Habib Zaidi *Editor*

Molecular Imaging of Small Animals

Instrumentation and Applications

Springer

Molecular Imaging of Small Animals

Habib Zaidi
Editor

Molecular Imaging of Small Animals

Instrumentation and Applications

Springer

Editor
Habib Zaidi
Department of Radiology & Medical Informatics
Geneva University Hospital
Geneva, Switzerland

ISBN 978-1-4939-0893-6 ISBN 978-1-4939-0894-3 (eBook)
DOI 10.1007/978-1-4939-0894-3
Springer New York Heidelberg Dordrecht London

Library of Congress Control Number: 2014939119

Printed on acid-free paper

Springer is part of Springer Science+Business Media (www.springer.com)

Contents

About the Editor

Habib Zaidi, Ph.D., is Chief Physicist and head of the PET Instrumentation & Neuroimaging Laboratory at Geneva University Hospital and faculty member at the Medical School of Geneva University. He is also a Professor of Medical Physics at the University Medical Center of Groningen (The Netherlands) and visiting Professor at Ecole Nationale Supérieure d'Electronique et de ses Applications (ENSEA, France). He received a Ph.D. and habilitation (PD) in medical physics from Geneva University. Dr. Zaidi is actively involved in developing imaging solutions for cutting-edge interdisciplinary biomedical research and clinical diagnosis in addition to lecturing undergraduate and postgraduate courses on medical physics and medical imaging. His research centres on modelling nuclear medical imaging systems using the Monte Carlo method, dosimetry, image correction, reconstruction and quantification techniques in emission tomography as well as statistical image analysis in molecular brain imaging, and more recently on novel design of dedicated high-resolution PET and combined PET-MRI scanners. He was guest editor for seven special issues of peer-reviewed journals and serves as Deputy Editor for the *British Journal of Radiology*, Associate editor and member of the editorial board of many scientific journals including *Medical Physics, the International Journal of Biomedical Imaging*, *Nuclear Medicine Communications, Computer Methods and Programs in Biomedicine*, and serves as scientific reviewer for leading journals in medical imaging. He is a senior member of the IEEE and liaison representative of the International Organization for Medical Physics (IOMP) to the World Health Organization (WHO) in addition to being affiliated to several International medical physics and nuclear medicine organisations. He is involved in the evaluation of research proposals for European and International granting organisations and participates in the organisation of International symposia and top conferences as member of scientific committees. His academic accomplishments in the area of quantitative PET imaging have been well recognized by his peers and by the medical imaging community at large since he is a recipient of many awards and distinctions among which the prestigious *2003 Young Investigator Medical Imaging Science Award* given by the *Nuclear Medical and Imaging Sciences Technical Committee of the IEEE*, the *2004 Mark Tetalman Memorial Award* given by the

Society of Nuclear Medicine, the *2007 Young Scientist Prize in Biological Physics* given by the *International Union of Pure and Applied Physics* (*IUPAP*), the prestigious (100,000$) *2010 kuwait Prize of Applied sciences* (known as the *Middle Eastern Nobel Prize*) given by the *Kuwait Foundation for the Advancement of Sciences* (*KFAS*) for "*outstanding accomplishments in Biomedical technology*", the 2013 *John S. Laughlin Young Scientist Award* given by the American Association of Physicists in Medicine (AAPM) and the 2013 *Vikram Sarabhai Oration Award* given by the Society of Nuclear Medicine (India). Dr. Zaidi has been an invited speaker of many keynote lectures at an international level, has authored over 400 publications, including ~180 peer-reviewed journal articles (h-index = 31), conference proceedings and book chapters and is the editor of three textbooks including this volume.

E-mail: habib.zaidi@hcuge.ch; Web: http://pinlab.hcuge.ch/

Contributors

Abass Alavi Division of Research, Department of Radiology, University of Pennsylvania, Philadelphia, PA, USA

Carina Mari Aparici Department of Radiology & Biomedical Imaging, San Francisco and Nuclear Medicine Service, San Francisco Veterans Affairs Medical Center, University of California, San Francisco, CA, USA

Nicola Belcari Dipartimento di Fisica, Università di Pisa, and INFN Sezione di Pisa, Pisa, Italy

Andrew M. Blamire Newcastle Magnetic Resonance Centre, Newcastle University, Newcastle upon Tyne, UK

Cindy Casteels Nuclear Medicine Department, Leuven University Hospital, Leuven, Belgium

Xiaoyuan Chen National Institute of Biomedical Imaging and Bioengineering (NIBIB), National Institutes of Health (NIH), Bethesda, MD, USA

June-key Chung Department of Nuclear Medicine, Cancer Research Institute, Tumor Micro-environment Global Core Research Center, College of Medicine, Seoul National University, Seoul, South Korea

Eri F.J. de Vries Department of Nuclear Medicine and Molecular Imaging, University of Groningen, University Medical Centre Groningen, Groningen, The Netherlands

Alberto Del Guerra Dipartimento di Fisica, Università di Pisa, and INFN Sezione di Pisa, Pisa, Italy

Filippo Galli Nuclear Medicine Unit, II Faculty of Medicine and Surgery, 'Sapienza' University of Rome, St. Andrea Hospital, Rome, Italy

Andrew L. Goertzen Department of Radiology, University of Manitoba, Winnipeg, MB, Canada

Joo Hyun Kang Molecular Imaging Research Center, Korea Institute of Radiological and Medical Science, Seoul, South Korea

Keon Wook Kang Department of Nuclear Medicine, Cancer Research Institute, College of Medicine, Seoul National University, Seoul, South Korea

Institute of Radiation Medicine, Medical Research Center, Seoul National University, Seoul, South Korea

Peter L. Kench Faculty of Health Sciences, Brain and Mind Research Institute, University of Sydney, Sydney, NSW, Australia

Craig S. Levin Departments of Radiology, and by courtesy, Physics, Electrical Engineering, and Bioengineering; Molecular Imaging Instrumentation Laboratory (MIIL); Stanford Molecular Imaging Scholars (SMIS) Program; Stanford Center for Innovation in In-Vivo Imaging (SCI3); Molecular Imaging Program at Stanford (MIPS); Division of Nuclear Medicine, Stanford University School of Medicine, Stanford, CA, USA

Tom K. Lewellen Department of Radiology, University of Washington, Seattle, WA, USA

Jianyu Lin Department of Electrical and Computer Engineering, Curtin University, Perth, WA, Australia

Yongjian Liu Mallinckrodt Institute of Radiology, Washington University School of Medicine, St. Louis, MO, USA

Eckart Lorenz Max Planck Institute for Physics, Munich, Germany

Eidg. Technische Hochschule, Zurich, Switzerland

Yujie Lu Center for Molecular Imaging, Institute of Molecular Medicine, University of Texas Health, Science Center at Houston, Houston, TX, USA

Gaurav Malviya Department of Nuclear Medicine and Molecular Imaging, University of Groningen, University Medical Centre Groningen, Groningen, The Netherlands

Ravi Marfatia Cardiovascular Molecular Imaging Laboratory, Yale University School of Medicine, New Haven, CT, USA

Dirk Meier Integrated Detector Electronics AS, Fornebu, Norway

Steven R. Meikle Faculty of Health Sciences, School of Medical Radiation Sciences, University of Sydney, Sydney, NSW, Australia

Robert Miyaoka Department of Radiology, University of Washington, Seattle, WA, USA

Gang Niu National Institute of Biomedical Imaging and Bioengineering (NIBIB), NIH, Bethesda, MD, USA

Bradley E. Patt Gamma Medica-Ideas (USA), Northridge, CA, USA

Jörg Peter Division of Medical Physics in Radiology, German Cancer Research Center (DKFZ), Heidelberg, Germany

Marybeth A. Pysz Departments of Radiology and MIPS, Stanford University, Stanford, CA, USA

Bosky Ravindranath Biomedical Engineering Department, SUNY Stony Brook, Stony Brook, NY, USA

Mallinckrodt Institute of Radiology, Washington University School of Medicine, St. Louis, MO, USA

Dieter Renker Paul Scherrer Institute, Villigen, Switzerland

Erik L. Ritman Department of Physiology and Biomedical Engineering, Mayo Clinic College of Medicine, Rochester, MN, USA

Paolo Russo Dipartimento di Fisica, Università di Napoli Federico II, and INFN Sezione di Napoli, Napoli, Italy

Mehran M. Sadeghi Cardiovascular Molecular Imaging Laboratory, Yale University School of Medicine, New Haven, CT, USA

David Schlyer Biosciences Department, Brookhaven National Laboratory, Upton, NY, USA

Youngho Seo UCSF Physics Research Laboratory, Department of Radiology & Biomedical Imaging, University of California, San Francisco, CA, USA

Alberto Signore Nuclear Medicine Unit, II Faculty of Medicine and Surgery, 'Sapienza' University of Rome, St. Andrea Hospital, Rome, Italy

Department of Nuclear Medicine and Molecular Imaging, University of Groningen, University Medical Centre Groningen, Groningen, The Netherlands

Virginia Ch. Spanoudaki Department of Radiology, Molecular Imaging Program at Stanford (MIPS), Massachusetts Institute of Technology, Massachusetts, CA, USA

The David Koch Institute for Integrative Cancer Research, Massachusetts Institute of Technology, Cambridge, MA, USA

David B. Stout Department of Molecular and Medical Pharmacology, University of California, Los Angeles, CA, USA

Sina Tavakoli Cardiovascular Molecular Imaging Laboratory, Yale University School of Medicine, New Haven, CT, USA

Koen Van Laere Division of Nuclear Medicine, Leuven University Hospital, Leuven, Belgium

Douglas J. Wagenaar Gamma Medica-Ideas (USA), Northridge, CA, USA

Ge Wang Biomedical Imaging Cluster, Center for Biotechnology and Interdisciplinary Studies, Department of Biomedical Engineering, Rensselaer Polytechnic Institute, Troy, NY, USA

Jürgen K. Willmann Departments of Radiology and MIPS, Stanford University, Stanford, CA, USA

Hyewon Youn Department of Nuclear Medicine, Cancer Research Institute, Tumor Micro-environment Global Core Research Center, College of Medicine, Seoul National University, Seoul, South Korea

Cancer Imaging Center, Seoul National University Hospital, Seoul, South Korea

Habib Zaidi Department of Radiology & Medical Informatics, Geneva University Hospital, Geneva, Switzerland

Pat Zanzonico Department of Medical Physics, Memorial Sloan Kettering Cancer Center, New York, NY, USA

Chapter 1
Scintillation Detectors for Small-Animal Imaging

Tom K. Lewellen and Robert Miyaoka

1 Introduction

The detection of high energy photons (i.e. gamma rays or X-rays) is one of the main tools in small animal imaging. Imaging systems with external radiation sources (e.g., X-ray computed tomography—CT) and internal sources (e.g., single photon emission computed tomography—SPECT; and positron emission tomography—PET) are used routinely in pre-clinical investigations and are under active development both commercially and in research laboratories. In all cases, the detection process requires conversion of the energy carried by the photon into some sort of electrical signal. Further, the conversion process needs to be efficient and provide information on the amount of energy deposited (to allow discrimination of events by the amount of energy carried by the photon). For imaging systems, the detector must also provide spatial position information (e.g., the point in the detector that the photon interacted). For this chapter, we will not address optical light systems, but focus only X-ray and gamma ray technologies.

For internal sources, we are normally dealing with radiolabeled compounds with the goal of imaging the distribution of labelled molecules in-vivo. Further, such images are used to obtain metabolic information as was recently summarized in a review article by Cherry [1]. The details of how the radionuclide is labelled to molecules of interest is beyond the scope of this chapter, but there is a large number of such labelled compounds in everyday use in the clinic and the research laboratory. The radionuclides used for imaging fall into two general categories: beta and positron emitters. In the case of positron emitters (e.g., ^{18}F, ^{15}O, ^{14}N, ^{11}C, ^{82}Rb, etc.), a positron is emitted by the decay of the nuclide and travels a short distance until it annihilates with an electron. At the point, two 511 keV gamma rays are produced. It is the paired annihilation photons (detected in coincidence) that we normally use

T.K. Lewellen (✉) • R. Miyaoka
Department of Radiology, University of Washington, Seattle, WA 98195, USA
e-mail: tkldog@u.washingtons.edu; rmiyaoka@u.washington.edu

H. Zaidi (ed.), *Molecular Imaging of Small Animals: Instrumentation and Applications*,
DOI 10.1007/978-1-4939-0894-3_1,

for imaging. Some of the heavier positron-emitting nuclides (e.g., ^{124}I, ^{94}Tc) are also associated with other gamma rays emitted by the daughter nucleus from the decay. These daughter gamma rays are normally not used for imaging and present a complication in terms of unwanted events in the detector systems. The important fact here is that for positron imaging, we want to optimize the detector system for detecting 511 keV gamma rays.

A wide range of beta emitters are used. Some of the more common for imaging include ^{99m}Tc, ^{131}I, ^{111}In, ^{201}Tl, ^{123}I, and ^{67}Ga. The energies of the gamma rays to be detected can range from less than 80 keV to more than 300 keV and all come from the daughter nuclide formed as a result of the beta decay. Some of the decays emit more than one gamma ray energy (e.g., ^{67}Ga has three primary gamma rays used for imaging: 93, 185, and 300 keV). Thus, the detectors for beta emitters (often termed single photon emitters as compared to the annihilation radiation produced in positron decay) must be able to detect gamma rays over a range of energies. Both single photon and coincidence detection systems, the detectors operate in single pulse mode—that is, each event is recorded as a separate event and its energy deposited measured.

X-ray detectors, in particular those for CT, are detecting photons in the range of 30–120 keV produced by an X-ray tube. For most applications, a large photon flux is needed to achieve the statistics needed for measurement of small attenuation coefficient differences. As a result, most CT scanners operate the detectors in current mode and do not measure the energy deposited on an event by event basis. There are now efforts to develop high flux detector systems that can provide some degree of energy discrimination, but they are not yet a commercial reality.

There are many types of technologies that can be used for photon detection. There are various types of gas, solid state, and scintillator systems that have been described in the literature (e.g., [2–12]). However, the majority of pre-clinical imaging systems based on X-ray or gamma ray detection utilize scintillators. Scintillators provide a cost effective solution with a wide range of options for specific imaging tasks. In this chapter, we will review the basics of scintillators and the basic detector properties associated with their use.

2 Basic Scintillator Concepts

The basic concept of scintillators is that they transfer the energy of a detected X-ray or gamma ray into a large number of photons in the optical region. As the photon interacts in the scintillator, electrons within the crystal lattice are excited to higher energy states. If the material has the appropriate band gap between excited and ground states, scintillation light is produced. For many inorganic scintillators, impurity atoms are required to “activate” the scintillator, i.e., the impurity atoms provide additional energy levels that support light production. Besides the production of light, there are many other important physical properties that determine the utility of a scintillator for small animal X-ray and nuclear medicine applications. A description of those basic properties follows.

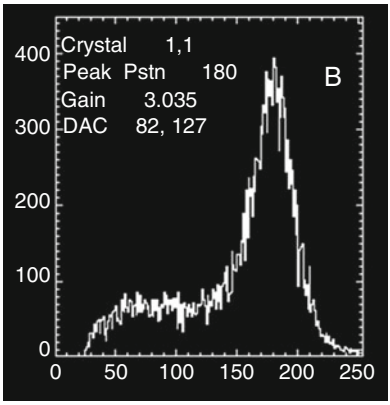

Fig. 1.1 Example of a Ge-68 energy spectrum from a crystal in a PET block detector using BGO crystals. The x-axis values are relative channel numbers (not calibrated in energy units)

2.1 Energy Resolution

The energy resolution of a scintillator is defined by the full width at half maximum of the photopeak of the energy spectrum divided by the peak channel of the energy spectrum, as illustrated in Fig. 1.1. In the example, the energy resolution of the detector system for the 511 keV photons produced by Ge-68 is 15 % (full width at half maximum—FWHM). Note that energy resolution will vary depending upon the energy of the photons being detected. Detection of higher energy photons produces more light within a scintillator that in turn improves the statistical estimate of the amount of light collected. The energy resolution for a detector system is very important as better energy resolution improves the discrimination between true unscattered events (i.e., the desirable events for image formation) and Compton scatter events (i.e., undesirable events that affect quantitation and reduce contrast) within the object being imaged.

The intrinsic energy resolution of a scintillator is mostly governed by the amount of light produced per energy deposited in the scintillator, but is also affected by non-proportional response and inhomogeneities of the scintillator [27]. In addition other physical effects contribute to the overall energy resolution of a detector assembly. These include the index of refraction of the crystal (described below); the photon detection efficiency of the photoreceptor used to convert the light signal to an electrical signal; and electronic noise associated with the photosensor. Thus the energy resolution of a detector assembly depends on both the scintillator characteristics and the physical characteristics of the photoreceptors. The main variable being how well the light photon detection efficiency of the photoreceptor is matched to the emission wavelength of the scintillator. The characteristics and properties of photosensors are further covered in Chap. 3.

2.2 Stopping Power (Detection Efficiency)

The photon detection efficiency is a measure of what fraction of true unscattered photons will be detected by the scintillation crystal. The stopping power depends upon both the photoelectric and Compton cross-section of the crystal, where the photoelectric cross-section mainly depends upon the effective Z of the material and the Compton cross-section depends upon the density of the material. Ideally photons will be photoelectrically absorbed on the first interaction. However, that is generally not the case for many applications. For example, NaI(Tl) at 140.5 keV approximately 80 % of first interactions will be photoelectric; however, at 511 keV a majority of first interactions will be Compton for all the common scintillators used for small animal PET imaging systems. For 511 keV detection, the main scintillators currently in use are BGO and lutetium-based materials. While the lutetium-based scintillators have a higher density than BGO, BGO because of it higher effective Z has better overall stopping power for 511 keV photons.

The stopping power for the scintillator is especially important for small animal imaging systems. This is because of the very small structures that one often desires to image and the tiny amounts of activity that will be taken up in these structures. In comparison to whole-body human imaging, the activity concentration per voxel for small animal imaging procedures needs to be factors of a thousand times higher to achieve comparable image quality. While the attenuation differences between humans and small animals favor small animal imaging, there is still the need for very high detection efficiency small animal imaging systems. For single photon imaging the detection efficiency is quite high for Tc-99m and extremely good for I-125 with its low energy photons and X-rays.

When considering high resolution imaging systems—in particular small animal systems, the issue of parallax is important. Parallax refers to the phenomenon of a gamma ray entering one crystal but passing through it to interact in a neighbouring crystal or region of the detector (Fig. 1.2). One approach to reduce parallax for small diameter rings is to use short crystals (perhaps <10 mm long) so that if a gamma ray passes through the first crystal, it will exit the detector ring before interacting. However, this leads to less than desired sensitivity. As a result, many groups are working on detectors with depth-of-interaction (DOI) capability to allow estimation of the point of first interaction in the detector array (maintaining the high spatial resolution while increasing sensitivity with longer crystals). Dense scintillators (with high photoelectric cross sections) would be ideal for DOI applications if all the other needed parameters (see below) are acceptable.

2.3 Speed

The speed of the crystal refers to the decay constant of the light produced in the scintillator. A short decay time is important for two main reasons. First the count rate capabilities of the detector depend upon the light decay constant for the

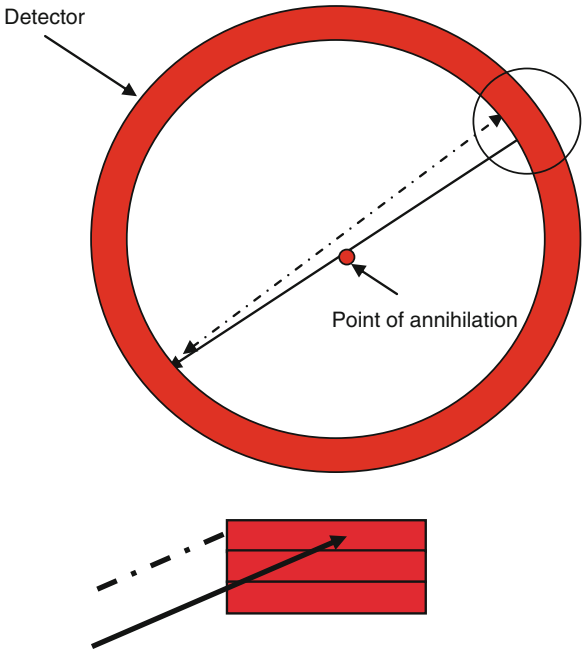

Fig. 1.2 Illustration of the parallax error. The gamma ray (*solid line*) penetrates the first crystal and interacts in the second crystal. Without depth of interaction information, the detection electronics will assign the event to the wrong line of response (the *dotted line*). The lower portion of the figure is an enlargement of the section of the detector ring that is circled

scintillator. The shorter the decay time, the higher the counting rate capability of the detector (less pile-up where the signals from two events overlap and distort the light output from the scintillator). The lutetium-based scintillators with their relatively short decay times are ideal for the higher photon flux associated with PET imaging. Because collimators are generally used for single photon imaging, the count rate requirements are usually significantly lower than for PET imaging applications. For detector systems using NaI(Tl) or BGO that need to achieve higher counting rates, there are pulse shortening techniques (i.e., pulse tail clipping or pulse tail extrapolation) that facilitate higher count rate capabilities in these slower decay time scintillators.

The second performance variable that the light decay time of the scintillator effects is the timing resolution of the detector. In general, faster decay times corresponded to better timing resolution. This is largely the case because the faster the decay time the larger the initial burst of light photons when the event is first detected. While not critical for small animal PET imaging applications, coincidence timing is still important for limiting the collection of random events.

2.4 Physical Properties

Physical properties refer to the characteristics of the scintillator that might affect manufacturing and fabrication costs. These properties include the hardness of the scintillator; whether the crystal has cleavage planes and whether or not the

scintillator is hygroscopic. The hardness of the scintillator and whether it has cleavage planes affects the machinability of the material. In general, crystals that have cleavage planes are more difficult and expensive to fabricate, whether into small discrete crystals or larger monolithic designs.

Crystals that are hygroscopic affect the design of detector systems in two ways. First, they have to be encapsulated to prevent moisture from reaching the crystal. This adds cost to the detector assembly. Second, they can affect the packing fraction (the amount of the face area of the detector assembly that can actually be used to detect photons) of the detector system because of the packaging.

2.5 Index of Refraction

The index of refraction mainly affects the amount of light that can be extracted from a scintillating crystal. A high index of refraction is good for piping light down a high cross-section to length aspect ratio; however, it also makes extraction of the light from the crystal more challenging. Matching the indices of refraction of the scintillator, the optical coupling glue, and the window of the photosensor optimizes light collection efficiency. Unfortunately, all the current scintillators in use have reasonably high indices of refraction that make light collection more challenging.

2.6 Light Yield

The light yield reflects how efficient a scintillator is at converting the energy deposited by a detected photon or X-ray to light. The light yield of a scintillator impacts the energy resolution, spatial resolution and timing resolution of a detector. In general, the higher the light yield the better the energy resolution. This is almost always the case; however, for scintillators that have non-proportional light output (e.g., lutetium-based materials) the energy resolution is not as good as one would expect from the measured light yield.

In general, scintillators with higher light yield can also provide better spatial resolution. For monolithic style crystals that are often used in gamma cameras this is because having more light reduces noise in the measured signals and improves the accuracy of the positioning algorithm. For discrete crystal detectors, higher light yield can facilitate decoding more or smaller cross-section crystals. Decoding smaller cross-section crystals leads to better intrinsic spatial resolution for a detector.

The light yield can also affect coincidence timing resolution for PET detectors. Both light yield and decay time in combination effect timing resolution. This is because the timing resolution is strongly affected by the slope of the rising edge of the pulse (i.e., the light photon flux at the start of the pulse). The combination of a short decay time and high light output yields the steepest slope to the rising edge of the pulse from a scintillator.

2.7 Peak Wavelength

The wavelength of the light produced by the scintillator can have a significant impact on the light collection efficiency. This is both in regards to the amount of light that makes it to the photosensor and the quantum efficiency of the photosensor to the light produced by the scintillator. Ultraviolet (UV) wavelength light is more difficult to collect and requires special quartz windowed photosensors for signal processing. Blue light is well matched to the quantum efficiency of bialkali photocathodes, while green and longer wavelength light is better matched to silicon-based photodiodes. As described in Chap. 3 the quantum efficiency of different photosensors can widely vary depending upon the wavelength of the light and thus can have a significant impact on effective light yield.

2.8 Fabrication Complications

Fabrication complications are factors that affect the cost of a scintillator. The three main variables are the cost of the raw materials used to grow the scintillator; the melting temperature of the scintillator; and the yield for the growth process (also may affect the pull rate—i.e., how fast the scintillator material can be grown). Of course, hydroscopic scintillators require additional handling precautions during fabrication (e.g., dry boxes for assembly), but handling such scintillators have long since been worked out by the manufactures.

2.9 Afterglow

After a gamma or X-ray interacts in a crystal, there is a period of time while scintillation light is still being produced as the electrons excited by the interaction process return to ground states. Many scintillators have some small fraction of these excited electrons that take a long time to return to ground states resulting in a prolonged period of low light output. These long decay components can be many milliseconds or even hours long for some scintillators. For high count rate (or high flux) applications, the after glow can lead to bias errors in estimating the amount of energy deposited in the scintillator.

2.10 Radiation Hardness

Radiation hardness refers to the potential of damage to a scintillator due to prolonged exposure to radiation. Such damage usually manifests as optical transparency (optical light transmission) in the scintillator. For most imaging applications,

radiation damage is not an issue. However, for specialized applications such as in-beam imaging system, selection of scintillators should include consideration of potential radiation damage effects. Most designers consider a scintillator as "radiation hard" if there are no measurable effects with doses of 10,000 Gray. Most such effects, other than radio-activation, will at least partially reverse once the scintillator is removed from a high radiation environment.

3 Basic Scintillator Geometries

Most imaging systems use scintillators in one of two basic geometries: pixilated and monolithic detector designs.

In pixilated designs, arrays of individual scintillators or blocks cut into many segments (Fig. 1.3) are readout by photosensors. Early PET systems [13–17] used one photo-multiplier tube (PMT) per scintillation crystal. There are several major limitations to this approach. For high spatial resolution, you need to use small crystals and existing PMTs are too large to allow a full ring of very small crystals; also, it becomes difficult or impossible to make multi-ring systems. For large numbers of crystals, this type of design also leads to a large number of electronic channels and PMTs, thus increasing the cost of the system. This led to the kind of geometry shown in Fig. 1.3b where a block of crystals (or a segmented block) are viewed by a coarse array of large photosensors. The arrays are then decoded by measuring the amount of light that reaches each photosensor. In many designs, the amount of light that is shared between the photosensors is partially controlled by changing the interfaces between the crystals in designs like Fig. 1.3a or changing the depth of the saw cuts in block such as those shown in Fig. 1.3b. The resulting signals can produce

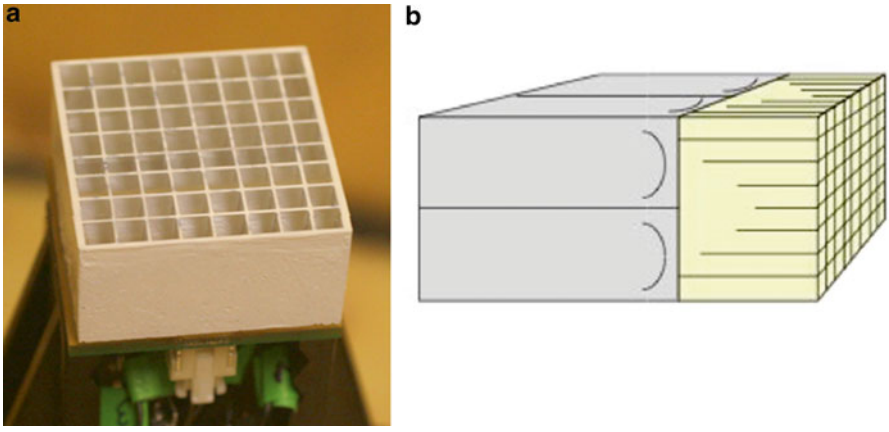

Fig. 1.3 Pixilated detectors. (**a**) An example of an array of individual crystals mounted on a GM-APD array. (**b**) A diagram of a block of crystal sawed into segments mounted on a set of PMTs

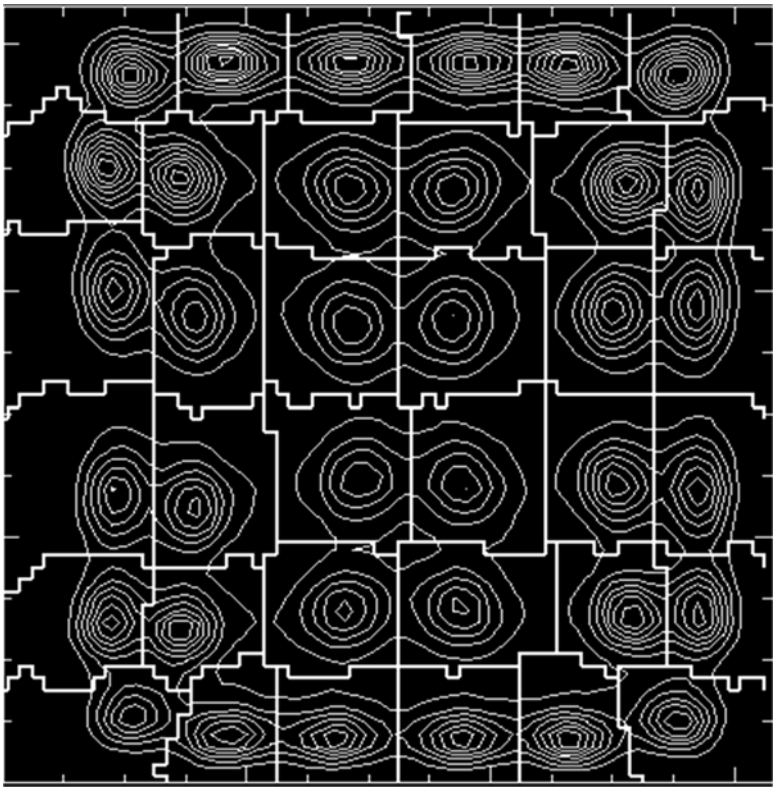

Fig. 1.4 A 2D block map of a 6×6 BGO crystal array viewed by four PMTs. The relative light output is indicated by the isocount curves. The "*straight*" *lines* indicate what regions will be assigned to each crystal position

"crystal maps" much like that shown in Fig. 1.4 which depicts a two dimensional crystal map from a detector block using a 6×6 array of BGO crystals. Four PMTs are placed over the crystals in a rectangular pattern $\left[\frac{A \mid B}{C \mid D}\right]$. To form the ratios, the two PMTs across the top of the block are summed for the x value (A+B) and the two PMTs along the left side are summed for the y value (A+C). For both ratios, the signals from all four PMTS are summed for the denominator $\left(x = \frac{A+B}{A+B+C+D}; y = \frac{A+C}{A+B+C+D}\right)$.

The electronics can then assign an event to a crystal by determining which region the event corresponds to in the crystal map. With the advancements in photosensors (see Chap. 3) and electronics devices such as field programmable gate arrays (FPGA) and application specific integrated circuits (ASIC), we now have the option to return to one-on-one coupling with fine pitched solid state photosensor arrays where each photosensor is coupled directly to a single crystal in the array.

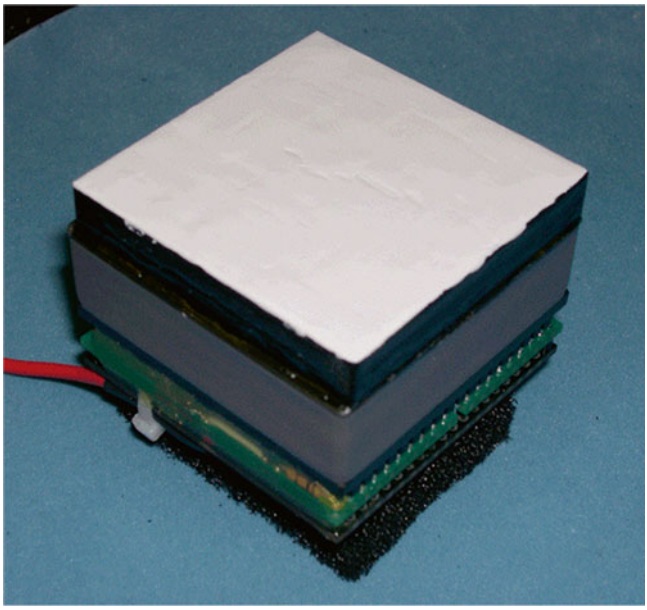

Fig. 1.5 Example of a monolithic crystal block (50×50 mm) mounted on a Hamamatsu 8×8 anode PMT

The choice of using cut blocks or discrete crystals depends on many issues including cost of fabrication, packing fraction, and crystal size. As the crystal pitch and size become smaller (e.g., those used in small animal scanners), it is often best to use discrete crystals both in terms of packing fraction and overall ease of manufacture.

Another approach is to use monolithic "slabs" of crystal and decode the event position by analyzing the light distribution from the event within the crystal. The approach is basically the same as used in Anger cameras and has been applied to PET systems using NaI(Tl) crystal modules [30]. Figure 1.5 depicts such a detector module with a relatively small monolithic crystal (50×50 mm). Traditionally, the position of an event in an Anger camera is determined by calculating the centroid of the emitted light; $X = \sum(x_i * S_i)/\sum(S_i)$, where x_I is the weight associated with the i^{th} PMT and S_i is the integrated PMT signal. More recently, investigators have been using statistical estimation techniques to determine the event position, even including estimates of the depth of the event within the monolithic slab [2, 18–20].

Whatever design is chosen, there are factors that impact performance. One problem is resolution loss. We have already mentioned parallax (depth-of-interaction in Fig. 1.6a). In pixilated detectors (Fig. 1.6a), other factors contributing to spatial resolution include: finite crystal width; scattering within the detector array (more than one source of light); and statistical uncertainty related to the amount of light detected. As shown in Fig. 1.6b, similar factors limit resolution in monolithic detectors.

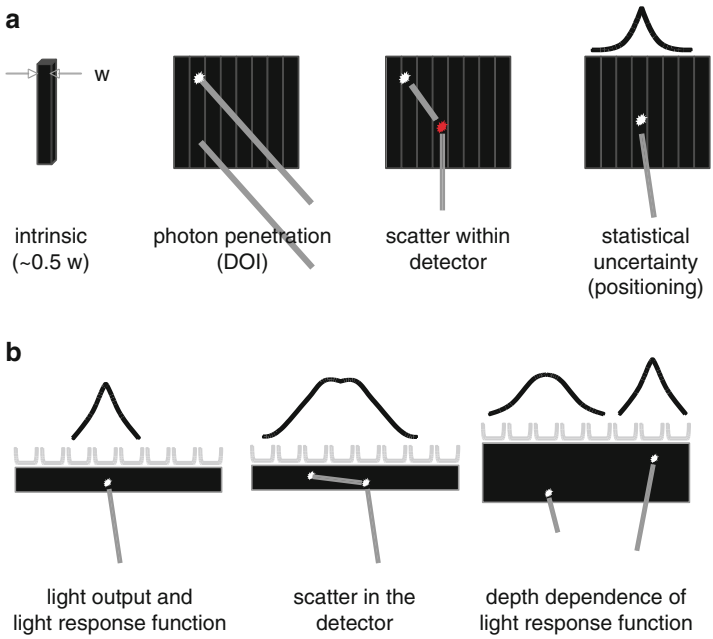

Fig. 1.6 Some of the causes of spatial resolution loss in: (**a**) pixilated detectors and (**b**) monolithic detectors

Other factors that can impact detector performance include pulse pileup (where a second event is detected before the light has fully decayed from the previous event) and multiple gamma ray interactions due to Compton scatter in the same detector array.

Positron emission tomography (PET) and single photon emission computed tomography (SPECT) and planar imaging are based on detecting events one at a time (pulse counting) and tend to emphasize the properties related to energy resolution, sensitivity, and fast timing when detectors are designed. Computed X-ray tomography (CT) most commonly measures X-ray flux and does not do event-by-event detection. Such detector systems rely on integrating the flux rate and tend to emphasize sensitivity and low after glow.

4 Types of Scintillators

For the X-ray and gamma rays encountered in PET, SPECT, and CT, the most common interactions of the primary radiation in a detector material are Compton scattering and Photoelectric absorption. An ideal detector would have high enough Photoelectric cross section and density to assure that all interactions were single events (Photoelectric absorption). Real world detectors generally have a mix of

Compton and Photoelectric events (although that mix is highly dependent on the energy of the primary radiation). Scintillators are a class of detector materials that convert the energy deposited in them by X-ray and gamma ray interactions into visible light [21]. The primary radiation excites electrons in the scintillator. Typically the primary radiation ionizes atoms via both Compton and Photoelectric interactions producing a multiplication effect (one incoming X-ray/gamma ray produces a cascade of excited electrons). The excited electrons eventually de-excite and in the process emit visible or near visible light photons. Thus a single incoming X-ray or gamma ray produces a large number of visible light photons which, in turn, can be detected by a photosensor.

Scintillators can generally be separated into two main groups—organic and inorganic. Organic scintillators are hydrocarbon compounds [6] that produce light through molecular excitation. Typically, the primary fluorescent compound emits light in the ultraviolet (UV) region during de-excitation. A second compound is usually added to the mix to shift the UV light into visible light for use with most photosensors. These compounds can be used as a liquid in which materials containing radiotracers are dissolved (often beta emitters such as tritium) and the resulting scintillation light collected by photosensors—but that application is not in the scope of this book since such counters are used for sample counting, not imaging. These organic scintillation compounds can also be made into plastics (polymerized) to form solid detector materials commonly referred to as plastic scintillators. Such scintillators have the advantages of being easily machined or cast into a wide variety of shapes and sizes and have been used extensively for large area detectors in high energy physics applications. The can also be incorporated into optical fibres to make scintillating fibres. Plastic scintillators typically have good light output [25–30 % of NaI(Tl)] and very fast rise and fall times (rise times of 1 ns or less). They have been the standard reference detector for many fast timing measurements. There are a wide variety of plastic scintillators optimized for different applications (e.g., fast timing, neutron detection, etc.), as illustrated by the more than 24 plastic scintillator formulations listed by Saint-Gobain (a major commercial scintillator company) in their standard catalogue.

Plastic scintillators have been used or proposed for some applications for PET. Some examples include in-beam monitoring systems for high energy radiation therapy applications, time-of-flight scanner designs, and alternative detector decoding schemes, and small animal PET scanners [22–26]. The low-Z materials in these scintillators result in X-ray and gamma rays detection being dominated by Compton interactions. The low photoelectric cross sections and low densities result in low stopping power which is not ideal for imaging applications. As a result, plastic scintillators have not been used in most imaging system designs.

Inorganic scintillators have been the primary detector used in the majority of imaging system designs. Scintillation in these materials is due to lattice effects rather than the molecular effects of organic scintillators. Inorganic materials are often characterized as having electrons in valence (bound at the lattice sites) and conduction (free to move around the crystal) bands. The aforementioned ionization process of primary radiation interaction moves electrons from the valence band into

Table 1.1 List of some of the properties of inorganic scintillators used in imaging system designs

	NaI(Tl)	BaF_2	BGO	LSO	GSO	LYSO	$LaBr_3$	LFS	LuYAP	LuI_3
Effective atomic no. (Z)	51	54	74	66	59	60	47	63	65	60
Linear atten. coef. (cm^{-1})	0.34	0.44	0.92	0.87	0.62	0.86	0.47	0.82	0.9	~0.56
Density (g/cm^3)	3.67	4.89	7.13	7.4	6.7	7.1	5.3	7.3	8.34	5.6
Index of refraction	1.85	–	2.15	1.82	1.85	1.81	1.88	1.78	1.95	?
Light yield (k/MeV)	41	2(6)*	7	26	10	26	60	26	5	76
Peak wavelength (nm)	410	220	480	420	430	420	370	430	365	470
Decay constant (ns)	230	0.8	300	40	65	41	18	35	18	30
Hydroscopic	Yes	Slight	No	No	No	No	No	No	No	Yes

*fast (slow) light component yield
?Not known at the time of publication

the conduction band. As electrons move back into the valence band (releasing energy), many go through trapping centers in the gap between the conduction and valence bands. These trapping (or activation) centers allow the electrons to return to the valence band in a series of steps, releasing light photons at each transition [27]. Part of the development of good scintillators is creating the activation centers such that a large amount of the released energy as electrons de-excite are in the visible light region and to control the rate at which the de-excitation occurs (the light decay time in the scintillator). Table 1.1 lists some of the cardinal properties of many of the scintillators that have been considered for use in scanner systems.

4.1 Scintillator Imaging Characteristics and Applications

4.1.1 NaI(Tl)

NaI(Tl) is the scintillator material used in the first gamma camera developed by Hal Anger [28]. It has outstanding properties for imaging the 140.5 keV photons emitted by ^{99m}Tc, the most used radioisotope for nuclear medicine imaging. The three most important physical characteristics of NaI(Tl) for single photon imaging are its high light output; its excellent detection efficiency including photoelectric cross-section at 140.5 keV; and its relatively low cost. In addition NaI(Tl) can be grown into large crystals that support economical fabrication of large area imaging detectors. The light output of NaI(Tl) is the reference by which other inorganic scintillator materials are commonly compared. The main limitations to NaI(Tl) for imaging purposes are threefold. First, it is hygroscopic. Therefore it must be housed in hermetically sealed packaging. This limits it utility for imaging systems requiring an array or ring of smaller sized detector modules; however, this is not a serious limitation for large area detectors such as the ones use for clinical nuclear medicine gamma cameras. Second, NaI(Tl) also has a relatively long decay time in comparison to the other scintillator materials listed. Again this is not a significant limitation for clinical nuclear medicine imaging where the flux of photons to the detector is moderated

by the collimator. While very innovative methods were developed to extend the count rate capabilities of large area NaI(Tl) detectors which led to the development of NaI(Tl) based PET imaging systems [29, 30], the discovery of new scintillator materials with more optimum properties for PET imaging (i.e., better detection efficiency at 511 keV and better coincidence timing characteristics) has led to the discontinuation of clinical NaI(Tl) based PET imaging systems. Finally, NaI(Tl) does have a long decay component that can lead to baseline shifts in the detector signal at high flux rates. Again this is usually not a problem for gamma camera imaging as pulse pile-up effects usually distort the acquired energy spectra before baseline shifts occur. As stated above, NaI(Tl) has outstanding properties for clinical nuclear medicine imaging and is still by far the most common detector material used for single photon imaging applications. NaI(Tl) because of it relatively low cost and excellent energy resolution properties is also often used in well counters and spectroscopy detectors.

4.1.2 BGO

While NaI(Tl) has been the scintillator material of choice for single photon imaging cameras, for years BGO (discovered in 1973 [31]) was the scintillator material of choice for human whole-body, clinical PET systems. This was predominantly driven by the excellent stopping power (i.e., high effective atomic number and material density) of BGO. Even though LSO is more dense than BGO, BGO has better detection efficiency at 511 keV due to its higher effective atomic number which translates to a better photoelectric cross-section. During the developmental years of human whole-body PET, most systems acquired data in two dimensions through the use of collimation in the imaging system. Collimating septa were used to reduce deleterious random and scattered coincidences associated with PET imaging. Since random and scattered events were limited by collimating septa, the most important physical properties for 2D PET imaging are the ones associated with detection efficiency. While BGO has a rather long decay time, detector dead time was not a problem for 2D PET imaging because the septa also significantly reduced the photon flux to the detectors. The other design feature that helps reduce dead time is by using relatively compact detector modules. The light output from BGO is also on the low end of the scintillators listed. The low light output effects energy resolution and the decoding capabilities of a detector module. Because of the low light output, BGO is not a candidate for gamma camera imaging at 140.5 keV. However with modern BGO crystals, better than 20 % detector energy resolution can be achieved at 511 keV that allows for relatively good discrimination against scattered events. Further using standard detector designs, 8×8 BGO crystals arrays can be accurately decoded using a 2×2 array of photomultiplier tubes. Using a quadrant sharing detector design even higher decoding efficiency can be achieved with BGO crystals and standard photomultiplier tubes. The index of refraction of BGO is 2.15 which makes extracting light from a crystal a little more difficult than many of the other listed scintillators. This is because of internal reflections within the crystal due to

index of refraction mismatch between the crystal and optical resins used to couple the crystal to an optical sensor. BGO is relatively rugged and easy to cut for fabrication purposes. Thus the main limitations of BGO are it relatively low light output and relatively long decay time. While these weaknesses are not significant for 2D PET imaging systems, they become more problematic when one goes to three dimensional PET data acquisition mode (i.e., without collimating septa in the field of view). While modern PET imaging systems using BGO can be operated in three dimensional data acquisition mode, BGO's properties are most well suited for 2D PET imaging.

4.1.3 LSO, LYSO, LFS, LuAP

The development of LSO in 1992 [32] was met with high expectations because of its high density, high light output and fast decay time. After the introduction of LSO additional lutetium based scintillators with similar physical characteristics were developed. These scintillators include LYSO, LFS LuAP [33], and LuYAP. While the lutetium based scintillators were touted to replace the need for BGO, clinical, whole body, BGO PET systems have continued to be built due to BGO's better detection efficiency and lower cost. Additional reasons for this are that the lutetium-based scintillators have non-proportional light output and therefore the energy resolution achieved by early model systems was only slightly better than that achieved by BGO systems. Thus the scatter fraction for lutetium based systems were similar to BGO based systems. However as the growth processes for the lutetium scintillators have improved, the light output characteristics have also improved to the point where current generation LYSO based PET systems report a system energy resolution of ~12 % at 511 keV (i.e., compared to ~18 % energy resolution for BGO). LuAP has not made a major impact on scanner designs due to its relatively low light output and emission wavelength (Table 1.1). As an alternative to LuAP, crystal developers have proposed LuYAP which has higher light output (e.g., ~12,000 photons/MeV) than LuAP.

While improved energy resolution is helping with the performance characteristics of lutetium based detector systems, the main reason there is currently significant interest in lutetium based scintillators is the potential for time-of-flight PET imaging. For non-time-of-flight PET, a detected event is localized to a line of response defined by the two coincidence detectors. On the other hand for time-of-flight PET, the detected event is localized to a segment of the line of response defined by two coincident detectors. The time of flight information leads to an improvement in the signal to noise ratio of the reconstructed image. It has also been shown to improve contrast in the image [34–36]. The achievable coincidence timing resolution of a scintillator is correlated with the decay time and light output of the scintillator. Therefore, lutetium scintillators hold significant promise at for time-of-flight PET detectors. The first commercially available time-of-flight PET system offered since the 1980s was developed by Philips Medical Systems and is marketed as the Gemini

TF64 [37]. Both General Electric Healthcare and Siemens Medical Solutions have prototype time-of-flight PET systems under evaluation.

In addition to being the current detector material of choice for human whole body TOF PET systems, lutetium based scintillators are also the crystal material of choice for most preclinical PET imaging. This is mainly because of the high light output of lutetium based scintillators. The high light output facilities decoding very small cross-section discrete crystal arrays. For the same PMT assembly significantly more lutetium based scintillators can be accurately decoded versus discrete BGO crystals.

While lutetium scintillators are great for PET imaging detectors, they have not found much utility for single photon detector applications. This is because about 2 % of lutetium found in nature is radioactive. This leads to a background count rate in lutetium scintillators. While it has been demonstrated that preclinical PET imaging systems can also be used as preclinical, pinhole SPECT imaging systems, lutetium based scintillators have not found great interest as a single photon imaging detector.

4.1.4 GSO

GSO is a scintillator that was developed after the introduction of BGO but before the discovery of LSO. It has many good properties; however, it does not have any one outstanding property that leads to a significant performance advantage for PET imaging. As a PET detector material there was more interest in the use of GSO before the current widespread availability of lutetium based scintillators. One interesting characteristic of GSO is that while it produces less light than LSO, GSO PET detectors can provide better energy resolution. This is an advantage for 3D whole body PET imaging because the better energy resolution can be used to better discriminate against scatter events. This was more of an advantage during the developmental years of LSO. As previously mentioned the energy resolution of current lutetium based scintillators has improved as the growth process has been refined.

4.1.5 YAP

YAP was introduced in the 1990s and has very good light output. The high light output allows for the decoding of very small cross-section crystals. The main disadvantage of YAP is that it has a very poor photoelectric cross-section. A preclinical PET imaging system has been built using YAP detectors. To highlight its poor photoelectric cross-section, when operating in its high resolution mode the electronics rejects events that have deposited energy in the 511 keV photopeak because it is highly likely that those events have had at least two interactions within the crystal array. Multiple interactions within a crystal array leads to broadening of the spatial resolution.

4.1.6 CsI(Tl)

CsI(Tl) can be grown as discrete crystals for single photon gamma camera detectors or as thin films for X-ray imaging systems. As a discrete crystal scintillator, CsI(Tl) has many physical properties that surpass NaI(Tl) for general single photon imaging. It is denser and brighter than NaI(Tl). In addition, it is only slightly hygroscopic. One the other hand, its decay time is significantly longer and the peak wavelength of the light its produces (i.e., 540 nm) is not well matched to the quantum efficiency of photomultiplier tubes. To alleviate these weaknesses, a discrete crystal CsI(Tl) based detector system where the CsI(Tl) crystals were individually coupled to silicon PIN photodiodes was proposed. This design circumvents the two main weaknesses of CsI(Tl). By individually coupling crystals to the silicon PIN photodiode array, there is effectively very little dead time associated with the detector system because of the large number of data channels. And while PMTs are not very sensitive to 540 nm wavelength light, silicon PIN photodiodes have very good detection efficiency at that wavelength. The key to this design is the availability of photodiodes with high enough signal to noise that they can be operated at room (or close to) temperature.

The second way that CsI(Tl) can be used for imaging instrumentation is as a thin film for X-ray imaging systems. This will be further described below (Sect. 4.2).

There are many investigators developing new scintillators. In recent years, the search for new materials has generally concentrated on better scintillators for TOF applications (fast timing, high light output). The challenge has been to find such high performance scintillators that also have stopping power competitive with the more "conventional" scintillators already in general use. Examples include $LaBr_3$ [38] and LuI_3 [39]. Some of the characteristics for these two scintillators are included in Table 1.1. $LaBr_3$ has been used for at least one TOF scanner [40], but TOF is currently not of use in small animal scanners since timing resolutions of one to two orders of magnitude better than currently achieved would be needed to improve the images for most pre-clinical applications. For small animal applications most system designers are looking for high light output and high stopping power. As noted earlier, the high light output aids in detector decoding and extraction of information such as depth-of-interaction. Such requirements make a scintillator such as LuI_3 of interest since it has high light output and has a high effective atomic number (Table 1.1). However, the linear attenuation coefficient is not as high as the Lutetium compounds or BGO—making it less attractive. The search continues for the ideal detector [41–44]. No one scintillator is the perfect solution, but the current available crystals and ceramics offer a wide range of options for the designers of imaging systems.

4.2 Scintillation Detectors for CT Imaging

There are three types of scintillation detectors that have been used for small animal CT imaging systems. A common scintillator used for small animal CT is CsI(Tl). Using thin film deposition techniques, CsI(Tl) can be grown into a micro-columnar

thin film structure. When X-rays are detected in the array, the scintillation light can be channelled down the micro-columnar structure to a lens coupled CCD camera. Other readout devices include an array of amorphous silicon photodiodes, CMOS arrays or X-ray film. Other thin film scintillators include yttrium aluminum garnet (YAG) and lutetium aluminum garnet (LuAG) both doped with cerium (Ce). Another scintillator commonly used as a CT detector is $CdWO_4$. Because of their structural characteristics, CsI(Tl) has been mostly used for cone-beam geometry systems while $CdWO_4$ has been used for fan beam systems. The second style of scintillator that has been used for CT imaging is ceramic scintillating detectors. This includes versions of gadolinium oxysulfide, Gd_2O_2S (GOS) with different dopant materials (e.g., Pr, Ce, and F) and $Y_{1.34}Gd_{0.60}O_3$:(Eu, Pr)$_{0.06}$ (YGO). By using codopants these ceramic scintillators and can good light yield and low afterglow [45]. Further, there has been recent interest in the use of the same scintillator detector for both PET and CT [48]. The first such testing was done using a discrete crystal LSO scintillator array where the crystal elements were individually coupled to an avalanche photodiode (APD) [46, 47]. Because of the large difference between the photon flux of PET and CT, the detector module needed to have very high count rate capability. This was supported by the individual crystal readout. Because the detector operated in photon counting mode rather than flux mode, less X-ray photons are required to produce an image. The concept of a photon counting CT detector is still a research endeavor. In a study looking at other potential X-ray photon counting scintillators [48], the best performing scintillators were GSO:Ce, BGO and $LaBr_3$.

5 Summary

Scintillators have long been a main stay in detectors for energetic photons. This is because of the detection efficiency and/or cost advantage they possess over most other detector materials. While semiconductor materials are in use for detection of photons to convert the photon energy directly into a current pulse without the use of scintillators (e.g., CdTl, CZT, intrinsic germanium [5]), scintillators continue to offer a wide range of performance parameters in robust, well-understood detector designs. There continues to be a considerable effort to find scintillators that are closer to the ideal (i.e., dense, high photo-electric cross section, non-hydroscopic, high light output, fast decay time, and inexpensive). While the perfect material has yet to be found, the current selection described in this chapter provides many options for system designers and many of the new compounds do offer considerable promise for continued improvements in the ultimate performance of scintillator based small animal molecular imaging instrumentation systems.

Acknowledgments The authors would like to thank all the members of the Nuclear Medicine Physics Group at the University of Washington for making it possible for us to find the time to write this chapter—and for their insight and good work that has allowed our laboratory to work on detector and scanner development so consistently over the years. We also wish to acknowledge the support of the NIH, DOE, GE Medical Systems, Philips Medical Systems, Altera, and Zecotek Photonics in our research in detectors and electronics.

References

1. Cherry, S.R.: "In vivo molecular and genomic imaging: new challenges for imaging physics.", *Phys. Med. Biol.* **49**, pp. R13-48 (2004).
2. Maas, M.C., Schaart, D.R., van der Lann, D.J., Bruyndonckx, P., Lemaitre, C., Beekman, F.J., van Ekjk, C.W.E.: "Monolithic scintillator PET detectors with intrinsic depth-of-interaction correction", *Phys. Med. Biol.* **54**, pp. 1893 - 908 (2009)
3. Eriksson, L., Melcher, C.L., Eriksson, M., Rothfuss, H., Grazioso, R., Aykac, M.: "Design considerations of phoswich detectors for high resolution positron emission tomography", *IEEE Trans. Nucl. Sci.* **56**, pp. 182 - 8 (2009)
4. Ueno, Y., Morimoto, Y., Tsuchiya, K., Yanagita, N., Kojima, S., Ishitsu, T., Kitaguchi, H., Kubo, N., Zhao, S., Tamaki, N., Amemiya, K.: "Basic performance test of a prototype PET scanner using CdTe semiconductor detectors", *IEEE Trans. Nucl. Sci.* **56**, pp. 24 - 8 (2009)
5. Lewellen, T.K.: "Recent Developments in PET detector technology", *Phys. Med. Biol.* **53**, pp. R287-R317 (2008)
6. Leroy, C.: "Review of radiation detectors", *AIP Conf. Proc.* **958**, pp. 92 - 100 (2007)
7. D'Ambrosio, C., Anulli, F., Bencivenni, G., Domenici, D., Felici, G., Morone, M.C., Murtas, F.: "A hybrid parallel plate gas Counter for medical imaging", *Nucl. Instrum. Methods Phys. Res. A, Accel. Spectrom. Detect. Assoc. Equip.* **572**, pp. 244 - 5 (2007).
8. Couceiro, M., Blanco, A., Ferreira Nuno, C., Ferreira Marques, R., Fonte, P., Lope, L.: "RPC-PET: Status and perspectives", *Nucl. Instrum. Methods Phys. Res. A, Accel. Spectrom. Detect. Assoc. Equip.* **580**, pp. 915 - 918 (2007).
9. Hadong, K., Cirignano, L., Dokhale, P., Bennett, P., Stickel, J.R., Mitchell, G.S., Cherry, S.R., Squillante, M., Shah, K.: "CdTe orthogonal strip detector for small animal PET", *IEEE Nuclear Science Symposium and Medical Imaging Conference Record,* pp. 3827 - 3830 (2007)
10. Boston, H.C., Boston, A.J., Cooper, R.J., Cresswell, J., Grint, A.N., Mather, A.R., Nolan, P.J., Scraggs, D.P., Turk, G., Hall, C.J., Lazarus, I., Berry, A., Beveridge, T., Gillam, J., Lewis, R.: "Characterization of the SmartPET planar Germanium detectors", *Nucl. Instrum. Methods Phys. Res. A, Accel. Spectrom. Detect. Assoc. Equip.* **579**, pp. 104 - 107 (2007).
11. Arnaud, D., Olivier, M., Francoise, M., Guillaume, M., Loick, V.: "CdZnTe detectors for small field of view positron emission tomographic imaging", *Nucl. Instrum. Methods Phys. Res. A, Accel. Spectrom. Detect. Assoc. Equip.* **571**, pp. 465 - 470 (2007).
12. Doke, T., Kikuchi, J., Nishikido, F.: "Time-of-flight positron emission tomography using liquid xenon scintillation", *Nucl. Instrum. Methods Phys. Res. A, Accel. Spectrom. Detect. Assoc. Equip.* **569**, pp. 863 - 71 (2006).
13. Burnham, C., Bradshaw, J., Kaufman, D., Chesler, D., Brownell, G.L.: "One dimensional scintillation cameras for positron ECT ring detectors", *IEEE Trans Nucl. Sci.* **NS-28**, pp. 109-113 (1981)
14. Hoffman, E.J., Phelps, M.E., Huang, S.C., Kuhl, D.E.: "A new tomograph for quantitative positron emission computed tomography of the Brain", *IEEE Trans. Nucl. Sci.* **NS-28**, pp. 99-103 (1981)
15. Ter-Pogossian, M.M., Ficke, D.C., Yamamoto, M., Hood Sr., J.T.: "Super PETT I: a positron emission tomograph utilizing photon time-of-flight information", *IEEE Trans. Med. Imag.* **MI-1**, pp. 179-186 (1982)
16. Hoffman, E.J., Ricci, A.R., van der Stee, L.M.A.M., Phelps, M.E.: "ECAT III--basic design considerations", *IEEE Trans. Nucl. Sci.* **NS-30**, pp. 729-733 (1983)
17. Moses, W.W., Derenzo, S.E., Geyer, A.B., Huesman, R.H., Uber, D.C.: "The tuning algorithms used by the Donner 600 crystal tomograph", *IEEE Trans. Nucl. Sci.* **36**, pp. 1025-1029 (1989)
18. Joung, J., Miyaoka, R.S., Kohlmyer, S.G., Lewellen, T.K.: "ML based positioning algorithms for scintillation cameras", *IEEE Nuclear Science Symposium and Medical Imaging Conference* pp. 1455-1459 (1999)

19. Milster, T.D., Selberg, L.A., Barrett, H.H., Landesman, A.L., Seacat III, R.H.: "Digital position estimation for the modular scintillation camera", *IEEE Trans. Nucl. Sci.* **NS-32**, pp. 748-752 (1985)
20. Miyaoka, R.S., Sung-Kwan, J., Kisung, L.: "Detector light response modeling for a thick continuous slab detector", *J. Nucl. Sci. Technol.* **45**, pp. 634 - 638 (2008)
21. Cherry, S.R., Sorenson, J.A., Phelps, M.E.: *Physics in Nuclear Medicine* (Saunders, Orlando, 2003)
22. Braem, A., Chesi, E., Joram, C., Rudge, A., Seguinot, J., Weilhammer, P., De, L., R., Nappi, E., Lustermann, W., Schinzel, D., Johnson, I., Renker, D., Albrecht, S.: "Wavelength shifter strips and G-APD arrays for the read-out of the z-coordinate in axial PET modules", *Nucl. Instrum. Methods Phys. Res. A, Accel. Spectrom. Detect. Assoc. Equip.* **586**, pp. 300 - 308 (2008).
23. Chaney, R.C., Fenyves, E.J., Nelson, G., Anderson, J.A., Antich, P.P., Atac, M.: "Application of scintillating fiber gamma ray detectors for medical imaging", *Proc. SPIE - Int. Soc. Opt. Eng.* **1737**, pp. 37 - 40 (1993)
24. Fernando, J.L., Xiong, R., Nguyen, T., Anderson, J.A., Arbique, G., Challa, S., Constantinescu, A., Fenyves, E.J., Kulkarni, P.V., Raheja, A., Thambi, G., Antich, P.P.: "Small animal PET imager built with plastic scintillating fibers", *Proc. SPIE - Int. Soc. Opt. Eng.* **2551**, pp. 102 - 127 (1995)
25. Kulkarni, P.V., Anderson, J.A., Antich, P.P., Prior, J.O., Zhang, Y., Fernando, J., Constantinescu, A., Goomer, N.C., Parkey, R.W., Fenyves, E., Chaney, R.C., Srivastava, S.C., Mausner, L.F.: "New approaches in medical imaging using plastic scintillating detectors", *Nucl. Instrum. Methods Phys. Res. B, Beam Interact. Mater. At.* **B79(1-4)**, pp. 921 - 925 (1993).
26. McIntyre, J.A., Allen, R.D., Aguiar, J., Paulson, J.T.: "A positron emission tomograph designed for 3/4 mm resolution", *IEEE Trans. Nucl. Sci.* **42(4)**, pp. 1102 - 1106 (1995)
27. Moszynski, M.: "Inorganic scintillation detectors in gamma-ray spectrometry", *Nucl. Instrum. Methods Phys. Res. A, Accel. Spectrom. Detect. Assoc. Equip.* **505**, pp. 101-110 (2003).
28. H.O. Anger, in *Instrumentation in Nuclear Medicine*, edited by Hine, G.J. (Academic Press, New York, 1967), Chap. 19.
29. Karp, J.S., Mankoff, D.A., Muehllehner, G.: "A positron-sensitive detector for use in positron emission tomography", *Nucl. Instr. Meth. Phys. Res.* **A273**, pp. 891-897 (1988)
30. Muehllehner, G., Karp, J.S., Mankoff, D.A., Beerbohm, D., Ordonez, C.E.: "Design and performance of a new positron tomograph", *IEEE Trans Nucl. Sci*. **35**, pp. 670-674 (1988)
31. Weber, M.J., Monchamp, R.R.: "Luminescence of Bi4Ge3O12: Spectral and decay properties", *J. Appl. Phys.* **44**, pp. 5495 - 9 (1973)
32. Melcher, C.L., Schweitzer, J.S.: "Cerium-doped lutetium oxyorthosilicate: a fast, efficient new scintillator", *IEEE Trans. Nucl. Sci.* **39(4)**, pp. 502 - 5 (1992)
33. van Eijk, C.W.E.: "Inorganic scintillators in medical imaging", *Phys. Med. Biol.* **47**, pp. 85 - 106 (2002)
34. Surti, S., Karp, J.S., Daube-Witherspoon, M., Wener, M.: "Investigation of image quality and NEC in a TOF capable PET scanner.", *IEEE Nuclear Science Symposium and Medical Imaging Conference*, pp 4032-4037 (2004)
35. Surti, S., Karp, S., Popescu, L.M., Daube-Witherspoon, E., Werner, M.: "Investigation of time-of-flight benefit for fully 3-DPET", *IEEE Trans. Med. Imaging* **25**, pp. 529 - 38 (2006)
36. Manjeshwar, R.M., Yiping, S., Jansen, F.P.: "Image quality improvements with time-of-flight positron emission tomography for molecular imaging", *IEEE International Conference on Acoustics, Speech, and Signal Processing* **Vol. 5**, pp. 853 - 6 (2005)
37. Surti, S., Kuhn, A., ME, W., Perkins, A.E., Kolthammer, J., Karp, J.S.: "Performance of Philips Gemini TF PET/CT scanner with special consideration for its time-of-flight imaging capabilities", *J Nucl. Med.* **46**, pp. 471-480 (2007)
38. van Loef, E.V.D., Dorenbos, P., van Eijk, C.W.E., Kramer, K., Gudel, H.U.: "High-energy-resolution scintillator: Ce3+ activated LaBr3", *Appl. Phys. Lett.* **79**, pp. 1573 - 5 (2001)
39. Birowosuto, M.D., Dorenbos, P., van Eijk, C.W.E., Kramer, K.W., Gudel, H.U.: "Scintillation properties of LuI3:Ce3+-high light yield scintillators", *IEEE Trans. Nucl. Sci.* **52**, pp. 1114 - 18 (2005)

40. Kuhn, A., Surti, S., Karp, J.S., Newcomer, F.M., VanBerg, R., Muehllehner, G.: "Performance assessment of pixelated LaBr3 detector modules for TOF PET.", *IEEE Nuclear Science Symposium and Medical Imaging Conference*, pp 3402-3406 (2004)
41. Porter-Chapman, Y.D., Bourret-Courchesne, E.D., Bizarri, G.A., Weber, M.J., Derenzo, S.E.: "Scintillation and luminescence properties of undoped and cerium-doped LiGdCl4 and NaGdCl4", *IEEE Trans. Nucl. Sci.* **56**, pp. 881 - 6 (2009)
42. Derenzo, S.E., Boswell, M.S., Bourret-Courchesne, E., Boutchko, R., Budinger, T.F., Canning, A., Hanrahan, S.M., Janecek, M., Qiyu, P., Porter-Chapman, Y., Powell, J.D., Ramsey, C.A., Taylor, S.E., Lin-Wang, W., Weber, M.J., Wilson, D.S.: "Design and implementation of a facility for discovering new scintillator materials", *IEEE Trans. Nucl. Sci.* **55**, pp. 1458 - 63 (2008)
43. Hawrami, R., Batra, A.K., Aggarwal, M.D., Roy, U.N., Groza, M., Cui, Y., Burger, A., Cherepy, N., Niedermayr, T., Payne, S.A.: "New scintillator materials (K2CeBr5 and Cs2CeBr5)", *J. Cryst. Growth* **310**, pp. 2099 - 102 (2008)
44. Van Loef, E.V., Yimin, W., Glodo, J., Brecher, C., Lempick, A., Shah, K.S.: "Recent advances in ceramic scintillators", *Nuclear Radiation Detection Materials,* pp. 87 - 94 (2008)
45. Van Eijk, C.W.E.: "Inorganic scintillators in medical imaging detectors", *Nucl. Instrum. Methods Phys. Res. A, Accel. Spectrom. Detect. Assoc. Equip.* **509**, pp. 17-25 (2003).
46. Berard, P., Pepin, C.M., Rouleay, D., Cadorette, J., Lecomte, R.: "CT acquisition using PET detectors and electronics", *IEEE Trans. Nucl. Sci.* **52**, pp. 634-637 (2005)
47. A. Nassalski, M. Moszynski, T. Szczesniak, D. Wolski, T. Batsch, The Road to the common PET/CT Detector, IEEE Trans Nucl. Sci. vol. 54, no. 3, pp. 1459-63, 2007
48. Nassalski, A., Kapusta, M., Batsch, T., Wolski, D., Mockel, D., Enghardt, W., Moszynski, M.: "Comparative study of scintillators for PET/CT detectors", *IEEE Trans. Nucl. Sci* **54**, pp. 3-10 (2007)

Chapter 2
Solid-State Detectors for Small-Animal Imaging

Paolo Russo and Alberto Del Guerra

1 Introduction

Semiconductor detector technology, initially developed for high energy physics applications, has found a distinctive role in high performance systems for X-ray and gamma-ray medical imaging applications, including small animal imaging. Single-Photon Emission Computed Tomography (SPECT) small animal imaging requires the development of compact detectors with intrinsically ultrahigh spatial resolution, high energy resolution and good detection efficiency, in addition to suitable radiation collimation strategies. This overall performance can only partly be guaranteed by scintillator based systems with photomultiplier tube readout, the most used technology at present for small animal SPECT scanners. On the other hand, with respect to scintillator based detectors, semiconductor detectors can offer a gain by approximately a factor two in energy resolution at typical radionuclide energies, a factor greater than two in intrinsic spatial resolution, and a comparable intrinsic detection efficiency, though usually at a reduced field of view. Moreover, their compactness could be crucial in devising animal "personalized" miniature scanners. An additional interesting feature of semiconductor based small animal SPECT scanners is that the detector technology can be used both for gamma-ray imaging and for X-ray imaging, when coupling the SPECT scanner to a low resolution X-ray CT scanner for anatomical registration. The requirement of high spatial resolution, coupled to high sensitivity, becomes also stringent in microPET systems, where semiconductor detectors could be the technology of choice for future high performance PET scanners.

P. Russo (✉)
Dipartimento di Fisica, Università di Napoli Federico II,
and INFN Sezione di Napoli, Napoli, Italy
e-mail: Paolo.Russo@na.infn.it

A. Del Guerra
Dipartimento di Fisica, Università di Pisa, and INFN Sezione di Pisa, Pisa, Italy
e-mail: alberto.delguerra@df.unipi.it

H. Zaidi (ed.), *Molecular Imaging of Small Animals: Instrumentation and Applications*,
DOI 10.1007/978-1-4939-0894-3_2,

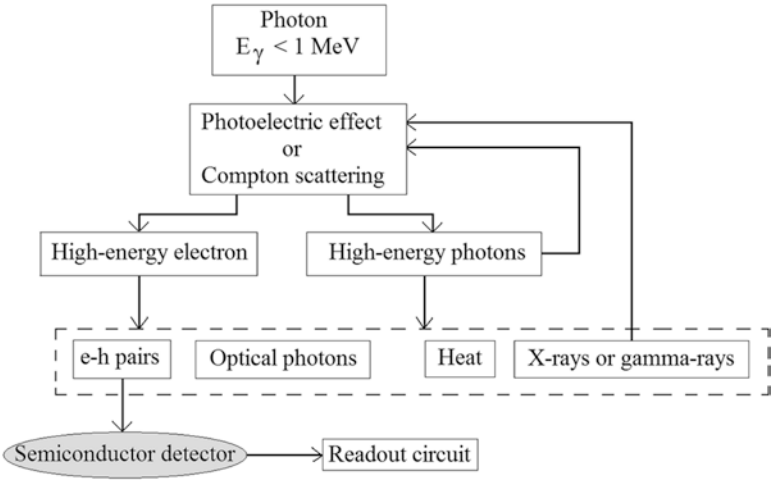

Fig. 2.1 Schematics of the inelastic interaction of a gamma ray in the detector material, up to energies below 1 MeV

This chapter illustrates the basic technology of pixel and microstrip semiconductor detectors for these small animal imaging applications, with reference to the most used technologies, relative to the CdTe, CdZnTe (CZT) and Si semiconductors. Still at its early stage, but of increasing interest, is the technology of semiconductor detectors—CdTe, CdZnTe, Si room-temperature semiconductors, in addition to liquid nitrogen cooled Ge—specifically for Positron Emission Tomography (PET) in ultra high resolution small animal scanners. Examples of development of semiconductor SPECT and SPECT/CT scanners, and of semiconductor PET scanners for small animal imaging, are presented. In illustrating those systems, the emphasis will be on their technical description.

In order to illustrate the application of semiconductor detectors to small animal imaging in the area of microSPECT and microPET, a brief outline follows on the physical characteristics of those detectors. Basic terminology, relevant data and basic techniques will be introduced for completeness of illustration.

1.1 Basic Principles of Radiation Semiconductor Detectors

Semiconductor detectors for X-rays and gamma-rays in the diagnostic energy range for radiography and nuclear medicine (from tens of keV up to some hundreds of keV) work by converting the energy of interacting photons into a number of electron–hole (e–h) pairs transported to the corresponding collection electrodes and then by recording this charge (Fig. 2.1). Once a photoelectric or a Compton interaction occurs in the semiconductor substrate, a high-kinetic-energy electron is created. The probability of this event determines the quantum efficiency of the detector.

Table 2.1 Physical properties of some semiconductors for X-ray and gamma-ray imaging [2]

	Material			
	Si	CdTe	$Cd_{0.9}Zn_{0.1}Te$	Ge
Atomic number(s)	14	48; 52	48; 30; 52	32
Effective atomic number	14	50	49.1	32
Density (g/cm^3)	2.33	5.85	5.78	5.33
Bandgap, E_g (eV)	1.12	1.44	1.572	0.67
Electron mobility, μ_e (cm^2/V s)	1,400	1,100	1,000	3,900
Electron lifetime, τ_e (s)	$>10^{-3}$	3×10^{-6}	3×10^{-6}	$>10^{-3}$
Hole mobility, μ_h (cm^2/V s)	480	100	50–80	1,900
Hole lifetime, τ_h (s)	2×10^{-3}	2×10^{-6}	10^{-6}	10^{-3}
$\mu_e\tau_e$ (cm^2/V)	>1	3.3×10^{-3}	$3–5\times10^{-3}$	>1
$\mu_h\tau_h$ (cm^2/V)	1	2×10^{-4}	5×10^{-5}	>1
Pair creation energy (eV/e–h pairs)	3.62	4.43	4.64	2.95
Dielectric constant	11.7	11	10.9	16
Resistivity (Ω cm) @ 20 °C	$<10^4$	10^9	3×10^{10}	50

This high energy electron loses its energy in the material by producing phonons and energetic e–h pairs, and these electrons and holes can, in turn, produce phonons or create secondary e–h pairs, up to the end of their energy loss process where they recombine radiatively or through phonon excitation [1].

Semiconductor detectors collect the electrons and holes and produce a signal in the readout circuit. Since a part of the charge created can be trapped in semiconductor bulk or anyway is unable to contribute to the electrical signal at the collecting electrode, the charge collection efficiency (CCE) can be less than unity: this occurs, e.g., with compound semiconductor detectors in the presence of impurities, crystal defects, trapping centers etc. The amount of energy deposited in the detector volume by each interacting photon is directly proportional to the total number of e–h pairs created: for semiconductors, this pair creation energy is roughly in the range 3–5 eV/e–h pair (Table 2.1), against, e.g., 13 eV/e–h pair in NaI:Tl scintillator material. This implies a large signal generated in the semiconductor detector: for example, in CdTe a 100-keV photon can generate an average number of ≅23,000 e–h pairs, so that even in the presence of inefficiencies in the transport and collection of electron and hole charges, the electric signal can be conveniently amplified and the interaction event recorded. To this purpose, the detector dark (leakage) current must be kept low, so that the radio-induced signal is well separated from the detector noise.

There are two basic schemes for working in low-dark current conditions, which employ the diode structure (junction) or the resistive mode. In the first scheme (Fig. 2.2, which illustrates the case of high resistivity n-type Si wafers) p-n junctions are realized on the doped detector substrate by implanting p^+ regions on one side in the form of single detector elements or multi-detector elements (strips, pixels) and n^+ regions are on the opposite side. Then this diode structure is reverse-biased: in this case the leakage current flowing in the external circuit is largely reduced with respect to forward bias operation.

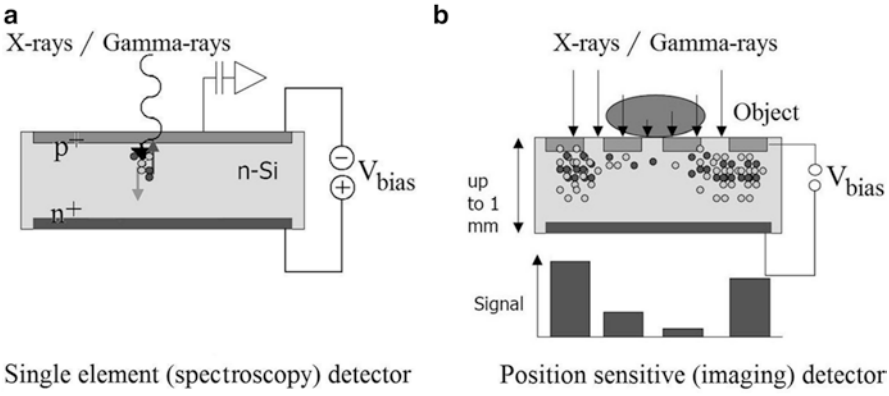

Fig. 2.2 Basic scheme of Si p–n junction detectors for spectroscopy (single element, **a**) or imaging applications (**b**), illustrating the generation, drift and collection of e–h pairs from interacting X-rays or gamma-rays

1.2 Charge Generation and Transport in Semiconductor Detectors

Application of a suitable high reverse bias voltage (increasing with the square of the substrate thickness) allows to extend the depletion (active) region to the whole detector thickness. Once fully depleted, the bias voltage can be further increased (before breakdown) in order to increase the strength E of the electric field in the drift region of the charge carriers. Alternatively, the (reverse biased) diode structure with a surface barrier can be realized by metal–semiconductor (Schottky) anode contact on one side, and low-resistive ("ohmic" or "injecting") metal–semiconductor contact on the opposite side (Fig. 2.3). This structure is used, e.g., with CdTe room-temperature compound semiconductors by using indium (or titanium/indium) for the anode electrode (which forms a high Schottky barrier at the In/CdTe interface) and platinum for the cathode electrode; alternatively, p-n junction type contacts can be created. In the second scheme (Fig. 2.3), photoconductive operation can be implemented by depositing ohmic contacts on both opposite sides of the detector substrate (e.g., in a Pt/CdTe/Pt detector). The irradiation geometry is typically head-on and from the cathode, but edge-on irradiation can be used as well (Fig. 2.3a), e.g. with thin detectors, in order to exploit a higher interaction depth and to assure good lateral resolution. Application of a high voltage bias assures high E values (e.g., 10^3–10^4 V/cm) and, hence, high drift velocities ($v_e = \mu_e \cdot E$; $v_h = \mu_h \cdot E$, with μ_e and μ_h electrical mobilities for electrons and holes, respectively) of the charge carriers generated by the interacting radiation. Then, in order to keep the leakage current low in photoconductive detectors, the semiconductor detector substrate must have a high bulk resistivity (e.g., 10^8–10^{10} Ω cm) (Table 2.1). Choice of the voltage polarity on

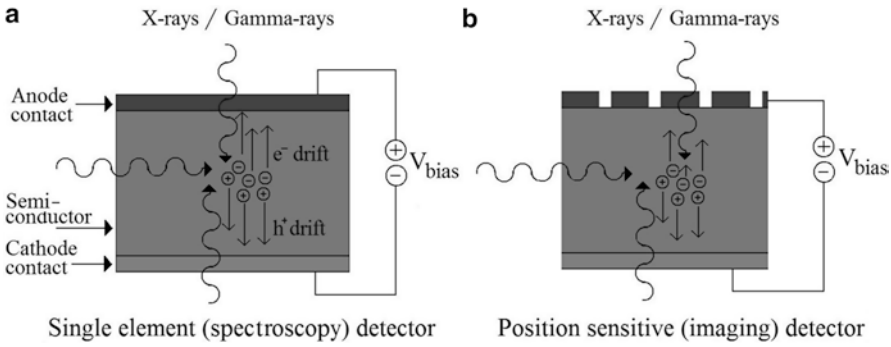

Fig. 2.3 Radiation detectors for spectroscopy (single element, **a**) or imaging applications with segmented contact electrodes (**b**) can be realized on semiconductor substrates equipped with ohmic or with Schottky contacts. As shown by the photon paths, they can be irradiated from the front side, from the back side or edge-on

the signal readout side allows to select the charge carrier type (electrons or holes), on dependence of their different electrical mobilities μ_e and μ_h, and on their lifetime τ_e, τ_h, respectively.

Due to presence of electronic levels in the forbidden gap region of the semiconductor corresponding to crystal defects, some electrons and holes are trapped in those levels during the drift process, reducing the values of τ_e, τ_h for compound semiconductors (e.g., CdTe, CdZnTe) to levels (≅ μs) orders of magnitude lower than for Si and Ge (≅ ms) (Table 2.1). Typically, charge transport parameters (μ, τ), are significantly higher for electrons than for holes and these low μ_h, τ_h values cause hole trapping and charge loss. This asymmetry of charge carrier transport between electrons and holes introduces a dependence of the pulse shape and of the induced charge at the anode and cathode collecting electrodes, respectively, on the depth of interaction, z, inside the semiconductor detector active thickness, L. If the interaction event occurs close to the cathode ($z \cong 0$), hole movement contributes little to the charge signal. For interaction at a depth $0 \ll z < L$ from the cathode, the charge pulse shape depends on the contribution of holes. If the hole drift distance z from the cathode is long compared to the average distance before trapping $\lambda_h = v_h \cdot \tau_h = \mu_h \cdot \tau_h \cdot E$, then the CCE for the induced charge signal Q_{anode} at the anode is reduced, according to the following Hecht relation (where q is the elementary charge and N_0 is the number of e–h pairs created by the interacting photon at depth z):

$$CCE = \frac{Q_{anode}}{qN_0} = \frac{\mu_e \tau_e E}{L}\left(1 - e^{-(L-z)/\mu_e \tau_e E}\right) + \frac{\mu_h \tau_h E}{L}\left(1 - e^{-z/\mu_h \tau_h E}\right).$$

Due to the low $\mu_h \cdot \tau_h$ value, the above relationship shows that if the detector thickness L is greater than $\mu_h \cdot \tau_h \cdot E$, the collected charge Q_{anode} is less than qN_0 by a variable quantity in dependence of the interaction depth z. This implies that the peak spectral shape due to photoelectric absorption of a gamma ray presents a shoulder (tailing)

on the lower-energy side. For example, for CdTe, with the data in Table 2.1, and from the above equation, in a 1-mm thick detector biased at −100 V, the estimated CCE is 82 % for interaction at 0.1 mm from the anode, 94 % for interaction at detector mid-depth and 99 % for interaction at 0.1 mm distance from the cathode. For these reasons, gamma-ray irradiation from the cathode side and collection of the charge signal from the anode side (either continuous or pixelated) are preferred, where the electrons are mostly contributing to the signal. In semiconductor arrays of gamma-ray detectors, Barrett et al. [3] showed that the effect of hole trapping depends on the ratio of the size of the pixel ω to the detector thickness L, and that for small pixels ($\omega \ll L$) the largest contribution to the pixel signal arises from charge carriers moving to within a distance ω from the anode plane. Then, if the pixels are the anode contacts, the largest signal contribution comes from the electrons, which are less trapped than holes, thus preserving CCE and energy resolution. In the case of room-temperature semiconductors like CdTe or CdZnTe, this so-called "small-pixel effect" favors the use of detector arrays with pixels on the anode side and irradiation from the cathode (continuous electrode). However, the pixel size has not to be too small with respect to the detector thickness: in this case, spreading of the charge to adjacent pixels ("charge sharing") causes partial or total loss of spectroscopic information. Intermediate values of the aspect ratio L/ω (e.g., $L/\omega \cong 4$–5) may provide better energy resolution at energies up to 511 keV. For example, a CdTe array detector with 75 μm pixels on a 750 μm thickness ($L/\omega = 10$) has poor energy resolution (according to simulations at 60 keV [4]) and a CdTe array detector with 55 μm pixels on a 1 mm thickness ($L/\omega = 18$) has no spectroscopic resolution at all [5]; a 5 mm thick CdTe detector had an estimated energy resolution with a minimum of 4 % at 140 keV, for an aspect ratio $L/\omega = 4$ [6]. For high-aspect-ratio pixel detectors, summing up the analog signal from a sub-array of adjacent pixels should be able to recover the energy resolution, while preserving the spatial resolution.

1.3 From Semiconductor to Semi-insulating Detectors

Room-temperature operation with low leakage current is achieved with high-resistivity compound semiconductors like CdTe, semi-insulating GaAs and CdZnTe equipped with rectifying contacts as well as with ohmic contacts, thanks to their large energy bandgap >1.4 eV (Table 2.1). Since detector-grade compound semiconductor crystals (e.g., CdTe) present impurities in their growth which decrease the crystal resistivity, doping with suitable atoms during crystal growth (e.g. using Cl in the case of CdTe:Cl) is used to electrically compensate such impurities. This produces a semi-insulating electrical behavior of the crystal. For example, if all impurities are fully compensated ($n_i \cong n \cong p$), then the bulk resistivity ρ_i can be calculated as [7]:

$$\rho_i = \frac{1}{q n_i \left(\mu_e + \mu_h \right)}$$

where n_i is the intrinsic carrier concentration, n and p are equilibrium concentrations of free electrons and holes, respectively: at room-temperature, for $Cd_{0.9}Zn_{0.1}Te$, the above formula allows to derive a resistivity as large as 4×10^{10} Ωcm (i.e., one order of magnitude higher than for CdTe).

2 Semiconductor Based Imaging Detectors

2.1 Semiconductor vs. Scintillator Based Detectors

Semiconductor materials have been employed at room-temperature as substrates for X-ray and gamma-ray direct-detection imaging systems for small animal imaging (10–150 keV), since they are expected to provide a better performance, at least for some image quality parameters, than conventional indirect-detection systems, based on scintillator crystals coupled to position-sensitive light detection devices. From a schematic point of view, there is similarity between the direct and indirect detection modes (Fig. 2.4), and both can be operated at room temperature. In indirect-detection systems, gamma-rays are absorbed in a phosphor/scintillator layer and their energy is converted in a proportional number of visible or UV light photons, following primary photoelectron and electron–hole pairs creation processes. The optical photons migrate isotropically in the scintillator toward the crystal faces. Then, this optical signal is readout by a photodetector which converts the light photons into an

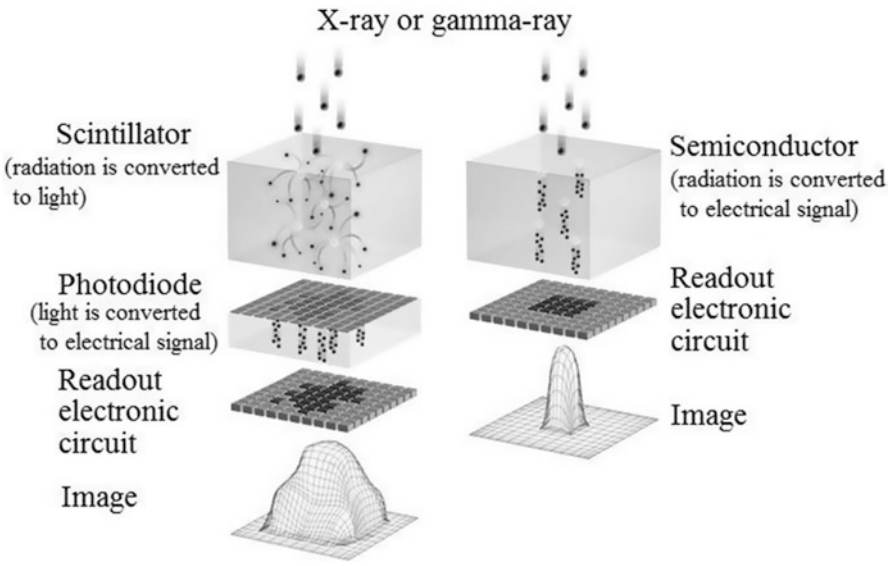

Fig. 2.4 Schematic representation of the conversion processes in a scintillator based and in a semiconductor based imaging system (adapted from [15])

intense electron current, after a large amplification. In direct-detection systems, gamma-ray photons interact in the (semiconductor) detector volume where the signal is generated as a proportional number of e–h pairs: under an intense applied electric field, these charge carriers are separated and migrate toward the corresponding electrodes, where this drift induces a current which is integrated by a charge-sensitive amplifier and converted into a voltage pulse. The photodetector + readout circuit in indirect-detection systems could be bulky (e.g. a photomultiplier tube, PMT), and this can give relatively more compactness to direct-detection systems, though the situation could also be reversed (e.g., with very compact indirect-detection systems employing a thin scintillator layer coupled to a Charge Coupled Device, CCD). Quantitative differences between the two schemes arise when considering the statistical fluctuations and the efficiency in the conversion process, the total amplification gain, the signal loss processes. All these effects determine the detector energy resolution, a spectroscopic parameter considered of importance in gamma-ray systems for human imaging as well as for small animal imaging, for isotope identification and for scatter rejection. It is of interest to examine briefly the above differences, in order to appreciate the merits of semiconductor detectors versus scintillator based detectors, for gamma-ray small animal imaging.

In the optical detection scheme with scintillators, light signal losses are present since it is not possible, in a continuous or in a pixelated scintillator crystal, to transport the scintillation light only toward the crystal side facing the photodetector surface. Indeed, this condition of light guiding toward the output surface can be realized in needle-structured scintillators like can be done for CsI:Tl, but in this case the absorption thickness is typically limited to a fraction of a millimeter, so that their use is limited to low-energy gamma-rays. The light which reaches the other scintillator faces is either absorbed (e.g. by black finishing) in order to avoid distortions in the position evaluation due to light reflections, or reflected (e.g. by reflective painting) in order to increase the light output. In addition, optical losses are present when transferring the output light signal to the photodetector window, since coupling between two optical surfaces is normally associated with lossy reflections and to light loss at the surface borders. A conservative estimate for the efficiency of light transport from the point of interaction to the photodetector window is 0.75.

Analogously, charge losses in a semiconductor detector occur in the drift process when electrons or holes are trapped in crystal defects, nonuniformities and trapping centers, so that the CCE at the electrodes is not unity, even using high-strength applied electric fields. For Si the CCE can be close to 1, but for room-temperature compound semiconductors one can assume as a conservative estimate CCE $\cong$ 0.9. In the case of a scintillator, the inefficiencies in the conversion processes—including the creation of a given number of photoelectrons at the photocathode of the light detector—determine the overall energy resolution. Fluctuations in the number of e–h pairs radiation-generated in a material are governed by a distribution whose variance is proportional, via the Fano factor F, to the average number of e–h pairs generated. Let us consider the case of NaI:Tl, where 7,500 e–h pairs are generated by a 100 keV interacting photon. These charge carrier produce, via excitation and radiative de-excitation, light photons with an efficiency of about 0.54, i.e. about

4,000 photons are generated, but of these only 3,000 reach the photocathode (75 % light collection efficiency), where they are converted to 600 photoelectrons (assuming 20 % photocathode quantum efficiency). This implies that for NaI:Tl, about 13 e–h pairs are needed to create one photoelectron in the readout photodetector. For high light yield scintillators like $LaBr_3$:Ce (6,300 photons/100 keV) and CsI:Tl (6,600 photons/100 keV) the situation is better, with about 1,000 photoelectrons generated at the photocathode, for a 100 keV interacting photon. All these factors, leading to inefficiencies in the generation of the useful photoelectron signal, are independent of each other and ultimately determine a Fano factor $F \cong 1$ (i.e., Poisson statistics applies) to the process of photoelectron generation with scintillator based detectors. On the other hand, an improved overall efficiency in the conversion from gamma-ray energy to photoelectron signal is shown by a semiconductor detector. For crystalline silicon the conversion factor is 28,000 e–h pairs/100 keV photons, and for CdTe it is 22,600 e–h pairs/100 keV photons. F at room temperature is close to 0.10 ± 0.04 for Si and for semiconductors of interest (e.g., CdTe, CdZnTe, GaAs) at gamma-ray energies of interest [8]. This means that the signal generation process has fluctuations governed by a sub-Poissonian statistical distribution. As a result, while with $LaBr_3$:Ce scintillators an energy resolution of 2.6–2.9 % at 662 keV has been reached [9], the corresponding figure for CdTe is 0.9 % [10]. At 140 keV, a continuous $LaBr_3$:Ce crystal 5-mm thick, coupled to a flat panel position-sensitive PMT, shows 9 % energy resolution. For CdZnTe, at 140 keV, a 5 mm thick detector can have an energy resolution between 3.6 % [11] and 6 % [12], the performance being dependent also on the readout electronics.

Analysis of signal conversion gain G and Fano factor F is also useful to clarify differences between indirect and direct-detection systems in terms of X-ray intrinsic detection efficiency, η, and Detective Quantum Efficiency at zero spatial frequency (DQE(0)). It can be shown (e.g., [13]) that for a direct-detection system

$$DQE(0) = \frac{\eta}{1 + \left(\frac{F}{G}\right)} \cong \eta$$

where the term in parentheses is close to zero since F is close to zero and G is large, for semiconductor detectors. For an indirect-detection system, the above expression is modified so as to take into account the first conversion stage (scintillator) as well as the second conversion stage from light photons to electrical charge, with corresponding parameters F_2 and G_2, so that we have

$$DQE(0) = \frac{\eta}{1 + \left(\frac{F_1}{G_1}\right) + \left(\frac{F_2}{G_1 G_2}\right)} \cong \eta.$$

The approximation holds after considering that, for scintillators, $F_1 \cong 1$, $G \gg G_1$, $G_1 \gg 1$, $G_1 G_2 \gg 1$. One can conclude that, on a quantitative basis, the $DQE(0)$ of

Table 2.2 Photon cross sections (linear attenuation coefficients) in semiconductor detectors at characteristic energies for small animal imaging

Material	Energy (keV)	Compton (cm^{-1})	Photoelectric (cm^{-1})	Total attenuation (cm^{-1})	Mean free path (mm)
Si	27.5	0.347	3.542	4.241	2.4
Si	140.5	0.310	0.020	0.350	28.6
Si	511	0.200	4.1×10^{-4}	0.202	49.5
CdTe	27.5	0.570	154.4	159.7	0.06
CdTe	140.5	0.614	3.223	4.148	2.4
CdTe	511	0.415	0.091	0.534	18.7
CdZnTe	27.5	0.570	150.3	155.5	0.06
CdZnTe	140.5	0.613	3.052	3.965	2.52
CdZnTe	511	0.413	0.086	0.525	19.0
Ge	511	0.402	0.018	0.433	23.1
BGO	511	0.509	0.396	0.963	10.4

For comparison, cross section data for a $Bi_4Ge_3O_{12}$ (BGO) scintillator crystal at 511 keV are also reported (data from [14])

semiconductor- or scintillator-based detectors for gamma-ray imaging differ more on the basis of their intrinsic detection efficiency η rather than on their principle of operation.

The faint light signal from a scintillator for a single gamma-ray needs to be amplified with high gain (and using high voltages ≅kV) by the readout photodetector (e.g., a PMT), whereas the charge (electrons or holes) from a single gamma-ray in a semiconductor can be collected with a relatively low voltage (≅0.1 kV) and integrated with a low gain. These are additional practical advantages of the semiconductor-based systems.

2.2 *Detection Efficiency of Semiconductor Detectors*

For semiconductor detectors with low Z and low density (e.g., Si) (Tables 2.1 and 2.2, Fig. 2.5) η is unacceptably low for high-energy gamma-rays (e.g., 140 keV) due to their limited active thickness (typically ≤1 mm) with respect to scintillator crystal thicknesses (several mm). With this major limitation, silicon based detectors have find a role in imaging detectors for low-energy X-ray or gamma-ray applications (e.g., ^{125}I, microCT), where this mature detector technology can offer high intrinsic spatial resolution for in vivo imaging. On the other hand, edge-on irradiation geometry of thin low Z detectors permitted to reach great attenuation lengths even for high-energy for 511-keV PET imaging. Conversely, high Z, high density semiconductor based detectors (e.g., CdTe, CdZnTe) (Tables 2.1 and 2.2) offer higher absorption efficiency than scintillator based detectors of the same active thickness (Fig. 2.6). However, the active substrate thickness of those compound semiconductor detectors for direct-detection imaging applications is limited to few millimeters,

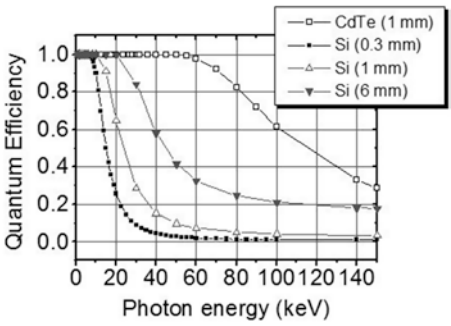

Fig. 2.5 Quantum efficiency of Si (0.3, 1 and 6 mm thickness) and CdTe (1 mm thickness) detectors (calculated with XCOM data from [14])

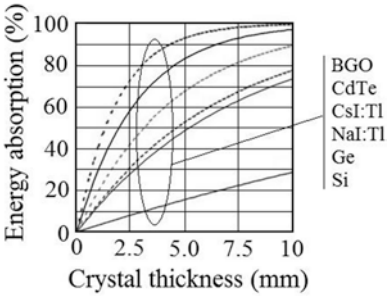

Fig. 2.6 Comparison of the radiation energy absorption at 150 keV in various thicknesses of scintillator and semiconductor detectors (adapted from [15])

while scintillator crystals are available thick enough to provide high absorption efficiencies at high gamma-ray energies (Fig. 2.6). On the other hand, an increased thickness of the scintillator layer increases the light spread and decreases the intrinsic spatial resolution obtainable with indirect-detection systems.

For semiconductor detectors, their intrinsic spatial resolution depends on the lateral charge spread which can be controlled via electrode configuration and by application of a high electric field, since most drift charge collection occurs close to the collecting electrode. This implies that for semiconductor detectors, the pixel size can be optimized down to dimensions as small as technically feasible or down to otherwise physically limited dimensions (e.g., small pixel effect, lateral charge diffusion, charge sharing due to photon fluorescence or Compton scatter) whilst for scintillator detectors, the spatial resolution is related inversely to absorption thickness and hence to absorption efficiency.

2.3 Hybrid Pixel Detectors

The term hybrid detector indicates an assembly made by coupling electrically a semiconductor X-ray or gamma-ray radiation detector (the sensor) with a microelectronic circuit for signal readout. These detectors were originally developed for

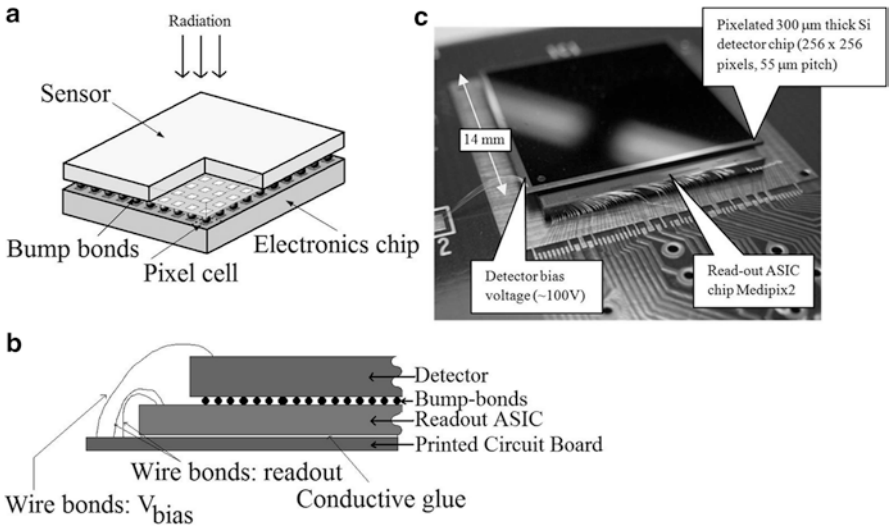

Fig. 2.7 (**a**) Scheme of a hybrid pixel detector, (**b**) scheme of detector connections, (**c**) photo of a hybrid pixel detector (Medipix2) on the printed circuit board [17]

high energy physics applications [16] (Fig. 2.7). Hence, at variance with a monolithic detector in which both the sensor and the readout functions are implemented on the same semiconductor substrate, in a hybrid detector one can optimize independently the efficiency of radiation detection and the performance of the signal processing, since the two functions are implemented on two separate semiconductor substrates which can have completely different properties. For example, the analog (micro) electronics for signal amplification and discrimination as well as the digital logic for signal processing are usually realized on low-resistivity silicon wafers, whereas the semiconductor substrate for the realization of the radiation detector can be, e.g., high-resistivity silicon, Si:Li, epitaxial GaAs, semi-insulating GaAs, CdTe, CdZnTe. These semiconductor detectors have a large energy bandgap and they usually work at room-temperature, but a moderate cooling may be employed for reducing the detector leakage current and for managing the heat load of the associated readout electronics.

For imaging applications, either a pixel geometry or a microstrip geometry have been implemented for the detector. In a hybrid pixel detector, the radiation field is sampled spatially by a 2D matrix arrangement of detector elements—pixels—and the semiconductor sensor is electrically connected pixel by pixel to a pixelated readout integrated circuit, *ad hoc* designed (Application Specific Integrated Circuit, ASIC) [18] whose pattern geometry matches that of the pixel detector. The high-density interconnection uses typically the bump-bonding technology, i.e. interposition of micro (≅10 μm) metal bumps (gold, indium, solder) between the pixel and the electronic cell [19] (Figs. 2.8 and 2.9). The production yield of bump-bonding in terms of fraction of good contacts over the detector array is usually

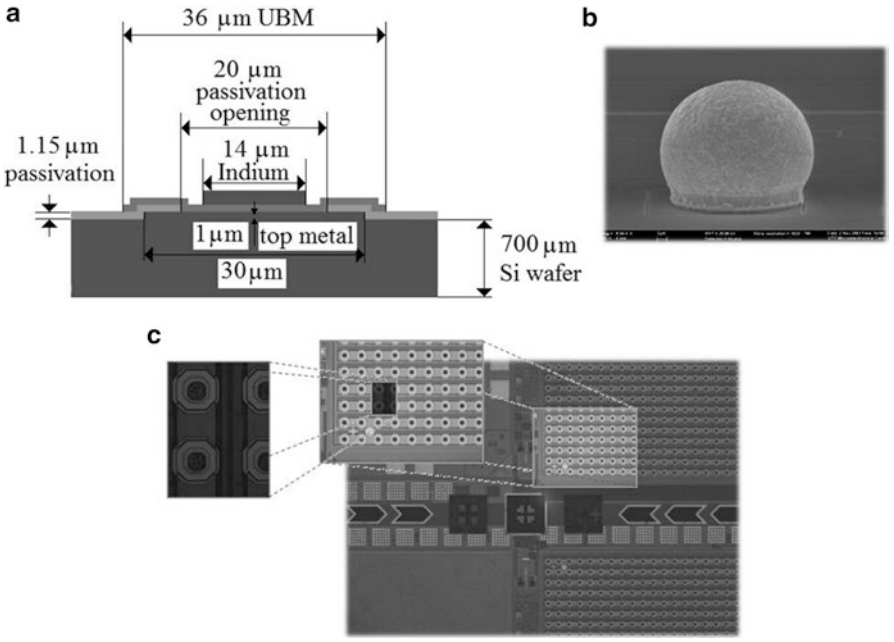

Fig. 2.8 Example of high-density indium bump-bonding: the Medipix2 hybrid pixel detector bump-bonded to a 700-µm thick silicon pixel detector with 55-µm-pitch pixels. (**a**) Scheme of the detector pixel, where a 36-µm square under-bump metallization (UBM) deposition is made at detector and ASIC substrates. (**b**) Scanning electron micrography of a 14 µm indium bump. (**c**) Patterning at the ASIC substrate showing, in successive magnifications, the pixel matrix array and the pixel bonding pads (courtesy of Z. Vykydal, IEAP, CTU, Prague)

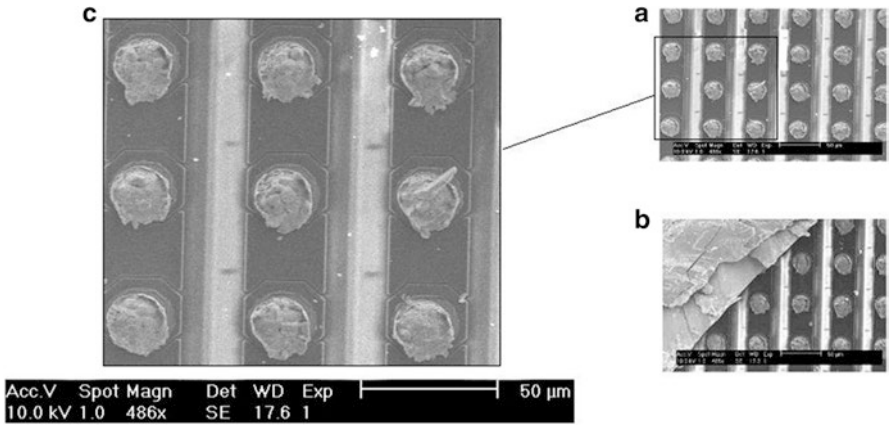

Fig. 2.9 (**a**) Scanning electron microscopy of a hybrid pixel detector, showing the indium bumps deposited with a pitch of 55 µm on the ASIC circuit. In (**b**), after hybridization, the sensor (a 1-mm thick CdTe detector) has been partially removed with a high strength force (scratched assembly). In (**c**) is a zoomed image of the bumps (courtesy of E. Manach, CEA-LIST, Saclay, France)

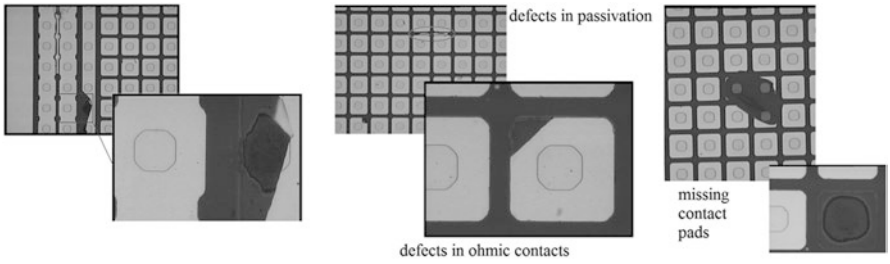

Fig. 2.10 Microphotography of a semiconductor pixel detector (CdTe, ohmic contacts) with square pixels of 55 μm pitch, prior to hybridization with the readout ASIC, showing various types of localized defects in contacts manufacturing. In the case shown the fraction of defective contacts over the matrix array was found to be only 10^{-4} (courtesy of J. Ludwig, Freiburg University, Germany)

>95 % and it may be >99.9 %; a high yield is found as well for pixel detector contact technology (Fig. 2.10).

The bump-bonding can be obtained either at high temperature (e.g., from 400 °C down to 180 °C, at the temperatures of solder bonding) or in a "cold" condition (e.g., 80 °C), as occurs in the flip-chip indium bonding technique where typically a bump is positioned on a specific bonding pad realized on both wafers (sensor and readout chip) and the two wafers are then pressed together with a force of some tens of N per chip, in order to establish mechanical and electrical connection [20]. The choice of the bonding technology depends also on the temperature requirements of the semiconductor substrate: for example, CdZnTe detector arrays are sensitive to high temperature exposures, so that hybridization is carried out in the range 60–150 °C [21]. External connection of the readout chip to the readout interface is normally done with fine pitch ultrasonic wire bonding. In this imaging detector one continuous electrode is on one side (into which the radiation is incident) and a pixelated electrode structure is on the other side (Fig. 2.11).

In a hybrid detector each pixel may correspond to the junction of a diode structure (e.g., Fig. 2.11, where a p^+n junction is formed on the pixel side), or the detector works in the photoconductive (ohmic) mode. By applying a voltage bias between the two electrode sides, an active region is formed as the depletion layer in a junction detector or as the whole semiconductor substrate volume, for ohmic detectors. The electron–hole pairs—generated by the interaction of gamma-ray photons in the detector active region—are separated by a high-strength electric field, fast enough to prevent recombination. Charge drift then occurs towards corresponding electrodes, and at the end of the drift process an induced charge (either electrons or holes, depending on the voltage polarity) can be collected at the pixel side.

The bias voltage polarity is selected so as to prefer the collection of the charge carrier type which exhibits the best transport properties in the semiconductor substrate, in the presence of charge trapping and de-trapping effects, material defects, different electron and hole mobilities, lateral charge diffusion (Fig. 2.12). The coordinate of the hit pixel(s) identifies the interaction position, while the information on

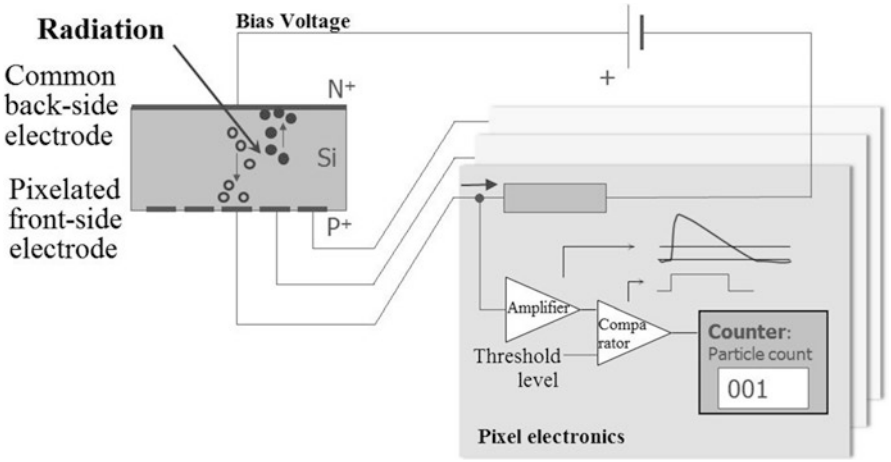

Fig. 2.11 Explaining the principle of operation of a hybrid pixel detector working in single photon counting. A single detector pixel is shown, realized as a p–n junction on a high resistivity Si substrate. The radiation-generated electron–hole pairs drift in the sensor active region under the applied electric field and the total charge reaching the pixel electrode is collected and processed by the pixel cell electronics. Either holes (as in the case depicted) or electrons can be collected, in dependence of the bias voltage polarity. The signal is passed through a charge-sensitive amplifier, its level is compared with a set threshold level and the number of interaction events (photons) is counted, for which the signal is higher than the threshold (courtesy of J. Jakubek, IEAP, CTU, Prague)

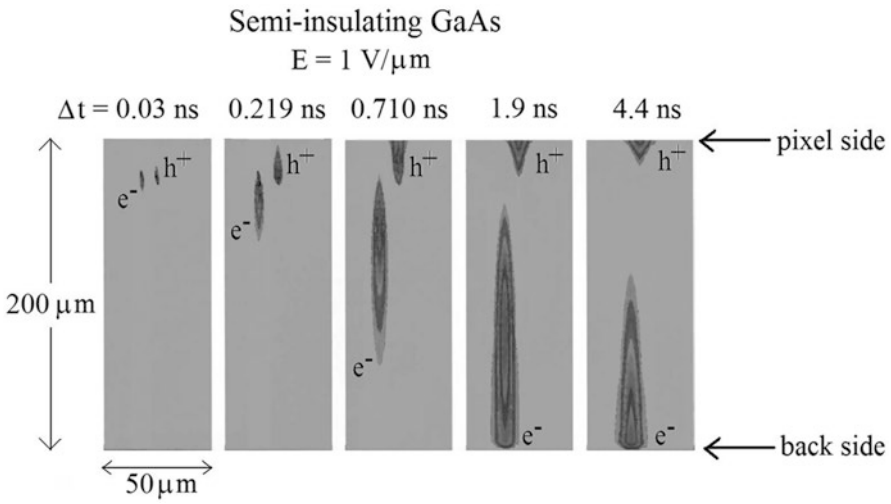

Fig. 2.12 Plot of the time evolution of the spatial distribution of 10,000 e–h pairs generated by a 42-keV photon interacting in a semi-insulating GaAs pixel detector, as determined by simulations. The 200-μm thick detector is biased at 200 V with the pixel side grounded (hole collection). The detector has 50-μm pitch pixels and the charge creation is supposed to occur at a depth of 25 μm below the surface on the pixel side, at the center between two adjacent pixels. For display convenience, the cloud of electrons (e^-) has been slightly separated laterally with respect to the cloud of holes (h^+). The five plots show the drift of the e^- and h^+ clouds towards the collecting anode and cathode, respectively, as well as their lateral and vertical spread by electrical diffusion, at different time intervals Δt from the creation time, from 0.03 up to 4.4 ns. The grey scale of the e^- and h^+ distributions indicates the charge carrier concentrations in the semiconductor bulk (data from [28], reproduced with permission)

the photon energy is given by the total collected charge, which is proportional to the deposited energy in the pixel(s). The signal due to the collection of the charge generated by a single photon or by many interacting photons is processed in each pixel electrode.

A hybrid detector can work in current mode or in photon counting mode. In single photon counting—where the pixel electronics in the readout chip is fast enough to identify and process each interacting photon during the exposure—the readout electronics of each cell may include a charge sensitive preamplifier, a single- or multiple-level discriminator and a counter or a series of counters (Fig. 2.11). A matrix-level global discriminator is normally settable for all pixels, while fine regulation of this threshold at pixel level is generally available in readout ASICs in order to compensate for small differences in the amplification of the cells. The global threshold can be regulated via the interface electronics which connects the hybrid pixel detector to the digital acquisition system. With just one discriminator level, the image matrix readout at the end of the exposure contains the total number of photons depositing, in each pixel, an energy higher than the threshold. A usual setting for this energy threshold is just above the system noise. With two discriminator thresholds available per pixel, energy windowing can be implemented for discriminating single photons on the basis of their energy, e.g. as required in gamma-ray imaging in nuclear medicine with radioactive tracers for radionuclide identification and tissue scatter rejection. With the availability of more than one counter per pixel and multiple thresholds, multi-energy ("color") single photon imaging is feasible (e.g., [22]), thus adding spectroscopic performance to the photon counting scheme.

In current mode, the collected signal at readout electrodes is due to the total induced current by all photons interacting in the detector pixel during the exposure time. This mode is typically used for high intensity radiation fields as occurs, e.g., for X-ray Computed Tomography imaging.

2.4 Microstrip Imaging Detectors

Microstrip detectors, originally developed for high energy physics and then used in medical imaging for digital radiography [23–25] and digital autoradiography [26, 27] use a semiconductor substrate (e.g. Si, CdTe, CdZnTe, GaAs, HgI_2) of thickness typically a fraction of a mm, on which segmented electrodes are deposited in the form of thin (≅10–20 μm), long (e.g. 3–6 cm) strip metal contacts. These strips act as charge collecting electrodes for the underlying detector structures, which are either *p–n* junctions or Schottky barrier strip diodes (Fig. 2.13).

For Cd(Zn)Te, ohmic contacts as well as metal–semiconductor barriers can be realized on either or both detector sides. In very schematic and simple terms, the principle of operation of microstrip detectors is the following. For the realisation of a 1D detector, only one side of the detector (Junction side) is equipped with *n* parallel microstrips, and the opposite side is covered with a uniform contact. Under external bias, radio-induced charges (electrons and holes) drift toward their respective collecting electrode, and on the Junction side, single-polarity charge is

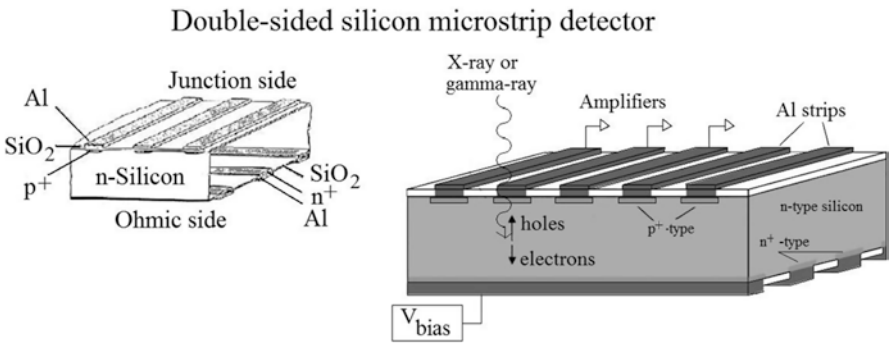

Fig. 2.13 Schematic drawings of a double-sided silicon microstrip detector, showing principle-of-operation of the device for 2D photon counting. On a (Junction) side a high-resistivity *n*-type silicon substrate, p^+ strip are implanted to form a series of parallel junctions; n^+ parallel strips are implanted on the back (Ohmic) side, orthogonally to the other set of strips. An aluminum contact is deposited on the strips for electrical connection to the readout circuit

collected only in one or a few adjacent strips. This gives the 1D position information of the coordinate of photon interaction. In 2D (double-sided) microstrip detectors, the back (Ohmic) contact is also equipped with *m* parallel microstrips, but orthogonal to the *n* microstrips on the junction side.

The Ohmic microstrips collect single-polarity charge carriers (electrons, in the case of reverse-biased microstrip detectors) and provide a 1D position information, too. The charge drift motion lasts a few ns, typically. By analyzing the temporal coincidence of signals on the Junction and Ohmic sides, the coordinate on one side (*X*) can be coupled (electronically on-line or via software, off-line in list-mode acquisition) with the orthogonal coordinate (*Y*) on the other side, giving a hit count in the projected (*X*, *Y*) coordinates of the photon interaction point. This allows one to reconstruct the number of interacting photons in each "pixel" of the $n \times m$ image matrix. In the case of charge sharing between adjacent microstrips, which produces above-threshold signals in (a few) close strips, the derivation of a *center-of-charge* (spatially weighted sum of strip charge signals) allows the spatial resolution to increase beyond the limit intrinsically given by the strip pitch ω (mm), up to $(2.35/\sqrt{12})\cdot\omega$ (mm FWHM) for a uniform distribution of irradiation position between strips.

3 Imaging Requirements of SPECT and PET Small-Animal Scanners

3.1 MicroSPECT

^{99m}Tc and ^{125}I are the basic radionuclides in small animal SPECT imaging [1]. The latter has gained attention recently due to its low-energy X-ray (27.5 and 31.0 keV, with total emission probabilities ≅90 %) and gamma-ray emissions (35.5 keV),

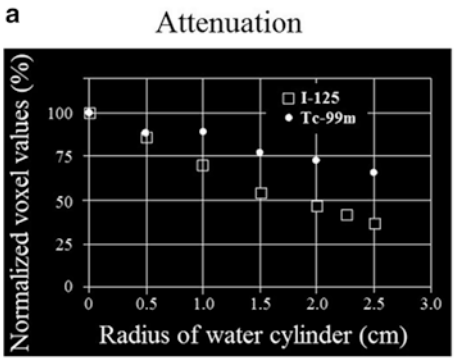

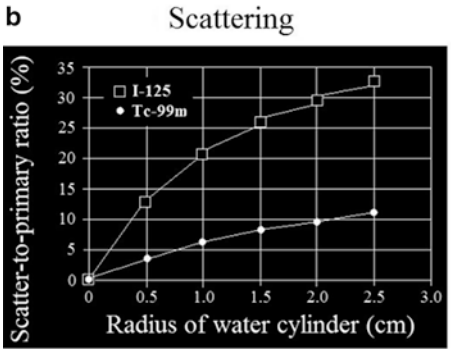

c

Simulation parameters

	I-125	Tc-99m
Source energy	27.5 keV	140 keV
Energy resolution FWHM	26%	12%
Energy window	10–50 keV	126–161 keV
Compton scattering	0.182 cm^{-1}	0.150 cm^{-1}
Photoelectric absorption	0.194 cm^{-1}	0.0009 cm^{-1}
Rayleigh scattering	0.0541 cm^{-1}	0.0028 cm^{-1}
Total attenuation	0.430 cm^{-1}	0.154 cm^{-1}

Interaction data for water

Fig. 2.14 (**a**) Simulation of the level of radioactivity for a ^{125}I source (*open squares*) or a ^{99m}Tc source (*filled squares*) as a function of the radius of a water cylinder in which the source is immersed axially. The source is a radioactive sphere of 2 mm radius. Data show that due to photon attenuation, the reconstructed radioactivity can be underestimated. (**b**) In the same geometry, the simulated scatter-to-primary ratio is significantly higher for ^{125}I than for ^{9m}Tc. The parameters and interaction data used in the simulation are indicated in the table in (**c**) (data from [32], reproduced with permission)

which allow to use collimators with small apertures and provide high system spatial resolution [29], but which also cope with the detection efficiency of low Z (e.g. Si:Li) [30] or thin (e.g. 1 mm CdTe) [31] semiconductor detectors. For imaging tasks and quantification of radioactive distribution in small animal organs, tissue scattering and attenuation have to be considered, since the different photon energies of the two radionuclides determine a specific different scenario. In fact, at 27.5 keV the Compton and photoelectric attenuation coefficients in water are comparable, while at 140 keV photoelectric absorption is negligible with respect to scattering (Fig. 2.14c, Table 2.3).

Monte Carlo simulations [32] showed that in a water cylinder of a few cm radius, used as a mouse phantom, the scatter-to-primary ratio (SPR) can be as high as 30 % for ^{125}I and 10 % for ^{99m}Tc (Fig. 2.14b). The total attenuation can determine an underestimation of the reconstructed activity at the center of the phantom by as much as ≅25 % (^{99m}Tc)–50 % (^{125}I) (Fig. 2.14a).

Table 2.3 Photon cross sections (linear attenuation coefficients) in water at characteristic energies for small animal imaging (data from [14])

Energy (keV)	Compton (cm^{-1})	Photoelectric (cm^{-1})	Rayleigh (cm^{-1})	Total attenuation (cm^{-1})
27.5	1.82×10^{-1}	1.94×10^{-1}	5.41×10^{-2}	4.30×10^{-1}
140.5	1.50×10^{-1}	9.05×10^{-4}	2.77×10^{-3}	1.54×10^{-1}
511	9.58×10^{-2}	1.78×10^{-5}	2.15×10^{-4}	9.60×10^{-2}

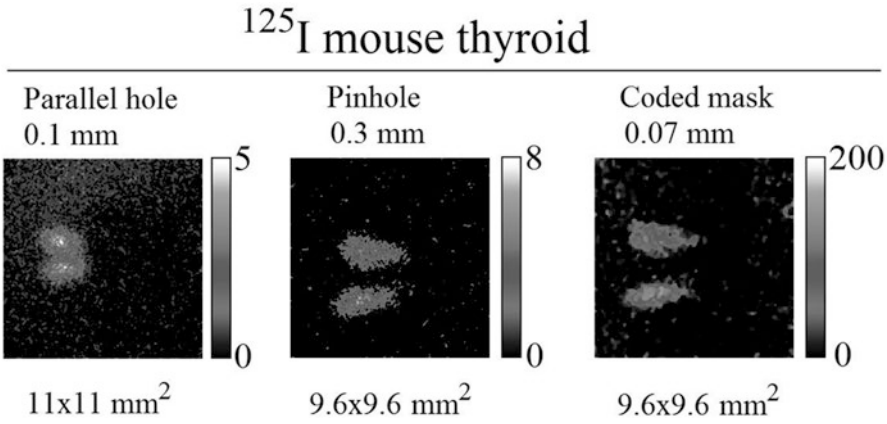

Fig. 2.15 Example of the improvement in sensitivity and a high spatial resolution provided by collimator aperture multiplexing. The mouse thyroid was imaged in vivo with ^{125}I radiotracer using the same CdTe detector (1 mm thick, 55 μm pixel pitch) coupled either to a parallel hole collimator, or to a 0.3 mm pinhole or to a coded mask with 460 apertures of 70 μm size. The exposure time per image was fixed to 20 min. The coded mask image was median filtered with a two pixel kernel

Thus, high energy resolution as a method of scatter rejection could more be of concern at low photon energies than at 140 keV, where SPR values are expected to be below 10 % in the injected mouse.

At variance with scintillator based detectors, semiconductor detectors offer good energy resolution at ^{125}I energies. However, tissue Compton discrimination at ≅30 keV is difficult since the scattered photon energy is too close to the primary photon energy. On the other hand, the actual influence of tissue scattering in low-count rate small animal imaging is task dependent (and observer dependent), and in imaging of small organs at a reduced Field of View (FoV) with a low injected activity, the system *sensitivity* could play a more crucial role. System sensitivity in SPECT with semiconductor detectors can be recovered by exploiting signal multiplexing (e.g., multi-pinhole apertures) and/or complex detector structures with multiple heads. As an example of the first solution, Fig. 2.15 shows a planar in vivo ^{125}I image of the mouse thyroid taken with a high resolution CdTe pixel detector, successively coupled to a parallel hole collimator with 0.1 mm holes, or to a 0.3 mm pinhole or to a coded mask with 460 holes of 70 μm size. Here, the count rate was increased by two orders of magnitude with the coded mask as compared to a 0.3 mm aperture pinhole, yet providing sub-mm spatial resolution.

A distinctive feature of semiconductor array detectors is that they could in principle be used for both SPECT and X-ray Computed Tomography (CT) small animal imaging. Indeed, in addition to working in current mode with high-flux X-ray imaging capabilities, Si, CdTe and CdZnTe based pixel detectors working in single photon counting have been produced, which can be used at the same time for low-count rate gamma-ray imaging and for high-count rate X-ray (micro)CT. An example is the CdTe gamma-ray/X-ray camera built by AJAT Oy Ltd. (Espoo, Finland) with 44×44 mm^2 sensitive area of 0.25×0.5 mm^2 pixels on a 0.75-mm thick substrate [4], or the Si [33] or CdTe [34, 35] based pixel detectors realized by the Medipix2 collaboration for X-ray imaging as well as for gamma-ray imaging [6, 36]. Those semiconductor detectors provide a useful spatial resolution for combined X-ray/gamma-ray imaging on the same small animal SPECT/CT semiconductor system.

3.2 MicroPET

There are two basic requirements for high performance small-animal PET imaging: high sensitivity and high spatial resolution; current commercial systems show 1–2 mm FWHM resolution with 2–7 % sensitivity (see Sect. 6). Spatial resolution in microPET is limited by fundamental processes of positron emission and annihilation, and improvements come from the reduction of limitations from detector geometry (detector dimensions and depth of interaction effects) and from detector physics (detector internal scatter and multiple interactions). A semiconductor based scanner can provide the solution toward sub-millimeter resolution, but improvements in sensitivity are expected as well, in a technological trend toward a target performance of detecting in vivo 0.1–1 mm^3 active volumes with 20 % sensitivity. High sensitivity results from high solid angle coverage, high detection efficiency and efficient use of all interaction events. As a typical strategy to improve sensitivity, the high density detector material should surround the animal body and its absorption thickness should be sufficient at 511 keV. A stack of thin (semiconductor) detectors is a possible solution. Gamma mean free path at 511 keV in semiconductor detectors range from 18 to 19 mm for CdTe and CZT, to 23.1 mm for Ge and 49.5 mm for Si, as opposed to 10.4 mm for a BGO crystal (Table 2.2). These figures imply that adequate sensitivity would be provided by a detector with $\cong$20 mm absorption thickness for CdTe, CZT and Ge, and $\cong$50 mm for Si. For adequate field coverage in mouse PET imaging with semiconductor crystals, the axial FoV could be $\cong$40 mm and the transaxial FoV $\cong$ 50 mm, with available detectors.

As described in Sect. 3.1, imaging in small animals may not require necessarily the precise determination of the energy of photons transmitted by the animal body, since the tissue interaction volume is very limited and Compton scattering in the animal body is of decreasing relevance as the photon energy increases (Table 2.3) and can be modeled. For PET energies, at 511 keV, the Compton scattering cross

section in water is 64 % of that at 140 keV, so that following the discussion related to Fig. 2.14, the scatter-to-primary ratio in a small-animal is estimated to be less than 10 % and it is less important than in clinical PET. This implies that in small animal PET imaging, photon counting (without energy information) could be a suitable acquisition strategy. As a consequence, it may not be necessary to determine the full energy peak in the spectroscopic analysis of the energy deposition by a 511-keV photon in the detector material. This signal analysis is usually performed in PET detectors where photons are counted if their energy deposit in the detector material is higher than a given high threshold (e.g., 350 keV). If Compton interaction in the detector is to be exploited for event identification, then low Z semiconductors can play a role. For example, at 511 keV, for BGO scintillator the Compton cross section is 53 % of the total attenuation coefficient whilst for Si, the Compton fraction is 99 % (Table 2.2). Moreover, in low Z materials the probability of multiple incoherent scattering is low with respect to high Z scintillator crystals of comparable thickness, this meaning that for 511-keV incident photons the fraction of single Compton interaction events is large. As a consequence, identification of the position of the (first) Compton interaction is favored and the line of flight of the two back-to-back 511 keV photons can be determined with greater accuracy than in the case of multiple interactions in the scintillator(s).

4 CdTe and CdZnTe Semiconductor Detectors

CdTe:Cl single crystals are typically grown by the Traveling Heater Method (THM) in ingots as large as 75–100 mm in diameter: this allows to cut wafers up to 50×50 mm^2 from which imaging detectors as large as 25×25 mm^2 can be derived [37], with a typical thickness of 1 mm. On such crystals, either ohmic or Schottky contacts are realized, in order to fabricate an ohmic-type (photoconductive) detector or a Schottky-type detector (Fig. 2.16).

CdTe detectors equipped with ohmic contacts show a stable response over long times and moderately good energy resolution (8–9 % at 122 keV), whereas Schottky contacts result in CdTe detectors with higher energy resolution (4–5 % at 122 keV) and count rate capabilities (Fig. 2.16). Stability of response refers to the so-called *polarization* phenomenon, observed for Schottky CdTe detectors, whereby soon after applying the detector bias voltage the energy resolution degrades and the photopeak channel decreases, this process continuing for some hours after start of functioning. Working at high bias voltages, as well as periodically interrupting the bias, helps reducing the polarization effect [37].

CdTe diode detectors show less leakage current than CdZnTe detectors of comparable thickness and this allows to use higher bias voltages: this, in turn, permits to exploit the better charge transport properties of CdTe with respect to CdZnTe which results in better energy resolution. At 22 keV, the resolution of a $3 \times 3 \times 1$ mm^3 commercial CdTe diode detector can be as good as 0.43 keV [10] (see Fig. 2.16).

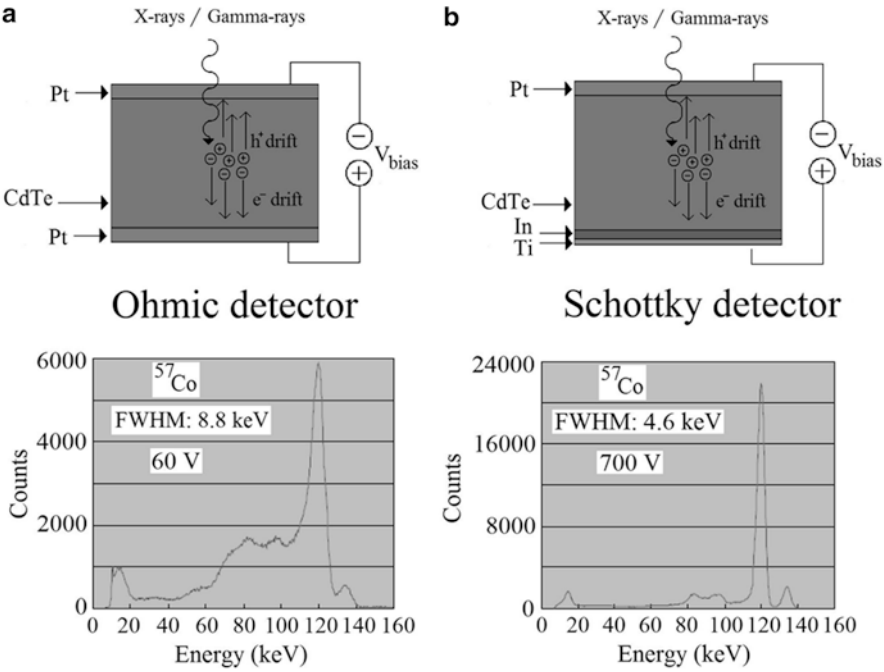

Fig. 2.16 Scheme of ohmic (**a**) a Schottky-type (**b**) CdTe detectors, and corresponding typical spectroscopic performance for 1-mm thick single-element detector of 4×4 mm^2 [37]

CdTe and CdZnTe semiconductor detectors allow to assemble compact and lightweight gamma cameras. However, since it is difficult and expensive to produce large volume semiconductor crystals with good spectroscopic quality, typical detector arrays can be realized on volumes up to 20–30 mm by side and 1–2 mm thickness. The pixel size is around 1 mm but pitch values of a fraction of a mm have been realized, and a pitch of ≅50 μm is feasible. The limited sensitive area suggests to cover a large FoV and to increase system sensitivity by assembling a few detector heads around the animal. Several groups have developed compact gamma cameras based on thick CdTe or CdZnTe semiconductor detectors, for small animal planar and SPECT imaging, with single-head units as well as multiple-head detectors disposed around the animal with suitable collimators. In its turn, a single detector unit may be composed of a mosaic of small matrices detectors (e.g., 4×4): this approach allows to work with thick detector substrates (e.g., 5-mm thick) which however are typically of small-size pixels (e.g., 1.6×1.6 mm^2) [12]. Array matrices of pixel detectors based on CdTe or CdZnTe substrates can be as large as 48×48 [38] or 64×64 at 380 μm pitch [39], 120×80 at 130 μm pitch [40], 256×256 at 55 μm pitch [5] (Table 2.4).

Table 2.4 Characteristics (substrate thickness L, pixel pitch ω, aspect ratio L/ω, energy resolution $\Delta E/E$ at 122 keV) of some CdTe and CdZnTe detectors for gamma-ray imaging

Material	L (mm)	ω (mm)	L/ω	$\Delta E/E$ (%)	References
CdTe	0.5	0.675	0.7	7.3	[41]
CdTe	0.75	0.5	1.5	3.9	[4]
CdTe	1	0.055	18.2	–	[5]
CdTe	1	0.35	2.9	2.5	[42]
CdTe	1.2	1.4	0.9	4	[43]
CdTe	1.5	0.38	3.9	–	[44]
CdTe	2	3.07	0.7	5	[45]
CdTe	5	1.4	3.6	7.8[a]	[46]
CdZnTe	2	0.38	5.3	10[a]	[38, 39, 47, 48]
CdZnTe	3	0.5	6.0	4.7	[21]
CdZnTe	5	2	2.5	3–4	[49]
CdZnTe	5	2.46	2.0	–	[50]
CdZnTe	5	2.1	2.4	4.5[a]	[51, 52]
CdZnTe	5	1.8	2.8	3.6[a]	[53]
CdZnTe	5	1.6	3.1	4.4	[54]
CdZnTe	6	4.5	1.3	6.5	[55]

[a]At 140 keV

5 Semiconductor Based SPECT Scanners for Small-Animal Imaging

In the following, some experimental scanners based on semiconductor detectors, designed for small animal SPECT imaging, will be described, with the aim of providing technical details useful for detector technology evaluation.

5.1 University of Arizona SPECT/CT System

The University of Arizona group (Center for Gamma-Ray Imaging, CGRI) has developed CdZnTe detector arrays for gamma-ray imaging with sub-millimeter pitch, with most work dedicated to the development of 380-μm-pitch 64 × 64 detector arrays [38, 39, 44, 47, 56, 57]. A prototype SPECT system (combined with a CT head for dual-modality SPECT/CT imaging) for small animal imaging using one such detector head has been realized in 2002 [44, 47] and is currently in use for ^{99m}Tc mouse imaging studies (Fig. 2.17). Its spatial resolution is 1–2 mm [44].

The 25 × 25 × 1.5 mm^3 CdZnTe detector ([44], or 25 × 25 × 2 mm^3 CdZnTe detector, [47]) is segmented on one side, via gold contact electrodes, in 330 μm square pixels with 50 μm inter-pixel gap, while a continuous gold contact is on the other

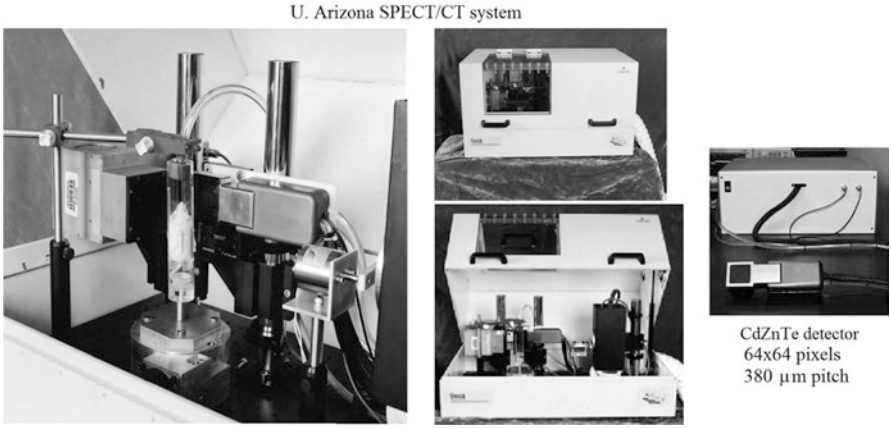

Fig. 2.17 Views of the dual modality SPECT/CT system developed by the Center for Gamma-Ray Imaging at the University of Arizona [60], based on a CdZnTe hybrid pixel detector. The detector head (*rightmost image*) is also used for spot imaging

Table 2.5 Projects done or ongoing with the small animal SPECT/CT system at U. Arizona [58]

Study	Radiotracer
Induced lung adenomas in mice	^{99m}Tc-sestamibi, glucarate, depreotide
Lymphedema in mouse models	^{99m}Tc-sulphur colloid
Detection of bone metastasis in mice	^{99m}Tc-MDP
Imaging mouse femora attached by strain gauges	^{99m}Tc-MDP
Neuroblastoma bone metastases	^{99m}Tc-MDP
Mechanism of Glucarate uptake in tumors	^{99m}Tc-glucarate
Tumor targeting of ^{99m}Tc-VIP	^{99m}Tc-VIP-Taxol
Apoptosis imaging in tumors	^{99m}Tc-C2A-GST
Dynamic SPECT imaging of mouse and rat lung	^{99m}Tc-MAA
Imaging bone metastasis in mice	^{99m}Tc-MDP
Tumor glucose uptake	^{99m}Tc-ECDG

side. The continuous electrode is at a negative −140 V potential with respect to the pixel side, where the charge collected is due to electrons. The acrylic mouse holder (a 1-in. diameter tube) is vertical. A polyacetal (Delrin™) nose piece is used to further restrain the animal and to connect to the tube for gas anesthesia. The pixel detector is indium bump-bonded to a readout ASIC. The system is mounted on an optical table and contained in an Al enclosure of $79 \times 48 \times 46$ cm^3 with 1.5 mm Pb shielding. This is a very compact imaging system whose basic design is a potential provider of reliability, ease of operation, low cost of realization and maintenance. It is in use since 2002 for various mouse imaging studies, a list of which is provided in Table 2.5.

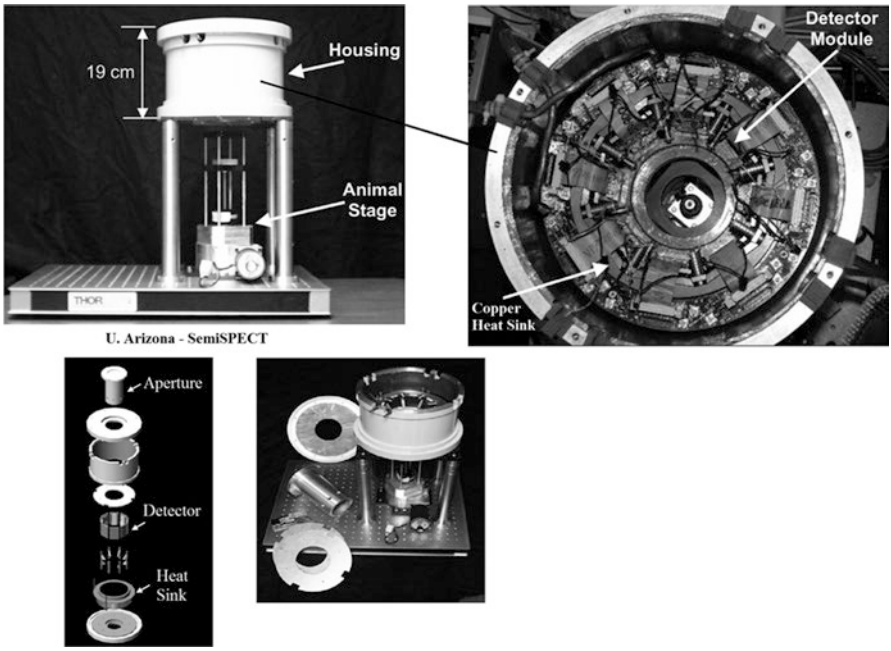

Fig. 2.18 Views of the small animal SPECT system SemiSPECT developed by the CGRI group at the University of Arizona [48, 60]. The system is based on eight CdZnTe semiconductor detector modules each of $27 \times 27 \times 2$ mm^3 and 64×64 pixels

5.2 University of Arizona SemiSPECT System

The evolution of the combined SPECT/CT system realized by the CGRI group at U. Arizona is the SemiSPECT small animal SPECT system (Fig. 2.18) [48, 59]. This is a very complex and high performance small animal SPECT imager, which employs eight compact detector heads based on CdZnTe detectors each realized on $27 \times 27 \times \cong 2$ mm^3 substrates (64×64 pixels each, 380 μm pitch, $\cong 2$ mm thickness) biased at −180 V. This detector has 31 % detection absorption efficiency at 140 keV ±15 % photopeak, and 54 % in the full energy range 30–200 keV. In order to reduce the leakage current, the detector heads are cooled, usually in the range from −10 to +10 °C, thus also removing the heat generated by the readout ASIC. The readout frame rate for each array is as large as 1,000 fps. The cylindrical FoV is 32 mm diameter × 32 mm height and the magnification at the center of the FoV is $m = 0.8$. The scanner is equipped with eight 0.5-mm aperture pinholes (0.77-mm effective diameter at 140 keV) which provide a calculated planar resolution of 1.80 mm at FoV center and a system sensitivity of 5×10^{-5}. The performance of the single detector head is 10 % energy resolution at 140 keV, obtained by summing the signal in a 3×3 array of adjacent pixels. A resolution of 1.45 mm FWHM has been reported

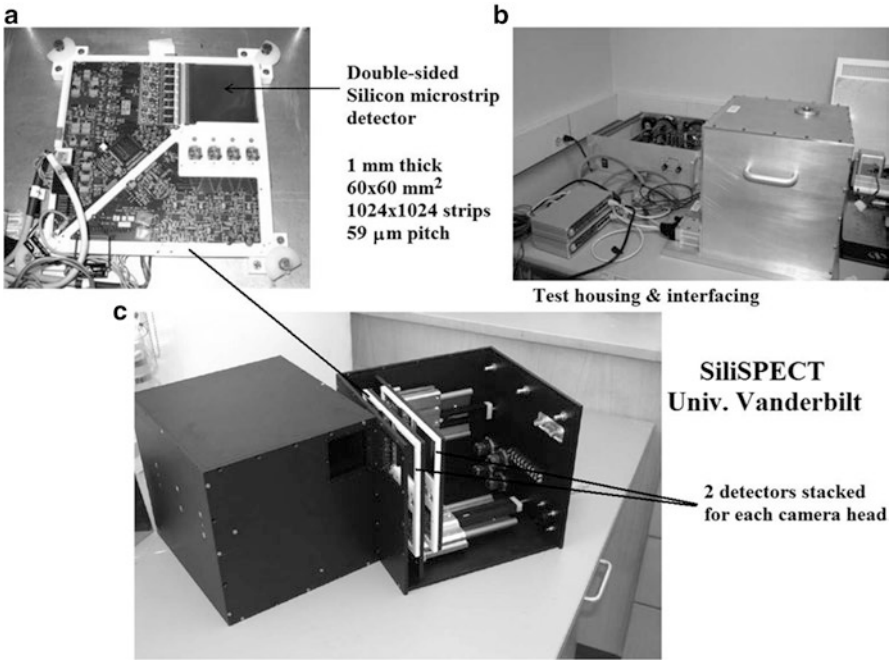

Fig. 2.19 (**a**) The detector plane of SiliSPECT, a small animal scanner based on double-sided silicon microstrip detectors built at Vanderbilt University. The figure shows the module hosting the semiconductor detector, the readout ASICS and the data acquisition electronics. (**b**) Lab test setup for housing the detector head and for interfacing. (**c**) View of the SiliSPECT prototype, made by two heads positioned at 90°, each containing two stacked detector planes ([67, 68], reproduced with permission)

[48]. Projects ongoing on small animals with the use of SemiSPECT include a study on "human lung-cancer xenografts using ^{99m}Tc-glucarate" and "Myocardial infarction in mouse heart model using ^{99m}Tc-tetrofosmin, ^{99m}Tc-glucarate" [58].

5.3 University of Vanderbilt SiliSPECT System

The group at Vanderbilt University (Nashville, TN, USA), with collaborations from University of Arizona and University of Pennsylvania, has designed and realized a small animal scanner based on double-sided silicon microstrip detectors for SPECT imaging with ^{125}I [61–66]. This is a semiconductor based, high-resolution, stationary imager which employs focused multi-pinhole collimators for imaging small-sized objects (10–15 mm in diameter), e.g. the mouse brain, at a distance of 20–30 mm (Fig. 2.19). The SiliSPECT system is an example of a highly specialized imaging system in which apparently sub-optimal parameters (low detection

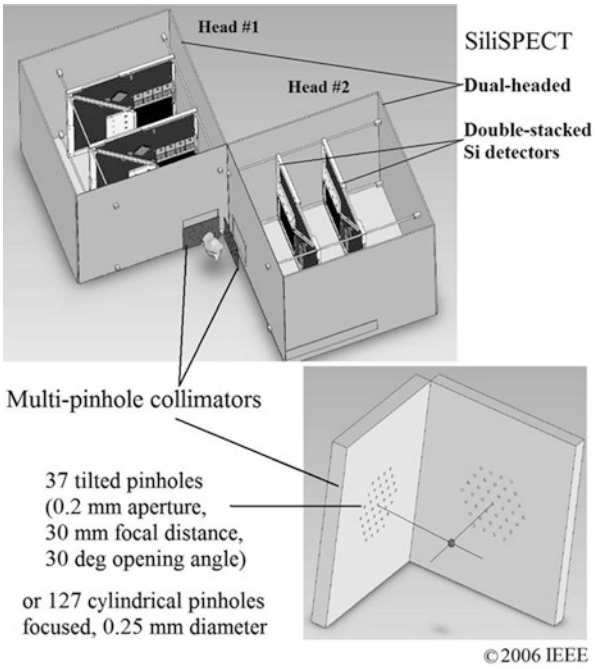

Fig. 2.20 Schematic diagram of SiliSPECT, showing the two detector heads each made of two stacked silicon microstrip detectors and coupled to a focused multi-pinhole array of small-aperture collimators (adapted from [61], reproduced with permission)

efficiency of silicon detectors, low geometric efficiency of small-aperture pinholes, small FoV, high image multiplexing) are used with advantage by focusing on specialized imaging tasks, e.g. in vivo imaging of Amyloid Beta plaques in a mouse brain with 0.1 mm resolution [66]. These systems will likely be developed in larger numbers in the future, since each animal imaging task has its own peculiarities, to be matched by specialized hardware and software solutions.

The silicon detectors of SiliSPECT have a (fully depleted) active thickness of 1 mm, starting from the first tests with a 0.3 mm thick substrate; the strip pitch is 59 μm and the detector strips are 1,024 (J side) + 1,024 (Ω side), for an equivalent sensitive area of 60.4×60.4 mm^2. The use of two stacked detectors (Fig. 2.20) allows to increase the detection efficiency, which is less than 29 % at 30 keV for a single 1-mm thick Si detector (Fig. 2.5). In the list-mode acquisition and readout circuit, time stamping for coincidence processing between J-side and Ω-side microstrips is at 40 MHz clock frequency: the strip number, event time, event ADC value, are stored in two separate lists for the two detector sides, and coincident events are recovered off-line with a resolution of about 300 ns [67]. The use of a large number of close imaging apertures determines a large multiplexing on the image plane, so that image quality parameters (sensitivity, spatial resolution, noise, SNR) are not related by simple relationships to the geometrical parameters (pinhole shape, aperture, orientation and position on the collimator plane, object distance). These relationships must describe the uncertainty in the source ray direction arising from the uncertain identification of the aperture which the gamma-ray has passed

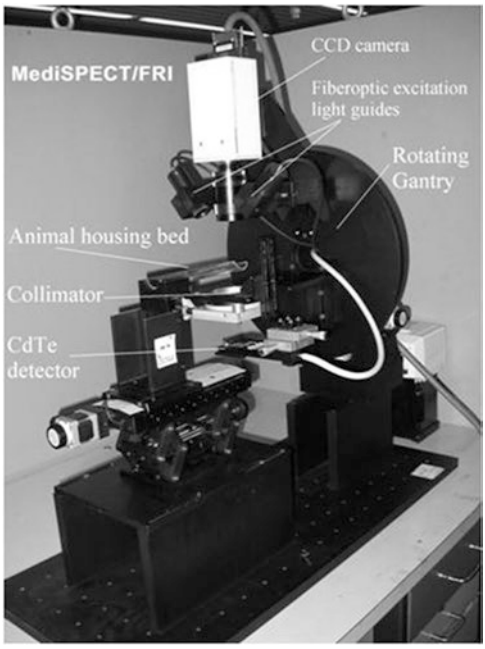

Fig. 2.21 Photo of the MediSPECT/FRI scanner for combined SPECT and planar optical imaging in small animals. The Fluorescence Reflectance Imaging part is based on a cooled monochrome CCD camera, halogen lamp with fiber optic light guides, excitation/fluorescence filters. The SPECT scanner is based on a CdTe hybrid pixel detector of the Medipix2 series, coupled to high resolution pinhole, parallel hole or coded aperture mask collimators

through. Moreover, imaging performance depends on the imaging task. For SiliSPECT, Monte Carlo simulations indicate that by using small acceptance angle (30°) knife-edge pinholes, or cylindrically shaped pinholes, focused toward the center of the FoV, the system sensitivity can reach 0.07–0.08 % using 127 focused pinholes of 0.25 mm diameter for each detector head [68]. The reported intrinsic resolution (59 μm) is the strip pitch [62], and the system sensitivity can be as good as 0.27 mm FWHM [61]. The SiliSPECT project is on-going, and experimental SPECT images of the mouse brain in vivo are expected.

5.4 University and INFN Napoli MediSPECT System

The MediSPECT small animal scanner is the SPECT part of a combined radionuclide/optical fluorescence reflectance imaging system (MediSPECT/FRI) realized by the University and INFN Napoli, Italy [36, 69–71] (Fig. 2.21). Most of the work has been dedicated to the development of the radionuclide subunit. MediSPECT is based on a CdTe detector (1-mm thick substrate) [34] hybridized via solder bump-bonding (AJAT, Finland) with the Medipix2 single photon counting ASIC [72] realized by the European Medipix2 collaboration [34, 73–75] (Figs. 2.22 and 2.23a). The semiconductor detector is a CdTe:Cl pixel detector fabricated on customer's specifications by ACRORAD (Japan) with the Traveling Heater Method (Fig. 2.23b).

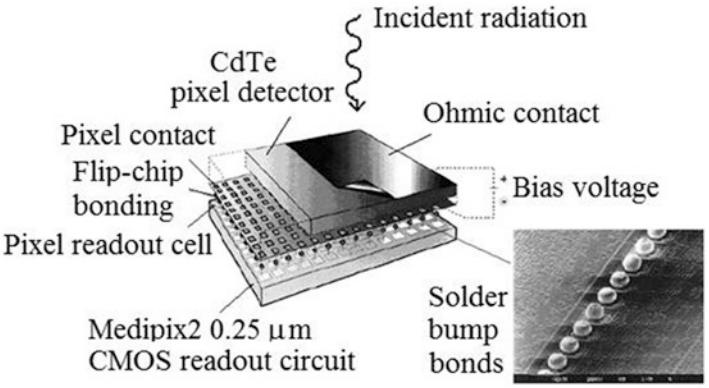

Fig. 2.22 MediSPECT is based on a hybrid pixel detector consisting of a CdTe pixel detector (1 mm thick, with ohmic contacts on both sides) and a Medipix2 readout ASIC with 55 µm square cells, as shown in this scheme

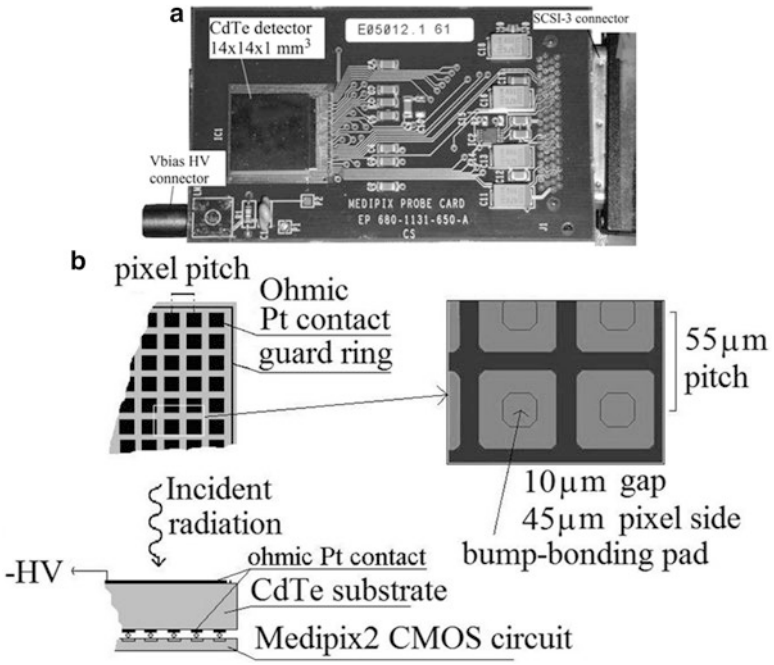

Fig. 2.23 (**a**) Printed circuit board hosting the CdTe pixel detector hybridized with the Medipix2 CMOS readout ASIC, adopted in the MediSPECT scanner. (**b**) Scheme of the CdTe pixel detector of the MediSPECT scanner

The detector has platinum ohmic contacts on both sides and its thickness is 1 mm. The contact side facing the Medipix2 readout chip side is pixelated in a matrix array of 256×256 square pixels of 45 μm side, 10 μm interpixel gap and 55 μm pitch (Fig. 2.23b), for a sensitive area of 14.08×14.08 mm^2. The detector is operated in the photoconductive mode with a bias voltage of −100 V (0.5 μA detector leakage current), determining electron collection at the pixel side. The Medipix2 cell is 55×55 μm^2 and it contains a charge sensitive preamplifier, a double threshold discriminator and a 13-bit pseudo-random counter. The Medipix2 photon counting microelectronic circuit has demonstrated a counting linearity up to 330 kHz/cm^2 [75], while the readout frame rate with the serial readout interfaces can be set typically to a maximum of a few frame per second (fps), though 50 fps have been reached with this serial interface [76] and frame rates up to 500 Hz have been reported. The dark count rate of this hybrid detector in the laboratory at room temperature is 8×10^{-3} cps/mm^2 [5]. A dedicated serial electronic interface and a software interface are used for connection to a personal computer, in order to read out the data stream from the Medipix2 ASIC and to display the 256×256×13 bits raw image.

The Medipix2 readout ASIC has two detection thresholds, which permit photon energy discrimination via counting all interacting photons with energy in a window. This feature is a common basic requirement of a gamma camera, where photon energy selection around the main photopeak of the injected radionuclide emission allows to efficiently reject the Compton scattering in the tissue. Compton rejection is normally considered important for ^{99m}Tc (140 keV) imaging, due to predominance of Compton scattering over photoelectric absorption in tissue. For ^{125}I mouse imaging the low energy of the X-ray and gamma-ray emission peaks (27.5, 31.0, 35.5 keV) increases the proportion of photoelectric events in tissue, but the scatter-to-primary ratio is even higher than that at 140 keV, as shown in Sect. 3, so that in principle Compton rejection strategies are of concern in ^{125}I imaging. On the other hand, the overall image blurring effect of Compton scattering cannot be too relevant for mouse imaging, due to limited tissue absorption length (a few cm).

This is shown in Figs. 2.24 (for ^{99m}Tc) and 2.25 (for ^{125}I), where CdTe-detector spectroscopy of the radiation emitted by an injected mice or a PMMA phantom shows limited influence of Compton scattering in the sample. However, the MediSPECT CdTe hybrid pixel detector has such a fine pitch (55 μm) that a single 140-keV gamma-ray interacting in the detector volume deposits its energy in more than one pixel, due to photoelectron range and to the emission of fluorescent radiation absorbed at a small distance from the first interaction point. This “charge sharing” effect imposes a limit to the ultimate spatial resolution of fine pitch pixel detectors. Extensive studies for this specific CdTe hybrid detector [34, 77–79] permit to derive that, on the average, a single 122 keV gamma-ray deposits its energy in 2.1 detector pixels of 55 μm pitch. This implies that the energy deposition is fractioned in two or more pixels, so that spectroscopy information is not preserved in the pixel. For this reason, the Medipix2 CdTe detector employed in the MediSPECT scanner is operated with a single low-energy detection threshold of about 20 keV, thus counting all interacting photons with energy above this threshold.

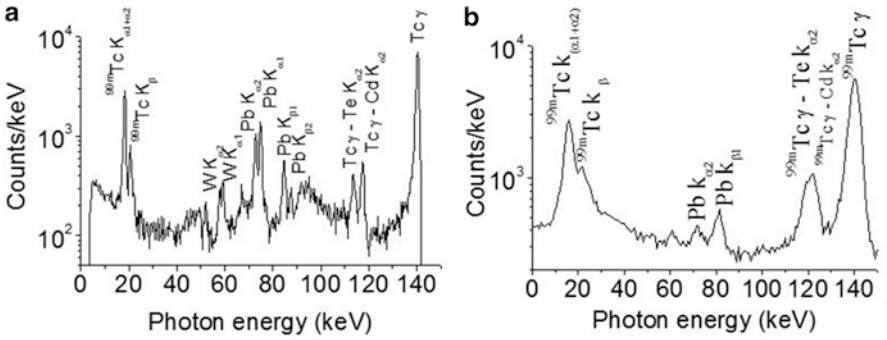

Fig. 2.24 (**a**) Pulse height spectrum of the radiation emitted from the body of a mouse injected with ^{99m}Tc radiotracer, acquired with a XR-100T-CdTe 1-mm thick detector (Amptek, Bedford, MA, USA). Photoelectric peaks are identified, arising from primary or scattered radiation from the radionuclide, from the tungsten collimators and from the lead shield around the mouse, as well as escape peaks from interaction in the CdTe detector substrate. The 140-keV photopeak has a width of 1.3 keV FWHM. (**b**) The same spectroscopy setup has been used to record the ^{99m}Tc emission from a PMMA (Lucite) phantom, so that there are 4 cm of acrylic between the source and the detector. The 140 keV photopeak has a width of 5.6 keV FWHM. The spectra have not been corrected for the energy-dependent CdTe detection efficiency

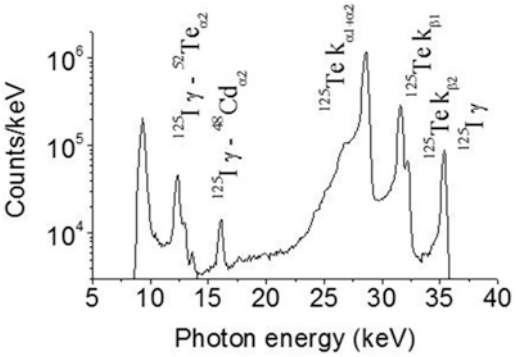

Fig. 2.25 Pulse height spectrum of the radiation emitted from a 1-mm diameter capillary source of ^{125}I inside a PMMA cylindrical phantom of 26 mm diameter, acquired with a 1-mm thick CdTe diode detector (XR-100 T-CdTe, Amptek). Main photopeaks and escape peaks are identified; the measured energy resolution is 0.42 keV at 35.5 keV. While some peak tailing is present, the effect of Compton scattering is limited and evident only on the main photopeak at 27.5 keV

For ^{125}I imaging in small animals (4–5 cm thick) this condition of spectroscopy deficit could deteriorate, according to simulations in [32], the detection performance due to the relevance of Compton scattering (see Fig. 2.14). However, in vivo ^{125}I thyroid imaging in the mouse has demonstrated a spatial resolution down to ≅0.1 mm in planar imaging [31] and sub-mm resolution in SPECT imaging (see below). Analogously, it has been observed that for ^{99m}Tc imaging in a 5-cm thick Lucite phantom the use of just a single low-energy threshold does not impair the spatial resolution (Fig. 2.26) [5], in accordance with simulations reported in [32].

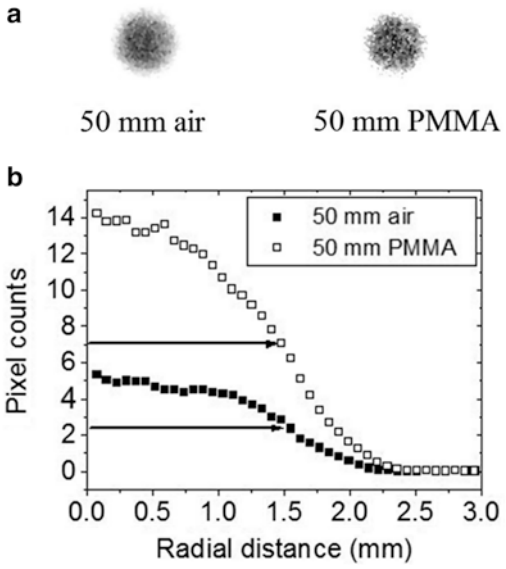

Fig. 2.26 (**a**) Planar images of a ^{57}Co (122 keV) point-like radioactive source acquired with the Medipix2 CdTe hybrid pixel detector with a threshold of 20 keV, either in air or by interposing a 50 mm thick PMMA block between the detector and the source. (**b**) Radial profile of the point-like source images, indicating attenuation but limited effect of Compton scattering in 50 mm PMMA: indeed, the half-width at half maximum (indicated by the *arrows*) is practically the same for the two radial profiles

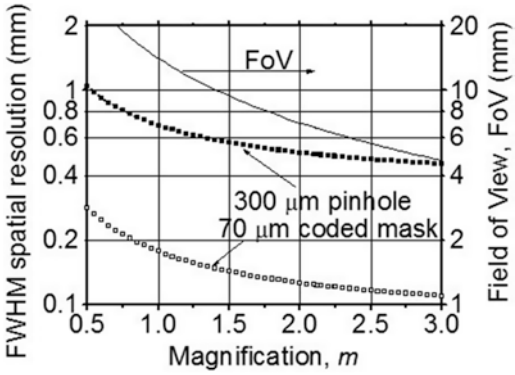

Fig. 2.27 Calculated spatial resolution and FoV in planar imaging of the CdTe detector unit of the MediSPECT scanner, equipped with a 300 µm aperture pinhole or with a NTHT coded aperture mask with 480 square holes of 70 µm side

This hybrid pixel detector has a sensitive area of 1.98 cm^2, an intrinsic spatial resolution around 0.1 mm at 122 keV due to the detector pixels of 55 µm pitch, an intrinsic detection efficiency of 45 % at 122 keV [5]. Note that for this detector, the space-bandwidth-efficiency product [1] as a Figure Of Merit (FOM = detector area × detector efficiency/pixel area) at 122 keV is

$$FOM = \frac{\left(14.08 \cdot 14.08 \text{mm}^2\right) \cdot 0.45}{\left(0.055 \cdot 0.055 \text{mm}^2\right)} \cong 30000$$

a remarkable value higher than that of clinical gamma cameras (≅20,000). Once coupled to high resolution pinhole or coded aperture collimators [31], a trade-off between FoV coverage and spatial resolution allows to select the proper geometrical settings for the imaging task (Fig. 2.27). However, with such a limited detector

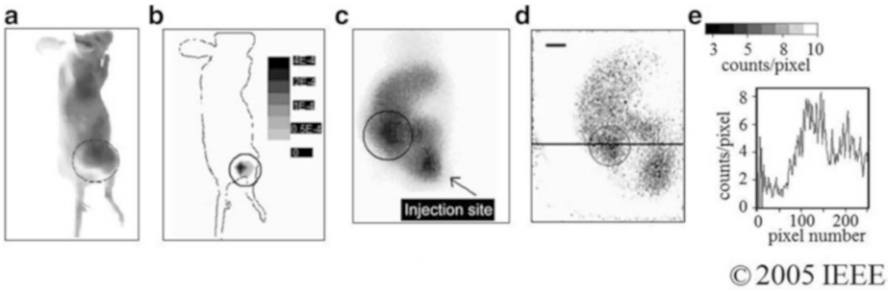

Fig. 2.28 Images of a tumor-bearing mouse (tumor area circled) injected with 74 MBq of $^{99m}TcO_4^-$ and with hematoporphyrin fluorescence marker. (**a**) white light image; (**b**) red optical fluorescence image excited in the green, superimposed on the mouse silhouette; (**c**) whole body mouse image obtained with a clinical pinhole gamma camera; (**d**) planar image (195 × 293 pixels, 47 × 71 mm^2, magnification = 0.45, 1 mm pinhole aperture) acquired with the Medipix2 CdTe hybrid pixel detector of the MediSPECT/FRI scanner; (**e**) counts profile along the horizontal line across the tumor shown in **d**). The Medipix2 image is the result of the composition of two partially overlapped images (data from [36])

sensitive area, in order to have a sub-millimeter spatial resolution the FoV is limited to ≅20 mm or lower: thus, this scanner is best suited for specialized imaging of animal (mouse) organs, like the mouse brain, heart, thyroid, or for solid tumor implanted in the mouse body.

Preliminary combined fluorescence and radionuclide imaging tests have been reported (Fig. 2.28), but major work has been dedicated to the development of the SPECT system. The MediSPECT magnification allows to have a planar FoV ranging from 2.4 to 29 mm using pinhole collimators and from 6.3 to 24.3 mm with a coded aperture mask. The collimator unit can host different types of pure tungsten collimators (knife-edge pinhole with 0.3, 0.4 or 1 mm aperture, a parallel hole collimator with 100 μm round holes, two NTHT (No Two Holes Touching) MURA (Modified Uniformly Redundant Array) coded aperture masks with 70 or 80 μm holes).

With MediSPECT, a deep sub-millimeter system planar spatial resolution in the 0.1–0.2 mm range has been demonstrated with the usage of coded aperture mask with 70 μm holes (NTHT masks, 62 × 62 matrix array of open/close positions, with 460 holes). Such a hole size can be realized only in thin metal (tungsten) foils of ≅0.1 mm thickness, so that this coded mask can be used only for low-energy radionuclides as ^{125}I. This type of collimator allows to preserve a high spatial resolution (related to the single aperture size) while providing a high geometrical efficiency, up to the maximum given by the sensitivity of a pinhole of equal aperture to that of a single hole, multiplied by the number of apertures in the mask. In planar imaging, raw images produced by the overlapping of projections of the source by single apertures on the image plane (a condition known as multiplexing) are decoded off-line with a linear analysis code. In SPECT imaging, reconstruction occurs via a specific 3-D OS-EM algorithm which processes all multiplexed data from all projections at each iteration step, rather than decoding the data from each projection and then

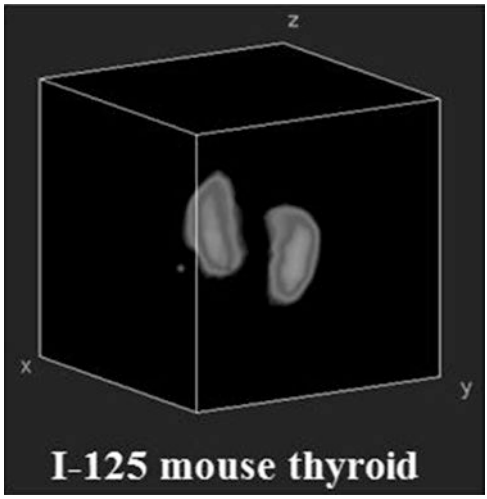

Fig. 2.29 Volume rendered ^{125}I SPECT image of a mouse thyroid, obtained with the MediSPECT CdTe based scanner equipped with a 300 μm pinhole (magnification 1.47, ^{125}I injected activity 31.8 MBq). Acquisition parameters: 72 views at 5° steps, exposure time 1 min/view. OS-EM reconstruction parameters: 31^3 pixels with 450 μm isotropic pixel size, 15 iterations and 5 subiterations. Image FoV = 14 × 14 × 14 mm^3

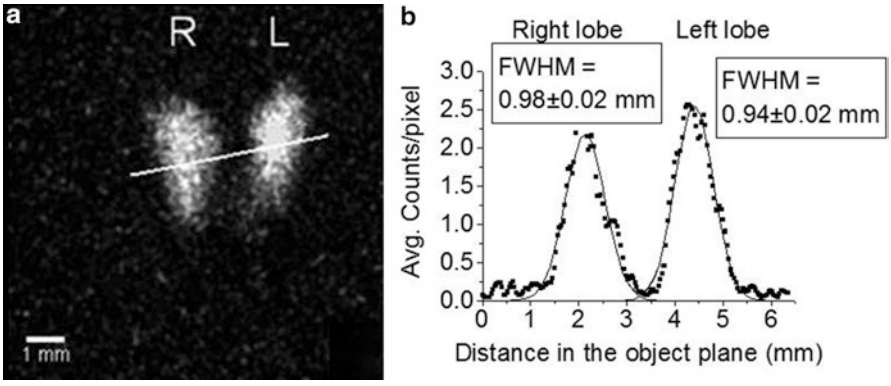

Fig. 2.30 (**a**) Planar image of an ^{125}I injected mouse thyroid taken with MediSPECT scanner equipped with a 300 μm pinhole (magnification 1.47; FoV 9.6 × 9.6 mm^2). The raw image has been low-pass filtered with a Gaussian kernel of two pixels FWHM. Injected activity = 31.8 MBq, acquisition time = 20 min. (**b**) The profile along the line shown on the image in **a**) indicates a size of the thyroid lobes less than 1 mm FWHM

perform reconstruction. MediSPECT has shown in in vivo mouse imaging to resolve thyroid lobes of less than 1 mm FWHM (Figs. 2.29 and 2.30). The ^{125}I sensitivity was 1.6×10^{-4} [70].

5.5 Philips Medical System's SOLSTICE System

The group at Philips Medical Systems (Cleveland, OH, USA) has developed a semiconductor gamma camera (SOLSTICE, Solid State Imager with Compact Electronics) [11, 53]. An intended application is ^{99m}Tc small animal SPECT

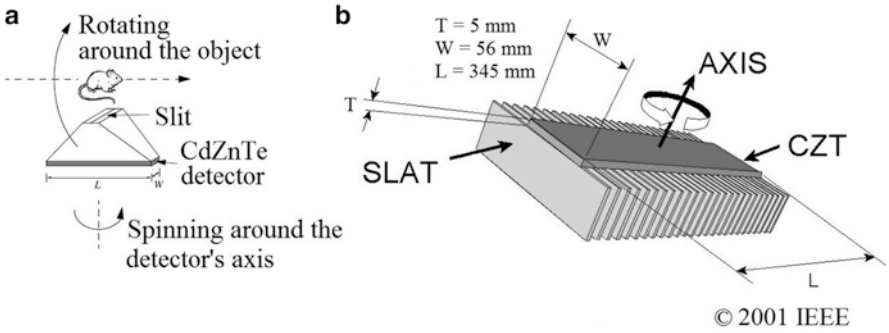

Fig. 2.31 (**a**) Acquisition geometry of the SOLSTICE small animal SPECT imager (adapted from [80], with permission). (**b**) Scheme of the CdZnTe detector and slat collimator of the SOLSTICE semiconductor gamma camera (adapted from [11], with permission)

imaging [80] (Fig. 2.31). SOLSTICE employs a series of CdZnTe detector with 5-mm-thick substrates. The SOLSTICE camera is coupled to a rotating slat collimator (Fig. 2.31a) for improved sensitivity, matching the collimator resolution with the pitch of the semiconductor detector.

The camera has a 345 mm FoV (*L* in Fig. 2.31a, b). The design requirements at 140 keV are excellent energy resolution (below 4–5 %) and high spatial resolution (a few mm). The slit camera detector axis spins around the detector's axis so that it creates 1-D projections (spinograms) of the 3-D radioactive distribution. Then, the camera is rotated around the animal to provide SPECT imaging. Essentially, this configuration requires a linear detector array in the form of a strip detector, and tests have been performed with a strip CZT detector with 192 pixels of 1.8 mm pitch [80]. Since a 1-D gamma-ray collimation is necessary, the W/Pb collimators can be made with relatively close-spaced slats (1.5 mm) matching the detector pitch, and large height (40 mm) to provide good spatial resolution. A study of CZT detector performance was made which employed sub-pixelization of the CZT detector, producing a better energy resolution. The anode side (opposite to the cathode radiation side) of each crystal (14.4×14.4 mm^2) was segmented into a matrix array of 4×8 pixels, with a pixel size of 1.5×3.3 mm^2 and a 0.3 mm inter-pixel gap.

A test of 88 CZT crystals has been reported, with negative bias voltages ranging from 275 to 420 V. The average energy resolution over the array was as good as 3.6 % at 122 keV and generally lower than the 5 % energy resolution design parameter at 140 keV [11]. The design planar spatial resolution is 5 mm FWHM at 10 cm distance. Application to small animal imaging has been reported [81] with resolution below 2.5 mm, and superior energy and spatial resolution with respect to a "conventional NaI detector" with a ultra-high-resolution parallel-hole collimator. The excellent energy resolution of the SOLSTICE/CZT camera (3.8 % at 140 keV) allowed also to perform dual isotope imaging tests with ^{99m}Tc (140 keV) and ^{123}I (159 keV) both in phantoms and in vivo on rats [81].

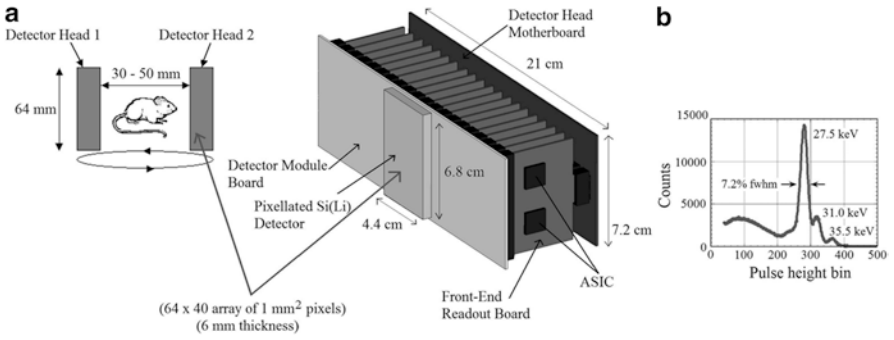

Fig. 2.32 (**a**) Scheme of the small animal ^{125}I SPECT system designed at LBNL using Si:Li pixel detectors. (**b**) Best spectroscopic performance of the Si:Li detector for ^{125}I (7.2 % at 27.5 keV) (adapted from [82])

5.6 LBNL Si:Li System

A high-resolution SPECT system for ^{125}I in vivo mouse imaging has been designed at Lawrence Berkeley National Laboratory, based on thick Si:Li detectors [30] (Fig. 2.32). Lithium-drifted silicon (Si:Li) crystals can be made by drifting Li in order to compensate for impurities in Si, so that an "intrinsic" Si bulk substrate can be obtained with a large thickness (e.g., 1 cm). In the LBNL design, a detector array of 64×40 square pixels of 1-mm pitch with 50–100 μm inter-pixel gap, on a 6-mm thick substrate is used, operated at room temperature since the $1 \times 1 \times 6$ mm^3 voxels have a leakage current in the order of just a few nA. The 6-mm detector thickness produces an intrinsic detection efficiency ≅90 % at ^{125}I energies (Fig. 2.5). Two such detector modules rotate around the animal for SPECT imaging. An energy resolution of 8.5 % FWHM at 27.5 keV has been reported (best result is 7.2 % FWHM at 27.5 keV, Fig. 2.32b) with the available discrete readout, and an energy resolution of 15 % is foreseen with the redesign of the 64-channel readout CMOS ASIC.

5.7 Gamma Medica-Ideas System

The group at Gamma Medica-Ideas (Canada/Norway/USA), in collaboration with groups at the University of California, Irvine, and Johns Hopkins University, have developed a CZT based gamma camera, compatible with Magnetic Resonance Imaging, for a small animal scanner [54]. The system is based on modules of pixelated CZT crystals, 5-mm thick, operated at −500 V bias applied to the top (non pixelated) contact, with 16×16 pixels of 1.6 mm pitch, and associated electronic readout. Each detector module is coupled to a pinhole with 0.5–2 mm aperture. By using flexible circuit boards, eight modules can be arranged in a compact "ring"

around the animal for a 30-mm FoV. A few "rings" of modules can be stacked so as to cover a larger transaxial FoV. An energy resolution of 5.4 keV at 122 keV has been reported [54].

6 Semiconductor Detectors for Small-Animal PET

There are two major issues in image quality in small animal PET: sensitivity and spatial resolution [83]. For ^{18}F imaging, scanner sensitivity currently ranges 1–7 % and spatial resolution is above 1 mm, and less than 2 mm, in state-of-the-art systems (see Fig. 2.35). However, the fundamental limiting spatial resolution in small animal PET imaging—related to positron range and non-collinearity of annihilation gamma-rays—is roughly ¼ of a mm FWHM, as estimated by summing in quadrature the contribution from ^{18}F positron range in water (0.10 mm FWHM, non Gaussian distribution) and that from photon non-collinearity (0.22 mm for a 100 mm ring diameter, Gaussian distribution) [84]. Most scanners are based on scintillator detector technology, and intrinsic spatial resolution is related to the transverse size (currently about 1 mm) of individual elements of the crystals. Further reduction in the size of the pixels in scintillator crystals is not likely to occur due to manufacturing difficulties and, in addition, a scintillator pixel with a small cross section produces a reduced light output at the readout side: this degrades significantly both energy resolution and position identification. As a consequence, in order to reach a sub-millimeter spatial resolution, several groups started dedicating efforts to the development of a new class of small animal PET scanners based on room-temperature semiconductor detectors, including CdTe and CdZnTe [85], and Si and Ge as well. In fact, for most-used PET tracers as ^{18}F and ^{11}C, simulations show that the crystal pitch is the prevalent parameter over non-collinearity and positron range effects, in determining the spatial resolution of high resolution systems. Such semiconductor detectors have been investigated for PET applications long ago (e.g., [86]), in particular for their coincidence timing properties [87, 88] which at that time was poor with respect to scintillator technology. Small animal PET involves detector rings of small diameter (several cm), and this helps reducing the influence of the detector pixel size on the intrinsic spatial resolution of the scanner.

The intrinsic resolution of such pixel or strip detectors is ultimately limited only by the pixel pitch, which—as we have seen in the case of small animal SPECT scanners—can be well below 1 mm, thus providing the potential for an intrinsic sub-millimeter spatial resolution of semiconductor-based small animal PET scanners. Semiconductor detectors of choice, due to their high attenuation for 511 keV photons, have been considered CdTe and CdZnTe (Table 2.2). In such detectors, which are available in size of 2–3 cm by side, sufficient detection efficiency can be obtained by irradiating them by the side (planar transverse field configuration), thus exploiting a 2–3 cm attenuation length: in CdTe, this corresponds to 65–80 % intrinsic detection efficiency at 511 keV. This situation refers to gamma rays incident normally to the detector side; in this case information on the depth of

interaction (DOI) in the detector crystal is not necessary for source position determination. In the case of gamma rays incident on one of the detector faces, uncertainty in the localization of an off-axis source arises and DOI information is needed. If a stack of such semiconductor detectors is assembled for the realization of a "detector block" as the basic unit of a fixed-gantry PET ring, then the spatial resolution improvement is related to the high level of crystal segmentation, to the availability of DOI datum for each stack layer, and to a dense packing of the detector planes. Such solutions have been investigated recently in the case of CdZnTe [89], but single large CZT detectors ($15 \times 15 \times 7.5$ mm^3) with a coplanar grid electrode geometry have been tested as well [90].

In order to illustrate the technical details related to the development of a semiconductor based small animal PET scanner with ultra-high spatial resolution, in the following a few experimental realizations will be illustrated, based on Si, CdTe, CdZnTe and Ge semiconductors.

6.1 University of Ferrara SiliPET System

As described in Sect. 3.2, low Z semiconductors can be used in small-animal PET scanners where the detection strategy is identification of the position of Compton interaction in the detector. In 4-cm thick Si, the fraction of single Compton interaction events can be as large as 52 % [91]. On the basis of these considerations, the Medical Physics group at University and INFN Ferrara, Italy, proposed the realization of a small animal PET scanner (SiliPET) based on double-sided microstrip silicon detectors [92]. In SiliPET, in order to reach a suitable intrinsic detection efficiency, a stack of forty 1-mm thick Si planar detectors is used (Figs. 2.33 and 2.34), for a total absorption thickness of 40 mm Si for normally incident photons, which is close to one mean free path (49.5 mm) at 511 keV in Si (Table 2.2). Indeed, this innovative approach to photon detection in small animal PET has a number of advantages with respect to scintillator based scanners, potentially providing a very high spatial resolution (below 1 mm) coupled to high sensitivity (a few percent). In fact, Si microstrip detectors can be made large enough (e.g., 60×60 mm^2 in SiliPET) to cover a large solid angle when positioned around the animal in a box-like arrangement (Fig. 2.33a), thus increasing the scanner sensitivity. Moreover, the Si detector pitch can be small enough (e.g., 0.5 mm in SiliPET) so that the intrinsic position resolution is adequate for one-hit identification of the planar position of the (first) Compton event in a single detector plane (Fig. 2.33b): in fact, the range of Compton recoil electrons in Si from a 511-keV photon is 0.34 mm on the average and 0.57 mm at most.

The third coordinate of the position of the first interaction event is given by the position of the detector plane in the detector stack: for thin detector substrates (e.g., 1 mm in SiliPET), the resolution in this depth-of-interaction coordinate is high (with respect to a detector stack thickness of 40 mm in SiliPET). For event identification, an equivalent threshold of 50 keV in the analysis of the strip signal is set in

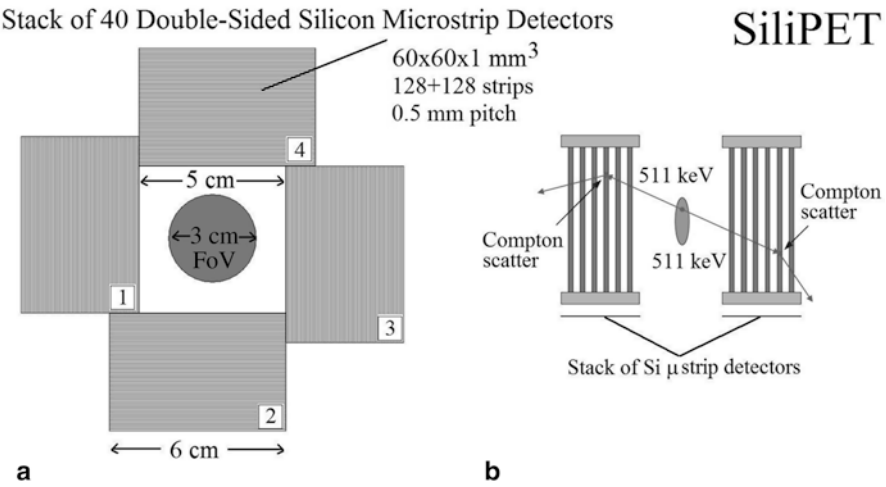

Fig. 2.33 Scheme of the SiliPET small animal PET scanner, based on a stack of double-sided microstrip silicon detectors. (**a**) Top view of the scanner geometry with the four stacks arranged box-like around the animal FoV. (**b**) Photon interaction scheme, based on the detection of Compton scatter events in two of the four stacks

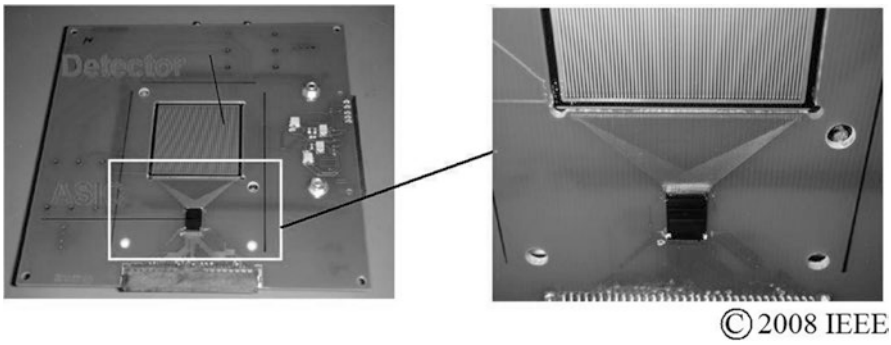

Fig. 2.34 A single detector plane (double-sided silicon strip detector, 1 mm thick, 0.5 mm pitch) of the SiliPET scanner, coupled to a commercial VATAGP2.5 128-channel analog ASIC (Ideas) for strip signal readout (adapted from [95])

the design of the SiliPET scanner. A further advantage is the reduction in complexity of the acquisition and readout electronics since no energy information is to be recorded and processed. The design and realization of a readout ASIC for fast timing measurement for the SiliPET scanner is underway at Politecnico di Milano, Italy [93]: first measurements give a time resolution of 16.5 ns [94]. Double-sided silicon strip detectors are designed and realized at ITC- Fondazione Bruno Kessler (FBK-irst), Trento, Italy, where first prototypes of 30×30 mm^2 with 0.5 mm pitch and 1 or 1.5 mm thickness have been tested [95].

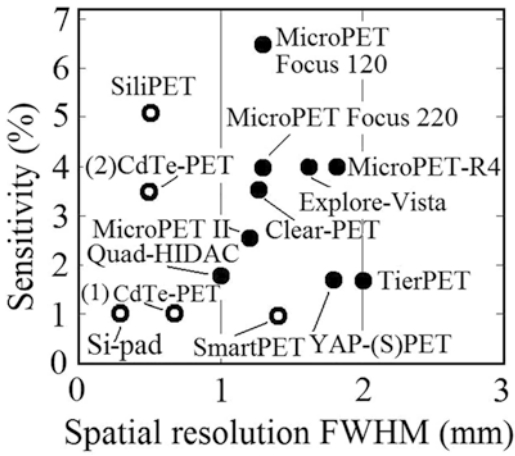

Fig. 2.35 Comparison of the performance of some scintillator based and semiconductor based small animal PET scanners, for a spatial resolution below 2 mm. CdTe-PET (*1*) refers to University of Tohoku scanner described in paragraph 6.2, CdTe-PET (2) refers to University of California scanner described in Sect. 6.3, and Si-pad refers to the system of the CIMA collaboration described in Sect. 6.7 (modified with inclusion of semiconductor data, from original data provided by courtesy of G. Zavattini, Ferrara University, Italy)

Overall, the above features of the design of the SiliPET scanner potentially provide (a) a high accuracy in the determination of the position of interaction, (b) a reduction of the parallax error through the determination of the depth of interaction in the detector, (c) a high solid angle coverage, and (d) a simplification in the associated readout electronics. The realization of the full SiliPET scanner is on-going and laboratory tests with prototype setups have been reported [94]. In Monte Carlo simulations for assessing its basic performance, with a point-like ^{18}F source at the center of a 3-cm diameter water phantom, SiliPET showed an intrinsic spatial resolution of 0.52 mm FWHM and a sensitivity of 5.1 % at the center of the system [91, 92]. This potential performance of SiliPET would represent a significant technological advancement in small animal PET scanners (Fig. 2.35).

6.2 University of Tohoku System

A group at Tohoku University (Sendai, Japan) proposed [96] and then developed [97, 98] a small animal PET scanner based on arrays of Schottky CdTe detectors. Initial motivations for using commercially available, thin (0.5 mm) CdTe Schottky type detectors (Pt(cathode)/CdTe/In(anode)) were their high energy resolution and low noise, when operated at high reverse bias voltages (200 V). A suitable absorption length for 511 keV gamma rays is obtained by irradiating the detectors from the side, i.e., perpendicular to the direction of the electric field inside the detector.

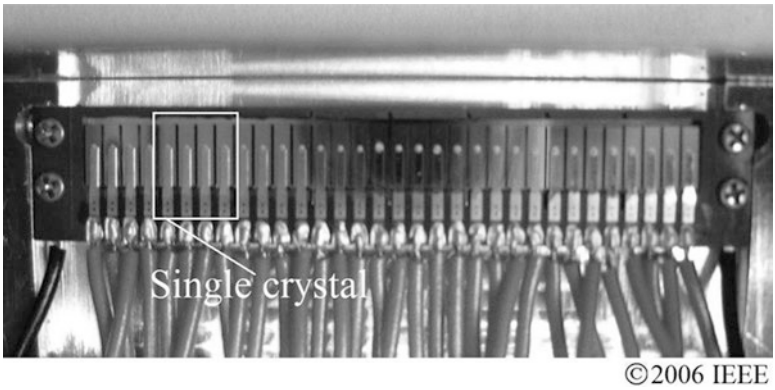

Fig. 2.36 The 32-channel CdTe detector array of the prototype University of Tohoku PET scanner, consisting of eight crystals with segmented anodes; single channels have $1.2 \times 1.15 \times 4.5$ mm^3 size (adapted from [97])

Moreover, a thin detector ($\cong$1 mm) assures (relatively) short transit times for charge carriers to the collecting electrodes and hence, short signal rise times, which are improved by operating at applied electric fields of 300–400 V/mm or higher. For example, with a bias voltage of 400 V over a 1 mm distance between the electrodes, data in Table 2.1 for CdTe provide an estimate of 23 and 250 ns for the maximum transit times of electrons and holes, respectively.

In a preliminary report [96], two detector units were realized each one consisting of eight detectors sub-divided into two arrays of four detectors ($5.0 \times 5.0 \times 0.5$ mm^3) aligned with 2.4 mm spacing between them. The second array of four detectors is placed behind the first array, so that practically the attenuation length in the radial direction is 5.0+5.0 mm: for CdTe, this total thickness provides 41 % intrinsic detection efficiency at 511 keV. Moreover, the second array is translated in 0.6 mm step laterally with respect to the first array, so as to sample the (transaxial) gap region between two detectors. Two opposing detector units, placed at 10 cm distance and readout in coincidence, with a rotating 0.6 mm diameter ^{22}Na source at the center, were able to resolve the source with 0.9 mm FWHM resolution, thus demonstrating the proof-of-principle of the sub-millimeter resolution small animal PET scanner.

The next technological step was the demonstration of array detectors with suitable detector multiplicity. An array of 32 Schottky detectors was built, consisting of eight CdTe crystals; on each crystal four detectors were produced by segmenting the readout anode electrode in four strips. This 32-channel CdTe array resulted in single channels of $1.2 \times 1.15 \times 4.5$ mm^3 size distributed over a 1.4 mm pitch (Fig. 2.36).

In a coincidence system, with a rotating 0.6 mm diameter ^{22}Na source at the center, two such detector arrays at 10 cm distance showed a time resolution of 13 ns by biasing the detector at 700 V, and a resolution of 1.0 mm [96]. Based on this detector array, a rotating gantry setup was realized (Fig. 2.37), which demonstrated an energy resolution of 3 % FWHM at 511 keV and 5 ns FWHM time resolution [97]. This

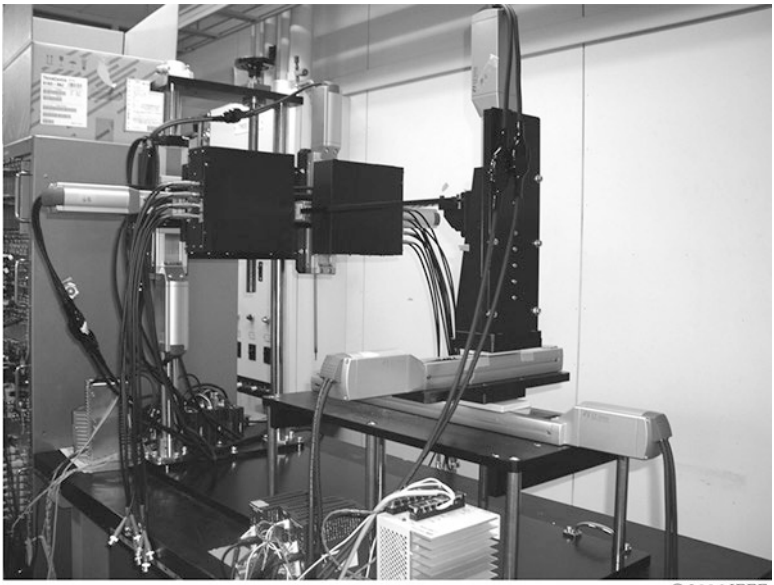

Fig. 2.37 Prototype of the University of Tohoku PET scanner with a dual head rotating gantry setup (from [97])

demonstrator showed a constant overall resolution of 1.0 mm (including 0.5 mm source diameter) with a ^{18}F phantom, with a distance between the detector heads from 50 to 150 mm, thus indicating potential performance for mouse as well as for rat imaging.

The potential of this prototype was shown in a ultra high resolution PET scanner with a fixed gantry consisting of ten detector heads arranged in a ring structure with a FoV of 64 mm diameter (transaxial) and 26 mm length (axial) (Fig. 2.38a) [98]. Full front-end and readout electronics have been realized: each one of the ten "detector buckets" consists of a detector block and ASIC amplifier unit. In the detector block there are 16 stacked detector units. Each detector unit consists of two linear arrays of 16 Schottky CdTe detectors, with one array placed in the same plane of the stack and behind the front array, shifted laterally by 0.6 mm.

Each ASIC contains 32 charge sensitive preamplifiers and is connected to the 32 signal lines from one detector unit and 16 ASICs are contained in a detector bucket (Fig. 2.38b). Ten FPGA-based digital processing boards connect to the ten detector buckets, respectively: they process above-threshold (215 keV) signals from the ASIC amplifier unit, by time-stamping the arrival of gamma rays with a 100 MHz clock (20 ns time coincidence window). The stacked detector unit contains CdTe strip detectors in two linear arrays of 19.7 mm length each, with single detectors in the array having a size of $1.1 \times 1.0 \times 5.0$ mm^3, the longer dimension being in the radial direction in the transaxial plane (Fig. 2.39). The pitch of the array is 1.2 mm. Separation between single elements in the detector array is achieved by a track of 0.1 mm width, 0.2 mm depth and 5.0 mm length on the Schottky (In/CdTe) side.

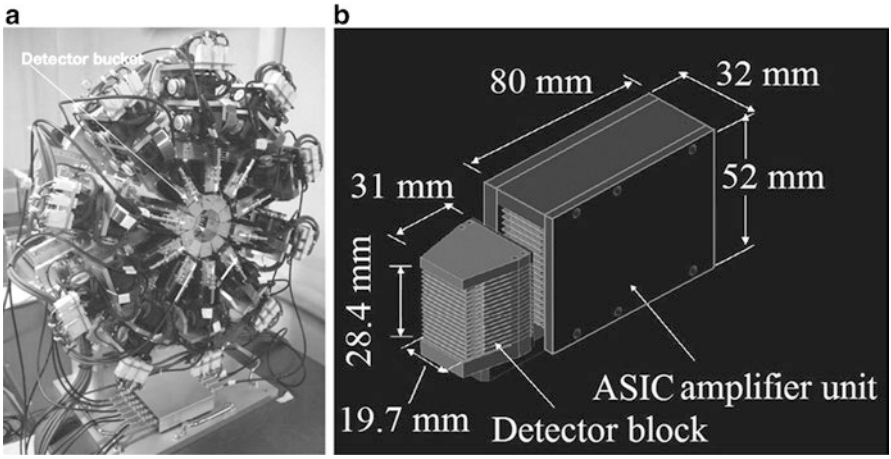

Fig. 2.38 (**a**) University of Tohoku small animal PET scanner, consisting of ten CdTe detector heads, with a FoV diameter of 64 mm. (**b**) A detector bucket (adapted from [98], reproduced with permission)

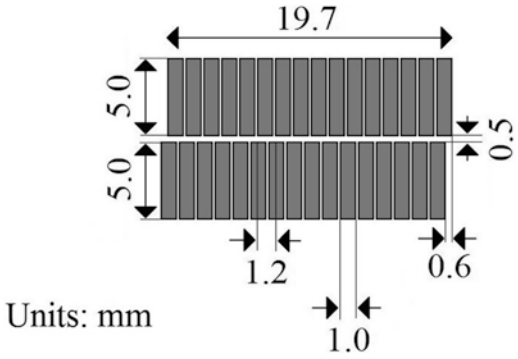

Fig. 2.39 Scheme of the dual detector arrays of 16 CdTe Schottky detectors of the University of Tohoku small animal PET scanner (adapted from [98], reproduced with permission)

The arrangement of two detector arrays shifted by half the detector pitch allows to register up to three cross line of response in 1.2 mm transaxial distance, and to determine depth of interaction in the detector. Tests with a ^{22}Na source of 0.5 mm diameter showed a tangential resolution of 0.74 mm FWHM at the center of the FoV (Fig. 2.35); mouse and rat in vivo preliminary tests with this scanner showed high resolution performance (Fig. 2.40) [98]. The simulated sensitivity for an array of 16 layers of $1.2 \times 1.15 \times 10$ mm^3 detectors was 1 % [97].

An improvement in the position resolution of the Schottky CdTe detectors studied during the development of the University of Tohoku PET small animal scanner is represented by the realization of so-called (one-dimensional) position-sensitive CdTe detectors, i.e., Schottky devices (In/CdTe/Pt) which give the single coordinate of the interaction of the gamma rays in the direction perpendicular to the applied

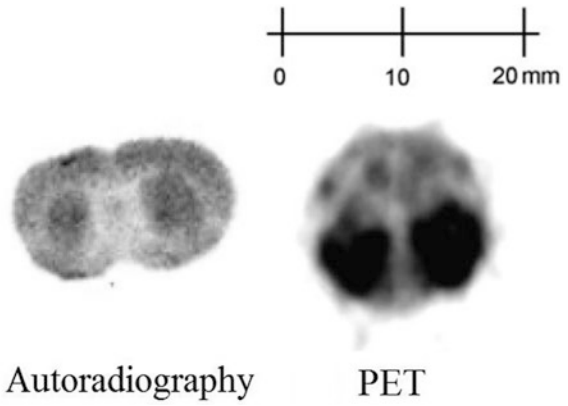

Fig. 2.40 First mouse images of the University of Tohoku small animal PET scanner: a transaxial image of a mouse brain compared to *post mortem* digital autoradiography of a brain slice of the mouse. The mouse was injected with 44.4 MBq of ^{18}F-FDG (adapted from [98], reproduced with permission)

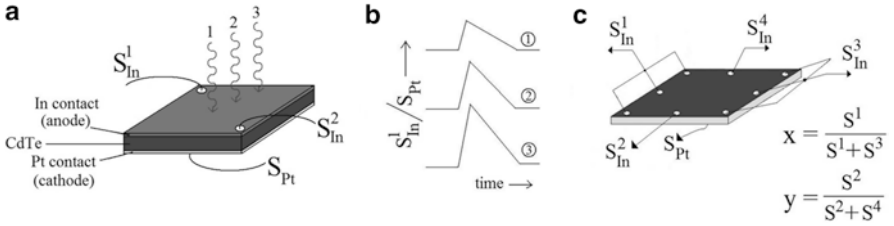

Fig. 2.41 (**a**) Schematic representation of the principle of operation of a resistive-anode Schottky CdTe detector. The ratio of the signal S^1 or S^2 from the anode side to the signal S_{Pt} from the cathode side has an amplitude (**b**) which depends on the position (e.g., 1, 2, 3) of interaction of the radiation. (**c**) By placing several readout electrodes on the In anode, the x–y coordinates of the position of interaction on the surface electrode can be recovered

electric field. It was found that if the surface resistance of the In contact is high enough, one could record a signal S_{In}/S_{Pt} as the ratio of the signal S_{In} picked up on the In anode contact to the signal S_{Pt} from the rear Pt cathode contact, whose amplitude depends on the position of the interaction of incident ionizing radiation [99] (Fig. 2.41).

The increase of the surface resistance of the In contact was obtained by decreasing the thickness of the In electrode (e.g., a thickness of 40 nm produces a resistance of 150 kΩ between two Au wires contacted at a distance of 10 mm on the surface of the In electrode), so realizing a "resistive electrode" configuration [99]. Then, the next technological step would be to place several readout electrodes on the surface of the resistive electrode, so as to derive the two-dimensional coordinates of the position of interaction of incident radiation: the University of Tohoku group has recently reported that a suitable arrangement of six readout electrode (Fig. 2.41c) is apt to recover linearly the x–y coordinates of the position of the interaction on the detector surface [100].

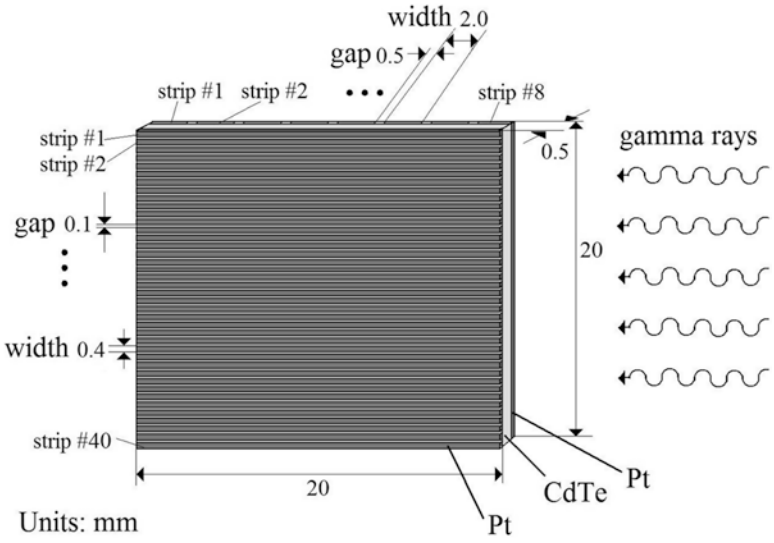

Fig. 2.42 Scheme of the double-sided CdTe strip detector employed in the University of California small animal PET scanner. The $20 \times 20 \times 0.5$ mm^3 detector has 40 strips of 0.5-mm pitch along the direction of the incident gamma rays, and eight orthogonal strip of 2.5-mm pitch for providing DOI information (from data in [101])

6.3 University of California at Davis and RMD System

When irradiated from the side, i.e., orthogonally to the applied electric field determined by the bias voltage, a thin semiconductor detector can show good lateral resolution (determined by the thickness of the active substrate) and sufficient intrinsic detection efficiency (determined by the width of the detector surface). Then, 1D position sensitivity of the detector allows to obtain DOI information. In the University of Tohoku PET scanner described in the previous section, single-sided strip CdTe detectors have been used, and linear arrays of such detectors are arranged. In the case of the small animal PET scanner designed at University of California, Davis, in collaboration with Radiation Monitoring Devices, Inc. (Watertown, MA, USA), the basic detector element is a double-sided (orthogonal) CdTe strip detector of $20 \times 20 \times 0.5$ mm^3 equipped with ohmic (Pt) contacts, fabricated by ACRORAD (Fig. 2.42).

In this irradiation geometry, transaxial resolution is related to the 0.5-mm pitch of the 40 contact strips of 0.4 mm width, along the direction of the incident gamma rays, and DOI information is provided by eight orthogonal strips of 2.5-mm pitch and 2.0-mm width. The absorption length of 20 mm is to be compared with the gamma mean free path of 18.7 mm for CdTe, at 511 keV (Table 2.2). Preliminary tests indicate an energy resolution of 3 % at 511 keV and a coincidence timing resolution (with respect to a LSO scintillator coupled to a PMT) of less than 11 ns down

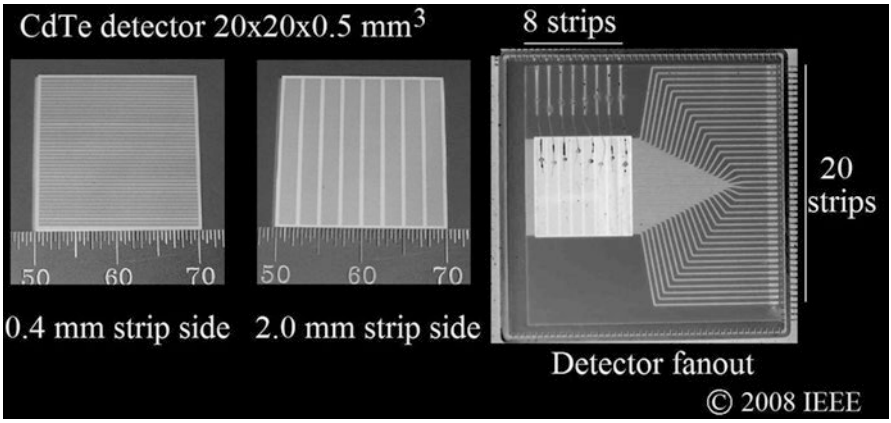

Fig. 2.43 View of the CdTe strip detector unit of the University of California small-animal PET scanner (adapted from [102])

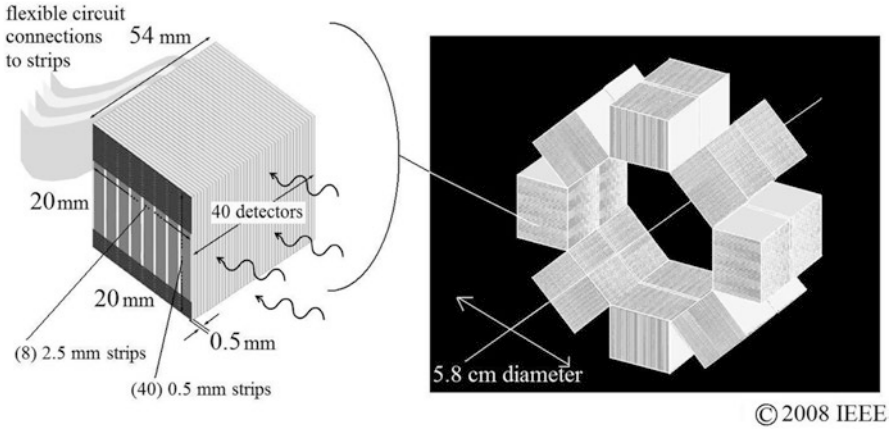

Fig. 2.44 The proposed detector block and gantry of the University of California CdTe PET small animal scanner (adapted from [102])

to 3 ns in dependence of the applied voltage bias, recorded from the 0.4-mm wide, 20-mm long strips [101] (Fig. 2.43).

Two dimensional FWHM position resolution was found to be equal to the strip pitch values (2.5, 0.5 mm, respectively). In timing coincidence measurements between two CdTe detector units, the timing resolution was 8 ns at 350 keV energy threshold [102]. A $20 \times 20 \times 24$ mm^3 detector block was designed, made by stacking 40 such detector elements, and two such blocks are coupled for increasing the axial FoV, in a gantry arrangement of 16 detector blocks with an inner ring diameter of 5.8 cm (Fig. 2.44). Such a scanner has potential for 3.4 % sensitivity [102]

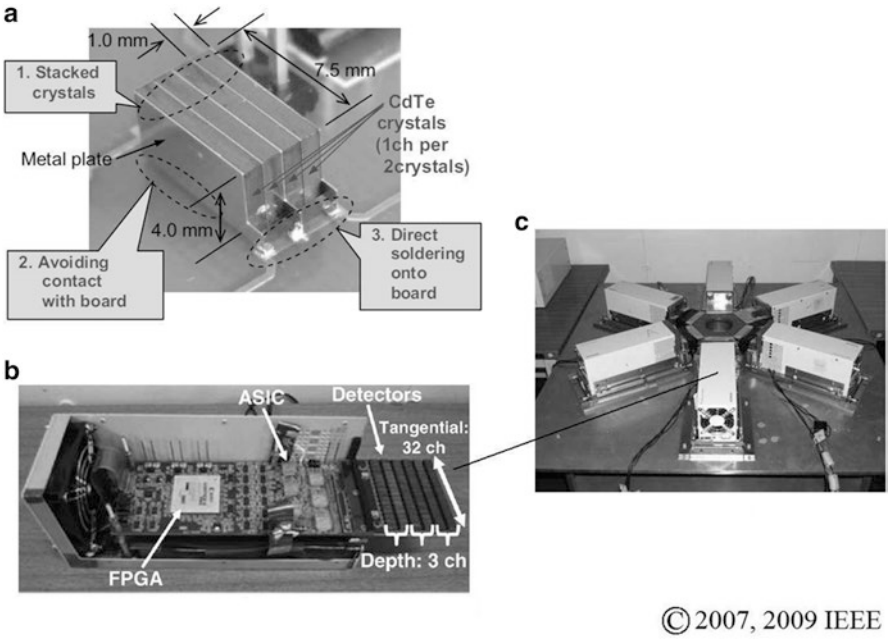

Fig. 2.45 (**a**) The CdTe detector module consisting of four crystals and two channels, (**b**) the detector unit with 32×3 detector channels and (**c**) the single slice ring (82 mm inner diameter) of the prototype PET scanner developed by Hitachi Ltd. and University of Hokkaido (from [103, 104])

(Fig. 2.35). Given its complexity, it represents a major technological challenge for detector assembling, interconnection, data acquisition and processing. However these challenges compete with the major potential of semiconductor detectors vs. scintillator detectors for sub-millimeter spatial resolution and high sensitivity in small animal PET imaging.

6.4 Hitachi and University of Hokkaido System

In view of the realization of a 3D PET scanner for human brain imaging using CdTe detectors, a group at Hitachi Ltd. (Ibaraki, Japan) in collaboration with Hokkaido University (Sapporo, Japan) has made a single-slice prototype of a PET scanner based on six stacks of CdTe detectors [103], useful for small animal, e.g., rat imaging. Each detector module is a stack of four crystals, each of size 1.0×7.5×4.0 mm^3, and 96 detector modules are arranged in six detector units in a single slice ring (Fig. 2.45).

A single detector channel is composed of two adjacent crystals with 2.3 mm pitch (1 + 1 mm thickness + 0.3 mm gap) in the tangential direction, and two crystals with 17.5 mm pitch in the radial direction (7.5 + 7.5 mm

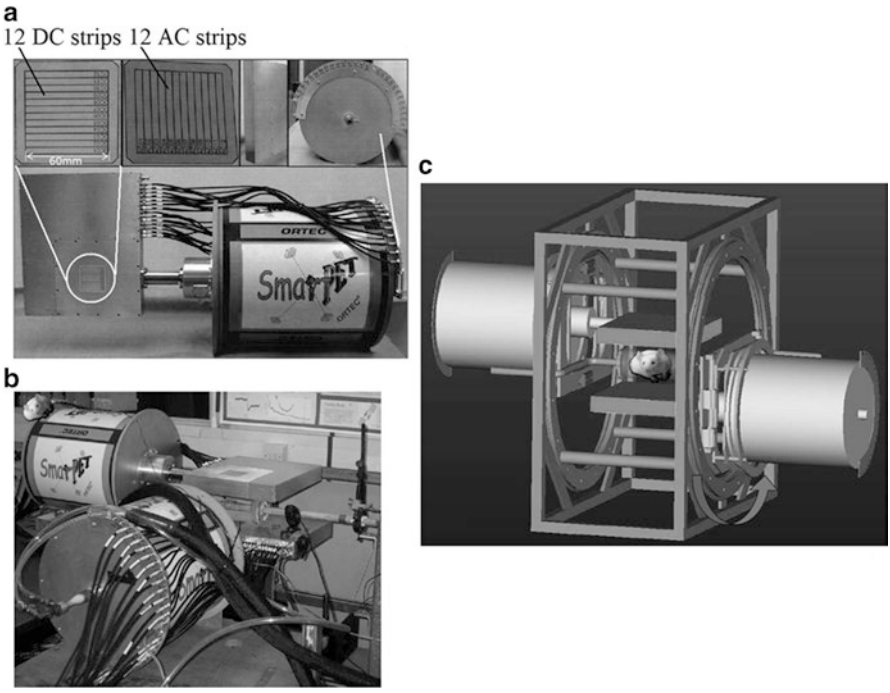

Fig. 2.46 (**a**) The HPGe planar detector module consisting of a double-sided strip detector ($60 \times 60 \times 20$ mm^3) with $12 + 12$ orthogonal strips of 5-mm pitch, (**b**) the two detector heads and (**c**) the dual-head rotating gantry of SmartPET, the small animal PET demonstrator developed by University of Liverpool. The large cylinders are the 72 h dewars for cryogenic cooling of the detectors with liquid nitrogen (from [108])

thickness + 2.5 mm gap). Under tests, the timing resolution was 6.0–6.8 ns FWHM (450 keV threshold), the energy resolution was 4.1–5.4 % FWHM and the spatial resolution was 2.6 mm FWHM.

6.5 University of Liverpool SmartPET System

In their analysis of image blurring in scintillator based PET systems for human imaging, caused by scattering of one or both of the collinear 511 keV gamma rays, the group at University of Liverpool identified the need for a very high energy resolution for rejection of background events and improved image quality. Hence, they proposed [105, 106] to use High Purity Germanium (HPGe) planar detectors for PET imaging, due to their excellent spectroscopic properties, and their detection properties approaching that of CdTe at 511 keV (Tables 2.1 and 2.2). In order to investigate this technology, in the framework of a 5-year hardware/software study started in 2003, they built a demonstrator that works as a small animal PET scanner (SmartPET) (Fig. 2.46),

but that has been used also in Compton imaging configuration [107]. The SmartPET prototype is a dual head, rotating gantry system based on a pair of double-sided high purity Germanium strip detectors. The p-type Ge crystals are $74 \times 74 \times 20$ mm^3 each with an active volume of $60 \times 60 \times 20$ mm^3; a 7 mm wide guard ring surrounds the active surface on the two detector surface. The outer contacts are segmented into 12 strips per side with a pitch of 5 mm, thus defining equivalent voxels of $5 \times 5 \times 20$ mm^3. The strips are defined by p^+ AC coupled contacts (49.82 mm wide and 0.18 mm inter-strip gap) on one side, and orthogonal DC coupled n^+ contacts (49.70-mm wide and 0.30 mm inter-strip gap) on the opposite side (Fig. 2.46a) The separation between the two detector planes is 130 mm (Fig. 2.46b, c); the detectors are operated at −1,800 V bias. The raw spatial resolution of such a detector would be equal to the (equivalent) detector pixel, i.e. 5 mm on the detector planes and 20 mm in the direction perpendicular to the scanner axis, implying no DOI information. On the other hand, Pulse Shape Analysis (PSA) of the charge signals on the AC and DC strips allows to recover a higher intrinsic spatial resolution [109]. The improvement in lateral spatial resolution using PSA techniques derives from the analysis of the charge signals induced, by the e–h carriers drift motion, both on the hit strip and on adjacent strips. When a pixel strip is hit by an interacting gamma-ray, the area under the signal waveforms in the left-side and right-side strips varies in dependence of the actual position of interaction across the 5-mm wide strip: by evaluating an asymmetry parameter between the two area values, a lateral position resolution of 1 mm has been demonstrated [109]. As regards DOI information, an event-by-event analysis of the pulse shape rise time—which depends on the depth of interaction below the detector surface—showed that, away from the detector edges, it depends linearly on the event DOI, thus permitting to reconstruct the interaction depth [110]. The rise time distribution of single-pixel events could be divided into five regions, thus permitting a coarse resolution of about 4 mm along the 20 mm detector depth [109].

The timing resolution was approximately 10 ns [106, 111], and initial tests at 122 keV indicated an energy resolution less than 1.5 keV FWHM for the SmartPET detectors [106], though the excellent energy discrimination of the HPGe detectors seemed not play a determinant role in the overall performance of the scanner, in subsequent works of the Liverpool group. As regards the detection sensitivity, measured for a ^{22}Na source at the center of the FoV and without full-energy event recover analysis, the dual-head SmartPET prototype showed an absolute sensitivity of 0.99 %; this value reduces to 0.12 % by limiting the data analysis to single pixel events, and to 0.001 % to single pixel photopeak events [112]. This demonstrates that for a significant sensitivity, all interaction events had to be considered. By accepting, in the event selection stage of data analysis, all events where one or both detector heads recorded either one or two strip hits per interaction, the SmartPET prototype showed a resolution of 1.4 mm FWHM with a statistical reconstruction and of 2.7 mm FWHM with an analytical reconstruction algorithm, for a point-like ^{22}Na source at the center of the FoV.

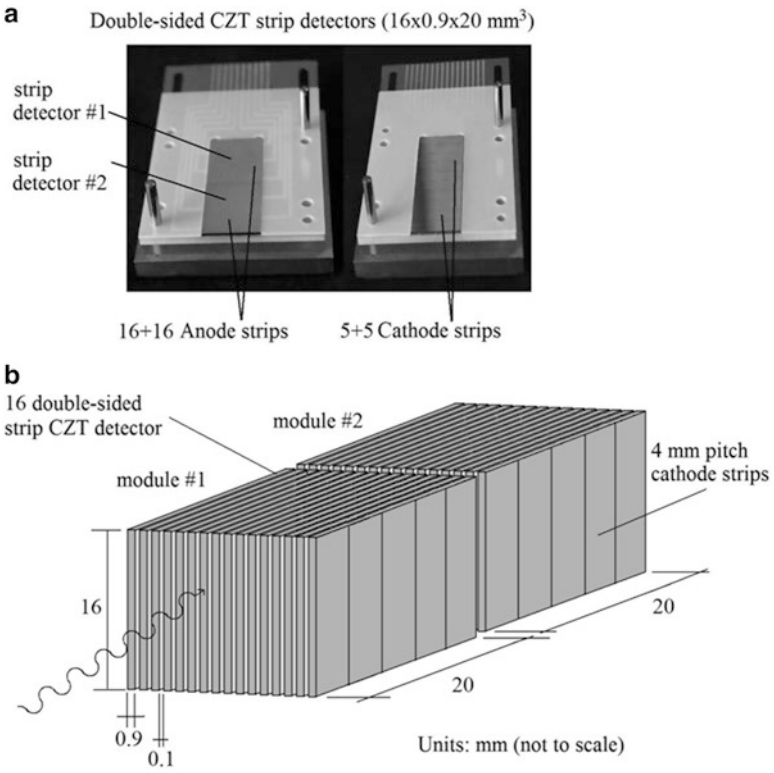

Fig. 2.47 (**a**) View of anode and cathode sides of CZT orthogonal strip detectors fabricated by CEA-Leti for microPET. Two detectors are placed in the same plane one behind the other, in order to double the attenuation thickness to 40 mm for gamma-rays incident edge-on along the detector length. (**b**) Sixteen detector planes are stacked with a 0.1 mm plastic sheet in between, for realizing a detector block of $16 \times 16 \times 40$ mm^3 active volume (adapted from [114])

6.6 CEA-Leti CZT System

The group at CEA-Leti (Grenoble, France) has been pursuing the realization of a PET scanner based on CdZnTe detectors. The higher resistivity and the absence of polarization effects with respect to CdTe, motivated their choice of CZT as a suitable material for their PET prototype. First experimental tests have been shown with detector modules consisting of arrays of double-sided CZT strip detectors 0.9-mm thick, irradiated edge-on along their length, with 20 mm length and 16×16 mm^2 faces, with 1 mm pitch on the anode side and 4-mm pitch on the cathode side (for DOI measurement), respectively (Fig. 2.47a) [113]. The detector planes are made by two 20-mm long arrays, put one behind the other for 40 mm total attenuation thickness, each array being made of 16 $16 \times 20 \times 0.9$ mm^3 strip detectors with a separating polyimide sheet of 0.1 mm thickness (Fig. 2.47b). Coincidence timing tests

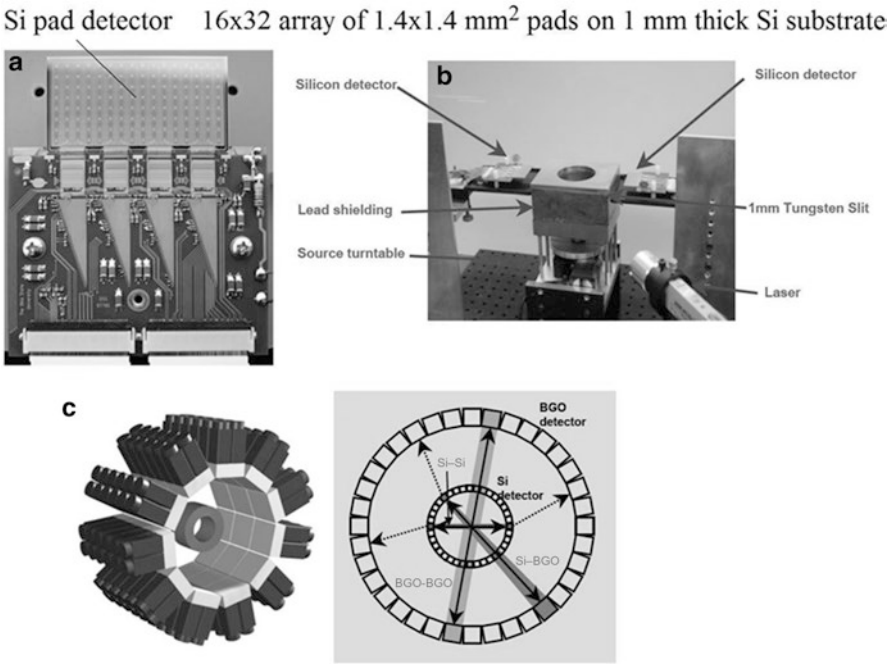

Fig. 2.48 The CIMA collaboration has designed a small animal PET scanner (**c**) based on a conventional BGO ring detector with an internal ring of silicon pad detector. One such detector is shown in (**a**) while in (**b**) is a photo of the dual head prototype setup of the silicon pad detectors, where the laser is used for detector alignment [117]

in planar geometry with two CZT detectors gave a resolution of 2.6 ns FWHM, and with a CZT detector and a fast BaF_2 scintillator gave 2.1 ns FWHM on anodic signals at 500 V bias voltage [89].

6.7 CIMA Collaboration Si Pad System

The Computer Imaging for Medical Applications (CIMA) collaboration [114] has developed a dual head prototype of a silicon detector small animal PET scanner, to be used as a high-resolution insert for a conventional scintillator based PET scanner [115]. The silicon detector ring, internal to the BGO detector ring (Fig. 2.48c), is made of 1-mm thick Si diode detectors (p^+–n junction at pad contacts and n–n^+ contact on the back) contacted with a 32×16 array of 512 pads (Fig. 2.48a). A double metal layer is used for routing pad connections to the bonding pads to commercial 128-channel readout ASICs. The inner ring is designed to Compton scatter 511 keV photons: in fact, most events are either direct absorption interactions in the scintillators, or single Compton scatter events in the low Z semiconductor detector followed by absorption in the scintillator detector (Fig. 2.48c). This

introduces the distinction between Si–Si interactions, Si–BGO interactions and BGO–BGO coincident interactions. The single scattering event in the Si detector can be localized with high spatial resolution due to the short range of the Compton recoil electron: then, the intrinsic spatial resolution in this detector would be limited only by the pad size. Again, as in other semiconductor-based PET scanners described previously, the realization of a stack of such thin detectors (irradiated from the side, Fig. 2.48b, or face-on) would provide axial field coverage with high resolution DOI information [117].

A prototype based on two front Si detector heads (separated by 170 mm) and four BGO detectors (non-position sensitive) has been assembled (Fig. 2.48b shows the Si detector heads), and the performance has been reported for ^{18}F sources [118]. The measured spatial resolution for Si–Si events was 0.98 mm FWHM at the center of the FoV, against a theoretical value (including photon non-collinearity contribution of 0.374 mm FWHM, positron range and source size contributions of 0.254 mm FWHM) of 1.04 mm FWHM. This gave indications that a Si detector with smaller size pads would improve significantly the overall spatial resolution for Si–Si events (e.g., 0.34 mm FWHM for 0.3×0.3 mm^2 pads [115]). Using a ^{18}F line source with 1.1 mm internal diameter, the resolution was 1.45 mm FWHM, with excellent resolution uniformity across the FoV up to 20 mm from the center [117]. Si–Si events contributed only $\cong$1 % to the system sensitivity, but the consideration of Si–BGO composite events allowed to increase the sensitivity up to 9 %, for a corresponding system resolution of 1 mm FWHM [115].

7 Summary

Most of the commercially available small animal SPECT and PET imaging systems are based on scintillator detectors coupled to position sensitive photomultiplier tubes. The requirement of improved performance, mainly in spatial resolution, has led to the application of microstrip or pixel semiconductor detectors for X-rays and gamma-rays. Compact, high spatial resolution, high energy resolution detector units are now assembled in microSPECT (Table 2.6) and microPET (Table 2.7) scanners.

Table 2.6 Comparison of performance (sensitivity and spatial resolution, simulated or measured for ^{99m}Tc imaging) of semiconductor based small animal SPECT prototypes

System	Technology	Sensitivity (%)	Spatial resolution (mm)	References
Univ. Arizona SPECT/CT	CdZnTe pixel	1×10^{-3}	1–2	[44, 47]
SemiSPECT	CdZnTe pixel	5×10^{-3}	1.45	[48, 59]
SiliSPECT	Si microstrip	$7–8 \times 10^{-2}$	0.27	[61, 68]
MediSPECT	CdTe pixel	1.6×10^{-2}	<1	[31, 69, 70]
SOLSTICE	CdZnTe strip	NA	<2.5	[11, 53, 81, 82]
LBNL	Si:Li pixel	1.8×10^{-2}	1.6	[30]

For MediSPECT and LBNL, data are reported for ^{125}I imaging (*NA* not available)

Table 2.7 Comparison of performance (sensitivity and spatial resolution, simulated or measured) of semiconductor based small animal PET prototypes (*NA* not available)

System	Technology	Sensitivity (%)	Spatial resolution (mm)	References
SiliPET	Si strips	5.1	0.52	[91–95]
Univ. Tohoku	CdTe strips	1	0.74	[96–100]
Univ. Davis, CA	CdTe strips	3.4	0.5	[101, 102]
Univ. Hokkaido	CdTe	NA	2.6	[103, 104]
SmartPET	HPGe strips	0.99	1.4	[105–112]
CEA-Leti	CdZnTe strips	NA	<1	[89, 113]
CIMA Si-pad	Si pads	1	0.34	[114–118]

This was also possible because of the technical advancements in minute segmentation of the readout electrodes of such detectors, with pitch values well below 1 mm. The potential drawback of the semiconductor detectors—their limited quantum efficiency at medium (140 keV) and high (511 keV) gamma-ray energies, for thin detector substrates—has been bypassed by using side-on irradiation geometries. This allows also to manage the problem of limited active area (a few cm by side) of semiconductor detectors; in fact, for small animal imaging a limited number of closely packed detectors irradiated by their side can be arranged around the animal so as to obtain an adequate FoV coverage. Good spectroscopic performance—often better than scintillator based detectors—is achieved by improved material fabrication and electrical contact technologies, which permit the use of high bias voltages. The major potential for improvement and technological innovation of semiconductor imaging detectors could be in the field of microPET, where high sensitivity (≈4–5 %) with high resolution (≈0.5 mm) are already feasible, as well as integration with semiconductor based microCT. Once available in significant production volumes, all-semiconductor based SPECT/CT and PET/CT systems may contribute to the reduction of the high end-user price of such pre-clinical systems, this being one of the major limitation to the diffusion of small animal imaging systems with ionizing radiation.

References

1. Barrett HH and Hunter WCJ (2005) Detectors for small-animal SPECT I. In: Kupinski MA and Barrett HH (eds.), Small animal SPECT imaging, pp. 26–27. Springer, Heidelberg.
2. (eV Products 2009) http://www.evproducts.com/material_prop.pdf (accessed May 2009).
3. Barrett HH, Eskin JD, and Barber HB (1995) Charge transport in arrays of semiconductor gamma-ray detectors. Phys Rev Lett 5: 156–159.
4. Spartiotis K, Leppänen A, Pantsar T, Pyyhtiä J, Laukka P, Muukkonen K, Maännistö O, Kinnari J, and Schulman T 2005 A photon counting CdTe gamma- and x-ray camera. Nucl Instrum Methods Phys Res A **550**: 267–277.
5. Russo P, Mettivier G, Pani R, Pellegrini R, Cinti MN, and Bennati P (2009) Imaging performance comparison between a $LaBr_3$:Ce scintillator based and a CdTe semiconductor based photon counting compact gamma camera. Med Phys 36: 1298–1317.

6. Guerra P, Santos A, and Darambara DG (2009) An investigation of performance characteristics of a pixellated room-temperature semiconductor detector for medical imaging. J Phys D: Appl Phys 42: 175101.
7. Prokesch M and Szeles C (2006) Accurate measurements of electrical bulk resistivity and surface leakage current of CdZnTe radiation detector crystals. J Appl Phys 100: 014503.
8. Devanathan R, Corrales LR, Gao F, and Weber WJ (2006) Signal variance in gamma-ray detectors—A review. Nucl Instrum Methods Phys Res A **565**: 637–649.
9. "BrilLanCe™380 scintillation material," Technical Data Sheet (2007) (available online at websitehttp://www.detectors.saint-gobain.com/Media/Documents/S00000000000000001004/SGC_BrilLanCe_380_data_sheet.pdf) (accessed May 2009).
10. AMPTEK website (http://www.amptek.com/CdTe.html) (accessed May 2009).
11. Gagnon D, Zeng GL, Links JM, Griesmer JJ, and Valentino FC (2001) Design considerations for a new solid-state gamma-camera: SOLSTICE. Nuclear Science Symposium Conference Record, IEEE, vol. 2: 1156–1160.
12. Ogawa K, Hota A, Shuto K, Motomura N, Kobayashi H, Makino S, Nakahara T, and Kubo A (2006) Development of semiconductor gamma-camera system with CdZnTe detectors. Nuclear Science Symposium Conference Record, 2006, IEEE, vol. 4: 2426–2429.
13. Shulman T (2006) Si, CdTe and CdZnTe radiation detectors for imaging application. PhD thesis, University of Helsinki, Finland, 2006 (available online at website http://ethesis.helsinki.fi/julkaisut/mat/fysik/vk/schulman/sicdtean.pdf) (accessed May 2009).
14. XCOM: Photon Cross Sections Database. Available online at website (http://physics.nist.gov/PhysRefData/Xcom/Text/XCOM.html) (accessed May 2009).
15. ACRORAD Co. website (http://www.acrorad.co.jp/us/cdte.html) (accessed May 2009).
16. Heijne EHM (2001) Semiconductor micropattern pixel detectors: a review of the beginnings. Nucl Instrum Methods Phys Res A **465**: 1–26.
17. Institute of Experimental and Applied Physics, Czech Technical University, Prague, CZ. Available online at website (http://aladdin.utef.cvut.cz/ofat/Methods/Xray_radiography/XrayRadiography.html) (accessed May 2009).
18. Mikulec B, Campbell M, Heijne E, Llopart X, and Tlustos L (2003) X-ray imaging using single photon processing with semiconductor pixel detectors. Nucl Instrum Methods Phys Res A **511**: 282–286.
19. Heijne EHM (2001) Future semiconductor detectors using advanced microelectronics with post-processing, hybridization and packaging technology. Nucl Instrum Methods Phys Res A **541**: 274–285.
20. Alimonti G, Andreazza A, Bulgheroni A, Corda G, Di Gioia S, Fiorello A, Gemme C, Koziel M, Manca F, Meroni C, Nechaeva P, Paoloni A, Rossi L, Rovani A, and Ruscino E (2006) Analysis of the production of ATLAS indium bonded pixel modules. Nucl Instrum Methods Phys Res A **565**: 296–302.
21. Szeles C, Soldner SA, Vydrin S, Graves J, and Bale DS (2008) CdZnTe semiconductor detectors for spectroscopic X-ray imaging. IEEE Trans Nucl Sci **55**: 572–582.
22. Ballabriga R, Campbell M, Heijne EHM, Llopart X, and Tlustos L (2007) The Medipix3 prototype, a pixel readout chip working in single photon counting mode with improved spectrometric performance. IEEE Trans Nucl Sci **54**: 1824–1829.
23. Rönnquist C, Santps F, Toker O, Weilhammer P, Yoshioka K, Nygård E, Czermak E, Jalocha P, Dulinski W, and Hu Y (1994) Double-sided silicon microstrip detectors and low noise self-triggering multichannel readout chips for imaging applications. Nucl Instrum Methods Phys Res A 348: 440–443.
24. Beccherle R Bertolucci E, Bisogni MG, Bottigli U, Collins T, Conti M, Del Guerra A, Fantacci ME, Gambaccini M, Kipnis I, Marchesini R, Marziani M, Rosso V, Russo P, Russo S, Stefanini A, Taibi A, and Tripiccione R (1996) Development of a digital radiography system based on silicon microstrip detector. Physica Medica XII: 17–24.
25. Speller RD, Royle GJ, Triantis FA, Manthos N, Van der Stelt PF, and di Valentin M (2001) Digital X-ray imaging using silicon microstrip detectors: a design study. Nucl Instrum Methods Phys Res A 457: 653–664.

26. Bertolucci E, Conti M, Grossi G, Madonna G, Mancini E, Russo P, Caria M, Randaccio P, Del Guerra A, Gambaccini M, Marchesini R, Marziani M, Taibi A, Beccherle R, Bisogni MG, Bottigli U, Fantacci ME, Rosso V, Stefanini A, Tripiccione R, and Amendolia SR (1996) Autoradiography with silicon strip detectors. Nucl Instrum Methods Phys Res A 381: 527–530.
27. Overdick M, Czermak A, Fischer P, Herzog V, Kjensmo A, Kugelmeier T, Ljunggren K, Nygård E, Pietrzik C, Schwan T, Strand S-E, Straver J, Weilhammer P, Wermes N, and Yoshioka K (1997) A Bioscope system using double-sided silicon microstrip detectors and self-triggering read-out chips. Nucl Instrum Methods Phys Res A 392: 173–177.
28. Chmeissani M and Mikulec B (2001) Performance limits of a single photon counting pixel system. Nucl Instrum Methods Phys Res A 460: 81–90.
29. Beekman FJ, McElroy DP, Berger F, Gambhir SS, Hoffman EJ, and Cherry SR (2002) Towards in vivo nuclear microscopy: iodine-125 imaging in mice using micro-pinholes. Eur J Nucl Med 29: 933–938.
30. Choong WS, Moses WW, Tindall CS, and Luke PN (2005) Design for a high-resolution small-animal SPECT system using pixelated Si:Li detectors for in ^{125}I imaging. IEEE Trans Nucl Sci **52**: 174–180.
31. Accorsi R, Celentano L, Laccetti P, Lanza RC, Marotta M, Mettivier G, Montesi MC, Roberti G, and Russo P (2008) High resolution I-125 small animal imaging with a coded aperture and a hybrid pixel detector. IEEE Trans Nucl Sci **55**: 481–490.
32. Huang AB, Franc BL, Gullberg GT, and Hasegawa BH (2008) Assessment of the sources of error affecting the quantitative accuracy of SPECT imaging in small animals. Phys Med Biol 53: 2233–2252.
33. Belcari N, Bisogni MG, Carpentieri C, Del Guerra A, Delogu P, Panetta D, Quattrocchi M, Rosso V, and Stefanini A (2007) Preliminary characterization of a single photon counting detection system for CT application. Nucl Instrum Methods Phys Res A 576: 204–208.
34. Chmeissani M, Frojdh C, Gal O, Llopart X, Ludwig J, Maiorino M, Manach E, Mettivier G, Montesi MC, Ponchut C, Russo P, Tlustos L, and Zwerger A (2004) First experimental tests with a CdTe photon counting pixel detector hybridized with a Medipix2 readout chip. IEEE Trans Nucl Sci **51**: 2379–2385.
35. Blanchot G, Chmeissani M, Díaz A, Díaz F, Fernández J, García E, García J, Kainberger F, Lozano M, Maiorino M, Martínez R, Montagne JP, Moreno I, Pellegrini G, Puigdengoles C, Sentís M, Teres L, Tortajada M, and Ullán M (2006) Dear-Mama: a photon-counting X-ray imaging project for medical applications. Nucl Instrum Methods Phys Res A 569: 136–139.
36. Autiero M, Celentano L, Cozzolino R, Laccetti P, Marotta M, Mettivier G, Montesi MC, Riccio P, Roberti G, and Russo P (2005) Experimental study on in vivo optical and radionuclide imaging in small animals. IEEE Trans Nucl Sci **52**: 205–209.
37. Funaki M, Ando Y, Jinnai R, Tachibana A, and Ohno R (2007) Development of CdTe detectors in Acrorad. *International Workshop on Semiconductor PET*. Unpublished. Available online at website (http://www.acrorad.co.jp/pdf/Development_of_CdTe_detectors.pdf) (accessed May 2009).
38. Marks DG, Barber HB, Apotovsky BA, Augustine FL, Barrett HH, Dereniak EL, Doty FP, Eskin JD, Hamilton WJ, Matherson KJ, Venzon JE, Woolfenden JM, and Young ET (1996) A 48×48 CZT array with multiplexer readout. IEEE Trans Nucl Sci **43**: 1253–1259.
39. Matherson KJ, Barber HB, Barrett HH, Eskin JD, Dereniak EL, Marks DG, Woolfenden JM, Young ET, and Augustine FL (1998) Progress in the development of large-area modular 64×64 CdZnTe imaging arrays for nuclear medicine. IEEE Trans Nucl Sci **45**: 354–358.
40. Basolo S, Berar JF, Boudet N, Breugnoa P, Chantepia B, Clemens JC, Delpierre P, Dinkespiler B, Hustache S, Medjoubi K, Menouni M, Morel C, Pangaud P, and Vigeolas EA (2008) 20 k pixels CdTe photon-counting imager using XPAD chip. Nucl Instrum Methods Phys Res A 589: 268–274.
41. Takahashi T, Wataname S, Kouda M, Sato G, Okada Y, Kubo S, Kuroda Y, Onishi M, and Ohno R (2001) High-resolution CdTe detector and applications to imaging devices. IEEE Trans Nucl Sci **48**: 287–291.

42. Meng L-J, Tan JW, Spartiotis K, and Schulman T (2009) Preliminary evaluation of a novel energy-resolved photon-counting gamma ray detector. Nucl Instrum Methods Phys Res A **604**: 548–554.
43. Mitani T, Nakamura H, Uno S, Takahashi T, Nakazawa K, Watanabe S, Tajima H, Nomachi M, Fukazawa Y, Kubo S, Kuroda Y, Onishi M, and Ohno R (2003) Large area Gamma-ray Imaging Detector Based on High Resolution CdTe Diode. IEEE Trans Nucl Sci **50**: 1048–1052.
44. Kastis GA, Wu MC, Balzer SJ, Wilson DW, Furenlid LR, Stevenson G, Barrett HH, Barber HB, Woolfenden JM, Kelly P, and Appleby M (2002) Tomographic small-animal imaging using a high-resolution semiconductor detector. IEEE Trans Nucl Sci **49**: 172–175.
45. Chambron J, Arntz Y, Eclancher B, Scheiber Ch, Siffert P, Hage Hali M, Regal R, Kazandjian A, Prat V, Thomas S, Warren S, Matz R, Jahnke A, Karman M, Pszota A, and Nemet L (2000) A pixelated γ-camera based on CdTe detectors clinical interests and performances. Nucl Instrum Methods Phys Res A **448**: 537–549.
46. Tsuchimochi M, Sakahara H, Hayama K, Funaki M, Ohno R, Shirahata T, Orskaug T, Maehlum G, Yoshioka K, and Nygard E (2003) A prototype small CdTe gamma camera for radioguided surgery and other imaging applications. Eur J Nucl Med Mol Imaging **30**: 1605–1614.
47. Kastis GA, Furenlid LR, Wilson DW, Peterson TE, Barber HB, and Barrett HH (2004) Compact CT/SPECT small-animal imaging system. IEEE Trans Nucl Sci **51**: 63–67.
48. Kim H, Furenlid LR, Crawford MJ, Wilson DW, Barber HB, Peterson TE, Hunter WCJ, Liu Z, Woolfenden JM, and Barrett HH (2006) SemiSPECT: A small-animal single-photon emission computed tomography SPECT imager based on eight cadmium zinc telluride (CZT) detector arrays. Med Phys **33**: 465–474.
49. Parnham KB, Grosholz J, Davis RK, Vydrin S, and Cupec CA (2001) Development of a CdZnTe-based small field of view gamma camera. Proc SPIE **4508**: 134–140.
50. Wagenaar DJ, Chowdhury S, Engdahl JC, and Burckhardt DD (2003) Planar image quality comparison between a CdZnTe prototype and a standard NaI(Tl) gamma camera. Nucl Instrum Methods Phys Res A **505**: 586–589.
51. Eisen Y, Mardor I, Shor A, Baum Z, Bar D, Feldman G, Cohen H, Issac E, Haham-Zada R, Blitz S, Cohen Y, Glick B, Falk R, Roudebush S, and Blevis I (2002) NUCAM3—A gamma camera based on segmented monolithic CdZnTe Detectors. IEEE Trans Nucl Sci **49**: 1728–1732.
52. Eisen Y, Shor A, and Mardor I (2004) CdTe and CdZnTe x-ray and gamma-ray detectors for imaging systems. IEEE Trans Nucl Sci **51**: 1191–1198.
53. Griesmer JJ, Kline B, Grosholz J, Parnham K, and Gagnon D (2001) Performance evaluation of a new CZT detector for nuclear medicine: SOLSTICE. Nuclear Science Symposium Conference Record, IEEE, vol. 2: 1050–1054.
54. Azman S, Gjaerum J, Meier D, Muftuler LT, Maehlum G, Nalcioglu O, Patt BE, Sundal B, Szawlowski M, Tsui BMW, Wagenaar DJ, and Wang Y (2007) A nuclear radiation detector system with integrated readout for SPECT/MR small animal imaging. Nuclear Science Symposium Conference Record, IEEE, vol. 3: 2311–2317.
55. Mestais C, Baffert N, Bonnefoy JP, Chapuis A, Koenig A, Monnet O, Ouvrier Buffet P, Rostaing JP, Sauvage F, and Verger L (2001) A new design for a high resolution, high efficiency CZT gamma camera detector. Nucl Instrum Methods Phys Res A **458**: 62–67.
56. Barber HB, Barrett HH, Augustine F., Hamilton WJ, Apotovsky BA, Dereniak EL, Doty FP, Eskin JD, Garcia JP, Marks DG, Matherson KJ, Woolfenden JM, and Young ET (1997) Development of a 64×64 CZT array and associated readout integrated circuit for use in nuclear medicine. J Electron Mater **26**: 765–772.
57. Kastis GA, Barber HB, Barrett HH, Balzer SJ, Lu D, Marks DG, Stevenson G, Woolfenden JM, Appleby M, and Tueller J (2000) Gamma-ray imaging using a CdZnTe pixel array and a high-resolution, parallel-hole collimator. IEEE Trans Nucl Sci 47: 1923–1927.
58. http://www.radiology.arizona.edu/CGRI/research-projects/animal.html (accessed May 2009).

59. Peterson TE, Hyunki K, Crawford MJ, Gersham BM, Hunter WCJ, Barber HB, Furenlid LR, Wilson DW, Woolfenden JM, and Barrett HH (2002) SemiSPECT: a small-animal imaging system based on eight CdZnTe pixel detector. Nuclear Science Symposium Conference Record (2002), IEEE, vol. 3: 1844–1847.
60. http://www.radiology.arizona.edu/CGRI/research-projects/Adaptive_Modality_Imaging/adaptive_modality.html (accessed May 2009).
61. Shokouhi S, Fritz MA, McDonald BS, Wilson M.D., Metzler SD, and Peterson TE (2006) Design of a Multi-Pinhole Collimator in a Dual-Headed, Stationary, Small-Animal SPECT. Nuclear Science Symposium Conference Record, IEEE, vol. 4: 2399–2402.
62. Shokouhi S, Durko HL, Fritz MA, Furenlid LR, and Peterson TE (2006) Thick silicon strip detectors for small-animal SPECT imaging. Nuclear Science Symposium Conference Record, IEEE, vol. 6: 3562–3566.
63. McDonald BS, Shokouhi S, Barrett HH, and Peterson TE (2006) Multi-energy, single-isotope pinhole imaging using stacked detectors. Nuclear Science Symposium Conference Record (2006), IEEE, vol. 3: 1797–1801.
64. Shokouhi S, McDonald BS, Durko HL, Fritz MA, Furenlid LR, Peterson TE (2007) Performance characteristics of thick silicon double sided strip detectors. Nuclear Science Symposium Conference Record, IEEE, vol. 2: 1656–1660.
65. Shokouhi S, Fritz MA, McDonald BS, Durko HL, Furenlid LR, Wilson DW, and Peterson TE (2007) A silicon SPECT system for molecular imaging of the mouse brain. Nuclear Science Symposium Conference Record, IEEE, vol. 4: 2782–2784.
66. Shokouhi S, Wilson DW, Pham W, and Peterson TE (2007) System evaluation for in vivo imaging of amyloid beta plaques in a mouse brain using statistical decision theory. Nuclear Science Symposium Conference Record, IEEE, vol. 6: 4528–4530.
67. http://www.radiology.arizona.edu/CGRI/SiliSPECT.pdf (accessed May 2009).
68. Shokouhi S, Metzler SD, Wilson DW, and Peterson TE (2009) Multi-pinhole collimator design for small-object imaging with SiliSPECT: a high resolution SPECT. Phys Med Biol 54: 207–225.
69. Accorsi R, Autiero M, Celentano L, Chmeissani M, Cozzolino R, Curion AS, Frallicciardi P, Laccetti P, Lanza RC, Lauria A, Maiorino M, Marotta M, Mettivier G, Montesi MC, Riccio P, Roberti G, and Russo P (2007) MediSPECT: Single photon emission computed tomography system for small field of view small animal imaging based on a CdTe hybrid pixel detector. Nucl Instrum Methods Phys Res A **571**: 44–47.
70. Accorsi R, Curion AS, Frallicciardi P, Lanza RC, Lauria A, Mettivier G, Montesi MC, and Russo P (2007) Preliminary evaluation of the tomographic performance of the MediSPECT small animal imaging system. Nucl Instrum Methods Phys Res A **571**: 415–418.
71. Autiero M, Celentano L, Cozzolino R, Laccetti P, Marotta M, Mettivier G, Montesi MC, Riccio P, Roberti G, and Russo P (2006) Multimodal system for in vivo tumor imaging in mice. Proc SPIE 6191: 340–352.
72. Llopart X, Campbell M, Dinapoli R, SanSegundo D, and Pernigotti E (2002) Medipix2, a 64 k pixel read-out with 55 μm square elements working in single photon counting mode. IEEE Trans Nucl Sci **49**: 2279–2283.
73. Medipix2 collaboration website: www.cern.ch/medipix (accessed May 2009).
74. Russo P (2002) Hybrid semiconductor pixel detectors for low- and medium-energy X- and gamma-ray single photon imaging using the Medipix read-out chip. In: Hornak JP (ed.), *Encyclopedia of Imaging Science and Technology*. Wiley Interscience, John Wiley & Sons, Inc., New York.
75. Tlustos L, Ballabriga R, Campbell M, Heijne E, Kincade K, Llopart X, and Stejskal P (2006) Imaging properties of the Medipix2 system exploiting single and dual energy thresholds. IEEE Trans Nucl Sci **53**: 367–372.
76. Mettivier G, Montesi MC, Sebastiano A, and Russo P (2006) High frame rate X-ray imaging with a 256×256 pixel single photon counting Medipix2 detector. IEEE Trans Nucl Sci **53**: 1650–1655.

77. Maiorino M, Pellegrini G, Blanchot G, Chmeissani M, Garcia J, Martinez R, Lozano M, Puigdengoles C, and Ullan M (2006) Charge sharing observations with a CdTe pixel detector irradiated with a ^{57}Co source. Nucl Instrum Methods Phys Res A **563**: 177–181.
78. Pellegrini G, Chmeissani M, Maiorino M, Blanchot G, Garcia J, Lozano M, Martinez R, Puigdengoles C, Ullan M, and Casado P (2006) Performance limits of a 55-μm pixel CdTe detector. IEEE Trans Nucl Sci **53**: 361–366.
79. Pellegrini G, Maiorino M, Blanchot G, Chmeissani M, Garcia J, Lozano M, Martinez R, Puigdengoles C, and Ullan M (2007) Direct charge sharing observation in single-photon-counting pixel detector. Nucl Instrum Methods Phys Res A **573**: 137–140.
80. Zeng GL and Gagnon D (2004) CdZnTe strip detector SPECT imaging with a slit collimator. Phys Med Biol 49: 2257–2271.
81. Gagnon D, Penn MS, Lee D, Urbain J-L, Chi-Hua T, Kline B, Bender PJ, Mercer DL, and Griesmer JJ (2002) Use of SOLSTICE rotating slat solid-state camera for small animal imaging. Nuclear Science Symposium Conference Record, IEEE, vol. 3: 1367–1369.
82. Moses WW Nuclear medical imaging: Techniques and challenges. Available online at website (http://instrumentationcolloquium.lbl.gov/Nuclear%20Medical%20Imaging.pdf) (accessed May 2009).
83. Stickel JR and Cherry SR (2005) High-resolution PET detector design: modeling components of intrinsic spatial resolution. Phys Med Biol 50: 179–195.
84. Levin CS and Hoffman EJ (1999) Calculation of positron range and its effects on the fundamental limit of positron emission tomography system spatial resolution. Phys Med Biol 44: 781–799.
85. Drezet A, Monnet O, Montémont G, Rustique J, Sanchez G, and Verger L (2004) CdZnTe detectors for the positron emission tomographic imaging of small animals. Nuclear Science Symposium Conference Record, IEEE, vol. 7: 4564–4568.
86. Conti M, Del Guerra A, Mazzei D, Russo P, Bencivelli W, Bertolucci E, Messineo A, Rosso V, Stefanini A, Bottigli U, Randaccio P, and Nelson WR (1992) Use of EGS4 Monte Carlo code to evaluate the response of HgI2 and CdTe semiconductor detectors in the diagnostic energy range. Nucl Instrum Methods Phys Res A 322: 591–595.
87. Baldazzi G, Bollini D, Casali F, Chirco P, Donati A, Dusi W, Landini G, Rossi M, and Stephen JB (1993) Timing response of CdTe detectors. Nucl Instrum Methods Phys Res A 326: 319–324.
88. Bertolucci E, Conti M, Curto CA, and Russo P (1997) Timing properties of CdZnTe detectors for positron emission tomography. Nucl Instrum Methods Phys Res A **400**: 107–112.
89. Drezet A, Monnet O, Mathy F, Montémont G, and Verger L (2007) CdZnTe detectors for small field of view positron emission tomographic imaging. Nucl Instrum Methods Phys Res A **571**: 465–470.
90. Vaska P, Bolotnikov A, Carini G, Camarda G, Pratte J-F, Dilmanian FA, Park S-J, and James RB (2005) Studies of CZT for PET Applications. Nuclear Science Symposium Conference Record, IEEE, vol. 5: 2799–2802.
91. Zavattini G, Cesca N, Di Domenico G, Moretti E, and Sabba N (2006) SiliPET: an ultra high resolution design of a small animal PET scanner based on double sided silicon strip detector stacks. Nucl Instrum Methods Phys Res A **568**: 393–397.
92. Auricchio N, Cesca N, Di Domenico G, Moretti E, Sabba N, Gambaccini M, Zavattini G, Andritschke R, Kanbach G, and Schopper F (2005) SiliPET: design of an ultra high resolution small animal PET scanner based on stacks of semiconductor detectors. Nuclear Science Symposium Conference Record, IEEE, vol. 5: 3010–3013.
93. Gola A, Fiorini C, Di Domenico G, Zavattini G, and Auricchio N (2006) An ASIC circuit for timing measurements with strip detectors, designed for the SiliPET project. Nuclear Science Symposium Conference Record, IEEE, vol. 1: 370–374.
94. Auricchio N, Di Domenico G, Zavattini G, Gola A, Fiorini C, Frigerio M, Ambrosi G, Ionica M, Fiandrini E, Zorzi N, and Boscardin M (2007) First measurements of the SiliPET project: a small animal PET scanner based on stacks of silicon detectors. Nuclear Science Symposium Conference Record, IEEE, vol. 4: 2926–2929.

95. Auricchio N.; Di Domenico G.; Milano L.; Malaguti R.; Ambrosi G, Ionica M, Fiandrini E, Zorzi N, Boscardin M, and Zavattini G (2008) Experimental measurements for the SiliPET project: a small animal PET scanner based on stacks of silicon detectors. Nuclear Science Symposium Conference Record, IEEE: 366–369.
96. Kikuchi Y, Ishii K, Yamazaki H, Matsuyama S, Yamaguchi T, Yamamoto Y, Sato T, Aoki Y, and Aoki K (2005) Preliminary report on the development of a high resolution PET camera using semiconductor detectors. Nucl Instrum Methods Phys Res B **241**: 727–731.
97. Kikuchi Y, Ishii K, Yamazaki H, Matsuyama S, Momose G, Ishizaki A, Kisaka J, and Kudo T (2006) Feasibility of ultra high resolution better than 1 mm FWHM of small animal PET by using CdTe detector arrays. Nuclear Science Symposium Conference Record, IEEE, vol. 4: 2454–2457.
98. Ishii K, Kikuchi Y, Matsuyama S, Kanai Y, Kotani K, Ito T, Yamazaki H, Funaki Y, Iwata R, Itoh M, Kanai Km Hatazawa J, Itoh N, Tanizaki N, Amano D, Yamada M, and Yamaguchi T (2007) First achievement of less than 1 mm FWHM resolution in practical semiconductor animal PET scanner. Nucl Instrum Methods Phys Res A **576**: 435–440.
99. Kikuchi Y, Ishii K, Terakawa A, Matsuyama S, Yamazaki H, Hatazawa J, and Kotani K (2007) Prototype of high resolution PET using resistive electrode position sensitive CdTe detectors. Nuclear Science Symposium Conference Record, IEEE, vol. 4: 2669–2672.
100. Kikuchi Y, Ishii K, Yamazaki H, Matsuyama S, Nakhostin M, Sakai T, Nakamura K, and Kouno M (2008) Fundamental study of two-dimensional position sensitive CdTe detector for PET camera. Nuclear Science Symposium Conference Record, IEEE, vol. 4: 4924–4926.
101. Kim H, Cirignano LJ, Dokhale P, Bennet P, Stickel JR, Mitchell GS, Cherry SR, Squillante M, and Shah K (2006) CdTe orthogonal strip detector for small animal PET. Nuclear Science Symposium Conference Record, IEEE, vol. 6: 3827–3830.
102. Mitchell GS, Sinha S, Stickel JR, Bowen SL, Cirignano LJ, Dokhale P, Kim H, Shah K, and Cherry SR (2008) CdTe strip detector characterization for high resolution small animal PET. IEEE Trans Nucl Sci **55**: 870–876.
103. Yanagita N, Morimoto Y, Ishitsu T, Suzuki A, Takeuchi W, Seino T, Takahashi I, Ueno Y, Amemya K, Inoue S, Suzuki M, Kozawa F, Kubo N, and Tamaki N (2007) Physical performance of a prototype 3D PET scanner using CdTe detectors. Nuclear Science Symposium Conference Record, IEEE, vol. 4: 2665–2668.
104. Ueno Y, Morimoto Y, Tsuchiya K, Yanagita N, Kojima S, Ishitsu T, Kitaguchi H, Kubo N, Zhao S, Tamaki N, and Amemiya K (2009) Basic performance test of a prototype PET scanner using CdTe semiconductor detectors. IEEE Trans Nucl Sci **56**: 24–28.
105. Hall CJ, Nolan PJ, Boston AJ, Helsby WI, Berry A, Lewis RA, Gillam J, Beveridge T, Mather AR, Turk G, Norman J, and Gross S (2003) A gamma tracking detector for nuclear medicine. Nuclear Science Symposium Conference Record, IEEE, vol. 3: 1877–1881.
106. Boston HC, Boston AJ, Cooper RJ, Cresswell J, Grint AN, Mather AR, Nolan PJ, Scraggs DP, Turk G, Hall CJ, Lazarus I, Berry A, Beveridge T, Gillam J, and Lewis R (2007) Characterization of the SmartPET planar Germanium detectors. Nucl Instrum Methods Phys Res A **579**: 104–107.
107. Gillam J, Beveridge T, Svalbe I, Grint A, Cooper R, Boston A, Boston H, Nolan P, Hall C, and Lewis R (2008) Compton imaging using the SmartPET detectors. Nuclear Science Symposium Conference Record, IEEE: 624–628.
108. http://ns.ph.liv.ac.uk/imaging-group/group-members/andrew-mather.php (accessed August 2009).
109. Cooper RJ, Boston AJ, Boston HC, Cresswell J, Grint AN, Mather AR, Nolan PJ, Scraggs DP, Turk G, Hall CJ, Lazarus I, Berry A, Beveridge T, Gillam J, and Lewis RA (2007) SmartPET: applying HPGe and pulse shape analysis to small-animal PET. Nucl Instrum Methods Phys Res A **579**: 313–317.
110. Cooper RJ, Turk G, Boston AJ, Boston HC, Cresswell J, Mather AR, Nolan PJ, Hall CJ, Lazarus I, Simpson J, Berry A, Beveridge T, Gillam J, and Lewis RA (2007) Position sensitivity of the first SmartPET HPGe detector. Nucl Instrum Methods Phys Res A **573**: 72–75.

111. Cooper RJ, Boston AJ, Boston HC, Cresswell JR, Grint AN, Harkness LJ, Nolan PJ, Oxley DC, D.P. Scraggs DP, Lazarus I, Simpson J, Dobson J (2008) Charge collection performance of a segmented planar high-purity germanium detector. Nucl Instrum Methods Phys Res A **595**:401–409.
112. Cooper RJ, Boston AJ, Boston HC, Cresswell J, Grint AN, Harkness LJ, Nolan PJ, Oxley DC, Scraggs DP, Mather AR, Lazarus I, and Simpson J (2009) Positron emission tomography imaging with the SmartPET system. Nucl Instrum Methods Phys Res A **606**: 523–532.
113. Peyret O (2006) Towards digital X-ray imaging. Available online at website(http://www.minatec-crossroads.com/pdf-AR/Peyret.pdf) (accessed August 2009).
114. CIMA Collaboration website (http://www.cima-collaboration.org).
115. Park S-J, Rogers WL and Clinthorne NH (2007) Design of a very high-resolution small animal PET scanner using a silicon scatter detector. Phys Med Biol 52: 4653–4677.
116. Clinthorne N (2009) Methods for High Resolution PET. Stanford Linear Accelerator Center, Advanced Instrumentation Seminar, 1April 2009. Available online at website (http://www-group.slac.stanford.edu/ais/publicDocs/presentation113.pdf) (accessed August 2009).
117. Park S-J, Rogers WL, Huh S, Kagan H, Honscheid K, Burdette D, Chesi E, Lacasta C, Llosa G, Mikuz M, Studen A, Weilhammer P, and Clinthorne NH (2007) A prototype of very high-resolution small animal PET scanner using silicon pad detectors. Nucl Instrum Methods Phys Res A **570**: 543–555.
118. Park S-J, Rogers WL, Huh S, Kagan H, Honscheid K, Burdette D, Chesi E, Lacasta C, Llosa G, Mikuz M, Studen A, Weilhammer P, and Clinthorne NH (2007) Performance evaluation of a very high resolution small animal PET imager using silicon scatter detectors. Phys Med Biol 52: 2807–2826.

Chapter 3
Photon Detectors for Small-Animal Imaging Instrumentation

Dieter Renker and Eckart Lorenz

1 Introduction

In nearly all detectors for small animal studies using the imaging technique, the first step in the detection of X-rays or gamma-rays (shortcut γ) is the conversion of the absorbed X-rays or γ's into photons mostly in the visible spectrum by high z, high density scintillation crystals (see Chap. 1). In this process, normally only a small fraction of the absorbed X-ray or γ-energy is converted into light. Typical conversion efficiencies for commonly used scintillation crystals range between 20 and 100 eV energy loss for the generation of a single photon in the few eV range. As most scintillation crystals emit in the spectral range between 300 and 700 nm (with only a few exceptions) the typical conversion fraction in energy is between 0.1 and 0.02. Table 3.1 lists some parameters of common scintillation crystals, their peak spectral emission and the number of photons/keV deposited energy in that scintillation crystal. The numbers are typical values because many subtle effects can change the listed values, for example nonlinearities in the light emission as a function of the γ-energy or self-absorption losses of the scintillation material. For the physics of the main γ-absorption processes by the photoelectric effect or Compton scattering the reader is referred to Chap. 1.

After the conversion of high energy radiation into photons in the eV range the next processes are the photon transport to a photon detector and the conversion of the photons into an electrical signal by means of an optimally adapted photon detector. In the following we skip details of photon transport inside the crystals as well as

D. Renker (✉)
Paul Scherrer Institute, Villigen, Switzerland
e-mail: dieter.renker@ph.tum.de

E. Lorenz
Max Planck Institute for Physics, Munich, Germany

Eidg. Technische Hochschule, Zurich, Switzerland
e-mail: e.lorenz@mac.com

H. Zaidi (ed.), *Molecular Imaging of Small Animals: Instrumentation and Applications*,
DOI 10.1007/978-1-4939-0894-3_3,

Table 3.1 Some key parameters of common scintillation crystals for X-ray and γ-ray detection

Scintillation crystals	Density (g/cm^3)	Atomic number Z	Photo fraction @ 511 keV (%)	Peak emission wavelength (nm)	Refractive index	Photons per keV	Decay time τ of main comp. (ns)	Hygroscopic
NaI(Tl)	3.67	43	18	410	1.85	38–40	250	Yes
CsI(Tl)	4.51	54		540	1.79	55	≈1,000	(Yes)
CsI(Na)	4.51	54		420	1.84		630	Yes
LSO[a]	7.4	65	34	420	1.81	27	40	No
LuI_3[a]	5.6	59		470		47	30	Yes
BGO	7.13	73	43	480	2.15	8	300	No
YAG	4.55	15		550	1.82	8	60–70	No
$LaCl_3$(Ce)	3.79	36		350	1.9	49	28	Yes
$LaBr_3$(Ce)	5.29	43	15	380	1.9	63	26	Yes

[a]Radioactive

the problem of light extraction and efficient coupling of the scintillation crystals to the photon detector, referring the reader to Chap. 1 of this volume, and concentrate on the issue of the photon detection efficiency. Nevertheless, we make some simplifying assumption that only typically a fraction of light can be extracted and coupled to the photon detectors because of geometrical limitations.

While for CT detectors a high photon extraction efficiency is possible, the photon extraction efficiency in SPECT or PET detectors is typically only between 10 and 30 %, because one normally couples the photon detector to the rear cross section of the crystals. If intermediate light guides are used the extraction efficiency can be even lower. From the data in Table 3.1 a number of conclusions can be derived for the requirements for the photon detectors.

- The conversion of photons into photoelectrons should be as high as possible, i.e. the photon detector should have a high quantum efficiency (QE).
- The photon detection efficiency[1] (PDE), i.e. the efficiency to convert photons into measurable photoelectrons, should be close to the QE of the photon detector, i.e. losses of photoelectrons inside the photon detectors should be minimal.
- If the transfer of the photons from the scintillation location to the photon detector is inefficient, which normally is the case, and only a small fraction of the total number of produced photons impinge onto the photon detector, the requirements in high PDE in the detector will have to be even more demanding.
- Photons in the eV energy range can only be converted in common photon detectors into at most one photoelectron. Therefore the number of expected electrons from common scintillation crystals is much smaller than normally needed for data processing. Therefore signal amplification is needed. If possible, the amplifiers, either internal or external, should not degrade the signal.
- A timing signal in the (sub)-nsec range is frequently needed for PET but nearly all suitable scintillating crystals have a decay time in the range of 20–1,000 ns. In most cases only a few photons are emitted during the first (few) nsec(s) and could be used for deriving a timing signal. Therefore, suitable photon detectors require a good single photoelectron response (SER)
- It follows that for nsec timing measurements the photon detectors and the needed amplifiers (internally or externally) should have an intrinsic bandwidth equal to or superior to the goals in timing to be achieved.
- The spectral sensitivity of a photon detector should be optimally matched to the emission spectrum of the scintillation crystals.
- As scintillation crystals normally are of high refractive index (n in the range of 1.7–2.2) efficient optical coupling to the photon detector is needed.

[1] It is quite common to use the QE to specify the number of photoelectrons in a photon detector. The QE ignores the subsequent losses of photoelectrons inside the photon detector, for example in the front-end of a PMT. The PDE, respectively effective QE specifies the more realistic number of photoelectrons that are amplified and processed in the subsequent electronics system following the photon converter of the photon detector.

It should be mentioned that both in PET and SPECT one normally tries to measure the time and energy of single γ-quanta with relatively high precision, while in CT one measures integrated fluxes and deposited energy as a function of time because the X-ray flux is normally much too high to allow counting and a measurement of the energy of individual X-rays hitting a detector pixel. A precise energy measurement of the individual X-ray quanta is currently not needed because of the broad energy spectrum of the X-ray generator and the lack of a method to determine the initial energy of X-rays before interaction in the body under examination. The γ-detectors for PET and SPECT should have at least an energy resolution of a few percent to separate the 'γ'-line from the Compton edge.

Also, some other conditions should be fulfilled for practical applications:

- The photon detectors should be unaffected by magnetic fields or at least be easily protected by suitable shielding materials.
- Nearly all devices for radiation detection normally work in an environment of high electromagnetic background. Therefore, a high immunity against EMI is needed.
- The devices must be easy to operate and should not drift over time in an uncontrolled way.
- Radiation damage is, in general, not an issue because most sensors were initially developed for other applications used in much higher radiation environments compared to that in small animal imaging devices.

Particularly for small animal imaging some requirements related to the small dimensions of the objects to be studied should be fulfilled:

- The resolution of the instruments should be well adapted to the dimensions of structures to be studied. This requires small pixel elements to achieve sub-mm resolution.
- As objects to be studied normally have dimensions comparable to the crystal length, parallax errors become important and need to be corrected.
- Scintillation crystals and particularly the photon detectors should be as compact as possible. This condition is a 'must' in case mobile applications are needed (see example in Fig. 3.17).
- As the volume to detector surface of a small animal PET is normally much smaller than in the case of a human PET the radiation levels will normally be smaller, simply because of the reduced uptake. Therefore, the timing resolution for separating events in PET and SPECT is less demanding than in human PET. Similarly, Compton scattering background inside the small animals is also much lower in small animal PET and SPECT compared to human PET/SPECT.
- In case of very compact detectors minimizing heat developed by the local electronics is an issue.

Currently, four families of photon sensors are used for fast, low light flux detection

(a) Photomultipliers (PMT), i.e. vacuum photon detectors with secondary photoelectron multiplication by means of a number of dynodes at different electrostatic potentials.
(b) Solid state photon sensors based on silicon without internal amplification:

- PIN photodiodes, currently of very restricted use in PET or SPECT.
- CCD arrays, only for CT.
- Drift photodiodes

(c) Solid state sensors, based on silicon, with internal amplification:

- Avalanche photodiodes (APD) operated in the linear amplification mode just below breakdown voltage.
- Geiger-mode avalanche photodiodes (G-APD) operated slightly above breakdown voltage but using avalanche induced current quenching following the Geiger principle

(d) Exotic photon detectors.

There are quite a few special photon detectors (exotic photon detectors) allowing one in principle to detect low light level signals, such as for example hybrid photomultipliers, gaseous photon detectors, cryogenic photon detectors, or non-silicon solid state photon detectors. All these detectors have either severe deficiencies concerning the discussed application (large size, low QE, complex operation) or are not yet mature, respectively are not yet produced at large industrial levels.

PMTs are the long-term 'workhorse' for fast and low level light detection and are well established in the field of nuclear medical applications Unfortunately, they are not suited to being operated in magnetic fields, such as inside Magnetic Resonance (MRI) scanners, and small pixel sizes are difficult to achieve. Nowadays, multianode PMTs with pixel sizes down to 2×2 mm^2 are available. Equally suited for the readout of fine pixilated scintillating crystal matrices is the Anger-camera principle, i.e. the sharing of light from a pixel by a few larger area PMTs. While for human PET detectors the block detector principle is strongly favored because it allows for a large reduction in readout channels, a coupling of one photon detector to one crystal slab (1:1 coupling) is also possible for small animal PET detectors because the number of channels is still manageable.

The main deficiencies of APDs are their low gain, their sensitivity to temperature changes and to even small voltage drifts, all of which are difficult to control. It is quite likely that the use of linear mode APDs is only an intermediate step towards the use of G-APDs as readout elements in the near future. G-APDs are still under development, but rapidly approaching maturity. They offer a number of advantages making them the most promising photon detectors in PET/SPECT for small animal imaging.

Before discussing the different sensors in detail we present in Table 3.2 a comparison of the advantages and disadvantages of the PMTs, APDs and G-APDs for the use in PET and SPECT detectors using scintillation crystals as γ-detectors.

Table 3.2 Comparison of some basic features (typical) of PMTs, APDs and G-APDS for PET and SPECT crystal readout. Some parameters are expected to improve in the near future[a]

Feature	PMT	APD	G-APD
Volume, compared to crystals	*Very large*	Very compact	Very compact
Readout Pixel structure	*Limited*	Very fine	Very fine
Block readout	Well established	First tests	First tests
Area limitations	No	Few cm^2	<1 cm^2
User experience	High	Some	Prototype
Costs	Very high	Medium	Still high, long-term lowest
Operation voltage (V)	*1,000–1,500*	300–500	30–100
Voltage regulation needed	High	*Very high*	High
Gain	10^5–10^6	*50–300*	10^5 to *few* 10^6
Dynamic range	High	High	Some limitations
High rate operation	High	*Limited*	Minor limitations
Sensitivity to magnetic fields	*Very high*	No	No
Need for high quality preamp	No	*Yes*	No
Sensitivity for pick-up	Medium	*Very high*	Low
Requirement for shielding	Some	*Necessary*	Optional
Quantum efficiency (%)	20–25	60–80	25–50
Can detect single photons	Yes	No	Yes
Pulse risetime single photoel.	1–2 ns		<1 ns
Noise	Very low	High	High, uncritical
Excess noise factor	1.2–1.5	*5–10 at gain* 1,000	1.0–1.2
Temperature sensitivity	Very low	Very high	Medium for high overvoltage
Sensitivity to bias drifts	Low	Very high	Medium for high overvoltage
Commercially available	Yes	Yes, new	Yes
Damage due to light exposure	High	No	No
Radiation damage	Modest	Low	*Modest*
Potential for mass production	*Low, hand assembled*	Medium, ion implantation	Very high, CMOS technology

[a]In italics: parameters that can seriously affect performance

The structure of the section on photon detectors is the following: in Sect. 2 we will briefly review the general principle of photon detection. In Sect. 3 we will give a short survey of the processes influencing the signal losses from the conversion in the crystal to the detection of the photons in the photon detector influencing the energy resolution and timing. In Sect. 4 we will discuss the classical photon detector, the photomultiplier, reviewing its basic design principle, features and limitations. In Sects. 5 and 6 we will discuss solid state photon detectors without and with internal gain, their basic construction and their features and limitations relevant for photon detection in small animal imaging. Also in Sect. 6, we will briefly mention some application examples, while in Sect. 7 some special requirements not specific

to photon detection will be discussed. In Sect. 8, a short outlook on prospects on improving photon detection in the future will be given. It should be mentioned that in this report emphasis is mainly put on more recent photon detector developments, which are at present mostly driven by the requirements for PET or SPECT. In particular, we will only briefly mention their uses and details in CT because the photon detection technology in this area is rather static since a few years and well documented. On the other hand, the solid state photon detectors, based on the Geiger mode avalanche photodiodes (G-APD), are given more room, because these detectors are undergoing rapid progress and have the potential of becoming soon the leading photon detector for scintillation crystal readout in small animal PET. It is perhaps interesting to mention that at the recent photon detector conference in Aix-les Bains (2008) more than half of the submitted contributions were dealing with developments of G-APDs.

2 Some Comments on Resolution Issues

Before discussing details of the photon detectors we will briefly discuss some issues concerning resolution requirements. Emphasis is again put mostly on PET and SPECT.

In small animal imaging instruments using radiation detectors, one has to deal with three issues of resolution[2] linked in part to the photon detectors:

- The spatial resolution,
- The energy resolution,
- The timing resolution.

The spatial resolution is mostly influenced by the geometry and crystal subdivision of the detector. In case of a geometry with a 1:1 coupling the energy resolution and noise contribution of the photon detector has very little impact on the image resolution, except an uncertainty of the depth of interaction (DOI) in PET, resulting in a parallax error along the crystal length. In principle, one is able to measure the DOI by means of a readout from both crystal ends and a comparison of the pulse heights. Other methods consist of combining two shorter crystal slabs of very different decay time to a longer slab thus allowing one to tag the interaction in one of the two sections by pulse shape discrimination. A high energy resolution as well as a good pulse shape measurement will reduce false associations. The situation is quite different in the block detector readout. Here, the energy resolution and the contribution from the detector noise can influence the image resolution.

In the following we use the example of PET to demonstrate the limitations and benefits of standard photon detectors concerning the image resolution.

[2] Here we follow the convention in nuclear medical applications for the definition of the resolution as the FWHM (FWHM = 2.35 σ) of the distribution.

Moses and Derenzo proposed an empirical formula, which nicely describes the reconstructed FWHM spatial resolution [2]:

$$FWHM = a\sqrt{\left(d/2\right)^2 + b^2 + r^2 + \left(0.0022D\right)^2}$$

where d is the detector size, b the position decoding accuracy, r the positron range, D is the system diameter used to describe the photon annihilation non-colinearity, a is a correction factor and depends on the algorithm used to reconstruct the images a ranges typically from 1.1 to 1.3.

The photon non-colinearity is almost negligible in a scanner for small animals and the positron range r is given by the isotope used, while d and b can be minimized in the design. In case of installing the PET detector inside a high field MRI magnet, the range of the positrons is shortened by 'spiraling'.

"Block" detectors using light sharing and Anger-like logic, the only choice when standard PMTs are used, have in average a value $b \sim 2$ mm [3–7]. A better value of $b \sim 1$ mm can be achieved with 1:1 direct coupling of crystals to position-sensitive or multi-anode PMTs [8–13].

Only the third category, where the crystals are individually coupled to photon detectors and independent electronics, achieves an intrinsic resolution that is equal to the geometric resolution ($b \sim 0$) [14–17]. This readout scheme can be currently only realized with solid state photon detectors which can be tailored to the required geometry. An image resolution of 1 mm has been achieved with 0.8 mm wide crystals [18].

The energy resolution is of less importance provided one is able to separate the photopeak events from the Compton events. The energy resolution is influenced by quite a few different processes, which can eventually prevent a clear separation of the photopeak from the Compton edge. In the following we assume for simplicity that we deal with only 511 keV γ-quanta, which are fully absorbed in a single crystal slab. The following processes will all contribute to a degradation of the energy resolution:

(a) The scintillation light yield will depend on the local 'quality' of the crystal, i.e. from the local crystal defects and local admixture of activation material.
(b) A small but important broadening of the resolution will be the so-called non-proportionality of the light yield at very low γ or electron energies. This effect is strongest at lowest energies and broadens the intrinsic scintillation resolution beyond the 2.35/N, N being the mean number of scintillating photons. A very good scintillation crystal, such as YAP:Ce or $LaCl_3$:Ce can have an intrinsic energy resolution of around 5 % at 511 keV.
(c) The next process in broadening the scintillation photon distribution seen from an end of the crystal is the variable light collection influenced by geometrical effects, absorption losses inside the crystal, surface scattering losses and effects of the reflector material (diffuse reflection, specular reflection). In case of a truncated pyramid shape of the crystals in a radial arrangement and a readout by

the rear crystal end one can easily get a higher light yield from the far side than from the side of the readout. This results in a broadening of the resolution when averaging over the crystal. By appropriate surface treatment it is possible to improve the uniformity and in turn the resolution. Generally one can collect at most 25–50 % of all photons in a not too long crystal at the rear surface to be coupled to a photon detector. In case of long crystals these numbers will significantly decrease.

(d) At the end-face one normally couples the crystal to the photon detector by means of optical grease or optical glue matched closely to the refractive index of the PMT glass window or the silicon photon detectors, which are normally protected by a thin layer of transparent plastic material. As most useful crystals for PET or SPECT have a refractive index well above the optical coupling material, a sizeable fraction of the light remains trapped inside the crystal.

(e) The next class of loss is the backreflection of photons by the photon detector, which in case of a PMT can vary between a few percent to up to around 30 % (wavelength dependent). Also silicon photon detectors have quite some backreflection. Part of the backreflected photons might be 'recycled' a second time onto the photon detector in case of small and compact crystals while for long crystals most of the backreflected photons are lost.

(f) Not all the photons entering either the photocathode in a PMT or the silicon of the silicon photon detectors are converted into free electrons. The relevant number is the quantum efficiency (QE), which is the ratio of the number of 'freed' photoelectrons to the number of impinging photons. Typical QE values for classical PMTs range between 20 and 30 % at peak sensitivity, close to 80 % for PIN and avalanche photodiodes and anywhere between 20 and 70 % for G-APDs (depending of the active to total area ratio, often called the fill factor).

(g) Not all the photoelectrons can be collected and amplified. It is therefore more appropriate to replace the QE by the so-called photon detection efficiency (PDE). The ratio of the PDE/QE has typical values between 0.8 and 0.9 for the best PMTs[3] (≈0.6–0.7 for mesh dynode PMTs, due to geometrical effects), close to 1 for PIN and avalanche photodiodes and between ≈0.2 and 0.6 for current G-APDs (strongly dependent on operation parameters).

(h) The amplification normally adds some additional broadening of the resolution distribution on the amplified photoelectrons. This number is commonly named the excess noise factor F (see Sect. 4.4). Best PMTs have an F-factor of 1.1–1.2, PIN photodiodes an intrinsic F factor of 1 (plus the intrinsic noise contribution from the amplifier), linear mode APDs have a typical F-factor ranging from 5 to 10 at a gain of 500 (see Fig. 3.13) with a very strong gain dependence while G-APDs have a value of about 1.1–1.3, again gain and geometry dependent.

[3] There exists another source of loss in the PMT front-end. Photoelectrons are sometimes backscattered when impinging on the first dynode and have a very low chance to produce a secondary electron. This process is up to now not well measured and often ignored.

In the above list we ignored small effects like trapping effects, phosphorescence or wavelength shifting, etc.

It is obvious that due to the multitude and diversity of processes affecting the energy resolution it is difficult to predict the resolution beforehand. Monte Carlo simulation might predict the resolution within 30 %. Experimental optimization is currently the most frequently used procedure to determine the resolution. For example, single LSO crystals coupled to selected PMTs can give about 10 % resolution for 511 keV γs, while one normally achieves a resolution of 12–25 % in densely packed arrangements and a block readout. At around 25 % resolution one already has considerable overlap between the photopeak and Compton events.

As mentioned before, timing resolution in the 0.5–1 ns range is in most cases sufficient, because it is very difficult to achieve high counting rates in small animals due to the limited uptake.

As nearly all scintillation crystals, except a few unsuited materials such as ZnO or the J9758 from Hamamatsu, have quite long decay times, one generates timing signals from the very first detected photon respectively from the rise time of the scintillation pulses by using standard methods, such as constant fraction discriminators, leading edge discriminators, or the high-low discrimination technique. As the crystals are normally only a few (10–20) mm long, time dispersion inside the crystal can be ignored.

A reason for generating timing signals is the need for coincidence triggers from the two gammas. With PMTs and G-APDs it is possible to achieve sub-ns time resolutions, while photodiodes and avalanche photodiodes allow only a considerably worse timing resolution of, at best, a few ns.

A good pulse shape discrimination is essential for DOI measurements when combining two scintillation crystals of a different decay time.

3 General Principle of Photon Detection

Two processes, the external and the internal photoeffect, are used for the detection of photons. Both are based on the transfer of the photon energy to an electron in a collision. When a photon impinges on the surface of any material it can liberate an electron, provided the energy of the photon is higher than the photoelectric work function ϕ. This was first formulated by A. Einstein in 1905 [1]:

$$W_{kin} = h\nu - \phi$$

The kinetic energy W_{kin} of the electron can be sufficient to bring the electron not only from the surface, but also from the volume of the material, to the free space. Semiconductors have a very small work function ϕ. Consequently, the threshold wavelength of the incoming photon can be in the near infrared. Standard bialkali photocathodes in photomultipliers (Sb–Rb–Cs, Sb–K–Cs) have a threshold at 630 nm (red light).

The internal process needs less energy. In a semiconductor it is sufficient to lift an electron from the valence band to the conduction band. Therefore a silicon crystal (bandgap 1.1 eV) can be a very efficient photon detector in the complete range of visible light. If the electron does not recombine with the hole in the conductive band due to the electric field of a silicon photodiode it can be collected and the signal amplified.

4 Classical Readout Using PMTs

4.1 History

In 1913, Elster and Geitel invented the first photoelectric tube. Some years earlier, in 1889, they had reported the photoelectric effect induced by visible light striking an alkali metal [19]. The first photomultiplier tube (PMT) was invented in 1930 by L. Kubetsky. In 1939, V. Zworykin and his colleagues from the RCA laboratories developed a PMT with electrostatic focusing [20], the basic structure of current PMT's (Fig. 3.1). A short time afterwards it became a commercial product. Single photons were detectable from now on.

Further innovations have led to highly sophisticated devices available nowadays. The bulky shape turned into a flat design with a length of a few centimeters and with pixilated anodes the PMTs became position sensitive. While early PMTs allowed only a block readout, a 1:1 coupling of crystals to a position sensitive PMT became possible, a scheme where the end faces of small crystals are coupled to a matching pixel of the PMT (Fig. 3.2). A vacuum container is still needed, but the fraction of the active faceplate area compared to the total faceplate of the PMT is now close to 90 %.

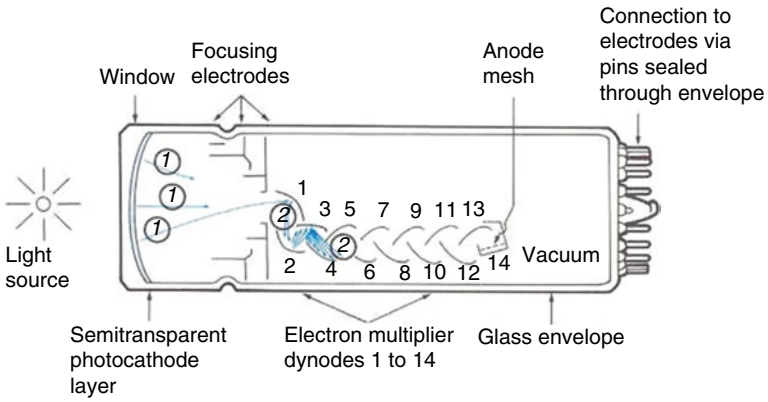

Fig. 3.1 Cross section of a photomultiplier tube. (*1*) Indicates the electrons liberated by photons from the photocathode and (*2*) shows the cascade of secondary electrons in the first stages of the multiplier dynodes

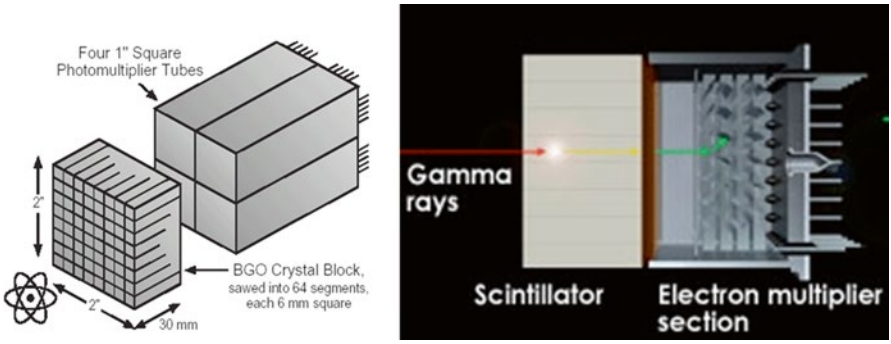

Fig. 3.2 Crystal block design with conventional PMTs (*left*), and 1:1 coupling with state of the art position sensitive flat panel PMTs (*right*). Shown are the small scintillating crystals and the individual dynode structure and anode of the PMT pixels

4.2 Gain

The gain of standard PMTs is very high with typical values of 10^6–10^7. It is almost completely independent of the temperature and in a wide dynamic range independent of the rate that needs to be handled. Without the need for an amplifier the output signals can be directly fed into standard readout electronics.

4.3 Photon Detection Efficiency

The main characteristic of a photomultiplier is its quantum efficiency (QE), which describes the probability of a photon creating a free electron, which can be amplified in the dynode structure. Several effects influence the QE: the photon can be reflected by the glass of the window, it can pass through the photocathode without interaction and it can produce an electron in the volume of the photocathode which electron is stopped inside the material. The overall effect limits the QE to typically 25 %. Manufacturers usually provide the radiant sensitivity (the cathode photocurrent divided by the radiant power), not the QE. An example is shown in Fig. 3.3.

As can be seen from Fig. 3.3, it is possible to select a photocathode material, which matches the emission wavelength of the crystal scintillator used.

The QE can be calculated from the radiant sensitivity $S_k(\lambda)$ by

$$\mathrm{QE} = S_k(\lambda) \cdot \frac{hc}{e\lambda} \Rightarrow QE(\%) = 1.24 \cdot \frac{S_k(\lambda)}{\lambda}$$

with the Planck's constant h, the speed of light c, the wavelength λ expressed in nm and $S_k(\lambda)$ in mA/W.

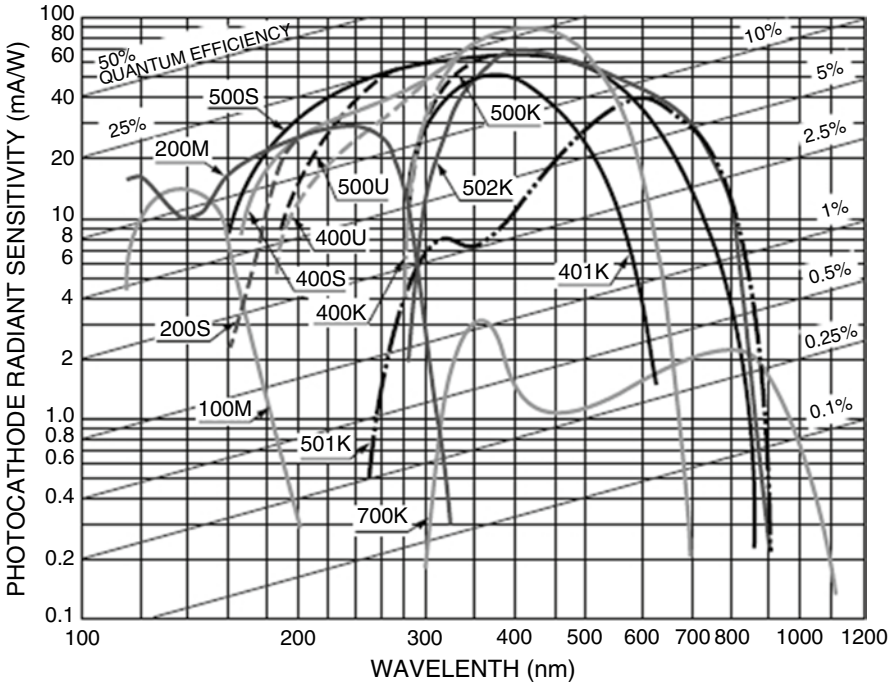

Fig. 3.3 Radiant sensitivity for several photocathode materials. The QE is indicated by the *inclined lines* (Hamamatsu PMT handbook)

Recently, the QE was boosted to values above 40 % by employing extremely pure bialkali photocathode materials and precise control of the vapor deposition process [21]. Photocathodes made of GaAsP(Cs), a new material, which is difficult to deposit, also provides a QE of more than 50 % in a wide range of wavelengths.

Usually the collection efficiency (CE), i.e. the probability that an electron, liberated from the photocathode, reaches the first dynode, is neglected. The CE can be as low as 70 %. The photon detection efficiency (PDE), the probability of an incoming photon creating an output signal is:

$$\mathrm{PDE} = \mathrm{QE} \times \mathrm{CE}$$

Actually, some other effect might further reduce the PDE, even if the photoelectron hits the first dynode. Depending on the dynode material and the acceleration voltage, the photoelectron might, with some probability, be backscattered (elastically or inelastically) and will thus not produce any secondary electrons at all or only a few. Backscattering is not fully understood and is normally treated as part of the collection efficiency.

Hybrid photon detectors are a variant of the photomultiplier. The vacuum container and the photocathode are the same, but multiplication is not realized in a

chain of dynodes. The electrons liberated in the photocathode by a photon are accelerated in a high electric field (15–25 kV) and are focused onto a silicon diode or onto an avalanche photodiode (APD). In the silicon, the electrons lose their energy by ionization. They produce electron–hole pairs, which can be collected in case they are produced in the depletion layer. The diodes (avalanche diodes) need a very thin $p^+(n+)$ top layer, because the pairs created in this layer recombine immediately and are lost. An energy loss of 3.6 eV is needed to create an electron–hole pair. The ratio of the gained electron energy (corrected by the loss in the dead area) divided by 3.6 eV sets the amplification, which is about 5,000 when using a PIN diode while in case of an APD this has to be multiplied by the APD internal gain (resulting in a total gain of a few 10^5–10^6).

4.4 The Excess Noise Factor

The energy resolution σ(E)/E of a crystal-PMT assembly is dominated by the stochastic distribution of the produced and collected photons (N_{photon}).

$$\frac{\sigma(E)}{E} = \sqrt{\frac{1}{N_{photon} \cdot PDE}}$$

The resolution is degraded by the excess noise factor F, which is mainly caused by the secondary electrons produced in the first dynode. The resolution becomes:

$$\frac{\sigma(E)}{E} = \sqrt{\frac{F}{N_{photon} \cdot PDE}}$$

A typical value is $F \approx 1.2$ for standard PMTs (The character F is also used for the Fano factor which affects the photon statistics or the statistics of electron–hole generation in semiconductors and is used in Sect. 2. In the light production in scintillating crystals, Poisson statistics apply and the Fano factor is $\cong 1$).

4.5 Time Resolution

The output signal of PMTs is very fast (rise time of about 1 ns) provided the proper dynode structure is used. In such cases it is possible to achieve an excellent time resolution, which is limited by the so-called transit time spread (TTS). This is a measure of the variations of time an electron needs for travelling from the photocathode to the first dynode. Typical values are about 200 ps. Some PMT types, in which mesh dynodes or micro channel plates are used as electron multipliers, show a very small TTS, and a time resolution of only 50 ps or even less can be achieved. The caveats of such structures are a higher price and a reduced CE.

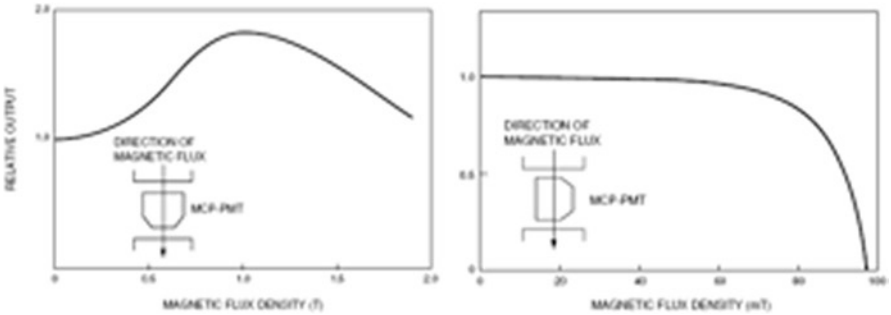

Fig. 3.4 Relative output of an MCP–PMT when its axis is oriented parallel (*left*) and perpendicular (*right*) to a magnetic field

Besides the transit time spread, some PMTs also show different delay effects of photoelectrons emitted in the central area and those emitted at the outer area because of the longer flight path and in turn lower field strength when focusing photoelectrons onto a small dynode area.

Like the energy resolution, the time resolution improves in first order with the number of detected photons:

$$\sigma(t) \propto \sqrt{\frac{1}{N_{photon} \cdot PDE}}$$

4.6 Operation in Magnetic Fields

Both normal and hybrid PMTs, are extremely sensitive even to small (mT) magnetic fields. Specialized devices with micro channel plates (MCP) instead of the dynode structure work in magnetic fields, but only if it is strictly parallel to the axis of the PMT (Fig. 3.4).

4.7 Advantages and Disadvantages

For many decades, PMTs have been the workhorse for single photon and low level light detection. Their advantages are obvious:

- The gain is high (10^6–10^7) and in most cases no amplifier is needed.
- The operation is relatively stable because the temperature dependence of the gain is very small. Nevertheless, some gain drift can occur, particularly immediately after biasing.

- A very good energy resolution can be achieved when state of the art scintillating crystals are used (i.e. lutetium–oxyorthosilicate or the newly developed $LaCl_3$(Ce) or $LaBr_3$(Ce) crystals).
- Compared to most other photon detectors the excess noise factor is small.
- An excellent time resolution can be obtained.
- The multiplication in a chain of dynodes is one of the best known low noise amplifications.

There are a number of disadvantages:

- Most severe is the strong sensitivity to magnetic fields (preventing any use in MRI magnets).
- PMTs need a high operating voltage of about 2 kV and special devices (hybrid PMTs) need about 20 kV.
- State of the art PMTs have a peak QE of typically 25 % and a typical front-end photoelectron collection efficiency of 70–80 %, i.e. a peak PDE of around 20 %.
- It is very difficult to produce a very fine pixilated ($<2\times2$ mm^2) PMT.
- State of the art PMTs have rather large volumes compared to the crystals commonly used in small animal detectors. It is therefore difficult to build high resolution detectors with a 1:1 coupling.
- It is impossible to stabilize the gain by some feedback mechanism like in operation amplifiers
- The fabrication of PMTs is costly because 30 or more parts have to be assembled by hand in a vacuum container which afterwards has to be well sealed.

5 Readout with Solid State Photo Sensors Without Internal Gain

5.1 History

Semiconductor photodiodes were developed in the early 1940s approximately at the time when the photomultiplier tube became a commercial product. Only in recent years, with the invention of the Geiger-mode avalanche photodiodes, semiconductor photon detectors have reached a sensitivity comparable to that of photomultiplier tubes. The evolution started in the 1960s with the p-i-n (PIN) photodiode, a very successful device, which is still used in many detectors for high energy physics and in a large number of other applications like radiation detection and medical imaging. The next step was the development of the avalanche photodiode (APD), leading to a substantial reduction of noise but not yet achieving single photon response.

The weakest light flashes that can be detected by the PIN diode need to contain several hundreds of photons. An improvement of the sensitivity by two orders of magnitude was achieved by the development of the avalanche photodiode, a device

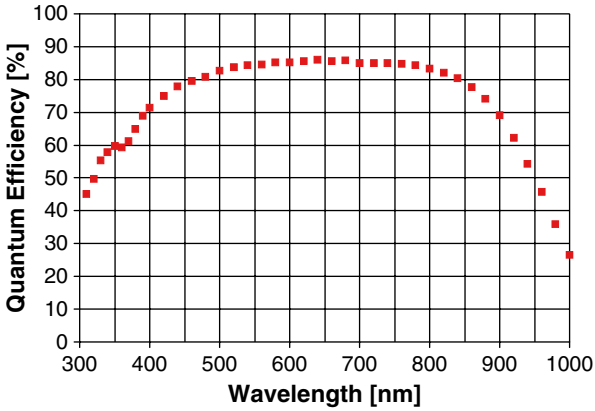

Fig. 3.5 QE as function of the wavelength of a silicon photodiode. Reprinted with permission from [22]

with internal gain. At the end of the millennium, the semiconductor detectors evolved with the Geiger-mode avalanche photodiode into highly sensitive devices, which have an internal gain comparable to the gain of photomultiplier tubes and a response to single photons.

Solid state devices have the big advantage that they can be produced in standard fully automated processes and can therefore be cheap. They can be customized to individual needs in a short time, i.e. within few months, they have low mass and very small space consumption, and they need only a low operating voltage. The detector by itself is only about 0.3 mm thick, and the housing thickness can be less than 0.5 mm. In addition, they are insensitive to magnetic fields with a theoretical limit of about 15 T. The quantum efficiency is very high in all solid state devices, because basically only the reflection at the surface reduces the detection probability. A silicon photodiode has a QE of 85 % in almost the whole range of visible light [22]. In the blue range of the spectrum, where most scintillating crystals have their peak emission, the QE is still 70–80 % (Fig. 3.5). It is difficult to achieve a high QE below ≈400 nm because of the very short absorption lengths of UV photons.

5.2 Detectors Integrating Over Many Photons

In detectors integrating over many photons (subsequently called integrating detectors) the signal is proportional to the number of photons per time interval. Integrating light detectors nowadays are mostly found in image processing for consumer or medical applications. Best known are simple versions, called Charged Coupled Devices (CCD), which can be found in digital cameras as well as in highly sophisticated devices in astronomical telescopes or as X-ray detectors on satellites. CCDs made of an array of pixels have a quantum efficiency of 70 % and more over a rather wide spectral range, making them far more sensitive than photographic films, which capture only about 2 % of the incident light.

Faster, cheaper and less power-consuming are the Monolithic Active Pixel Sensors (MAPS) or Complementary Metal Oxide (CMOS) image sensors, which, in contrast to CCDs, are compatible with the Complementary Metal Oxide production technology. All components necessary for the readout can be implanted on one single piece of silicon.

In hybrid pixel detectors, a pixelized sensor chip made of any kind of semiconductor material is bump-bonded to a readout chip. Photon detection with this technique is only possible when the photon energy exceeds several keV. In imaging applications, the hybrid pixel detectors define the incident radiation through the counting of the radiation quanta in every pixel [23].

For radiography, the MEDIPIX (versions 1, 2 and 3) chip [24] and the MPEC chip [25] have been developed. These chips can be combined with sensors made of various semiconductor materials including the high-Z material CdTe.

The first large-scale hybrid pixel detector in operation is the PILATUS detector [26], developed at the Paul-Scherrer-Institute in Switzerland for proton crystallography experiments like at the Swiss Light Source (SLS). A remarkably low energy threshold below 3 keV has been obtained with 320 μm thick Si sensors [27]. PILATUS is a modular system. Each module consists of a Si sensor bump-bonded to an array of 8×2 chips using indium balls. It has 487×195 pixels with a pixel size of 0.172 mm. The 16 chips of a module are read out in parallel within a read-out time of ~2 ms. The PILATUS 6 M contains 6×12 modules, spans an area of 424×435 mm^2 and has six million pixels in total. With thin (20 μm) YAG(Ce) or LuAG(Ce) scintillating screens coupled to CCD cameras a spatial resolution of a few micron has been achieved. Very high efficiency can be achieved in fiber optics plates with CsI scintillators, again coupled to CCDs. CsI can be grown in a column structure. The scintillation light is confined to the columns in a similar way as in fibers and is guided towards the sensor, which typically is a CCD, but can as well be a sensor of the MEDIPIX type. The spatial resolution is defined by the diameter of the columns, which can be as small as 10–20 μm.

5.3 The PIN Photodiode

The PIN photodiode is one of the simplest types of photodiodes. It is an intrinsic piece of high ohmic semiconductor sandwiched between two heavily doped n^+ and p^+ regions (Fig. 3.6). It is produced by standard semiconductor processes: boron diffusion on one side and phosphor diffusion on the other side of a high purity n-type silicon wafer. This configuration produces a field, which, even without an external field supplied, will tend to separate charges produced in the depleted region. The separated charges will be swept to the terminals and detected as current provided that they do not already recombine inside the semiconductor. The thick layer of intrinsic silicon (300 μm) reduces the capacitance of the diode and, thus, the serial noise, and makes it sensitive to red and infrared light, which has a rather long absorption length in silicon. Since this layer has a very low concentration of

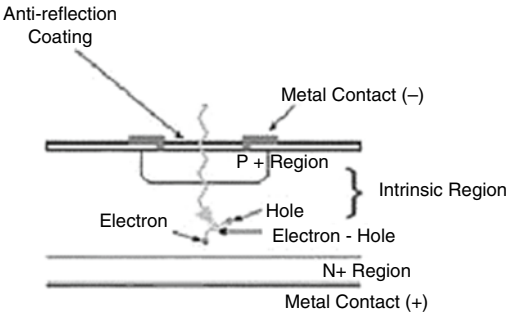

Fig. 3.6 Structure of a PIN photodiode

dopants, only a small voltage is required to deplete the device completely. An additional advantage is the fact that the recombination/generation time constant is longest in case of undoped materials, which also provide a minimal thermal generation current. Clearly the top p-layer, which cannot be depleted, needs to be transparent to incoming light. A thin, but highly doped layer is used in silicon photodiodes.

The operation of a PIN photodiode is simple and reliable, but, since it has no internal gain, a charge sensitive amplifier and a low bandwidth filter amplifier are needed for the detection of low light level signals above the sizeable noise caused by the leakage current and the large diode capacitance, which is typically some 40 pF/cm^2. On the other hand, due to the absence of internal gain, PIN photodiodes offer an exceptional stability. For the treatment of noise, we refer to [28]. The use of a charge-sensitive preamplifier and a filter amplifier makes the signal slow. The lowest intensity light flash detectable above noise needs to be several hundred photons for state of the art cm^2 PIN photodiodes and filter time constants of a few μs.

Nowadays, PIN diodes with areas of 10 cm^2 and more are available, and it is easy to manufacture position sensitive arrays—even monolithic ones—with a large number of elements. As mentioned before, the noise of large PIN photodiodes increases proportionally to the area, respectively to the diode capacitance.

The low signal-to-noise ratio requires long integration times in the electronics, reducing the ability to determine the arrival of the pulses, which is an important aspect for PET. Therefore, PIN photodiodes are generally not suitable for use in PET. In combination with PMTs PIN photodiodes have been used to measure the depth of interaction in a PET detector [29].

5.4 Silicon Drift Photodiode

If a low noise for a large area readout is required, a possible way out is drifting the photoelectrons to a small collection area with a low capacitance. A caveat is that the drift collection times can be quite long and again the readout will be rather slow; in addition, the flux has to be low to avoid pileup. The silicon drift photon detector (SDD) is a fully depleted diode in which an electric field nearly parallel to the

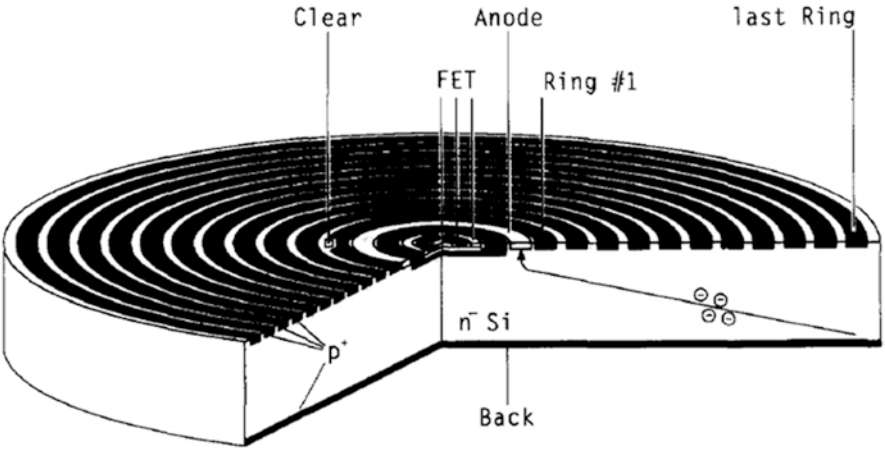

Fig. 3.7 Cross section of a cylindrical silicon drift detector with an integrated n-channel JFET. The entrance window is the non-structured backside. Reprinted with permission from [30]

surface is created by properly biased continuous field strips. Figure 3.7 shows a typical example. The field configuration drives free electrons created anywhere in the depleted volume towards a collecting anode in the center. The unique feature is a low noise due to an extremely low anode capacitance, which is, moreover, independent of the detector area. It is possible to achieve a noise level of only a few electrons, albeit with a jitter in time due to the normally unknown photon conversion location and thus due to the drift delay. To take full advantage of the low output capacitance, the front-end n-channel JFET of an amplifier can be integrated on the detector chip close to the n^+ implanted anode.

Examples for the excellent performance of these devices are given in [31, 32]. A circular SDD with an active area of 30 mm^2 has been coupled to the high light yield scintillator $LaBr_3(Ce)$ and yielded an energy resolution of 2.7 % FWHM for the 662 keV line of ^{137}Cs when converted in the scintillator.

Gamma cameras of the Anger type with the excellent spatial resolution of 0.35 mm FWHM (Fig. 3.8) have been built [33] or are under construction [34].

6 Solid State Photon Detectors with Internal Amplification

6.1 Avalanche Photodiodes

A modification of the photodiode leads to a device known as the avalanche photodiode (APD). The APD is another step towards increasing the sensitivity of photon detectors by reducing the noise at high bandwidth. An avalanche photodiode (APD) is a p–n device with internal gain due to the high internal field at the

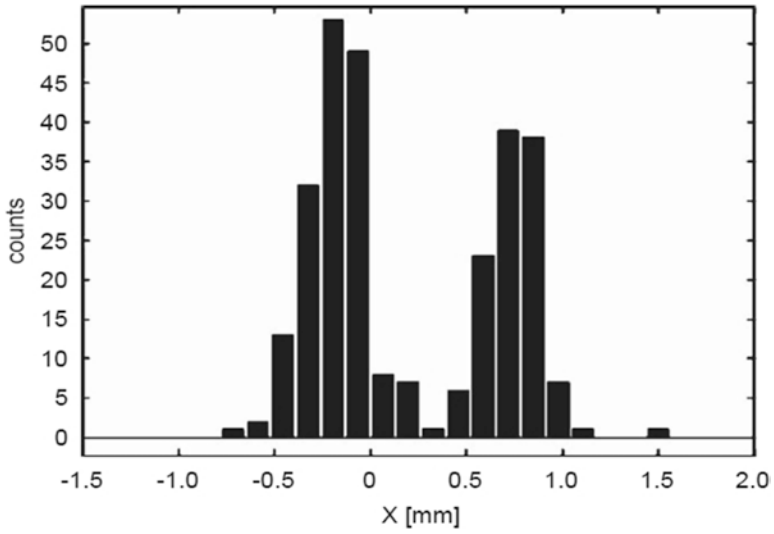

Fig. 3.8 One-dimensional section of two irradiation spots of a collimated ^{57}Co source. The average spatial resolution is 0.35 mm FWHM. Reprinted with permission from [33]

junction of positive and negative doped silicon. In an APD, a photoelectron in this field gains enough energy to create an electron–hole pair by impact ionization; both the initial electron and the additional electron again undergo high acceleration and can initiate further electron–hole pairs—thus starting an avalanche. The electric field must reach a critical value, called the impact ionization threshold, which is approximately 1.75×10^5 V/cm for silicon, before electrons can gain sufficient kinetic energy to generate electron/hole pairs [35]. The field strength for holes to generate impact ionization is around 2.5×10^5 V/cm [36]. The impact ionization process generates M additional carriers on average, where M is called the multiplication gain. The multiplication in practical APDs is moderate, between 50 and 200. A gain of 10^4 is in principle possible, but at gain values higher than a few hundred, the environment (e.g. temperature and voltage supply) needs to be strongly regulated because the APD has to be operated extremely close to the breakdown voltage.

Again, the QE is in the of 70–85 % range. When combined with the relative high gain, this leads to roughly equivalent performance for energy and timing compared with PMT-based detectors. APDs allow for a more compact PET scanner design, which together with the insensitivity of APDs to magnetic fields, makes it possible to place the detectors inside of a MRI magnet. Other design possibilities can be considered, for example multiple concentric rings of detectors (see Sect. 6.1.7), or the use of APD arrays on both front and back surfaces of scintillator arrays. Both these designs provide depth of interaction information.

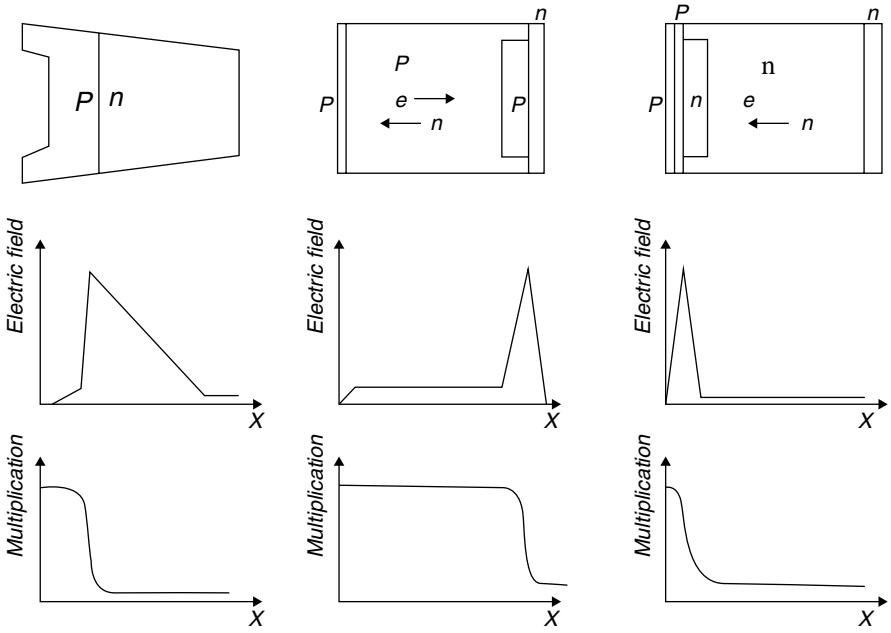

Fig. 3.9 Device structures, electric field profiles and electron/hole multiplication for (*left*) beveled-edge, (*center*) reach-through and (*right*) shallow junction APDs, modified from Webb et al. [37]

6.1.1 Structure of Common APDs

Commonly three alternative APD structures are used:

- Beveled-edge,
- Reach-through,
- Reverse or buried junction APD.

Here we discuss the p-on-n structures with a peak sensitivity in the 'blue' region. The n-on-p structure is basically a mirrored construction with highest sensitivity for red light.

The basic structure of these APDs is shown in the top row of Fig. 3.9, the electric field distributions as a function of depth for all three devices in the middle and the corresponding multiplication at the bottom. Electrons in both the beveled-edge and the reach-through structure have high multiplication rates throughout almost the entire device structure while hole multiplication is kept to a minimum. In the shallow junction APD (also called reverse APD), by contrast, photoelectrons must be generated in front of the p–n junction buried at a depth of a few microns to undergo multiplication. Full amplification can only be achieved when the diode is illuminated by blue light which has a very short absorption length of less than 1 μm.

Due to the production yield, the size of APDs is limited to achieve an extremely uniform field distribution over the sensitive area. The biggest area available commercially is 2.5 cm^2.

Advanced Photonix Inc. was the first to bring a large area APD on the market. The APDs have beveled edges to reduce the surface currents. It has a traditional p–n junction, in which the n-type resistivity is chosen such that it makes the breakdown voltage very high (~2,000 V). Due to a neutron transmutation process (the naturally occurring and uniform distributed ^{30}Si isotope is converted to P), the internal field and the gain are very uniform. Consequently, an excellent energy resolution of 4.3 % FWHM for the 662 keV line from ^{137}Cs has been measured with this so-called Large Area Avalanche Photo Diode (LAAPD) from Advanced Photonix in combination with a YAP:Ce crystal [38] and 3.7 % have been achieved in combination with a $LaCl_3$:Ce crystal [39]. The deep UV scintillation light of Argon (128 nm) has been detected with a LAAPD at a quantum efficiency greater than 40 % [40].

A reach-through APD has a wide low-field drift region (>100 μm) at the front of the device and the multiplying region at the back. Almost the full thickness is active. Since most of the thermally generated dark current inside the thick p layer undergoes electron multiplication, large area devices tend to be noisy.

The third type, the shallow junction APD has its p–n junction close to the front surface. An example is the APD developed for the CMS electromagnetic calorimeter [41].

The basic structure is low resistivity silicon with an epitaxial grown layer of low doped n-silicon on top. In this top layer with a thickness of 40–50 μm, the p–n junction is created by diffusion and ion implantation at a depth of ~5 μm. About 30–40 μm of the epitaxial grown layer of low doped n-silicon remains unaltered and acts only as a drift region. However, this reduces the capacitance and, consequently, the noise of the device. A groove close to the edge of the device prevents the flow of surface currents (Fig. 3.10).

The reverse APD has a number of advantages in PET applications:

- Fast response,
- Small dark current,
- Reduced temperature dependence.

6.1.2 Quantum Efficiency

The QE of a reverse APD is similar to the QE of a PIN photodiode (Fig. 3.5), but only photoelectrons created in front of the shallow p–n junction undergo full amplification while those produced close to the junction or behind see only part of the potential, and thus the amplification is reduced. The holes contribute little because they have a much smaller ionization coefficient than electrons at the same field strength. Photons with long wavelengths often penetrate deeper into the silicon (Fig. 3.11) and the photoelectrons have, therefore, less chance to undergo full amplification (Fig. 3.12) [42].

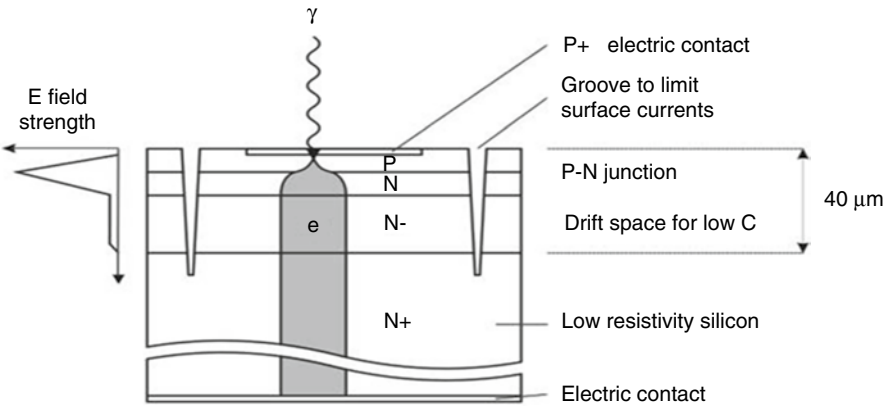

Fig. 3.10 Structure of the Hamamatsu S8148 APD used by CMS

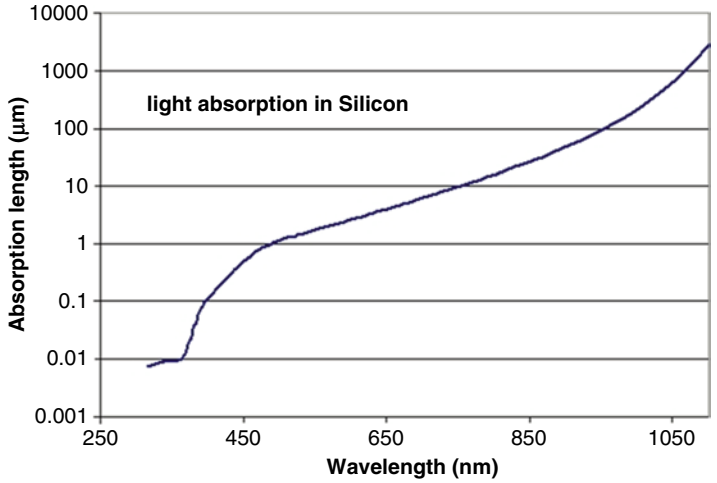

Fig. 3.11 The photon absorption length in **µ**m of silicon versus wavelength [43]

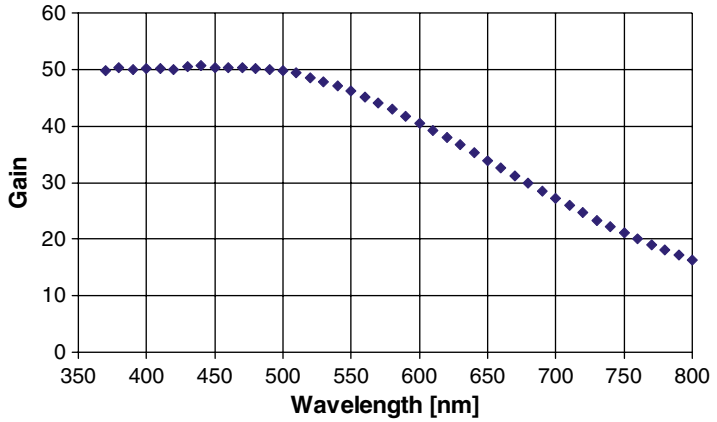

Fig. 3.12 Gain of a reverse type APD (Hamamatsu S8148) as a function of the wavelength of the incident light. Reprinted with permission from [42]

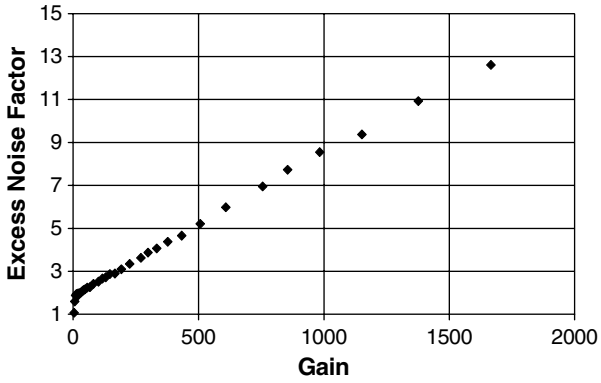

Fig. 3.13 Excess noise factor for different gains (Hamamatsu APD, type S8148). Reprinted with permission from [45]

State of the art crystal scintillators with elements with high atomic number (needed for PET because of best ratio of the photoelectric absorption to Compton scattering) have a peak light emission in the range of 350–500 nm, a range which is well covered by reverse APDs.

6.1.3 Excess Noise Factor

The avalanche multiplication in an APD is a stochastic process. The fluctuations are described by the excess noise factor *F*. In theory, it is at high gain (>10) mostly attributed to the contribution of the holes to the multiplication [44].

$$F = k_{eff} \cdot M + \left(2 - 1/M\right) \cdot \left(1 - k_{eff}\right)$$

$$\text{for } M > 10 : F = 2 + k_{eff} \cdot M$$

$$k_{eff} \approx k = \beta/\alpha$$

α and β are the ionization coefficients for electrons and holes, $\alpha \gg \beta$ in APDs biased below breakdown.

The theoretical lower limit of *F* at small gain is 2. It increases linearly with the gain and is ~10 at a gain of 1,000 (Fig. 3.13).

6.1.4 Stability

The gain of an APD exponentially depends on the bias voltage and, therefore, the relative change of the gain with voltage is a linear function of the gain. At a gain of 50, the relative change is ~3.1 %/V and increases linearly to more than 30 %/V at

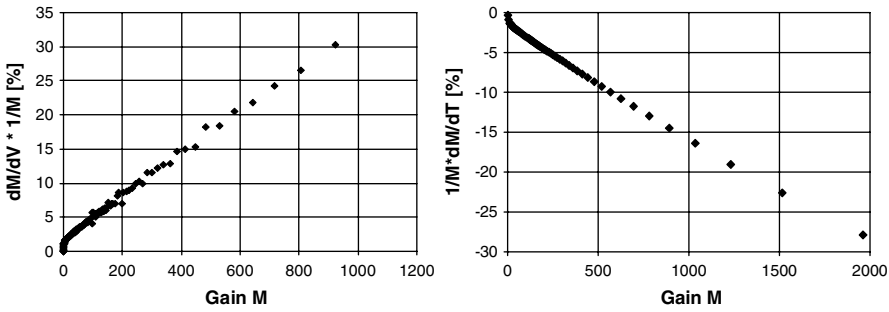

Fig. 3.14 Relative change of the gain for variations of the bias voltage (*left*) and the temperature (*right*) plotted as function of the gain for the Hamamatsu S8148. Reprinted with permission from [22]

gain 1,000. Similarly, the gain depends on temperature changes, which are caused by the energy loss in interactions of the electrons with phonons (Fig. 3.14). The relative change is ≈2.4 %/C at gain 100 and ≈15 %/C at gain 1,000 (Fig. 3.12, all values for the S8148 APD from Hamamatsu [22]). Because of the strong sensitivity to small changes in the bias voltage and temperature when operated close below the breakdown voltage, APDs have to be operated at moderate internal gain and need low noise preamplifiers.

6.1.5 Contribution of the APD Parameters to the Energy Resolution

In a scintillation detector with an APD as a readout element, the APD contributes to all three conventionally used terms describing the energy resolution:

$$\frac{\sigma_E}{E} = \frac{a}{\sqrt{E}} \oplus b \oplus \frac{c}{E}$$

In detail, APDs contribute to the stochastic term, a of the energy resolution of a crystal-APD system with their area (mismatch of the APD area and the crystal face), the quantum efficiency and the excess noise factor. The gain sensitivity to voltage and temperature variation increases the constant term b and the capacitance, serial resistance and dark current all add to the noise term c.

The dark current of state of the art APDs is very small and the excess noise factor is close to the theoretical limit as long as the gain is not too high. Therefore, the parallel noise (caused by the dark currents as shown in the first summand in the formula below) can only be improved by a short shaping time, which is anyhow needed in high rate calorimeters with state of the art scintillation crystals. Unfortunately, the short shaping time increases the series noise (caused by the capacitance of the APDs as shown in the second summand in the formula below), which becomes the dominant part. The APD should have the lowest possible

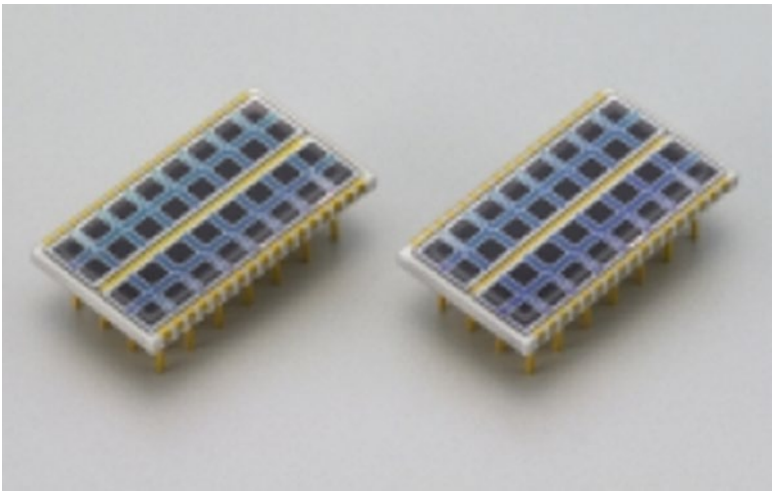

Fig. 3.15 Array of APDs from Hamamatsu with pixels of 1.6×1.6 mm^2 and a pitch of 2.3 mm

capacitance to achieve the best possible energy resolution. To first order, the ENC is expressed by Eq. (17) from [46]:

$$ENC^2 \approx 2q \cdot \left(\frac{I_{ds}}{M^2} + I_{db} \cdot F \right) \cdot \tau + 4kTR_s \cdot \frac{C^2}{M^2} \cdot \frac{1}{\tau}$$

τ is the shaping time, q the electron charge, I_{ds} the dark surface current, I_{db} the dark bulk current created before the p–n junction, M is the gain, F the excess noise factor, R_s the series resistance of the APD and the amplifier input, C the capacitance of the APD and the amplifier input, k the Boltzmann constant, and T the absolute temperature.

6.1.6 Arrays of APDs

Arrays are available from several manufacturers for applications in nuclear medical imaging (SPECT and PET). An array with 32 reverse APDs, for example, is produced by Hamamatsu [47] specifically for small animal PET scanner design (Fig. 3.15). The area of the individual APDs is 1.6×1.6 mm^2. Radiation Monitoring Devices (RMD) produces arrays with up to 169 reach-through APDs with an element size of 1×1 mm^2 [48].

6.1.7 Examples of Small Animal PET Detectors Using APDs

In the following we will show some small animal PET examples, all using the new miniaturized photon sensors. Figure 3.16 shows the early prototype small animal PET named MADPET (Munich Avalanche Diode PET) using avalanche

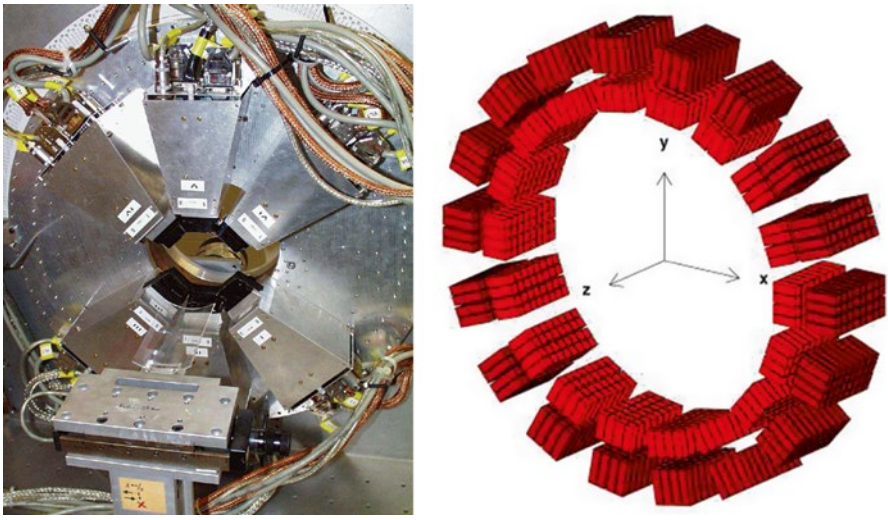

Fig. 3.16 MADPET with 48 detectors in 6 sectors (*left*) and arrangement of 1,152 crystals in MADPET II with two coaxial layers (*right*) with improved spatial resolution (<1.5 mm). Reprinted with permission from [49]

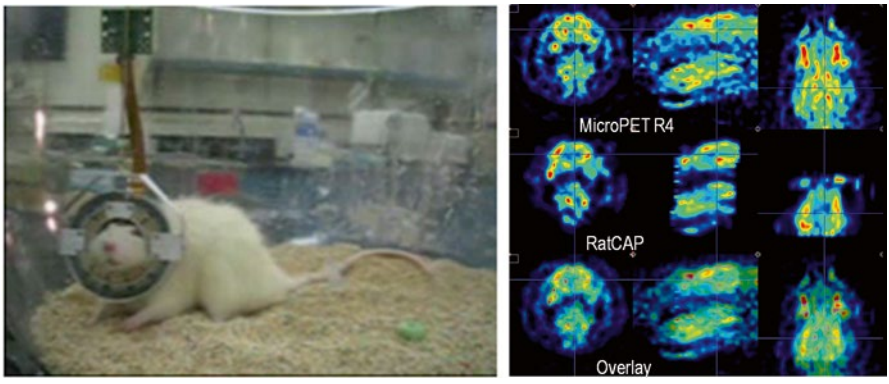

Fig. 3.17 *Left*: Awake rat wearing the RatCAP that is supported by the tether and mechanical counterbalance system. *Right*: ^{18}F-FDG rat brain images from the RatCAP compared to the same animal imaged with a MicroPET R4. *Vertical lines* show the axial coverage of the RatCAP. Reprinted with permission from [50]

photodiodes and its advanced version MADPET II, using the APD arrays shown in Fig. 3.15. The readout uses the 1:1 coupling. For reducing the parallax error the crystals in MADPET II were divided into two radial rings and read out separately, allowing for a resolution of less than 1.5 mm [49].

Figure 3.17 shows another design by Dr Woody et al., the so-called RatCAP, demonstrating clearly the potential of much more compact designs compared with those based on PMT readouts. A comparison with a measurement with the MicroPET R4 shows nearly the same resolution [50].

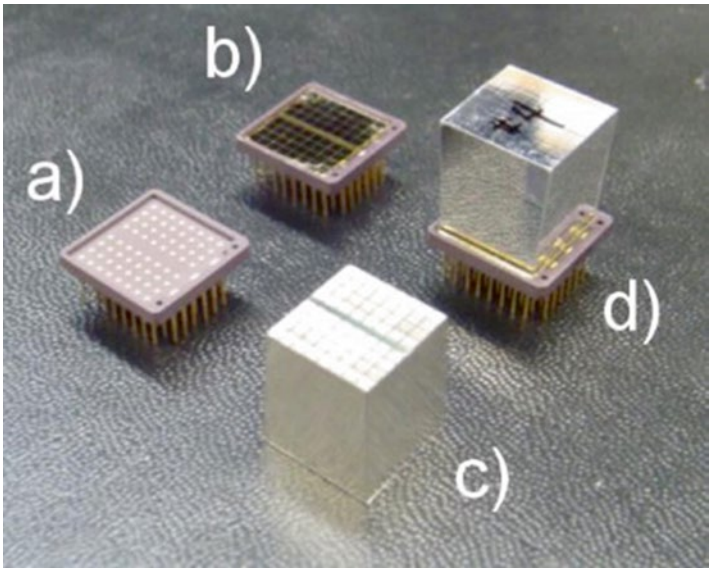

Fig. 3.18 Picture of: (**a**) ceramic case with bump bonding pads; (**b**) two APD arrays mounted in the ceramic; (**c**) custom tapered LYSO array; (**d**) assembled LabPET II module. Reprinted with permission from [51]

Dr Lecomte and co-workers were the first to realize a PET scanner with APD readout at Université de Sherbrooke in Canada. The most recent development which employs APDs is the LabPET II [51] shown in Fig. 3.18.

Also, the very compact design of APDs and their insensitivity to magnetic fields triggered the construction of first prototypes of combining MRI and PET. A PET–MRI combination for multimodality imaging was built in 2006/2007 at the University of Tuebingen (Fig. 3.19) for the simultaneously acquired images [52].

6.2 Geiger-Mode Avalanche Photodiodes

At the beginning of this millennium the Geiger-mode avalanche photodiode (G-APD) was developed. This device can detect single photons just like a PMT with a very high gain first dynode and therefore some people call it a 'Silicon Photo Multiplier' (SiPM). The pulse height spectrum measured with a G-APD shows a resolution even better than what can be achieved with the best hybrid photomultiplier tubes (Fig. 3.20). "Geiger-mode" describes the feature of these devices whereby a photo-generated carrier in the depletion region can trigger a diverging avalanche multiplication of carriers by impact ionization. Both positive and negative carriers (and also photons generated in the avalanche multiplication, see Sect. 6)

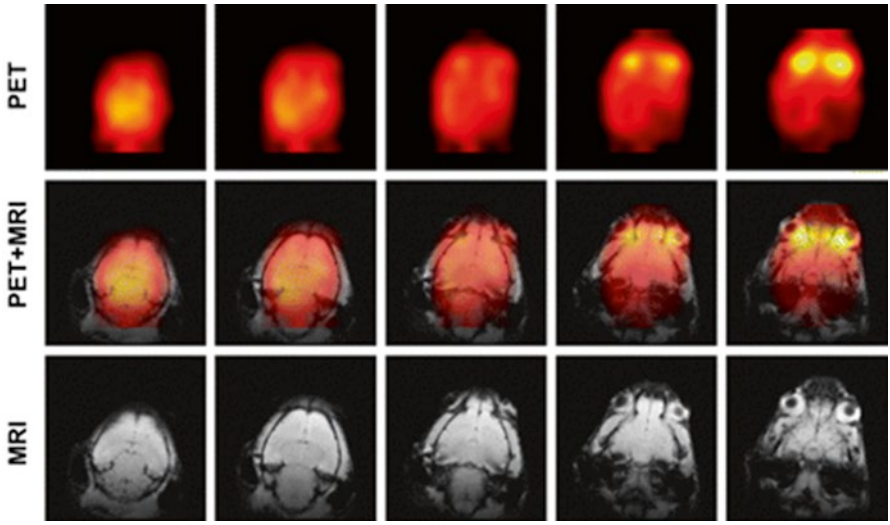

Fig. 3.19 Simultaneously acquired PET (filtered back projection, 2.5-mm Gaussian postsmoothing filter) and coronal unenhanced fast low-angle shot MRI (394/5.9, 40° flip angle, six signals acquired, 1-mm section thickness, 256×256 pixels) images of a mouse head injected with FDG. The fused PET/MRI images show good alignment of images acquired with the two imaging modalities. The increased uptake of the PET images correlates with the location of the Harderian glands behind the eyes in the MRI images. Reprinted with permission from [52]

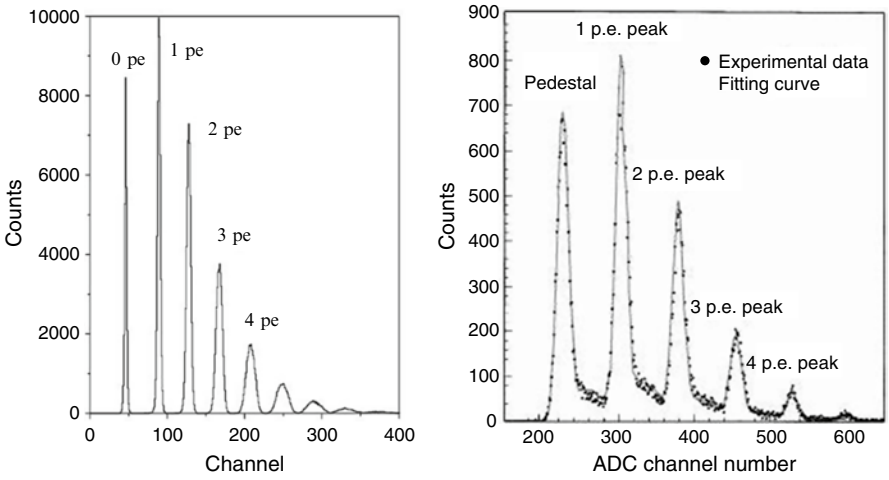

Fig. 3.20 Pulse height spectrum of light pulses with very low intensity recorded with a G-APD (*left*) and a HPD. Reprinted with permission from [53]

are involved with a positive feedback effect, which, when the electric field is high enough, makes the carrier multiplication self-sustaining. In linear mode APDs, avalanches develop basically only in one direction (from the p- towards the n-material) and stop multiplying when the charge carriers reach the low field area of the n-zone.

Very rarely secondary avalanches are started by holes or secondary photons in the p-layer. In G-APDs, the essential new process is the additional initiation of secondary avalanches, triggered by holes and secondary photons in the p-layer. A G-APD, therefore, does not turn off by itself and, as a consequence, the avalanche process must be quenched by the voltage drop across a high ohmic serial resistor or by an active quenching circuit. Another important feature of G-APDs is that it is possible to bias small depleted volumes at the p–n junction well over the so-called breakdown voltage much longer in time than on average a free electron is generated, which would lead to an avalanche breakdown, i.e. it is possible to keep small volumes for a sufficient amount of time in a 'supercritical state'. It is obvious that large depleted volumes with a high electrical field could never be kept biased well over the breakdown voltage for a sufficiently long period because enough free electrons would always be thermally generated. Initially, the idea to 'overbias' small, single volumes was tried out in the 1970s of the last century [54, 55].

It is obvious that semiconductors of low band-gap (unless they are strongly cooled) or of high impurity will be completely unsuited for G-APDs because it is not possible to keep even very small depleted volumes free of charge carriers for sufficiently long periods of time. It is also obvious that materials with a high photon production (III–V materials for LED or laser diodes) are unsuited because, in the case of large secondary photon emission, secondary avalanches can be triggered in the entire ensemble of small cells by optical crosstalk.

6.2.1 History

Pioneering work in the development of solid state single photon detectors, biased above the breakdown voltage, was carried out in the 1960s of the last century in the RCA company by R.J. McIntyre and coworkers [54] and by R.H. Haitz and his colleagues in the Shockley research laboratory [55]. The main problem was that only very small volumes of Si could be kept depleted for sufficient time above breakdown voltage to keep the diodes sensitive for photons. In most cases, the high internal bulk current in the depleted volume triggered an instant breakdown when the diode bias rose just above the breakdown voltage. Due to improved technologies it was possible to keep the depleted volume free of electrons biased well above breakdown for a sufficiently long time. The development led to the so-called Single Photon Avalanche Diode (SPAD).

Around 1990, the MRS (metal–resistor–semiconductor) APDs were invented in Russia. A very thin metal layer (Ti, ~0.01 μm) and a layer of SiC or Si_XO_Y with a resistivity of 30–80 MΩ cm limits the Geiger breakdown by a local reduction of the electric field. The technology is complicated because all parameters need to be controlled very precisely. The next step was logical: subdivide the MRS structure into many cells and connect them all in parallel by an individual limiting resistor (Fig. 3.21). The Geiger-mode avalanche photodiode (G-APD) was born. Key personalities in this development were Golovin [56] and Sadygov [57]. The G-APD is produced by a standard MOS (metal–oxide–silicon) process and promises to eventually be relatively simple and therefore cheap.

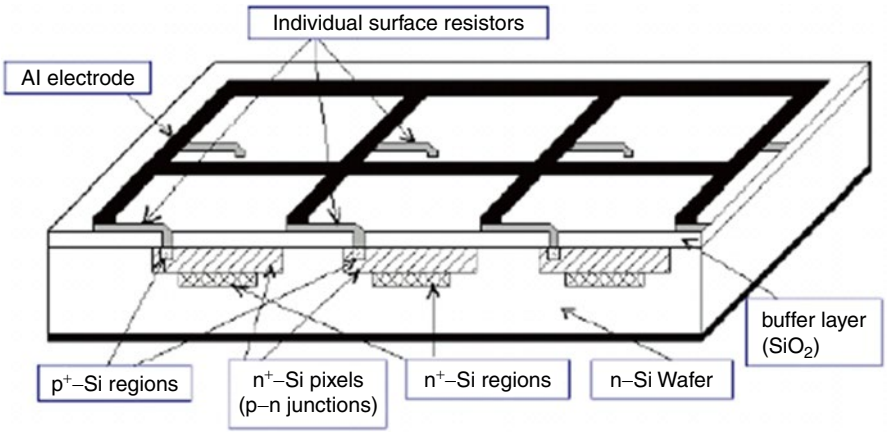

Fig. 3.21 Basic structure of a Geiger-mode avalanche photodiode. Reprinted with permission from [57]

6.2.2 Properties of G-APDs

High Gain

G-APDs produce a standard signal when any of the cells goes to breakdown. The amplitude A is proportional to the capacitance of the cell divided by the electron charge times the overvoltage:

$$A_i \sim C / q \cdot (V - V_b)$$

where V is the operating bias voltage and V_b is the breakdown voltage.

When many cells are fired at the same time, the output is the sum of the standard pulses

$$A = \sum A_i$$

In this way the basically digital device has a linear response. The gain is typically in the range of 10^5–10^7 but there are also designs with a gain of only 10^4 (see later discussion). Single photons produce a signal of several millivolts on a 50 Ω load (Fig. 3.22).

No (or at most a simple) amplifier is needed for many applications for single photon detection. Particularly low-level light detection with PIN photodiodes or linear mode APDs requires high quality shielding to prevent pickup. Because of the extremely small extension of the cell size and the high gain, G-APDs have practically no pickup noise and often need no shielding at all. Since there are no avalanche fluctuations as in normal APDs, the excess noise factor is very small and it could eventually be negligible if other contributions from optical crosstalk could be suppressed. Groom's theorem [58] is not valid. This theorem states that the

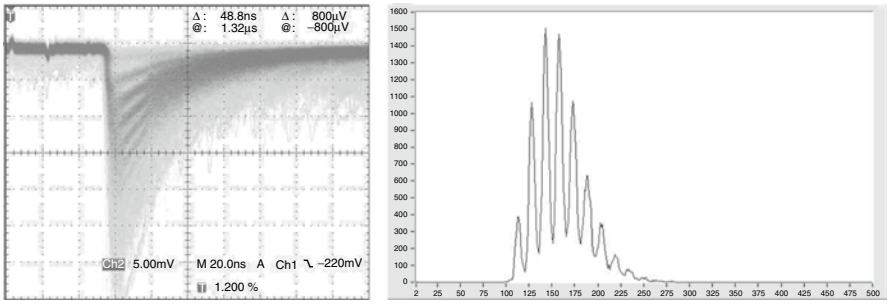

Fig. 3.22 *Left*: Oscilloscope picture of the signal from a G-APD (Hamamatsu 1-53-1A-1) recorded without an amplifier. *Right*: The corresponding pulse height spectrum. The mean number of photons in the recorded light flashes is about 2.5. Horizontal scale in arbitrary units

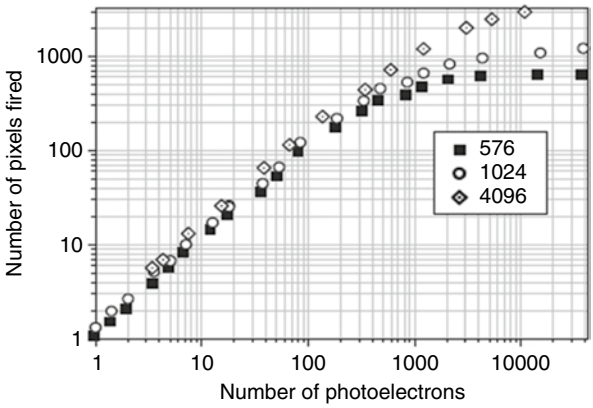

Fig. 3.23 Nonlinear response to a 40 ps laser light signal for G-APDs with different number of cells. Reprinted with permission from [59]

resolution of an assembly of a scintillator and a semiconductor photon detector is independent of the area of the photon detector because, in first order, the photon statistic improves linearly with the photon detector area while equally the noise increases linearly with the detector capacitance, which is again proportional to the area.

Saturation in Case of Bright Light Flashes

The output signal is proportional to the number of fired cells as long as the number of photons in a pulse (N_{photon}) times the PDE is significantly smaller than the number of cells N_{total} (Fig. 3.23). The equation given below is not exact but describes the data very well.

$$A \approx N_{firedcells} = N_{total} \cdot \left(1 - e^{-\frac{N_{photon} \cdot PDE}{N_{total}}} \right)$$

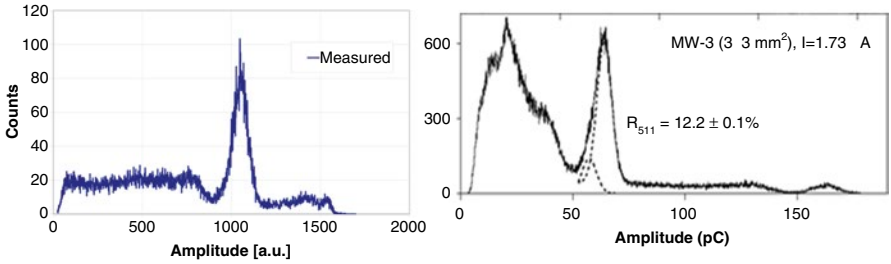

Fig. 3.24 *Left*: Energy spectrum measured with a ^{22}Na sources and a LYSO crystal (2×2×12 mm^3) coupled to a G-APD from CPTA/Photonique with ~400 cells/mm^2. *Right*: LYSO of the same size and a G-APD from Zecotek with 15,000 cells/mm^2

Two or more photons which convert within the same time in one cell produce exactly the standardized signal of 1 single photon. When the number of impinging photons times the PDE exceeds 50 % of the available cells, the deviation from linearity becomes more than 20 %. When a spectrum of the response of a scintillator and G-APD detector is measured the nonlinear response acts as a compression and fakes an energy resolution which looks better than it is in reality.

In PET, SPECT applications this is not a severe disadvantage provided the dynamic compression is not too high and easy calibration is possible. G-APDs with a very large number of cells (up to 40,000 cells/mm^2) have been produced and are available from Zecotek Photonics Inc. Fig. 3.24 highlights the deviation from linearity when observing a ^{22}Na source with a crystal read out by a G-APD with 400 cells/mm^2 and with a G-APD of 15,000 cells/mm^2.

Sensitivity of the Gain to the Bias Voltage Stability

The G-APD signal stability depends mainly on (a) the stability of the applied bias and (b) on temperature changes (see next section). To describe the dependence of the G-APD response on the bias voltage one can introduce a voltage dependent coefficient $k_V(V)$ as follows:

$$k_V(V) = \frac{1}{A} \cdot \frac{dA}{dV} \cdot 100\%$$

Examples of the voltage dependence are shown in Fig. 3.25. The amplitude A of the signals of 2 G-APDs from Hamamatsu and Photonique/CPTA have been measured and the coefficients derived [60].

For precision measurements, the voltage has to be regulated at the diode and not before the bias resistor, to avoid gain drops due to large temporary light signals, resulting in current changes in the resistor and, in turn, a voltage drop.

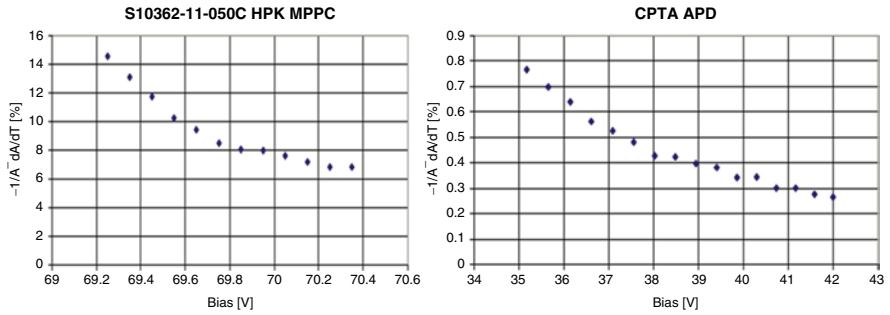

Fig. 3.25 Voltage coefficients $k_V(V)$ of a G-APD from Hamamatsu (*left*) and from Photonique/CPTA (*right*) depending on the bias voltage at T = 22 °C. Reprinted with permission from [60]

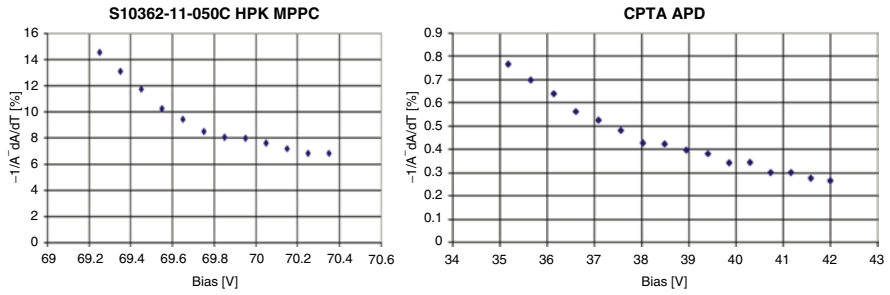

Fig. 3.26 Temperature coefficients of a G-APD from Hamamatsu (*left*) and from Photonique/CPTA (*right*) as a function of the bias voltage. Reprinted with permission from [60]

Temperature Dependence of the Gain

The breakdown voltage of a silicon diode depends strongly on the temperature because of the interactions of the carriers with phonons. Almost all parameters of a G-APD are a function of the overvoltage $V–V_b$. Here we discuss the influence of temperature changes on the gain. Similar to the coefficient $k_V(V)$, which describes the dependence on the bias voltage, we define

$$k_T(V) = \frac{1}{A} \cdot \frac{dA}{dT} \cdot 100\%$$

Again, the amplitudes A of the signals of 2 G-APDs from Hamamatsu and Photonique/CPTA were measured at different temperatures and the coefficients derived (Fig. 3.26) [60].

For a stable operation, the temperature needs to be controlled with a precision of a fraction of a degree. Alternatively, the applied bias voltage has to be corrected to compensate for the shift of the breakdown voltage caused by temperature changes.

For the device from Hamamatsu, the bias voltage needs to be increased by ~50 mV when the temperature rises by 1 °C and if the device is operated with at least a $V_{OV} > 1$ V, while for the Photonique/CPTA device the compensation of bias voltage is ~20 mV/°C for $V_{OV} > 1$ V.

Photon Detection Efficiency (PDE)

The PDE is the product of (a) the quantum efficiency (QE) of the active area, (b) the geometric fill factor ε (ε = ratio of sensitive to total area), and (c) the probability that an incoming photon triggers a breakdown ($P_{trigger}$). A small correction for the hit cell still recovering from a previous breakdown (from noise or a previous light signal) is neglected in the current discussions

$$PDE = QE \cdot \varepsilon \cdot P_{trigger}$$

The geometric factor ε needs to be optimized depending on the application. Since some space is needed between the cells for separation and the individual resistors, the best filling can be achieved with a small number of big cells, and a geometric fill factor of 80 % or more is possible. A pixel with cells of large size generally has the disadvantage of a low dynamic range and of a larger number of periods of insensitivity due to the accumulation of cells in the recovery phase caused by the more frequent noise triggers in the larger depleted volume.

G-APDs for SPECT and PET need a large number of cells for unit area. One of the preferred materials for PET nowadays, Lutetium Oxyorthosilicate (LSO) crystals, produce many photons (≈15,000 per a 511 keV) and up to a few 1,000s can be collected at the end face of the crystals. To avoid saturation effects, the number of cells needs to be big for the given viewing area and, in turn, the cells must be small. The currently achieved geometric fill factor ε in suitable models is in the range of 40–60 %. An example is shown in Fig. 3.27.

The triggering probability depends on the position where the primary electron–hole pair is generated. Compared to holes, electrons have a better chance to trigger a breakdown in silicon. Therefore, a conversion of the photon in the p-layer has the highest probability to trigger a breakdown. This has been calculated by Oldham et al. [61]. They define an avalanche region with a width W and the position x, which runs from 0 to W starting at the n-edge (Fig. 3.28).

Oldham and coworkers verified their calculations by illuminating a diode with short (390 nm) and long (1,050 nm) wavelengths and achieved good agreement.

G-APDs with an n-on-p structure (sketch in the right pane of Fig. 3.28) operated just above the breakdown voltage V_b are inefficient for short wavelength photons because these photons must penetrate into the p layer to generate electrons that initiate avalanches when moving towards the n-layer (see Fig. 3.11 for the absorption length of photons in silicon). When raising the voltage well above V_b, holes generated by short wavelength photons in the n-layer will be able to initiate a measurable signal. According to Fig. 3.28, a much higher overvoltage is required for obtaining

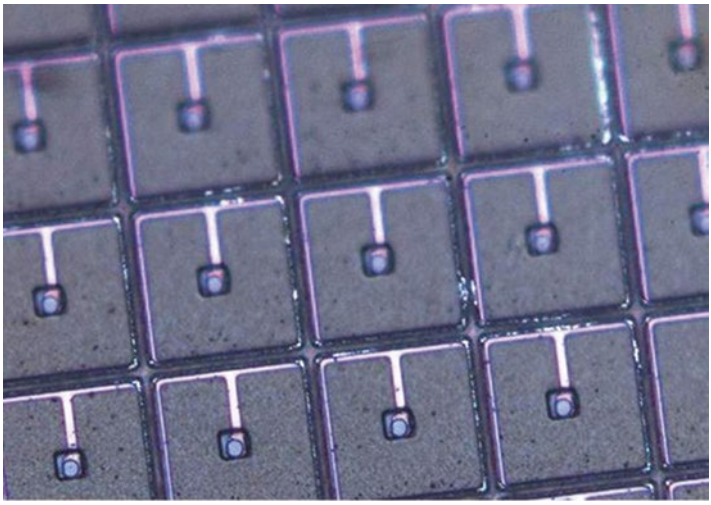

Fig. 3.27 Magnified photo of a G-APD produced by Photonique/CPTA

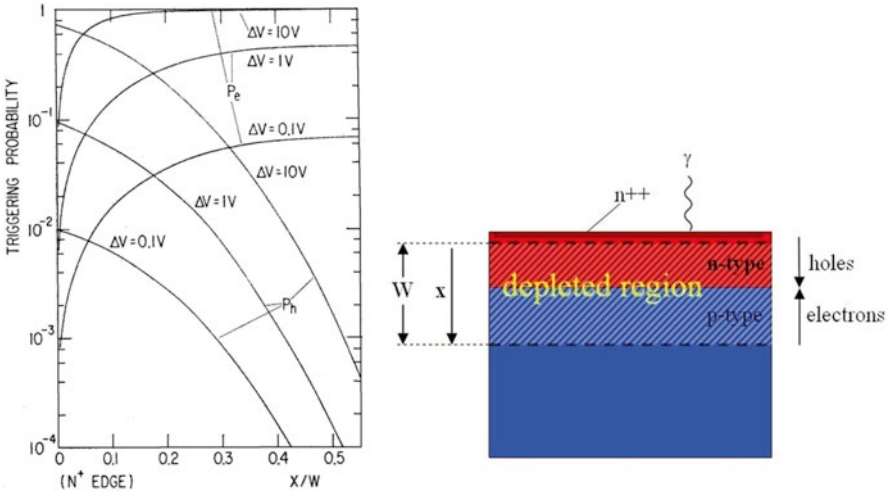

Fig. 3.28 Triggering probability for different positions of carrier generation (*left*, see text, modified [61]) and sketch of the structure for an explanation of the parameters W and x (*right*)

a reasonable blue-sensitivity of n-on-p structures compared to that required in the case of a p-on-n structure.

The QE of the active area can reach 80–90 % depending on the wavelength. It peaks in a relatively narrow range of wavelengths compared to the QE distribution of a PIN diode (Fig. 3.29) because the sensitive layer of silicon is very thin. In the case shown in Fig. 3.29, the G-APD structure is p-silicon on an n-substrate. The p-layer is 0.5 µm thick on a 4 µm epitaxial n-layer.

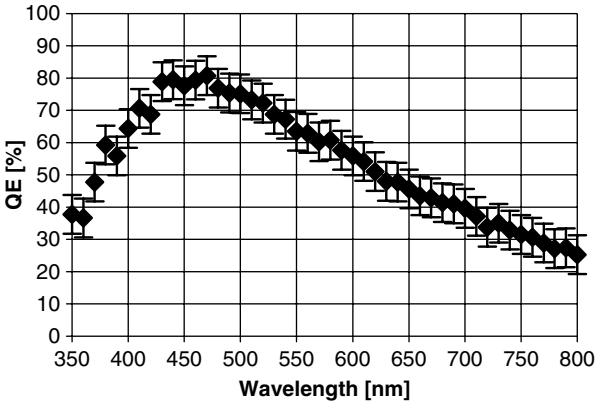

Fig. 3.29 Quantum efficiency of the active area as a function of the wavelength for Hamamatsu 0-50-2 with 400 cells/mm^2. The error bars denote the systematic measuring errors. The unpublished measurements shown in this figure and in Fig. 3.30 have been done by Y. Musienko [INR (Moscow) and Northeastern University (Boston)], and some in the following figures without a reference (Figs. 3.32, 3.33, and 3.35) by D. Renker

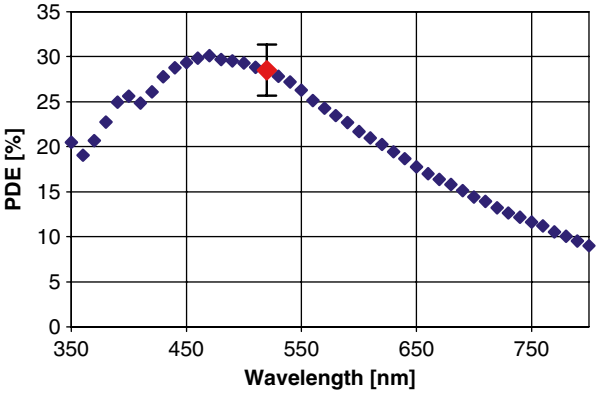

Fig. 3.30 PDE of a so-called p-on-n G-APD produced by Hamamatsu (PSI-33-050C) operated 1 V over the breakdown voltage. The *red data point with error bars* indicates the size of the systematic error

The overall PDE is shown in Fig. 3.30 for a blue sensitive device (p-on-n structure) for the detection of scintillation light from crystals used in PET (BGO, LSO or $LaBr_3$), and in Fig. 3.31 for a device with the inverted n-on-p structure useful together with CsI(Tl) in SPECT.

The PDE depends on the overvoltage (Fig. 3.32). Operation at high gain (high bias voltage) is favored but, in most cases, a compromise needs to be found because at high gain the dark currents and the dark count rate become very high and the optical crosstalk increases.

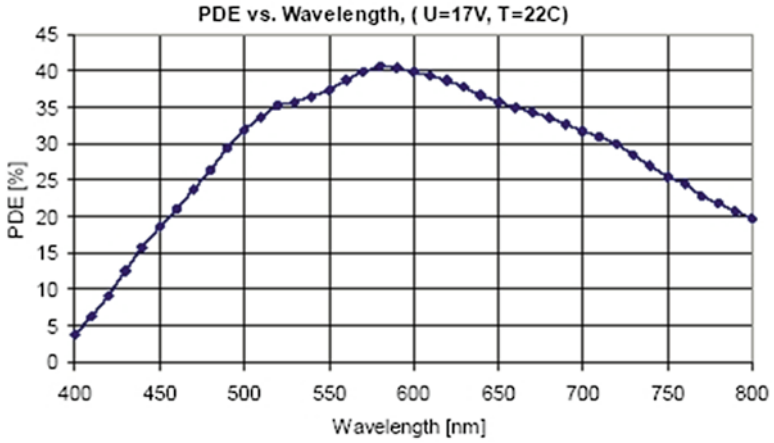

Fig. 3.31 PDE of an n-on-p G-APD produced by Photonique/CPTA (SSPM_0710G9MM) operated about 4 V over the breakdown voltage [62]

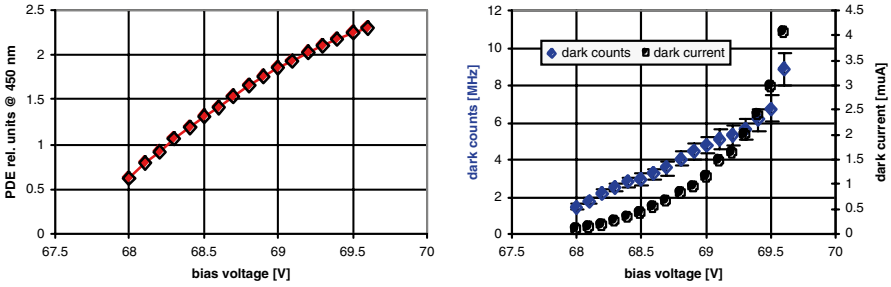

Fig. 3.32 PDE of Hamamatsu MPPC-33-050C as a function of the applied bias voltage in relative units (*left pane*) and the dark currents and dark counts measured at 25 °C in the same voltage range (*right pane*)

Dark Counts

A breakdown can be triggered by an incoming photon or by any generation of free carriers in the depleted layer of a few micron thickness. The latter produces dark counts with a rate of 100 kHz to several MHz per mm^2 at 25 °C and with a threshold at half of the one photon amplitude (Fig. 3.32). Two main processes are responsible for dark counts, thermally generated e–h pairs and so-called field-assisted generation of free electrons.

Thermally generated free carriers can be reduced by cooling. There is a factor 2 reduction of the thermally generated dark counts with every 8 °C drop in temperature.

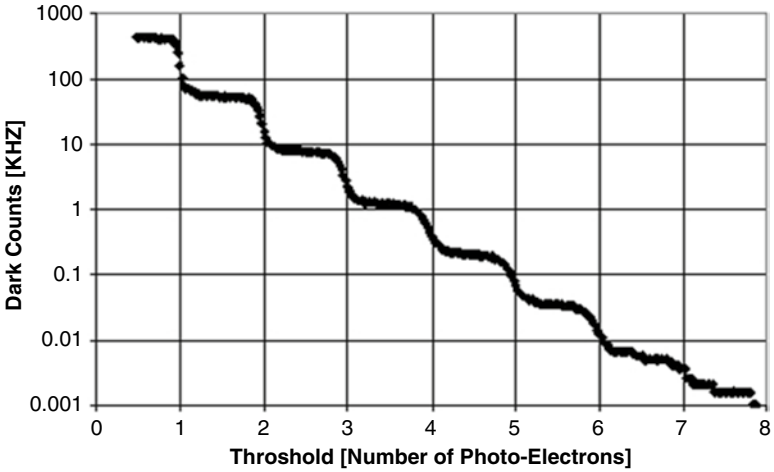

Fig. 3.33 Dark count rate for different values of the discriminator threshold. The G-APD used in this measurement is the S10362-11-050C from Hamamatsu operated at a gain of 7.5×10^5

Field-assisted generation without the help of a phonon (trap-assisted tunneling [63, 64]) has, compared to the thermal generation, a relatively small effect. It can only be reduced by operating the G-APDs at a smaller electric field, thereby lowering the gain and reducing the PDE.

In medical imaging inorganic crystals with a high light yield are used and the dark counts are not giving cause for concern because the number of recorded events falls rapidly with a high setting of the threshold.

Optical Crosstalk

In an avalanche breakdown, there are on average three photons emitted per 10^5 carriers with a photon energy higher than 1.14 eV, the band gap of silicon [65]. When these photons travel to a neighboring cell they can trigger a breakdown there like any external photon. This effect is called optical crosstalk. It can be visualized in the dark count distribution shown in Fig. 3.33. An avalanche from a dark count can, by optical cross talk, occasionally trigger a few additional cells to fire.

The optical crosstalk acts like shower fluctuations in an APD. It is a stochastic process and introduces an excess noise factor F as in a normal APD or in a PMT. Neglecting saturation effects and contributions from afterpulses and dark counts in the wide gate needed for the measurement of light from a scintillating crystal F can be approximated:

$$F \approx 1 + p_{ct}$$

The probability p_{ct} is defined by the rate of dark count events with crosstalk (threshold 1.5 fired cells) divided by the total dark count rate (threshold 0.5 fired cells).

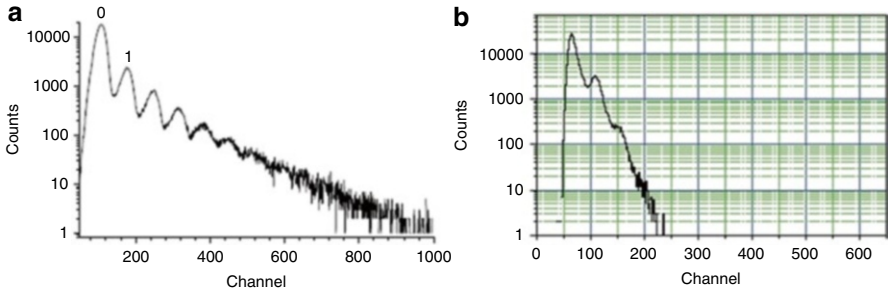

Fig. 3.34 Optical crosstalk in a 1×1 mm^2 G-APD produced by MEPHI/Pulsar, measured as the dark count pulse height distribution: no suppression (**a**); with suppression of the optical crosstalk (**b**) by grooves. Reprinted with permission from [67]

With a dedicated design, which has an additional junction and with grooves between the cells acting as an optical isolation, the optical crosstalk can be reduced [66–68]. The effect of grooves is highlighted by the change in the dark count pulse height spectrum shown in Fig. 3.34. Operation at relatively low gain is advantageous for reducing optical crosstalk, albeit with the disadvantage of significantly reducing the PDE. A quite convenient alternative method of suppressing optical crosstalk is inserting narrow grooves between cells and filling them with an optical absorber. The disadvantage is the need for space reducing the active area, i.e. reducing the fill factor ε and, in turn, the PDE.

A concern in compact scintillator-G-APD arrangements is the fact that photons generated in a breakdown of a G-APD penetrate into a crystal that is coupled to the G-APD, are then reflected at the end of the crystal and come back to the G-APD where some additional cells might be triggered. This effect was simulated by a reflector made of aluminized Mylar, which was mounted in front of a G-APD from Hamamatsu (type PSI-11-100C operated at a gain of 2.4×10^6) to simulate the emission into a crystal and reflection of the light at the other end of the crystal.

The peaks from dark counts with internal cross talk (two or more cells fired) were enhanced by ~18 % (from 15.7 % crosstalk probability to 18.6 %) by reflected photons (Fig. 3.35). With a diffuse reflector (eight layers of Teflon foil) the enhancement was ~12 %.

Afterpulsing

In the silicon volume where a breakdown happened, a plasma with high temperatures (a few 1,000 °C) is formed and deep-lying traps in the silicon are filled. Carrier trapping and delayed release causes afterpulses during a period of several 100 ns after a breakdown.

The afterpulse probability of the device Hamamatsu S10362-33-050C was measured by counting dark counts in a gate with a fixed width but variable delay (Fig. 3.36). Two components were found with a 50 and 140 ns time constant, respectively [69].

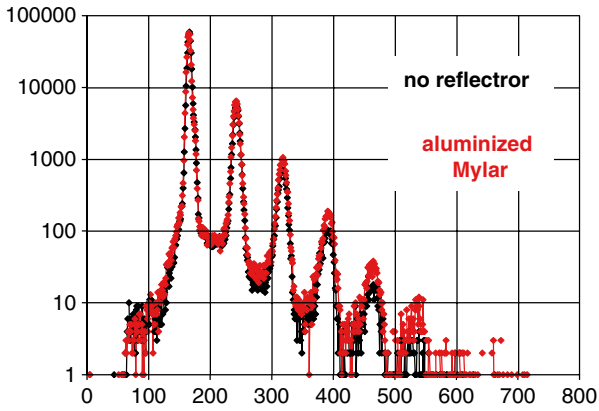

Fig. 3.35 Spectrum of dark count events with and without a reflector made of aluminized Mylar in front of a G-APD (Hamamatsu PSI-11-100C) operated at a gain of 2.4×10^6

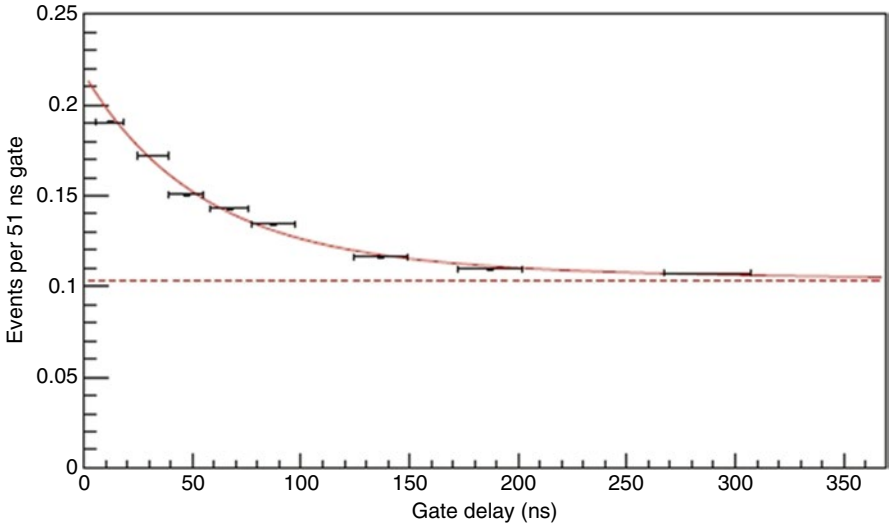

Fig. 3.36 The probability for a delayed release of carriers as a function of time after a breakdown event. The level of dark counts is indicated by the *dashed line*. Reprinted with permission from [69]

Scintillator-G-APD detectors need rather long electronic integration times (200 ns and more). Therefore the afterpulses contribute to the output signal. Since this is a stochastic process the afterpulses contribute to the excess noise factor in a way similar to the optical crosstalk.

Recovery Time and Pulse Shape

The time needed to recharge a cell after a breakdown has been quenched depends mostly on the cell capacitance and the individual quenching resistor ($\tau \sim RC$). Afterpulses can prolong the recovery time, because the recharging starts anew.

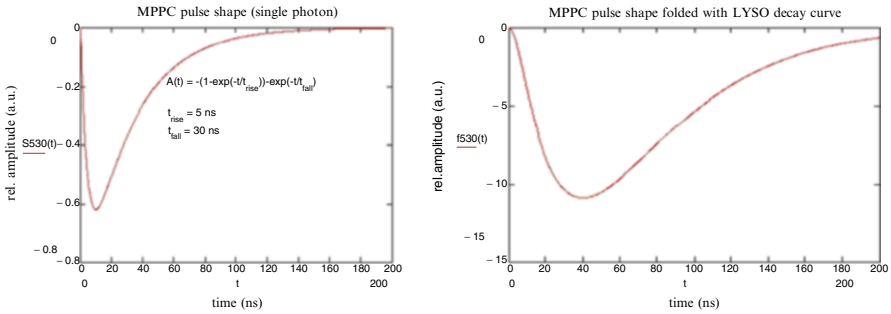

Fig. 3.37 Pulse shape of a G-APD from Hamamatsu (S10362-330050C) for single photons (*left*) and for photons from a LYSO crystal with a decay time of 40 ns (*right*). Reprinted with permission from [70]

Some G-APDs need hundreds of microseconds after a breakdown until the amplitude of a second signal reaches 95 % of the first signal. The shortest recovery times is found in G-APDs with small cells and small resistors. State of the art devices (for example Hamamatsu S10362-33-050) have a recovery time of less than 50 ns (see Fig. 3.37 left). A short recovery time is crucial because the saturation effect is enhanced when many cells are in a recovery state.

The recharging of the cells defines the fall time of the signals, which is the same as the recovery time. When a G-APD is coupled to a scintillating crystal like lutetium–yttrium–oxyorthosilicate (LYSO), the rise time of the signals can become quite long (see Fig. 3.37, right). This can be explained by a convolution of the G-APD signal fall time with the time distribution of the photon emission of the LYSO scintillation [70].

Timing

The active layer of silicon in a G-APD is very thin (2–4 μm) and the process of the breakdown development is fast. In addition, the signal amplitude is large because of the high cell capacitance. Therefore, very good timing properties even for single photons can be expected. Fluctuations in the avalanche development are mainly due to a lateral spreading by diffusion and by the photons emitted in the avalanche [71, 72]. The vertical avalanche build-up contributes only little to the timing. Figure 3.38 shows a measurement of the time response of a G-APD in the case of single photon triggers [53]. The authors state a 40 ps contribution from both the used laser and the electronics. The result, then, is a time resolution with a standard deviation of 42 ps. Operation at high overvoltage (high gain) improves the time resolution.

The time resolution of PET detectors based on LYSO crystals and G-APDs is dominated by the spread of the arrival time of the scintillation photons at the entrance window of the G-APD caused mainly by the variation in path length in the crystal with a high index of refraction (n = 1.82). With two types of G-APDs, the so-called

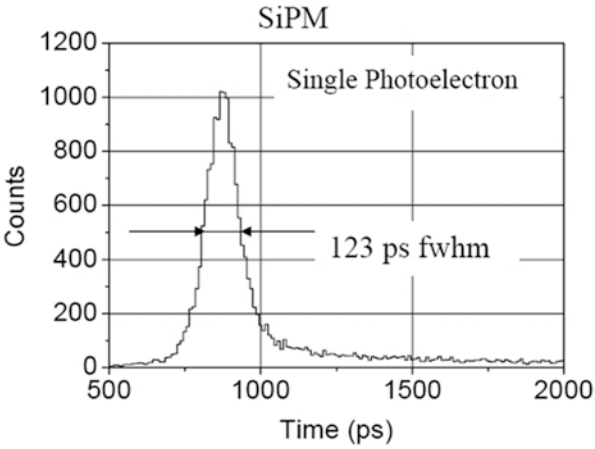

Fig. 3.38 Time resolution for single photons. Reprinted with permission from [53]

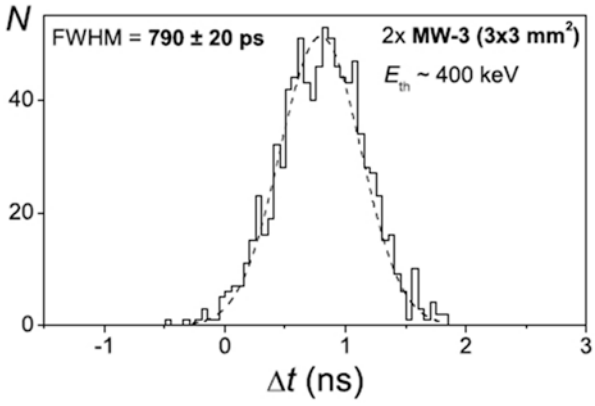

Fig. 3.39 Time difference between the signals from two identical detectors made of LYSO ($2\times2\times12$ mm^3) coupled to G-APDs at the registration of two 511 keV γ-quanta emitted simultaneously at 180° from a ^{22}Na source positioned between the detectors. The *dashed line* is a Gaussian fit to the data. Reprinted with permission from [74]

SiPM produced in MEPHI/Pulsar and the MW-3 produced by Zecotec Photonics, similar time resolutions of about 800 ps have been measured [73, 74]. Figure 3.39 shows an example of such a measurement.

Radiation Hardness

G-APDs have been irradiated with ionizing radiation (^{60}Co) and started to show damage effects at doses of about 200 Gy. This is several orders of magnitude more than the dose that can be expected in SPECT or PET even in a long operation period of 10 years. For medical application G-APDs can be considered as radiation hard.

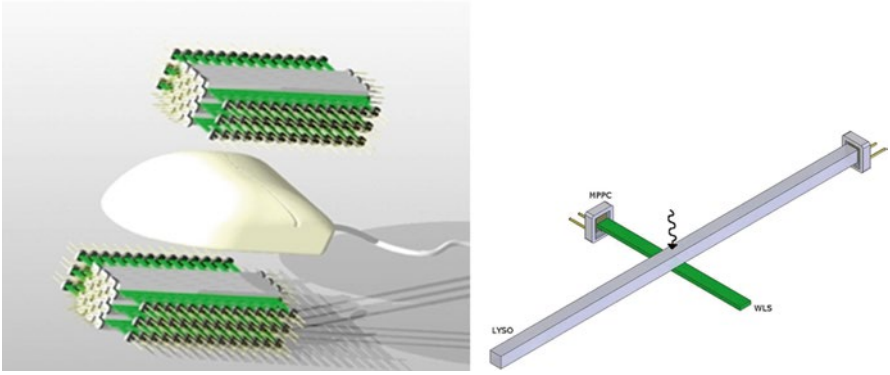

Fig. 3.40 Sketch of the principle and the building components (LYSO crystal, WLS strips and readout by G-APDs)

6.3 Examples of Some Detectors Using G-APDs as Readout Sensors

As G-APDs are still in the developmental phase, nuclear medical instruments using G-APDs are rather sparse. Currently, the efforts concentrate on PET developments and on the proof of concept demonstrators for small animal imaging devices. The two main drawbacks are the much higher price per unit of sensitive area compared to PMTs, and the requirement to wait for maturity of the device before starting on the design of large detectors for human medical applications. On the other hand, the development of small animal imaging devices is an excellent training ground for what might be achieved later in large scale production. In the following we briefly mention two developments, the AX-PET and a development pursued at the University of Tuebingen.

The AX-PET is a novel concept for a 3-D axial PET geometry [75]. It allows for a new way of measuring the interaction point in the detector with very high precision. Figure 3.40 shows the basic concept of the AX-PET. It is based on a matrix of long LYSO crystals oriented in the axial direction, each coupled to one G-APD array. To derive the axial coordinate, WLS (Wave Length Shifter) strips are mounted orthogonally and interleaved between the crystals. The light from the WLS strips is read by custom-made G-APDs. The weighted mean of the signals in the WLS strips has proven to give a very precise axial position information. The achievable resolution along the three axes is mainly driven by the dimensions of the LYSO crystals and WLS strips. This concept is inherently free of parallax errors. Furthermore, it will allow identification of most Compton interactions in the detector and reconstruction of a fraction of them, which is expected to enhance image quality and sensitivity.

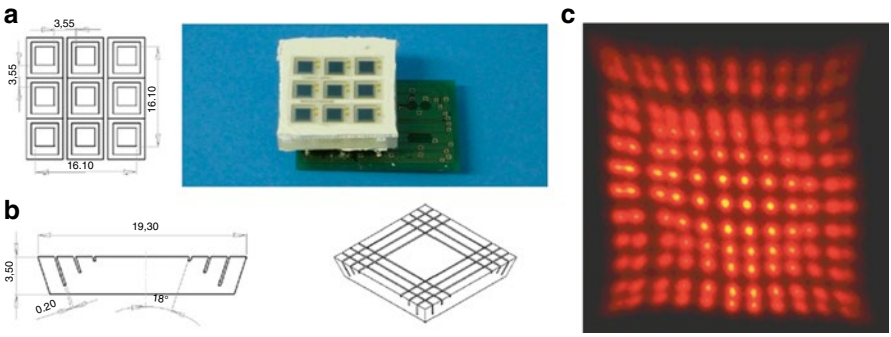

Fig. 3.41 Detector components (**a**: the G-APD array and a photograph of the array, **b**: the projection of the light guide and configuration of cuts) and (**c**) first result of the crystal map

The results are [75]:

- Energy resolution: 11.5 % FWHM @ 511 keV
- High achieved light collection and accordingly a large number of photo electrons created in the G-APD (~1,000 pe @511 keV)
- Axial spatial resolution: 1.1 mm FWHM

The second example is a study of the block detector concept for reading out a matrix of 144 small LSO crystal bars, $1.5 \times 1.5 \times 10$ mm^3 each, by only 9 G-APDs [76]. It was decided to use 9 G-APDs instead of only four for the block readout concept, because the currently largest available commercial G-APDs have an area of only 3×3 mm. By using simple summing amplifiers the signals of the 9 G-APDs were reduced to only four signals. The matrix was coupled by means of a simple and not yet optimised light guide to the G-APDs, which cover only ≈29 % of the crystal block end face. Figure 3.41 shows the basic elements and the achieved crystal map. The mean energy resolution achieved over the entire block was 24 % (FWHM) and the averaged timing resolution 0.96 ns. The group also tested the influence of a strong magnetic field by placing such a detector inside a MRI magnet. Nearly no degradation of performance was observed, i.e. it was confirmed that such a block readout could be used for a PET–MRI simultaneous acquisition.

7 Additional Comments

In this section, we to briefly mention some rather special issues beyond the main function of photon sensors.

7.1 A Comment on Photon Sensor Costs

Photon sensor costs are now a major factor in the entire imaging device: in the typical component chain: scintillator crystals → photon detectors → electronics → readout, the photon detector development is progressing at slowest speed. Better crystal quality as well as a reduction of prices has been seen in recent years. The production of better, cheaper and more complex electronics with a higher potential of integration is progressing fastest. The performance of data storage and computing power is doubling nearly by a factor 2 within 18 months. Not following the trend are the costs of photon sensors. The unit price for the active area of a G-APD is still between factors 10 and 100 higher than that of PMTs. The high price prevents rapid progress and, in turn, the commercialisation of cost effective small animal imaging devices.

7.2 Integration of Electronics onto the Semiconductor Photon Sensors

Semiconductor photon sensors bear another potential. Extrapolating a few years into the future it is quite likely that step by step the control electronics (bias control, temperature control…) and later the signal processing electronics (amplifiers, summing amplifiers, digital electronics for the trigger, etc.) will be integrated on the same chip. The potential for linear mode APDs is much lower than that for the G-APDs because of quite disjunctive production methods and much higher operation voltage. As G-APDs production methods are close to the MOS technology it is a natural path towards integrating electronics on the same chip by MOS technology (preferentially by the high voltage MOS production procedure).

7.3 The Trend Towards Multimodal Imaging

In small animal imaging one would also prefer to simultaneously retrieve physiological and morphological data in coincidence, i.e. by combing for example CT with PET or MRI with PET. Particularly the increase in special resolution can only be fully used if one knows the morphological structure in the time of data acquisition. Especially the combination of MRI and PET should soon be realisable, because the interference of a PET detector using miniature semiconductor photon sensors and an MRI installation would be minimal except for a small reduction of the FoV inside the MRI magnet. Therefore, the need of combining PET and MRI will be a strong driving force to further improve solid state photon detectors. While the proof of concept has already been demonstrated last year for linear mode APD readout, the first demonstration of using the more robust G-APDs will very likely happen within late 2009 or 2010. The combination of CT and PET will be more complex because of the incoherence of the detection processes.

8 Outlook

Photon detectors are an essential element in nearly all modern small animal imaging detectors. The usual strong need to miniaturise detectors and to improve their performance, as well as the need to reduce costs, nowadays results in intense developments for replacing the classical workhorse of past times for PET and SPECT, the PMT, by solid-state photon detectors. Developments concentrate on G-APDs for both PET and SPECT and very soon detectors combing PET and MRI will be available, first as prototypes and a few years later as commercial products. The main drive behind such a development is the large step in miniaturisation on the photo sensor size and the insensitivity to magnetic fields. It will take at least 2–4 years until G-APDs will have reached a high level of maturity.

In the typical component chain: scintillation crystals → photon detectors → electronics → readout' the photon detector development is progressing with the slowest speed. The developments for CT sensors are going on with even slower speed. What is missing is a persuading idea of how to change from analogue readout to a simpler, high rate digital readout, which might allow one to reduce the very high radiation load by about a factor 10 without spoiling the resolution.

In the following years we might expect some major improvements in G-APDs produced on other indirect semiconductor materials with a higher bandgap than that of Silicon, the successive integration of electronics onto the semiconductor photon sensor chip moreover the production of large monolithic matrices of G-APDs for coupling to crystal matrices of fine pixelisation. Figure 3.42 shows a first monolithic matrix of 8×8 G-APDs.

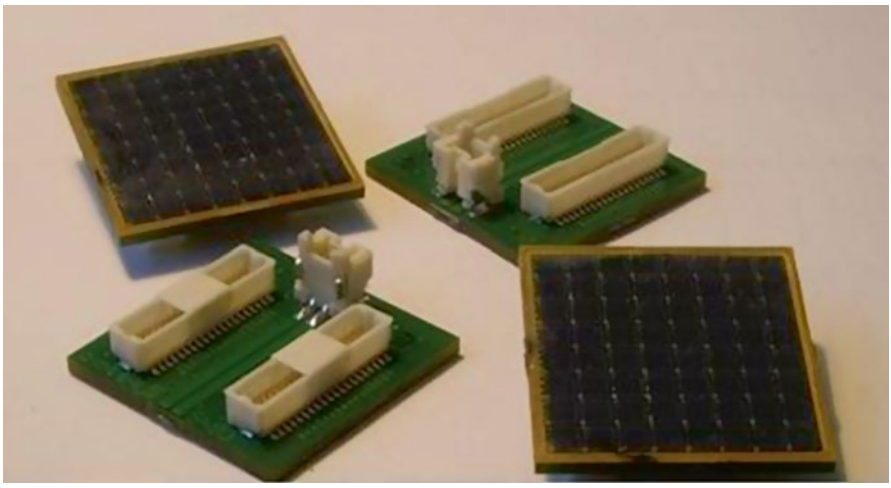

Fig. 3.42 8×8 Arrays of Geiger-mode APDs produced by Zecotek Photonics Inc

Acknowledgements Herewith we would like to thank many of our colleagues for comments and useful suggestions. We also thank Sybille Rodriguez for corrections and formatting the chapter.

References

1. A. Einstein (1905) Über einen die Erzeugung und Verwandlung des Lichtes betreffenden heuristischenGesichtspunkt, Ann Physik **322:** 132-148.
2. W.W. Moses and S.E. Derenzo (1993) Empirical observation of performance degradation in positron emission tomographs utilizing block detectors, J Nucl Med 34: 101P.
3. M. Watanabe, H. Uchida, H. Okada et al. (1992) A high resolution PET for animal studies, IEEE Trans Med Imaging **11:** 577-580.
4. P.D. Cutler, S.R. Cherry et al. (1992) Design features and performance of a PET system for animal Research, J Nucl Med **33:** 595-604.
5. P.M. Bloomfield, S. Rajeswaran, T.J. Spinks et al. (1995) The design and physical characteristics of a small animal positron emission tomography, Phys Med Biol **40:** 1105-1126.
6. K. Wienhard, M. Dahlbohm, L. Eriksson et al. (1994) The ECAT EXACT HR: Performance of a new high resolution positron scanner, J Comput Assist Tomogr **18:** 110-118.
7. K. Wienhard, M. Schmand, M.E. Casey et al. (2002) The ECAT HRRT: performance and first clinical application of the new high resolution research tomography, IEEE Trans Nucl Sci **49:** 104-110.
8. P. Bruyndonckx, X. Liu, S. Tavernier and Z. Shuping. (1997) Design and physical characteristics of a small animal PET using BaF_2 crystals and a photosensitive wire chamber, Nucl Instr Meth Phys Res A **392:** 407-413.
9. S.R. Cherry, Y. Shao, R.W. Silverman et al. (1997) MicroPET: a high resolution PET scanner for imaging small animals, IEEE Trans Nucl Sci **44:** 1161-1166.
10. A. Del Guerra, G. Di Domenico, M. Scandola and G. Zavattini (1998) High spatial resolution small animal YAP-PET, Nucl Instr Meth A **409:** 537-541.
11. M. Watanabe, H. Okada, K. Shimizu et al. (1997) A high resolution animal PET scanner using compact PS-PMT detectors, IEEE Trans Nucl Sci **44**: 1277-1282.
12. Y.C. Tai, A.F. Chatziioannou, Y. Yang et al. (2003) MicroPET II: design, development and initial performance of an improved microPET scanner for small-animal imaging Phys Med Biol **48:** 1519-1537.
13. T. Tomitani, N. Nohara, H. Muramaya et al., (1985) Development of a high resolution positron CT for animal studies, IEEE Trans Nucl Sci **32**: 822-825.
14. R. Lecomte, J. Cadorette, S. Rodrigue et al. (1996) Initial results from the Sherbrooke avalanche photodiode positron tomography, IEEE Trans Nucl Sci **43**:1952-1957.
15. A.P. Jeavons, R.A. Chandler and C.A.R. Dettmar (1999) A 3D HIDAC-PET camera with sub-millimetre resolution for imaging small animals, IEEE Trans Nucl Sci **46:** 468-473.
16. S.E. Derenzo, R.H. Huesman, J.L. Cahoon et al. (1988) A positron tomograph with 600 BGO crystals and 2.6 mm resolution, IEEE Trans Nucl Sci **35**: 659-664.
17. R. Lecomte, C. Martel and J. Cadorette (1991) Study of the resolution performance of an array of discrete detectors with independent readouts for positron emission tomography, IEEE Trans Med Imaging **10**: 347-357.
18. R.S. Miyaoka, S.G. Kohlmyer and T.K. Lewellen (2001) Performance characteristics of micro crystal element (MiCE) detectors, IEEE Trans Nucl Sci **48**: 1403-1407.
19. J. Elster and H. Geitel (1889) Einige Demonstrationsversuche zum Nachweis einseitiger Elektricitätsbewegung in verdünnten Gasen bei Anwendung glühender Elektroden, Ann. Physik, **274:** 27-39.
20. V.K. Zworykin and J.A. Rajchman (1939) The electrostatic electron multiplier, Proc. IRE **27:** 558-566.

21. http://sales.hamamatsu.com/assets/pdf/catsandguides/UBA_SBA_TPMH1305E03.pdf
22. D. Renker (2002) Properties of avalanche photodiodes for applications in high energy physics, astrophysics and medical imaging, Nucl Instr Meth A **486:** 164-169.
23. P. Fischer (1996) An area efficient 128 channel counter chip, Nucl Instr Meth A **378:** 297-300.
24. R. Ballabriga et al. (2007) The Medipix3 prototype, a pixel readout chip working in single photon counting mode with improved spectrometric performance, IEEE Trans Nucl Sci **54:** 1824-1829.
25. M. Locker et al. (2004) Single photon counting X-ray imaging with Si and CdTe single chip pixel detectors and multichip pixel modules, IEEE Trans Nucl Sci **51:** 1717-1723.
26. C. Broennimann et al. (2006) The PILATUS 1 M detector, J Synchrotron Rad **13:** 120-130.
27. A. Bergamaschi et al. (2007) Experience and results from the 6 Megapixel PILATUS system, *Proc. 16th International Workshop on Vertex detectors*, Lake Placid, NY, USA, 2007, paper PoS(Vertex 2007)049.
28. V. Radeka (1987) Semiconductor detectors and readout electronics: Present directions and outstanding problems: An introduction to the symposium Nucl Instr Meth A **253:** 309-312.
29. W.W. Moses, S.E. Derenzo, C.L. Melcher, R.A. Manente (1995) A room temperature LSO/ PIN photodiode PET detector module that measures depth of interaction, IEEE Trans Nucl Sci **42:** 1085-1089.
30. P. Lechner et al. (1996) Silicon drift detectors for high resolution room temperature X-ray spectroscopy, Nucl Instr Meth A **377:** 346-351.
31. C. Fiorini et al. (2006) Gamma-ray spectroscopy with $LaBr_3Ce$ scintillator readout by a Silicon drift detector, IEEE Trans. Nucl. Sci. Vol. **53:** 2392-2397.
32. M. Moszynski et al. (2009) A comparative study of Silicon drift detectors with photomultipliers, avalanche photodiodes and PIN photodiodes in gamma spectroscopy with $LaBr_3$ crystals, IEEE Trans Nucl Sci **56:** 1006-1011.
33. C. Fiorini et al. (2009) Imaging performances of the DRAGO gamma camera, Nucl Instr Meth A **604:** 101-103.
34. C. Fiorini et al.(2008) Silicon Drift Detectors arrays for the HICAM gamma camera, 2008 IEEE NSS Conference Record, pp. 2981-2983.
35. R.J. McIntyre (1999) A new look at impact ionization-Part I: A theory of gain, noise, breakdown probability, and frequency response**,** IEEE Trans Elec Dev **46:** 1623-1631.
36. C.A. Lee et al. (1964) Ionization rates of holes and electrons in Silicon, Phys Rev A **134:** 761-773.
37. P. P. Webb, R. J. McIntyre and J. Conradi (1974) Properties of avalanche photodiodes, RCA Review, Vol. 35, pp. 234-278.
38. M. Moszynski et al. (2000) Large Area Avalanche Photodiodes in X-rays and scintillation detection, Nucl. Instr. and Meth. A **442:** 230-237.
39. C.P. Allier et al. (2002) Readout of a $LaCl_3(Ce^{3+})$ scintillation crystal with a large area avalanche photodiode, Nucl Instr Meth A **485:** 547-550.
40. R. Chandrasekharan et al. (2006) Detection of VUV light at high quantum efficiency with large area avalanche photodiodes (LAAPDs), Nucl Instr Meth A **567:** 45-47.
41. K. Deiters et al. (2000) Properties of the most recent avalanche photodiodes for the CMS electromagnetic calorimeter, Instr Meth. A **442:** 193-197.
42. Th. Kirn et al. (1997) Wavelength dependence of avalanche photodiode (APD) parameters, Nucl. Instr. Meth. A **387:** 202-204.
43. K. Rajkanan, R. Singh and J. Shewchun (1979) Absorption coefficient of silicon for solar cell calculations, Solid-State Electronics **22:** 793-795.
44. R.J. McIntyre (1972) The distribution of gains in uniformly multiplying avalanche photodiodes: Theory, IEEE Trans Elec Dev **19:** 703-713.
45. K. Deiters et al. (2001) Investigation of the avalanche photodiodes for the CMS electromagnetic calorimeter operated at high gain, Nucl Instr Meth A **461:** 574-576.

46. V. Radeka (1968) Optimum signal-processing for pulse-amplitude spectrometry in the presence of high-rate effects and noise, IEEE Trans Nucl Sci 15: 455-470.
47. http://sales.hamamatsu.com/assets/pdf/parts_S/S8550.pdf
48. http://www.rmdinc.com/products/p006.html
49. Ziegler, S. (2005) Positron Emission Tomography: Principles, Technology and Recent Developments, Nucl Phys A **752:** 679-687.
50. C. Woody et al. (2007) Initial studies using the RatCAP conscious animal PET tomograph, Nucl Instr Meth A **571:** 14-17.
51. Ph. Berard et al. (2009) Development of a 64-channel APD detector module with individual pixel readout for sub-millimeter spatial resolution in PET, Nucl Instr Meth A **610:** 20-23.
52. M. Judenhofer et al. (2007) PET/MR Images Acquired with a compact MR-compatible PET Detector in a 7-T Magnet, Radiology **244:** 807-814.
53. P. Buzhan et al. (2003) Silicon photomultiplier and its possible applications, Nucl Instr Meth A **504:** 48-52.
54. R.J. McIntyre (1961) Theory of Microplasma Instability in Silicon, J Appl Phys **32:** 983-995.
55. R.H. Haitz. (1964) Model for the electrical behavior of a microplasma, J Appl Phys **35:** 1370-1376.
56. V. Golovin (1999) Avalanche Photodetector, Russian Agency for Patents and Trademarks, Patent No. RU 2142175.
57. Z. Sadygov (1998) Avalanche Detector, Russian Agency for Patents and Trademarks, Patent No. RU 2102820.
58. D.E. Groom (1984) Silicon photodiode detection of bismuth germanate scintillation light, Nucl Instr Meth **219:** 141-148.
59. V. Andreev et al. (2005) A high-granularity scintillator calorimeter readout with silicon photomultipliers, Nucl Instr Meth A **540:** 368-380.
60. Y. Musienko et al. (2007) Tests and performance of multipixel Geiger mode APD's and APD's for the CMS ECAL, Proc. of Science (PD07) 012.
61. W.G. Oldham et al. (1972) Triggering phenomena in avalanche diodes**,** IEEE Trans Elec Dev **19:** 1056-1060.
62. http://www.photonique.ch/Prod_0710G9MM.html
63. G.A.M. Hurkx et al. (1992) A new recombination model for device simulation including tunneling, IEEE Trans Elec Dev **39:** 331-338.
64. G.A.M. Hurkx et al. (1992) A new analytical diode model including tunneling and avalanche breakdown, IEEE Trans Elec Dev **39:** 2090-2998.
65. A. Lacaita et al. (1993) On the bremsstrahlung origin of hot-carrier-induced photons in silicon devices**,** IEEE Trans Elec Dev **40:** 577-582.
66. N. Basharuli et al. (2002) Registration of charged particles by scintillating fibers coupled with micro-cell Si APD, Advanced Technology and Particle Physics, World Scientific, Singapore, pp. 627-632.
67. P. Buzhan et al. (2006) Large area silicon photomultipliers: Performance and applications, Nucl. Instr. Meth. A **567:** 78-82.
68. W.J. Kindt (1999) Geiger mode avalanche photodiode arrays for spatially resolved single photon counting, PhD Thesis, Delft University Press, The Netherlands.
69. Th. Kraehenbuehl (2008) G-APD arrays and their use in axial PET modules, Diploma thesis, ETH Zuerich, Switzerland.
70. Ch. Casella et al. (2008) Readout of a LYSO crystal with MPPCs. Calculations and measurements of the signal shape, AX-PET note 2008-001.
71. A. Lacaita et al. (1990) Observation of avalanche propagation by multiplication assisted diffusion in *p-n* junctions, Appl Phys Letters **57:** 489-491.
72. A. Lacaita et al. (1993) Photon-assisted avalanche spreading in reach-through photodiodes, Appl Phys Letters **62:** 606-608.
73. P. Buzhan et al. (2006) Timing by silicon photomultiplier: A possible application for TOF measurements, Nucl. Instr. Meth. A **567:** 353-355.

74. I. Britvitch et al., (2006) Study of avalanche microchannel photodiodes for use in scintillation detectors, 2006 JINST 1 P08002
75. E. Bolle et al. (2008) A demonstrator for a new axial PET concept, IEEE Nuclear Science Symposium Conference Record, 2008, pp 4571-4571.
76. A. Kolb, E. Lorenz, M.S. Judenhofer, D. Renker, K. Lankes, BJ. Pichler, 2010. Evaluation of Geiger-mode APDs for PET block detector designs. Phys Med Biol **55:** 1815-1832.

Chapter 4
Design Considerations of Small-Animal SPECT Cameras

Steven R. Meikle, Peter L. Kench, and Jianyu Lin

1 Introduction

1.1 Rationale for Small Animal SPECT as a Research Tool

Single photon emission computed tomography (SPECT) is a tomographic imaging modality based on the radiotracer principle [1]. It is used to measure the 3D distribution of radiolabelled molecules in vivo using very sensitive radiation detectors and mathematical image reconstruction algorithms. Although SPECT has been used as a clinical tool for several decades, it is also well suited to imaging small animal models of human disease, such as laboratory mice and rats, for pre-clinical research. Because of the relatively long physical half-lives of single photon emitters (Table 4.1), SPECT is best suited to the study of macromolecules, such as antibodies and proteins, which have relatively slow rates of accrual at their target sites and slow plasma clearance. Additionally, proteins and antibodies are easily labelled with one of the radioisotopes of iodine (^{125}I, ^{123}I or ^{131}I), or else by attaching a chelating agent incorporating one of the other common single photon emitters with suitable imaging properties, such as ^{99m}Tc or ^{111}In. Conversely, the closely related radiotracer technique positron emission tomography (PET), which is discussed in the following chapter, is best suited to the study of small molecules such as synthetic drugs which have relatively fast kinetics in the body. Thus, the two techniques are highly complementary in the pre-clinical research environment.

S.R. Meikle (✉) • P.L. Kench
Faculty of Health Sciences, Brain and Mind Research Institute, University of Sydney, Sydney, NSW, Australia
e-mail: s.meikle@usyd.edu.au; peter.kench@sydney.edu.au

J. Lin
Department of Electrical and Computer Engineering, Curtin University, GPO Box U1987, Perth, WA 6845, Australia
e-mail: jianyulin@hotmail.com

H. Zaidi (ed.), *Molecular Imaging of Small Animals: Instrumentation and Applications*,
DOI 10.1007/978-1-4939-0894-3_4,

Table 4.1 Single photon-emitting radionuclides commonly used in small animal imaging studies and their physical characteristics

Radionuclide	Main emission energy (keV)	Half-life
^{99m}Tc	140	6.02 h
^{123}I	159	13.3 h
^{131}I	364	8.2 days
^{125}I	20–35 (X-rays)	59 days
^{111}In	171, 245	2.8 days

1.2 Pre-clinical Applications of SPECT

The instruments and techniques used to acquire a small animal SPECT study are determined by the research question, the species of animal, the structure and physiology of the organ(s) of interest and the desired spatial resolution and sensitivity. The size of the smallest structure to be imaged and the activity distribution within tissue are important considerations for determining the required spatial resolution of the system [2]. Imaging of the rodent brain, myocardium, skeletal system or a tumour may have different spatial resolution and sensitivity requirements. For example, the brain is a complex structure requiring high spatial resolution and sensitivity in order to quantify radiopharmaceutical uptake in structures such as the striatum and cerebellum for studying the dopaminergic system [3, 4]. Imaging the rodent skeleton requires high spatial resolution; sensitivity is less critical, however an extended axial FOV is required to image the whole skeleton. Engrafted tumours often exhibit a heterogeneous distribution of radiopharmaceutical due to rapid tumour growth and tissue necrosis, which require high spatial resolution for accurate quantification. With appropriate collimation and detector configuration, whole body sub-millimetre spatial resolution can be achieved for rodent skeletal and tumour imaging [5].

High system sensitivity is required when investigating tracer kinetics and quantifying uptake. Many SPECT systems support dynamic acquisition for studying tracer kinetics, but reliability of kinetic parameter estimates is dependent not only on temporal resolution but also good signal to noise ratio (SNR). For cardiac and lung imaging, physiological motion may cause excessive blurring. Using a physiological trigger, such as the 'R' wave from an electrocardiograph (ECG), SPECT projections can be divided into discrete time bins that represent different parts of the physiological (e.g. cardiac) cycle. Reconstructing and sequentially displaying each frame in the cycle allows visualisation and quantification of radiopharmaceutical uptake during different phases of the periodic motion. Gated SPECT also allows quantitative analysis of myocardial contractile function and/or motion correction of the respiratory cycle.

Some applications require the capability to simultaneously image multiple radionuclides with different emission energies. For example, Zhou et al. co-injected animals with ^{111}In-oxyquinoline labelled stem cells and ^{99m}Tc-sestamibi, enabling simultaneous imaging of the engraftment of stem cells and perfusion defects in the infarcted rat myocardium [6]. Here, the 245 keV photons of ^{111}In and the 140 keV

photons of ^{99m}Tc were imaged simultaneously in separate energy windows. Such studies require good energy resolution to minimise cross-talk between radionuclide measurements.

These are just some of the very broad areas of application of small animal SPECT in preclinical research. More specific examples are given in later chapters. The key point is that the performance parameters of small animal SPECT systems are very application dependent. Therefore, the intended research applications are an important consideration in the design of small animal SPECT systems.

2 Design Principles

The basic unit of a SPECT system is the radiation imaging detector, also called a gamma camera. The gamma camera senses the photon emitted by a radiation source and determines the two-dimensional position of its interaction within the detector plane (in some detector designs, depth within the finite thickness of the absorber may also be encoded) and the resulting energy deposited within the detector. Thus, typically a gamma camera produces an X and Y signal representing the position coordinates of the absorbed photon and a Z signal representing its energy. The different types of radiation detector and the technologies that underpin them were described in detail in Chaps. 1 and 2. The specific choices appropriate for SPECT are discussed in Sect. 3.5 of this chapter.

In PET, the position coordinates recorded on two opposing detectors are sufficient to determine the trajectory of the annihilation photon pair. This is not the case in SPECT. The position coordinates recorded by a gamma camera tell you where the photon was absorbed but not where it came from. To determine the trajectory of the photon, another key component of the gamma camera is required—the collimator. This is a device attached to the gamma camera and constructed of material with sufficient density and thickness to absorb most of the emitted photons, allowing only a small fraction to pass through one or more open apertures and reach the detector along certain preferred trajectories. For small animal SPECT, the pinhole collimator is the most common design as it provides the best resolution-sensitivity trade-off for imaging small objects. However, there are other alternatives and there are various pinhole designs optimized for different imaging conditions. These are discussed in detail in Sec. 3.6.

Since SPECT is not affected by positron range or non-collinearity effects, it is capable of higher spatial resolution than PET, especially when pinhole collimation is employed, but at the expense of considerably lower sensitivity (approximately 1–2 orders of magnitude lower than PET). The sensitivity of SPECT can be improved by designing the collimator aperture(s) to allow more photons to pass through per unit of radioactivity, or by increasing the number of pinholes and detectors surrounding the animal. However, increased collimator sensitivity comes at the cost of poorer spatial resolution, while increasing the number of detectors increases the cost of the system. For certain types of collimation—in particular focusing

collimators, such as pinholes—sensitivity and spatial resolution can both be improved by minimizing the distance between the pinhole(s) and the subject, at the same time constraining the size of the field of view (FOV). These choices need to be carefully considered in view of the species and organs to be imaged.

Thus, the key trade-offs in SPECT system design are between sensitivity, spatial resolution and the size of the FOV, with cost being an additional, sometimes limiting, constraint. Other considerations include the requirement for quantitative measurements (e.g. absolute tracer concentrations and/or physiological parameter estimates) and the importance of accurately co-registered structural images, such as those provided by X-ray computed tomography (CT) or magnetic resonance imaging (MRI). These considerations drive choices about system configuration and integration of complementary imaging modalities. There are a number of commercial small animal SPECT systems now available, including SPECT–CT hybrid systems. Most are capable of sub-millimeter spatial resolution and have sufficient sensitivity and quantitative capability to perform studies of tracer kinetics. There remain many challenges to further improving the spatial resolution, sensitivity and functionality of preclinical SPECT systems through the development of new instrumentation, imaging techniques and data analysis algorithms. The key drivers for addressing these design challenges are discussed in the following sections.

2.1 Spatial Resolution Versus Sensitivity

There is a trade-off between system spatial resolution and sensitivity which is ultimately determined by appropriate choice of detector and collimator design. The parameters of these are further constrained by several other factors such as FOV size and energy of photons. For parallel hole and pinhole collimator designs, improvements in spatial resolution are usually at the cost of sensitivity [2]. As the diameter of the collimator hole increases the number of photons that can pass through to the detector (sensitivity) also increases but the precise origin of the photon (spatial resolution) becomes more difficult to determine. Parallel collimators are sometimes useful for whole body small animal planar imaging, but the spatial resolution is limited by the intrinsic resolution of the detector, collimator design parameters and distance from the animal. Pinhole collimators are more frequently used for small animal imaging as they offer the best trade-off between spatial resolution and sensitivity for small objects [5, 7]. Magnification of the projection image due to the pinhole geometry improves the observed spatial resolution beyond the intrinsic resolution of the detector. Moving the object closer to the pinhole aperture magnifies the projection, resulting in further improvement in spatial resolution and sensitivity of the system, but at the cost of a smaller FOV as shown in Fig. 4.1. For parallel-hole collimators, the sensitivity is approximately independent of the distance between the collimator and object, as illustrated in Fig. 4.1b.

A mouse is approximately 3,000 times smaller by volume and weight than a human [8, 9]. Given that a typical clinical SPECT system has volumetric spatial

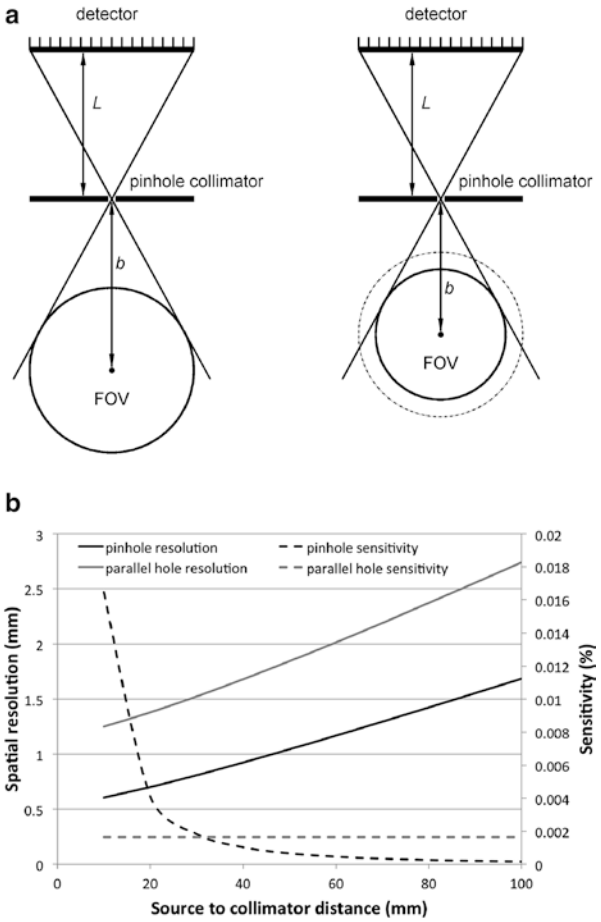

Fig. 4.1 The effect of source to collimator distance on system spatial resolution and sensitivity for pinhole and parallel hole collimators. Intrinsic resolution of the detector is assumed to be 1 mm and the aperture diameter is 0.5 mm for the pinhole and 0.5 mm for the parallel hole collimator. Focal length of the pinhole is 80 mm while septal length and thickness of the parallel hole collimator are 25 and 0.15 mm respectively. Note that at short distances the pinhole collimator leads to both improved resolution and sensitivity compared with the parallel hole collimator, but also a reduced FOV

resolution of approximately 1 cm^3 at the centre of the FOV, a mouse SPECT system would require volumetric resolution of 3×10^{-4} cm^3 (i.e. linear spatial resolution of 0.7 mm) in order to achieve comparable delineation of organs and structures of interest. This may seem a daunting challenge but Fig. 4.1 indicates that a target resolution of 0.7 mm can be achieved with pinhole collimation when the centre of the FOV is approximately 20 mm from the pinhole focus, a realistic distance for a mouse. The greater challenge is to acquire enough counts in each voxel to support this resolution and, thus, achieve similar signal-to-noise to a clinical SPECT study with much larger voxels.

The relatively poor sensitivity of pinhole SPECT can be offset by increasing the administered dose of radioactivity to the animal. This tends to result in higher radiation doses being administered to rodents than humans relative to their volume and mass [8]. Hence, careful consideration needs to be given to the potential impact of a high radiation dose to the animal. This is particularly true for longitudinal studies

where multiple doses of radiopharmaceutical are administered. Researchers need to be confident that SPECT measurements as a function of time are a result of disease progression or intervention and not radiation induced changes. Funk, Sun and Hasegawa estimated the whole body radiation dose for radionuclides commonly used in small animal SPECT and PET imaging [10]. The radiation dose for a mouse is generally greater than that for a rat by a factor of 10 for the same administered activity, due to its smaller body mass. They found that the whole body radiation dose in mice varied between 6 cGy and nearly 1 Gy which is only an order of magnitude less than the lethal dose (LD50/30 approx. 7 Gy) for a mouse. Thus, it is recommended to limit the radiation dose to 10 cGy or less for mice involved in longitudinal studies. The need for high spatial resolution and low radiation dose is driving the development of small animal SPECT systems with higher sensitivity.

2.2 The Need for Quantification

The observed distribution of radiopharmaceutical within a small animal is usually a qualitative or semi-quantitative measure. The uptake within organs and various tissues can be visually compared to uptake in surrounding structures. The ability to provide an absolute measure of tracer concentration in tissue, and/or quantify physiological kinetic parameters, may enhance understanding of the in vivo behaviour of the radiopharmaceutical and the pathophysiology of disease. The impact of an intervention may also be better understood with quantitative measurements of tracer distribution as a function of time within the same animal. When quantification is performed the tracer distribution is expressed as absolute radioactivity or percentage of injected dose per unit tissue volume. Tracer kinetics can be observed by acquiring a dynamic sequence of tomographic data over an extended time, typically up to 90 min following administration. PET is considered ideal for such studies because of its high sensitivity and temporal resolution. Recent advances in small animal SPECT have seen greatly improved sensitivity and full ring systems making tracer kinetic studies now possible [5, 11].

The small size of a rodent makes the bias caused by photon attenuation much less than that which occurs in larger animals and humans. However, for accurate quantification, this error needs to be considered and corrected for. One approach is to assume a constant linear attenuation coefficient for the whole animal (i.e. uniform tissue density) and correct for attenuation based on the distance travelled by the gamma ray within the animal. This approach works well for soft tissue within the abdomen but problems arise when quantifying myocardial tissue uptake due to the different densities of myocardial and surrounding lung tissue. A more accurate approach is to create an attenuation map from a CT volume and correct for SPECT attenuation errors during reconstruction. The CT derived attenuation data need to be calibrated for the difference in photon energy between the X-ray source and SPECT radioisotope. The accuracy of this technique has been demonstrated in several studies (e.g. [12]).

Li et al. [13] demonstrated the feasibility of using highly magnified pinhole SPECT for quantification by accurately (<7% bias) determining the activity of point sources in air and water. The method used a filtered backprojection reconstruction algorithm that considered the impact of attenuation, scatter, pinhole geometric response and system misalignment. Acton et al. [3] quantified dopamine transporters in the mouse brain using ^{99m}Tc TRODAT-1 and a triple detector clinical system fitted with custom made single pinhole collimators. The investigators used a simplified reference tissue model to quantify kinetic parameters [14], which had been previously validated in primates, thus avoiding the need for arterial blood sampling, which is difficult to perform in mice.

High spatial resolution is important when quantifying tissue uptake of radiopharmaceutical as borders can be clearly defined and the impact of the partial volume (PV) effect is reduced. When an imaging system has low spatial resolution, events from an adjacent projection pixel or reconstructed voxel spill in or out of the area of interest. This problem causes a loss of accuracy within the area of interest known as the PV effect. In the study by Acton et al. [3] the pinhole SPECT spatial resolution was 0.83 mm at 30 mm radius of rotation, which is better than can be achieved with current small animal PET systems. The in vivo SPECT tissue uptake measurements correlated strongly with ex vivo tissue counting, validating the quantification method used. The test–retest value was a low 2.6 %, indicating that this method is a useful technique for longitudinal studies. Future improvements in the sensitivity of small animal SPECT systems will allow shorter time frames between acquisitions and include anatomical localisation for correctly identifying tissue boundaries.

In summary, quantitative errors can be corrected in small animal imaging but their magnitude is influenced by the spatial and energy resolution of the SPECT system, the choice of radionuclide and the geometry of the radiopharmaceutical distribution within the animal.

2.3 The Need for Anatomical Localisation

It is desirable to localise foci of increased or decreased radiopharmaceutical uptake in relation to surrounding anatomical structures to ensure correct interpretation of the image. It is often the case that radiopharmaceuticals with high specificity for their target site also exhibit less non-specific uptake in surrounding organs and tissues. Paradoxically, radiopharmaceuticals with a lot of non-specific uptake in surrounding tissues provide information that helps to localize uptake in the target tissues.

Methods of identifying the localisation of a radiopharmaceutical include using external markers or the administration of a second radiopharmaceutical with different pattern of uptake. Placing an external radionuclide marker on the animal in a known location provides a reference point for identifying radiopharmaceutical uptake. External markers can be difficult to secure to the animal's fur or skin but are an easy method for providing a gross estimate of radiopharmaceutical location.

Administering a different radiopharmaceutical that localises within or adjacent to the organ of interest can provide a more accurate method of localisation. If radionuclides with the same or similar photon energies are used, the study of primary importance to the research question should be performed prior to administration of the radiopharmaceutical for anatomical localisation. If the radiopharmaceuticals have quite different photon energies then simultaneous dual isotope imaging can be performed [6]. It is desirable for the radiopharmaceutical of interest to have the higher photon energy to minimise Compton or 'down' scatter into the lower energy window, which would otherwise reduce the quality of the SPECT study.

It is becoming increasingly important in research applications to accurately localise radiopharmaceutical biodistribution relative to known anatomical structures, particularly for new targeted radiopharmaceuticals with low non-specific binding. X-ray CT and MRI can provide detailed anatomical information which is highly complementary to the SPECT study. Thus, it is common in commercial systems for SPECT to be one component of a dual- or even tri-modality imaging system. There are several possible combinations and approaches to multi-modality imaging which are discussed in later chapters, including SPECT/CT (Chap. 12) and SPECT/MRI (Chap. 14). The detector developments that give rise to these possibilities are discussed in Chaps. 2 and 3.

3 System Design

3.1 Angular Sampling

To perform SPECT, multiple projections must be acquired from a large number of uniformly spaced angles around the subject. Certain conditions for the acquisition geometry must be met for the projection data to be successfully reconstructed into a volume representing the distribution of radiopharmaceutical. Orlov and Tuy described the geometrical requirements for parallel hole and pinhole tomography respectively [15, 16]. For a successful SPECT reconstruction, the volume of interest must be fully sampled in each of the projections, i.e. the volume must not be truncated, otherwise reconstruction artefacts may result. Additionally, Tuy's condition states that for pinhole SPECT (or any other cone beam geometry), the pinhole focus must trace out an arc of a great circle as the detector rotates around the subject in order to obtain an accurate reconstruction [15]. In the case of single pinhole SPECT, this condition is only satisfied for the central slice through the subject that is coplanar with the pinhole aperture. Multiple pinhole collimation can be used to overcome this limitation, as discussed below.

A key consideration is the number of projection angles around the object, referred to as angular sampling, which may affect the quality of the reconstructed SPECT volume. For SPECT systems there is a trade-off between the number of projection angles and the acquisition time for each projection. If the time for each projection is

too short the data will contain increased noise relative to signal, resulting in poor reconstruction results. The kinetics of the radiopharmaceutical, injected activity, system sensitivity and duration of anaesthesia all limit the total SPECT acquisition time and, hence, limit the acquisition time per projection and/or number of projections.

Sufficient angular sampling for SPECT can be achieved by rotating the detector around a stationary animal [17], rotating the animal in front of a stationary detector [18] or completely surrounding the animal with stationary detectors [5, 19]. From Shannon's sampling theorem [20], it is necessary to sample at least twice the achievable spatial resolution to ensure resolution is not degraded. The optimal number of projections to faithfully reconstruct the object and prevent angular under sampling for the available spatial resolution is therefore given by:

$$N = \pi D \Big/ \left(\frac{\delta x}{2} \right) \tag{4.1}$$

where D is the diameter of the FOV (or object of interest centred on the AOR) and δx is the system spatial resolution [21, 22].

To increase the FOV the animal can be translated in the axial and/or transaxial directions through the focal area of the detector(s) during SPECT acquisition. Since the locations of the detector and animal are known for each projection the lines of response can be determined allowing the extended FOV to be reconstructed into a larger volume.

3.2 Retrofitted Clinical SPECT Systems

The initial feasibility studies of small animal pinhole SPECT imaging were performed using human SPECT systems [23]. Clinical SPECT systems usually have one or more rectangular or round monolithic inorganic scintillation crystals, each 300–500 mm wide, coupled to an array of single anode photomultiplier tubes (PMT). When a gamma ray interacts with the scintillation crystal some or all of the energy is transferred into visible light. The number of light photons is proportional to the energy deposited in the scintillation crystal. The location and energy of a scintillation within the crystal is determined by analyzing the relative intensity of signals produced in the PMTs directly beneath and surrounding the event, a method known as 'Anger Logic' [24].

Early small animal SPECT imaging studies used existing clinical SPECT systems retrofitted with specially designed pinhole collimators to obtain high spatial resolution and sensitivity for small animal imaging [25]. To overcome the low intrinsic spatial resolution of a clinical pinhole SPECT system, a large magnification factor must be used. The use of a clinical SPECT system fitted with a small aperture pinhole collimator provides a cost effective method of small animal SPECT imaging, as the cost of new equipment and ongoing maintenance are avoided. The large surface of the detector allows for highly magnified projections, and placing the

animal close to the pinhole produces reasonable sensitivity. Unfortunately, there is some loss of spatial resolution near the edge of the detector due to parallax error caused by the oblique incidence angle of the photon and the finite thickness of the crystal. Because clinical SPECT systems are optimised for photon energies of 140–300 keV they are not well suited to small animal studies using low photon energy radionuclides such as ^{125}I (20–35 keV) which produce low light output within the crystal. When a SPECT system is used for human and small animal imaging, careful consideration needs to be given to scheduling of studies and regulatory requirements for shared human and animal imaging equipment. The size and cost of a clinical SPECT system make it less than ideal for a dedicated small animal imaging facility [26].

3.3 Systems Based on Compact High Resolution Detectors

The need for dedicated small animal SPECT and breast imaging systems resulted in the development of radiation detectors with higher intrinsic spatial resolution [27, 28]. This was achieved by developing new approaches in PMT and inorganic scintillation crystal designs. The array of single anode PMTs used in a clinical SPECT system was replaced by one or more position sensitive PMTs (PS-PMT) which are capable of very high intrinsic spatial resolution. These devices, which are discussed in detail in Chap. 3, have multiple anodes whose outputs are used to calculate an X and Y position signal for each detected scintillation event. The sum of the signals from all anodes is proportional to the number of light photons detected in the photocathode, hence the energy of the gamma ray absorbed in the crystal. A limitation of PS-PMTs is their relatively poor uniformity and linearity of response, particularly near the edge. However, their spatial response is very stable over time. A linearity correction or event position lookup map is created to ensure that all events are mapped to the correct position.

To further improve spatial resolution the scintillation crystal can be made thinner. With decreasing crystal thickness, the light from a scintillation event is better localised, but at the cost of reduced detection efficiency. There is also an improvement in energy resolution and a decrease in the non-linear edge effects when the diameter/thickness ratio of an inorganic scintillation crystal disc is increased. Wirrwar et al. [29] recommend scintillation crystal diameter/thickness ratios to be greater than 30 for new detector designs.

A pixelated crystal array comprising small (typically 1–2 mm wide) tightly packed crystals is an alternative approach to achieving high intrinsic spatial resolution. The crystal needles in a pixelated array are separated by a reflective material such as Teflon to prevent scintillation light from escaping to adjacent crystals and to reflect light photons from within the crystal towards the photocathode of the PMT. As the width of the crystal needle decreases the amount of packing material becomes a larger percentage of the total detector area, resulting in loss of detection efficiency. The distance between the centres of adjacent crystals (crystal pitch) includes the

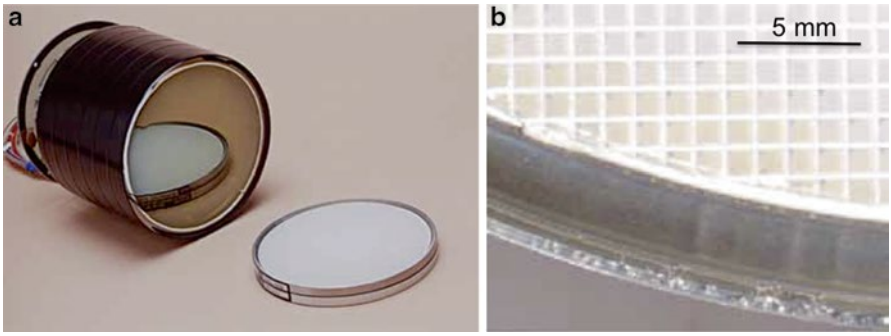

Fig. 4.2 (**a**) Hamamatsu R3292-02 PS-PMT and pixelated NaI(Tl) crystal array. (**b**) A zoomed section of the crystal array showing individual elements and reflective packing. The array comprises 1 mm crystals on a 1.25 mm pitch

crystal width and packing material. The intrinsic spatial resolution of the detector is approximately the same as the crystal pitch, provided it is coupled to a high resolution detector such as a PS-PMT (Fig. 4.2). Since the individual crystal needles of a multiple crystal array are precisely positioned, a map of all crystal locations can be used to correct for the non-linear response of the PS-PMT. Scintillation events are assigned to the location of individual crystals based on the measured map of crystal locations derived from a high count flood acquisition. It is desirable to make the crystal pitch small (e.g. 1 mm or less) for high resolution but the needles must be sufficiently thick to absorb most photons for good detection efficiency. However, as the crystal needle length-to-width ratio increases light output decreases due to internal reflections resulting in a loss of energy resolution [26, 29, 30].

3.4 Rotating Versus Stationary SPECT Systems

A variety of SPECT system designs are used to acquire sufficient angular samples of the animal for tomography. These include rotating or translating animals in front of a stationary collimator and detector, rotating collimators with stationary detector(s) and animal, rotating detectors and collimators with a stationary animal, and completely stationary systems (Fig. 4.3). Each design has specific advantages and disadvantages that need to be considered.

The simplest small animal SPECT system involves the vertical or horizontal rotation of the anaesthetised animal in front of a stationary detector [31]. The design should allow the AOR to be centred over the pinhole. The animal gantry needs to be rotated through at least 180° using incremental steps. Vertical rotation is preferred over horizontal rotation to reduce the chance of organ movement during the scan, although horizontal rotation systems have also been developed that address the organ motion issue [18]. Vertical positioning should be done for short periods of

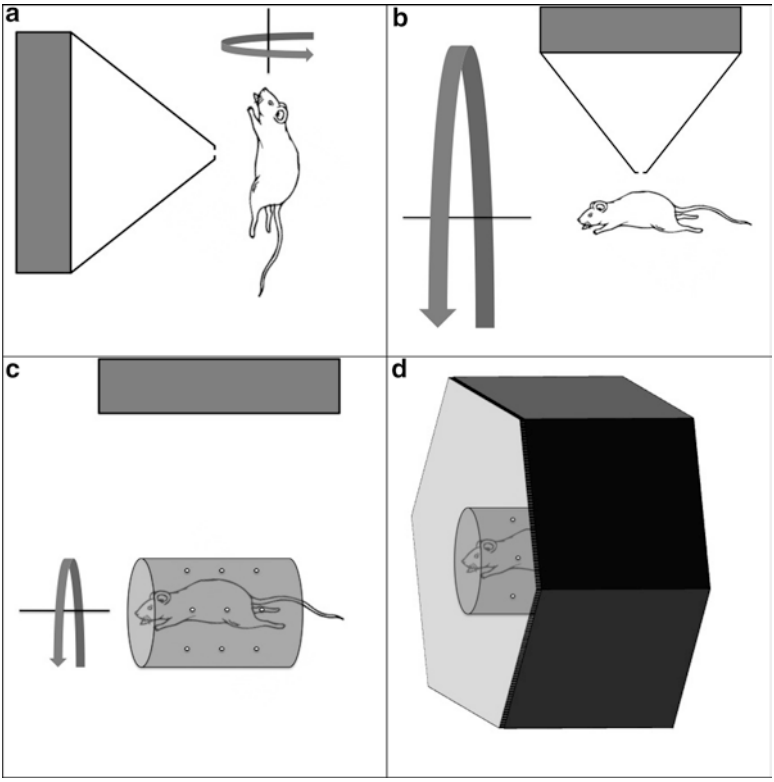

Fig. 4.3 The common SPECT system designs are illustrated. These include systems where (**a**) the mouse rotates in front of a stationary detector and collimator, (**b**) the detector and collimator rotate around a stationary animal, (**c**) the collimator and the animal rotates in front of a stationary detector and (**d**) the system and animal are stationary

time only, as it is not well suited to the rodent's physiology and has been related to an increased incidence of mortality [32]. The advantage of rotating the animal instead of the SPECT detector is that the weight of the animal is considerably less than that of the detector and the gantry is simpler and cheaper to design. The weight of a detector with collimation and shielding may introduce mechanical misalignments resulting in reconstruction artefacts when the detector is rotated around the animal [18]. The drawbacks of rotating the animal are difficulties with accommodating apparatus for gas anaesthesia and physiological monitoring and positioning may be difficult to reproduce for longitudinal studies.

Most clinical and small animal SPECT systems have the detector and collimator mounted on a gantry that rotates 360° around the subject in precise incremental steps or continuous motion. The gantry allows the detector and collimator to move in and out perpendicular to the AOR, to adjust the radius of rotation and hence the projection magnification when pinhole collimation is used. Magnification may also be altered by changing the distance between the pinhole collimator aperture and the

detector surface [33]. The gantry must be sturdy enough to rotate the detectors without varying the radius of rotation or causing the detectors to sag. The detector must be precisely positioned to ensure that its surface is parallel and centred over the AOR. The incremental angular rotation and translation of the detector must also be precise and reproducible over extended periods of time. These engineering requirements add to the cost of designing, building and maintaining a small animal SPECT based on rotating detectors.

To improve the sensitivity and reduce the imaging times of a small animal imaging system additional detectors may be added. Multiple detector SPECT systems using two, three or four rotating detectors have been developed [3, 33–37]. Multiple detector systems reduce the need for a system to acquire projection data over a full 180° or 360°. The uniformity and sensitivity must be similar for each detector to ensure that reconstruction artefacts are not introduced. Each additional detector adds weight to the gantry and cost to the system, although multiple equally placed detectors may help to balance the gantry as it rotates.

The FOV is often limited for small animal pinhole SPECT systems that use high magnification or small compact detectors. Some imaging protocols require a greater FOV to image a larger organ such as the rat skeleton. The FOV can be enlarged by increasing the radius of rotation but this also reduces the spatial resolution and sensitivity of pinhole systems. Another approach is to move the animal stepwise through the FOV during the SPECT acquisition allowing a degree of projection overlap. The acquired data can be reconstructed separately and the volumes stitched together or the entire dataset can be reconstructed as one extended volume (Fig. 4.4) [5]. In the case of a rotating SPECT system, translating the animal in the axial direction while acquiring projection data results in the detectors travelling in a helical path around the AOR. Stepwise or helical acquisition not only increases the FOV but also reduces the incomplete sampling artefact in the axial direction sometimes observed in highly magnified circular SPECT orbits. Increasing the number of detectors for helical SPECT acquisitions also increases the likelihood of an object being sampled close to a pinhole aperture. Thus, the use of multiple detectors and a helical SPECT orbit can produce a more uniform reconstruction volume, better sensitivity and improved resolution.

Several systems have been developed with stationary detectors that surround the animal and multiple stationary or rotating pinholes. Surrounding the animal with detectors and pinholes improves system sensitivity, and rotating the collimator instead of the detector reduces gantry construction costs and avoids mechanical misalignments due to gantry rotation. For example, Goertzen et al. modified a human brain scanner, the Ceraspect, with a rotating multiple pinhole tungsten collimator insert [19]. The Ceraspect has a ring of stationary NaI(Tl) inorganic scintillation crystals coupled to PMTs. The rotating tungsten pinhole collimator has 8×1 mm^2 aperture pinholes evenly spaced with non-overlapping projections, and requires only a 45° rotation which can be completed in 1.25 s. The reconstructed spatial resolution measures 1.7 mm FWHM with a sensitivity of 373 counts s^{-1} MBq^{-1} (or 0.00037 %) with a transaxial FOV suitable for mouse imaging.

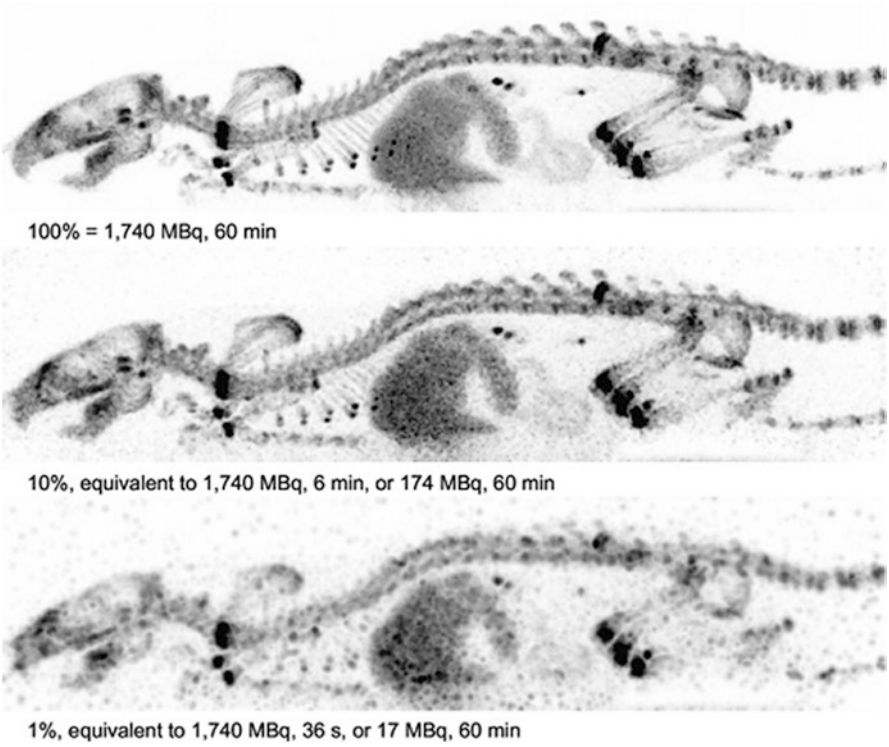

Fig. 4.4 Whole body ^{99m}Tc-HDP bone SPECT study of a rat. Images were reconstructed using 100 % (*top*), 10 % (*middle*) and 1% (*bottom*) of available counts from list-mode data (reproduced from [5] with permission of the Society of Nuclear Medicine)

Furenlid et al. [38] developed a stationary small animal SPECT system (FastSPECT II) based on 16 fixed individual pinhole collimators and detectors capable of imaging a mouse with photon collection efficiency of 0.04 %. Beekman et al. [11] described a small animal SPECT system (U-SPECT I) based on three stationary clinical detectors and a cylinder with five rows of 15 gold pinholes focused towards the centre of the cylinder. Projection overlap was avoided by placing additional shielding between the pinhole and the detector. Peak sensitivity is as high as 0.22 % using 0.6 mm aperture pinholes for a mouse sized collimator, making dynamic SPECT feasible. The detectors have intrinsic spatial resolution of 3.2 mm FWHM but the reconstructed spatial resolution is sub-millimetre. Since the pinholes are focused, the FOV for a single bed position is limited to 10.5 mm diameter (transaxial) and 5 mm axial [5]. Imaging larger organs or a whole body requires imaging at multiple bed positions. van der Have et al. [5] reported the sensitivity and spatial resolution of the U-SPECT II, a commercial stationary small animal SPECT system. Sensitivity was measured to be 1,500 and 525 counts s^{-1} MBq^{-1} for the 0.6 and 0.35 mm aperture collimators respectively. Whole body imaging is achieved by moving the animal through the focal spot of the multiple pinhole collimator using a

computer controlled system that can translate the bed in three directions. An important advantage of stationary SPECT systems is that all the required projections are acquired simultaneously, eliminating reconstruction errors due to redistribution of the radiopharmaceutical [38]. SPECT systems without moving detectors or collimators also have more stable geometric calibration and are less susceptible to mechanical misalignments.

3.5 Detector Choice

The ideal detector would have 100 % likelihood of absorbing the full energy of an incident gamma ray within a small volume via a single photoelectric interaction and it would release a large number of light photons at a wavelength that matches the peak sensitivity of the photodetector.

Scintillation detectors are constructed of an inorganic crystal coupled to one or more photodetectors via a light guide. The most common inorganic scintillation crystals are sodium iodide doped with thallium [NaI(Tl)] and caesium iodide doped with thallium [CsI(Tl)] or sodium [CsI(Na)]. The thallium and sodium impurity atoms create an 'activity centre' within the crystal matrix which allows scintillation to occur at room temperature. Important properties of scintillation crystals include density, light decay time, light yield and wave length, refractive index and environmental stability. These properties are discussed in detail in Chap. 1, including the scintillation properties of the common SPECT scintillators NaI(Tl), CsI(Tl) and CsI(Na).

NaI(Tl) is a good scintillator for SPECT due to its stopping power for 140 keV gamma rays, high light output and the close match between its 410 nm emission wavelength and the peak efficiency of bialkali PMTs. CsI(Tl) has greater density and light output but slower decay time than NaI(Tl). They have a similar refractive index but CsI(Tl) is only slightly hygroscopic, making it less likely to deteriorate over time. CsI(Na) exhibits the best characteristics of NaI(Tl) and CsI(Tl) but has a longer decay time, which may be a problem for high count rate applications. Inorganic scintillators must be coupled to a photodetector, usually via a light guide matched to the refractive index of the crystal that converts light photons into an electrical signal. The most common photodetectors are PMTs (and PS-PMTs), silicon photodiodes and charge coupled devices (CCDs). PMTs have reasonable quantum efficiency (15–40 %) for converting light photons into photoelectrons, which is required for good spatial and energy resolution. Photodiodes are efficient at converting light into electrical current but produce very weak noisy signals, especially when the detectors are larger than a few mm. Geiger-mode APDs show significant promise as alternatives to PS-PMTs as they have similar gain to PMTs (10^5–10^7), fast timing properties and are MRI-compatible. Improvements in performance of CCDs make these devices viable alternatives to PMTs. Modern CCDs do not suffer from dark current when modestly cooled, and achieve quantum efficiencies as high as 90 %. Some CCDs are suitable for both optical (bioluminescence and/or fluorescence) and SPECT imaging with suitable modifications [26].

Recent developments in semiconductor radiation imaging detectors make them a viable choice for small animal SPECT in place of inorganic scintillators coupled to photodetectors. Semiconductor detectors are solid state ionisation chambers that produce one ionisation event per 3–5 keV of photon energy absorbed. Materials commonly used as semiconductors for radiation detection are silicon (Si), germanium (Ge) and, more recently, cadmium telluride (CdTe) or cadmium zinc telluride (CZT). Silicon and germanium semiconductors have similar densities (2.33 and 5.32 g cm^{-3} respectively) to inorganic crystals, hence similar probability of a gamma ray interaction. However, they are not suitable for imaging due to the high thermal noise generated when operated at room temperature, making ionizing events difficult to distinguish from the background noise.

CZT, on the other hand, is a high density semiconductor material (6.06 g cm^{-3}) with good performance at room temperature. The probability of interaction for a 140 keV gamma ray is 83 % for 5.0 mm of CZT and energy resolution is approximately 6–7 % for a typical array element, which is better than the energy resolution of similar sized scintillation array detectors [39, 40]. CZT detectors have the added advantage of being insensitive to magnetic field strengths of up to 7 T, making them a suitable choice for hybrid SPECT/MRI systems.

3.6 Collimation

The purpose of collimation is to restrict gamma rays impinging on the detector to those travelling in certain preferred and, therefore, known directions. Collimators are constructed from gamma ray absorbing material which has a high atomic number and electron density, such as lead, tungsten, gold and depleted uranium. There are a wide variety of collimator designs which provide different trade-offs between spatial resolution and detection efficiency. They can be broadly categorized as multi-channel, pinhole and slit–slat collimators.

3.6.1 Multi-Channel Collimation

Multi-channel collimators are constructed from a series of adjacent channels or tubes within gamma ray absorbing material that covers the entire surface of the detector. The channels may be circular, square or hexagonal. They may be drilled, die-cast or constructed from foil. Lead alloy is most commonly used for collimator construction due to its high gamma ray absorption properties, machinability and cost effectiveness. Factors that affect the spatial resolution and geometric efficiency (sensitivity) of a multi-channel collimator include the septal (wall) thickness, hole width and height of the channel. The septal wall needs to be sufficiently thick to prevent gamma rays from passing through the channel wall and interacting with the detector material. However, increased septal thickness decreases geometric

efficiency and spatial resolution. Decreasing the channel width and increasing its length increases spatial resolution but at the cost of geometric efficiency, so the choice of collimator parameters is a trade-off between spatial resolution and efficiency.

The multi-channel parallel hole collimator is designed with all the channels parallel to each other and perpendicular to the detector surface. This configuration allows only gamma rays travelling perpendicular to the detector surface and parallel to the channels to be detected. When the distance between the source of radiation and collimator is increased there is a loss of spatial resolution but the geometric efficiency of the collimator remains constant. Resolution decreases because gamma rays travelling at a larger acceptance angle from the source can now pass through more channels, resulting in a loss of detail about the photon's origin. Geometric efficiency remains stable within a range of distances because photon intensity is inversely related to distance from the source but this is offset by the increasing number of channels "seen" by the source as distance increases. The channels can be arranged so that they are all not aligned in the same direction and the channel width can vary along its length. Collimators that magnify the projection of radionuclide distribution onto the detector surface are referred to as converging or fan-beam and those that minify the projection are diverging.

The application of multi-channel collimators to small animal imaging has been limited due to their inferior spatial resolution and geometric efficiency compared with pinhole collimation for small sources. The parallel-hole collimator cannot achieve spatial resolution greater than the intrinsic spatial resolution of the detector, in fact normally it is substantially worse. The magnification of the converging collimator could increase the detector's spatial resolution, but other types of magnifying small animal collimators achieve higher geometric efficiency for objects less than 30 mm in size [41]. The multi-channel parallel collimator is, however, suitable for whole body rodent imaging using compact high resolution detectors as it does not require the animal to be translated through the FOV.

3.6.2 Pinhole Collimation

The main factors that influence spatial resolution and sensitivity in pinhole SPECT are magnification, aperture diameter, the distances between the source and pinhole and pinhole to detector, and the number of pinholes. Other influencing factors include the acceptance angle, the shape of the pinhole edge profile and collimator material. The ability of the pinhole collimator to magnify the projection view of the object compensates for the limited intrinsic resolution of the detector. Magnification occurs when the distance b from the pinhole centre to the AOR is smaller than the distance from the pinhole centre to the detector, i.e. the focal distance L (Fig. 4.1). The magnification factor is given by

$$M = \frac{L}{b} \tag{4.2}$$

Fig. 4.5 Cross sections of pinhole collimators with (**a**) knife and (**b**) keel edges

Moving the animal closer to the pinhole has the added advantage of improving system sensitivity but this also decreases the FOV.

The contribution of the pinhole collimator to spatial resolution R_{coll} and efficiency g of the imaging system are proportional to the pinhole aperture diameter d. When calculating the R_{coll} and g for a pinhole collimator it is necessary to take into account the penetration of gamma rays through the knife edge of the pinhole (Fig. 4.5a) by using the effective pinhole aperture diameter d_{eff} instead of d:

$$d_{eff} = \sqrt{d\left[d + 2\mu^{-1}\tan\left(\alpha/2\right)\right]} \tag{4.3}$$

$$R_{coll} \approx d_{eff}\left(1 + \frac{1}{M}\right) \tag{4.4}$$

$$g \approx d_{eff}\frac{\cos^3\theta}{16b^2} \tag{4.5}$$

where α is the acceptance angle of the pinhole opening, μ is the linear attenuation coefficient of the pinhole material for the energy of the gamma ray being imaged and θ is the angle the photon trajectory subtends with the pinhole axis, i.e. the angle of incidence.

Materials proposed for pinhole collimation include tungsten, lead, gold, platinum and depleted uranium. Lead has less attenuation than tungsten, and gold and platinum are expensive compared to tungsten alloy. The cost of gold and platinum pinholes can be reduced by creating small pinhole inserts within a tungsten plate [11, 42]. Pure tungsten has an atomic number of 74 and density of 19.3 g cm^{-3} but is a difficult material to machine. However, tungsten alloys containing small amounts of Fe, Ni and Cu have favourable machining properties for collimator manufacture with a density of 18.5 g cm^{-3} and a linear attenuation coefficient of 34.48 cm^{-1} for 140 keV gamma rays [43]. The tenth value thickness (ln10/μ) for tungsten alloy with a 140 keV photon is 0.67 mm.

Keel-edge pinholes are recommended for medium energy (approx. 200–380 keV) photons and high resolution imaging, as the extra thickness of the edge reduces penetration [44]. They are constructed with a small channel instead of a knife edge (Fig. 4.5). With a keel-edge, sensitivity decreases as the angle between the source and the central axis of the collimator increases due to narrowing of the apparent

aperture. The geometric response of a keel-edge pinhole collimators is, therefore, different from that of a knife-edge pinhole which should be considered when reconstructing projections from a keel-edge pinhole collimator.

For a given SPECT application the desired or achievable FOV determines the pinhole magnification required. The magnification and intrinsic spatial resolution of the detector, in turn, determine the achievable system spatial resolution. The pinhole aperture size can be designed to provide the desired spatial resolution for a known pinhole magnification and detector configuration. The total system resolution R_t for a pinhole system and detector with intrinsic spatial resolution R_i is given by

$$R_t = \sqrt{R_{coll}^2 + \left(\frac{R_i}{M}\right)^2} \tag{4.6}$$

It can be shown that the most efficient (but not necessarily optimal) trade-off between resolution and sensitivity is obtained when the two terms in Eq. (4.6) are approximately equal, i.e.

$$R_{coll} = d_{\text{eff}}\left(1+\frac{1}{M}\right) = \frac{R_i}{M} \tag{4.7}$$

Therefore, an efficient trade-off between sensitivity and resolution is achieved when the pinhole aperture size is

$$d_{\text{eff}} = \frac{R_i}{M+1} \tag{4.8}$$

Note, for pixelated sensors the pixels are square and the response is discrete. Then, d_{eff} can be chosen to be somewhat larger than that specified by Eq. (4.8). Equation (4.8) also tells us that for a given intrinsic detector resolution R_i, when magnification M is increased the aperture size needs to be decreased accordingly to achieve the most efficient trade-off between resolution and sensitivity. Theoretically one can continue increasing magnification to improve resolution, however magnification cannot be increased without limit. The first limit comes from the size of the object to be imaged, which constrains the pinhole to AOR distance, and the configuration of the SPECT system, which constrains the focal length of the pinhole. The second limit is the size of the FOV. If b is too small (pinhole too close to the object), truncation of projections may occur. Thus, there is a limit to the extent to which adjustment of a single pinhole parameter can achieve the desired trade-off between resolution and sensitivity.

3.6.3 Multi-Pinhole Collimation

In many cases, the constraints on magnification mean that the projection of the object occupies a small proportion of the available detector area and the remaining detector area is wasted. To make more efficient use of the detector and, in turn,

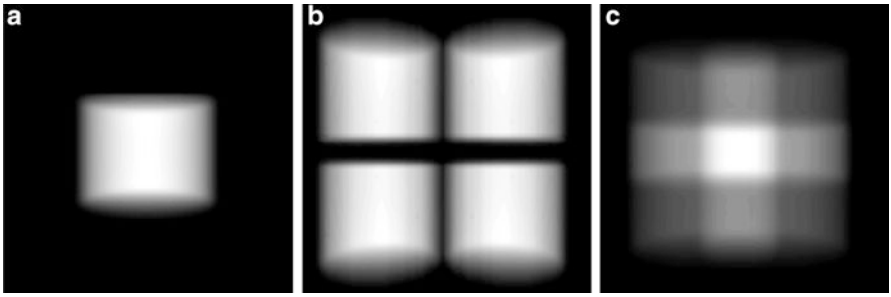

Fig. 4.6 Projections of a simulated cylinder through (**a**) one pinhole, (**b**) four pinholes without multiplexing and (**c**) four pinholes with multiplexing

increase sensitivity, one can employ multiple pinholes to project additional projections of the object onto the available detector area. Multiple pinhole collimators can be designed such that they produce overlapping or non-overlapping projections of the object on the detector (Fig. 4.6). When the projections overlap, the acquired data are said to be multiplexed, which means that detector elements in the overlap region record data from more than one channel (i.e. more than one ray path). Thus, the data in the overlap region are ambiguous.

At first, such ambiguity may be thought to be problematic with regard to producing an accurate artefact-free reconstruction of the object. However, provided the projection data acquired from all angles are consistent with each other, the object can be faithfully reconstructed from multiplexed data (Fig. 4.7), although iterative algorithms typically take longer to converge compared with non-multiplexed data. The key question is whether the additional sensitivity in the overlap region outweighs the increased noise due to slower convergence. We shall return to this question after considering the effects of multiplexing and inconsistent projections and how to avoid them.

In Fig. 4.7a, the condition of an inconsistent projection is shown. The part labelled "inconsistently projected volume" in the object is projected to the detector through pinhole 2 (PH2) but not through pinhole 1 (PH1). As a result, the part of the multiplexed region indicated by the dashed line is formed by inconsistent projections. When reconstruction is performed, back projection errors arise from the missing projection of the "inconsistently projected volume" through pinhole 1, i.e. the back projection through PH1 would evaluate the inconsistently projected volume as zero, while the back projection through PH2 would not. This inconsistency makes it difficult or impossible for the iterative algorithm to match the multiplexed part correctly during forward projection. As a result, the reconstructed image may contain artefacts, or the iterative algorithm may never converge.

Thus, if a multi-pinhole collimator allows multiplexing, it should be designed in such a way that the imaging volume is projected consistently through all pinholes. To address the problem of an inconsistently projected volume, one can employ

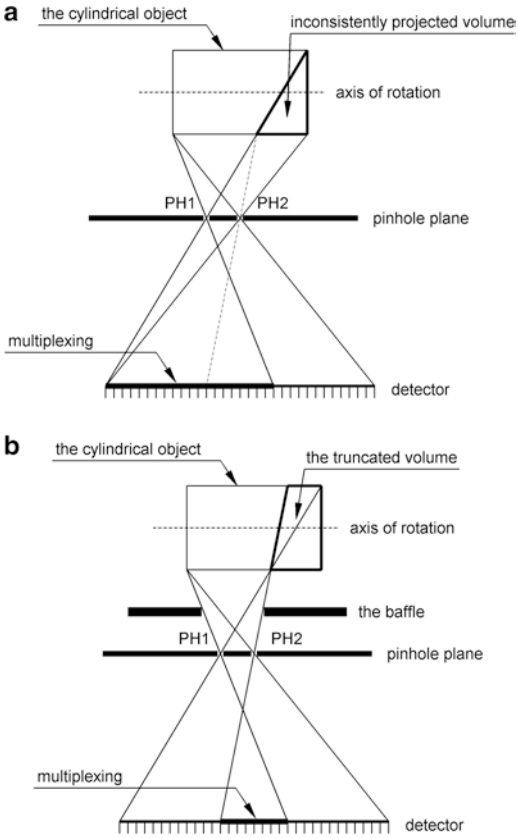

Fig. 4.7 Effects of multiplexing and inconsistent projections in multi-pinhole collimation. Multiplexing arises when parts of the object project through different pinholes into the same area of the detector. (**a**) Inconsistency arises when different parts of the object are partially projected through each of the pinholes. (**b**) These effects can be mitigated by including appropriate shielding (i.e. a baffle) to minimise overlap and inconsistency

focused pinholes or insert a gamma ray absorbing baffle in front of the pinhole plate as shown in Fig. 4.7b. By blocking some of the projections from PH2, inconsistent projections are effectively removed from the multiplexed region, and at the same time multiplexing is reduced [45].

There have been detailed theoretical and numerical simulation studies to investigate the image quality trade-offs associated with multiplexed and non-multiplexed designs [46, 47], but the value of multiplexing remains an open question. However, one clear advantage that multiple pinhole collimation (with or without overlapping) has over single pinhole designs is that it improves sampling in the axial direction. According to Tuy's condition [15], when single pinhole collimation is used projection data in the off-axis slices (the top and bottom parts of the coronal image) are incompletely sampled. Only the central region is properly sampled. This problem is largely overcome by positioning multiple pinholes such that they increase sampling along the axial direction.

3.6.4 Slit–Slat Collimation

Slit–slat collimation is a combination of pinhole (slit) and fan-beam (slat) designs. It may be suitable for SPECT imaging of medium sized animals where the optimal sensitivity and FOV lie between converging multi-channel and pinhole collimation for a specified spatial resolution. A narrow slit is positioned close to the object aligned with the AOR. The image of the object is magnified through the slit, as in pinhole geometry. Between the slit and detector are positioned a series of thin slats aligned perpendicular to the AOR. The slats behave like the septa of a multi-channel collimator, providing complete sampling in the axial direction. This addresses the limited off-axis sampling of circular orbit single pinhole SPECT where there is insufficient data to avoid reconstruction artefacts. The slit provides magnification and improved spatial resolution in the transaxial direction and high sensitivity for objects close to the slit, like a pinhole collimator. The axial resolution is less than that of an equivalent pinhole design because of the distance between the object and the slats [48].

Zeng [41] proposed a modified slit–slat design for small animal SPECT imaging, referred to as 'skew-slit' collimation. A vertical slit is aligned with the AOR and positioned close to the object, providing magnification in the transaxial direction. Between the vertical slit and collimator are positioned a number of horizontal slits. These provide no magnification in the axial direction, as the distance of the vertical slits from the object and the collimator are identical. The distance between the horizontal slits maximises the detector area but reduces overlapping of the projection data. Initial simulation and phantom results demonstrate an improvement in reconstructed transaxial spatial resolution over the multi-pinhole design [41].

4 SPECT Image Reconstruction

Tomographic data are reconstructed from a series of 2D projections into a 3D volume, allowing visualisation of the radiopharmaceutical distribution without interference from over- and underlying activity. There are two broad categories of tomographic reconstruction methods for emission tomography, analytic and iterative [49]. The main analytic method is filtered backprojection (FBP) [50, 51], which is a discrete implementation of a mathematical solution that is exact for noiseless and continuous functions [52]. However, real SPECT data is neither noiseless nor continuous. Thus analytical methods, although computationally efficient, are limited in their ability to deal with noisy data, finite discrete linear sampling and photon attenuation [53, 54]. Iterative methods, such as maximum likelihood expectation maximization (ML-EM) [55, 56] require greater computation than analytic methods but they use an appropriate statistical model to describe the data. They also allow for more realistic modelling of physical effects such as scatter, attenuation and detector properties, resulting in a potentially more accurate representation of the radiopharmaceutical distribution within the subject. Iterative methods have become routinely used in both PET and SPECT due to rapid improvements in computational power and the advantages they confer.

The FBP method of tomographic reconstruction is commonly used with parallel ray geometry such as that encountered with parallel hole collimation in SPECT. It can also be adapted for converging ray geometries such as fan beam and cone beam X-ray CT. However, in small animal SPECT using single and multiple pinhole geometries, iterative algorithms based on EM and its variants are much more commonly used.

The ML-EM method starts with an initial estimate of the object to be reconstructed, usually a uniform cylinder. The estimate of the object is forward projected to create a series of estimated projection data. The forward projection may include modelling of scatter, attenuation, collimator and detector response, and the ML-EM method explicitly models Poisson noise. The estimated and measured projection data are compared (cost function), and the difference is expressed as a ratio (projection space error) which is backprojected (image space error) and multiplied by the previous volume estimate (update step). The process is then repeated iteratively until the projection space error reduces to an acceptably small value or the reconstructed volume reaches an acceptable solution [49, 54]. The ML-EM algorithm is guaranteed to converge to a maximum likelihood solution but since the projection data are noisy, that may mean fitting primarily to the noise if the algorithm is allowed to continue for too many iterations. Thus, it is common to either terminate the algorithm early in the iterative process or, preferably, to post smooth the reconstruction after it has substantially converged [57].

Ordered subsets expectation maximisation (OS-EM) is a modification of ML-EM which speeds up the reconstruction process [58]. SPECT projections are organised into groups of symmetric projections which represent subsets of the total number of projections, e.g. 64 projections can be divided into 2, 4, 8, 16 or 32 subsets. Subsets of 1 and 64 can also be used, but these are equivalent to ML-EM and multiplicative algebraic reconstruction technique (MART) [59] respectively. Forward projection, back projection and update steps are performed using all projections within a given subset. The process is repeated in a sequence that maximises the spread of subsets around the object (referred to as subset balance), until all subsets have been forward and back projected. This is referred to as one full iteration of OS-EM, which consists of several updates (equivalent to the number of subsets) to the volume estimate. It has been demonstrated that one iteration of OS-EM is almost exactly equivalent to N iterations of ML-EM where N is the number of subsets, hence it accelerates the reconstruction by a factor of approximately N [58]. OS-EM combines the benefits of ML-EM with greatly improved processing speed, making it an important algorithm for SPECT reconstruction [49, 58].

5 State-of-the-Art Pre-clinical SPECT Systems

At the time of writing there are six small animal SPECT systems available commercially. These systems encompass a wide variety of detector and collimator designs, covering most of the technologies discussed in this chapter. Most are also

Table 4.2 Commercial small animal SPECT systems and the technologies they employ

System	Detector	Photodetector	Collimation
X-SPECT	CZT	N/a	Single or multiple pinhole
EXplore speCZT	CZT	N/a	Multi-slit or multi-pinhole
NanoSPECT	Monolithic NaI(Tl)	PMT	Multi-pinhole with multiplexing
U-SPECT-II [5]	Monolithic NaI(Tl)	PMT	Multiple focussed pinholes
Inveon SPECT	Pixelated NaI(Tl)	PS-PMT	Single and multi-pinhole
YAP-(S)PET	Pixelated YAP:Ce	PS-PMT	Parallel hole

available as dual modality SPECT/CT systems and, in the case of the YAP-(S)PET system, as a dual purpose SPECT–PET scanner. The commercial systems and the technologies they employ are listed in Table 4.2. The performance specifications are not included as these are dependent on several variable parameters, including the pinhole aperture diameter (most systems offer several choices for different applications) and radius of rotation. Nor have the companies marketing these systems been included, mainly because such information is subject to change and likely to become out of date quickly. However, all these systems are capable of achieving sub-millimetre spatial resolution with a FOV suitable for mice and/or rats and most have sufficient temporal sampling and sensitivity for performing kinetic studies. All systems offer both analytical and iterative 3D OS-EM reconstruction as a minimum, with at least some form of system modeling such as spatially variant point source response modeling.

6 Summary and Future Perspectives

Small animal SPECT systems have come a long way since the first converted clinical systems were used to image laboratory animals using pinhole collimation in the early 1990s [23, 25, 36]. After two decades of continuous development, dedicated small animal SPECT systems are routinely being used in research laboratories and the pharmaceutical industry to image a wide range of animal models with an equally wide range of labelled compounds at sub-millimetre spatial resolution.

It is interesting to note that most of the commercially available systems still use the same basic form of collimation used in the early prototypes, i.e. pinhole collimation, and some still use large area monolithic NaI(Tl) detectors with conventional photomultiplier tubes. Nevertheless, several of the novel technologies discussed in this chapter have found their way into commercial systems, including pixelated scintillators, semiconductor detectors, position sensitive photodetectors and multi-pinhole collimation and reconstruction.

It is difficult to predict what future technologies might be around the corner, but it is possible to make some general observations. First, despite the impact of novel multi-pinhole designs and associated image reconstruction developments, the main challenge for small animal SPECT remains increasing the sensitivity of these

systems. This is an important goal for two reasons: (1) the radiation dose to experimental animals is relatively high and needs to be reduced to enable longitudinal studies to be performed on the same animal; (2) for the full potential of small animal SPECT to be realised, higher sensitivity is needed to ensure accurate quantification of tracer kinetics and associated physiological parameters.

The second observation is that it continues to be the case that experimental small animal imaging systems are an ideal platform for testing new technologies. Many of the technologies discussed in this chapter, including pixelated detectors and position sensitive photodetectors, were incorporated into early prototype small animal imaging systems, both SPECT and PET. It is also worth noting that some new technologies like CZT are better suited to the relatively low gamma ray energies of single photon emitters than PET. CZT is also more likely to be used in small animal systems than clinical systems in the near future because growing large uniform detectors with this semiconductor material remains a significant manufacturing challenge.

Finally, multimodality imaging has made a major impact on both the pre-clinical and clinical realms [60]. SPECT/CT is widely available and is almost essential for optimal interpretation and quantification of the radiopharmaceutical distribution. Several laboratories are also developing combined SPECT and optical imaging systems. The current major challenge is to develop stable, reliable SPECT/MRI systems that combine the advantages of both modalities without compromising the performance of either. With the recent developments in solid state radiation detectors, photodetectors and low noise multi-channel amplifiers, such systems are not far away.

References

1. Hevesy G, Chiewitz O (1935) Radioactive indicators in the study of phosphorous metabolism in rats. Nature 136:754–755.
2. Jansen FP, Vanderheyden J-L (2007) The future of SPECT in a time of PET. Nucl Med Biol 34:733–735.
3. Acton PD, Choi SR, Plossl K, Kung HF (2002) Quantification of dopamine transporters in the mouse brain using ultra-high resolution single-photon emission tomography. Eur J Nucl Med Mol Imaging 29:691–8.
4. Pissarek MB, Oros-Peusquens AM, Schramm NU (2008) Challenge by the murine brain: multi-pinhole SPECT of ^{123}I-labelled pharmaceuticals. J Neurosci Meth 168:282–92.
5. van der Have F, Vastenhouw B, Ramakers RM, Branderhorst W, Krah JO, Ji C, et al. (2009) U-SPECT-II: An Ultra-High-Resolution Device for Molecular Small-Animal Imaging. J Nucl Med 50:599–605.
6. Zhou R, Thomas DH, Qiao H, Bal HS, Choi SR, Alavi A, et al. (2005) In vivo detection of stem cells grafted in infarcted rat myocardium. J Nucl Med 46:816–22.
7. Beekman FJ, van der Have F (2007) The pinhole: gateway to ultra-high-resolution three-dimensional radionuclide imaging. Eur J Nucl Med Molec Imaging 34:151–161.
8. Acton PD, Kung HF (2003) Small animal imaging with high resolution single photon emission tomography. Nucl Med Biol 30:889–95.
9. Loudos GK (2007) Advances in small animal imaging systems. AIP Conference Proceedings 958:127–30.

10. Funk T, Sun M, Hasegawa BH (2004) Radiation dose estimate in small animal SPECT and PET. Med Phys 31:2680–6.
11. Beekman FJ, van der Have F, Vastenhouw B, van der Linden AJA, van Rijk PP, Burbach JPH, et al. (2005) U-SPECT-I: A Novel System for Submillimeter-Resolution Tomography with Radiolabeled Molecules in Mice. J Nucl Med 46:1194–1200.
12. Hwang AB, Taylor CC, VanBrocklin HF, Dae MW, Hasegawa BH (2006) Attenuation correction of small animal SPECT images acquired with¹²⁵I-iodorotenone. IEEE Trans Nucl Sci 53:1213–20.
13. Li J, Jaszczak RJ, Coleman RE (1995) Quantitative small field-of-view pinhole SPECT imaging: initial evaluation. 1994 Nuclear Science Symposium and Medical Imaging Conference, NSS/MIC. Norfolk, VA, 30 Oct.-5 Nov., pp.
14. Acton PD, Kushner SA, Kung MP, Mozley PD, Plossl K, Kung HF (1999) Simplified reference region model for the kinetic analysis of [99mTc]TRODAT-1 binding to dopamine transporters in nonhuman primates using single-photon emission tomography. Eur J Nucl Med 26: 518–26.
15. Tuy HK (1983) An Inversion-Formula for Cone-Beam Reconstruction. Siam J Appl Math 43:546–552.
16. Metzler SD, Bowsher JE, Jaszczak RJ (2003) Geometrical similarities of the Orlov and Tuy sampling criteria and a numerical algorithm for assessing sampling completeness. IEEE Trans Nucl Sci 50:1550–5.
17. Acton PD, Hou C, Kung MP, Plossl K, Keeney CL, Kung HF (2002) Occupancy of dopamine D2 receptors in the mouse brain measured using ultra-high-resolution single-photon emission tomography and [123]IBF. Eur J Nucl Med Molec Imaging 29:1507–15.
18. Habraken JBA, de Bruin K, Shehata M, Booij J, Bennink R, van Eck Smit BLF, et al. (2001) Evaluation of High-Resolution Pinhole SPECT Using a Small Rotating Animal. J Nucl Med 42:1863–1869.
19. Goertzen AL, Jones DW, Seidel J, King Li AKL, Green MVAGMV (2005) First results from the high-resolution mouseSPECT annular scintillation camera. IEEE Trans Med Imaging 24:863–867.
20. Shannon CE (1949) Communication in the presence of noise. Proc IRE 37:10–21.
21. Rosenthal MS, Cullom J, Hawkins W, Moore SC, Tsui BMW, Yester M (1995) Quantitative SPECT Imaging: A Review and Recommendations by the Focus Committee of the Society of Nuclear Medicine Computer and Instrumentation Council. J Nucl Med 36:1489–1513.
22. Hutton B (1996) Angular Sampling Necessary for Clinical SPECT. J Nucl Med 37:1915–1916.
23. Jaszczak RJ, Li J, Wang H, Zalutsky MR, Coleman RE (1994) Pinhole collimation for ultra-high-resolution, small-field-of-view SPECT. Phys Med Biol 39:425–437.
24. Anger HO (1958) Scintillation Camera. Rev Sci Instrum 29:27–33.
25. Weber DA, Ivanovic M, Franceschi D, Strand SE, Erlandsson K, Franceschi M, et al. (1994) Pinhole SPECT: An approach to in vivo high resolution SPECT imaging in small laboratory animals. J Nucl Med 35:342–348.
26. Barrett HH, Hunter WCJ (2005) Detectors for small-animal SPECT I. Overview of Technologies. In: Kupinski MA, Barrett HH, eds. *Small animal SPECT imaging*. New York: Springer, pp.
27. Schramm N, Wirrwar A, Sonnenberg F, Halling H (2000) Compact high resolution detector for small animal SPECT. IEEE Trans Nucl Sci 47:1163–1167.
28. Meikle SR, Kench P, Weisenberger AG, Wojcik R, Smith MF, Majewski S, et al. (2002) A prototype coded aperture detector for small animal SPECT. IEEE Trans Nucl Sci 49:2167–71.
29. Wirrwar A, Schramm N, Halling H, Muller-Gartner HW (2000) The optimal crystal geometry for small-field-of-view gamma cameras: arrays or disks? Nuclear Science Symposium Conference Record, 2000 IEEE, vol. 3, pp. 21/91-21/93 vol.3.
30. Wirrwar A, Schramm N, Vosberg H, Muller-Gartner HW (1999) Influence of crystal geometry and wall reflectivity on scintillation photon yield and energy resolution. Nuclear Science Symposium, 1999. Conference Record. 1999 IEEE, vol. 3, pp. 1443–1445 vol.3.

31. MacDonald LR, Patt BE, Iwanczyk JS, Tsui BMW, Wang Y, Frey EC, et al. (2001) Pinhole SPECT of mice using the LumaGEM gamma camera. IEEE Trans Nucl Sci 48:830–836.
32. Stevenson G (2005) The animal in animal imaging. In: Kupinski MA, Barrett HH, eds. *Small Animal SPECT Imaging*. New York: Springer, pp 87–100.
33. Meikle SR, Kench P, Wojcik R, Smith MF, Weisenberger AG, Majewski S, et al. (2003) Performance evaluation of a multipinhole small animal SPECT system Nuclear Science Symposium Conference Record, IEEE. Volume 3, 19–25 Oct. 2003 Page(s):1988–1992, 19–25 Oct., vol. 3, pp. 1988–1992.
34. Zimmerman RE, Moore SC, Mahmood A (2004) Performance of a triple-detector, multiple-pinhole SPECT system with iodine and indium isotopes. Nuclear Science Symposium Conference Record, 2004 IEEE, vol. 4, pp. 2427–2429.
35. Forrer F, Valkema R, Bernard B, Schramm N, Hoppin J, Rolleman E, et al. (2006) In vivo radionuclide uptake quantification using a multi-pinhole SPECT system to predict renal function in small animals. Eur J Nucl Med Molec Imaging 33:1214–1217.
36. Ishizu K, Mukai T, Yonekura Y, Pagani M, Fujita T, Magata Y, et al. (1995) Ultra-high resolution SPECT system using four pinhole collimators for small animal studies.[see comment]. J Nucl Med 36:2282–7.
37. Metzler SD, Jaszczak RJ, Patil NH, Vemulapalli S, Akabani G, Chin BB (2005) Molecular imaging of small animals with a triple-head SPECT system using pinhole collimation. IEEE Trans Med Imaging 24:853–862.
38. Furenlid LR, Wilson DW, Yi-chun C, Hyunki K, Pietraski PJ, Crawford MJ, et al. (2004) FastSPECT II: a second-generation high-resolution dynamic SPECT imager. IEEE Trans Nucl Sci 51:631–5.
39. Izaguirre EW, Mingshan S, Vandehei T, Despres P, Yong H, Funk T, et al. (2006) Evaluation of a Large Pixellated Cadmium Zinc Telluride Detector for Small Animal Radionuclide Imaging. Nuclear Science Symposium Conference Record, 2006. IEEE 6:3817–3820.
40. Seo HK, Choi Y, Kim JH, Im KC, Woo SK, Choe YS, et al. (2000) Performance evaluation of the plate and array types of NaI(Tl), CsI(Tl) and CsI(Na) for small gamma camera using PSPMT. Nuclear Science Symposium Conference Record, 2000 IEEE, vol. 3, pp. 21/94-21/97 vol.3.
41. Zeng GL (2008) A skew-slit collimator for small-animal SPECT. J Nucl Med Technol 36:207–12.
42. Tenney CR (2000) Gold pinhole collimators for ultra-high resolution Tc-99m small volume SPECT. IEEE Nuclear Science Symposium., Piscataway, NJ, USA., vol. 3, pp. 22/44-6.
43. Tenney CR, Tornai MP, Smith MF, Turkington TG, Jaszczak RJ (2001) Uranium pinhole collimators for 511-keV photon SPECT imaging of small volumes. IEEE Trans Nucl Sci 48:1483–9.
44. Tenney CR (2004) Pinhole edge penetration and scatter in small-animal energy-integrating pinhole emission computed tomography. 2003 IEEE Nuclear Science Symposium. Conference Record. Portland, OR, 19–25 Oct., pp.
45. Kench PL, Lin J, Gregoire MC, Meikle SR (2011) An investigation of inconsistent projections and artefacts in multi-pinhole SPECT with axially aligned pinholes. Phys Med Biol 56:7487–7503.
46. Rentmeester MCM, Have Fvd, Beekman FJ (2007) Optimizing multi-pinhole SPECT geometries using an analytical model. Phys Med Biol 52:2567–2581.
47. Vunckx K, Bequé D, Defrise M, Nuyts J (2008) Single and multipinhole collimator design evaluation method for small animal SPECT. IEEE Trans Med Imaging 27:36–46.
48. Metzler SD, Accorsi R, Novak JR, Ayan AS, Jaszczak RJ (2006) On-Axis Sensitivity and Resolution of a Slit-Slat Collimator. J Nucl Med 47:1884–1890.
49. Wernick MN, Aarsvold JN (2004) *Emission Tomography. The Fundamentals of PET and SPECT*. San Diego: Elsevier Academic Press.
50. Bracewell RN (1956) Strip integration in radio astronomy. Aust J Phys 9:198–217.
51. Ramachandran GN, Lakshminarayanan AV (1971) Three-dimensional reconstruction from radiographs and electron micrographs: Application of convolutions instead of Fourier transforms. Proc Nat Acad Sci 68:2236–2240.

52. Radon J (1917) Über die Bestimmung von Funktionen durch ihre Integralwerte längs gewisser Mannigfaltigkeiten. Berichte Sächsische Akademie der Wissenschaften, Leipzig. Mathematisch - Physikalische Klasse 69:262–277.
53. Madsen MT (2007) Recent advances in SPECT imaging. J Nucl Med 48:661–673.
54. Cherry SR, Sorenson JA, Phelps ME (2003) *Physics in Nuclear Medicine*, 3 ed. Philadelphia: Saunders.
55. Shepp LA, Vardi Y (1982) Maximum likelihood reconstruction for emission tomography. IEEE Trans Med Imaging MI-1:113–22.
56. Lange K, Carson R (1984) EM reconstruction algorithms for emission and transmission tomography. J Comput Assist Tomogr 8:306–16.
57. Nuyts J, Fessler JA (2003) A penalized-likelihood image reconstruction method for emission tomography, compared to postsmoothed maximum-likelihood with matched spatial resolution. IEEE Trans Med Imaging 22:1042–1052.
58. Hudson HM, Larkin RS (1994) Accelerated image reconstruction using ordered subsets of projection data. IEEE Trans Med Imaging 13:601–609.
59. Gordon R, Bender R, Herman GT (1970) Algebraic reconstruction techniques (ART) for three-dimensional electron microscopy and x-ray photography. J Theoret Biol 29:471–481.
60. Townsend DW, Cherry SR (2001) Combining anatomy and function: the path to true image fusion. Eur Radiol 11:1968–1974.

Chapter 5
Design Considerations for Small Animal PET Scanners

Virginia Ch. Spanoudaki and Craig S. Levin

1 Introduction

Positron emission tomography (PET) is an established imaging technique currently used for the clinical management of disease in oncology, cardiology and neurology [1–3]. PET is nowadays integrated in the clinical routine and is acknowledged as a sensitive molecular imaging method. In addition to clinical applications, PET is also an active research tool in preclinical imaging with somewhat different applications. In order to highlight the specific goals of preclinical the following sub-sections will outline the differences between clinical and preclinical PET imaging in terms of applications and system performance requirements. Following that, this chapter will cover in more detail basic design considerations of preclinical PET scanners.

1.1 Applications

Preclinical PET plays a key role in the evaluation of new pharmaceuticals as well as in the assessment of the biological origin of various human diseases through imaging of appropriate animal models. Typically rodents (mice and rats) are used as

V.Ch. Spanoudaki
Department of Radiology, Molecular Imaging Program at Stanford (MIPS), Massachusetts Institute of Technology, Massachusetts, CA, USA
e-mail: vspan@mit.edu

C.S. Levin (✉)
Departments of Radiology, and by courtesy, Physics, Electrical Engineering, and Bioengineering; Molecular Imaging Instrumentation Laboratory (MIIL); Stanford Molecular Imaging Scholars (SMIS) Program; Stanford Center for Innovation in In-Vivo Imaging (SCI3); Molecular Imaging Program at Stanford (MIPS); Division of Nuclear Medicine, Stanford University School of Medicine, Stanford, CA, USA
e-mail: cslevin@stanford.edu

H. Zaidi (ed.), *Molecular Imaging of Small Animals: Instrumentation and Applications*,
DOI 10.1007/978-1-4939-0894-3_5,

such models due to their genetic similarity to humans [4, 5]; however primate imaging, typically monkeys, as well as imaging of other mammalians such as swine has also been reported [6, 7].

PET allows for non-invasive, in-vivo imaging of biological processes, thus each animal may be used for several different studies or the same study may be performed in the same animal over several days. In this way the experimental accuracy is improved and the number of sacrificed animals is reduced significantly resulting in a corresponding cost reduction of each study.

1.2 General Performance Requirements

Compared to clinical PET imaging the regions of interest under investigation in preclinical imaging are several orders of magnitude smaller. For that reason, the required spatial resolution of preclinical systems is accordingly higher. In addition, the specific activity (activity per unit mass) that may be administered to the animal is restricted due to limitations in the delivered dose. Proper detection of the limited amounts of activity requires high photon sensitivity of the imaging system, in order to be able to visualize and quantify as accurately as possible small amounts of radiotracer concentrations.

An ideal preclinical PET system should have the following characteristics:

- It should have *sub-millimeter spatial resolution* which should be uniform throughout the field of view. Thus the system should be able to detect lesions of all sizes with the same accuracy.
- Due to the limited amount of radioactivity administered to the animal, the ideal system should be able to detect a large fraction (optimally larger than 10 %) of the occurred annihilation events (*high photon sensitivity*), namely it should provide sufficient geometric coverage of the imaged animal and in addition it should absorb efficiently the energy of the emitted photons.
- If the system employs multiple small detector elements for improved spatial resolution, there should be an accurate correction for *non-uniformities* in the aforementioned photon efficiency among the various detector elements.
- It should be able to distinguish photons of different energies (*high energy resolution*, optimally smaller than 10 %) and precisely detect each annihilation photon's arrival time (*high time resolution*, optimally smaller than 1 ns).
- The system should respond linearly to a large range of photon emission rates with a *live-time* fraction of more than 95 %.
- The *system design* should allow for accurate readout of a large number of detector elements in a *cost effective* way.

These requirements pose a number of hardware design challenges which will be addressed in more detail in the following sections.

2 Specific Performance Requirements

2.1 Spatial Resolution and Partial Volume Effect

As mentioned above (Sect. 1.2) a spatial resolution below 1 mm is desired. For the majority of current system designs this is a rather difficult goal to achieve given the impractical small sizes of the detector elements required in combination with other blurring factors discussed in this section. The spatial resolution of an imaging system is a quantitative measure of the system's ability to localize a structure. It is defined as the minimum detectable size of a focal point of tracer accumulation or, otherwise stated, the minimum distance between two foci such that they can still be distinguished from each other (Fig. 5.1). Typical spatial resolutions (for a point source in the center with high statistics) of preclinical systems lie in the range between 1.5 and 2 mm, significantly smaller compared to the 4–8 mm resolution limits in clinical imaging [8–10] (where low statistics necessitate image smoothing), however recent advances in detector designs have led to sub-millimeter resolutions [11–13].

For systems based on discrete scintillation crystal elements read out by photodetectors, the intrinsic limit in spatial resolution is determined by the crystal element width. For systems based on alternative detector technologies, such as gas or semiconductor detectors, spatial resolution is determined by the pitch of the readout electrode wires, strips or pads.

The nature of positron annihilation poses some additional limitations to spatial resolution which are rather difficult to be addressed by technical approaches. The first is the positron range, namely the finite distance that the positron traverses inside a subject prior to its annihilation. This distance depends on the positron maximum energy E_{max} as well as on the tissue in which the positron migrates. The larger E_{max} is, the larger the positron range variance within a specific tissue thus causing degradation of the spatial resolution. Studies have shown that for the widely used ^{18}F positron emitter ($E_{max} = 635$ keV), the positron range in water has a distribution with 0.1 mm full width at half maximum (FWHM), which is well below the current spatial resolution limits of both clinical and preclinical PET [14].

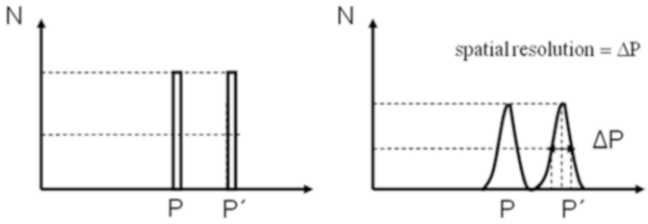

Fig. 5.1 Illustration of the concept of spatial resolution: the ideal intensity profiles of two neighboring point sources (*left*) appear in reality smoother (*right*) due to the imaging system's spatial resolution. The latter is defined as the FWHM of the resulting intensity profile. If two adjacent profiles are separated by a distance greater than ΔP, the point sources will be resolved

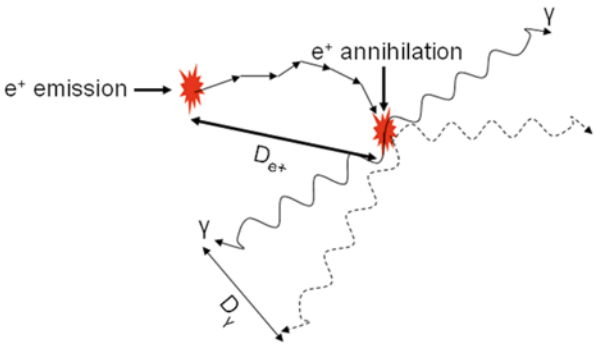

Fig. 5.2 Effect of positron range and photon acolinearity on spatial resolution of PET. Their variations contribute to spatial resolution blurring. The respective spatial blurring components D_{e+} and D_γ contribute in quadrature to the achievable spatial resolution

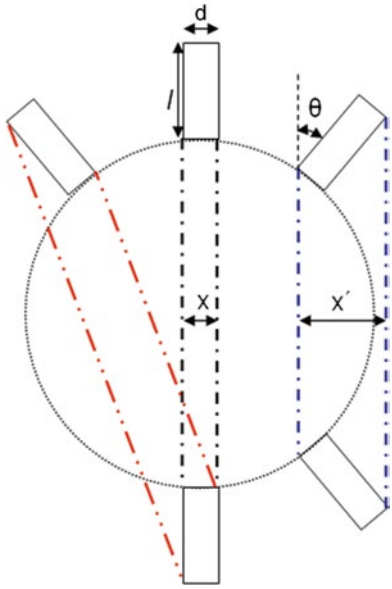

Fig. 5.3 Illustration of the parallax effect for lines of response (LoRs) with different obliqueness. For a non-oblique detector pair the depth of interaction of the 511 keV photons along the detector length *l* does not affect the width *x* of the ToR (*black dashed lines*). For oblique detector pairs the ToR width *x′* broadens (*red* or *blue dashed lines*) depending on the crystal element length (*l*) and element size (*d*) as well as on the detector obliqueness θ and the angle of photon incidence

During annihilation of a positron with an electron there is the possibility that the two produced annihilation photons are emitted at an angle with respect to each other which slightly deviates from 180° due to residual positron or electron momentum. This photon acolinearity produces a spatial deviation that increases linearly with the tomograph's diameter and thus is more prominent in clinical PET [14, 15]. As in positron range, it is the variance in this deviation that further degrades spatial resolution. Both the effects of positron range and photon acolinearity are illustrated in Fig. 5.2.

The length of the crystal element also affects the spatial resolution of a PET system, especially for small fields of view (FoV), such as in preclinical PET. The so called parallax error, namely the non-uniformity of spatial resolution throughout the FoV is illustrated in Fig. 5.3. The finite crystal element length and the penetration of the 511 keV photons in the crystal volume, translate to an uncertainty of where

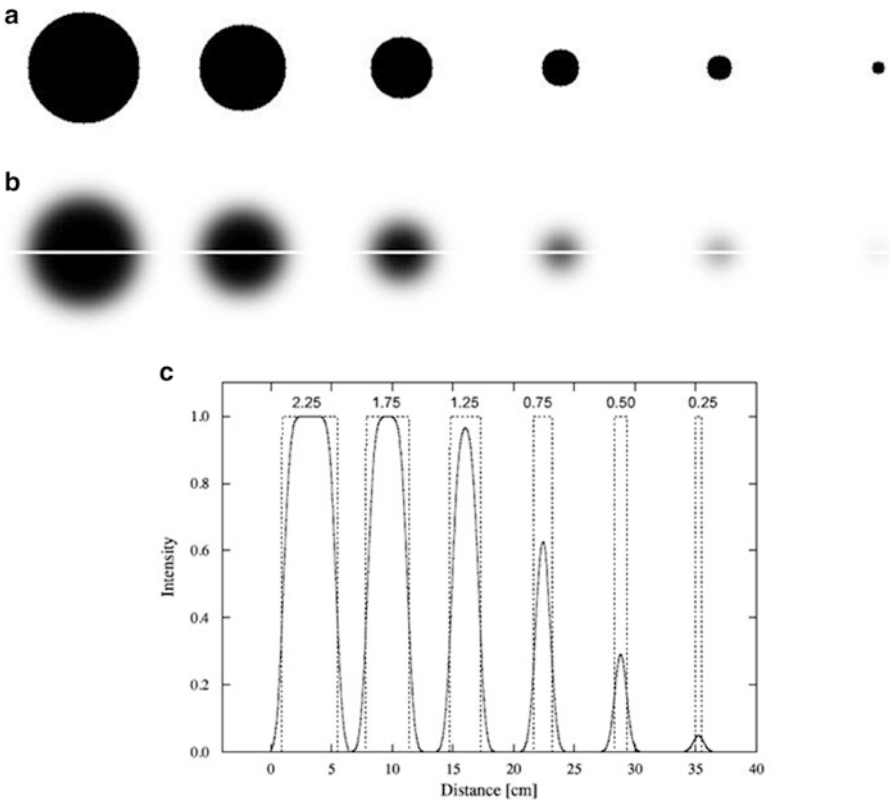

Fig. 5.4 Illustration of the partial volume effect. (**a**) Simulated spheres of different sizes and the same activity concentration. (**b**) Reconstructed images of the spheres imaged by a 10 mm resolution system. (**c**) Position profiles of the images shown in (**b**) indicating that the activity concentration appears to be smaller for smaller objects. Reproduced from [16] with permission

within the width of the response tube (ToR) defined by a detector element pair the positron annihilation took place.

A side effect of the limited spatial resolution in PET is the so called partial volume effect (PVE), illustrated in Fig. 5.4. PVE is the underestimation of the radioactivity concentration in a region of interest (RoI) in the reconstructed image if this RoI is smaller than the spatial resolution of the system. PVE effects can also lead to overestimation of the radioactivity concentration depending on the background surrounding the RoI [16].

2.2 Photon Sensitivity

Photon sensitivity of a PET system is the ratio of the detected coincident photon pair event rate (measured in counts per second or cps) to the emitted radioactivity from the object to be imaged (measured in Ci or Bq). However it is common to quote

absolute photon sensitivity as the percentage (%) of emitted coincident photons that are detected. The ideal photon sensitivity limit (>10 %) mentioned in Sect. 1.2 still deviates significantly from the typically achieved values given the limited solid angle coverage as well as the inherently limited detector intrinsic photon detection efficiency.

In general, radiation detection is a process dominated by Poisson statistics and therefore, in the case of PET imaging, it will inevitably result in fluctuations in photon sensitivity. Because in Poisson statistics any fluctuation or variance is directly associated with the mean value, the photon sensitivity fluctuations in a PET system are associated with the mean detected number of coincident events. A general rule is that the relative fluctuations on the mean detected number of radiation events over this mean value is inversely proportional to the square root of this mean. Thus it is desirable that photon detection systems have high photon sensitivity (high mean detected number of photon events) in order to minimize statistical variations. Typical photon sensitivities of preclinical systems lie in the range between 1 and 7 % and are significantly larger than the typical values of clinical systems due to the smaller system diameter and thus the larger solid angle coverage of the imaged object. This fact allows the use of small detector elements in preclinical imaging while maintaining an adequate number of detected counts per element.

One of the most important factors which affect the photon sensitivity of a system is the crystal material. The effective atomic number Z and the density ρ of the material define its photon stopping power and thus the intrinsic detector efficiency. High Z and high ρ values are desired for enhanced possibility of absorption of the emitted annihilation photons in the detector material. In addition, the obliqueness of a detector with respect to the incident radiation as well as the inevitable dead space between detectors affects the intrinsic efficiency. Additional to the intrinsic efficiency, the geometric efficiency of the PET system plays a large role to the overall photon sensitivity. Systems with detectors placed as close as possible to the object to be imaged (i.e. small ring diameter for cylindrical systems) and with a radial/axial extent are typically designed in order to enhance the overall photon sensitivity.

The actual sensitivity of a PET system will be further degraded by the fact that not all registered coincident events are actually the ones we want; depending on the energy and time resolution of the system, which will be explained in more detail in Sects. 2.3 and 2.4, true coincidences will be contaminated by background scattered and accidental coincident photon events. The former coincidence type originates from scatter of one or both of the annihilation photons within the imaged object thus resulting in detection of the two photons from a different detector pair. In order to avoid such localization errors, scattered coincidences are rejected by setting a proper threshold in the recorded photon energies. The latter coincidence type is a false coincidence between two photons that originate from two independent positron annihilations which happen to occur within the same time window. Accidental coincidences may be rejected by setting a proper time coincidence window. The different types of coincident events (true, random and scattered coincidences) are outlined in Fig. 5.5.

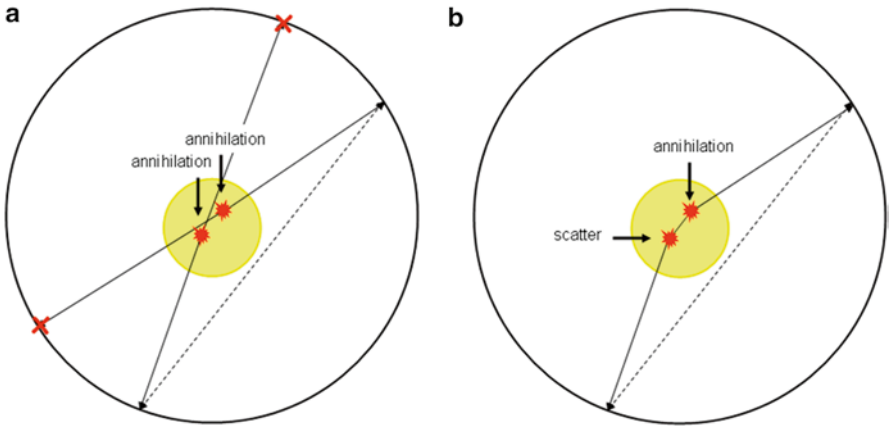

Fig. 5.5 (**a**) Random coincidences: two photon events registered within the same time window may result in the assignment of a LoR (*dashed line*) even though the two events originate from independent annihilations. (**b**) Scatter coincidences: the scatter of one or both annihilation photons may result in localization errors by assigning a LoR to a different detector pair than the expected one (*dashed line*)

Two-dimensional (2D) acquisition mode was performed by the early clinical PET systems in order to reduce the number of registered random or scattered coincidences. In this mode, only coincidences between detectors belonging to the same detector element ring (direct plane coincidences) or to the immediate neighboring rings (cross-plane coincidences) are registered. Thus the number of scattered or random coincidences is decreased significantly, however so is the good or "true" photon sensitivity. Modern PET systems adopt the three-dimensional (3D) acquisition mode in which coincidences between all detector pairs (belonging to any detector element ring) are registered. This acquisition mode greatly enhances the system's photon sensitivity; however accurate corrections for scattered and random coincidences are necessary.

A PET system comprises of many individual detectors and thus variations in photon detection efficiency among the various detectors may be observed. Even though minor differences in the intrinsic detection efficiency are possible from crystal to crystal, the vast majority of variations may be observed either due to their position in the PET system or due to intrinsic detector gain variations.

2.3 Energy Resolution

The accuracy at which a PET system responds to a specific amount of photon energy absorbed by its detectors defines its energy resolution. One of the requirements, outlined in Sect. 1.2, for an ideal preclinical PET system was an energy resolution of less than 10 %. Especially for standard system designs based on scintillation

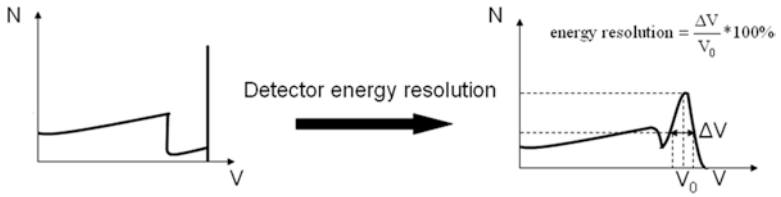

Fig. 5.6 Illustration of the concept of energy resolution: an ideal histogram of the deposited energies in the detector (including both Compton scatter and photoelectric absorption) is shown on the *left drawing*. The detector response on the absorbed 511 keV photon energy (photopeak) is a "delta function". The limited energy resolution of the detector results in a histogram similar to the one shown on the *right drawing*. The photopeak follows approximately a Gaussian distribution

crystal readout by photodetectors the relatively low conversion efficiency of the incident photon energy to electric charge results in energy resolution degradation, so that typical energy resolutions for these designs lie between 15 and 25 %. In PET the energy of interest is 511 keV, namely the energy of each of the two anti-parallel annihilation photons per event, thus resolution is typically defined with respect to this energy.

For a detector with ideal (infinitively precise) energy resolution, a histogram of the PET system's response to the absorbed 511 keV energy (in form of collected detector charge or detector pulse height) would be a "spike" at a single energy (such "spikes" are mathematically described by the so-called delta function). However for a detector with non-ideal energy resolution, the 511 keV line will appear to have a Gaussian distribution with a FWHM of, typically, several tens of keV about the 511 keV value (Fig. 5.6).

In a PET system employing many detectors, differences in the energy resolution values characterizing each individual detector may be observed. These differences are most commonly attributed to gain and noise variations between the photodetectors and if not properly identified and corrected for, they may hinder the system's ability to represent in a quantitative way the true radiotracer concentration.

Energy information requires a high level of accuracy in order to properly distinguish scattered from unscattered events. The former will deposit only part of their energy in the detector while the latter will fully deposit their energy. The worse (higher value) the energy resolution the more difficult it is to distinguish scatter from photopeak events. Scattered events lead to localization errors as outlined in Fig. 5.5b and subsequently to a uniform background in the reconstructed image thus affecting image contrast, signal to noise ratio (SNR) and quantitative accuracy.

The annihilation photons may scatter both in the object to be imaged as well as in the crystal material itself. Although scatter in small animals is less than in humans due to the smaller object volume within the FoV, the effect is still significant [17]. Crystal scatter is apparent in both clinical and especially preclinical PET since the crystal elements are smaller. As previously mentioned, given adequate energy resolution, the effects of object scatter, which effectively lead to mispositioning of annihilation events, is reduced. However, scatter in the crystal may still be exploited to

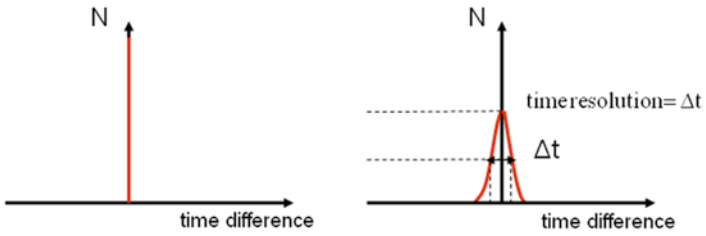

Fig. 5.7 Illustration of the concept of time resolution: Ideally the time difference between two photon detection events that occurred simultaneously would be zero, thus a histogram of the time differences over many simultaneous events would be a delta function centered around zero (*left*). Due to the system's limited time resolution the histogram appears to be smooth following a Gaussian distribution (*right*)

identify annihilation events provided that the position of the first interaction can be determined. Detector designs based on individual readout of finite crystal elements have the ability of identification of crystal scatter [18, 19].

2.4 Time Resolution

PET imaging is based on coincident photon detection and thus photon arrival time information needs to be extracted as accurately as possible. In counting systems whose detection principle is based on the measured time difference between detector signals, such as PET systems, the precision to which this time difference is determined is of utmost importance. This precision is directly related to the PET detector's time (or temporal) resolution which is defined as the uncertainty to which the arrival time of an event is estimated by the detector system (Fig. 5.7). Recent advances in improving the response speed of scintillators and photodetectors have made the desired time resolution limits mentioned in Sect. 1.2 feasible.

Typically, time information about the occurrence of an event is extracted from the produced detector voltage signal $V(t)$. The time resolution is then described by the following formula:

$$\sigma_t = \sqrt{\left(\frac{\sigma_V}{\frac{dV}{dt}}\right)^2 + \sigma_{TTS}^2} \tag{5.1}$$

where σ_V is the signal root-mean-square (RMS) noise, $\frac{dV}{dt}$ is the signal slope at the point of time pick-off and σ_{TTS} is the transit time variance of the optical photons within the scintillation crystal and the electric charge within the photodetector. As it can be seen from the above formula, the time resolution of a single PET detector depends on a number of parameters:

– The light output, the decay time and the geometry of the scintillator. A scintillator with high optical photon rate (eventually translated as $\frac{dV}{dt}$ in the detector output) will reduce the effect of statistical variations (on the amount of light contributing to σ_V in the detector output) in the determination of the arrival time and will allow timing pick-off at early stages of scintillation photon production. The crystal geometry, and more specifically the crystal aspect ratio (width-to-length ratio), is also an important factor. A crystal with high aspect ratio will minimize the variation in distance between the point of optical photon production and the point of optical photon detection. Thus with short crystal elements photon losses at the crystal interfaces (affecting V) and flight time variations (as reflected by σ_{TTS}) are minimized.
– The noise (represented by σ_V), gain (represented by V) and transit time spread (represented by σ_{TTS}) of the photodetector or any other means used to detect the annihilation photons, such as gas or semiconductor crystals.

As already outlined in the previous section for the case of energy resolution, in a complete PET system, which employs several (hundreds to thousands) detector and electronic channels, the overall system time resolution will be affected by the individual detector time resolutions and indeed might be broadened due to inherent temporal shifts between detectors. Proper correction of these temporal variations through a procedure known as time calibration will minimize the system time resolution for coincidence detection from all possible detector pairs in the system.

In PET imaging it is essential that time resolution is kept as low as possible in order to minimize contamination of true coincident photon events from accidental (random) coincidences. The latter typically add a uniform background in the PET reconstructed image thus reducing image contrast, SNR and quantitative accuracy. From theory, the number of random coincidences increases proportionally to the time coincidence window and to the product of event flux seen by each detector in a coincident detector pair. Thus, minimization of random events requires that the time coincidence window selected for coincidence detection be as low as possible and the activity is as low as possible.

In addition to controlling the accidental coincidence rate, the time resolution poses a lower limit in the minimum temporal difference between two subsequent coincident photon events in order for the detector to identify them as distinct. However this minimum time difference between events is further degraded by the detector recovery time as well as by the dead time of the subsequent electronics, as will be explained in more detail in Sect. 3.4.

Detectors that demonstrate sub-nanosecond time resolution are currently used in clinical imaging in order to exploit the actual time of flight (ToF) information of the two annihilation photons and improve the SNR of the reconstructed image. The benefits of ToF are more obvious for large sized patients however the current time resolution limitations of PET detectors limit the applicability of ToF methodology to clinical PET only.

Table 5.1 summarizes the aforementioned performance requirements and compares their significance for clinical and preclinical PET.

Table 5.1 Summary of the performance parameters in PET imaging and significance in clinical and preclinical PET

Feature	Clinical PET	Preclinical PET
Spatial resolution	4–8 mm	1–2 mm
Effect of time resolution (randoms/count rate)	Significant	Not as significant (depends on application)
Effect of energy resolution (scatter)	Significant	Not as significant
Photon sensitivity	$O(10^{-2})$	$O(10^{-2})$
Effect of DoI	For points close to detectors	Significant
Effect of ToF	In image SNR	Currently none

3 Detector Designs

3.1 Materials

The fundamental components of PET detectors have been reviewed in detail in previous chapters of this book. In the following sections, we will summarize the various detector configurations employed in PET scanners, we will outline their advantages and disadvantages and emphasize the significance of their special features in preclinical PET imaging.

3.1.1 Scintillation Crystal–Photodetector

The large majority of PET systems consist of detectors whose basic components are a scintillation crystal coupled to a photodetector. This detector configuration provides an indirect means of detection of 511 keV photons through the two-step process of conversion to scintillation light via a scintillation crystal and a subsequent conversion to electric charge via a photodetector. Through this multi-step process inevitable signal losses and additional statistical variations and dispersions are introduced. Nevertheless, to date a scintillator/photodetector configuration is the standard choice in the design of PET systems [15].

As described, scintillators with high effective atomic number (Z), density (ρ), light output and short decay time are preferred for optimum PET performance in terms of time/energy resolution and photon sensitivity. A major breakthrough in PET detector technology has been enabled with the invention of fast inorganic scintillators such as lutetium oxyorthosilicate (LSO) which demonstrates a good compromise between high light output and fast timing. However, its natural radioactivity may pose a number of design issues which nevertheless are addressed without implying significant design limitations [20, 21].

Photomultiplier tubes (PMTs) have mostly been used as the preferred photodetectors due to their excellent performance features (see Chap. 3). However, their relatively large sizes result in large dead spaces and thus poor packing fraction. This has motivated the development of specialized detector designs where the readout of

the scintillation light by the PMT is interfaced by means of a light guide [22]. In this way, good crystal packing fraction is guaranteed independent of the gaps between photodetectors. This is of particular importance in the case of preclinical scanners where the available space is limited by the small system diameters. A new generation of preclinical PET systems is based upon Avalanche Photodiodes (APDs) due to their availability in small sizes and compact arrays allowing thus for direct interfacing between the miniscule scintillator elements and the photodetector. An additional advantage of APDs over PMTs is that the former are able to operate reliably under the presence of magnetic fields which makes them appropriate for simultaneous PET/MRI, as will be emphasized in Chap. 15.

3.1.2 Gas Filled Detectors

In order to overcome the inevitable signal losses of the aforementioned indirect scintillation detection methods, researchers have looked into alternative detection techniques. The architecture of multiwire proportional counters (MWPCs) used in high energy physics experiments have been implemented in the quad-HIDAC small animal PET scanner [11].

Lead honey-comb structures are used to convert the 511 keV photons into electrons. The charge subsequently migrates within a gas medium under the influence of an electric field and is detected by a network of anode electrodes. A major advantage of such systems is the high spatial resolution defined by the electrode pitch which however comes at the expense of energy information, poor time resolution and poor photon sensitivity.

3.1.3 Semiconductor Detectors

Another detector configuration employing direct conversion of 511 keV photons to charge are semiconductor detectors. Semiconductor detectors such as germanium (Ge) or cadmium telluride (CdT) can be highly efficient in 511 keV detection resulting in excellent energy resolution [23]. Currently there is increasing interest in the latter material for high resolution PET because it operates in room temperature and, similar to MWPCs, sub-millimeter intrinsic spatial resolutions may be achieved due to the fine pitch of the anode and/or cathode electrodes. The poor time resolution of these detectors is however still a limitation [10].

Figure 5.8 shows pictures of the three different PET detector types.

3.2 Readout Designs

Since the most common detector components are scintillation crystals with photodetector readout, our discussion in the following sub-sections will focus on readout configurations of designs based on those components.

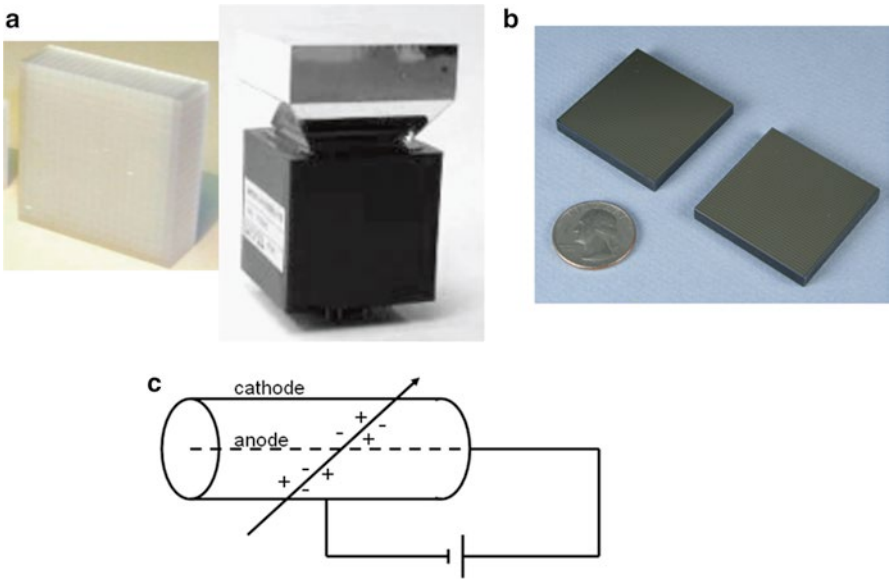

Fig. 5.8 Three different detector types currently used in preclinical PET systems: (**a**) *left*: 20×20 LSO crystal array (crystal element size 1.5×1.5×10 mm^3). *Right*: LSO crystal array, tapered light guide and PSPMT (courtesy of Robert Nutt, Siemens Preclinical Solutions). (**b**) Anode view of two CZT detectors (courtesy of Yi Gu, Stanford University). (**c**) Basic detection principle of gas-filled detectors

3.2.1 Block Detector Readout

The block detector design refers to the indirect readout of many crystal array elements by a fewer number of photodetectors based on scintillation light sharing. Three different block detector designs can be identified:

– Readout of a crystal slab by a number of photodetectors [15, 24]. The scintillation light produced by the interaction of a 511 keV photon with the crystal is shared among the various photodetectors and information about the position of interaction is extracted by the relative amplitudes of the different photodetector signals and is estimated using appropriate positioning algorithms. This design is based on the Anger gamma camera architecture and its advantage lies in the simplicity of its implementation [15].
– Readout of a crystal array by a coarse photodetector array [15]. In the same way as in the previous design the scintillation light produced in crystal array elements is shared among the various photodetectors and the position information is extracted by positioning algorithms. However, in this case the crystal elements are optically isolated using reflectors and the scintillation light is thus more focused and confined within the volume of one or two crystal elements. Thus light sharing among the photodetectors should be facilitated by means of an

additional optical medium, typically a light guide in between the crystal array and the photodetector.
– Alternative to photodetector arrays, position sensitive photodetectors, such as position sensitive photomultiplier tubes (PSPMTs) [25, 26] or position sensitive avalanche photodiodes (PSAPDs) may be used [27]. These photodetectors consist of a single photosensitive area (as opposed to the discrete elements in an array) whose produced charge is collected by multiple anodes or a resistive charge multiplexing network connecting the anodes. This network will yield a number of signals (typically four) which are subsequently used in conjunction with positioning algorithms for interaction localization. This design, which is apparent in most clinical and preclinical PET systems, offers the advantage of significant reduction of the readout channels while using a large number of small scintillation crystal elements for improved spatial resolution.

Some disadvantages of the block detector readout scheme are the dependence of position localization accuracy, and consequently of spatial resolution, on the algorithm used and on the effectiveness of the light sharing with respect to electronic SNR. Additionally, in cases of high counting rates, block detectors are sensitive to pulse pile up effects as will be explained in Sect. 3.4.2. Finally, this design cannot differentiate between object scatter and scatter in the crystal. The latter is an effect that is especially important in preclinical PET systems since the crystal elements are small and scatter in small animal tissues is less likely than in patients.

3.2.2 Individual Crystal Readout

A limited number of PET scanners have adopted the individual crystal readout scheme where the crystal elements are coupled one-to-one to the photodetectors [28]. This readout scheme overcomes the positioning limitations of block detectors because the detector intrinsic spatial resolution is determined by the scintillation crystal element size. Unlike block detectors, in this detector design intercrystal scatter mentioned in Sect. 2.3 can be identified. In addition, detectors with individual crystal readout are capable of higher count rates (less pulse pile up) compared to block detectors given the fact that each photodetector reads a single scintillation crystal element. However the aforementioned advantages come at the expense of increased number of detector and electronic channels which further implies increased costs as well as construction and signal processing complexity.

Figure 5.9 depicts the various aforementioned detector designs. The PET detectors are typically arranged in ring geometry to allow acquisition from different angular views (Fig. 5.10a). However initial alternative PET system architectures suggest arrangement of the PET detectors in partial ring geometry (Fig. 5.10b) [29]. Tomographic acquisition is performed by rotating the detectors around the animal. Partial ring geometries can be more cost effective although the overall duration of the PET scan can be significantly increased and rotational artifacts may be introduced. It is also possible to arrange detectors into other shapes, such as a box [30].

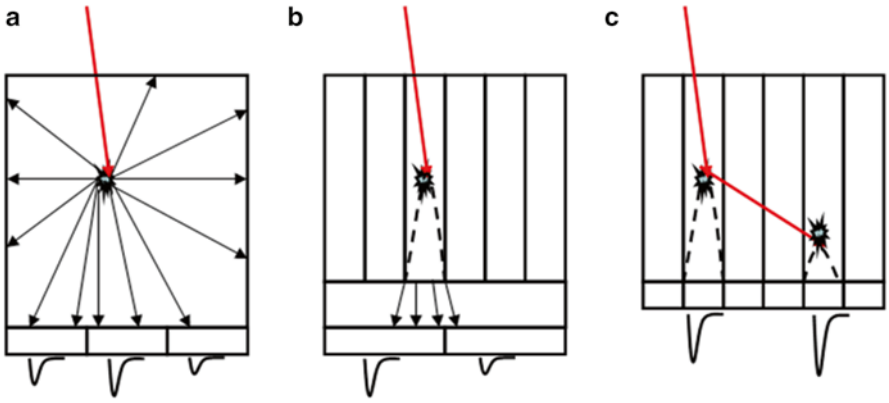

Fig. 5.9 (**a**) Block detector readout of a crystal slab, (**b**) block detector readout of a crystal array, (**c**) individual crystal readout

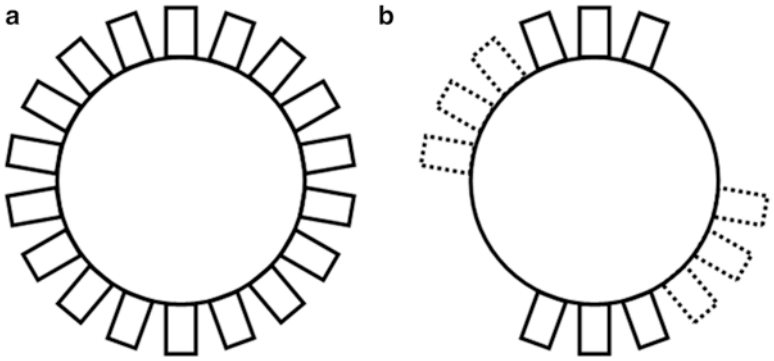

Fig. 5.10 PET system designs. (**a**) Full ring geometry, (**b**) partial ring geometry. The detectors marked with a *dashed line* indicate different rotation for tomographic acquisition

3.3 Special Design Features

The need for increased quantitative accuracy in preclinical PET has lead to the development of specific detector designs aimed to address a number of current limitations. In the following, the discussion will focus on design features which compensate for non uniform spatial resolution and motion artifacts.

3.3.1 Depth of Interaction

In PET scanners with small FoV, especially in preclinical tomographs, significant spatial resolution non-uniformity across the FoV may be observed depending on the radial extent (or length) of the scintillation crystal element used and the radial

position within the system. This effect is called the parallax error and is illustrated in Fig. 5.3. The exponential attenuation of the 511 keV photons in the scintillation crystal implies a statistical likelihood of the interaction along the crystal length with enhanced probability close to the photon's entrance point and exponentially decreasing probability with increasing distance from that point. Thus, in a crystal of finite length the exact interaction point is not known, but rather its likelihood results in an additional position blurring especially for oblique photon incidence that occurs for emission points away from the center [10].

As emphasized in Sect. 2.2, PET photon sensitivity is enhanced by the use of long (thick) crystals of high atomic number and density. Consequently, there is a trade-off between photon sensitivity and spatial resolution uniformity which is successfully addressed by a number of specialized detector designs described in the following:

– Dual ended crystal readout: A common DoI detector design employs crystal elements read out by two photodetectors on both sides [31]. In this way the depth of interaction of the annihilation photon inside the crystal is determined by the difference in the amount of light detected by the two photodetectors. An advantage of this method is the availability of continuous DoI information; however the light sharing between the two photodetectors may result in poor detector performance in terms of energy and/or timing resolution. Positioning nonlinearity near the two photodetectors is also apparent in this design. In addition, detailed detector calibration (particularly with respect to gain variability between the two photodetectors) is a prerequisite for extraction of reliable DoI information.
– Individual crystal readout: This detector design has been adopted as a straightforward method of acquiring quantized DoI information [32]. The design consists of two or more crystal layers each read out by individual photodetectors. The DoI resolution is determined by the dimension of the crystal layer along the radial direction and at the same time the detector performance is maintained due to the individual readout. However, the basic drawback of this design is the increasing number of electronic readout channels and thus the potential development costs. Alternatively, the crystal layers are read out collectively by position sensitive photodetectors [33, 34]. Such designs are more cost effective given the reduced number of readout channels compared to the number of crystal elements in the detectors, and they provide much better DoI resolution.
– Phoswich design: The phoswich detector comprises two different types of scintillation crystal materials read out by the same photodetector [35, 36]. Identification of the crystal of interaction (and thus DoI) is realized by pulse shape discrimination given the different decay time constants of the two scintillation crystal types. A major drawback of this detector design is the interdetector performance variability due to the different types of scintillation material used. This variability may especially hinder timing performance given the fact that one of the crystals should have a slower decay time compared to the other.
– Monolithic crystal design: More recently there have been detector designs based on a single monolithic crystal layer read out by either individual photodetectors

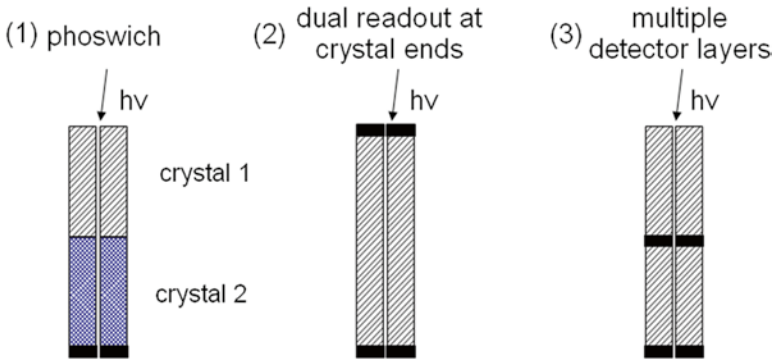

Fig. 5.11 Detector designs with DoI capabilities. (*1*) Phoswich, (*2*) dual ended crystal readout, (*3*) individual crystal readout of layered detectors

or position sensitive photodetectors employing a resistive network able to identify the scintillation light spread profile on the photodetector entrance surface [24, 37–39]. The light spread profile depends on the depth of interaction and several algorithms have been developed that associate the acquired profiles with DoI [38, 39]. Despite the detector simplicity implied by the use of a single monolithic crystal layer, the complexity of this design lies mostly in the photodetector readout scheme and the associated algorithms and calibrations. In addition this design is subject to the general spatial resolution limitations, especially near corners and edges, as are all designs employing continuous crystals.

The most common DoI detector designs are summarized in Fig. 5.11.

3.3.2 Motion Correction

Quantitative studies performed in PET require accurate calculation of the radiotracer distribution within a region of interest. The RoI is typically drawn based on the reconstructed image, thus its accuracy will directly depend on the quality and accuracy of the PET image.

Quantitative accuracy dictates that a number of corrections be performed post acquisition and during reconstruction. Apart from the rejection of scattered and random coincident events, as well as attenuation correction, localization errors may originate from inevitable movement of the imaged object such as respiration and cardiac motion. Especially in the case of preclinical imaging, the heart beat and respiration rates are significantly higher compared to humans (60–100 heartbeats/min and 15–20 respirations/min for humans vs. approximately 500 heartbeats/min and 160 respirations/min for mice). This fact, in combination with the higher spatial resolution of small animal systems makes the imaging system performance more sensitive to motion artifacts.

Several methods for motion correction have been developed from various groups [40–42]. Typically, for cardiac motion ECG sensors are used and respiratory motion is monitored via motion sensors placed near the abdominal area of the animal. List

mode data acquisition, namely acquisition of the energy and time of individual photon events in a list, is suitable for incorporating the motion sensors' signal into the data stream. The list mode data is then rearranged in groups belonging to the same stage of each cardiac/breathing cycle during the course of measurement in order to produce images free of motion artifacts.

3.4 Data Acquisition Electronics

The signals produced by the PET detectors are further processed by subsequent electronics in order to extract two types of information: Energy, as represented by the integrated pulse height, and time, as represented by the signal time stamp. The latter is essential in PET for determining coincident photon pairs from single photon events whereas the former is used to identify and remove scatter events that may degrade image quality and accuracy. Even though the first PET scanners based their acquisition chain in coincidence detection hardware modules, modern systems record single photon events and their corresponding energy and time information (list-mode data format) and coincidence detection is performed either in software post-acquisition or in field programmable gate array (FPGA) based hardware architectures during or post-acquisition. The basic issues that need to be addressed when designing data acquisition systems for PET are the number of electronic channels and the processing speed as reflected by the system's dead time.

Typically the current or charge produced by the photodetector is converted to a voltage signal with the use of preamplifiers. These preamplifiers provide a pulse in their output whose height is typically proportional to the photodetector charge which in turn is proportional to the scintillation crystal light and thus to the absorbed incident photon energy. Especially in the case of low gain detectors the preamplifier needs to be placed as close as possible to the detector in order to avoid signal attenuation. A charge sensitive preamplifier integrates the photodetector charge through a capacitor (C) and a resistive load (R) for a time window defined by the time constant $\tau = RC$. Typically, the R and C values are chosen in such a way so that the integration occurs for a time window at least three times larger compared to the scintillation decay time. The resulting pulse will have a rising edge following the photodetector response and a trailing edge dominated by the time constant τ.

Subsequent electronics are used to further shape the signal, mainly increasing SNR and restoring a faster return to the baseline. The shaped signal is used for the extraction of energy and time information by means of a peak detector circuit for the former and a time pick-off circuit for the latter. All the aforementioned steps of the electronic chain require a minimum processing time for each detector signal affecting thus the overall system dead time.

More recent data acquisition systems are based on sampling of the shaped signal and extracting energy and time information from the digitized samples based on various algorithms applied either in software or in FPGAs. This acquisition option leads to increased flexibility in the choice of processing algorithms, however it may result in increased cost and analysis complexity following acquisition.

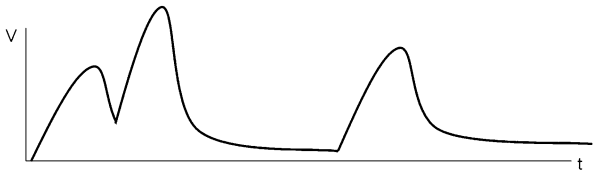

Fig. 5.12 Illustration of the signal pile up effect. The finite scintillator decay time dictates a signal charge integration time of typically at least two to three times the decay time, resulting in pulses with a relatively long trailing edge. In cases of high counting rates the possibility of detector pulses adding to the trailing edge of the preceding pulse increases, resulting in distorted pulse shapes

3.4.1 Signal Multiplexing

The need to reduce the number of electronic channels in the described detector designs (Sects. 3.2.1 and 3.2.2) has lead to the development of several channel reduction techniques at the front end readout electronics [43, 44]. For front-end channel reduction, signals from multiple photodetector channels are multiplexed either resistively or capacitively. Special care is given to the design of the multiplexing architectures so that the multiplexed signals carry accurate position information and at the same time lead to minimal degradation of energy and time resolution. Successful signal multiplexing schemes have lead to a four-fold or higher reduction on the number of electronic channels.

3.4.2 Signal Pile Up and Dead Time Effects

In imaging situations involving high amounts of tracer radioactivity, such as cardiac imaging, the response of the data acquisition system to high counting rates may be subject to signal pile up and dead time effects. Specifically these effects are more prominent in preclinical PET systems due to the smaller system diameter and thus higher photon sensitivity.

Signal pile up occurs mainly at the early stages of the signal processing chain. If the intensity of the incident photon flux is such that the detection of a photon event, and the associated generation of a detector signal, occurs before a signal from a previous detection has returned to its baseline, the former will be superimposed on the trailing edge of the previous detector signal, as illustrated in Fig. 5.12. The pulse shape is thus distorted resulting in inaccurate information about both the height and time of the pulse. Pulse pile up is significantly suppressed by reducing the duration of the pulse trailing edge via appropriate shaping. In Sect. 3.2.1 it was pointed out that block detector designs are more subject to pile up effects compared to designs with individual crystal readout. This is due to the fact that in the former design each photodetector reads out the scintillation photon fluxes from multiple crystals. In moderate count rates pile up is not apparent given the fact that it is rather unlikely that two crystals seen by the same photodetector in a PET system will produce signals close together in time.

Dead time is usually defined as the minimum temporal difference between two events in order for the imaging system to identify them as two separately detected events. Dead time is essentially a property of the imaging system as a whole, originating from both the detector front end and the data acquisition electronics.

Detector dead time is related to the recovery of the scintillator and the photodetector after the detection of a photon event. Data acquisition dead time is related to the time it takes for the peak detector, time pick-off circuits, digitizers and data transfer architectures to reset in order to be able to process the next event.

Counting systems can be distinguished in terms of their dead time behavior, in two different categories [23]:

- Paralyzable systems: if two or more events are incident within a time window which is smaller than the minimum processing time required for that system, the system will not process any events during this time window. Thus the system's dead time is effectively increased depending on the rate of incident events.
- Non-paralyzable systems: if two or more events are incident within a time window which is smaller than the minimum processing time required for that system, the system will process those events as a single event.

Depending on the complexity of the PET data acquisition system, its dead time may not belong to either of the above categories. Several groups have been working in developing appropriate dead time models for specific PET systems in order to correct for counting losses [45].

4 State-of-the-Art Preclinical Systems

A number of preclinical PET tomographs initially developed by research groups have been commercialized and are currently used by several research centers around the world.

- **MicroPET/Focus/Inveon (CTI/Siemens):** The MicroPET technology is based on pixellated LSO crystals readout by PSPMTs by means of optical fibers. Different versions of this technology varying in crystal and FoV sizes have been realized [46–48].
- **Mosaic (Philips):** This system is based on GSO pixellated crystals coupled to hexagonal arrays of individual PMTs via a continuous light guide [49].
- **Argus (Suinsa):** The Argus system is the first commercially available PET system employing DoI capability [50]. Its detector architecture consists of a dual phoswich detector (LYSO/LGSO) read out by PSPMTs.
- **ClearPET (Raytest):** This preclinical system also employs DoI capabilities by means of a phoswich detector (LYSO/LuYAP) read out by PSPMTs [51]. The scanner has adjustable FoV allowing thus for both rodent and primate imaging.
- **LabPET (Gamma Medica-Ideas):** The LabPET system is the first commercially available APD based PET scanner. The system employs a phoswich detector (LYSO/LGSO) where the two different crystals are arranged next to each other in order to read out two detectors with the same APD [52].

Table 5.2 Performance summary of commercially available preclinical PET systems

System	Detector material	Radial FoV (mm)	Axial FoV (mm)	Transaxial/axial spatial resolution @ center (mm)	Photon sensitivity (%)
MicroPET	LSO	112	18	1.8, 2.0	0.56 @ 250 keV
Focus	LSO	258	76	1.3, 1.3	3.4 @ 250 keV
Inveon	LSO	161	127	<1.8	9.3 @ 250 keV
Mosaic	GSO	197	128	2.7, 3.4	0.65 @ 410 keV
Argus	LYSO/GSO	118	48	1.4	2.1 @ 400 keV
ClearPET	LYSO/LuYAP	135	110	1.3	4.5 @ 250 keV
LabPET	LYSO/LGSO	100	37.5/75	1.4, 1.3	1/2 @ 250 keV
Quad-HiDAC	Lead/Argon gas	170	280	1.1	1.0 @ 0 keV
FLEX™	BGO	100	118	1.8–2.0	8 @ 250 keV

– **Quad HiDAC (Oxford Positron Systems):** The quad-HiDAC system, also mentioned in Sect. 3.1.2, makes use of gas detectors equipped with lead converters and read out by electrode meshes. The system achieves sub-millimeter spatial resolution despite the poor time resolution, no energy resolution and poor photon sensitivity [11].
– **FLEX™ (Gamma Medica-Ideas):** The XPET system of the tri-modality FLEX™ tomograph (PET/SPECT/CT) consists of a detector ring based on quadrant sharing of BGO crystal arrays by arrays of PMTs. The detector block has the shape of a pentagon with tapered ends resulting in high detector packing fraction [53].

Table 5.2 summarizes quantitatively the basic performance features of these systems. Several other research systems employ special features:

– **RatCAP:** The Rat Conscious Animal PET (RatCAP) is a prototype PET scanner aimed to perform brain studies in conscious rats thus avoiding anesthesia which may inhibit several brain processes under study. Its architecture is based on individual readout of LSO crystal arrays by APD arrays with the detectors fixed in the animal's skull [54].
– **VP-PET:** The Virtual Pinhole PET (VP-PET) is a technology aiming to improve the spatial resolution of already existing systems by implementing a high resolution detector insert within the FoV [55]. Coincidences are registered between all possible detector pairs from both the existing system and the insert resulting in magnification similar to pinhole SPECT [56–59].

5 Summary

In this chapter, an overview of the design considerations for small animal PET scanners was given. Preclinical imaging is widely used in PET research for the evaluation of new pharmaceuticals and for the study of the biology of various human diseases.

However, the performance requirements for preclinical imaging differ from those for clinical imaging due to the significantly different volumes to be imaged. Differences in energy, time and spatial resolution between preclinical and clinical PET were explained and current trends in the PET detector designs were presented. A summary of state-of-the-art small animal PET scanners was also given.

Acknowledgments This work was supported by the National Institutes of Health (NIH) with grants R01CA119056 from NCI, R33EB003283 from NIBIB, R01CA120474 from NCI and P50CA114747 from NCI. The authors would also like to acknowledge the support of GE Healthcare and the AXA Research Fund.

References

1. Chen W (2007) Clinical applications of PET in brain tumors. J Nucl Med 48:1468-81.
2. Schwaiger M, Ziegler S, Nekolla SG (2005) PET/CT: challenge for nuclear cardiology. J Nucl Med 46:1664-78.
3. Strauss LG, Conti PS (1991) The applications of PET in clinical oncology. J Nucl Med 32:623-48; discussion 649-50.
4. Pellegrino D, Cicchetti F, Wang X, Zhu A, Yu M, Saint-Pierre M, et al. (2007) Modulation of dopaminergic and glutamatergic brain function: PET studies on Parkinsonian rats. J Nucl Med 48:1147-53.
5. Stegger L, Hoffmeier AN, Schafers KP, Hermann S, Schober O, Schafers MA, et al. (2006) Accurate noninvasive measurement of infarct size in mice with high-resolution PET. J Nucl Med 47:1837-44.
6. Fowler JS, Kroll C, Ferrieri R, Alexoff D, Logan J, Dewey SL, et al. (2007) PET studies of d-methamphetamine pharmacokinetics in primates: comparison with l-methamphetamine and (--)-cocaine. J Nucl Med 48:1724-32.
7. Munk OL, Bass L, Roelsgaard K, Bender D, Hansen SB, Keiding S (2001) Liver kinetics of glucose analogs measured in pigs by PET: importance of dual-input blood sampling. J Nucl Med 42:795-801.
8. Brix G, Zaers J, Adam LE, Bellemann ME, Ostertag H, Trojan H, et al. (1997) Performance evaluation of a whole-body PET scanner using the NEMA protocol. National Electrical Manufacturers Association. J Nucl Med 38:1614-23.
9. Levin CS (2005) Primer on molecular imaging technology. Eur J Nucl Med Mol Imaging 32 Suppl 2:S325-45.
10. Levin CS (2008) New imaging technologies to enhance the molecular sensitivity of positron emission tomography. Proceedings of the IEEE 96:439-467.
11. Schafers KP, Reader AJ, Kriens M, Knoess C, Schober O, Schafers M (2005) Performance evaluation of the 32-module quadHIDAC small-animal PET scanner. J Nucl Med 46:996-1004.
12. Stickel JR, Qi J, Cherry SR (2007) Fabrication and characterization of a 0.5-mm lutetium oxyorthosilicate detector array for high-resolution PET applications. J Nucl Med 48:115-21.
13. Visvikis D, Lefevre T, Lamare F, Kontaxakis G, Santos A, Darambara D (2006) Monte Carlo based performance assessment of different animal PET architectures using pixellated CZT detectors. Nucl Instr Meth A 569:225-229.
14. Levin CS, Hoffman EJ (1999) Calculation of positron range and its effect on the fundamental limit of positron emission tomography system spatial resolution. Phys Med Biol 44:781-99.
15. Cherry SR, Phelps ME, Sorenson JA (2003) *Physics in nuclear medicine*, 3rd ed. Philadelphia, PA: Saunders.

16. Phelps ME (2004) *PET molecular imaging and its biological applications*. New York: Springer.
17. Yang YF, Cherry SR (2006) Observations regarding scatter fraction and NEC measurements for small animal PET. IEEE Trans Nucl Sci 53:127-132.
18. Pratx G, Levin CS (2009) Bayesian reconstruction of photon interaction sequences for high-resolution PET detectors. Phys Med Biol 54:5073-94.
19. Rafecas M, Boning G, Pichler BJ, Lorenz E, Schwaiger M, Ziegler SI (2003) Inter-crystal scatter in a dual layer, high resolution LSO-APD positron emission tomograph. Phys Med Biol 48:821-48.
20. Huber JS, Moses WW, Jones WF, Watson CC (2002) Effect of 176Lu background on singles transmission for LSO-based PET cameras. Phys Med Biol 47:3535-41.
21. Watson CC, Casey ME, Eriksson L, Mulnix T, Adams D, Bendriem B (2004) NEMA NU 2 performance tests for scanners with intrinsic radioactivity. J Nucl Med 45:822-6.
22. Surti S, Karp JS, Freifelder R, Liu F (2000) Optimizing the performance of a PET detector using discrete GSO crystals on a continuous lightguide. IEEE Trans Nucl Sci 47: 1030-1036.
23. Knoll GF (2000) *Radiation detection and measurement*, 3rd ed. New York ; Toronto: Wiley.
24. Joung J, Miyaoka RS, Lewellen TK (2002) cMiCE: a high resolution animal PET using continuous LSO with a statistics based positioning scheme. Nucl Instr Meth A 489:584-598.
25. Monzo JM, Lerche CW, Martinez JD, Esteve R, Toledo J, Gadea R, et al. (2009) Analysis of time resolution in a dual head LSO plus PSPMT PET system using low pass filter interpolation and digital constant fraction discriminator techniques. Nucl Instr Meth A 604: 347-350.
26. Seidel J, Vaquero JJ, Barbosa F, Lee IJ, Cuevas C, Green MV (2000) Scintillator identification and performance characteristics of LSO and GSO PSPMT detector modules combined through common X and Y resistive dividers. IEEE Trans Nucl Sci 47:1640-1645.
27. Levin CS (2002) Design of a high-resolution and high-sensitivity scintillation crystal array for PET with nearly complete light collection. IEEE Trans Nucl Sci 49:2236-2243.
28. Pichler BJ, Bernecker F, Boning G, Rafecas M, Pimpl W, Schwaiger M, et al. (2001) A 4×8 APD array, consisting of two monolithic silicon wafers, coupled to a 32-channel LSO matrix for high-resolution PET. IEEE Trans Nucl Sci 48:1391-1396.
29. Ziegler SI, Pichler BJ, Boening G, Rafecas M, Pimpl W, Lorenz E, et al. (2001) A prototype high-resolution animal positron tomograph with avalanche photodiode arrays and LSO crystals. Eur J Nucl Med 28:136-43.
30. Habte F, Foudray AM, Olcott PD, Levin CS (2007) Effects of system geometry and other physical factors on photon sensitivity of high-resolution positron emission tomography. Phys Med Biol 52:3753-72.
31. Yang Y, Dokhale PA, Silverman RW, Shah KS, McClish MA, Farrell R, et al. (2006) Depth of interaction resolution measurements for a high resolution PET detector using position sensitive avalanche photodiodes. Phys Med Biol 51:2131-42.
32. Rafecas M, Boning G, Pichler BJ, Lorenz E, Schwaiger M, Ziegler SI (2001) A Monte Carlo study of high-resolution PET with granulated dual-layer detectors. IEEE Trans Nucl Sci 48: 1490-1495.
33. Zhang J, Foudray AMK, Cott PD, Farrell R, Shah K, Levin CS (2007) Performance characterization of a novel thin position-sensitive avalanche photodiode for 1 mm resolution positron emission tomography. IEEE Trans Nucl Sci 54:415-421.
34. Zhang J, Olcott PD, Chinn G, Foudray AM, Levine CS (2007) Study of the performance of a novel 1 mm resolution dual-panel PET camera design dedicated to breast cancer imaging using Monte Carlo simulation. Med Phys 34:689-702.
35. Mosset JB, Devroede O, Krieguer M, Rey M, Vieira JM, Jung JH, et al. (2006) Development of an optimized LSO/LuYAP phoswich detector head for the Lausanne ClearPET demonstrator. IEEE Trans Nucl Sci 53:25-29.

36. Seidel J, Vaquero JJ, Green MV (2003) Resolution uniformity and sensitivity of the NIH ATLAS small animal PET scanner: Comparison to simulated LSO scanners without depth-of-interaction capability. IEEE Trans Nucl Sci 50:1347-1350.
37. Lerche CW, Benlloch JM, Sanchez F, Pavon N, Escat B, Gimenez EN, et al. (2005) Depth of gamma-ray interaction within continuous crystals from the width of its scintillation light-distribution. IEEE Trans Nucl Sci 52:560-572.
38. Maas MC, Schaart DR, van der Laan DJ, Bruyndonckx P, Lemaitre C, Beekman FJ, et al. (2009) Monolithic scintillator PET detectors with intrinsic depth-of-interaction correction. Phys Med Biol 54:1893-908.
39. Schaart DR, van Dam HT, Seifert S, Vinke R, Dendooven P, Lohner H, et al. (2009) A novel, SiPM-array-based, monolithic scintillator detector for PET. Phys Med Biol 54:3501-12.
40. Lucignani G (2009) Respiratory and cardiac motion correction with 4D PET imaging: shooting at moving targets. Eur J Nucl Med Mol Imaging 36:315-9.
41. Dawood M, Kosters T, Fieseler M, Buther F, Jiang X, Wubbeling F, et al. (2008) Motion correction in respiratory gated cardiac PET/CT using multi-scale optical flow. Med Image Comput Comput Assist Interv 11:155-62.
42. Lamare F, Cresson T, Savean J, Cheze Le Rest C, Reader AJ, Visvikis D (2007) Respiratory motion correction for PET oncology applications using affine transformation of list mode data. Phys Med Biol 52:121-40.
43. Pichler BJ, Swann BK, Rochelle J, Nutt RE, Cherry SR, Siegel SB (2004) Lutetium oxyorthosilicate block detector readout by avalanche photodiode arrays for high resolution animal PET. Phys Med Biol 49:4305-19.
44. Siegel S, Silverman RW, Shao YP, Cherry SR (1996) Simple charge division readouts for imaging scintillator arrays using a multi-channel PMT. IEEE Trans Nucl Sci 43:1634-1641.
45. Daube-Witherspoon ME, Carson RE (1991) Unified deadtime correction model for PET. IEEE Trans Med Imaging 10:267-75.
46. Bao Q, Newport D, Chen M, Stout DB, Chatziioannou AF (2009) Performance evaluation of the Inveon dedicated PET preclinical tomograph based on the NEMA NU-4 standards. J Nucl Med 50:401-8.
47. Cherry SR, Shao Y, Silverman RW, Meadors K, Siegel S, Chatziioannou A, et al. (1997) MicroPET: A high resolution PET scanner for imaging small animals. IEEE Trans Nucl Sci 44:1161-1166.
48. Tai YC, Ruangma A, Rowland D, Siegel S, Newport DF, Chow PL, et al. (2005) Performance evaluation of the microPET Focus: a third-generation microPET scanner dedicated to animal imaging. J Nucl Med 46:455-63.
49. Huisman MC, Reder S, Weber AW, Ziegler SI, Schwaiger M (2007) Performance evaluation of the Philips MOSAIC small animal PET scanner. Eur J Nucl Med Mol Imaging 34:532-40.
50. Wang Y, Seidel J, Tsui BM, Vaquero JJ, Pomper MG (2006) Performance evaluation of the GE healthcare eXplore VISTA dual-ring small-animal PET scanner. J Nucl Med 47:1891-900.
51. Roldan PS, Chereul E, Dietzel O, Magnier L, Pautrot C, Rbah L, et al. (2007) Raytest ClearPET (TM), a new generation small animal PET scanner. Nucl Instr Meth Phys Res A 571: 498-501.
52. Bergeron M, Cadorette J, Beaudoin JF, Lepage MD, Robert G, Selivanov V, et al. (2009) Performance evaluation of the LabPET APD-based digital PET scanner. IEEE Trans Nucl Sci 56:10-16.
53. Parnham KB, Chowdhury S, Li J, Wagenaar DJ, Patt BE (2006) Second-generation, tri-modality, pre-clinical imaging system. NSS/MIC Conf Rec: 1802-1805
54. Vaska P, Woody CL, Schlyer DJ, Shokouhi S, Stoll SP, Pratte JF, et al. (2004) RatCAP: Miniaturized head-mounted PET for conscious rodent brain imaging. IEEE Trans Nucl Sci 51:2718-2722.
55. Tai YC, Wu H, Pal D, O'Sullivan JA (2008) Virtual-pinhole PET. J Nucl Med 49:471-9.
56. Beekman FJ, van der Have F, Vastenhouw B, van der Linden AJ, van Rijk PP, Burbach JP, et al. (2005) U-SPECT-I: a novel system for submillimeter-resolution tomography with radiolabeled molecules in mice. J Nucl Med 46:1194-200.

57. DiFilippo FP (2008) Design and performance of a multi-pinhole collimation device for small animal imaging with clinical SPECT and SPECT-CT scanners. Phys Med Biol 53: 4185-4201.
58. Palmer J, Wollmer P (1990) Pinhole emission computed tomography: method and experimental evaluation. Phys Med Biol 35:339-50.
59. Shokouhi S, Metzler SD, Wilson DW, Peterson TE (2009) Multi-pinhole collimator design for small-object imaging with SiliSPECT: a high-resolution SPECT. Phys Med Biol 54:207-225.

Chapter 6
Design Considerations of Small-Animal CT Systems

Erik L. Ritman

1 Introduction

This chapter focuses on the ability of small-animal CT to provide information about molecular species and their spatial distribution in tissues. Over the past several decades radionuclide imaging methods have been the mainstay of in vivo molecular imaging by virtue of the variety of biologically active molecules that can be labeled with a radioactive marker. CT image data has been used to provide both attenuation correction of the SPECT and PET images as well as provide the anatomic localization of the radionuclide accumulation. This important contribution of CT to molecular imaging is presented in those chapters directly addressing the radionuclide imaging approaches. Although, the presence of higher atomic weight atomic labels (e.g., iodine) of biologically active tracer molecules can be conveyed by conventional X-ray attenuation-based imaging methods (in milli-molar concentrations as compared to pico-molar concentrations by radionuclide methods), molecular species can be conveyed by non-attenuating aspects of X-ray interaction with matter by virtue of their molecular bonds that are characteristic of polymeric molecules. These non-attenuating X-ray imaging methods are now starting to emerge from the feasibility demonstrations and hence will be explored in some depth in this chapter.

Micro-CT was first developed in the early 1980s [1–3]. In the later 1980s bench-top micro-CT was greatly facilitated by the development of a cone beam reconstruction algorithm by Feldkamp et al. [4] because the bench-top systems use the X-ray cone-beam to magnify the X-ray image itself.

Figure 6.1 is a schematic of a typical small animal CT scanner. CT is a 3D X-ray imaging method that involves obtaining X-ray projection images at many angles of view around an axis through an object and then applying a tomographic reconstruction

E.L. Ritman (✉)
Department of Physiology and Biomedical Engineering, Mayo Clinic College of Medicine, Rochester, MN, USA
e-mail: elran@mayo.edu

H. Zaidi (ed.), *Molecular Imaging of Small Animals: Instrumentation and Applications*,
DOI 10.1007/978-1-4939-0894-3_6,

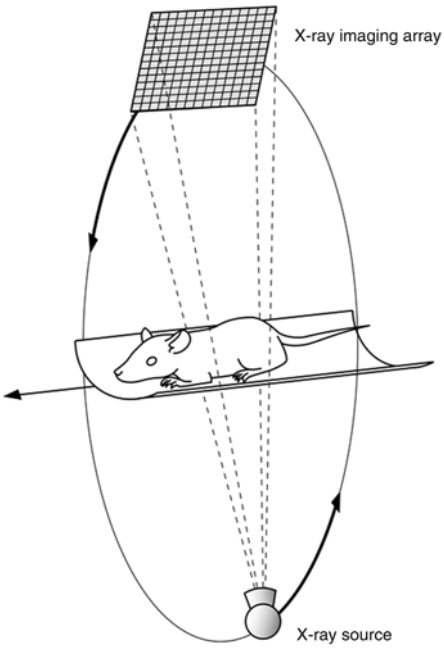

Fig. 6.1 Schematic of a small-animal CT scanner system. The small animal is anesthetized and lies on an horizontal table. If the animal's ECG and/or thoracic movement is monitored, then either prospective or retrospective gated scans and/or reconstructions can be performed by incremental recording/selection of the different angles of view required to generate transaxial CT images. The X-ray source and its opposite X-ray imaging array rotate about the cephalocaudal axis of the animal. Some scanners have dual X-ray source/detector arrays arranged at right angles to each other, which halves the scan time required. The animal table can be translated axially (i.e., at right angles to the plane described by the X-ray source trajectory) so that the length of the body scanned can be several times the length of animal exposed by the X-ray source [5]

algorithm to generate a stack of thin tomographic images of transaxial slices through the object. The transaxial images are made up of voxels (three-dimensional pixels).

Utilization and availability of small-animal CT systems has increased markedly over the past decade. It has evolved from custom-made scanners (applied mostly to imaging small-animal bones and segments of larger animal bones) to commercially available scanners designed for in vivo imaging of skeletal and soft tissues. Numerous reviews of the development and applications of micro-CT have been published [6–9]. A number of commercially marketed micro-CT scanners are now available for in-vivo small animal imaging. Some performance characteristics of a selected set of available small-animal CT scanners are summarized in Table 6.1. As this is a rapidly evolving market, this table is likely to be incomplete and in part obsolete in the not too distant future. Nonetheless, the message remains, in that the different functional characteristics of these scanners and the different imaging needs of the potential purchaser, will need to be carefully matched.

Table 6.1 Commercially-available small-animal CT scanners

Scanner	Diameter (mm)	Length (mm)	Voxel (μm)	kVp
Gamma Medica X-O	93	97	17	75
GE eXplore CT120	85	275	25–100	70–120
GE eXplore Lotus	55	275	27–90	70–120
Imtek micro-CATII	54	80	15–27	0–130
LaTheta LCT-200	30–120	300	24–60	80
ScanCo vivaCT 40	20–38	145	10–38	50–70
ScanCo vivaCT 75	40–78	145	20–79	50–70
SkyScan 1076 in vivo	68	210	9–35	20–100
SkyScan 1178	82	210	80–160	20–65

Similarly, because some scanners have a range of operational characteristics while others are more suitable for "turn-key" operation, an investigator will need to consider the positives and negatives of the operational flexibility of a scanner.

The grey-scale of those voxels is proportional to the attenuation coefficient of the material at the spatial location depicted by the voxel. The voxel is usually of the order of approximately 50–100 μm on-a-side when intact small animals are scanned—perhaps more appropriately called *mini-CT* because its CT images are scaled so as to provide voxel resolution such that the number of voxels per organ are similar to that obtained in human CT images. This generally involves clinical level X-ray photon energy. However, as small animals have higher heart and respiratory rates than humans do, scanning of the thorax involves scans that provide incremental scan data acquired over a number of sequential heart and/or respiratory cycles, so-called gated scanning. To provide CT image signal-to-noise comparable to clinical CT scanners the X-ray exposure of the animal or specimen should increase by an amount proportional to at least the inverse of the voxel volume [10–12]. As the radiation itself might affect the pathophysiology of interest in, for instance angiogenesis or cancer [6] a voxel size less than $(50\ \mu m)^3$ could result in excessive radiation exposure in living animals if repeated scans are involved.

True *micro-CT*, which has voxel resolution of the order of approximately 5–50 μm, is suitable for scanning isolated organs from small animals or tissue biopsies from larger animals or indeed intact dead small animals. For isolated specimens, for which higher resolution is often desired, the scanner generally operates at lower X-ray photon energy which is optimally matched to the diameter of the specimen [13].

In recent years several bench-top *nano-CT* scanners with sub-micrometer voxel resolutions have been developed and are commercially available. These can provide 3D images at cellular level of resolution, but scan only small volumes.

2 Rationale for Use of Small-Animal CT

CT has been used primarily to provide 3D images of anatomic structures and function of those structures by virtue of motion of those structures and/or of dynamic distribution of contrast agent within the vascular tree. Traditional clinical CT and

small-animal CT approaches have rarely been used to generate images of the spatial distribution of specific molecules by virtue of the CT image data itself. The uses of small-animal CT in biology include the following.

2.1 *Phenotype Characterization by Anatomic Structures and Material Composition*

Organ dimensions (e.g., dimensions of airways or volumes of lung, heart wall or chambers [14, 15]), bone mineralization [16, 17], micro-architecture of the cancellous bone and cortical bone thickness [18], blood vessel lumen diameter and branching geometry [19–21], tumor size and impact on its surrounding tissues (e.g., bone erosion or compression of adjacent blood vessels). Such measurements would be seen to change in response to maturation and/or disease or due to exposure to various pharmacological agents, environmental conditions or radiation exposure. These dimensions and local CT grey-scales can be measured directly from the 3D CT image data and thereby represent the main application of small-animal CT imaging to date.

2.2 *Physiological Spaces and Their Contents*

In addition to anatomic structures, especially entire organs, there are "macroscopic" physiological spaces such as the intravascular lumens, the lumens of ducts (e.g., renal tubules, ureters, bowel, bladder and bile ducts which tend to vary with time or pathophysiological conditions) or less well-defined microscopic spaces such as the extravascular space between the vessel endothelium and the parenchymal cells. This space swells with edema or with deposition of pathological proteins such as occurs in amyloidosis, or lipids such as occurs in atherosclerosis. These spaces can be detected and thereby delineated by use of contract agents which selectively accumulate (or avoid) those spaces. For the vascular tree iodinated-molecule solutions are used and bile and renal ducts can be opacified by virtue of intravascular injection of contrast agents that are selectively taken up and excreted by the liver or kidney respectively. Very transient labelling of those spaces can still be scanned despite the relatively slow micro-CT scans if incremental scans acquired from repeated contrast injections [22], use of long-duration contrast agent concentration in the blood stream [9] or snap-freezing of the tissue of interest for subsequent cryo-static scanning [23], are used to acquire the needed scan data. The volume of these spaces can be computed from the increase in CT values of those spaces.

2.3 Tissue Perfusion, Drainage and Secretion: Molecular Transport

Tissue perfusion (F) can be estimated from CT scans if they provide images at each heart cycle during the passage of a bolus of intravascular contrast agent [24]. Given the values of F and the extraction (e) of the contrast from the blood stream into the extra-vascular space, then the rate of influx or washout of the contrast agent from a physiological space can be used to estimate the transport into or out of that space from the Crone–Renkin relationship [25]: $PS = -F \cdot \ln(1 - e)$, where P is the endothelial permeability and S is the surface area of the endothelial surface. The value of S can be estimated from the intravascular blood volume of the microcirculation.

2.4 Need to Scan Entire Organ and Resolution

The volume that needs to be scanned is determined by several, sometimes conflicting, needs. Thus, we would need to scan an entire organ if we are looking for a focal lesion such as early cancer. On the other hand, at high voxel resolution it may technically not be possible to scan an entire organ at that resolution due to, for instance, limits on the X-ray detection system resolution and size. For estimation of organ volume, relatively large voxel sizes can be tolerated (e.g., a $(2\ \text{cm})^3$ heart needs approximately 4,000 voxels of $(30\ \mu\text{m})^3$ if better than a 1 % uncertainty is desired). However, if a 200 μm diameter basic functional units (i.e., BFU, the smallest accumulation of diverse cells that behave like the organ it is in, e.g., an hepatic lobule or a Haversian canal-centered osteome) is of interest, then voxel resolutions of better than $(100\ \mu\text{m})^3$ will be needed just to unambiguously detect it, but a $(3\ \mu\text{m})^3$ voxel would be needed if the volume of the BFU is to me estimated within 10 %.

3 Types of Small-Animal CT Approaches

The above considerations apply to most current uses of small-animal CT. These applications can also provide some information about atomic content and therefore relate to molecular discrimination and quantitation at only an indirect level. There are, however, other aspects of X-ray/matter interaction that can be used to discriminate and quantitate atom concentration as well as some chemical bonds, i.e., a more direct aspect of molecular characteristics.

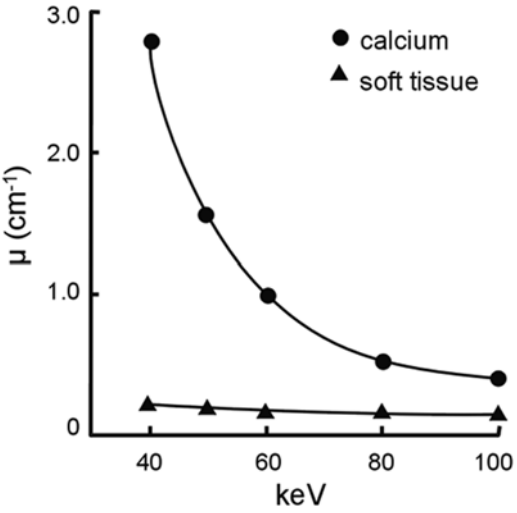

Fig. 6.2 Attenuation of X-rays passing through tissues differs depending on the tissue elemental content and the energy of the X-ray photons. In this example of a filtered 80 kVp source (effective 54 keV) the difference between calcium and soft tissue is dramatic. If the calcium is diluted so that its attenuation is comparable to the soft tissue, then by generating images at two energies, e.g., 80 and 50 keV, the Ca component will change more rapidly than the soft tissue, hence a subtraction of the two images will tend to leave a calcium signal but eliminate the tissue signal [26]

3.1 Attenuation-Based Scanning

This is the basis for the most common and most technically straightforward mode of CT scanning. The basic mechanism is the generation of a shadowgraph which is quantitated by measurement of the reduction in local X-ray intensity. By use of the Beer–Lambert law, $I = I_o \cdot e^{-\mu x}$, where I is the detected X-ray intensity at a detector pixel after passing through an object of thickness x, I_o is the incident X-ray intensity at the same pixel and μ is the attenuation coefficient of the specimen's material. As shown in Fig. 6.2 the attenuation coefficient (expressed as "/cm" of matter traversed) decreases exponentially with increasing X-ray photon energy up to an energy of up to approximately 50 keV due to the photo-electric effect (proportional to Z^3/E^3, where Z is the atomic number and E is the photon energy), beyond 50 keV μ decreases slowly with photon energy due to the Compton effect (largely independent of Z).

This image can be converted to a projection of the attenuation x thickness product (i.e., the line integral) along the X-ray beam traversing the object. With multi-angular projection data this can be mathematically converted to the three-dimensional distribution of the local attenuation coefficient at the site of each voxel making up the 3D image data set [27]. The X-ray beam should be monochromatic if beam hardening is to be avoided. This is readily achievable with a synchrotron [28, 29] by

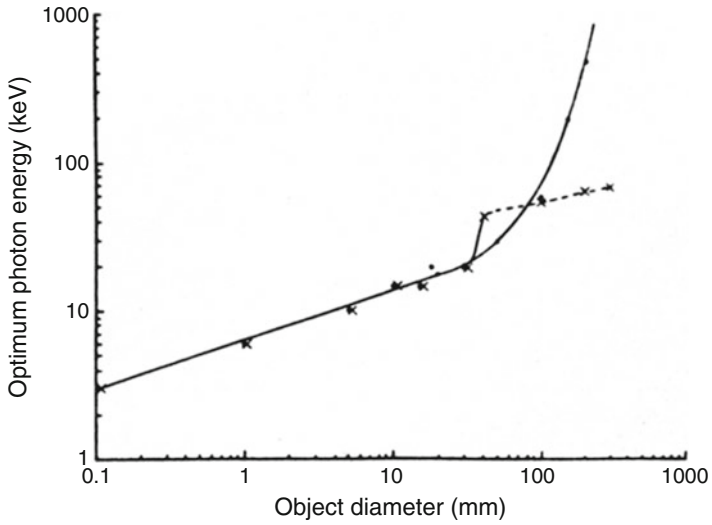

Fig. 6.3 The optimal photon energy for the detection of a 1 % density difference in circular water phantoms as a function of the diameter of the phantom. The diameter of the contrasting detail is 1/200 of the phantom diameter. Optimization criteria: *cross symbol*, minimum absorbed dose at center of phantom; *filled square*, minimum number of incident photons [31]

use of a diffraction crystal which can select those X-ray photons within a ±50 eV energy range. This can also be achieved in part by filtering the X-ray beam prior to it encountering the specimen. This generally involves use of a layer of aluminium which preferentially removes the lower energy photons, but if the K_α emission of the anode is to be used as the primary source (e.g., 17.5 keV for a Molybdenum anode), then a suitably matched filter with a Kedge absorption energy just greater than the K_α energy would also selectively reduce the photons with energy greater than the K_α energy [30] (e.g., 18 keV for a zirconium filter). This approach is effective but for the bench-top X-ray source results in a greatly diminished X-ray flux and hence requires long scan periods which are generally incompatible with in vivo scanning.

Finally, the signal (i.e., the change in local contrast of the shadowgraph) in all attenuation-based imaging approaches involves local reduction of X-ray intensity, which is accompanied by a reduced signal-to-noise ratio due to the reduction in the number of photons impinging on each detector pixel. Noise in this context is the variation of signal in adjacent pixels that should have identical signals due to the line integral of the specimen along the X-ray beam illuminating each pixel being identical. For specimens higher contrast resolution can be achieved by use of lower energy photons. As shown in Fig. 6.3, Spanne [31] showed that E has to increase with sample diameter (actually μx product) if noise is to be kept constant. Grodzins [13] showed that the optimal trade-off between signal and contrast resolution occurs when 10 % of the incident beam is transmitted. If the duration of the scan is important (especially in living animals) then higher X-ray photon energy is used because

of the higher signal (due to less attenuation). However, this is at the "cost" of lower "density" resolution.

This image can be converted to a projection of the attenuation x thickness product (i.e., the line integral) along the X-ray beam traversing the object. With multiangular projection data this can be mathematically converted to the three-dimensional distribution of the local attenuation coefficient at the site of each voxel making up the 3D image data set [27]. The X-ray beam should be monochromatic if beam hardening is to be avoided. This is readily achievable with a synchrotron [28, 29] by use of a diffraction crystal which can select those X-ray photons within a ±50 eV energy range. This can also be achieved in part by filtering the X-ray beam prior to it encountering the specimen. This generally involves use of a layer of aluminium which preferentially removes the lower energy photons, but if the K_α emission of the anode is to be used as the primary source (e.g., 17.5 keV for a Molybdenum anode), then a suitably matched filter with a Kedge absorption energy just greater than the K_α energy would also selectively reduce the photons with energy greater than the K_α energy [30] (e.g., 18 keV for a zirconium filter). This approach is effective but for the bench-top X-ray source results in a greatly diminished X-ray flux and hence requires long scan periods which are generally incompatible with in vivo scanning.

The absolute value and rate of decrease of attenuation coefficient differs depending on the element and the density of the material. Thus, the attenuation value of muscle tissue decreases 765-fold from 1 to 10 keV but only 31-fold from 10 to 100 keV whereas blood decreases 690 and 32-fold over the same ranges of photon energies. Subtracting the image obtained at a low from that obtained at higher photon energy would differentiate blood and muscle tissue better than their attenuation coefficient alone would at any one photon energy.

At 10 keV tissues of different density (e.g., fat, muscle and bone) show considerable differences in attenuation coefficients (3.1, 5.6 and 54/cm respectively) and hence can be distinguished from each other by their attenuation coefficient alone.

The attenuation coefficient can change dramatically at the so-called Kedge. As illustrated in Fig. 6.4 for iodine the attenuation coefficient increases from 6.55/cm to 35.8/cm when the photon energy increases by a mere electron volt at 33.1694 keV. Certain biologically relevant elements (such as iodine which occurs naturally in the thyroid gland or when purposely bound chemically to biological molecules of interest) can be identified and quantitated by subtracting images generated at a photon energy just below and just above the Kedge transition voltage. Unfortunately none of the common elements that occur naturally in the tissues of the body (e.g., Na, K, Ca, P etc.) have Kedges at sufficiently high keV photon energy that can be used for imaging of even isolated mouse organs, much less intact mice.

This is because at these very low photon energies (i.e., <10 keV) the attenuation of the X-ray is so large (i.e., only 0.5 % of photons pass through 1 cm of water—the thickness of a mouse abdomen) that useful images cannot be generated at acceptable radiation exposure levels.

This methodology generally involves use of either two energies of monochromatic photon radiation with narrow spectral bandwidth that "straddle" the Kedge

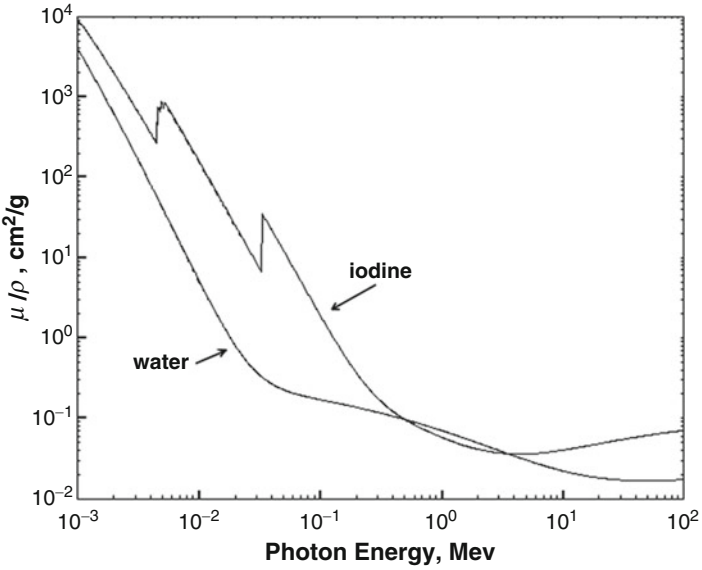

Fig. 6.4 Attenuation of X-ray, normalized for gravimetric density, by iodine decreases with increasing energy, but at approximately 5 and 33 keV there are step changes in attenuation. These are the so-called Ledge and Kedge of Iodine which correspond to the energy of the electrons in the L and K shells of the iodine atom. Water (the main component of living tissues) has those discontinuities due to the hydrogen and oxygen at 16 and 500 eV respectively, well below the X-ray photon energies used in small-animal-CT. Subtraction of two X-ray images involving X-ray photon energies at 32 and 34 keV would show a large difference in iodine signal but a relatively small change in the water signal—resulting in an essentially iodine-only image. Micromolar (15 μg/cm^3) concentrations of iodine can be detected by this method [32]

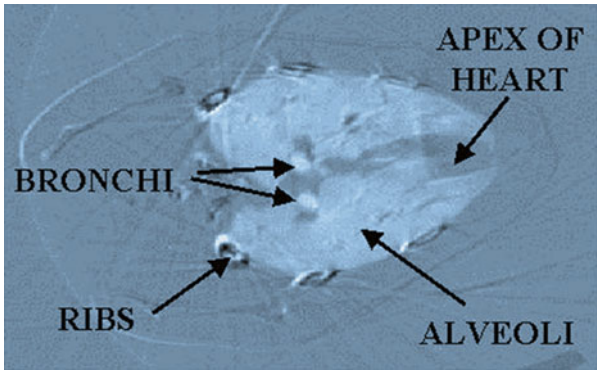

Fig. 6.5 A dual energy subtraction CT image of a rabbit lung obtained during inhalation of xenon gas (Kedge 34.56 keV). Note, the bright left and right bronchi and the less bright parenchymal signal of the xenon in the alveoli [33]

energy of the atom of interest or an energy selective X-ray detection system used with broad spectrum X-ray exposure. Narrowing of the spectral bandwidth (i.e., range of X-ray photon energy) down to levels of 50 eV can be achieved by use of a diffraction crystal at a synchrotron because even with this great restriction of X-ray flux there is still adequate X-ray flux to allow rapid imaging (Fig. 6.5).

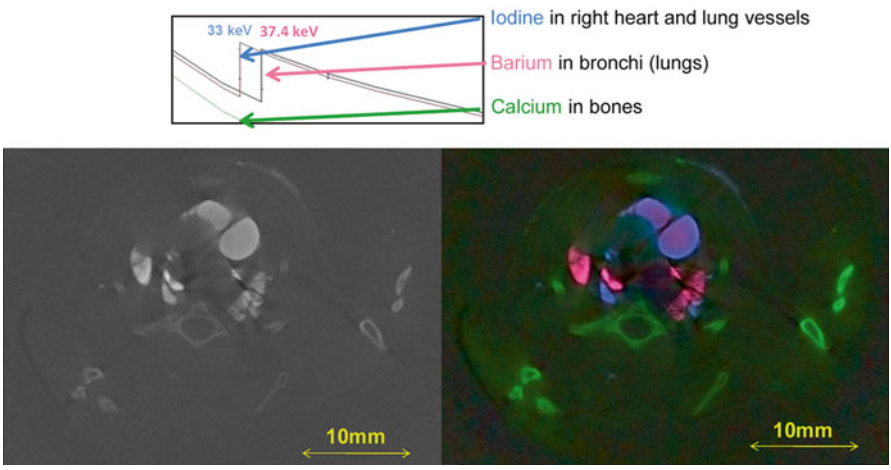

Fig. 6.6 *Left panel*: A CT image of a transaxial cross section of a mouse thorax. The bronchial tree had barium sulphate infused and the pulmonary artery had an iodine-based contrast injected. These different materials and the skeletal features cannot be distinguished unambiguously on the basis of their CT grey-scale values. *Right panel*: The use of Principal Component Analysis by virtue of the ability to extract the different X-ray photon energy components from the bremsstrahlung X-ray exposure allowed identification and quantitation of the three elements by virtue of their different attenuation-to-photon energy relationships—as illustrated in the *upper panel* [34, 35]

With conventional X-ray sources which produce broad spectrum bremsstrahlung suitable selection of the anode material for its characteristic K_α emission of the material, combined with a thin metal foil filter which has an absorption K edge just above the K_α photon energy, the spectral bandwidth can be reduced to 30 % or less. If an energy discriminating detector is used then those photons with energies of interest can be selected from the X-ray image data [34–38].

Recently detector arrays with 55 μm^2 pixels, energy discrimination and photon counting (up to 8,000 photons/s per pixel) have become available [34] for energies up to 18 keV (silicon-based array), 50 keV (GaAs array) and 75 keV (CdTe array) at 50 % detector efficiency (Fig. 6.6).

3.2 Fluorescence-Based Scanning

As shown in Fig. 6.7, elements that are irradiated with X-rays also fluoresce with X-ray photons that have an energy that is characteristic of that element. This so-called K_α emission also has low energy for most biological elements (e.g., Na 1 keV, P 2 keV, K 3.3 keV). However, by exposing a specimen to X-rays with photon energies higher than the K_α energy of the element of interest, chemically surrogate elements (e.g., Rb, a surrogate for potassium, has a K_α of 13.4 keV and Sr, a surrogate for Ca, has a K_α of 14 keV) or elements that can be used to label

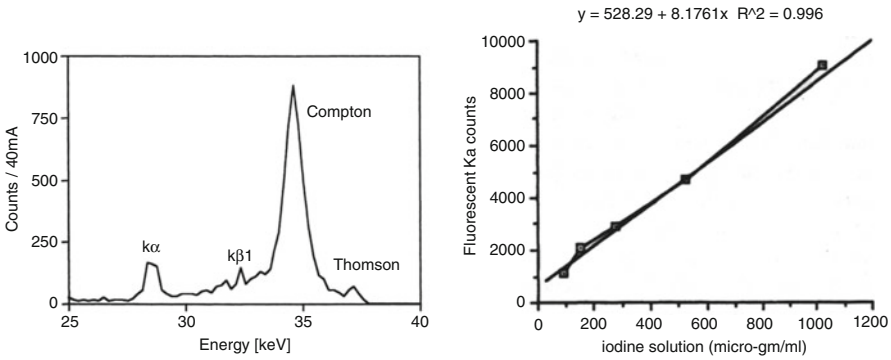

Fig. 6.7 *Left panel*: X-ray photon energy spectrum in scattered radiation measured at an angle to an illuminating X-ray pencil beam passing through an iodine solution. Thomson scatter is coherent and occurs at angles generally less than 15°. The energy is identical to the illuminating, 37 keV, X-ray beam. This deflection is used to generate a CT image of the location and concentration of a specific molecule. Compton scatter is predominant and its photon energy and intensity change with angle (0–180°) from the illuminating beam. The K_α and K_β peaks are the characteristic fluorescence of iodine. The intensity falls off with increasing angle to the illuminating X-ray beam. When the X-ray intensity at these peaks is used to generate a CT image, it is an image of the location and concentration of the element with that characteristic emission spectrum [39]. *Right panel* shows the linear relationship between the fluorescent counts and the concentration of iodine. Note that in attenuation-based CT the detectable concentrations are in the milli-molar range (10 mg/cm^3) rather than the micro-molar range (60 μg/cm^3) possible with fluorescence CT [40]

molecules or particles of interest (e.g., with Iodine which has a $K_\alpha = 28.5$ keV). This approach is particularly useful for detection of heavy metal contamination such as lead deposited in bone.

This approach can have several source/detector configurations, but as illustrated in Fig. 6.8, all detect the fluorescent X-rays at an angle to the illuminating beam. Thus, the regular transmission image can also be recorded during this scan.

If the fluorescence detector is sufficiently far from the object, then it will detect a line integral of emissions along each transilluminating pencil beam. If a collimated detector is used then each point along the transilluminated beam can have its emissions quantitated. This is straightforward if just a pencil beam is used because then the emissions are coming from a known location in the specimen. The only correction that has to be made is for the attenuation of the illuminating beam as it proceeds to the voxel of interest within the object and of the fluorescent emissions as they exit the specimen from that voxel. This can be done by use of the 3D attenuation map generated with the regular attenuation-based scan. To generate a 3D image would require scanning the X-ray beam transaxially relative to the object, which would require long scan durations. If, however, the specimen is illuminated with a thin, planar X-ray beam, along with a Suitable 2D collimator, then an axial plane of the specimen is illuminated, thereby speeding up the 3D scan process.

If the entire specimen is illuminated by, for instance, a cone beam of X-ray and observed with a multi-hole collimator, then each detector pixel records a line

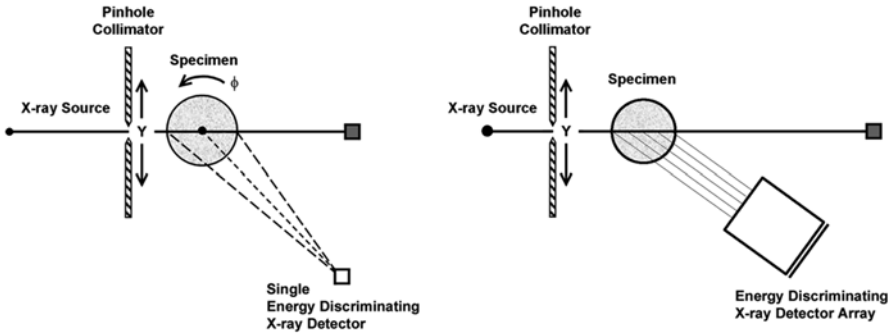

Fig. 6.8 Schematic of system for fluorescent X-ray tomographic imaging. *Left panel*: Involves trans-illuminating the specimen with a pencil beam of X-ray with narrow spectral bandwidth so that the lower photon energy K_α can be discriminated from the scattered X-ray. In order to generate the set of line-integral data needed for Radon-based tomographic reconstruction, this X-ray beam has to be translated across the specimen and this is repeated at each angle of rotation of the specimen about its axis. This is a very laborious process generally incompatible with live-animal scanning. *Right panel*: Involves a collimator which records the fluorescence from each location along the beam traversing the specimen so now no rotation of the specimen is needed to complete the scan of a single cross section. Indeed, a plane (oriented at right angles to the plane of the figure) is exposed then with a 2D collimator a volume can then be scanned in single rotation [41]

integral of fluorescence emissions, which would require multi-angular data, just as in a regular CT scan, to unravel the line integrals.

The fluorescent radiation is preferentially in the "forward" 2π steradians. This means that multiple detectors could be arranged around the transmission detector so as to decrease the duration of the scan because of the increased number of photons emitted at each point in the specimen being detected. Use of an energy discriminating detector system is needed to separate the Compton scatter from the fluorescent emissions.

3.3 Scatter-Based Scanning

Coherent scatter is a function of charge distribution within the scattering medium. As material with highly periodic charge distribution will scatter into well defined angles (so-called Bragg angles), various factors will tend to blur this discrete interference effect. Incoherent scatter can be separated from the coherent scatter by virtue of the fact that incoherent (i.e., Compton) scatter is diminished over the range of angles of importance for coherent scatter. Coherent scatter of X-rays which has the same photon energy as the illuminating X-ray and incoherent X-ray that has less energy than the illuminating beam. Figure 6.9 shows that these two scattering mechanisms distribute their photons over different solid angles relative to the illuminating beam.

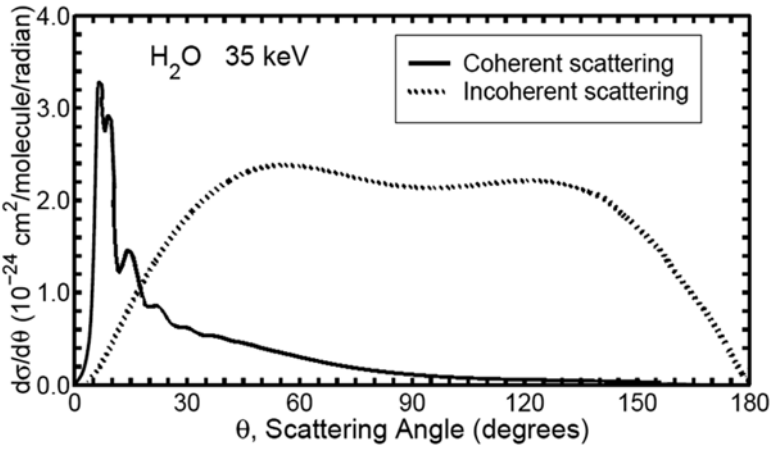

Fig. 6.9 Two mechanisms of X-ray scattering—coherent scatter has photon energy equal to that of the illuminating beam and is limited to approximately 0–15° from the illuminating beam, the actual angular distribution being dependant on the illuminating photon energy and the chemical bonds in the material. Incoherent (Compton) scatter has photon energy less than that of the illuminating beam. Its angular distribution is essentially constant over all but the acute and obtuse angles relative to the illuminating beam [42]

The scanner arrangement and subsequent processing of the detected signals is very similar to that of the fluorescence approach. The angular distribution of the coherent X-ray scatter is characteristic for different materials, especially for polymeric molecules such as collagen by virtue of the repetitive nature of the chemical bonds which have lengths of the order of an X-ray wavelength.

As illustrated in Fig. 6.10, the angle-dependant pattern of coherent X-ray scatter is characteristic for the material being illuminated. This pattern is called the momentum transfer curve (q).

It is generally generated by observing the scatter over a range of angles θ. Use of an energy-discriminating detector system can be used to reduce (or even eliminate) the need for multiple angles of view because $q=(1/\lambda)\sin(\theta/2)$ where λ is the X-ray photon wavelength and θ is the angle between the illuminating X-ray beam and the scatter direction can also be represented by $q=(E/12.3)\sin(\theta/2)$ where θ is fixed and the range in photon energy E (keV) is provided by the breakdown of the broad X-ray spectrum into a number of energy "bins". The energy discrimination could also help separate the Compton scatter from the coherent scatter.

This characteristic curve can be used to identify the material. Molecules with strings of repetitive chemical bonds include proteins (e.g., collagen) and synthetic materials such as often used in prosthetic devices made of synthetic polymer-based materials. The wavelength of the K_α X-ray emission of tungsten is 20 pm and of molybdenum is 71 pm, hence it is repetitive structures such as chemical bonds (e.g., C–C 154 pm, C–H 109 pm) that produce strong coherent scatter patterns. As shown in Fig. 6.11, collagen or protein, which contain strings of repetitive chemical bonds,

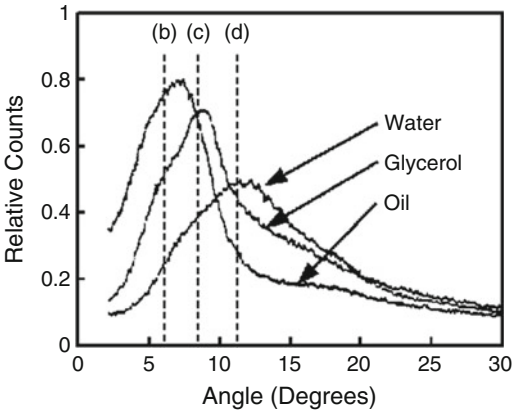

Fig. 6.10 X-ray scatter curves (more generally expressed as momentum transfer curves in which the X-ray wavelength is also accounted for) recorded from water, glycerol and oil which were illuminated by a pencil beam of 17.5 keV X-rays. Even though these curves were not corrected for the Compton scatter contribution, the different curves clearly allow discrimination of glycerol and oil which have very similar attenuation coefficients [43]

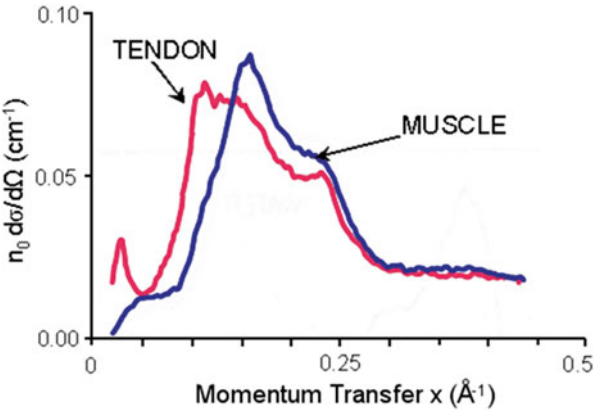

Fig. 6.11 Two momentum transfer curves—one from muscle and one from tendon. The greater collagen content of the tendon shifts the peak of the curve to the left (by a ratio of 0.47) and thus allows discrimination of muscle from tendon more readily than is possible by conventional coefficients of tendon and muscle [45]

differ distinctly in their scattering characteristics. Attenuation coefficients differ by a ratio of 0.02 of clinical kVp levels [44].

Different collagen types differ in their X-ray scattering characteristics such as occurs when the collagen is malformed in cancerous tissues, can be detected [46]. This is perhaps the most promising aspect of X-ray imaging with respect to the ability to detect and discriminate a variety of molecules directly with X-ray imaging. At this stage imaging of coherent X-ray scatter has been demonstrated only in test phantoms and isolated tissue specimens. Thus, the peak coherent scattering intensity for tendon was found to be approximately at a momentum transfer value of 10 Å^{-1} whereas skeletal muscle had a value of 17 Å^{-1} [45]. Unfortunately, due

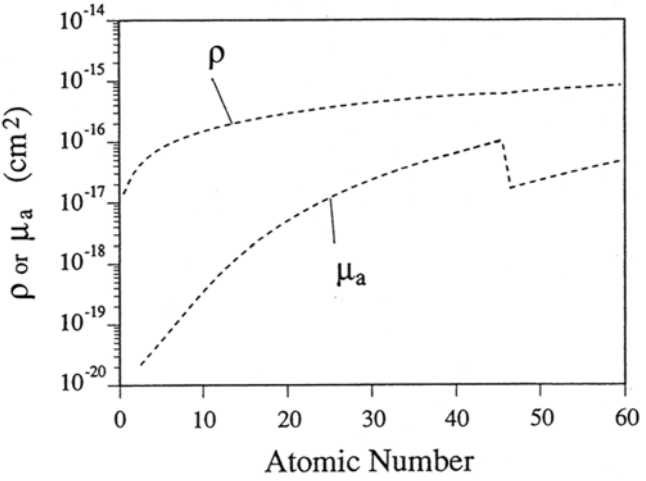

Fig. 6.12 Atomic X-ray phase shift (ρ) and absorption (μ) of 24 keV X-ray as a function of atomic number. The X-ray refractive index of matter $n = 1 - \delta - i \cdot \beta$, where δ is the phase shift related component and β the attenuation related component. The step-change in the absorption curve corresponds to the Kedge effect. Note that the ρ value is orders of magnitude higher than the μ value at any one atomic number, indicating that either the X-ray refractive properties of matter can either be exploited to provide higher contrast resolution or reduced radiation exposure [47]

to the low signal-to-noise of this imaging approach at the radiation levels tolerable in living animals, scatter-based CT is probably practical only when the accumulation of the molecules of interest are locally widespread (so that large voxels can be used to increase signal-to-noise) and concentrated. These conditions are most likely to be achieved with pathological accumulations of proteins such as in amyloid disease and when applied to imaging prosthetic device materials (especially when the μ of the prosthetic material is close to the μ of the surrounding tissues) in living small animals.

3.4 Phase Contrast Scanning

X-rays, like light, are refracted by matter, resulting in slight deviations of the X-ray beam from its initial straight-line trajectory. However, the refractive index of X-ray in water is very small, 7.4×10^{-7} [46]. Nonetheless, as shown in Fig. 6.12, the phase-shift component (δ) of the refractive index is orders of magnitude greater than the attenuation component (β) of the compound refractive index n: $n = 1 - \delta - i \cdot \beta$, where $i = \sqrt{-1}$. At 17.5 keV there is a 180° phase shift caused by 50 μm of tissue whereas the change in attenuation caused by 50 μm water is only 0.25 %.

The deflection of the X-ray results from a shift in the phase of the X-ray, which in turn is the result of the X-ray's interaction with the molecular structure of the

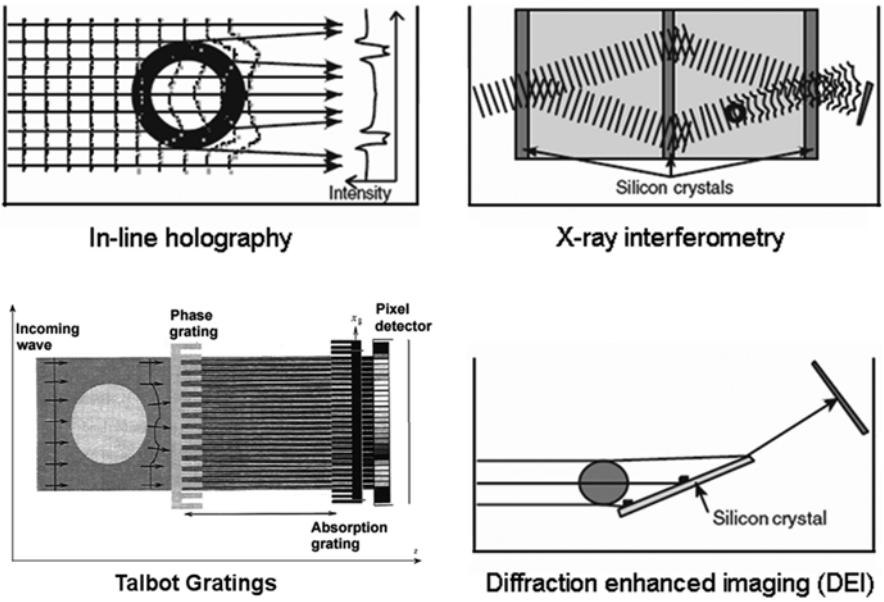

Fig. 6.13 Four methods of using the very slight deviation of X-ray due to change in refractive index of material along the path of an X-ray beam. This effect can also be detected quantitatively by virtue of the phase shift of the X-ray. *Left upper panel* shows how the slight deviation of the X-ray can be used by inverting the image data obtained in many views around the object [48]. This method involves placing the detector array at increasing distance away from the X-ray source. The change in local image brightness distribution can then be used to deduce the refraction at each location in the transmitted X-ray image. *Right upper panel* shows how use of the interference between the phase of a reference beam and the beam transmitted (and phase shifted) by an object can be used to generate a moiré pattern that can be "unravelled" to provide the local phase shift in the transmitted beam [49]. *Right lower panel* shows how a silicon crystal diffractometer can be used to directly measure the small angular deflection of individual X-ray beams by rocking the crystal [50]. *Left lower panel* shows how gratings can be used to generate "coded" X-ray images such that the distortion of that coded image by the phase shift can then be used to estimate the local refraction [51]

material. Phase shift cannot be measured directly with imaging systems because the frequency of approximately 10^{18}/s is much too fast. However, phase shift can be detected much more readily by virtue of interference patterns that can be generated by several means. This can be achieved by four methods as illustrated in Fig. 6.13 The first demonstration of this approach involved use of a parallel beam of narrow bandwidth monochromatic X-ray that is split into a reference beam which bypasses the specimen so that the interference pattern generated by mixing the reference beam and the beam passing through the specimen can be used to generate a map of the line integrals of phase shift at each angle of view.

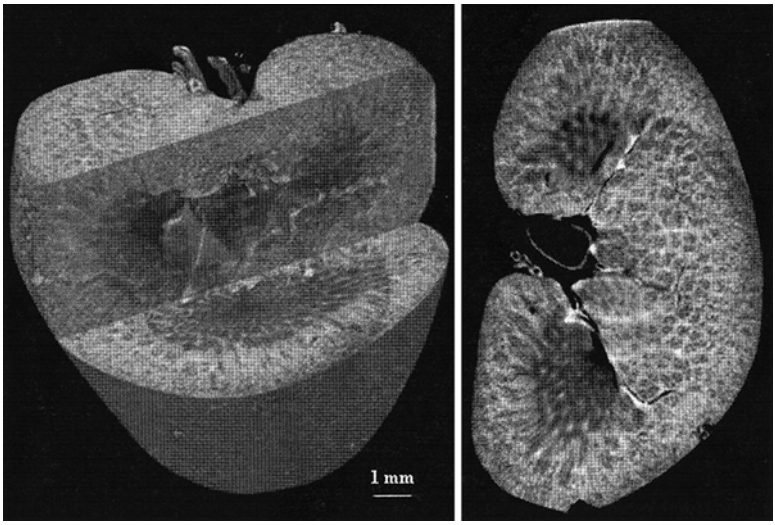

Fig. 6.14 Phase-contrast X-ray CT image of rat kidney obtained at 35 keV. Whole structures of renal cortex, medulla and pelvis were observed [59]

This method is very effective but would be technically very difficult to scale up for intact animals or large tissue specimens. Another method involves using a Bragg diffraction crystal which is used to differentiate the very slight angle between the refracted and transmitted X-ray beam. This also requires a parallel beam of very narrow bandwidth X-rays and involves rotating (rocking) the analyzer crystal over a range of angles to generate the multiple images of X-ray intensities at each angle of view about the specimen and for each pixel at that angle of view around the specimen.

The most practical method, and the method that most readily can accommodate a broad spectrum, non-parallel X-ray beam, involves use of multiple venetian blind-like gratings (for instance consisting of micrometer wide layers of gold on silicon) placed between the source and specimen (to convert the full area beam into a series of parallel linear sources) and between the specimen and the detector array (to analyze the transmitted X-ray image). The slight deflection of the X-rays due to the refraction in the specimen can be quantitatively detected by moving the analyzer grating across the image in steps that are fractions of the interval between adjacent slats in the source grid, much like the function of a vernier micrometer [52–58]. Figure 6.14 is an example of the high contrast that is achievable with this methodology [59].

The phase shift can be shown to be proportional to mass density for most biological materials, except when there is a high proportion of hydrogen present which has almost double the effect on phase due to its unique electron charge to Z ratio.

4 Technical Issues

If the X-ray source/detector system is stationary (which is always true if the X-ray source is a synchrotron) and the specimen is rotated, then this has the advantage that the heavy components of the scanner can be rigidly and accurately positioned with great precision. This works very well for in vitro specimens, but this generally involves use of a vertical rotation of the specimen (rather than horizontal) as this minimizes the gravity-induced movement or distortion of the specimen, relative to its axis of rotation. The living animal and its contents cannot be secured sufficiently rigidly to prevent motion as it rotates about a horizontal axis. While rotation of a living animal about a vertical axis minimizes this problem, maintenance of a vertical position over an extended period of time is not physiological for larger quadrupeds and may interfere with cardiopulmonary function, although it is generally acceptable for small rodents.

Rotation of the X-ray source/detector system about a horizontal axis ensures that the animal is in its physiological horizontal position, and thus it will not distort with angle of view. A technical requirement for this arrangement is that the generally heavy source/detector components have to rotate so that deviation from the ideal trajectory about the axis of rotation is smaller than the detector pixel size.

The duration of a complete scan depends on the X-ray flux that can be generated by the X-ray source as this governs the duration required to generate a projection image of sufficient quality (i.e., signal-to-noise and motion blurring) to be used for tomographic imaging and to a lesser extent the speed with which the necessary X-ray detection information can be recorded and transferred to an off-scanner memory. These factors vary greatly depending on the specific X-ray modality used to generate the tomographic image data.

If a synchrotron is used to generate the X-ray, then this very brilliant source can be used to generate a very narrow bandwidth monochromatic X-ray beam [60]. State-of-the-art synchrotrons can generate monochromatic X-ray beams of up to 100 keV photon energy. This beam can be sufficiently intense that the main factor in the duration of the scan is the time required for image recording and transfer to a memory. The method is also limited in the width and height of the field-of-view that is exposed by X-ray. If a bench-top roentgen X-ray source is used then the divergence of the X-ray beam can be used to expose a large field-of-view. However, use of a point-source X-ray the cone-beam geometry introduces some mathematical complications which may limit the resolution of the tomographic images at the upper and lower axial extents of the specimen. This effect is largely overcome by combining a translation with the rotation trajectory, most commonly achieved by either a “step and shoot”, in which the animal is advanced one axial field-of-view length after completing each sequential scan. The helical CT scanning mode, in which the specimen is translated along the axis of rotation during the scan, allows coverage over a long axial extent but this reduces the temporal resolution of the tomographic image data set.

5 Radiation Exposure

X-ray exposure results in direct disruption of chemical bonds and generates super radicals which in turn damage near by molecules, the DNA being of particular concern as this affects cell reproduction and its control [11, 61–63]. The number of photons absorbed in a voxel determines the noise in the CT image (i.e., the variation in grey scale from voxel-to-voxel differs even though they represent the same material). For a given exposure of the subject the number of photons interacting within a voxel decreases in direct relationship with the voxel volume. This, combined with some other consequences of the scanning process, results in the radiation exposure to the subject having to increase with the fourth power of the voxel side dimension if the noise per voxel is to remain unchanged [10]. Consequently, the higher the spatial resolution the higher the radiation exposure. The LD50/30 dose (following which 50 % animals die within 30 days) for small animals is somewhat less than eight Grey. A scan generating $(65\ \mu m)^3$ voxels would involve five Grey exposure [63], tolerable in a terminal study, but not in the first of several sequential scans of the same animal in a longitudinal study.

6 Conclusions

Molecular structure, in terms of elemental components (either as part of the molecule or as a synthetically labeled molecule) and certain chemical bonds (especially if they repeat along the length of long molecules) can be detected and somewhat characterized by X-ray micro-CT imaging methods. Conventional, attenuation-based, micro-CT often plays an integral part of non-attenuation-based micro-CT, because it provides the high spatial resolution confines of organs and physiological spaces in which molecules of interest tend to be confined, excluded or washout from and it provides the spatial distribution of X-ray attenuation that is needed to correct the non-attenuation-based micro-CT image data for attenuation of the X-ray used for image generation using the non-attenuation aspect.

Although the attenuation aspect and the other modalities can readily be individually integrated into a single micro-CT scanner, so that time is saved and more importantly that registration of the two different images is greatly facilitated, no one micro-CT combination is likely to meet all needs.

A major strength of small-animal-CT is that it provides clinically relevant image information of pathophysiology, both at scale-equivalent of clinical CT scan resolution. Micro-CT can provide image data at resolutions much higher than achievable with clinical scanners so that deeper insights into pathophysiological processes can be expected. Another strength of small-animal-CT is that it provides a test-bed for development and evaluation of novel, clinically applicable, X-ray imaging approaches.

Acknowledgments Dr. Ritman's micro-CT work was supported in part by National Institutes of Health Grant, EB000305.

References

1. Elliot JC, Dover SD (1982) X-ray tomography. J Microsc 162(2): 211–213.
2. Flannery BP, Deckman HW, Roberg WG et al (1987) Three dimensional x-ray microtomography. Science 237: 1439–1444.
3. Sasov A (1987) Non-destructive 3D imaging of the objects internal microstructure by microCT attachment for SEM. J Microsc 147: 169–192.
4. Feldkamp LA, Davis LC, Kress JW (1984) Practical cone-beam algorithm. J Opt Soc Am A1: 162–191.
5. Ritman EL (2014) Cone beam micro-CT for small-animal research. IN: Shaw C (ed): Cone Beam Computed Tomography. Chapter 12, pp171–179. CRC Press (Taylor and Francis).
6. Paulus MJ, Geason SS, Kennel SJ et al (2000) High resolution x-ray tomography: an emerging tool for small animal cancer research. Neoplasia 2: 36–45.
7. Holdsworth DW, Thornton MM (2002) Micro-CT in small animal and specimen imaging. Trends Biotech 20(8): S34–39.
8. Ritman EL (2004) Micro-computed tomography: Current status and developments. Annual Rev Biomed Eng 6: 185–208.
9. Badea CT, Drangova M, Holdsworth DW et al (2008) In vivo small-animal imaging using micro-CT and digital subtraction angiography. Physics in Med Biol 53: R319–R350.
10. Brooks RA, Di Chiro G (1976) Statistical limitations in x-ray reconstructive tomography. Med Phys 3: 237–240.
11. Ford NL, Thornton MM, Holdsworth DW (2003) Fundamental image quality limits for micro-computed tomography in small animals. Med Phys 30: 2869–2898.
12. Faulkner K, Moores BM (1984) Noise and contrast detection in computed tomography images. Phys Med Biol 29: 329–339.
13. Grodzins L (1983) Optimum energies for x-ray transmission tomography of small samples. Nucl Instrum Methods 206: 541–545.
14. Drangova M, Ford NL, Detombe SA et al (2007) Fast retrospectively gated quantitative four-dimensional (4D) cardiac microcomputed tomography imaging of free-breathing mice. Invest Radiol 42: 85–94.
15. Badea CT, Hedlund LW, Johnson GA et al (2004) Micro-CT with respiratory and cardiac gating. Med Phys 31: 3324–3329.
16. Cowan CM, Aghaloo T, Chou YF et al (2007) Micro-CT evaluation of three dimensional mineralization in response to BMP-2 doses in vitro and in critical sized rat calvarial defects. Tissue Eng 13: 501–512.
17. Borah B, Ritman EL, Dufresne TE et al (2005) The effect of residronate on bone mineralization as measured by micro-computed tomography with synchrotron radiation: Correlation to histomorphometric indices of turnover. Bone 37(1): 1–9.
18. Kinney JH, Lane NE, Haupt DL (1995) In vivo three dimensional microscopy of trabecular bone. J Bone Miner Res 10(2): 264–270.
19. Lee J, Beighley P, Ritman E et al (2007) Automatic segmentation of 3D micro-CT coronary vascular images. Med Image Analysis 11(6): 630–647.
20. Op den Buijs J, Bajzer Z, Ritman EL (2006) Branching morphology of the rat hepatic portal vein tree: A micro-CT study. Ann Biomed Eng 34(9): 1420–1428.
21. Nordsletten D, Blackett S, Bentley MD et al (2006) Structural morphology of renal vasculature. Am J Physiol: Heart Circ Physiol 291: H296–H309.
22. Badea CT, Hedlund LW, Mackel JF et al (2007b) Cardiac micro-computed tomography for morphological and functional phenotyping of muscle LIM protein null mice. Mol Imaging 6: 261–268.
23. Kantor B, Jorgensen SM, Lund PE et al (2002) Cryostatic micro-computed tomography imaging of arterial wall perfusion. Scanning 24: 186–190.
24. Schmermund A, Bell MR, Lerman LO et al (1997) Quantitative evaluation of regional myocardial perfusion using fast x-ray computed tomography. Herz 22(1): 29–39.

25. Crone C (1963) The permeability of capillaries in various organs as determined by the use of the indicator diffusion method. Acta Physiol Scand 58: 292–305.
26. Cann CE, Gamsu G, Birnbert FA et al (1982) Quantification of calcium in solitary pulmonary nodules using single and dual-energy CT. Radiology 145: 493–496.
27. Herman GT (1980) Image Reconstruction from Projections: The Fundamentals of Computerized Tomography. Academic Press, New York.
28. Dilmanian FA (1992) Computed tomography with monochromatic x-rays. Am J Physiol Imaging 7(3-4): 175–179.
29. Bonse U, Johnson Q, Nicols M et al (1986) High resolution tomography with chemical specificity. Nucl Instrum Methods Phys Res A 246(1-3): 644–648.
30. Ross PA (1928) A new method of spectroscopy for faint x-radiations. J Opt Soc Am 16: 433–437.
31. Spanne P (1989) X-ray energy optimization in the computed tomography. Phys Med Biol 34(6): 679–690.
32. http://physics.nist.gov/PhysRefData/XrayMassCoef/
33. Le Duc et al (1999) ESRF HighLights. http://www.esrf.eu/UsersAndScience?Publications/Highlights/1999/life-sci/broncho.html
34. Butzer JS, Butler APH, Butler PH et al (2008) Image and Vision Comput New Zealand, pgs. 1-6, doi:10.1109/IVNZ.2008.4762080.
35. Anderson NG, Butler AP, Scott N et al (2009) Medipix imaging – evaluation of data sets with PCA. Eur Radiol B-393: S228.
36. Panetta D, Belcari N, Baldazzi G et al (2007) Characterization of a high-resolution CT scanner prototype for small animals. Nuovo Cimento B 122: 739–747.
37. Firsching M, Butler AP, Scott N et al (2009) Contrast agent recognition in small animal CT using the Medipix2 detector. Nucl Inst Meth A 607: 179–182.
38. Gleason SS, Sari-Sarraf H, Paulus MJ et al (1999) Reconstruction of multi-energy x-ray computed tomography images of laboratory mice. IEEE Trans Nucl Sci 46: 1081–1086.
39. Takeda T, Yuasa T, Hoshino A et al (1997) Fluorescent x-ray computed tomography to visualize specific material distribution. IN: Developments in X-ray Tomography. Proc SPIE 3149: 160–172.
40. Takeda T, Tu Q, Yashiro T et al (1999) Human thyroid specimen imaging by fluorescent x-ray computed tomography with synchrotron radiation. Proc SPIE 3772: 258–267.
41. Cui CW, Jorgensen SM, Eaker DR et al (2008) Coherent x-ray scattering for discriminating biocompatible materials in tissue scaffolds. Proc SPIE: Development X-ray Tomogr VI 7078: 70781S-1-70781S-10.
42. Johns PC, Leclair RJ, Wismayer MP (2002) Medical x-ray imaging with scattered photons. IN: Opto-Canada: SPIE Regional Meeting on Optoelectronics, Photonics, and Imaging, Proc SPIE TDO1:355–357.
43. Grant JA, Morgan MJ, Davis JR et al (1993) X-ray diffraction microtomography. Meas Sci Technol 4: 83–87.
44. Pelc JS (2001) Volume rendering of tendon-bone relationships using unenhanced CT. Am J Roentgenol 176: 973–977.
45. Kosanetzky J, Knoerr B, Harding G et al (1987) X-ray diffraction measurements of some plastic materials and body tissues. Med Phys 14(4): 526–532.
46. Lewis RA, Hall CJ, Hufton AP et al (2003) X-ray refraction effects: application to the imaging of biological tissues. British J Radiol 76: 301–308.
47. Momose A, Fukuda J (1995) Phase-contrast radiographs of nonstained rat cerebellar specimen. Med Phys 22: 375–379.
48. Cloetens P, Ludwig W, van Dyck D, et al (1999) Quantitative phase tomography by holographic reconstruction. Proc SPIE 3772: 279–290.
49. Beckman F, Bonse U, Busck F et al (1997) X-ray microtomography (μCT) using phase contrast for the investigation of organic matter. J Comput Assist Tomogr 21: 539–553.
50. Chapman D, Thomlinson W, Johnston RE et al (1997) Diffraction enhanced x-ray imaging. Phys Med Biol 42: 20115–20125.

51. Momose A, Yashiro W, Takeda Y et al (2008) Sensitivity of x-ray phase tomography based on Talbot and Talbot-Lau interferometer. Proc SPIE 7078: 707811-1-707811-8.
52. Nugent KA, Gureyev TE, Cookson DJ et al (1996) Quantitative phase imaging using hard x-rays. Phys Rev Letters 77: 2961–2964.
53. Pfeiffer F, Weitkamp T, Bunk O et al (2006) Phase retrieval and differential phase-contrast imaging with low brilliance x-ray sources. Nature Physics 2: 256–261.
54. Wilkins SW, Gureyev TE, Gao D et al (1996) Phase-contrast imaging using polychromatic hard x-rays. Nature 384: 335–338.
55. Donnelly EF, Price RR, Lewis KG et al (2007) Polychromatic phase-contrast computed tomography. Med Phys 34: 3165.
56. Olivo A, Speller R (2007) Polychromatic phase contrast imaging as a basic step towards a widespread application of the technique. Nucl Instrum Methods A580: 0179–1082.
57. Olivo A, Speller R (2007) A coded-aperture technique allowing x-ray phase contrast imaging with laboratory sources. Appl Phys Lett 91: 074106.
58. Zhou SA, Brahme A (2008) Development of phase-contrast x-ray imaging techniques and potential medical applications. Physica Medica 24: 129–148.
59. Takeda T, Wu J, Yoneyama A et al (2004) SR biomedical imaging with phase-contrast and fluorescent x-ray CT. Proc SPIE 5535: 380–391.
60. Dilmanian FA, Garrett RF, Thomlinson WC et al (1990) Multiple energy computed tomography for neuroradiology with monochromatic-rays from the National Synchrotron Light Source. Physica Medica VI, n.3-4: 301–307.
61. Bond VP, Robertson JS, (1957) Vertebrate radiobiology (lethal actions and associated effects). Annu Rev Nucl Sci 7: 135–62.
62. Boone JM, Velazquez O, Cherry SR (2004) Small-animal x-ray dose from micro-CT. Mol Imaging 3: 149–158.
63. Carlson SK, Classic KL, Bender CE et al (2007) Small animal absorbed radiation dose from micro-computed tomography imaging. Mol Imaging Biol 9: 78–82.

Chapter 7
Small-Animal MRI Instrumentation

Andrew M. Blamire

1 Introduction

Magnetic resonance imaging (MRI) emerged in the 1970s from the laboratories of physical scientists where the basic phenomenon of nuclear magnetic resonance (NMR) was being investigated, and has rapidly expanded to permeate most areas of biological and clinical research. MRI is undoubtedly the most versatile of all the non-invasive imaging modalities. The MRI signal originates from the nucleus of the hydrogen atom (the proton) and while the intrinsic contrast of the MRI image reflects differences in proton density within the tissue, selection of appropriate signal preparation schemes allows image intensity to be linked to other important processes such as blood flow (e.g. bulk flow for angiography or micro flow for tissue perfusion), Brownian water motion (e.g. diffusion imaging to assess tissue microstructure), tissue oxygenation (for functional information), etc. Further, the local chemical environment of the nucleus modulates the MRI signal frequency allowing the identification of molecular groups using the allied technique of MRI spectroscopy (MRS) allowing metabolic measurements. No other imaging modality can rival this inherent flexibility. For all of these MRI measurement, the scanning instrumentation remains essentially constant, with selection of the contrast type determined by the specific imaging sequence alone. In this chapter we describe in detail the basic instrumentation required for small animal MRI.

2 Background to Magnetic Resonance

In this section we give a brief overview of the fundamentals of the MRI experiment as a background to describing the design and selection of MRI instrumentation.

A.M. Blamire (✉)
Newcastle Magnetic Resonance Centre, Newcastle University, Newcastle upon Tyne, UK
e-mail: andrew.blamire@newcastle.ac.uk

H. Zaidi (ed.), *Molecular Imaging of Small Animals: Instrumentation and Applications*,
DOI 10.1007/978-1-4939-0894-3_7,

2.1 The Fundamentals of MRI Signal Generation

A complete description of the MRI experiment is beyond the scope or purpose of this chapter and has been described in many good texts on that subject [1, 2]. However, in order to understand the design criteria and selection of MRI instrumentation it is necessary to first introduce some basic concepts.

MRI is based on the fundamental physical property of some nuclei known as nuclear magnetic resonance (NMR) which was first shown experimentally in 1945, and for which Felix Bloch and Edward Purcell shared the 1952 Nobel Prize for Physics. Key nuclei (e.g. ^{1}H, ^{13}C, ^{31}P, ^{23}Na, ^{19}F, ^{7}Li) possess a property described by quantum mechanics as *spin* (which equates well to a classical description of the nucleus rotating on its axis), and which leads to a property called the magnetic moment (μ). (Classically a rotating charged object can be decomposed into a series of circulating charged sub-particles which constitute an electric current, which has an associated magnetic field.) When placed in a strong uniform magnetic field (denoted B_o and by convention aligned along the z axis) these nuclei polarize between several discrete energy levels (the number of which is nucleus specific). In the case of conventional MRI the nucleus of interest is the proton which has two discrete (quantized) energy levels.

The energy separation (ΔE) for a two level system is given by

$$\Delta \mathrm{E} = \gamma h \mathrm{B}_{\mathrm{o}} / 2\pi \tag{7.1}$$

where γ is a nucleus specific constant known as the magnetogyric ratio and h is Planks constant. In the NMR experiment this energy is imparted to the nuclei via an applied electromagnetic wave of angular frequency ω which has associated energy given by

$$\mathrm{E} = h\omega / 2\pi \tag{7.2}$$

For MRI the frequency of this electromagnetic wave is within the radio-frequency (RF) band. For resonant absorption of energy by the nuclei we can equate Eqs. (7.1) and (7.2) to obtain the expression

$$\omega_{\mathrm{o}} = \gamma \mathrm{B}_{\mathrm{o}} \tag{7.3}$$

which describes the required RF frequency for nuclear resonance at a given magnetic field strength. This frequency ω_o is known as the *Larmor* frequency.

On a macroscopic scale the effect of polarizing the individual magnetic moments is to create a net *magnetization* along the axis of the magnet. A pulse of RF energy applied to the system causes a rotation of the magnetization vector away from the z axis towards the x–y plane (Fig. 7.1). The precise angle (α) through which the magnetization is rotated is known as the *flip angle* and is determined by the strength of the magnetic component of the applied RF pulse (B_1) and the pulse duration t_p.

$$\alpha = \int_0^{t_p} \gamma B_1(t')\, dt' \tag{7.4}$$

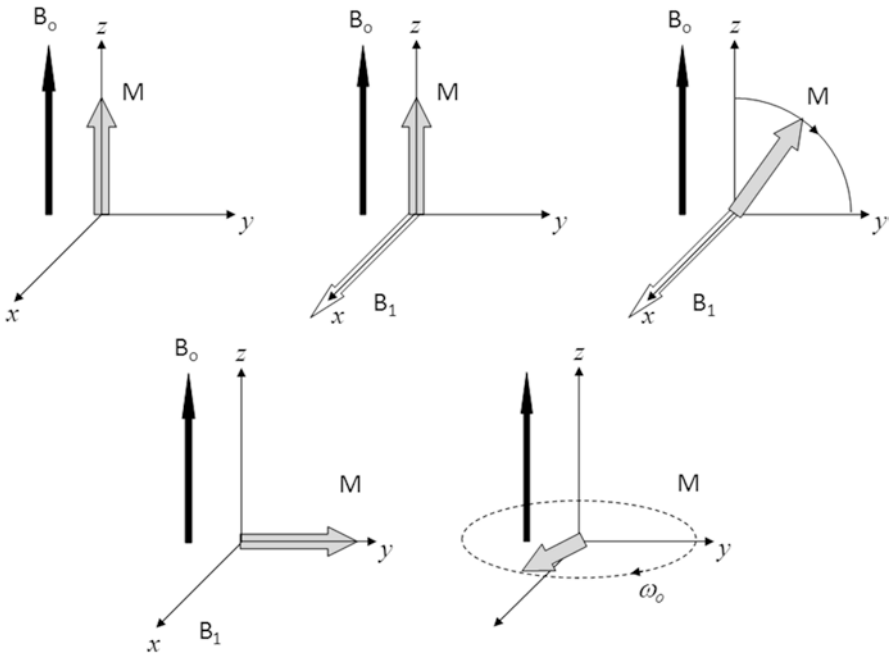

Fig. 7.1 The classical description of the nuclear magnetic resonance (NMR) experiment. In the presence of a polarizing field $B_o(z)$ the sample has a net magnetization M. The magnetic field component (B_{1x}) of an applied pulse of RF energy causes the magnetization to rotate into the transverse (*xy*) plane. The main field exerts a torque on the transverse magnetization causing it to precess in the *xy* plane where it can induce a current in a suitably placed receiver coil

The interaction between the main magnetic field and the magnetization component in the *x*–*y* plane is a torque which causes the magnetization to precess about the axis of the main field at the Larmor frequency. This precession can be detected by electromagnetic induction in a suitably placed detector coil.

2.2 Properties of the MRI Signal

Once the MRI signal has been excited, two main processes take over to return the nuclei to their equilibrium state. These are known as *relaxation* and act to destroy the observable magnetic resonance signal, and restore the original polarization of the nuclei in the applied magnetic field.

2.2.1 Transverse, T_2 or Spin–Spin Relaxation

Following excitation by an RF pulse the transverse component of magnetization precesses under the action of the main applied magnetic field. At the atomic level fluctuations occur in the local environment of each nucleus due to interactions

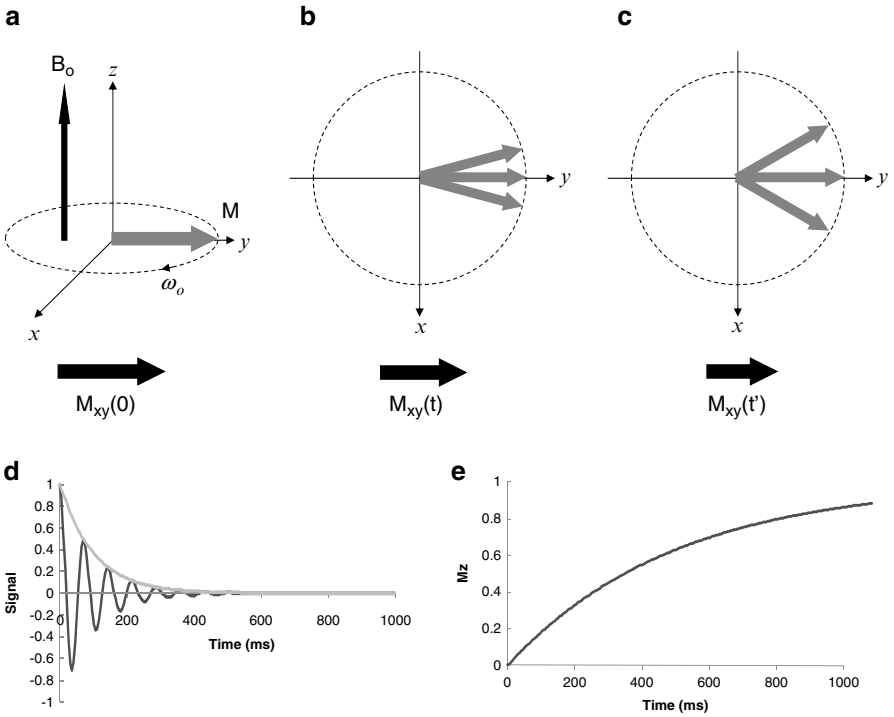

Fig. 7.2 Illustration of the precession of magnetization and relaxation processes. (**a**–**d**) Interactions between individual nuclei (spin–spin interactions) causes loss of the coherent precession within the net magnetization leading to the decay of the M_{xy} component of magnetization, (**e**) recovery of the longitudinal magnetization M_z due to spin–lattice or T_1 relaxation

between closely located nuclei (termed spin–spin interactions), such that energy is transferred from nuclei to nuclei. These fluctuations cause loss of coherence in the precession of individual nuclei and the observable magnetization (and hence the detected signal) decays or "relaxes" exponentially (Fig. 7.2) with a time constant T_2.

$$M_{xy}(t) = M_{xy}(0)\exp(-t/T_2) \tag{7.5}$$

As the strength of the detected MRI signal is dependent on the total macroscopic magnetization precessing within the *x*–*y* plane, the detected signal also decays with the same time constant.

2.2.2 Longitudinal, T_1 or Spin–Lattice Relaxation

The second relaxation process (termed longitudinal relaxation) determines the rate at which the nuclei return to their equilibrium longitudinal polarization aligned back along the z axis with the main static field. During longitudinal relaxation, energy is

lost from the nuclei to the tissue with a second exponential time constant T_1 (Fig. 7.2e). If the applied RF pulse is calibrated to impart a 90° flip angle the recovery of the magnetization to equilibrium is described by:

$$M_z(t) = M_z(0)\left\{1 - \exp\left(-t / T_1\right)\right\} \tag{7.6}$$

The T_1 relaxation process is always slower than the T_2 decay of transverse magnetization, and in vivo, the observable signal disappears some time before the nuclei have returned to their equilibrium polarization (Fig. 7.2d, e). The processes driving relaxation at the tissue level are determined by the precise environment experienced by each proton. Differing tissue compartments therefore have different relaxation times which can be exploited to generate contrast in MRI images [2].

2.3 Localizing the Origin of the NMR Signal: MRI

In 1973 Paul Lauterbur published pioneering data demonstrating the potential for using the nuclear magnetic resonance phenomenon to generate images [3] and for which he shared the 2004 Nobel Prize for Medicine and Physiology with Peter Mansfield. MRI is based around a simple extension to Eq. (7.3). If a linear magnetic field gradient (G_r) is superimposed on the main static field B_o, the frequency of the resonant condition becomes dependent on the location in space, i.e.

$$\omega(r) = \gamma\left(B_o + G_r r\right) \tag{7.7}$$

as illustrated in Fig. 7.3. By applying the field gradient simultaneously with the applied RF pulse Eq. (7.7) indicates that the pulse will only (selectively) excite a signal from the region of sample with resonant frequency matching the bandwidth properties of the applied pulse. Alternatively by applying a field gradient during the time when the signal is being sampled a distribution of frequencies will be present in proportion to the distribution of nuclei in space, which can be determined by the mathematical construct of the Fourier transformation [4].

2.4 The Basic Elements of MRI Instrumentation

From the above description it is possible to identify the main components of the MRI instrumentation, these being

1. a uniform static magnetic field,
2. a RF system arranged to efficiently irradiate the sample with radio-waves,
3. a system to transiently impose a linear field gradient to localize the MRI signal,
4. a RF system to detect, demodulate and sample the excited MRI signal, and
5. a reconstruction and display system.

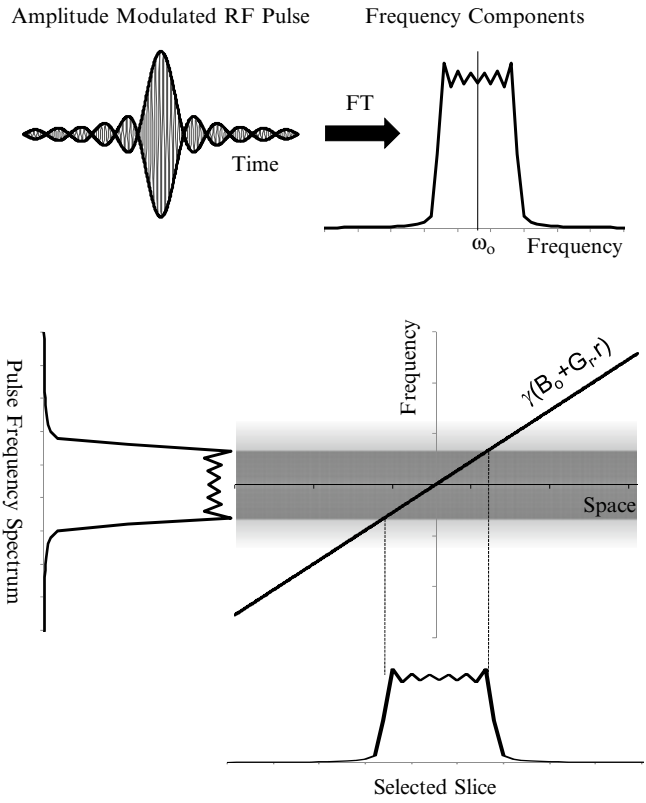

Fig. 7.3 The relationship between gradient field strength, MRI resonant frequency and the principle of slice selection. An amplitude modulated pulse of RF waves at the Larmor frequency (ω_o) has an effective set of frequency components given by the Fourier transform (FT). When applied in the presence of a field gradient G_r, the frequency spectrum of the pulse matches the resonant condition for only a small section of the object, exciting a signal from a selected slice

3 The MRI Scanner

A schematic diagram of the entire MRI instrument is shown in Fig. 7.4. In this section we consider the design criteria and selection of each of these components.

3.1 Magnet

The largest single component of the MRI scanner is the magnet system which generates the applied field B_o. Magnet design must be such that the field is highly uniform (homogeneous) and temporally extremely stable. It is convenient to describe these design specifications by considering the spatial frequency variation and

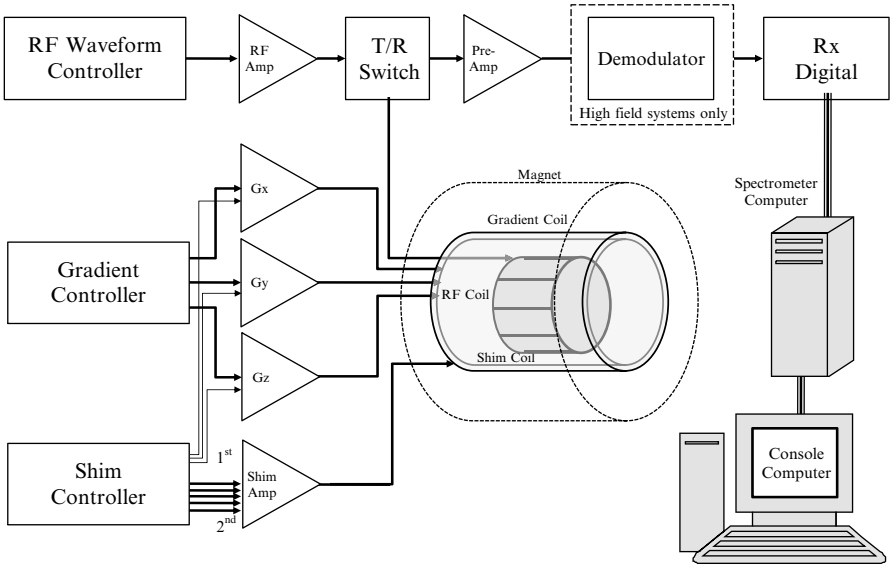

Fig. 7.4 Schematic diagram of the MRI scanner instrumentation

frequency stability they impart to an extended sample placed within the MRI scanner. Typically basic magnet homogeneity must be better than 0.1 parts per million (ppm) and stability must be of the order of a few Hz per hour (equating to a field drift of 1 part in 10^8 or better).

Examples of typical commercially available small-animal magnets are shown in Fig. 7.5, together with schematic illustrations of the internal design in Fig. 7.6. The majority of magnets for in vivo imaging are based around a similar design using a cryogenically cooled, superconducting, solenoid-type coil to provide a powerful and stable magnetic field. The solenoid itself is generally constructed from a niobium/titanium or niobium/tin alloy which becomes superconducting (the wire resistance is zero) below a critical temperature (T_c, 10 K for Nb/Ti, 18 K for Nb/Sn). The solenoid is suspended in a bath of liquid helium (boiling point 4.2 K). Once the main current has been established the ends of the solenoid can be joined via a superconducting switch to form a continuous loop, and the power-supply can be removed. The homogeneity of the magnetic field can be adjusted by passing current through additional field profile coils (the cryoshim coils) within the cryostat until the measured field is as uniform as possible. Slight residual resistance causes the field to decay with time, but this downward field drift is less than 1 part in 10^8 per hour. To maintain the superconducting state the solenoid is carefully thermally isolated from the rest of the magnet structure to minimize helium boil-off. Thermal isolation is enhanced by vacuum vessels and heat-shields. In traditional magnet designs a liquid nitrogen (boiling point, 77 K) vessel is also used (Fig. 7.6, lower left) as an additional heat shield for the helium bath. Boil-off of the relatively inexpensive liquid nitrogen is sacrificed in a bid to minimize helium boil-off. In this design, both

Fig. 7.5 Typical commercially available small animal MRI magnet systems. *Left*: A cryogenic unshielded ultra-high field 16.4 T small animal MRI magnet. For scale, the free bore diameter is 260 mm (courtesy of Varian Inc). *Right*: A 7 T, 300 mm bore ultra-shielded magnet with pulse-tube cryocooler for minimal helium boil-off (courtesy of Bruker Biospin Ltd)

cryostats must be refilled with cryogens on a frequent basis (weeks to months). More recent magnet designs incorporate a refrigeration system (the "cold head" and associated components, based on the pulse-tube refrigeration method of Gifford and Longsworth [5]) to re-liquify helium vapor within the magnet, minimizing boil-off (Fig. 7.6, lower right) and reducing cryogen costs, but at the expense of refrigeration costs. All magnet systems must be connected to a *quench pipe* to allow safe release of cryogen gas in the event of magnet failure when rapid and uncontrolled boil-off of cryogens can occur.

3.1.1 Selection of Magnetic Field Strength

In Sect. 2.1 we described that the proton nucleus has two energy levels in the applied magnetic field. From a macroscopic perspective the many nuclei within a sample are distributed between these two levels and, on average, the difference in the number of nuclei (Δn) which populate each of these energy levels can be described by

$$\Delta n = n_{\alpha} - n_{\beta} = N\Delta E / 2KT \tag{7.8}$$

where N is the total number of nuclei, n_{α} and n_{β} are the number of nuclei in each of the two levels, K is the Boltzmann constant and T is the sample temperature. Equation (7.8) shows that this distribution is driven by the thermal energy of the nuclei. Combining Eqs. (7.1) and (7.8) we find that the fractional difference in occupancy of the energy levels is

$$\frac{\Delta n}{N} = \frac{\gamma h B_o}{4\pi KT} \tag{7.9}$$

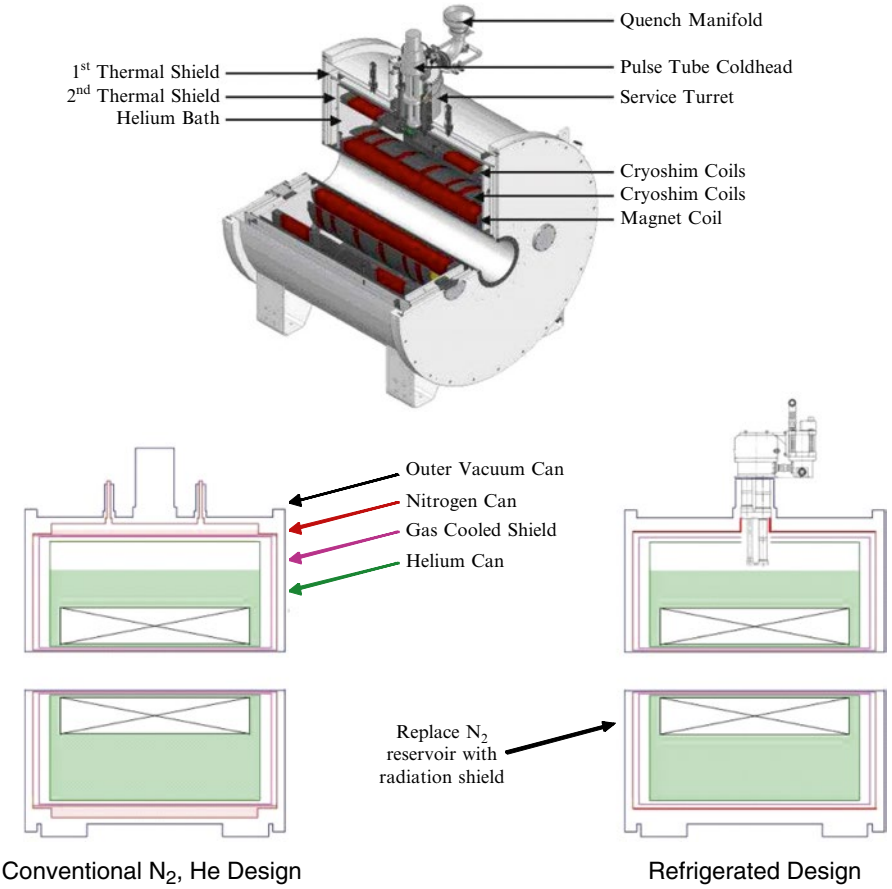

Fig. 7.6 Schematic diagrams of the internal structure of the cryogenic and cryocooled magnet systems. The main magnetic field is produced by the *Magnet Coil* with additional field from the *Cryoshim Coils* which are adjusted to obtain the optimum magnetic field uniformity. *Left*: A cryogenic magnet design where liquid nitrogen and helium boil-off requires regular re-filling of the magnet dewars to maintain superconductivity. *Right*: A cryocooled magnet design where the nitrogen vessel is no longer necessary and helium vapor is recondensed back into the dewar leading to minimal boil-off in normal operation. The heat exchanger and chiller system required to cool the "cold head" are not shown in this illustration (courtesy of Varian Inc)

The observable signal strength depends directly on this excess difference in occupancy between the energy levels which at achievable field strengths of between 0.1 and 10.0 T is only 1 in 2,870,000–28,700 nuclei. Thus the basic nuclear magnetic resonance phenomenon is actually inherently insensitive.

From Eq. (7.9) it is clear that there are two options to obtain a stronger MRI signal; operate at the highest possible magnetic field strength B_o, or decrease the sample temperature. This second approach is not compatible with in vivo imaging where core body temperature must be maintained within physiological limits, which

Table 7.1 Typical field strengths used for in vivo MRI investigation together with proton frequency ($\gamma(^1H) = 4.25 \times 10^7$ Hz/T) and available bore sizes (maximum size of object)

Field strength (T)	Proton frequency (MHz)	Typical bore size (mm)	Purpose
1.5	63.75	600	Clinical imaging
3.0	127.5	600	Human/pre-clinical imaging
4.7	200.0	160–400	Human/pre-clinical imaging
7.0	300.0	160–400	Human/pre-clinical imaging
9.4	400.0	160–400	Human/pre-clinical imaging
11.7	500.0	160–400	Pre-clinical imaging

leaves field strength as the only viable option. We will discuss advanced methods to generate hyperpolarization in Sect. 4.2. Therefore in general, higher field strength equates with increased signal to noise ratio in the MRI image and the highest possible field strength (within economic limits) is strived for. Table 7.1 lists typical field strengths used for in vivo imaging and the respective proton frequencies.

3.1.2 Siting-Shielding, Filtering, Fringe Field

Since the signal detection system is a high sensitivity RF receiver, shielding from stray RF signal sources in the local environment is critical for obtaining maximum sensitivity and eliminating image artifacts. Radio-frequency signals can penetrate down the scanner bore where they are detected by the system RF coil and enter the scanner via the signal pathway. The degree of penetration of RF noise along the bore depends on the dimensions (bore radius to magnet length ratio) with the bore itself acting as a waveguide providing some signal attenuation. To eliminate all extraneous noise sources the magnet is normally sited within, and earthed to a Faraday cage. All electrical connections to and from the magnet (e.g. scanner hardware connections, or user equipment such as animal monitoring) pass through electronic filters in the Faraday cage wall to remove signal within any of the required operating frequency ranges of the system. An alternative to a full Faraday cage is to electrically "seal" the ends of the magnet bore with metal plates once the sample is positioned with the magnet, essentially creating a Faraday cage from the scanner bore and the end plates (Fig. 7.7).

The polarizing field present at the magnet isocentre is many thousands of times the earth's field (the earth's field is typically 0.05 mT) and decays with distance from the magnet structure. This *fringe field* extends into the scanner laboratory and poses several hazards to MRI scientists and must be carefully controlled [6], (Fig. 7.8). The largest hazard is to staff with active implanted medical devices such as cardiac pacemakers. These devices can be activated or damaged by interaction with the magnet fringe field, with potentially life threatening consequences. A safe working zone outside the 0.5 mT fringe field line must be established and inside which persons with such devices must not be allowed. Careful screening of staff can

Fig. 7.7 Illustration showing a magnet with integral Faraday cage (courtesy of Bruker Biospin Ltd)

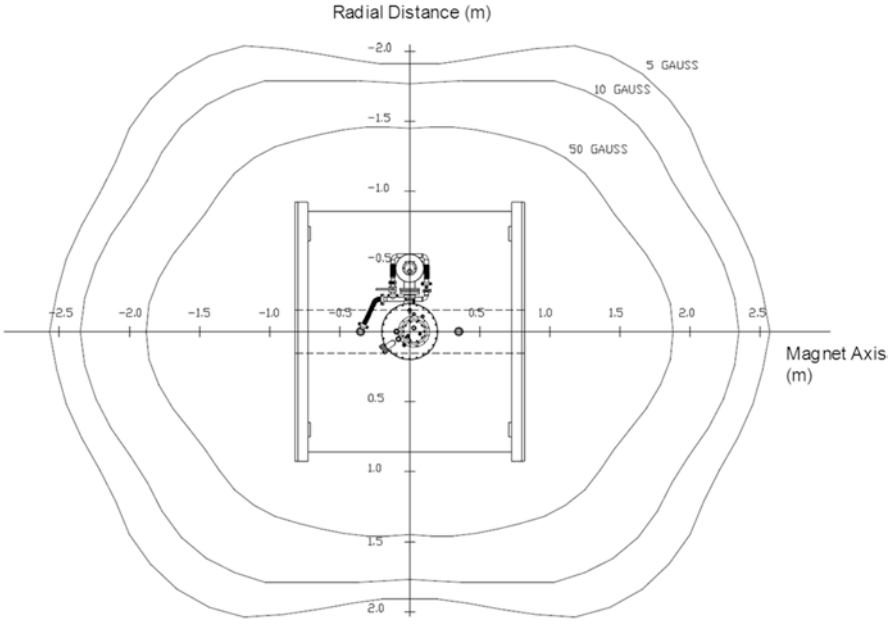

Fig. 7.8 Fringe field plot for a typical self-shielded small animal MRI scanner with 210 mm bore operating at 9.4 T (courtesy of Varian Inc)

eliminate risk. The fringe field however also exerts an attractive force on any ferromagnetic items in the vicinity. Loose metal objects can be attracted to the scanner with such force that they become projectiles, injuring staff and causing major damage to the magnet structure. Again, careful design and monitoring of the scanner environment is crucial and can minimize this risk. Typically the requirements for a Faraday cage and safe working zone can be combined such that the 0.5 mT line is contained entirely within the Faraday cage.

Current magnet systems for small animal studies incorporate a self-shielding magnet design, whereby a second set of coil windings are positioned within the magnet cryostat. These are counter-wound to the main coils with a density of turns such that the fringe field from the primary windings is partially counteracted by the field from these screening windings. This design creates a compact installation footprint for the system. As an alternative to active self-shielding passive shielding can be incorporated by designing a steel enclosure around the magnet which contain the magnetic field.

3.2 Gradient System

In Sect. 2.3, we described how the localization of the MRI signal is performed using time-varying linear field gradients which are modulated during the MRI sequence. These fields are created by the system gradient coils. The desired gradient waveform is generated by the spectrometer gradient waveform control processor and fed to the gradient coils via high power linear constant current gradient amplifiers.

3.2.1 Gradient Coils

In order to localize the MRI signal in three dimensions the scanner is equipped with three orthogonal and independent gradient coils constructed around a series of concentric cylindrical formers. These are largely based on a Maxwell coil design for the z gradient and Golay coil designs [7] for the x and y gradients as illustrated in Fig. 7.9. As with the magnet structure, the magnetic field created by current flowing in the gradient coils is not confined to the gradient tube bore but has a fringe field component which extends around the coil structure. Rapid switching of the field gradients can induce eddy currents to flow within any conducting surface in the vicinity, particularly in components of the magnet cryostat. These eddy currents generate their own time-varying magnetic field which distorts the field generated by the gradient coil itself, leading to image artifacts and instabilities. The time constant of these eddy-currents is inversely proportional to the resistance of the conductors in which they flow, so it is imperative that no eddy currents are allowed to form in the cooled internal structures of the magnet system, where time constants can be several seconds. To counteract this problem, Mansfield introduced the concept of actively shielded gradient coils [8] which again contain a second counter-wound set

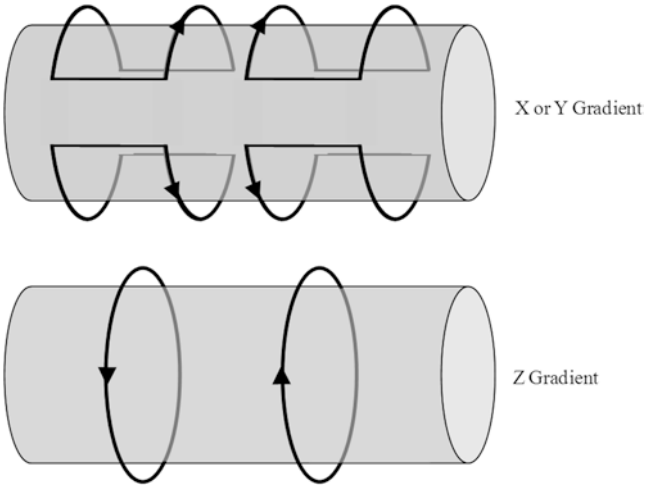

Fig. 7.9 Schematic diagram of the current windings for the three axes of the gradient coil. Over the useable volume of the scanner the windings all produce linear variations in the Z magnetic field (i.e. $\partial B_z/\partial x$, $\partial B_z/\partial y$ and $\partial B_z/\partial z$ the z axis being defined along the magnet bore)

of windings on a co-axial former surrounding the main gradient coils. Typically active shielding of the gradient coils reduces eddy currents to below 1 % of the equivalent unshielded design. A commercial gradient system (un-mounted from the magnet) is shown in Fig. 7.10.

Image resolution Δr is determined by the maximum gradient strength which can be established across the sample during detection of the MRI signal. The precise relationship is defined by the expression

$$\Delta r = \frac{2\pi}{\int_0^t \gamma . G_r\left(t'\right).dt'} \tag{7.10}$$

where $G_r(t')$ is the time-varying field applied over duration t for which the MRI signal is sampled.

Gradient strength is determined by the coil geometry and the current (I) passing through the windings. Gradient strength is inversely proportional to the coil radius so choice of the optimum gradient coil is dictated by the largest sample size which is to be imaged. The rate at which each gradient field can be switched to encode spatial information during the imaging sequence is determined by the self-inductance (L) of the coil, the applied voltage (V) and the total resistance of the system (R, from the coils and cabling). This can be expressed as

$$V = IR + L\frac{dI}{dt} \tag{7.11}$$

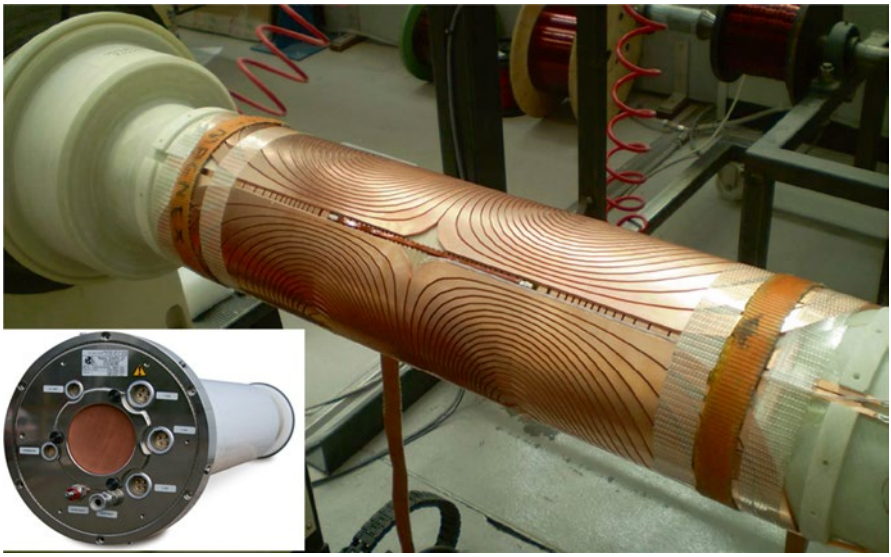

Fig. 7.10 View of a gradient coil during construction. The current paths illustrated in Fig. 7.9 are translated into patterns of continues arcs of copper cut from a single sheet. Sheets for each of the primary and secondary (shielding) windings are positioned around a glass reinforced plastic former interspersed with insulation. Shown is one of the transverse windings (X or Y), with another winding visible below. The whole structure is finally embedded in epoxy resin under pressure. *Inset*: View of the complete gradient coil showing connections for the three gradient coils, integrated shim coils, thermometry and water cooling (courtesy of Varian Inc)

Rapid gradient response (dI/dt) is essential for modern ultra-rapid imaging sequences and gradient coils are therefore designed to have low self-inductance and resistance and are driven at high current and high voltage. Small animal systems typically are driven with amplifiers supplying peak voltage of 300 V and peak current of 200 A generating gradient fields between 400 and 1,000 mT/m depending on gradient coil diameter.

The final element of the gradient hardware is the cooling system. High duty cycle scanning leads to intense heat dissipation in the gradient coils. In the context of the imaging experiment this heating can alter the coil resistance changing the coil performance, while in the context of the coil hardware the heating can cause damage to the coil windings. Water cooling systems are therefore incorporated within the coil structure in close thermal contact with the coil windings and supplied with chilled water to maintain a constant working temperature.

3.2.2 Pre-emphasis

In Sect. 3.2.1 the concept of active gradient shielding was introduced as a method to reduce eddy current interactions with the magnet structure. While good gradient design is effective in eliminating ~99 % of the stray field effects, residual eddy

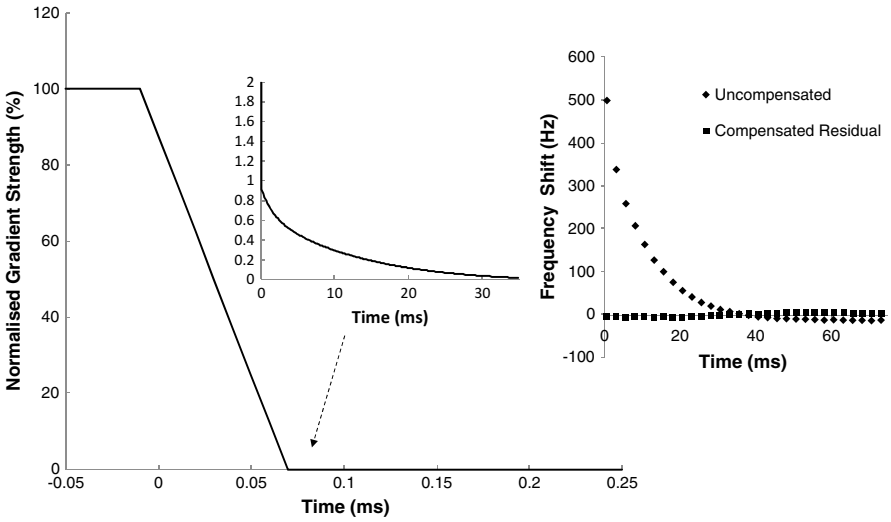

Fig. 7.11 Illustration showing the falling edge of a requested trapezoidal gradient waveform. Experimental measurement of field stability in the scanner bore following the gradient waveform showed time-varying eddy-current gradient fields within the magnet bore with three different time constants of 1.5, 13.5 and 65.5 ms. Pre-emphasis adjustment to provide a stable measured field required addition of time-decaying components with these time constants at –0.09, 0.75 and 0.24 % of the requested gradient amplitude and leads to a gradient function which has a long tail (insert, note the much longer time scale). Also shown is the measured frequency shift in a small object in the scanner as a function of time after the end of the ideal gradient event, with and without pre-emphasis compensation

currents are still present in the system. Gradient field strengths of 100 mT/m are not uncommon in small-animal scanners which amounts to a proton frequency dispersion [Eq. (7.7)] of 425,000 Hz/cm. The frequency stability of the scanner is measurable within the receiver electronics (see Sect. 3.4.3) to typically better than 0.1 Hz and several data acquisition methods (notably MRI spectroscopy acquisitions and the echo-planar imaging or EPI sequence) are sensitive to field changes of ~0.1–5 Hz. Therefore residual eddy currents of 1 % are still intolerable for high sensitivity imaging. The residual field can however be reduced significantly using the technique of *pre-emphasis*.

Pre-emphasis refers to the adaptation of the driving waveform such that the magnetic field gradient produced by the coil combined with the field produced by the induced eddy currents produce the true desired gradient field modulation within the sample (Fig. 7.11). Pre-emphasis is a function of the interaction between the individual system components (magnet, gradient coil and RF coil) and is pre-measured for each configuration during system installation. The time-varying eddy currents are mapped for each gradient axis and decomposed into a series of exponentially decaying functions and amplitudes. From these parameters the gradient driving function is “pre-emphasized” before passing to the gradient coils.

3.3 Shims

In Sect. 3.1 we noted that the applied magnetic field B_o must be highly homogeneous so that the Larmor frequency is as close to uniform as possible. However, even if a *perfect* magnet design could be constructed this would not achieve optimal conditions. Differences in the magnetic susceptibility (χ) between air and the object to be scanned lead to spatial variations in the magnetic field established within the sample, and hence to local variations in B_o. As static field strength is increased the magnitude of the inhomogeneity variation increases, while the size of the object typically decreases (higher field systems generally have smaller bore size, Table 7.1) and the relative proportion of the object experiencing unacceptable field variation increases. This field distortion must be therefore compensated in each object which is scanned via a process known as magnetic field *shimming*.

Within the magnet bore an additional set of field profile coils (the *shim coils*) are added. The winding geometry of these coils is designed to create static fields with first, second and in some cases third order spatial spherical harmonic distributions [7, 9]. The spatial field variation can be mapped using specific data acquisition sequences (e.g. [10]), decomposed into their spatial harmonics and then corrected by driving appropriate current into each shim coil. In general shim fields are static fields, but in some conditions dynamic shimming to alter the field shim on a per collection basis can improve sensitivity [11, 12]. Shim coils can be mounted separately within the magnet bore, but in most system designs they are incorporated within the gradient coils located in the space between the primary and secondary (screening windings), thus saving valuable free bore space.

3.4 RF System

The second major system within the MRI instrument is the radio-frequency (RF) chain, consisting of components to transmit the initial excitation pulse and subsequently detect and demodulate the returning MRI signal.

3.4.1 RF Coils

The radio-frequency coil is required to transmit the excitation pulse into the sample. The coil is in essence a RF antenna which has been specifically designed to deposit RF energy within a confined volume (rather than to radiate energy away from the coil as in a RF aerial). RF coil systems fall into two basic categories, (1) single transmit-receive coils and (2) separate transmit and receive coil pairs. In either case, the basic coil design consists of a tuned circuit (inductance and capacitance networks with the main inductance formed from the coil winding) which resonates at the Larmor frequency of the nucleus of interest. It is well recognized in electronic theory that resonant circuits provide a scaling of the current flowing within the circuit by the quality

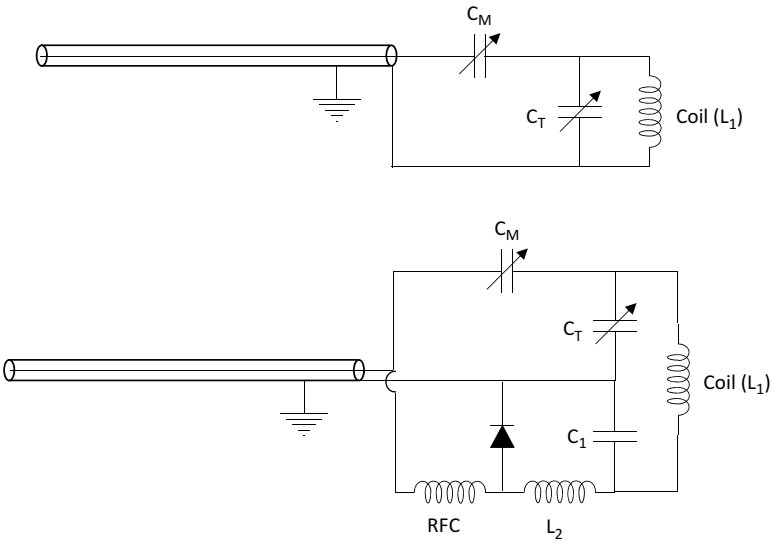

Fig. 7.12 Basic circuit diagrams for RF coil designs. The coil conductors which produces the RF field form the main inductance (L1) of the system while additional tuning (CT) and matching capacitors (CM) complete the resonant circuit and allow the coil to be tuned to the appropriate scanner frequency and matched to 50 W impedance for optimum power transfer between the coil and rest of the system electronics. A more advanced coil design (*lower*) is also illustrated which could be used as a receive only coil within a larger volume transmit coil. Additional components in this design allow the coil to be detuned from the Larmor frequency via PIN diode switching. During RF excitation by a second coil a DC bias is supplied to the PIN diode via the RF choke (RFC) placing the additional inductance L2 in parallel with tuning capacitor C1 leading to an altered resonant frequency. During signal reception the PIN diode is off and inductance L2 no longer contributes to the coil resonant frequency

factor Q of the coil (Q being the ratio of the resonant frequency to the half width of the resonance), providing increased performance when working at that resonant frequency relative to an untuned circuit. Simple circuit diagrams showing the essential elements of the RF coil are shown in Fig. 7.12. As the electronics of the RF chain are designed to operate at 50 Ω impedance (resistive) the RF coil must also be matched to 50 Ω to maximize power transfer between the components of the RF chain.

Current flowing within the windings or conductors forming the coil generates a magnetic field oscillating at the driving (Larmor) frequency and it is the magnetic component of this near field (denoted B_1) which interacts with the nuclei in the imaging experiment.

When a simple imaging experiment such as a "spoiled gradient recalled imaging" [13] (SPGR) measurement is performed in a sample with relaxation times T_1 and using a sequence with repetition time TR, the strength of the excited MRI signal, $S(r)$ arising from a location r is described by the expression

$$S(r) \propto \rho(r) \frac{\left(1 - e^{-TR/T_1}\right) \sin \alpha}{1 - \cos \alpha . e^{-TR/T_1}} \tag{7.12}$$

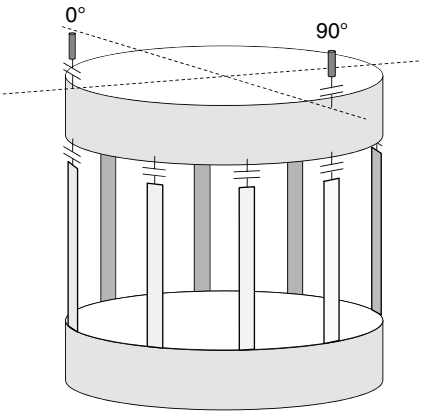

Fig. 7.13 Schematic diagram of the birdcage volume coil design. The coil is tuned to the Larmor frequency by adjusting the capacitance at each "rung". Although this structure will resonate at a number of frequencies, the required mode occurs when a RF standing-wave of wavelength equal to the circumference of the end rings propogates within the structure. In this case current flow down each rung is distributed sinusoidally around the coil leading to a uniform magnetic field distribution within the active volume of the coil

where $\rho(r)$ is the density of nuclei at location r and α is the flip angle produced by the RF pulse [Eq. (7.4)]. Flip angle α is determined by the RF pulse duration tp and the local B_1 field strength which can vary with position r depending on the design of the RF coil (see below) leading to the expression

$$\alpha(r) = \int_{o}^{tp} \gamma B_1(r,t')\,dt' \tag{7.13}$$

Further, via a principle known as *reciprocity* [14], the sensitivity of the RF coil used in signal detection is proportional to the effective $B_1(r)$ distribution of that coil. From these two expressions it is clear the careful control of the B_1 field distribution within the sample is essential.

In general the larger the RF coil, the lower the inherent sensitivity. (This follows from reciprocity since the magnetic field generated by unit current flowing in a larger coil structure will be less than the same current flowing in a smaller structure). Close coupling of the smallest coil system with the object being imaged provides maximal signal to noise ratio. It follows that for optimum sensitivity RF coil design must be tailored to the investigation or object being scanned.

Typically for body imaging a surrounding "volume" coil is used which may be used to both transmit and receive the MRI signals, or may be used in transmit only mode with a local receiver coil positioned over the target region to obtain greater sensitivity. A simple volume coil based on the birdcage design [15] is illustrated in Fig. 7.13. The birdcage design was the first MRI coil to have essentially uniform B_1 field distribution. Through appropriate distribution of capacitance around the rungs

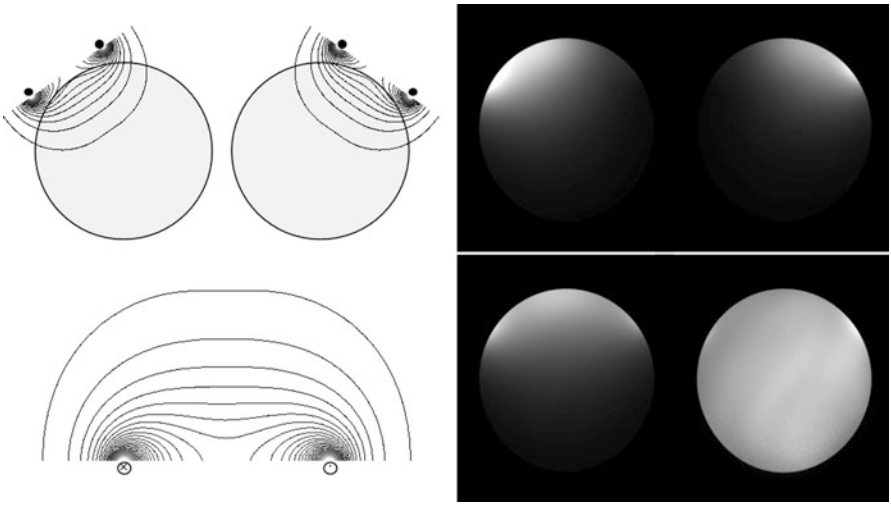

Fig. 7.14 Theoretical and experimental images showing the received signal from individual coil elements of a phased array coil and the image created by mathematical combination of the signal from the individual elements. *Lower left*: Theoretical B_1 field variation with distance from the plane of a single circular loop surface coil. *Upper left*: Contour plots of the theoretical B_1 profiles for a phased array surface coil pair overlaid on schematic of a test object. *Upper right*: Experimental data showing individual images reconstructed from signals received through each independent receiver coil. *Lower right*: Quadrature combination of the signals from the two coils (*left*) and SENSE reconstruction of the signals using a sensitivity reference scan (*right*)

or end-rings of the structure current flow down each rung is arranged to be sinusoidal in amplitude when driven at the resonant frequency, leading to constructive interference of the field from each rung and generating the uniform B_1 distribution. When driven from a single location on the end-ring (linear drive), current flow around the structure can be in either direction, generating two counter rotating B_1 fields, only one of which couples to the sample nuclei. However, by driving the coil from two locations 90° apart and with signal phase also separated by 90° (in *quadrature*, Fig. 7.13) a single rotating field is produced, providing a factor of 2 in power performance for RF pulse transmission. In receive mode, the precessing magnetization inductively couples to the coil structure and in the case of the quadrature design is coherently detected through both channels. Although the signal source is coherent, noise is incoherent and quadrature combination of the two channels leads to a $\sqrt{2}$ improvement in signal to noise ratio compared to linear mode reception.

Surface coils and phased array coils. When the volume to be imaged is superficial and is limited in lateral extent (for example if investigating a subcutaneous tumor where the precise location is known, or for brain imaging investigations) then alternative coils termed *surface coils* can be employed to give high sensitivity images. A surface coil consists of an approximately planar coil configuration which is positioned adjacent to the area of interest [16]. The theoretical B_1 field distribution [17] for one such a coil consisting of a single circular loop is illustrated in Fig. 7.14. It can be seen that the strongest B_1 field is produced close to the loop and falls away

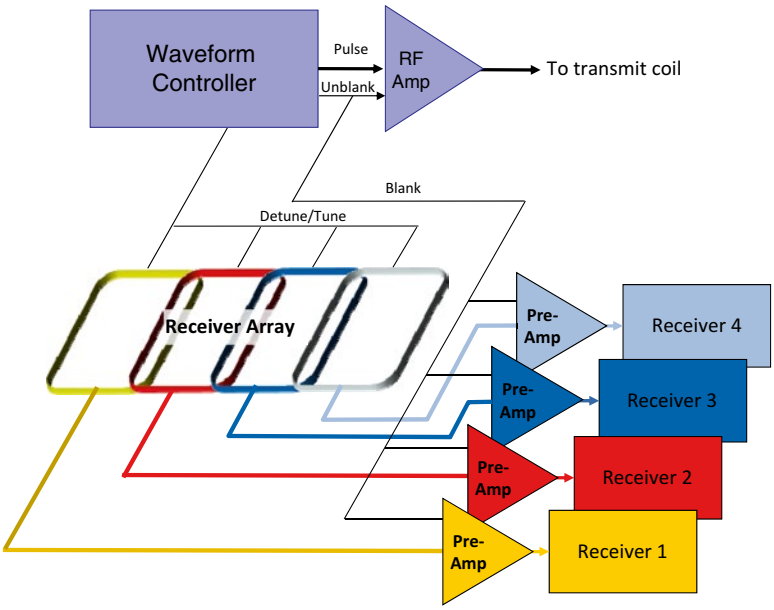

Fig. 7.15 Schematic diagram of a phased array coil system

rapidly with distance from the coil. By reciprocity the imaging sensitivity is also maximal close to the coil. Surface coils can also be designed to work as quadrature systems using two uncoupled, angled and overlapping coils. Although true quadrature coils require perfectly orthogonal B_1 fields, which can never be produced from the field distribution from a planar structure, a focused area of the B_1 field from the quadrature surface coil does meet this criteria and signal from that region of the sample does benefit from quadrature signal to noise ratio (SNR) improvement.

The concept of surface coils was developed further for clinical MRI applications by the introduction of phased-array RF coils by Roemer in 1990 [18]. This coil design uses an array of overlapping but electrically uncoupled surface coils each connected to its own complete receiver channel (Fig. 7.15). Individually each coil element provides the high sensitivity expected from the small loop coil with the associated limited field of view, but the data from the whole array can be combined to provide a much greater total imaging field of view (Fig. 7.14). Volume coils can be also constructed using similar principles by positioning the array of smaller coil elements around a cylindrical former. Multi-element array coils are most often used as "receive only" coils in conjunction with a separate surround volume coil which provides uniform RF excitation. In this configuration the transmit and receive coils must be electrically uncoupled for maximum performance and most importantly to prevent the high power excitation pulse from entering the high sensitivity RF receiver chain. Coil system are therefore actively uncoupled using PIN diode switches to tune or detune each coil [19], (Fig. 7.12).

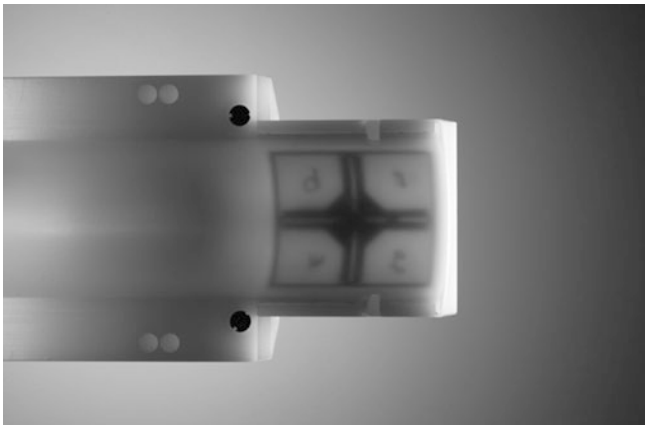

Fig. 7.16 Commercially available surface coil array for neuroimaging. The internal coil elements can be seen through the housing (courtesy of Bruker Biospin Ltd)

The engineering challenge in constructing separate transmit and multi-element receive array coils structures at small scale into devices for small animal MRI has recently been addressed (Fig. 7.16).

Cryocooled Coils. The sensitivity of the scanner hardware can be quantified in term of the signal to noise ratio of the acquired images. As we have discussed above, the signal strength depends on many factors including static field strength, the amount of magnetization within the active volume of the RF coil, the RF coil size and geometry. Likewise, noise within the image dataset (the random fluctuations seen on top of the image) has several potential source; noise arising within the object being scanned and coupled into the RF coil, electronic noise generated within the RF coil itself, and electronic noise generated downstream of the RF coil in the receiver electronics (see below). In a well designed system this latter source is small. The source of electronic or "*Johnson*", "*Nyquist*" or simply "*thermal*" noise is attributed to the chaotic motion of electrons within any components giving resistance to the circuit. This thermal noise N can be expressed by

$$N \propto \sqrt{4KTR} \tag{7.14}$$

where R is the electronic resistance and T the temperature of the electronic circuitry or coil (K is the Boltzmann constant). Electronic noise originating in the RF coil components can therefore be reduced by cooling the coil structure. *Cryocooled coils* are common in chemistry applications of NMR and are becoming available for in vivo use based on both helium and nitrogen refrigeration systems (Fig. 7.17). Design of cryocooled coils for animal imaging requires careful insulation of the cold components from the animal which necessarily increases coil size and hence the separation between the coil and the animal. There is therefore a trade-off between lowering noise and lowering signal.

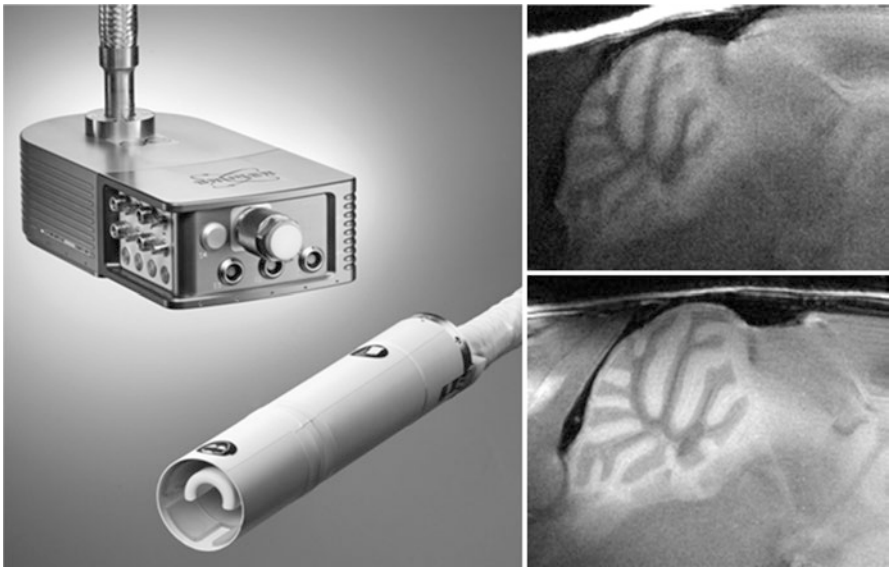

Fig. 7.17 Illustration showing a commercial cryo-cooled RF coil and illustrating the improvement in image quality which can be obtained by cooling the coil structure and associated pre-amplifier. Images were collected under identical conditions using a RARE sequence, eight echoes; TR/TE: 5,000/53 ms, 1 mm slice thickness and in-plane resolution of 40 μm × 40 μm (courtesy of Bruker Biospin Ltd)

3.4.2 RF Generation System

The RF pulse applied to excite the MRI signal is generally a complex amplitude and phase modulated pulse whose characteristics determine the precise nature of the excitation such as the profile of the selected slice. The pulse waveform is generated by a dedicated processor board in the spectrometer console. The basic pulse frequency must match the Larmor condition for the imaging slice of interest [Eq. (7.7)]. This process is performed by direct digital synthesis of the amplitude modulated pulse which is then shifted in frequency to the desired carrier signal produced by a highly stable synthesizer (e.g. PTS, Fig. 7.18). The final pulse shape is then fed to a high power (typically ~1 kW) linear amplifier which drives the RF coil. Since the RF pulse is an intense burst of energy with peak powers of many hundreds of Watts, the receiver electronics is "blanked" to prevent penetration into the high gain pre-amplifiers used to detect the micro-milliWatt MRI signal returning from the sample.

3.4.3 Receiver System

The receiver system is illustrated schematically in Fig. 7.19. The system begins with the receiver RF coil collecting the MRI signal from the precessing magnetization. This is fed directly to a high gain, low noise pre-amplifier which is often integral to

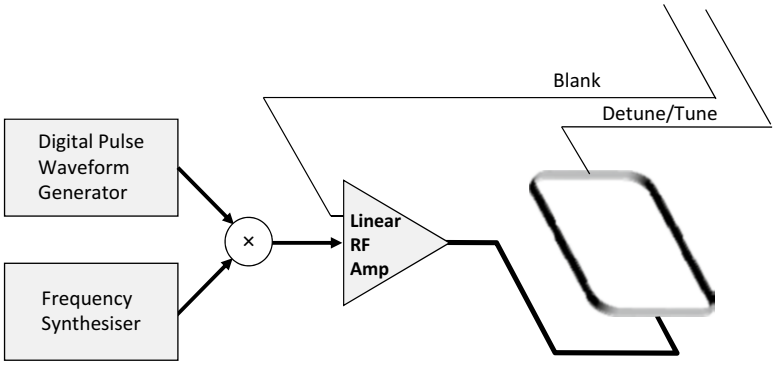

Fig. 7.18 Schematic of a typical RF transmission stage for a high field MRI scanner. The basic amplitude and phase characteristics of the required pulse are generated in digital form by the RF pulse waveform controller before being combined with a carrier signal at the required Larmor frequency

the RF coil. Amplification of the weak MRI signal at this earliest stage minimizes the potential for contamination by external noise sources. The RF signal is then demodulated down to the audio frequency range and split into a complex signal using a pair of phase sensitive detectors. Finally the two channels of the complex signal are digitized and stored in spectrometer memory before being saved to disk. Signals are filtered to eliminate noise from outside of the sampled signal bandwidth which may be performed using analogue filtering prior to sampling or digital filtering of the sampled signal.

3.4.4 Specific Absorption Rate

It is clear from the discussion above that significant amounts of RF energy may be applied to the sample, the majority of which will be absorbed by the tissue. This RF energy has the potential to raise tissue temperature which can lead to alterations in tissue physiology and in extreme cases RF burns. In clinical MRI scanners RF energy (or *specific absorption rate*, SAR) is closely monitored (both by calculation of the requested RF power and by experimental monitoring of RF output) and must remain below stringent legal requirements. SAR levels are defined in terms of local and global heating effects such that temperature rises of no more than 1 °C can be induced in patients [6]. Similar requirements are not so rigidly enforced in small animal MRI and many instruments do not contain the same RF monitoring circuitry found in their clinical counterparts. However, careful assessment of SAR is still essential as part of rigorous scientific practice.

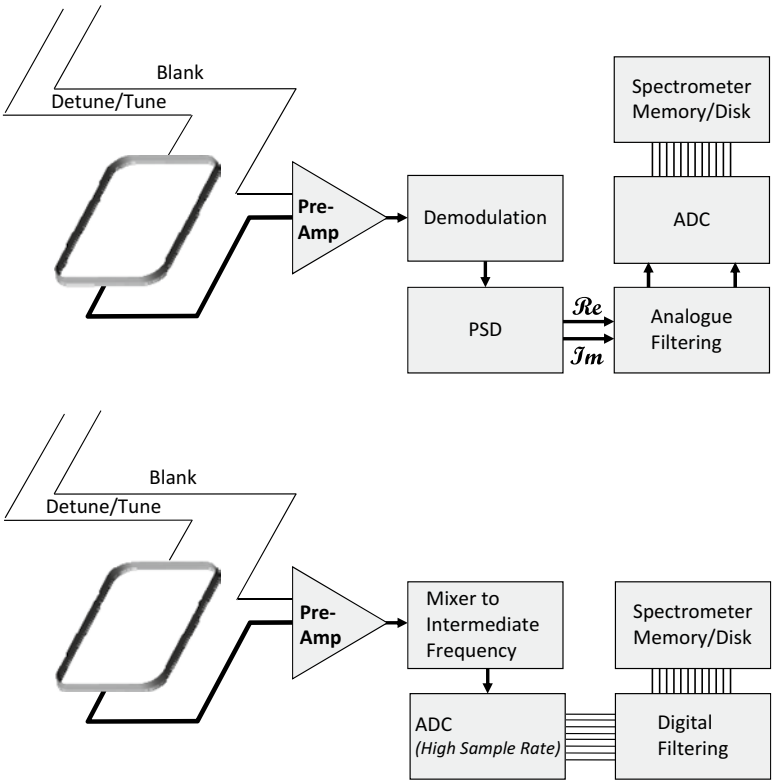

Fig. 7.19 Schematics of RF receiver systems for a high field MRI scanner. *Upper*: Traditional design based on analogue circuitry. The weak MRI signal is detected in the RF coil and immediately amplified using a low noise preamplifier circuit. The RF signal is then demodulated down to the audio frequency range and split into a complex signal using a pair of phase sensitive detectors. Signals are filtered to eliminate noise from outside of the desired signal bandwidth using analogue filtering prior to sampling. Finally the two channels of the complex signal are digitised and stored in spectrometer memory before being saved to disk. *Lower*: Digital design. The pre-amplified signal is mixed down to an intermediate frequency still in the 10 s of MHz range before being directly sampled at high bandwidth (e.g. 80 MHz). Digital filtering is applied to achieved the normal quadrature signal

3.5 Data Reconstruction

The sampled MRI data consists of time-varying signals whose frequency components are determined by the spatial water distribution and the applied spatial encoding gradient [Eq. (7.7)]. The generalized expression describing the MRI signal is given by

$$S(t) = \oint M_{xy}(r) \exp(-t/T_2) \exp\left(-i\left[\omega_o + \int_0^t \gamma G_r(t')\, r\, dt'\right]\right) dr \qquad (7.15)$$

Ignoring relaxation and demodulating the signal from the basic Larmor frequency simplifies this expression to

$$S(t) = \oint M_{xy}(r) \exp\left(-i \int_0^t \gamma G_r(t') r dt' \right) dr \tag{7.16}$$

The gradient-time integral can be combined [20, 21] to introduce the term

$$k_r = \int_0^t \gamma G_r(t') dt' \tag{7.17}$$

to describe the effect of gradient modulation, which further simplifies Eq. (7.16) to

$$S(t) = \oint M_{xy}(r) \exp(-ik_r.r) dr \tag{7.18}$$

indicating that the time varying signal is simply the Fourier transformation of the spatial magnetization distribution measured along the direction of the applied magnetic field gradient G_r. Recovering the image is a simple matter of Fourier transformation (in one, two or three dimensions depending on the nature of the imaging sequence used).

Modern PCs have sufficiently fast processing speed that fast Fourier transformation can be performed by the console computer without the need for dedicated processing systems.

4 Advanced MRI Methods and Instrumentation for Molecular Imaging

So far we have described the generic instrumentation for MRI which measures the abundant proton signal from water molecules. While the anatomical images created by conventional MRI provide useful detail on tissue structure they do not achieve the goal of molecular imaging to provide information on the distribution of cellular and metabolic processes in vivo. With additional advanced instrumentation and the use of nuclei other than the proton, magnetic resonance can also contribute directly to molecular imaging.

4.1 Non-proton Techniques

Many (but not all) nuclei exhibit the phenomenon of nuclear magnetic resonance and can in theory be used in molecular or metabolic imaging studies. Key nuclei which have been used in biological investigations are given in Table 7.2, together

Table 7.2 Important nuclei for MRI and spectroscopy applications in vivo

Nucleus	Isotope	Natural abundance (%)	Magnetogyric ratio ($\times 10^7$ rad s^{-1} T^{-1})	Relative sensitivity (to ^1H)
Lithium	^7Li	92.4	10.398	6.52×10^{-4}
Carbon	^{13}C	1.07	6.728	1.76×10^{-4}
Fluorine	^{19}F	100	25.162	8.33×10^{-1}
Sodium	^{23}Na	100	7.081	9.27×10^{-2}
Phosphorus	^{31}P	100	10.839	6.65×10^{-2}

Note that all are *stable isotopes*. Imaging sensitivity is calculated by multiplying NMR sensitivity $\gamma^3 I(I+1)$ by natural abundance assuming for equimolar concentrations of each nucleus. To obtain imaging sensitivity, relative sensitivity must be scaled by expected tissue concentration

with indications of their relative sensitivity (relative to the proton used in conventional MRI), MRI characteristics, and natural abundance.

It is clear that all nuclei have lower sensitivity than the proton, although fluorine-19 has almost the same NMR sensitivity. The low sensitivity of these nuclei provide a challenge in terms of the concentration which must be present in the tissue for detection above background noise. Since MRI sensitivity depends on the concentration within the sampled region, one method to overcome low concentration is to simply sample much larger tissue volumes. (In proton MRI on high field animal scanners image pixels may represent tissue volumes of dimension 50 μm, whereas pixels for nuclei such as ^{31}P or ^{13}C will be several mm in dimension.) It is natural to then ask what is the attraction of working with such low sensitivity nuclei?

4.1.1 Spectroscopy Versus Imaging

The answer to this question lies in some of the earliest observations of the NMR phenomenon which underpin the field of chemical analysis by NMR. The Larmor frequency of a nucleus within a molecular environment is partially screened from the applied magnetic field by its electrons. The density of electrons associated with the nucleus depends on the nature of the chemical bond formed within the molecule, such that small variations in the Larmor frequency can be detected between differing molecular groups (known as the *chemical shift*). Using magnetic resonance spectroscopy (MRS) sequences the precessing magnetization is detected in the *absence* of any spatial encoding gradients allowing the frequency distribution due to chemical shift to be measured. Fourier transformation of the MRI signal now yields a *spectrum* rather than an image.

Carbon-13 has the advantage of low natural abundance which allows infusion of ^{13}C enriched compounds to be detected. Importantly metabolism of such infused compounds can be followed entirely non-invasively as breakdown of the original compound, and transfer of the ^{13}C atoms to other molecules can be seen via enhancement of the peaks at varying chemical shift [22–24]. Fluorine-19 and lithium (-6 or -7) have zero background concentration in vivo and so their detection can be uniquely attribute to infused labelled compounds or cells [25–27].

4.1.2 RF Systems for Non-proton Methods

From Table 7.2 we note that the magnetogyric ratio of each nuclei is different and so the Larmor frequency also varies with nucleus. MRI instrumentation must reflect these differences if nuclei other than proton are to be detected. The RF chain of the entire spectrometer—RF coils, RF amplifier and receiver—must be retuned to the new nucleus. Typically this requires the MRI spectrometer to be equipped with a second complete *broadband* RF system.

4.2 Hyperpolarization

In Sect. 3.1.1 it was noted that the strength of the MRI signal is determined by the bulk magnetization of the sample when placed in the main field B_o. Equation (7.8) showed that the number of nuclei in each available energy level is almost equal, even at very high static fields. Increasing the difference in occupancy in the energy levels can be achieved using the techniques of hyperpolarization which create large increases in magnetization and which have largely been applied to date in ^{13}C nuclei. Two broad categories of hyperpolarization method have been developed known respectively as dynamic nuclear polarization (DNP) and parahydrogen induced polarization (PHIP). These methods cannot be applied directly in vivo and as such require additional instrumentation to the basic MRI scanner, but they can however be used to increase the polarization of substrate compounds which can be injected into the animal as high sensitivity probes, in a analogous way to positron emission tomography (PET) probes.

4.2.1 Dynamic Nuclear Polarization (DNP)

The technique of dynamic nuclear polarization (DNP) enhances nuclear magnetization by transferring the polarization of the spin state of *unpaired electrons* into polarization of the nuclear spin states. Successful experiments using this technology for solution state NMR [28] and subsequently MRI [29] led to introduction of commercial instrumentation for DNP in 2005.

The DNP process is a complex multi-stage method. Initially the compound to be polarized is mixed with a trityl radical (as the source of unpaired electrons) and appropriate solvents such that the mixture will form a glass when frozen. The mixture is cooled in liquid helium under vacuum to less than 4 K, placed in a magnetic field (typically ~3.35 T) and irradiated with microwaves (typically at 94 GHz), which transfers electron polarization to the nucleus. Build-up of nuclear polarization occurs exponentially with a time constant of hundreds to thousands of seconds and consequently total irradiation time can be many hours to reach maximal polarization. When polarization is complete the sample is raised out of the helium bath but maintained in the magnetic field while it is rapidly thawed by injection of a pressurized hot solvent.

4.2.2 Parahydrogen

A full description of the technique of parahydrogen induced polarization is beyond the scope of this chapter and has been reviewed elsewhere [30]. However, a brief summary is worthwhile as an introduction to this subject. As we have noted above (Sect. 2.1) the proton has spin states α and β which are associated with the two energy levels of the nucleus when in the polarizing MRI field. Parahydrogen is a form of molecular hydrogen gas in which the two hydrogen nuclei have opposing spin states either αβ or βα. If a molecule of interest is subject to a hydrogenation reaction with parahydrogen, the resulting population of only certain energy levels of the resulting compound are significantly enhanced, leading to enhanced effective polarization of the sample. Parahydrogen is present naturally in molecular hydrogen at approximately 25 % at room temperature. The proportion of parahydrogen increases as the gas temperature is decreased (approximately 50 % of molecular gas is in the parahydrogen form at 77 K) but can also be significantly enhanced by passing the gas through a catalyst such as charcoal to prepare parahydrogen for reaction. Equipment and techniques for performing parahydrogen based MRI experiments of biomolecules have been described [31] and in vivo experiments have been performed [32]. While early experiments using parahydrogen required chemical hydrogenation of the biomolecule of interest, recent advances have shown that coordination of the biomolecule with parahydrogen via a catalyst but without direct chemical interaction can also achieve significant hyperpolarization [33]. These developing techniques of PHIP are simple, quick and cheaper to perform that DNP experiments, although no direct comparisons of efficiency are yet published.

In vivo applications of hyperpolarization techniques are still in their infancy but are being developed at a rapid pace and are already beginning to have a major impact on small animal molecular and cellular imaging studies by MRI.

5 Summary

The MRI spectrometer is a complex but highly versatile instrument offering the widest range of possibilities of all non-invasive scanning techniques. Many instrument configurations are possible depending on the precise nature of the imaging experiment to be conducted. The optimal configuration for any in vivo MRI measurement depends on careful selection of the most appropriate gradient and RF coil hardware.

Acknowledgments The author acknowledges the assistance of Dr Roy Gordon, Bruker Biospin Limited and Dr Simon Pittard, Varian Inc in providing images of components of commercial small animal MRI scanners.

References

1. Gadian DG (1996) NMR and Its Applications to Living Systems 2nd Edition ed: Oxford University Press.
2. McRobbie DW, Moore EA, Graves MJ, Prince MR (2007) MRI from picture to proton, 2nd Edition ed: Cambridge University Press.
3. Lauterbur PC (1973) Image Formation by Induced Local Interactions - Examples Employing Nuclear Magnetic-Resonance. Nature 242:190–191.
4. Bracewell RN (1999) The Fourier Transform & Its Applications 3rd Edition ed: McGraw-Hill Science/Engineering/Math.
5. Gifford WE, Longsworth RC (1964) Pulse tube refrigeration. Trans Am Soc Mec Eng 86: 264–268.
6. IEC (2002) Medical Electrical Equipment. Part 2–33. Particular requirements for basic safety and essential performance of magnetic resonance equipment for medical diagnosis., Vol. IEC 60601-2-33:2002. Geneva: International Electrotechnical Commission.
7. Romeo F, Hoult DI (1984) Magnet Field Profiling - Analysis and Correcting Coil Design. Magn Reson Med 1:44–65.
8. Mansfield P, Chapman B (1986) Active Magnetic Screening of Gradient Coils in NMR Imaging. J Magn Reson 66:573–576.
9. Gruetter R, Boesch C (1992) Fast, noniterative shimming of spatially localized signals - in vivo analysis of the magnetic-field along axes. J Magn Reson 96:323–334.
10. Gruetter R (1993) Automatic, localized in vivo adjustment of all 1st-order and 2nd-order shim coils. Magn Reson Med 29:804–811.
11. Blamire AM, Rothman DL, Nixon T (1996) Dynamic shim updating: A new approach towards optimized whole brain shimming. Magn Reson Med 36:159–165.
12. Zhao YS, Anderson AW, Gore JC (2005) Computer simulation studies of the effects of dynamic shimming on susceptibility artifacts in EPI at high field. J Magn Reson 173:10–22.
13. Haase A, Frahm J, Matthaei D, Hanicke W, Merboldt KD (1986) FLASH IMAGING - RAPID NMR IMAGING USING LOW FLIP-ANGLE PULSES. J Magn Reson 67:258–266.
14. Chen C-N, Hoult DI (1989) Biomedical magnetic resonance technology: IOP Publishing Limited.
15. Hayes CE, Edelstein WA, Schenck JF, Mueller OM, Eash M (1985) An Efficient, Highly Homogeneous Radiofrequency Coil for Whole-Body NMR Imaging at 1.5-T. J Magn Reson 63:622–628.
16. Axel L (1984) Surface Coil Magnetic-Resonance Imaging. J Comp Assist Tom 8:381–384.
17. Haase A, Hanicke W, Frahm J (1984) The Influence of Experimental Parameters in Surface-Coil NMR. J Magn Reson 56:401–412.
18. Roemer PB, Edelstein WA, Hayes CE, Souza SP, Mueller OM (1990) The NMR Phased-Array. Magn Reson Med 16:192–225.
19. Garbow JR, McIntosh C, Conradi MS (2008) Actively Decoupled Transmit-Receive Coil-Pair for Mouse Brain MRI. Concepts in Magnetic Resonance Part B-Magnetic Resonance Engineering 33B:252–259.
20. Mansfield P, Grannell PK (1973) NMR 'diffraction' in solids? J Phy C: Solid State Physics 6:L422-L426.
21. Ljunggren S (1983) A simple graphical representation of Fourier-based imaging methods. J Magn Reson 54:338–343.
22. Henry PG, Tkac I, Gruetter R (2003) H-1-localized broadband C-13 NMR spectroscopy of the rat brain in vivo at 9.4 T. Magn Reson Med 50:684–692.
23. Nabuurs C, Klomp DWJ, Veltien A, Kan HE, Heerschap A (2008) Localized sensitivity enhanced in vivo C-13 MRS to detect glucose metabolism in the mouse brain. Magn Reson Med 59:626–630.

24. van der Zijden JP, van Eijsden P, de Graaf RA, Dijkhuizen RM (2008) 1H/13C MR spectroscopic imaging of regionally specific metabolic alterations after experimental stroke. Brain 131:2209–19.
25. Procissi D, Claus F, Burgman P, Koziorowski J, Chapman JD, Thakur SB, et al. (2007) In vivo F-19 magnetic resonance spectroscopy and chemical shift imaging of tri-fluoro-nitroimidazole as a potential hypoxia reporter in solid tumors. Clin Cancer Res 13:3738–3747.
26. Srinivas M, Morel PA, Ernst LA, Laidlaw DH, Ahrens ET (2007) Fluorine-19 MRI for visualization and quantification of cell migration in a diabetes model. Magn Reson Med 58: 725–734.
27. van Heeswijk RB, Uffmann K, Comment A, Kurdzesau F, Perazzolo C, Cudalbu C, et al. (2009) Hyperpolarized Lithium-6 as a Sensor of Nanomolar Contrast Agents. Magn Reson Med 61:1489–1493.
28. Ardenkjaer-Larsen JH, Fridlund B, Gram A, Hansson G, Hansson L, Lerche MH, et al. (2003) Increase in signal-to-noise ratio of >10,000 times in liquid-state NMR. Proc Nat Acad Sci USA 100:10158–10163.
29. Golman K, Ardenaer-Larsen JH, Petersson JS, Mansson S, Leunbach I (2003) Molecular imaging with endogenous substances. Proc Nat Acad Sci USA 100:10435–10439.
30. Natterer J, Bargon J (1997) Parahydrogen induced polarization. Progress in Nuclear Magnetic Resonance Spectroscopy 31:293–315.
31. Hovener JB, Chekmenev EY, Harris KC, Perman WH, Robertson LW, Ross BD, et al. (2009) PASADENA hyperpolarization of C-13 biomolecules: equipment design and installation. Magnetic Resonance Materials in Physics Biology and Medicine 22:111–121.
32. Golman K, Axelsson O, Johannesson H, Mansson S, Olofsson C, Petersson JS (2001) Parahydrogen-induced polarization in imaging: Subsecond C-13 angiography. Magn Reson Med 46:1–5.
33. Adams RW, Aguilar JA, Atkinson KD, Cowley MJ, Elliott PIP, Duckett SB, et al. (2009) Reversible Interactions with para-Hydrogen Enhance NMR Sensitivity by Polarization Transfer. Science 323:1708–1711.

Chapter 8
Preclinical Optical Molecular Imaging

Yujie Lu and Ge Wang

1 Introduction

Molecular imaging, especially small-animal preclinical molecular imaging, is a rapidly developing area in the biomedical imaging field [1–3]. Given tremendous needs in biological research and drug development, it becomes imperative to have in vivo imaging strategies for gene expression, protein interactions, and cell behaviours [4]. Molecular imaging has been demonstrated to be instrumental or promising in observing all these biological processes at the cellular and molecular levels. Since optical labelling methods with probes based on fluorescence and bioluminescence have been extensively applied in vitro, it was natural to transfer corresponding strategies to in vivo settings, and there have been successful over the past several years [1, 5].

Currently, planar imaging methods are the most popular in various in vivo applications because of their ease of operation, high sensitivity, high throughput, low cost and non-ionizing nature [2]. Fluorescence imaging strategies require external illumination [6], and their sensitivity is affected by tissue autofluorescence and illumination leakage. On the other hand, bioluminescent probes, such as luciferase enzymes, are more suitable for in vivo gene encoded imaging, more sensitive than

Y. Lu
Center for Molecular Imaging, Institute of Molecular Medicine, University of Texas Health Science Center at Houston, 1825 Pressler Street SRB 330, Houston, TX 77030, USA
e-mail: yujie.lu@uth.tmc.edu

G. Wang (✉)
Biomedical Imaging Center, Center for Biotechnology and Interdisciplinary Studies, Department of Biomedical Engineering, Rensselaer Polytechnic Institute, Troy, NY 12180, USA
e-mail: wangg6@rpi.edu

H. Zaidi (ed.), *Molecular Imaging of Small Animals: Instrumentation and Applications*,
DOI 10.1007/978-1-4939-0894-3_8,

fluorescent probes, and have made bioluminescence imaging a powerful optical molecular imaging tool complementary to fluorescence imaging [5]. The probes used in autoluminescence/bioluminescence imaging are not confined to biochemical enzyme reactions. Recently, several different types of autoluminescent probes were developed to enrich the probe library. To enable 3D visualization and quantitative analyses, tomographic imaging methods were proposed, including fluorescence molecular tomography (FMT) [7] and bioluminescence tomography (BLT) [8]. The commercial instruments and laboratory prototypes have all shown the tomographic potential compared with their planar counterparts [1, 9].

In this chapter, we review the state of art of optical molecular imaging. Given the availability of excellent reviews on fluorescence imaging such as that by Ntziachristos [6], this review will be largely focused on bioluminescence imaging, with relatively brief mentions of fluorescence imaging related issues as appropriate. First, we detail the latest progress in probes and discuss planar optical molecular imaging. Then, in a comprehensive fashion we describe bioluminescence tomography, covering instrument design, multimodality fusion and tomographic reconstruction, along with discussions on fluorescence molecular tomography. Finally, we highlight important biomedical applications with bioluminescence and fluorescence imaging.

2 Optical Probes

2.1 Bioluminescent Probes

2.1.1 Classic Bioluminescent Probes

Optical probes/reporters are a prerequisite for bioluminescence/autoluminescence imaging. Some living organisms, especially marine vertebrates and invertebrates, naturally emit bioluminescence [12], generated by specific enzymes and corresponding substrates when oxygen and ATP co-exist. Each of these photoluminescent enzymatic reaction products has unique spectral characteristics. The responsible genetic fragment can be exacted and engineered as a bioluminescent probe. When coupled to the experimental regulatory elements, the genetic fragment will drive enzyme expression in a pattern representing the typical expression of the experimental gene. Four types of enzymes from firefly (FLuc), click beetle (CBGr68, CBRed) and *Renilla reniformins* (hRLuc) (Fig. 8.1a) have been widely used so far [10]. Because of the optical window for biological tissues [13], Fluc and CBRed are more suitable for small animal imaging. However, in more sophisticated studies, it is necessary to observe several biological targets simultaneously for better understanding of systems biology. In these scenarios, multiple bioluminescent probes with different spectral peaks are desirable. The photons emitted at each signal wavelength can be detected using a highly sensitive detector coupled with band-pass filters.

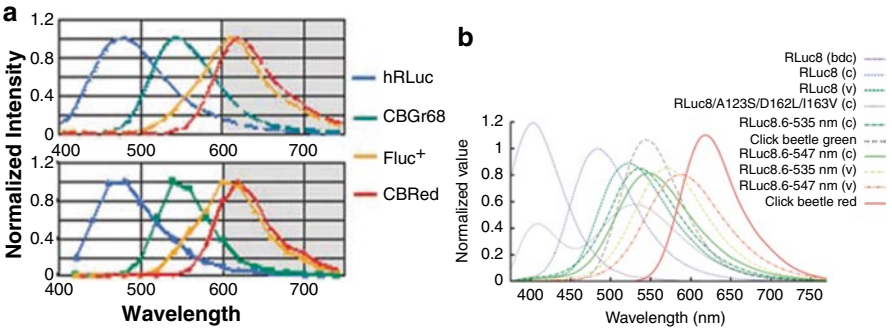

Fig. 8.1 Spectra of four classic bioluminescent probes (**a**) and a series of bioluminescent probes obtained via genetic mutation (**b**) (reproduced from [10, 11] with permission)

Thus, the library of bioluminescent probes needs to be constantly enhanced. A series of enzymes with different spectral peaks (Fig. 8.1b) were obtained via genetic mutation [11]. More probes of this type will emerge in the future.

2.1.2 BRET-Based Probes

Fluorescence resonance energy transfer (FRET) [15] is realized by the energy transfer from a donor to an acceptor chromophore. In microscopy imaging, it is a useful tool to observe molecular dynamics, especially protein–protein interactions and protein–DNA interactions. However, tissue autofluorescence significantly compromises the performance of small animal FRET imaging. In organisms that are not naturally bioluminescent, spontaneous bioluminescent signal is much lower than levels of autofluorescence. Thus, bioluminescence resonance energy transfer (BRET), a complementary technique to FRET, realizes optically labeled detection without external excitation [14]. In this strategy, a bioluminescent luciferase (generally firefly or *Renilla* luciferase) is used to provide energy rather than an external fluorescent source. Figure 8.2 shows the schematic that a quantum dot covalently coupled to Luc8 emits photons after receiving the energy from the latter. The application of BRET-based probes further extends the range of bioluminescence imaging.

2.1.3 Radioactive Isotope-Based Probes

Cerenkov radiation is a type of electromagnetic radiation that generates visible light when a charged particle travels through an electrically insulating material with a speed greater than the speed of light in the same medium. Many high energy isotopes may generate Cerenkov radiation. High-energy positron emitters, such as ^{14}C, ^{18}F, ^{32}P, used in positron emission tomography (PET), have potential to induce

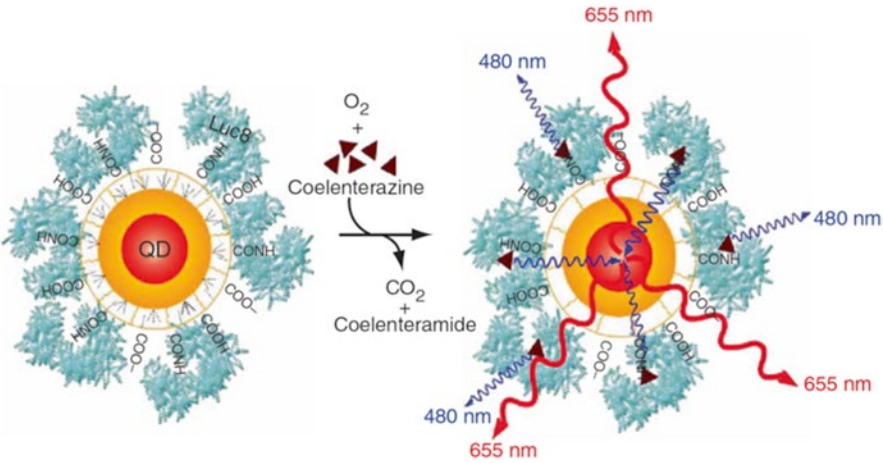

Fig. 8.2 BRET-based probes. A quantum dot is covalently coupled to a BRET donor, Luc8, and emits photons. The spectral peaks of Luc8 and the quantum dot are 480 and 655 nm respectively (reproduced from [14] with permission)

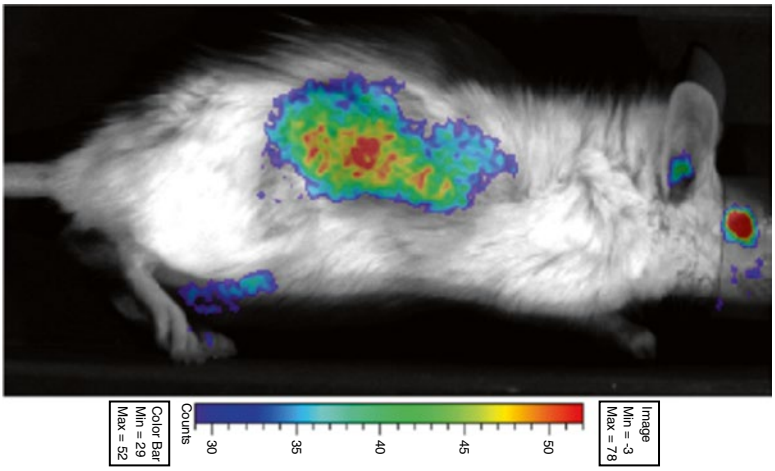

Fig. 8.3 Cerenkov luminescence imaging. Optical imaging of a mouse bearing a CWR22-RV1 xenograft is performed after injecting 270 μCi FDG (reproduced from [16] with permission)

Cerenkov radiation in biological tissues [17]. Recently, the possibility of in vivo mouse Cerenkov luminescence imaging (Fig. 8.3) was demonstrated [16]. With the development of optical imaging techniques, Cerenkov luminescence imaging can be done at lower cost than scintillator-based positron imaging systems. Cerenkov luminescence imaging provides an alternative for radiotracer detection in small animal models. Hence, radioactive isotopes can serve as autoluminescent probes, similar to bioluminescent probes.

2.2 Fluorescent Probes

A major advantage of gene-encoded optical probes is that the optical signal increases with cell division. This type of signal is very useful to observe tumor occurrence and metastasis. A few gene-encoded fluorescent probes are already available. Green fluorescent protein (GFP) obtained from the jellyfish *Aequorea victoria* and its variants are commonly used in fluorescence imaging [18]. However, the emission spectral peak of GFP is around 509 nm. Due to the high absorption of biological tissues in this wavelength and tissue autofluorescence, it is difficult to detect weak emission signals in small animal fluorescence imaging. Recently, infrared-fluorescence protein was developed, whose emission spectral peak is around 708 nm, significantly improving fluorescence molecular imaging at the whole-body small animal level [19]. Most other fluorescent probes are fluorochromes. Based on their labeling functions, they are classified into active (like radioactive probes) and activatable (quenchable) probes [6]. When the number and types of fluorescent probes are increased, there will be more preclinical and clinical applications in the future.

3 Planar Optical Molecular Imaging

3.1 Planar Bioluminescence Imaging

3.1.1 Signal Detection

Bioluminescent probes can be used to label biological targets of interest. The photons emitted by bioluminescent probes inside a small animal body can be externally detected since they may propagate through biological tissue and reach the surface. Planar bioluminescence/autoluminescence imaging can be realized by collecting escaped photons. Due to the high absorption characteristics of biological tissues, the detectable optical signals are very weak. It is pivotal to select suitable detectors for data acquisition with high signal sensitivity and high spatial resolution. Conventional optical detector types include photomultiplier (PMT), avalanche photodiode (APD), and charge-coupled devices (CCD) [20]. PMT devices have very high gain (typically 10^6–10^7), but their quantum efficient (QE) is very low (typically less than 10 %) when the wavelength is beyond 600 nm. Although PMT arrays, such as multi-anode PMT, are available to acquire images, the pixel sizes of PMT arrays are large, not suitable for high resolution optical detection. APD has higher quantum efficiency (typically 60–80 % at 600–800 nm) and lower gain than PMT. The development of integrating APD technology is slow and usually used in single photon counting. Clearly, CCD is the method of choice for bioluminescence imaging. The QE of the back-illuminated integrated CCD is beyond 80 % at 500–800 nm and is higher than front-illuminated counterpart [21]. In terms of the signal-to-noise ratio (SNR), the integrating CCD is better in the case of low photon rates than the

intensified CCD. When the working temperature is decreased to −100 °C using liquid nitrogen or Peltier thermoelectric cooling device, the dark current noise of the integrating CCD can be effectively controlled. With an optical coupling system of a low f-number, photons emitted from ~500 tumor cells ~0.5 mm under the skin of a mouse can be sensed with a decent SNR, showing the high sensitivity of the back-illuminated integrating CCD-based detection system [21].

3.1.2 Photometric Calibration

Over a suitable exposure time, a photon distribution can be acquired from the body surface of a small animal. However, a number of factors determine a bioluminescent view as directly recorded by a CCD camera. As a result, this bioluminescent view does not precisely reflect the actual photon distribution on the body surface. A lens system usually distorts the acquired images. Because more photons are collected at the center of the field of view (FOV) than are acquired peripherally, a technique known as flat fielding is performed to correct light intensities across the FOV, typically utilizing a uniform area source. Background noise is another important factor in the imaging process. The conventional method is to subtract a background image from an acquired bioluminescent view, using the same exposure time. Additionally, bias noise from data readout and isolated "hot" pixels are removed in the calibration process. Finally, data rebinning is often used as appropriate to improve SNR substantially.

How should the calibrated images be expressed in physical units? It is evident that the pixel values of the calibrated images do not directly tell how many photons are involved. Nevertheless, a key goal of molecular imaging is to objectively measure biological activities and treatment responses of the same animal over time. Therefore, we must find a physically-oriented reference framework independent of optical imaging instruments to compare the research results. To address this issue, a relationship between the pixel reading and its photometric value can be established using an absolutely calibrated integrating sphere [21]. For that purpose, portable calibration devices are available [22].

3.1.3 Anatomical Registration

In planar bioluminescence imaging, the anatomical correspondence cannot be easily established only based on the photon distribution on the body surface of a small animal. Hence, it becomes natural to combine a bioluminescent view and a photograph of a small animal in planar bioluminescence imaging [21]. Because the bioluminescent view and the photograph are obtained using the same camera when fixing the mouse, co-registration of the two images is straightforward (Fig. 8.4a). In order to localize optically labeled biological objects, information on internal anatomical structures is necessary. Thus, an in vivo optical imaging system combined with anatomical X-ray imaging was developed. In this system, the scintillator is used to transduce X-rays to visible light. The capture of X-ray and optical signals using the same camera facilitates the registration and reduces the equipment cost (Fig. 8.4b).

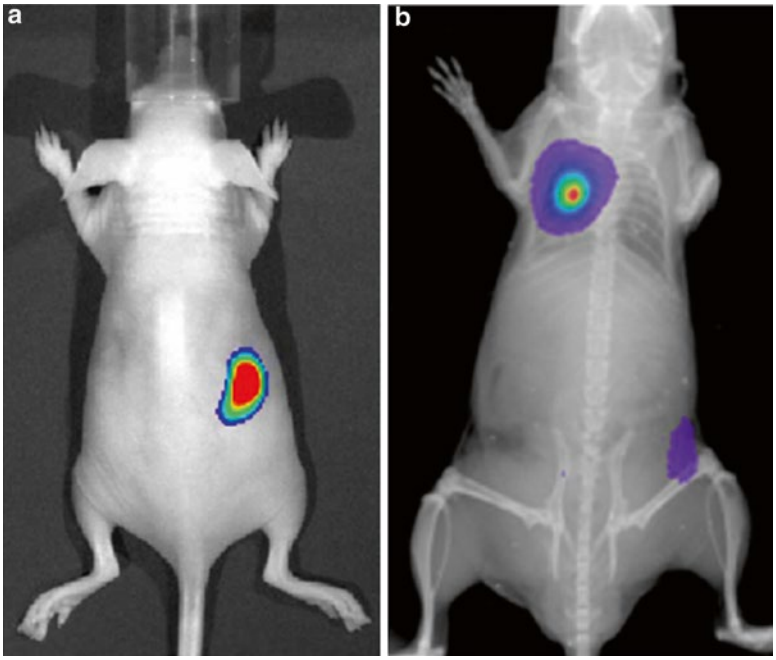

Fig. 8.4 Image registration of mice between bioluminescence images and a photograph (**a**) or a radiograph (**b**) of mice, respectively [reproduced from Caliper Life Sciences (Hopkinton, MA, USA) with permission]

X-ray imaging is a form of ionizing radiation but it is particularly good at revealing bony structures and air-tissue interfaces. Recently, an all-optical anatomic imaging method was invented [23]. It utilizes the differences of the in vivo bio-distribution dynamics of the dye in different organs of small animals to acquire the anatomical information. The corresponding commercial system has become available [24].

3.2 Planar Fluorescence Imaging

In vivo fluorescence microscopic imaging is a popular tool for subsurface imaging of biological tissues. Typical imaging methods include confocal, two-photon and multi-photon microscopies [25–27]. These imaging methods can obtain high resolution (submicron to several microns) at a shallow depth (several hundred microns). Recently, using endoscopic methods, images can be acquired at deep depths while keeping the same lateral spatial resolution [28].

Generally speaking, planar fluorescence imaging is implemented using the macroscopic imaging methods. Currently, two types of planar imaging are usually used, that is, epi-illumination imaging [29–34] and transillumination imaging [35–37]. Epi-illumination imaging is also referred to as fluorescence reflectance imaging,

since the fluorescence emission signals are detected from the same side of the illumination. A sophisticated detection design is necessary to remove reflected illuminating signals for detection of a small amount of fluorescent probes at a deep [38]. Transillumination imaging is realized by placing the illumination and detection devices on the opposite sides of a small animal. Due to the high absorption of tissue, transillumination imaging is suitable at longer wavelengths, such as 650–900 nm. Quantitative information of fluorescent probes cannot be generally obtained because of the unknown nonlinear dependence of the detected signal on the source depth. In transillumination imaging, improved contrast can be gained using post-processing techniques, such as normalization of transmission data [39].

4 Multi-Modality for Optical Molecular Tomography

Planar optical molecular imaging is only able to map the photon distribution on the body surface of a small animal. Then, the changes of the observed biological objects can be roughly inferred aided by projective anatomical information. The complexity of in vivo biological tissues makes it too imprecise to meet the quantitative requirements demanded by sophisticated studies in systems biology and molecular medicine [40]. In contrast, bioluminescence tomography (BLT) is an emerging and promising molecular imaging technology that aims to reconstruct a 3D bioluminescent source distribution reflecting the concentration of bioluminescent cells in a living mouse from external views around the animal. Similar to the development of X-ray CT after planar radiography, BLT allows a localized and quantitative analysis of bioluminescent source/probe distributions while existing planar bioluminescent imaging is primarily qualitative.

In CT, we may assume X-rays propagate in biological tissues along straight paths, although scattering correction needs to be performed to improve image quality. In optical imaging, almost all the photons are scattered by biological tissues in highly zigzag patterns. Hence, BLT is much more difficult than CT in terms of tomographic reconstruction [9]. To enable BLT reconstruction, the multi-modality fusion approach is necessary to collect all available information and reconstruct an underlying bioluminescent source distribution. Furthermore, various imaging modalities rely on different physical contrast mechanisms, and images from independent sources are complementary to each other.

4.1 Multi-Modality Fusion for Bioluminescence Tomography

To reconstruct tomographic images of an underlying bioluminescent source distribution within a small animal, three types of *a priori* information were used: anatomical information of an individual small animal (at least topographical information for

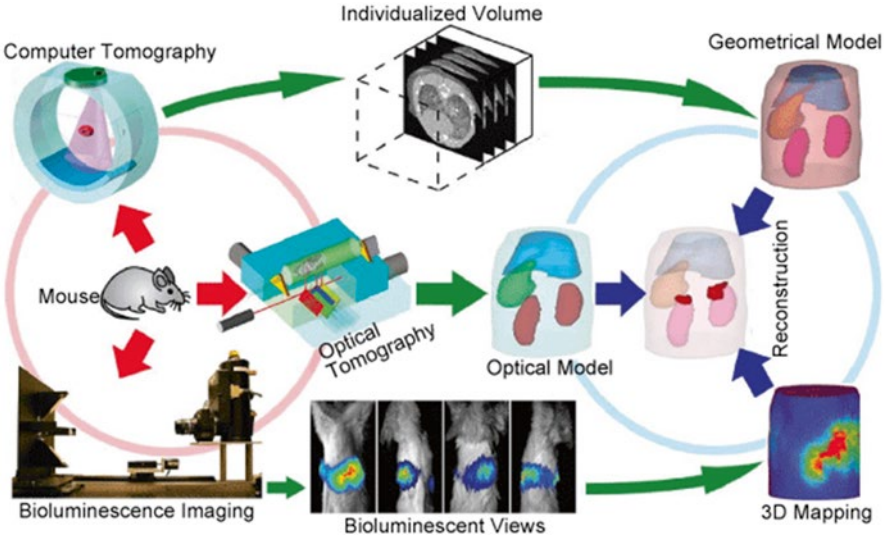

Fig. 8.5 Multi-modality fusion approach for BLT with anatomical *a priori* information from micro-CT [reproduced from the Optical Molecular Imaging Laboratory (Virginia Tech, USA) with permission]

atlas-based elastic registration) [41–43], corresponding tissue optical properties [42], and spectrally-resolved measurements on the body surface of the small animal [42–47]. Clearly, multimodality BLT reconstruction is intimately related to the acquirement of detailed *a priori* information (Fig. 8.5).

4.1.1 Geometrical Modeling

To obtain anatomical information, a simple method is to acquire the surface topology of a small animal [44]. This method is sufficient if we consider an in vivo small animal optically homogeneous. However, in BLT studies, it has been shown that the assumption of a homogeneous optical background is inadequate, especially for deeper bioluminescent sources [41, 42]. It is necessary to consider an in vivo small animal as an optically heterogeneous object. It has been reported that the optical properties especially absorption of biological tissues depend to a large degree on the resident concentrations of oxy-haemoglobin (HbO), deoxy-haemoglobin (HHb) and water [48]. Although these concentrations vary significantly in different organs of small animals, we may assume that the concentrations are uniform in the same organ or tissue structure. Anatomical imaging modalities such as CT, MRI, ultrasound and so on can be used to define a geometrical model of a small animal. Due to the easy realization and low cost of CT, it was first used to realize multimodality tomographic optical imaging. However, a major disadvantage of CT is that it cannot

distinguish the soft tissues well. It becomes difficult to delineate the organs with segmentation methods. MRI is an alternative due to its predominant soft tissue imaging ability. As an approximate and cost-effective option, several digital mouse atlases were established using MRI or cryo-section images [49, 50]. These can be elastically matched to individualized topographic surfaces of small animals, and used for BLT reconstruction.

4.1.2 Optical Characterization

The aforementioned anatomical imaging process gives us a high-quality geometrical model of a small animal. Then, optical properties of the small animal must be mapped onto the geometrical model to build the complete forward imaging model. Through in vivo tissue sampling, the absorption and reduced scattering coefficients of biological tissues can be optically obtained. The reflectance imaging techniques are also used to determine the optical properties using an in vivo mouse [51]. Another attractive method is diffusive optical tomography (DOT) [52]. Because the spectra of HbO and HHb differ markedly at visible and near-infrared (NIR) wavelengths, DOT techniques were originally developed to acquire this type of information and produce spatially resolved images in terms of absorption and/or scattering properties of tissues, or relevant physiological parameters. When DOT is applied in multi-modality BLT, it can provide the optical properties of tissues. When applied to interpretation of anatomical information of small animals, DOT can significantly improve the accuracy of the acquired optical properties [53].

Since the tissue absorption coefficient is subject to more changes depending on the wavelength than the scattering property, photoacoustic tomography (PAT), targeting the tissue absorption coefficient, becomes another promising imaging modality [54]. The physical principle of PAT is that acoustic waves are generated when the tissue absorbs pulsed optical energy (typically, laser pulses of several nanoseconds in period). Ultrasound scattering in biological tissues is usually lower than optical scattering. Therefore, PAT can achieve higher spatial resolution than DOT. However, PAT requires water immersion of the animal, which is inconvenient [55].

4.1.3 Temperature Modulation

A temperature-modulated BLT approach [56] is based on the temperature-dependent spectral shifts of some classic bioluminescent probes (Fig. 8.6a). A focused ultrasound array can heat small regions containing the bioluminescent probe (Fig. 8.6b). The detectable change in the optical signal can improve the BLT reconstruction quality. In this method, temperature monitoring is critical. MRI has the ability of detecting the 3D temperature distribution in vivo, thus suggesting MRI-based temperature-modulated BLT. Since photoacoustic tomography also performs thermal imaging [57], it might become an alternative in this context.

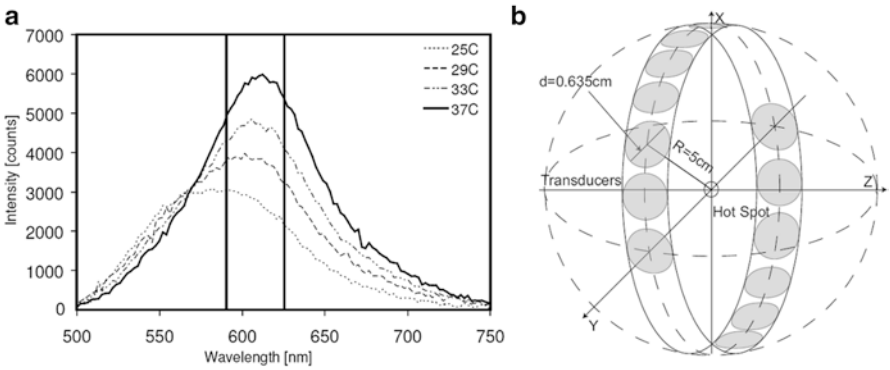

Fig. 8.6 Temperature-dependent spectral changes of Fluc (**a**) and a cylindrical ultrasound transducer array for temperature-modulated BLT (**b**) (reproduced from [10, 56] with permission)

4.2 Multi-Modality Fusion for Fluorescence Molecular Tomography

The acquisition of anatomical structures and optical properties applied in bioluminescence tomography are also suitable for fluorescence molecular tomography [58–62]. Similar to bioluminescence tomography, when combining nuclear imaging and fluorescence molecular tomography, improved imaging quality can be obtained [63, 64]. With photoacoustic tomography, optical characterization may be better performed for fluorescence tomography, and moreover absorption characteristics of fluorescent probes could be extracted as well, at least when an animal is small or the depth is shallow [65].

5 System Architecture

5.1 System Architecture for Bioluminescence Tomography

5.1.1 Multi-View Configurations

The conventional detection system with a CCD camera works in one single view mode [21]. At the initial stage of the BLT system development, a rotated stage fixing the phantom or mouse realizes noncontact multi-view detection sequentially [41, 66]. However, this setup easily introduces data inconsistency and complicates the biological experiments. Another solution is mirror-based multi-view setup. Different mirror configurations were proposed to obtain photon distributions on the body surface of a small animal from several views (typically four views as seen in Fig. 8.7b) [45, 67].

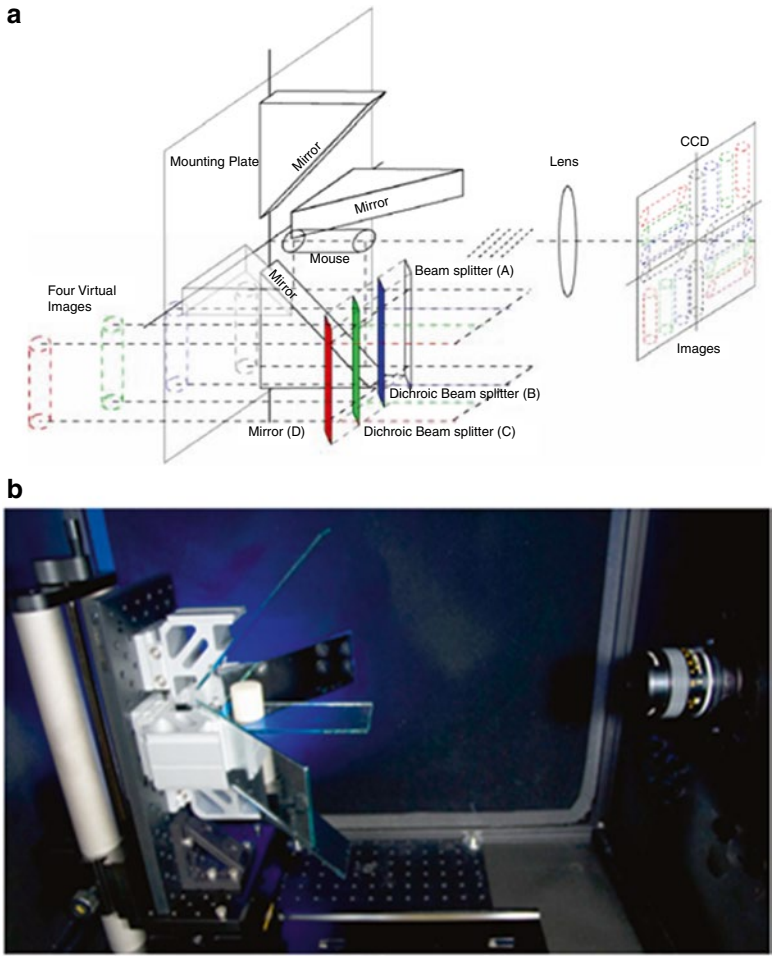

Fig. 8.7 Multi-view and multi-spectral detection concept (**a**) and a four-view bioluminescent signal acquisition system (**b**) [reproduced from [9] and the Optical Molecular Imaging Laboratory (Virginia Tech, USA) respectively with permission]

A truncated cone-shaped mirror setup was developed to perform the measurement from the entire view [68]. However, a sophisticated signal recovery algorithm would be needed because of the distortion of the measured photon distribution.

Bandpass filters are commonly used to acquire multi-spectral data. The traditional bandpass filter only works at one wavelength range. A rotated wheel is necessary for multi-spectral measurement [44]. An alternative solution is the liquid crystal tunable filter (LCTF) [69, 70]. The specific wavelength can be selected by electrically controlled liquid crystal elements. Although its transmission efficiency (typically ~60 % as shown in Fig. 8.8b) is lower than the high performance traditional bandpass filters (typically >85 % as seen in Fig. 8.8a), the rotated wheel is not needed, simplifying the system design.

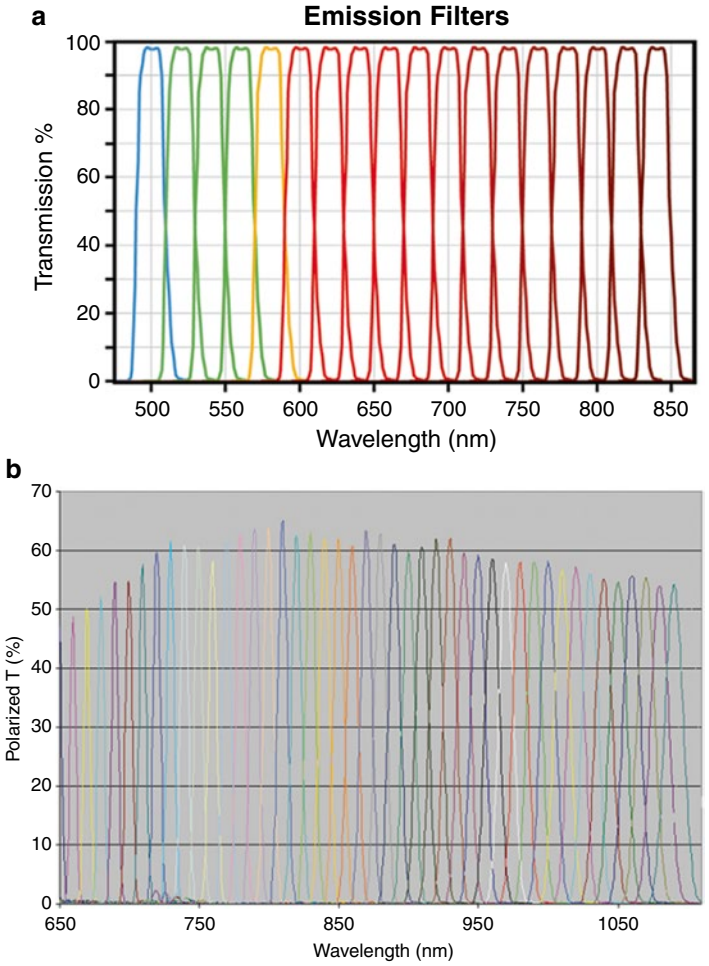

Fig. 8.8 Transmission efficiency of high performance bandpass filters (**a**) and the liquid crystal tunable filter (LCTF) (**b**) [reproduced from Caliper Life Sciences (Hopkinton, MA, USA) and CRi (Woburn, MA, USA) respectively with permission]

Experimental observations have revealed that the source intensity of bioluminescent probes varies significantly over time [9]. Since the optical signals generated by bioluminescent probes are very weak, a long exposure time is necessary to obtain a high SNR. The simultaneous signal acquisition from multi-view and multi-spectral detection methods can shorten the data detection time and improve the overall signal quality (Fig. 8.7a). Based on a rainbow mouse holder for multispectral detection, the simultaneous acquisition is attempted [67]. Beam splitters and cone-shaped mirror are used to improve the detection performance. Furthermore, a digital spectral separation method was developed to extract multi-spectral information more efficiently [71].

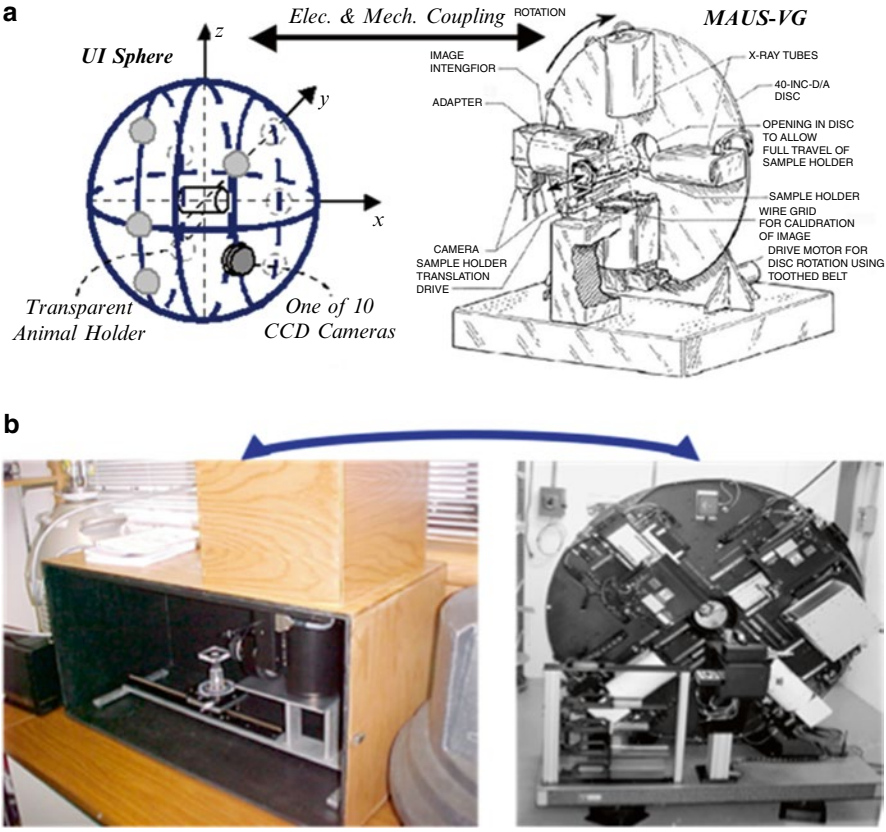

Fig. 8.9 Original hybrid BLT system design (**a**) and experiment prototype (**b**) [reproduced from the Optical Molecular Imaging Laboratory (Virginia Tech and BIR Inc., USA) with permission]

5.1.2 Multi-Spectral Schemes

It has been widely recognized that *a priori* information is critically important for BLT reconstruction. In the first prototype BLT system, multiple CCD cameras for high efficiency optical signal detection were coupled with a micro-CT system (BIR, Inc.), as seen in Fig. 8.9a. Due to the cost issue, the first BLT system used a CCD camera of 1,340×1,300 16-bit pixels (Princeton Instruments VA 1300B, Roper Scientific, Trenton, NJ) to collect bioluminescent views sequentially. A rotated stage under computer control was used to realize multi-view acquisition. A Nikon Normal Macro 55 mm f/2.8 Micro Nikkor Manual Focus Lens helped capture more photons. A holder clamped onto the rotation stage maintained the mouse in a vertical position. Artificial marks on the mouse skin were used for registration with a CT image volume. To perform bioluminescence imaging in a totally dark environment, a light-tight enclosure was built out of 1/2″ plywood lined with aluminum and black

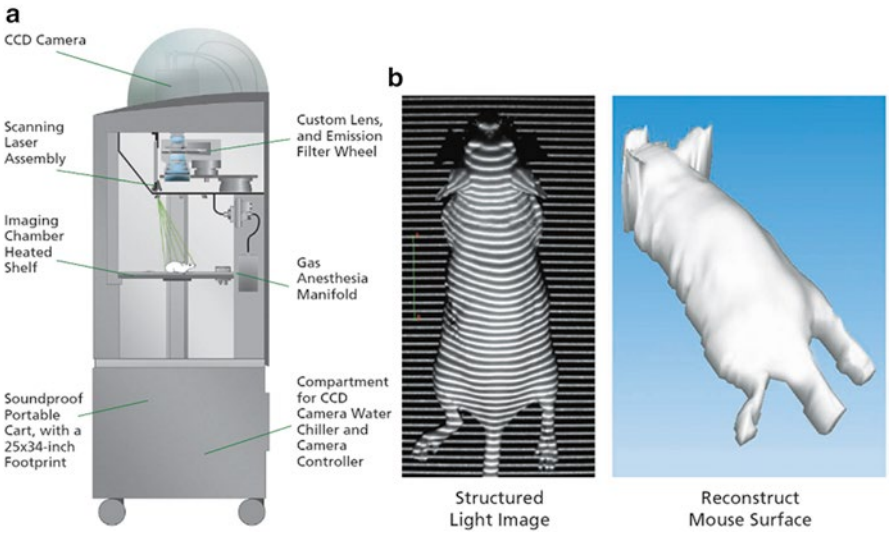

Fig. 8.10 Single view bioluminescence imaging system aided by structured light scanning (**a**) to acquire a mouse body surface (**b**) [reproduced from Caliper Life Sciences (Hopkinton, MA, USA) with permission]

felt, with an entry hatch to accommodate the wires and minimize light leakage. Typically, at each orientation, two images are obtained with light on and off for exposure time 0.1 s and 5–25 min, respectively. The former image indicates the mouse body surface. The latter image represents the bioluminescent view from the corresponding orientation relative to the mouse body. After finishing the data acquisition, a micro-CT scanner scans the mouse in the same body posture for anatomical structures. The experiment prototype is shown in Fig. 8.9b. Then, in-house software reconstructs a bioluminescent source distribution within the animal.

5.1.3 Multi-Modality Setups

Obtaining the surface topology of small animals in vivo is an issue when performing tomographic reconstruction. A simple method is to use the structured light technique, as seen in Fig. 8.10a [44]. This technique projects a series of parallel laser lines down on the subject at a certain angle. A CCD camera is used to acquire the structured light images of the illuminated subject. The surface topology of the small animal can be determined by analyzing the measured data (Fig. 8.10b). However, this method is simple only if we consider the small animal as an optically homogeneous object. The entire or partial topology of the small animal can then be obtained based on different hardware design [44, 72, 73].

To combine BLT with PET, an integrated PET and bioluminescence imaging system (OPET) was developed [42, 73–75]. This system is able to simultaneously

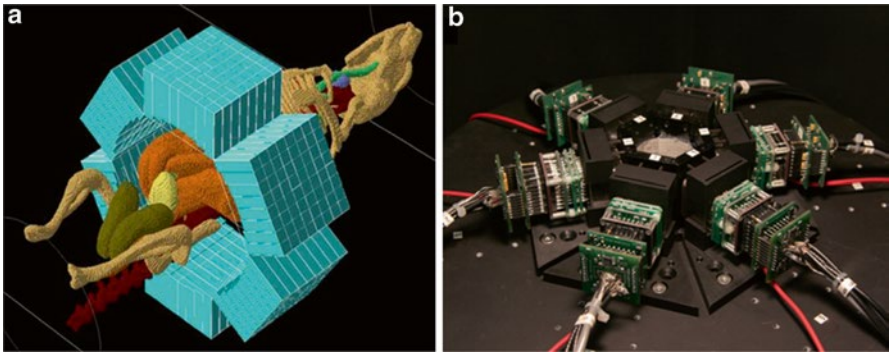

Fig. 8.11 OPET system (**a**) and its detection system composing of six detection modules (**b**) [reproduced from [42] and the Crump Institute for Molecular Imaging (UCLA, USA) respectively with permission]

image high energy annihilation photons emanating from the decay of positron emitting probes and bioluminescent photons emitted from bioluminescent probes. The schematic is shown in Fig. 8.11a. A ring-shaped detection module consists of six detectors with 64-channel multi-channel photomultiplier tubes (MCPMT) and an 8×8 scintillator crystal array, as seen in Fig. 8.11b. A field-programmable gate array (FPGA) is used for data acquisition [77]. This 3.5 cm diameter system is only slightly larger than a mouse, and provides the multi-view detection ability naturally. A higher detection sensitivity to optical photons in the contact mode can be potentially obtained than systems in the noncontact mode. Preliminary tests of the detector yielded promising data [74].

5.2 System Architecture for Fluorescence Molecular Tomography

Because of the use of illumination, flexible system design and different domain modes can be selected for fluorescence based imaging. More information can be detected when FMT works in time- and frequency-domain modes [77, 78]. In theory, frequency-domain detection information can be obtained from time-domain mode because time-domain mode can obtain photon information at the entire frequency. However, high noise is generated in time-domain mode especially at high frequency. An intensified CCD camera is used to detect the modulated photon signal [79, 80]. The SNR is significantly improved. Compared with the fiber-based contact detection mode, the CCD camera can obtain more detection information, improving the reconstruction quality [81]. Regarding the illumination mode, more information about fluorescent probes can be acquired by area illumination compared with point illumination [82]. Similar to CT imaging, more detection information is obtained when illumination-detector pairs rotate around the small animal [83].

Similar to system architecture for bioluminescence tomography, fluorescence molecular tomography can obtain anatomical information from micro-CT, surface topology from structured light scanning, and functional information from PET/SPECT imaging.

6 Optical Molecular Tomography Algorithms

6.1 Bioluminescence Tomography Algorithms

BLT is an ill-posed inverse source problem [84–86]. First, we need to find a mathematical model to describe the photon propagation process in the biological tissue, which allows prediction of the photon distribution on the small animal body surface. It is usually called the forward problem [48]. Then, we can solve the inverse problem, that is, recovering the bioluminescent source distribution with a suitable reconstruction algorithm [87].

6.1.1 Photon Propagation Modeling

To understand photon propagation in the biological tissue, two types of mathematical descriptions can be used: statistical modeling and deterministic modeling [52].

Statistical modeling methods track individual photon trajectories in biological tissues. In the optical imaging field, a popular technique is the Monte Carlo (MC) simulation [88–90]. Poisson noise can be naturally combined into the simulation, realistically mimicking the actual measurement. MC methods are considered the "gold standard" because of their precision given a large number of simulated photons. At the beginning, Monte Carlo methods were implemented using simple analytic geometry (such as slabs, cylinders, spheres, and so on) [88]. However, to simulate the bioluminescent or fluorescent photon propagation in small animals, MC methods need to be performed in complex heterogeneous geometry. Voxel-based MC methods were used to simulate photon propagation in models such as in a digital mouse atlas [89]. However, voxels cannot model irregular geometry precisely. Based on the triangular surface mesh, a more accurate simulation platform was developed [90]. Figure 8.12 shows the simulated photon distribution using the triangular surface mesh. A recent effort was made to perform MC simulation based on tetrahedrons to achieve a higher computational efficiency. Although the MC methods provide precise results, it is still very time-consuming because large numbers of photons need to be tracked. Parallel acceleration becomes natural, especially using popular GPU hardware because of the parallel nature of the MC methods [91–93]. These MC simulation packages are useful tools for system design and performance evaluation, especially to avoid the *inverse crime* problem [93–95].

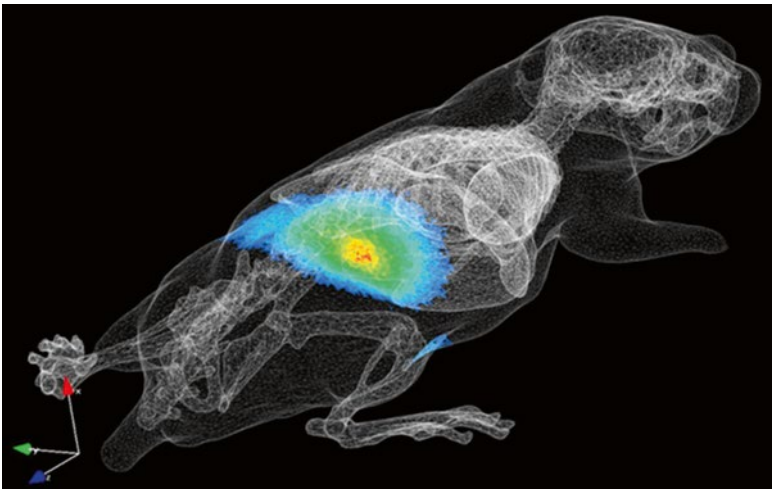

Fig. 8.12 Simulated photon distribution on the mouse surface using Monte Carlo methods (http://www.mosetm.net) [reproduced from the Life Sciences Research Center (Xidian University, China), the Medical Image Processing Group (Institute of Automation, Chinese Academy of Sciences (CAS), China) and the Optical Molecular Imaging Laboratory (Virginia Tech, USA) with permission]

Deterministic modeling methods mainly solve the radiative transfer equation (RTE, also called as Boltzmann equation) and its approximations [96]. The RTE can also provide precise results. In bioluminescence imaging, the source intensity is generally assumed to be time invariant during the data acquisition. Hence, the RTE can be expressed as [97]:

$$\hat{s}\cdot\nabla\psi(r,\hat{s})+(\mu_s(r)+\mu_a(r))\psi(r,\hat{s})=\mu_s(r)\int_{4\pi}p(\hat{s},\hat{s}')\psi(r,\hat{s}')d\hat{s}'+S(r,\hat{s})$$

where $\psi(r,\hat{s})$ denotes photons in the unit volume traveling from point r in direction $\hat{s}$. $p(\hat{s},\hat{s}')$ is the scattering phase function and gives the probability of a photon scattering anisotropically from direction $\hat{s}'$ to direction $\hat{s}$. Generally, the Henyey–Greenstein (HG) phase function is used to characterize this probability. Based on the principle of energy conservation, the RTE states that the radiance $\psi(r,\hat{s})$ is equal to the sum of all component contributions including absorption $\mu_a(r)$, scattering $\mu_s(r)$, and source energy $S(r,\hat{s})$ when light interacts with a unit volume. Currently, the diffusion approximation to the RTE is extensively applied [48]. Diffusion approximation is the first-order spherical harmonics approximation to the RTE and assumes that the phase function is independent of the absolute angle and the sources are isotropic. For simple geometries, analytic formulas can be obtained based on the diffusion approximation [21, 98]. When the simulation domain is homogeneous, the analytic solution can be obtained using a tangential planar approximation method for complex boundaries [44]. The most popular computational approach is the finite

element method (FEM) [52, 99]. Generally, the FEM solution on the fine discretized domain is more precise than that on the coarse counterpart. However, simulation time significantly increases with the domain refinement. An adaptive finite element method was introduced to obtain a satisfactory solution efficiently via local mesh refinement [100].

Diffusion approximation becomes inaccurate in some important cases, such as near source and surface, in anisotropic tissues, in domains of high absorption, and so on [52, 101]. To obtain more precise solutions, it is necessary to solve the RTE and its high-order approximations. A generalized delta-Eddington phase function was proposed to simplify the RTE [102]. As a result, an integral equation was developed to calculate the photon flux vector. A precise simulated solution can be obtained using this formula. The simulation speed is fast in a homogeneous domain but fast algorithms need to be developed in heterogeneous domains. Regarding the partial differential operator, the first- and second-order formulations of the RTE are usually used to solve the RTE directly [96]. Discrete ordinates (S_N) and spherical harmonics (P_N) methods, as two common numerical approximations, can yield excellent solutions. Compared with first-order formulations, the distinct advantage of the second-order forms such as the even-odd parity (EOP) equations is that the acquired FEM matrix is sparse positive-definite (SPD), easily being solved using iterative methods. In order to generate a precise simulation solution, and regardless of the first- and second-order equations, one has to set N as large as possible and then $N(N+2)$ and $(N+1)^2$ coupled equations corresponding to S_N and P_N methods need to be solved. This computational complexity becomes extremely high, especially on a large volume. A multigrid solver of the radiative transfer equation was developed through a direct angular discretization using the finite element method, providing encouraging numerical results at a relatively fast simulation speed [103]. Recently, the simplified spherical harmonics (SP_N) method was developed for optical imaging, improving computational efficiency significantly [104]. Furthermore, a parallel adaptive FEM method was proposed to improve the simulation speed [105].

6.1.2 Mouse Domain Triangulation

Anatomical images can be obtained from scanning a mouse using micro-CT, micro-MRI, or an alternative imaging modality. Domain triangulation is necessary for modeling the photon propagation and BLT reconstruction [9]. Tetrahedral element based modeling is quite suitable to represent a complex domain. To reflect optical properties of biological tissues, major organs in a mouse must be considered for mesh generation. Since raw anatomical images are rather detailed, interactive segmentation methods aided by expert knowledge are often used for precise organ segmentation [106]. Based on the segmented images, surface extraction can be performed using the classic Marching Cubes (MC) algorithm or its variants [107]. Recently, a Marching Tetrahedra (MT) algorithm was proposed to avoid the ambiguity problem in the MC algorithm [108]. The quality of the surface mesh can be improved via mesh smoothing (typically Laplacian smoothing) and simplification [109].

Note that the methods similar to the multiple-material marching cubes algorithm (M3C) [110] or multiregional Marching Tetrahedra (MMT) algorithm [108] are necessary for heterogeneous domain-based surface generation. Several triangulation methods, such as the octree-based algorithm, advancing front method and Delaunay technique, were developed to generate a volumetric mesh from the surface mesh [111]. Several open-source packages and commercial software are available to facilitate domain triangulation [112].

6.1.3 Bioluminescent Source Reconstruction

BLT is an ill-posed inverse source problem. The theoretical study shows that the uniqueness can only be obtained with sufficient *a priori* information [84–86]. Practically, the richer the *a priori* information we apply, the more improvement we have in BLT reconstruction. Using a physical heterogeneous phantom, Fig. 8.13 shows the importance of *a priori* optical properties distinctly. Three types of *a priori* information are extensively applied in reconstruction algorithms, that is, anatomical information [40, 42, 113–116], optical properties of each structural component [41, 42, 117], spectrally-resolved measurements on the body surface of a small animal [42, 45–47, 118]. Anatomical information yields a geometrical model. The forward imaging model is enabled after relevant optical properties are assigned to the geometrical model. Spectrally resolved data allows incorporation of the bioluminescent source spectra into account. Recently, the sparse characteristics of the bioluminescence probes was also explored as *a priori* information [93]. The use of *a priori* information significantly reduces the ill-posedness of this source reconstruction problem. This underscores that the value of analytic modeling-based reconstruction methods are limited to homogeneous geometries [44]. Due to the curved surface topography of the mouse and the necessity of addressing the heterogeneous characteristics of mouse tissues, numerical reconstruction algorithms, such as those based on FEM, are more accurate than the over-simplified analytical method and more efficient than the Monte Carlo simulation-based methods [41, 52].

BLT is, somehow, similar to single photon emission computed tomography (SPECT) and positron emission tomography (PET), since they all target source reconstructions despite dramatic differences in photon propagation trajectories. As a result, reconstruction algorithms for PET and SPECT can be adapted to realize the BLT reconstruction [42, 119, 120]. Specifically, the system response P-matrix needs to be computed, which is a very time-consuming step, although it can be obtained prior to acquiring the measured data. The BLT reconstruction is sensitive to multiple factors. Pre-calculating the P-matrix can affect the reconstruction quality due to the different heterogeneous geometries between what is assumed in the calculation and that used in the experiment [121]. Diffuse optical tomography (DOT) has been investigated for several decades, and the DOT algorithms can be applied to estimate source distribution for BLT [115, 122]. Since the BLT problem is linear, the least-square solution can be sought to produce the BLT reconstruction [41, 123, 124].

The feasibility of the BLT reconstruction was initially demonstrated using basic reconstruction algorithms and well-known *a priori* information [41, 42, 45, 46, 66, 118].

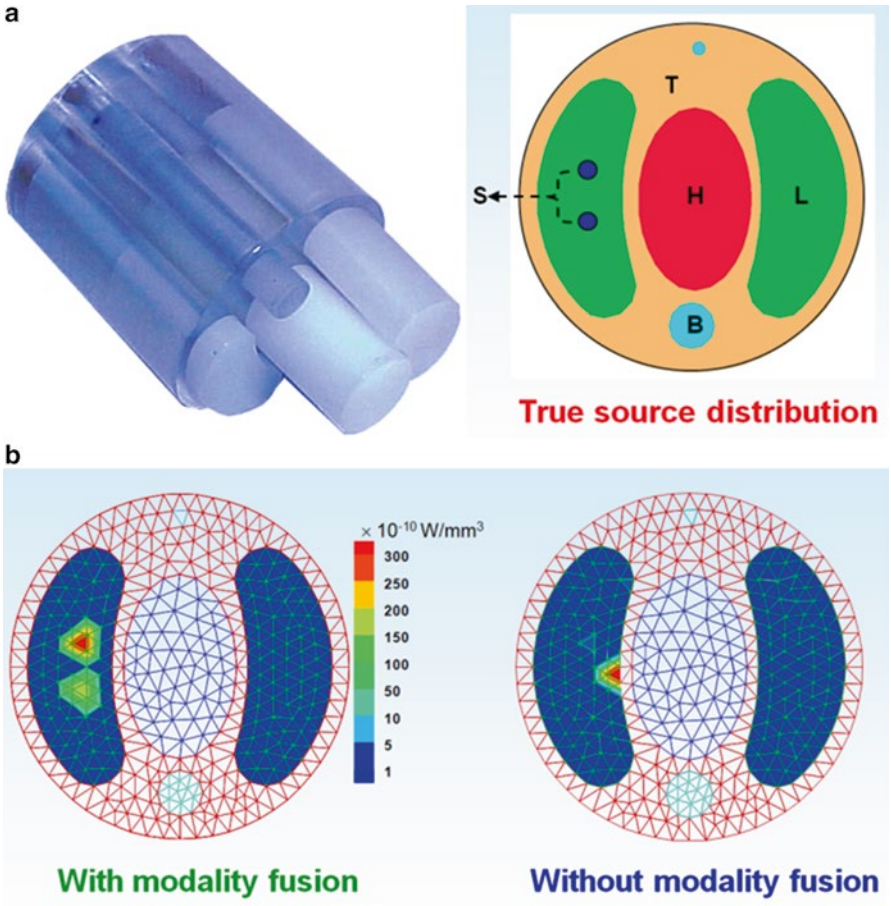

Fig. 8.13 BLT reconstruction with and without compensation of optical heterogeneity. (**a**) A physical heterogeneous phantom and the cross section of the phantom and the true source position; (**b**) the reconstructed results with/without compensation of optical heterogeneity [reproduced from the Optical Molecular Imaging Laboratory (Virginian Tech, USA) with permission]

To improve the BLT reconstruction quality, more ideas and theories were then developed. Stable BLT reconstruction with a low computational cost on a coarse discretized domain can be obtained because of fewer unknown variables involved and thus a less ill-poseness. The fine domain discretization means high spatial resolution, and may be subject to "the dimensionality curse". A multilevel adaptive finite element reconstruction algorithm was developed to harvest *a priori* reconstruction from the coarse mesh for the reconstruction on adaptively refined meshes [43, 95]. Compressed sensing (CS) theory is attractive because the real signals or images can be recovered using fairly fewer measurements if they are sparse on some basis, and the measurement operator and sparsity basis satisfy certain conditions [125, 126]. The improved BLT reconstruction was obtained based on the l_1 minimization strategy when the sparse characteristic of the bioluminescence probes holds [93].

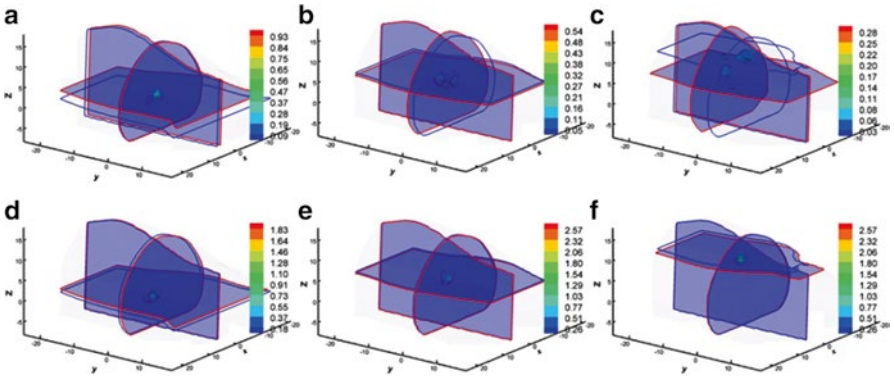

Fig. 8.14 Simulated BLT reconstruction with diffusion approximation (**a**–**c**) and SP_3 (**d**–**f**) using a mouse-shaped geometry when a single solid spherical source of 1.0 mm radius is located at different position. Cross-sections with *blue* and *red* boundaries are the center position of the actual and reconstructed sources, respectively. The mesh denotes reconstructed values larger than 10 % of the reconstructed maximum [reproduced from [70] with permission]

Earlier BLT reconstruction is mostly based on diffusion approximation theory. However, when performing BLT reconstructions on small animals, several approximations and assumptions can lead to poor source localization and quantification [40]. For example, the use of spectrally resolved information in the whole-body small animal reconstruction violates the assumptions of the diffusion approximation theory in cases of high absorption tissues, void-like domains, small tissue geometries and so on [40, 119]. BLT reconstruction with high-order approximations to the RTE was then investigated. The improved reconstructions were obtained using the RTE model in simple geometries [119, 127]. SP_N-based reconstruction also improved the imaging performance, as seen in Fig. 8.14 [70].

The use of *a priori* information, such as the heterogeneous tissue characteristics and spectrally resolved measurements significantly increases the computational cost. The introduction of high-order approximation models further increases the computational complexity of the BLT reconstruction on small animals, which is practically impossible to achieve if the computation is sequentially conducted. A fully parallel radiative-transfer-based reconstruction framework was proposed to make the BLT reconstruction for the whole-body of a small animal feasible [124]. The flowchart is shown in Fig. 8.15.

6.2 *Fluorescence Molecular Tomography Algorithms*

To model the photon propagation for fluorescence molecular tomography, two processes are involved, which are due to illumination and emission. Furthermore, time- and frequency-domain modes further complicate the situations. The Monte Carlo

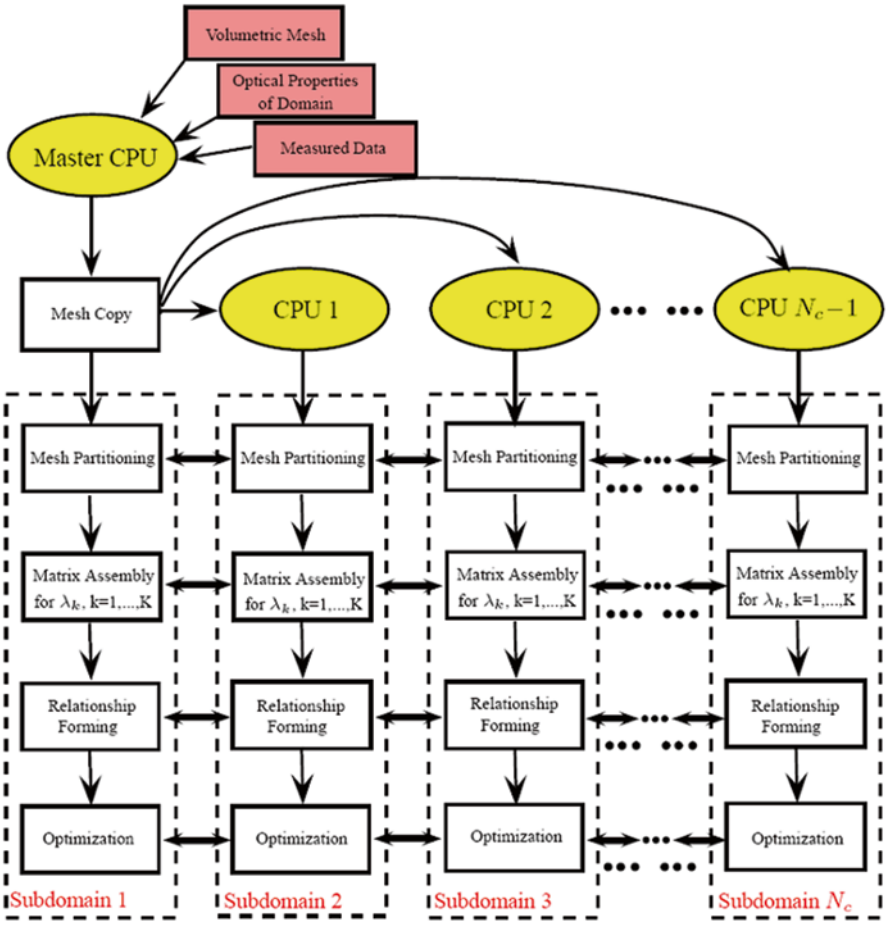

Fig. 8.15 Flowchart of a fully parallel reconstruction framework for BLT reconstruction using the approximation to the RTE. Four major steps are implemented in parallel, involving mesh partitioning, FEM-based matrix assembly, relationship forming between the unknown source distribution and the spectrally resolved measured data, and optimization (reproduced from [124] with permission)

methods, the RTE and relevant variants are widely used to study fluorescence molecular tomography. Generally, time- and frequency-dependent measurements bring more challenges. For development of reconstruction algorithms, analytical methods based on the Born and Rytov approximations are popular [128–130]. To handle the heterogeneous domain, finite element and finite difference methods are successful [127, 131]. Additionally, the adaptive mesh evolution strategy can provide the improved reconstruction [132].

7 Biomedical Applications

7.1 Bioluminescence Imaging

Classic bioluminescence probes are well established in biological research. By inserting the genetic fragment expressing luciferase into the gene sequence, various cell lines have developed, thanks to the good biocompatibility of classic bioluminescence probes. Mouse xenograft models are now widely available. Transgenic mice used to observe specific biological and disease processes can be labeled using bioluminescent probes. Planar bioluminescence imaging has been extensively applied in small animal models of human diseases in many biological research areas. Typical applications include tumor studies [133], cancer diagnosis [134, 135], drug discovery [136], and gene therapies [137].

While classic imaging modalities, such as micro-CT, micro-MRI, and micro-PET/SPECT, have been instrumental, planar bioluminescence imaging provides critical information, and bioluminescence tomography maximizes the potential of bioluminescent probes for in vivo biological research, especially in a synergistic combination with these mature imaging modalities [138]. When specific radioactive probes are used to label biological features of interest, it is difficult to control the high-energy photon emission. The circulation and metabolism of the radioactive probes generate a high background noise. Using a mouse xenograft model, the reconstruction results from the micro-PET/BLT multimodality imaging have shown precise tumor location and low background noise. Using the murine glial fibrillary acidic protein (GFAP) promoter (GFAP-luc mice), the BLT reconstruction can reveal the spatiotemporal distribution of bioluminescent signals correlated with GFAP immunoreactivity [139].

The analysis of the reconstruction results from several groups has shown that less than 3 mm accuracy in source center localization and less than 30 % error in source intensity estimation can be obtained using current BLT systems [44, 66]. Several studies on xenograft mouse models using different tumor cell lines have confirmed the potential of BLT in biomedical applications. Relevant results are shown in Figs. 8.16 and 8.17.

7.2 Fluorescence Molecular Imaging

Biological applications of fluorescence imaging are wide spread. Since the original FMT feasibility studies were performed on small animal brains [7], FMT has been highly developed for biological research [140–143]. Clinical applications of fluorescence imaging have also been reported with promising results. Typical clinical applications include fluorescence imaging of breast tumors [144] and lymphatic statuses [145]. Since FDA is much more tolerant of fluorescence than bioluminescence in the clinical settings, fluorescence imaging has a much greater translational potential than bioluminescence imaging.

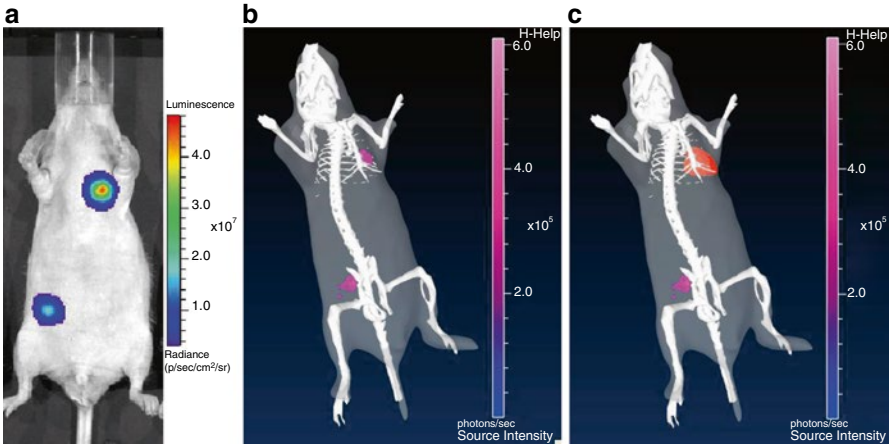

Fig. 8.16 Planar bioluminescence imaging of a mouse injected with PC-3M-luc cells (**a**) and the source reconstruction in *pink* with the display of the atlas skeleton (**b**) and additionally with the atlas heart (**c**) [reproduced from Caliper Life Sciences (Hopkinton, MA, USA) with permissions]

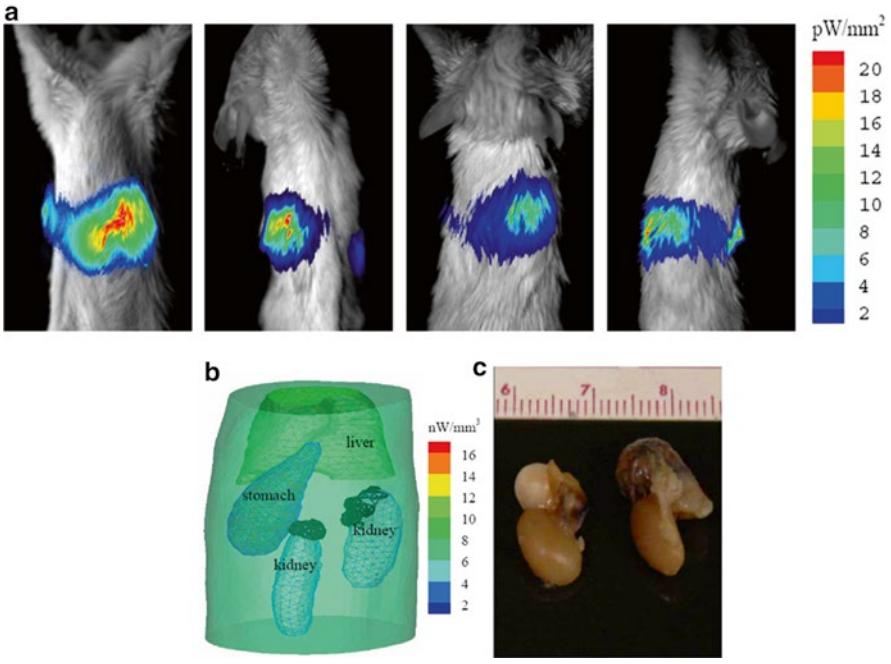

Fig. 8.17 Four-view detection of bioluminescent photon surface distribution of a mouse injected 22Rv1-luciferase human prostate cancer cells (**a**). (**b**) and (**c**) show the source reconstruction and dissection validation (reproduced from [66] with permission)

8 Summary

The development of optical molecular imaging helps understand biological processes in a totally new way. The unique advantages of bioluminescent and fluorescent probes are now recognized in extensive preclinical applications. Optical tomography promises to provide more accurate and rich imaging information compared with planar imaging methods. As a new imaging modality, current progress in the optical molecular tomography methods summarized in this chapter suggests a bright future despite the fact that this field is still in its infancy. Multidisciplinary collaboration is necessary to develop the next generation of probes, systems and methods to improve the reconstruction quality significantly. More photons can be generated from new optical probes by probe signal amplification. Tumors of small volume at deeper position can be detected using more sensitive detection systems. More precise localization and quantification can be achieved through better utilization of more *a priori* information, based on more precise photon propagation models and more advanced reconstruction algorithms.

Since the FMT and BLT concepts were proposed in early this century, several laboratory prototypes and commercial systems have been proposed. We believe that optical molecular tomography will grow from this beginning to develop into a major molecular imaging modality for modern biology and medicine.

Acknowledgments We would like to thank Dr. Ming Jiang for constructive discussions, Dr. Arion F. Chatziioannou for encouragement and advice, and Dr. Chaincy Kuo for Fig. 8.16. This work is supported by grants NIH R01 EB001458, DOE DE-SC0001234, NIH CA127189, EB001685, CA127189 and EB006036.

References

1. Ntziachristos V, Ripoll J, Wang LV, Weisslder R (2005) Looking and listening to light: the evolution of whole body photonic imaging. Nature Biotechnology 23 (3):313–320
2. Weissleder R (2002) Scaling Down Imaging: Molecular Mapping of Cancer in Mice. Nature Reviews Cancer 2:11–18
3. Herschman H (2003) Molecular imaging: looking at problems, seeing solutions. Science 302 (5645):605–608
4. Weissleder R (1999) Molecular Imaging: exploring the Next Frontier. Radiology 212 (3):609–614
5. Contag CH, Bachmann MH (2002) Advances in bioluminescence imaging of gene expression. Annual Review of Biomedical Engineering 4:235–260
6. Ntziachristos V (2006) Fluorescence molecular imaging. Annual Review of Biomedical Engineering 8:1–33
7. Ntziachristos V, Tung C-H, Bremer C, Weissleder R (2002) Fluorescence-mediated tomography resolves protease activity in vivo. Nature Medicine 8 (7):757–760
8. Wang G, Hoffman EA, McLennan G, Wang LV, Suter M, Meinel JF (2003) Development of the first bioluminescence CT scanner. Radiology 566:229
9. Wang G, Cong W, Shen H, Qian X, Henry M, Wang Y (2008) Overview of bioluminescence tomography--a new molecular imaging modality. Frontiers in Bioscience 13:1281–1293

10. Zhao H, Doyle TC, Coquoz O, Kalish F, Rice BW, Contag CH (2005) Emission spectra of bioluminescent reporters and interaction with mammalian tissue determine the sensitivity of detection in vivo. Journal of Biomedical Optics 10:041210–041210
11. Loening AM, Wu AM, Gambhir SS (2007) Red-shifted Renilla reniformis luciferase variants for imaging in living subjects. Nature Methods 4 (8):641–643
12. Wilson T, Hastings J (1998) Bioluminescence. Annual Review of Cell and Developmental Biology 14 (1):197–230
13. Jobsis F (1977) Noninvasive, infrared monitoring of cerebral and myocardial oxygen sufficiency and circulatory parameters. Science 198 (4323):1264–1267
14. So MK, Xu C, Loening AM, Gambhir SS, Rao J (2006) Self-illuminating quantum dot conjugates for in vivo imaging. Nature Biotechnology 24 (3):339–343
15. Villalobos V, Naik S, Piwnica-Worms D (2007) Current state of imaging protein-protein interactions in vivo with genetically encoded reporters. Annual Review of Biomedical Engineering 9:321–349
16. Robertson R, Germanos MS, Li C, Mitchell GS, Cherry SR, Silva MD (2009) Optical imaging of Cerenkov light generation from positron emitting radiotracers. Physics in Medicine and Biology 54 (16):N355–365
17. Cho JS, Taschereau R, Olma S, Liu K, Chen YC, Shen CK, van Dam RM, Chatziioannou AF (2009) Cerenkov radiation imaging as a method for quantitative measurements of beta particles in a microfluidic chip. Physics in Medicine and Biology 54 (22):6757–6771
18. Tsien R (2005) Building and breeding molecules to spy on cells and tumors. FEBS letters 579 (4):927–932
19. Shu X, Royant A, Lin MZ, Aguilera TA, Lev-Ram V, Steinbach PA, Tsien RY (2009) Mammalian expression of infrared fluorescent proteins engineered from a bacterial phytochrome. Science 324 (5928):804–807
20. Ohnukia T, Michaletb X, Tripathia A, Weissb S, Arisaka K Development of an Ultra-fast Single-Photon Counting Imager for Single-Molecule Imaging. In: Biomedical Optics, 2006. International Society for Optics and Photonics, pp 60920P–60920P
21. Rice BW, Cable MD, Nelson MB (2001) In vivo imaging of light-emitting probes. Journal of Biomedical Optics 6 (4):432–440
22. Nelson M, Rice B, Bates B, Beeman B, Cable M (2005) Light calibration device for use in low level light imaging systems. U.S. Patent No. 6919919
23. Hillman EM, Moore A (2007) All-optical anatomical co-registration for molecular imaging of small animals using dynamic contrast. Nature Photonics 1 (9):526–530
24. Mayes P, Dicker D, Liu Y, El-Deiry W (2008) Noninvasive vascular imaging in fluorescent tumors using multispectral unmixing. Biotechniques 45 (4):459–464
25. Jain R, Munn L (2002) Dissecting tumour pathophysiology using intravital microscopy. Nature Reviews Cancer 2 (4):266–276
26. Condeelis J, Segall J (2003) Intravital imaging of cell movement in tumours. Nature Reviews Cancer 3 (12):921–930
27. Wei X, Runnels J, Lin C (2003) Selective uptake of indocyanine green by reticulocytes in circulation. Investigative Ophthalmology & Visual Science 44 (10):4489–4496
28. Wang T, Contag C, Mandella M, Chan N, Kino G (2003) Dual-axes confocal microscopy with post-objective scanning and low-coherence heterodyne detection. Optics Letters 28 (20):1915–1917
29. Yang M, Baranov E, Jiang P, Sun F, Li X, Li L, Hasegawa S, Bouvet M, Al-Tuwaijri M, Chishima T (2000) Whole-body optical imaging of green fluorescent protein-expressing tumors and metastases. Proceedings of the National Academy of Sciences of the United States of America 97 (3):1206–1211
30. Ke S, Wen X, Gurfinkel M, Charnsangavej C, Wallace S, Sevick-Muraca E, Li C (2003) Near-infrared optical imaging of epidermal growth factor receptor in breast cancer xenografts. Cancer Research 63 (22):7870–7875
31. Zaheer A, Lenkinski R, Mahmood A, Jones A, Cantley L, Frangioni J (2001) In vivo near-infrared fluorescence imaging of osteoblastic activity. Nature Biotechnology 19 (12):1148–1154

32. Weissleder R, Tung C, Mahmood U, Bogdanov A (1999) In vivo imaging of tumors with protease-activated near-infrared fluorescent probes. Nature Biotechnology 17:375–378
33. Wunder A, Tung C, Müller-Ladner U, Weissleder R, Mahmood U (2004) In vivo imaging of protease activity in arthritis. Arthritis and Rheumatism 50:2459–2465
34. Mahmood U Near infrared optical imaging system to detect tumor protease activity. 1999. Radiology 213:866–870
35. Franceschini M, Moesta K, Fantini S, Gaida G, Gratton E, Jess H, Mantulin W, Seeber M, Schlag P, Kaschke M (1997) Frequency-domain techniques enhance optical mammography: initial clinical results. Proceedings of the National Academy of Sciences of the United States of America 94 (12):6468–6473
36. Grosenick D, Moesta K, Wabnitz H, Mucke J, Stroszczynski C, Macdonald R, Schlag P, Rinneberg H (2003) Time-domain optical mammography: initial clinical results on detection and characterization of breast tumors. Applied Optics 42:3170–3186
37. Taroni P, Danesini G, Torricelli A, Pifferi A, Spinelli L, Cubeddu R (2004) Clinical trial of time-resolved scanning optical mammography at 4 wavelengths between 683 and 975 nm. Journal of Biomedical Optics 9 (03):464–473
38. Hwang K, Houston J, Rasmussen J, Joshi A, Ke S, Li C, Sevick-Muraca E (2005) Improved excitation light rejection enhances small-animal fluorescent optical imaging. Molecular Imaging 4 (3):194
39. Ntziachristos V, Turner G, Dunham J, Windsor S, Soubret A, Ripoll J, Shih H (2005) Planar fluorescence imaging using normalized data. Journal of Biomedical Optics 10:064007
40. Virostko J, Powers AC, Jansen ED (2007) Validation of luminescent source reconstruction using single-view spectrally resolved bioluminescence images. Applied Optics 46:2540–2547
41. Cong W, Wang G, Kumar D, Liu Y, Jiang M, Wang LV, Hoffman EA, McLennan G, McCray PB, Zabner J, Cong A (2005) Practical reconstruction method for bioluminescence tomography. Optics Express 13 (18):6756–6771
42. Alexandrakis G, Rannou FR, Chatziioannou AF (2005) Tomographic bioluminescence imaging by use of a combined optical-PET (OPET) system: a computer simulation feasibility study. Physics in Medicine and Biology 50:4225–4241
43. Lv Y, Tian J, Cong W, Wang G, Yang W, Qin C, Xu M (2007) Spectrally resolved bioluminescence tomography with adaptive finite element analysis: methodology and simulation. Physics in Medicine and Biology 52:4497–4512
44. Kuo C, Coquoz O, Troy TL, Xu H, Rice BW (2007) Three-dimensional reconstruction of in vivo bioluminescent sources based on multispectral imaging. Journal of Biomedical Optics 12:024007
45. Chaudhari AJ, Darvas F, Bading JR, Moats RA, Conti PS, Smith DJ, Cherry SR, Leahy RM (2005) Hyperspectral and multispectral bioluminescence optical tomography for small animal imaging. Physics in Medicine and Biology 50 (23):5421–5441
46. Dehghani H, Davis SC, Jiang S, Pogue BW, Paulsen KD, Patterson MS (2006) Spectrally resolved bioluminescence optical tomography. Optics Letters 31:365–367
47. Cong A, Wang G (2006) Multispectral bioluminescence tomography: methodology and simulation. International Journal of Biomedical Imaging 2006
48. Arridge SR (1999) Optical tomography in medical imaging. Inverse problems 15:R41-R93
49. Segars WP, Tsui BMW, Frey EC, Johnson GA, Berr SS (2004) Development of a 4D digital mouse phantom for molecular imaging research. Molecular Imaging and Biology 6:149–159
50. Dogdas B, Stout D, Chatziioannou AF, Leahy RM (2007) Digimouse: a 3D whole body mouse atlas from CT and cryosection data. Physics in Medicine and Biology 52 (3):577–587
51. Comsa D, Farrell T, Patterson M (2006) Quantification of bioluminescence images of point source objects using diffusion theory models. Physics in Medicine and Biology 51 (15):3733–3746
52. Gibson AP, Hebden JC, Arridge SR (2005) Recent advances in diffuse optical imaging. Physics in Medicine and Biology 50:R1-R43

53. Guven M, Yazici B, Intes X, Chance B (2005) Diffuse optical tomography with a priori anatomical information. Physics in Medicine and Biology 50:2837–2858
54. Wang X, Pang Y, Ku G, Xie X, Stoica G, Wang LV (2003) Noninvasive laser-induced photoacoustic tomography for structural and functional in vivo imaging of the brain. Nature Biotechnology 21 (7):803–806
55. Wang L (2009) Multiscale photoacoustic microscopy and computed tomography. Nature Photonics 3 (9):503–509
56. Wang G, Shen H, Cong W, Zhao S, Wei Wei G (2006) Temperature-modulated bioluminescence tomography. Optics Express 14:7852–7871
57. Shah J, Park S, Aglyamov S, Larson T, Ma L, Sokolov K, Johnston K, Milner T, Emelianov S (2008) Photoacoustic imaging and temperature measurement for photothermal cancer therapy. Journal of Biomedical Optics 13:034024
58. Barbour R, Graber H, Chang J, Barbour S, Koo P, Aronson R (1995) MRI-guided optical tomography: prospects and computation for a new imaging method. IEEE Computational Science & Engineering 2 (4):63–77
59. Brooksby B, Dehghani H, Pogue B, Paulsen K (2003) Near-infrared (NIR) tomography breast image reconstruction with a priori structural information from MRI: algorithm development for reconstructing heterogeneities. IEEE Journal of Selected Topics in Quantum Electronics 9 (2):199–209
60. Schweiger M, Arridge S (1999) Optical tomographic reconstruction in a complex head model using a priori region boundary information. Physics in Medicine and Biology 44:2703–2722
61. Pogue B, Paulsen K (1998) High-resolution near-infrared tomographic imaging simulations of the rat cranium by use of a priori magnetic resonance imaging structural information. Optics Letters 23 (21):1716–1718
62. Ntziachristos V, Yodh A, Schnall M, Chance B (2002) MRI-guided diffuse optical spectroscopy of malignant and benign breast lesions. Neoplasia (New York, NY) 4 (4):347
63. Li C, Mitchell G, Dutta J, Ahn S, Leahy R, Cherry S (2009) A three-dimensional multispectral fluorescence optical tomography imaging system for small animals based on a conical mirror design. Optics Express 17 (9):7571–7585
64. Li C, Wang G, Qi J, Cherry S (2009) Three-dimensional fluorescence optical tomography in small-animal imaging using simultaneous positron-emission-tomography priors. Optics Letters 34 (19):2933–2935
65. Razansky D, Distel M, Vinegoni C, Ma R, Perrimon N, Köster R, Ntziachristos V (2009) Multispectral opto-acoustic tomography of deep seated fluorescent proteins in vivo. Nature Photonics 3 (7):412–417
66. Wang G, Cong W, Durairaj K, Qian X, Shen H, Sinn P, Hoffman E, McLennan G, Henry M (2006) In vivo mouse studies with bioluminescence tomography. Optics Express 14:7801–7809
67. Wang G, Shen H, Durairaj K, Qian X, Cong W (2006) The First Bioluminescence Tomography System for Simultaneous Acquisition of Multiview and Multispectral Data. International Journal of Biomedical Imaging 2006:Article ID 58601
68. Wang G, Cong A, Han W, Jiang M, Shen H, Cong W (2007) Systems and methods for multispectral bioluminescence tomography.
69. Hardeberg J, Schmitt F, Brettel H (2002) Multispectral color image capture using a liquid crystal tunable filter. Optical Engineering 41:2532
70. Lu Y, Douraghy A, Machado H, Stout D, Tian J, Herschman H, Chatziioannou A (2009) Spectrally resolved bioluminescence tomography with the SP3 approximation. Physics in Medicine and Biology 54:6477–6493
71. Wang G, Shen H, Liu Y, Cong A, Cong W, Wang Y, Dubey P (2008) Digital spectral separation methods and systems for bioluminescence imaging. Optics Express 16 (3):1719–1732
72. Kuo C, Coquoz O, Troy T, Zwarg D, Rice B (2005) Bioluminescent Tomography for in vivo Localization and Quantification of luminescent Sources from a Multiple-view Imaging System. Molecular Imaging 4 (3):370

73. Rannou F, Kohli V, Prout D, Chatziioannou A (2004) Investigation of OPET performance using GATE, a Geant4-based simulation software. IEEE Transactions on Nuclear Science 51 (5):2713–2717
74. Prout D, Silverman R, Chatziioannou A (2005) Readout of the optical PET (OPET) detector. IEEE Transactions on Nuclear Science 52 (1):28–32
75. Douraghy A, Prout D, Silverman R, Chatziioannou A (2006) Evaluation of scintillator afterglow for use in a combined optical and PET imaging tomograph. Nuclear Instruments and Methods in Physics Research Section A: Accelerators, Spectrometers, Detectors and Associated Equipment 569 (2):557–562
76. Douraghy A, Rannou F, Alexandrakis G, Silverman R, Chatziioannou A (2008) FPGA electronics for OPET: a dual-modality optical and positron emission tomograph. IEEE Transactions on Nuclear Science 55:2541–2545
77. Sevick E, Chance B, Leigh J, Nioka S, Maris M (1991) Quantitation of time-and frequency-resolved optical spectra for the determination of tissue oxygenation. Analytical Biochemistry 195 (2):330–351
78. Chance B (1991) Optical method. Annual Review of Biophysics and Biophysical Chemistry 20 (1):1–30
79. Godavarty A, Eppstein M, Zhang C, Theru S, Thompson A, Gurfinkel M, Sevick-Muraca E (2003) Fluorescence-enhanced optical imaging in large tissue volumes using a gain-modulated ICCD camera. Physics in Medicine and Biology 48 (12):1701–1720
80. Thompson A, Sevick-Muraca E (2003) Near-infrared fluorescence contrast-enhanced imaging with intensified charge-coupled device homodyne detection: measurement precision and accuracy. Journal of Biomedical Optics 8:111–120
81. Schulz R, Peter J, Semmler W, D'Andrea C, Valentini G, Cubeddu R (2006) Comparison of noncontact and fiber-based fluorescence mediated tomography. Optics Letters 31 (6):769–771
82. Joshi A, Bangerth W, Sevick-Muraca EM (2006) Non-contact fluorescence optical tomography with scanning patterned illumination. Optics Express 14(14):6516–6534
83. Turner G, Zacharakis G, Soubret A, Ripoll J, Ntziachristos V (2005) Complete-angle projection diffuse optical tomography by use of early photons. Optics Letters 30 (4):409–411
84. Wang G, Li Y, Jiang M (2004) Uniqueness theorems in bioluminescence tomography. Medical Physics 31 (8):2289–2299
85. Jiang M, Wang G (2007) Uniqueness results for multi-spectral bioluminescence tomography (invited). Paper presented at the An Interdisciplinary Workshop on Mathematical Methods in Biomedical Imaging and Intensity-Modulated Radiation Therapy (IMRT), Centro di Ricerca Matematica Ennio De Giorgi, Scuola Normale Superiore di Pisa, Italy, October 15 - 20
86. Han W, Cong W, Wang G (2006) Mathematical theory and numerical analysis of bioluminescence tomography. Inverse problems 22 (5):1659
87. Wang G, Jiang M, Tian J, Cong W, Li Y, Han W, Kumar D, Qian X, Shen H, Zhou T, Cheng J, Lv Y, Li H, Luo J (2006) Recent Development in Bioluminescence Tomography. Current Medical Imaging Reviews 4:453–457
88. Wang L, Jacques SL, Zheng L (1995) MCML - Monte Carlo modeling of photon transport in multi-layered tissues. Computer Methods and Programs in Biomedicine 47:131–146
89. Boas D, Culver J, Stott J, Dunn A (2002) Three dimensional Monte Carlo code for photon migration through complex heterogeneous media including the adult human head. Optics Express 10:159–169
90. Li H, Tian J, Zhu F, Cong W, Wang LV, Hoffman EA, Wang G (2004) A mouse optical simulation environment (MOSE) to investigate bioluminescent phenomena in the living mouse with the Monte Carlo method. Academic Radiology 11 (9):1029–1038
91. Alerstam E, Svensson T, Andersson-Engels S (2008) Parallel computing with graphics processing units for high-speed Monte Carlo simulation of photon migration. Journal of Biomedical Optics 13:060504
92. Fang Q, Boas D (2009) Monte Carlo Simulation of Photon Migration in 3D Turbid Media Accelerated by Graphics Processing Units. Optics Express 17 (22):20178–20190

93. Lu Y, Zhang X, Douraghy A, Stout D, Tian J, Chan T, Chatziioannou A (2009) Source reconstruction for spectrally-resolved bioluminescence tomography with sparse a priori information. Optics Express 17 (10):8062–8080
94. Holder S (2005) Electrical Impedance Tomography. Institute of Physics Publishing, Bristol and Philadelphia
95. Lv Y, Tian J, Cong W, Wang G, Luo J, Yang W, Li H (2006) A multilevel adaptive finite element algorithm for bioluminescence tomography. Optics Express 14 (18):8211–8223
96. Lewis EE, Warren F. Miller J (1984) Computational Methods of Neutron Transport. John Wiley & Sons, New York
97. Ishimaru A (1997) Wave propagation and scattering in random media. IEEE Press,
98. Cong W, Wang LV, Wang G (2004) Formulation of photon diffusion from spherical bioluminescent sources in an infinite homogeneous medium. Biomedical Engineering Online 3:12
99. Arridge SR, Schweiger M, Hiraoka M, Delpy DT (1993) A finite element approach for modeling photon transport in tissue. Medical Physics 20:299–309
100. Lv Y, Tian J, Li H, Luo J, Cong W, Wang G, Kumar D Modeling the forward problem based on the adaptive FEMs framework in bioluminescence tomography. In: SPIE Optics+ Photonics, 2006. p 631801
101. Hielscher A, Alcouffe R, Barbour R (1998) Comparison of finite-difference transport and diffusion calculations for photon migration in homogeneous and heterogeneous tissues. Physics in Medicine and Biology 43 (5):1285–1302
102. Cong W, Cong A, Shen H, Liu Y, Wang G (2007) Flux vector formulation for photon propagation in the biological tissue. Optics Letters 32(19):2837–2839
103. Gao H, Zhao H (2009) A Fast-Forward Solver of Radiative Transfer Equation. Transport Theory and Statistical Physics 38 (3):149–192
104. Klose AD, Larsen EW (2006) Light transport in biological tissue based on the simplified spherical harmonics equations. Journal of Computational Physics 220 (1):441–470
105. Lu Y, Chatziioannou A (2009) A parallel adaptive finite element method for the simulation of photon migration with the radiative-transfer based model. Communications in Numerical Methods in Engineering 25 (6):751–770
106. Pham DL, Xu C, Prince JL (2000) Current Methods in Medical Image Segmentation. Annual Review of Biomedical Engineering 2:315–337
107. Lorensen WE, Cline HE (1987) Marching cubes: a high resolution 3D surface construction algorithm. Proceedings of the 14th annual conference on Computer graphics and interactive techniques 21 (4):163–169
108. Cong A, Liu Y, Kumar D, Cong W, Wang G Geometrical modeling using multiregional marching tetrahedra for bioluminescence tomography. In: Robert L. Galloway JKRC (ed) Medical Imaging 2005: Visualization, Image-Guided Procedures, and Display, 2005. pp 756–763
109. Cignoni P, Montani C, Scopigno R (1998) A comparison of mesh simplification algorithms. Computers & Graphics 22:37–54
110. Wu Z (2001) Accurate and Efficient Three-Dimensional Mesh Generation for Biomedical Engineering Applications. Worcester Polytechnic Institute
111. Owen SJ A Survey of Unstructured Mesh Generation Technology. In: Proceedings of the 7th International Meshing Roundtable, 1998. Pp 239–267
112. Owen SJ (1998) Meshing Software Survey, Hexahedra and Tetrahedra Mesh Generation Software, http://www.andrew.cmu.edu/user/sowen/software/hexahedra.html; http://www.andrew.cmu.edu/user/sowen/software/tetrahedra.html.
113. Cong W, Wang G (2006) Boundary integral method for bioluminescence tomography. Journal of Biomedical Optics Letters 11(2):020503–020503
114. Cong W, Durairaj K, Wang LV, Wang G (2006) A Born-type approximation method for bioluminescence tomography. Medical Physics 33:679–686
115. Dehghani H, Davis S, Pogue B (2008) Spectrally resolved bioluminescence tomography using the reciprocity approach. Medical Physics 35:4863
116. Jiang M, Zhou T, Cheng J, Cong W, Wang G (2007) Image reconstruction for bioluminescence tomography from partial measurement. Optics Express 15 (18):11095–11116

117. Lv Y, Tian J, Cong W, Wang G (2007) Experimental study on bioluminescence tomography with multimodality fusion. International Journal of Biomedical Imaging 2007:86741
118. Kuo C, Coquoz O, Stearns DG, Rice. BW Diffuse luminescence imaging tomography of in vivo bioluminescent markers using multi-spectral data. In: Society for Molecular Imaging 3rd Annual Meeting (St. Louis), 2004. Cambridge: MIT Press, p 227
119. Klose AD (2007) Transport-theory-based stochastic image reconstruction of bioluminescent sources. Journal of the Optical Society of America A 24:1601–1608
120. Slavine N, Lewis M, Richer E, Antich P (2006) Iterative reconstruction method for light emitting sources based on the diffusion equation. Medical Physics 33:61
121. Alexandrakis G, Rannou FR, Chatziioannou AF (2006) Effect of optical property estimation accuracy on tomographic bioluminescence imaging: simulation of a combined optical-PET (OPET) system. Physics in Medicine and Biology 51:2045–2053
122. Gu X, Zhang Q, Larcom L, Jiang H (2004) Three-dimensional bioluminescence tomography with model-based reconstruction. Optics Express 12:3996–4000
123. Cong W, Kumar D, Liu Y, Cong A, Wang G A practical method to determine the light source distribution in bioluminescent imaging. In: Bonse U (ed) Developments in X-Ray Tomography IV, 2004. pp 679–686
124. Lu Y, Machado HB, Douraghy A, Stout D, Herschman H, Chatziioannou AF (2009) Experimental bioluminescence tomography with fully parallel radiative-transfer-based reconstruction framework. Optics Express 17:16681–16695
125. Donoho D (2006) Compressed sensing. IEEE Transactions on Information Theory 52 (4):1289–1306
126. Candès E, Romberg J, Tao T (2006) Stable signal recovery from incomplete and inaccurate measurements. Communications on Pure and Applied Mathematics 59 (8):1207
127. Klose AD, Ntziachristos V, Hielscher AH (2005) The inverse source problem based on the radiative transfer equation in optical molecular imaging. Journal of Computational Physics 202:323–345
128. O'Leary M, Boas D, Li X, Chance B, Yodh A (1996) Fluorescence lifetime imaging in turbid media. Optics Letters 21 (2):158–160
129. Chang J, Graber H, Barbour R (1997) Luminescence optical tomography of dense scattering media. Journal of the Optical Society of America A 14 (1):288–299
130. Ntziachristos V, Weissleder R (2001) Experimental three-dimensional fluorescence reconstruction of diffuse media by use of a normalized Born approximation. Optics Letters 26 (12):893–895
131. Jiang H (1998) Frequency-domain fluorescent diffusion tomography: a finite-element-based algorithm and simulations. Applied Optics 37:5337–5343
132. Joshi A, Bangerth W, Sevick-Muraca E (2004) Adaptive finite element based tomography for fluorescence optical imaging in tissue. Optics Express 12 (22):5402–5417
133. Lyons S, Meuwissen R, Krimpenfort P, Berns A (2003) The generation of a conditional reporter that enables bioluminescence imaging of Cre/loxP-dependent tumorigenesis in mice. Cancer Research 63 (21):7042
134. Rehemtulla A, Stegman L, Cardozo S, Gupta S, Hall D, Contag C, Ross B (2000) Rapid and quantitative assessment of cancer treatment response using in vivo bioluminescence imaging. Neoplasia (New York, NY) 2 (6):491
135. Jenkins D, Oei Y, Hornig Y, Yu S, Dusich J, Purchio T, Contag P (2003) Bioluminescent imaging (BLI) to improve and refine traditional murine models of tumor growth and metastasis. Clinical and Experimental Metastasis 20 (8):733–744
136. Rudin M, Weissleder R (2003) Molecular imaging in drug discovery and development. Nature Reviews Drug Discovery 2 (2):123–131
137. Ray P, Bauer E, Lyer M Monitoring gene therapy with reporter gene imaging. In: Seminars in nuclear medicine, 2001. vol 4. Elsevier, pp 312–320
138. Ray P, Wu A, Gambhir S (2003) Optical bioluminescence and positron emission tomography imaging of a novel fusion reporter gene in tumor xenografts of living mice. Cancer Research 63 (6):1160

139. Cordeau Jr P, Lalancette-Hebert M, Weng Y, Kriz J (2008) Live imaging of neuroinflammation reveals sex and estrogen effects on astrocyte response to ischemic injury. Stroke 39 (3):935
140. Graves E, Ripoll J, Weissleder R, Ntziachristos V (2003) A submillimeter resolution fluorescence molecular imaging system for small animal imaging. Medical Physics 30:901
141. Patwardhan S, Bloch S, Achilefu S, Culver J (2005) Time-dependent whole-body fluorescence tomography of probe bio-distributions in mice. Optics Express 13 (7):2564–2577
142. Montet X, Ntziachristos V, Grimm J, Weissleder R (2005) Tomographic fluorescence mapping of tumor targets. Cancer Research 65 (14):6330
143. Ntziachristos V, Schellenberger E, Ripoll J, Yessayan D, Graves E, Bogdanov A, Josephson L, Weissleder R (2004) Visualization of antitumor treatment by means of fluorescence molecular tomography with an annexin V–Cy5. 5 conjugate. Proceedings of the National Academy of Sciences 101 (33):12294
144. Godavarty A, Thompson A, Roy R, Gurfinkel M, Eppstein M, Zhang C, Sevick-Muraca E (2004) Diagnostic imaging of breast cancer using fluorescence-enhanced optical tomography: phantom studies. Journal of Biomedical Optics 9:488
145. Sevick-Muraca E, Sharma R, Rasmussen J, Marshall M, Wendt J, Pham H, Bonefas E, Houston J, Sampath L, Adams K (2008) Imaging of Lymph Flow in Breast Cancer Patients after Microdose Administration of a Near-Infrared Fluorophore: Feasibility Study. Radiology 246 (3):734

Chapter 9
Advances in Radiotracer Development for Molecular Imaging

Yongjian Liu and Michael J. Welch*

1 Introduction

Molecular imaging is currently defined by the society of nuclear medicine as the visualization, characterization and measurement of biological processes at the molecular and cellular levels in humans and other living systems [1]. Historically, molecular imaging can be traced back to France in 1896, when Henri Becquerel discovered that certain materials emitted energetic "rays", a physical process that called radioactive decay later [2]. In 1950s, Michel Ter-Pogossian and his colleagues conducted some pioneering molecular imaging studies in the determination of oxygen content in malignant neoplasms by using ^{15}O-labeled gas mixture. Later, based on ^{15}O-labeled radiopharmaceuticals, Ter-Pogossian et al developed quantitative in vivo tracer techniques and carried out a series of brain imaging studies such as the first quantitative measurements of regional brain oxygen consumption in human etc [3, 4].

In general, due to the advance in molecular biology, including genomics and proteomics etc, the development of biologically targeted markers has become feasible, which in turn propels the rapid growth of applications in molecular imaging field consisting of various modalities such as nuclear imaging including positron emission tomography (PET), single photon emission computed tomography (SPECT), magnetic resonance imaging (MRI), magnetic resonance spectroscopy (MRS), computed tomography (CT), ultrasound, bioluminescence, fluorescence imaging and also the combination of multimodalities, for example, PET/CT, SPECT/CT and PET/MRI [5–10] etc. In the past few decades, significant progress in these imaging instrumentations has been achieved, which enhances the in vivo imaging capability in small animals and human, improves the smooth transfer of

*This work is dedicated to Dr. Welch, who passed away on May 6th, 2012.

Y. Liu (✉)
Mallinckrodt Institute of Radiology, Washington University School of Medicine,
510 S Kingshighway Blvd, Campus Box 8225, St Louis, MO 63110, USA
e-mail: liuyo@mir.wustl.edu

H. Zaidi (ed.), *Molecular Imaging of Small Animals: Instrumentation and Applications*,
DOI 10.1007/978-1-4939-0894-3_9,

understanding and characterization information between species, and eventually facilitates the translation into clinical application [11–13].

Molecular imaging has its roots in molecular and cell biology as well as imaging technology [14]. In general, it exploits specific molecular probes as well as intrinsic tissue characteristics as the source of image contrast, and provides the potential for understanding of integrative biology, earlier detection and characterization of disease, and evaluation of treatment [15]. In contradistinction to the conventional readouts, one of the advantages of molecular imaging is that it can be performed in the intact organism with sufficient spatial and temporal resolution for studying biological processes in vivo [11].

In the design of imaging probe, several key criteria must generally be met: (a) availability of high affinity probes with reasonable pharmacodynamics; (b) the ability of these probes to overcome biological delivery barriers (vascular, interstitial, cell membrane); (c) use of amplification strategies (chemical or biologic); and (d) availability of sensitive, fast, high resolution imaging techniques. In a typical scenario, all four prerequisites must be met for successful in vivo imaging at the molecular level [10]. Historically, imaging of cell-specific surface antigens or epitopes with radiolabeled monoclonal antibodies (i.e., IgG) represented some of the earliest molecular imaging studies [16]. With the advances in molecular and cellular biology techniques, more and more imaging probes with high affinity to the molecular targets have been developed [9, 12]. In general, most of the imaging probes could be categorized into three strategies: direct imaging, indirect imaging, and surrogate imaging [17]. Direct imaging is based on imaging the target directly and usually uses a target-specific probe for cell surface receptors, intracellular molecules or gene expression, which interacts directly with the target providing an image intensity correlating to the amount of target actively present. This imaging strategy is common in nuclear medicine such as the monoclonal antibody targeting of a particular cell membrane epitope, imaging the activity of an enzyme with enzyme-specific probe, imaging the receptor density with radiolabeled small molecule, and targeting mRNA or protein in vivo with radiolabeled antisense probes etc [17–21]. The indirect imaging is more complicated because it is composed of multiple elements. One paradigm is "reporter imaging" which contains a marker/reporter gene and a marker/reporter probe. The reporter gene product can be an enzyme that converts a reporter probe to a metabolite that is selectively trapped within transduced cells. The main advantage of this strategy is the enzymatic amplification of the probe-signal that facilitates imaging the magnitude and location of reporter gene expression [12]. This strategy is quite popular in radionuclide-based imaging, optical imaging, as well as MRI [14, 22–29]. Surrogate imaging usually detects downstream effects of endogenous molecular genetic processes using established radiopharmaceuticals and clinical imaging protocols. This approach is particularly attractive for potential translation into clinical studies in the short-term, because existing radiopharmaceuticals and imaging paradigms may be useful for monitoring downstream effects of changes in specific molecular genetic pathways in diseases such as cancer [14, 30–33]. So far, hundreds of molecular imaging probes have been developed based on the three imaging strategies and there are more under development. In this chapter, we will focus on the recent advance of radionuclide-based molecular imaging probe.

2 Radionuclides for Molecular Imaging

A radionuclide is an unstable form of a chemical element that radioactively decays, resulting in the emission of nuclear radiation. Radioactive decay is a spontaneous nuclear transformation that has been shown to be unaffected by pressure, temperature, and chemical forms etc (except for a few special cases). This insensitivity to extranuclear conditions allows us to characterize radioactive nuclei by their decay periods, modes, and energies of decay without regard to their physical or chemical condition. The mode of radioactive decay is dependent on the particular nuclide involved. In general, the radioactive decay can be characterized by α-, β- and γ-radiation. Alpha-decay is the emission of helium nuclei. Beta-decay is the creation and emission of either electrons (β^-) or positrons (β^+) or the process of electron capture. Gamma-decay is the emission of electromagnetic radiation where the transition occurs between the different energy levels of same nucleus. Internal conversion is another mode of radioactive decay that a nucleus loses its energy by interaction of the nuclear field with that of the orbital electrons, causing ionization of an electron instead of γ-ray emission. In some circumstances, spontaneous fission will be observed in the heaviest nuclei that the nucleus dissociates spontaneously into two roughly equal parts, leading to the emission of electromagnetic radiation and of neutrons. In addition, there are some unusual decay modes observed for nuclides very far from the stability line, such as neutron emission, proton emission, and ^{12}C-emission.

In molecular imaging, the radionuclides used for imaging probes (PET and SPECT) are mostly positron emitters or gamma-emitters. The positron decay can be described symbolically as:

$$ {}^{A}_{Z}X \rightarrow {}^{A}_{Z-1}X^{-} + {}^{0}_{+1}\beta + \nu \rightarrow {}^{A}_{Z-1}X + {}^{0}_{+1}e^{-} + {}^{0}_{+1}\beta + \nu \tag{9.1} $$

A proton-rich nucleus emits a positron after the conversion of a proton into a neutron, with simultaneous emission of a neutrino (ν). The positron is the antiparticle to the electron and the energy of emission can take a continuum of values up to a maximum, which depends on the difference between the energetic states of the parent–daughter nuclei. After emission from the nucleus, the positron loses kinetic energy by interactions with surrounding matter such as inelastic/elastic collision or scattering. Eventually, the positron combines with an electron and annihilates, which releases two 511 keV photons in (the rest-mass equivalent of each particle) opposite directions (ca. 180° to each other) to conserve momentum. The distance traveled by the positron before annihilation depends on its initial energy.

In γ decay, electromagnetic radiation is emitted as a nucleus undergoes transitions from its higher excited state to lower excited state or ground state. The excited state of the nucleus and the lower-energy daughter state that is reached as a result of the γ emission are referred to as nuclear isomers only when the half-life of the excited state is long enough to be easily measurable. In this case, the γ decay is described as an isomeric transition. Gamma ray emissions are characteristic of the radionuclides, and the energies of the emitted photons depend on the energy differences between the initial excited state and the next one.

Table 9.1 Radionuclides commonly used in SPECT imaging

Nuclide	$T_{1/2}$	Decay %	β Energy (keV) Max.	Mean	Main photon keV (%)	Production
^{67}Ga	3.26 day	EC			93 (39.2); 185 (21.2) 300 (16.8)	^{68}Zn (p, 2n) ^{67}Ga
^{99m}Tc	6.01 h	IT			140 (89.1)	^{99}Mo/^{99m}Tc generator
^{111}In	2.8 day	EC			171 (90.7); 245 (94.1)	^{111}Cd (p, n) ^{111}In ^{112}Cd (p, 2n) ^{111}In
^{123}I	13.27 h	EC			159 (83.3)	^{124}Te (p, 2n) ^{123}I ^{124}Xe (p, 2n)^{123}I
^{125}I	59.41 day	EC			35.5 (6.68 %)	^{124}Xe (n, γ)$^{125m/125g}$Xe→ ^{125}I
^{201}Tl	72.91 h	EC			167 (10.0)	^{203}Tl (p, 3n)^{201}Pb:^{201}Tl
^{133}Xe	5.24 day	β^-	346	100	81 (38.0)	^{235}U fission

According to the production modes, the radionuclides used for PET and SPECT imaging can be differentiated into three groups: reactor nuclides, cyclotron nuclides, and generator nuclides. The production and application of radionuclide-based tracers and recent progress of radiochemistry and radiopharmacy is reviewed elsewhere [34–41]. The most commonly used radionuclides in SPECT and PET imaging are listed in Tables 9.1 and 9.2, respectively [36].

Radiotracers are chemical species that contain a radionuclide, and it is the activity of the radioisotope that is monitored to follow the process under investigation. The first radiotracer application in biological process was done in 1913 with radium-D (^{210}Pb) by Georg Hevesy in tracing the movement of radionuclides from soil into plants and the movement of food through animal systems [42, 43]. For the radionuclides listed in Table 9.1, technetium-99m (^{99m}Tc) is the most widely used γ-emitter for nuclear imaging due to its suitable half-life and nuclear properties. Even now, about 80 % of diagnostic scans are performed using ^{99m}Tc labeled radiotracers. Technetium-99m decays with a half-life of 6.0 h by isomeric transition to ^{99g}Tc, thereby emitting a single photon with energy of 141 keV, which is almost ideal in meeting the sensitivity maximum of SPECT camera system [44]. However, the most important reason for the special role of ^{99m}Tc in SPECT is the cost effectiveness and the on-demand availability of the isotope through the ^{99}Mo/^{99m}Tc generator system. The mother nuclide molybdenum-99 can be produced either by ^{98}Mo(n, γ)^{99}Mo reaction or the fission of uranium-235, with the later method is more preferred because of the high yield and almost carrier-free and thus of the high specific activity. In addition, the use of Al_2O_3 matrix reduces the risk of ^{99}Mo breakthrough, resulting in the high radionuclide purity of ^{99m}Tc eluate. Molybdenum-99 has a half-life of 66 h and decays by β^- emission; 87 % of the decay goes ultimately to the metastable state ^{99m}Tc and the remaining 13 % to the ground state ^{99g}Tc. ^{99m}Tc can be separated from ^{99}Mo by column chromatography with sterile and pyrogen free saline. Since the half-life of ^{99}Mo is ten times higher than that of ^{99m}Tc, transient equilibrium is achieved, which allows the daily use of ^{99m}Tc up to 1 week. In addition, the rich chemistry of technetium at various oxidation states facilities the widespread of ^{99m}Tc radiopharmaceuticals in brain, heart, renal, hypoxia imaging etc [44–47].

Table 9.2 Radionuclides commonly used in PET imaging

Nuclide	$T_{1/2}$	Decay %	β Energy (keV) Max.	Mean	Main photon keV (%)	Production
^{11}C	20.4 min	β^+ (99.8) EC (0.2)	959	386	511 (199.5)	^{14}N (p, α) ^{11}C
^{13}N	9.96 min	β^+ (99.8) EC (0.2)	1,198	492	511 (199.6)	^{16}O (p, α) ^{13}N
^{15}O	2.07 min	β^+ (99.9) EC (0.1)	1,732	735	511 (199.8)	^{15}N (p, n) ^{15}O
^{18}F	109.7 min	β^+ (96.7) EC (0.1)	634	245	511 (193.5)	^{18}O (p, n) ^{18}F
^{60}Cu	23.7 min	β^+ (93) EC (7)	3,772	970	511 (185); 826 (21.7) 1,332 (88); 1,792 (45.4)	^{60}Ni (p, n) ^{60}Cu
^{61}Cu	3.33 h	β^+ (61) EC (39)	1,215	500	511 (123); 656 (10.8)	^{61}Ni (p, n) ^{61}Cu
^{62}Cu	9.7 min	β^+ (97) EC (3)	2,926	1,314	511 (194.9)	$^{62}Zn/^{62}Cu$ generator
^{64}Cu	12.7 h	β^+ (17) EC (44)	653	278	511 (34.8)	^{64}Ni (p, n) ^{64}Cu
^{66}Ga	9.49 h	β^+ (56) EC (44)	4,153	1,740	511 (112); 1,039 (36) 2,752 (23.3)	^{63}Cu (α, n) ^{66}Ga
^{68}Ga	67.7 min	β^+ (89) EC (11)	1,899	829	511 (178.3)	$^{68}Ge/^{68}Ga$ generator
^{75}Br	96.7 min	β^+ (73) EC (27)	2,008	719	511 (146); 287 (90)	^{76}Se (p, 2n) ^{75}Br ^{76}Se (d, 3n) ^{75}Br
^{76}Br	16.2 h	β^+ (55) EC (45)	3,941	1,180	511 (109); 559 (74) 657 (15.9); 1,854 (14.7)	^{76}Se (p, n) ^{76}Br ^{76}Se (d, 2n) ^{76}Br
^{82}Rb	1.25 min	β^+ (96) EC (4)	3,378	1,417	511 (191)	$^{82}Sr/^{82}Rb$ generator
^{86}Y	14.7 h	β^+ (33) EC (66)	3,141	664	511 (63.9); 1,077 (82.5) 1,115 (30.5); 627 (32.6)	^{86}Sr (p, n) ^{86}Y
^{94m}Tc	52.0 min	β^+ (70) EC (30)	2,438	1,072	511 (140.4); 871 (94.2)	^{94}Mo (p, n) ^{94m}Tc
^{124}I	4.18 day	β^+ (23) EC (77)	2,138	820	511 (46); 603 (62.9) 723 (10.3)	^{124}Te (p, n) ^{124}I ^{124}Te (d, 2n) ^{124}I

Due to the wide application of ^{99m}Tc in SPECT, technetium-94m has been examined for the potential in PET imaging taking the advantage of the rich technetium chemistry and the appropriate nuclear properties ($t_{1/2}$ = 52 min, 2.4 MeV positron with 72 % abundance). The commercially available ^{94m}Tc-teboroxime kits showed consistent results with those reported for ^{99m}Tc, indicating the potential opportunities for study many of new technetium compounds with PET [48, 49].

Radioiodine became available for medical application (i.e. thyroid uptake measurement) from cyclotron production since late 1930s on a limited basis. With the development of nuclear reactor, iodine-131 became the "classic" radioiodine for both diagnosis and therapy. However, due to the attractive nuclear (159 keV γ with 83 % abundance, $t_{1/2}$ = 13.3 h) properties (Table 9.1), and high purity production, and the versatile radioiodination approaches such as isotopic exchange,

oxidation etc, leading to the regio-specific iodination, iodine-123 is becoming the "ideal" radioiodine for SPECT imaging [50].

Another important isotope for SPECT imaging is indium-111 produced from cyclotron. The use of ^{111}In in medical application started from the late 1960s. Due to the 2.8 days physical half-life, In-111 is mostly used to study the biomolecules with relatively slow in vivo kinetics such as antibodies and peptides etc. with diethylenetriaminepentaacetic acid (DTPA) chelation and conjugation [51].

The greatest advantage of PET is the potential to image and study the biochemical processes in vivo without altering or affecting in any way the homeostasis due to some organic positron-emitters. Among the list of the positron emitting radionuclides (Table 9.2), carbon-11, nitrogen-13, oxygen-15 and fluorine-18 are the most important PET isotopes. The physical half-lives of these radionuclides are relatively short (<2 h), leading to the feasibility of high specific activity.

The most common method for the production of carbon-11 is the proton bombardment of nitrogen-14 by using the natural nitrogen as target [34]. By using the high purity nitrogen gas, 185–740 GBq/μmol of [^{11}C]CO_2 can be obtained. Because of the appropriate nuclear properties ($t_{1/2}$ = 20.4 min, 99.8 % by β^+, 0.2 % by EC), C-11 can be used for repeated PET imaging studies in the same subject within a relatively short time frame and multi-step syntheses given the fact that there is no distinguishable difference from the stable natural counterpart with respect to biological properties. The C-11 based tracer can majorly be radiolabeled with biosynthetic methods, recoil labeling, organic synthetic methods and enzyme catalysis etc and the primary precursors used for the labeling are generally [^{11}C] carbon dioxide, [^{11}C] methane, and [^{11}C] carbon monoxide [52].

The medical application of nitrogen-13 started from the [^{13}N] ammonia (NH_3 or NH_4^+ ion). One important application of ^{13}N based radiotracer is the labeling of amino acids. Although the cyclotron produced ^{13}N has specific activity more than 400 GBq/μmol, the short physical half-life ($t_{1/2}$ = 9.98 min) limited the application in the multi-step synthesized tracer [53]. For oxygen-15, the 2.07 min half-life determined the rapid synthesis of ^{15}O labeled radiotracer such as [^{15}O]H_2O, [^{15}O]CO, and [^{15}O]CO_2 etc [3, 4, 53].

Fluorine-18 is no less a remarkable and versatile positron-emitting radionuclide due to the appropriate nuclear properties ($t_{1/2}$ = 109.7 min, β^+ = 634 keV, positron range = 2.4 mm in water). However, the medical application only got burst about 50 years after its discovery because of the improvement on the fluorination strategies through nucleophilic form of fluorine-18 ([^{18}F]fluoride ion) or an electrophilic form ([^{18}F]F_2). Among all the F-18 based radiotracers, [^{18}F]-2-fluoro-2-deoxyglucose (FDG) is the most widely used tracer [54–56].

Both bromine-75 and bromine-76 are produced by bombarding the [^{76}Se] enriched (96 %) Cu_2Se target. The physical half-life of Br-76 ($t_{1/2}$ = 16.2 h) is favorable for radiotracer synthesis and application in long physiologic process such as slowly proliferating tumors. For the fast physiologic process, Br-75 ($t_{1/2}$ = 96.7 min) is more suited for imaging [57].

Gallium has three isotopes gallium-66, gallium-67 and gallium-68 that can be used for diagnosis/therapy purpose in nuclear medicine. Of these radionuclides, Ga-67 had been widely used in SPECT to detect both chronic and acute abscesses

and inflammatory processes because of the emission of 185 keV γ-ray. In addition, the relatively long half-life ($t_{1/2}$ = 3.26 day) favored the commercialization of Ga-67 without losing significant amount of activity. Gallium-66 ($t_{1/2}$ = 9.49 h) is a cyclotron-produced position emitter and can be used for both imaging and therapy. The labeling with DOTA-(D)Phe^1-Tyr^3-octreotide is one of the best somatostatin analogues developed [48, 58]. Gallium-68 ($t_{1/2}$ = 67.7 min) is produced from the ^{68}Ge/^{68}Ga generator and decays 89 % by positron emission. The long half-life of the parent nuclide ^{68}Ge ($t_{1/2}$ = 280 days) gives the generator a useful life of 1–2 years, allowing PET imaging at facilities without an on-site cyclotron. The chelate chemistry of gallium is dominated by ligands containing nitrogen, oxygen and sulfur as the electron donor. By functionalization of bioactive molecule to the bifunctional chelator, the target-specific tracer can be designed for medical applications provided that it is stable to hydrolysis and more stable than the Ga (II)-transferrin complexes [51].

The radionuclides of copper offer a selection of diagnostic (^{60}Cu, ^{61}Cu, ^{62}Cu and ^{64}Cu) and therapeutic (^{64}Cu, ^{67}Cu) isotopes. The positron-emitting isotopes produced by cyclotron or generator have a wide range of half-lives (23.7 min for ^{60}Cu, 3.33 h for ^{61}Cu, 9.7 min for ^{62}Cu, and 12.7 h for ^{64}Cu), which makes the application of copper radiotracer particularly attractive. With the enriched nickel target, high yields of copper isotopes (33.3GBq of ^{60}Cu, 5.55GBq of ^{61}Cu, and 37GBq of ^{64}Cu) can be produced [48]. Among the copper radionuclides, the shorter-lived copper isotopes can be used for lipophilic copper complexes measuring blood flow and hypoxia. The longer-lived copper isotopes such as ^{64}Cu have been mostly used in the early investigation for tumor targeting. Recently, more and more efforts have been put on the Cu-labeled biological molecules (antibodies, peptides etc.) for pathological models (i.e. cardiovascular disease, inflammation) [49, 59–61].

Yttrium-86 can be produced on small biomedical cyclotrons via the ^{86}Sr (p, n)^{86}Y reaction using a [^{86}Sr]CO_3 target. The appropriate nuclear properties ($t_{1/2}$ = 14.7 h, 511 keV gamma with abundance of 63.9 %) of ^{86}Y make it attractive as a surrogate for ^{90}Y to monitor the therapeutic effectiveness [48].

Rubidium-82 ($t_{1/2}$ = 1.25 min, 511 keV gamma with abundance of 191 %) is available from the ^{82}Sr–^{82}Rb generator. The ^{82}Sr ($t_{1/2}$ = 25.6 days) is loaded on a SnO_2 column and ^{82}Rb can be eluted with saline solution. Because of its short half-life, ^{82}Rb can be eluted repeatedly every 10–15 min with maximum yield. Clinically, ^{82}Rb is primarily used for myocardial perfusion imaging with PET in conjunction with an infusion system [62].

2.1 Specific Activity

In the design of a radiotracer, some aspects have to be considered:

- the kind of nuclide
- the position of labeling
- the specific activity
- the chemical purity
- the radiochemical purity

For quantitative PET/SPECT imaging, all the results are based on the tracer principle that requires high effective specific activity of the radiopharmaceutical produced [63]. Specific activity is generally defined as amount of radioactivity per unit mass of a radionuclide or a labeled compound, which implies the mass represents the combined mass of radioactive species and the non-radioactive (stable or "cold") counterpart. The unit of specific activity (SA) can be described as GBq/mg, GBq/mmol, or GBq/μmol. Specific activity of a radiopharmaceutical is a function of natural abundance, radionuclide half life, production method, radiolabeling strategy, and purification technique etc. The theoretical maximum specific activity for a radionuclide with a half-life (in hours) of $T_{1/2}$ is:

$$SA_{max}\,(Bq/mol) = 1.16 \times 10^{20}/T_{1/2}$$

In practice, due to the various physical and biological influencing factors such as the cyclotron target purification, the theoretical maximum specific activity is never really achieved in the routine production. However, the concept of specific activity is very important in dealing with PET radiotracers. For example, for some ligand-receptor imaging, due to the low population of receptors expressed on the cell surface, the tracer with low specific activity may saturate the receptor, disobey the tracer principle, and change the pharmacokinetics in vivo etc, causing poor imaging quality and misleading results [64].

Table 9.3 presents examples of specific activities of the radionuclides following production as well as examples of the specific activities of the final labeled products.

2.2 Problems and Challenges

In small-animal nuclear imaging study, there are some issues that need to be carefully considered. Some of these are related to the physical side such as the design and optimization of PET/SPECT scanners to achieve high spatial resolution and sensitivity. Some are focused on the biological feature addressing the interaction between the radiotracer and the biological system. Some are connected to the radiochemistry aspect specific to the radiotracer etc. In this chapter, we will just focus on the problems and challenges encountered in the design and synthesis of radiotracers.

As pointed out before [65, 66], an ideal radiotracer should have high affinity and suitability to the disease specific target, appropriate nuclear properties, superior specific activity and stability. The real challenge in radiotracer based molecular imaging therefore is the search for the "optimal" nuclear imaging probes. The tracer must have high specificity to the characteristic target of disease in order to serve as diagnostic tool prior to any planning therapeutic treatment. The selection of a new target for a given disease, and thus the development of a new radiotracer, is dependent on the reliable molecular and cell biology information base.

As a rule of thumb, for example B_{max}/K_D, (the ratio of available receptor proteins (B_{max}) and dissociation equilibrium constant (K_D)) should preferably be higher than 2 to ensure that a sufficiently large signal is obtained, in order to detect changes in receptor occupancy following dosing with the study tracer. It is, however, of

Table 9.3 Reported specific activities of selected radiotracers[a]

Radionuclide (theoretical specific activity, GBq/μmol)	Radiochemical	Specific activity (GBq/μmol)	References
^{60}Cu (293,500 GBq/μmol)	[^{60}Cu]Cl_2	178–666	[70]
^{61}Cu (34,800 GBq/μmol)	[^{61}Cu]Cl_2	45.1–183	[70]
^{64}Cu (8,695 GBq/μmol)	[^{64}Cu]Cl_2	2,221–734	[71]
	[^{64}Cu]DOTA-ReCCMSH(Arg^{11})	22.3	[72]
	[^{64}Cu]ATSE	7.47	[73]
	[^{64}Cu]ASSM	6.40	[73]
	[^{64}Cu]DOTA-bististatin	83.5	[74]
^{66}Ga (11,636 GBq/μmol)	[^{66}Ga]DOTA-Tyr^3-Octreotide	0.984	[75]
^{76}Br (6,819 GBq/μmol)	[^{76}Br]progestin 16α,17α-dioxolane	7.4–46.2	[76]
	[^{76}Br]L19-SIP	14.8	[77]
^{124}I (1,106 GBq/μmol)	[^{124}I]dRFIB	0.100	[78]
^{86}Y (7,603 GBq/μmol)	[^{86}Y]DOTA-ReCCMSH(Arg^{11})	231	[72]
^{18}F (63,270 GBq/μmol)	[^{18}F]Isatin analog 2	96.2 ± 47.2	[79]
	[^{18}F]2-amino-4-methylpyridine analogue 9	37	[80]
	[^{18}F]WC-II-89	55.5	[81]
	[^{18}F]FDG	37	[82]
^{11}C (341,140 GBq/μmol)	[^{11}C]Isatin analog 4	207	[79]
	[^{11}C]PJ34	74	[83]
^{99m}Tc (19,314 GBq/μmol)	[^{99m}Tc]2PEG$_4$-dimer	370	[84]
	[^{99m}Tc]Annexin V	13,262–265,233	[85]
^{67}Ga (1,480 GBq/μmol)	[^{67}Ga]citrate	596	[39]
^{111}In (1,739 GBq/μmol)	[^{111}In]DNE-B72.3	24.4–44.4	[86]
^{123}I (8,769 GBq/μmol)	[^{123}I]RGD	1.37–2.05	[87]

[a]The data presented in Table 9.3 should be reviewed with caution. The values listed in the literature are specific activities quoted at different times during radiopharmaceutical production (e.g., end of bombardment vs. end of synthesis) using different chemical synthetic routes (e.g., direct reaction or via a precursor) and have also been calculated using different analytical methodologies

importance to realize that the affinity of a tracer for a target is only one of several important parameters. A very high affinity in combination with a high B_{max} may present a problem if the rate-limiting step in the process is shifted from interaction between target and tracer to transport to tissue by blood [40, 67, 68].

Another challenge we would like to discuss is the specific activity. In PET/SPECT imaging, in order to get sufficient contrast and accurate quantification, a radiotracer with high specific activity is critical. However, due to the isotopic dilution and radioactive decay, either in the radionuclide production step or in the subsequent synthesis of a proper reactive secondary precursor, the practical specific activity will be much lower than the theoretical maximum specific activity as illustrated in Table 9.3. For example, the average ratio of $^{11}C/^{12}C$ in the final synthesized radiotracer is approximately 1/7,000 given the specific activity of the tracer is between 50 and 500 GBq/μmol. Although the ^{11}C labeled tracer is still sufficiently sensitive for biomedical imaging study, there is a great potential and urgent need to enhance the specific activity of the tracer [40, 69].

3 Application of Radiotracers as Molecular Imaging Probes

In molecular imaging, the most outstanding advantage of the use of radiotracer is the opportunity afforded to trace dynamic mechanisms in living organism with high sensitivity. The trace amount of radiopharmaceutical (in the range from pictograms to micrograms) conforms to true tracer kinetics and has only marginal or negligible pharmacological effect and toxicity with the ability of imaging the low abundance targets such as receptors, antigens etc.

In the following sections, we would like to briefly discuss some applications of PET and SPECT radiotracers developed for imaging of tumor, cardiovascular disease, brain, inflammation and cells. More examples on the imaging of these targets with various modalities will be discussed in detail in other chapters of this volume.

3.1 Tumor Imaging

3.1.1 Tracer for Imaging Tumor Metabolism

Nuclear imaging (PET/SPECT) of tumor metabolism has gained considerable interest, since numerous studies have demonstrated that malignant tumors can be detected with high sensitivity and specificity by imaging their increased metabolic rates for glucose, amino acids, or lipids. Cancer imaging with [^{18}F]FDG-PET takes advantage of increased glucose metabolism in cancer cells first described by Otto Warburg in the 1930s [88]. [^{18}F]FDG is taken up by cells with glucose transporters such as GLUT-1. Once in the cytoplasm, [^{18}F]FDG enters the first step of the glycolytic pathway and is converted to [^{18}F]FDG-6-phosphate. Unlike glucose-6-phosphate, [^{18}F]FDG-6-phosphate is not a substrate of phosphoglucose isomerase, the second enzyme in the glycolytic pathway. Hence, the radioactivity accumulates inside cells [89]. In this way, [^{18}F]FDG-PET provides a functional image of the underlying changes of glucose metabolism in normal and abnormal tissues. Because most malignancies exhibit increased glucose metabolism for energy needs, the accumulation of radioactivity in cancer cells produces a high contrast to the surrounding tissue [90]. The advantages of [^{18}F]FDG-PET imaging has been reviewed elsewhere [91]. Currently, [^{18}F]FDG is the most widely available and dominant PET tracer in both clinical and pre-clinical research [92–94].

Based on FDG, a series of ^{99m}Tc labeled deoxyglucose analogues such as ^{99m}Tc-labeled ethylenedicysteineglucosamine (EC-DG) and diethylenetriaminepentaacetic acid-deoxyglucose (DTPA-DG) have been built up for tumor metabolic imaging with SPECT taking advantage of glucose metabolism. The results showed access of the radiotracers to cell nuclei and high uptake in tumor cells, indicating the potential of serving as metabolic imaging agents with SPECT [95–99].

In addition to elevated glucose metabolism, tumor cells also show increased protein synthesis and membrane transport of amino acids, making amino acid another important target for tumor metabolic imaging [100]. So far, almost all the existing amino acids have been radiolabeled and evaluated as potential probe for metabolism

imaging. Among the various radiolabeled amino acids, L-[methyl-^{11}C]methionine (Met), reported to be more specific to tumor cells, has been extensively evaluated. Recent studies showed that Met was able to differentiate benign and malignant tumors (granuloma and astrocytomas, etc). In addition to ^{11}C-labeled amino acids, a number of ^{18}F labeled tracers based on tyrosine and phenylalanine amino acids such as L-3,4-dihydroxy-6-[^{18}F]fluorophenylalanine (FDOPA), O-(2-[^{18}F]fluoroehtyl)-L-tyrosine (FET) and L-3-[^{18}F]fluoro-methyltyrosine (FMT) etc have also been explored and some of them showed great diagonostic potential in brain tumor imaging [101]. Furthermore, some ^{123}I-labeled tracers have also shown high uptake in tumor cells [102–104].

Additionally, radiolabeled choline ([^{11}C]-choline) [105] and choline analogs ([^{18}F]-choline and [^{18}F]-fluoroethylcholine) [106, 107] have been used to study tumor lipid metabolism by PET, showing significantly high accumulation of radioactivity in tumor cells. A recent study suggested that choline transport and not phosphorylation is the key factor for choline uptake of cancer cells [108].

Another interesting imaging probe is [^{11}C]acetate which has been used to study oxidative metabolism of the myocardium for a long time. Recently, some results have shown that [^{11}C]acetate is also accumulated in various malignancies [109, 110], indicating a different metabolic fate of acetate in cancer cells, which is thought to be relevant to fatty acid synthesis. Blocking studies showed significant decrease of uptake in both cell culture and mouse tumor model by pharmacologic inhibition of fatty acid synthase and acetyl-CoA carboxylase, confirming the specificity of [^{11}C] acetate for imaging FAS expression [111].

3.1.2 Tracer for Imaging Tumor Cell Proliferation

Uncontrolled cell proliferation is the primary hallmark of cancer, which consequently increases the number of cells undergoing DNA replication. Due to the irreplaceable role of thymidine in DNA synthesis, the upregulated thymidine transport and mammalian thymidine kinases in cancer cells provides a molecular target for imaging by radiolabeling the thymidine analogues. The application of radiotracer in assessing tumor cell proliferation started about 50 years ago. In general, there are two strategies to image the tumor cell proliferation with non-invasive nuclear probe. One is the radiotracer imaging indirectly related to cell proliferation such as [^{18}F]FDG and L-[^{11}C methyl]methionine etc. Another strategy is directly related to cell proliferation such as [^{11}C] thymidine and 32-deoxy-32[^{18}F] fluorothymidine (FLT) etc [112].

The indirect imaging approach is mostly related to tumor metabolism. Although some studies showed positive results in tumor uptake both in vivo and in vitro [113, 114], most studies revealed poor or weak correlation between the cell proliferation and tumor uptake [115–118].

It is well known that thymidine is uniquely incorporated into DNA during the synthesis, which is an indicator of cell proliferation. A series of thymidine analogues have been studied for direct cell proliferation imaging through radiolabeling such as ^{11}C and ^{18}F etc. Among the ^{11}C labeled agents, the most studied radiotracers are [^{11}C] methyl-thymidine and 2-[^{11}C]thymidine. Following the intravenous injection, the

two tracers were metabolized and the majority of activities were accumulated in tumor cells and incorporated into DNA of proliferating cells [119–121]. The limitation for the widespread clinical application is the rapid metabolism and short physical half-life of ^{11}C. In addition, a number of halogenated thymidine analogues have also been investigated for tumor cell proliferation imaging. However, most of them suffered the dehalogenation in vivo and poor contrast [122, 123], which propelled the drive toward finding thymidine analogs readily labeled with the longer-lived ^{18}F isotope, such as [^{18}F]FLT or [^{18}F]FMAU [124].

FLT was originally synthesized as an antineoplastic and antiretroviral agent and is similar in concept to azidothymidine, the first approved anti-HIV agent. It acts as a chain terminator in the synthesis of DNA. The replacement of the hydroxyl group at the 3′ position of deoxyribose prevents cleavage of the sugar from the thymine base by thymidine phosphorylase, therefore, improves the in vivo stability of FLT. The first FLT-PET application was performed to measure the cellular thymidine kinase activity and thereby to infer the rate of cell proliferation [116]. A number of studies have been performed to compare the [^{18}F]FLT to the other tracers in various tumor models and the results showed elevated specificity and therefore high contrast to surrounding tissue of FLT in assessment of cellular proliferative activity, which makes it one of the best tracers in tumor cell proliferation imaging [125–128]. Recently, the applications of FLT in monitoring therapeutic response have drawn a lot of attention. Both pre-clinical and clinical studies showed decreased FLT uptake after radiation/chemotherapy [129, 130].

1-(2′-Deoxy-2′-fluoro-1-β-D-arabinofuranosyl)-thymine (FMAU) is another promising radiotracer (^{11}C labeling at 5-methyl group of the pyrimidine or ^{18}F labeling at the 2′-fluoro position of the sugar) for cell proliferation imaging. Preclinical studies have shown its high resistance to catabolism in animals and incorporation into DNA [131–134], indicating the potential of FMAU as tumor proliferation marker [135].

3.1.3 Tracer for Imaging Tumor Hypoxia

Tumor hypoxia is the situation where tumor cells have been deprived of oxygen. As a tumor grows, it rapidly outgrows its blood supply, leaving portions of the tumor with regions where the oxygen concentration is significantly lower than in healthy tissues. Hypoxic tumor cells usually resistant to radiotherapy and chemotherapy [136]. In addition, tumor hypoxia promotes angiogenesis through the induction of pro-angiogenic factors such as the vascular endothelial growth factor [137].

For radiotracer based hypoxia imaging, there are generally two approaches. One is based on the intracellular retention of nitroimidazoles [138, 139] such as [^{18}F]fluoromisonidazole ([^{18}F]FMISO) or [^{18}F]fluoroazomycin arabinoside following transmembrane diffusion and reduction to a radical form by ubiquitous nitroreductases. Under hypoxic conditions, these radicals cannot be reoxidized, which results in a binding to intracellular macromolecules, preventing back diffusion across the cell membrane. A subtle adjustment of the redox potential is a prerequisite for these tracers [140].

Another approach is based on a radioactive copper (^{60}Cu, ^{62}Cu, ^{64}Cu) complex with diacetyl-bis-N^4-methylthiosemicarbazone (ATSM). Although the targeting and

retention mechanisms have not been fully understood, the reduction of Cu (II) to Cu (I) has been identified as the crucial step [141–144].

[^{18}F]FMISO is the prototype hypoxia imaging agent and has been widely used for hypoxia image in both pre-clinical and clinical studies [145]. Its high partition coefficient leads to homogeneous uptake in most normal tissues [146]. [^{18}F]FMISO accumulates in tissues by binding to intracellular macromolecules when $pO_2 < 10$ mmHg and the retention profile depends on nitroreductase activity and accumulation in hypoxic tissues over a range of blood flows, including within the intestinal lumen where it is retained in anaerobes [147]. Due to its hydrophobicity, the blood clearance is slow, causing low tumor-to-background ratio, which gives rise to the search of more hydrophilic radiolabeled nitroimidazole derivatives such as [^{18}F]fluoroerythromisonidazole ([^{18}F]FETNIM) [148], [^{18}F]fluoro-azomycinarabinofu ranoside ([^{18}F]FAZA) [149], [^{18}F]-fluoroetanidazole ([^{18}F]-FETA) [150] and 2-nitroimidazole [^{18}F]EF5 [151, 152] etc. In addition, some SPECT based tracers ([^{99m}Tc]N2IPA) have also been developed for tumor hypoxia imaging and showed promising results [153, 154].

The pre-clinical applications of Cu-ATSM in tumor hypoxia imaging have been evaluated many times due to its high specificity and enhanced sensitivity [144]. Its retention mechanism in hypoxic tissues is largely attributed to the low oxygen tensions and the subsequently altered redox environment of hypoxic tumors (increased NADH levels) [155, 156]. Additionally, ^{60}Cu-ATSM can be used as a predictor of response and survival in patients after tumor chemoradiotherapy [157]. Recently, a combination of glucose-ATSM labeled with ^{64}Cu ([^{64}Cu]ATSE/A-G) showed improved hypoxic/normoxic uptake ratio in vivo with remained hypoxia selectivity in vitro [158].

3.1.4 Tracer for Imaging Tumor Receptors

Tumor receptors imaging offers complementary information including evaluation of the entire tumor burden, as well as characterization of the heterogeneity of tumor receptor expression. The common to all receptor imaging is the receptor-ligand interaction where the specific binding of ligand to the receptor results in downstream biochemical or physiologic changes [159, 160]. The nature of the ligand-receptor interaction poses a challenge for imaging the requirement for a low molecular concentration of the imaging probe with high affinity to acquire sufficient target-to-background ratio, which makes the nuclear imaging probe (PET/SPECT) the best candidate for tumor receptor imaging [161].

Many intracellular and cell-surface receptors are up-regulated in cancer cells. In general, small ligands, peptides, as well as larger proteins such as antibodies and their fragments, have been radiolabeled as tracers to target specific tumor receptors. To target potential receptors, it would be optimal to use tracers that have high affinity for the target receptor and a minimal background accumulation. This could be achieved by lowering tracer's lipophilicity. In addition, the specific activity of the radiotracer is critical for imaging tumor receptor due to the low receptor population on cell surface, especially for the small molecule based tracers. The most recent applications of radiotracers targeting a variety of tumor receptors are listed in Table 9.4.

Table 9.4 Representative applications of radiotracer imaging of tumor receptors

Receptor	Imaging probe	Tumor	Modality	References
	Peptide			
GRP-R	[^{68}Ga]bombesin	Prostate, breast	SPECT	[175]
	[^{18}F]BBN-RGD		PET	[176]
	[^{68}Ga]NOTA-BBN-RGD		PET	[177]
CCK-2	[^{111}In]DOTA-sCCK$_8$	Thyroid, lung	SPECT	[178]
	[^{99m}Tc]EDDA/HYNIC-MG11		SPECT	[179]
GLP-1-R	Lys^{40}(Ahx-DTPA-^{111}In)NH$_2$exendin-4	Pancreas, prostate	SPECT	[180]
	[^{123}I]GLP-1		SPECT	[181]
NPY-R	[^{111}In][Lys(DOTA)^4, Phe^7, Pro^{34}]NPY	Breast, ovary	SPECT	[182]
NT-R1	[^{99m}Tc]NT-XIX	Pancreas, brain	SPECT	[183]
	[^{99m}Tc]Demotensin 4		SPECT	[184]
NK1	[^{11}C]R116301	Glial tumor	PET	[185]
	[^{18}F]FE-SPA-RQ		PET	[186]
VPAC$_1$	[^{64}Cu]TP3939	Breast, ovary	PET	[187]
	[^{18}F](R^{8,15,21,} L^{17})-VIP		PET	[188]
	[^{64}Cu]TP3982		PET	[189]
	[^{99m}Tc]TP3982, ^{99m}Tc-TP3654		SPECT	[189]
MC1R	[^{111}In]DOTA-Re-(Arg^{11})CCMSH	Skin	SPECT	[190]
	[^{99m}Tc](Arg^{11})CCMSH		SPECT	[190]
	[^{64}Cu]CBTE2A-Re(Arg^{11})CCMSH		PET	[191]
	[^{68}Ga]DOTA-ReCCMSH(Arg^{11})		PET	[192]
sst2	[^{64}Cu]CB-TE2A-Y3-TATE	Pancreas, lung	PET	[168]
	Gluc-S-Dpr([^{11}C]MBOA)-TOCA		PET	[193]
	Gluc-S-Dpr([^{18}F]FBOA)-TOCA		PET	[194]
	[^{99m}Tc/EDDA/tricine/HYNIC]NATE		SPECT	[166]
	[^{67}Ga]KE88		SPECT	[167]
	Small molecule			
Sigma	[^{18}F]WC59	Liver, kidney	PET	[195]
	[^{76}Br] 1 and [^{76}Br] 2		PET	[196]
	[^{18}F]SA4503		PET	[197]
	[^{123}I]BPB		SPECT	[198]
Folate	[^{64}Cu]TETA-SCK-folate	Kidney, placenta	PET	[41]
	[^{18}F]click-folate		PET	[199]
	[^{99m}Tc]EC20		SPECT	[200]
ER	CpT[^{94m}Tc]	Ovary, uterus	PET	[201]
	[^{99m}Tc]GAP-EDL		SPECT	[202]
PR	[^{76}Br]Progestin 16α, 17α-dioxolane	Breast, prostate	PET	[76]
AR	7α-[^{18}F]FM-DHT/7α-^{18}F-FM-norT	Prostate	PET	[203]
	[^{18}F]FMDHT		PET	[204]
	Monoclonal antibody and fragment			
HER2	[^{111}In]DTPA-trastuzumab	Skin	SPECT	[205]
	[^{99m}Tc]ZHER2:2,395-Cys		SPECT	[206]
	[^{18}F]FBEM-Z(HER2:342)		PET	[207]
	[^{18}F]FBO-Z(HER2:477)		PET	[208]
	[^{124}I]PIB-Z(HER2:342)		PET	[209]

In small molecule imaging, one of the most extensively studied systems is radiolabeled steroid for targeting hormone-receptor-positive tumors. The steroid receptors are proteins located in both the cytoplasmic and nuclear fractions of the cell. Steroid hormones such as progestins, estrogens, and androgens are likely to influence carcinogenesis since they have profound effects on cellular proliferation, and up-regulation of steroid receptors may have clinical implication. Therefore, various radiolabeled small molecules such as [^{18}F]FES have been developed to image the steroid receptors such as estrogen receptor (ER), androgen receptor (AR), as well as progesterone receptor (PgR). The imaging applications of these receptors have been discussed by the author elsewhere [162].

For the peptide-based nuclear probe for tumor imaging, the receptors for regulatory peptides are over-expressed in a variety of cancers, which is the molecular basis for in vivo imaging. Among all the peptide-based probes, the somatostatin-derived SPECT/PET tracers designed to image the sst_2-overexpressing neuroendocrine tumors, have enjoyed almost two decades of successful development and extensive clinical applications [163]. Since the commercialization of [^{111}In-DTPA^0]octreotide (^{111}In-pentetreotide, octreoscan), a number of SPECT tracers such as [^{99m}Tc] Depreotide have been developed for sst receptors imaging [164, 165]. Lately, more PET isotopes (^{64}Cu, ^{11}C, ^{18}F, ^{68}Ga) have been conjugated to sst analogs and investigated for tumor diagnosis due to the achievable high specific activities and sensitivities [166–170].

Antibodies are also potential tracers targeting cell-surface receptors. Although primarily exploration for tumor imaging initialized with gamma emitters conjugated with monoclonal antibodies, efforts have been recently focused in the systematic construction of engineered antibody fragments such as HER2 fragment with PET isotopes for tumor receptor imaging due to the rapid blood clearance, improved target-to-background ratio and high sensitivity [171].

3.2 Cardiovascular Imaging

The goal of cardiovascular imaging is to detect and quantify at the molecular and cellular level the pathways that regulate heart and blood vessel function, and to understand abnormalities in these pathways. Current methods for imaging the cardiovascular system, such as CT, MRI, and ultrasound focus predominantly on anatomical and bulk functional measurements (e.g., flow, perfusion, and wall motion). In contradistinction to "classical" diagnostic imaging, molecular imaging probes the molecular abnormalities that are the basis of disease rather than imaging the result of these molecular alterations. In this section, we will focus on the recent development of nuclear imaging probes on atherosclerosis, angiogenesis, apoptosis, cardiac receptor, and reporter gene imaging etc [172].

3.2.1 Tracer for Imaging of Atherosclerosis

The development of atherosclerotic plaques is a process of complex, consecutive, and interacting steps involving chemokines, the up-regulation of adhesion molecules, recruitment of inflammatory cells to the arterial wall, transmigration of these cells, and the development of lipid-laden macrophages (the so-called foam cells) from invading monocytes. With the identification of the distinct mediators and regulators in the cascade of atherosclerosis, non-invasive radionuclide-based molecular imaging probes have been developed such as lipoproteins, components of the coagulation system, cytokines, and mediators of the matrix-metalloproteinase (MMP) system, cell receptors and even whole cells [173]. A review of radionuclide based approaches for atherosclerosis imaging has been published elsewhere [174].

Due to the high metabolic activity of the atherosclerotic plaque, [^{18}F]FDG has been widely used for plaque inflammation imaging [210, 211]. A recent study showed high aortic uptake-to-blood ratio in atherosclerotic rabbit model and correlation to the macrophage content [212]. However, a potential limitation of coronary atherosclerotic plaque imaging of [^{18}F]FDG is the poor target-to-background ratio due to the high myocardial background uptake. In addition, [^{18}F]choline has also been used for murine plaque macrophage imaging [213]. But, the atherosclerotic lesion uptake was low [214].

Low density lipoprotein (LDL) based nuclear tracers had been extensively studied for atherosclerosis imaging. Although focal accumulation could be observed for the radiotracers ([^{123}I]LDL, [^{99m}Tc]LDL etc) on the atherosclerotic lesion, the target-to-background ratio was always hampered by the slow clearance of the tracer [215].

Annexin A5 labeled with ^{99m}Tc remains the most largely studied radiotracer for atherosclerotic plaque imaging. The feasibility of [^{99m}Tc]Annexin A5 imaging apoptosis/macrophage burden in atherosclerotic lesion of animal model has been demonstrated in various animal models showing positive correlation [216]. A recent study indicated that [^{99m}Tc]Annexin A5 might possibly have a greater potential than [^{18}F]FDG as an indicator of last stage, vulnerable plaques as compared with early lesions [217].

Lately, radiolabeled cells (monocytes/macrophages) have also been used for atherosclerotic plaque imaging. An [^{111}In]oxine monocytes study showed avid monocytes recruitment to plaques within days of adoptive transfer and created new insights into the pathogenesis of atherosclerosis and other inflammatory diseases [218]. In addition, a ^{64}Cu labeled nanostructure showed improved sensitivity and direct correlation of PET signal with an established macrophage biomarker (CD68) [219].

Additionally, some probes are also developed to target the molecules expressed by the endothelial/smooth muscle cells during the progression of atherosclerosis plaque, such as vascular cell adhesion molecule-1 ([^{99m}Tc]VCAM-1), with satisfactory sensitivity [220].

3.2.2 Tracer for Imaging of Angiogenesis

Angiogenesis is a complex multistep process and usually has four different phases, endothelial cell activation, basement degradation, endothelial cell migration, and vessel formation and stabilization. During the phase transformation, a number of

molecular targets have been employed to image angiogenesis such as vascular endothelial growth factor (VEGF), extracellular matrix (ECM), matrix metalloproteinases (MMP), $\alpha_v\beta_3$ integrin etc [221].

The angiogenic actions of VEGF are mainly mediated via two endothelium-specific receptor tyrosine kinases, VEGFR-1(Flt-1/FLT-1) and VEGFR-2 (Flk-1/KDR), leading to VEGF/VEGFR pathway a new paradigm for assessing the both tumor and ischemia induced angiogenesis [222, 223]. VEGFR imaging with different VEGF isoforms ($VEGF_{121}$, $VEGF_{165}$ etc) initialized from the γ-emitters (^{111}In, ^{99m}Tc etc) with SPECT [224]. Recently, more PET based tracers have been investigated due to the improved sensitivity [225]. For example, [^{64}Cu]DOTA-$VEGF_{121}$ showed high (15%ID/g) and specific uptake in small U87MG tumor [226]. In mouse hindlimb ischemia model, this tracer showed significantly higher accumulation at injury site in contrast to the control site [227]. Lately, a VEGFR-2 specific tracer, $VEGF_{DEE}$ offered comparable uptake to $VEGR_{121}$ in 4T1 tumor model but much lower kidney burden [228].

Extracellular matrix based tracers for angiogenesis imaging were majorly focused on the radioiodine isotopes. A recent study showed [^{123}I]L19(scFv)(2) was able to distinguish between quiescent and actively growing lesions with no side effects observed, indicating the potential as angiogenesis marker [229].

Matrix metalloproteinases family has five members, collagenases, gelatinases, stromolysins, membrane type (MT)-MMPs, and nonclassified MMPs. Among them, gelatinases MMP-2 and MMP-9 are consistently detected in malignant tissue and their expressions correlate with tumor aggressiveness and metastatic potential. Thus, great efforts have been made to develop MMP inhibitors [230].

In general, there are two approaches to target MMP. One is peptide-based inhibitors and the other one is small molecule-based inhibitors [231]. Using phage display libraries, a disulfide bridged decapeptide (CTTHWGFTLC) was found which selectively inhibits MMP-2 and MMP-9 [232]. Therefore, a number of tracers (^{125}I, ^{99m}Tc, ^{64}Cu) based on this peptide have been investigated. However, all the tracers suffered the low metabolic stabilities and high lipophilicities, resulting in moderate uptake in tumor but high accumulation in liver and kidney [233–235]. Recently, an [^{111}In]DTPA labeled CTT showed reduced uptake in non-target organs and significant correlation between tracer accumulation in tumor as well as tumor-to-blood ratio and gelatinase activity [236].

A lot of small molecule MMP inhibitors have also been developed for anti cancer therapy. Based on CGS27023A, a broad range of MMP inhibitors belong to the family of *N*-sulfonylamino acid derivatives. With ^{11}C/^{18}F labeling, these tracers showed great binding affinity to MMP with μM to nM level IC_{50} observed [231]. In addition, biphenylsulfonamide derivatives were also prepared as radiotracers. (S)-2-(4′-Methoxybiphenyl-4-sulfonylamino)-3-methylbutyric acid and CGS 25966 exhibited high inhibitory activities for MMPs with nM level IC_{50}. However, most of these tracers showed low tumor uptake and poor tumor-to-background ratios in various animal models [230, 237, 238].

Integrins are heterodimeric transmembrane glycoproteins that function in cellular adhesion, migration and signal transduction. Up to now, 18α and 8β subunits have been described, which assemble into more than 20 different receptors. Among them, the $\alpha_v\beta_3$ integrin is significantly up-regulated on activated endothelial cells

during angiogenesis but not on quiescent endothelial cells. A common feature of many integrins like $\alpha_v\beta_3$ is that they bind to extracellular matrix proteins via the three amino acid sequence (Arginine-Glycine-Aspartic Acid, RGD). Due to its important role in tumor angiogenesis, imaging the expression of $\alpha_v\beta_3$ has become a popular topic recently, and was reviewed elsewhere [239–242].

In general, there are three approaches for $\alpha_v\beta_3$ targeting with various radiolabeled RGD peptides. The first strategy is to use the monomeric radiolabeled RGD peptide. It was reported that the cyclic RGD pentapeptide Arg-Gly-Asp-$_D$-Phe-Val (cRGDfV) was a 100-fold better inhibitor of cell adhesion to vitronection than the linear variant and had an affinity for $\alpha_v\beta_3$ in the nanomolar range [243]. However, some of the RGD radiotracers would cause heavy burden in liver and intestine, resulting in different strategies to improve the pharmacokinetics, although the tracers showed receptor-specific tumor uptake [244]. One approach is to conjugate sugar derivatives to the ε-amino function of a corresponding lysine in the peptide sequence, such as [^{18}F] galacto-RGD. With the retention of specific binding in vitro, an improved pharmacokinetics with dominant renal clearance pathway was observed [245]. In addition, some bifunctional chelators (DTPA/DOTA) have also been introduced via a lysine to chelate radioactive metals such as ^{111}In, ^{99m}Tc, ^{64}Cu etc. Among them, the ^{99m}Tc labeled RGD peptide (NC100692) showed high uptake in neovascularization area expressing $\alpha_v\beta_3$. The subsequent study confirmed the localization of binding on the endothelial cells [246]. Another interesting tracer is [^{64}Cu]DOTA-MEDI-522 which showed high tumor accumulation in U87MG tumor model and receptor mediated uptake [247]. In addition, the cross-bridge chelator, [^{64}Cu]-CB-TE2A-c(RGDyK) was compared to [^{64}Cu]-diamsar-c(RGDfD) for targeting $\alpha_v\beta_3$ in M21 tumor model due to its improved blood, liver and kidney clearance. The results showed that [^{64}Cu]-CB-TE2A-c(RGDyK) had higher tumor uptake in contrast to [^{64}Cu]-diamsar-c(RGDfD) due to the different linkers, charges and lipophilicities [248].

Another approach is the introduction of hydrophilic d-amino acids into the RGD sequence, such as [^{18}F]dAsp3-RGD. In contrast to [^{18}F]galacto-RGD, although the tumor uptake was low due to the fast clearance, the tumor-to-background ratio benefitted from that and showed comparable results.

The binding between $\alpha_v\beta_3$ integrin and RGD-containing ECM-proteins involves multivalent binding sites with clustering of integrins. In order to improve the binding affinity, multimeric cyclic RGD peptide could be used and provide more effective antagonist with enhanced targeting capability and cellular uptake. The validity of this concept was demonstrated by labeling divalent and tetravalent scFv's of mAb CC49 with ^{99m}Tc ([^{99m}Tc]-[sc(Fv)2]2) and the results showed threefold higher tumor uptake than [^{99m}Tc]-sc(Fv)2 [249]. By pegylation and polyvalency, the dimer of [^{18}F] FB-E[c(RGDyK)]2 showed almost twice as much tumor uptake as its monomer [250]. In another study, the tetrameric [^{99m}Tc]RAFG-RGD showed significantly higher $\alpha_v\beta_3$ binding affinity compared with the monomer and dimer [251]. Based on these, a systematic study on the influence of multimerization on receptor affinity and tumor uptake was carried out with monomeric, dimeric, tetrameric and octameric RGD peptides both in vitro and in vivo. The results showed increasing binding affinity and tumor uptake along with the multimerization from monomer to octamer [239].

Recently, the nanoparticle based imaging probe has drawn more attention in targeting $\alpha_v\beta_3$ in tumor angiogenesis due to the multi-functionalities [239, 252]. In a recent study, an [^{111}In]-labeled perfluorocarbon nanoparticles (approximately 250 nm, ten ^{111}In per particle) was used to target $\alpha_v\beta_3$ in a Vx-2 rabbit model. At 18 h, the mean tumor activity of the targeting nanoparticles was fourfold higher than the non-targeted control particles [253]. In consideration of the size of the nanoparticle, the stealth property and tunable chemistry to adjust the blood circulation of nanoparticle in vivo, a biodegradable dendrimer (approximately 12 nm) conjugated with RGD peptide was synthesized, labeled with ^{76}Br and tested in murine hindlimb ischemia model. The in vitro binding assay showed a 50-fold enhancement of the affinity to $\alpha_v\beta_3$ integrin receptor with respect to the monovalent RGD peptide. The in vivo pharmacokinetics studies exhibited no specific organ accumulation and fast clearance through urine and feces. The PET imaging studies showed significantly higher uptake at injured site with the targeted dendrimer than that of non-targeted dendrimer, indicating the potential implication of this nanoprobe in imaging and therapy [254].

3.2.3 Tracers for Imaging Cardiac Receptor

Various cardiac receptors have been identified as playing a role in cardiovascular pathophysiology and thus represent attractive targets for imaging. In general, muscarinic and adrenergic receptors are the major receptors investigated for both PET and SPECT imaging.

Musccarinic receptor was the first myocardial receptors targeted with PET [255], and has several subtypes (M_1–M_5) [162]. The antagonist of muscarinic, methylquinuclidinyl benzilate (MQNB) has been labeled with ^{11}C and showed specific binding to muscarinic receptor [162]. In addition, some other radiotracers have also been developed to target the receptor such as (R)-[^{11}C]VC002, [^{11}C]butylthio-TZTP, [^{18}F] FP-TZTP etc [256]. However, the major applications of these tracers are brain imaging with only limited application in cardiac imaging. Based on [^{18}F]FP-TZTP, a series of TZTP derivatives was labeled with ^{11}C to monitor the effect of structural variations on the pharmacokinetics and behavior in blood and seek the possibility of using [^{11}C]FP-TZTP as an alternative for [^{18}F]FP-TZTP [257]. More recently, with a modified precursor, a new radiosynthesis method has been optimized offering comparable specific activity to previous study but 10 % higher radiochemical yield and 25 min shorter synthesis time for [^{18}F]FP-TZTP [258, 259].

The adrenergic system plays the major role in modulation of heart rate and contractility. The adrenergic signaling is initiated by the binding of the adrenergic agonists, norepinephrine, and epinephrine, to adrenergic receptors. There are three types of adrenergic receptors, alpha 1, alpha 2, and beta receptors and each of these has several sub-types. The selection, design and evaluation of radiotracers for PET studies of these receptors were reviewed elsewhere [260].

The nuclear imaging of cardiac α1 receptor initiated from ^{11}C labeled prazosin which showed high selectivity and homogenous uptake, but high non-specific

binding as well. By changing the lipophilicity (log $P = 3$) of the tracer, the prazosin derivative [^{11}C]GB67 showed high selectivity and uptake in myocardium [261]. However, alpha1 density was reported to be ten times higher in rat heart compared to that in man. In order to transfer the tracer to clinical study, a recent study in pig was performed and showed specific binding of [^{11}C]GB67 to myocardial α1 receptor accounted for approximately 50 % of volume of distribution, indicating the potential of this tracer in clinical study [262].

The imaging studies on adrenergic alpha 2 receptors are mostly concentrated on brain and almost all the tracers suffering the low uptake and non-specific binding in lung and heart [162].

For the beta receptors, in myocardium the β_1-subtype predominates in concentration over the β_2-subtype although both have important functions. (S)-[^{11}C]CGP 12177 is a widely studied tracer for selectively imaging beta receptor but not selective for β_1 over β_2 subtype due to the low lipophilicity (log $P = 1.8$) and high affinity ($pK_D = 9.91$, for the S-enantiomer) [263]. Due to the cumbersome synthesis of [^{11}C] phosgene, the isopropyl analogue (S)-[^{11}C]CGP 12388 was developed and showed little non-specific binding and radioactive metabolites in plasma, indicating the potential for clinical application [264]. In order to offer better cardiac imaging, some selective β_1 receptor ligands such as [^{123}I]ICI89406 have also been studied. However, this tracer suffered the fast dehalogenation in vivo [265]. For the β_2 selective tracer, the [^{18}F]FEFE showed specific binding both in vitro and in vivo [266, 267]. More recently, a lot of effort has been put in the search for new radiotracer imaging β receptors. However, none of them could show the applicability in clinical study due to the slow clearance and non-specific binding [268, 269].

3.2.4 Tracers for Imaging of Apoptosis

Cell death is central to normal physiology and numerous disease states. In general, it can be characterized as apoptosis (programmed cell death) and necrosis (accidental passive and unregulated form of cell death) [270, 271]. Apoptosis and necrosis seem to have different biochemical, morphological and physiological characteristics. However, the two processes of cell death are not so far separated from each other [268]. In molecular imaging, apoptosis probes can either bind to externalized phospholipids at the cell membrane or inside the cells to enzymes like caspases. Imaging of necrosis is mainly based on the loss of the cell membrane integrity allowing exchange of macromolecules between the intracellular and extracellular environment. In this section, we mainly focus on the imaging of apoptosis.

Apoptosis plays an essential role in the development and maintenance of a multicellular organism and contributes to both normal physiology and pathology. This highly regulated and genetically defined cellular process forms the main mechanism by which cells die, both in healthy and diseased tissue. During the apoptotic process, some potential targets (phosphatidylserine (PS) and phosphatidylethanolamine (PE) aminophospholipids, caspase-3, -7, -8, and -9 etc) will be exposed for molecular imaging due to the specific biochemical changes, which propels the

development of imaging probe to assess the pathogenesis of various cardiovascular diseases, as well as tumor response to cancer therapy [272].

Cells undergoing apoptosis signal their neighbors by expressing PS on the external leaflet of the cell membrane, which leads to the application of annexin V based radiotracer for imaging apoptosis. Annexin V (MW ≈ 36 kDa) is an endogenous human protein and binds to rafts of PS exposed on a cell's surface with internalization via a newly discovered unique pathway of pinocytosis [273]. Annexin V has been radiolabeled with ^{125}I, ^{124}I, ^{18}F, ^{68}Ga, and ^{99m}Tc etc for imaging. Among them, the [^{99m}Tc]N_2S_2-rh-annexin has been widely studied in cardiovascular disease models and gone into clinical trials [273–275]. However, due to the cumbersome labeling procedure, a bifunctional agent hydrazinonicotinamide (HYNIC) has been selected to improve the labeling. In a mouse tumor model, the potential of [^{99m}Tc]HYNIC-Annexin V in imaging apoptosis after systematic chemotherapy was evaluated. The tumor uptakes in the treated mice were significantly higher than those in the control group, indicating the great potential of this agent for imaging apoptosis in response to treatment in a thymoma tumor bearing mouse model [276]. In addition, [^{99m}Tc]HYNIC was conjugated to a murine anti-MUC1 monoclonal antibody (RP81) and showed specific accumulation at tumor and minimum uptake at non-target organs [277]. Yet, it accumulates in the cortex of kidney, limiting the visualization of any paranephric structures [278]. Alternatively, a number of annexin mutants such as V117 and V128 have been developed [279, 280]. With the site-specific modification at the N terminus, [^{99m}Tc]annexin-V128 showed twice as much apoptosis-specific liver uptake as did all forms of annexin V derivatized randomly via amino groups, and 88 % less renal retention [281]. Recently, a site-specific labeled [^{18}F]annexin-V128 radiotracer was developed and showed satisfactory binding affinity, suggesting its potential in apoptosis imaging [282].

Apart from Annexin V, a smaller PS targeting agent based on the C2A domain (14.2 kDa) of another vesicle associated protein, synaptotagmin-I has been labeled with ^{99m}Tc. The tracer uptake was clearly observed in the area at risk due to the specific binding and passive leakage [283]. In non-small cell lung tumor model, the tracer uptakes of treated group were significantly higher than that of control group. The radiotracer uptake was positively correlated to the apoptotic index, as well as caspase-3 activity [284]. In addition, some peptide based tracer such as duramycin with high binding affinity to the head group of phosphatidylethanolamine has also been developed. The in vivo studies showed more than 30-fold enhancement of [^{99m}Tc]duramycin uptake in apoptotic cells with respect to the control cells [285].

Besides the PS targeting probes, a number of small molecule based tracers targeting the caspase-3/-7 have also been synthesized and tested in vivo. An isatin sulfonamide analog, WC-II-89 was labeled with ^{18}F and showed high uptake in the rat liver with chemically induced apoptosis in contrast to the control group [97]. Based on [^{18}F]WC-II-89, a ^{11}C labeled tracer WC-98 showed retained activity in liver and good correlation with caspase-3 enzyme activity [97]. Furthermore, an ^{18}F labeled 5-fluorophentyl-2-methyl-malonic acid ([^{18}F]ML-10) was developed to target the membrane of the apoptotic cell. The in vivo studies showed high uptake in the region of interest of the infarct and good correlation with histologic results [286].

Table 9.5 Representative examples of probe for reporter gene imaging

Reporter type	Tracer	Reporter gene	Application	References
Enzyme	[^{18}F]FPrDU	HSV1-tk	PET	[291]
	[^{18}F]-FHBG	HSV1-sr39tk	PET	[292]
	[^{124}I, ^{18}F]-FIAU	Human mitochondrial TK	PET	[293]
Receptor	[^{125}I]IBF	D_2R	SPECT	[294]
	[^{18}F]FES-hERL	Estrogen receptor	PET	[295]
	[^{94m}Tc]-Demotate	SSTr	PET	[296]
Transporter	$^{99m}TcO_4^-$	NIS	SPECT	[297]

3.2.5 Tracers for Imaging of Reporter Gene

Reporter genes are nucleic acid sequences encoding for easily assayed proteins. Reporter gene imaging is the indirect imaging strategy and the prerequisite is the pre-delivery of a reporter gene to the target tissue by transfection or transduction. It usually includes transcriptional control components that can function as "molecular genetic sensors" that initiate reporter gene expression [287]. A general paradigm for non-invasive reporter gene imaging using radiolabeled probe was initialized from 1995 [288]. Then, this strategy has been widely used for reporter gene imaging, therapeutic gene imaging, monitoring gene therapy, and imaging biological processes etc. The summaries of reporter gene/probe system have been reviewed elsewhere [289, 290]. Some representative examples of reporter gene systems are listed in Table 9.5.

Herpes simplex virus type 1 thymidine kinase (HSV1-tk) is the most widely used reporter gene for radiotracer-based molecular imaging, and has been used as a therapeutic "suicide" gene in clinical anti-cancer gene therapy trials as well as a research tool in gene targeting strategies. In general, the substrates served as PET/SPECT reporter probes for HSV1-tk can be classified into two main categories: pyrimidine nucleoside derivatives, such as FIAU (5-iodi-2′-fluoro-2′-deoxy-1-β-D-arabinofuranosyl-uracil) and FEAU (2′-fluoro-2′-deoxyarabinofuranosyl-5-ethyluracil) [298], and acycloguanosine derivatives, for example FPCV (fluoropenciclovir) [299] and FHBG (9-[4-fluoro-3-(hydrommethyl) butyl] guanine) [300] etc. In a recent study, some ^{18}F labeled 5-[^{18}F]fluoroalkyl pyrimidine nucleosides have also been developed for HSV1-tk imaging. However, most of these imaging probes suffered the low sensitivity [291]. In order to improve the sensitivity, a mutant HSV1TK (HSV1-sr39tk gene), was derived using site-directed mutagenesis to obtain an enzyme more effective at phosphorylating ganciclovir (GCV) with consequent gain in imaging signal. It has been reported that the combination of [^{18}F]FHBG and HSV1-sr39tk is the most effective PET system [290].

HSV1-tk and HSV1-sr39tk are nonhuman genes and pose a small risk of generating an immune response against cells and tissue transduced with these genes, although in some cancer applications an immune response may be desirable. Alternatively, human thymidine kinase 2 (hTK2) can be used to reduce the risk. The pre-clinical studies have shown the levels of FIAU accumulation in cells expressing

DeltahTK2 and DeltahTK2 GFP was at least tenfold higher than in wild-type cells in vitro and about six times higher in vivo, indicating the potential of imaging DeltahTK2 reporter gene expression [293].

The dopamine 2 receptor (D_2R) gene has also been used as an imaging reporter gene on the cell surface in the form of receptors. A widely used nuclear probe is [^{18}F]fluoroethylspipersone (FESP), which showed significant uptake at areas expressing D_2R gene. Recently, an ^{125}I labeled probe [^{125}I]5-iodo-7-*N*-[(1-ethyl-2-pyrrolidinyl)methyl]carboxamide-2,3-dihydrobenzofuran ([^{125}I]IBF) was developed and showed correlation ($r=0.900$, $P<0.001$) between areas that expressed HA-D(2)R by immunostaining and areas in which [^{125}I]IBF accumulated [294].

Similarly, estrogen receptor is also used as a PET gene. Recently, an ^{18}F labeled estradiol and human estrogen receptor ligand (hERL) binding domain has been developed and high FES uptake accompanied by hERL and hTP expression was obtained both in vitro and in vivo by the test adenovirus infection [295]. Additionally, the human somatostatin receptor subtype 2 (hSSTR2) gene has also been suggested as a potential reporter gene for human studies due to its limited expression on carcinoid tumors. A recent study showed high affinity and in vivo tumor uptake [296].

The sodium iodide symporter (NIS) is expressed primarily on the basolateral membrane of thyroid epithelial cells, and at low levels in some other organs such as salivary glands etc. The NIS can transfer a lot of anions into cells such as $^{99m}TcO_4^-$[290]. A recent study showed the tracers ($^{99m}TcO_4^-$/^{124}I) accumulation in vitro and clear vision at the locations injected with cells [297]. A further discussion of the NIS has been published elsewhere [301].

3.3 Brain Imaging

The brain is a vastly complex organ, with numerous functions that are inadequately assessed with anatomical imaging such as MRI. Functional brain imaging, for example nuclear imaging, can detect the neurological abnormalities beyond the confines of structural deterioration with trace amount of radiotracer. The roles of functional PET/SPECT played in brain research include a broad range of issues such as regional cerebral functions, molecular metabolism, receptor binding capacity, monitoring pathophysiological processes etc. In this chapter, we only focus the recent radiotracer development in imaging Alzheimer's disease.

Alzheimer's disease (AD) is the most devastating neurodegenerative disorder. In 2006, the number of AD patients worldwide was approximately 26.6 million. A recent study showed that the overall estimate of the doubling time was 5.5 years, which meant 8 years later from now, the total number of patients will be more than 100 million globally [302]. Therefore, there is an urgent need to develop sensitive and specific imaging technique to reduce the diagnostic uncertainty. So far, a lot of radiotracers have been developed as molecular imaging probes to target the biomarkers in AD [303]. Besides the widely used [^{18}F]FDG [304], due to the major pathological feature of β-amyloid in AD, a number of β-amyloid labeled nuclear imaging probes have been evaluated in the diagnosis of AD.

The first attempt to image brain β-amyloid deposition in AD was reported in human using a ^{99m}Tc labeled monoclonal antibody fragment ([^{99m}Tc]10H3) targeting β-amyloid 1–28 ($A\beta_{1-28}$). However, no cerebral uptake of the antibody was observed, possibly due to the cross reaction of the 10H3 with another protein [305]. However, this first study was instructive for the subsequent efforts. Currently, for the development of β-amyloid tracer, a set of selection criteria is established (a) a high affinity and selectivity for the target β-amyloid structure; (b) a low molecular weight compound (MW < 400) and medium lipophilicity (log *P* in the range of 1–3) to ensure a high initial brain uptake with rapid clearance from normal brain; (c) functional groups in the molecule for introduction of radionuclides; (d) high stability of the PET/SPECT tracer in the brain as well as no brain uptake of peripherally generated metabolites of the tracer; (e) high availability of the tracer for clinical application; (f) appropriate half-life of the radionuclide to allow the clearance of non-specific binding and background [306].

So far, there are several radiotracers that have gone in clinical studies such as [^{18}F]1,1-dicyano-2-[6-(dimethylamino)-2-naphtalenyl] propene ([^{18}F]FDDNP), *N*-methyl [^{11}C]2-(4′-methylaminophenyl)-6-hydroxy-benzothiasole ([^{11}C]PIB), 4-*N*-methylamino-4′-hydroxystilbene ([^{11}C]SB13), 2-(2-[-dimethylaminothizol-5-yl] ethenyl)-6-(2-[fluoro]benzoxazole ([^{11}C]BF-227), and trans-4-(*N-methylamino*)-4ÅL-{2-[2-(2-[^{18}F]fluoro-ethoxy)-ethoxy]-ethoxy}-stilbene ([^{18}F]BAY94-9172) etc [307].

In the search of small molecule based probe for amyloid imaging, there are some interesting structures discovered meeting the selection criteria, such as Congo red, thioflavin, stilbene and FDDNP etc [308]. Among these radiotracers, [^{11}C]PIB is probably the most widely investigated radiotracer for β-amyloid imaging. Therefore, many PIB analogues have been synthesized and evaluated. A recent study illustrated the specific in vitro binding of ^{11}C labeled structural isomers of 6-hydroxy-2-(4′-aminophenyl)-1,3-benzothiazole to amyloid plaques and high brain uptake and fast clearance kinetics, indicating the potential in clinical application [309]. In another study, an ^{18}F labeled PIB analogue 2-(4′-[^{18}F]fluorophenyl)-1,3-benzothiazole has been demonstrated to have high brain uptake at 2 min post injection (p.i.) (3.2 % ID/g) and fast clearance (0.21 % ID/g at 60 min p.i.), showing excellent preclinical characteristics comparable with those of the ^{11}C-PIB [310]. In addition, some ^{18}F-labeled 2-phenylbenzothiazoles have also showed promising pharmacokinetics in vivo. More importantly, [^{18}F]5, or 6-methyl-2-(4′-[^{18}F]fluorophenyl)-1,3-benzothiazole, seemed to be metabolically stable in the brain and little background signal from the plasma radiometabolites [311]. Furthermore, an automatic radiosynthesis strategy has been recently established showing fast synthesis and high specific activity (20–60 GBq/μmol), indicating the prospective of this method for commercialization [312].

Another approach to develop new small molecule tracer for β-amyloid imaging is to synthesize stilbene derivatives by lowering the lipophilicity. The compounds [^{18}F] 3-{4-[2-(4-Dimethylaminophenyl)vinyl]phenoxy}-2-fluoromethyl-propan-1-ol and [^{18}F] 2-Fluoromethyl-3-{4-[2-(4-methylaminophenyl)vinyl]-ph-enoxy}propan-1-ol with log *P* = 3.13 and 2.94, respectively, showed high binding affinity and brain uptakes (5.55 and 9.75 % ID/g at 2 min), as well as the fast clearance [313].

Alternatively, pegylation technique was also employed to increase the hydrophilicity. The results showed medium log *P* values (2.05 -2.52) and high brain uptake (6.6-8.1 % ID/g) [314, 315].

Recently, an ^{18}F labeled phenylacetylene derivatives 5-((4-(2-(2-(2-fluoroethoxy) ethoxy)ethoxy) phenyl) ethynyl)-1H-indole 14 has been reported with good binding affinity and initial brain uptake to β-amyloid plaque [316]. In addition, another ^{18}F-labeled biphenylalkyne, AV-138 ([^{18}F]AV-138) also showed some promising results in β-amyloid imaging [317].

[^{123}I]-IMPY (6-iodo-2-(4′-dimethylamino-) phenyl-imidazo[1,2-a]pyridine) is another tracer going into clinical trial with SPECT imaging. In the effort of seeking new IMPY derivatives for β-amyloid imaging, a structure-affinity relationship was discussed shining insight into the topography of the binding site for IMPY-like ligands in β-amyloid plaques [318]. Based on this, a number of 6-thiolato-substituted 2-(4′-*N*,*N*-dimethylamino)phenylimidazo[1,2-a] pyridines (RS-IMPYs; 1-4) labeled with ^{11}C were synthesized and evaluated in vivo, showing the ratio of radioactivity at maximal uptake in brain to that at 60 min reached 18.7 for ^{11}C labeled methyl 3-(2-(4-(dimethylamino)phenyl) imidazo[1,2-*a*]pyridin-6-ylthio) propanoate, suggesting the necessity for further evaluation [319].

3.4 Other Imaging Targets

3.4.1 Tracers for Inflammation and Infection

Inflammation is the response of tissues to injury in order to bring plasma proteins and immune cells to the site of damage. This tissue damage can be caused by contamination with a foreign species (bacteria, viruses, fungi, asbestos, and others) neoplasm or trauma. If the inflammation is due to contamination with microorganisms, the inflammation is referred to as an infection [320]. In clinical research, adequate delineation and diagnosis of inflammatory foci is of critical importance to enable clinicians to quickly apply the most appropriate treatment. Till now, there are some well established radiopharmaceuticals for infection/inflammation imaging such as ^{67}Ga citrate, radiolabeled white blood cells ([^{99m}Tc]hexamethyl-propylene amine oxime, [^{99m}Tc]HMPAO), radiolabeled anti-granulocyte antibody preparations ([^{99m}Tc]anti-stage-specific embryonic antigen-1 IgM, [^{99m}Tc]anti-SSEA-1 IgM), and the most investigated tracer [^{18}F]FDG [321]. However, each of the radiotracers has its own limitations, for example, the limited applicability of ^{67}Ga citrate due to the physiological bowel uptake and the high radiation dose, the cumbersome preparation of labeling white blood cells, the diagnostic accuracy of radiolabeled anti-granulocyte antibody, and limited commercialization of [^{18}F]FDG etc, which propel the search of new radiotracers for imaging infection and inflammation such as tracers targeting receptors expressed on the cells involved in the inflammatory processes.

Interleukin-8 (IL-8) is a small protein (MW = 8.5 kDa) and belongs to the chemokine (C-X-C motif) subfamily of the chemokines. IL-8 binds to both types of CXC receptors

(CXCR1 and CXCR2) on neutrophils with high affinity ($K_d = 0.3–4 \times 10^{-9}$ M). The pharmacokinetics analysis of [^{99m}Tc]IL-8 showed high accumulation of tracer in the inflamed tissue, mainly bound to peripheral neutrophils, suggesting a highly specific, neutrophil-driven process [322]. In a lung infection study, [^{99m}Tc]IL-8 was reported to enable early visualization of localization and extent of pulmonary infection with significantly higher uptake in lung with respect to the control animal [323]. Recently, a ^{99m}Tc labeled leukocyte-avid peptide-glycoseaminoglycan complex, [^{99m}Tc]P1827DS has been synthesized and evaluated in vivo, showing significant accumulation in abscess [324].

Leukotriene B_4 (LTB_4) is a potent chemoattractant that activates granulocytes and macrophages. It is involved as an important mediator in both acute and chronic inflammatory disease. LTB_4 binds to leukotriene receptors BLT1expressed on neutrophils with high affinity, and BLT2 expressed more ubiquitously with low affinity. Recently, a LTB_4 antagonist was reported to be able to reveal infectious and inflammatory foci in distinct animal models with high sensitivity. A following study revealed that [^{111}In]DPC11870 accumulation in infectious and inflammatory foci was because of binding to LTB_4 receptors expressed on activated hematopoietic cells that subsequently migrated to the site of infection, which led to visualization of the infectious lesions [325]. In addition, a ^{99m}Tc labeled LTB_4 antagonist MB88 was synthesized for infection imaging and showed superior characteristics relative to [^{111}In]DPC11870 [326]. Recently, the LTB_4 antagonist was also labeled with ^{18}F and showed feasibility for infection imaging [327].

Furthermore, a number of ^{99m}Tc labeled antibody fragments have been developed for infection imaging such as [^{99m}Tc]ciprofloxacin [328], [^{99m}Tc]N-CPFXDTC [329], [^{99m}Tc]CFT [330, 331], [^{99m}Tc]UBI 29-41 etc, and discussed elsewhere [320].

3.4.2 Tracers for Cell Labeling

Direct visualization of cell migration patterns in vivo by means of nuclear imaging greatly assists the appraisal of a multitude of variable like production, administration and host associated with cell-mediated diagnosis and therapy [332]. Cell tracking has been employed as an important tool in many fields such as chronic inflammatory disease, rheumatoid arthritis etc. Recently, in vivo cell tracking of stem cells has become popular since evaluation of treatment efficacy requires quantitatively and qualitatively monitoring of administered cells [333].

The cell labeling with radionuclide started from leukocyte [334]. Currently, leukocyte, monocytes, and stem cells are the widely investigated cells for radiolabeling. In general, there are two labeling strategies, direct labeling and indirect labeling. For the direct labeling, [^{99m}Tc]hexamethylpropylene amino oxime ([^{99m}Tc]HMPAO), [^{18}F]FDG, and [^{118}In] hydroxyquinoline ([^{111}In]-oxime) etc. have been widely used for pre-clinical and clinical studies and summarized elsewhere [335–337]. However, the applications have been limited by the stability of the labeled cells due to the cleavage process leading to incomplete trapping mechanism of the cell-ligand complex, thus producing a signal from the labeled moiety distinct from that of the

labeled cell [338]. With regard to the indirect labeling, reporter gene system has been used for long term step cell monitoring [339]. However, the reporter gene technology requires genetic modification and it is unclear whether this may alter the cell function etc.

There is considerable effort being expended in searching suitable radiotracer for cell labeling with minimal chemical, physical or emission toxicity to the cell, and not affect cell's nature. Recently, the lipophilic hexadecyl-4-[^{18}F]fluoroben-zoate ([^{18}F]-HFB) was used to radiolabel rat mesenchymal stem cells (MSCs) by absorption into cell membrane. This tracer had cell labeling efficiency of 25 % , more than 90 % cell retention over 4 h period, at least 90 % cell viability, and high specific activity (>3.7 GBq/μmol). The in vivo studies showed accumulation of radioactivity in the lung with no other organ observed on PET images, supporting the efficient retention of the radiolabel in the cells trapped in the lungs [340]. As a contrast, the non-selective agent *N*-succimidyl-4-[^{18}F] fluorobenzoate ([^{18}F]SFB) labeled dendritic cells did not show significant accumulation at the target organ and unexpected loss of the label from cells, possibly due to the metabolic release of the labeled alkylated moiety [341]. In addition, ^{64}Cu-pyruvaldehyde-bis(N_4-methylthiosemicarbazone) ([^{64}Cu]PTSM) has also been used for cell labeling and offered more efficient labeling relative to [^{18}F]-FDG with no change to the viability or proliferation rate of cells in contrast to the unlabeled controls, indicating the potential of this tracer in imaging the cell migration [342]. More recently, [^{64}Cu]polyethylenimine ([^{64}Cu]PEI) had been compared to [^{64}Cu]PTSM for U87MG cell labeling. Although the labeling efficiency was lower, [^{64}Cu]PEI had significantly higher tumor uptake than that of [^{64}Cu]PTSM. With the pegylation, [^{64}Cu]PEI-PEG had decreased toxicity, higher tumor uptake, and better tumor-to-background contrast in U87MG xenograft model [343].

4 Summary

Nuclear imaging including PET and SPECT offers unique possibilities for highly sensitive in vitro and in vivo imaging applications, especially in the perspective of molecular imaging. Understanding the fundamentals of nuclear imaging and grasping the essentials of available imaging techniques is a must for researchers interested in the field. This chapter summarized the radionuclides used for PET/SPECT imaging, important concepts of radiotracer development, as well as brief description of state-of-the-art imaging applications. For more detailed discussions of the subject, the reader is kindly referred to the articles below.

References

1. Mankoff DA (2007) A definition of molecular imaging. J Nucl Med 48:18N, 21N.
2. Domper MG, Gelovani JG (2008) Molecular imaging in oncology. New York: Informa healthcare USA.

3. Ter-Pogossian MM, WE P (1957) The use of radioactive oxygen 15 in the determination of oxygen content in malignant neoplasms. Radioisotopes in scientific research, Paris, pp.
4. Raichle ME (1998) Imaging the mind. Semin Nucl Med 28:278–89.
5. Cassidy PJ, Radda GK (2005) Molecular imaging perspectives. J R Soc Interface 2:133–44.
6. von Schulthess GK, Schlemmer HP (2009) A look ahead: PET/MR versus PET/CT. Eur J Nucl Med Mol Imaging 36 Suppl 1:S3–9.
7. Heiss WD (2009) The potential of PET/MR for brain imaging. Eur J Nucl Med Mol Imaging 36 Suppl 1:S105–12.
8. Schober O, Rahbar K, Riemann B (2009) Multimodality molecular imagin--rom target description to clinical studies. Eur J Nucl Med Mol Imaging 36:302–14.
9. Rossin R, Welch MJ (2005) Molecular imaging probes for PET and SPECT. In: Schuster DP, Blackwell TS, eds. Molecular imaging of the lungs. New York: Taylor and Francis, pp 3–39.
10. Weissleder R, Mahmood U (2001) Molecular imaging. Radiology 219:316–33.
11. Willmann JK, van Bruggen N, Dinkelborg LM, Gambhir SS (2008) Molecular imaging in drug development. Nat Rev Drug Discov 7:591–607.
12. Dobrucki LW, Sinusas AJ (2005) Cardiovascular molecular imaging. Semin Nucl Med 35:73–81.
13. Dobrucki LW, Sinusas AJ (2005) Molecular cardiovascular imaging. Curr Cardiol Rep 7:130–5.
14. Serganova I, Mayer-Kukuck P, Huang R, Blasberg R (2008) Molecular imaging: reporter gene imaging. Handb Exp Pharmacol:167–223.
15. Massoud TF, Gambhir SS (2003) Molecular imaging in living subjects: seeing fundamental biological processes in a new light. Genes Dev 17:545–80.
16. Brumley CL, Kuhn JA (1995) Radiolabeled monoclonal antibodies. Aorn J 62:343–50, 353–5; quiz 356–8, 361–2.
17. Blasberg RG (2003) Molecular imaging and cancer. Mol Cancer Ther 2:335–43.
18. Bonasera TA, O'Neil JP, Xu M, Dobkin JA, Cutler PD, Lich LL, et al. (1996) Preclinical evaluation of fluorine-18-labeled androgen receptor ligands in baboons. J Nucl Med 37:1009–15.
19. Dewanjee MK, Ghafouripour AK, Kapadvanjwala M, Dewanjee S, Serafini AN, Lopez DM, et al. (1994) Noninvasive imaging of c-myc oncogene messenger RNA with indium-111-antisense probes in a mammary tumor-bearing mouse model. J Nucl Med 35:1054–63.
20. Anderson CJ, Connett JM, Schwarz SW, Rocque PA, Guo LW, Philpott GW, et al. (1992) Copper-64-labeled antibodies for PET imaging. J Nucl Med 33:1685–91.
21. Phelps ME (2000) Inaugural article: positron emission tomography provides molecular imaging of biological processes. Proc Natl Acad Sci U S A 97:9226–33.
22. Ponde DE, Dence CS, Schuster DP, Welch MJ (2004) Rapid and reproducible radiosynthesis of [^{18}F] FHBG. Nucl Med Biol 31:133–8.
23. Serganova I, Blasberg R (2005) Reporter gene imaging: potential impact on therapy. Nucl Med Biol 32:763–80.
24. Gheysens O, Mottaghy FM (2009) Method of bioluminescence imaging for molecular imaging of physiological and pathological processes. Methods
25. Sadikot RT, Blackwell TS (2008) Bioluminescence: imaging modality for in vitro and in vivo gene expression. Methods Mol Biol 477:383–94.
26. Weissleder R, Simonova M, Bogdanova A, Bredow S, Enochs WS, Bogdanov A, Jr. (1997) MR imaging and scintigraphy of gene expression through melanin induction. Radiology 204:425–9.
27. Louie AY, Huber MM, Ahrens ET, Rothbacher U, Moats R, Jacobs RE, et al. (2000) In vivo visualization of gene expression using magnetic resonance imaging. Nat Biotechnol 18:321–5.
28. Shu CJ, Radu CG, Shelly SM, Vo DD, Prins R, Ribas A, et al. (2009) Quantitative PET reporter gene imaging of CD8+ T cells specific for a melanoma-expressed self-antigen. Int Immunol 21:155–65.
29. Likar Y, Dobrenkov K, Olszewska M, Shenker L, Cai S, Hricak H, et al. (2009) PET imaging of HSV1-tk mutants with acquired specificity toward pyrimidine- and acycloguanosine-based radiotracers. Eur J Nucl Med Mol Imaging.

30. Zhao B, Schwartz LH, Larson SM (2009) Imaging surrogates of tumor response to therapy: anatomic and functional biomarkers. J Nucl Med 50:239–49.
31. Schelling M, Avril N, Nahrig J, Kuhn W, Romer W, Sattler D, et al. (2000) Positron emission tomography using [(18)F]Fluorodeoxyglucose for monitoring primary chemotherapy in breast cancer. J Clin Oncol 18:1689–95.
32. Thomas GV, Tran C, Mellinghoff IK, Welsbie DS, Chan E, Fueger B, et al. (2006) Hypoxia-inducible factor determines sensitivity to inhibitors of mTOR in kidney cancer. Nat Med 12:122–7.
33. Weber WA, Petersen V, Schmidt B, Tyndale-Hines L, Link T, Peschel C, et al. (2003) Positron emission tomography in non-small-cell lung cancer: prediction of response to chemotherapy by quantitative assessment of glucose use. J Clin Oncol 21:2651–7.
34. Schlyer DJ (2003) Production of radionuclides in accelerators. In: Welch MJ, Redvanly CS, eds. Handbook of radiopharmaceuticals: radiochemistry and applications. Chichester: Wiley, pp 1–71.
35. Mausner LF, Mirzadeh S (2003) Reactor Production of Radionuclides. In: Welch MJ, Redvanly CS, eds. Handbook of radiopharmaceuticals: radiochemistry and applications. Chichester: Wiley, pp 87–119.
36. Welch MJ, Redvanly CS (2003) Handbook of radiopharmaceuticals: radiochemistry and applications. Chichester: Wiley.
37. Schubiger PA, Lehmann L, Friebe M (2007) PET Chemistry The Driving Force in Molecular Imaging. Berlin: Springer.
38. Saha GB (2004) Basics of PET Imaging Physics, Chemistry, and Regulations. New York: Springer.
39. Anderson CJ, Welch MJ (1999) Radiometal-labeled agents (non-technetium) for diagnostic imaging. Chem Rev 99:2219–34.
40. Antoni G, Langstrom B (2008) Radiopharmaceuticals: Molecular Imaging using Positron Emission Tomography. In: Semmler W, Schwaiger M, eds. Molecular Imaging I. Berlin: Springer, pp 177–203.
41. Rossin R, Pan D, Qi K, Turner JL, Sun X, Wooley KL, et al. (2005) 64Cu-labeled folate-conjugated shell cross-linked nanoparticles for tumor imaging and radiotherapy: synthesis, radiolabeling, and biologic evaluation. J Nucl Med 46:1210–8.
42. Hevesy GCd, Peneth F (1938) A manual of radioactivity, 2nd ed. London Oxford University Press.
43. Eckelman WC (2005) The use of positron emission tomography in drug discovery and development. In: Bailey DL, Townsend DW, Valk PE, et al., eds. Positron emission tomography: basic sciences. London: Springer, pp 327–341.
44. Banerjee S, Pillai MR, Ramamoorthy N (2001) Evolution of Tc-99m in diagnostic radiopharmaceuticals. Semin Nucl Med 31:260–77.
45. Jurisson SS, Lydon JD (1999) Potential technetium small molecule radiopharmaceuticals. Chem Rev 99:2205–18.
46. Mahmood A, Jones AG (2003) Technetium radiopharmaceuticals. In: Welch MJ, Redvanly CS, eds. Handbook of radiopharmaceuticals: radiochemistry and applications. Chichester: Wiley, pp 323–362.
47. Liu S, Edwards DS (1999) 99mTc-Labeled Small Peptides as Diagnostic Radiopharmaceuticals. Chem Rev 99:2235–68.
48. McQuade P, Rowland DJ, Lewis JS, Welch MJ (2005) Positron-emitting isotopes produced on biomedical cyclotrons. Curr Med Chem 12:807–18.
49. Bigott HM, Welch MJ (2002) Technetium-94 m-sestamibi. Preparation and quality control for human use. . In: Nicolini M, Mazzi U, eds. Technetium, rhenium and other metals in chemistry and nuclear medicine, vol 6. Padova: SG Editoriali, pp 559–561.
50. Finn R (2003) Chemistry applied to iodine radionuclides. In: Welch MJ, Redvanly CS, eds. Handbook of radiopharmaceuticals: radiochemistry and applications. Chichester: Wiley, pp 423–440.

51. Weiner RE, Thakur ML (2003) Chemistry of gallium and indium radiopharmaceuticals. In: Welch MJ, Redvanly CS, eds. Handbook of radiopharmaceuticals: radiochemistry and applications.Chichester: Wiley, pp 363–400.
52. Antoni G, Kihlbert T, Langstrom B (2003) Aspects on the synthesis of ^{11}C-labeled compounds. In: Welch MJ, Redvanly CS, eds. Handbook of radiopharmaceuticals: radiochemistry and applications. Chichester: Wiley, pp 141–194.
53. Clark JC, Aigbirhio FI (2003) Chemistry of nitrogen-13 and oxygen-15. In: Welch MJ, Redvanly CS, eds. Handbook of radiopharmaceuticals:radiochemistry and applications. Chichester: Wiley, pp 119–140.
54. Snyder SE, Kilbourn MR (2003) Chemistry of fluorine-18 radiopharmaceuticals. In: Welch MJ, Redvanly CS, eds. Handbook of radiopharmaceuticals: radiochemistry and applications. Chichester: Wiley, pp 195–228.
55. Ferrieri RA (2003) Production and application of synthetic precursors labeled with carbon-11 and fluorine-18. In: Welch MJ, Redvanly CS, eds. Handbook of radiopharmaceuticals: radiochemistry and applications. Chichester: Wiley, pp 229–282.
56. Fowler JS, Ido T (2003) Design and synthesis of 2-deoxy-2-[^{18}F]fluoro-D-glucose [^{18}FDG]. In: Welch MJ, Redvanly CS, eds. Handbook of radiopharmaceuticals: radiochemistry and applications.Chichester: Wiley, pp 307–322.
57. Rowland DJ, McCarthy TJ, Welch MJ (2003) Radiobromine for imaging and therapy. In: Welch MJ, Redvanly CS, eds. Handbook of radiopharmaceuticals: radiochemistry and applications.Chichester: Wiley, pp 441–466.
58. Ugur O, Kothari PJ, Finn RD, Zanzonico P, Ruan S, Guenther I, et al. (2002) Ga-66 labeled somatostatin analogue DOTA-DPhe1-Tyr3-octreotide as a potential agent for positron emission tomography imaging and receptor mediated internal radiotherapy of somatostatin receptor positive tumors. Nucl Med Biol 29:147–57.
59. Sun X, Anderson CJ (2004) Production and application of copper-64 radiopharmaceuticals Methods in enzymology. 386:237–261.
60. Sun G, Hagooly A, Xu J, Nystrom AM, Li Z, Rossin R, et al. (2008) Facile, efficient approach to accomplish tunable chemistries and variable biodistributions for shell cross-linked nanoparticles. Biomacromolecules 9:1997–2006.
61. Rossin R, Muro S, Welch MJ, Muzykantov VR, Schuster DP (2008) In vivo imaging of 64Cu-labeled polymer nanoparticles targeted to the lung endothelium. J Nucl Med 49:103–11.
62. Saha GB (2004) Basics of PET Imaging Physics, Chemistry, and Regulations. New York: Springer.
63. Lewis JS, Singh RK, Welch MJ (2008) Long lived and unconventional PET radionuclides. In: Pomper MG, Jelovani JG, eds. Molecular imaging in oncology. New York: Informa Healthcare, pp 282–292.
64. Hume SP, Gunn RN, Jones T (1998) Pharmacological constraints associated with positron emission tomographic scanning of small laboratory animals. Eur J Nucl Med 25:173–6.
65. Ding YS, Fowler J (2005) New-generation radiotracers for nAChR and NET. Nucl Med Biol 32:707–18.
66. Wester HJ (2007) Nuclear imaging probes: from bench to bedside. Clin Cancer Res 13:3470–81.
67. Fowler JS, Wang GJ, Logan J, Xie S, Volkow ND, MacGregor RR, et al. (1995) Selective reduction of radiotracer trapping by deuterium substitution: comparison of carbon-11-L-deprenyl and carbon-11-deprenyl-D2 for MAO B mapping. J Nucl Med 36:1255–62.
68. Eckelman WC (2003) Mechanism of Target Specific Uptake Using Examples of Muscarinic Receptor Binding Radiotracers. In: Welch MJ, Redvanly CS, eds. Handbook of radiopharmaceuticals: radiochemistry and applications. Chichester: Wiley, pp 487–500.
69. Velikyan I, Beyer GJ, Bergstrom-Pettermann E, Johansen P, Bergstrom M, Langstrom B (2008) The importance of high specific radioactivity in the performance of 68Ga-labeled peptide. Nucl Med Biol 35:529–36.

70. McCarthy DW, Bass LA, Cutler PD, Shefer RE, Klinkowstein RE, Herrero P, et al. (1999) High purity production and potential applications of copper-60 and copper-61. Nucl Med Biol 26:351–8.
71. McCarthy DW, Shefer RE, Klinkowstein RE, Bass LA, Margeneau WH, Cutler CS, et al. (1997) Efficient production of high specific activity 64Cu using a biomedical cyclotron. Nucl Med Biol 24:35–43.
72. McQuade P, Miao Y, Yoo J, Quinn TP, Welch MJ, Lewis JS (2005) Imaging of melanoma using 64Cu- and 86Y-DOTA-ReCCMSH(Arg11), a cyclized peptide analogue of alpha-MSH. J Med Chem 48:2985–92.
73. McQuade P, Martin KE, Castle TC, Went MJ, Blower PJ, Welch MJ, et al. (2005) Investigation into 64Cu-labeled Bis(selenosemicarbazone) and Bis(thiosemicarbazone) complexes as hypoxia imaging agents. Nucl Med Biol 32:147–56.
74. McQuade P, Knight LC, Welch MJ (2004) Evaluation of 64Cu- and 125I-radiolabeled bitistatin as potential agents for targeting alpha v beta 3 integrins in tumor angiogenesis. Bioconjug Chem 15:988–96.
75. Lewis MR, Reichert DE, Laforest R, Margenau WH, Shefer RE, Klinkowstein RE, et al. (2002) Production and purification of gallium-66 for preparation of tumor-targeting radiopharmaceuticals. Nucl Med Biol 29:701–6.
76. Zhou D, Sharp TL, Fettig NM, Lee H, Lewis JS, Katzenellenbogen JA, et al. (2008) Evaluation of a bromine-76-labeled progestin 16alpha,17alpha-dioxolane for breast tumor imaging and radiotherapy: in vivo biodistribution and metabolic stability studies. Nucl Med Biol 35:655–63.
77. Rossin R, Berndorff D, Friebe M, Dinkelborg LM, Welch MJ (2007) Small-animal PET of tumor angiogenesis using a (76)Br-labeled human recombinant antibody fragment to the ED-B domain of fibronectin. J Nucl Med 48:1172–9.
78. Stahlschmidt A, Machulla HJ, Reischl G, Knaus EE, Wiebe LI (2008) Radioiodination of 1-(2-deoxy-beta-D-ribofuranosyl)-2,4-difluoro-5-iodobenzene (dRFIB), a putative thymidine mimic nucleoside for cell proliferation studies. Appl Radiat Isot 66:1221–8.
79. Zhou D, Chu W, Chen DL, Wang Q, Reichert DE, Rothfuss J, et al. (2009) [^{18}F]- and [11C]-labeled N-benzyl-isatin sulfonamide analogues as PET tracers for apoptosis: synthesis, radiolabeling mechanism, and in vivo imaging study of apoptosis in Fas-treated mice using [11C]WC-98. Org Biomol Chem 7:1337–48.
80. Zhou D, Lee H, Rothfuss JM, Chen DL, Ponde DE, Welch MJ, et al. (2009) Design and Synthesis of 2-Amino-4-methylpyridine Analogues as Inhibitors for Inducible Nitric Oxide Synthase and in Vivo Evaluation of [(18)F]6-(2-Fluoropropyl)-4-methyl-pyridin-2-amine as a Potential PET Tracer for Inducible Nitric Oxide Synthase. J Med Chem.
81. Zhou D, Chu W, Rothfuss J, Zeng C, Xu J, Jones L, et al. (2006) Synthesis, radiolabeling, and in vivo evaluation of an 18F-labeled isatin analog for imaging caspase-3 activation in apoptosis. Bioorg Med Chem Lett 16:5041–6.
82. Jagoda EM, Vaquero JJ, Seidel J, Green MV, Eckelman WC (2004) Experiment assessment of mass effects in the rat: implications for small animal PET imaging. Nucl Med Biol 31:771–9.
83. Tu Z, Chu W, Zhang J, Dence CS, Welch MJ, Mach RH (2005) Synthesis and in vivo evaluation of [11C]PJ34, a potential radiotracer for imaging the role of PARP-1 in necrosis. Nucl Med Biol 32:437–43.
84. Wang L, Shi J, Kim YS, Zhai S, Jia B, Zhao H, et al. (2009) Improving tumor-targeting capability and pharmacokinetics of (99m)Tc-labeled cyclic RGD dimers with PEG(4) linkers. Mol Pharm 6:231–45.
85. Kolodgie FD, Petrov A, Virmani R, Narula N, Verjans JW, Weber DK, et al. (2003) Targeting of apoptotic macrophages and experimental atheroma with radiolabeled annexin V: a technique with potential for noninvasive imaging of vulnerable plaque. Circulation 108:3134–9.
86. Mohsin H, Fitzsimmons J, Shelton T, Hoffman TJ, Cutler CS, Lewis MR, et al. (2007) Preparation and biological evaluation of 111In-, 177Lu- and 90Y-labeled DOTA analogues conjugated to B72.3. Nucl Med Biol 34:493–502.

87. Johnson LL, Schofield L, Donahay T, Bouchard M, Poppas A, Haubner R (2008) Radiolabeled RGD Peptides to Image Angiogenesis in Swine Model of Hibernating Myocardium. JACC Cardiovasc Imaging 1:500–510.
88. Warburg O (1931) The Metabolism of Tumors. New York: Richard Smith.
89. Plathow C, Weber WA (2008) Tumor cell metabolism imaging. J Nucl Med 49 Suppl 2:43S–63S.
90. Jerusalem G, Hustinx R, Beguin Y, Fillet G (2003) PET scan imaging in oncology. Eur J Cancer 39:1525–34.
91. Belhocine T, Driedger A (2008) 8F-Fluorodeoxyglucose Positron Emission Tomography in Oncology Advantages and Limitations. In: Hayat MA, ed. Cancer Imaging: Instrumentation and Applications, vol 2. Burlington: Elsevier, pp 193–200.
92. von Schulthess GK, Steinert HC, Hany TF (2006) Integrated PET/CT: current applications and future directions. Radiology 238:405–22.
93. Nomori H, Ohba Y, Yoshimoto K, Shibata H, Shiraishi K, Mori T (2009) Positron emission tomography in lung cancer. Gen Thorac Cardiovasc Surg 57:184–91.
94. Allen-Auerbach M, Weber WA (2009) Measuring Response with FDG-PET: Methodological Aspects. Oncologist.
95. Sun YY, Chen Y (2009) Cancer drug development using glucose metabolism radiopharmaceuticals. Curr Pharm Des 15:983–7.
96. Chen Y, Xiong Q, Yang X, Huang Z, Zhao Y, He L (2007) Noninvasive scintigraphic detection of tumor with 99mTc-DTPA-deoxyglucose: an experimental study. Cancer Biother Radiopharm 22:403–5.
97. Chen Y, Huang ZW, He L, Zheng SL, Li JL, Qin DL (2006) Synthesis and evaluation of a technetium-99m-labeled diethylenetriaminepentaacetate-deoxyglucose complex ([99mTc]-DTPA-DG) as a potential imaging modality for tumors. Appl Radiat Isot 64:342–7.
98. Yang DJ, Kim CG, Schechter NR, Azhdarinia A, Yu DF, Oh CS, et al. (2003) Imaging with 99mTc ECDG targeted at the multifunctional glucose transport system: feasibility study with rodents. Radiology 226:465–73.
99. Yang DJ, Kim EE (2005) Tracer development and hybrid imaging. Eur J Nucl Med Mol Imaging 32:1001–2.
100. Jager PL, Vaalburg W, Pruim J, de Vries EG, Langen KJ, Piers DA (2001) Radiolabeled amino acids: basic aspects and clinical applications in oncology. J Nucl Med 42:432–45.
101. Vallabhajosula S (2007) (18)F-labeled positron emission tomographic radiopharmaceuticals in oncology: an overview of radiochemistry and mechanisms of tumor localization. Semin Nucl Med 37:400–19.
102. Keyaerts M, Lahoutte T, Neyns B, Caveliers V, Vanhove C, Everaert H, et al. (2007) 123I-2-iodo-tyrosine, a new tumour imaging agent: human biodistribution, dosimetry and initial clinical evaluation in glioma patients. Eur J Nucl Med Mol Imaging 34:994–1002.
103. Hellwig D, Romeike BF, Ketter R, Moringlane JR, Kirsch CM, Samnick S (2008) Intra-individual comparison of p-[123I]-iodo-L-phenylalanine and L-3-[123I]-iodo-alpha-methyl-tyrosine for SPECT imaging of gliomas. Eur J Nucl Med Mol Imaging 35:24–31.
104. Biersack HJ, Coenen HH, Stocklin G, Reichmann K, Bockisch A, Oehr P, et al. (1989) Imaging of brain tumors with L-3-[123I]iodo-alpha-methyl tyrosine and SPECT. J Nucl Med 30:110–2.
105. Hara T, Kosaka N, Kishi H (1998) PET imaging of prostate cancer using carbon-11-choline. J Nucl Med 39:990–5.
106. Hara T, Kosaka N, Kishi H (2002) Development of (18)F-fluoroethylcholine for cancer imaging with PET: synthesis, biochemistry, and prostate cancer imaging. J Nucl Med 43:187–99.
107. DeGrado TR, Baldwin SW, Wang S, Orr MD, Liao RP, Friedman HS, et al. (2001) Synthesis and evaluation of (18)F-labeled choline analogs as oncologic PET tracers. J Nucl Med 42:1805–14.
108. Bansal A, Shuyan W, Hara T, Harris RA, Degrado TR (2008) Biodisposition and metabolism of [(18)F]fluorocholine in 9L glioma cells and 9L glioma-bearing fisher rats. Eur J Nucl Med Mol Imaging 35:1192–203.

109. Kotzerke J, Volkmer BG, Neumaier B, Gschwend JE, Hautmann RE, Reske SN (2002) Carbon-11 acetate positron emission tomography can detect local recurrence of prostate cancer. Eur J Nucl Med Mol Imaging 29:1380–4.
110. Kato T, Tsukamoto E, Kuge Y, Takei T, Shiga T, Shinohara N, et al. (2002) Accumulation of [11C]acetate in normal prostate and benign prostatic hyperplasia: comparison with prostate cancer. Eur J Nucl Med Mol Imaging 29:1492–5.
111. Vavere AL, Kridel SJ, Wheeler FB, Lewis JS (2008) 1-11C-acetate as a PET radiopharmaceutical for imaging fatty acid synthase expression in prostate cancer. J Nucl Med 49:327–34.
112. Bading JR, Shields AF (2008) Imaging of cell proliferation: status and prospects. J Nucl Med 49 Suppl 2:64S–80S.
113. Chung JK, Kim YK, Kim SK, Lee YJ, Paek S, Yeo JS, et al. (2002) Usefulness of 11C-methionine PET in the evaluation of brain lesions that are hypo- or isometabolic on 18F-FDG PET. Eur J Nucl Med Mol Imaging 29:176–82.
114. Watanabe K, Nomori H, Ohtsuka T, Naruke T, Ebihara A, Orikasa H, et al. (2006) [F-18] Fluorodeoxyglucose positron emission tomography can predict pathological tumor stage and proliferative activity determined by Ki-67 in clinical stage IA lung adenocarcinomas. Jpn J Clin Oncol 36:403–9.
115. de Wolde H, Pruim J, Mastik MF, Koudstaal J, Molenaar WM (1997) Proliferative activity in human brain tumors: comparison of histopathology and L-[1-(11)C]tyrosine PET. J Nucl Med 38:1369–74.
116. Shields AF, Grierson JR, Dohmen BM, Machulla HJ, Stayanoff JC, Lawhorn-Crews JM, et al. (1998) Imaging proliferation in vivo with [F-18]FLT and positron emission tomography. Nat Med 4:1334–6.
117. van Waarde A, Been LB, Ishiwata K, Dierckx RA, Elsinga PH (2006) Early response of sigma-receptor ligands and metabolic PET tracers to 3 forms of chemotherapy: an in vitro study in glioma cells. J Nucl Med 47:1538–45.
118. Buck AK, Halter G, Schirrmeister H, Kotzerke J, Wurziger I, Glatting G, et al. (2003) Imaging proliferation in lung tumors with PET: 18F-FLT versus 18F-FDG. J Nucl Med 44:1426–31.
119. Vander Borght T, Lambotte L, Pauwels S, Labar D, Beckers C, Dive C (1991) Noninvasive measurement of liver regeneration with positron emission tomography and [2-11C]thymidine. Gastroenterology 101:794–9.
120. Vander Borght T, Labar D, Pauwels S, Lambotte L (1991) Production of [2-11C]thymidine for quantification of cellular proliferation with PET. Int J Rad Appl Instrum [A] 42:103–4.
121. Goethals P, van Eijkeren M, Lemahieu I (1999) In vivo distribution and identification of 11C-activity after injection of [methyl-11C]thymidine in Wistar rats. J Nucl Med 40:491–6.
122. Toyohara J, Gogami A, Hayashi A, Yonekura Y, Fujibayashi Y (2003) Pharmacokinetics and metabolism of 5-125I-iodo-4'-thio-2'-deoxyuridine in rodents. J Nucl Med 44:1671–6.
123. Cho SY, Ravasi L, Szajek LP, Seidel J, Green MV, Fine HA, et al. (2005) Evaluation of (76) Br-FBAU as a PET reporter probe for HSV1-tk gene expression imaging using mouse models of human glioma. J Nucl Med 46:1923–30.
124. Wells P, Price P (2008) Tumor proliferation:2-[^{11}C]-thymidine positron emission tomography. In: Hayat MA, ed. Cancer Imaging: instrumentation and applications, vol 2. Burlington: Elsevier, pp 181–191.
125. Kameyama R, Yamamoto Y, Izuishi K, Takebayashi R, Hagiike M, Murota M, et al. (2009) Detection of gastric cancer using 18F-FLT PET: comparison with 18F-FDG PET. Eur J Nucl Med Mol Imaging 36:382–8.
126. Yamamoto Y, Nishiyama Y, Ishikawa S, Nakano J, Chang SS, Bandoh S, et al. (2007) Correlation of 18F-FLT and 18F-FDG uptake on PET with Ki-67 immunohistochemistry in non-small cell lung cancer. Eur J Nucl Med Mol Imaging 34:1610–6.
127. Krohn KA, Mankoff DA, Muzi M, Link JM, Spence AM (2005) True tracers: comparing FDG with glucose and FLT with thymidine. Nucl Med Biol 32:663–71.
128. Muzi M, Mankoff DA, Grierson JR, Wells JM, Vesselle H, Krohn KA (2005) Kinetic modeling of 3'-deoxy-3'-fluorothymidine in somatic tumors: mathematical studies. J Nucl Med 46:371–80.

129. Dittmann H, Jusufoska A, Dohmen BM, Smyczek-Gargya B, Fersis N, Pritzkow M, et al. (2009) 3'-Deoxy-3'-[(18)F]fluorothymidine (FLT) uptake in breast cancer cells as a measure of proliferation after doxorubicin and docetaxel treatment. Nucl Med Biol 36:163–9.
130. Yang YJ, Ryu JS, Kim SY, Oh SJ, Im KC, Lee H, et al. (2006) Use of 3'-deoxy-3'-[18F]fluorothymidine PET to monitor early responses to radiation therapy in murine SCCVII tumors. Eur J Nucl Med Mol Imaging 33:412–9.
131. Sun H, Mangner TJ, Collins JM, Muzik O, Douglas K, Shields AF (2005) Imaging DNA synthesis in vivo with 18F-FMAU and PET. J Nucl Med 46:292–6.
132. Bading JR, Shahinian AH, Vail A, Bathija P, Koszalka GW, Koda RT, et al. (2004) Pharmacokinetics of the thymidine analog 2'-fluoro-5-methyl-1-beta-D-arabinofuranosyluracil (FMAU) in tumor-bearing rats. Nucl Med Biol 31:407–18.
133. Mangner TJ, Klecker RW, Anderson L, Shields AF (2003) Synthesis of 2'-deoxy-2'-[18F] fluoro-beta-D-arabinofuranosyl nucleosides, [18F]FAU, [18F]FMAU, [18F]FBAU and [18F] FIAU, as potential PET agents for imaging cellular proliferation. Synthesis of [18F]labelled FAU, FMAU, FBAU, FIAU. Nucl Med Biol 30:215–24.
134. Sun H, Sloan A, Mangner TJ, Vaishampayan U, Muzik O, Collins JM, et al. (2005) Imaging DNA synthesis with [18F]FMAU and positron emission tomography in patients with cancer. Eur J Nucl Med Mol Imaging 32:15–22.
135. van Waarde A, Elsinga PH (2008) Proliferation markers for the differential diagnosis of tumor and inflammation. Curr Pharm Des 14:3326–339.
136. Denny WA (2001) Prodrug strategies in cancer therapy. Eur J Med Chem 36:577–95.
137. Brown JM (1999) The hypoxic cell: a target for selective cancer therap--ighteenth Bruce F. Cain Memorial Award lecture. Cancer Res 59:5863–70.
138. Padhani AR, Krohn KA, Lewis JS, Alber M (2007) Imaging oxygenation of human tumours. Eur Radiol 17:861–72.
139. Padhani AR (2005) Where are we with imaging oxygenation in human tumours? Cancer Imaging 5:128–30.
140. Piert M, Machulla HJ, Picchio M, Reischl G, Ziegler S, Kumar P, et al. (2005) Hypoxia-specific tumor imaging with 18F-fluoroazomycin arabinoside. J Nucl Med 46:106–13.
141. Dehdashti F, Grigsby PW, Mintun MA, Lewis JS, Siegel BA, Welch MJ (2003) Assessing tumor hypoxia in cervical cancer by positron emission tomography with 60Cu-ATSM: relationship to therapeutic response-a preliminary report. Int J Radiat Oncol Biol Phys 55:1233–8.
142. Dehdashti F, Mintun MA, Lewis JS, Bradley J, Govindan R, Laforest R, et al. (2003) In vivo assessment of tumor hypoxia in lung cancer with 60Cu-ATSM. Eur J Nucl Med Mol Imaging 30:844–50.
143. Dehdashti F, Grigsby PW, Lewis JS, Laforest R, Siegel BA, Welch MJ (2008) Assessing tumor hypoxia in cervical cancer by PET with 60Cu-labeled diacetyl-bis(N4-methylthiosemicarbazone). J Nucl Med 49:201–5.
144. Holland JP, Lewis JS, Dehdashti F (2009) Assessing tumor hypoxia by positron emission tomography with Cu-ATSM. Q J Nucl Med Mol Imaging 53:193–200.
145. Krohn KA, Link JM, Mason RP (2008) Molecular imaging of hypoxia. J Nucl Med 49 Suppl 2:129S–48S.
146. Rajendran JG, Krohn KA (2005) Imaging hypoxia and angiogenesis in tumors. Radiol Clin North Am 43:169–87.
147. Padhani A (2006) PET imaging of tumour hypoxia. Cancer Imaging 6:S117–21.
148. Yang DJ, Wallace S, Cherif A, Li C, Gretzer MB, Kim EE, et al. (1995) Development of F-18-labeled fluoroerythronitroimidazole as a PET agent for imaging tumor hypoxia. Radiology 194:795–800.
149. Sorger D, Patt M, Kumar P, Wiebe LI, Barthel H, Seese A, et al. (2003) [18F]Fluoro azomycinarabinofuranoside (18FAZA) and [18F]Fluoromisonidazole (18FMISO): a comparative study of their selective uptake in hypoxic cells and PET imaging in experimental rat tumors. Nucl Med Biol 30:317–26.

150. Barthel H, Wilson H, Collingridge DR, Brown G, Osman S, Luthra SK, et al. (2004) In vivo evaluation of [18F]fluoroetanidazole as a new marker for imaging tumour hypoxia with positron emission tomography. Br J Cancer 90:2232–42.
151. Komar G, Seppanen M, Eskola O, Lindholm P, Gronroos TJ, Forsback S, et al. (2008) 18F-EF5: a new PET tracer for imaging hypoxia in head and neck cancer. J Nucl Med 49:1944–51.
152. Ziemer LS, Evans SM, Kachur AV, Shuman AL, Cardi CA, Jenkins WT, et al. (2003) Noninvasive imaging of tumor hypoxia in rats using the 2-nitroimidazole 18F-EF5. Eur J Nucl Med Mol Imaging 30:259–66.
153. Tatum JL, Kelloff GJ, Gillies RJ, Arbeit JM, Brown JM, Chao KS, et al. (2006) Hypoxia: importance in tumor biology, noninvasive measurement by imaging, and value of its measurement in the management of cancer therapy. Int J Radiat Biol 82:699–757.
154. Chu T, Li R, Hu S, Liu X, Wang X (2004) Preparation and biodistribution of technetium-99m-labeled 1-(2-nitroimidazole-1-yl)-propanhydroxyiminoamide (N2IPA) as a tumor hypoxia marker. Nucl Med Biol 31:199–203.
155. Lewis JS, Laforest R, Dehdashti F, Grigsby PW, Welch MJ, Siegel BA (2008) An imaging comparison of 64Cu-ATSM and 60Cu-ATSM in cancer of the uterine cervix. J Nucl Med 49:1177–82.
156. Wood KA, Wong WL, Saunders MI (2008) [(64)Cu]diacetyl-bis(N(4)-methyl-thio semicarbazone) - a radiotracer for tumor hypoxia. Nucl Med Biol 35:393–400.
157. Dietz DW, Dehdashti F, Grigsby PW, Malyapa RS, Myerson RJ, Picus J, et al. (2008) Tumor hypoxia detected by positron emission tomography with 60Cu-ATSM as a predictor of response and survival in patients undergoing Neoadjuvant chemoradiotherapy for rectal carcinoma: a pilot study. Dis Colon Rectum 51:1641–8.
158. Bayly SR, King RC, Honess DJ, Barnard PJ, Betts HM, Holland JP, et al. (2008) In vitro and in vivo evaluations of a hydrophilic 64Cu-bis(thiosemicarbazonato)-glucose conjugate for hypoxia imaging. J Nucl Med 49:1862–8.
159. Krohn KA, Link JM (2003) Interpreting enzyme and receptor kinetics: keeping it simple, but not too simple. Nucl Med Biol 30:819–26.
160. Krohn KA (2001) The physical chemistry of ligand-receptor binding identifies some limitations to the analysis of receptor images. Nucl Med Biol 28:477–83.
161. Mankoff DA, Link JM, Linden HM, Sundararajan L, Krohn KA (2008) Tumor receptor imaging. J Nucl Med 49 Suppl 2:149S–63S.
162. Hagooly A, Rossin R, Welch MJ (2008) Small molecule receptors as imaging targets. Handb Exp Pharmacol:93–129.
163. Rufini V, Calcagni ML, Baum RP (2006) Imaging of neuroendocrine tumors. Semin Nucl Med 36:228–47.
164. Reubi JC, Maecke HR (2008) Peptide-based probes for cancer imaging. J Nucl Med 49:1735–8.
165. Vallabhajosula S, Moyer BR, Lister-James J, McBride BJ, Lipszyc H, Lee H, et al. (1996) Preclinical evaluation of technetium-99m-labeled somatostatin receptor-binding peptides. J Nucl Med 37:1016–22.
166. Gandomkar M, Najafi R, Shafiei M, Mazidi M, Ebrahimi SE (2007) Preclinical evaluation of [99mTc/EDDA/tricine/HYNIC0, 1-Nal3, Thr8]-octreotide as a new analogue in the detection of somatostatin-receptor-positive tumors. Nucl Med Biol 34:651–7.
167. Ginj M, Zhang H, Eisenwiener KP, Wild D, Schulz S, Rink H, et al. (2008) New pansomatostatin ligands and their chelated versions: affinity profile, agonist activity, internalization, and tumor targeting. Clin Cancer Res 14:2019–27.
168. Wadas TJ, Eiblmaier M, Zheleznyak A, Sherman CD, Ferdani R, Liang K, et al. (2008) Preparation and biological evaluation of 64Cu-CB-TE2A-sst2-ANT, a somatostatin antagonist for PET imaging of somatostatin receptor-positive tumors. J Nucl Med 49:1819–27.
169. Win Z, Al-Nahhas A, Rubello D, Gross MD (2007) Somatostatin receptor PET imaging with Gallium-68 labeled peptides. Q J Nucl Med Mol Imaging 51:244–50.

170. Maecke HR, Hofmann M, Haberkorn U (2005) (68)Ga-labeled peptides in tumor imaging. J Nucl Med 46 Suppl 1:172S–8S.
171. Friedman M, Stahl S (2009) Engineered affinity proteins for tumour-targeting applications. Biotechnol Appl Biochem 53:1–29.
172. Wu JC, Bengel FM, Gambhir SS (2007) Cardiovascular molecular imaging. Radiology 244:337–55.
173. Brown TM, Bittner V (2008) Biomarkers of atherosclerosis: clinical applications. Curr Cardiol Rep 10:497–504.
174. Langer HF, Haubner R, Pichler BJ, Gawaz M (2008) Radionuclide imaging: a molecular key to the atherosclerotic plaque. J Am Coll Cardiol 52:1–12.
175. Henze M, Dimitrakopoulou-Strauss A, Milker-Zabel S, Schuhmacher J, Strauss LG, Doll J, et al. (2005) Characterization of 68Ga-DOTA-D-Phe1-Tyr3-octreotide kinetics in patients with meningiomas. J Nucl Med 46:763–9.
176. Li ZB, Wu Z, Chen K, Ryu EK, Chen X (2008) 18F-labeled BBN-RGD heterodimer for prostate cancer imaging. J Nucl Med 49:453–61.
177. Liu Z, Niu G, Wang F, Chen X (2009) (68)Ga-labeled NOTA-RGD-BBN peptide for dual integrin and GRPR-targeted tumor imaging. Eur J Nucl Med Mol Imaging.
178. Laverman P, Roosenburg S, Gotthardt M, Park J, Oyen WJ, de Jong M, et al. (2008) Targeting of a CCK(2) receptor splice variant with (111)In-labelled cholecystokinin-8 (CCK8) and (111)In-labelled minigastrin. Eur J Nucl Med Mol Imaging 35:386–92.
179. von Guggenberg E, Dietrich H, Skvortsova I, Gabriel M, Virgolini IJ, Decristoforo C (2007) 99mTc-labelled HYNIC-minigastrin with reduced kidney uptake for targeting of CCK-2 receptor-positive tumours. Eur J Nucl Med Mol Imaging 34:1209–18.
180. Wild D, Macke H, Christ E, Gloor B, Reubi JC (2008) Glucagon-like peptide 1-receptor scans to localize occult insulinomas. N Engl J Med 359:766–8.
181. Gotthardt M, Fischer M, Naeher I, Holz JB, Jungclas H, Fritsch HW, et al. (2002) Use of the incretin hormone glucagon-like peptide-1 (GLP-1) for the detection of insulinomas: initial experimental results. Eur J Nucl Med Mol Imaging 29:597–606.
182. Zwanziger D, Khan IU, Neundorf I, Sieger S, Lehmann L, Friebe M, et al. (2008) Novel chemically modified analogues of neuropeptide Y for tumor targeting. Bioconjug Chem 19:1430–8.
183. Garcia-Garayoa E, Blauenstein P, Blanc A, Maes V, Tourwe D, Schubiger PA (2009) A stable neurotensin-based radiopharmaceutical for targeted imaging and therapy of neurotensin receptor-positive tumours. Eur J Nucl Med Mol Imaging 36:37–47.
184. Maina T, Nikolopoulou A, Stathopoulou E, Galanis AS, Cordopatis P, Nock BA (2007) [99mTc]Demotensin 5 and 6 in the NTS1-R-targeted imaging of tumours: synthesis and preclinical results. Eur J Nucl Med Mol Imaging 34:1804–14.
185. Van der Mey M, Janssen CG, Janssens FE, Jurzak M, Langlois X, Sommen FM, et al. (2005) Synthesis and biodistribution of [(11)C]R116301, a promising PET ligand for central NK(1) receptors. Bioorg Med Chem 13:1579–86.
186. Haneda E, Higuchi M, Maeda J, Inaji M, Okauchi T, Ando K, et al. (2007) In vivo mapping of substance P receptors in brains of laboratory animals by high-resolution imaging systems. Synapse 61:205–15.
187. Zhang K, Aruva MR, Shanthly N, Cardi CA, Rattan S, Patel C, et al. (2008) PET imaging of VPAC1 expression in experimental and spontaneous prostate cancer. J Nucl Med 49:112–21.
188. Cheng D, Yin D, Zhang L, Wang M, Li G, Wang Y (2007) Radiosynthesis of 18F-(R8,15,21, L17)-vasoactive intestinal peptide and preliminary evaluation in mice bearing C26 colorectal tumours. Nucl Med Commun 28:501–6.
189. Thakur ML, Aruva MR, Gariepy J, Acton P, Rattan S, Prasad S, et al. (2004) PET imaging of oncogene overexpression using 64Cu-vasoactive intestinal peptide (VIP) analog: comparison with 99mTc-VIP analog. J Nucl Med 45:1381–9.
190. Miao Y, Benwell K, Quinn TP (2007) 99mTc- and 111In-labeled alpha-melanocyte-stimulating hormone peptides as imaging probes for primary and pulmonary metastatic melanoma detection. J Nucl Med 48:73–80.

191. Wei L, Butcher C, Miao Y, Gallazzi F, Quinn TP, Welch MJ, et al. (2007) Synthesis and biologic evaluation of 64Cu-labeled rhenium-cyclized alpha-MSH peptide analog using a cross-bridged cyclam chelator. J Nucl Med 48:64–72.
192. Wei L, Miao Y, Gallazzi F, Quinn TP, Welch MJ, Vavere AL, et al. (2007) Gallium-68-labeled DOTA-rhenium-cyclized alpha-melanocyte-stimulating hormone analog for imaging of malignant melanoma. Nucl Med Biol 34:945–53.
193. Henriksen G, Schottelius M, Poethko T, Hauser A, Wolf I, Schwaiger M, et al. (2004) Proof of principle for the use of 11C-labelled peptides in tumour diagnosis with PET. Eur J Nucl Med Mol Imaging 31:1653–7.
194. Schottelius M, Poethko T, Herz M, Reubi JC, Kessler H, Schwaiger M, et al. (2004) First (18) F-labeled tracer suitable for routine clinical imaging of sst receptor-expressing tumors using positron emission tomography. Clin Cancer Res 10:3593–606.
195. Chu W, Xu J, Zhou D, Zhang F, Jones LA, Wheeler KT, et al. (2009) New N-substituted 9-azabicyclo[3.3.1]nonan-3alpha-yl phenylcarbamate analogs as sigma2 receptor ligands: synthesis, in vitro characterization, and evaluation as PET imaging and chemosensitization agents. Bioorg Med Chem 17:1222–31.
196. Rowland DJ, Tu Z, Xu J, Ponde D, Mach RH, Welch MJ (2006) Synthesis and in vivo evaluation of 2 high-affinity 76Br-labeled sigma2-receptor ligands. J Nucl Med 47:1041–8.
197. Kawamura K, Tsukada H, Shiba K, Tsuji C, Harada N, Kimura Y, et al. (2007) Synthesis and evaluation of fluorine-18-labeled SA4503 as a selective sigma1 receptor ligand for positron emission tomography. Nucl Med Biol 34:571–7.
198. Staelens L, Oltenfreiter R, Dumont F, Waterhouse RN, Vandenbulcke K, Blanckaert P, et al. (2005) In vivo evaluation of [123I]-4-iodo-N-(4-(4-(2-methoxyphenyl)-piperazin-1-yl)butyl)-benzamide: a potential sigma receptor ligand for SPECT studies. Nucl Med Biol 32:193–200.
199. Ross TL, Honer M, Lam PY, Mindt TL, Groehn V, Schibli R, et al. (2008) Fluorine-18 click radiosynthesis and preclinical evaluation of a new 18F-labeled folic acid derivative. Bioconjug Chem 19:2462–70.
200. Fisher RE, Siegel BA, Edell SL, Oyesiku NM, Morgenstern DE, Messmann RA, et al. (2008) Exploratory study of 99mTc-EC20 imaging for identifying patients with folate receptor-positive solid tumors. J Nucl Med 49:899–906.
201. Bigott HM, Parent E, Luyt LG, Katzenellenbogen JA, Welch MJ (2005) Design and synthesis of functionalized cyclopentadienyl tricarbonylmetal complexes for technetium-94 m PET imaging of estrogen receptors. Bioconjug Chem 16:255–64.
202. Takahashi N, Yang DJ, Kohanim S, Oh CS, Yu DF, Azhdarinia A, et al. (2007) Targeted functional imaging of estrogen receptors with 99mTc-GAP-EDL. Eur J Nucl Med Mol Imaging 34:354–62.
203. Parent EE, Dence CS, Sharp TL, Welch MJ, Katzenellenbogen JA (2008) 7alpha-18F-fluoromethyl-dihydrotestosterone and 7alpha-18F-fluoromethyl-nortestosterone: ligands to determine the role of sex hormone-binding globulin for steroidal radiopharmaceuticals. J Nucl Med 49:987–94.
204. Garg S, Doke A, Black KW, Garg PK (2008) In vivo biodistribution of an androgen receptor avid PET imaging agent 7-alpha-fluoro-17 alpha-methyl-5-alpha-dihydrotestosterone ([(18) F]FMDHT) in rats pretreated with cetrorelix, a GnRH antagonist. Eur J Nucl Med Mol Imaging 35:379–85.
205. McLarty K, Cornelissen B, Scollard DA, Done SJ, Chun K, Reilly RM (2009) Associations between the uptake of 111In-DTPA-trastuzumab, HER2 density and response to trastuzumab (Herceptin) in athymic mice bearing subcutaneous human tumour xenografts. Eur J Nucl Med Mol Imaging 36:81–93.
206. Ahlgren S, Wallberg H, Tran TA, Widstrom C, Hjertman M, Abrahmsen L, et al. (2009) Targeting of HER2-Expressing Tumors with a Site-Specifically 99mTc-Labeled Recombinant Affibody Molecule, ZHER2:2395, with C-Terminally Engineered Cysteine. J Nucl Med.
207. Kramer-Marek G, Kiesewetter DO, Martiniova L, Jagoda E, Lee SB, Capala J (2008) [18F] FBEM-Z(HER2:342)-Affibody molecule-a new molecular tracer for in vivo monitoring of HER2 expression by positron emission tomography. Eur J Nucl Med Mol Imaging 35:1008–18.

208. Cheng Z, De Jesus OP, Namavari M, De A, Levi J, Webster JM, et al. (2008) Small-animal PET imaging of human epidermal growth factor receptor type 2 expression with site-specific 18F-labeled protein scaffold molecules. J Nucl Med 49:804–13.
209. Orlova A, Wallberg H, Stone-Elander S, Tolmachev V (2009) On the selection of a tracer for PET imaging of HER2-expressing tumors: direct comparison of a 124I-labeled affibody molecule and trastuzumab in a murine xenograft model. J Nucl Med 50:417–25.
210. Chen W, Bural GG, Torigian DA, Rader DJ, Alavi A (2009) Emerging role of FDG-PET/CT in assessing atherosclerosis in large arteries. Eur J Nucl Med Mol Imaging 36:144–51.
211. Zhang Z, Machac J, Helft G, Worthley SG, Tang C, Zaman AG, et al. (2006) Non-invasive imaging of atherosclerotic plaque macrophage in a rabbit model with F-18 FDG PET: a histopathological correlation. BMC Nucl Med 6:3.
212. Worthley SG, Zhang ZY, Machac J, Helft G, Tang C, Liew GY, et al. (2009) In vivo non-invasive serial monitoring of FDG-PET progression and regression in a rabbit model of atherosclerosis. Int J Cardiovasc Imaging 25:251–7.
213. Wyss MT, Weber B, Honer M, Spath N, Ametamey SM, Westera G, et al. (2004) 18F-choline in experimental soft tissue infection assessed with autoradiography and high-resolution PET. Eur J Nucl Med Mol Imaging 31:312–6.
214. Matter CM, Wyss MT, Meier P, Spath N, von Lukowicz T, Lohmann C, et al. (2006) 18F-choline images murine atherosclerotic plaques ex vivo. Arterioscler Thromb Vasc Biol 26:584–9.
215. Riou LM, Broisat A, Dimastromatteo J, Pons G, Fagret D, Ghezzi C (2009) Pre-clinical and clinical evaluation of nuclear tracers for the molecular imaging of vulnerable atherosclerosis: an overview. Curr Med Chem 16:1499–511.
216. Ishino S, Kuge Y, Takai N, Tamaki N, Strauss HW, Blankenberg FG, et al. (2007) 99mTc-Annexin A5 for noninvasive characterization of atherosclerotic lesions: imaging and histological studies in myocardial infarction-prone Watanabe heritable hyperlipidemic rabbits. Eur J Nucl Med Mol Imaging 34:889–99.
217. Zhao Y, Kuge Y, Zhao S, Morita K, Inubushi M, Strauss HW, et al. (2007) Comparison of 99mTc-annexin A5 with 18F-FDG for the detection of atherosclerosis in ApoE−/− mice. Eur J Nucl Med Mol Imaging 34:1747–55.
218. Kircher MF, Grimm J, Swirski FK, Libby P, Gerszten RE, Allport JR, et al. (2008) Noninvasive in vivo imaging of monocyte trafficking to atherosclerotic lesions. Circulation 117:388–95.
219. Nahrendorf M, Zhang H, Hembrador S, Panizzi P, Sosnovik DE, Aikawa E, et al. (2008) Nanoparticle PET-CT imaging of macrophages in inflammatory atherosclerosis. Circulation 117:379–87.
220. Broisat A, Riou LM, Ardisson V, Boturyn D, Dumy P, Fagret D, et al. (2007) Molecular imaging of vascular cell adhesion molecule-1 expression in experimental atherosclerotic plaques with radiolabelled B2702-p. Eur J Nucl Med Mol Imaging 34:830–40.
221. Dobrucki LW, Sinusas AJ (2007) Imaging angiogenesis. Curr Opin Biotechnol 18:90–6.
222. Hicklin DJ, Ellis LM (2005) Role of the vascular endothelial growth factor pathway in tumor growth and angiogenesis. J Clin Oncol 23:1011–27.
223. Choe YS, Lee KH (2007) Targeted in vivo imaging of angiogenesis: present status and perspectives. Curr Pharm Des 13:17–31.
224. Cai W, Chen X (2008) Multimodality molecular imaging of tumor angiogenesis. J Nucl Med 49 Suppl 2:113S–28S.
225. Cai W, Gambhir SS, Chen X (2008) Chapter 7. Molecular imaging of tumor vasculature. Methods Enzymol 445:141–76.
226. Cai W, Chen K, Mohamedali KA, Cao Q, Gambhir SS, Rosenblum MG, et al. (2006) PET of vascular endothelial growth factor receptor expression. J Nucl Med 47:2048–56.
227. Willmann JK, Chen K, Wang H, Paulmurugan R, Rollins M, Cai W, et al. (2008) Monitoring of the biological response to murine hindlimb ischemia with 64Cu-labeled vascular endothelial growth factor-121 positron emission tomography. Circulation 117:915–22.
228. Wang H, Cai W, Chen K, Li ZB, Kashefi A, He L, et al. (2007) A new PET tracer specific for vascular endothelial growth factor receptor 2. Eur J Nucl Med Mol Imaging 34:2001–10.

229. Santimaria M, Moscatelli G, Viale GL, Giovannoni L, Neri G, Viti F, et al. (2003) Immunoscintigraphic detection of the ED-B domain of fibronectin, a marker of angiogenesis, in patients with cancer. Clin Cancer Res 9:571–9.
230. Haubner R (2008) Noninvasive rracer techniques to characterize angiogenesis. In: Semmler W, Schwaiger M, eds. Molecular Imaging II. Heidelberg: Springer, pp 323–341.
231. Haubner RH, Wester HJ, Weber WA, Schwaiger M (2003) Radiotracer-based strategies to image angiogenesis. Q J Nucl Med 47:189–99.
232. Koivunen E, Arap W, Valtanen H, Rainisalo A, Medina OP, Heikkila P, et al. (1999) Tumor targeting with a selective gelatinase inhibitor. Nat Biotechnol 17:768–74.
233. Medina OP, Kairemo K, Valtanen H, Kangasniemi A, Kaukinen S, Ahonen I, et al. (2005) Radionuclide imaging of tumor xenografts in mice using a gelatinase-targeting peptide. Anticancer Res 25:33–42.
234. Sprague JE, Li WP, Liang K, Achilefu S, Anderson CJ (2006) In vitro and in vivo investigation of matrix metalloproteinase expression in metastatic tumor models. Nucl Med Biol 33:227–37.
235. Kuhnast B, Bodenstein C, Haubner R, Wester HJ, Senekowitsch-Schmidtke R, Schwaiger M, et al. (2004) Targeting of gelatinase activity with a radiolabeled cyclic HWGF peptide. Nucl Med Biol 31:337–44.
236. Hanaoka H, Mukai T, Habashita S, Asano D, Ogawa K, Kuroda Y, et al. (2007) Chemical design of a radiolabeled gelatinase inhibitor peptide for the imaging of gelatinase activity in tumors. Nucl Med Biol 34:503–10.
237. Zheng QH, Fei X, Liu X, Wang JQ, Stone KL, Martinez TD, et al. (2004) Comparative studies of potential cancer biomarkers carbon-11 labeled MMP inhibitors (S)-2-(4'-[11C] methoxybiphenyl-4-sulfonylamino)-3-methylbutyric acid and N-hydroxy-(R)-2-[[(4'-[11C] methoxyphenyl)sulfonyl]benzylamino]-3-methylbutanamide. Nucl Med Biol 31:77–85.
238. Breyholz HJ, Wagner S, Levkau B, Schober O, Schafers M, Kopka K (2007) A 18F-radiolabeled analogue of CGS 27023A as a potential agent for assessment of matrix-metalloproteinase activity in vivo. Q J Nucl Med Mol Imaging 51:24–32.
239. Beer AJ, Schwaiger M (2008) Imaging of integrin alphavbeta3 expression. Cancer Metastasis Rev 27:631–44.
240. Dijkgraaf I, Beer AJ, Wester HJ (2009) Application of RGD-containing peptides as imaging probes for alphavbeta3 expression. Front Biosci 14:887–99.
241. Haubner R, Decristoforo C (2009) Radiolabelled RGD peptides and peptidomimetics for tumour targeting. Front Biosci 14:872–86.
242. Haubner R (2006) Alphavbeta3-integrin imaging: a new approach to characterise angiogenesis? Eur J Nucl Med Mol Imaging 33 Suppl 1:54–63.
243. Aumailley M, Gurrath M, Muller G, Calvete J, Timpl R, Kessler H (1991) Arg-Gly-Asp constrained within cyclic pentapeptides. Strong and selective inhibitors of cell adhesion to vitronectin and laminin fragment P1. FEBS Lett 291:50–4.
244. Haubner R, Wester HJ, Reuning U, Senekowitsch-Schmidtke R, Diefenbach B, Kessler H, et al. (1999) Radiolabeled alpha(v)beta3 integrin antagonists: a new class of tracers for tumor targeting. J Nucl Med 40:1061–71.
245. Haubner R, Wester HJ, Weber WA, Mang C, Ziegler SI, Goodman SL, et al. (2001) Noninvasive imaging of alpha(v)beta3 integrin expression using 18F-labeled RGD-containing glycopeptide and positron emission tomography. Cancer Res 61:1781–5.
246. Hua J, Dobrucki LW, Sadeghi MM, Zhang J, Bourke BN, Cavaliere P, et al. (2005) Noninvasive imaging of angiogenesis with a 99mTc-labeled peptide targeted at alphavbeta3 integrin after murine hindlimb ischemia. Circulation 111:3255–60.
247. Cai W, Wu Y, Chen K, Cao Q, Tice DA, Chen X (2006) In vitro and in vivo characterization of 64Cu-labeled Abegrin, a humanized monoclonal antibody against integrin alpha v beta 3. Cancer Res 66:9673–81.
248. Wei L, Ye Y, Wadas TJ, Lewis JS, Welch MJ, Achilefu S, et al. (2009) (64)Cu-Labeled CB-TE2A and diamsar-conjugated RGD peptide analogs for targeting angiogenesis: comparison of their biological activity. Nucl Med Biol 36:277–85.

249. Goel A, Baranowska-Kortylewicz J, Hinrichs SH, Wisecarver J, Pavlinkova G, Augustine S, et al. (2001) 99mTc-labeled divalent and tetravalent CC49 single-chain Fv's: novel imaging agents for rapid in vivo localization of human colon carcinoma. J Nucl Med 42:1519–27.
250. Chen X, Tohme M, Park R, Hou Y, Bading JR, Conti PS (2004) Micro-PET imaging of alphav-beta3-integrin expression with 18F-labeled dimeric RGD peptide. Mol Imaging 3:96–104.
251. Sancey L, Ardisson V, Riou LM, Ahmadi M, Marti-Batlle D, Boturyn D, et al. (2007) In vivo imaging of tumour angiogenesis in mice with the alpha(v)beta (3) integrin-targeted tracer 99mTc-RAFT-RGD. Eur J Nucl Med Mol Imaging 34:2037–47.
252. Cormode DP, Skajaa T, Fayad ZA, Mulder WJ (2009) Nanotechnology in Medical Imaging. Probe Design and Applications. Arterioscler Thromb Vasc Biol.
253. Hu G, Lijowski M, Zhang H, Partlow KC, Caruthers SD, Kiefer G, et al. (2007) Imaging of Vx-2 rabbit tumors with alpha(nu)beta3-integrin-targeted 111In nanoparticles. Int J Cancer 120:1951–7.
254. Almutairi A, Rossin R, Shokeen M, Hagooly A, Ananth A, Capoccia B, et al. (2009) Biodegradable dendritic positron-emitting nanoprobes for the noninvasive imaging of angiogenesis. Proc Natl Acad Sci U S A 106:685–90.
255. Syrota A, Paillotin G, Davy JM, Aumont MC (1984) Kinetics of in vivo binding of antagonist to muscarinic cholinergic receptor in the human heart studied by positron emission tomography. Life Sci 35:937–45.
256. Elsinga PH, van Waarde A, Vaalburg W (2004) Receptor imaging in the thorax with PET. Eur J Pharmacol 499:1–13.
257. Reid AE, Ding YS, Eckelman WC, Logan J, Alexoff D, Shea C, et al. (2008) Comparison of the pharmacokinetics of different analogs of 11C-labeled TZTP for imaging muscarinic M2 receptors with PET. Nucl Med Biol 35:287–98.
258. van Oosten EM, Wilson AA, Stephenson KA, Mamo DC, Pollock BG, Mulsant BH, et al. (2009) An improved radiosynthesis of the muscarinic M2 radiopharmaceutical, [18F] FP-TZTP. Appl Radiat Isot 67:611–6.
259. Kiesewetter DO, Vuong BK, Channing MA (2003) The automated radiosynthesis of [18F] FP-TZTP. Nucl Med Biol 30:73–7.
260. Pike VW, Law MP, Osman S, Davenport RJ, Rimoldi O, Giardina D, et al. (2000) Selection, design and evaluation of new radioligands for PET studies of cardiac adrenoceptors. Pharm Acta Helv 74:191–200.
261. Law MP, Osman S, Pike VW, Davenport RJ, Cunningham VJ, Rimoldi O, et al. (2000) Evaluation of [11C]GB67, a novel radioligand for imaging myocardial alpha 1-adrenoceptors with positron emission tomography. Eur J Nucl Med 27:7–17.
262. Park-Holohan SJ, Asselin MC, Turton DR, Williams SL, Hume SP, Camici PG, et al. (2008) Quantification of [11C]GB67 binding to cardiac alpha1-adrenoceptors with positron emission tomography: validation in pigs. Eur J Nucl Med Mol Imaging 35:1624–35.
263. Kopka K, Law MP, Breyholz HJ, Faust A, Holtke C, Riemann B, et al. (2005) Non-invasive molecular imaging of beta-adrenoceptors in vivo: perspectives for PET-radioligands. Curr Med Chem 12:2057–74.
264. Momose M, Reder S, Raffel DM, Watzlowik P, Wester HJ, Nguyen N, et al. (2004) Evaluation of cardiac beta-adrenoreceptors in the isolated perfused rat heart using (S)-11C-CGP12388. J Nucl Med 45:471–7.
265. Wagner S, Kopka K, Law MP, Riemann B, Pike VW, Schober O, et al. (2004) Synthesis and first in vivo evaluation of new selective high affinity beta1-adrenoceptor radioligands for SPECT based on ICI 89,406. Bioorg Med Chem 12:4117–32.
266. Helisch A, Schirrmacher E, Thews O, Schirrmacher R, Buchholz HG, Dillenburg W, et al. (2005) Demonstration of pulmonary beta2-adrenergic receptor binding in vivo with [18F] fluoroethyl-fenoterol in a guinea pig model. Eur J Nucl Med Mol Imaging 32:1324–8.
267. Schirrmacher E, Schirrmacher R, Thews O, Dillenburg W, Helisch A, Wessler I, et al. (2003) Synthesis and preliminary evaluation of (R,R)(S,S) 5-(2-(2-[4-(2-[(18)F]fluoroethoxy) phenyl]-1-methylethylamino)-1-hydroxyethyl)-ben zene-1,3-diol ([(18)F]FEFE) for the in vivo visualisation and quantification of the beta2-adrenergic receptor status in lung. Bioorg Med Chem Lett 13:2687–92.

268. Stephenson KA, van Oosten EM, Wilson AA, Meyer JH, Houle S, Vasdev N (2008) Synthesis and preliminary evaluation of [(18)F]-fluoro-(2S)-Exaprolol for imaging cerebral beta-adrenergic receptors with PET. Neurochem Int 53:173–9.
269. van Waarde A, Doorduin J, de Jong JR, Dierckx RA, Elsinga PH (2008) Synthesis and preliminary evaluation of (S)-[11C]-exaprolol, a novel beta-adrenoceptor ligand for PET. Neurochem Int 52:729–33.
270. Fink SL, Cookson BT (2005) Apoptosis, pyroptosis, and necrosis: mechanistic description of dead and dying eukaryotic cells. Infect Immun 73:1907–16.
271. Levine B, Kroemer G (2008) Autophagy in the pathogenesis of disease. Cell 132:27–42.
272. Blankenberg FG (2008) In vivo imaging of apoptosis. Cancer Biol Ther 7:1525–32.
273. Kenis H, van Genderen H, Bennaghmouch A, Rinia HA, Frederik P, Narula J, et al. (2004) Cell surface-expressed phosphatidylserine and annexin A5 open a novel portal of cell entry. J Biol Chem 279:52623–9.
274. Doue T, Ohtsuki K, Ogawa K, Ueda M, Azuma A, Saji H, et al. (2008) Cardioprotective effects of erythropoietin in rats subjected to ischemia-reperfusion injury: assessment of infarct size with 99mTc-annexin V. J Nucl Med 49:1694–700.
275. Zhao Y, Kuge Y, Zhao S, Strauss HW, Blankenberg FG, Tamaki N (2008) Prolonged high-fat feeding enhances aortic 18F-FDG and 99mTc-annexin A5 uptake in apolipoprotein E-deficient and wild-type C57BL/6J mice. J Nucl Med 49:1707–14.
276. Wong E, Kumar V, Howman-Giles RB, Vanderheyden JL (2008) Imaging of Therapy-Induced Apoptosis Using (99m)Tc-HYNIC-Annexin V in Thymoma Tumor-Bearing Mice. Cancer Biother Radiopharm.
277. Salouti M, Rajabi H, Babaei MH, Rasaee MJ (2008) Breast tumor targeting with (99m) Tc-HYNIC-PR81 complex as a new biologic radiopharmaceutical. Nucl Med Biol 35:763–8.
278. Boersma HH, Liem IH, Kemerink GJ, Thimister PW, Hofstra L, Stolk LM, et al. (2003) Comparison between human pharmacokinetics and imaging properties of two conjugation methods for 99mTc-annexin A5. Br J Radiol 76:553–60.
279. Tait JF, Brown DS, Gibson DF, Blankenberg FG, Strauss HW (2000) Development and characterization of annexin V mutants with endogenous chelation sites for (99m)Tc. Bioconjug Chem 11:918–25.
280. Tait JF, Smith C, Blankenberg FG (2005) Structural requirements for in vivo detection of cell death with 99mTc-annexin V. J Nucl Med 46:807–15.
281. Tait JF, Smith C, Levashova Z, Patel B, Blankenberg FG, Vanderheyden JL (2006) Improved detection of cell death in vivo with annexin V radiolabeled by site-specific methods. J Nucl Med 47:1546–53.
282. Li X, Link JM, Stekhova S, Yagle KJ, Smith C, Krohn KA, et al. (2008) Site-specific labeling of annexin V with F-18 for apoptosis imaging. Bioconjug Chem 19:1684–8.
283. Zhao M, Zhu X, Ji S, Zhou J, Ozker KS, Fang W, et al. (2006) 99mTc-labeled C2A domain of synaptotagmin I as a target-specific molecular probe for noninvasive imaging of acute myocardial infarction. J Nucl Med 47:1367–74.
284. Wang F, Fang W, Zhao M, Wang Z, Ji S, Li Y, et al. (2008) Imaging paclitaxel (chemotherapy)-induced tumor apoptosis with 99mTc C2A, a domain of synaptotagmin I: a preliminary study. Nucl Med Biol 35:359–64.
285. Zhao M, Li Z, Bugenhagen S (2008) 99mTc-labeled duramycin as a novel phosphatidylethanolamine-binding molecular probe. J Nucl Med 49:1345–52.
286. Reshef A, Shirvan A, Waterhouse RN, Grimberg H, Levin G, Cohen A, et al. (2008) Molecular imaging of neurovascular cell death in experimental cerebral stroke by PET. J Nucl Med 49:1520–8.
287. Blasberg R (2002) PET imaging of gene expression. Eur J Cancer 38:2137–46.
288. Tjuvajev JG, Stockhammer G, Desai R, Uehara H, Watanabe K, Gansbacher B, et al. (1995) Imaging the expression of transfected genes in vivo. Cancer Res 55:6126–32.
289. Sundaresan G, Gambhir S (2002) Radionuclide imaging of reporter gene expression. In: Toga A, Mazziotta J, eds. Brain mapping the methods, second ed. San Diego: Academic Press, pp 799–818.

290. Kang JH, Chung JK (2008) Molecular-genetic imaging based on reporter gene expression. J Nucl Med 49 Suppl 2:164S–79S.
291. Chacko AM, Qu W, Kung HF (2008) Synthesis and in vitro evaluation of 5-[(18)f]fluoroalkyl pyrimidine nucleosides for molecular imaging of herpes simplex virus type 1 thymidine kinase reporter gene expression. J Med Chem 51:5690–701.
292. Yaghoubi SS, Couto MA, Chen CC, Polavaram L, Cui G, Sen L, et al. (2006) Preclinical safety evaluation of 18F-FHBG: a PET reporter probe for imaging herpes simplex virus type 1 thymidine kinase (HSV1-tk) or mutant HSV1-sr39tk's expression. J Nucl Med 47:706–15.
293. Ponomarev V, Doubrovin M, Shavrin A, Serganova I, Beresten T, Ageyeva L, et al. (2007) A human-derived reporter gene for noninvasive imaging in humans: mitochondrial thymidine kinase type 2. J Nucl Med 48:819–26.
294. Shiba K, Torashima T, Hirai H, Ogawa K, Akhter N, Nakajima K, et al. (2009) Potential usefulness of D2R reporter gene imaging by IBF as gene therapy monitoring for cerebellar neurodegenerative diseases. J Cereb Blood Flow Metab 29:434–40.
295. Lohith TG, Furukawa T, Mori T, Kobayashi M, Fujibayashi Y (2008) Basic evaluation of FES-hERL PET tracer-reporter gene system for in vivo monitoring of adenoviral-mediated gene therapy. Mol Imaging Biol 10:245–52.
296. Rogers BE, Parry JJ, Andrews R, Cordopatis P, Nock BA, Maina T (2005) MicroPET imaging of gene transfer with a somatostatin receptor-based reporter gene and (94m)Tc-Demotate 1. J Nucl Med 46:1889–97.
297. Terrovitis J, Kwok KF, Lautamaki R, Engles JM, Barth AS, Kizana E, et al. (2008) Ectopic expression of the sodium-iodide symporter enables imaging of transplanted cardiac stem cells in vivo by single-photon emission computed tomography or positron emission tomography. J Am Coll Cardiol 52:1652–60.
298. Alauddin MM, Shahinian A, Park R, Tohme M, Fissekis JD, Conti PS (2007) In vivo evaluation of 2'-deoxy-2'-[(18)F]fluoro-5-iodo-1-beta-D-arabinofuranosyluracil ([18F]FIAU) and 2'-deoxy-2'-[18F]fluoro-5-ethyl-1-beta-D-arabinofuranosyluracil ([18F]FEAU) as markers for suicide gene expression. Eur J Nucl Med Mol Imaging 34:822–9.
299. Cai H, Yin D, Zhang L, Yang X, Xu X, Liu W, et al. (2007) Preparation and biological evaluation of 2-amino-6-[18F]fluoro-9-(4-hydroxy-3-hydroxy-methylbutyl) purine (6-[18F] FPCV) as a novel PET probe for imaging HSV1-tk reporter gene expression. Nucl Med Biol 34:717–25.
300. Johnson M, Karanikolas BD, Priceman SJ, Powell R, Black ME, Wu HM, et al. (2009) Titration of Variant HSV1-tk Gene Expression to Determine the Sensitivity of 18F-FHBG PET Imaging in a Prostate Tumor. J Nucl Med 50:757–764.
301. Min JJ, Gambhir SS (2008) Molecular imaging of PET reporter gene expression. Handb Exp Pharmacol:277–303.
302. Ziegler-Graham K, Brookmeyer R, Johnson E, Arrighi HM (2008) Worldwide variation in the doubling time of Alzheimer's disease incidence rates. Alzheimers Dement 4:316–23.
303. Herholz K, Carter SF, Jones M (2007) Positron emission tomography imaging in dementia. Br J Radiol 80 Spec No 2:S160–7.
304. Coleman RE (2005) Positron emission tomography diagnosis of Alzheimer's disease. Neuroimaging Clin N Am 15:837–46, x.
305. Friedland RP, Kalaria R, Berridge M, Miraldi F, Hedera P, Reno J, et al. (1997) Neuroimaging of vessel amyloid in Alzheimer's disease. Ann N Y Acad Sci 826:242–7.
306. Henriksen G, Yousefi BH, Drzezga A, Wester HJ (2008) Development and evaluation of compounds for imaging of beta-amyloid plaque by means of positron emission tomography. Eur J Nucl Med Mol Imaging 35 Suppl 1:S75–81.
307. Nordberg A (2008) Amyloid imaging in Alzheimer's disease. Neuropsychologia 46:1636–41.
308. Cai L, Innis RB, Pike VW (2007) Radioligand development for PET imaging of beta-amyloid (Abeta)--current status. Curr Med Chem 14:19–52.
309. Serdons K, Verduyckt T, Vanderghinste D, Borghgraef P, Cleynhens J, Van Leuven F, et al. (2009) 11C-labelled PIB analogues as potential tracer agents for in vivo imaging of amyloid beta in Alzheimer's disease. Eur J Med Chem 44:1415–26.

310. Serdons K, Verduyckt T, Vanderghinste D, Cleynhens J, Borghgraef P, Vermaelen P, et al. (2009) Synthesis of 18F-labelled 2-(4'-fluorophenyl)-1,3-benzothiazole and evaluation as amyloid imaging agent in comparison with [11C]PIB. Bioorg Med Chem Lett 19:602–5.
311. Serdons K, Terwinghe C, Vermaelen P, Van Laere K, Kung H, Mortelmans L, et al. (2009) Synthesis and Evaluation of (18)F-Labeled 2-Phenylbenzothiazoles as Positron Emission Tomography Imaging Agents for Amyloid Plaques in Alzheimer's Disease. J Med Chem.
312. Verdurand M, Bort G, Tadino V, Bonnefoi F, Le Bars D, Zimmer L (2008) Automated radiosynthesis of the Pittsburg compound-B using a commercial synthesizer. Nucl Med Commun 29:920–6.
313. Zhang W, Oya S, Kung MP, Hou C, Maier DL, Kung HF (2005) F-18 stilbenes as PET imaging agents for detecting beta-amyloid plaques in the brain. J Med Chem 48:5980–8.
314. Stephenson KA, Chandra R, Zhuang ZP, Hou C, Oya S, Kung MP, et al. (2007) Fluoropegylated (FPEG) imaging agents targeting Abeta aggregates. Bioconjug Chem 18:238–46.
315. Zhang W, Oya S, Kung MP, Hou C, Maier DL, Kung HF (2005) F-18 Polyethyleneglycol stilbenes as PET imaging agents targeting Abeta aggregates in the brain. Nucl Med Biol 32:799–809.
316. Qu W, Choi SR, Hou C, Zhuang Z, Oya S, Zhang W, et al. (2008) Synthesis and evaluation of indolinyl- and indolylphenylacetylenes as PET imaging agents for beta-amyloid plaques. Bioorg Med Chem Lett 18:4823–7.
317. Wey SP, Weng CC, Lin KJ, Yao CH, Yen TC, Kung HF, et al. (2009) Validation of an 18F-labeled biphenylalkyne as a positron emission tomography imaging agent for beta-amyloid plaques. Nucl Med Biol 36:411–7.
318. Cai L, Cuevas J, Temme S, Herman MM, Dagostin C, Widdowson DA, et al. (2007) Synthesis and structure-affinity relationships of new 4-(6-iodo-H-imidazo[1,2-a]pyridin-2-yl)-N-dimethylbenzeneamine derivatives as ligands for human beta-amyloid plaques. J Med Chem 50:4746–58.
319. Cai L, Liow JS, Zoghbi SS, Cuevas J, Baetas C, Hong J, et al. (2008) Synthesis and evaluation of N-methyl and S-methyl 11C-labeled 6-methylthio-2-(4'-N,N-dimethylamino) phenylimidazo[1,2-a]pyridines as radioligands for imaging beta-amyloid plaques in Alzheimer's disease. J Med Chem 51:148–58.
320. Chianelli M, Boerman OC, Malviya G, Galli F, Oyen WJ, Signore A (2008) Receptor binding ligands to image infection. Curr Pharm Des 14:3316–25.
321. Rennen H, Bleeker-Rovers C, Oyen WJ (2006) Imaging infection and inflammation. In: Schiepers C, ed. Diagnostic nuclear medicine, second edition ed. Berlin: Springer, pp 113–126.
322. Rennen HJ, Boerman OC, Oyen WJ, Corstens FH (2003) Kinetics of 99mTc-labeled interleukin-8 in experimental inflammation and infection. J Nucl Med 44:1502–9.
323. Rennen HJ, Bleeker-Rovers CP, van Eerd JE, Frielink C, Oyen WJ, Corstens FH, et al. (2004) 99mTc-labeled interleukin-8 for scintigraphic detection of pulmonary infections. Chest 126:1954–61.
324. Krause S, Rennen HJ, Boerman OC, Baumann S, Cyr JE, Manchanda R, et al. (2007) Preclinical evaluation of technetium 99m-labeled P1827DS for infection imaging and comparison with technetium 99m IL-8. Nucl Med Biol 34:925–32.
325. van Eerd JE, Oyen WJ, Harris TD, Rennen HJ, Edwards DS, Corstens FH, et al. (2005) Scintigraphic imaging of infectious foci with an 111In-LTB4 antagonist is based on in vivo labeling of granulocytes. J Nucl Med 46:786–93.
326. van Eerd JE, Broekema M, Harris TD, Edwards DS, Oyen WJ, Corstens FH, et al. (2005) Imaging of infection and inflammation with an improved 99mTc-labeled LTB4 antagonist. J Nucl Med 46:1546–51.
327. Rennen HJ, Laverman P, van Eerd JE, Oyen WJ, Corstens FH, Boerman OC (2007) PET imaging of infection with a HYNIC-conjugated LTB4 antagonist labeled with F-18 via hydrazone formation. Nucl Med Biol 34:691–5.
328. Britton KE, Wareham DW, Das SS, Solanki KK, Amaral H, Bhatnagar A, et al. (2002) Imaging bacterial infection with (99m)Tc-ciprofloxacin (Infecton). J Clin Pathol 55:817–23.

329. Zhang J, Guo H, Zhang S, Lin Y, Wang X (2008) Synthesis and biodistribution of a novel (99m)TcN complex of ciprofloxacin dithiocarbamate as a potential agent for infection imaging. Bioorg Med Chem Lett 18:5168–70.
330. Diniz SO, Rezende CM, Serakides R, Ferreira RL, Ribeiro TG, Martin-Comin J, et al. (2008) Scintigraphic imaging using technetium-99m-labeled ceftizoxime in an experimental model of acute osteomyelitis in rats. Nucl Med Commun 29:830–6.
331. Gomes Barreto V, Rabiller G, Iglesias F, Soroa V, Tubau F, Roca M, et al. (2005) [99mTc-ceftizoxime scintigraphy in normal rats and abscess induced rats]. Rev Esp Med Nucl 24:312–8.
332. Thompson M, Wall DM, Hicks RJ, Prince HM (2005) In vivo tracking for cell therapies. Q J Nucl Med Mol Imaging 49:339–48.
333. Van Hemert FJ, Voermans C, Van Eck-Smit BL, Bennink RJ (2009) Labeling monocytes for imaging chronic inflammation. Q J Nucl Med Mol Imaging 53:78–88.
334. McAfee JG, Subramanian G, Gagne G (1984) Technique of leukocyte harvesting and labeling: problems and perspectives. Semin Nucl Med 14:83–106.
335. Palestro CJ, Love C, Bhargava KK (2009) Labeled leukocyte imaging: current status and future directions. Q J Nucl Med Mol Imaging 53:105–23.
336. Zhou R, Acton PD, Ferrari VA (2006) Imaging stem cells implanted in infarcted myocardium. J Am Coll Cardiol 48:2094–106.
337. Lee Z, Dennis JE, Gerson SL (2008) Imaging stem cell implant for cellular-based therapies. Exp Biol Med (Maywood) 233:930–40.
338. Zhang Y, Ruel M, Beanlands RS, deKemp RA, Suuronen EJ, DaSilva JN (2008) Tracking stem cell therapy in the myocardium: applications of positron emission tomography. Curr Pharm Des 14:3835–53.
339. Sheikh AY, Wu JC (2006) Molecular imaging of cardiac stem cell transplantation. Curr Cardiol Rep 8:147–54.
340. Ma B, Hankenson KD, Dennis JE, Caplan AI, Goldstein SA, Kilbourn MR (2005) A simple method for stem cell labeling with fluorine 18. Nucl Med Biol 32:701–5.
341. Olasz EB, Lang L, Seidel J, Green MV, Eckelman WC, Katz SI (2002) Fluorine-18 labeled mouse bone marrow-derived dendritic cells can be detected in vivo by high resolution projection imaging. J Immunol Methods 260:137–48.
342. Adonai N, Nguyen KN, Walsh J, Iyer M, Toyokuni T, Phelps ME, et al. (2002) Ex vivo cell labeling with 64Cu-pyruvaldehyde-bis(N4-methylthiosemicarbazone) for imaging cell trafficking in mice with positron-emission tomography. Proc Natl Acad Sci U S A 99:3030–5.
343. Li ZB, Chen K, Wu Z, Wang H, Niu G, Chen X (2009) (64)Cu-Labeled PEGylated Polyethylenimine for Cell Trafficking and Tumor Imaging. Mol Imaging Biol.

Chapter 10
Image Registration for Multimodality Small-Animal Imaging

Pat Zanzonico

1 Introduction

Since the discovery of X-rays, imaging has been a vital component of clinical medicine. Increasingly, in vivo imaging of small laboratory animals, i.e. mice and rats, has emerged as an important component of basic biomedical research as well. Historically, clinical and laboratory imaging modalities have often been divided into two general categories, structural (or anatomical) and functional (or physiological). Anatomical modalities, i.e. depicting primarily morphology, include X-rays (plain radiography), CT (computed tomography), MRI (magnetic resonance imaging), and US (ultrasound). Functional modalities, i.e. depicting primarily information related to underlying genetics and metabolism, include (planar) scintigraphy, SPECT (single-photon emission computed tomography), PET (positron emission tomography), MRS/MRSI (magnetic resonance spectroscopy and spectroscopic imaging), fMRI (functional magnetic resonance imaging), and, in small animals, optical (i.e. bioluminescence and fluorescence) imaging modalities. The functional modalities form the basis of the rapidly advancing field of "molecular imaging," defined as the direct or indirect non-invasive monitoring and recording of the spatial and temporal distribution of in vivo molecular, genetic, and/or cellular processes for biochemical, biological, diagnostic, or therapeutic applications [1].

Since information derived from multiple modalities is often complementary, e.g. localizing the site of an apparently abnormal metabolic process to a pathologic structure such as a tumor, integration of this information may be helpful and at times critical. In addition to anatomic localization of "signal" foci, image registration and fusion provide intra- as well as inter-modality corroboration of diverse images and more accurate and reliable diagnostic and treatment-monitoring information.

P. Zanzonico (✉)
Department of Medical Physics, Memorial Sloan Kettering Cancer Center, New York, NY, USA
e-mail: zanzonip@mskcc.org

H. Zaidi (ed.), *Molecular Imaging of Small Animals: Instrumentation and Applications*,
DOI 10.1007/978-1-4939-0894-3_10,

The problem, however, is that differences in image size and dynamic range, voxel dimensions and depth, image orientation, subject position and posture, and information quality and quantity make it difficult to unambiguously co-locate areas of interest in multiple image sets. The objective of image *registration* and *fusion*, therefore, is (a) to appropriately modify the format, size, position, and even shape of one or both image sets to provide a point-to-point correspondence between images and (b) to provide a practical integrated display of the images thus aligned. This process entails spatial registration of the respective images in a common coordinate system based on optimization of some "goodness-of-alignment," or "similarity," criterion (or metric). This chapter is a brief, largely non-mathematical review of the basics of image registration and fusion and of software approaches to three-dimensional (3D) image alignment and presents illustrative examples of registered and fused multi-modality images in laboratory settings. Hardware approaches (i.e. multi-modality instruments such as PET–CT scanners) [2] are discussed elsewhere in this volume.

2 General Principles of Image Registration and Fusion

The general image registration and fusion process [3–7] is illustrated diagrammatically in Fig. 10.1. The first step is re-formatting of one image set (the "floating," or secondary, image) to match that of the other image set (the reference, or primary, image). Alternatively, both image sets may be transformed to a new, common image format. Three-dimensional (3D), or tomographic, image sets are characterized by: the dimensions (e.g. in mm), i.e. the length (ΔX), width (ΔY), and thickness (ΔZ), of each voxel; the image matrix, XxYxZ = number of rows, X x number of columns, Y x number of tomographic images (or "slices"), Z; and the image depth (e.g. in bytes), which defines the dynamic range of signal display-able in each voxel (e.g. a word-mode, i.e. one word- or two byte-"deep," image can display up to $2^{16} = 65{,}536$ signal levels for 16-bit words). The foregoing image parameters are provided in the image "header," a block of alphanumeric data which may either be in a stand-alone text file associated with the image file or incorporated into the image file itself. Among the image sets to be registered, either the finer matrix is re-formatted to the coarser matrix by combining of voxels or the coarser matrix is re-formatted to the finer matrix by interpolation of voxels. One of the resulting 3D image sets is then magnified or minified to yield primary and secondary images with equal voxel dimensions. Finally, the "deeper" image is re-scaled to match the depth of the "shallower" matrix. Usually, the higher-spatial resolution and finer-matrix structural (e.g. CT) image is the primary image and the functional (e.g. PET) image the secondary image.

The second step in image registration is the actual transformation [translation, rotation, and/or deformation (warping)] of the re-formatted secondary image set to spatially align it, in three dimensions, with the primary image set.

The third and fourth steps are, respectively, evaluation of the accuracy of the registration of the primary and transformed secondary images and adjustment, iteratively, of the secondary-image transformation until the registration (i.e. the goodness-of-alignment metric) is optimized.

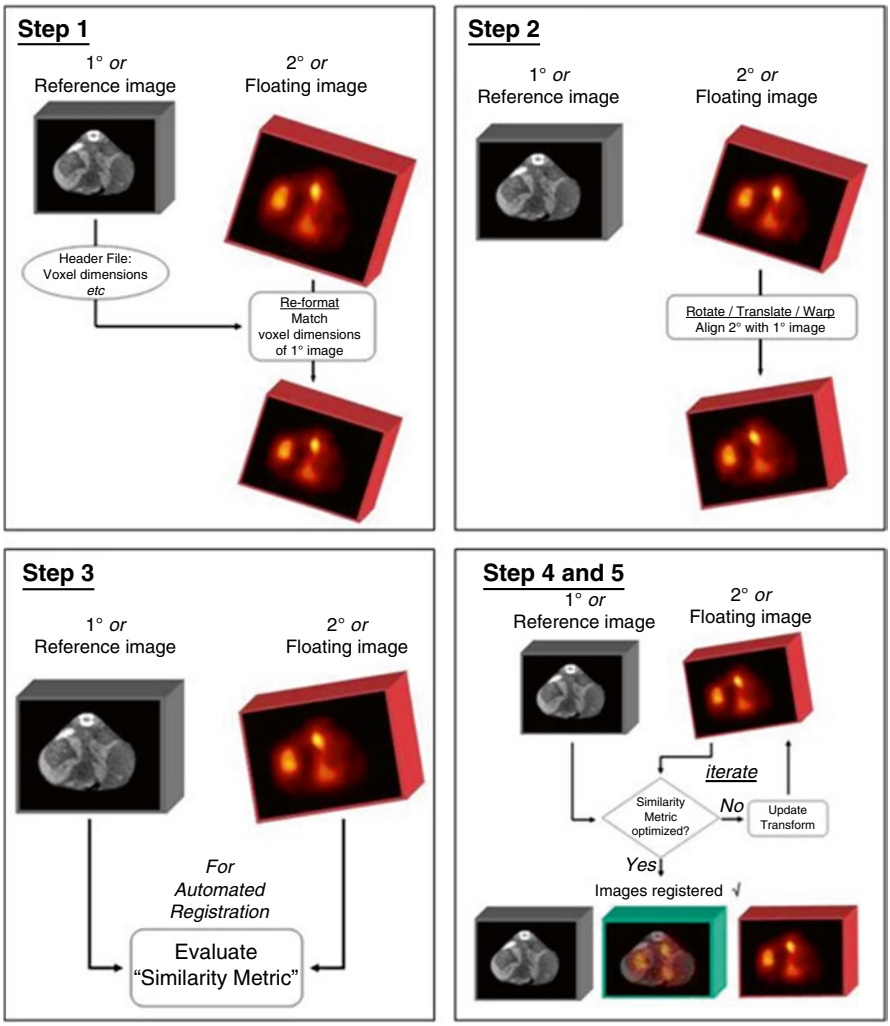

Fig. 10.1 The image registration and fusion process. See text for details. Adapted from [2] by permission of the authors

The fifth and final step is image fusion, the integrated display of the registered images.

3 Software Methods for Image Registration

As noted, there are two practical approaches to image registration and fusion, software and hardware approaches. In the software approach, images are acquired on separate devices, imported into a common image-processing computer platform,

and registered and fused using the appropriate software. In the hardware approach, images are acquired on a single, multi-modality device and transparently registered and fused with the manufacturer's integrated software. Both approaches are dependent on software sufficiently robust to recognize and import diverse image formats. The availability of industry-wide standard formats, such as the ACR-NEMA DICOM standard (i.e. the American College of Radiology (ACR) and National Electrical Manufacturers Association (NEMA) for Digital Imaging and Communications in Medicine (DICOM) standard [8–11], is therefore critical.

3.1 Rigid Versus Non-rigid (Warping) Transformations

Software-based transformations of the secondary image set to spatially align it with the primary image set are commonly characterized as either "rigid" or "non-rigid" [3–7]. In a rigid transformation, the secondary image is only translated and/or rotated with respect to the primary image. The Euclidean distance between any two points (i.e. voxels) within an individual image set remains constant, however. In non-rigid, or deformable, transformations (commonly known as "warping"), selected sub-volumes within the image set may be expanded or contracted and/or their shapes altered. Translations and/or rotations may be performed as well. Such warping is therefore distinct from any magnification or minification performed in the re-formatting step, where distances between points *all* change by the same *relative* amount. Unlike rigid transformations, which may be either manual or automated, non-rigid transformations are generally automated.

3.2 Feature- and Intensity-Based Approaches

Registration transformations are often based on alignment of specific landmarks visible in the image sets; this is sometimes characterized as the "feature-based" approach [3–7]. Such landmarks may be either intrinsic, i.e. one or more well-defined anatomic structure(s) or the body contour (i.e. surface outline), or extrinsic, i.e. one or more fiducial markers placed in or around the subject. Feature-based registration generally requires some sort of pre-processing "segmentation" of the image sets being aligned, that is, identification of the corresponding features (e.g. fiduciary markers) of the image sets. Feature-based image registration algorithms may be automated by minimization of the difference(s) in position of the pertinent feature(s) between the image sets being aligned.

Other registration algorithms are based on analysis of voxel intensities (e.g. counts in a PET or SPECT image) and are characterized as "intensity-based" approaches [3–7]. These include: alignment of the respective "centers of 'mass'" (e.g. counts) and orientation (i.e. principal axes) calculated for each image set; minimization of absolute or sum-of-square voxel intensity differences between the

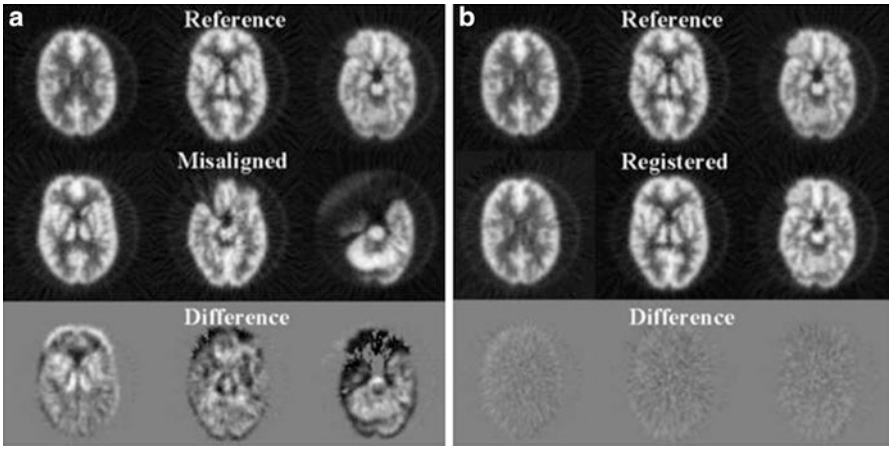

Fig. 10.2 Intra-modality image registration based on minimization of voxel intensity differences. (**a**) Selected brain images of sequential misaligned (i.e. non-registered) PET studies of the same patient, with the section-by-section difference images in the *bottom row*. (**b**) The same image sets as in (**a**), now aligned by minimization of the voxel-by-voxel intensity differences. From [4] by permission of the authors

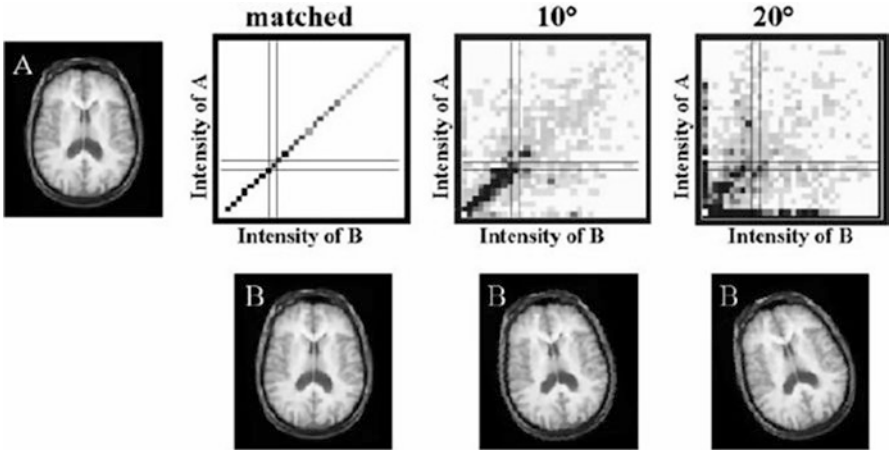

Fig. 10.3 Intra-modality image registration based on matching of voxel intensity histograms. The joint intensity histograms of a transverse-section brain MRI image with itself when the two image sets are originally matched (i.e. aligned) and when misaligned by counterclockwise rotations of 10° and 20°, respectively. See text for details. Adapted from [4] by permission of the authors

image sets; cross-correlation (i.e. maximizing the voxel intensity correlation between the image sets); minimization of variance (i.e. matching of identifiable homogeneous regions in the respective images sets); and matching of voxel intensity histograms [3, 4] (Figs. 10.2, 10.3, and 10.4).

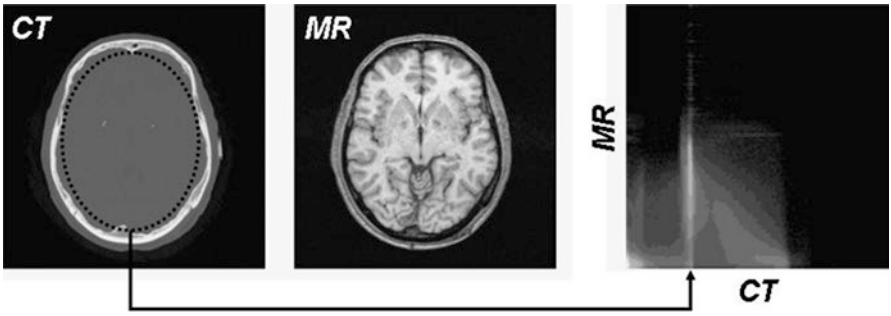

Fig. 10.4 An inter-modality (CT and MRI) joint intensity histogram. The featureless (i.e. uniform) area corresponding to brain tissue in the transverse-section head CT image (*left panel*), in contrast to the anatomic detail in the corresponding area of the MRI image (*middle panel*), yields a distinct vertical cluster (*arrow*) in the CT-MRI joint histogram (*right panel*). Adapted from [5] by permission of the authors

As illustrated in Fig. 10.2 showing sequential PET brain images of the same patient [4], misalignment of the image sets produces visualizable structure in the difference images (the bottom row of Fig. 10.2a), i.e., the voxel-by-voxel intensity differences are not zero. In contrast, accurate registration yields differences images whose voxel-by-voxel intensity differences are equal to zero within statistical uncertainty (i.e. "noise") and therefore an absence of visualizable structure (bottom row of Fig. 10.2b).

For two image sets *A* and *B*, a two-dimensional joint histogram (also known as the "feature space") (Fig. 10.3) [4] can be constructed by plotting, for each combination of intensity *a* in image A and intensity *b* in image *B*, the point (*a, b*) whose darkness or lightness reflects the number of occurrences of the combination of intensities *a* and *b*. Thus, a darker point in the joint histogram indicates a larger number and a lighter point a smaller number of occurrences of the combination (*a*, *b*). When two identical image sets are aligned (matched), all voxels coincide and the plot in the voxel intensity histogram is the line of identity (i.e. $a = b$ for all voxels). As one of the image sets is rotated relative to the other (by 10° and then by 20°), for example, the joint histogram becomes increasingly blurred (i.e. dispersed) (Fig. 10.3). Alignment of the images can therefore be achieved by minimizing the dispersion in the joint intensity histogram. Like other intensity-based approaches, this approach is most readily adaptable to similar (i.e. intra-modality) images sets but in principle can be applied to dissimilar (i.e. inter-modality) images by appropriate mapping of one image intensity scale to the other intensity scale (Fig. 10.4) [5].

Such intensity-based approaches implicitly assume that the voxel intensities in the images being aligned represent the same, positively correlated parameters (e.g. counts) and thus are directly applicable only to intra-modality image registration.

3.3 Mutual Information

A relatively new but already widely used automated registration algorithm is based on the statistical concept of mutual information [5, 12], also known as trans-information or relative entropy. The mutual information of two random variables *A* and *B* is a quantity that measures the statistical dependence of the two variables, that is, the amount of information that one variable contains about the other. Mutual information measures the information about *A* that is shared by *B*. If *A* and *B* are independent, then *A* contains no information about *B* and vice versa and their mutual information is therefore zero. Conversely, if *A* and *B* are identical, then all information conveyed by *A* is shared with *B* and their mutual information is maximized. Accurate spatial registration of two such image sets thus results in maximization of their mutual information and vice versa.

The concepts of entropy and mutual information are developed more formally in the following. Given "events" (e.g. gray-scale values) e_1, e_2,…, e_n with probabilities (i.e. frequencies of occurrence) p_1, p_2,…, p_n in an image set, the entropy (specifically, the so-called "Shannon entropy") H is defined as follows [5]:

$$\mathrm{H} \equiv \sum_{1}^{n} \mathrm{p_i}\, log \frac{1}{p_i} \tag{10.1a}$$

$$= -\sum_{1}^{n} \mathrm{p_i}\, log\, p_i \tag{10.1b}$$

The term, $log \frac{1}{p_i}$, indicates that the amount of information provided by an event is inversely related to the probability (i.e. frequency) of that event: the less frequent an event, the more significant is its occurrence. The information per event is thus weighted by the frequency of its occurrence. The uniform "background" (e_{BG}) occupies a large portion of a CT image (i.e. p_{BG} is large), for example, and therefore contributes relatively little information (i.e. $log \frac{1}{p_{BG}}$ is small)—and would not contribute substantially to accurate alignment with an MRI image. The Shannon entropy is also a measure of the uncertainty of an event. When all events (e.g. all gray-scale values in an image) are equally likely to occur (as in an highly heterogeneous image), the entropy is maximal.[1] When an event or a range of events are more likely to occur (as in a uniform image), the entropy is minimal. Additionally, the entropy is a measure of dispersion of an image's probability distribution (i.e. the probability of a grey-scale value versus the grey-scale value): a highly heterogeneous image has a broad dispersion and a high entropy while a uniform image has

[1] The analogy between signal entropy, used in the context of mutual information, and thermodynamic entropy thus becomes clear.

no dispersion and minimal entropy. Entropy thus has several interpretations: the information content per event (e.g. grey-scale value), the uncertainty per event, and the statistical dispersion of events in an image.

For two images *A* and *B*, the mutual information MI(*A*, *B*) may be defined as follows [5][2]:

$$\mathrm{MI}(A,B) \equiv \mathrm{H}(B) - \mathrm{H}(B|A) \tag{10.2}$$

H(*B*) is the Shannon entropy of image B (derived from the probability distribution of its grey-scale value) and H(*B*|*A*) is the conditional entropy of image *B* with respect to image *A* (derived from the conditional probabilities p(*b*|*a*), the probability of grey-scale value *b* occurring in image *B* given that grey-scale value *a* occurs in the corresponding voxel in image *A*). When interpreting entropy in terms of uncertainty, MI(*A*,*B*) thus corresponds to the uncertainty in image *B* minus the uncertainty in image *B* when image *A* is known. Intuitively, therefore, MI(*A*,*B*)—the image-*B* information in image *A*—is the amount by which the uncertainty in image *B* decreases when image *A* is given. Because images *A* and *B* can be interchanged, MI(*A*,*B*) is also the information image *B* contains about image *A* and it is therefore *mutual* information. Registration thus corresponds to maximizing mutual information: the amount of information images have about each other is maximized when, and only when, they are aligned. If a subject is imaged by two different modalities, there is presumably considerable mutual information between the spatial distribution of the respective signals in the two images sets no matter how diverse (i.e. unrelated) they may appear to be. For example, the distribution of fluorine-18-labeled fluoro-deoxyglucose (FDG) visualized in a PET scan is, *at some level*, dictated by (i.e. dependent on) the distribution of different tissue types imaged by CT.

3.4 Goodness-of-Alignment Metrics

Regardless of the algorithm employed, the evaluation and adjustment of the registration requires some metric of its accuracy. It may be as simple as visual (i.e. qualitative) inspection of the aligned images and a judgment by the operator that the registration is or is not "acceptable." A more objective and, ideally, quantitative evaluation of the accuracy of the registration is, of course, preferred. One goodness-of-alignment metric, for example, is the sum of the Euclidean distances between corresponding fiduciary markers (or anatomic landmarks) in the two image sets; the optimum alignment corresponds to the transformation yielding the minimum sum of distances. Another similarity metric, as discussed above, is the mutual information: when the mutual information between the two image sets is maximized, they

[2] In information theory, there are actually a number of different definitions of mutual information.

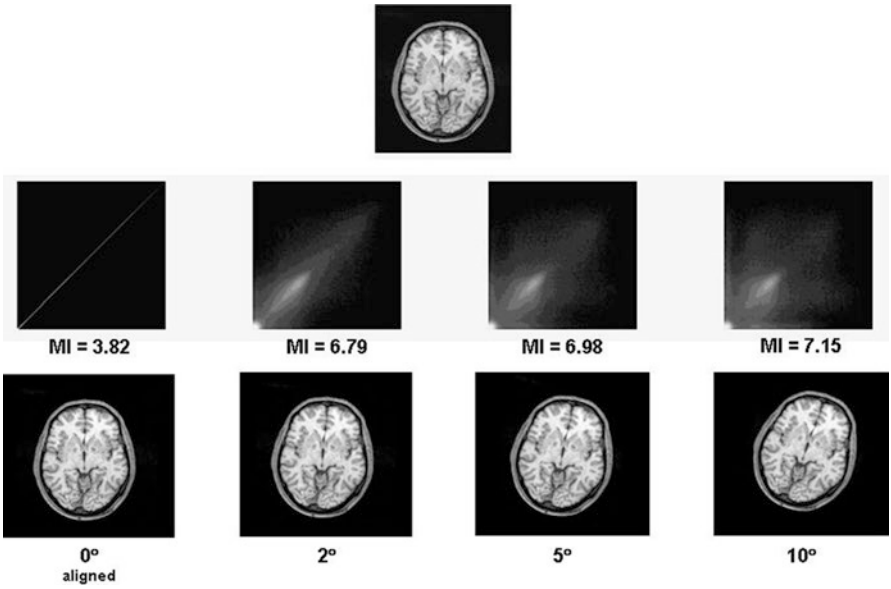

Fig. 10.5 Effect of misregistration on joint intensity histograms and mutual information (MI) between a transverse-section brain MRI image (*top row*) and itself. Shown are the joint intensity histograms and mutual information (MI) (*middle row*) when the two image sets are originally matched (i.e. aligned) and when misaligned by clockwise rotations of 2°, 5°, and 10°, respectively (*bottom row*). See text for details. Adapted from [5] by permission of the authors

are optimally aligned. As illustrated in Fig. 10.5 [5] for registration of a brain MRI image with itself, the joint histogram of two images changes as the alignment of the images changes. When the images are registered, corresponding signal foci overlap and the joint histogram will show certain clusters of grey-scale values. As images become increasingly misaligned (illustrated in Fig. 10.5 with rotations of 2°, 5°, and then 10° of the brain MRI relative to the original image), signal foci will increasingly overlap that are not their respective counterparts on the original image. Consequently, the cluster intensities for corresponding signal foci (e.g. skull and skull, brain and brain etc) will decrease and new non-corresponding combinations of grey-scale values (e.g. of skull and brain) will appear. The joint histogram will thus become more dispersed; as described above, minimization of this dispersion is the basis of certain intensity-based registration algorithms. At the same time, the mutual information (MI) (See Eqs. (10.1a and 10.1b) and (10.2)), which is minimized when the two images are aligned, will increase. However, unlike other intensity-based approaches, *no* assumptions are made in the MI approach regarding the nature of the relationship between image intensities (e.g. a positive or a negative correlation). MI is thus a completely general goodness-of-alignment metric and can be applied to inter- as well as intra-modality registration and automatically without prior segmentation.

4 Impact of Non-simultaneity of Multi-Modality Image Acquisition

An important consideration in multi-modality image registration is that, in almost all cases, images are acquired sequentially, not simultaneously [13]; the one notable exception is related to hardware-registered PET or SPECT and MRI images [14] (discussed elsewhere in this volume). Implicit in the registration of such sequentially acquired images is the assumption that the subject is morphologically and functionally stable over the time interval between and during the image acquisitions. Otherwise, one may be attempting to register images of what are effectively different subjects. Intuitively, registration of functional and structural images (e.g. PET and CT images) or of different structural images (e.g. CT and MRI images) is rather forgiving of the time interval between sequential image acquisitions, as anatomy generally changes quite slowly (typically over days to weeks). Importantly, however, this may not be the case in tumor xenograft models in rodents. Such xenografts may grow significantly over a matter of hours, with size-dependent alteration of its functional as well as structural properties; for example, as tumor mass increases, the intra-tumoral number and distribution of hypoxic cells may also vary. For multi-modality imaging devices, where one image is acquired immediately following the other, the time interval between acquisitions is typically of the order of only several minutes, with, of course, no significant structural alterations expected. Registration of sequentially acquired functional images is potentially more problematic in this respect, as functional properties such as blood flow, hypoxia etc may change transiently over time frames of minutes and even seconds. One must be cognizant of this possibility in designing and interpreting multi-modality functional imaging studies and must take care to maintain the physiological parameters (e.g. body temperature, hydration, blood oxygenation, and depth of anesthesia) as constant as possible over the duration of and time between imaging studies.

5 Special Considerations of Small-Animal Image Registration

Mice and rats and their internal structures (i.e. organs and tumors) are, of course, much smaller than human subjects and their internal structures. Intuitively, therefore, a greater degree of accuracy is required for useful registration of small-animal images than of patient images. While difficult to generalize, with organ and tumor dimensions of the order of 10 mm a registration accuracy of approximately $\pm$1 mm appears reasonable for mouse and rat images for many applications. In contrast, with human organ and tumor dimensions typically of the order of 10 cm or greater a registration accuracy of approximately $\pm$1 cm is probably sufficient. Of course, the registration accuracy required is ultimately dependent on the particular application and the spatial scale of significant heterogeneities in the images under consideration.

Another consideration specific to small-animal image registration is the obvious inability of animals to maintain a fixed body posture (i.e. to lie still on command) over a period of time required to perform multiple imaging studies. As result, animals must be anesthetized for imaging (whether or not image registration is performed).

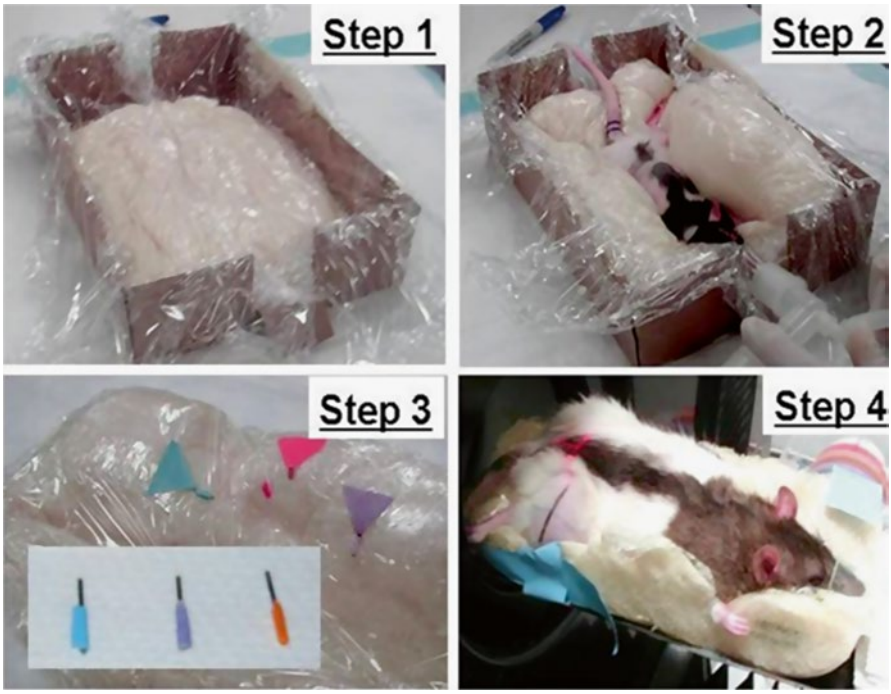

Fig. 10.6 Step-by-step fabrication and use of an animal-specific mold for immobilization and reproducible positioning of a tumor-bearing rat for repeat imaging studies. Rapid-Foam™ (Soule Medical, Lutz, FL), a commercial quick-setting mold kit, was used to fabricate the molds. Three custom-manufactured ^{68}Ge fiduciary markers (10 μCi each, 1 × 10 mm) (Sanders Medical Products, Knoxville, TN) were used to subsequently register sequential microPET™ images. Adapted from [15] by permission of the authors

In our experience, inhaled isoflurane is preferable to injectable anesthetics such as ketamine/xylazine—it is easier to safely maintain anesthesia over a prolonged period of time and animals generally recover (i.e. regain consciousness) quickly. Any long-term anesthesia (i.e. in excess of ~10 min) disrupts thermoregulation, among other effects, and generally requires warming of the animal with a heating lamp, heating pad etc. To properly maintain heating of the animal, such a device may be connected to a rectal temperature probe and control unit which automatically cycles the device on and off and thus maintains body temperature within a physiologic range. In addition, the animal may need to be immobilized in a whole-body mold to ensure constancy of body posture, depending on the accuracy of image registration required. This is particularly important in studies in which serial images are acquired over a protracted period of time (e.g. over several days or longer) and the animal is therefore allowed to awaken between imaging studies and then must be reproducibly positioned. An inexpensive (~$5 per animal), rapid (less than 30 min per animal), and well-tolerated method for immobilization and reproducible positioning of small laboratory animals is based on commercial quick-setting mold kits used for fabrication of patient-specific molds for radiation therapy (Fig. 10.6) [15]. The kit reagents are mixed, poured into a plastic-lined container, covered with plastic and allowed to

cure (harden) for ~5 min (Step 1). The anesthetized mouse or rat, with its legs extended as for imaging, is gently pressed supine into the still-soft mixture and left in place for 15 min (Step 2). The mouse or rat is then removed and the hardened mold trimmed to fit into the imaging gantry. For PET imaging, for example, the mold is placed on the animal palette and fiduciary markers (e.g. three steel-encased germanium-68 (^{68}Ge) rods (370 kBq = 10 μCi each, 1 × 10 mm) are placed on or inserted into the hardened mold at specific positions (Step 3). Of course, by using "MRI-visible" (e.g. non-metallic gadolinium-filled) markers, this method is adaptable to MRI. The fiduciary markers allow for either manual or automated registration of the image sets among the serial intra-modality or consecutive inter-modality image sets. The animal is then placed in its custom mold and imaged (Step 4).

6 Illustrative Examples of Small-Animal Image Registrations

Our laboratory has focused on the development and validation of various approaches to imaging of tumor hypoxia, and two examples of small-animal image registration derived from this ongoing effort are presented. In the first example (Fig. 10.7) [15], the intra-tumoral distributions of sequentially administered fluoro-deoxyglucose

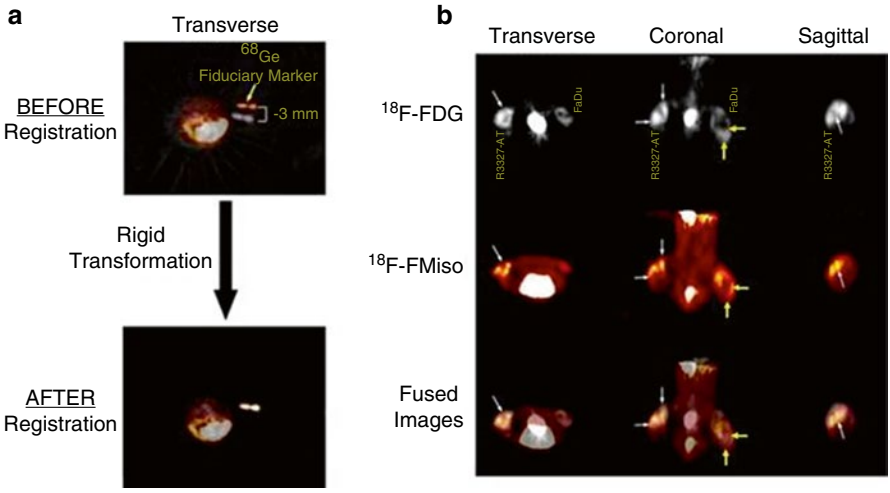

Fig. 10.7 (**a**) The appearance, in a selected transverse section, of the ^{68}Ge markers on overlaid F18-FDG and -FMiso transverse R4 microPET™ images before and after registration based on a rigid transform consisting of translations Δx, Δy, and Δz and rotations $\Delta\theta_x$, $\Delta\theta_y$, and $\Delta\theta_z$. (**b**) Registered and fused ^{18}F-FDG (*gray scale*) and -FMiso (hot iron) transverse, coronal, and sagittal images; the sagittal views are through a R3327-AT tumor xenograft in the animal's right hindlimb. Discordant areas of FDG and FMiso uptakes are indicated by the *white arrows* for the R3327-AT tumor and by the *yellow arrows* for a FaDu tumor xenograft in the animal's left hindlimb. Adapted from [15] by permission of the authors

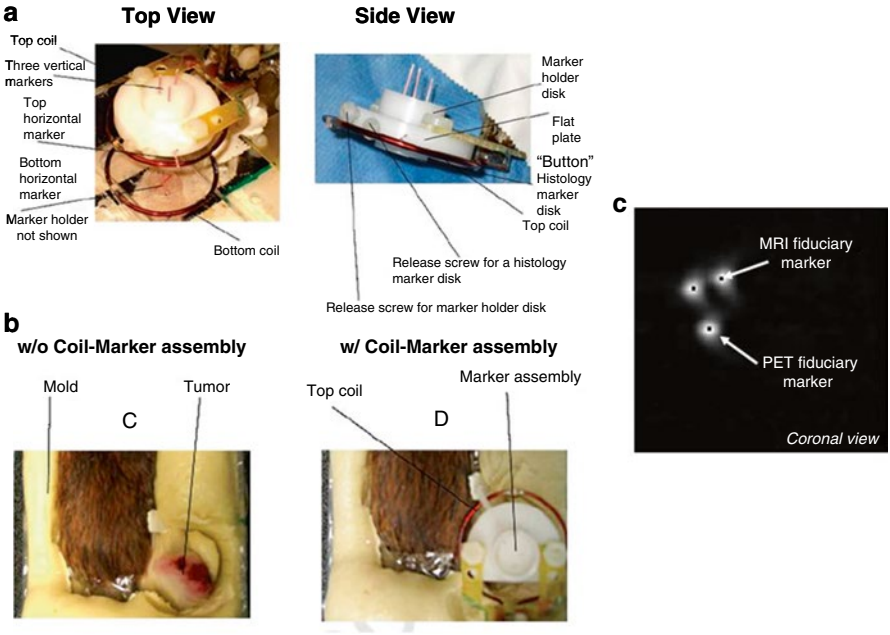

Fig. 10.8 (**a**) Magnetic coil-fiduciary marker assembly for 3D registration of MRI, PET, and histological images. (**b**) Dorsal view of tumor-bearing caudal end of tumor-bearing rat. (**c**) Registered (by rigid transform) MRI and PET images of the three vertical fiduciary markers. For MRI the fiduciary markers are filled with an aqueous Gd solution and for PET imaging with an aqueous ^{18}F solution. Adapted from [17] by permission of the authors

(FDG) and the hypoxia tracer ^{18}F-fluoromisonidazole (FMiso) were compared in rats by registered R4 microPET™ (Concorde Microsystems, Knoxville, TN) imaging with positioning of each animal in its custom-fabricated whole-body mold. Three ^{68}Ge rods were reproducibly positioned in the mold as external fiduciary markers. The registered microPET™ images unambiguously demonstrate grossly similar though not identical distributions of FDG and FMiso in the tumors—a high-activity rim surrounding a lower-activity core. There were subtle but possibly significant differences in the intra-tumoral distributions of FDG and FMiso, however, and these may not have been discerned without careful image registration.

In the second example [16, 17], a multi-modality (i.e. PET and MRI) imaging study using stereotactic fiduciary markers in a Dunning R3327-AT rat prostate tumor model was performed, focusing on the relationship between dynamic contrast-enhanced (DCE)-MRI using Magnevist® (Gd-DTPA) and dynamic ^{18}F-FMiso PET (Figs. 10.8, 10.9, and 10.10). A novel component of this work was registration not only of in vivo (i.e. PET and MRI) images but of in vivo and ex vivo (i.e. histological) images. Specifically, in vivo imaging results were corroborated by comparison to tumor sections stained for hematoxylin and eosin (H&E) to identify viable and necrotic tissue areas and pimonidazole to identify hypoxic tissue areas.

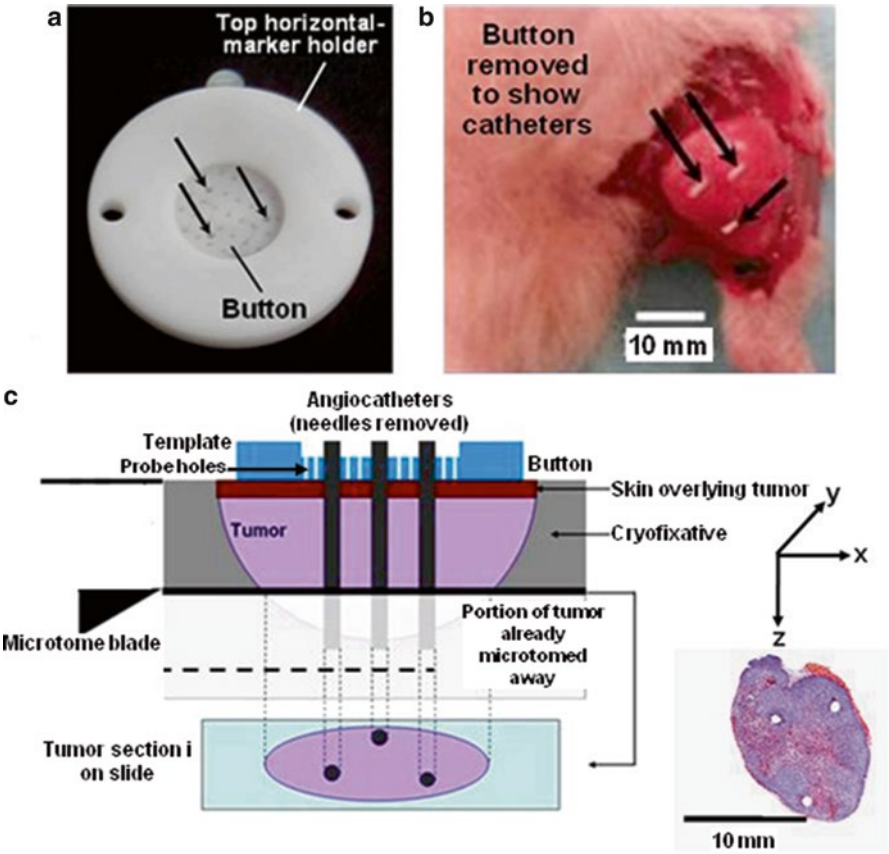

Fig. 10.9 (**a**) Close-up view of the top horizontal-marker holder (or "button") showing the three holes for the vertical catheters; the multiple smaller holes (not used in the study being described) are for various interstitial probes. (**b**) A post-sacrifice photograph of the tumor in situ with the overlying skin and fiduciary-marker assembly removed but with the three plastic angiocatheters, used for registration of the histological images with the in vivo (i.e. PET and MRI) images, in place. The tumor is removed with the horizontal-marker holder (button) and angiocatheters in place and the entire tumor-button-angiocatheter assembly is frozen in cryofixative for sectioning. (**c**) The procedure for the depth (or z-axis) registration of the in vivo and histological images. The button, frozen held in place with the angiocatheters against the shallow surface of the excised tumor, is placed against the microtome chuck. As a result, the cryosections thus cut are parallel to the in vivo (PET and MRI) coronal images. The first (i.e. the deepest) cryosection in which tumor is visible is matched with the first PET and MRI coronal images in which the tumor is also visible, thus achieving depth-wise alignment of the cyrosections and the PET and MRI images. Histological sections and PET and MRI images at the same depth are then aligned in the coronal (or xy-plane) by rigidly transforming the three angiocatheter holes visible in the section with the fiduciary markers visible in the PET/MRI images. Adapted from [17] by permission of the authors

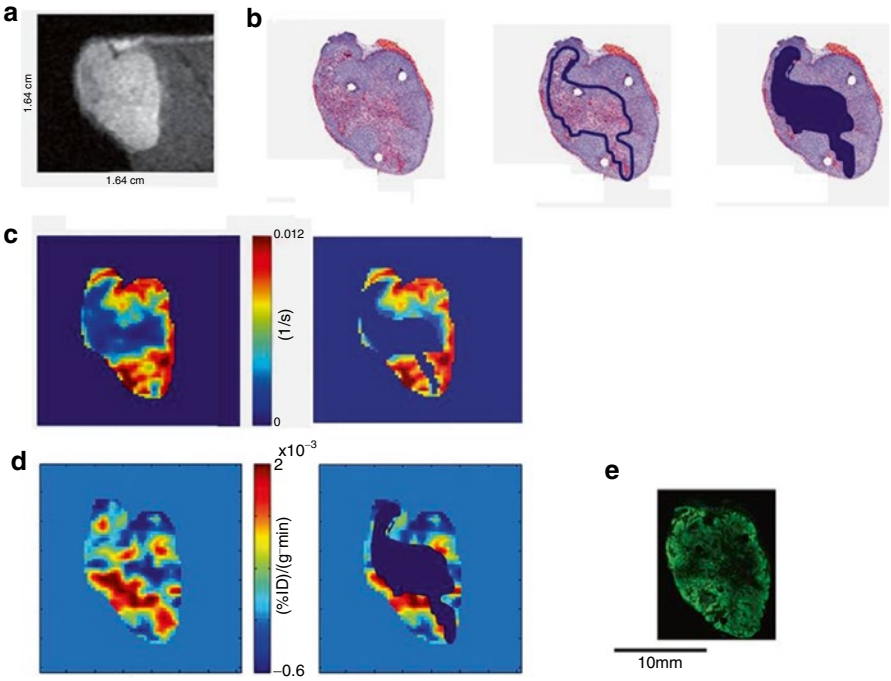

Fig. 10.10 (**a**) A T2-weighted coronal MRI image of the tumor xenograft in the animal shown in Fig. 10.8b. (**b**) The registered H&E-stained section of the same tumor showing the channels created by the three angiocatheters and the necrotic and viable areas of the tumor stained *purple* and *blue*, respectively (*left panel*). The necrotic area of the tumor outlined (*middle panel*) and a mask overlying the necrotic area of the tumor as outlined in the *middle panel* (*right panel*) are also shown. (**c**) The registered DCE-MRI-derived Akep parametric map of the same tumor without (*left panel*) and with (*right panel*) the necrotic area of the tumor segmented out using the "necrosis mask" created in (**b**). (**d**) The registered dynamic ^{18}F-FMiso PET late-slope parametric map also without (*left panel*) and with (*right panel*) the necrotic area of the tumor segmented out. (**e**) The registered pimonidazole-stained section of the same tumor showing the hypoxic areas of the tumor stained green. Note the spatial concordance of the hypoxic tumor areas as identified by the segmented ^{18}F-FMiso parametric map and the pimonidazole-stained section, with the elimination of possible false-positive hypoxic areas corresponding to necrosis (perhaps due to FMiso diffusing from viable but hypoxic areas of tumor into nearby necrotic areas). Adapted from [17] by permission of the authors

A Helmholtz MRI coil was constructed in two parts (Fig. 10.8), with the upper part of the coil and a fiduciary-marker assembly initially detached to facilitate positioning of the animal bearing a tumor xenograft in its hindlimb. The fiduciary-marker assembly is shown in Fig. 10.8a attached to the coil-marker system. The marker assembly was composed of two cylindrical disks and one flat plate. The top disk, or marker holder (or "button"), had three holes for Gd (for MRI)- or ^{18}F (for PET)-filled vertical markers. A bottom disk with identically aligned holes was separated from the marker holder disk by a flat plate. Separate release screws fastened each disk to the flat plate, which was fixed to the top of the MRI coil. At the end of

the imaging experiments, the bottom marker disk was detached from the rest of the marker. The flat plate had one side-hole for a horizontal marker. An additional holder was placed in the center of the bottom coil with a grooved disk for holding another horizontal marker. The three vertical markers (forming an oblique triangle with lengths of 0.9, 0.7 and 0.5 cm, respectively) and the two horizontal markers were composed of cut lengths of 22-G catheter tubing which were heat-sealed once filled. The vertical markers allowed in-plane registration of the PET and MRI images and the two horizontal markers depth-wise registration. The three vertical markers were pushed into the 0.9 mm-sized holes through separate channels. The separation of the top and bottom coils was adjustable over a range of 2–3 cm to accommodate tumors of various sizes. As illustrated in Fig. 10.8b, the magnetic coil-fiduciary marker assembly was placed in the animal's whole-body mold (See above.), which was fabricated in a semi-cylindrical Lucite holder compatible with both the MRI and PET scanner palettes. Close-up views of the top horizontal-marker holder (button) and the three angiocatheters in place are shown in Fig. 10.9a, b, respectively; the procedure for registration of the in vivo (PET and MRI) and ex vivo (histological) images is explained in Fig. 10.9c.

The comparison of the registered DCE-MRI "Akep" parametric maps (Akep is a parameter related to blood flow and vascular permeability and therefore considered a measure of tissue perfusion) [18] and the H&E-stained sections and of the registered ^{18}F-FMiso PET late-slope maps and pimonidazole-stained sections (Fig. 10.10) confirm the capability of combined MRI-PET measurements to functionally image the tumor microenvironment and to distinguish regions of necrosis, hypoxia and normoxia. This multi-modality approach to functional tissue segmentation, validated by registration with histological images, should minimize the possibility of false-positive findings of tumor hypoxia likely to result if one only were to perform static PET imaging of ^{18}F-FMiso or other "hypoxia" radiotracers.

7 Concluding Remarks

Image registration and fusion have rapidly emerged as an invaluable component of both clinical and small-animal imaging. However, rigorous registration and fusion of in vivo images with ex vivo microscopy images has been particularly challenging and has been largely ignored—despite the detailed structural information discernible with histology and the richness of specific molecular imaging probes now available for immunohistochemistry. A unique system has been now designed, fabricated, and tested for image registration of coarser-resolution in vivo imaging modalities such as PET and MRI and ultra-high-resolution ex vivo imaging techniques such as histology, autoradiography, and immunohistochemistry. This system can potentially be used to guide interstitial probe measurements of tissue parameters such as partial pressure of oxygen (pO_2) and to spatially index such measurements to allow correlation between the measured values and in vivo image and parametric-map voxel values. This novel paradigm provides a powerful approach to the validation of functional imaging techniques.

References

1. RSNA News, RSNA, SNM urge interdisciplinary cooperation to advance molecular imaging, 2005.
2. Zanzonico P. and Heller H. Developments in instrumentation. Seminars Nucl Med, vol. 38, pp. 149–222, 2008.
3. P. Zanzonico. Multimodality image registration and fusion. In Dhawan AP, Huang HK, and Kim DS (Eds), Principles and Advanced Methods in Medical Imaging and Image Analysis, World Scientific Publishing, Singapore, pp. 413–435, 2008.
4. B.F. Hutton, M. Braun, L. Thurfjell, et al. Image registration: An essential tool for nuclear medicine. Eur J Nucl Med, vol. 29, pp. 559–577, 2002.
5. J.B.A. Maintz and M.A. Viergever, "A survey of medical image registration," Med Image Anal, vol. 2, pp. 1–36, 1998.
6. J.V. Hajnal, D.L.G. Hill DLG, and D.J. Hawkes DJ (Eds.). Medical image registration, Boca Raton, FL: CRC Press, 2001.
7. D.L.G. Hill, P.G. Batchelor, M. Holden, et al. Medical image registration. Phys Med Biol, vol. 46, pp. R1–R45, 2001.
8. American College of Radiology, National Electrical Manufacturers Association. ACR-NEMA Digital Imaging and Communications Standard. NEMA Standards Publication No. 300-1985, Washington, DC, 1985.
9. American College of Radiology, National Electrical Manufacturers Association. ACR-NEMA Digital Imaging and Communications Standard: Version 2.0. NEMA Standards Publication No. 300-1988, Washington, DC, 1988.
10. American College of Radiology, National Electrical Manufacturers Association. Digital Imaging and Communications in Medicine (DICOM): Version 3.0. Draft Standard, ACR-NEMA Committee, Working Group VI, Washington, DC, 1993.
11. P. Mildenberger, M. Eichelberg, and E. Martin. Introduction to the DICOM standard. Eur Radiol, vol. 12, pp. 920–927, 2002.
12. P. Viola and W.M. Wells III. Alignment by maximization of mutual information. Inter J Computer Vision, vol. 22, pp. 137–154, 1997.
13. P. Zanzonico and S.A. Nehmeh. Introduction to clinical and laboratory (small-animal) image registration and fusion. Conf Proc IEEE Eng Med Bio Soc, vol. 1, pp. 1580–1583, 2006.
14. B.J. Pichler, H.F. Wehrl, A. Kolb, et al. Positron emission tomography/magnetic resonance imaging: the next generation of multimodality imaging? Seminars Nucl Med, vol. 38, pp. 199–208, 2008.
15. Zanzonico P, Campa J, Polycarpe-Holman D ,et al, Animal-specific positioning molds for registration of repeat imaging studies: Comparative microPET™ imaging of F18-labeled fluoro-deoxyglucose and fluoro-misonidazole in rodent tumors. Nucl Med Biol, vol. 33, pp. 65–70, 2006.
16. J.L. Humm, D. Ballon, J. Hu, et al. A stereotactic method for the three-dimensional registration of multi-modality biologic images in animals: NMR, PET, histology, and autoradiograph. Med Physics, vol. 30, pp. 2303–2314, 2003.
17. H. Cho, E. Ackerstaff E, S. Carlin S, et al. Noninvasive multimodality imaging of the tumor microenvironment: registered dynamic magnetic resonance imaging and positron emission tomography studies of a preclinical tumor model of tumor hypoxia. Neoplasia, vol. 11, pp. 247–259. 2009.
18. U.Hoffmann, G.Brix, M.V.Knopp, et al. Pharmokinetic mapping of the breast: a new method for dynamic MR mammography. Magnet Resonance Med, vol. 33, pp. 506–514, 1995.

Chapter 11
Dual-Modality Preclinical SPECT/PET Instrumentation

Alberto Del Guerra and Nicola Belcari

1 Rationale for Dual-Modality SPECT/PET

Present multimodality imaging strategies are mostly based on the combination of complementary imaging technique such as PET/CT and SPECT/CT where functional and morphological information on the same subject can be derived and combined. On the shadow of the successful application of combined PET/CT scanners in the clinical environment, multimodality techniques have been recently transferred to small animal scanners.

On the other hand, there is a growing interest for the pre-clinical application of nuclear imaging techniques able to perform dual-tracer imaging [1]. It is defined as the application of two radionuclide-labelled tracers to image two different biological or molecular targets at the same time. In this way a direct comparison between the two targets can be derived so as to provide additional diagnostic value that is difficult for a single tracer imaging to provide. Dual-tracer imaging is now a well established technique. It has been in use for over a decade for parathyroid [2], liver and cardiac [3] disease (for example in metabolic and perfusion studies for the assessment of myocardial viability), and for studies in brain receptors and perfusion (for example in the imaging of dopamine neurotransmission and brain perfusion in differential diagnosis of Parkinson's disease) [4]. Dual isotope imaging is performed both in clinical and pre-clinical environments with SPECT by using two different isotopes with well separated γ ray emission energies. When injected together, the two isotopes can produce two different images that are obtained by applying different energy windows around the energy of the two primary photons. However, the main limitation of the dual-radionuclide imaging is the crosstalk between the two radionuclides [5]. Such a crosstalk is mainly due to the scattered (in the object, in the detector or

A. Del Guerra (✉) • N. Belcari
Dipartimento di Fisica, Università di Pisa, and INFN Sezione di Pisa,
Largo Bruno Pontecorvo, 3, 56127 Pisa, Italy
e-mail: alberto.delguerra@df.unipi.it; belcari@df.unipi.it

H. Zaidi (ed.), *Molecular Imaging of Small Animals: Instrumentation and Applications*,
DOI 10.1007/978-1-4939-0894-3_11,

in the collimator) radiation from the higher energy radionuclide that is detected in the lower energy window or to the higher energy secondary emission peaks from the lower energy radioisotope that can be detected in the higher energy window.

The following step would be the combination of PET and SPECT for dual-tracer imaging that will potentially open new possibilities for the design of many new clinical and pre-clinical protocols. In this case one single γ emitting isotope is used in combination with a β^+ emitting isotope. For years PET and SPECT were considered as antagonist techniques. In practice, each of the two modalities has peculiar advantages: PET can usually provide superior imaging performance in sensitivity and quantification as compared to SPECT and the PET tracers can offer several advantages with respect to SPECT tracers from the biological compatibility point of view; on the other hand SPECT is not intrinsically limited in spatial resolution and can be potentially better than PET in this issue on limited field-of-view by using pinhole collimators. Hence, the combination of the two modalities is a real plus and can be technically advantageous in certain aspects as compared to conventional SPECT dual-tracer. A significant improvement in dual tracer PET/SPECT imaging would be the possibility to perform the two modalities simultaneously (simultaneous SPECT/PET).

2 Instrumentation for Dual-Modality SPECT/PET

In principle, a dual tracer study with PET and SPECT could also be done with two separate scanners that share the same type of animal bed holder. In fact, the animal can be subjected to a series of scans with the two modalities by transferring the animal bed from one scanner to the other, once the animal is well fixed on the bed. The image fusion for dual tracer study can be done a-posteriori by knowing the relative position of the animal with respect to the PET and SPECT field-of-view, respectively.

On the other hand, a scanner where PET and SPECT detectors are physically integrated with a common bed will potentially ease the imaging procedure and speed up post-processing.

Dual-modality SPECT/PET systems are now available and a number of prototypes have been proposed in last years. Present systems are very different in integration level and detector technology. Examples of solutions for SPECT/PET are illustrated in the following Sections.

2.1 Integrated or Dockable Solutions

The simplest way to combine two imaging modalities is to physically integrate two separate imaging systems in a single gantry. This was the way PET and CT gave birth to a new imaging paradigm: the PET/CT. On the shadow of the clinical PET/CT and SPECT/CT a growing number of combined emission/transmission small animal scanners became available. The first multi-modality small animal system to

be available was SPECT/CT. A pre-clinical SPECT/CT is typically made of separate SPECT (usually one or two opposing detector heads) and CT components that share the same scanner axis and animal bed. The field-of-view of the two systems is usually overlapping. This kind of mechanical arrangement facilitates the combination of mutual information from the two modalities, e.g. for image fusion and CT based attenuation correction of SPECT data.

The step towards a fully integrated PET/SPECT/CT system was short. In 2004, Gamma Medica (Nortridge, CA) introduced the first multi-modality platform, called FLEX^{TM}, able to perform PET, SPECT and CT with separate systems installed on the same gantry. Due to the typical ring geometry the PET system field-of-view does not overlap with that of the SPECT/CT but is axially shifted like in clinical PET/CT systems. For this reason, with this kind of system PET and SPECT modalities cannot be performed at the same time.

Another way to combine different imaging modality is to juxtapose back-to-back two stand alone systems in such a way that they have the same axis and can share the same animal bed. Once combined, the two systems can be controlled by the same user console. The advantage of this solution, called "dockable", is a greater flexibility in exchange for a higher cost.

2.2 Co-planar Hybrid Solutions

A further step toward a full combination of the SPECT and PET modalities is to have a solution where the two fields-of-view are overlapping. In this way, in addition to the possibility of performing both emission techniques on the same animal, it allows, in principle, the simultaneous execution of PET and SPECT investigation. To make it feasible, a possible solution is to combine two rotating dual head parallel plane detectors where a pair is dedicated to PET and the other is for SPECT. An example of this solution can be found in [6].

2.3 Single and Dual Layer Scintillator Solutions

Various research groups have shown a growing interest in developing detectors able to perform PET and SPECT acquisitions in a single device. In principle a high light output pixilated scintillator suitable for PET can be used for the detection of single medium energy γ-rays commonly used in SPECT. An example of this solution for a system using a single scintillator for both PET and SPECT is the YAP-(S)PET scanner [7] (see also Sect. 4.2). A more complicated solution is based on a dual layer scintillator read out by a common photodetector (e.g. photomultiplier tubes or avalanche photodiodes). In this case a first layer is optimized for the detection of medium energy γ-rays for SPECT commonly used in SPECT, whilst a second layer is optimized for the high energy annihilation radiation used in PET. Such a detector

module can be used as the basic detection unit in a multi-modality scanner capable of performing PET and SPECT imaging simultaneously. Pulse shape discrimination is used to separate the signals originating from the different detector materials. Good candidates for the first layer are high light output scintillator, while the second layer should be made of fast, high density crystals. Examples of possible dual layer scintillators for SPECT/PET are (first layer/second layer) YSO/LSO [8, 9], LSO/GSO [8], NaI/LSO [10, 11], YAP/LSO [12].

3 Examples of Dockable and Combined SPECT/PET Instrumentation

3.1 SIEMENS Inveon

The SIEMENS Inveon is a scalable platform able to perform PET, SPECT and/or Computed Tomography (CT). The system comprises three separate imaging subsystems for PET, SPECT and CT. The subsystems are able to work individually or in combination. Two possible combinations of mechanical integration between the systems, "integrated" or "dockable" are offered. In the "integrated" solution the three subsystems are physically integrated on the same gantry. The systems have the same tomographic axis and share the same animal bed. The SPECT and CT systems have also overlapping field-of-views. In the "dockable" solution the PET and the SPECT/CT systems are mounted on two separate gantries that can be physically combined by docking the two systems back-to-back. Once docked the two systems are equivalent to the "integrated" solution (Fig. 11.1).

Fig. 11.1 Drawings of the two solutions available from SIEMENS medical. *Left*: integrated solution, the PET, SPECT and CT systems are available in a single gantry. *Right*: the "dockable" solution, the PET stand alone system (*left*) can be plugged on the back of the SPECT/CT system (*right*) to obtain a fully combined scanner (http://www.medical.siemens.com/siemens/en_US/gg_nm_FBAs/files/multimedia/inveon/index.htm)

3.1.1 Inveon PET Module

The scanner uses $1.51 \times 1.51 \times 10$ mm^3 LSO crystals grouped in 20×20 blocks; a tapered light guide couples the LSO crystals of a block to a position-sensitive photomultiplier tube. The crystal pitch is 1.63 mm × 1.59 mm in transaxial and axial directions, respectively. There are 80 rings with 320 crystals per ring and the ring diameter is 161 mm. The transaxial and axial fields of view (FOV) are 100 and 127 mm, respectively. The scanner has a spatial resolution at the center of the FOV of about 1.6 mm (FWHM) in the transaxial plane and 2.2 mm (FWHM) axially in images reconstructed using the filtered back projection algorithm [13]. A higher resolution in the reconstructed image can be achieved with iterative reconstruction algorithms. A continuous bed motion acquisition modality effectively extends the axial FOV to 50 cm, offering better image quality due to the over sampling. The maximum absolute sensitivity in the center of the FOV is greater than 10 %.

3.1.2 Inveon SPECT Module

The SPECT detectors on the SIEMENS Inveon system are constructed using 10 mm thick pixellated NaI crystal on a 2.2 mm pitch [14]. The NaI crystal is coupled to a light guide that is attached to a 3 × 3 array of 50 mm × 50 mm square position sensitive photomultiplier tubes. The total active imaging area of the detector is 150 mm × 150 mm.

Pinhole collimators with up to seven pin-holes can be used. The SPECT detectors are mounted on a rotating gantry and rotate together with the CT components. Up to four SPECT heads can be installed on the gantry. With the CT installed the maximum number of SPECT heads is limited to 2.

The spatial resolution and field-of-view size depend on the pinhole size and magnification factor. The maximum spatial resolution is 0.7 mm (FWHM) and is reached with a 0.5 mm diameter pinhole and with a field of view of 25 mm (pinhole magnification factor 4.9).

3.2 GE Triumph™

As the SIEMENS Inveon the GE Triumph™ is a multi modality pre-clinical imaging platform that includes PET, SPECT and CT subsystems. In this case the three subsystems are integrated in a common gantry. The system can accommodate various size animals from mouse to rhesus monkey (Fig. 11.2).

3.2.1 LabPET™: APD-Based PET Sub-system

The LabPET system consists in a 15.6 cm diameter ring configuration PET systems [15]. Each detector is made of a phoswich pair consisting of one LYSO and one LGSO scintillator optically coupled along one long side and read out by a single APD sitting

Fig. 11.2 The Triumph™ multi modality system from GE (mouse solution) (http://www.gehealthcare.com/euen/fun_img/products/pre-clinical/triumph/triumph.html)

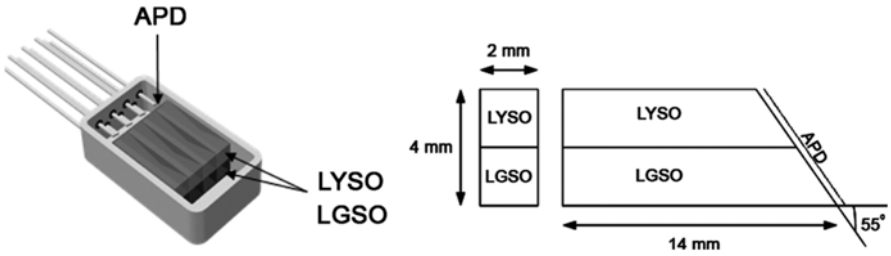

Fig. 11.3 Arrangement of the scintillating crystal elements and the APD photodetectors in the LabPET system from GE

on a 55° wedge (Fig. 11.3). The two crystals can be identified since the crystal decay times are sufficiently different (40 ns for LYSO and 65 ns for LGSO). This side-by-side phoswich configuration was selected to achieve a quasi-individual crystal readout. Options of 3 different axial fields of view (3.75, 7.5, and 11.25 cm) are available. The absolute sensitivity at the center of the field-of-view is about 3 % for the 11.25 cm scanner. The scanner has a spatial resolution at the center of the FOV of about 1.2–1.3 mm (FWHM) for images reconstructed using an MLEM algorithm [16].

3.2.2 X-SPECT®: CZT-Based SPECT Subsystem

The SPECT subsystem is based on one, two, or four Cadmium Zinc Telluride (CZT) digital gamma camera, with 1.6 mm pixels. Single and multiple pinholes are available. The maximum spatial resolution is better than 0.5 mm (FWHM). A feature of

the CZT based detectors is the excellent energy resolution. In this case it reaches a value of 4.5 % (FWHM) at 140 keV. This could help the reduction of radiation scatter and enables simultaneous multi-isotope imaging that covers a wide range of energies (30–300 keV, i.e. ^{99m}Tc, ^{125}I, ^{123}I, ^{201}Tl, and ^{111}In isotopes).

4 Simultaneous SPECT/PET

PET and SPECT dual-tracer imaging, particularly the simultaneous acquisition, may open the door for many potentially new clinical and preclinical applications.

Even if designed to integrate multi-modality PET and SPECT imaging techniques, none of the above mentioned systems are specifically designed for true simultaneous PET/SPECT acquisitions.

4.1 Challenges for Simultaneous SPECT/PET Acquisitions

The requirements for simultaneous PET and SPECT goes beyond the ability to simply detect single low energy (for SPECT) and coincidence 511 keV (for PET) γ rays. The technical challenges for this imaging method are multifold and are related to the type of system in use. In fact, a possible solutions for simultaneous PET/SPECT can use either a common detector working simultaneously in PET and SPECT (*joint modality*), or PET and SPECT can be performed using separate detectors either of the same type (*split modality*) or using different technologies (*separate modality*).

A common challenge for any solution is related to the fact that the simultaneous PET/SPECT acquisition implies the simultaneous presence of single photon and positron emitting isotopes. Hence, each modality should be able to work in presence on a secondary γ source.

The effect of the simultaneous presence of two kinds of γ sources is twofold.

- On one side the SPECT data are contaminated by down scattered 511 keV photons to low energy. In fact, since the thickness of the collimators is optimized to stop low energy γ rays, usually the 140 keV γ rays of ^{99m}Tc, the high energy radiation (511 keV) passes or scatters through the collimator. When using scintillators for γ ray detection, a non negligible fraction of the 511 keV photons, because of the scattering within the crystal, will be recorded within the energy window used for SPECT imaging. Due to the fact that such events are not selected by the collimator (or in the joint modality only partially attenuated), the number of such events is usually more than one order of magnitude greater than the total number of SPECT counts within the selected energy window, when a γ and a β^+ source of similar activity are used. This effect can significantly degrade SPECT performance adding a strong background, hence generating significant artefacts in the reconstructed images. A correction procedure for this effect, similar to those described in the next paragraph, is then mandatory. In addition, to

further limit the cross contamination, the activity of the single γ ray source should be at least ten times higher than the β^+ activity.

- On the other hand the PET data are less influenced by the presence of the single γ ray source. In fact, the cross contamination is limited, on one side by the time coincidence acquisition modality, and on the other by the fact that the single γ counts are limited in a relatively narrow low energy window, that can be excluded for the PET data analysis. In addition, when using a high γ/β^+ activity ratio the PET acquisition system is subjected to a high singles count rate that can limit the PET count rate performance due to system dead time, pile-up effects and an increased difficulty for estimating random counts. In the split and separate modalities a hardware solution for limiting the single γ ray flux reaching the PET detectors can be obtained by adding an attenuation slab whose thickness can be chosen as a compromise between stopping the larger fraction as possible of low energy γ's and letting the annihilation γ's passing through it. For example, a 2 mm thick lead slab is a possible solution.
- A peculiar challenge for the joint modality is the difficulty in designing a common acquisition for PET and SPECT. In addition, a necessary collimator for SPECT will strongly attenuate PET coincidence events that should be further corrected for this effect.

4.1.1 Down Scatter Correction

The fraction of down-scatter events (C_{PET}) with respect to the true single photon SPECT events (C_{SPECT}) depends on the photofraction of the detector (scintillator or solid state) used in the SPECT system. The higher is the photofraction at 511 keV, the lower will be the down-scatter fraction. However, due to the relatively low efficiency of the SPECT collimators the number of scattered events in the SPECT energy window exceeds the number of true SPECT events by more than one order of magnitude when using similar activity values for PET and SPECT tracers for any scintillator to be used for this purpose.

Several algorithms were proposed to correct down-scatter events. In the auxiliary energy window method [17] the counts in an auxiliary energy window (AEW) (e.g. 160–170 keV when using ^{99m}Tc) just above the main energy window (MEW) (e.g. 135–145 keV) are used as an estimation of the down-scatter. By considering that the energy spectrum of the down-scattered events is quite flat in this region, the events in the AEW are a good approximation of the down-scattered events in the MEW ($C_{PET}(AEW) \approx C_{PET}(MEW)$). In this case the value of C_{SPECT} can be estimated from the total counts in the original data (C_{DATA}) as: $C_{SPECT}(MEW) = C_{DATA}(MEW) - C_{DATA}(AEW)$, where $C_{DATA}(AEW)$ is assumed to be completely obtained from down-scattering of PET photons (i.e., $C_{DATA}(AEW) \approx C_{PET}(AEW)$). In this way $C_{DATA}(AEW)$ is a good approximation of $C_{PET}(MEW)$. An alternative method is the so called extra shielding method [17]. In this case, the down-scatter events are measured by placing an additional lead sheet (~2.0 mm thickness) in front of the collimator and performing a calibration immediately after the acquisition, using the same object. The lead

sheet blocks most of the 140 keV photons while still lets most of the 511 keV photons passing through. In this case the value of C_{SPECT}(MEW) is obtained from the number of counts in the calibration acquisition with the lead slab C_{SLAB} as: $C_{SPECT}(MEW) = C_{DATA}(MEW) - k \times C_{SLAB}(MEW)$, where k is a factor that estimates the 511 keV γ ray attenuation of the lead sheet for each crystal. A third example of down scatter correction is somewhat a merge of the two previously described methods and is based on the following approximation: the background events produced by the 511 keV gamma rays scattered radiation that are detected by each pixel i in the MEW are a fraction (f_i) of the events registered in the previously defined AEW, i.e. $f_i = C_{PET,i}(MEW)/C_{DATA,i}(AEW)$. An approximated value of f_i can be determined from a calibration acquisition of the same object using a lead sheet as described above, or with a phantom mimicking the animal geometry (e.g. a cylinder 2.5 cm in diameter, 5.6 cm in height for a mouse) filled with a β^+ source only (no lead sheet is used in this case). The solution based on the use of the same object where low energy γ rays are attenuated by the lead slab is in principle better in reproducing the spatial variation of f_i but the obtained values are biased by the presence of the slab itself. On the other hand, since the distribution of f_i does not contain high frequency information from the object the phantom method is usually preferred, since it does not need the slab measurement and allows for the possibility of using the same calibration acquisition (with high statistics) for many acquisitions (no interruption in the workflow). In any case f_i can be calculated, for each pixel i as $f_i = C_{CAL,i}(MEW)/C_{CAL,i}(AEW)$. A direct measurement of f_i is obtained by taking the ratio between the SPECT sinogram produced in the MEW and AEW, respectively. A better statistics is gained by averaging f_i over the angular coordinates. The value of SPECT counts in the MEW $C_{SPECT,i}(MEW)$ can be then obtained as: $C_{SPECT,i}(MEW) = C_{DATA,i}(MEW) - f_i \times C_{DATA,i}(AEW)$. Again this operation can be directly performed on the relative sinograms.

4.2 YAP-(S)PET II: An Example of Combined/Simultaneous SPECT/PET

The YAP-(S)PET scanner (Fig. 11.4) from Imaging System Europe (ISE), is made up of four detector heads: each one is composed of a 4.05×4.05 cm^2 $YAlO_3$:Ce (or YAP:Ce) matrix of 27×27 elements, $1.5 \times 1.5 \times 20$ mm^3 each. The matrix is directly coupled to a PS-PMT (Hamamatsu R2486). The four modules are positioned on a rotating gantry; the opposite detectors are in time coincidence when used in PET mode. The rotation is controlled via PC thus permitting the acquisition of the tomographic views. The system can operate in 3-D PET data acquisition mode [18].

Thanks to the rotating planar detector configuration the scanner can also work as SPECT. The switching to the SPECT modality can be easily made by replacing the tungsten septum (used in PET for shielding the scintillators from the background outside the FOV) with a high resolution parallel-hole, lead collimator (0.6 mm diameter, 0.15 mm septum) in front of each crystal. For SPECT the system uses the same acquisition electronics with no coincidence.

Fig. 11.4 *Left*: the YAP-(S)PET II scanner from ISE. *Right*: arrangement of the four heads when used in simultaneous PET/SPECT configuration. In this case heads 1 and 2 are used for PET, while heads 3 and 4 are equipped with a collimator and used in SPECT mode

For both PET and SPECT modalities the scanner has an axial field of view of 4.05 cm and the diameter of the transaxial FOV is 4.05 cm. Exploiting the YAP-(S) PET scanner capability of performing both PET and SPECT imaging, it is possible to perform simultaneous PET/SPECT acquisitions [19]. In this case two opposing heads (e.g. heads 1 and 2 in Fig. 11.4, right) are used for PET (coincidence mode) while the other pair (detectors 3 and 4) are equipped with the collimators and independently acquire single events (SPECT mode).

The SPECT data analysis procedure for reducing the cross contamination includes a procedure that uses a direct measurement of f_i as illustrated in the previous section (third method). In order to further reduce the background produced by the Compton scattering of 511 keV gamma rays, each SPECT head is set in anticoincidence with the opposing one. On the other side, the events detected by the PET pair are only slightly influenced by the increase in random coincidence rate due to the increased singles count rate (most of the singles are now originated by the single γ emission).

Two techniques were adopted to reduce the incidence of SPECT γ-rays (e.g. 140 keV photons from ^{99m}Tc) on PET coincidence imaging: a) an hardware procedure consisting in placing a lead layer of about 2 mm in front of the scintillator of the heads used for the PET acquisition or b) a software procedure based on selecting only the coincidence events registered in an energy window excluding all the possible contamination from ^{99m}Tc. The energy window used is 200–850 keV, just above the ^{99m}Tc photo-peak energy window. The two procedures provide comparable results. They are both good in eliminating the SPECT γ ray contribution to PET images with a small reduction in coincidence 511 keV γ ray detection. The hardware procedure is usually preferred since it further reduces the radiation scattered in the object. Figure 11.5 shows an example of the application of the simultaneous PET/SPECT with the YAP-(S)PET scanner.

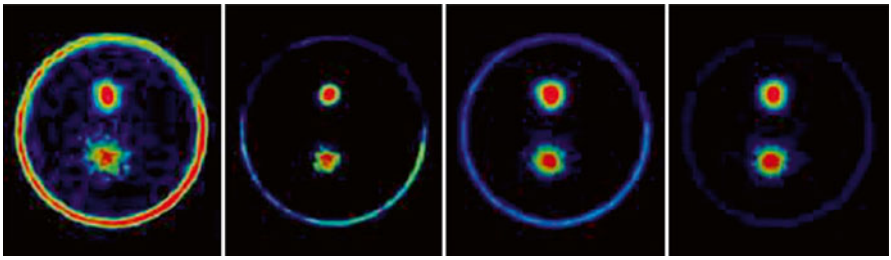

Fig. 11.5 Transaxial images of a simultaneous PET/SPECT acquisition of two small syringes. the *top* syringe was filled with ^{99m}Tc while the *bottom* one was filled with ^{18}F. The SPECT/PET activity ratios are, from *left* to *right*: 5:1, 10:1, 30:1, 50:1

4.3 Slit–Slat Collimator Insert for MicroPET

In the previous example the same detectors are used both for PET and SPECT but each detector head is specifically dedicated to one (PET or SPECT) modality only. The simultaneous PET/SPECT is obtained by setting half of the heads in PET and half in SPECT.

On the other hand, in the example reported in this section, a whole system is actually used simultaneously for PET and SPECT. In particular, this is an example of a modification of a PET system based on a ring geometry to perform SPECT and also simultaneous PET/SPECT.

A microPET Focus 120™ has been used to build this prototype [17]. This scanner is made up of 96 detector blocks arranged in 4 rings. Each block is composed of 12×12 arrays of $1.59 \times 1.59 \times 10$ mm^3 LSO crystals. The diameter of the ring of the scanner is about 14.7 cm. The transaxial and axial field-of-view are 10.0 and 7.7 cm, respectively. The measured image resolution at the center of FOV is around 1.4 mm (FWHM). The SPECT capability is obtained by inserting a slit-slat collimator within the ring aperture. The slit-aperture is made of wedge-shaped lead plates that form a limited angle collimation with an aperture of 45° and a 0.5 mm gap between the two plates. The septa are made of stacked parallel annular-shape tungsten sheets to form a 2D collimation. Each Tungsten sheet is 0.2 mm thick, with a 0.6 mm spacer between neighbouring sheets. The in-plane effective FOV is about 4.0 cm. To obtain the tomography acquisition the object is rotated around the scanner axis with a computer controlled rotating stage. The acquisition mode was set to be able to acquire single counts.

The correction of the SPECT data is similar to the previous example, especially for the case of the down-scatter of the 511 keV photons. In fact, even if LSO shows a good photofraction at 511 keV (32 %) the down-scatter counts are still 18 times higher than the true SPECT counts from ^{99m}Tc, with mixed sources at equal activities. In this case the extra shielding method was found to be the best solution for down-scatter correction. To measure down-scatter an additional cylindrical lead sheet (~2.0 mm thickness) was placed inside the collimator after the SPECT acquisition.

Using LSO scintillators an additional problem is the ^{176}Lutetium background radiation. From experimental measurements the energy spectrum of LSO background is quite flat in the regions around the 140 keV ^{99m}Tc photopeak. Hence, the contribution of the background can be subtracted from SPECT data by measuring the background count rate for each crystal.

In this case 511 keV PET γ rays are measured after passing through the collimators. Hence, collimator attenuation to PET coincidence acquisition has to be measured. Collimator attenuation is directly measured in coincidence mode with a Ge/Ga-68 line source that is inserted inside the collimator and rotated along the inner surface of the collimator to cover the entire FOV. This transmission is then used as the basis to calculate the attenuation factor associated with each line of response.

5 Summary

The demand for multi-probe molecular imaging of small-animals using both single-photon and positron emitting radiotracers has stimulated the development of dedicated small-bore high-resolution systems for rodents' imaging allowing concurrent acquisition of SPECT and PET data. Multi-probe scanning can be performed through energy discrimination which allows the acquisition of SPECT and PET data in different energy windows.

The peculiar architecture of some small animal scanners gives the opportunity to implement simultaneous PET/SPECT acquisition. The coincidence detection (PET mode) is almost unaffected by the presence of low energy photons (i.e., ^{99m}Tc). Single-photon acquisition (SPECT mode), instead, is seriously affected by the crosstalk from 511 keV photons scattering or depositing a fraction of their energy in the crystal and mimicking ^{99m}Tc photons. This technology opens the way to new and interesting protocols for the investigation of many biological phenomena, more effectively than when using PET or SPECT modalities alone.

References

1. Rahmim A, Zaidi H (2008) PET versus SPECT: strengths, limitations and challenges. Nucl Med Commun 29:193–207.
2. Neumann DR (1992) Simultaneous dual-isotope SPECT imaging for the detection and characterization of parathyroid pathology. J Nucl Med 33:131–134.
3. Berman DS, Kang X, Tamarappoo B, Wolak A, Hayes SW, Nakazato R et al. (2009) Stress Thallium-201/rest Technetium-99m sequential dual isotope high-speed myocardial perfusion imaging. JACC: Cardiovas Imag 2:273–282.
4. Links JM (1996) Simultaneous dual-radionuclide imaging: are the images trustworthy? Eur J Nucl Med 23:1289–1291.
5. Chang CJ, Huang WS, Su KH, Chen JC (2006) Separation of two radionuclides in simultaneous dual-isotope imaging with independent component analysis. Biomed Eng Appl Basis Comm 18:264–269.

6. US Patent 6303935. Combination PET/SPECT nuclear imaging system.
7. Del Guerra A, Damiani C, Di Domenico G, Motta A, Giganti M, Marchesini R et al. (2000) An integrated PET-SPECT small animal imager: preliminary results. IEEE Trans Nucl Sci 47:1537–1540.
8. Saoudi A, Lecomte R (1999) A novel APD-based detector module for multi-modality PET/SPECT/CT scanners. IEEE Trans Nucl Sci 46: 479–484.
9. Dahlbom M, MacDonald LR, Schmand M, Eriksson L, Andreaco M, Williams C (1998) A YSO/LSO phoswich array detector for single and coincidence photon imaging. IEEE Trans Nucl Sci 45:1128–1132.
10. Schmand M, Dahlbom M, Eriksson L, Casey ME et al. (1998) Performance of a LSO/NaI(Tl) phoswich detector for a combined PET/SPECT imaging system [abstract]. J Nucl Med 39:9P.
11. Pichler BJ, Gremillion, Ermer T, Schmand V, Bendriem B, Schwaiger M, et al. (2003) Detector characterization and detector setup of a NaI-LSO PET/SPECT camera. IEEE Trans Nucl Sci 50:1420–1427.
12. Guerra P, Rubio JL, Ortuño JE, Kontaxakis G, Ledesma MJ, Santos A (2007) Performance analysis of a low-cost small animal PET/SPECT scanner. Nucl Instr and Meth Phys Res A 57:98–101.
13. Kemp BJ, Hruska CB, McFarland AR, Lenox MW, Lowe VJ (2009) NEMA NU 2–2007 performance measurement of the Siemens Inveon™ preclinical small animal PET system. Phys Med Biol 54: 2359–2376.
14. Austin DW, Paulus MJ, Gleason SS, Mintzer RA, Siegel SB, Figueroa SD, et al. (2006) Design and performance of a new SPECT detector for multimodality small animal imaging platforms. IEEE Nuclear Science Symposium Conference Record, Vol. 5, pp 3008–3011.
15. Tetrault MA, Viscogliosi N, Riendeau J, Belanger F, Michaud JB, Semmaoui H, et al. (2008) System architecture of the LabPET™ small animal PET scanner. IEEE Trans Nucl Sci 55:2546–2550.
16. Bergeron M, Cadorette J, Beaudoin JF, Rousseau JA, Dumoulin M, Lepage MD, et al. (2009) Performance Evaluation of the LabPET APD-Based Digital PET Scanner. IEEE Trans Nucl Sci 56:10–16.
17. Shao Y, Yao R, Ma T, Manchiraju P (2007) Initial studies of PET-SPECT dual-tracer imaging, IEEE Nuclear Science Symposium Conference Record, Vol. 6, pp 4198–4204.
18. Del Guerra A, Bartoli A, Belcari N, Herbert D, Motta A, Vaiano A, et al. (2006) Performance evaluation of the fully engineered YAP-(S)PET scanner for small imaging. IEEE Trans Nucl Sci 53:1078–1083.
19. Bartoli A, Belcari N, Del Guerra A, Fabbri S (2007) Simultaneous PET/SPECT imaging with the small animal scanner YAP-(S)PET. IEEE Nuclear Science Symposium Conference Record, Vol. 5, pp 3408–3413.

Chapter 12
Dual-Modality Preclinical SPECT/CT Instrumentation

Youngho Seo and Carina Mari Aparici

1 Limitations of Standalone Preclinical SPECT

Preclinical imaging using SPECT and small animal models provides a very high spatial resolution using pinhole geometries or other convergent collimator geometries [1, 2], typically in submillimeters [3]. In addition, multiple apertures of pinholes in combination with multiple radionuclide detectors potentially provide a desirable high detection efficiency of radionuclide gamma-ray photons [4, 5]. However, the utility of preclinical SPECT imaging is limited especially when the imaging studies require more than the functional information that SPECT alone can provide [6–8].

1.1 Localizing Tracer Distribution in Small Animal Models

When the physiologic target of a radiotracer used in preclinical SPECT imaging studies is located anywhere within the animal body, correlating tracer uptake seen by SPECT to its anatomy is sometimes challenging. A similar issue occurs with clinical SPECT studies. In the clinical setting, nuclear medicine physicians are trained to distinguish abnormal uptake versus normal physiologic uptake of a known radiotracer; however, in the preclinical setting, it is rare to have a specifically

Y. Seo (✉)
UCSF Physics Research Laboratory, Department of Radiology & Biomedical Imaging, University of California, San Francisco, CA, USA
e-mail: youngho.seo@ucsf.edu

C. Mari Aparici
Department of Radiology & Biomedical Imaging, San Francisco and Nuclear Medicine Service, San Francisco Veterans Affairs Medical Center, University of California, San Francisco, CA, USA
e-mail: carina.mari@radiology.ucsf.edu

H. Zaidi (ed.), *Molecular Imaging of Small Animals: Instrumentation and Applications*,
DOI 10.1007/978-1-4939-0894-3_12,

trained interpreter who understands the small animal anatomy and the radiotracer distribution well. The complication is augmented when a preclinical evaluation of a new radiotracer is the main utilization of the preclinical SPECT.

1.2 Quantification of Radiotracer

As in clinical SPECT studies, preclinical SPECT studies using dedicated small animal SPECT scanners basically result in images of tracer distribution in small animal models in an arbitrary unit (e.g., pixel value, not in Bq/ml). Tracer quantification is only possible if the user of the preclinical SPECT scanner is confident that most physical compensations are implemented in image generation [9, 10]. Additionally, the poor photon statistics in preclinical SPECT scanners without innovative designs like multidetectors [11] and multipinholes limits quantitative accuracies to an unreliable level.

It is known that out of physical perturbations in SPECT imaging, photon attenuation errors contribute the most when the object size is large and the energy of emission photons from a radiotracer is low (e.g., I-125's 20–30 keV photopeaks). In other words, for small body size of rodents, particularly in mice, physical compensations may not be critical in terms of obtaining quantitative accuracies of tracer distribution in reconstructed images. Yet, when the attenuation correction is necessary, the standalone preclinical SPECT scanners should rely on some external transmission scans for attenuation map generation.

1.3 Limitations of Standalone SPECT Scanners Specific to Preclinical Systems

The anatomical localization capability and the tracer quantification aspect have been widely recognized because these issues are also found in clinical SPECT systems. With regards to preclinical SPECT systems more specifically, the limitations are caused by (a) unfamiliarities of animal anatomies that are not comparable to human anatomy, (b) inherent geometrical limitations such as limited field of view (FOV) caused from focusing collimators like pinholes used in small animal SPECT, and (c) lack of robust correction methods for physical perturbations in SPECT imaging such as photon attenuation errors [12].

2 Preclinical SPECT Combined with CT

Fortunately, most of the limitations mentioned earlier can be completely or partially overcome by having a structural imaging combined with SPECT. The combined SPECT/CT systems have become a common form of clinical SPECT scanners, and it is no wonder that preclinical SPECT/CT systems followed the trend [13]. Magnetic resonance imaging (MRI) integration with SPECT is also an interesting area for discussion [14]; but this chapter focuses only on the SPECT/CT in preclinical settings.

An X-ray computed tomography (CT) has been available in small animal imaging applications in parallel with most other noninvasive imaging modalities. A microfocus X-ray tube producing X-ray current on the order of 1 mA at 50 kVp (50 Watt) and an X-ray detector such as a charge-coupled device (CCD) or a complementary metal oxide semiconductor (CMOS) usually comprise a small animal CT scanner. Combined with SPECT, small animal SPECT/CT systems acquire SPECT radionuclide data and CT X-ray data mostly sequentially without moving an animal from the bed, which benefits to in vivo animal studies that often require a gas anesthesia system with often bulky gas delivery plumbing fixtures. For the sequential imaging, the bed movement is minimal or translational only when required. By performing a sequential imaging of SPECT and CT at known positions, coregistration between the two imaging modalities can be achieved by rigid transformation assuming the animal is stationary during both imaging sequences. Besides, image units in CT can be also converted to energy-dependent linear attenuation coefficients useful for attenuation correction in SPECT reconstruction [15, 16]. There is also a potential use of CT information to model scatter components in SPECT reconstruction. Figure 12.1 illustrates the significance of CT-based attenuation correction even for a small size object (approximately one inch across) when a low-energy gamma emitter like iodine-125 is used for SPECT studies.

CT provides details of small animal anatomies with reconstruction resolutions in the range of 10–200 μm, and the details can be enhanced by either conventional clinical iodinated contrast media or animal-specific iodinated contrast materials [17]. With CT providing both the attenuation coefficients and anatomical details, small animal SPECT/CT is more visually pleasing than standalone SPECT systems, and is capable of providing accurate tracer localization and quantification which are desirable characteristics for drug and new tracer evaluation processes using noninvasive preclinical imaging [18]. The resolution requirements from CT vary depending on how much anatomical details are needed in SPECT investigations. For example, if attenuation correction is the only use of CT, the resolution of CT can be as poor as the typical resolution of SPECT, ~1 mm full-width at half-maximum (FWHM). In contrary, when a full anatomic detail is essential in SPECT/CT investigations of small animals, even 10–20 μm spatial resolution with contrast enhancement is marginal.

Although the promises of preclinical SPECT/CT are strong and implementations in system instrumentations seem straightforward assuming both preclinical SPECT and CT are separately mature technologies, there are still inherent issues when combining the two systems together. These issues are not negligible in most applications, and occasionally application and animal specific.

– Coregistration between SPECT and CT: In preclinical SPECT systems, convergent collimation geometries such as pinholes or multipinholes are of a common use. The convergent geometry introduces imaging magnification or minification of the object so that applying reconstruction algorithms needs inputs from collimator geometries. In addition, the projection data for both preclinical SPECT and CT are collected typically in a cone-beam geometry which also introduces other geometry complications that include cone-beam artifacts and image truncation issues. As a result, the geometry defined in preclinical SPECT/CT needs

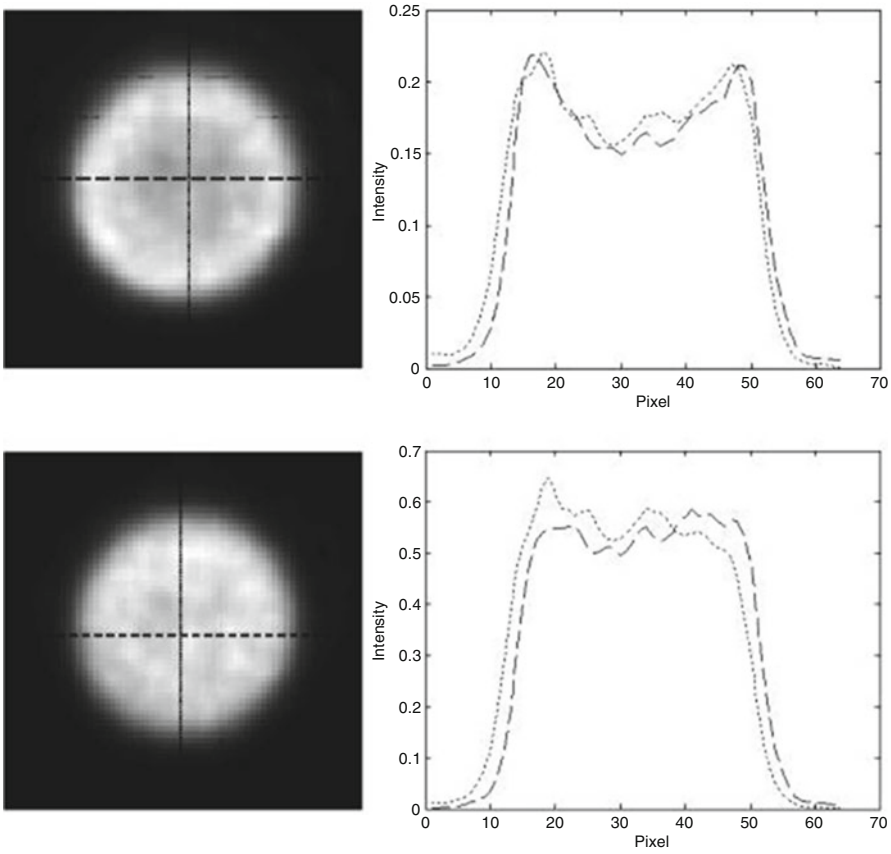

Fig. 12.1 Photon attenuation corrected reconstruction versus uncorrected reconstruction using a uniform cylindrical phantom filled with iodine-125 solution (Reprinted with permission from [6])

a coregistration strategy that includes adjustments for complex geometries from reconstructed SPECT and CT images.

– Temporal resolution difference between SPECT and CT: Surprisingly, currently available preclinical CT scanners on the market do not yet provide a very fast multidetector CT acquisition capability except for very few products or prototypes. What is not surprising is that still the data acquisition of preclinical CT even on the current market, typically in the range of 1–10 min to achieve approximately 150 μm in-plane spatial resolution, is faster than that of preclinical SPECT. This difference in temporal resolutions does not always cause serious problems when CT is only used for anatomic localization of radiotracer or attenuation map generation. A more serious problem is that the preclinical CT using small animal models suffers motion-related spatial resolution degradation, resulting in blurred CT images because the breathing of the animal model induces a non-negligible movement during the CT acquisition. In a volume where SPECT radiotracer localization can potentially benefit greatly from anatomical details

such as brain and thorax, the anatomy provided by CT can be less valuable in determining precise location of radiotracer concentrations.

– Approaches to prospective gating in SPECT and CT: The two common gating strategies to reduce any motion-related image artifacts using electrocardiogram (ECG) or respiratory signals are implemented and can be used in both preclinical SPECT and CT studies [19, 20]. The caveat of performing either ECG-gated or respiratory-gated SPECT/CT studies is the degradation of temporal resolution for both imaging modalities. Without significant innovations for which some of implementable technologies are mentioned in other chapters, the total image acquisition time could be very impractical considering the speed of both SPECT and CT in preclinical settings and the small amount of radiotracer that can be administered without altering the biology of given studies (e.g., radiation-related carcinogenesis) [21].

3 Historical Perspective on Dual-Modality Preclinical SPECT/CT Developments

Similarly to its human scale version, a pioneering work on developing a dual-modality preclinical SPECT/CT system was first conducted at the University of California, San Francisco (UCSF) in early 2000 [22–26]. However, the development of the full scale preclinical SPECT/CT scanner from the UCSF project had been plagued by complications of the system design and novelty of the technology. The system was actually built (shown in Fig. 12.2), and evaluated for small animal SPECT/CT studies. Although the details of technical design considerations will be discussed in the following section for this scanner, notable features include the slip-ring gantry that enables continuous rotations of SPECT and CT and the use of a solid-state detector material (CdZnTe or CZT) for the SPECT module.

During this period of developments, Gamma Medical-Ideas went ahead with commercialization of preclinical SPECT/CT system combining its A-SPECT preclinical scanner with a CMOS-based X-ray CT subsystem in a scanner gantry rotating around a horizontal axis [27]. After the success of this commercial platform, most of other commercial vendors and academic researchers started to offer or build other preclinical SPECT/CT systems.

4 Design Considerations of Dual-Modality Preclinical SPECT/CT

The following list is a list of implemented dual-modality preclinical SPECT/CT systems. Although this list probably does not include all of the systems developed or being developed, key features that are generally applicable to any other developments of the combined SPECT/CT system are mentioned for each development. Also, the status of the development, either research or commercial, is indicated for each system. Some different flavors of SPECT/CT integrations are depicted in Fig. 12.3.

Fig. 12.2 UCSF MoHawk SPECT/CT scanner with two CZT-based pinhole SPECT cameras and X-ray cone-beam CT subsystem placed on a disk-gantry attached to a slip-ring (*left*). This system is designed to mount up to four pinhole/multipinhole CZT-based gamma cameras with a retractable in-plane microfocus CT (*right*) built on the same disk-gantry

4.1 University of California, San Francisco (Research)

The preclinical SPECT/CT scanner built at UCSF is also known as MoHawk ("Mo"use "Hawk"eye) named after the Hawkeye technology from GE Healthcare's clinical SPECT/CT products for which the UCSF group contributed significantly in its original innovation. The key features of the MoHawk SPECT/CT are:

- SPECT/CT integration type: In-plane,
- Helical scan capability: Both imaging modalities (continuous rotation),
- SPECT detector material: CdZnTe,
- CT detector material: GOS (gadolinium oxysulfide)/CCD,
- Collimators: single pinholes down to 0.5 mm diameter,
- Other notable features: Slip-ring platform and a large disk-shape optical table for mounting scalable CT and SPECT components.

4.2 Gamma Medica-Ideas, Inc. (Commercial)

The first preclinical integrated SPECT/CT scanner was from Gamma Medica-Ideas' X-SPECT™ that combined their NaI(Tl)-based LumaGEM® gamma camera with a microfocus conebeam X-ray CT scanner (X-O™). As of June 2009, Gamma Medica-Ideas has a product line FLEX Triumph™ preclinical platform that can consist of a combination of SPECT, CT, and PEt all in one platform.

Fig. 12.3 Different flavors of preclinical SPECT/CT integration. (**a**) Compact box system that includes both small FOV X-ray CT and SPECT components from University of Arizona (Reprinted with permission from [28]). (**b**) An inside view drawing of Gamma Medica-Idea's FLEX Triumph™ gantry that shows the triple-modality (SPECT–CT–PET) configuration. (**c**) Another triple-modality configuration of a large gantry design with sufficient room around the scanner components (Siemens Inveon Multimodality gantry). (**d**) Docked SPECT/CT configuration–U-SPECT/CT from MILabs (figures of (**b**–**d**) are from product brochures)

The key features of Gamma Medica-Ideas' preclinical multimodality imaging systems for SPECT/CT offering are (from http://www.gm-ideas.com/):

- SPECT/CT integration type: In-plane,
- Helical scan capability: Spiral SPECT, but not continuous rotation over one spiral,
- SPECT detector material: NaI(Tl) or CdZnTe,
- CT detector material: GOS/CMOS,

– Collimators: parallel hole, single pinholes, multipinholes with different fields of view (FOVs) for mice and rats separately,
– Other notable features: Offered as the triple modality (SPECT–PET–CT) configuration.

4.3 University of Arizona (Research)

University of Arizona's Center for Gamma-Ray Imaging has had a long history of gamma imaging technology developments. Based on their enormous resources and accumulated expertise, a combined SPECT/CT system for small animal imaging applications was developed with a focus on its compact design [28]. The key features for this compact SPECT/CT system are:

– SPECT/CT integration type: In-plane,
– Helical scan capability: No,
– SPECT detector material: CdZnTe,
– CT detector material: GOS (gadolinium oxysulfide)/CCD,
– Collimators: high resolution parallel-hole with a matching pitch on detector pixels,
– Other notable features: Compact size (79 cm × 48 cm × 46 cm outside box dimension) and rotation stage (vertical animal holder).

4.4 Jefferson Lab and Johns Hopkins University (Research)

There are two generations of the preclinical SPECT/CT development from the group from Jefferson Lab and University of Virginia in collaboration with Johns Hopkins University [29, 30]. Their original system was configured to be a triple-modality that had an option of adding an optical imaging component to SPECT/CT. The current generation of their preclinical SPECT/CT system is based on a modified Siemens MicroCAT II gantry. The key features of the current generation system design are:

– SPECT/CT integration type: In-plane,
– Helical scan capability: No,
– SPECT detector material: NaI(Tl)-PSPMT (position sensitive photomultiplier tube),
– CT detector material: CsI/CCD,
– Collimators: parallel-hole and pinholes,
– Other notable features: Currently configured to image awake mice using infrared tracking system for animal motion.

4.5 Siemens Medical Solutions (Commercial)

Siemens at its Knoxville, Tennessee facility has developed a high-end line of preclinical imaging systems with a universal platform line named as Inveon. The Inveon Multimodality (MM) can be built as a triple-modality (PET–CT–SPECT) configuration on a single gantry [31]. The key features of Siemens preclinical SPECT/CT configured in the Inveon MM gantry are:

- SPECT/CT integration type: In-plane
- Helical scan capability: No
- SPECT detector material: NaI(Tl)-PSPMT (position sensitive photomultiplier tube)
- CT detector material: GOS/CCD
- Collimators: parallel-holes, single pinholes, and multipinholes
- Other notable features: The Inveon MM can be configured as a triple modality system (SPECT and CT in-plane and PET module next to it).

4.6 Bioscan and MILabs (Commercial)

Bioscan's NanoSPECT and MILabs' U-SPECT II are both multipinhole SPECT systems that provide stationary acquisition modes and very high spatial resolution of SPECT imaging. Unlike other preclinical SPECT/CT systems described above, these two SPECT scanners are also offered as SPECT/CT systems (NanoSPECT/CT and U-SPECT/CT) with a docked or serial configuration combining two separate SPECT and CT modules attached together. The docked or serial configuration is different in many ways from the other SPECT/CT systems described above. The most notable difference is that the in-plane SPECT/CT systems (all systems except Bioscan or MILabs systems) have a stationary animal bed during both SPECT and CT acquisitions. The docked or serial configuration by Bioscan or MILabs systems needs an animal bed that translates between two imaging modalities. Besides, the docked configuration applied to U-SPECT/CT (MILabs) has one clear advantage when separate operations of SPECT and CT are fully utilized for independent applications that do not need both imaging capabilities.

5 Applications of Dual-Modality Preclinical SPECT/CT

The specific applications that absolutely need dual-modality preclinical SPECT/CT systems simultaneously are actually rare. However, the addition of CT to SPECT for the benefits described above makes most SPECT studies more quantitative, easier to the eyes, and provides more confidence in their interpretations than when standalone preclinical SPECT systems are utilized.

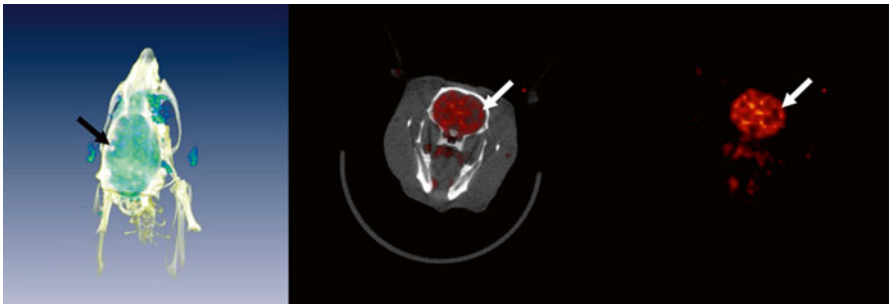

Fig. 12.4 SPECT and CT images obtained from a rat brain imaging study using ^{99m}Tc-exametazime [35]. The rat model of ischemic stroke was imaged by Gamma Medica-Idea's FLEX X-SPECT/X-O system. From *left* to *right*: 3D volume rendered SPECT and CT images fused together, transaxial view of SPECT–CT images, and transaxial SPECT-only image. *Arrows* indicate the hypoperfusive area affected by regional cerebral blood flow

5.1 Drug Discovery and Evaluation

SPECT/CT for drug discovery and evaluation has a significant potential because SPECT/CT is one of few strategies toward quantitative SPECT evaluations of new drug candidates. In this application, tracer quantification is the most essential because in vivo animal imaging with a new drug candidate can be quantified from SPECT reconstructed images without sacrificing animal models at many different time points for biodistribution studies. Technically, when quantitative accuracy of SPECT reconstruction is robust and reliable, a pharmaceutical's concentration (in unit of mg/ml) estimation is feasible, and has a possibility of accelerating the drug evaluation process [18].

5.2 Neurological Applications

Although brain imaging using SPECT in small animals is often conducted [32, 33], there is little use of preclinical CT for neurological applications. In addition, the CT addition to SPECT reconstruction for brain sometimes minimally useful because the brain anatomy is easily identifiable from SPECT-only studies. For example, cerebral blood flow studies using ^{99m}Tc-exametazime SPECT in animal models (as shown in Fig. 12.4). However, neurological applications demand the highest-possible spatial resolution; thus controlling the movement of small animal heads during both SPECT and CT is important to achieve best possible image resolution. One way to maximize spatial resolution in brain imaging using SPECT and CT in small animal models is to use a X-ray-transparent stereotactic device to fix the movement of animal heads during acquisitions [34]. With help of iodinated contrast agent, small animal

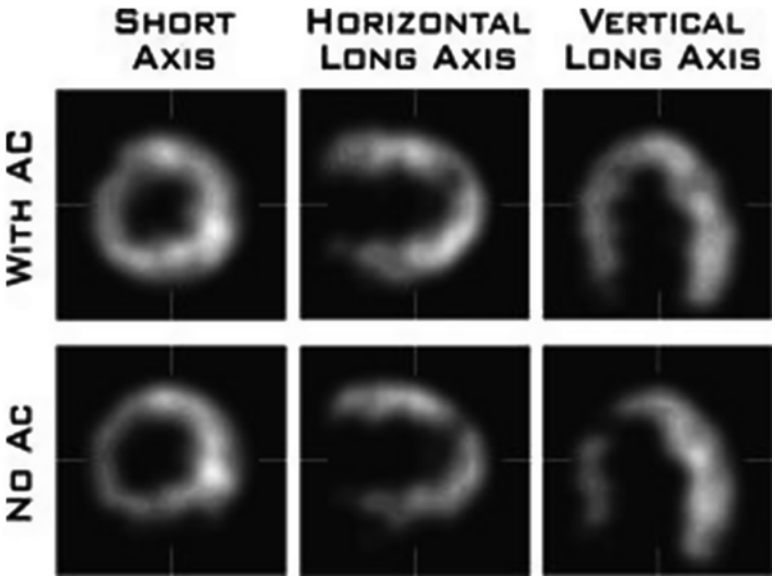

Fig. 12.5 Reconstructed SPECT images with CT-based attenuation correction (*above*) and without AC (*bottom*) visualizing the heart of a normal rat. The imaging agent was iodine-125-labeled iodorotenone, myocardial perfusion imaging agent (Reprinted with permission from [6])

brain CT for cerebrovascular investigation can be combined with brain SPECT applications using a combined preclinical SPECT/CT scanner [35].

5.3 Cardiovascular Applications

Cardiovascular SPECT using small animal models is an emerging and ever-evolving field [36, 37]. Cardiovascular CT using small animal models also witnesses the same enthusiasm from researchers. The motion of the animal's thorax, where the heart sits, is what makes the biggest influence on cardiovascular investigations. Controlling organ motion by ECG or respiratory gating is often another complication of the use of SPECT/CT imaging systems in cardiovascular applications. Prospective ECG/respiratory gating strategies for both systems are desired in quantitative evaluations of cardiovascular disease processes in small animal models.

CT-based attenuation correction (AC) for preclinical SPECT studies also can make a difference in the appearance of SPECT reconstructed images. An example to elucidate the impact of CT-based AC is shown in Fig. 12.5. As in this figure, myocardial perfusion imaging agent radiolabeled with iodine-125 without attenuation correction could lead to false positive reading of perfusion deficit where photon attenuation diminishes image intensity.

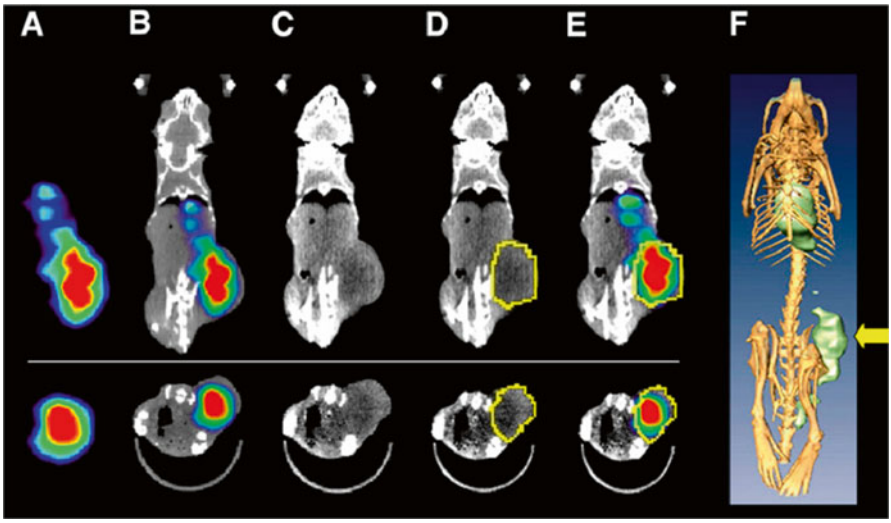

Fig. 12.6 Small animal SPECT/CT in an oncologic preclinical application. Coronal (*top*, **a–e**) and transaxial (*bottom*, **a–e**) are shown. The colored superimposed images are from SPECT, and the *black* and *white* images are from CT. (**f**) depicts 3D rendered volumes simultaneously showing SPECT and CT images (Reprinted with permission from [13])

5.4 Oncologic Applications

In oncologic applications, having SPECT/CT capability in preclinical studies is potentially significant because CT guides exact anatomical localization of uptake of SPECT oncologic agents, and provides a gateway to tracer quantification [24, 38]. Figure 12.6 elucidates this point. The tracer distribution seen by SPECT using prostate specific membrane antigen (PSMA) targeting 7E11 antibody radiolabeled with indium-111, pinpoints tracer accumulation in mouse xenograft model (LNCaP) [39]. CT overlay images provide means to delineate the tumor boundaries for tracer uptake quantification.

6 Perspectives on Future Developments

The progress on advanced SPECT/CT preclinical systems is dependent on technological advances on each modality independently. The integration of SPECT and CT will hardly change because there are benefits for both in-plane or side-by-side configurations, and few other configurations are practical. However, one should note that cost-effective rail- or track- based modular imaging systems for SPECT/CT using existing standalone SPECT and CT scanners can be also realized although this approach should be not confused with integrated SPECT/CT systems.

This approach has been implemented using clinical systems [40] as well as small animal systems [41]. Commercializations of emerging technologies such as use of solid-state detectors like CZT will also depend on the progress of each imaging modality separately. The progress of the field itself is expected to be centered around biological applications of the systems. One example is that MRI integration of SPECT may provide better anatomical reference of SPECT studies because of high soft-tissue contrast provided by MRI over CT. In small animal applications, this combination may prove a wider spectrum of applications than its human version because the FOV from both SPECT and MRI can be implemented sufficiently large to cover the whole animals.

Acknowledgments This work was partially supported by National Cancer Institute Grant #5K25 CA114254 (Y.S.), and by the University of California Industry-University Cooperative Research Program Grant dig 06–10210 (C.M.A.).

References

1. Beekman F, van der Have F (2007) The pinhole: gateway to ultra-high-resolution three-dimensional radionuclide imaging. Eur J Nucl Med Mol Imaging 34:151–161.
2. Zeniya T, Watabe H, Aoi T, Kim KM, Teramoto N, Takeno T, et al. (2006) Use of a compact pixellated gamma camera for small animal pinhole SPECT imaging. Ann Nucl Med 20:409–416.
3. Vastenhouw B, Beekman F (2007) Submillimeter total-body murine imaging with U-SPECT-I. J Nucl Med 48:487–493.
4. van der Have F, Vastenhouw B, Rentmeester M, Beekman FJ (2008) System calibration and statistical image reconstruction for ultra-high resolution stationary pinhole SPECT. IEEE Trans Med Imaging 27:960–971.
5. Nuyts J, Vunckx K, Defrise M, Vanhove C (2009) Small animal imaging with multi-pinhole SPECT. Methods 48:83–91.
6. Hwang AB, Hasegawa BH (2005) Attenuation correction for small animal SPECT imaging using x-ray CT data. Med Phys 32:2799–2804.
7. Panetta D, Belcari N, Baldazzi G, Carpentieri C, Cicalini E, Del Guerra A, et al. (2007) Characterization of a high-resolution CT scanner prototype for small animals. Nuovo Cimento B 739–747.
8. DiFilippo FP (2008) Design and performance of a multi-pinhole collimation device for small animal imaging with clinical SPECT and SPECT-CT scanners. Physics in Medicine and Biology 53:4185–4201.
9. Wieczorek H (2007) SPECT image quality and quantification. 2006 IEEE Nuclear Science Symposium Conference Record (IEEE Cat. No.06CH37832):5–5.
10. Chen CL, Wang Y, Lee JJ, Tsui BM (2009) Toward quantitative small animal pinhole SPECT: assessment of quantitation accuracy prior to image compensations. Mol Imaging Biol 11:195–203.
11. Funk T, Despres P, Barber WC, Shah KS, Hasegawa BH (2005) A high efficiency small animal imaging system based on position sensitive avalanche photodiodes. Proceedings of the SPIE - The International Society for Optical Engineering 5923:1–9.
12. Boutchko R, Balakrishnan K, Reutter BW, Sauve A, Gullberg GT (2007) Small animal imaging with attenuation correction using clinical SPECT/CT scanners. 2007 IEEE Nuclear Science Symposium Conference Record 4294–4295.
13. Franc BL, Acton PD, Mari C, Hasegawa BH (2008) Small-animal SPECT and SPECT/CT: important tools for preclinical investigation. J Nucl Med 49:1651–1663.

14. Goetz C, Breton E, Choquet P, Israel-Jost V, Constantinesco A (2008) SPECT low-field MRI system for small-animal imaging. Journal of Nuclear Medicine 49:88–93.
15. Vanhove C, Defrise M, Bossuyt A, Lahoutte T (2009) Improved quantification in single-pinhole and multiple-pinhole SPECT using micro-CT information. Eur J Nucl Med Mol Imaging 36:1049–1063.
16. Zaidi H, Hasegawa B (2003) Determination of the attenuation map in emission tomography. J Nucl Med 44:291–315.
17. Badea CT, Fubara B, Hedlund LW, Johnson GA (2005) 4-D micro-CT of the mouse heart. Mol Imaging 4:110–116.
18. Seo Y (2008) Quantification of SPECT and PET for drug development. Curr Radiopharm 1:17–21.
19. Vandehei T, Li J, Iwata K, Patt BE, Caravaglia G, Hartsough NE, et al. (2004) Gated cardiac SPECT in rodents using a dedicated SPECT system: X-SPECT. Proceedings of the SPIE 5541:165–170.
20. Tsui BMW, Segars WP, Lalush DS (2000) Effects of upward creep and respiratory motion in myocardial SPECT. IEEE Transactions on Nuclear Science 47:1192–1195.
21. Funk T, Mingshan S, Hasegawa BH (2004) Radiation dose estimate in small animal SPECT and PET. Medical Physics 31:2680–2686.
22. Iwata K, Wu MC, Hasegawa BH (1999) Design of combined x-ray CT and SPECT systems for small animals. 1999 IEEE Nuclear Science Symp/Medical Imaging Conf.,Seattle, WA, vol. 3, pp. 1608–1612.
23. Izaguirre EW, Sun M, Carver J, Thompson S, Hasegawa BH (2005) Dual modality micro-SPECT and micro-CT for small animal imaging: technical advances and challenges. Proceedings of the SPIE 5923:59230C.
24. Izaguirre EW, Mingshan S, Drummond DC, Kirpotin DB, Funk T, Thompson S, et al. (2006) SPECT-CT study of directed drug delivery using sup 111/In-labeled liposomes in a murine mammary carcinoma model. 2005 IEEE Nuclear Science Symposium Conference Record (IEEE Cat. No.05CH37692C):4–4.
25. Sun M, Izaguirre EW, Funk T, Hwang AB, Carver J, Thompson S, et al. (2006) A small animal helical SPECT scanner. 2005 IEEE Nuclear Science Symposium Conference Record (IEEE Cat. No.05CH37692C):2066–2069.
26. Sakdinawat AE, Iwata K, Hwang AB, Tang HR, Wong KH, Hasegawa BH (2003) Development of external fiducial markers for image registration in small animal SPECT/CT. 2002 IEEE Nuclear Science Symposium Conference Record (IEEE Cat. No.02CH37399) 2:842–845.
27. Iwata K, MacDonald LR, Li J, Williams SP, Sakdinawat AE, Hwang AB, et al. (2002) Dual isotope imaging with a dedicated small animal CT-SPECT system. Mol Imaging Biol 4:S21.
28. Kastis GA, Furenlid LR, Wilson DW, Peterson TE, Barber HB, Barrett HH (2004) Compact CT/SPECT small-animal imaging system. IEEE Trans. Nucl. Sci. 51:63–67.
29. Stolin A, Pole D, Majewski S, Kross B, Weisenberger A, Wojcik R, et al. (2005) Design and characteristics of a small animal multi-modality scanner. 2005 IEEE Nuclear Science Symp/ Medical Imaging Conference Record 2183–2186.
30. Weisenberger A, Kross B, Majewski S, Popov V, Smith MF, Tran VH, et al. (2006) Instrumentation development of a SPECT-CT system to image awake mice. 2006 IEEE Nuclear Science Symp/Medical Imaging Conf.,San Diego, CA, vol. pp. 3000–3003.
31. Gleason SS, Austin DW, Beach RS, Nutt R, Paulus MJ, Yan S (2006) A new highly versatile multimodaltiy small animal imaging platform. 2006 IEEE Nuclear Science Symp/Medical Imaging Conf.,San Diego, CA, vol. pp. 2447–2449.
32. Bal H, Thomas D, Zixiong C, Ferrari V, Horowitz J, Acton PD (2006) A novel method for the estimation of infarct size in a reperfused rat model for pinhole SPECT. 2005 IEEE Nuclear Science Symposium Conference Record (IEEE Cat. No.05CH37692C) 4–4.
33. Zixiong C, Bal G, Accorsi R, Acton PD (2005) Optimal number of pinholes in multi-pinhole SPECT for mouse brain imaging-a simulation study. Physics in Medicine and Biology 50: 4609–4624.

34. Seo Y, Hashimoto T, Nuki Y, Hasegawa BH (2008) In vivo microCT imaging of rodent cerebral vasculature. Phys Med Biol 53:N99–107.
35. Seo Y, Gao DW, Hasegawa BH, Dae MW, Franc BL (2007) Rodent brain imaging with SPECT/CT. Med Phys 34:1217–1220.
36. Acton PD, Thomas D, Zhou R (2006) Quantitative imaging of myocardial infarct in rats with high resolution pinhole SPECT. International Journal of Cardiovascular Imaging 22:429–434.
37. Zhou R, Thomas DH, Qiao H, Bal HS, Choi SR, Alavi A, et al. (2005) In vivo detection of stem cells grafted in infarcted rat myocardium. Journal of Nuclear Medicine 46:816–822.
38. Muller C, Forrer F, Schibli R, Krenning EP, de Jong M (2008) SPECT study of folate receptor-positive malignant and normal tissues in mice using a novel sup 99m/Tc-radiofolate. Journal of Nuclear Medicine 49:310–317.
39. Pan MH, Gao DW, Feng J, He J, Seo Y, Tedesco J, et al. (2009) Biodistributions of 177Lu- and 111In-labeled 7E11 antibodies to prostate-specific membrane antigen in xenograft model of prostate cancer and potential use of 111In-7E11 as a pre-therapeutic agent for 177Lu-7E11 radioimmunotherapy. Mol Imaging Biol 11:159–166.
40. Bailey DL, Roach PJ, Bailey EA, Hewlett J, Keijzers R (2007) Development of a cost-effective modular SPECT/CT scanner. Eur J Nucl Med Mol Imaging 34:1415–1426.
41. Beekman F, Hutton BF (2007) Multi-modality imaging on track. Eur J Nucl Med Mol Imaging 34:1410–1414.

Chapter 13
Dual-Modality Preclinical PET/CT Instrumentation

Andrew L. Goertzen and Habib Zaidi

1 Introduction

In vivo molecular imaging techniques, such as positron emission tomography (PET) utilize imaging probes that are targeted to specific biochemical pathways, bind to specific receptors, or that accumulate in a specific fashion in cells expressing particular genes or proteins. The use of these imaging probes and techniques in vivo has enabled the non-invasive, longitudinal study of animal models of human disease, allowing each animal to serve as its own control, reducing experimental uncertainty. The use of longitudinal imaging of a single animal is particularly important for studying animal models of disease that have variable time of onset and degree of severity, such as metastatic cancer models or diseases with genetic causes. The power of preclinical PET imaging to enable non-invasive imaging of molecular level processes has led to a growing market for preclinical PET cameras and its widespread use in basic medical research.

An unavoidable limitation of in vivo PET imaging is that the high specificity of many of the positron-emitting radiopharmaceuticals (PERs) used results in images that have little anatomical information available and thus can be difficult to interpret. The integration of PET with an anatomical imaging technique provides an obvious solution to this problem by providing a high resolution subject specific anatomical map that is automatically coregistered with the functional PET image.

A.L. Goertzen (✉)
Department of Radiology, University of Manitoba, Winnipeg, MB, Canada
e-mail: Andrew.Goertzen@med.umanitoba.ca

H. Zaidi
Department of Radiology & Medical Informatics, Geneva University Hospital, Geneva, Switzerland
e-mail: habib.zaidi@hcuge.ch

H. Zaidi (ed.), *Molecular Imaging of Small Animals: Instrumentation and Applications*,
DOI 10.1007/978-1-4939-0894-3_13,

Beyond the advantage of facilitating interpretation this anatomical map can also be used to enhance the accuracy of the PET data by acting as an input for correction algorithms such as attenuation, scatter, and partial volume. The obvious synergy of functional and anatomical imaging modalities has led to significant interest in the development of multimodal imaging systems for preclinical imaging applications, with research groups working on combining PET with X-ray computed tomography (CT), PET with magnetic resonance imaging (MRI), single photon emission computed tomography (SPECT) with CT, SPECT with MRI, and even PET and SPECT with CT. This rapid expansion in multimodality preclinical imaging systems has been enabled by the maturing of dedicated preclinical imaging systems and an increasing demand from researchers using animal models for combined functional and anatomical imaging. Another key factor in the push for preclinical dual-modality imaging systems was the introduction of dual-modality clinical PET/CT imaging in the late 1990s [1]. Clinical PET/CT has proved so successful that virtually all new clinical PET cameras installed today are hybrid PET/CT devices.

X-ray CT has several distinct advantages as a complementary anatomical imaging technique for use in combination with PET. Firstly, the image formation process is based on measuring the attenuation of energetic X-ray photons in the object being imaged so that the resultant image has intensity proportional to the attenuation properties of the material in the image voxel. This image formation process makes CT images well suited for use in attenuation correction of PET images since the μ values measured with the lower energy X-ray beam can be scaled to the respective values at the 511 keV PET photon energy. This is in sharp contrast to MRI, where the image intensity is not related to the attenuation properties of the object, making the generation of MRI based attenuation corrections for PET a challenging problem. Secondly, there is not a fundamental incompatibility between standard PET and CT imaging hardware in the same way that there is with photomultiplier tube (PMT) based PET detectors and MRI systems. This greatly simplifies the integration of PET and CT imaging techniques. Finally, preclinical CT imaging has advanced to the point where scanning times can be relatively short as compared to the time required for PET imaging. The additional time required to generate a high quality CT image can thus be much shorter than the time required to measure an attenuation map on the PET system using an external radioisotope source such as ^{68}Ge or ^{57}Co.

In this chapter we will examine the development of preclinical PET/CT imaging systems from bench-top prototype to commercial product. We will then examine current approaches to PET/CT imaging and examine the benefits and problems associated with each method. Applications of dual-modality PET/CT imaging will be explored and finally we will look at future directions in preclinical PET/CT imaging.

2 Development of Preclinical PET/CT Systems

In the past decade preclinical PET/CT instrumentation has undergone a rapid evolution from laboratory bench-top prototype to fully integrated, commercially produced system. This evolution been driven by a maturing of the technology behind animal

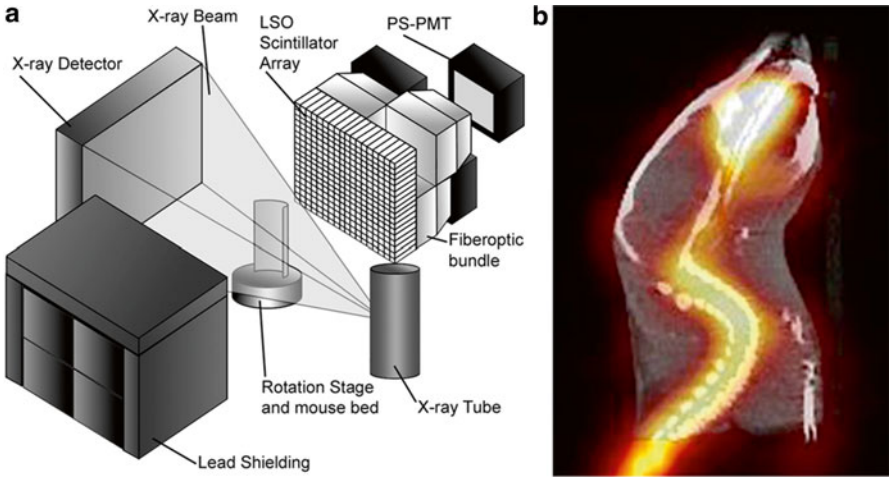

Fig. 13.1 Example of prototype PET/CT system. (**a**) Schematic of coplanar PET and CT systems and vertically positioned mouse bed. (**b**) PET/CT scan of a mouse following 18F- administration. Adapted with permission from [31]

imaging systems, advancements in software for data handling and processing, and a consolidation in the preclinical imaging system industry so that manufacturers came to include expertise in both PET and CT in the same company. The potential for combining PET with an anatomical imaging technique was recognized early in the development of dedicated preclinical tomographs. In the mid-1990s, dedicated preclinical CT systems did not exist yet, so work on dual-modality systems focused on developing MRI compatible PET systems [2–5] that could fit within the bore of a clinical 1.5 T MRI system. This early work, while demonstrating the feasibility of multimodality imaging, did not immediately translate into practical use due to the highly limited field of view (FOV) of the single slice PET systems developed for this purpose and the need for utilizing a clinical MRI system.

By the late 1990s there were two developments in preclinical imaging instrumentation that would ultimately enable the preclinical PET/CT systems that would appear over the following decade. The first development was a focused research effort on development of animal PET cameras that led to the creation of a number of prototype imaging PET systems [6–14] and was followed shortly after by the commercial availability of systems based on these designs [15–20]. The second key development was a similar effort on developing preclinical CT systems [21–27] that ultimately led to the availability of a number of commercial preclinical CT systems [28–30]. We refer the reader to Chaps. 5 and 6 for discussions of the development of these systems. With viable hardware existing for both preclinical PET and CT systems, work could begin on integrated dual-modality imaging systems.

By the early 2000s a number of groups were actively working on developing approaches to achieve dual-modality preclinical PET/CT imaging. At the time, access to commercially produced imaging systems was still very limited so that centres with both a PET and CT system for animal imaging were rare. Development work thus focused on constructing proof of principle devices [31] such as that shown in Fig. 13.1.

At the time, CT acquisitions required 10–15 min due to the slow readout rate of the detectors used so simultaneous acquisition strategies were seen as viable despite the inherent compromise in PET imaging performance due to the required shielding for scattered X-rays. These devices demonstrated the possibility for PET/CT imaging but similar to early PET/MRI devices, were not practical for high throughput in vivo imaging situations as they were generally bench-top devices which featured vertically oriented mouse beds [22, 31]. As commercially produced preclinical PET and CT systems became more widespread, development work shifted to integration of stand-alone PET and CT systems [32–34] with the two systems being arranged in a coaxial manner so that the bed with the animal could be passed through the FOV of each system. An alternative approach was to develop an animal bed that would hold the mouse in a stable position and could be moved between the PET and CT system [35, 36]. The increasing reliability of the data collected through these approaches allowed work on software that could make use of the multimodality nature of the data.

Due to the long X-ray exposure times routinely used in early preclinical CT systems a common concern was the magnitude of the radiation dose being delivered to the mouse. In PET/CT imaging, both imaging modalities deliver radiation dose to the subject unlike PET/MRI, where MRI does not use ionizing radiation. A fundamental goal of any in vivo imaging technique is to avoid the situation in which the imaging technique affects the process being followed. Early measurements by Paulus et al. [28] suggested that the dose from a screening CT scan could exceed 5 % of the LD50/30 values for radiation exposure in mice. The need for these high exposure levels was well described in an important paper by Ford et al. [37] in which the dose vs. image noise tradeoff for small image voxel sizes was described. Subsequent work to better characterize the radiation dose by Monte Carlo simulation [38–40] and thermoluminescent dosimeter (TLD) measurements [28, 38, 41–44] showed that the radiation dose to a mouse could be kept below 2 cGy for a screening CT scan such as one might expect to perform on a PET/CT system. At the same time researchers were becoming increasingly aware of the radiation dose delivered by PERs to the animals being imaged, with dosimetry calculations showing that tens of cGy could be delivered to a mouse from a PET study [45–48]. While these radiation exposures are an unavoidable consequence of using PET/CT techniques, researchers must be aware of them to ensure that the disease model under study is not being influenced by the imaging being employed.

3 Current Approaches to Preclinical PET/CT Imaging

3.1 Standalone PET and CT Systems with a Moveable Bed

With the increasing availability of both preclinical PET and CT in imaging centres there is a growing interest in performing sequential imaging studies with the two modalities and using software to register and fuse the images. This approach requires fixation of the animal being imaged to an imaging bed that can be moved between imaging systems so that there is no movement of the animal between the two studies [35, 49, 50].

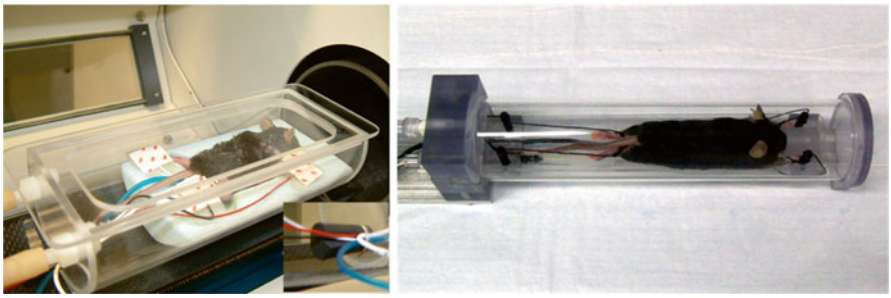

Fig. 13.2 Two examples of multimodality imaging beds designed for mouse imaging. Multimodality chamber compatible with PET, MRI, CT and optical imaging (*left*). Multimodality chamber designed for PET and CT imaging (*right*). Both devices feature built in restraint systems, gas anesthesia delivery lines, and leads for physiological monitoring. *Left* and *right panels* adapted with permission from [49] and [35], respectively

A simple rigid body registration is then sufficient for fusing the PET and CT images with sub millimeter accuracy [36]. Figure 13.2 shows two examples of this type of multimodality imaging bed designed specifically to be compatible with PET and CT imaging and Fig. 13.3 illustrates examples of preclinical data collected using this technique. Common features on beds of this design include a method to keep the animal in a stable position, built in gas anaesthesia delivery lines, leads for physiological monitoring equipment, a method of heating the animal to maintain body temperature, and fiducial markers visible with multiple imaging techniques to aid in image registration. An important additional design consideration for this type of bed is that the chamber can be sealed to maintain barrier conditions within the chamber, allowing animals to be imaged and then returned to the primary care facility. Several companies now offer commercial versions of these types of multimodality imaging beds [51, 52]. More refined immobilization devices were also suggested with registration accuracy in the order of 0.2–0.3 mm [53].

Using two standalone systems for multimodality imaging has several advantages over a single integrated device. In high throughput environments, two animals can be imaged at one time when two systems are used, as opposed to having one animal tie up both imaging modalities on an integrated device. The use of multiple imaging beds allows additional animals to be prepared for imaging while the camera systems are in use, thus minimizing the setup time normally associated with positioning an animal on the imaging bed at the start of a scan. Having two systems also allows for greater flexibility in upgrading and/or replacement of imaging systems since they can be treated independently. In addition, access to the animal being imaged is often better with this arrangement than in a single integrated unit. Among the advantages, perhaps the most significant is that there need be no compromise in the quality of the PET or CT system being used since they can be independently chosen from the best manufacturer for each type of system. Acquiring PET and CT images from two separate cameras does however require in-house expertise in data management in order to register and fuse the two image data sets [36, 54]. This requirement can be a limiting factor to implementing PET/CT imaging on two cameras at a smaller imaging centre.

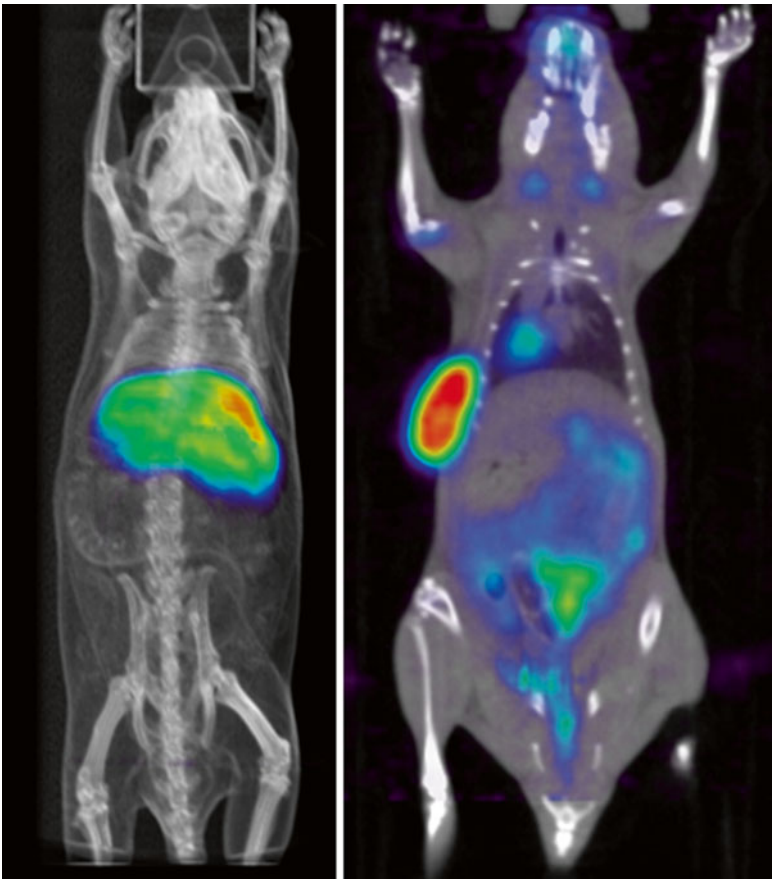

Fig. 13.3 Example of a projection image showing all the 3D data for a combined FDG-PET/CT scan of a tumor bearing mouse (*left*). Using this view, all parts of the data are visible as one image. Example of coronal view of a second FDG PET/CT image. Tomographic views enable detailed examination of all the image data on a slice by slice basis. Adapted with permission from [56]

Another drawback to this approach is that there can be shifting of the animal during movement between the two systems, leading to registration errors which lead to artifacts in the image due to errors data corrections such as attenuation [55].

3.2 Docking PET and CT Systems

Integration of PET and CT imaging into a single system can be accomplished by docking separate PET and CT systems together so that they share a common bed which passes through the FOV of both cameras. Docking type systems, such as the one shown in Fig. 13.4, have been developed by a number of research groups

Fig. 13.4 Photo of a docking-type PET–CT system constructed by combining a custom built micro-CT scanner (*left panel*) with a commercially produced Siemens microPET R4, shown together in the *right panel*. Reprinted with permission from [33]

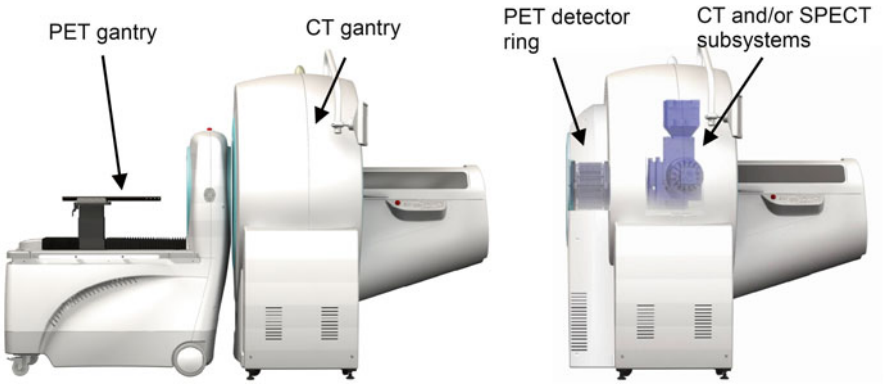

Fig 13.5 Example of preclinical commercially available PET/CT system, the Siemens Inveon, shown in docking format (*left*) which is comprised of stand-alone PET and CT systems docked together, and an integrated multimodality format (*right*). For clarity the internal component are shown schematically in the integrated system. Adapted with permission from [57]

[32–34] by combining either custom or commercially built PET and CT systems. These devices are commonly independently controlled by separate data acquisition consoles so that they can be separated and operated independently. At the present time, there is at least one commercially available system of this design [57] shown in Fig. 13.5. This approach to combined PET/CT imaging follows along the same path as the clinical implementation of PET/CT imaging, in which complete PET and CT systems are placed axially adjacent to each other [58].

A key advantage of a docked PET/CT system over independent PET and CT cameras is that the animal and imaging bed are not moved between the two scans, thus reducing errors and artifacts introduced by movement of the animal in between scans. Docked systems offer some degree of flexibility in choice of PET and CT system but are unlikely to be independently upgradeable with the same ease as for independent systems due to the requirement of needing systems from the same manufacturer.

3.3 Integrated PET/CT Imaging Systems

In the past 3 years, integrated preclinical PET/CT imaging systems have become commercially available. An example of such a system, the FLEX Triumph™ from Gamma Medica-Ideas (now commercialized by GE Healthcare) [59], features a complete ring PET system with an X-ray CT and optional semiconductor-based SPECT system. The FLEX system can be configured with either the RRPET/X-PET [60] or the LabPET™ [61] as a PET sub-system. Another example of this design is the Siemens Inveon Multimodality system [57, 62], shown in Fig. 13.5, which combines an Inveon PET system with an X-ray CT and optional SPECT system in a single gantry. Both of these systems are similar to the docked system design in that they incorporate a full ring high performance PET system with a high performance standard X-ray CT system placed axially adjacent to each other. This approach to combining PET and CT is the most technically challenging from a hardware point of view but is perhaps the simplest approach from an end user point of view since all imaging functions and corrections are implemented in a single machine. Integrating PET and CT into a single gantry has many of the same advantages of a docking system in that the animal does not need to be moved from one system to another but rather only the bed needs to be translated through the axial field of view of both cameras. In addition, these types of systems allow the user to set up and acquire a complete PET/CT protocol with minimal intervention between scans. The key benefit of this design is that the integration of the PET and CT data acquisitions can be transparent to the end user, simplifying the training of users and minimizing the data handling and processing infrastructure required to integrate the two imaging modalities.

While integrated systems have many benefits, they also have drawbacks. A common complaint of this type of system is that the long tunnel design of these systems can serve to limit access to the animal during an imaging study, making it difficult to perform dynamic PET studies that require an injection of the PER at the start of the study. This can be problematic for monitoring respiratory and ECG-gating signals, motion problems and can make blood sampling difficult or even impossible. Another key drawback of this type of system is that the PET and CT systems must come from a single manufacturer and the upgrade path is limited to devices that will fit within the existing gantry.

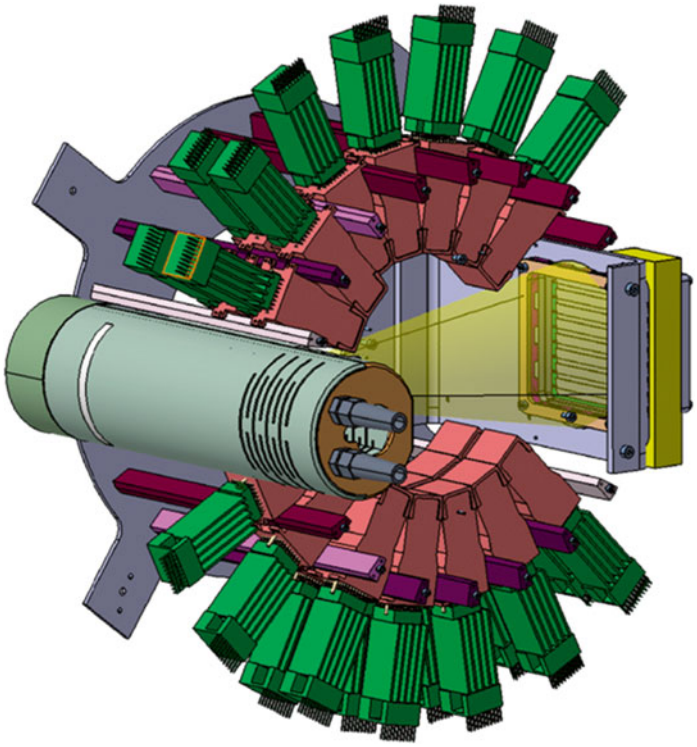

Fig. 13.6 Gantry design for a combined PET/CT system allowing simultaneous dual-modality imaging. Reprinted with permission from [64] (© 2007 IEEE)

More recently, several groups have developed novel dual-modality preclinical scanners with coplanar geometries that overcome some of the limitations imposed by the long axial tunnel length of other multimodality systems. An example of this type of system is the ClearPET/XPAD shown in Fig. 13.6 which combines a modified design of the ClearPET preclinical PET scanner [63] with the XPAD hybrid pixel X-ray detector to allow simultaneous dual-modality PET/CT imaging [64]. Due to the simultaneous acquisition of PET and CT data, an important consideration for this design is the shielding of PET detector blocks to prevent their saturation by the low energy scattered X-ray CT photons. Another design, the VrPET/CT [65] combines a partial-ring PET system and a small-animal CT assembled on a rotating gantry without axial displacement between the geometric centers of both fields of view. The PET subsystem performance characteristics were evaluated using the recently adopted NEMA NU-4 protocol [66]. Inter-modality alignment accuracy of less than half the PET system's spatial resolution (radial and tangential FWHM at the center were 1.48 and 1.88 mm, respectively) was reported. Unlike the ClearPET/XPAD system, the VrPET/CT is designed to acquire PET and CT data sequentially rather than simultaneously, thus removing the need for shielding the

PET detectors from the scattered X-rays. Both of these system designs use partial ring geometries for the PET system, thus requiring rotation of the PET detector ring to acquire full tomographic data which ultimately limits the minimum frame time for dynamic studies to the time required for a full rotation of the PET detector ring.

3.4 Preclinical PET/CT Using a Clinical System

A few studies involving preclinical imaging on large-bore clinical PET scanners, particularly for tumor-bearing mice, have demonstrated the need for the high resolution of dedicated small-animal PET units to enhance the detectability of small tumors [67, 68]. However, for some studies a clinical PET/CT camera can represent a viable alternative to dedicated preclinical instrumentation [69, 70]. For larger animal subjects, such as woodchucks [71] or larger primates, a dedicated animal system may be too small. Therefore, this is a plausible alternative for studies involving larger animals or for centers without animal imaging infrastructure. Dedicated high resolution brain PET scanners such as the High Resolution Research Tomograph (HRRT) [72] and many other designs [73] have also been widely used for preclinical and primate PET studies in many facilities. The recent availability of high resolution breast PET/CT scanners [74, 75] might also offer additional opportunities for laboratory animal imaging. Similar dual-use opportunities may exist for low-cost transformable PET cameras that can be configured into either a large-bore whole-body (e.g. 83 cm detector ring diameter, 13 cm axial field-of-view) or a smaller-bore brain/breast/axilla (54 cm detector ring diameter, 21 cm axial field-of-view) scanner [76].

The quantitative analysis of ^{124}I PET images of a small-animal phantom scanned on a clinical PET system revealed the viability of this approach for preclinical imaging [77]. One of the advantages is the ability to perform high-throughput studies to assess the performance of novel PET tracers in a timely and cost-effective manner by imaging many animals simultaneously. Promising tracers as judged by this screening technique can then be further assessed using conventional necropsy studies.

4 Integration of PET and CT Data

The advantages of improved image quality and quantitative accuracy that are available for clinical applications of dual-modality imaging also are being investigated as a means of facilitating biological research, especially those that involve small-animals such as mice and rats [78–80]. The arguments for combining multimodality data in the context of clinical imaging still hold for preclinical imaging where the potential advantages of combining anatomical and functional imaging have been well recognized by biomedical researchers. Multimodality molecular imaging has become an essential tool for the development of new tracers, to study the molecular

pathways of disease, including factors such as gene expression, in living subjects, and to test new therapeutic approaches in animal models of human disease. However, multi-modality imaging requires robust registration of images generated by various modalities. A substantial number of techniques have been proposed to achieve the goal of multimodal medical image registration [81, 82]. However, image registration algorithms widely used in clinical studies have not been well characterized in small-animal setting [83]. However, despite progress made during the last few years, many image registration problems particularly for small animal imaging remain unsolved, and this is likely to continue to be an active field of research in the future (see Chap. 10).

Preclinical molecular imaging has a long tradition of incorporating quantitative analysis in research protocols even when using non-standard nuclides where the problem becomes more complex owing to the concurrent emission of other gamma rays during the decay process [84]. Much worthwhile effort has been spent on the development of accurate models for improved quantification of molecular targets using combined PET/CT imaging (see Chap. 17). Several studies reported on the improvement of the quantitative capability of small-animal PET studies through accurate image correction strategies [85–90]. For example, Fahey et al. [85] reported that the microPET P4 scanner provides accurate quantitation to within 6 % for features larger than 10 mm. In addition, 60 % of object contrast was preserved for features as small as 4 mm. To take full advantage of the quantitative capabilities of PET imaging, data normalization [90–92] and object-specific correction of background (randoms) and physical degrading factors such as attenuation [54, 93–95], scatter [96–101], partial volume effect (PVE) [102, 103], and motion [104–106] must be performed prior to reconstruction or incorporated within advanced iterative image reconstruction techniques [107, 108]. Until recently, the analysis was based on functional or metabolic images as the sole input although the importance of the complementary information available from other anatomical modalities or from earlier scans has long been recognized. In addition, the visual quality and quantitative accuracy of small-animal imaging can be improved using anatomical imaging techniques to guide the reconstruction procedure [109, 110] and to correct the PET data for physical errors.

On the other hand, sophisticated kinetic modeling tools are needed to quantify physiological processes in vivo in basic science research investigations involving small-animal studies [111]. Absolute quantification using PET generally requires accurate measurement of activity concentrations in arterial blood, which provides the input function to the kinetic model used. Although many dedicated blood sampling devices have been specifically designed for this purpose (e.g. [112, 113]), this remains a challenging task in small-animal imaging.

The above referenced issues are reviewed in detail in Chap. 17 of this volume and will not be discussed here except for a brief discussion of the photon attenuation problem owing to the impact of combined PET/CT systems on attenuation correction. Photon attenuation is recognized as one of the major issues impacting image quality and quantitative analysis of PET images [95, 114]. CT-based attenuation correction (CTAC) is one the well established techniques in combined clinical and preclinical PET/CT

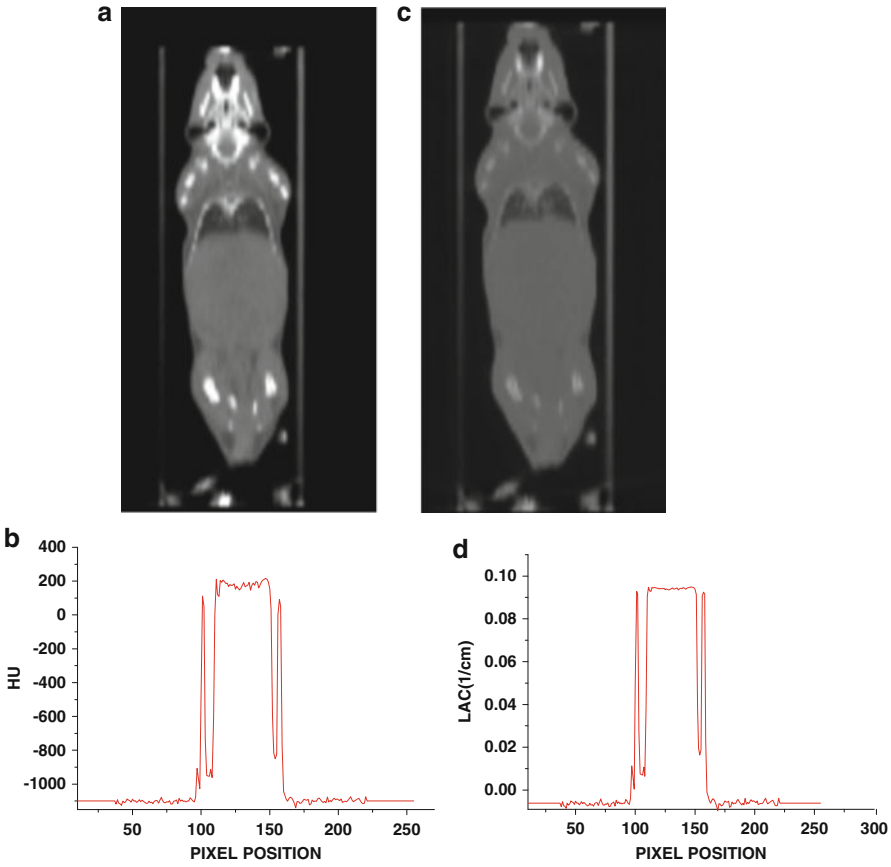

Fig. 13.7 Coronal original CT image (in HU) of a mouse (**a**) and its corresponding horizontal profile (**b**). Attenuation map (in cm^{-1}) obtained by conversion of the CT image shown in (**a**) using the bilinear method (**c**) and its corresponding horizontal profile (**d**)

scanners owing to the low statistical noise and high-quality anatomical information, small crosstalk between PET annihilation photons and low energy X-rays, and higher throughput imaging protocols [54, 93, 115]. However, precise and accurate conversion of CT numbers derived from low-energy polyenergetic X-ray spectra from a CT scanner to linear attenuation coefficients at 511 keV has become essential in order to apply accurate CTAC to the acquired PET data [54, 116].

The practical implementation of CT-based attenuation correction usually requires X-ray CT scanning of a cylindrical phantom containing cylindrical holes filled with a mixed solution of K_2HPO_4 and water with varying concentrations to simulate biological tissues with different densities. The calibration curve obtained can then be used for conversion of CT images of the animal to an attenuation map that can be used for attenuation correction purposes at the 511 keV photon energy in PET (Fig. 13.7) [115]. Despite the fact that the use of CTAC is recognized to lead to more accurate quantification in high resolution preclinical PET imaging, further work is

still needed to explore its broad potential, in particular in combination with scatter and beam hardening correction of cone-beam CT data [117].

5 Applications of Preclinical PET/CT Imaging

During the first days of their inception, the role of small-animal PET scanners was rather unclear and controversial [118]. It was later recognized with a more pronounced enthusiasm that this technology is essential for molecular imaging-based biomedical research [119–122]. However, the success and widespread adoption of combined PET/CT systems in clinical environments has not yet materialized in the preclinical setting.

An impressive literature exists on the use of PET and PET/CT in preclinical research, ranging from the mouse up to the monkey. A comprehensive overview of published literature is beyond the scope of this chapter. Dedicated high-resolution small-animal PET scanners have been used in a wide variety of fields including tracer development [123, 124], drug discovery [125–128], development of therapeutic targets and targeted therapies [129, 130] and many other applications [131]. Interested readers are encouraged to consult other chapters of this volume addressing the applications of preclinical imaging in neurology and psychiatry (Chap. 19), cardiology (Chap. 20), oncology (Chap. 21), inflammation and infection (Chap. 22), gene expression (Chap. 23), and drug development (Chap. 24).

6 Future Directions of Preclinical PET/CT

The future of preclinical PET/CT imaging lies in the design of systems that make multimodality imaging simple, easy, accurate and reproducible. The target information is not so much pretty images, but rather the information content related to how much of the imaging probe went to what specific location. The latter can be easily achieved through the availability of anatomical imaging in the combined system. The process of creating fused co-registered images from multiple modalities will become increasingly automated and require less user interaction. One issue does remain clear, which is that the more information that can be obtained, whether sequentially or simultaneously, the better a biological system can be understood. Often the imaging modalities are complimentary, providing different information about the same animal, thus multimodality is likely to become the normal way imaging-based research is conducted in the future.

In this respect, there are many different design paths being pursued in academic and corporate settings and it will be interesting to see what technologies become the most successful in the future. As an alternative to the above described designs, the Sherbrooke group is working towards a combined PET-CT system based on the LabPET™ scanner [20, 61] developed by the same group (now commercialized by GE Healthcare), where PET and CT data are acquired using the same detector

channels and electronics thus allowing true simultaneous PET-CT scanning with the possibility to count and discriminate individual X-ray photons in CT mode [132–134]. This can be achieved by sampling the analog signal using high-speed analog-to-digital converters (ADC) and digital processing in field programmable gate arrays (FPGAs) [135, 136]. The parallel architecture and fast digital processing electronics allow high count rates for both PET and CT modes whereas the modularity of the system design allows the extension of the number of channels up to 10^4 or more. Another approach to simultaneous acquisition of PET and CT data is described by Nassalski et al. in which a detector consisting of $LaBr_3$ [137] or LSO [138] pixellated crystals are coupled to an avalanche photodiode (APD) array.

An important issue which is worth mentioning in this context is the radiation dose delivered to animals, which remains one of the critical issues in preclinical imaging and can be very high depending on the experiments and should be monitored carefully as it might change tumor characteristics, induce significant biological effects thus changing the animal model being studied or even cause lethality [46, 48]. The same applies to other imaging modalities such as CT [39], particularly when performed on multimodality imaging systems where the resulting absorbed dose is the sum of the individual contributions of each modality. While much worthwhile effort has been devoted towards the assessment of radiation dose delivered to human subjects, few research studies addressed this issue for small animals [39, 46, 139–141].

Acknowledgments This work was supported by the National Sciences and Engineering Research Council of Canada under Discovery Grant 341628 and the Swiss National Science Foundation under grant SNSF 31003A-125246.

References

1. Beyer T, Townsend DW, Brun T, Kinahan PE, Charron M, Roddy R, et al. (2000) A combined PET/CT scanner for clinical oncology. J Nucl Med 41:1369–79.
2. Shao YP, Cherry SR, Farahani K, Meadors K, Siegel S, Silverman RW, et al. (1997) Simultaneous PET and MR imaging. Phys Med Biol 42:1965–1970.
3. Slates R, Cherry S, Boutefnouchet A, Shao YP, Dahlbom M, Farahani K (1999) Design of a small animal MR compatible PET scanner. IEEE Trans Nucl Sci 46:565–570.
4. Raylman RR, Hammer BE, Christensen NL (1996) Combined MRI-PET scanner: a Monte Carlo evaluation of the improvements in PET resolution due to the effects of a static homogeneous magnetic field. IEEE Trans Nucl Sci 43:2406–2412.
5. Pichler B, Lorenz E, Mirzoyan R, Pimpl W, Roder F, Schwaiger M, et al. (1997) Performance test of a LSO-APD PET module in a 9.4 Tesla magnet. IEEE Nuclear Science Symposium Conference Record, vol. 2, pp. 1237–1239.
6. Del Guerra A, Di Domenico G, Scandola M, Zavattini G (1998) YAP-PET: first results of a small animal positron emission tomograph based on YAP:Ce finger crystals. IEEE Trans Nucl Sci 45:3105–3108.
7. Jeavons AP, Chandler RA, Dettmar CAR (1999) 3D HIDAC-PET camera with sub-millimetre resolution for imaging small animals. IEEE Trans Nucl Sci 46:468–473.
8. Lecomte R, Cadorette J, Rodrigue S, Lapointe D, Rouleau D, Bentourkia M, et al. (1996) Initial results from the Sherbrooke avalanche photodiode positron tomograph. IEEE Trans Nucl Sci 43:1952–1957.

9. Pichler B, Boning G, Lorenz E, Mirzoyan R, Pimpl W, Schwaiger M, et al. (1998) Studies with a prototype high resolution PET scanner based on LSO-APD modules. IEEE Trans Nucl Sci 45:1298–1302.
10. Cherry SR, Shao Y, Silverman RW, Meadors K, Siegel S, Chatziioannou A, et al. (1997) MicroPET: A high resolution PET scanner for imaging small animals. IEEE Trans Nucl Sci 44:1161–1166.
11. Bruyndonckx P, Liu XA, Tavernier S, Zhang SP (1997) Performance study of a 3D small animal PET scanner based on BaF2 crystals and a photo sensitive wire chamber. Nucl Instr Meth A 392:407–413.
12. Siegel S, Vaquero JJ, Aloj L, Seidel J, Jagoda E, Gandler WR, et al. (1999) Initial results from a PET planar small animal imaging system. IEEE Trans Nucl Sci 46:571–575.
13. Tavernier S, Bruyndonckx P, Shuping Z (1992) A Fully 3D Small PET scanner. Phys Med Biol 37:635–643.
14. Seidel J, Vaquero JJ, Green MV (2003) Resolution uniformity and sensitivity of the NIH ATLAS small animal PET scanner: Comparison to simulated LSO scanners without depth-of-interaction capability. IEEE Trans Nucl Sci 50:1347–1350.
15. Tai YC, Chatziioannou A, Siegel S, Young J, Newport D, Goble RN, et al. (2001) Performance evaluation of the microPET P4: a PET system dedicated to animal imaging. Phys Med Biol 46:1845–1862.
16. Knoess C, Siegel S, Smith A, Newport D, Richerzhagen N, Winkeler A, et al. (2003) Performance evaluation of the microPET R4 PET scanner for rodents. Eur J Nuc Med Mol Imaging 30:737–747.
17. Surti S, Karp JS, Perkins AE, Freifelder R, Muehllehner G (2003) Design evaluation of A-PET: A high sensitivity animal PET camera. IEEE Trans Nucl Sci 50:1357–1363.
18. Wang Y, Seidel J, Tsui BMW, Vaquero JJ, Pomper MG (2006) Performance Evaluation of the GE Healthcare eXplore VISTA Dual-Ring Small-Animal PET Scanner. J Nucl Med 47:1891–1900.
19. Missimer J, Madi Z, Honer M, Keller C, Schubiger A, Ametamey SM (2004) Performance evaluation of the 16-module quad-HIDAC small animal PET camera. Phys Med Biol 49:2069–81.
20. Fontaine R, Belanger F, Viscogliosi N, Semmaoui H, Tetrault MA, Michaud JB, et al. (2009) The hardware and signal processing architecture of LabPET™, a small animal APD-based digital PET scanner. IEEE Trans Nucl Sci 56:3–9.
21. Paulus MJ, Sari-Sarraf H, Gleason SS, Bobrek M, Hicks JS, Johnson DK, et al. (1999) New x-ray computed tomography system for laboratory mouse imaging. IEEE Trans Nucl Sci 46:558–564.
22. Khodaverdi M, Pauly F, Weber S, Schroder G, Ziemons K, Sievering R, et al. (2001) Preliminary studies of a micro-CT for a combined small animal PET/CT scanner. IEEE Nuclear Science Symposium Conference Record, vol. 3, pp. 1605–1606.
23. Goertzen AL, Nagarkar V, Street R, Paulus M, Bonne J, Cherry SR (2004) A comparison of x-ray detectors for mouse CT imaging. Phys Med Biol 49:5251–5265.
24. Colijn AP, Zbijewski W, Sasov A, Beekman FJ (2004) Experimental validation of a rapid Monte Carlo based micro-CT simulator. Phys Med Biol 49:4321–4333.
25. Corrigan NM, Chavez AE, Wisner ER, Boone JM (1999) A multiple detector array helical x-ray microtomography system for specimen imaging. Med Phys 26:1708–13.
26. Reimann DA, Hames SM, Flynn MJ, Fyhrie DP (1997) A cone beam computed tomography system for true 3D imaging of specimens. Appl Radiat Isot 48:1433–6.
27. Ruegsegger P, Koller B, Muller R (1996) A microtomographic system for the nondestructive evaluation of bone architecture. Calcif Tissue Int 58:24–9.
28. Paulus MJ, Gleason SS, Kennel SJ, Hunsicker PR, Johnson DK (2000) High resolution X-ray computed tomography: an emerging tool for small animal cancer research. Neoplasia 2:62–70.
29. Sasov A (2002) In-vivo micro-CT for small animals imaging. Proceedings IEEE International Symposium on Biomedical Imaging, pp. 377–380.

30. Marxen M, Thornton MM, Chiarot CB, Klement G, Koprivnikar J, Sled JG, et al. (2004) MicroCT scanner performance and considerations for vascular specimen imaging. Med Phys 31:305–13.
31. Goertzen AL, Meadors AK, Silverman RW, Cherry SR (2002) Simultaneous molecular and anatomical imaging of the mouse *in vivo*. Phys Med Biol 47:4315–4328.
32. Liang H, Yang Y, Yang K, Wu Y, Boone JM, Cherry SR (2007) A microPET/CT system for invivo small animal imaging. Phys Med Biol 52:3881–3894.
33. Jan ML, Ni YC, Chen KW, Liang HC, Chuang KS, Fu YK (2006) A combined micro-PET/CT scanner for small animal imaging. Nucl Instr Meth A 569:314–318.
34. Seidel J, Vaquero JJ, Pascau J, Desco M (2002) Features of the NIH atlas small animal PET scanner and its use with a coaxial small animal volume CT scanner. Proceedings IEEE International Symposium on Biomedical Imaging, pp. 545–548.
35. Suckow C, Kuntner C, Chow P, Silverman R, Chatziioannou A, Stout D (2009) Multimodality rodent imaging chambers for use under barrier conditions with gas anesthesia. Mol Imaging Biol 11:100–116.
36. Chow PL, Stout DB, Komisopoulou E, Chatziioannou AF (2006) A method of image registration for small animal, multi-modality imaging. Phys Med Biol 51:379–390.
37. Ford NL, Thornton MM, Holdsworth DW (2003) Fundamental image quality limits for microcomputed tomography in small animals. Med Phys 30:2869–77.
38. Chow PL, Goertzen AL, Berger F, DeMarco JJ, Chatziioannou AF (2001) Monte Carlo model for estimation of dose delivered to small animals during 3D high resolution x-ray computed tomography. IEEE Nuclear Science Symposium Conference Record, vol. 3, pp. 1678–1681.
39. Taschereau R, Chow PL, Chatziioannou AF (2006) Monte Carlo simulations of dose from microCT imaging procedures in a realistic mouse phantom. Med Phys 33:216–24.
40. Boone JM, Velazquez O, Cherry SR (2004) Small-animal X-ray dose from micro-CT. Mol Imaging 3:149–58.
41. Carlson SK, Classic KL, Hadac EM, Bender CE, Kemp BJ, Lowe VJ, et al. (2006) *In vivo* quantitation of intratumoral radioisotope uptake using micro-single photon emission computed tomography/computed tomography. Mol Imaging Biol 8:324–32.
42. Goertzen AL (2003) Development of a combined microPET and microCT system for mouse imaging [Thesis (Ph.D.)]. University of California, Los Angeles; 2003.
43. Figueroa SD, Winkelmann CT, Miller HW, Volkert WA, Hoffman TJ (2008) TLD assessment of mouse dosimetry during microCT imaging. Med Phys 35:3866–74.
44. Obenaus A, Smith A (2004) Radiation dose in rodent tissues during micro-CT imaging. J Xray Sci Technol 12:241–249.
45. Liang H, Cherry SR. Monte Carlo Simulation of Combined MicroPET/CT Dose Delivered to Mice. IEEE Nuclear Science Symposium and Medical Imaging Conference. Rome, Italy, 2004.
46. Funk T, Sun M, Hasegawa BH (2004) Radiation dose estimate in small animal SPECT and PET. Med Phys 31:2680–6.
47. Goertzen AL, Janicki C, Rosa-Neto P (2005) Dosimetry of PET tracers in mice using microPET scans as an input function. IEEE Nuclear Science Symposium Conference Record, vol. 3, pp. 1628–1632.
48. Taschereau R, Chatziioannou AF (2007) Monte Carlo simulations of absorbed dose in a mouse phantom from 18-fluorine compounds. Med Phys 34:1026–36.
49. Bahadur AN, Wu IQ, Weinstein DM, Davis MD, Lewis DA, Kochunov P, et al. (2007) Multimodality Chamber for coregistered anatomical and molecular imaging of small animals. Lab Anim (NY) 36:29–35.
50. Stout DB, Chatziioannou AF, Lawson TP, Silverman RW, Gambhir SS, Phelps ME (2005) Small animal imaging center design: the facility at the UCLA Crump Institute for Molecular Imaging. Mol Imaging Biol 7:393–402.
51. Bioscan, Inc. Minerve Small-Animal Environment. Available at http://www.bioscan.com/molecular-imaging/minerve

52. M2M Imaging. Split top mouse chamber for Preclinical Imaging Systems. Available at http://www.m2mimaging.com/products/accessories/animalhandling/multimodal_mouse_siemens.html
53. Christian N, Lee JA, Bol A, De Bast M, Gallez B, Gregoire V (2008) Immobilization device for *in vivo* and in vitro multimodality image registration of rodent tumors. Radiother Oncol 87:147–151.
54. Chow PL, Rannou FR, Chatziioannou AF (2005) Attenuation correction for small animal PET tomographs. Phys Med Biol 50:1837–1850.
55. Zaidi H, Hasegawa B (2003) Determination of the Attenuation Map in Emission Tomography. J Nucl Med 44:291–315.
56. Stout DB, Zaidi H (2008) Preclinical multimodality imaging *in vivo*. PET Clin 3:251–273.
57. Siemens Medical Solutions USA Inc. Inveon Product Brochure. Available at https://www.medical.siemens.com/siemens/en_INT/gg_nm_FBAs/files/broch/br_09_inveon.pdf
58. Townsend DW (2008) Multimodality imaging of structure and function. Phys Med Biol 53:R1–R39.
59. Gamma Medica-Ideas. FLEX Triumph. Available at http://www.gm-ideas.com/index.php?option=com_content&task=view&id=5&Itemid=2
60. Xie S, Ramirez R, Liu Y, Xing TXA-T, Uribe JA-U, J., Li HLA-H, et al. (2005) A pentagon photomultiplier-quadrant-sharing BGO detector for a rodent research PET (RRPET). IEEE Trans Nucl Sci 52:210–216.
61. Bergeron M, Cadorette J, Beaudoin JF, Lepage MD, Robert G, Selivanov V, et al. (2009) Performance Evaluation of the LabPET APD-Based Digital PET Scanner. IEEE Trans Nuc Sci 56:10–16.
62. Gleason SS, Austin DW, Beach RS, Nutt R, Paulus MJ, Shikui Y (2006) A new highly versatile multimodality small animal imaging platform. IEEE Nuclear Science Symposium Conference Record, vol. 4, pp. 2447–2449.
63. Ziemons K, E. Auffray, Barbier R, Brandenburg G, Bruyndonckx P, Choi Y, et al. (2005) The ClearPET™ project: development of a 2nd generation high-performance small animal PET scanner. Nucl Instr Meth A 537:307–311.
64. Khodaverdi M, Nicol S, Loess J, Brunner FC, Karkar S, Morel C (2007) Design study for the ClearPET/XPAD small animal PET/CT scanner. IEEE Nuclear Science Symposium Conference Record, vol. 6, pp. 4300–4302.
65. Lage E, Vaquero JJ, Sisniega A, Espana S, Tapias G, Abella M, et al. (2009) Design and performance evaluation of a coplanar multimodality scanner for rodent imaging. Phys Med Biol 54:5427–5441.
66. National Electrical Manufacturers Association (2008) NEMA Standards Publication NU 4 – 2008. Performance Measurements of Small Animal Positron Emission Tomographs. National Electrical Manufacturers Association, Rosslyn, VA.
67. Tatsumi M, Nakamoto Y, Traughber B, Marshall LT, Geschwind JF, Wahl RL (2003) Initial experience in small animal tumor imaging with a clinical positron emission tomography/computed tomography scanner using 2-[F-18]fluoro-2-deoxy-D-glucose. Cancer Res 63:6252–7.
68. Seemann MD, Beck R, Ziegler S (2006) *In vivo* tumor imaging in mice using a state-of-the-art clinical PET/CT in comparison with a small animal PET and a small animal CT. Technol Cancer Res Treat 5:537–542.
69. Ziemer LS, Evans SM, Kachur AV, Shuman AL, Cardi CA, Jenkins WT, et al. (2003) Noninvasive imaging of tumor hypoxia in rats using the 2-nitroimidazole 18F-EF5. Eur J Nucl Med Mol Imaging 30:259–266.
70. Seemann MD (2004) Human PET/CT scanners: feasibility for oncological *in vivo* imaging in mice. Eur J Med Res 9:468–72.
71. Salem N, MacLennan G, Kuang Y, Anderson P, Schomisch S, Tochkov I, et al. (2007) Quantitative evaluation of 2-Deoxy-2[F-18]fluoro-d -glucose-Positron Emission Tomography imaging on the woodchuck model of hepatocellular carcinoma with histological correlation. Mol Imaging Biol 9:135–143.
72. Wienhard K, Schmand M, Casey ME, Baker K, Bao J, Eriksson L, et al. (2002) The ECAT HRRT: performance and first clinical application of the new high resolution research tomograph. IEEE Trans Nuc Sci 49:104–110.

73. Zaidi H, Montandon M-L (2006) The new challenges of brain PET imaging technology. Curr Med Imag Rev 2:3–13.
74. Wu Y, Bowen SL, Yang K, Packard N, Fu L, Jr GB, et al. (2009) PET characteristics of a dedicated breast PET/CT scanner prototype. Phys Med Biol 54:4273–4287.
75. Bowen SL, Wu Y, Chaudhari AJ, Fu L, Packard NJ, Burkett GW, et al. (2009) Initial Characterization of a Dedicated Breast PET/CT Scanner During Human Imaging. J Nucl Med 50:1401–1408.
76. Li H, Wong W-H, Baghaei H, Uribe J, Wang Y, Zhang Y, et al. (2007) The engineering and initial results of a transformable low-cost high-resolution PET camera. IEEE Trans Nucl Sci 54:1583–1588.
77. Gonzalez Trotter DE, Manjeshwar RM, Doss M, Shaller C, Robinson MK, Tandon R, et al. (2004) Quantitation of small-animal (124)I activity distributions using a clinical PET/CT scanner. J Nucl Med 45:1237–1244.
78. Cherry SR (2006) The 2006 Henry N. Wagner lecture: of mice and men (and positrons)-Advances in PET Imaging Technology. J Nucl Med 47:1735–1745.
79. Beekman F, Hutton B (2007) Multi-modality imaging on track. Eur J Nuc Med Mol Imaging 34:1410–1414.
80. Weissleder R, Pittet MJ (2008) Imaging in the era of molecular oncology. Nature 452:580–589.
81. Maintz JB, Viergever MA (1998) A survey of medical image registration. Med Image Anal 2:1–36.
82. Pluim JP, Maintz JB, Viergever MA (2003) Mutual-information-based registration of medical images: a survey. IEEE Trans Med Imaging 22:986–1004.
83. Zanzonico PB, Nehmeh SA (2006) Introduction to clinical and laboratory (small-animal) image registration and fusion. Conf Proc IEEE Eng Med Biol Soc 1:1580–1583.
84. Laforest R, Liu X (2009) Cascade removal and microPET imaging with 76Br. Phys Med Biol 54:1503–1531.
85. Fahey FH, Gage HD, Buchheimer N, Smith HC, Harkness BA, Williams RC, et al. (2004) Evaluation of the quantitative capability of a high-resolution positron emission tomography scanner for small animal imaging. J Comput Assist Tomogr 28:842–848.
86. Toyama H, Ichise M, Liow JS, Modell KJ, Vines DC, Esaki T, et al. (2004) Absolute quantification of regional cerebral glucose utilization in mice by 18F-FDG small animal PET scanning and 2-14C-DG autoradiography. J Nucl Med 45:1398–1405.
87. Kesner AL, Dahlbom M, Huang SC, Hsueh WA, B SP, Czernin J, et al. (2006) Semiautomated analysis of small-animal PET data. J Nucl Med 47:1181–1186.
88. Aide N, Louis MH, Dutoit S, Labiche A, Lemoisson E, Briand M, et al. (2007) Improvement of semi-quantitative small-animal PET data with recovery coefficients: A phantom and rat study. Nucl Med Commun 28:813–822.
89. Vaska P, Rubins DJ, Alexoff DL, Schiffer WK (2006) Quantitative imaging with the microPET small-animal PET tomograph. Int Rev Neurobiol 73:191–218.
90. Torres-Espallardo I, Spanoudaki VC, Rafecas M, Ziegler SI (2007) Quantification issues in imaging data of MADPET-II small animal scanner using a system matrix based on Monte Carlo techniques. IEEE Nuclear Science Symposium Conference Record, vol. 6, pp. 4192–4197.
91. Foudray AMK, Chinn C, Levin CS (2005) Component based normalization for PET systems with depth of interaction measurement capability. IEEE Nuclear Science Symposium Conference Record, vol. 4, pp. 2108–2111.
92. Rodriguez M, Barker WC, Liow JS, Thada S, Chelikani S, Mulnix T, et al. (2006) Count rate dependent component-based normalization for the HRRT [abstract]. J Nucl Med 47:197P.
93. Yao R, Seidel J, Liow J-S, Green MV (2005) Attenuation correction for the NIH ATLAS small animal PET scanner. IEEE Trans Nucl Sci 52:664–668.
94. Yu J, Seidel J, Pomper M, Tsui BMW (2007) Experimental evaluation of the bilinear transformation used in the CT-based attenuation correction for small animal PET imaging. IEEE Nuclear Science Symposium Conference Record, vol. 5, pp. 3747–3750.
95. Zaidi H, Montandon M-L, Alavi A (2007) Advances in attenuation correction techniques in PET. PET Clinics 2:191–217.

96. Lubberink M, Kosugi T, Schneider H, Ohba H, Bergstrom M (2004) Non-stationary convolution subtraction scatter correction with a dual-exponential scatter kernel for the Hamamatsu SHR-7700 animal PET scanner. Phys Med Biol 49:833–842.
97. Yang Y, Cherry SR (2006) Observations regarding scatter fraction and NEC measurements for small animal PET. IEEE Trans Nucl Sci 53:127–132.
98. Laforest R, Longford D, Siegel S, Newport DF, Yap J (2007) Performance evaluation of the microPET®—FOCUS-F120. IEEE Trans Nucl Sci 54:42–49.
99. Zaidi H, Montandon M-L (2007) Scatter compensation techniques in PET. PET Clinics 2:219–234.
100. Ferrero A, Poon JK, Badawi RD. Characterization of the scatter fraction arising from different sized objects - a simulation study. IEEE Nuclear Science Symposium and Medical Imaging Conference. Orlando, FL, USA, 2009.
101. Bentourkia M, Sarrhini O (2009) Simultaneous attenuation and scatter corrections in small animal PET imaging. Comput Med Imaging Graph 33:477–488.
102. Rousset O, Rahmim A, Alavi A, Zaidi H (2007) Partial volume correction strategies in PET. PET Clinics 2:235–249.
103. Soret M, Bacharach SL, Buvat I (2007) Partial-volume effect in PET tumor imaging. J Nucl Med 48:932–945.
104. Rahmim A, Rousset O, Zaidi H (2007) Strategies for motion tracking and correction in PET. PET Clinics 2:251–266.
105. Zhou VW, Kyme AZ, Meikle SR, Fulton R (2008) An event-driven motion correction method for neurological PET studies of awake laboratory animals. Mol Imaging Biol 10:315–324.
106. Kyme AZ, Zhou VW, Meikle SR, Fulton RR (2008) Real-time 3D motion tracking for small animal brain PET. Phys Med Biol 53:2651–2666.
107. Qi J, Leahy RM (2006) Iterative reconstruction techniques in emission computed tomography. Phys Med Biol 51:R541-R578.
108. Reader AJ, Zaidi H (2007) Advances in PET image reconstruction. PET Clinics 2:173–190.
109. Comtat C, Kinahan PE, Fessler JA, Beyer T, Townsend DW, Defrise M, et al. (2002) Clinically feasible reconstruction of 3D whole-body PET/CT data using blurred anatomical labels. Phys Med Biol 47:1–20.
110. Baete K, Nuyts J, Van Paesschen W, Suetens P, Dupont P (2004) Anatomical-based FDG-PET reconstruction for the detection of hypo-metabolic regions in epilepsy. IEEE Trans Med Imaging 23:510–519.
111. Dupont P, Warwick J (2009) Kinetic modeling in small animal imaging with PET. Methods 48:98–103.
112. Convert L, Morin-Brassard G, Cadorette J, Archambault M, Bentourkia Mh, Lecomte R (2007) A new tool for molecular imaging: The microvolumetric {beta} blood counter. J Nucl Med 48:1197–1206.
113. Wu H-M, Yu AS, Lin H-D, Ladno W, Huang S-C, Phelps ME (2007) The feasibility of performing longitudinal measurements in mice using small animal PET imaging and a microfluidic blood sampling device. IEEE Nuclear Science Symposium Conference Record, vol. 6, pp. 4174–4175.
114. Huang SC, Hoffman EJ, Phelps ME, Kuhl DE (1979) Quantitation in positron emission computed tomography: 2. Effects of inaccurate attenuation correction. J Comput Assist Tomogr 3:804–14.
115. Prasad R, Ay M, Ratib O, Zaidi H (2009) CT-based attenuation correction on the FLEX Triumph™ preclinical PET/CT scanner. IEEE Trans Nucl Sci. 58:66–75.
116. Kinahan PE, Hasegawa BH, Beyer T (2003) X-ray-based attenuation correction for positron emission tomography/computed tomography scanners. Semin Nucl Med 33:166–179.
117. Ay M, Zaidi H (2006) Assessment of errors caused by x-ray scatter and use of contrast medium when using CT-based attenuation correction in PET. Eur J Nucl Med Mol Imaging 33:1301–1313.
118. Hichwa R (1994) Are Animal Scanners Really Necessary for PET? J Nucl Med 35:1396–1397.

119. Tornai MP, Jaszczak RJ, Turkington TG, Coleman RE (1999) Small-animal PET: advent of a new era of PET research. J Nucl Med 40:1176–1179.
120. Nanni C, Rubello D, Fanti S (2007) Role of small animal PET for molecular imaging in preclinical studies. Eur J Nuc Med Mol Imaging 34:1819–1822.
121. Tai YC, Laforest R (2005) Instrumentation aspects of animal pet. Annu Rev Biomed Eng 7:255–285.
122. Levin CS, Zaidi H (2007) Current trends in preclinical PET system design. PET Clinics 2:125–160.
123. Nanni C, Rubello D, Khan S, Al-Nahhas A, Fanti S (2007) Role of small animal PET in stimulating the development of new radiopharmaceuticals in oncology. Nucl Med Commun 28:427–429.
124. Wester H-J (2007) Nuclear imaging probes: from bench to bedside. Clin Cancer Res 13:3470–3481.
125. Aboagye EO (2005) Positron emission tomography imaging of small animals in anticancer drug development. Mol Imaging Biol 7:53–8.
126. Richter W (2006) Imaging biomarkers as surrogate endpoints for drug development. Eur J Nuc Med Mol Imaging 33:6–10.
127. Pien HH, Fischman AJ, Thrall JH, Sorensen AG (2005) Using imaging biomarkers to accelerate drug development and clinical trials. Drug Discovery Today 10:259–266.
128. Lucignani G (2007) Imaging biomarkers: from research to patient care — a shift in view. Eur J Nuc Med Mol Imaging 34:1693–1697.
129. Stephen R, Gillies R (2007) Promise and progress for functional and molecular imaging of response to targeted therapies. Pharmaceutical Research 24:1172–1185.
130. Czernin J, Weber WA, Herschman HR (2006) Molecular imaging in the development of cancer therapeutics. Annu Rev Med 57:99–118.
131. Cherry SR, Gambhir SS (2001) Use of positron emission tomography in animal research. ILAR J 42:219–32.
132. Fontaine R, Belanger F, Cadorette J, Leroux JD, Martin JP, Michaud JB, et al. (2005) Architecture of a dual-modality, high-resolution, fully digital positron emission tomography/computed tomography (PET/CT) scanner for small animal imaging. IEEE Trans Nucl Sci 52:691–696.
133. Berard P, Riendeau J, Pepin CM, Rouleau D, Cadorette J, Fontaine R, et al. (2007) Investigation of the LabPET (TM) detector and electronics for photon-counting CT imaging. Nucl Instr Meth A 571:114–117.
134. Saoudi A, Lecomte R (1999) A novel APD-based detector module for multi-modality PET/SPECT/CT scanners. IEEE Trans Nuc Sci 46:479–484.
135. Fontaine R, Michaud JB, Leroux JD, Viscogliosi N, Riendeau J, Semmaoui H, et al. (2007) Roadmap to fully-digital PET/CT scanners. IEEE Nuclear Science Symposium Conference Record, vol. 5, pp. 3332–3336.
136. Riendeau J, Berard P, Viscogliosi N, Tetrault MA, Lemieux F, Lecomte R, et al. (2008) High rate photon counting CT using parallel digital PET electronics. IEEE Trans Nucl Sci 55:40–47.
137. Nassalski A, Moszynski M, Szczesniak T, Wolski D, Batsch T (2007) The road to the common PET/CT detector. IEEE Trans Nucl Sci 54:1459–1463.
138. Nassalski A, Moszynski M, Syntfeld-Kzuch A, Swiderski L, Szczesniak T, Wolski D, et al. (2008) Application of Hamamatsu S8550 APD array to the common PET/CT detector. IEEE Trans Nucl Sci 55:2460–2464.
139. Stabin MG, Peterson TE, Holburn GE, Emmons MA (2006) Voxel-based mouse and rat models for internal dose calculations. J Nucl Med 47:655–659.
140. Hindorf C, Ljungberg M, Strand SE (2004) Evaluation of parameters influencing S values in mouse dosimetry. J Nucl Med 45:1960–1965.
141. Carlson SK, Classic KL, Bender CE, Russell SJ (2007) Small animal absorbed radiation dose from serial micro-computed tomography imaging. Mol Imaging Biol 9:78–82.

Chapter 14
Dual-Modality Preclinical SPECT/MRI Instrumentation

Douglas J. Wagenaar, Dirk Meier, and Bradley E. Patt

1 Introduction

Single photon emission tomography (SPET or SPECT) and magnetic resonance imaging (MRI) are in use routinely in hospitals worldwide. Each of these modalities is steadily growing in study volume and makes a major contribution to healthcare, with approximately 40 million SPECT and 60 million MRI patient exams completed every year. Also in the preclinical research field both SPECT and MRI are found to play important roles, with an installed base of about 200 microSPECT and 400 small animal MRI systems in use as of the beginning of 2009. The high magnetic field strengths of modern MRI machines, both clinical and preclinical, preclude the use of conventional photomultiplier-tube based SPECT equipment in the vicinity of the magnet. If a patient or a laboratory animal is to be imaged by *both* modalities, the two studies must be done in separate imaging sessions—always in different rooms and often in different departments and sometimes even in different buildings within a medical facility. Combined SPECT/MRI imaging is important since non-invasive probing of intact, living biological organisms—human or laboratory animal—bridges the gap between exponentially growing understanding of molecular and genetic mechanisms and the phenotypical embodiments of diseases and their response to treatments.

The main goal of this chapter is to review the progress that has been made in dual-modality SPECT/MRI in preclinical imaging using an integrated hardware design. The main innovation of SPECT/MRI lies in the engineering of the two

D.J. Wagenaar • B.E. Patt
Gamma Medica-Ideas (USA), Northridge, CA, USA

D. Meier (✉)
Integrated Detector Electronics AS, Fornebu, Norway
e-mail: dirk.meier@ideas.no

H. Zaidi (ed.), *Molecular Imaging of Small Animals: Instrumentation and Applications*,
DOI 10.1007/978-1-4939-0894-3_14,

major imaging modalities such that data can be acquired *simultaneously* during the same imaging session. The related topics of PET/CT and PET/MRI are reviewed in Chaps. 13 and 15, respectively.

2 SPECT/MRI Applications

2.1 Clinical Applications

The success of whole-body PET/CT for oncology, beginning around the year 2000 and continuing to grow after nearly a decade, clearly demonstrates the clinical efficacy of molecular imaging by cost-efficient patient management and therapy follow-up. The example of whole-body PET/CT leads researchers to pursue other combinations of modalities which will lead to additional changes in patient management that result in demonstrated improved outcomes. Supporters of these efforts claim that refinement of patient management decisions can result in reduced healthcare costs—mostly through the avoidance of ineffective yet expensive therapies.

The applications for a combined SPECT/MRI instrument can be deduced from an examination of the trajectories of the growth of each modality into new fields. For example, dynamic, contrast-enhanced (DCE) breast imaging is rapidly growing in the field of MRI, with more than 800,000 studies expected to be performed in the United States in 2009, and a growth rate of about 20 % per year. At the same time, Molecular Breast Imaging [1], or MBI, [1] using ^{99m}Tc-sestamibi is demonstrating efficacy in detecting small (<1 cm) breast lesions especially in women with radiographically dense breasts. Since SPECT (in the form of MBI) and MRI are probing different and perhaps complementary biological processes, it suggests itself to consider the benefits of acquiring both image sets *simultaneously*, thereby removing several experimental variables from the imaging session.

Although whole-body FDG-PET/CT has proven to be valuable for most oncologic applications, it is not useful in prostate cancer imaging due to poor FDG uptake in this relatively non-aggressive cancer. As with the preceding paragraph on breast imaging in women, a potential SPECT/MRI clinical application for men could be prostate imaging with SPECT agents such as ^{111}In-labeled Prostascint [2], ^{111}In-labeled antibody J591 [3] or ^{99m}Tc-labeled PMSA inhibitors [4]. The high-sensitivity of antibody or receptor-targeted SPECT can complement the soft tissue, functional, and chemical information provided by MRI or MRSI [5]. For breast and prostate cancer imaging applications, it may be beneficial to use SPECT/MRI to image, and non-invasively evaluate axillary and inguinal lymph nodes, respectively, for staging and treatment planning.

[1] Also known as Breast-Specific Gamma Imaging (BSGI)

MRI has high study volumes in the imaging of connective tissues. This is because MRI has the unique ability to image soft tissues whereas X-ray computer tomography (CT) currently is limited in its ability to differentiate between soft tissues based on differences in the attenuation of a spectrum of incoherent X-rays.

The addition of SPECT for the imaging of inflammation, repair processes (growth factors, angiogenesis), apoptosis, or other biological processes associated with musculo-skeletal injury or abnormality is a logical addition of complementary information. Another important, though not popularized, application for both SPECT and MRI is the imaging of hyperfunctioning parathyroid [6]. The small size and dispersed anatomic location of the parathyroid calls for the high resolution, soft tissue contrast of MRI. Hyperfunctioning parathyroid has been shown to avidly uptake ^{99m}Tc-sestamibi in SPECT [7]. Evidence of the utility of functional-plus-anatomic imaging of primary hyperparathyroidism is reported for combined SPECT/CT [8].

2.2 Preclinical Applications

As outlined in the preceding section, clinical applications can be extrapolated from the known trajectories of clinical imaging research in the separate modalities. In the area of preclinical research, the number of potential applications grows dramatically because there are many applications in each research modality that are not currently being performed clinically. *This distinction is important:* preclinical imaging is the subject of this chapter because the pool from which potential dual-modality applications can be extracted is far larger and more varied—and hence statistically more likely to find a successful application that can be translated into the clinic.

There are now two main sub-categories in the preclinical area: (1) disease-based imaging; and (2) therapy response imaging. A third, emerging sub-category has grown in the past ten years and will likely overtake the other two categories within the next decade: namely, molecular imaging methods. We will introduce each of these sub-categories in the following paragraphs.

2.2.1 Disease-Based Imaging Research

- *Neurology:* There are two sub-categories of research in neurological imaging—neuro-degenerative diseases and receptor imaging. Neuro-degenerative research involves Alzheimer's disease imaging of plaques and tangles, Parkinson's disease imaging of receptor uptake rates, and diffusion-tensor imaging in Huntington's disease. Changes in brain blood flow due to activation are seen in the MRI technique known as "blood oxygen, level dependent" (BOLD). Although BOLD exhibits low spatial resolution, it can be combined with perfusion imaging using ^{99m}Tc-HMPAO, a common brain perfusion SPECT agent. Nuclear imaging of receptor sites has high molar sensitivity, and applications such as dopamine, serotonin, norephenephrine, muscarinic, nicotinic, and benzodiazepine receptors have been reported extensively in the SPECT literature during the past two decades. The combination of receptor

SPECT and activation or diffusion MRI is a good example of the complementary nature of these modalities in neurology research. The dynamic nature of uptake in the receptors and perfusion in the brain tissues makes simultaneous acquisition of the two modalities imperative. Localized MRI spectroscopy (MRS) of cerebral metabolites can achieve spatial resolution on the order of 1.5 mm, providing another path for dual-modality neurology investigations.

- *Cardiology:* As with the receptors/perfusion combination in neurology, cardiology has a similar combination of vulnerable plaques and left ventricular perfusion. Vulnerable plaque imaging research has matured in both MRI and SPECT over the past 10 years. MRI is uniquely capable of differentiating fatty from fibrous plaques. SPECT agents have been used to image matrix metalloproteases, apoptosis, angiogenesis, cytokine and chemokine signaling in vulnerable plaques. The anatomy of the heart can be imaged in real time by MRI, and this high-resolution data set can be used to provide gated and resolution-corrected SPECT images. Global tissue perfusion, innervations, oxygenation, and fatty acid metabolism can be imaged with SPECT agents. MRI might also be used to image tissue perfusion, coronary vessel blockage, and hypokinesis.
- *Oncology:* SPECT can be used in many oncologic processes: receptor-targeted antibodies, angiogenesis, hypoxia, signaling (cytokines, chemokines), growth factors, invasion (matrix breakdown), lymph node metastasis and global metastasis. Preclinical MRI, with resolution better than 0.1 mm per voxel, provides anatomical context for the specific oncologic process probed by the SPECT agents listed above. The high resolution of MRI can distinguish between encapsulated and invasive cancers. More sophisticated MRI techniques can image oxygenation and perfusion, and MRI spectroscopy can be used to image endogenous molecular densities associated with early stage cancer development, albeit with diminished spatial resolution.
- *Musculo-skeletal:* Research into the processes of injury and repair of the musculo-skeletal system is of importance to trauma physicians dealing with automobile, athletic, or combat injuries. Cartilage, ligament, tendon, and muscular imaging with MRI have experienced growth in the past 20 years. Imaging of bone disease and micro- and stress fractures is a strength of SPECT using phosphonated bone agents. Since MRI does not image bone well, a bone agent such as ^{99m}Tc-methylene diphosphonate (MDP) can augment MRI in musculo-skeletal imaging. SPECT can also be used to image repair mechanisms such as inflammation, signaling, growth factors, angiogensis, and metabolism. The combination of SPECT and MRI in musculo-skeletal disease and injury gives the researcher a clear view of the biological functions of natural response and repair mechanisms of all the tissues involved—soft tissues as well as bone.

2.2.2 Therapy Response Imaging

Many of the preclinical imaging laboratories in operation today are dedicated to drug development. The use of imaging techniques has been a great advance in drug development research through the use of a vastly reduced population of animals to

perform the standard ADME-Tox[2] experiments that are required when a drug has succeeded beyond the in vitro stage of development. Each of these steps is required to be well documented and understood in an intact, living laboratory specimen prior to clinical trials with human beings. The pharmacokinetics of each drug can be studied with preclinical imaging. Pharmacokinetics is the documentation of "the action of the body on the drug". Likewise, the pharmacodynamics—or "the action of the drug on the body" can also be measured with preclinical imaging. It can be seen that the field of drug development, in which large R&D investments are made, has been streamlined by the introduction of and growing use of preclinical imaging techniques. SPECT and MRI, operated simultaneously in the drug development setting, will allow the delivery of the drug, its distribution and uptake, washout, and ultimately its action on the system to be imaged over the course of the original injection and following up over several weeks if necessary. In particular, in longitudinal drug studies the effects of oncologic agents on the size and aggressiveness of tumors can be measured with MRI and SPECT, respectively. In longitudinal studies, sequential acquisitions will suffice, since the extended time periods between imaging sessions obviate simultaneous imaging with the two modalities. For neurological or psychiatric agents, the dynamics of receptor uptake using SPECT or changes in activation or diffusion in MRI can indicate a positive response to a new psychiatric agent.

2.2.3 Molecular Imaging Methods

Research in the fields of stem cell therapies, nanoparticles, and genetic engineering is increasing rapidly in the preclinical realm. Each of these therapies has in common the fact that they are highly potent yet clinically silent and relatively slow-acting. Traditionally, stem cell therapy calls for animal studies with high statistics in which many end-points are analyzed to establish the behavior (or misbehavior through oncogenesis) of therapeutic stem cells. Molecular Imaging—through non-invasive imaging of labeled cells—can allow significantly fewer animals to be used while providing refined experimental conclusions. Reporter genes, for example the sodium-iodide symporter, can be engineered into cells of interest and used after many cell divisions to monitor the behavior of stem cells (or genetically altered cells) throughout their life cycles. Reporter techniques can also monitor the differentiation and behavior of the progeny of stem cells through successive cell divisions. The term "nanoparticles" represents a fast-growing family of human-designed biological entities on the 10-1000 nm scale, i.e., from large molecules to small cells in size. These designer cells are envisioned to be capable of carrying genetic information, imaging contrast agents for both SPECT, MRI, or other imaging modalities and instructions on which actions to carry out—from targeting cells to penetrating them and delivering their therapeutic payload—and providing imaging signals that tell the physician of their location and the success of their actions. In this sense,

[2] ADME-Tox stands for Absorption, Distribution, Metabolism, Elimination, and Toxicity.

nanoparticles represent the convergence of stem cell and genetic engineering research in which specific instructions for repair and cure can be carried and monitored through molecular imaging techniques such as reporter gene imaging. The SPECT modality has been imaging nanoparticles, in the form of simple radiolabeled nanocolloids, for more than 30 years.

3 Nuclear Imaging: SPECT and PET

The authors reviewed the combination of MRI with the nuclear modalities of SPECT and PET [9]. SPECT nuclides in general are larger (i.e., heavier elements such as iodine, technetium, and thallium) compared with positron emitting nuclides which generally are smaller atoms found in living organisms (e.g., ^{11}C, ^{13}N, ^{15}O, and ^{18}F). Also, SPECT nuclides tend to have established production and distribution channels and hence are less costly, generally, than PET nuclides. PET nuclides tend to have shorter half-lives than SPECT nuclides—usually on the order of minutes-to-hours, whereas the SPECT agents have half-lives on the order of hours to days. Thus when the action of a small, biologically-relevant molecule must be monitored, the substitution of the ^{12}C atom with the positron-emitter ^{11}C and an accurate map of the fate of the molecule can be acquired with PET. This "biologically relevant" advantage of PET as a modality is important in preclinical research, especially in the area of drug development.

Nevertheless, advantages of SPECT over PET in preclinical research can make SPECT/MRI a powerful combination. One of the advantages of SPECT over PET is the theoretically unlimited spatial resolution that results from the emission of the single photon from the exact location of the atom that is intended to be imaged. This is contrasted with positron imaging, in which the annihilation location can be up to a few millimeters (and always several hundred microns) from the location of the radioactive decay. The uncertainty in the location of the decay in PET imaging is further degraded by the center-of-mass momentum of the positron-electron (positronium) prior to annihilation—which adds an uncertainty in the 180-degree angle between the two 511 keV annihilation photons. The advantage of resolution is especially pronounced in the organs and anatomical structures of small animals such as mice.

In order to fully realize the spatial resolution advantage of SPECT, *multiple* pinholes must be employed to collect the additional photons needed to fill the three-dimensional voxel space. The number and configuration of pinholes is limited by the physical size of the surrounding SPECT detectors, and therefore the smaller the resolution element the more pinholes that can be employed, that is, the more pinhole images that can be projected onto the detector surface. Conventional Anger gamma cameras have resolution elements of about 3 mm. Current semiconductor CZT modules employ 1.6 mm pixels, and researchers are aiming toward sub-0.5 mm pixel CZT in the future. Therefore developments in smaller-pixel SPECT detectors lead directly to simultaneous improvements in sensitivity and spatial resolution in multi-pinhole imaging.

Another advantage of SPECT is the ability to image two isotopes simultaneously. Dual-isotope techniques using NaI Anger cameras have been reported in the literature for at least 20 years. Examples of SPECT nuclide combinations include: ^{99m}Tc-with-^{111}In (140 and 171, 245 keV), and ^{99m}Tc-with-^{123}I (140 keV and 159 keV). Note that these radionuclides are labeled to different pharmaceuticals such that separate biological processes are simultaneously probed. The MRI-compatible detector material, CZT, happens to have especially good energy resolution compared with the conventional NaI/PMT combination that has been in use for more than 50 years, thereby giving dual-isotope images with superior contrast. CZT's energy resolution is now less than 4.5 % FWHM at 140 keV compared with the typical >9.0 % FWHM value of NaI for the 140 keV photon energy that ^{99m}Tc emits. Therefore, two or even three SPECT-labeled pharmaceuticals can be imaged with the CZT camera while MRI provides the anatomical, functional, or spectroscopic information from either the inherent molecules or an additional MRI-contrast agent. This "multi-wavelength" advantage is often touted for preclinical optical techniques and is the advantage of complementary, simultaneous molecular information also can be realized with CZT-based SPECT.

Another advantage of SPECT over PET in general is the longer half-lives of the SPECT nuclides. As mentioned above, the biologically-relevant PET nuclides are useful in drug development, especially to monitor the effects of small molecules without the labeling atom interfering with the chemistry. However, these four nuclides have half-lives of 110 min (^{18}F), 20.4 min (^{11}C), 10 min (^{13}N), and 2 min (^{15}O). Therefore, the price one pays for the small, biologically relevant nuclides is that one cannot monitor their action in vivo for an extended time period. Furthermore, chemistry processes have to be accelerated in the formulation of the labeled pharmaceuticals such that the labeled injectate must be ready well within an hour of the creation of the nuclide via nuclear reaction in a cyclotron. Therefore, SPECT nuclides, along with MRI-relevant elements such as gadolinium, can be incorporated into nanoparticle "cells" that may take more than an hour to fabricate and fill. A labeled nanoparticle admittedly cannot serve as a small molecule probe for drug development, but when receptor-targeted ligands are attached they can be highly-specific molecular probes despite their relatively large size.

Nuclear medicine imaging can be quantitative in that the number of radioactive atoms in a given imaging volume (voxel) can be estimated to an uncertainty in accuracy of less than 20 %. In order to achieve accurate quantification of the concentration of radioactive atoms in a given voxel, a number of "corrections" have to be performed. The accuracy of these corrections can be aided by the simultaneous acquisition of MRI data and the use of the MRI image upon which to base the corrections. For example, absolute quantification and pharmacokinetic modeling are dependent upon the knowledge of the "input function" which represents the time-course of the delivery of the radioactive bolus to the targeted lesion or organ-of-interest. Traditionally, the nuclear modalities PET [10] and SPECT [11] have used blood sampling to estimate the time-dependent input function. However, blood sampling can be tedious and often invasively affect the experiment (especially with very small animals with a limited blood volume). It would be preferred to use blood

flow MRI sequences through major vessels [12] to estimate the input function rather than extract and assay blood samples on a continuous basis throughout the imaging session. Other recent MRI approaches to estimating the input function [13] developed in 2D in mice could be more promising.

Another correction that must be made in nuclear quantification is that for attenuation of the emitted photons. Attenuation encompasses both the photo-electric interaction which removes photons from possible contribution to the image, as well as the Compton-scattered interaction which reduces the energy of the photons and redirects their trajectory. Although PET and SPECT used external radioactive sources to create "attenuation maps" throughout the 1990s and into the new millennium, these external sources have been superseded by CT-generated attenuation maps. Nowadays CT hardware is nearly always sold in combination with PET rings and increasingly with dual-headed SPECT systems. The CT attenuation map is converted to the correct (known) PET energy (511 keV) or SPECT energy for the given nuclide in use. Tissues are segmented in software and these segmented tissues are used to provide scatter correction to the nuclear data. In SPECT/MRI, the MRI would take the place of the CT for estimating the attenuation map to be used for the quantitative correction. This is more complicated than CT energy scaling, since MRI signal generation is unrelated to attenuation properties [14]. One must segment the MRI data into tissues, and an assignment of a "mean" value of attenuation must be made to each tissue type. This approach is under development for PET/MRI [15].

Quantitative accuracy is diminished when the object being imaged is smaller than or of-the-order-of the spatial resolution of the imaging system. This is called the "partial volume effect". The partial volume effect can be partially corrected for if the resolution response function of the system is well known. However, it is always preferred to begin the quantification process with better spatial resolution. With MRI's superior spatial resolution, the boundaries determined by MRI can be used to provide a-priori information to enable an improved correction for the partial volume effect for the SPECT quantification calculation.

Because SPECT does not require further corrections for random coincidences and changes in detection efficiency due to count-rate dead time effects, SPECT enjoys an advantage compared with PET in that the uncertainties in quantitative accuracy from these corrections are not present in the SPECT measurements. Especially in the preclinical imaging arena, where SPECT resolution now is routinely superior to PET by about a factor of two (0.5 mm compared with 1.0 mm FWHM), the partial volume effect offers SPECT an advantage over PET in preclinical quantification accuracy.

4 Review of SPECT/MRI Development Efforts

Over the centuries physicians have observed symptoms and physical manifestations of disease and used them to render a curative recommendation. The role of medical imaging to aid the physician's diagnosis is summarized in the timeline of Table 14.1.

Table 14.1 The historical progression of multi-modality advances with emphasis on imaging contributions

Time	Development	Example(s)
Pre-modern era	Tribal wisdom, knowledge of natural medicine	Herbs, fungi, acupuncture
~1500	Dissection of cadavers; basic understanding of musculo-skeletal and vascular anatomy	Anatomical atlases
~1900	X-ray discovery	In vivo visualization of blockages, foreign bodies, and malformations using film
~1970	Tomography (MRI, CT, nuclear), computers	3D visualization of anatomy (CT, MRI), function (MRI, nuclear), and molecular (nuclear) conditions in vivo
1995	Dual-modality, sequential	SPECT/CT and PET/CT
2005	Dual-modality, simultaneous	PET/MRI, SPECT/MRI
Future	Single-modality, simultaneous, two 3D datasets	Multiple wavelength optical and SPECT

Note that the ultimate multi-modality configuration of the future might be a single modality which simultaneously acquires multiple image datasets via multiple wavelength channels such as allowed by optical or SPECT techniques

Beginning in the Renaissance era, the dissection of cadavers for the purpose of documenting the human anatomy allowed physicians to "imagine" the fluid flow, swelling, inflammation, abscess formation, and other phenomena in living subjects. This was aided by palpation techniques used with knowledge of normal anatomy to deduce the presence of abnormalities. In the period after the discovery of X-rays, the use of imagination was superseded by definitive X-ray images. New modalities arose during the preceding century—ultrasound, nuclear, and magnetic resonance imaging each contributed its unique clinical data to the physician's diagnostic observations. With new modalities that probed different biological processes, the physician again was required to use imagination or "mental fusion" to combine the impressions from the various imaging modalities to formulate an improved diagnostic judgment. The practice of radiology during the period from ~1940 (after which ultrasound and nuclear medicine were added to X-ray imaging) to ~1995 (when dual-modality imaging was introduced) required mental fusion of imaging data acquired at different times and under varying physical conditions.

Computers were introduced to medical imaging in the 1970s. By the 1990s the efficient transfer of image data by removable media or over first-generation networks allowed the "software fusion" of digital image data from individual modalities. The use of computers to combine image datasets is a necessary first step to justify the development of multimodality systems. If radiologists are "mentally fusing" image sets on a regular basis, there is obviously a growing demand for a software solution to perform this task. The existence of mental and software fusion of two imaging datasets provides the impetus for the development of a hardware solution that will remove experimental variables and reduce costs and inconvenience associated with separate imaging sessions.

With this review of the history of Radiology in mind we examine the developments in the field of SPECT/MRI.

Image registration is the scaling and orientation (and, if necessary, warping) of two 3D image datasets in preparation for the display of the fused images. Early efforts in the development of SPECT/MRI explored techniques to register the two datasets [16] and to use the high resolution MRI data as a-priori information to improve the SPECT reconstruction [17]. An early software fusion example of clinical SPECT combined with MRI was for brain imaging—matching anatomical MRI with perfusion SPECT [18]. The fixed confines of the skull provide a known backdrop for the development of registration and quantitative analysis routines [19] for the two modalities. Software fusion of SPECT with MRI has also been done with clinical prostate images [20].

The first step in developing SPECT/MRI hardware is to push the current technologies to their operational limits. Although it is generally assumed that PMT-based gamma cameras cannot operate effectively in magnetic fields stronger than the earth field, careful experimental layout allows the operation of a PMT-based system in a magnetic field of 0.1 T using a "low-field" MRI (roughly an order of magnitude lower than used in the clinical) and a rotating, PMT-based SPECT system (Gaede, Freiburg, Germany) [21, 22]. This system cannot be used for simultaneous SPECT and MRI acquisitions, but served as a useful example of a "same-room" prototype that is similar to PET/CT in sequential operation.

The magnetic field-sensitive PMTs can be substituted with semiconductor detectors, thereby allowing researchers to bring SPECT imagers directly into the high magnetic fields in use today in small animal MRI research. A 2-mm thick, 5-mm × 5-mm CZT single crystal was introduced into a 7 T animal MRI imager by researchers at the University of California, San Francisco [23]. An ultra-high resolution (350-micrometer pixels), 1.1-cm × 2.2-cm CdTe prototype has demonstrated feasibility as an imaging detector in a 4.7 T MRI scanner [24]. Together with the work of the authors, these supporting efforts confirm that the CZT and CdTe family of radiation imaging detectors is currently the preferred choice for high-performance, simultaneous SPECT/MRI.

5 Detector Technologies for Simultaneous SPECT/MRI

The magnetic field strength, B, in state-of-the-art preclinical MRI systems is fixed typically at 4.7 T, 7.0 T, 9.4 T or 11.7 T.[3] B determines the polarization of the magnetizations, which directly determines the achievable signal-to-noise of the MRI image. The very high magnetic field strength precludes the use of conventional

[3] Varian, Inc. (Palo Alto, California) and Bruker Biospin GmbH (Ettingen, Germany are the primary vendors of preclinical MRI instruments.

SPECT camera hardware, in particular photomultiplier tubes (PMTs), inside an MRI system. The failure of PMTs in strong magnetic fields, even with shielding by metals, is the most important technical hurdle for the design of an integrated SPECT/MRI hardware. To solve the problem of mutual interference between SPECT and MRI there are two possibilities: (1) to develop low-field MRI systems which might allow one to use PMT based SPECT, or (2) to use high-field MRI systems and develop a SPECT system based on new gamma radiation detectors that work in strong magnetic fields. Possible alternatives to PMTs include solid state semiconductor radiation detectors, typically based on silicon, germanium or much heavier compounds, like cadmium zinc telluride (CZT). Solid state detectors offer additional advantages over PMTs, e.g., higher stability, smaller size, lower power dissipation and potentially lower costs. Possible detector technologies for high field MRI-compatible SPECT include: (1) direct detection in a semiconductor based radiation sensors, (2) and a combination of scintillation crystals and semiconductor photosensors.

In a PMT the primary and secondary electrons move in a vacuum of about 10-4 mbar. The electrons accelerate between the focusing electrodes (dynodes) due to the electrostatic field [25]. However, when exposed to a magnetic field the PMT gain changes depending on its orientation relative to the magnetic field. Due to the Lorentz force, the electrons move in a helix with a radius of curvature r. The radius, r, and the momentum component, $p \times \cos(\lambda)$, perpendicular to the magnetic field are related by [26]:

$$r_{[\mu m]} = 3.3 \frac{p_{[keV/c]}}{B_{[T]}} \cdot \cos(\lambda) \tag{14.1}$$

The angle, λ, is the pitch angle of the helix. The radius is relatively small: for a given electron momentum $p \times \cos(\lambda)$ in the range from a few eV/c up to 100 eV/c, one calculates the radius of less than 1 μm at 1 T, which is much smaller than the distance between the photocathode and the first dynode. The Lorentz force causes the gyro-center to move with respect to the electric field lines (Lorentz drift), and thereby deflects the electrons from their proper trajectory. The signal amplitude in a PMT depends on the correct trajectories of secondary electrons among the dynodes, and therefore small changes in the steering greatly affect the amplified signal.

Figure 14.1 illustrates the effect of a magnetic field on the image acquired with a PMT-based gamma camera from five straight line sources. The arcs denote the magnetic field of equal strength for 1, 3, 10 and 30 G (1 G = 10^{-4} T, where G = Gauss and T = Tesla are the units of magnetic field strength). The line sources give a good image at a magnetic field of less than 3 G. The image becomes distorted for a magnetic field higher than 10 G and it disappears at 30 G.

The magnetic field affects semiconductors differently than PMTs due to the differences in charge transport and charge collection. In a semiconductor the photoelectron generates electrons in the conduction band and vacancies (holes) in the valence band. The semi-classical model of conduction predicts the movement of charge carriers (electrons and holes) in the crystal [27]. The drift velocity for electrons and holes in a semiconductor is proportional to the electric field strength and

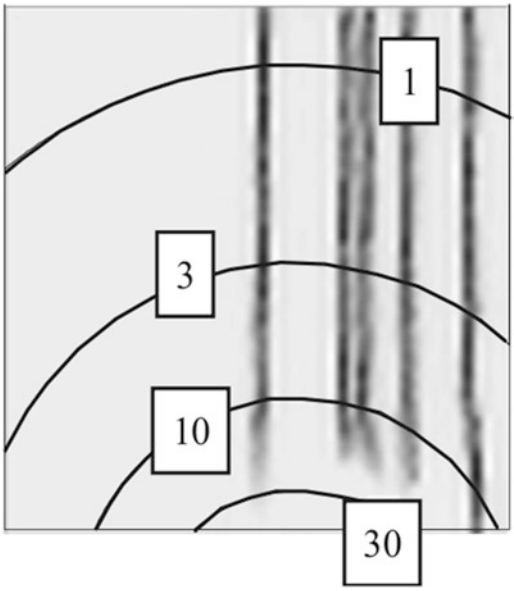

Fig. 14.1 The effect of a magnetic field on the image of ^{99m}Tc-filled line sources acquired with a PMT-based gamma camera. The line images distort at 10 G and disappear above 30 G

to their respective drift mobilities. The drift mobility characterizes the effect of scattering for electrons and holes with the crystal lattice. In the absence of a magnetic field, electrons and holes move along the electric field lines in opposite directions. In the presence of a magnetic field, charges curl according to equation 14.1 with a sub-micron radius and move along an inclined trajectory due to the Lorentz force. The Lorentz angle, θ, between the charge velocity and the electric field vector is given by Eq. (14.2) [28]:

$$\theta = \arctan\left(\mu B\right) \tag{14.2}$$

The Hall mobility, μ, is almost equal to the drift mobility. The electron Hall mobility in silicon at room temperature is 1670 cm^2/Vs, thus yielding θ=9.5° at B=1 T [28]. In a PMT the electron mobility is much larger than in a semiconductor crystal which increases the drift away from the electric field much more than in a semiconductor. The effects of the Lorentz angle has been studied in position sensitive silicon detectors [29] and its effect on charged particle tracking and imaging can be corrected for after data acquisition.

5.1 MRI-Compatible Indirect Radiation Sensors

Indirect gamma radiation sensors typically consist of an inorganic scintillator and a photosensor. Many types of scintillators have been developed for Nuclear Physics and High Energy Physics experiments [30], where they are routinely used in strong magnetic fields. Experiments in MRI systems show that scintillators only minimally affect

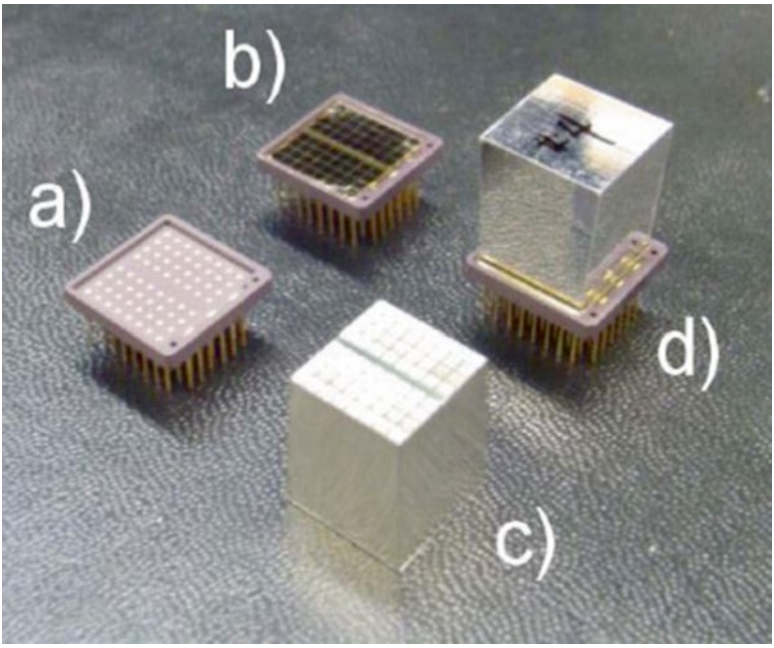

Fig. 14.2 Ceramic package and pin grid array (**a**), APD array (**b**), scintillator array (**c**), and assembly of scintillators and APDs (**d**)

image quality depending on their susceptibility and distance from the field-of-view [31]. New developments in scintillators [32] and new developments in photosensors [33], especially on semiconductor photosensors with large gain, might enable new MRI-compatible high resolution, position-resolved gamma spectroscopy in preclinical and clinical imaging. Figure 14.2 shows a photograph of a gamma radiation detector module, originally designed for preclinical PET/CT applications. The module consists of an LYSO scintillator crystal array and two arrays of monolithic avalanche photodiodes (APDs) [34]. The APDs are semiconductor photosensors designed for the 1-to-1 readout of the LYSO scintillator array. The scintillator array is made of 64 crys tals, 12-mm long, and 1.2-mm pitch at the photosensor. The mean energy resolution is 27.5 % FWHM at 511 keV, and the intrinsic spatial resolution is 0.82 mm FWHM. This energy resolution precludes SPECT applications, but can enable MRI-compatible gamma radiation detection and MRI-compatible PET. The combination of scintillators and APDs [35] or SiPMs/MPPCs[4] [36] has been shown to work inside MRI systems. Conventional SPECT systems based on monolithic NaI scintillators and PMTs have an energy resolution of about 14 keV FWHM at 140 keV. Using arrays of SiPMs it might be possible to obtain sufficient energy resolution for SPECT [37].

[4] Silicon photomultipliers (SiPMs) and multi-pixel photon counters (MPPCs) are two names for silicon photosensors operated in Geiger-mode.

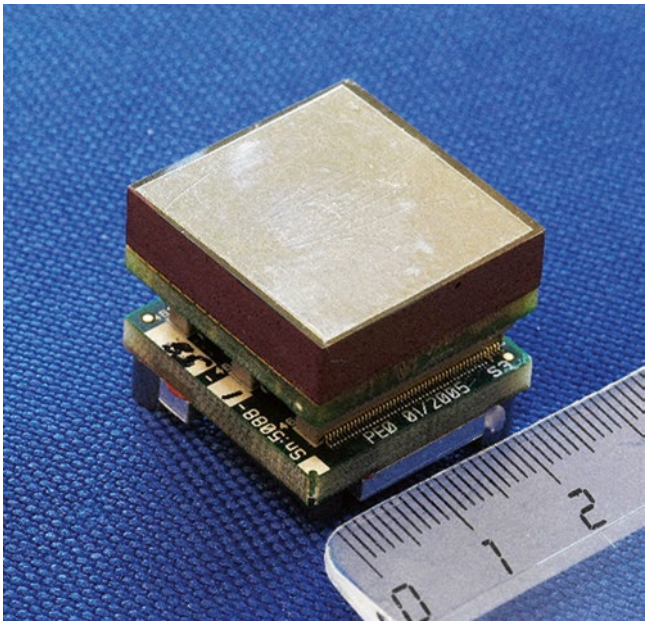

Fig. 14.3 Cadmium zinc telluride (CZT) crystal in a gamma radiation detector module

5.2 MRI-Compatible Direct Radiation Sensors

The intrinsic energy resolution of scintillators is determined by crystal properties, photon statistics, and electron scattering [38]. Direct conversion radiation detectors can achieve higher energy resolution than scintillators. Figure 14.3 shows a photograph of a radiation detector module designed for SPECT applications. The module contains a 5-mm thick crystal of cadmium zinc telluride (CZT) (eV Products, Saxonburg, PA USA) which converts a gamma quantum "directly" into an electric signal. The radiation entrance side is covered by a solid metallic electrode (cathode), while the opposite side of the crystal has a pattern of 16×16 pixels (anodes). A gamma-ray that interacts in the crystal generates electrons in the conduction band and holes in the valence band. Electrons and holes move in opposite directions in the electric field and thereby induce a current in the pixels closest to the point of interaction. The detector module was designed for SPECT applications and allows one to measure the energy and the position of gamma rays in the range from 20 to 350 keV. The intrinsic spatial resolution of this module is equal to the pixel pitch of 1.6 mm. The energy resolution is 5 keV FWHM at 140 keV.

Experiments show that the signal amplitude and energy resolution in CZT pixels at magnetic field strengths of 3 and 4 T are minimally degraded compared with operation in the Earth's field (Fig. 14.5). Experiments also show that the presence and operation of the CZT module does not degrade the MRI performance within the field-of-view [39]. CZT appears to be well suited for MRI-compatible gamma cameras.

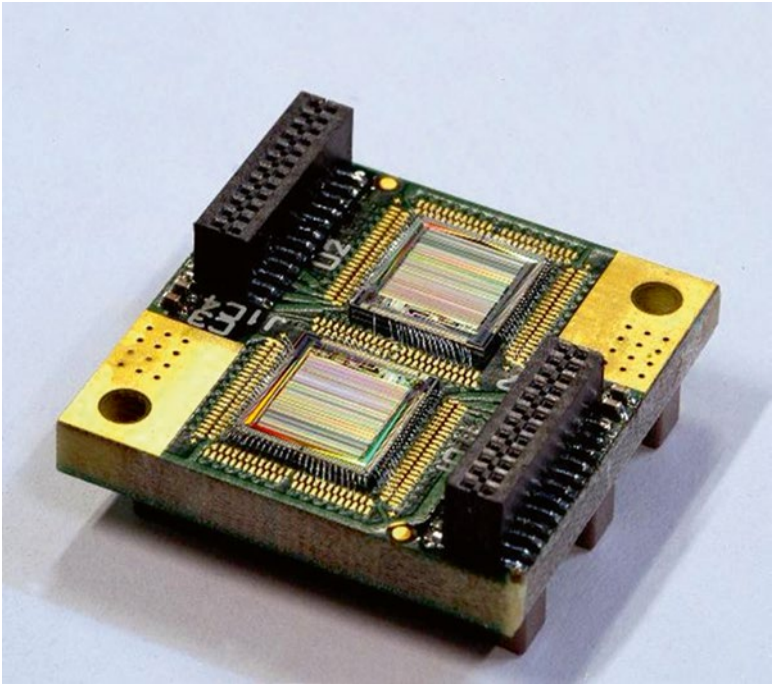

Fig. 14.4 Application specific integrated circuits (ASICs)

5.3 Integrated Front-End Electronics

An imaging system of detector heads (or rings) comprised of radiation detector modules from Figs. 14.2 and 14.3 would necessarily feature several thousand pixels.[5] The electrical currents from pixels are relatively small (several thousand electrons in less than a micro second) and it would be impractical to conduct the signals from all pixels over long distances. It is therefore important to design application specific integrated circuits (ASICs) which process the currents in close proximity to the pixels and provide information on energy, position, and time. The signal processing on the ASIC can include signal amplification, filtering, discrimination, multiplexing of analog and digital data and further digital logic. In Fig. 14.3 the pixels are directly connected to an ASIC electronic readout located underneath the CZT [40]. Tests have shown that the ASICs are MRI-compatible and operate well inside and outside of the MRI system [41]. Each pixel is an independent gamma-ray energy spectrometer and with CZT this discrimination enables imaging of multiple isotopes simultaneously. The electronic readout for 256 pixels (two ASICs) is shown in Fig. 14.4.

[5] For example, the Triumph™ (Gamma Medica-Ideas, Inc.) preclinical microSPECT system uses 4 heads, with 25 modules per head, and 256 CZT pixels per module, for a total of 25,600 pixels.

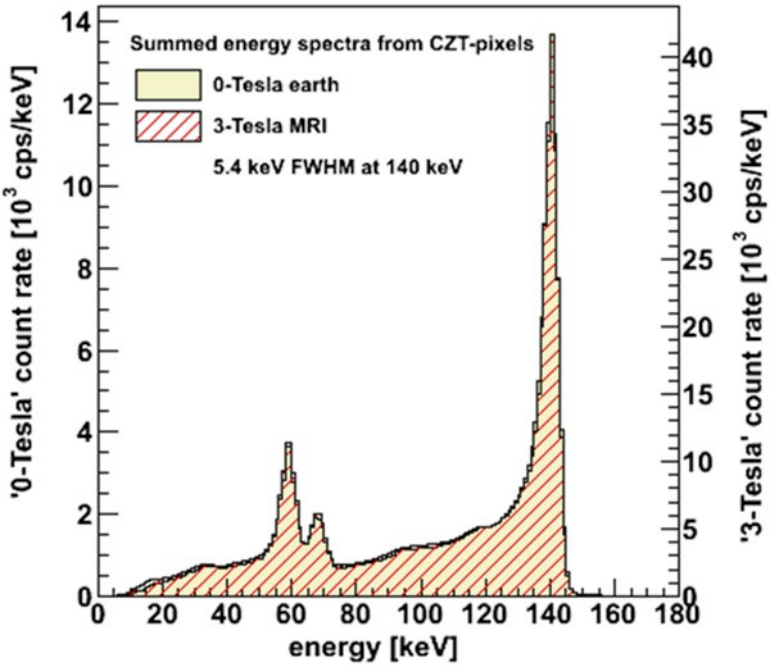

Fig. 14.5 CZT energy spectra from ^{99m}Tc measured at Earth's field and at 3 T

The ASICs are normally covered with a cap which was not mounted in this photograph. The two connectors near the ASICs provide connections for power, control signals and data lines. A data acquisition system acquires radiation events from many ASICs and delivers list mode data to a computer outside the MRI system. All electronics inside the MRI has been shielded against electromagnetic interference with the MRI.

5.4 Experimental Results

The modules shown in Fig. 14.3 were used inside a high-field MRI and at Earth's magnetic field to acquire gamma-radiation energy spectra with ^{99m}Tc. The gain was measured for each pixel and calibrated using the 140-keV ^{99m}Tc photopeak and a 59-keV tungsten X-ray fluorescence peak. Figure 14.5 shows the two calibrated energy spectra superimposed. The energy spectrum has a sharp photo peak at 140 keV and smaller X-ray fluorescence peaks at 59 and 68 keV. The lowest energy threshold in all pixels is less than 20 keV which is excellent for preclinical SPECT applications. There is no difference in the shape of the summed spectra between 3 T and Earth's magnetic field which confirms that CZT with ASICs retains its spectroscopic performance inside the MRI.

Figure 14.6 shows images from a uniform phantom (top) and a resolution phantom (bottom) acquired with a 3 T MRI system (left two) and a SPECT system (right

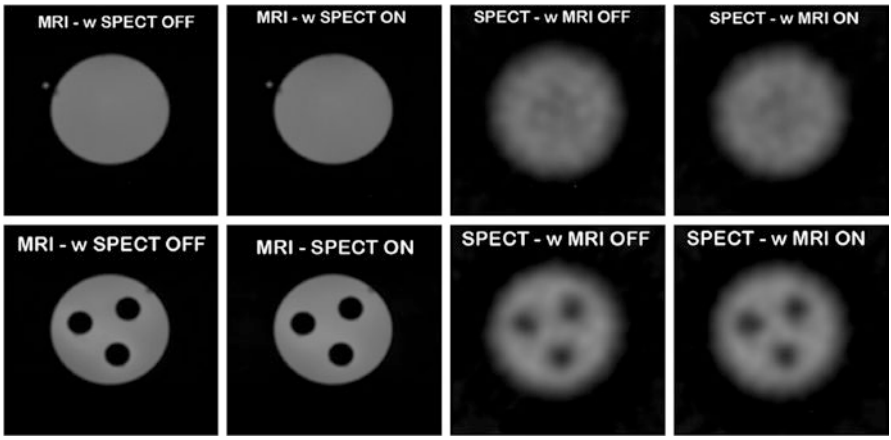

Fig. 14.6 MRI and SPECT images from phantoms: uniform (*top*) and resolution phantom (*bottom*). The system resolution (pixel resolution convolved with collimator) was about 3 mm FWHM

two). The phantom has a diameter of 25 mm and was filled with water and ^{99m}Tc (20 MBq). The SPECT images have been acquired with a CZT module (1.6 mm pixels) and a parallel-hole collimator by rotating the phantom with respect to the CZT module [39]. The images show that both SPECT and MRI can acquire images from objects simultaneously in the same field-of-view.

5.5 MRI-Compatible SPECT Camera

Figure 14.7 shows a photograph of an MRI-compatible small animal SPECT camera. The camera has a barrel shape to fit into an MRI magnet bore of larger than 12-cm diameter. The barrel structure (white), made from MRI-compatible materials, supports 32 SPECT imaging modules (see Fig. 14.3) which are connected by MRI-compatible flexible circuit boards (brown and green). The cradle (white) is optional and allows one to use the SPECT inside large-bore MRI systems or as a stand-alone SPECT system. The 32 imaging modules are arranged in 4 octagons, providing a spherical or cylindrical field-of-view inside the camera bore, depending upon the configuration of pinholes in a cylindrical collimator sleeve. A mouse, located at the center, is surrounded by a radio-frequency (RF) coil, the cylindrical collimator sleeve, and imaging modules.

The imaging modules are arranged in concentric octagons which are rotated with respect to each other (i.e., non-aligned, as shown in Fig. 14.7) to provide tomographic angular sampling in the tangential direction. This SPECT camera surrounds the entire field-of-view and has no moving parts. Tomographic images are reconstructed from projections acquired from the different angles. This SPECT configuration allows one to sample all projection views simultaneously from a subject in the FOV which improves sensitivity over conventional SPECT and is particularly attractive for dynamic SPECT imaging.

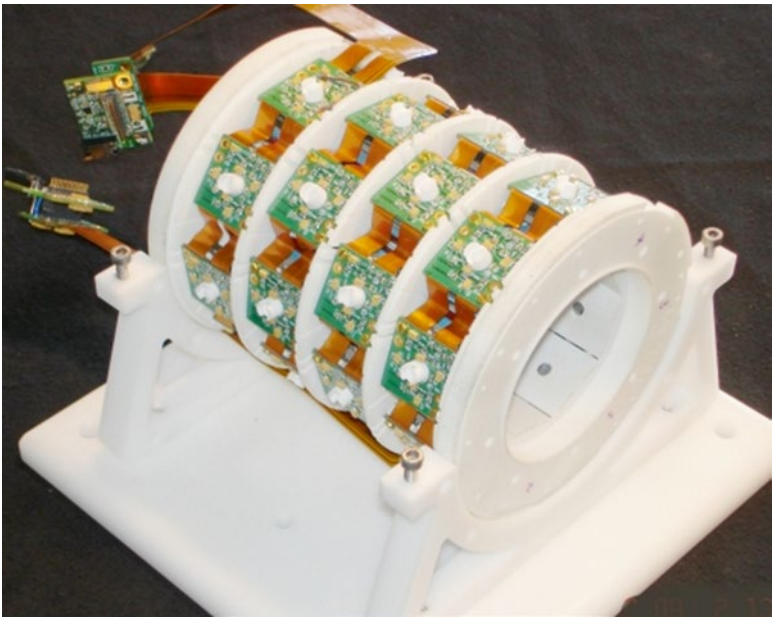

Fig. 14.7 MRI-compatible SPECT camera head

Conventional SPECT systems use a gamma radiation collimator normally made from solid lead located between the subject and the radiation detectors. It is possible to build MRI-compatible gamma radiation shields and collimators from heavy metals [42]. Multiple pinholes can be designed into the material to collimate the gamma radiation and projects gamma radiation from the subject through the pinholes to the radiation detector modules. The pinhole principle is well known from visible light pinhole cameras. The concept of multi-pinhole collimators combined with high spatial resolution detectors and magnification of less than one improves the SPECT sensitivity [43]. It is important that the pinhole collimator effectively collimates and shields the gamma radiation but allows one to transmit the MRI radio-frequency (RF) and avoids distortion of the MRI static magnetic fields or MRI gradient fields. Tests regarding MRI safety and compatibility follow the recommended guidelines [44].

6 Summary

Multimodality imaging has grown rapidly since the first PET/CT scanners were made available on the clinical market about 10 years ago. Because of developments in semiconductor radiation and photosensor detector technologies, recent research efforts have concentrated on combining PET or SPECT with MRI. We have described above the rationale for building a combined SPECT/MRI for preclinical research,

with an eye toward future clinical applications. Pixellated CZT modules with ASIC microelectronic circuitry can provide a flexible foundation upon which preclinical imaging systems (e.g., Fig. 14.7) can be built. Future SPECT/MRI applications in the clinic will likely be based upon the most successful of the three preclinical areas we have described: (1) Disease-based research; (2) Therapy response/drug development; and (3) Molecular Imaging (stem cells, reporter imaging, and nanoparticles).

Acknowledgments The authors wish to thank the following individuals for their substantial contributions to the SPECT/MRI progress: Benjamin M.W. Tsui, Orhan Nalcioglu, Si Chen, Mark Hamamura, Jingyan Xu, Werner Roeck, Yuchuan Wang, Seung-Hoon Ha, Samir Chowdhury, Gunnar Maehlum, Bjorn Sundal, Jon Gjaerum, Marek Szawlowski, Maciej Kapusta, and Ryan Gomez. Funding from the U.S. NIH NIBIB Grant R44 EB006712 and the Research Council of Norway is gratefully acknowledged.

References

1. Hruska CD, Phillips SW, Whaley DH, Rhodes DJ and O'Connor MK (2008) Molecular breast imaging: use of a dual-head dedicated gamma camera for detection of small breast tumors. Am J Roentgenol **191**(6):1805–1815.
2. Brassell SA (2005) Update on magnetic resonance imaging, Prostascint, and novel imaging in prostate cancer. Curr Opin Urol **15**(3):163–166.
3. Bander NH, Trabulsi EJ, Kostakoglu L et al (2003) Targeting metastatic prostate cancer with radiolabeled monoclonal antibody J591 to the extracellular domain of prostate specific membrane antigen. J Urol **170**:1717–1721.
4. Banerjee SR, Foss CA, Mease RC et al (2007) Synthesis and evaluation of 99mTc/Re labeled PSMA inhibitors. J Nucl Med **48**(Suppl 2):18P.
5. Shukla-Dave A, Hricak H, Ishill NM et al (2009) Correlation of MR imaging and MR spectroscopic imaging findings with Ki-67, phosphor-67, phosphor-Akt, and androgen receptor expression in prostate cancer. Radiology **250**:803–812.
6. Saeed S, Yao M, Philip B and Blend M (2006) Localizing hyperfunctioning parathyroid tissue: MRI or nuclear study or both? Clin Imaging **30**(4):257–265.
7. Eslamy HK and Ziessman HA (2008) Parathyroid scintigraphy in patients with primary hyperparathyroidism: 99mTc sestamibi SPECT and SPECT/CT. Radiographics **28**(5):1461–1476.
8. Neumann DR, Obuchowski NA and DiFilippo FP (2008) Preoperative 123I/99mTc-sestamibi subtraction SPECT and SPECT/CT in primary hyperparathyroidism. J Nucl Med **49**: 2012–2017.
9. Wagenaar DJ, Kapusta M, Li J and Patt BE (2006) Rationale for the combination of nuclear medicine with magnetic resonance for preclinical imaging. Technol Cancer Res Treat **5**: 343–350.
10. Lecomte R (2004) Technology challenges in small animal PET imaging. Nucl Instrum Methods Phys Res **A527** (1–2):157–165.
11. Ito H, Koyama M, Goto R et al (1995) Cerebral blood flow measurement with 123I-IMP SPECT, calibrated standard input function and venous blood sampling. J Nucl Med **36**(12):2339–2342.
12. Fritz-Hansen T, Rostrup E, Larsson HBW et al (1996) Measurement of the arterial concentration of Gd-DTPA using MRI: a step toward quantitative perfusion imaging. Magn Reson Med **36**(2):225–231.
13. Ribot EJ, Miraux S, Delville MH et al (2009) Study of the MR relaxation of microglia cells labeled with Gd-DTPA-bearing nanoparticles. Contrast Media Mol Imaging **4**(3):109–117.

14. Zaidi H (2007) Is MR-guided attenuation correction a viable option for dual-modality PET/MR imaging? Radiology **244**:639–642.
15. Martinez-Möller A, Souvatzoglou M, Delso G et al (2009) Tissue Classification as a Potential Approach for Attenuation Correction in Whole-Body PET/MRI: Evaluation with PET/CT Data. J Nucl Med **50**:520–526.
16. Yong Z, Fessler JA, Clinthorne NH and Rogers WL (1994) Joint estimation for incorporating MRI anatomic images into SPECT reconstruction. Proc IEEE Nucl Sci Symp/Med Imag Conf **3**:1256–1260.
17. Calvini P, Vitali P, Nobili F and Rodriquez G (2001) Enhancement of SPECT reconstructions by means of coregistered MR data. IEEE Trans Nucl Sci **48**(3, part 2):750–755.
18. Colin A and Boire JY (1997) MRI-SPECT image fusion for the synthesis of high resolution functional images: a prospective study. Proceedings of the 19th Annual International Conference of the IEEE **2**:499–501.
19. Knutsson L, Boerjesson S, Larsson EM et al (2007) Absolute quantification of cerebral blood flow in normal volunteers: correlation between Xe-133 SPECT and dynamic susceptibility contrast MRI. J Mag Res Imag **26**(4):913–920.
20. Seo Y, Kurhanewicz J, Franc BL, Hawkins RA and Hasegawa BH (2005) Improved prostate cancer imaging with SPECT/CT and MRI/MRSI. IEEE Trans Nucl Sci **52**(5, part 1):1316–1320.
21. Breton E, Choquet C, Goetz C et al (2007) Dual SPECT/MR imaging in small animals. Nucl Instrum Methods Phys Res **A571** (1–2):446–448.
22. Goetz C, Breton E, Choquet P, Israel-Jost V and Constantinesco A (2008) A. SPECT low-field MRI system for small-animal imaging. J Nucl Med **49**:88–93.
23. Després P, Izaguirre EW, Siyuan L etal (2007) Evaluation of an MR-compatible CZT detector. Proc IEEE Nucl Sci Symp/Med Imag Conf **6**:4324–4326.
24. Meng LJ, Tan JW and Fu G (2007) Design study of an MRI compatible ultra-high resolution SPECT for in vivo mice brain imaging. Proc IEEE Nucl Sci Symp/Med Imag Conf **4**:2956–2960.
25. Burle Industries Inc (1980) Photomultiplier Handbook. printed in U.S.A.
26. Amsler C et al (2008) Particle Detectors. Physics Letters **B667** (1) available on the Particle Data Group website URL: http://pdg.lbl.gov/.
27. Ashcroft NW and Mermin ND (1976) in: Solid State Physics. Saunders College Publishing.
28. Lutz G (2001) Semiconductor Radiation Detectors. Device Physics. Springer 2nd Edition.
29. Bartsch V, de Boer W, Bol J etal (2003) An algorithm for calculating the Lorentz angle in silicon detectors. Nucl Instrum Methods Phys Res **A497**:389–396.
30. Dorenbos SE, Weber MJ, Bourret-Courchesne E and Klintenberg MK (2003) The quest for the ideal inorganic scintillator. Nucl Instrum Methods Phys Res **A505**:111–117.
31. Yamamoto S, Kuroda K and Senda M (2003) Scintillator selection for MR-Compatible Gamma Detectors. IEEE Trans Nucl Sci **50**(5, part 2):1683–1685.
32. Lecoq P (2009) New crystal technologies for novel calorimeter concepts. J Phys Conference Series. **160**:paper 012016. Online at www.iop.org/EJ/toc/1742-6596/160/1.
33. Renker D (2007) New trends on photodetectors. Nucl Instrum Methods Phys Res **A571**:1–6.
34. Berard P, Bergeron M, Pepin CM et al (2009) Development of a 64-channel APD detector module with individual pixel readout for submillimetre spatial resolution in PET. Nucl Instrum Methods Phys Res **A610**:20–23.
35. Pichler BJ, Judenhofer MS, Catana C et al (2006) Performance Test of an LSO-APD Detector in a 7-T MRI Scanner for Simultaneous PET/MRI. J Nucl Med **47**:639–647.
36. Schaart DR, van Dam HT, Seifert S et al (2009) A novel, SiPM-array-based, monolithic scintillator detector for PET. Phys Med Biol **54**:3501–3512.
37. Majewski S, Proffitt J, McKisson J et al (2009) Imaging Tests with Silicon Photomultipliers Made from MPPC Arrays in Magnetic Fields up to 14 Tesla. IEEE Nucl Sci Symp/Med Imag Conf, abstract M13–249.
38. Moszynski M, Balcerzyk M, Czarnacki W et al (2004) Intrinsic Energy Resolution and Light Yield Nonproportionality of BGO. IEEE Trans Nucl Sci **51**(3, part 3):1074–1079.

39. Hamamura MJ, Ha SH, Roeck WW et al (2009) Development of an MR-compatible SPECT system (MRSPECT) for simultaneous data acquisition. Phys Med Biol in press.
40. Mikkelsen S, Meier D, Maehlum G et al (2008) Low-Power and Low-Noise Multi-Channel ASIC for X-ray and Gamma Ray Spectroscopy. Proc 2nd Int Workshop Analog Mixed Signal Integrated Circuits for Space Applications AMICSA.
41. Azman S, Gjaerum J, Meier D et al (2007) A Nuclear Radiation Detector System with Integrated Readout for SPECT/MR Small Animal Imaging. Proc IEEE Nucl Sci Symp/Med Imag Conf **3**:2311–2317.
42. Strul D, Cash D, Keevil SF et al (2003) Gamma Shielding Materials for MR-Compatible PET. IEEE Trans Nucl Sci **50**(1, part 1):60–69.
43. Rogulski MM, Barber HB, Barrett HH et al (1993) Ultra-High-Resolution Brain SPECT Imaging: Simulation Results. IEEE Trans Nucl Sci **40**(4, part 1–2):1123–1129.
44. Schaefers G (2008) Testing MR safety and compatibility – An Overview of the Methods and Current Standards. IEEE Eng Med Biol Mag, **27:** 23–27.

Chapter 15
Dual-Modality Preclinical PET/MRI Instrumentation

David Schlyer and Bosky Ravindranath

1 Introduction

Multimodality imaging using positron emission tomography (PET) and Magnetic resonance imaging (MRI) is emerging as an extremely valuable tool for investigating disease and physiological processes in small animal models. MRI has high spatial resolution but low sensitivity for detecting low abundance molecules and PET has very high sensitivity for the detection of radiotracers but relatively poor spatial resolution. The combination of these two molecular imaging techniques offers synergistic advantages over either modality alone. A fused anatomical and functional image affords complementary information that clearly improves our understanding. Images acquired simultaneously offer distinct advantages over sequential image acquisition since this gives "perfect" coregistration and observing the same process from two different vantage points can ensure the correlation of information that is impossible in separate experiments.

PET/CT has become the standard for clinical imaging studies because CT also gives anatomical detail not possible with PET. However, PET/MRI is better in several respects as a diagnostic tool than PET/CT, and even more so in pre-clinical, small-animal studies. In the simplest application, using MRI data to detect and correct for motion during a PET scan, and making optimum use of dynamic data is likely to lead to better, more detailed images. The study of tumor uptake and dynamics with dual-labeled, functionalized nanoparticle contrast agents [1], and simultaneous PET and fMRI monitoring of brain activity are just two examples of the possibilities with this dual-modality system. PET employs radiotracers that target

D. Schlyer (✉)
Biosciences Department, Brookhaven National Laboratory, Upton, NY, USA
e-mail: schlyer@bnl.gov

B. Ravindranath
Biomedical Engineering Department, SUNY Stony Brook, Stony Brook, NY, USA
e-mail: bosky@bnl.gov

H. Zaidi (ed.), *Molecular Imaging of Small Animals: Instrumentation and Applications*,
DOI 10.1007/978-1-4939-0894-3_15,

specific sites or molecules with a sensitivity many orders-of-magnitude greater than is possible with current MRI techniques, but PET cannot distinguish the molecular species to which the radioactive atom is attached. Combining PET radiotracers with magnetic resonance spectroscopy (MRS) using C-13 labeled tracers could significantly improve our insight into molecular processes occurring in the body [2]. Some additional advantages are listed below:

- Radiation dose is reduced. MRI does not contribute to the patient's radiation dose whereas the dose from a CT scan is significant.
- Excellent spatial registration is obtained between the MRI and PET images. This ability is particularly important for organs and tissues whose position and shape can shift even between temporally proximal scans.
- Soft-tissue contrast is enhanced, and tissue boundaries are more clearly delineated than is possible with CT. This may support reliable partial-volume correction of PET data that can be very important for quantitative clinical data.
- Accurate temporal registration between the MRI and PET scans allows the determination of pharmacokinetics and pharmacodynamics. The MRI data also could be used to obtain blood flows and to correct for the effects of blood-vessel partial volume, effects that are inherent in the PET data sets, potentially enabling accurate measurement of input functions from this data without requiring arterial sampling.
- The magnetic field of the MRI may slightly improve the PET spatial resolution for high energy positron emitters, as is the case for some non-traditional PET radionuclides being used in preclinical studies.

Several approaches have been explored in the pursuit of the goal of simultaneous PET and MRI. There has been significant progress in identifying PET scintillators with magnetic properties [3] which are compatible with MRI. PET/MRI tomographs have been designed that use optical fibers to transmit the scintillation light from the crystal out of the magnetic field of the MRI to photomultiplier tubes (PMTs) [4–9]. Several groups favor a design that replaces the PMTs in the PET tomograph with magnetic field-insensitive avalanche photodiodes (APD) [10–16]. Since one issue in running PET and MRI simultaneously is the potential for the two modalities to interfere, there has been some effort to design shielded PET electronics to avoid electromagnetic interference [17]. However, several technical challenges remain that must be met to reduce or eliminate such interference. We describe the history of the development of this instrumentation, and its current state-of-the art in the following sections.

2 Instrumentation Development

2.1 PET Using PMTs and Optical Fiber Technology

Early commercial PET scanners for human and animal imaging were built on the concept of directly coupling a scintillator, such as Bismuth Germanate (BGO), to a PMT. The earliest commercially available animal PET scanner, the CTI/Siemens

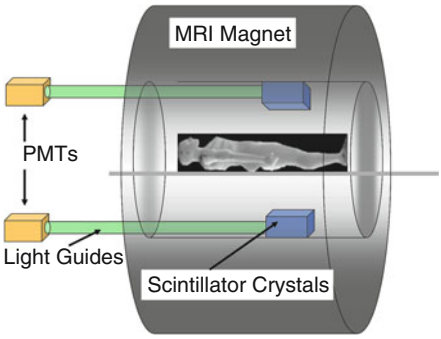

Fig. 15.1 Schematic of combined PET and MRI scanner where light from scintillator blocks inside the MRI scanner is guided to PMTs placed in a low magnetic field via light guides, as described by Hammer [19]

Animal Tomograph—model 713 [18] was built on this concept. It utilized Anger type logic for locating the event position and had a reconstructed transaxial radial spatial-resolution ranging from 3.8 mm full-width-at-half-maximum (FWHM) at the center of the scanner, to 6.7 mm FWHM at a radius of 12 cm; the scanner's tangential resolution was consistent at 3.8 mm FWHM.

The prospect for simultaneous PET and MRI imaging has intrigued researchers since the early 1980s. Complimentary imaging information offered by the two modalities and the improvement in the PET's spatial resolution when using high-energy isotopes in strong magnetic fields engendered new approaches for combining these two imaging modalities. The most logical approach towards integrating them was to develop an MRI-compatible PET insert; the first such device was patented by Hammer in 1990 [19]. The then-available scintillator-PMT combination for PET scanners was not MRI-compatible due to the sensitivity of the PMT to magnetic fields. The presence of PMTs also made the magnetic field inhomogeneous, so distorting the MRI image. Researchers recognized that the key to making the two imaging modalities compatible was to position PMTs in a region of low magnetic-field strength where they could function normally and not disturb the homogeneity of the MRI's magnetic field. Guiding the optical photons from the scintillator blocks to the PMTs via light guides accomplished this aim (Fig. 15.1). The portion of the PET detector that is positioned in the MRI's field-of-view is free of ferromagnetic material, so minimizing inhomogeneities and susceptibility artifacts in the MRI image.

Such a design was implemented in a prototype system with two NaI(T1) scintillation crystals placed inside a 5 T magnet and coupled to the PMTs via a cylindrical Lucite rod [4]. A measurement of the point-spread function of a Ge-68 source inside the 5 T magnet showed a FWHM of 1.64 mm, while outside the magnet the FWHM was 2.19 mm, suggesting an improvement in resolution from a reduction in the range of the positrons perpendicular to the 5 T field.

To image and quantify a radiotracer's concentration in the organs of small animals, a small animal PET must have high resolution. Resolution using block detector technology is limited by the size of the individual crystals in the block detector array, mispositioning of events by the light-sharing technology used and the inability to identify interactions undergoing multiple scatter within a block. BGO scintillators was chosen for its high density, but had the limitations of being difficult to

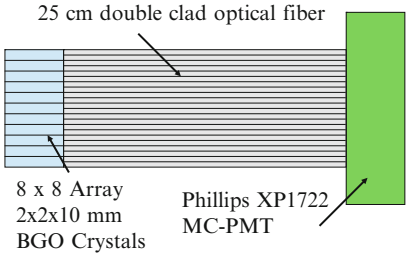

Fig. 15.2 Schematic of array of BGO crystals with one-to-one coupling with multi-channel PMT via optical fibers used in the microPET module

saw into finer crystals and having low light output making positioning of events using Anger logic for larger array of finer crystals difficult [20].

Cherry et al. [21, 22] developed an approach to work around this problem. Instead of using saw cuts to divide a block of scintillator into array of smaller crystals, finer individual crystal elements were stacked together and coupled on a one-to-one basis with an individual pixel of a multi-channel photomultiplier tube through optical fibers. This approach overcomes the size limitation of individual crystal pixels, thereby increasing the intrinsic resolution possible, reducing errors in event positioning, eliminating light-sharing, and correctly identifying and rejecting scattered events. Figure 15.2 is a schematic of such a detector array, which is the building block of the Concord microPET® high-resolution small animal imaging system.

As Fig. 15.2 shows, such an arrangement of scintillators and PMT lends itself to simultaneous PET/MRI imaging, similar to the design proposed by Hammer. The scintillator array is placed inside the MRI's bore and connected on a one-to-one basis by optical fibers to the PMT placed in a low magnetic field area well outside the magnet. Shao and Cherry utilized this design as the McPET (MRI Compatible PET) system [7]. This scanner produced the first simultaneous PET/MRI images.

The McPET I system consisted of a ring of forty eight $2\times2\times10$ mm^3 Lutetium Oxyorthosilicate (LSO) crystals of inner diameter 38 mm, connected via 2 mm diameter, 4 m long double clad optical fibers to three multi channel PMTs (MC-PMT). Each 2×2 mm^2 LSO crystal face was coupled to each individual element of the MC-PMT. The crystals were arranged such that their 10 mm side formed the scanner's axial length. The crystal ring of McPET I was placed inside the radio frequency receiver coil of a 0.2 T open magnet MRI. The MC-PMTs were positioned at 3 m from the center of the MRI's bore, where the magnetic field was less than 0.1 mT and the MC-PMTs could be operated properly (B less than or equal to 10 mT). A steel box shielded the MC-PMTs and their associated readout electronics from ambient light, magnetic fields, and radio frequencies. Figure 15.3 is an image of a newer version of the McPET system, showing its positioning in the MRI machine.

McPET I had a reconstructed spatial resolution of 2.1 mm at the center, an energy resolution of 41 % at 511 keV, and a coincidence timing resolution of 20 ns FWHM.

A second prototype (McPET II) was fabricated [8] consisting of seventy two $2\times2\times5$ mm^3 LSO crystals arranged in a ring with an inner diameter of 54 mm. The crystals of McPET II are arranged such that their 5 mm length forms the thickness of the scanner in the radial direction. This arrangement increases the system's stopping efficiency from 14 % in the McPET I to 34 % in the McPET II. McPET II has

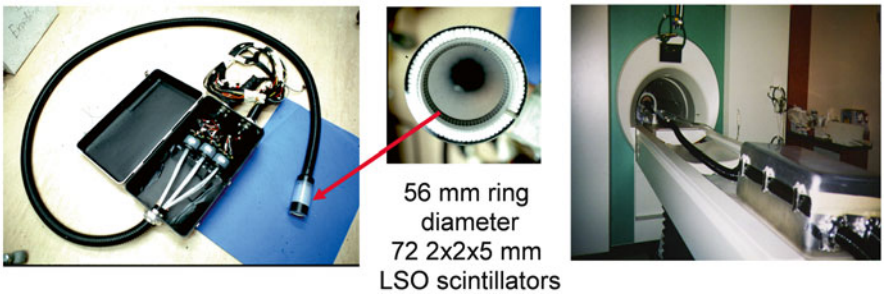

Fig. 15.3 *Left*: picture of the McPET system's detector module. *Right*: detector system installed inside the MRI magnet (Pictures courtesy of Simon Cherry)

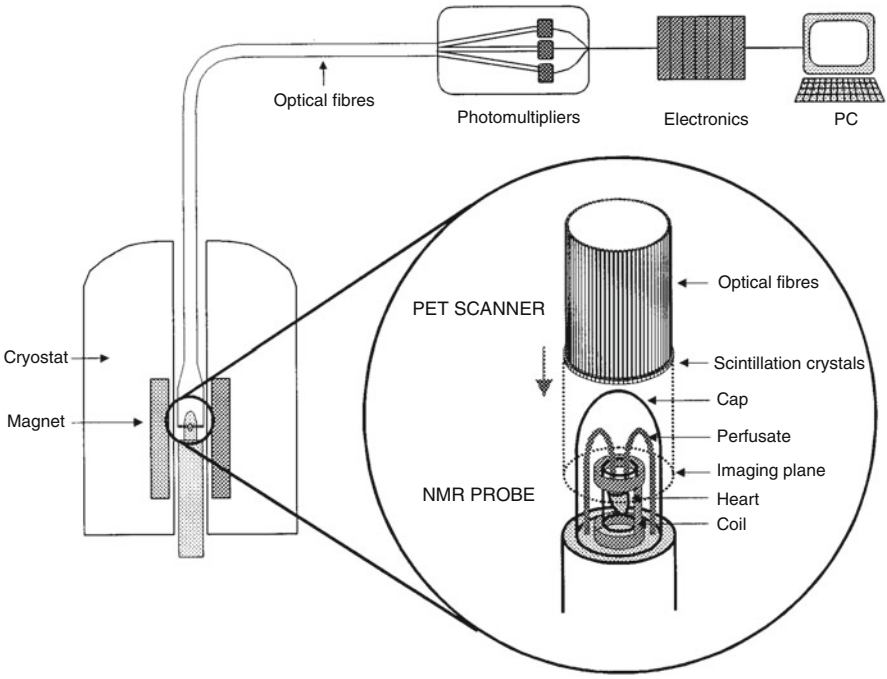

Fig. 15.4 Arrangement of McPET II inside the Bruker 9.4 T spectrometer with a custom-designed NMR probe in place. Reprinted with permission from Garlick et al. [23]

an energy resolution of 45 % and a coincidence timing resolution of 26 ns, both lower than McPET I due to light loss from the optical fibers being coupled to the crystal's side face (2×5 mm).

Along with simultaneous PET/MRI images, McPET II was used to acquire the first simultaneous PET- P-31 NMR spectroscopy of an isolated perfused rat heart in the 9.4 T Bruker NMR spectrometer [23], the so-called PANDA acquisition system (PET and NMR dual acquisition). Figure 15.4 illustrates the positioning of McPET II and the NMR probe.

The use of fiber optic cables to position MRI sensitive equipment far from the magnet, and avoiding ferromagnetic material in the PET system, minimizes interference between the two imaging modalities. An analysis of the quality of MRI and PET images obtained with McPET inside the MRI revealed no significant artifacts due to such interferences [24].

2.2 Development of Solid-State Electronics

The major drawbacks of photomultiplier tubes that prevented their use in an MRI were overcome with the development of semiconductor detector technology. In particular, the development of Avalanche Photodiodes (APDs) paved the way for much of the PET technology possible today. The operation principle of an APD is based on the conversion of photon energy into free charge carriers in the semiconductor bulk, and their multiplication via the process of impact ionization. The basic element of the structure is the p-n junction. When a reverse bias is applied, a volume close to the junction is depleted of free charge carriers. The charge carriers created in the depleted region drift in the electric field towards the corresponding electrodes, and while traversing this region, acquire enough energy to produce electron–hole pairs by impact ionization. The newly created charge carriers may create new ones, and so on. Thus, there is an avalanche of electrons and holes moving through the detector. An external circuit then detects these current pulses.

Although other types of semiconductor detectors, such the pin photodiodes, were studied as an alternative to PMTs, their poor timing resolution and high noise characteristics limited their use in PET [25]. On the other hand, APDs with their reasonable timing- and energy-resolution, and, very importantly, magnetic-field insensitivity, were extremely attractive for high-resolution PET and multi-modality imaging, such as simultaneous PET/MRI. The small size and ruggedness of APDs allowed the development of PET architectures with very small crystals and high packing fraction which was not possible with traditional PMT based designs without employing light guides or the light sharing block detector techniques.

Rapid growth in semiconductor technology in the 1980s resulted in several improvements, such as higher gain and gain uniformity, due to better doping and growth techniques of the Si wafer, and higher quantum efficiency in the blue range of the spectrum (surpassing PMT quantum efficiencies) thereby making them suitable for coupling with scintillators. APDs also have an advantage over PMTs in not requiring high bias voltages to operate. Nevertheless, APDs are prone to high noise due to factors such as shot noise from internal and surface currents, capacitance noise from downstream electronics such preamplifiers, and statistical noise due to the avalanche processes. Hence, low-noise front-end electronics are required to minimize the noise and assure a good signal-to-noise ratio from such detectors. Another disadvantage is that APD gains are sensitive to temperature and, consequently, temperature monitoring or control is needed when operating APD-based devices [25, 26].

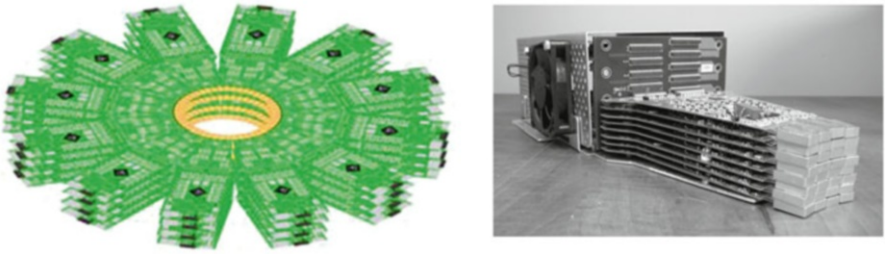

Fig. 15.5 *Left*: diagram of the Sherbrooke Small Animal Tomograph, the first LSO-APD based PET scanner (Fontaine et al. [30] used with permission, © [2005] IEEE). *Right*: a detector "cassette" making up the ring of the scanner. Reprinted with permission from Bergeron et al. [31], © [2009] IEEE

The combination of APDs with scintillators for application in PET began with Petrillo et al.'s studies of APD-scintillator detector units [26]. Using reach-through APDs (RAPDs), the first test that coupled APDs to NaI(T1) crystals, yielded an energy resolution of 10.4 % FWHM for the Cs-137 photopeak at 662 keV, with a quantum efficiency of over 50 % at NaI's emission wavelength (415 nm).

Work continued by making detector units of BGO, at that time the crystal of choice for PET scanners and APDs [25, 27, 28]. Those detector modules consisted of two individual $3 \times 5 \times 20$ mm^3 BGO crystals coupled to 4×4 mm^2 APDs. In principle, the modules could be stacked to form larger arrays. Tests demonstrated an average energy-resolution of 20 % for 662 keV Cs-137 γ rays, and a coincidence-timing resolution of 15 ns FWHM (511 keV) between two such modules, performance characteristics suitable for PET. The outcome of these and further studies was the construction of the first APD-based PET system for small animals, The Sherbrooke Avalanche Photodiode Positron Tomograph. This scanner consisted of 256 BGO APD detector modules [29] and a transaxial FOV of 118 mm and an axial FOV of 10.5 mm. Figure 15.5 illustrates the tomograph and its detector modules.

The introduction of Ce-doped LSO crystals ushered in new detector modules containing this scintillator with APDs. LSO was superior to BGO in having a much faster decay time (40 ns vs. 300 ns), hence leading to better timing-resolution. Several tests of LSO–APD detector modules established the feasibility of this approach, especially by achieving nanosecond timing resolution [32, 33]. Various detector configurations were explored, such as the one to one coupling of LSO crystal arrays to a matching APD array (Fig. 15.6) as well as position encoding using APDs [14, 34, 35]. Furthermore, progress was made in designing ultra low noise front end electronics [36, 37].

Pichler et al. evaluated the performance parameters of this LSO APD combination. Studies were conducted at 9.4 T [38] by wrapping a polished $3.7 \times 3.7 \times 12.0$ mm^3 LSO crystal in Teflon tape, coupling it to a 3 mm active diameter APD via a silicone rubber disc, and placing them in a magnet bore. The output of the APD was connected by a coaxial cable to a preamplifier also situated inside the magnet (Fig. 15.7).

Two aluminum boxes enclosed the LSO APD module, the Na-22 point source, and the preamplifier, shielding their electronics from any kind of interference from

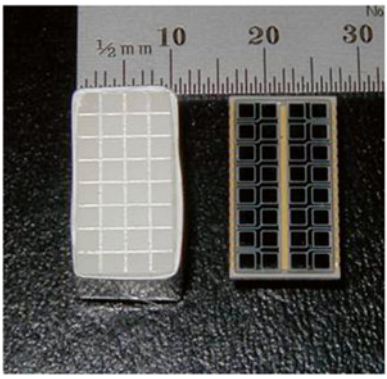

Fig. 15.6 A 4×8 LSO crystal array next to a 4×8 array of non-magnetic APDs (Hamamatsu S 8550)

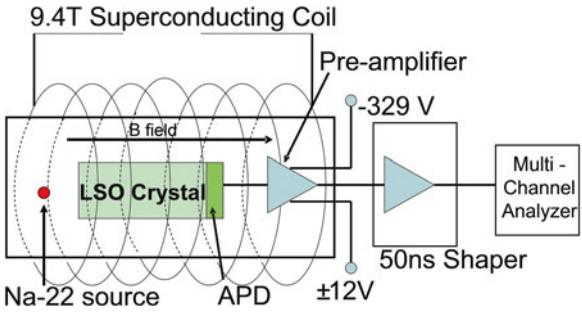

Fig. 15.7 Schematic of a LSO-APD detector module and preamplifier inside a 9.4 T magnet with the associated electronics outside the magnet

the MRI. Further, a copper tube surrounded the aluminum boxes. The output from the preamplifiers inside the magnet is fed to a preamplifier shaper outside the magnet via an 11 m long coaxial cable. Other components of the setup, such as the high-voltage supplies for the APD bias and a multichannel analyzer, were also situated outside the magnet. The study demonstrated the stable performance of the LSO APD detector module inside the 9.4 T, with no dependence in gain and energy resolution (14.4 % at 511 keV) of APD on the magnetic field. Also, there was no effect of changes in the orientation of the APD electric field with respect to the main magnetic field lines (parallel vs. perpendicular), hence proving the feasibility of operating such a PET detector module inside an MRI.

3 Current Instrumentation

Several groups developed operating PET/MRI systems for small animals, and several more formulated new technologies. In this section, we discuss current technologies and how they will take us into the future.

3.1 Current PET Systems

We have broadly classified current preclinical PET/MRI systems on the basis of the detector configuration as follows:

(a) Scintillator-PMT combination wherein the PMT is placed in a low magnetic field and light is directed into it from the scintillator via optical fibers. Section 2.1 details this system,
(b) Scintillator-APD combination that positions the APD and electronics in a low magnetic-field and directs light from the scintillator to the APD through optical fibers,
(c) Direct or closely coupled scintillator and APD detectors wherein the detector module is in the MRI's field of view (FOV), and hence experiences strong magnetic fields. Two such systems are summarized below,
(d) Silicon photomultipliers for APDs in a close coupled detector module.

In this section, we cover the design of two directly coupled APD scintillator PET/MRI systems, one developed by Judenhofer et al. at the University of Tubingen [15], and another developed by Schlyer et al. at Brookhaven National Laboratory (BNL) [39].

3.1.1 University of Tubingen Simultaneous PET/MRI Small Animal System

This PET system was built to function in a 7-T BioSpec 70/30 Ultra Shielded Refrigerated MRI, or a 7-T ClinScan MRI system (Bruker BioSpin MRI) [15]. The PET system consists of a detector module where a 12×12 array of individual $1.6 \times 1.6 \times 4.5$ mm^3 LSO crystals is coupled via 3-mm long light guides to a 3×3 APD array. The system comprises ten such detector blocks arranged in a ring. The RF coil of inner diameter 36 mm fits inside the PET ring that, in turn, fits inside the MRI gradient coil. This arrangement results in a transaxial PET/MRI FOV of 36 mm. Figure 15.8 shows the detector module and its positioning in the MRI.

The output of the APD is fed to a charge sensitive preamplifier after which it is buffered to electronics placed at a field <0.0005 T and shielded with non-magnetic coaxial cables. A copper-clad (10 μm thick) dual-sided printed circuit board (PCB) shields the detector modules. The shielded module is shown in Fig. 15.9c. These shielded modules then are assembled in a ring (Fig. 15.9b). The entire unit is positioned inside the MRI bore as illustrated in Fig. 15.9a.

3.1.2 BNL's Simultaneous PET/MRI Small Animal Imaging System

The BNL small animal PET/MRI system is based on the RatCAP technology [39]. The detector module consists of a 4×8 array of $2.2 \times 2.2 \times 5$ mm^3 LSO crystals, directly coupled to a 4×8 APD array. Each of these detector modules is mounted on a socket on a rigid flex circuit (Fig. 15.10). Twelve such detector modules on the circuit are rolled up to make the PET ring.

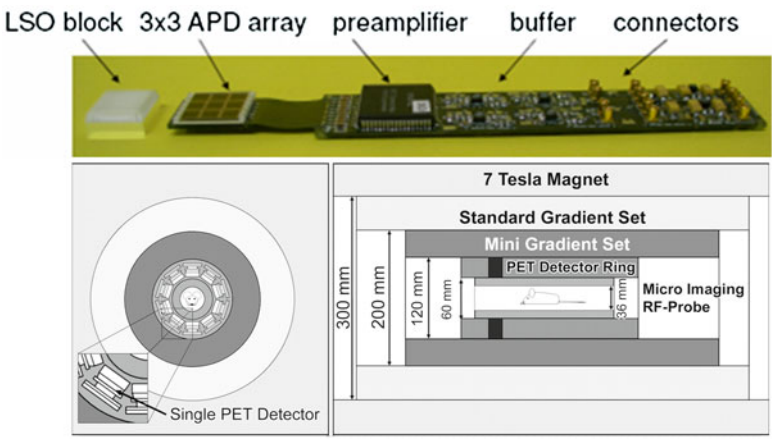

Fig. 15.8 *Top*: a detector module consisting of LSO crystals coupled to APDs and preamplifier unit printed-circuit board. *Bottom*: arrangement of PET system inside MRI showing its position between the RF and gradient coils. Adapted with permission from Judenhofer et al. [15]

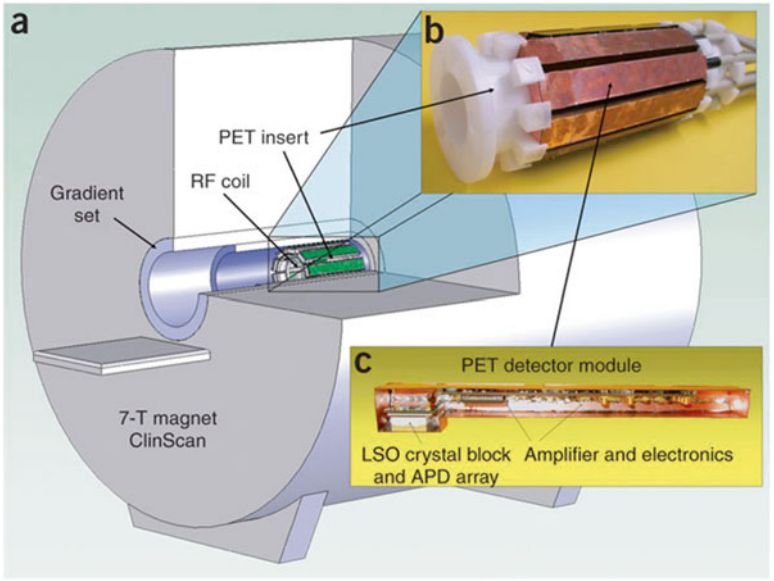

Fig. 15.9 (**a**) PET ring positioned inside scanner bore. (**b**) PET system consisting of ten shielded detector modules arranged in a ring. (**c**) PET detector module shielded by copper-clad printed circuit boards (PCBs). PET insert from the Tubingen group. Reprinted with permission from Judenhofer et al. [40])

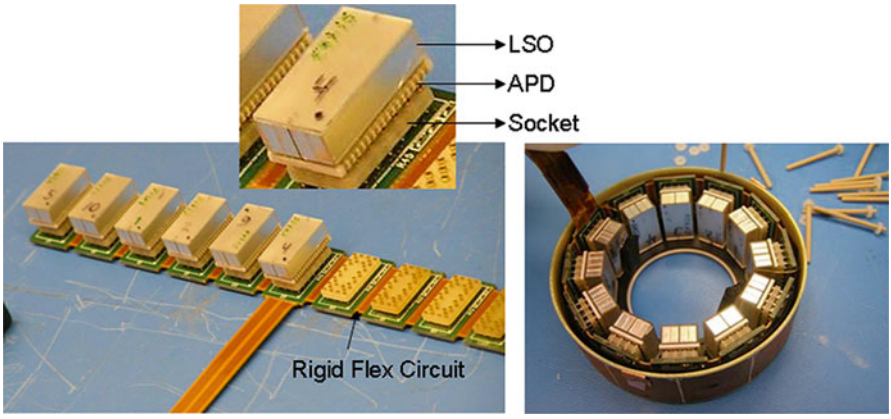

Fig. 15.10 *Left*: a rigid flex circuit partially populated with LSO-APD detector modules. *Right*: a rolled up rigid flex circuit showing the PET architecture

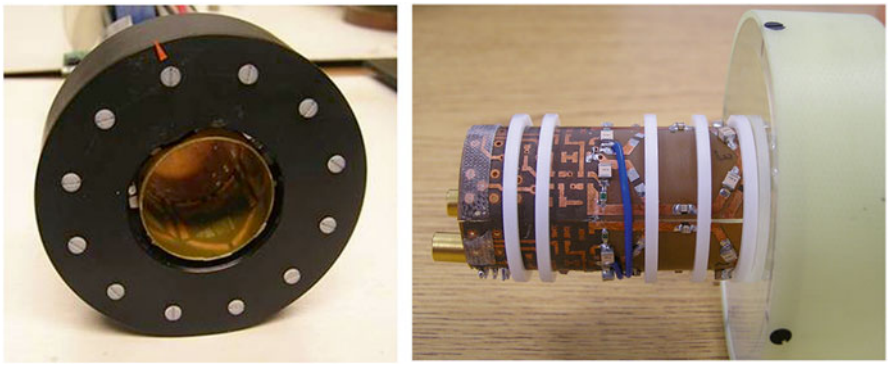

Fig. 15.11 *Left*: PET ring housed inside Delrin can with RF coil placed inside it. *Right*: the custom MRI coil used inside the PET ring

The APD signals are amplified and digitized using an application specific integrated circuit (ASIC) developed for this system [41]. The ASIC is mounted on the back of each socket on the flex circuit. The digital signal output from the ASIC is further routed to a time stamp and signal processing module (TSPM) via shielded coaxial cables; there, the events are processed further and buffered to a computer via optical fiber [42]. The TSPM is placed inside an aluminum box at the edge of the magnet bore. The power supply units and data acquisition computer also are outside the MRI room.

The PET system (Fig. 15.11) is housed in a Delrin (polyoxymethylene) plastic case, with a custom-designed RF coil that can operate in a quadrature mode positioned inside it. The PET assembly with the RF coil has a transaxial FOV of 31 mm. Cables transferring PET signals to the TSPM are housed in concentric segmented copper sheets to provide shielding and minimize eddy currents.

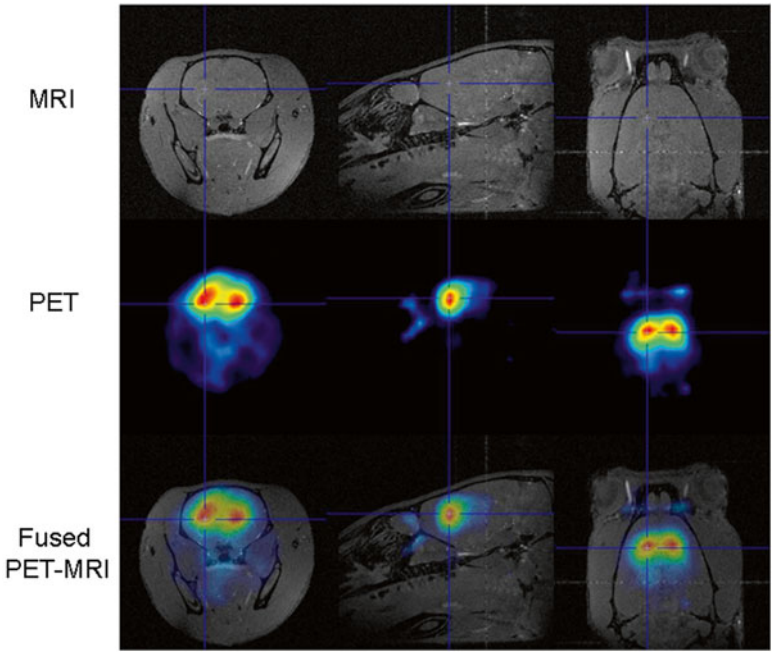

Fig. 15.12 *Top*: T1 weighted FLASH 3D isotropic MRI images of rat brain. *Middle*: PET images showing increased uptake of [^{11}C]Raclopride in the striata. *Bottom*: Fused PET/MRI images

In experiments, the PET ring and the RF coil were positioned at the center of the 9.4 T microMRI and simultaneous PET/MRI images of a rat's brain labeled with [^{11}C]raclopride were acquired. Raclopride binds specifically to dopamine receptors in the brain, and is reflected in the increased intensity of the PET signal in the brain striata, as shown in Fig. 15.12 [43].

3.2 Position Sensitive Avalanche Photodiodes (PSAPD)

One recent development in semiconductor technology for PET application was the introduction of position-sensitive APDs or PSAPDs [44]. Simply put, PSAPDs consist of a continuous layer of detector material (rather than pixelated arrays of traditional APDs) with output terminals positioned such that the relative intensity of the avalanche signal at these contacts serves to determine the exact location of the photon interaction, a principle similar to that underlying Anger logic positioning (Fig. 15.13).

With such a positioning logic, far fewer contact terminals are necessary for a PSAPD compared with a pixelated APD to achieve the same nominal spatial-resolution, thereby minimizing the electronics needed for downstream processing.

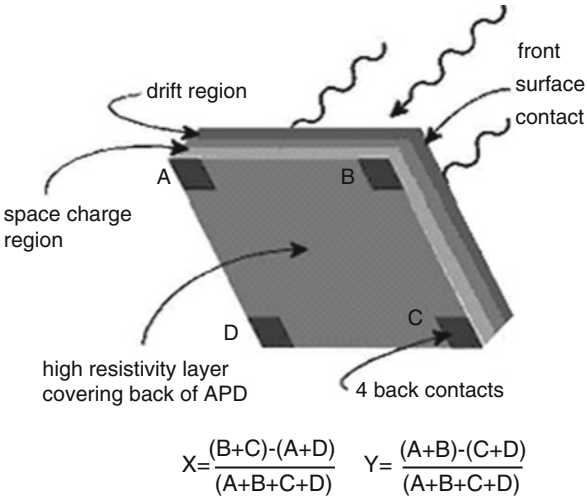

Fig. 15.13 A PSAPD with four corner-anode contacts A, B, C, D for position encoding, and a top cathode for energy and timing information. Positioning in the X and Y direction is computed for the A, B, C, D signals as shown. Reprinted with permission from Shah [45], © [2004] IEEE). For further details on the principles of PSAPDs and PET, see [45, 46]

This, in turn, reduces the cost and complexity of scanners being built using this technology, especially for small animal imaging systems where resolution is a crucial requirement, so that thousands of APD pixels have to be read out within only a small space to accommodate all the electronics. Tests with PSAPDs revealed energy and timing resolution sufficient for PET imaging and several groups have started incorporating PSAPDs into their scanner design [11, 47–49]. PSAPDs, similar to APDs, are insensitive to magnetic field and, with fewer electronics, are suitable candidates for simultaneous PET/MRI where PET detectors must fit in the space available inside a high-field MRI bore. Catana et al. implemented one such PET/MRI scanner in a 7 T magnet and acquired simultaneous PET/MRI images with it [11] (Fig. 15.14).

The PET detector in this setup consists of a module of an 8×8 array of LSO crystals ($1.43 \times 1.43 \times 6$ mm^3) coupled via optical fibers (approx. 10 cm long) to a 14×14 mm^2 PSAPDs whose terminals are further connected to charge sensitive preamplifiers (CSP) (Fig. 15.14, top). The PET ring consists of 16 modules arranged as shown in Fig. 15.14 (bottom). Concentric copper cylinders surround the CSP and associated electronics in the MRI bore minimizing electromagnetic interference between PET and MRI. The signals from the CSP are transmitted to signal processing electronics placed away from the magnet by using non-magnetic coaxial cables. The PET ring lies inside the MRI's bore between the RF and gradient coil (Fig. 15.15a). Simultaneous PET/MRI images of a mouse head acquired using this system is shown in Fig. 15.15b.

No visual artifacts were evident in the MRI images as a result of inserting the PET detectors. The effect of the MRI on PET involved a rotation in the flood histograms obtained during MRI pulsing, but unique crystal identification was still possible.

Another prominent application of PSAPDs is in depth of interaction (DOI) encoding. For small animal scanners that require high sensitivity, scintillator

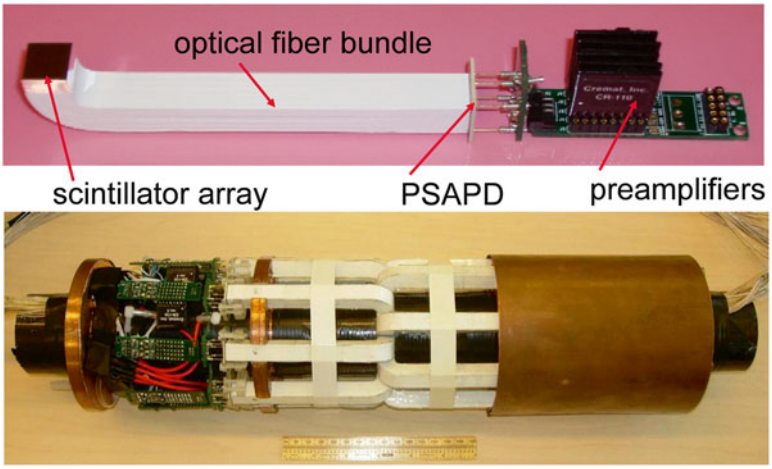

Fig. 15.14 *Top*: a detector module consisting of an LSO array coupled to PSAPD using optical fibers. *Bottom*: PET detector ring consisting of 16 such detector modules shielded with copper. (Photographs courtesy of Simon Cherry)

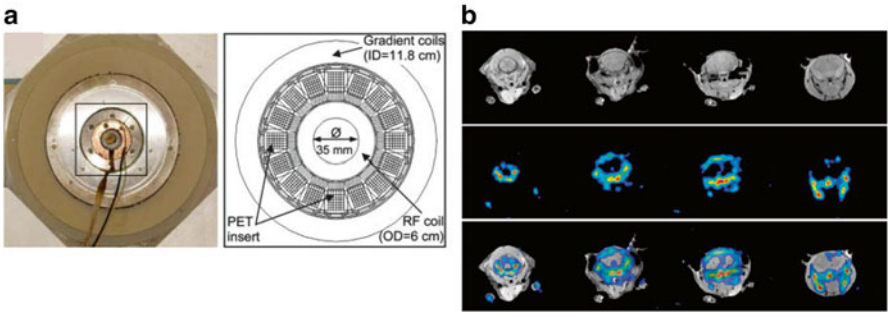

Fig. 15.15 (**a**) Arrangement of PET detector inside MRI's bore. (**b**) Simultaneous PET/MRI images of a mouse head using ^{18}F showing uptake of the radiotracer in the bones. *Top row*: MRI images, *Middle row*: PET Images, and, *Bottom row*: Fused PET/MRI images. Reprinted with permission from Catana et al. [11]

crystals need to be long (10–20 mm) to stop more annihilation gammas, and the detectors must be placed very close to the imaged object to increase solid-angle coverage. However, the combination of these two factors can result in severe parallax errors. With fewer electrical contacts and low gamma attenuation properties, depth of interaction encoding is feasible by placing PSAPDs on two opposite faces of the scintillator crystal. Several studies demonstrated the DOI encoding capabilities of PSAPDs [50, 51] thereby improving the spatial resolution attainable. Hence, PSAPD detectors can support high-sensitivity, high-resolution MRI compatible PET scanners.

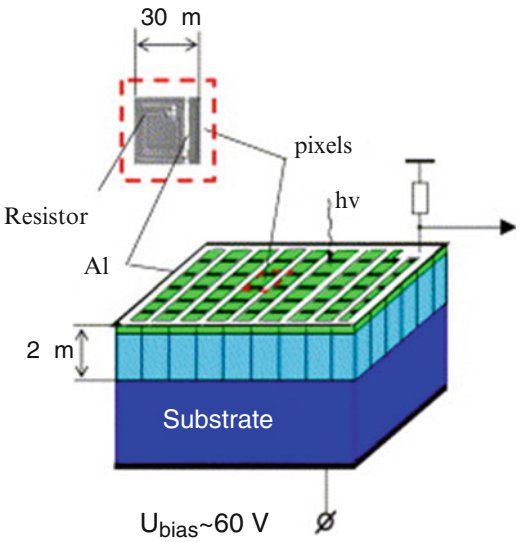

Fig. 15.16 A SiPM array consisting of several micropixels on a common substrate. Adapted from [53]

3.3 Silicon Photomultiplier

The Silicon Photomultiplier (SiPM) is a promising new technology that combines the high-gain, low-noise properties of a photomultiplier tube with the magnetic insensitivity of an APD. Also known as the Geiger Mode APD, these devices are, as the name suggests, APDs operating at a bias voltage slightly above their breakdown point, or in the Geiger mode [52]. Consequently, SiPMs exhibit very high internal gains on the order of 10^5–10^6, and have timing properties that act as a single-photon counter. Figure 15.16 illustrates the typical structure of a SiPM array. The array comprises a few hundred to a few thousand microcell or micropixel APDs on a common substrate of 1×1 mm^2.

An incident photon triggers the production of a charge carrier that, in turn, creates an avalanche breakdown. The SiPM is essentially a photon counter, and generates a standard output signal for one or more photon interactions per cell. This is where the structure of the microcell array, and the detector's single-photon counting capability come into play. With multiple photon interactions over a given area, multiple microcells are triggered into avalanche breakdown. Hence, the number of microcells fired in the array is proportional to the number of photon interactions taking place. This is true only if the rate of incoming photons is such that only a single photon interaction occurs in a microcell within its quenching time, i.e., the period it takes for a microcell APD to come back to its normal state after an avalanche breakdown. Passive quenching is achieved by connecting each of the microcell APDs in the series with a resistor to a common aluminum grid for reading out the signals from the array. The resistive layer also acts as a decoupling element between the adjacent microcells in an array. However, it also reduces the active area of the SiPM array, thereby reducing its overall detection efficiency.

From the perspective of using these detectors for PET, the following are its key advantages:

1. High intrinsic gain and low excess noise,
2. Insensitivity to magnetic field (particularly suitable for PET/MRI imaging),
3. Good timing-resolution (in picosecond range),
4. Low temperature-dependence compared traditional APDs,
5. Low operating voltages,
6. Low production costs.

Studies of SiPMs with scintillator crystals, such LSO/LYSO for PET have demonstrated good energy and timing resolution along with the listed favorable properties [53–55]. However, one drawback of SiPMs is their low detection-efficiency at the LSO/LYSO emission wavelengths (or the blue end of the spectrum). Hence, more work is needed here to fully exploit their usefulness for PET.

3.4 Modified MRI Scanner Architectures

Until recently, most work combining PET and MRI focused on modifying PET instrumentation to fit and function inside an existing MRI scanner. However, PET/MRI scanners have been designed wherein the MRI scanner instrumentation was modified to accommodate PET detectors. We describe two such systems below.

3.4.1 The microPET®-MRI System

The microPET®-MRI system, as the name suggests, implements the architecture of the microPET® (Focus 120) small animal scanner inside an MRI [5]. The MRI scanner is a novel 1 T superconducting magnet, fabricated in two halves with an intervening 80 mm gap, i.e., in a "split magnet" design that accommodates the PET detector modules in the gap. The modules, consisting of LSO crystals (12×12 array) are coupled to a position-sensitive PMT through optical fibers in a ring architecture. Figure 15.17 is a schematic of this arrangement.

As the illustration shows, the PMT is positioned outside the magnet bore at a radial position of 120 cm (length of optical fibres) where the field strength is about 30 mT. The PMTs are further shielded with soft iron, reducing the field strength experienced at the PMT to 1 mT. This configuration, with PET detectors positioned in the center of the MRI, supports simultaneous PET/MRI. There was minimal degradation in the sensitivity and energy spectra obtained from the PMT due to the magnetic field. However, using 120 cm long fiber-optic cables causes some degradation in energy resolution from loss of light. MRI images of a mouse brain obtained using this split magnet scanner verified that it generates good-quality, high-resolution images.

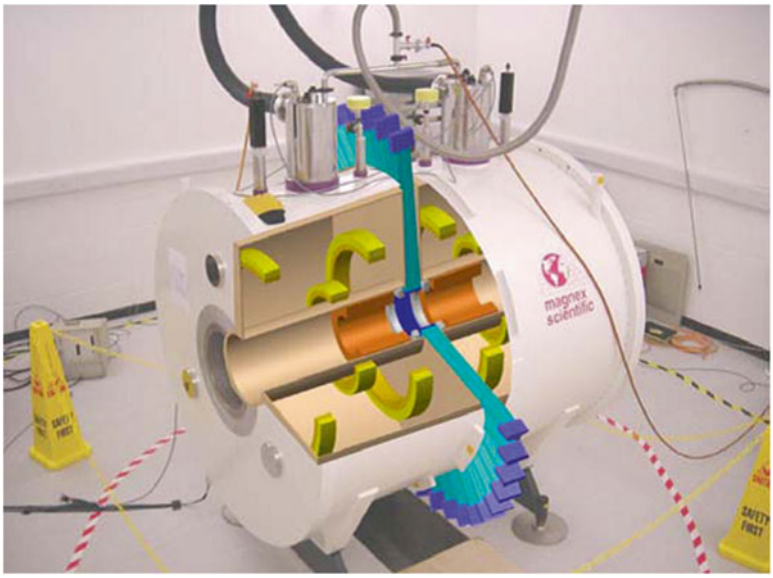

Fig. 15.17 Schematic drawing of PET detectors positioned in the split magnet space of the MRI. Reprinted with permission from Lucas et al. [57], © [2006] IEEE

3.4.2 Field Cycled MRI-PET System

The principle of operation of a field-cycled MRI-PET system is that PET data is acquired when the MRI magnetic field is turned off or cycled to zero [58]. This practice avoids the limitations faced when attempting to operate traditional PET systems in a magnetic field. A field-cycled MRI consists of two sets of magnets. The first one, called the polarizing magnet, is a high-strength magnet that polarizes the objects placed in its field of view. After polarization, this magnet is cycled to zero and the second magnet, a low field strength readout magnet is activated such that the polarized volume is precessing at the Larmor frequency of the readout magnet. During the readout magnet phase, excitation and readout pulse sequences are carried out by pulsing the RF and gradient coils. This phase of the pulse sequence is followed by a period when the readout magnet is cycled to zero and the magnets are allowed to cool, during which period, the PET images are acquired. Since there is no magnetic field during this period, readout can be accomplished by placing the PMTs in the field of view, hence allowing direct coupling and avoiding the use of light guides that degrade the PMT's performance. Gilbert [59] proposed this design (Fig. 15.18). A gap of 9 cm in the MRI system accommodates the PET system.

Other advantages of this mode are reduced distortion due to the magnetic field's homogeneity because the readout magnets are of low field-strength. This feature also reduces the requirements on RF and gradient power, thereby lowering their impact on the PET's electronics in comparison with standard high-field MRI systems.

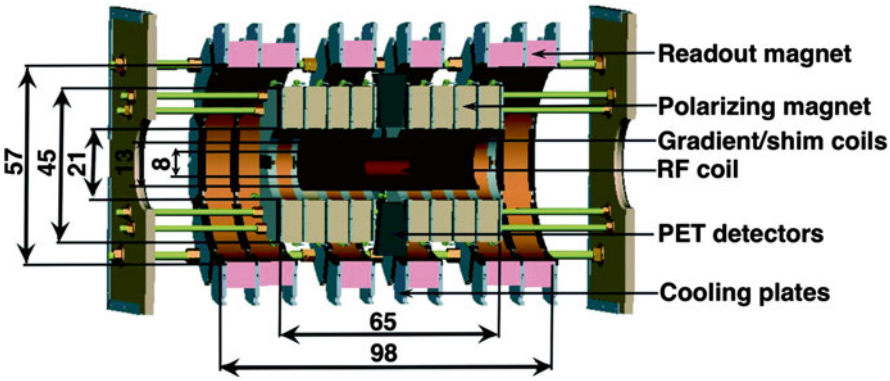

Fig. 15.18 Schematic of a field-cycled MRI with PET detectors. Reprinted with permission from Gilbert et al. [59]

4 MRI and PET Data Acquisition System Interactions

Potential interactions between the MRI system and the PET system could degrade their respective images. Interferences and artifacts might appear in the MRI images from the PET's electronics, and excess random counts in the PET's data stream might be created by the magnetic and radio frequency characteristics of the MRI data acquisition system. In this section, we a look at some potential interferences and describe different approaches to minimizing or eliminating them.

4.1 Shielding Approaches

There are three basic approaches to minimizing interference between the PET's electronics and the MRI data-acquisition system. The first is to move the electronics away from the MRI data system. This approach uses optical fibers to transmit the light from the scintillation crystals to the light detection devices, either PMTs or APDs. The second approach uses heavily shielded PET electronics situated inside the bore of the magnet and in close proximity to the MRI transmit and receive coils. This is the approach that has been used in the commercial PET system developed for human use and has also been employed for small animal scanning [12]. The third approach uses minimal or no shielding between the PET and MRI. This allows the maximum sensitivity for the MRI, but can result in a significant number of random counts in the PET system caused by the effects of the gradient fields and the RF pulses on the PET electronics.

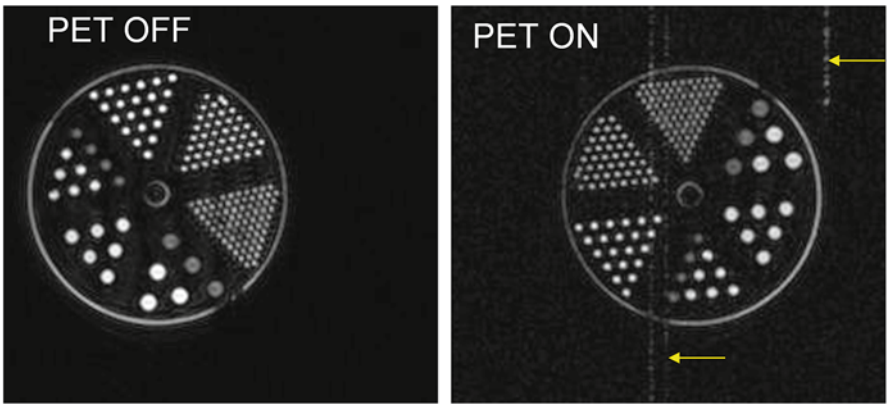

Fig. 15.19 MRI images and profiles of a resolution phantom containing water in some compartments and fat in others, without a PET system (*left*) and with a PET insert in place and powered on (*right*). Notice the line artifacts marked with the *yellow arrows* in the MRI image in the upper right and extending through the center of the image

4.2 Degradation of the MRI Image Due to PET Inserts

Using the configuration with light fibers and remote electronics seemingly guarantees minimal interference in the MRI images. In a study using a prototype MRI compatible PET system, subtraction images were used to delineate artifacts in the MRI images and none were observed [60]. Placing PET detectors and electronics that might contain metal components inside the MRI magnetic field can compromise the magnetic field's homogeneity, and may result in artifacts in the MRI images. Photodiodes or avalanche photodiodes are compatible with magnetic fields, but the acquisition of artifact free MRI images with these devices require assuring that components that do not contain any ferromagnetic materials.

In some PET systems, the PET events are timed using a high frequency "clock" signal that is propagated through the electronics on the PET insert. In this configuration, the clock signal might interfere with the MRI signal if the frequencies are close to each other, or are harmonics of each other. Offsetting the frequencies some amount will reduce the interference greatly. We studied the effects of PET electronics and hardware on MRI images with a 1.5 T MRI. These tests were performed without power on the PET circuits to demonstrate their potential effect. We filled one row in a Mini Deluxe Phantom (Data Spectrum Corporation, NC USA) hot spot insert with vegetable shortening to mimic fat, and the rest with 1 mM $CuSO_4$ solution. Figure 15.19 shows MRI images of the center slice of the phantom with no PET insert and with PET inserted and turned on. Yellow arrows mark the artifacts.

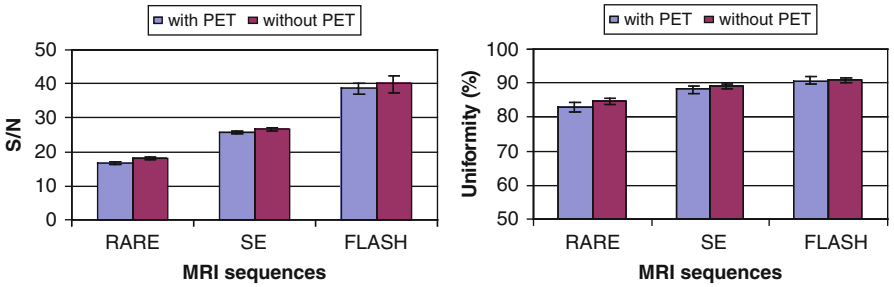

Fig. 15.20 Comparison of MRI image characteristics with and without the PET inserted (Plot courtesy of Simon Cherry)

Accordingly, we demonstrated that good MRI images are obtainable without RF shielding. Mild artifacts due to interference are represented in the form of streaks on the image. With RF filtering, we were able to eliminate these artifacts

Using shielding on the PET insert will allow essentially noise-free MRI images. Figure 15.20 plots the results of a study by Simon Cherry (private communication) on the signal-to-noise ratio in the MRI images; it shows the uniformity of this ratio as a function of the pulse sequence.

4.3 MRI Effects on Spatial and Temporal Resolution of the PET Images

Using the configuration of shielded light fibers and remote electronics, apparently there is minimal interference in the PET images. When the electronics are placed inside the MRI scanner, there can be significant effects. Using an unshielded case for the RatCAP and taking data in the 9.4 T magnet, we observed the following interference [39]. A very clear noise signal was generated in the unshielded PET electronics from the RF pulse sequence as shown in Fig. 15.21. The figure illustrates MRI pulse sequence on the upper part of the figure and the PET single counts below.

There are two ways to overcome this problem. The first is to remove the noise from the data by gating out the RF pulses, out. The second is to carefully shield the PET electronics from the RF pulse sequence. Figure 15.22 illustrates a case that we designed at BNL for this purpose.

The shield is constructed of G-10 material with a thin (5 μm) copper layer on the surface to block penetration of the RF power. The shielding is segmented to reduce eddy currents, and the electronics are placed inside a secondary shield shown on the right hand side of the figure.

In PET/MRI scanners that use shielded, short optical fibers and APDs, the number of counts per second is constant as the gradient coils are operated. Figure 15.23 plots the number of PET counts recorded as the gradient coils are turned.

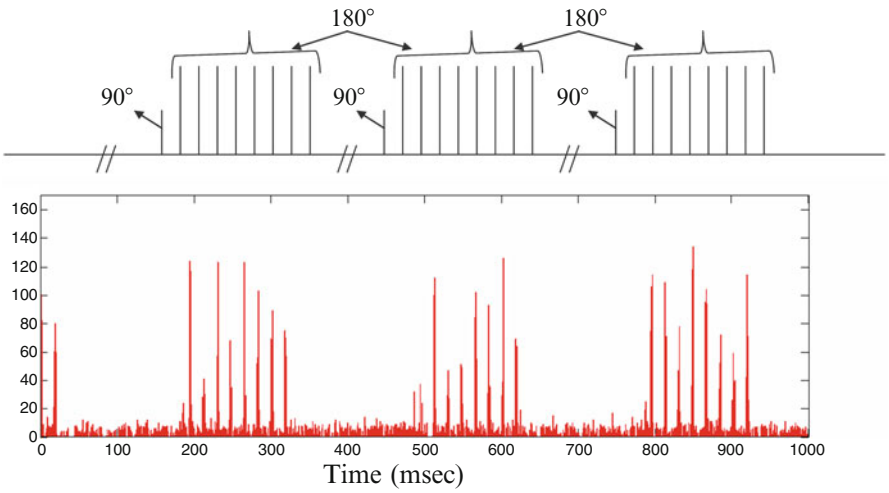

Fig. 15.21 PET data showing the noise introduced by the RF pulse sequence in an unshielded PET scanner

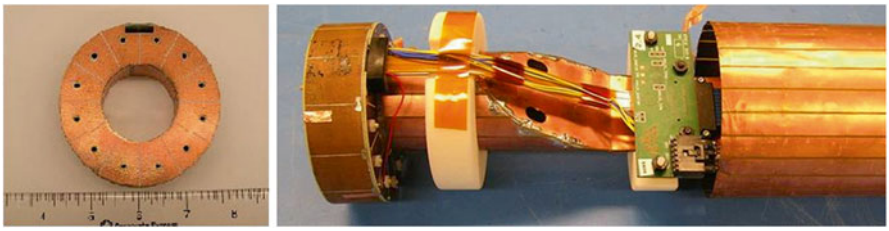

Fig. 15.22 *Left*: RF-shielded case for the RatCAP scanner used in the 9.4 T magnet at BNL; *Right*; RatCAP with RF shield before sliding the outer shield over the entire assembly

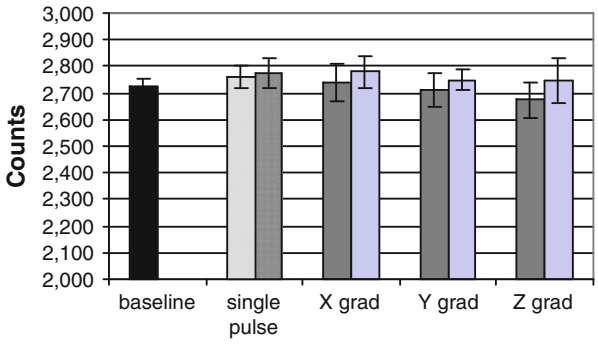

Fig. 15.23 Plot of number of counts during operation of the MRI gradient coils. *Dark gray bars* indicate that the gradients are off, and the *lighter blue bars* show that the gradients are on. (Plot courtesy of Simon Cherry)

4.4 PSAPD Detector Efficiencies in Magnetic Fields

Position Sensitive Avalanche Photodiodes (PSAPDs) provide similar noise, gain and quantum efficiencies to single channel APDs, but employ charge sharing amongst anodes to obtain position information. Only five contacts are needed to identify the position of the photon interaction, thereby greatly simplifying the electronic circuitry. In summary, PSAPDs offer good resolution in energy, timing, and space, and have greatly reduced electronic readout requirements.

When a uniform flood source is imaged in PET tomographs that use PSAPDs, the positional information is typically somewhat distorted showing a "pincushion" effect. This effect is a result of the Anger logic used to decode the position of the event using the four electrodes on the resistive sheet that comprises the PSAPD. This can complicate accurate segmentation of crystal positions if the distortion is very severe. Methods have been developed to correct for this effect [61].

The major potential problem of placing the PSAPD in the magnetic field is that the "pincushion" distortion may become more severe and events will be mispositioned and the energy resolution compromised due to the distortion from the magnetic field. In calibrating a PET system, the individual crystals are mapped by using a look-up table to normalize for the individual crystal's characteristics, such as energy, coincidence time-windows, and efficiencies. Plotting the maps in the magnetic field and applying this correction consistently eliminates such mispositioning. The only added complication is distortion due to the gradient fields. These effects were explored and algorithms developed to minimize the effects and produce an accurate segmentation of the crystals, even down to 1 mm resolution [61–64].

4.5 Magnetic Field Effect on Positron Range

Researchers have studied the effects of the magnetic field on the range of the positrons. Since the positrons' range is one of the limiting factors in the ultimate spatial resolution obtainable with PET, any improvement in it is an added benefit of the MRI environment, although this applies only in the 2-dimensional plane perpendicular to the magnetic field.

Raylman's Monte Carlo study [65], demonstrated that a substantial improvement in resolution can be achieved for higher energy positrons. Table 15.1 lists the findings for F-18, C-11, O-15, and Rb-82.

Raylman noted that there was some degradation in the annihilation non-collinearity that will degrade the resolution in large PET scanners, but which will be less important with a smaller diameter ring. There have been some experimental measurements of the improvement in spatial resolution in PET with magnetic fields [4, 66]. Using germanium-68 as the source of high energy positrons (Emax = 1.89 MeV), the results in Table 15.2 were obtained. These values are the ratio of the full width at half maximum of the point-spread function (PSF) in the

Table 15.1 Maximum positron energy and resolution change with and without an applied 10 T magnetic field [65]

Radionuclide	Max energy (Mev)	FWHM (0 T) (mm)	FWHM (10 T) (mm)
F-18	0.64	3.85	3.78
C-11	0.96	4.24	3.85
O-15	1.7	5.28	3.88
Rb-82	3.15	8.03	4.13

Table 15.2 Ratio of the full width at half maximum (FWHM) of the point spread function (PSF) with the field off, divided by the FWHM of the PSF with the field on as a function of magnetic field for Ge-68 in water

Field	$\frac{\text{FWHM off}}{\text{FWHM on}}$
0 T	1.0
4.0 T	1.22
5.0 T	1.42
9.4 T	2.05

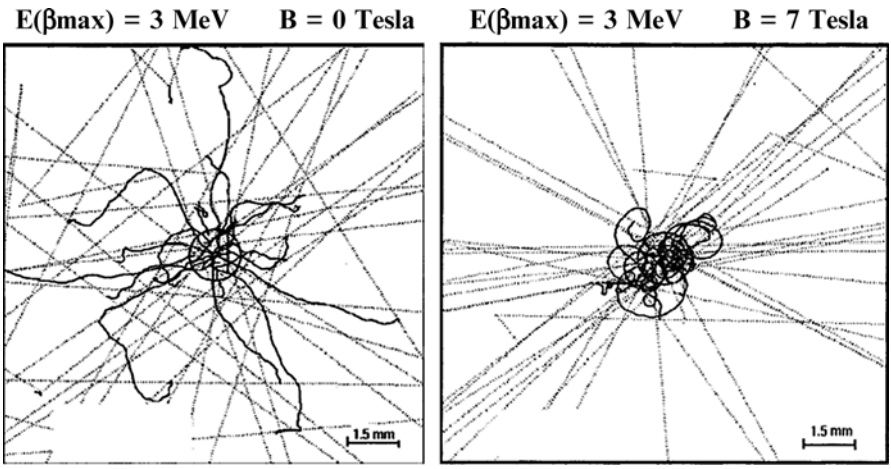

Fig. 15.24 Range of positrons with no magnetic field (*left*), and in a 7 T magnetic field (*right*). Reprinted with permission from Wirrwar et al. [68], © [1997] IEEE

transverse direction with the magnetic field off, divided the same measure with the magnetic field on as a function of the magnetic field (Table 15.2) [67].

A similar study, one with a very high-energy positron (3 MeV) and a 7 T magnet [68] encompassed theoretical and experimental measurements. Figure 15.24 is a graphical representation of the data generated from the GEANT simulation.

4.6 MRI Images for PET Attenuation Correction

One key advantage of PET is the possibility of gathering quantitative information on the distribution of radioactivity inside an object. However, for PET data to be quantitative, it is necessary to correct for the attenuation of the gamma rays as they pass through the object being scanned. The key characteristics of a material determining gamma attenuation are its atomic number and the electron density. When PET was being used alone, the attenuation was measured directly with either a ring source or with one or more rotating sources containing a positron emitter (usually Ge-68). Since the advent of PET/CT, the correction for attenuation is based on the data from the CT scan. This generates a relatively accurate attenuation map, although some concerns remain, such as the difference in attenuation of the 511 keV gammas compared to the attenuation of the much lower energy X-rays used in CT imaging.

With the move to MRI as the PET's complementary imaging modality, the attenuation correction must be based on the data available. A problem arises because the MRI signal is related to the proton density and not directly related to the electronic density that determines gamma attenuation in an object. Several approaches have been developed to obtain the attenuation map from MRI data and these methods are discussed here.

The attenuation of gamma rays by matter is a function of the electron density of the material through which they pass. Attenuation differs, depending on the energy of the gammas and the different processes contributing to attenuation. The X-ray CT maps are obtained with X-rays with maximum energy of 140 keV, while attenuation must be corrected in PET for photons of 511 keV. Thus, the attenuation-correction algorithm must convert the attenuation coefficients for 140 keV derived from CT maps, to the coefficients of 511 keV. This conversion may affect the accuracy of the attenuation corrected PET image for different tissue densities normally encountered in clinical studies such as lung and bone. However, in clinical practice the CT attenuation map often is more accurate than the traditional Ge-68-derived one, even with the extrapolations made due to the differences in energy, because the noise level of the CT image is very low, and therefore yields a very accurate map of the object.

The usual method in MRI is to segment the image in some way and then assign values for the attenuation based on this segmentation [69, 70]. One approach is to use the MRI image directly and assign different average values of attenuation for regions of bone, soft tissue, and air. There may be more regions, depending on the required level of complexity. An alternative is to obtain a CT attenuation map for several patients, and form an averaged attenuation map with the corresponding attenuation values. This attenuation map is then transformed (stretched and adjusted) to match the MRI image of the particular patient. This attenuation correction is then applied to the PET image to get an attenuation corrected image. This population based approach has some advantages and some disadvantages. The advantages are that it is relatively easy to implement, and does not require any additional scans. The disadvantages are that the general template must be adjusted for each patient using some either manual or automated fitting and that there is no easy way to adjust for differences in bone density.

Table 15.3 Typical attenuation coefficient values for MRI segmented

Region	Typical values (cm^{-1})
Brain	0.095–0.099
Skull	0.143–0.151
Nasal sinuses	0.054–0.055
Soft tissue, and skin	0.095–0.096

The most common approach for MRI attenuation correction of PET images is using some type of segmentation. The parameters employed for segmentation and the number of components determines the model's sophistication and accuracy. The simplest method of attenuation correction without using a transmission scan is to apply a uniform attenuation coefficient throughout the volume being imaged. For the brain, a simple elliptical model is often used. There was an improvement in the accuracy of the PET data using this approach, but it did not produce quantitative values. Early attempts to use MRI data to give an attenuation map followed that methodology [71]. The method was enhanced by adding more types of tissue with better estimates of the attenuation coefficients [72]. Table 15.3 gives typical segmentation values for these parameters for imaging several organs and tissues.

Correcting PET data for attenuation using MRI images still is being investigated actively. Several reviews [72–74] examined the possibilities and covered the work already done. The general conclusion is that using MRI for attenuation correction certainly is not as straightforward as using CT, but should be possible. Segmenting the skull into several regions and assigning attenuation coefficients seems to work well. For the torso, the favored approach seemingly is to fit the MRI images to a standard atlas by adjusting the standard organ sizes and shapes to match the patient.

5 Prospects for the Future

The first steps have been taken in the development of simultaneous PET/MRI scanners. There is a great deal left to do in terms of instrument improvements and the applications are just beginning. This is a very exciting time in multi-modality imaging that promises to get better.

5.1 Technical Challenges Still Ahead

Several technical challenges must be overcome before simultaneous PET/MRI is a mature technology. The ultimate goal is to design a system where the MRI does not degrade the PET image significantly, and the PET electronics do not interfere with the MRI electronics causing artifacts or decreasing the signal-to-noise in the MRI images. The greater the distance between the two systems, the easier this goal is to realize. Even a few millimeters will greatly reduce the interaction between the two

systems. Any conductive materials in the PET part of the system will need to be compensated by tuning the RF coil with the PET insert and object in place. For this reason, it is important to be able to tune the coil remotely from outside the machine.

Another consideration is the sensitivity of the gain of APDs to changes in temperature. Typically, a few degrees shift in temperature alters the gain by a large factor. The switching gradient's magnetic field and RF pulse sequences sometimes cause a notable rise in temperature from interactions with the PET system itself due to eddy currents, or even with the object being scanned. A temperature compensation mechanism should be incorporated in the PET electronics to deal with temperature drifts. PET electronics generate noise that can be picked up by the sensitive receivers in the MRI system. This is particularly true if there is a clock frequency running in the PET electronics to supply a timing signal. The frequency of this clock must be different from the MRI's fundamental or harmonic frequencies because the receivers are tuned specifically for this frequency and therefore, are particularly sensitive in this range. In our experience, the difference between 100 MHz and 105 MHz can be crucial for a 400 MHz (9.4 T) MRI system in terms of the signal-to-noise ratio of the MRI images.

5.2 MRI Spectroscopy with PET

Figure 15.25 shows a specific potential application of our hybrid PET/MRI system in a small-animal model. This mouse study illustrates how MRI spectroscopy, which can image flux rates throughout the tricarboxylic acid (TCA) cycle, when combined with PET, will afford a temporal correlation that is critical in meaningfully comparing these two functional datasets.

5.3 MRI Dynamic Domain Compared to PET Dynamic Domain

One interesting aspect of combining PET with MRI is the comparison of their time domains. The quality of a PET image mainly rests on the number of counts in it. It makes little difference if those counts are acquired over a few seconds or over several hours (neglecting deadtime considerations). MRI, on the other hand, has relatively constant signal and the accessible time-domain depends on the strength of the magnet, the pulse sequence used and, the relaxation constants of the environment.

One advantage of MRI is that an indefinite number of repeat studies can be done, so longitudinal studies are easy. On the other hand, for such studies in PET, with its short-lived positron emitters, usually necessitates two, three, or more injections of the radiotracer.

Under the right conditions the temporal information gained from PET can be closely correlated with the information from MRI. As an example of this, the study of brain function in small animal models requires both the localization of neural activity and the time sequence of the activation. Neuronal activation consumes

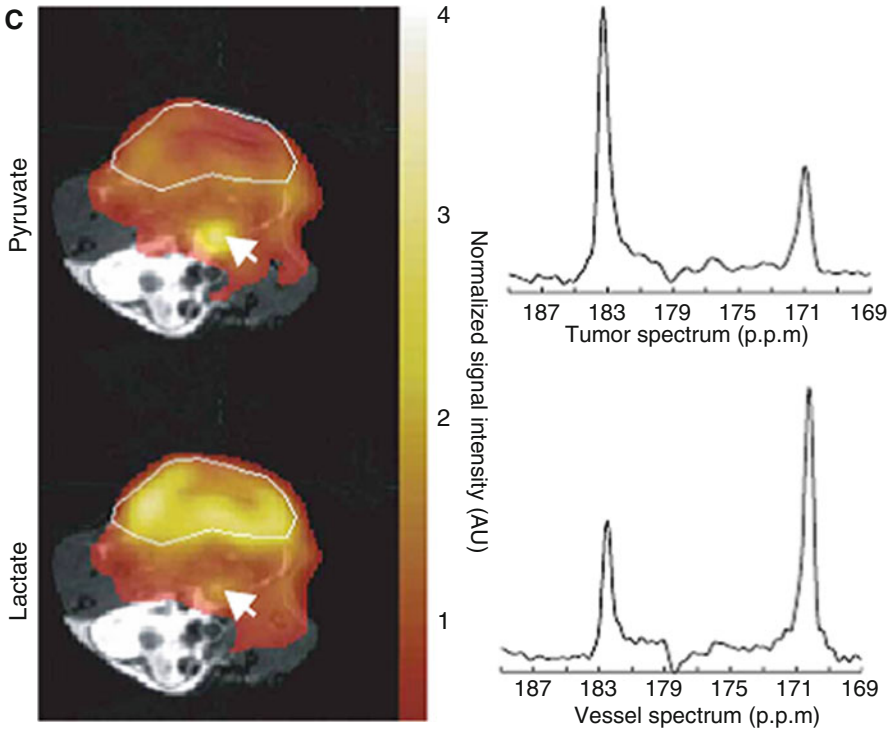

Fig. 15.25 Hyper-polarized ^{13}C-MRS in mouse-tumor imaging. Color maps representing [1-^{13}C]-lactate and [1-^{13}C]-pyruvate peak intensities and spectra from the tumor and a blood vessel (indicated by *arrow*) in mouse treated with an etoposide (chemotherapeutic agent). The ^{1}H images, shown in grayscale, were used to define the tumor's margins (indicated by *white lines*). Reprinted with permission from Day et al. [75]

oxygen [76]. After neural activation (particularly in the cerebral cortex), an increase in blood flow produces an influx of oxygenated hemoglobin. This influx reduces the local concentration of deoxygenated hemoglobin (deoxyhemoglobin). This effect is called the hemodynamic response (HR). This reduction can be measured using BOLD fMRI (blood oxygen level-dependent functional magnetic resonance imaging) [77], which now is the most popular method in functional magnetic resonance imaging (fMRI) and serves as one of the major experimental methods for analyzing neural function. However, vascular processes take at least an order of magnitude longer time than the underlying functional activation. The time-to-maximum of a HR due to a transient stimulus is typically delayed by 5–8 s and dispersed by 3–4 s. Oxygen-15 and PET can be used to correlate with the BOLD signal. This is a relatively new area, but promises to give new insight into neural activation. Oxygen-15 studies have been used extensively for the analysis of stroke in humans [78] although the possibility of doing both PET and MRI simultaneously will add a new dimension to these studies.

5.4 Preclinical and Research Applications

Imaging protocols are currently under development where MRI and PET are used in conjunction either to monitor the same physiological parameter for cross-validation, or to monitor different stages of metabolic activity and thus, different targets. We give examples of these types of investigations below.

A goal of neurophysiology is connect behavioral results with observables of non-specified or background mental functions, like awareness. The successes of PET and fMRI in non-invasively localizing sensory functions encouraged researchers to transform the subjective concepts of cognitive psychology into objective physical measures. Experimental results are interpreted in terms of flexible definitions of both cognitive concepts and the degree of localization. New approaches may connect measurements by fMRI, ^{13}C MRS, and PET of brain energy with observable behavior or more elusive parameters such as awareness. A sensory stimulation experiment could show whether the degree of localization found in BOLD signals is related to the global energy of the brain, which, when manipulated by anesthetics, will affect the degree of awareness. The influence of brain energy upon functional imaging maps is changing the interpretations of neuroimaging experiments [79]. Gerstl et al.'s study [80] is another example of correlating the regional distribution patterns of transmitters and the observable functional fields of the brain using fMRI and PET. They found that the distribution pattern of the major inhibitory serotonergic neurotransmitter-receptor, the 5-HT1A subtype, measured by PET is associated with the functional organization of the primary and secondary visual cortex defined by retinotopic mapping with fMRI. This work demonstrated study showed that multimodal neuroimaging combining PET and fMRI can clarify the relationship between the distribution of neurotransmitter receptors and functional specialization in human cortical areas in vivo.

One exciting area for combining PET and MRI is the ability to carry out functional and morphological imaging simultaneously. A specific example is employing advanced MRI techniques, such as diffusion tensor imaging (DTI), to delineate nerve tracks and correlate this with PET activation of nerve cells. This approach was used to demonstrate the invasion of tumor cells into pyramidal tracts and relate this information to the uptake of the PET tracer ^{18}F-fluoroethyl-L-tyrosine that measures cell proliferation [81]. Such data could prevent the destruction of important structures through more precise preoperative planning.

As another similar example of the complementary nature of PET and MRI is in ischemic stroke, where diffusion-weighted (DW), and perfusion-weighted (PW) magnet resonance imaging (MRI) are used to define the therapeutic target as the mismatch between the two volumes. Positron emission tomography (PET) can quantify the metabolic patterns of tissue compartments identified using this MRI technique. In one such study, the mismatch area did not reliably detect elevated Oxygen Extraction Fraction and overestimated the penumbra defined by PET [82].

Oxygen-15 labeled water imaging has become the gold standard for assessing cerebral blood flow (CBF). A new technique, arterial spin labeling (ASL), makes

it possible to measure CBF accurately with MRI without using contrast agents. In ASL, arterial blood water is first magnetically labeled just below the region (slice) of interest by applying a 180° radiofrequency (RF) inversion pulse which inverts the net magnetization of the blood water. After a period of time (called the transit time), this 'paramagnetic tracer' flows into the slice of interest where it exchanges with tissue water. The inverted spins carried with the blood coming into the volume of interest reduce total tissue magnetization. During this time, an image is taken (called the tag image) which highlights the change. The primary advantages are that completely noninvasive, absolute cerebral blood flow (CBF) measurements are possible with relative insensitivity to permeability, and that multiple repeated measurements can be obtained to evaluate one or more interventions or to perform perfusion-based functional MRI [83]. In one study, three patients with epilepsy and tuberous sclerosis underwent brain MRI with ASL and positron emission tomography (PET). The results were closely correlated with each other and with electrophysiological data [84]. Chen et al. [85] compared cerebral blood flow changes (ΔCBF) measured with flow-sensitive alternating inversion recovery (FAIR) ASL perfusion method to those obtained using $H_2{}^{15}O$ PET, the current gold standard for in vivo imaging of CBF. They imaged a group of healthy volunteers under identical conditions to study changes in regional and global CBF during five levels of visual stimulation and one level of hypercapnia. The CBF changes were compared using three types of region-of-interest (ROI) masks and found to be closely correlated [85].

There is some correlation between the size of the hippocampus and the development of Alzheimer's disease. Recently, a PET compound was developed and patented by researchers at the University of Pittsburg (Pittsburg Compound B or PIB) that apparently is a marker for amyloid plaque. One study aimed at relating the size of the hippocampus, the uptake of PIB, and the degree of cognitive impairment in an older population [86]. This study gives a preview of how anatomical detail as measured by MRI can be correlated with activation, enzyme concentration, or other measures physiological processes to give a clearer correlation between structure and function.

In a further application of simultaneous PET/MRI images, obtained with the Tubingen system, of the uptake by a mouse colon carcinoma [40] revealed selective uptake in its viable regions compared with degenerate areas (Fig. 15.26).

The corresponding MRI images also show increased contrast uptake in the viable regions of the tumor, while, at the same time, providing high-resolution structural information. Hence, the combination of PET/MRI accurately localizes the viable region versus regions with inflammation or necrosis on the tumor.

5.5 Multimodality Probes

Based on the discussion, it is clear that the total information that is obtained using PET and MRI simultaneously is greater than the sum of the parts. For PET and MRI probes to be truly simultaneous, they must have identical pharmacodynamic

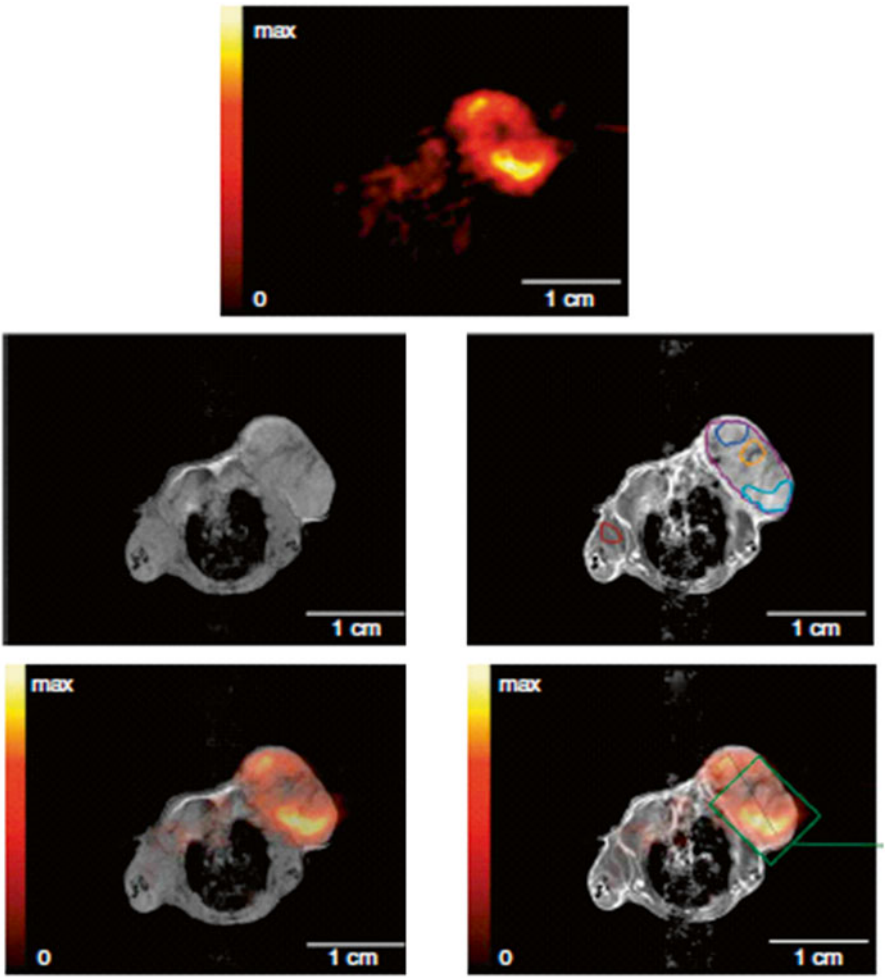

Fig. 15.26 *Top row*: F18- FLT PET image of colon carcinoma uptake. *Middle row*: corresponding T1-weighted MRI image. *Left*: pre-contrast enhanced MRI. *Right*: post-contrast enhanced MRI. *Bottom row*: fused PET/MRI image. Reprinted with permission from Judenhofer et al. [40]

properties. Multi-modal contrast agents and imaging probes under development will help solve this problem [87]. Despite the great wealth of information that such probes provide, their development is far from trivial, representing an important challenge to synthetic chemists [88]. An example of a multimodal probe based on a MRI active nanoparticle is shown in Fig. 15.27.

These probes may be made sensitive to other modalities, such as optical, by attaching the appropriate molecule to the nanoparticle. Disease processes often can be identified by altered molecular profiles and/or cell behavior before to anatomic alterations can be visualized. The more we learn in this regard, the more this seems

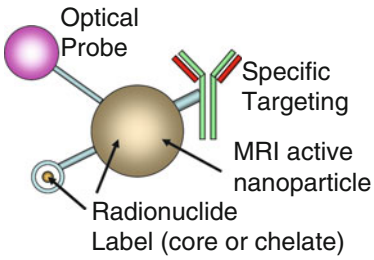

Fig. 15.27 Multimodal nanoparticle suitable for simultaneous PET and MRI imaging

to be a general phenomenon. Insight into these processes could potentially allow (1) the early detection of disease, (2) more accurate prognoses and personalized treatments, (3) the ability to monitor the effectiveness of therapeutic treatments, and, (4) improvements in our understanding of how cells behave and interact in their intact environment in living subjects. Molecular imaging with PEt already has profoundly affected our understanding in preclinical and clinical areas including cancer research and many aspects of neuroscience. MRI is in its early stages of moving from structural and functional imaging to molecular imaging, but this and requires considerable development. The combined use of PET and MRI with these proposed multi-modality imaging agents could be extraordinarily valuable in advancing our understanding of cellular pathophysiology.

Nanoparticles may not only provide sensitive and specific imaging information in cancer patients, but also selectively deliver anticancer drugs to tumor sites [89–91]. There are examples of using nanoparticles as drug delivery agents [92, 93]; more recently, magnetically guided nanoparticles have been used to deliver therapeutic drugs to the specific areas [94]. Although the feasibility of using targeted magnetic iron oxide nanoparticles (MINO) for tumor imaging and therapy is demonstrated, methods and strategies to produce tumor targeted imaging probes with a high specificity and sensitivity still are greatly needed [95, 96]. The added benefit of using nanoparticles for therapy requires that the therapeutic drug stays attached to the nanoparticle until it reaches the desired site. After two decades of effort, iron oxide nanoparticles have become a powerful platform, but are not yet in widespread use clinically [96]. There are questions about how to optimize the nanoparticle-therapeutic drug constructs for delivering the drug to the tumor site and how magnetic direction might be optimized for delivery using magnetically directed drug constructs. By combining the MRI visualization of these nanoparticles with the ability to quantify the concentration of the nanoparticles with PET, we have a powerful tool for investigating the fate of these nanoparticles. Labeling the therapeutic drug with a PET tracer and following the uptake of the nanoparticle with MRI, allows us to visualize clearly the fate of the drug versus that of the nanoparticle as they dissociate in vivo. It will be possible to label a magnetically active nanoparticle in the core and observe the loss in signal as the nanoparticle changes its magnetic properties over time in vivo, while concurrently tracking the total number and

distribution of iron atoms from the nanoparticles using the PET signal, which remains sensitive to the iron regardless of its chemical form.

Various biological molecules attached to nanoparticles have been used in vitro and in vivo. To date, studies showed that the polymer-coated nanoparticles have minimal impact on cell viability and function. Examples include:

- Monoclonal Antibodies. Two initial approaches were to conjugate dextran-coated particles to internalizing monoclonal antibodies and the HIV-tat-peptide. In the first case, the particles end up in the cell in small vesicles or endosomes, and, in the second case in the nucleus.
- Stem Cells. Using stem cells as delivery vehicles opens up the opportunity for targeting therapeutic proteins to the damaged or degenerating central nervous system. Most cellular imaging studies to date were conducted in disease models of the central nervous system (CNS); recently, the infarcted heart received attention.
- Cell Migration and Cell Trafficking. There are several examples of MRI imaging of cell migration following transplantation in the CNS.
- Transfection Agents. Another interesting area is employing iron-oxide nanoparticles coated with a transfection agent (TA). TAs usually are positively charged, bind rapidly to negatively charged cell membranes, and can shuttle associated macromolecules (i.e., oligonucleotides) into cells. The same concept applies for the intracellular delivery of SPIO particles.

We will be able to quantitatively map the dynamics of these molecular imaging probes, and measure their final concentrations. There is a difference in scale of the two types of imaging agents. Iron-based MRI contrast agents usually require about 50–100 μmol of iron per kilogram of body weight to give good semi-quantitative images, while PET tracers usually need about 1 nmol of tracer per kilogram of body weight. By using the two in conjunction, we gain the sensitivity and quantitation of the PET tracer, while using the anatomical sensitivity of the MRI agent to obtain their precise location and volume so that the PET images can be corrected for partial-volume effects in small structures.

6 Summary

The instruments and applications of PET combined with MRI are just beginning to scratch the surface of what is achievable with multi-modality imaging. The ability to view a metabolic or physiological process from several vantage points simultaneously gives us a new perspective in understanding nature. We believe PET/MRI is a cornerstone of these new developments. Even more modalities, such as optical, and ultrasound techniques might well be combined with PET/MRI, and undoubtedly will be valuable research tools for pre-clinical human and small-animal research in the near future.

Acknowledgments This work was supported by the U.S. Department of Energy (OBER) under Prime Contract No. DE-AC02-98CH10886.

References

1. Shokeen M, Fettig NM, Rossin R (2008) Synthesis, in vitro and in vivo evaluation of radiolabeled nanoparticles. Q J Nucl Med Mol Imaging 52:267–77.
2. Townsend DW, Cherry SR (2001) Combining anatomy and function: the path to true image fusion. Eur Radiol 11:1968–74.
3. Yamamoto S, Kuroda K, Senda M (2003) Scintillator selection for MR-compatible gamma detectors. Nuclear Science, IEEE Transactions on 50:1683–1685.
4. Christensen NL, Hammer BE, Heil BG, Fetterly K (1995) Positron emission tomography within a magnetic field using photomultiplier tubes and lightguides. Phys Med Biol 40:691–7.
5. Lucas AJ, Hawkes RC, Ansorge RE, Williams GB, Nutt RE, Clark JC, et al. (2006) Development of a combined microPET-MR system. Technol Cancer Res Treat 5:337–41.
6. Marsden PK, Strul D, Keevil SF, Williams SC, Cash D (2002) Simultaneous PET and NMR. Br J Radiol 75 Spec No:S53-9.
7. Shao Y, Cherry SR, Farahani K, Meadors K, Siegel S, Silverman RW, et al. (1997) Simultaneous PET and MR imaging. Phys Med Biol 42:1965–70.
8. Shao Y, Cherry SR, Farahani K, Slates R, Silverman RW, Meadors K, et al. (1997) Development of a PET detector system compatible with MRI/NMR systems. Nuclear Science, IEEE Transactions on 44:1167–1171.
9. Slates R, Cherry S, Boutefnouchet A, Yiping S, Dahlborn M, Farahani K (1999) Design of a small animal MR compatible PET scanner. Nuclear Science, IEEE Transactions on 46:565–570.
10. Catana C, Procissi D, Wu Y, Judenhofer MS, Qi J, Pichler BJ, et al. (2008) Simultaneous in vivo positron emission tomography and magnetic resonance imaging. Proc Natl Acad Sci U S A 105:3705–10.
11. Catana C, Wu Y, Judenhofer MS, Qi J, Pichler BJ, Cherry SR (2006) Simultaneous acquisition of multislice PET and MR images: initial results with a MR-compatible PET scanner. J Nucl Med 47:1968–76.
12. Pichler BJ, Judenhofer MS, Catana C, Walton JH, Kneilling M, Nutt RE, et al. (2006) Performance test of an LSO-APD detector in a 7-T MRI scanner for simultaneous PET/MRI. J Nucl Med 47:639–47.
13. Pichler BJ, Judenhofer MS, Wehrl HF (2008) PET/MRI hybrid imaging: devices and initial results. Eur Radiol 18:1077–86.
14. Schlyer D, Rooney W, Woody C, Vaska P, Kriplani A, Stoll S (2004) Development of a simultaneous PET/MRI scanner. Nuclear Science Symposium Conference Record, 2004 IEEE, vol. 6, pp. 3419–3421 Vol. 6.
15. Judenhofer MS, Catana C, Swann BK, Siegel SB, Jung WI, Nutt RE, et al. (2007) PET/MR images acquired with a compact MR-compatible PET detector in a 7-T magnet. Radiology 244:807–14.
16. Woody C, Schlyer D, Vaska P, Tomasi D, Solis-Najera S, Rooney W, et al. (2007) Preliminary studies of a simultaneous PET/MRI scanner based on the RatCAP small animal tomograph. Nuclear Instruments and Methods in Physics Research Section A: Accelerators, Spectrometers, Detectors and Associated Equipment 571:102–105.
17. Junnarkar SS, Fried J, O'Connor P, Radeka V, Vaska P, Purschke M, et al. (2006) MRI Compatible G-Link and PCI Based Data Acquisition Hardware for the RatCAP Scanner. Nuclear Science Symposium Conference Record, 2006. IEEE, vol. 1, pp. 380–383.
18. Cutler PD, Cherry SR, Hoffman EJ, Digby WM, Phelps ME (1992) Design features and performance of a PET system for animal research. J Nucl Med 33:595–604.
19. Hammer BE. NMR-PET scanner apparatus US Patent Number 4,939, 464. 1990.
20. Moses WW, Derenzo SE, Budinger TF (1994) PET detector modules based on novel detector technologies. Nuclear Instruments and Methods in Physics Research Section A: Accelerators, Spectrometers, Detectors and Associated Equipment 353:189–194.

21. Cherry SR, Shao Y, Siegel S, Silverman RW, Mumcuoglu E, Meadors K, et al. (1995) Optical fiber readout of scintillator arrays using a multi-channelPMT: a high resolution PET detector for animal imaging. vol. 3, pp.
22. Cherry SR, Shao Y, Tornai MP, Siegel S, Ricci AR, Phelps ME (1995) Collection of scintillation light from small BGO crystals. IEEE Transactions on Nuclear Science 42:1058–1063.
23. Garlick PB, Marsden PK, Cave AC, Parkes HG, Slates R, Shao Y, et al. (1997) PET and NMR dual acquisition (PANDA): applications to isolated, perfused rat hearts. NMR Biomed 10:138–42.
24. Slates RB, Farahani K, Shao Y, Marsden PK, Taylor J, Summers PE, et al. (1999) A study of artefacts in simultaneous PET and MR imaging using a prototype MR compatible PET scanner. Phys Med Biol 44:2015–27.
25. Lecomte R, Schmitt D, Lightstone AW, McIntyre RJ (1985) Performance characteristics of BGO-silicon avalanche photodiode detectors for PET. IEEE Transactions on Nuclear Science 32:482–486.
26. Petrillo GA, McIntyre RJ, Lecomte R, Lamoureux G, Schmitt D (1984) Scintillation detection with large-area reach-through avalanche photodiodes. IEEE Transactions on Nuclear Science 31:417–423.
27. Lecomte R, Martel C, Carrier C (1989) Status of BGO-avalanche photodiode detectors for spectroscopic and timing measurements. Nucl. Instrum. Meth. Phys. Res 278:585–597.
28. Lecomte R, Cadorette J, Jouan A, Heon M, Rouleau D, Gauthier G (1990) High resolution positron emission tomography with a prototypecamera based on solid state scintillation detectors. IEEE Transactions on Nuclear Science 37:805–811.
29. Lecomte R, Cadorette J, Rodrigue S, Lapointe D, Rouleau D, Bentourkia M, et al. (1996) Initial results from the Sherbrooke avalanche photodiode positron tomograph. Nuclear Science, IEEE Transactions on 43:1952–1957.
30. Fontaine R, Belanger F, Viscogliosi N, Semmaoui H, Tetrault MA, Michaud JB, et al. (2005) The architecture of LabPET/spl trade/, a small animal APD-based digital PET scanner. Nuclear Science Symposium Conference Record, 2005 IEEE, vol. 5, pp. 2785–2789.
31. Bergeron M, Cadorette J, Beaudoin JF, Lepage MD, Robert G, Selivanov V, et al. (2009) Performance Evaluation of the LabPET APD-Based Digital PET Scanner. Nuclear Science, IEEE Transactions on 56:10–16.
32. Schmelz C, Bradbury SM, Holl I, Lorenz E, Renker D, Ziegler S (1995) Feasibility study of an avalanche photodiode readout for a highresolution PET with nsec time resolution. IEEE Transactions on Nuclear Science 42:1080–1084.
33. Casey ME, Dautet H, Waechter D, Lecomte R, Eriksson L, Schmand M, et al. (1998) An LSO block detector for PET using an avalanche photodiode array. vol. 2, pp.
34. Pichler BJ, Swann BK, Rochelle J, Nutt RE, Cherry SR, Siegel SB (2004) Lutetium oxyorthosilicate block detector readout by avalanche photodiode arrays for high resolution animal PET. Phys Med Biol 49:4305–19.
35. Pichler B, Boning C, Lorenz E, Mirzoyan R, Pimpl W, Schwaiger M, et al. (1998) Studies with a prototype high resolution PET scanner based onLSO-APD modules. IEEE Transactions on Nuclear Science 45:1298–1302.
36. Binkley DM, Puckett BS, Casey ME, Lecomte R, Saoudi A (1999) A power efficient, low noise, wideband, integrated CMOSpreamplifier for LSO/APD PET systems. vol. 1, pp.
37. Lecomte R, Pepin CM, Lepage MD, Pratte JF, Dautet H, Binkley DM (2001) Performance analysis of phoswich/APD detectors and low-noise CMOSpreamplifiers for high-resolution PET systems. IEEE Transactions on Nuclear Science 48:650–655.
38. Pichler B, Lorenz E, Mirzoyan R, Pimpl W, Roder F, Schwaiger M, et al. (1997) Performance test of a LSO-APD PET module in a 9.4 Tesla magnet. Nuclear Science Symposium, 1997. IEEE, vol. 2, pp. 1237–1239 vol.2.
39. Schlyer D, Vaska P, Tomasi D, Woody C, Maramraju SH, Southekal S, et al. (2007) A Simultaneous PET/MRI scanner based on RatCAP in small animals. Nuclear Science Symposium Conference Record, 2007. NSS '07. IEEE, vol. 5, pp. 3256–3259.

40. Judenhofer MS, Wehrl HF, Newport DF, Catana C, Siegel SB, Becker M, et al. (2008) Simultaneous PET-MRI: a new approach for functional and morphological imaging. Nat Med 14:459–65.
41. Pratte JF, Junnarkar S, Deptuch G, Fried J, O'Connor P, Radeka V, et al. (2008) The RatCAP Front-End ASIC. Nuclear Science, IEEE Transactions on 55:2727–2735.
42. Junnarkar SS, Fried J, Southekal S, Pratte JF, O'Connor P, Radeka V, et al. (2008) Next Generation of Real Time Data Acquisition, Calibration and Control System for the RatCAP Scanner. Nuclear Science, IEEE Transactions on 55:220–224.
43. Maramraju SH, Junnarkar S, Ravindranath B, Southekal S, Stoll S, Smith SD, et al. (2008) An MR compatible PET scanner based on RatCAP for small animal imaging at 9.4T. Nuclear Science Symposium Conference Record, 2008. NSS '08. IEEE, pp. 3679–3682.
44. Karplus E, Farrell R, Shah K. Position sensitive solid state detector with internal gain. US patent No : 6,998,619 B2. 2004.
45. Shah KS, Grazioso R, Farrell R, Glodo J, McClish M, Entine G, et al. (2004) Position sensitive APDs for small animal PET imaging. IEEE Transactions on Nuclear Science 51:91–95.
46. Burr KC, Ivan A, LeBlanc J, Zelakiewicz S, McDaniel DL, Kim CL, et al. (2003) Evaluation of a position sensitive avalanche photodiode for PET. Nuclear Science, IEEE Transactions on 50:792–796.
47. Levin CS, Foudray AMK, Olcott PD, Habte F (2004) Investigation of position sensitive avalanche photodiodes for a new high-resolution PET detector design. Nuclear Science, IEEE Transactions on 51:805–810.
48. Yang Y, Wu Y, Qi J, St James S, Du H, Dokhale PA, et al. (2008) A prototype PET scanner with DOI-encoding detectors. Journal of Nuclear Medicine 49:1132.
49. Burr KC, Ivan A, Castleberry DE, LeBlanc JW, Shah KS, Farrell R, et al. (2004) Evaluation of a prototype small-animal PET detector with depth-of-interaction encoding. IEEE Transactions on Nuclear Science 51:1791–1798.
50. Dokhale PA, Silverman RW, Shah KS, Grazioso R, Farrell R, Glodo J, et al. (2004) Performance measurements of a depth-encoding PET detector module based on position-sensitive avalanche photodiode read-out. Physics in Medicine and Biology 49:4293–4304.
51. Yang Y, Dokhale PA, Silverman RW, Shah KS, McClish MA, Farrell R, et al. (2006) Depth of interaction resolution measurements for a high resolution PET detector using position sensitive avalanche photodiodes. Physics in Medicine and Biology 51:2131–2142.
52. Saveliev V, Golovin V (2000) Silicon avalanche photodiodes on the base of metal-resistor-semiconductor (MRS) structures. Nuclear Instruments and Methods in Physics Research Section A: Accelerators, Spectrometers, Detectors and Associated Equipment 442:223–229.
53. Otte AN, Barral J, Dolgoshein B, Hose J, Klemin S, Lorenz E, et al. (2005) A test of silicon photomultipliers as readout for PET. Nuclear Instruments and Methods in Physics Research Section A: Accelerators, Spectrometers, Detectors and Associated Equipment 545:705–715.
54. Llosa G, Belcari N, Bisogni MG, Collazuol G, Del Guerra A, Marcatili S, et al. (2008) Evaluation of the first Silicon Photomultiplier matrices for a small animal PET scanner. Nuclear Science Symposium Conference Record, 2008. NSS '08. IEEE, pp. 3574–3580.
55. Llosa G, Belcari N, Bisogni MG, Collazuol G, Marcatili S, Moehrs S, et al. (2009) Energy and Timing Resolution Studies With Silicon Photomultipliers (SiPMs) and 4-Pixel SiPM Matrices for PET. Nuclear Science, IEEE Transactions on 56:543–548.
56. Herbert DJ, Saveliev V, Belcari N, D'Ascenzo N, Del Guerra A, Golovin A (2006) First results of scintillator readout with silicon photomultiplier. Nuclear Science, IEEE Transactions on 53:389–394.
57. Lucas AJ, Hawkes RC, Guerra P, Ansorge RE, Nutt RE, Clark JC, et al. (2006) Development of a combined microPETÂ®-MR system. Nuclear Science Symposium Conference Record, 2006. IEEE, vol. 4, pp. 2345–2348.
58. Gilbert K, Handler W, Scholl T, Odegaard J, Chronik B (2006) Design of field-cycled magnetic resonance systems for small animal imaging. Physics in Medicine and Biology 51:2825–2842.

59. Gilbert KM, Scholl TJ, Handler WB, Alford JK, Chronik BA (2009) Evaluation of a positron emission tomography (PET)-compatible field-cycled MRI (FCMRI) scanner. Magn Reson Med.
60. Slates R, Shao Y, Farahani K, Marsden PK, Cherry SR, Meadors K, et al. (1997) Assessment of artifacts in simultaneous PET and MR imaging. Nuclear Science Symposium, 1997. IEEE, vol. 2, pp. 1357–1360 vol.2.
61. Zhang Z, Olcott PD, Levin CS (2007) A New Positioning Algorithm for Position-Sensitive Avalanche Photodiodes. Nuclear Science, IEEE Transactions on 54:433–437.
62. Chaudhari AJ, Joshi AA, Yibao W, Leahy RM, Cherry SR, Badawi RD (2008) Spatial distortion correction and crystal identification for position-sensitive avalanche photodiode-based PET scanners. Nuclear Science Symposium Conference Record, 2008. NSS '08. IEEE, pp. 5045–5052.
63. Chaudhari AJ, Joshi AA, Yibao W, Leahy RM, Cherry SR, Badawi RD (2009) Spatial Distortion Correction and Crystal Identification for MRI-Compatible Position-Sensitive Avalanche Photodiode-Based PET Scanners. Nuclear Science, IEEE Transactions on 56:549–556.
64. Zhang J, Foudray AMK, Olcott PD, Farrell R, Shah K, Levin CS (2007) Performance Characterization of a Novel Thin Position-Sensitive Avalanche Photodiode for 1 mm Resolution Positron Emission Tomography. Nuclear Science, IEEE Transactions on 54:415–421.
65. Raylman RR, Hammer BE, Christensen NL (1996) Combined MRI-PET scanner: a Monte Carlo evaluation of the improvements in PET resolution due to the effects of a static homogeneous magnetic field. Nuclear Science, IEEE Transactions on 43:2406–2412.
66. Hammer BE, Christensen NL (1995) Measurement of positron range in matter in strong magnetic fields. Nuclear Science, IEEE Transactions on 42:1371–1376.
67. Hammer BE, Christensen NL, Heil BG (1994) Use of a magnetic field to increase the spatial resolution of positron emission tomography. Med Phys 21:1917–20.
68. Wirrwar A, Vosberg H, Herzog H, Halling H, Weber S, Muller-Gartner HW (1997) 4.5 tesla magnetic field reduces range of high-energy positrons-potential implications for positron emission tomography. Nuclear Science, IEEE Transactions on 44:184–189.
69. Zaidi H, Hasegawa B (2003) Determination of the attenuation map in emission tomography. J Nucl Med 44:291–315.
70. Zaidi H, Montandon ML, Slosman DO (2003) Magnetic resonance imaging-guided attenuation and scatter corrections in three-dimensional brain positron emission tomography. Med Phys 30:937–48.
71. Rowell NP, Glaholm J, Flower MA, Cronin B, McCready VR (1992) Anatomically derived attenuation coefficients for use in quantitative single photon emission tomography studies of the thorax. Eur J Nucl Med 19:36–40.
72. Zaidi H (2007) Is MR-guided attenuation correction a viable option for dual-modality PET/MR imaging? Radiology 244:639–42.
73. Hofmann M, Pichler B, Scholkopf B, Beyer T (2009) Towards quantitative PET/MRI: a review of MR-based attenuation correction techniques. Eur J Nucl Med Mol Imaging 36 Suppl 1:S93–104.
74. Beyer T, Weigert M, Quick HH, Pietrzyk U, Vogt F, Palm C, et al. (2008) MR-based attenuation correction for torso-PET/MR imaging: pitfalls in mapping MR to CT data. Eur J Nucl Med Mol Imaging 35:1142–6.
75. Day SE, Kettunen MI, Gallagher FA, Hu DE, Lerche M, Wolber J, et al. (2007) Detecting tumor response to treatment using hyperpolarized 13C magnetic resonance imaging and spectroscopy. Nat Med 13:1382–7.
76. Thompson JK, Peterson MR, Freeman RD (2003) Single-neuron activity and tissue oxygenation in the cerebral cortex. Science 299:1070–2.
77. Belliveau JW, Cohen MS, Weisskoff RM, Buchbinder BR, Rosen BR (1991) Functional studies of the human brain using high-speed magnetic resonance imaging. J Neuroimaging 1:36–41.
78. Mountz JM (2007) Nuclear medicine in the rehabilitative treatment evaluation in stroke recovery. Role of diaschisis resolution and cerebral reorganization. Eura Medicophys 43:221–39.
79. van Eijsden P, Hyder F, Rothman DL, Shulman RG (2009) Neurophysiology of functional imaging. Neuroimage 45:1047–54.

80. Gerstl F, Windischberger C, Mitterhauser M, Wadsak W, Holik A, Kletter K, et al. (2008) Multimodal imaging of human early visual cortex by combining functional and molecular measurements with fMRI and PET. Neuroimage 41:204–11.
81. Stadlbauer A, Polking E, Prante O, Nimsky C, Buchfelder M, Kuwert T, et al. (2009) Detection of tumour invasion into the pyramidal tract in glioma patients with sensorimotor deficits by correlation of (18)F-fluoroethyl-L: -tyrosine PET and magnetic resonance diffusion tensor imaging. Acta Neurochir (Wien) 151:1061–9.
82. Sobesky J, Zaro Weber O, Lehnhardt FG, Hesselmann V, Neveling M, Jacobs A, et al. (2005) Does the mismatch match the penumbra? Magnetic resonance imaging and positron emission tomography in early ischemic stroke. Stroke 36:980–5.
83. Wolf RL, Detre JA (2007) Clinical neuroimaging using arterial spin-labeled perfusion magnetic resonance imaging. Neurotherapeutics 4:346–59.
84. Wissmeyer M, Altrichter S, Pereira VM, Viallon M, Federspiel A, Seeck M, et al. (2009) Arterial spin-labeling MRI perfusion in tuberous sclerosis: Correlation with PET. J Neuroradiol.
85. Chen JJ, Wieckowska M, Meyer E, Pike GB (2008) Cerebral Blood Flow Measurement Using fMRI and PET: A Cross-Validation Study. Int J Biomed Imaging 2008:516359.
86. Jack CR, Jr., Lowe VJ, Senjem ML, Weigand SD, Kemp BJ, Shiung MM, et al. (2008) 11C PiB and structural MRI provide complementary information in imaging of Alzheimer's disease and amnestic mild cognitive impairment. Brain 131:665–80.
87. Jennings LE, Long NJ (2009) 'Two is better than one'--probes for dual-modality molecular imaging. Chem Commun (Camb):3511–24.
88. Cheon J, Lee JH (2008) Synergistically integrated nanoparticles as multimodal probes for nanobiotechnology. Acc Chem Res 41:1630–40.
89. Gupta AK, Naregalkar RR, Vaidya VD, Gupta M (2007) Recent advances on surface engineering of magnetic iron oxide nanoparticles and their biomedical applications. Nanomed 2:23–39.
90. Hanessian S, Grzyb JA, Cengelli F, Juillerat-Jeanneret L (2008) Synthesis of chemically functionalized superparamagnetic nanoparticles as delivery vectors for chemotherapeutic drugs. Bioorg Med Chem 16:2921–31.
91. Yang CH, Huang KS, Lin YS, Lu K, Tzeng CC, Wang EC, et al. (2009) Microfluidic assisted synthesis of multi-functional polycaprolactone microcapsules: incorporation of CdTe quantum dots, Fe3O4 superparamagnetic nanoparticles and tamoxifen anticancer drugs. Lab Chip 9:961–5.
92. Peng XH, Qian X, Mao H, Wang AY, Chen ZG, Nie S, et al. (2008) Targeted magnetic iron oxide nanoparticles for tumor imaging and therapy. Int J Nanomedicine 3:311–21.
93. Murakami T, Tsuchida K (2008) Recent advances in inorganic nanoparticle-based drug delivery systems. Mini Rev Med Chem 8:175–83.
94. Barry SE (2008) Challenges in the development of magnetic particles for therapeutic applications. Int J Hyperthermia 24:451–66.
95. McCarthy JR, Weissleder R (2008) Multifunctional magnetic nanoparticles for targeted imaging and therapy. Adv Drug Deliv Rev 60:1241–51.
96. Xie J, Huang J, Li X, Sun S, Chen X (2009) Iron oxide nanoparticle platform for biomedical applications. Curr Med Chem 16:1278–94.

Chapter 16
Dual-Modality Preclinical PET-OI Concepts and Instrumentation

Jörg Peter

1 Motivation

Whereas interpreting functional and molecular data under anatomical cognizance as provided by CT or MRI offers a number of advantages, combining two molecular imaging modalities such as PET and optical imaging (OI), the latter comprising bioluminescence imaging (BLI), fluorescence mediated imaging (FMI), and possibly fluorescence mediated tomography (FMT), seems, at first sight, not very instinctive. However, there are a number of potential applications specifically in drug research and development such as translational study design or coadjutant pharmacokinetic modeling that could make use of fully integrated, time-resolved dual-modality PET-OI instrumentation. At the time of writing (2011), instrumentation development for in vivo imaging is still in its infant stage and—given the general limitation of light distribution in tissue to small volumes because of high scattering of light photons and, hence, given the complex inverse problem involved in three-dimensional tomographic image reconstruction with solutions not easily to be found in heterogeneous media—research is focused primarily on preclinical application to small animals (mice in particular). This chapter provides a review on the current state of dual-modal integration concepts including proposed and working systems respectively for small animal PET-OI through classification of approaches as reported in recent literature into the following instrumentation categories:

1. possible system approaches embodied through modular combination of sub-modalities;
2. a bi-modal system that use mirrors to deflect optical photons from the multi-energetic photon flux for external detection outside the field-of-view (FOV) of the PET system;

J. Peter (✉)
Division of Medical Physics in Radiology, German Cancer Research Center (DKFZ), Heidelberg, Germany
e-mail: j.peter@dkfz-heidelberg.de

H. Zaidi (ed.), *Molecular Imaging of Small Animals: Instrumentation and Applications*,
DOI 10.1007/978-1-4939-0894-3_16,

Table 16.1 Imaging considerations when employing positron and optical imaging modalities in small animals

	PET	OI
Particle cross-section	Scatter $\ll$ attenuation	Scatter $\gg$ attenuation
Spatial resolution	ca. 1 mm	Depth dependent
Temporal resolution	Seconds to hours	Seconds to days
Tissue penetration	Unlimited, whole body	Limited to few cm
Detector complexity	High (energy conversion)	Simple, high resolution
Image reconstruction	Fully 3D	Possible
Quantitative imaging	Yes	Possible (FMT)
Labeling probe	Direct/indirect	dir./indir./activatable
Detection sensitivity (mol/L)	10^{-10} to 10^{-12}	10^{-15} to 10^{-17} (BLI) 10^{-9} to 10^{-12} (FMI)
Background	Moderate to high	Low (BLI) Moderate (FMI)
Mass quantity	ngrams	µ/mgrams
Translational application	Yes	Very limited
Radiation hazard	Yes	No
Chemical synthesis	Complex	Straightforward
Cost per study	High	Low

3. a system proposal employing a single photon sensor for detecting both high-energy (PET) and low energy (optical) photons;
4. a fully-integrated system utilizing light detectors that are mounted directly in front and within the FOV of PET detectors.

1.1 Reasoning for Multimodal Molecular Imaging Techniques

Identification and selection of appropriate molecular targets (genes, proteins) is key prerequisite not only for the target being a critical component within the molecular pathway but also for it to be both a qualified target for molecular imaging and a potential candidate for therapeutic drug development. Once a target is selected it needs to be brought in contact with an imaging probe, employed to carry signal information from the target in vivo to the externally positioned imaging sensor. While there are various crucial criteria [1] that must be met when designing and applying imaging probes in order to effectively monitor specific molecular targets in living systems appropriate imaging instruments with high sensitivity and spatial (also temporal) resolution need to be available to detect the probe. However, as of today it is rather difficult to satisfy all criteria while only relying on a single imaging modality for intrinsic reasons (cf. Table 16.1). Moreover, various imaging modalities provide usually complementary diagnostic information. This holds not only for combining

high-sensitivity functional/molecular imaging (PET, OI) with high-resolution anatomical imaging (CT, MRI). Rather, it has also been demonstrated in a number of research studies that combining two (or even three) molecular imaging modalities can help to improve the diagnostic value of either single approach, or might have advantages in study accomplishment.

Comparing PET versus OI strategies, PET has the advantage of increased resolution and quantitation, lack of attenuation and absorption artifacts, and tomographic fully three-dimensional data representation. Conversely, bioluminescent optical imaging (of reporter gene expression, in particular) has frequently been more sensitive, is less expensive, more convenient, and more "user friendly" than PET imaging of the same target. Table 16.1 summarizes and compares various important aspects of PET and optical imaging when intended for applications in small animals.

There is a large difference in temporal resolution between the life times of the PET and optical probes. Whereas positron emission is representing a decay process—most radioisotopes as used for preclinical PET such as ^{18}F or ^{11}C have relative short half-lives, the optical signal can be detected even after several days or weeks after administration of the light generating substrate, and, very importantly, light emission can be activated or deactivated by various stimuli. This difference in time kinetics can be used, e.g., to perform longitudinal studies in which the PET probe is being evaluated for early probe distribution analysis while variations in the optical intensity can be observed at later time, for instance, to monitor therapy efficiency in the target tissue.

If multimodal imaging is carried out to monitor *multiple* molecular targets simultaneously, in this context by means of optical imaging and PET, then their might be the desire to acquire data simultaneously utilizing instrumentation as described in this chapter. If, however, a *single* molecular target is to be monitored by multiple, possibly fused imaging probes, or if a study is being carried out with the objective to cross-validate one imaging probe by another, amongst other study objectives, then fully integrated imaging instruments (with superimposed fields-of-view) might be obligatory. The same desire for simultaneous imaging—at least while cross-validating one sub-system for in vivo imaging against the other—might also hold when a probe is to be replaced with another probe of the complementary modality to produce an equivalent target signal because, e.g., replacing a radionuclide with a fluorescent dye might alter the in vivo probe distribution or rate of uptake on the target site. Another argument for multimodal molecular imaging lies in the fact that no single reporter gene probe system meets all molecular imaging criteria in an optimal fashion at present, being it related to probe design such as the ability to cross inherent biological barriers that would prevent a probe to reach its intended target, metabolic probe instability causing insufficient absorption and excretion, or probe accumulation in the target to establish image contrast, or being it related to physical and mathematical considerations such as for instance posing potentially advantageous constraints on optical image reconstruction strategies, e.g., by means of prior information from the spatial distribution of the PET probe after respective image reconstruction.

Table 16.2 Examples of reporter gene imaging systems employing positron and optical imaging modalities

Target protein	Modality (ligand/substrate)
Thymidine kinase	PET (FIAU, ganciclovir, penciclovir, FHPG) [10, 11]
Cytosine deaminase	PET (cytosine, fluorinated prodrugs) [12, 13]
Somatostatin receptor	PET (peptides) [14, 15]
Dopamine–2 receptor	PET (^{18}F spiperone) [16, 17]
GFP	OI (–) [18, 19]
Luciferase	OI (luciferin) [20, 21]
Protease	OI (quenched fluorescent molecules) [22, 23]

1.2 Multimodal PET-OI Probes

Most approaches in the field of in vivo molecular imaging aimed for visualization and quantitation of gene expression rely on the concept of reporter genes [2–5]. As of today, reporter gene imaging systems have been developed especially for optical [2, 6] and radionuclide [7–9] applications[1] (Table 16.2).

Recently, several groups have started synthesizing multimodal probes, incorporating a variety of modalities [24]. In fact, whereas combined *imaging instruments* is still in the research phase of development, utilizing multimodal *imaging probes* has been reported various times even though these fused multimodal probes were imaged sequentially in most cases. Instead of applying two different imaging agents that are distributed differently within the organism, true multimodal probes possess the signaling moieties for the two imaging systems into one molecule (monomolecular multimodality imaging agents). Such unique probe design ensures that both signals emanate from the same origin, allowing for the fusion of contrast data. Amongst the spectrum of multimodal probes fusion of nuclear and optical methods is still the less frequently used multimodal imaging strategy, as compared to MRI-OI [25]. Of the probes developed for PET-OI dual (or even triple, PET-FMI-BLI) imaging, many have been tested and have now been applied in vitro and in small animal imaging [26]. In the following, a short overview on some recent developments is assembled.

Detecting reporter gene expression is one of the fields in which small PET radionuclides combined with bioluminescence has proven very useful. Two reporter genes, mutant herpes simplex virus type 1 thymidine kinase (HSV1-sr39tk) and renilla luciferase (rl) which had been used many times in separate studies were fused together with a 20 amino acid long spacer sequence to form a single vector in order to study gene expression patterns in cancer development [27]. In that report,

[1] Fewer implementations have been reported for MRI/ MRS [4] such as for tyrosinase, arginine kinase, creatinine kinase, or β-galactosidase target proteins. Also, there are target proteins that can be imaged with SPECT.

the HSV1-sr39tk contained an FBDG tag and the rl contained the bioluminescence tag, coelenterazine. Chimeric fusion genes or bicistronic vectors monitored by PET and FMI [28] and by PET and BLI [29] have also been utilized for noninvasive imaging of reporter gene expression. In [30], cationic lipid-mediated monitoring of reporter gene expression of fl and HSV1-sr39tk in mice was also demonstrated. Multimodal reporter genes were also imaged in [31] in a breast tumor model.

Ottobrini et al. developed a cellular model for BLI (fl) and dopaminergic D2 receptor PET imaging for the assessment of estrogen receptor activity in vivo in a breast cancer model [32]. In vitro studies showed that the vector was efficient in coordinating the expression of the two genes. Moreover, stably transfected cells implanted in recipient animals maintained their capacity to express the reporters and reacted to systemic treatments, permitting the in vivo study of estrogen responsive activity by both PET and BLI imaging. Brader and colleagues [33], imaged bacteria using radiotracer and optical imaging techniques.

Various groups extensively investigated multimodal imaging strategies to analyze the molecular pathways of cancer initiation and progression and drug therapy in living subjects [34]. Fusion reporter genes encoding for fusion reporter proteins have found particularly promising for molecular imaging in that fusions between a fluorescent and a PET reporter protein can be adopted to translate information from a single cell in vitro to living animals in vivo, possibly at fully tomographic manner [35]. Even though fluorescence imaging can be tomographic, it has lower sensitivity than bioluminescence imaging and might be hampered by autofluorescence. Bioluminescent reporter genes on the other hand have emerged as a very sensitive detection tool for small animals. Ray and colleagues have therefore proposed triple-modality fusion proteins encoded by fusion reporter genes composed of a bioluminescent (rl enzyme), a red fluorescent (mRFP1 protein), and a PET reporter gene (HSV1-sr39tk enzyme) for bridging imaging gene expression from single cells to whole living animals with high sensitivity [36, 37]. This reporter vector has been used to identify cells in histological sections, to sort cells in the flow cytometer, to image reporter gene expression in living animals by BLI, and to noninvasively image reporter gene expression by PET. By imaging tumor xenografts in living mice, linear correlation of the signals from each component with all three modalities was found in all studies. In [38], the authors also monitored caspase-3 activation for which they synthesized a modified trimodal reporter gene construct that was fused through a caspase-3 recognizable polypeptide linker. Following induction with staurosporine, a significant increase in mRFP1, fl, and tk activity in 293 T cells was observed quantitatively through various normalization approaches verifying satisfactory correlation between the imaging signals. In another study, Ponomarev et al. have built two triple-modality reporter gene systems for whole-body fluorescent, bioluminescent, and nuclear imaging (both SPECT and PET) [39].

In all studies involving BLI, the bioluminescence signal was detected at a much higher sensitivity than that of HSV1-sr39tk resulting in the detection of a fewer numbers of cells with the OI approach compared to the PET approach. The presence of the PET reporter gene in the fusion protein, though, enabled tomographic visualization of reporter gene expression. Hence, a dualmodal PET-OI strategy provides a

unique approach of validating novel approaches in small animal models with a very low number of cells, while ultimately translating the approach to clinical use.

A multimodal imaging agent has also been designed for the somatostatin receptor [40]. Here, reporters for both optical (via the near-infrared (NIRF) fluorescent dye cypate) and PET (^{64}Cu) have been incorporated into a single molecule. In this study, however, the anticipated receptor-mediated accumulation in target tissues was not observed but there was excellent agreement between the optical and radiochemical biodistributions. Similar studies using a cys-tag for imaging of vascular endothelial growth factor (VEGF) receptors utilized the NIRF dye Cy5.5 and a ^{64}Cu-DOTA (1,4,7,10-tetraazacyclododecane-1,4,7,10-tetraacetic acid) unit for PET imaging [41]. Both probes retained VEGF activities in vitro and showed specific focal uptake in the vasculature of tumours and surrounding host tissue in mice. The fluorescence contrast agent exhibited long-term persistence and co-localized with endothelial cell markers, indicating that internalization is mediated by the receptors.

Further, it has been demonstrated that cationic amphiphilic drugs (CADs) can be labelled with ^{11}C coupled with the incorporation of a small organic fluorophore e.g. derivatised spiperone, a CAD and doperminergic ligand [42]. The small fluorophores are very advantageous because their lower molecular weights suppress tag distortion effects and allow crossing of biological interfaces such as the blood–brain barrier. With such approach, a chemically identical molecule was used to image drug binding in ex vivo cell lines and thin tissue sections whereas the positron-emitting equivalent could be visualized in vivo.

In recent years, quantum dots (QD) have been designed as optical probes for a number of biological systems [43, 44]. QDs are nanoparticulate clusters of semiconductor material possessing quantum confinement effects, that is, their optical properties are controlled by their size, rather than their composition, which makes them very useful optical imaging agents because of the ability to vary their emission spectra. Even though QDs are of great interest for their imaging capabilities, solubility and toxicity issues are potential problems which need be addressed prior to in vitro and in vivo biological applications. While most applications of QD probes are focused towards optical (and MRI) imaging, an increasing share of multimodal probes has been introduced very recently. VEGF receptor on tumor vasculature was assessed by an amine-functionalized QD conjugated with VEGF protein and DOTA chelator for VEGF receptor-targeted PET (^{64}Cu-labeled) optical (NIRF) imaging [45]. This study has been performed to examine the quantitative capability of the OI method which—in contrast to PET—could only maintain qualitative results, mainly because of limited tissue penetration and heterogeneous tissue constitution. Another QD approach has been reported in [46] in which a CdTe QD with an amine-functionalized surface has been modified with arginine-glycine-aspartic acid (RGD) peptides and DOTA chelators for integrin $\alpha_v\beta_3$-targeted PET-NIRF imaging. Linear correlation was obtained between the in vivo PET results and those measured by ex vivo OI and tissue homogenate fluorescence. Although this study focused on sensitivity, targeting efficacy, quantifiability and toxicity issues with regard to the QD probe, an interesting problem of the PET modality has been revealed by the authors in that the tumor-to-background ratios were similar in both the NIRF and PET

images except for bone marrow uptake which was significantly higher measured by OI than measured by PET. The reason likely can be contributed to the partial-volume effect of the PET system. It might be worth noting that the polyvalent nature of these multimodal nanomaterials can potentially be further exploited by normalizing the differences in the detection sensitivities of the different signals which could be achieved by adjusting the quanta of the signaling probes.

To deduct an overall conclusion for all presented studies, there is a commonly expressed hope in that dualmodal PET-OI systems should provide the convenience and sensitivity of OI (particularly BLI) merged with the resolution, quantification, and three-dimensional properties of PET. Prerequisite, though, is the availability of dualmodal PET-OI instruments. Further, using a single fusion reporter (PET-OI compatible) gene should accelerate the validation of reporter gene approaches developed in cell culture for translation into preclinical and clinical models. Another advantage of the PET-optical probe approach is the ability to accurately quantify light intensity in vivo. So, undoubtedly, any multimodal imaging approach helps to better understand each individual imaging modality involved. The multimodal approach also provides a link between high-throughput analysis, preclinical research and clinical studies. Taken all these aspects together, it is essential to understand which molecular probe or which imaging technique is best suited for molecular imaging of a specific molecular process in a specific field of application, being it related to oncology, neurology, pharmacology or pathophysiology.

2 Instrumentation Concepts

As multimodal radionuclide-optical probes where proposed and investigated using conventional, that is, sequential imaging strategies as explained before, the need for integrated instruments became obvious immediately. Consequently, a number of research groups started investigating possible instrumentation approaches for simultaneous imaging of optical (bioluminescence, fluorescence) and radioisotope (SPECT, PET) probes. Compared to the established clinical and by now successfully scaled down preclinical modalities, optical (tomographic) imaging in small animals is, in comparison, a very young discipline that did not have prior clinical heritage. Hence, various approaches towards quantitative data analysis or towards three-dimensional image reconstruction of optical probe distributions in heterogeneous media are intensely investigated at the time of this writing [47–51].

For investigating nuclear medicine instrumentation, Monte Carlo (MC) simulation has long been demonstrated of high value for understanding the complex physical and technological aspects of high-energy photon transport and detection [52–55]. Because of the more difficult approximation of light propagation in tissue (as compared to keV-photon distribution), MC simulation seems to carry an even higher value as a potent research tool for understanding, investigating and improving light-mediated imaging, particularly towards a more complete understanding of tissue optics with respect to the inverse relationship between measured light field

and tissue optical properties. Therefore, various MC simulation approaches and algorithms for light transport have been proposed [56–63]. In [64] a MC algorithm was developed for fully integrative simulation of optical (eV) and isotopic (keV) photons. This code has been involved in a number of radioisotope-optical instrumentation studies [69]. MC-based investigation of dualmodal PET-OI imaging instrumentation has also been carried out in [65–67].

The concept of MC simulation is mentioned here because most of the instrumentation concepts as described in the following sub-sections have been initially, or in parallel, investigated through visualization and validation of ideas utilizing this mathematical tool. Once these ideas carried enough potential towards further academic investigation prototypes were built in some cases. As of today, though, there are no integrated PET-OI instruments commercially available to the best knowledge of this author.

2.1 Complementary Integration Concepts

The most straightforward approach of dualmodal PET-OI probably is embodied by means of a modular instrumentation setup in which dedicated PET and optical cameras (including light sources for fluorochrome excitation) are located in close proximity whereby the imaged animal is placed on a support that has mounting clamps compatible with both imaging systems. In this case, the animal conceptional is imaged sequentially, though at very short time gap between the data acquisition runs.[2] Because the animal is restrained on the holder, and the holder might be equipped with fiducial markers, data registration can generally be readily performed.

Complete integration enabling *simultaneous* data acquisition can be achieved only when both cameras image the object simultaneously, requiring that the subsystem share identical fields-of-view during the entire imaging acquisition process. Figure 16.1 illustrates three feasible dualmodal PET-OI concept studies that consist of (micro)PET modules in which one or more optical cameras are integrated to detect optical photons.

Figure 16.1a shows a combination of a dual-head coincidence PET system with two integrated light cameras. In order to acquire tomographic data the gantry (not shown) holding the four detectors rotates at 180° single-step mode around the object during data acquisition. While temporal resolution is somewhat limited the advantage of using planar PET detectors is that these, and both adjacent optical cameras, can be adjusted in their radius of rotation, respectively, in order to optimize detection efficiency with different sized laboratory animals. In principle, this design could be extended toward arced detector block allocations, conceptionally comparable to the PET design as proposed for a small animal PET-CT scanner [68].

[2] This approach has been implemented by a number of companies for a multitude of instruments linking various modalities.

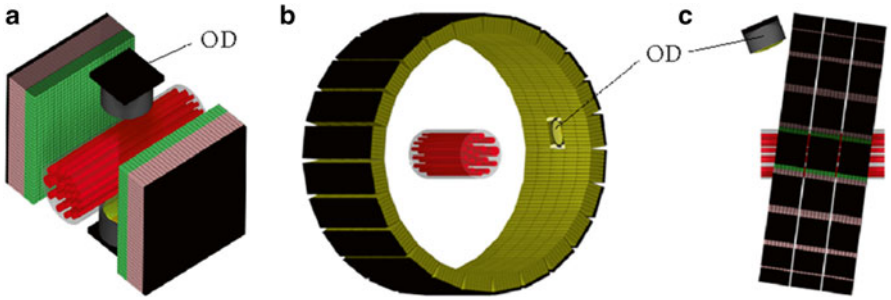

Fig. 16.1 Conceptual dualmodal PET-OI system layouts with identical fields-of-view: (**a**) dual-head coincidence PET system with two integrated optical detectors (OD), (**b**) cylindrical PET system whereby one PET detector block is replaced by an optical camera module, (**c**) tilted cylindrical PET system with an integrated tilted OD. In all designs, the sub-modalities (including light sources, not shown) are mounted on a common rotatable gantry

Figure 16.1b illustrates a design in which a conventional micro-PET has been modified by replacing one or more PET detector blocks by one or more light camera modules. Replacing PET detector blocks essentially corresponds to a truncated data acquisition problem which can be compensated for within the image reconstruction algorithm of the PET data. The prune angular section for the given geometry of the central ring constitutes to 15.65° for the proposal as depicted. In a variety of simulation studies that have been carried out in the author's laboratory quantifiable truncation artifacts were little (static 2D PET) or not (rotational 3D PET) evident in the reconstructed data using standard maximum-likelihood expectation-maximization (MLEM) reconstruction. Due to the integrated optical camera the entire sensitive area is reduced by 1.45 % compared to a dedicated PET system of the same geometry. Figure 16.1c shows a combination of a tilted cylindrical PET system with an integrated tilted light camera. In this conceptual proposal, the PET detector rings are rotated by −8° and the optical detector is rotated by +18° whereby the degree of tilting is adjustable, depending on object size and imaging task. For the example given, the PET system is rotated at a lesser quantity because its spatial resolution is non-isotropic, i. e. it is higher axially than it is transaxially, and because its field-of-view is axially limited, depending on the number of detector rings. Images acquired (and reconstructed) for both modalities could be corrected for the amount of camera tilt by simple numeric algebra.

In all conceptual system proposals illustrated in Fig. 16.1, the PET and light detector blocks are mounted on a common gantry that is fully rotational around the imaging object's long axis, as well as translatable along the long axis. The rotational/translatable common gantry would allow for unconstrained arbitrary orbital positioning of the optical detector(s) and (not shown in the sketch) integrated network of optical fiber bundles which guide laser excitation light from an external multi-wavelength laser to the imaged object. For the cylindrical PET detector geometry the fibers could have their exit points at the cross sections of the detector block offsets at fixed spacing. Individual fibers can be activated arbitrarily, allowing for a

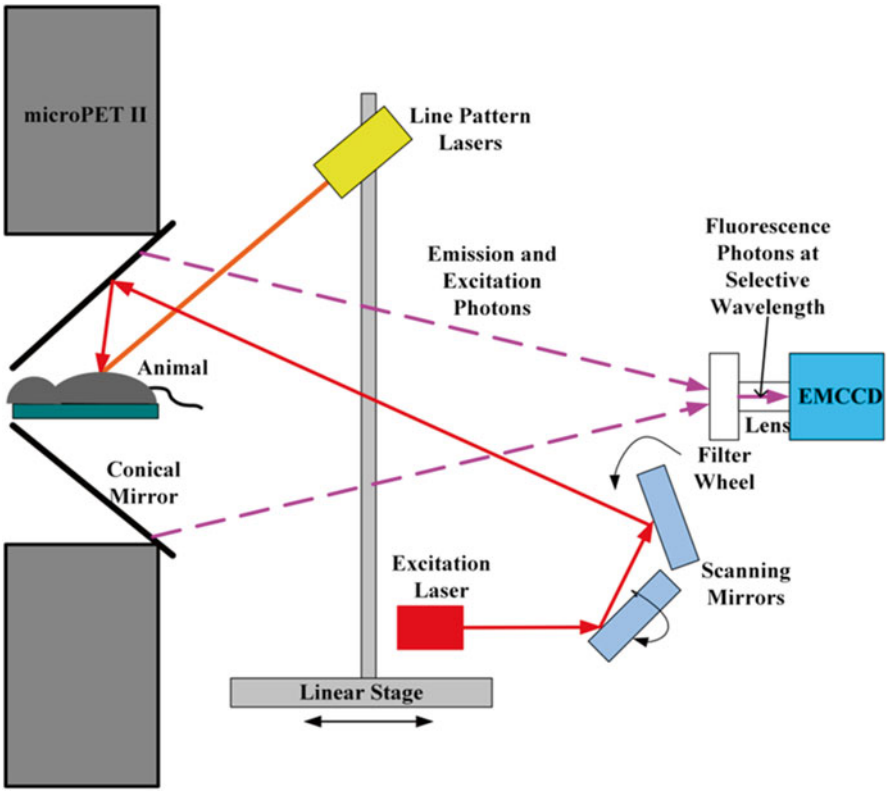

Fig. 16.2 Schematic of simultaneous PET and 3D fluorescence optical tomography (FOT) imaging system, where line pattern laser is used for the mouse surface extraction [71]

variety of laser excitation patterns. All these integrated imaging systems have been investigated in the author's laboratory at German Cancer Research Center. They all seem to represent valid concepts for dualmodal PET-OI. However, because various multimodal small animal imaging instruments were proposed and developed in that lab—among those the PET-OI instrument as described in Sect. 2.3—none of these concepts have been materialized.

Another dual-modal system for simultaneous PET and multispectral fluorescence optical imaging, illustrated in Fig. 16.2, has been proposed and constructed by Li and Cherry at the University of California, Davis. Intended for three dimensional fluorescence optical tomography (FOT), the authors employed a purposely manufactured truncated conical mirror allowing simultaneous viewing of the entire surface of the animal by an optical camera that is positioned outside of the field-of-view of the PET system.

The optical modality is laid out for multi-spectral emission data collection at ten wavelengths which is accomplished by a fast switching filter wheel. The conical mirror is made of aluminum and coated with silver and has an outside diameter

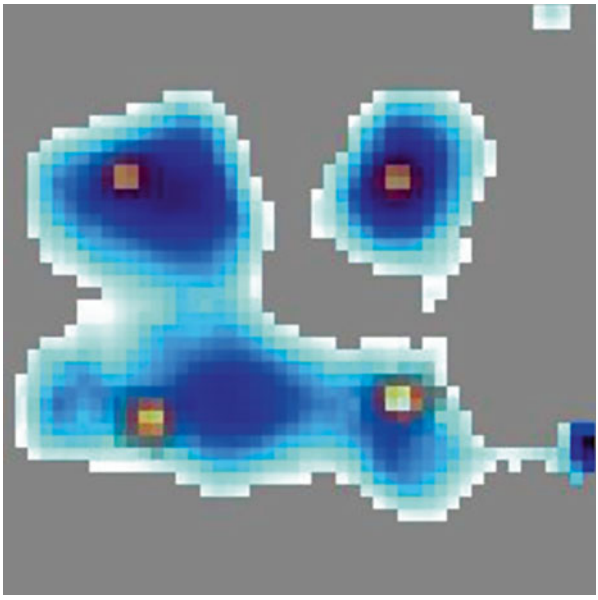

Fig. 16.3 Fused reconstructed PET (hot wire scale) and 3D fluorescence optical tomography (*white-blue scale*) images showing a transverse reconstructed section with four radioactive/fluorescent targets embedded in a cubic turbid medium [71]. PET and fluorescence data were acquired simultaneously

(155 mm) that is small enough to be inserted into the gantry of an existing microPET II scanner [70]. This conical mirror reflects light towards (for arbitrarily focused fluorochrome excitation) and away from the imaged object for simultaneous PET and 3D FOT imaging. With this conical mirror geometry, the CCD camera area is used more efficiently and more emission photons are detected compared with the use of multiple flat mirrors in a pyramidal configuration. Excitation beam positioning is achieved by an x–y mirror scanning system. Because the thickness of the conical mirror is 10 mm in the built prototype instrument a fraction of the annihilation photons is scattered and absorbed within it, causing a slight degradation in PET image quality. However, the thickness of the conical mirror might be reduced significantly, lowering its influence on the high energy photon flux. For FOT imaging, an array of specifically shaped neutral density filters, mounted on a linear stage, is used to increase the system measurement dynamic range. Both PET and FOT phantom experiments were performed, with a fused reconstructed PET and FOT image shown in Fig. 16.3, to evaluate the effects of the conical mirror on PET imaging, and PET effects on FOT imaging.

2.2 Detector Concept Based on Single-Sensor Design

At the UCLA Crump Institute for Molecular Imaging, a conceptual design for a dual-modal PET-BLI imaging instrument, called OPET, has been proposed and investigated [72–75]. This concept is very innovative in its own in that a single (modified) PET detector module is used to detect both the high-energy photons

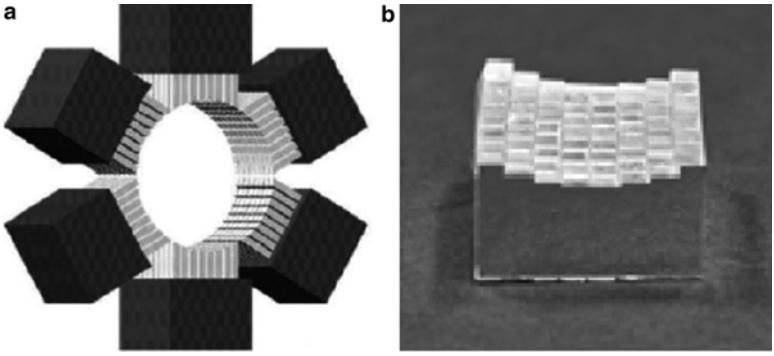

Fig. 16.4 (**a**) Illustration of an OPET detector ring showing individual detector modules [74]. Each module consists of a multichannel photomultiplier coupled to a specifically shaped scintillator array, (**b**), in which each crystal is optically isolated from the next

created by positron annihilation as well as the light as emitted from bioluminescence sources. The OPET system is illustrated in Fig. 16.4a.

The motivation of this concept is initiated by the fact that photomultiplier tubes (PMTs) do represent excellent light sensors. However, even in multichannel construction PMTs possess much less spatial resolution than CCD or CMOS photon sensors. The particular PMT used in the prototype assembly is an 8×8 multichannel photo multiplier tube with a multi-alkali photocathode for improved quantum efficiency in the red wavelength range. On the tube entrance window a specifically manufactured 8×8 array of optically isolated GSO crystal elements of 2×2 mm cross-section is attached. It is assembled in such way as to forming a conical shape side towards the imaged animal, as seen in Fig. 16.4b. This unusual crystal geometry is necessary because the crystal array serves also as light guide for the optical photons, in addition to its primary intended purpose as a scintillator for the interaction of the keV-photons. However, in optical mode the light guide operates only when the imaged object is brought in contact with the crystal elements because the elements themselves do not define an optically restrained field-of-view. In contrast to scintillators as used in dedicated PET imaging, the crystal has no light–tight seal towards the imaged space in order to accomplish its function as a light guide of optical photons from the imaged object to the PMT while detecting optical probe light. In PET mode, the detector operates as a normal gamma-ray detector block. It should be noted that selection of a proper scintillation material crucially effects both modalities. In addition to the requirements for high-energy photon detection while operating in PET mode, the crystal needs to be transparent also for the whole optical imaging spectrum, preferably also the NIRF range. Fortunately, a number of crystals suited for PET imaging such as GSO do have a fairly even transmission efficiency of about 70–75 % for a wavelengths above 600 nm up to NIRF range.

Initial measurement studies have demonstrated that the OPET design indeed sustains very good sensitivity for optical photons. However, as there are no optical elements such as collimating lenses used for the coupling of optical photons, the

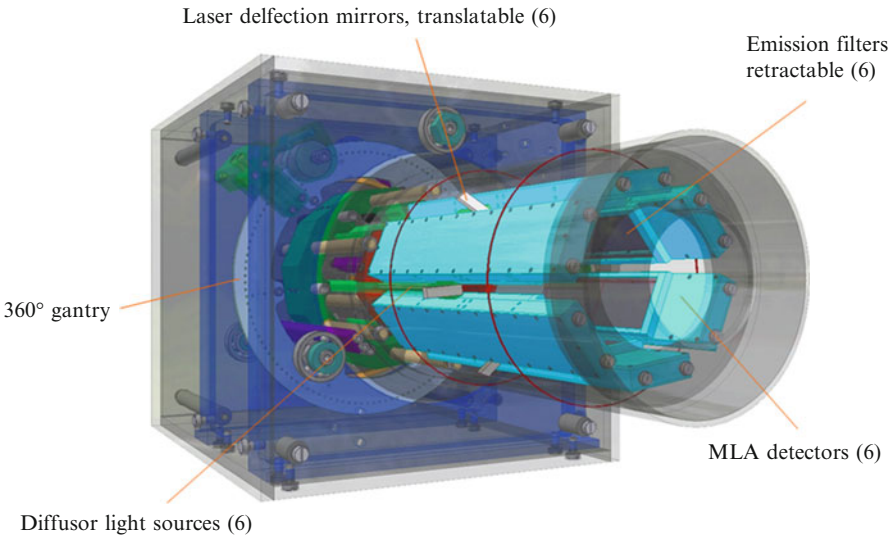

Fig. 16.5 Rendering of a microlens-based tomographic optical imaging assembly. The outer diameter of the cylindrical housing measures 125 mm. This part is being incorporated for multimodal imaging into the bore of an appropriate PET

optical field-of-view of individual optical detector channels cannot be separated well at a distance from the optical window. Thus, the imaged object needs to be in contact with the crystal around the entire perimeter, rendering its use in small animal imaging rather difficult.

2.3 Encapsulated Integration Concepts

A novel instrumentation concept for optical tomographic imaging, rendered in Fig. 16.5, is presented in [76, 77]. This optical imager is not only applicable for non-contact BLI and FMI/FMT but also for simultaneous multimodal PET-OI because the optical detector units have been designed to be very thin and rather translucent for high-energy photons. This optical tomopgraph consists of a hexagonal assembly of six microlens array based photon sensor detectors that completely enclose the imaged object circumferentially, forming an inner bore opening of 60 mm. The individual detector fields-of-view merge at a radius of 25 mm yielding complete, untruncated coverage of cylindrical objects equal or less than 50 mm in diameter (mice). The overall size of the assembly—in particular the cylindrical imaging enclosure with an outer diameter of 125 mm—is small enough for integration with secondary imaging modalities, here with PET. This allows for concurrent multimodal data acquisition at identical fields-of-view. Besides, the optical system carries a number of advantages such as complete object coverage with improved dynamic coverage as compared to mirror-based, single camera setups.

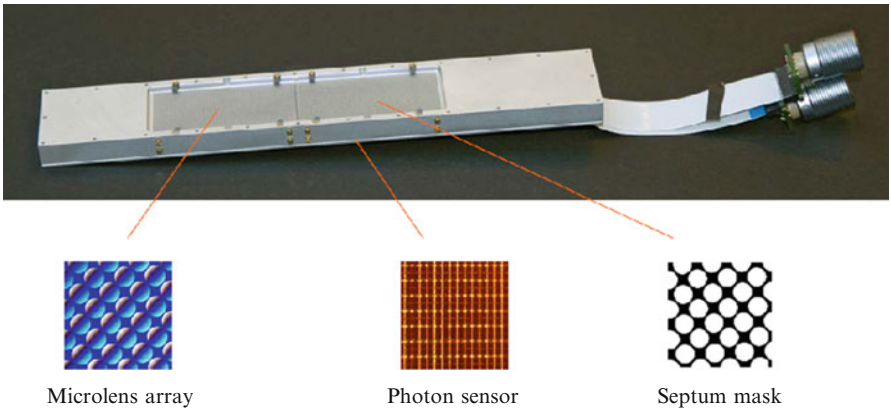

Fig. 16.6 MLA-based optical detector designed for whole-body mouse imaging (photographed before anodization)

A single optical detector unit of the tomographic imager illustarted in Fig. 16.5 is depicted in Fig. 16.6. To allow imaging of whole mice the active detector area has an effective area of 10 cm axially × 5 cm transaxially. A detector unit consists of four parts: a microlens array (MLA) intended for field-of-view (FOV) definition,[3] a large area complementary metal oxide semiconductor (CMOS) chip for light detection, a septum mask for cross-talk suppression, and an exchangeable filter for wavelength selection. The assembly of all parts allows for a very thin detector design yielding an effective complete detector thickness of less than 8.0 mm, including housing. The photon sensor is placed exactly at the focal plane of the MLA as determined by the uniform lens focal length. The gap between MLA and CMOS is filled out by the septum mask (400 μm hole diameter). Septum mask and the detector housing is cast from aluminum which causes a relatively low scatter und attenuation contribution for high-energy PET photons.

All detectors are mounted on a common rotatable gantry. Adjacent to each detector (Fig. 16.5) six laser diode generated light beams can be projected at any axial position towards the imaged object for fluorochrome excitation. Mechanically attached to the light beam assembly are retractable diffuser light fibers used for large area illumination. These sources are also deployed for extracting a set of reflectance images to be used for object surface reconstruction. Retractable filters can be moved in front of the detectors when fluorescence meditated imaging is performed. The imaged object is restrained inside a self-contained glass cylinder compartment of 45 mm in diameter that also provides mountings for ventilation and for miscellaneous monitoring equipment. Results of the application of this imager for a simple phantom experiment are shown in Fig. 16.7.

[3] An analogy for illustrating the purpose of the microlens array in this optical imaging application might be seen in the use of multi-hole collimators in high-energy detector physics such as in SPECT.

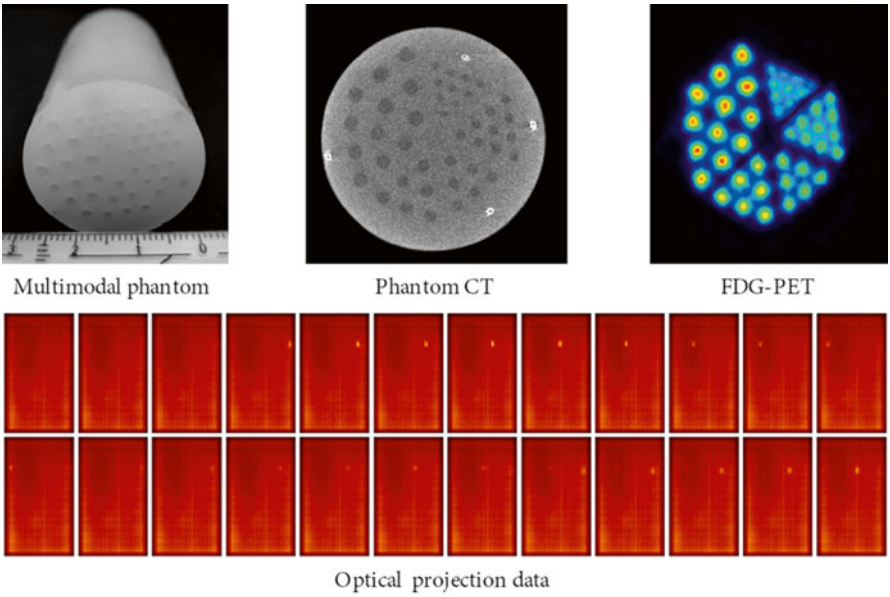

Fig. 16.7 Phantom setup and results of the PET-OI instrument as shown in Fig. 16.5. The CT was measured independently for illustrating the geometry of the Derenzo-type phantom, shown at *top left*. Aside from the fillable inclusions pattern the CT image also shows four small cylinder inclusions that, in fact, are light sources (tritium gas filled phosphor-coated cylinders emitting light at a maximum wavelength of 525 nm). PET (reconstructed image at *top right*) and optical imaging has been performed simultaneously inside a Siemens Inveon small animal PET. The phantom inclusions were filled with 12 MBq ^{18}F. All four light sources can be seen in the optical projection images (results from one detector at 24 angular gantry positions equally spaced around 360° are shown in the *lower two rows*, detector acquisition time was set to 6.7 s, data acquisition was performed at room temperature)

2.4 Summary and Outlook

Although the development of multimodality PET-optical imaging instruments is still in its infancy, significant progress has already been made towards the development of multimodality imaging probes. Recent advances in nanotechnology and imaging science have provided researchers with new tools for molecular imaging and it can be expected that nanotechnology-based multimodal probes will likely emerge and further drive the field of multimodal imaging.

Combining radioisotopes with optical probes has broadened the range of available molecular imaging applications and will continue to do so. With this advancement comes also an inherent potential to improve the performance and applicability of either imaging modality. In all studies reported, multimodal imaging was found very effective. As time goes on, a seamless transition from fluorescence/bioluminescence imaging in mice to nuclear imaging in patients might become a standard procedure.

This transition further facilitates the cross-comparison and cross-validation of the results obtained by these various modalities in vitro, in situ, and in vivo. Such study strategy is of foremost desire because it sheds light into investigating the effectiveness of individual molecular imaging modalities. In closing this section, the development of multimodality noninvasive imaging probes will enable investigators to choose the imaging technology most appropriate to the biological problem under investigation, not the other way around.

References

1. Herschman HR (2003) Molecular imaging: Looking at problems, seeing solutions. Science 302:605–608.
2. Contag CH, Spilman SD, Contag PR et al (1997) Visualizing gene expression in living mammals using a bioluminescent reporter. Photochemistry Photobiology 66:523–531.
3. Gambhir SS; Barrio JR, Wu L et al (1998) Imaging of adenoviral-directed herpes simplex virus type 1 thymidine kinase reporter gene expression in mice with radiolabeled ganciclovir. J. Nuclear Medicine 39:2003–2011.
4. Louie AY, Huber MM, Ahrens ET et al (2000) In vivo visualization of gene expression using magnetic resonance imaging. Nature Biotechnology 18:321–325.
5. Tjuvajev JG, Stockhammer G, Desai R et al (1995) Imaging the expression of transfected genes in-vivo. Cancer Research 55:6126–6132.
6. Mather S (2009) Molecular Imaging with Bioconjugates in Mouse Models of Cancer. Bioconjugate Chem. 20:631–643.
7. Blankenberg FG and Strauss HG (2002) Nuclear medicine applications in molecular imaging. J. Magnetic Resonance Imaging 16:352–361.
8. Blankenberg FG and Strauss HW (2007) Nuclear medicine applications in molecular imaging: 2007 update. Quarterly J. Nuclear Medicine Mol. Imaging 51:99–110.
9. Phelps ME (2000) Positron emission tomography provides molecular imaging of biological processes. Proc. National Acad. Sciences United States Am. 97:9226–9233.
10. Buursma AR, Rutgers V, Hospers GAP et al (2006) F–18-FEAU as a radiotracer for herpes simplex virus thymidine kinase gene expression: in-vitro comparison with other PET tracers. Nuclear Medicine Comm. 27:25–30.
11. Hospers GAP, Calogero A, van Waarde A et al (2000) Monitoring of herpes simplex virus thymidine kinase enzyme activity using positron emission tomography. Cancer Research 60:1488–1491.
12. Haberkorn U, Mier W and Eisenhut M (2005) Scintigraphic imaging of gene expression and gene transfer. Current Medicinal Chem. 12:779–794.
13. Haberkorn U, Oberdorfer F, Gebert J et al Monitoring gene therapy with cytosine deaminase: In vitro studies using tritiated–5-fluorocytosine. J. Nuclear Medicine 37:87–94.
14. Cornelio DB, Roesler R and Schwartsmann G (2003) Gastrin-releasing peptide receptor as a molecular target in experimental anticancer therapy. Annals Oncology 18:1457–1466.
15. Marka M, Semjeni M, Treszl A et al (2009) Expression of somatostatin receptor subtypes in human bladder carcinomas. Acta Physiologica Hungarica 96:100–101.
16. MacLaren DC, Gambhir SS, Cherry S et al (1998) Repetitive and non-invasive in vivo imaging of reporter gene expression using adenovirus delivered dopamine D2 receptor as a PET reporter gene and FESP as a PET reporter probe. J. Nuclear Medicine 39:130.
17. Shiba K, Torashima T, Hirai H et al (2009) Potential usefulness of D2R reporter gene imaging by IBF as gene therapy monitoring for cerebellar neurodegenerative diseases. J. Cerebral Blood Flow Metabolism 29:434 – 440.

18. Cao HST, Reynoso J, Yang M et al (2009) Development of the Transgenic Cyan Fluorescent Protein (CFP)-Expressing Nude Mouse for Technicolor Cancer Imaging. J. Cellular Biochem. 107:328–334.
19. Shimomura O (1998) The discovery of green fluorescent protein. Green Fluorescent Protein: Properties, Applications, Protocols :3–15.
20. Contag PR, Olomu IN, Stevenson DK et al (1998) Bioluminescent indicators in living mammals. Nature Medicine 4:245–247.
21. Zabala M, Alzuguren P, Benavides C et al (2009) Evaluation of bioluminescent imaging for noninvasive monitoring of colorectal cancer progression in the liver and its response to immunogene therapy. Mol. Cancer 8:2.
22. Jaffer FA, Kim DE, Quinti L et al (2007) Optical visualization of cathepsin K activity in atherosclerosis with a novel, protease-activatable fluorescence sensor. Circulation 115:2292–2298.
23. Tung CH, Bredow S, Mahmood U et al (1999) Preparation of a cathepsin D sensitive near-infrared fluorescence probe for imaging. Bioconjugate Chem. 10:892–896.
24. Lee S and Chen XY (2009) Dual-Modality Probes for In Vivo Molecular Imaging. Mol. Imaging 8:87–100.
25. Frullano L and Meade TJ (2007) Multimodal MRI contrast agents. J. Biological Inorg. Chem. 12:939–949.
26. Park JM and Gambhir SS (2005) Multimodality radionuclide, fluorescence, and bioluminescence small-animal imaging. Proc. IEEE 93:771–783.
27. Ray P, Wu AM and Gambhir SS (2003) Optical bioluminescence and positron emission tomography imaging of a novel fusion reporter gene in tumor xenografts of living mice. Cancer Research 63:1160–1165.
28. Dubey P, Su H, Adonai N et al (2003) Quantitative imaging of the T cell antitumor response by positron-emission tomography. Proc. National Acad. Sciences United States Am. 100:1232–1237.
29. De A, Lewis XZ and Gambhir SS (2003) Noninvasive imaging of lentiviral-mediated reporter gene expression in living mice. Mol. Therapy 7:681–691.
30. Iyer M, Berenji M, Templeton NS et al (2002) Noninvasive imaging of cationic lipid-mediated delivery of optical and PET reporter genes in living mice. Mol. Therapy 6:555–562.
31. Lin MM, Kim DK, El Haj AJ et al (2008) Development of Superparamagnetic Iron Oxide Nanoparticles (SPIONS) for Translation to Clinical Applications. IEEE Transactions On Nanobioscience 7:298–305.
32. Ottobrini L, Ciana P, Moresco R et al (2008) Development of a bicistronic vector for multimodality imaging of estrogen receptor activity in a breast cancer model: preliminary application. European J. Nuclear Medicine Mol. Imaging 35:365–378.
33. Brader P, Stritzker J, Riedl CC et al (2008) Escherichia coli Nissle 1917 facilitates tumor detection by positron emission tomography and optical imaging. Clinical Cancer Research 14:2295–2302.
34. Massoud TF and Gambhir SS (2003) Molecular imaging in living subjects: seeing fundamental biological processes in a new light. Genes & Development 17:545–580.
35. Ponomarev V, Doubrovin M, Serganova I et al (2003) A novel triple modality reporter gene for whole body fluorescent, bioluminescent and nuclear non-invasive imaging. J. Nuclear Medicine 44:150.
36. Ray P, De A, Min JJ et al (2004) Imaging tri-fusion multimodality reporter gene expression in living subjects. Cancer Research 64:1323–1330.
37. Ray P, Tsien R and Gambhir SS (2007) Construction and validation of improved triple fusion reporter gene vectors for molecular imaging of living subjects. Cancer Research 67:3085–3093.
38. Ray P, De A, Patel M et al (2008) Monitoring caspase–3 activation with a multimodality Imaging sensor in living subjects. Clinical Cancer Research 14:5801–5809.
39. Ponomarev V, Doubrovin M and Serganova I et al (2004) A novel triple-modality reporter gene for whole-body fluorescent, bioluminescent, and nuclear noninvasive imaging. European J. Nuclear Medicine Mol. Imaging 31:740–751.

40. Edwards WB, Xu B, Akers W et al (2008) Agonist–antagonist dilemma in molecular imaging: Evaluation of a monomolecular multimodal imaging agent for the somatostatin receptor. Bioconjugate Chem. 19:192–200.
41. Backer MV, Levashova Z, Patel V et al (2007) Molecular imaging of VEGF receptors in angiogenic vasculature with single-chain VEGF-based probes. Nature Medicine 13:504 –509.
42. Hostetler KY and Matsuzawa Y (1981) Studies on the mechanism of drug-induced lipidosis – cationic amphiphilic drug-inhibition of lysosomal phospholipases-a and phospholipases-c. Biochemical Pharmacology 30:1121–1126.
43. Medintz IL, Uyeda HT, Goldman ER et al (2005) Quantum dot bioconjugates for imaging, labelling and sensing. Nature Materials 4:435– 446.
44. Michalet X, Pinaud FF; Bentolila LA et al (2005) Quantum dots for live cells, in vivo imaging, and diagnostics. Science 307:538–544.
45. Chen K, Li ZB, Wang H et al (2008) Dual-modality optical and positron emission tomography imaging of vascular endothelial growth factor receptor on tumor vasculature using quantum dots. European J. Nuclear Medicine Mol. Imaging 35:2235–2244.
46. Cai WB and Chen XY (2007) Nanoplatforms for targeted molecular imaging in living subjects. Small, 3:1840–1854.
47. Bangerth W and Joshi A (2008) Adaptive finite element methods for the solution of inverse problems in optical tomography. Inverse Problems 24:034011.
48. Gibson A and Dehghani H (2009) Diffuse optical imaging. Philosophical Transactions Royal Soc. A-mathematical Phys. Engineering Sciences 367:3055–3072.
49. Hu G, Yao JJ and Bai J (2008) Full-angle optical imaging of near-infrared fluorescent probes implanted in small animals. Progress In Natural Science 18:707–711.
50. Kumar ATN, Raymond SB, Bacskai BJ et al (2008) Comparison of frequency-domain and time-domain fluorescence lifetime tomography. Optics Lett. 33:470– 472.
51. Wang DF, Liu X, Chen YP et al (2009) A Novel Finite-Element-Based Algorithm for Fluorescence Molecular Tomography of Heterogeneous Media. IEEE Transactions on Information Technology In Biomedicine 13:766–773.
52. Barret O, Carpenter TA, Clark JC et al (2005) Monte Carlo simulation and scatter correction of the GE Advance PET scanner with SimSET and Geant4. Phys. In Medicine Biol. 50: 4823– 4840.
53. Buvat I and Castiglion I (2007) Monte Carlo simulations in SPET and PET. Quarterly J. Nuclear Medicine 46:48–61.
54. Reaside D (1976) Monte Carlo principles and applications. Phys. In Medicine Biol. 21: 181–197.
55. Zaidi H (1999) Relevance of accurate Monte Carlo modeling in nuclear medical imaging. Medical Physics 26:574 –608.
56. Boas DA, Culver JP, Stott JJ and Dunn AK (2002) Three dimensional Monte Carlo code for photon migration through complex heterogeneous media including the adult human head. Optics Express 10:159–170.
57. Dehghani H, Srinivasan S, Pogue BW et al (2009) Numerical modelling and image reconstruction in diffuse optical tomography. Philosophical Transactions Royal Soc. A-mathematical Phys. Engineering Sciences 367:3073–3093.
58. Gardner CM and Welch AJ (1994) Monte-carlo simulation of light transport in tissue – unscattered absorption events. Appl. Optics 33:2743–2745.
59. Jagajothi G and Raghavan S (2007) Estimation of optical properties in biological tissues using Monte Carlo simulation. J. Mechanics in Medicine Biol. 7:449– 462.
60. Prahl SA, Fischer DG and Duncan DD (2009) Monte Carlo Green‹s function formalism for the propagation of partially coherent light. J. Opt. Soc. Am. A-Optics Image Science Vision 26:1533–1543.
61. Swartling J, Pifferi A, Enejder AMK et al (2003) Accelerated Monte Carlo models to simulate fluorescence spectra from layered tissues. J. Opt. Soc. Am. A-optics Image Science Vision 20: 714 –727.

62. Tian HJ, Liu Y, Wang LJ et al (2009) Hybrid diffusion approximation in highly absorbing media and its effects of source approximation. Chinese Optics Lett. 7:515–518.
63. Wang LH, Jacques SL and Zheng LQ (1995) MCML – Monte-Carlo modeling of light transport in multilayered tissues. Computer Methods Programs in Biomedicine 47:131–146.
64. Peter J and Semmler W (2007) vECTlab – A Fully Integrated Multi-Modality Monte Carlo Simulation Framework for the Radiological Imaging Sciences. Nuclear Instruments & Methods in Physics Research A 580:955–959.
65. Alexandrakis G, Rannou FR and Chatziioannou AF (2006) Effect of optical property estimation accuracy on tomographic bioluminescence imaging: simulation of a combined optical-PET (OPET) system. Phys. In Medicine Biol. 51:2045–2053.
66. Alexandrakis G, Rannou FR and Chatziioannou AF (2005) Tomographic bioluminescence imaging by use of a combined optical-PET (OPET) system: a computer simulation feasibility study. Phys. In Medicine Biol. 50:4225– 4241.
67. Rannou FR, Kohli V, Prout DL et al (2004) Investigation of OPET performance using GATE, a Geant4-based simulation software. IEEE Transactions On Nuclear Science 51:2713–2717.
68. Khodaverdi M, Nicol S, Loess J et al (2007) Design study for the ClearPET/ XPAD small animal PET/ CT scanner. Proceedings of the Nuclear Science Symposium Conference 4300– 4302.
69. Peter J, Unholtz D and Schulz R et al (2007) Development and Initial Results of a Tomographic Dual-Modality Positron/ Optical Small Animal Imager. IEEE Transactions On Nuclear Science 54:1553–1560.
70. Tai YC, Chatziioannou AF, Yang YF et al (2003) MicroPET II: design, development and initial performance of an improved microPET scanner for small-animal imaging. Phys. In Medicine Biol. 48:1519–1537.
71. Li C, Wang G, Qi J, Cherry SR (2009) Three-dimensional fluorescence optical tomography in small-animal imaging using simultaneous positron-emission-tomography priors. Optics Letters 34:2933–2935.
72. Prout DL, Silverman RW and Chatziioannou A (2004) Detector concept for OPET – A combined PET and optical Imaging system. IEEE Transactions On Nuclear Science 51:752–756.
73. Prout DL, Silverman RW and Chatziioannou A (2005) Readout of the optical PET (OPET) detector. IEEE Transactions on Nuclear Science 52:28–32.
74. Vu NT, Silverman RW and Chatziioannou AF (2006) Preliminary performance of optical PET (OPET) detectors for the detection of visible light photons. Nuclear Instruments & Methods In Phys. Research Section A-accelerators Spectrometers Detectors Associated Equipment 569:563–566.
75. Douraghy A, Rannou FR, Silverman RW et al (2008) FPGA Electronics for OPET: A Dual-Modality Optical and Positron Emission Tomograph. IEEE Transactions On Nuclear Science 55:2541–2545.
76. Unholtz D, Semmler W, Dössel W et al Image Formation with a Microlens-Based Optical Detector: a 3D Mapping Approach. Journal of Applied Optics 48:D273–D279.
77. Peter J, Schulz R and Semmler W (2005) Micro Lens Array Based Optical Detector Design for in Vivo Tomographic Imaging of Small Animals. Molecular Imaging 4: 373.

Chapter 17
Quantification of Small-Animal Imaging Data

Habib Zaidi

1 Introduction

The field of molecular imaging finds its roots in nuclear medicine, which since its inception had a major focus on task-based optimization of image quality, and on in vivo quantitative assessment of metabolic and physiological parameters [1]. This standpoint reflects the limited spatial resolution and high noise characteristics of SPECT and PET compared to high resolution structural imaging modalities (CT and MRI), which provide exquisite anatomical details. The disparities between performance characteristics of currently available scanners and their potential degradation with time can be delicate and tricky to put into evidence through qualitative visual interpretation. This has motivated the development of objective and reproducible metrics to observe and adjust changes in system performance, for intercomparison studies as well as for quality assurance and quality control tasks. The use of molecular imaging in the assessment of metabolic and physiological parameters linked to specific diseases further motivated quantitative molecular imaging.

The quantitative potential of molecular imaging made it possible to measure in vivo different physiological parameters including but not limited to organ function, tissue perfusion, tracer biodistribution and kinetics, and many other physiological parameters that necessitate accurate quantification. Quantitative analysis provides a direct link between the time-varying activity concentration in organs/tissues and relevant quantitative parameters representing biological processes taking place in the same organs/tissues [2].

The rate of specific tracer uptake in a tissue, organ or organ system depends on many aspects including its rate of delivery, local biochemical reactions, physical half-life and biological clearance. Quantitative molecular imaging using SPECT/

H. Zaidi (✉)
Department of Radiology & Medical Informatics, Geneva University Hospital, Geneva, Switzerland
e-mail: habib.zaidi@hcuge.ch

H. Zaidi (ed.), *Molecular Imaging of Small Animals: Instrumentation and Applications*,
DOI 10.1007/978-1-4939-0894-3_17,

PET considers all these factors to noninvasively provide a numerical estimate of discrete physiological characteristics of tissues or organs. Various physiological processes can be quantified from such measures, for example the rate at which the brain or a tumor is metabolizing glucose, referred to as metabolic rate for glucose (MRGlc), usually expressed in micromoles of glucose/100 g of tissue/min. These measures can then be correlated to clinical outcomes such as tumor evolution or response to therapy in such a way to relate disease physiology to its progression. These quantitative estimates can also serve as early surrogate endpoints in preclinical therapy trials.

Recent advances in dedicated small-animal imaging instrumentation enabled to contribute unique information in biomedical research [3]. Basic research laboratories focusing on molecular imaging-based preclinical research demand multiple competences, resources and trained personnel far beyond what is required to run clinical facilities. These laboratories usually consist of multidisciplinary teams working in close collaboration to solve basic research questions through quantitative regional estimation of physiologic or pharmacokinetic parameters from dynamic radiotracer studies.

To take full advantage of the quantitative capabilities of PET imaging, subject-specific correction of background and physical degrading factors must be performed [4]. While most of these corrections are performed in clinical imaging using sophisticated computational models, compensation for these effects is hardly considered in preclinical imaging where much attention has focused on physical performance of SPECT/PET scanners, namely the spatial resolution and sensitivity (see Chaps. 4 and 5) and animal preparation (see Chap. 18). The major challenges to quantitative preclinical PET imaging when the target is to quantify physiological or pharmacokinetic processes can be categorized in five classes [5]:

- Instrumentation and measurement factors: factors related to imaging system performance and data acquisition protocols;
- Physical factors: those related to the physics of photon interaction with biologic tissues;
- Reconstruction factors: issues related to assumptions made by image reconstruction algorithms;
- Physiological factors: factors related to motion and other physiological issues;
- Tracer kinetic factors: issues related to difficulties in developing and applying tracer kinetic models, especially at the voxel level (parametric imaging).

The above referenced issues (except instrumentation factors which are addressed in Chaps. 4 and 5 of this volume) are discussed at some level of detail in the following sections.

2 Advances in Image Reconstruction Strategies

The basic principle of image reconstruction is that an object can be accurately reproduced from a set of its projections taken at different angles by an inversion procedure. The analytic solution to this inverse problem has been known for about one century thanks to the pioneering work of the Austrian mathematician J. Radon.

In essence, two major classes of image reconstruction algorithms have emerged in PET: direct analytical methods and iterative methods. Until about two decades ago, the most widely used methods for image reconstruction in PET were direct analytical techniques because they are relatively quick and their derivation straightforward. However, the resulting image quality is limited by the over simplified line-integral model of the acquired projection data. Alternatively, iterative reconstruction techniques are computationally much more intensive but the resulting images demonstrate improvements (principally arising from more accurate statistical modeling of the system response) which have enabled them to replace analytic techniques not only in research settings but also in the clinic [6].

Time-dependent reconstruction can be handled either by considering series of independent 'static' reconstructions [7] or direct time-dependent 4D reconstructions [8]. The former remains the common approach to dynamic PET image reconstruction consisting of independent reconstruction of tomographic data within each dynamic frame. Following this step, one arrives at a set of dynamic images intended to specify the variation of activity over time throughout the reconstructed field-of-view (FOV). This is still the *de facto* standard approach applied in routine clinical and preclinical studies. As opposed to static imaging, dynamic PET reconstruction can provide additional very useful information, depending on the particular tracer and study design.

The foundations of image reconstruction are covered in detail in recent reviews [6, 7, 9] and textbooks [1, 10] that offer comprehensive coverage of image reconstruction techniques including appropriate representation of the object, measured data and the mathematical derivation of algorithms. There is also increasing interest in the use of advanced 4D image reconstruction strategies for research applications [8]. Therefore, this section only briefly summarizes novel developments in PET reconstruction algorithms, with particular emphasis on statistical iterative reconstruction techniques given their popularity, promise and wide adoption by the medical imaging community. Future directions for PET image reconstruction are also considered, addressing mainly the issues of improving the modeling of the data acquisition process and task-specific determination of the parameters to be estimated in image reconstruction [7].

2.1 Analytic Reconstruction Techniques

The inverse problem in the context of analytic reconstruction is expressed in a continuous framework with the algorithmic realization implemented as a discrete approximation of the continuous solution. Following the notation used in [7], let us recall that direct analytic inversion procedures in emission tomography assume that a 2D parallel projection representing a set of lines of response (LORs), $p\left(\mathbf{s},\hat{\mathbf{u}}\right)$, is equivalent to a set of line integrals through the radioatracer distribution $f(\mathbf{r})$ (the 3D X-ray transform) [11]:

$$p\left(\mathbf{s},\hat{\mathbf{u}}\right) = \int_{-\infty}^{+\infty} f\left(\mathbf{s} + x'\hat{\mathbf{u}}\right) dx' \tag{17.1}$$

where the 3D vector **r** in the imaging volume is decomposed into the 2D parallel projection position vector $\mathbf{s} = [y' \; z']^T$ and the 1D orientation unit vector $x'\hat{\mathbf{u}}$. This line-integral equation represents lines through the FOV, where each detector-pair is regarded as an LOR i (specified by a displacement **s** from the centre of the FOV and an orientation $\hat{\mathbf{u}} = (\varphi, \theta)$ and with the vector **q** replaced by the continuous function p.

The derivation of the image f given the projection data p is carried out through the inversion of equation (1) using the *central section theorem* [7, 12]. This theorem states that a central plane of the 3D Fourier transform $F(\mathbf{k})$ of the 3D image $f(\mathbf{r})$ is equal to the 2D Fourier transform $P(\mathbf{k})$ of the 2D parallel projection data at the same orientation $\hat{\mathbf{u}} = (\varphi, \theta)$. The equivalent in the 2D (slice-by-slice) image reconstruction case is that the 1D Fourier transform of a 1D parallel projection being equal to a single line through the 2D Fourier transform of f. One can observe that the superposition of these 1D Fourier transforms (one from each projection angle) creates the 2D Fourier transform of f. However, a $1/|r|$ weighting of the contributions to the 2D Fourier transform will result from this superposition. In other terms, the ramp filter defined as the inverse of this weighting, i.e. $|r|$ in frequency space is used to balance the irregular contributions. Filtering the projection using the convolution operator followed by backprojection is often used as an alternative to image reconstruction in Fourier space. As such, the tracer distribution f is reconstructed from the acquired projection data p in two steps: (1) *filtering* in which the projections are filtered by the ramp filter $|r|$, and (2) *backprojection* in which the intensity of each pixel is calculated from the contribution of the filtered projections.

A number of analytical reconstruction techniques were suggested in the literature, including simple backprojection, which produces a blurred version of the object to be reconstructed [13], backprojection followed by filtering (BPF) [14] and filtered backprojection (FBP)/convolution backprojection (CBP). In the context of 3D PET imaging, the 3D reprojection method (referred to as 3DRP) emerged as the most popular approach and has been commonly used in practice since its inception [15]. Given the considerable computational resources required by 3D reconstruction, various approximate techniques have been proposed to rebin the data from the oblique projections into 2D direct sinogram data sets to enable the application of 2D reconstruction techniques, thus decreasing the computation time. Fourier rebinning (FORE), in which oblique rays are binned to a transaxial slice using the frequency-distance relationship of the data in Fourier space [16], emerged as the most promising technique.

As mentioned earlier, despite the advantages of analytic reconstruction techniques (quick, simple, easy to implement…), their drawbacks (noise, streak artifacts, interference between regions of low and high tracer concentration…) motivated their replacement by iterative techniques both in clinical and research setting. Considering current state-of-the-art and recent progress in statistical reconstruction techniques, interest in analytic reconstruction approaches has substantially declined and, as such, this category of techniques will not be discussed further in this chapter.

2.2 Iterative Reconstruction Strategies

The main limitation of analytic reconstruction techniques discussed above is their reliance on the line-integral model [Eq. (17.1)], assuming that the measured projection data are perfectly consistent with the tracer distribution, a prerequisite that is certainly not materialized in practice owing to the presence of noise and considering the impact of other physical degrading factors [7]. The advantage of iterative techniques is their ability to not only accommodate more complex models of the PET data acquisition process in a realistic way, but they also enable to employ non-orthogonal basis functions. Iterative methods are frequently used to solve problems involving optimization. The image reconstruction problem can be regarded as a special situation where the aim is to determine the 'best' approximation of the tracer distribution given a set of measured projection data.

Iterative reconstruction strategies have been around since the early days of tomographic imaging but emerged as prominent techniques and potential replacements for analytic techniques following the introduction of statistical reconstruction approaches more than three decades ago [17]. The three major issues that delayed the widespread adoption of iterative reconstruction techniques in the clinic, namely the large memory requirements owing to the size of the transition matrix, the additional computational complexity compared to single-pass analytic techniques and the lack of a well defined stopping criterion that can be used to objectively choose the number of iterations in a given scenario, are no longer a matter of concern at the present time given recent advances in computer technology. Still the latter criteria remains a hot research topic which is attracting the interest of active research groups since excess numbers of iterations can lead to an unacceptable noise level in the reconstructed images if it is not appropriately controlled [18]. In practice, a preset number of iterations is commonly used and, as such, iterative algorithms are not run into convergence.

Similar to analytic techniques, iterative algorithms make use of a backprojection operator to estimate the tracer distribution from the projection data. However, contrary to analytic methods, they also include a forward projection operator which is used to compute the projection data corresponding to a given tracer distribution and attenuation map. The projection/backprojection operators are applied multiple times by iterative algorithms depending on the selected number of iterations and, as such, their algorithmic implementation in terms of accuracy and computational efficiency is crucial to achieve the best possible performance.

An iterative reconstruction technique consists of two basic components: (1) the parameters to estimate (a set of voxel intensities representing the tracer distribution) and, (2) the system model describing the relationship between the tracer distribution and the mean of the measured projection data. It should be emphasized that it is the mean of the measured projection data which is usually modeled. Iterative algorithms provide the flexibility required to appropriately model and parameterize this mean. Generally, the system model, mapping from the parameters to the mean, is time-invariant [7].

Several iterative reconstruction strategies have been devised with the expectation maximization (EM) algorithm applied in PET as an iterative method to compute maximum likelihood (ML) estimates of the tracer distribution, being the most popular approach [17]. This approach assumes that the measured projection data consist of samples from a set of random variables whose probability density functions are linked to the actual tracer distribution according to a mathematical model of the data acquisition process.

The EM algorithm entails two different steps [19]: (1) computation of current projection data from the tracer distribution estimated at the preceding iteration using the forward projection operator according to a predefined system matrix (a_{ij}), starting from an initial guess (usually a uniform cylinder) at the first iteration, (2) the present estimate f_j^{new} is updated by multiplying the preceding estimate f_j^{old} by the backprojection of the ratio of measured (p_i) over the estimated projections in such a way to maximise the likelihood. The ensuing ML-EM equation is therefore given by:

$$f_j^{new} = \frac{f_j^{old}}{\sum_l a_{lj}} \sum_i a_{ij} \frac{p_i}{\sum_k a_{ik} f_k^{old}} \tag{17.2}$$

Based on an ordered sets approach, an accelerated version of the EM algorithm referred to as the Ordered Subsets EM (OSEM) algorithm was proposed in 1994 [20]. This algorithm handles the projection data in subsets (blocks) within each iteration so as to speed up convergence by a factor proportional to the number of subsets. Many studies reported that OSEM generates images of comparable quality to those generated by the EM technique in a fraction of the processing time.

Traditionally, PET images were reconstructed using analytic techniques (FBP) following correction for the various physical degrading factors (attenuation, scatter, randoms, etc.). An appealing feature and attractive asset of iterative techniques is that the physical model of the data acquisition process and scanner geometry can be incorporated into the reconstruction algorithm through the use of weights or penalties. Statistical reconstruction methods often incorporate corrections for photon attenuation and degradation of spatial resolution (resolution recovery). Additional constraints and penalty functions can also be incorporated to reduce statistical noise or to ensure that the image has other desirable properties, thus allowing the algorithm to be tuned to meet the requirements of specific clinical protocols (task-specific). There is extensive literature demonstrating substantial improvement of image quality and quantitative accuracy of PET images when using iterative reconstruction techniques especially when applied to low count projection data (poor statistics) typically encountered in oncologic or other similar studies. Figure 17.1 compares an ^{18}F-NaF skeletal rat PET study reconstructed using analytic (3DRP) and iterative (ML-EM) reconstructions. Note the significant improvement in image quality and spatial resolution when using iterative reconstruction. Clinical and preclinical scanner manufacturers have gradually improved their reconstruction software by incorporating correction for photon attenuation, scatter, random events, spatial resolution degradation and other factors by modeling these effects into iterative reconstruction algorithms. This trend is expected to keep on into the future and traditional analytic algorithms will become obsolete.

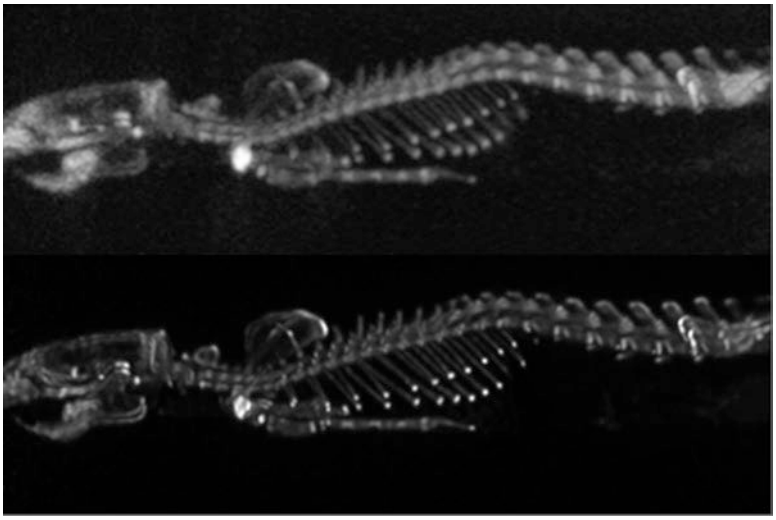

Fig. 17.1 Comparison of maximum intensity projections of an ^{18}F-NaF skeletal rat scan generated using analytic (3DRP) reconstruction (*top*) and iterative list-mode EM reconstruction (*bottom*). The iterative EM method benefits from improved modeling of the acquired PET data which significantly improves image quality and spatial resolution. Reprinted with permission from [7]

One of the main issues faced by iterative algorithms is the ill-conditioning of the inverse problem in PET image reconstruction. Regularization is often employed to counterbalance this through the use of appropriate techniques including post-reconstruction smoothing, early termination of the iterative process or Bayesian priors which are used to modify the ML objective to a *maximum a posteriori* (MAP) objective) [7].

If there is no a priori knowledge about the tracer distribution, maximising the likelihood is equivalent to maximising the posterior. However, some a priori knowledge is always available, i.e. the reconstructed image should not be too noisy [19]. A prior distribution favouring smooth solutions can be defined through a Markov random field or a Gibbs random field [21]. The probability of a voxel in a Markov random field depends on the intensities of voxels in the neighbourhood of that particular voxel according to a Gibbs distribution. This category of techniques has been successfully used in small-animal PET imaging and implemented on some commercial scanners [22]. Anatomical information derived from MRI has also been used to tune the noise suppressing prior in MAP-type algorithms by limiting smoothing to within organ boundaries revealed by the anatomical data [23, 24]. If the limited spatial resolution of the PET scanner is modelled, then this category of algorithms can produce a strong resolution recovery near anatomical boundaries.

Resolution recovery image reconstruction has received considerable attention during the last decade [25]. These techniques have been reported to improve both the noise properties and spatial resolution of the reconstructed images, potentially resulting in more accurate quantification. This is achieved by more accurate modeling of the relationship between the image and projection data within the system matrix.

These techniques can be implemented either in image or projection space based on accurate characterization of the spatially invariant or variant scanner-specific point spread function (PSF). The system matrix, usually combining various physics and instrumentation related factors, such as scanner geometry, positron range, parallax error, intercrystal scatter, and non-colinearity of annihilation photons, can be estimated using analytic calculations [26], Monte Carlo modeling [27] or experimental measurements [28–31]. The latter proved to be the favorite approach for deriving the spatially variant PSFs through accurate measurements of the spatial resolution characteristics of the PET scanner. For this purpose, a point source is commonly used to sample and parametrize the spatially varying PSF at different positions in the transaxial/axial FOV. Such algorithms have been recently implemented on clinical PET scanners and have proved to be useful for small-animal imaging [32].

Recent advances in the field focus on task-specific image reconstruction by incorporating the targeted objective within the reconstruction process, thus enabling to better suit the predefined task. This could be either the generation of high quality images with better spatial resolution and noise properties (usually required in clinical diagnostic imaging), or direct estimation of kinetic parameters of interest (usually needed in preclinical research involving small-animal studies). Estimating the metabolic rate of glucose from [^{18}F]-FDG PET scans instead of dynamic images of the time course of [^{18}F]-FDG concentration in tissue is one such example. PET images usually contain very complex noise distributions that need to be modeled for accurate tracer kinetic modeling. Strategies for direct estimation of kinetic parameters from the dynamic data set can simplify this task since such methods make use of the measured data, which are known to follow the simple independent Poisson distribution [8]. This concept was used in the framework of the EM algorithm to estimate kinetic parameters by maximizing the Poisson log-likelihood of obtaining the measured dynamic data [33]. Such approaches have been further extended and revisited by various groups and are described more in detail in the above referenced review [8].

3 Scatter Modeling and Correction

With the introduction of commercial preclinical PET scanners, small-animal imaging is becoming readily accessible and increasingly popular. The choice of a particular system being dictated in most cases by technical specifications, special attention has to be paid to methodologies followed when characterizing system performance. Since different methods can be used to assess the scatter fraction, differences may be methodological rather than reflecting any relevant difference in the performance of the scanner. Standardization of the assessment of performance characteristics is thus highly desired [34].

Little has been published on modeling the scatter component in small-animal PET scanners owing to the relatively small scatter fraction when imaging rodents (compared to clinical imaging). The origin of scatter for small-animal imaging has not been well characterized, but, has been proposed to stem mainly from the gantry

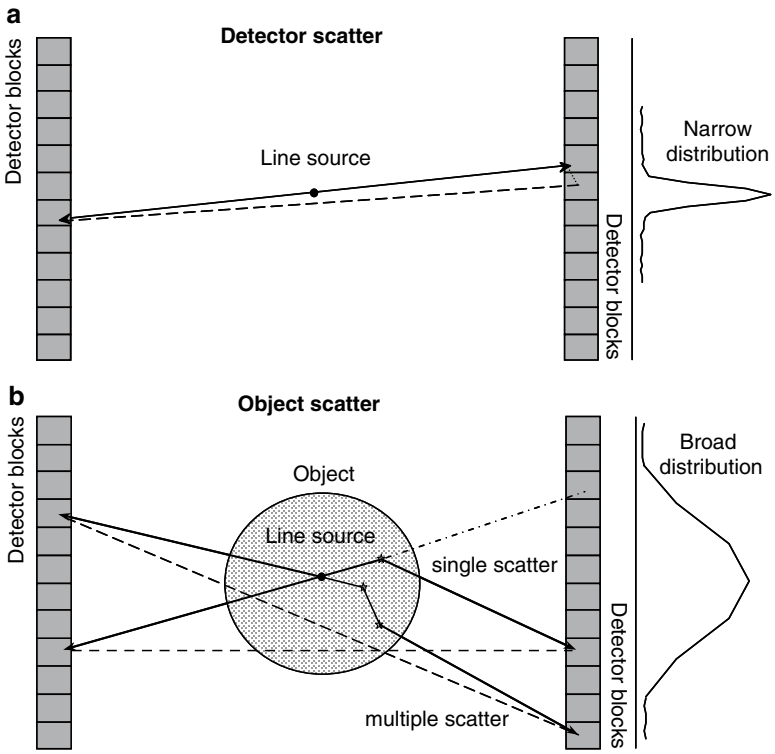

Fig. 17.2 (**a**) Schematic diagram of the origin and shape of detector scatter component for a cylindrical multi-ring PET scanner geometry estimated from a measurement in air using a line source. (**b**) Schematic diagram of the origin and shape of object scatter component estimated from measurements in a cylindrical phantom using a centred line source. Both single and multiple scatter are illustrated

and environment rather than the animal itself [35]. This point of view is supported by the fact that scatter correction usually does not involve correcting for scatter in the detector itself. Figure 17.2 illustrates the difference in terms of origin and shape between object and detector scatter components.

The scatter component for a prototype PET scanner based on avalanche photodiode (APD) readout of two layers of lutetium oxyorthosilicate (LSO) crystals with depth of interaction information, called the Munich-Avalanche-Diode-PET (MADPET), was assessed using Monte Carlo calculations [36]. In a more advanced version of this prototype (MADPET-II), the scatter fraction in a mouse-like cylindrical phantom (6 cm diameter, 7 cm height) containing a spherical source (diameter 5 mm) placed at its center was 16.2 % when the cylinder is cold and increased to 37.7 % when the cylinder is radioactive for a lower energy discriminator of 100 keV and no restrictions in the acceptance angle [37]. One study reported a scatter fraction of 25–45 % in the rat brain using ^{11}C-raclopride and an increase in distribution volume ratio of 3.5 % after scatter correction [38]. Monte Carlo simulations

showed that small-animal PET scanners are also sensitive to random and scattered coincidences from radioactivity outside the FOV [39].

Important contributions to the field were made by Bentourkia et al. [40] who used multispectral data acquisition on the Sherbrooke small-animal avalanche photodiode PET scanner to fit the spatial distribution of individual scatter components of the object, collimator and detector using simple mono-exponential functions. The scatter fraction of this scanner for rat imaging was estimated to be 33.8 % with a dominant contribution of the single-scatter component (27 %) as assessed by Monte Carlo calculations [41]. The position-dependent scatter parameters of each scatter component are then used to design non-stationary scatter correction kernels for each point in the projection. These kernels are used in a non-stationary convolution-subtraction method which consecutively removes object, collimator, and detector scatter from projections [42]. This technique served as basis for the implementation of a spatially variant convolution subtraction scatter correction approach using dual-exponential scatter kernel on the Hamamatsu SHR-7700 animal PET scanner [43].

The SF and noise equivalent count rate (NECR) are usually measured using various discrete phantoms of different uniform size [35, 44, 45]. The idea of the NEMA protocol for scatter fraction estimation is to use a uniform cylindrical phantom with a line source inserted at predefined radial displacements to give an estimate of the scatter fraction, which is representative of the whole phantom [46]. For this purpose, the scatter fraction and count rate performance are determined using a mouse- and rat-sized phantoms and an ^{18}F line source insert. The mouse-sized phantom is 70 ± 0.5 mm long and 25 ± 0.5 mm in diameter with a cylindrical hole (3.2 mm diameter) drilled parallel to the central axis at a radial distance of 10 mm. The rat-sized phantom has a diameter of 50 ± 0.5 mm and a length of 150 ± 0.5 mm with a cylindrical hole (3.2 mm diameter) drilled parallel to the central axis at a radial distance of 17.5 mm. For instance, the scatter fraction for the X-PET™ subsystem of the FLEX Triumph™ PET/CT scanner was measured to be 7.9 % for the mouse-sized phantom, whereas a value of 21 % was reported for the rat-sized phantom [47]. These values were measured to be 19 % and 31 %, respectively, for the LabPET™-8 scanner [48].

Monte Carlo simulation studies have shown that the optimum radial displacement of the line source required for relevant assessment of the scatter fraction for a range of phantom sizes was ~3/4 of the phantom radius from the center [44], which is very close to the position recommended by the NEMA NU-4 standard for animal scanners [46] contrary to the NU-2 standard for clinical whole-body scanners [49].

Exhaustive experimental measurements were also carried out to characterize the magnitude and origin of scattered radiation for the microPET II small-animal PET scanner [35]. It has been shown that for mice scanning, the scatter from the gantry and room environment as measured with a line source placed in air dominates over object scatter. The environmental scatter fraction rapidly increases as the lower energy discriminator decreases and can be over 30 % for an open energy window of 150–750 keV. The scatter fraction originating from the mouse phantom is very low (3–4 %) and does not change considerably when increasing the lower energy discriminator. The object scatter fraction for the rat phantom varies between 10 and 35 % for different energy windows and increases as the lower energy discriminator decreases.

Likewise, the measured scatter fractions for the mouse (rat) NEMA count rate phantom in the microPET-R4 and the microPET®—FOCUS-F120 were 14 % (29 %) and 12.3 % (26.3 %), respectively, when using a low energy discrimination of 250 keV [50]. If the discriminator is increased to 350 keV, the scatter fraction drops to 8.3 % (19.6 %) and 8.2 % (17.6 %), respectively. Scatter correction is thus more important for rat scanning whereas a large energy window (i.e., 250–750 keV) would be more appropriate for small objects (e.g. mouse brain scanning) to increase system sensitivity.

Several observations reported that within specific rodent species, especially rats or small rabbits, there is substantial variation in body size when rodents are litters or correspond to diabetic models put on high calorie diets. Also the rodents' body shape is not uniform throughout the axial direction. The body cross-section of rodents' specially rats and large species increases from head towards pelvic region [51]. Moreover, it has been suggested that a phantom representing a varying range of cross-sections and dimensions would be more suited for the assessment of these parameters for clinical PET systems [52]. Furthermore, it is nowadays common practice to increase the throughput of rodent PET studies by simultaneous scanning of multiple rodents placed at different radial offsets in the scanner's FOV [53].

More recently, Prasad et al. [51] reported on the design and development of a cone-shaped phantom for the measurement of object size-dependent SF and NECR and, second, to assess these parameters as a function of radial offset, object size and lower energy threshold for two small animal PET scanners, namely the X-PET™ and LabPET™-8, using the developed cone-shaped phantom. The optimized dimensions of the cone-shaped phantom were 158 mm (length), 20 mm (minimum diameter), 70 mm (maximum diameter) with taper angle of 9°. Depending on the radial offset from the centre of the central axial FOV (3–6 cm diameter), the SF for the cone-shaped phantom varied from 26.3 to 18.2 %, 18.6 to 13.1 % and 10.1 to 7.6 % for the X-PET™, whereas it varied from 34.4 to 26.9 %, 19.1 to 17.0 %, and 9.1 to 7.3 % for the LabPET™-8, for lower energy thresholds (LETs) of 250, 350 and 425 keV, respectively. The SF increases as the radial offset decreases, LET decreases and object size increases. Overall, the SF is higher for the LabPET™-8 compared to the X-PET™ scanner. Figure 17.3 illustrates a Monte Carlo model of the LabPET™-8 small animal PET scanner with a cone-shaped phantom in the FOV (left). The SF for FOV_{mouse} corresponding to the cone-shaped phantom for the LabPET™-8 scanner using a LET of 250, 350 and 425 keV is also shown (right). The SF estimates are shown for a line source located at the center and at 10 and 15 mm radial offset [51].

The same authors characterized the magnitude and spatial distribution of the scatter component in small-animal PET imaging when scanning single and multiple rodents simultaneously and assessed the performance of model-based scatter correction under similar conditions [54]. The modelled scatter component for the LabPET™-8 scanner using the single-scatter simulation (SSS) technique was compared to Monte Carlo simulation results. A good agreement was observed between calculated and Monte Carlo simulated scatter profiles for single- and multiple-subject imaging. In the LabPET™-8 scanner, the detector covering material (kovar)

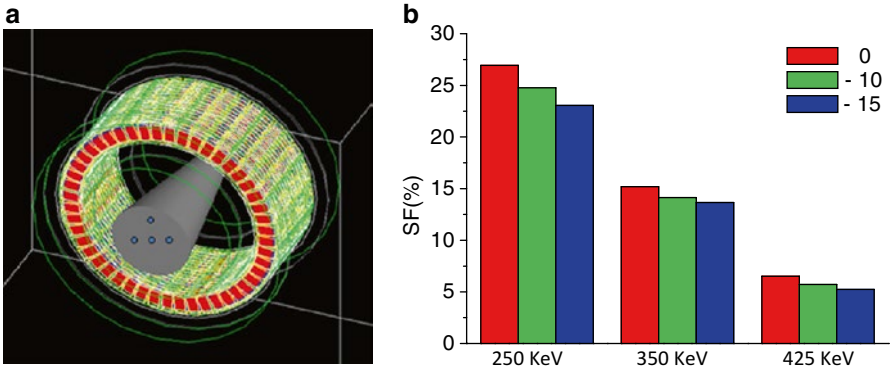

Fig. 17.3 Monte Carlo simulation model the LabPET™-8 small animal scanner (*left*). Reprentative example of the variation of the SF (in %) as a function of radial offsets for the cone-shaped phantom using a LET of 250, 350 and 425 keV for axial FOV_{mouse} (*right*)

contributed the maximum amount of scatter events while the scatter contribution due to lead shielding was negligible. The increase in SF ranged between 25 % and 64 % when imaging multiple subjects (three to five) of different size simultaneously in comparison to imaging a single subject.

Similar approaches were undertaken for positron emission mammography (PEM) units where both high spatial and contrast resolution and sensitivity are required to meet the needs of early detection of breast tumors, hence avoiding biopsy intervention. In this context, a scatter correction method for a regularized list-mode ML-EM reconstruction algorithm was proposed [55]. The object scatter component is modeled as additive Poisson random variable in the forward model of the reconstruction algorithm. The mean scatter sinogram, which only needs to be estimated once for each PEM configuration is estimated using lengthy Monte Carlo simulations [54].

A more recent approach aiming at simultaneous correction for attenuation and scatter was suggested [56]. This is achieved by analytical assessment of the spatial distribution of scattered photons using both emission and transmission images combined with prior knowledge of the probability of Compton scattering and scanner detection efficiency. The authors reported improved performance compared to the model-based approach proposed by Watson [57].

4 Attenuation Compensation

Similar to scatter correction [58], little has been published on attenuation correction (AC) in small-animal PET imaging owing to the low magnitude of attenuation factors when imaging rodents (compared to clinical imaging). The magnitude of the correction factors ranges from approximately 45 for a 40 cm diameter human

subject and decreases down to 1.6 for a 5 cm diameter rat) to nearly 1.3 for a 3 cm diameter mouse [59]. This elucidates why the problem of photon attenuation has been overlooked in small-animal imaging even in the third generation of preclinical PET scanners [60]. PET scanner calibration factors are usually determined with and without AC given that AC is till not well established in small-animal imaging.

Fahey et al. [61] have shown that the use of transmission (TX)-based AC improved the quantitative accuracy but also reduced the precision as indicated in the variability of the attenuation corrected data. This can be compensated by noise reduction schemes such as segmentation of the TX data. Another study compared several measured TX-based techniques for deriving the attenuation map on the microPET Focus 220 animal scanner [62]. This includes coincidence mode with and without rod windowing, singles mode with two different TX sources (^{68}Ge and ^{57}Co), and post-injection TX scanning. Moreover, the efficiency of TX image segmentation and the propagation of TX bias and noise into the emission images were examined. It was concluded that ^{57}Co-based AC provides the most accurate attenuation map having the highest SNR. Single-photon TX scanning using ^{68}Ge sources suffered from degradations resulting from object Compton scatter. Monte Carlo simulation studies also demonstrated that background contamination in the ^{68}Ge singles-mode data due to intrinsic ^{176}Lu radioactivity present in the detector crystals can be compensated using a simple technique [63]. Compensating for scatter improved the accuracy for a cylindrical phantom (10 cm diameter) but overcorrected for attenuation for a mouse phantom. Low-energy ^{57}Co-based AC also resulted in low bias and noise in post-injection TX scanning for activities in the FOV up to 20 MBq. Attenuation map segmentation was most successful using ^{57}Co single-photon sources, however, the modest improvement in quantitative accuracy and SNR may not rationalize its use, particularly for small-animals. More sophisticated techniques using multiple sources for TX scanning where each point source is surrounded by a plastic scintillator coupled to a miniature photomultiplier tube to allow collection of the energy the positron must lose before annihilation were also developed [64, 65]. The LoR joining the current source position and detector position is identified through the pulse provided by the energy lost in the plastic scintillator whereas scanner's conventional detectors provide the second pulse.

Combined anato-molecular PET/CT imaging also provides *a priori* subject-specific anatomical information that is needed to correct the PET data for photon attenuation and other physical effects. The potential use of small-animal CT for AC is now well established and is considered to be one of the potential applications of low-dose microCT imaging which can drive the further development of dual-modality small-animal PET/CT [66]. Similar to SPECT/CT [67, 68], the accuracy of CT-based attenuation correction (CT-AC) in preclinical imaging was demonstrated using phantom and animal studies where the low-dose CT was suitable for both PET data correction and PET tracer localization [59]. The principle of CT-AC is shown in Fig. 17.4. Some of the advantages of the technique are the low statistical noise and high-quality anatomical information, small crosstalk between PET annihilation photons and low energy X-rays, and higher throughput imaging protocols. Noise analysis in phantom studies with the TX-based method showed that noise in the TX data

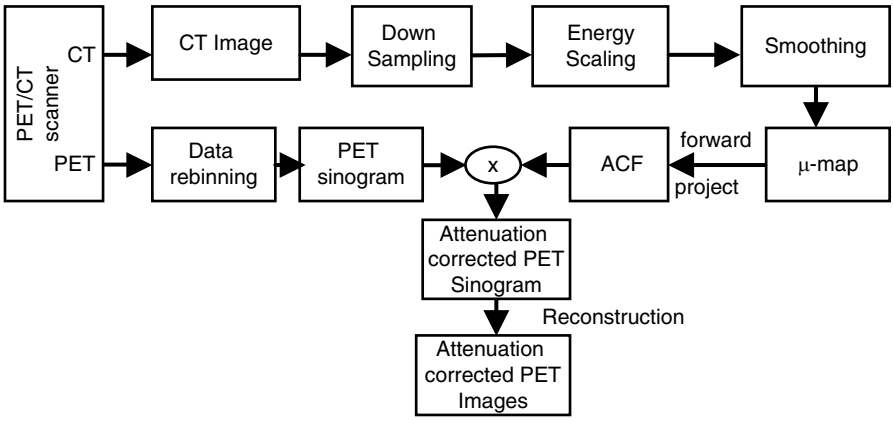

Fig. 17.4 Strategy for implementation of CT-based attenuation correction on a preclinical PET/CT scanner

increases the noise in the corrected PET emission data whereas the CT-based method was accurate and resulted in less noisy images. For small-animal imaging, hardware image registration approaches that rely on the use of custom made imaging chambers which can be rigidly and reproducibly mounted on separate PET and CT preclinical scanners [69] is a reasonable alternative to combined PET/CT designs [70–72]. Calculated AC was reported to provide similar correction compared to CT-AC for a cylindrical phantom and a mouse for which the attenuation medium volume matches the PET emission source distribution [73]. However, it undercorrects for attenuation when the emission image outline underestimates the attenuation medium volume (unmatched source distribution and attenuation medium).

One should note that accurate and robust conversion of CT numbers derived from low-energy polyenergetic X-ray spectra of a CT scanner to linear attenuation coefficients at 511 keV is essential for accurate implementation of CT-AC of PET data. Several conversion strategies have been reported in the literature including segmentation [74], scaling [75], hybrid (segmentation/scaling) [76], bilinear or piece-wise scaling [77], quadratic polynomial mapping [78, 79], and dual-energy decomposition methods [80]. Energy-mapping methods are generally derived at a preset tube voltage and current. These methods are widely used and validated on clinical PET systems [81]; however, they still need to be thoroughly investigated on dedicated high resolution, small FOV scanners such as those used for small-animal imaging. PET images of a transverse slice of the NEMA NU 4- 2008 image quality phantom reconstructed with and without attenuation correction are shown in Fig. 17.5. A horizontal line profile is also shown [79].

Despite the wide acceptance of CT-AC as a reliable technique allowing to achieve more accurate quantification in high resolution preclinical PET imaging, further work is still needed to explore its broad potential, in particular when combined with scatter and beam hardening correction of cone-beam CT data [82]. The impact of

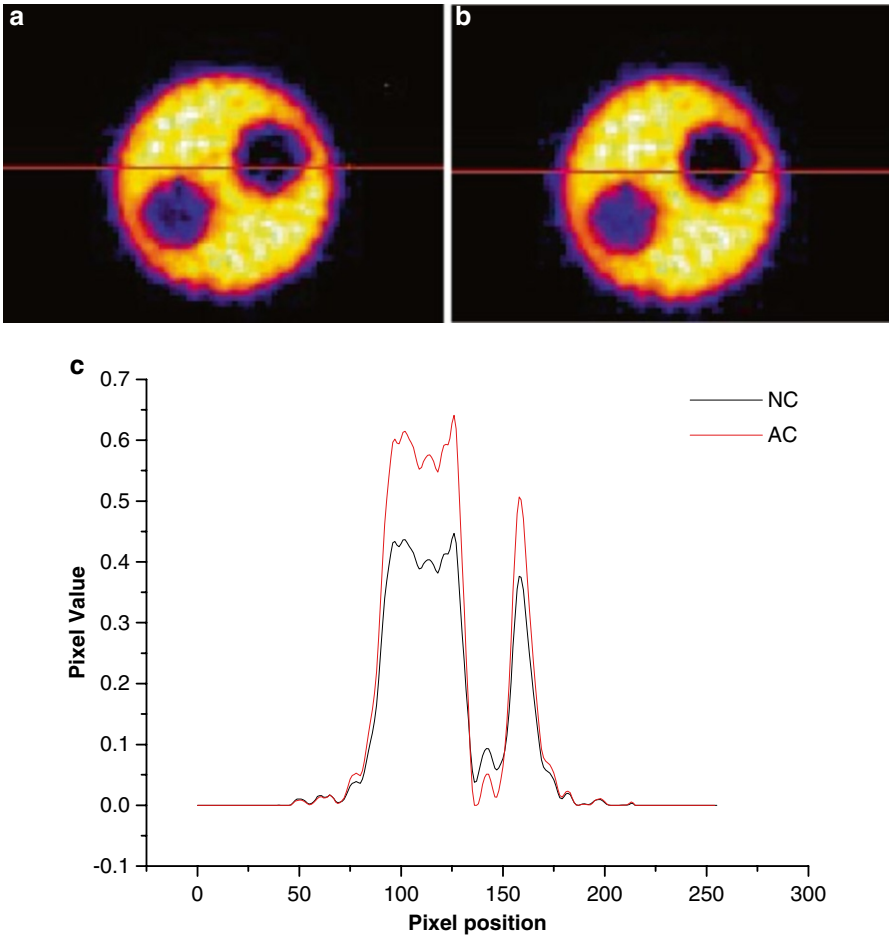

Fig. 17.5 Transaxial slices showing (**a**) uncorrected and (**b**) CT-based attenuated corrected PET images of the NEMA NU 4- 2008 image quality phantom acquired on the FLEX Triumph™ PET/CT scanner. (**c**) The corresponding horizontal profiles through images shown in (**a**) and (**b**)

X-ray scatter in cone-beam CT subsystems coupled to PET scanners on combined preclinical PET-CT systems has been investigated in a limited number of studies [83–85]. Most of the approaches estimate the scatter-to-primary ratio (SPR) from projections in the 3D cone-beam geometry using the beam stop method or from Monte Carlo simulations. Alternatively, analytical models were derived to estimate the first order X-ray scatter by approximating the Klein–Nishina formula so that the first order scatter fluence is expressed as a function of the primary photon fluence on the detector [86].

Following the introduction of hybrid small-animal PET/MRI systems [87–92] (see also Chap. 15), MRI-guided attenuation compensation has received a great deal

of attention in the scientific literature [93–95]. This is a very active research topic that will certainly impact the future of hybrid PET/MRI technology. The major difficulty facing MRI-guided attenuation correction lies in the fact that the MRI signal or tissue intensity level is not directly related to electron density which renders conversion of MRI images to attenuation maps less obvious compared to CT. One approach uses representative anatomical atlas registration where the MRI atlas is registered to the subject's MRI and prior knowledge of the atlas' attenuation properties (for example through coregistration to CT atlas) is used to yield a subject-specific attenuation map [96]. This is the basis of the method proposed by Chaudhari et al. [97] for mice imaging, using the Digimouse atlas. The critical and crucial part of the algorithm is the registration procedure which might fail in some cases with large deformations [98, 99]. The other fundamental question that remains to be addressed is: does the global anatomy depicted by an atlas really predict individual attenuation map? [93].

5 Partial Volume Effect Correction

The quantitative accuracy of PET is hampered by the low spatial resolution capability of currently available scanners. The well accepted criteria is that one can accurately quantify the activity concentration for sources having dimensions equal or larger than two to three times the system's spatial resolution measured in terms of its full width at half maximum (FWHM) [100, 101]. Sources of smaller size only partly occupy this characteristic volume and, as such, the counts are spread over a larger volume than the physical size of the object owing to the limited spatial resolution of the imaging system. It should be emphasized that the total number of counts is conserved in the corresponding PET images. In this case, the resulting PET images reflect the total amount of the activity within the object but not the actual activity concentration. This phenomenon is referred to as the partial volume effect (PVE) and can be corrected using one of the various strategies developed for this purpose [102].

In clinical PET imaging, partial volume errors are great sources of errors impacting PET image quantification. In preclinical PET imaging, partial volume errors are expected to be less severe owing to the higher spatial resolution of dedicated small bore systems. However, it is a matter of fact that the quantitative accuracy in small animal imaging still bears inherent limitations especially for quantification of tracer uptake in small organs such as mouse brain or heart [103]. It has been reported that dedicated preclinical PET scanners can provide accurate quantification to within 6 % for features larger than 10 mm. About 60 % of object contrast was retained for features as small as 4 mm [61].

The high cost of dedicated preclinical instrumentation and the interest expressed by several groups to conduct preclinical research studies in facilities equipped only with commercial scanners for clinical studies motivated the use of clinical PET scanners for imaging laboratory animals. Moreover, various strategies were developed to scan multiple rodents simultaneously at different radial offsets in the

scanner's FOV to increase the throughput of PET scanners [104]. However, the limited spatial resolution of clinical scanners deteriorates image quality and hampers the quantitative accuracy by enhancing the impact of partial volume errors in small-animal imaging. Despite these limitations, several investigators successfully carried out research experiments involving scanning laboratory animals on clinical PET scanners [105–107]. Many of these studies used simple approaches for partial volume correction using the method based on the calculation of recovery coefficients (RCs) [108, 109]. In this approach, the correction is performed by multiplying the uptake value in a specific region of interest (ROI) with a size-dependent RC. RCs are commonly calculated through experimental measurements using objects with known size, shape, activity concentration and location in the scanner's FOV [110]. Many of these approaches accounted for both 'spill-out' (loss of activity) and 'spill-in' (increase of activity) to and from the surrounding tissues, respectively. Few studies reported on partial volume correction for preclinical studies involving the use of small-animal PET scanners [103, 111]. Correction for partial volume even using this simple approach significantly improved both accuracy of small-animal PET semi-quantitative data in rat studies and their correlation with tumour proliferation, except for largely necrotic tumours [111].

More sophisticated approaches described in the literature were designed specifically to compensate for partial volume effect in rat brain imaging [112], tumour imaging [113] and cardiovascular imaging [114–117] including correction for partial volume effect when using image-derived input function for kinetic modelling [118, 119]. Most of these studies demonstrated significant improvement in quantitative accuracy when partial volume effect is applied. It has also been demonstrated that image correction and reconstruction techniques, object size and location within the FOV have a strong influence on the resulting partial volume effect [120]. Among the above referenced approaches, methods using the wavelet transform to incorporate the high resolution structural information (CT or MRI) into low resolution PET images seem to be promising and should be investigated further [121].

6 Issues Pertaining to Quantification and Kinetic Modelling

The kinetic modeling of PET data depends on the radiotracer used for imaging, the data acquisition protocol and the biological tissues or organs under study. Each radiotracer behaves differently in the body, and the same tracer could be affected differently in different types of tissue. The general principles of kinetic modeling are extensively reviewed elsewhere and will not be discussed here [122, 123]. Basically, two approaches were adopted for kinetic analysis: (1) tracer-dependent models performed on a voxel-by-voxel basis to produce parametric images and, (2) grouping voxels representing homogeneous tissues in volumes of interest (VOIs). The former approach bears the inherent drawback of generating noisy time-activity curves (TACs) at the voxel level and, as such, it is tricky to fit the model to the data for short-lived radionuclides. To this end, a number of approaches have been

suggested to tackle this challenge, including spatial noise reduction techniques, cluster analysis and spatial constrained weighted nonlinear least-square methods and wavelet denoising approaches [124]. Alternatively, the latter approach is more robust because of the averaging of the voxels contained in each VOI, thus enabling to handle the data with better statistical properties. This also allows significant reduction of computation time since the processing is limited to a predefined number of VOIs instead of a large number of voxels. Yet, this approach presents some fundamental limitations particularly when the assumption of tissue homogeneity within a VOI is questionable.

In the context of small-animal imaging, kinetic modeling of tracers presents several issues and additional challenges compared to human studies that need to be addressed through research before the technique can be exploited to its full potential [125]. This includes improved image correction, reconstruction and analysis techniques, and the use of blood plasma data coupled with advanced kinetic models. In addition to these technical concerns, two other issues still need to be carefully addressed. These include the impact of anesthesia on the physiological processes being studied [126] and the radiation dose delivered to the animals [127–129], particularly in longitudinal studies where the animal serves as its own control.

The data acquisition process in small-animal imaging involving kinetic modeling consists of the following steps [125]: (1) animal handling and preparation, (2) tracer injection, usually through the tail vein, (3) dynamic or list-mode PET data acquisition, and (4) direct blood sampling or acquisition of an early dynamic frame at the level of the heart if image-based derivation of the input function is sought. It is often common practice to launch the acquisition simultaneously with bolus injection. Special attention has to be paid to dead-time correction particularly at the beginning of the scan to measure the relatively high initial activity. Likewise, appropriate cross-calibration procedures between the PET scanner, dose calibrator and well counter should be performed. The different clocks used should also be synchronized to limit decay correction errors. The total acquisition time has consequences on the size of the data sets if acquired in list-mode format and on the animal's physiology. It is often assumed that the physiological and metabolic processes under investigation remain unchanged during the course of the study excluding cases where the aim of the study is to influence these processes (e.g. activation studies).

The input function is often required for kinetic modeling studies to determine the amount of the radiotracer in the blood (or plasma) delivered to tissue, and can be assessed from arterial blood samples. However, blood sampling is risky, and in the specific case of small animals, the procedure is very tricky and yet there may not be enough blood to extract especially in repetitive studies. Therefore, only a small fraction of the total blood volume is usually withdrawn to limit side effects. This obviously has an impact on the number of samples which have to be withdrawn either manually or automatically by means of blood sampling devices in a discrete or continuous fashion. Novel automated microfluidic blood sampling devices allow taking only few samples corresponding to a small fraction of the total blood volume [130, 131]. As mentioned above, alternative methods rely on extracting the input function directly from images. In this case, the radioactivity in the arterial blood can

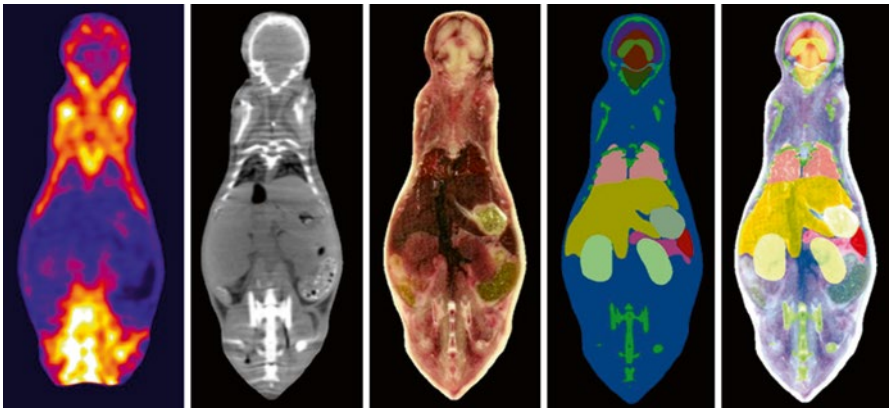

Fig. 17.6 Spatially registered (from *left* to *right*) PET, CT, cryosection, Atlas and overlay images for a coronal slice through the Digimouse model. Reprinted with permission from [147]

be assessed by defining VOIs on the left atrium chamber or on the left ventricle (in cardiac studies) [132, 133]. However, special attention has to be paid to correct for spillover from blood to tissues or from tissue to blood (owing to the small size of the heart relative to the scanner's spatial resolution) and for the metabolites. Another alternative is to use standard arterial input function derived from an automated slow bolus infusion of ^{18}F-FDG adjusted by few measured blood samples [134]. Promising approaches for derivation of the input function without blood sampling include reference tissue approaches [135, 136] and decomposition of images using factor analysis [137, 138] or independent component analysis [139]. Alternatively, beta-probes have also been used to determine the input function [140, 141], however, complex surgery might be needed to estimate accurately the input function [142].

Automatic quantitative analysis of molecular PET data is essential as it provides the potential to enhance the consistency among different interpreting observers regardless of their experience and to reduce the variability across institutions in multicentre trials. For example, the development of tracer-specific small animal PET probabilistic atlases [143] correlated with anatomical (e.g. MRI) templates enabled automated volume-of-interest or voxel-based analysis of small animal PET data with minimal end-user interaction [144]. One such software tool was developed by Kesner et al. [145] to enable the assessment of the biodistribution of PET tracers using small animal PET data. This is achieved though non-rigid coregistation of a digital mouse phantom with the animal PET image followed by automated calculation of tracer concentrations in 22 predefined VoIs representing the whole body and major organs. The development of advanced anatomical models including both stylized and more realistic voxel-based mouse [146–149] and rat [150–153] models obtained from serial cryo-sections or dedicated high resolution small animal CT and MRI scanners will certainly help to support ongoing research in this area [154, 155]. Figure 17.6 illustrates a representative slice of PET, CT, cryosection, and Atlas and overlay images through the Digimouse model [147]. More recently,

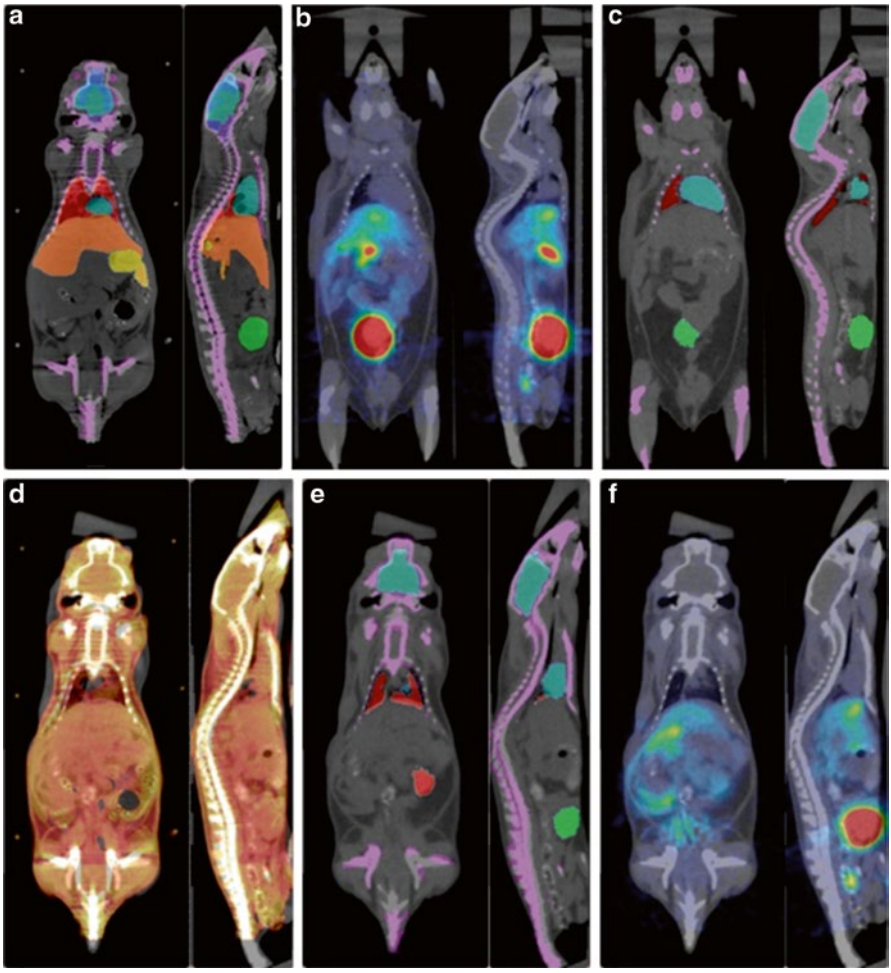

Fig. 17.7 Illustration of representative deformable registration example between the Digimouse and an experimental mouse studies showing: (**a**) overlay of the Digimouse atlas onto corresponding CT images, (**b**) actual ^{18}F-FDG PET/CT mouse study, (**c**) mouse study shown in (**b**) with overlay of the segmentation onto CT image (seven organs), (**d**) CT to CT registration of the Digimouse and actual mouse study shown in (**c**), (**e**) overlay of the transformed segmentation (seven organs) using registration parameters obtained in (**d**) onto CT image, and (**f**) transformed PET/CT study using registration parameters obtained in (**d**). Reprinted with permission from [156]

a methodology for fully automated atlas-guided analysis of small animal PET data through deformable registration to an anatomical mouse model was reported [156]. Representative image registration results between experimental mouse studies and the Digimouse atlas are shown in Fig. 17.7. Direct segmentation of functional PET images enabling to alleviate the need of the corresponding anatomical information

or an Atlas have also been reported [157]. Such approaches are useful for automated calculation of TACs for the various organs/tissues of interest, which is required for the purpose of kinetic modeling.

7 Summary and Future Directions

It is gratifying to see in overview the progress that quantitative analysis of small-animal PET data has made, from cumbersome manual techniques, through semi-automated approaches requiring the availability of multimodality imaging, and more recently towards atlas-guided fully automated analysis approaches. Significant attention has been devoted to optimizing algorithmic designs and computational performance and to balancing conflicting requirements. Approximate methods suitable for applications that do not require accurate quantitative measurements and more sophisticated approaches for research applications where there is greater emphasis on accurate quantitative measurements, are being addressed. Quantitative high resolution preclinical multimodality imaging will undoubtedly be an accurate and cost-effective method for conducting various basic research studies to enable the understanding of complex diseases and physiological processes and might also assist in drug discovery and many other applications relying on the use of small-animal models of human disease.

Technical challenges remain for quantitative imaging, particularly in the areas of motion tracking and correction when scanning freely moving awake rodents [158–160], in accurate image quantification predominantly when using exotic non-conventional radionuclides [161, 162], and in the development of more accurate kinetic models at the voxel level. As these challenges are met, and experience is gained, quantitative small-animal molecular imaging will attract more interest and make a more profound impact on biomedical research.

Acknowledgments This work was supported by the Swiss National Science Foundation under grant SNSF 31003A-125246. The author would like to thank Rameshwar Prasad (PhD student) for supplying some of the material used in this chapter.

References

1. H. Zaidi (2006) Ed., *Quantitative analysis in nuclear medicine imaging* (Springer, New York).
2. P. D. Acton, H. Zhuang, A. Alavi (2004) Quantification in PET. Radiol Clin North Am 42: 1055–1062
3. C. S. Levin, H. Zaidi (2007) Current trends in preclinical PET system design. PET Clinics 2: 125–160
4. M. A. Bahri, A. Plenevaux, G. Warnock, A. Luxen, A. Seret (2009) NEMA NU4-2008 image quality performance report for the microPET Focus 120 and for various transmission and reconstruction methods. J Nucl Med 50: 1730–1738

5. H. Zaidi, M.-L. Montandon, S. Meikle (2007) Strategies for attenuation compensation in neurological PET studies. Neuroimage 34: 518–541
6. J. Qi, R. M. Leahy (2006) Iterative reconstruction techniques in emission computed tomography. Phys Med Biol 51: R541–R578
7. A. J. Reader, H. Zaidi (2007) Advances in PET image reconstruction. PET Clinics 2: 173–190
8. A. Rahmim, J. Tang, H. Zaidi (2009) Four-dimensional (4D) image reconstruction strategies in dynamic PET: beyond conventional independent frame reconstruction. Med Phys 36: 3654–3670
9. R. M. Lewitt, S. Matej (2003) Overview of methods for image reconstruction from projections in emission computed tomography. Proceedings of the IEEE 91: 1588–1611
10. H. H. Barrett, K. Myers (2003) Foundations of Image Science John Wiley & Sons, Hoboken, New Jersey.
11. D. C. Solman (1976) The x-ray transform. J Math Anal Appl 56: 61-83
12. F. Natterer (1986) The mathematics of computerized tomography. Wiley, New York.
13. K. E. Kuhl, R. Q. Edwards (1963) Image separation radioisotope scanning. Radiology 80: 653–661
14. G. Chu, K.-C. Tam (1977) Three-dimensional imaging in the positron camera using Fourier techniques. Phys Med Biol 22: 245–265
15. P. E. Kinahan, J. G. Rogers (1989) Analytic 3D image reconstruction using all detected events. IEEE Trans Nucl Sci 36: 964–968
16. M. Defrise, P. E. Kinahan, D. W. Townsend, et al. (1997) Exact and approximate rebinning algorithms for 3-D PET data. IEEE Trans Med Imaging 16: 145–158
17. L. A. Shepp, Y. Vardi (1982) Maximum likelihood reconstruction for emission tomography. IEEE Trans Med Imaging 1: 113–122
18. H. Zaidi, B. H. Hasegawa (2003) Determination of the attenuation map in emission tomography. J Nucl Med 44: 291–315
19. B. Hutton, J. Nuyts, H. Zaidi: Iterative image reconstruction methods. In Quantitative analysis in nuclear medicine imaging. H. Zaidi, Ed. Springer, New York, 2006. 107–140
20. H. M. Hudson, R. S. Larkin (1994) Accelerated image reconstruction using ordered subsets of projection data. IEEE Trans Med Imaging 13: 601–609
21. S. Geman, D. E. McClure (1987) Statistical methods for tomographic image reconstruction. Bull Int Stat Inst 52–4: 5–21
22. J. Qi, R. M. Leahy, S. R. Cherry, A. Chatziioannou, T. H. Farquhar (1998) High-resolution 3D Bayesian image reconstruction using the microPET small-animal scanner. Phys. Med. Biol. 43: 1001–1013
23. S. Sastry, R. E. Carson (1997) Multimodality Bayesian algorithm for image reconstruction in positron emission tomography: a tissue composition model. IEEE Trans Med Imaging 16: 750–761
24. K. Baete, J. Nuyts, W. Van Paesschen, P. Suetens, P. Dupont (2004) Anatomical-based FDG-PET reconstruction for the detection of hypo-metabolic regions in epilepsy. IEEE Trans Med Imaging 23: 510–519
25. A. Rahmim, J. Qi, V. Sossi (2013) Resolution modeling in PET imaging: Theory, practice, benefits, and pitfalls. Med Phys 40: 064301–15
26. S. Moehrs, M. Defrise, N. Belcari, et al. (2008) Multi-ray-based system matrix generation for 3D PET reconstruction. Phys Med Biol 53: 6925–6945
27. M. Rafecas, B. Mosler, M. Dietz, et al. (2004) Use of a Monte Carlo-based probability matrix for 3-D iterative reconstruction of MADPET-II data. IEEE Trans Nucl Sci 51: 2597–2605
28. V. Y. Panin, F. Kehren, C. Michel, M. Casey (2006) Fully 3-D PET reconstruction with system matrix derived from point source measurements. IEEE Trans Med Imaging 25: 907–921
29. M. S. Tohme, J. Qi (2009) Iterative image reconstruction for positron emission tomography based on a detector response function estimated from point source measurements. Phys Med Biol 54: 3709–3725

30. A. M. Alessio, C. W. Stearns, S. Tong, et al. (2010) Application and evaluation of a measured spatially variant system model for PET image reconstruction. IEEE Trans Med Imaging 29: 938–949
31. F. A. Kotasidis, J. C. Matthews, G. I. Angelis, et al. (2011) Single scan parameterization of space-variant point spread functions in image space via a printed array: the impact for two PET/CT scanners. Phys Med Biol 56: 2917–2942
32. J. Zhou, J. Qi (2011) Fast and efficient fully 3D PET image reconstruction using sparse system matrix factorization with GPU acceleration. Phys Med Biol 56: 6739–6757
33. R. E. Carson, K. Lange (1985) The EM parametric image reconstruction algorithm. J Am Statist Assoc 80: 20–22
34. S. Weber, A. Bauer (2004) Small animal PET: aspects of performance assessment. Eur J Nucl Med Mol Imaging 31: 1545–1555
35. Y. Yang, S. R. Cherry (2006) Observations regarding scatter fraction and NEC measurements for small animal PET. IEEE Trans Nucl Sci 53: 127–132
36. S. I. Ziegler, W. K. Kuebler (1993) Monte Carlo simulation of the scatter component in small animal positron volume-imaging devices. Z Med Phys 3: 83–87
37. M. Rafecas, G. Boning, B. J. Pichler, et al. (2001) A Monte Carlo study of high-resolution PET with granulated dual-layer detectors. IEEE Trans Nucl Sci 48: 1490–1495
38. D. L. Alexoff, P. Vaska, D. Marsteller, et al. (2003) Reproducibility of 11C-raclopride binding in the rat brain measured with the microPET R4: effects of scatter correction and tracer specific activity. J Nucl Med 44: 815–822
39. A. Fulterer, S. Schneider, B. Gundlich, et al. (2007) Scatter analysis of the ClearPET™ Neuro using Monte Carlo simulations. In Advances in Medical Engineering. Springer, Heidelberg, pp 109–114
40. M. Bentourkia, P. Msaki, J. Cadorette, R. Lecomte (1995) Energy dependence of scatter components in multispectral PET imaging. IEEE Trans Med Imaging 14: 138–145
41. M. Bentourkia, M. Laribi, E. Lakinsky, J. Cadorette (2002) Scatter restoration in PET imaging, IEEE Nuclear Science Symposium Conference Record, 10-16.11.2002, Norlfolk, VA, USA.
42. M. Bentourkia, R. Lecomte (1999) Energy dependence of nonstationary scatter subtraction-restoration in high resolution PET. IEEE Trans Med Imaging 18: 66–73
43. M. Lubberink, T. Kosugi, H. Schneider, H. Ohba, M. Bergstrom (2004) Non-stationary convolution subtraction scatter correction with a dual-exponential scatter kernel for the Hamamatsu SHR-7700 animal PET scanner. Phys Med Biol 49: 833–842
44. A. Ferrero, J. K. Poon, A. J. Chaudhari, L. R. MacDonald, R. D. Badawi (2011) Effect of object size on scatter fraction estimation methods for PET- A computer simulation study. IEEE Trans Nucl Sci 58: 82–86
45. A. Konik, M. T. Madsen, J. J. Sunderland (2010) GATE simulations of human and small animal PET for determination of scatter fraction as a function of object size. IEEE Trans Nucl Sci 57: 2558–2563
46. National Electrical Manufacturers Association, "NEMA Standards Publication NU 4 – 2008. Performance Measurements of Small Animal Positron Emission Tomographs" (National Electrical Manufacturers Association, 2008)
47. R. Prasad, O. Ratib, H. Zaidi (2010) Performance evaluation of the FLEX Triumph™ X-PET scanner using the NEMA NU-04 standards. J Nucl Med 51: 1608–1615
48. R. Prasad, O. Ratib, H. Zaidi (2011) NEMA NU-04-based performance characteristics of the LabPET-8™ small animal PET scanner. Phys Med Biol 56: 6649–6664
49. National Electrical Manufacturers Association, "Standards Publication NU 2-2007. Performance measurements of positron emission tomographs." *NU 2-2007* (National Electrical Manufacturers Association, 2007)
50. R. Laforest, D. Longford, S. Siegel, D. F. Newport, J. Yap (2007) Performance evaluation of the microPET®—FOCUS-F120. IEEE Trans Nucl Sci 54: 42–49
51. R. Prasad, H. Zaidi (2012) A cone-shaped phantom for assessment of small animal PET scatter fraction and count rate performance. Mol Imaging Biol 14: 561–571

52. J. M. Wilson, S. J. Lokitz, T. G. Turkington (2011) Development of a fillable, tapered PET/CT phantom. IEEE Trans Nuc Sci 58: 651–659
53. A. Rominger, E. Mille, S. Zhang, et al. (2010) Validation of the octamouse for simultaneous 18F-fallypride small-animal PET recordings from 8 mice. J Nucl Med 51: 1576–1583
54. R. Prasad, H. Zaidi (2014) Scatter characterization and correction for simultaneous multiple small-animal PET imaging. Mol Imaging Biol 16: 199–209
55. J. Qi, R. H. Huesman (2002) Scatter correction for positron emission mammography. Phys Med Biol 47: 2759–2771
56. M. Bentourkia, O. Sarrhini (2009) Simultaneous attenuation and scatter corrections in small animal PET imaging. Comput Med Imaging Graph 33: 477–488
57. C. C. Watson (2000) New, faster, image-based scatter correction for 3D PET. IEEE Trans Nucl Sci 47: 1587–1594
58. H. Zaidi, M.-L. Montandon (2007) Scatter compensation techniques in PET. PET Clinics 2: 219–234
59. P. L. Chow, F. R. Rannou, A. F. Chatziioannou (2005) Attenuation correction for small animal PET tomographs. Phys Med Biol 50: 1837–1850
60. Y. C. Tai, R. Laforest (2005) Instrumentation aspects of animal PET. Annu Rev Biomed Eng 7: 255–285
61. F. H. Fahey, H. D. Gage, N. Buchheimer, et al. (2004) Evaluation of the quantitative capability of a high-resolution positron emission tomography scanner for small animal imaging. J Comput Assist Tomogr 28: 842–848
62. W. Lehnert, S. R. Meikle, S. Siegel, et al. (2006) Evaluation of transmission methodology and attenuation correction for the microPET Focus 220 animal scanner. Phys Med Biol 51: 4003–4016
63. E. Vandervoort, M. L. Camborde, S. Jan, V. Sossi (2007) Monte Carlo modelling of singles-mode transmission data for small animal PET scanners. Phys Med Biol 52: 3169–3184
64. C. J. Thompson, R. Lecomte, J. Cadorette (2000) Feasibility of using beta-gamma coincidence for 3D PET attenuation correction. IEEE Trans Nucl Sci 47: 1176–1181
65. M.-L. Camborde, C. J. Thompson, D. Togane, N. Zhang, A. Reader (2004) A positron-decay triggered transmission source for positron emission tomography. IEEE Trans Nucl Sci 51: 53–57
66. E. L. Ritman (2002) Molecular imaging in small animals-roles for micro-CT. J Cell Biochem Suppl 39: 116–124
67. A. Hwang, B. Hasegawa (2005) Attenuation correction for small animal SPECT imaging using x-ray CT data. Med Phys 32: 2799–2804
68. A. B. Hwang, C. C. Taylor, H. F. Vanbrocklin, M. W. Dae, B. H. Hasegawa (2006) Attenuation correction of small animal SPECT images acquired with 125I-Iodorotenone. IEEE Trans Nucl Sci 53: 1213–1220
69. P. L. Chow, D. B. Stout, E. Komisopoulou, A. F. Chatziioannou (2006) A method of image registration for small animal, multi-modality imaging. Phys Med Biol 51: 379–390
70. A. L. Goertzen, A. K. Meadors, R. W. Silverman, S. R. Cherry (2002) Simultaneous molecular and anatomical imaging of the mouse in vivo. Phys Med Biol 21: 4315–4328
71. R. Fontaine, F. Belanger, J. Cadorette, et al. (2005) Architecture of a dual-modality, high-resolution, fully digital positron emission tomography/computed tomography (PET/CT) scanner for small animal imaging. IEEE Trans Nucl Sci 52: 691–696
72. H. Liang, Y. Yang, K. Yang, et al. (2007) A microPET/CT system for in vivo small animal imaging. Phys Med Biol 52: 3881–3894
73. R. Yao, J. Seidel, J.-S. Liow, M. V. Green (2005) Attenuation correction for the NIH ATLAS small animal PET scanner. IEEE Trans Nucl Sci 52: 664–668
74. P. E. Kinahan, B. H. Hasegawa, T. Beyer (2003) X-ray-based attenuation correction for positron emission tomography/computed tomography scanners. Semin Nucl Med 33: 166–179
75. T. Beyer, P. E. Kinahan, D. W. Townsend, D. Sashin (1994) The use of X-ray CT for attenuation correction of PET data, *Proc.* IEEE Nuclear Science Symposium and Medical Imaging Conference, 30 Oct.–5 Nov., Norfolk, VA, USA

76. P. E. Kinahan, D. W. Townsend, T. Beyer, D. Sashin (1998) Attenuation correction for a combined 3D PET/CT scanner. Med Phys 25: 2046–2053
77. C. Bai, L. Shao, A. J. Da Silva, Z. Zhao (2003) A generalized model for the conversion from CT numbers to linear attenuation coefficients. IEEE Trans Nucl Sci 50: 1510–1515
78. M. R. Ay, M. Shirmohammad, S. Sarkar, A. Rahmim, H. Zaidi (2011) Comparative assessment of energy-mapping approaches in CT-based attenuation correction for PET. Mol Imaging Biol 13: 187–198
79. R. Prasad, M. R. Ay, O. Ratib, H. Zaidi (2011) CT-based attenuation correction on the FLEX Triumph™ preclinical PET/CT scanner. IEEE Trans Nucl Sci 58: 66–75
80. M. J. Guy, I. A. Castellano-Smith, M. A. Flower, et al. (1998) DETECT-dual energy transmission estimation CT-for improved attenuation correction in SPECT and PET. IEEE Trans Nucl Sci 45: 1261–1267
81. J. P. Carney, D. W. Townsend, V. Rappoport, B. Bendriem (2006) Method for transforming CT images for attenuation correction in PET/CT imaging. Med Phys 33: 976–983
82. M. Ay, H. Zaidi (2006) Assessment of errors caused by x-ray scatter and use of contrast medium when using CT-based attenuation correction in PET. Eur J Nucl Med Mol Imaging 33: 1301–1313
83. P. L. Chow, N. T. Vu, A. F. Chatziioannou (2004) Estimating the magnitude of scatter in small animal cone-beam CT, IEEE Nuclear Science Symposium Conference Record. Vol. 5; pp 2752–2754
84. Y. C. Ni, M. L. Jan, K. W. Chen, et al. (2006) Magnitude and effects of X-ray scatter of a cone-beam micro-CT for small animal imaging. Nucl Instr Meth A 569: 245–249
85. D. Gutierrez, H. Zaidi (2011) Assessment of scatter for the micro-CT subsystem of the trimodality FLEX Triumph preclinical scanner. Med Phys 38: 4154–4165
86. W. Yao, K. W. Leszczynski (2009) An analytical approach to estimating the first order x-ray scatter in heterogeneous medium. Med Phys 36: 3145–3156
87. M. S. Judenhofer, C. Catana, B. K. Swann, et al. (2007) Simultaneous PET/MR images, acquired with a compact MRI compatible PET detector in a 7 Tesla magnet. Radiology 244: 807–814
88. M. S. Judenhofer, H. F. Wehrl, D. F. Newport, et al. (2008) Simultaneous PET-MRI: a new approach for functional and morphological imaging. Nat Med 14: 459–465
89. C. Catana, D. Procissi, Y. Wu, et al. (2008) Simultaneous in vivo positron emission tomography and magnetic resonance imaging. Proc Natl Acad Sci U S A 105: 3705–3710
90. S. H. Maramraju, S. D. Smith, S. S. Junnarkar, et al. (2011) Small animal simultaneous PET/MRI: initial experiences in a 9.4 T microMRI. Phys Med Biol 56: 2459–2480
91. H. F. Wehrl, M. S. Judenhofer, A. Thielscher, et al. (2011) Assessment of MR compatibility of a PET insert developed for simultaneous multiparametric PET/MR imaging on an animal system operating at 7 T. Magn Reson Med 65: 269–279
92. S. Yamamoto, T. Watabe, H. Watabe, et al. (2012) Simultaneous imaging using Si-PM-based PET and MRI for development of an integrated PET/MRI system. Phys Med Biol 57: N1–N13
93. H. Zaidi (2007) Is MRI-guided attenuation correction a viable option for dual-modality PET/MR imaging? Radiology 244: 639–642
94. M. Hofmann, B. Pichler, B. Schölkopf, T. Beyer (2009) Towards quantitative PET/MRI: a review of MR-based attenuation correction techniques. Eur J Nuc Med Mol Imaging 36: S93–S104
95. H. Zaidi, A. Del Guerra (2011) An outlook on future design of hybrid PET/MRI systems. Med Phys 38: 5667–5689
96. M.-L. Montandon, H. Zaidi (2005) Atlas-guided non-uniform attenuation correction in cerebral 3D PET imaging. Neuroimage 25: 278–286
97. A. J. Chaudhari, A. A. Joshi, A. W. Toga, et al. (2009) Atlas-based attenuation correction for small animal PET/MRI scanners, IEEE Nuclear Science Symposium & Medical Imaging Conference, 25–31 October 2009, Orlando (FL), USA, *unpublished*.
98. E. Schreibmann, J. A. Nye, D. M. Schuster, et al. (2010) MR-based attenuation correction for hybrid PET-MR brain imaging systems using deformable image registration. Med Phys 37: 2101–2109

99. M. Hofmann, I. Bezrukov, F. Mantlik, et al. (2011) MRI-based attenuation correction for whole-body PET/MRI: Quantitative evaluation of segmentation- and Atlas-based methods. J Nucl Med 52: 1392–1399
100. O. Rousset, H. Zaidi: Correction of partial volume effects in emission tomography. In Quantitative analysis of nuclear medicine images. H. Zaidi, Ed. Springer, New York, 2006. pp 236–271
101. M. Soret, S. L. Bacharach, I. Buvat (2007) Partial-volume effect in PET tumor imaging. J Nucl Med 48: 932–945
102. O. Rousset, A. Rahmim, A. Alavi, H. Zaidi (2007) Partial volume correction strategies in PET. PET Clinics 2: 235–249
103. C. Kuntner, A. L. Kesner, M. Bauer, et al. (2009) Limitations of small animal PET imaging with [18F]FDDNP and FDG for quantitative studies in a transgenic mouse model of Alzheimer's disease. Mol Imaging Biol 11: 236–240
104. N. Aide, C. Desmonts, J. M. Beauregard, et al. (2010) High throughput static and dynamic small animal imaging using clinical PET/CT: potential preclinical applications. Eur J Nucl Med Mol Imaging 37: 991–1001
105. M. Tatsumi, C. Cohade, Y. Nakamoto, R. L. Wahl (2003) Fluorodeoxyglucose uptake in the aortic wall at PET/CT: possible finding for active atherosclerosis. Radiology 229: 831–837
106. M. D. Seemann, R. Beck, S. Ziegler (2006) In vivo tumor imaging in mice using a state-of-the-art clinical PET/CT in comparison with a small animal PET and a small animal CT. Technol Cancer Res Treat 5: 537–542
107. A. Helisch, O. Thews, H.-G. Buchholz, et al. (2010) Small animal tumour imaging with MRI and the ECAT EXACT scanner: application of partial volume correction and comparison with microPET data. Nucl Med Commun 31: 294–300
108. E. J. Hoffman, S. C. Huang, M. E. Phelps (1979) Quantitation in positron emission computed tomography: 1. Effect of object size. J Comput Assist Tomogr 3: 299–308
109. R. M. Kessler, J. R. Ellis, M. Eden (1984) Analysis of emission tomographic scan data: limitations imposed by resolution and background. J Comput Assist Tomogr 8: 514–522
110. L. Geworski, B. O. Knoop, M. L. de Cabrejas, W. H. Knapp, D. L. Munz (2000) Recovery correction for quantitation in emission tomography: a feasibility study. Eur J Nucl Med 27: 161–169
111. N. Aide, M. H. Louis, S. Dutoit, et al. (2007) Improvement of semi-quantitative small-animal PET data with recovery coefficients: A phantom and rat study. Nucl Med Commun 28: 813–822
112. W. Lehnert, M. C. Gregoire, A. Reilhac, S. R. Meikle (2012) Characterisation of partial volume effect and region-based correction in small animal positron emission tomography (PET) of the rat brain. Neuroimage 60: 2144–2157
113. L. Arhjoul, O. Sarrhini, M. Bentourkia (2006) Partial volume correction using continuous wavelet technique in small animal PET imaging, IEEE Nuclear Science Symposium Conference Record Vol. 5; pp 2717–2721
114. A. E. Spinelli, D. D'Ambrosio, G. Fiacchi, et al. (2008) Pixel-based partial volume correction of small animal PET images using Point Spread Function system characterization: Evaluation of effects on cardiac output, perfusion and metabolic rate using parametric images, IEEE Nuclear Science Symposium Conference Record, pp 4260–4265.
115. D. D'Ambrosio, G. Fiacchi, P. Cilibrizzi, et al. (2008) Partial volume correction of small animal PET cardiac dynamic images using iterative reconstruction: effects on glucose metabolic rate measurement, Proc. Conf. Computers in Cardiology, pp 1093–1096.
116. T. Dumouchel, R. A. deKemp (2011) Analytical-based partial volume recovery in mouse heart imaging. IEEE Trans Nucl Sci 58: 110–120
117. T. Dumouchel, S. Thorn, M. Kordos, et al. (2012) A three-dimensional model-based partial volume correction strategy for gated cardiac mouse PET imaging. Phys Med Biol 57: 4309–4334
118. Y. H. Fang, R. F. Muzic, Jr. (2008) Spillover and partial-volume correction for image-derived input functions for small-animal 18F-FDG PET studies. J Nucl Med 49: 606–614

119. K. H. Su, J. S. Lee, J. H. Li, et al. (2009) Partial volume correction of the microPET blood input function using ensemble learning independent component analysis. Phys Med Biol 54: 1823–1846
120. J. G. Mannheim, M. S. Judenhofer, A. Schmid, et al. (2012) Quantification accuracy and partial volume effect in dependence of the attenuation correction of a state-of-the-art small animal PET scanner. Phys Med Biol 57: 3981–3993
121. A. Le Pogam, M. Hatt, P. Descourt, et al. (2011) Evaluation of a 3D local multiresolution algorithm for the correction of partial volume effects in positron emission tomography. Med Phys 38: 4920–4923
122. R. Carson. Tracer kinetic modeling in PET (2003). In Positron Emission Tomography: Basic Science and Clinical Practice**.** P. E. Valk, D. L. Bailey, D. W. Townsend, M. N. Maisey, Eds. Springer-Verlag, London, pp 147–179
123. M. h. Bentourkia, H. Zaidi (2007) Tracer kinetic modeling in PET PET Clinics 2: 267–277
124. Y. Su, K. I. Shoghi (2008) Wavelet denoising in voxel-based parametric estimation of small animal PET images: a systematic evaluation of spatial constraints and noise reduction algorithms. Phys Med Biol 53: 5899–5915
125. P. Dupont, J. Warwick (2009) Kinetic modelling in small animal imaging with PET. Methods 48: 98–103
126. T. Hideo, S. Nishiyama, T. Kakiuchi, et al. (2001) Ketamine alters the availability of striatal dopamine transporter by [11C]ß-CFT and 11C]ß-CIT-FE in the monkey brain. Synapse 42: 273–280
127. T. Mauxion, J. Barbet, J. Suhard, et al. (2013) Improved realism of hybrid mouse models may not be sufficient to generate reference dosimetric data. Med Phys 40: 052501–11
128. T. Xie, H. Zaidi (2013) Effect of emaciation and obesity on small animal internal radiation dosimetry for positron-emitting radionuclides. Eur J Nucl Med Mol Imaging 40: 1748–1759
129. T. Xie, H. Zaidi (2013) Assessment of S-values in stylized and voxel-based rat models for positron-emitting radionuclides. Mol Imaging Biol 15: 542–551
130. H. M. Wu, G. Sui, C. C. Lee, et al. (2007) In vivo quantitation of glucose metabolism in mice using small-animal PET and a microfluidic device. J Nucl Med 48: 837–845
131. L. Convert, F. G. Baril, V. Boisselle, et al. (2012) Blood compatible microfluidic system for pharmacokinetic studies in small animals. Lab Chip 12: 4683–4692
132. S. Gambhir, M. Schwaiger, S. Huang, et al. (1989) Simple noninvasive quantification method for measuring myocardial glucose utilization in humans employing positron emission tomography and fluorine-18 deoxyglucose. J Nucl Med 30: 359–366
133. G. Germano, B. Chen, S. Huang, et al. (1992) Use of the abdominal aorta for arterial input function determination in hepatic and renal PET studies. J Nucl Med 33: 613–620
134. P. T. Meyer, V. Circiumaru, C. A. Cardi, et al. (2006) Simplified quantification of small animal [18F]FDG PET studies using a standard arterial input function. Eur J Nucl Med Mol Imaging 33: 948–954
135. F. Hermansen, A. A. Lammertsma (1996) Linear dimension reduction of sequences of medical images: III. Factor analysis in signal space. Phys Med Biol 41: 1469–1481
136. R. N. Gunn, S. R. Gunn, V. J. Cunningham (2001) Positron emission tomography compartmental models. J Cereb Blood Flow Metab 21: 635–652
137. J. Ahn, D. Lee, J. Lee, et al. (2001) Quantification of regional myocardial blood flow using dynamic H2(15)O PET and factor analysis. J Nucl Med 42: 782–787
138. H. Wu, S. Huang, V. Allada, et al. (1996) Derivation of input function from FDG-PET studies in small hearts. J Nucl Med 37: 1717–1722
139. M. Naganawa, Y. Kimura, T. Nariai, et al. (2005) Omission of serial arterial blood sampling in neuroreceptor imaging with independent component analysis. Neuroimage 26: 885–890
140. S. Yamamoto, K. Tarutani, M. Suga, et al. (2001) Development of a phoswich detector for a continuous blood-sampling system. IEEE Trans Nucl Sci 48: 1408–1411
141. F. Pain, P. Laniece, R. Mastrippolito, et al. (2004) Arterial input function measurement without blood sampling using a beta-microprobe in rats. J Nucl Med 45: 1577–1582

142. R. Laforest, T. L. Sharp, J. A. Engelbach, et al. (2005) Measurement of input functions in rodents: challenges and solutions. Nucl Med Biol 32: 679–685
143. C. Casteels, P. Vermaelen, J. Nuyts, et al. (2006) Construction and evaluation of multitracer small-animal PET probabilistic atlases for voxel-based functional mapping of the rat brain. J Nucl Med 47: 1858–1866
144. D. J. Rubins, W. P. Melega, G. Lacan, et al. (2003) Development and evaluation of an automated atlas-based image analysis method for microPET studies of the rat brain. Neuroimage 20: 2100–2118
145. A. L. Kesner, M. Dahlbom, S. C. Huang, et al. (2006) Semiautomated analysis of small-animal PET data. J Nucl Med 47: 1181–1186
146. W. P. Segars, B. M. Tsui, E. C. Frey, G. A. Johnson, S. S. Berr (2004) Development of a 4-D digital mouse phantom for molecular imaging research. Mol Imaging Biol 6: 149–159
147. B. Dogdas, D. Stout, A. F. Chatziioannou, R. M. Leahy (2007) Digimouse: a 3D whole body mouse atlas from CT and cryosection data. Phys Med Biol 52: 577–587
148. R. Taschereau, P. L. Chow, A. F. Chatziioannou (2006) Monte Carlo simulations of dose from microCT imaging procedures in a realistic mouse phantom. Med Phys 33: 216–224
149. A. Bitar, A. Lisbona, P. Thedrez, et al. (2007) A voxel-based mouse for internal dose calculations using Monte Carlo simulations (MCNP). Phys Med Biol 52: 1013–1025
150. M. G. Stabin, T. E. Peterson, G. E. Holburn, M. A. Emmons (2006) Voxel-based mouse and rat models for internal dose calculations. J Nucl Med 47: 655–659
151. L. Wu, G. Zhang, Q. Luo, Q. Liu (2008) An image-based rat model for Monte Carlo organ dose calculations. Med Phys 35: 3759–3764
152. P. H. Peixoto, J. W. Vieira, H. Yoriyaz, F. R. Lima (2008) Photon and electron absorbed fractions calculated from a new tomographic rat model. Phys Med Biol 53: 5343–5355
153. G. Zhang, T. Xie, H. Bosmans, Q. Liu (2009) Development of a rat computational phantom using boundary representation method for Monte Carlo simulation in radiological imaging. Proceedings of the IEEE 97: 2006–2014
154. H. Zaidi, X. G. Xu (2007) Computational anthropomorphic models of the human anatomy: The path to realistic Monte Carlo modeling in medical imaging. Annu Rev Biomed Eng 9: 471–500
155. H. Zaidi, B. M. W. Tsui (2009) Computational anthropomorphic anatomical models. Proceedings of the IEEE 97: 1935–1937
156. D. F. Gutierrez, H. Zaidi (2012) Automated analysis of small animal PET studies through deformable registration to an atlas. Eur J Nucl Med Mol Imaging 39: 1807–1820
157. R. Maroy, R. Boisgard, C. Comtat, et al. (2010) Quantitative organ time activity curve extraction from rodent PET images without anatomical prior. Med Phys 37: 1507–1517
158. A. Rahmim, O. Rousset, H. Zaidi (2007) Strategies for motion tracking and correction in PET. PET Clinics 2: 251–266
159. A. Z. Kyme, V. W. Zhou, S. R. Meikle, C. Baldock, R. R. Fulton (2011) Optimised motion tracking for positron emission tomography studies of brain function in awake rats. PLoS One 6: e21727
160. A. Kyme, S. Meikle, C. Baldock, R. Fulton (2012) Tracking and characterizing the head motion of unanaesthetized rats in positron emission tomography. J R Soc Interface 9: 3094–3107
161. R. Laforest, X. Liu (2009) Cascade removal and microPET imaging with 76Br. Phys Med Biol 54: 1503–1531
162. X. Liu, R. Laforest (2009) Quantitative small animal PET imaging with nonconventional nuclides. Nucl Med Biol 36: 551–559

Chapter 18
Animal Handling and Preparation for Imaging

David B. Stout

1 Introduction

Molecular Imaging refers to observations and measurements of molecular processes in living cells or animals [1]. Anything that alters physiological processes can change molecular pharmokinetics (PK) and pharmodynamics (PD), thus these factors are important to understand, control or eliminate wherever possible. Even with in-vitro or ex-vivo measurements, the environment during formation of the molecular target and conditions during exposure to the imaging probe may alter the experimental results. The capacity for biological systems to modify themselves, sometimes very quickly, means that the biological status is a potentially changeable condition.

In-vivo physiology can be influenced by a wide range of factors, including anesthetic agent, animal and room temperature, injection method and time of day [2]. These in turn can influence the specific accumulation and clearance of imaging agents and any endogenous background signals. In many cases it is possible to control these parameters, reducing or eliminating their effect on imaging experiments.

In addition to physiology, there are physical parameters that can be optimized to ensure the best possible data from the imaging systems. In most imaging devices there is a particular region where sensitivity or resolution may be highest, such as the center of a SPECT, PET or CT scanner. There are also times when sequential serial or longitudinal imaging may be useful, thus a fixed position for animals or cells can be quite useful. A positioning system ensures both optimal acquisition of image data, and also often aides in the subsequent data analysis.

D.B. Stout (✉)
Department of Molecular and Medical Pharmacology, University of California, Los Angeles, CA, USA
e-mail: davidstoutphd@gmail.com

H. Zaidi (ed.), *Molecular Imaging of Small Animals: Instrumentation and Applications*,
DOI 10.1007/978-1-4939-0894-3_18,

This chapter will discuss the various factors that can alter in vivo physiology and imaging probe signal, background and contrast between signal and background. Potential solutions for reducing physiological variability and the resulting impact on imaging experiments are described, along with the use of contrast agents for CT imaging.

2 Anesthesia

Molecular imaging systems are much like photographic cameras, in that they require a certain amount of time to collect data to form an image. It may take seconds or hours, and the systems may be tolerant or intolerant of motion during the imaging process. For example, current PET imaging systems have resolutions of 1–2 mm, so movements less than this distance might not seriously change the results. Some optical imaging systems can tolerate some amount of movement since light scatter substantially blurs the detected signal. Other systems such as MRI and CT, or high resolution SPECT, may not produce useful data at all if there is much movement of the animal. The tolerance for movement is set by the resolution, with high resolution imaging requiring little if any motion during data collection. In order to acquire high quality images, anesthesia is normally used to immobilize the animals. While anesthesia eliminates motion from the animals moving around, it does not stop cardiac or respiratory motion, which will be addressed in a later section.

Two types of anesthesia are used: injected and gas. Injected anesthetics such as pentobarbital, ketamine, midazolam and xylazine are controlled substances that require careful tracking, security and prescriptions, primarily because most are also drugs of abuse that alter the dopaminergic system. It is worth noting that if one wishes to study the dopaminergic system, it is important to understand the effects of anesthesia on the neuronal circuitry being investigated [3]. Injected anesthetics have a decided advantage, in that the only requirements are a syringe, needle and bottle of anesthetic. No other equipment is required to use injected anesthetics. This is particularly important for working with larger animals such as non-human primates, where in most cases gas cannot be safely used for the induction of anesthesia.

There are multiple disadvantages to injected anesthetics. Pentobarbital is very long lasting, which is both good and bad, since full recovery could take a long time, though this might be useful for long imaging sessions. Ketamine and xylazine are relatively short lasting, with some agents such as propofol very short lived, so these agents often require multiple injections or constant infusion. This can lead to a variable depth of anesthetic state, which also means variable physiology during imaging [4]. It may be difficult to inject additional anesthesia during imaging, and the right amount of additional dose may not be easy to determine. While it is possible to infuse injected anesthetics, it may be troublesome to titer the dose properly over time. Injected anesthetics also can easily lead to overdose, particularly with inexperienced personnel who are not at ease and adept with handling animals. The lethal dose is in most cases not much more than the amount required for deep

Fig. 18.1 *Left image*: wall mounted gas anesthesia system with manifold supplying isoflurane to multiple sites of use. *Right*: heated induction box with simple on/off gas control

anesthesia. There is also no way to recover from an accidental overdose if too much is injected. Despite these difficulties, injected anesthetics are commonly used and both safe and effective when used correctly.

Inhalant or gas anesthesia is the preferred method of keeping animals from moving for most molecular imaging research. Most common in use today is isoflurane, although there is increasing interest in using sevoflurane as it appears to have less effect on glucose levels in blood, which may be important for FDG imaging using PET [5]. Inhalant anesthetics have the advantage of creating a constant level of anesthesia that lasts as long as required, and it is less likely to kill animals by overdose. If the anesthesia setting is too high and the animal begins to have labored breathing, turning down the amount of anesthesia can quickly bring the animal back to a more appropriate respiratory rate. Both heart and respiratory rates are different between species and even between animal strains, so knowledge of what is normal is required to determine the optimal rates. Animals also recover very quickly from gas anesthesia, thus having less physiological impact, which may be important if animals are being imaged frequently. In addition to being safe, quick and effective, gas anesthetics are also readily available and are currently not controlled substances in the United States. Inhalant anesthetics can be used with induction boxes (Fig. 18.1), nose cones and through intubation either with our without ventilation. There is no need for analgesia and often the breathing rate remains much higher than with injected anesthetics.

Given that anesthetics alter animal physiology [5], there is considerable interest to image without anesthesia. In some cases this may mean restraining the conscious animals [6], or perhaps letting them roam free and tracking the movement [7]. One group has gone so far as building a miniature camera that is mounted on the animal [8]. A few groups have gone to great lengths to train animals to hold still during imaging, which provides interesting and valuable information, but at great cost in resources to train animals [9]. Other systems allow mice to roam freely and provide a video signal of optical signals [10]. Although the majority of molecular imaging in animals will continue to use anesthesia, conscious studies will always have an important role and may well expand as new ideas and imaging systems are developed.

The use of anesthesia is common in preclinical settings, yet rare in clinical settings. The impact on the physiology and probe signals may be profound and this

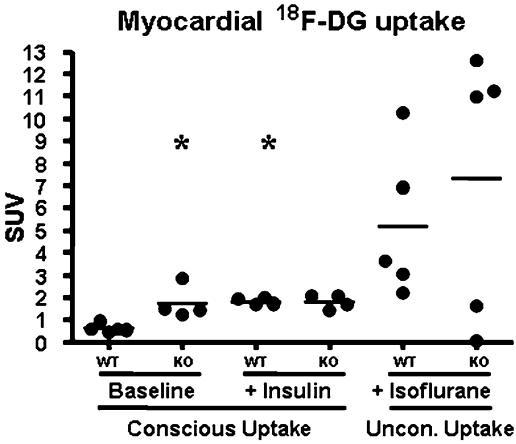

Fig. 18.2 Standardized uptake values (SUV) for FDG in mouse heart 60 min post-injection in both a wild type (wt) and insulin sensitivity knockout (ko) model. Right two columns show the high variability and increased heart uptake with the use of unconscious uptake under isoflurane. Stars indicate significant difference between mouse models (*left*) and wt baseline and wt insulin challenge (*right*)

represents a clear distinction between what may be observed in humans versus that seen in animals. One option is to use conscious injections and uptake time, followed by induction of anesthesia and immediate imaging. This is often referred to as conscious uptake, though it is followed by unconscious imaging. The idea is that the probe is already sequestered and the background activity eliminated, so that the signal and contrast levels are already set in place before the anesthetic agent is introduced. In some cases this has proven to be very successful, allowing signals to be seen that were otherwise masked by anesthetic effects, as shown in Fig. 18.2. The increased uptake of FDG using isoflurane during unconscious uptake masked the significance of the mouse knock-out model, which was observed by using conscious uptake (unpublished results). Note that with conscious uptake, not only was the heart uptake reduced, but the SUV variability was also substantially lower, making the differences between the mouse models and insulin status significant. One consideration with conscious work is that there may be stress related changes in the animal, leading to altered cortisone, glucose or other metabolic factors that can influence the experiment.

3 Temperature

Development of preclinical imaging systems with high resolution and sensitivity has enabled a shift from large to small animals for molecular imaging research. For example, the development of small animal PET systems such as microPET allowed researchers to move from primates, pigs, dogs and other larger species into working with rats and mice. There are tremendous advantages to using these rodents, including lower cost, they are not endangered, it is easy to work with many animals per day, they are easier to handle and housing larger numbers is possible in a small space. Perhaps the most important is that we know the genome and many different genetic knock out and knock in strains are available to study a wide range of diseases.

Animal supply vendors offer a huge range of mice with various genetic manipulations. One side effect of working with small animals is that temperature becomes a paramount issue to address since these small animals have little heat capacity.

With decreasing animal size, temperature control becomes increasingly important to regulate. Rodents are small, thus have relatively little thermal mass to maintain body temperature, especially when anesthetized. Anesthetized mice can quickly become hypothermic in as little as 5–6 min in a 20 °C room [11]. Larger species, such as primates or dogs, might not require heating during imaging, or might be sufficiently warmed using recirculating water baths or a heating blanket, though these systems provide little actual control over internal body temperature.

Biological systems are somewhat tolerant of low temperatures, with compensatory mechanisms to protect the animal's health. Surgeons sometimes take advantage of slowing physiological processes by chilling animals during surgery [12]. When cold, animals will divert blood flow from peripheral tissues to maintain core body temperature and this can cause the peripheral tumors to have significantly lower uptake, simply due to temperature [2]. Most work using tumors is focused on potential treatments and their effects, which is only confounded by variable uptake due to temperature changes. Frequently tumors are implanted in the shoulder region, which is well away from activity localizing in the bladder, GI and liver, however uptake of FDG in this region can be masked by high brown fat metabolism, as shown in Fig. 18.3. Given that mice thermoregulate by tail blood flow [13], it is especially important to keep animals warm if measurements or injections are going to make use of the tail vessels. In vivo metabolism is altered by hypothermia and can lead to variable or uncertain results depending on the conditions before and during uptake and imaging. There are also strain variations to consider, as different strains have differing responses to temperature, perhaps most obvious being nude mice, which do not have any insulating fur to help with temperature control [14].

Unlike lower temperatures, biological systems are rarely tolerant of high temperatures. Elevation of just 3–4 °C above normal is sufficient to denature proteins and cause heat shock [15]. For this reason, it is imperative that animals be carefully protected from overheating. Proper control requires monitoring of temperature to prevent overheating in any type of heating system. This is particularly important if the heating and sensing systems are separate, as would be the case if a thermocouple is used to sense the heat from a separate heating source. Thermocouples may work fine if the heating system is diffused before contact with the animal or well coupled to the heat source. One method that works well for certain cases is to use a resistive wire heating element, where the heat is applied and the temperature sensed by resistance from the same wire. This type of circuit enables precise control without overshooting the set point for the desired temperature. The precision and accuracy of control with resistive wire heating and quick equilibrium of animals to surrounding temperature also means that invasive thermocouple measurements are not necessary, saving cost, time and the potential to contaminate or damage the animals. Another heating method is the use of warmed air, often used with MRI systems. Air works well in a confined space such as the MRI gantry, however it does not carry much heat and can lead to dehydration over long usage times.

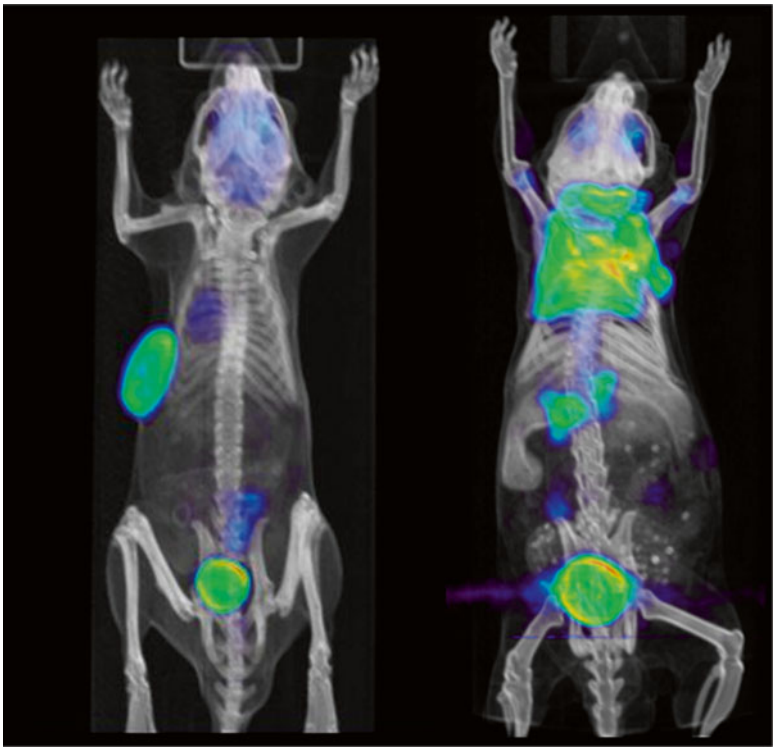

Fig. 18.3 PET/CT images of FDG uptake in a nude mouse. *Left* mouse is warmed prior to and during imaging, showing uptake in tumor and bladder. Mouse on *right* was not warmed and shows strong brown fat uptake in shoulder regions

4 Injection Methods

Animals can be injected using a variety of methods, from needles and catheters inserted into blood vessels, oral gavage, retro-orbital insertion and even by transdermal hypo spray [16]. Imaging agents are most commonly injected into the venous system via tail or leg veins (iv) or using intraperitoneal (ip) injections as shown in Fig. 18.3. Delivery can be as a single bolus pulse, or by infusion or sometimes is given as a bolus-infusion so as to reach a steady state in tissue [17]. The method used depends in the particular experiment and all have their advantages and disadvantages.

Tail vein injections are the most common with rodents, while other species such as rabbits have ear veins well suited for injections. Mouse blood vessels are very small, and many people struggle to inject imaging probes even in the readily accessible and visible tail vein. Venous injections are a quick and effective way to deliver imaging probes and contrast agents directly into the blood stream. Veins are often

Fig. 18.4 Injection methods commonly used; *Top Left*: Proper grip for holding mice, *Top right*: intraperitoneal injection, *Bottom left*: conscious tail vein, *Bottom right*: unconscious tail vein

near the surface of the skin and have thin walls and lower blood pressure, making them capable of distension to fit a comparatively large needle or catheter inside the vessel. Removal of the needle or catheter is not likely to cause any significant blood loss, unlike arterial punctures. Rats pose a bit more of a challenge for injection in the tail since the tough skin is relatively thick, so a small incision can help for getting good access to the tail vein.

Tail vein injections can be done under either conscious or unconscious conditions, as shown in the lower images of Fig. 18.4. Conscious injections require restraint, either by holding the animals or using a mouse holder. Awake animals have higher blood pressures, so vessels are easier to find, however animals often flinch when needles are inserted and this can cause difficulties with injections. Conscious injections can also cause stress in both the animal and investigator if there are any difficulties, mainly due to lack of experience. Unconscious uptake is challenging due to the lower blood pressure and reduced flow, but the advantage is that there is less stress, a sense of more time available and the tail can be heated to improve blood flow. The choice whether to use anesthesia for injections also depends on whether conscious uptake is needed to minimize the physiological effects of anesthesia (see Fig. 18.2).

With any tail vein injection, there is always a certain amount of extravasation, where some injection solution is left in the tissues surrounding the injection site.

This remaining solution is not bio-available through the bloodstream and usually should not be included when considering how much activity was injected into the animal. The amount can be trivial for a good injection, or quite substantial if the injection was not done properly. For this reason, it is much more accurate to image the entire body and calculate the activity within the animal based on the image data, rather than use the amount of activity drawn into the syringe. Using the image-based activity also avoids needing to calculate and convert injected activity or image count rate data into the same unit of measurement. One must be careful however when using images to calculate injected activity, since if the animal eliminates some of the activity through urine or feces, the image data will not be accurate. Other studies involving longer lived isotopes imaged over several days will require using the syringe-based activity measurement, unless images are acquired immediately following injection.

One limitation with the use of small animal such as mice is the small blood volume. The safe limit for either injection or removal of blood is about 10 % of the total volume, which for mice can mean a restricted volume of ~200 μl [18]. Removing more than this volume can leave mice anemic and alter the physiology in a variety of ways. Injecting too much volume can cause fluid buildup in the lungs and cause temperature shock if the injection solution is not warmed. The volume limitation may mean that the concentration of imaging agent used for humans is too dilute, so it may be necessary to concentrate the activity in order to have sufficient signal in a small volume.

Arterial blood is often preferred for sampling radioactivity over time, since it contains the activity presented to tissues for uptake. Venous blood has passed through the capillary bed and may contain less activity, metabolites or if the probe is first pass extracted, nothing at all. Arterial injections are sometimes useful, since the blood is directly delivered to any downstream tissues without first passing through the heart and lungs. The relatively thick muscle walls of arteries make it more difficult to penetrate without going through the far side of the vessel. The thicker walls also mean there is less distension of the vessel to accommodate a needle or catheter. One potential drawback of inserting an arterial catheter is that usually the artery needs to be cut and the catheter tied into place to prevent it slipping out over time. This means the artery is completely blocked and often tied off, thus there is no blood flow in the vessel except when sampling through the catheter. Cutting the artery is also usually considered a terminal experiment, so only a single use is possible for each animal.

Subcutaneous (subQ) and ip injections are very simple and relatively easy to do. If large numbers of animals are used, this is a quick efficient way to make sure animals are injected and makes it easy to stick to a schedule. Few probes are injected this way, in part because many may remain in place, or take considerable time for the lymphatic system to move the probe into the bloodstream. With ip injections, there is also the risk of puncturing the bowel or bladder, which may cause the probe to stay in the wrong region and can cause health problems for the animals. Nonetheless, if speed of delivery is not a crucial factor, these injection methods are the simplest and most reliable methods to inject animals, provided the imaging agent moves out of the skin or ip cavity and into the bloodstream.

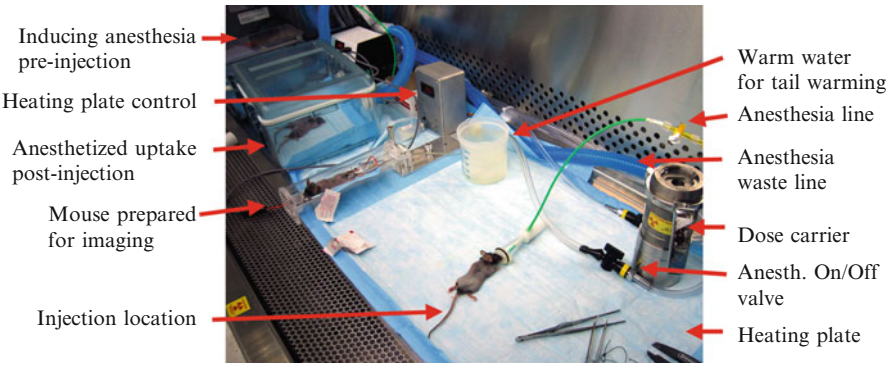

Fig. 18.5 Short imaging times following a period of uptake and clearance result in multiple mice at various stages of the injection and imaging process. This image shows mice in many stages, including anesthesia induction, injection, uptake and prepared for imaging

Retro-orbital injections or blood sampling is a method whereby the blood vessel rich area behind the eye is used to sample or insert imaging agents. While effective, this is hard to do inside an imaging system and often is restricted to only once every 2 weeks. The amount of volume that can be inserted or removed is very limited and blood sampling has the potential to cause infection and blindness. Similar to ip injections, in the hands of a skilled worker this technique can be done quickly and safely in large numbers of animals.

Oral gavage is a method where a syringe with a short tube is used to insert contrast agents, drugs and imaging probes directly to the stomach. Oral contrast delivery is needed for upper GI tract imaging using CT. Gavage subjects the drugs and probes to the digestive process, which may alter the molecules before they enter the bloodstream. In humans, taking drugs orally is the preferred method, primarily to avoid injections; therefore it is often useful to test out how well the compound gets into the bloodstream via the GI tract. There may also be a preference to use gavage for daily or frequent dosing, since it does not adversely damage the vascular system, which might be needed for injection of imaging agents.

Regardless of the injection method used, a well lit warm location is needed for injecting animals. Any support equipment required should be easily at hand, including alcohol wipes, needles and syringes, waste disposal containers, anesthesia control and a comfortable work environment. If immune compromised animals are in use (see section below), then the injection area is best located inside a biosafety cabinet, as shown in Fig. 18.5. This figure shows an experiment in process where animals are first anesthetized, then injected, then held under anesthesia for ~45 min, then placed into an imaging chamber for subsequent PET and CT imaging. At any one time, there may be up to eight animals in the process of being imaged, thus a well laid out and easy to use facility is essential given the challenging logistics of juggling so many tasks.

When mice are placed in an induction box and exposed to gas anesthesia, they tend to run around and get all mixed up, making it hard at times to keep track of

which animals have and have not been injected. Ear tags interfere with CT scans and animal marking tend to fade or may be hard to see, which can make it difficult to identify specific animals. This could easily lead to animals being injected twice or not injected at all. A simple solution is to have two induction boxes; one for animals being induced and a separate box for animals following injection. Since injected animals are already anesthetized, they do not move and can easily be laid out in the order in which they will be imaged. For conscious uptake studies, a separate clean cage for injected animals can be used to easily separate the animals; however careful marking will be needed to ensure that animals are imaged in the proper order. Simple, easy to follow solutions such as two induction boxes, simple on/off switches for heating and anesthesia, along with having all the necessary support equipment immediately on hand are the key to successful experiments.

5 Animal Access

During imaging experiments, usually animals are placed inside a space that is partially or completely enclosed. The enclosure may be present to keep out light (optical), contain radiation (CT) or the imaging detectors may be placed close to the animal to obtain the best possible image data (PET, SPECT, MRI). When imaging times are short, as with most optical methods, there may be little or no need to observe or otherwise have access to the animals. With longer imaging times, it is very important to observe the respiration and sometimes also heart rate to monitor the animal's physiological condition. These observations can be made by eye or by remote sensing systems (see section on gating below). Depth of anesthesia is something best checked every 10–15 min, both to ensure the animal is still alive and well, and to moderate the anesthesia dose. Typically the longer the animal is under anesthesia, the less anesthetic concentration is needed to keep the animal from moving. Depending on the heating system employed, monitoring of animal temperature may also be required.

Dynamic imaging is where animals are injected within the imaging system and imaged continuously for a period of time to observe changes in the probe biodistribution. This allows the fast temporal changes associated with delivery and early metabolism or elimination to be observed. Injecting within the imaging system is a task that may be simple or complex, depending on the ability to access the animal within the gantry. Direct injection using a needle is often extremely challenging in tight confined spaces, so most dynamic imaging is done using a short catheter inserted to a vein and connected to a syringe. The catheter has a certain volume based on the length and diameter of the tubing, termed the dead volume, which is not injected unless followed by a flush with saline. Often flushing is impractical, since it leads to a double-pulsed injection and it can be difficult to change syringes or have a switch that does not add its own considerable dead volume. In some cases a syringe pump can be used to inject the imaging agent; however it may be difficult

to have the pump close to the animal, leading to long catheter lines that may be filled with radioactivity. The dead volume in the syringe and tubing should be minimized to reduce radiation scatter and background, especially if they are left in place during imaging. Often it is best to leave the catheter in place after the injection; otherwise the pressure in the tubing and from the animal's blood pressure can cause blood and the injection fluid to drip or spill on the animal or surfaces within the imaging volume.

During the imaging time, it may be necessary to sample the blood to measure radioactivity, metabolites and blood concentrations of endogenous competitors to the imaging probes, such as glucose for FDG or thymidine for FLT. These endogenous molecules compete with the imaging probe for tissue uptake and may need to be measured to increase the accuracy of the measurements. As with injections, access to the animal for sampling can be challenging, especially in enclosed systems. If the animal is accessible, it may be possible to draw blood using catheters inserted before imaging or by nicking the tail vein and drawing off a small sample. A number of researchers have developed microfluidic sampling devices, which use a catheter to take small and sometimes frequent of continuous blood samples during the imaging process [19, 20].

When experiments last more than 60–90 min, it is advisable in mice to provide saline or Ringer's lactate to prevent dehydration. A simple method is to inject a small amount, ~100 μl, as a subQ injection between the shoulder blades just prior to imaging. Careful consideration is advised, since too much saline may lead to urination during imaging, which may cause artifacts or complicate the image analysis if the probe is excreted through the urine.

6 Circadian Rhythm Effects

It is well known that circadian rhythm alters the physiology of all animals [18], however the effect on imaging agents is not well understood. Rodents are nocturnal, thus imaging during the daytime when humans are active may have different results compared with imaging at night. Glucose levels, amino acid concentrations and even enzyme expression are known to follow a day/night cycle [18]. A simple way to avoid this is to conduct the experiments at approximately the same time of day when acquiring multiple measurements. Another alternative is to reverse the day/night cycle by changing the lighting sequence used within the vivarium.

In some cases, it appears that anesthesia may create an overriding physiological change, thus masking circadian effects [21]. While anesthesia may mask effects for FDG using PET, enzymatic expression cycles are less likely to be overridden since the time scale to change enzyme levels is longer than the glucose/insulin feedback cycle. This has implications for optical imaging using Luciferin/Luciferase, since work has shown substantial changes in enzyme expression based on time of day [22]. Research has shown that the cyclical nature of normal fluctuations of endogenous amino acids can alter PET probe uptake by competition for transport [23].

7 Reproducible Positioning and Multimodality Imaging

Most imaging systems have a central position within the field of view where resolution and/or sensitivity have the best values. The goal therefore is to put the area of interest to be imaged into this region, however there is often a trade-off if the goal is to survey the whole body or to examine two structures at once. One example is the desire to look at the brain for probe uptake, while at the same time imaging the heart to obtain image-based measurements of the left ventricular blood pool to use as an input function for kinetic modeling. For a mouse, the distance between brain and heart is small and it might not be a problem to see both regions, depending on the axial extent of the field of view. Often with brain imaging, the limited resolution in PET or SPECT requires the use of larger animals, such as a rats or small primates. Centering a rat between heart and brain may move both structures into positions of lower sensitivity and image quality, making the desired findings difficult to obtain. In this case, a series of multiple short acquisitions alternating over each structure might be a better option. Some systems also offer automated continuous bed motion, moving the animal back and forth between specified start and end positions, which can provide a more uniform sensitivity over the entire image [24].

For multimodality work involving two or more imaging methods, there are two types of positioning methods possible: single gantry and separate systems. A single gantry, or two systems rigidly connected together, requires only one positioning of the animal within an environmental support system. The animal is then imaged in the same location for both modalities or shuttled between imaging areas without removing the animal from the support or chamber. Shuttling of animals between positions is common for PET/CT, since the ring geometry of PET scanners does not easily allow space for the CT source and detectors, thus these two modalities are usually located adjacent to each other and require moving the animal from one location to another. The advantage with single gantry systems is that the animal is only placed in position once and in most cases the images can easily be co-registered from both systems. The best way to ensure that the animal position and physiological state is the same for both imaging modalities is to acquire simultaneous data, which is possible using SPECT/CT and PET/MRI systems. The disadvantage of a combined system is often little or no access to the animal for injections, blood sampling or monitoring of the animal's heart or breathing rate. This makes monitoring the health status of the animal difficult unless connected to heart and respiratory monitors. Although relatively easy to use monitoring systems are now available, their use adds to the complexity of the experiments and they may interfere with data acquisition. Electrical fields and more than tiny amounts of metal can cause artifacts in MRI and CT images.

The alternative option to an enclosed single gantry is the use of separate imaging systems, which requires the use of a common chamber or platform for animal support that can be used in both systems [11]. The advantage is that visibility and access can be very good for animals imaged in large bore PET systems, while the

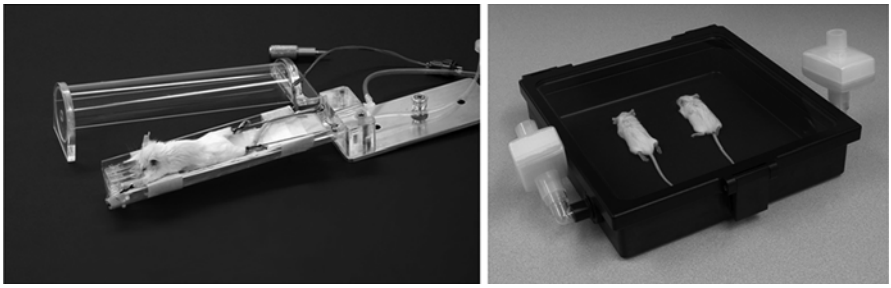

Fig. 18.6 Environmental chambers developed for PET/CT (*left*) and optical bioluminescence or fluorescent imaging (*right*)

limited access in an enclosed CT or MRI system may not be a problem if acquired after the PET scan. MRI and CT systems effectively isolate the animals from the investigators due to the long bore and shielding, however some PET and SPECT systems allow better access while imaging since they are not always completely enclosed. A trade off for PET and SPECT is that by bringing in the detectors closer to the animals, the sensitivity is improved and the system costs can be reduced. The choice of using a small or large bore PET scanner depends on the need for animal access or upon the availability of systems that enable monitoring and sampling using remote control.

Using separate systems can be challenging, since the animals must be accurately and most importantly be precisely placed within the systems in order to match the locations for the fused images. There is always the risk of changing the animal position during the move between imaging systems. A blind co-registration without using the image data to align the two image sets is often essential, since the anatomical information in CT and MRI may not have much, if anything, in common with the metabolic information within the SPECT or PET images. Coregistering the two image volumes, then using a fixed or known bed position for every scan allows the use of fixed reslice parameters to fuse the two images [25]. Another alternative is to use fiducial markers to align the images, however this may add unwanted signal within the data, be expensive or difficult to use routinely and adds complexity that might be avoided by using a well-designed chamber system. Fiducial markers also need to be replaced as the radioactivity source decays.

Several companies make imaging chambers and two examples are shown in Fig. 18.6. For 2D optical imaging, a flat surface is needed for the camera to see the light with minimal distortion. PET, CT and MRI work are best served with a rotationally symmetrical chamber to minimize any artifacts within the images. Chamber materials must be suitable for the particular modalities, such as non-phosphorescent for optical, no metal for CT, non-magnetic for MRI and low density for PET. Environmental support requirements typically require heating, positioning, anesthesia and temperature control, plus the ability to sterilize the surfaces.

8 Respiratory and Cardiac Gating

For some experiments, measurements of respiratory or cardiac motion may be desirable. Numerous systems are now available that can accurately monitor the relatively high heart and breathing rates found in rodents. Typical resting rates in mice can run as high as 600–700 beats per minute (bpm) [26]. Human and primate pulse oxymeters typically have a maximum of 250 bpm, thus are not suited for rodent work.

Heart and respiratory rates can be measured using several different physical means. Needles inserted under the skin have been used historically to provide electrocardiogram data. While this method works well, the presence of metal needles and wires may not be suitable for some imaging methods, such as MRI or CT. Carbon electrodes are a non-ferrous alternative, which are not magnetic and do not cause significant image artifacts in PET, CT and MRI images. Tail cuffs use a pressurized ring around the tail, however they are not well accepted by many investigators, mainly because tail blood flow is directly linked to mouse temperature and thus can be highly variable [13]. Perhaps the easiest system to use is a red light emitting diode and detector, used commonly for humans and primates. The light and sensor can be attached using spring clips, adhesive gauze, tape or other methods. Occasionally there can be problems getting a signal, especially when there is dark skin or too much light shining on the sensor, but this type of sensor is often very easy to use and provides good results without any invasive requirements.

The close link between anesthetic depth and respiratory rate means that the breathing rate needs to be monitored frequently and the anesthesia concentration changed as needed. This means that the breathing rate is not constant during an experiment, so a measurement system is needed that creates a signal for each breath and be recorded along with the image data. Similarly, the heart rate also changes with anesthetic depth.

Many imaging systems have the ability to accept heart rate and breathing data through an electrical connection. The signal can trigger acquisition of data, or be included into the data stream for later processing. Images can be created where the respiratory and/or heart cycle can be divided into multiple parts. Similar to dividing up time into a series of frames, the cycles can be divided into a series of gates, hence the term gated imaging. Dividing the data into separate gates results in larger data sets, and reduces the data events in each image. This may be important, since too many partitions of the data can result in very noisy and very large datasets. Under complete anesthesia sedation, the inhalation phase is about 1/4th or less of the respiratory cycle; so eight gates can describe the respiration motion reasonably well [27]. Light anesthesia can result in much more rapid breathing, as much as 2–3 per second, thus might require a finer sampling period. With deep anesthesia and little time spent in the inhalation phase, many people do not bother with respiratory gating as it may only provide minimal improvement in image data. The motion associated with breathing can be quite large if the animal is over anesthetized and exhibiting agonistic breathing, which is the gasping or large inhalation of air. Proper depth of anesthesia is therefore called for to reduce respiratory motion.

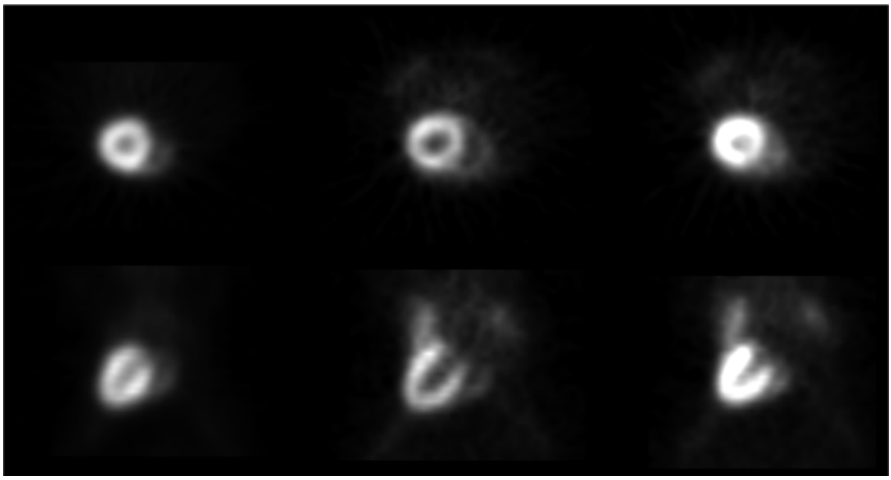

Fig. 18.7 Heart FDG images in a C57 mouse. *Top row*: transverse images of non-gated, diastole and systole. *Bottom row*: coronal view of the same data

Heart motion is fairly small, however gating can be used to separate systolic (contracted) from diastolic (relaxed) phases of the cardiac motion as seen in Fig. 18.7. Gating improves the visualization of both the cardiac wall and blood pools in the left and right ventricles and is particularly important for minimizing spillover and partial volume effect if the left ventricle blood pool is being used to derive the blood time activity data [28].

Unlike heart motion, respiratory motion can be controlled or eliminated by intubation and ventilation of the animals. A tube is inserted into the airway and a cuff inflated to block off any airflow around the tube. Using a pump, either air, oxygen or other gas mixtures can be forced in and out of the lungs. This approach enables controlled respiratory motion. The ventilation unit can trigger imaging, where data can be acquired during breath hold or at specific phases of the respiratory cycle. One interesting approach is high frequency oscillatory ventilation, where the equipment can bring in fresh gas and remove carbon dioxide without moving the animal at all [29]. This unique approach offers continuous ventilation without motion, which can be useful for long imaging times. The short tubing and magnetic pump does create some difficulties for use in certain imaging systems.

9 Immune Compromised Animals

Oncology research has greatly benefited from the creation of mice missing part or all of their immune system, which enables human tumors to be implanted and grown without rejection by the mouse immune system [30]. Nude hairless mice and rats are missing the thymus and ability to produce T cells. Severely compromised

immune deficient or SCID mice also do not have a thymus and additionally are unable to create B cells and have a defect in chromosome 16 that inactivates the DNA repair mechanism. Given the partial or complete lack of immune function, these animals are subject to illness unless protected under barrier conditions from environmental pathogens. These animals pose a special challenge to molecular imaging, since it is advisable to maintain the barrier conditions throughout all steps of the imaging process.

One option to control pathogen exposure is to have all the imaging work conducted in a clean environment, such as biosafety level 3 (BSL3) conditions or a clean room. This poses a challenge since humans have to carefully garb and contain themselves, plus it is difficult to disinfect the imaging systems between groups of animals. Service contract costs can become extremely expensive in BSL3 conditions and access for system repairs may be a problem for service personnel who visit multiple sites. BSL3 conditions may be required for infective and dangerous agents; however immune compromised animals need only be protected from exposure to pathogens if they do not contain biohazardous or carcinogenic agents.

Recently the author's university changed policy to reclassify human tumor xenografts from BSL1 to BSL2, which now requires additional safety requirements for housing and handling of these animals. The potential presence of biohazards such as herpes, AIDS or other blood borne pathogens, while perhaps not a threat to rodents, does represent a hazard to personnel handling these tissues. There is no widespread consistent interpretation about how xenograft tissues are treated, thus the requirements may differ concerning acceptable handling and environmental controls required. In some cases, the requirement of BSL2 conditions may require considerable and impractical changes to how things might have been done under BSL1. There are also AAALAC accreditation requirements that specify separate storage of BSL1 and BSL2 animals, which depending on the housing situation might be simple or very difficult to implement.

For immunocompromised work, a simpler solution is to contain the animals within imaging chambers (see Fig. 18.5) [11]. Animals can be handled, injected and prepared within biosafety cabinets, then imaged using sealed or positive pressure chambers. There are additional advantages of using chambers beyond pathogen control, including the ability to control heating, reproducibly position animals, ability to provide a constant level of gas anesthesia and providing a platform for imaging in multiple modalities.

10 Biohazardous and Infective Work

Unlike immune compromised research, where positive pressure is necessary to keep animals safe from the environment, animals containing biohazardous, carcinogenic or infectious agents must be isolated to protect people. These procedures require sealed or negative pressure containment. If the chambers are sealed and a BSL3 room is located nearby, it may be possible to assemble animals containing infectious,

carcinogenic or other biohazardous materials into chambers, disinfect the outside of the chamber, and conduct the imaging experiment in a BSL1 or BSL2 imaging facility. This approach allows the imaging systems to remain in an open environment and removes the need to disinfect the systems between different types of use.

Animals of different biosafety levels might not be allowed to be mixed together in the same space, which can cause some difficulty with housing, procedure areas and imaging. Chambers and separate preparation rooms may allow for multiple types of use; however the facility design and protocols for imaging work must be carefully determined to ensure this type of mixed use is allowed. It may be necessary to have separate housing and procedure spaces to enable the flexibility of imaging multiple types of biohazardous agents. Alternately, BSL1 animals might be allowed in a BSL2 environment if treated as if they were BSL2 level animals.

The creation of genetically altered animals often makes use of viral vectors for inserting genetic material [31]. These vectors are usually replicate incompetent; however they still require isolation and treatment as if they were infective for several days, depending on the viral agent. Many of the chemotherapeutic agents used to treat cancer are actually carcinogenic, thus are biohazardous agents and require special handling for injections and animal storage. Even though the amount of drug used is miniscule and large quantities are put into patients every day, protection strategies are required to keep personnel safe from exposure. In some cases microisolator cages can be used to house carcinogenic and biohazardous animals in a common vivarium with uninfected animals. More often however there is a requirement that these animals be kept isolated in a separate space, necessitating an additional room for housing. The procedures area where the viral vectors and biohazardous materials are used will require a ducted fume hood or biosafety cabinet, controlled access to the room and usage requirements equal to or greater than biosafety level 2 containment requirements.

11 Contrast Agents

In a broad sense, any imaging agent can be considered a contrast agent, since it is the difference between a specific signal and the background or reference tissue that provides the measured value. More commonly, contrast agents are defined as the agents used to distinguish anatomical structures when imaging with an anatomical system such as MRI or CT. For MRI, Gadolinium, Manganese and Iron are frequently used to give positive contrast in T1 images, while superparamagnetic iron oxides are used to create negative contrast. In CT, Iodine or Barium are used to create a higher density to visualize blood vessels and blood flow rates.

Preclinical imaging using CT poses a challenge when contrast agents are needed, as imaging can take from many seconds up to hours to acquire the data. Human CT systems and angiography studies are very rapid, requiring times of only a few seconds. In humans, contrast agents are injected rapidly at high concentrations and last only a few seconds. There is little persistence of the agents as they are quickly

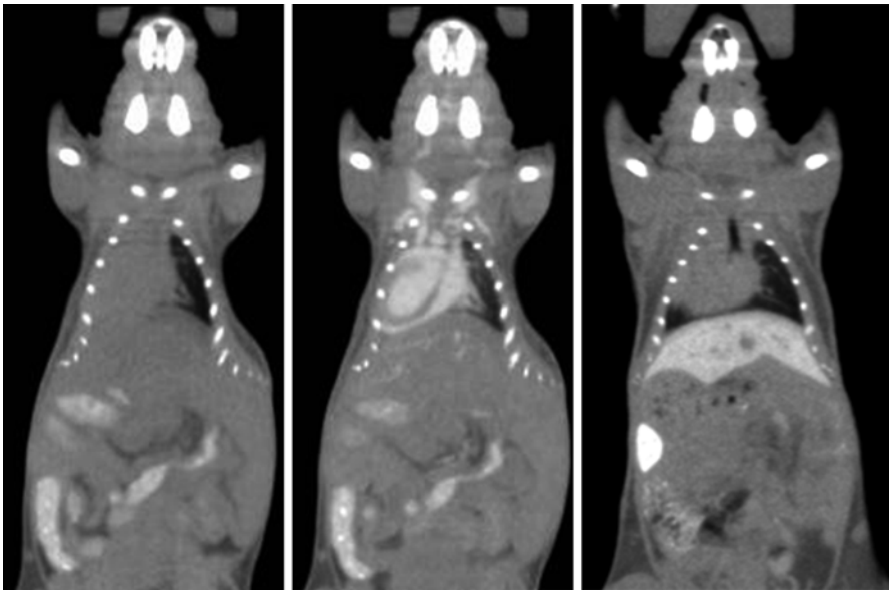

Fig. 18.8 Mouse CT images with no contrast (*left*), vascular Fenestra VC (*middle*) 10 min after a 100 µl injection and Fenestra LC showing liver and spleen (*right*) at 10 mg/kg after 2 h uptake

diluted and stop being useful very quickly. The long imaging times for preclinical systems mean that commercially available CT contrast agents for humans are unlikely to work for preclinical experiments. Fortunately, a number of long lasting agents are now available, which include Fenestra [32] and Exia [33], both of which have been characterized in mice. These agents are liposome encapsulated iodine agents, which depending on the surface treatment can target liver and spleen or remain in the vascular system, as seen in Fig. 18.8.

Care is required in the use of these CT agents, as the temperature and rate of injection can adversely affect the animals. At high concentrations these agents can be toxic, thus it is advisable to use only enough to achieve the desired minimum contrast in the images, typically 100 µl or at most 200 µl. Given that these agents last hours or days, and may require some time to reach peak effectiveness, a slow injection over a minute or two is much safer than a fast bolus injection. CT contrast agents have rather limited applications and are not currently in widespread use.

12 Diet

What animals are fed and when they eat can alter the images obtained using various modalities. With CT, there are often small bits of metal in the chow pellets, which come from the grinding process of the feed stock processing. These particles may also

affect MRI studies. The chlorophyll that makes rodent chow green is also a natural fluorophore, thus adds a signal when imaged using fluorescence optical methods. Switching to a chlorophyll free diet has been shown to eliminate the signal associated with chow, leaving the GI tract and abdominal area with a lower background signal and improving the ability to see fluorescent signals in these regions [34].

Fluorodeoxyglucose, FDG, is a frequently used PET imaging probe that is taken up by glucose transporters and phosphorylated by the hexokinase enzyme. Endogenous glucose competes with FDG for uptake, thus the amount of FDG signals is inversely proportional to glucose levels in blood [35]. Glucose levels are in turn linked to both time of day and feeding cycles [18], thus the fasting state of the animals will alter glucose and FDG uptake measurements. A special case is present with cardiac imaging, where the heart preferentially uses glucose, but under fasting conditions can switch to fatty acids as an energy source. Fasting the animals can actually turn off the heart FDG uptake [36], and also lower tumor signals [2, 37]. This may be a benefit for pulmonary work, but could be a detriment for cardiac imaging. For this reason, it is important to measure glucose levels in animals when imaging with FDG, so the image data can be normalized for endogenous glucose levels to remove some of the measurement variability. Mouse plasma glucose concentrations average about 100 mmol/l [18], however stress and other factors can easily triple this concentration, leading to substantial changes in FDG uptake.

Many imaging probes are taken up by transporter systems and are subsequently phosphorylated or metabolized into a molecule that is trapped in tissue, creating a signal as the uptake occurs and the background activity is washed away. Any endogenous molecules that would normally use those transporters and enzyme pathways would compete for the probe, thus changes in their concentrations would inversely affect probe uptake. One example is the competition of FDOPA for uptake into the brain with the plasma large neutral amino acid concentrations [23]. These amino acids vary based on diet and time of day. Another PET imaging probe subject to this effect is fluoro-L-thymidine (FLT), which is an amino acid analog subject to the same large neutral amino acid transport system as FDOPA.

13 Database and Archival Strategies

Images are only pretty pictures, unless provided with information about what they contain. Details of the imaging process need to be recorded and archived, such as the probe used, injection time and amount, processing details, anesthesia parameters, glucose levels and other associated meta data. By including information such as the people involved, time required, investigator name, recharge numbers, animal and radiation use authorizations, the database can be used to track usage and generate reports for radiation and animal use, billing statements and allows tracking of the operations within an imaging center. If web based, then investigators can be given password protected access to this data, enabling them to call up records from their lab on any computer. Web-based systems are also useful for viewing and modeling kinetic rate constants [38].

Tracking image data can be fairly simple by using a unique session identification number, which can be generated by many methods, from a simple table in a spreadsheet to a web-based database system. It may also be helpful to create animal identification numbers, since each animal may be imaged multiple times. The creation of a data record to be filled out as the imaging experiment progresses is often one of the first steps in starting an experiment.

An archival strategy is essential for an imaging center, regardless of how the data is stored. Imaging systems typically have a single hard drive for collecting data that does not have any redundancy for data preservation if the drive fails. Computer systems can also slow down considerably as the hard drive becomes full. Best transfer times and least chance of data loss can be achieved by archiving data and emptying the acquisition computer drives each day.

Several options exist for storing and retrieving data, which include a web-based retrieval system, network storage drives, DVDs, USB drives, tape and external hard drives. However the data is stored, a process to track, create, store and retrieve the data is necessary. Using the web or network via ftp server is a convenient way to enable the users of the center to obtain their data from any location for local processing. It also prevents any loss of data or physical archival media, since nothing physical is exchanged. The archival site can also be used to make software for image analysis easily available to investigators.

14 Summary

How animals are injected, handled and imaged has a profound effect on the resulting data, thus it becomes imperative that care is taken to minimize, measure or control these factors. While the array of factors and options might appear overwhelming, once these issues are understood, it is relatively straightforward to create an environment and procedures optimized to support the creation of the best possible data. Most imaging work is fairly routine, with only minor changes or the addition or subtraction of certain measurements. The ability to have various procedures ready to use and pre-approved helps greatly in many ways, from obtaining oversight approvals to writing methods in publications. Certain measures can be taken for all studies, such as heating and anesthesia, whereas others can be a toolbox of options available as resources to investigators. Wherever possible, solutions are best integrated into the procedures in ways that make it easy and simple for the investigator to carry out their research. Careful attention to detail will result in data with less variability, therefore capable of finding significant changes using fewer animals and with less work. The savings in cost and time are well worth the effort.

Acknowledgments The author would like to thank the many users of the Crump Preclinical Imaging Technology Center and our dedicated staff Waldemar Ladno. This work was supported by the National Cancer Institute (NCI) #R25 CA098010:01; the In Vivo Cellular and Molecular Imaging Center (NIH ICMIC) #R01 EB001943; the Small Animal Imaging Resource Program (SAIRP) #R24 CA92865; the Jonsson Comprehensive Cancer Center UCLA; and the NCI SPORE in Prostate Cancer.

References

1. Massoud TF, Gambhir SS (2007) Integrating noninvasive molecular imaging into molecular medicine: an evolving paradigm. Trends Mol Med 13:183–91.
2. Fueger BJ, Czernin J, Hildebrandt I, Tran C, Halpern BS, Stout D, et al. (2006) Impact of animal handling on the results of 18F-FDG PET studies in mice. J Nucl Med 47:999–1006.
3. Tsukada H, Nishiyama S, Kakiuchi T, Ohba H, Sato K, Harada N, et al. (1999) Isoflurane anesthesia enhances the inhibitory effects of cocaine and GBR12909 on dopamine transporter: PET studies in combination with microdialysis in the monkey brain. Brain Res 849:85–96.
4. Brandstater B, Eger, E., Edelist, G. (1965) Constant-depth halothane anesthesia in respiratory studies. J Appl Physiol 20:171–174.
5. Flores JE, McFarland LM, Vanderbilt A, Ogasawara AK, Williams SP (2008) The effects of anesthetic agent and carrier gas on blood glucose and tissue uptake in mice undergoing dynamic FDG-PET imaging: sevoflurane and isoflurane compared in air and in oxygen. Mol Imaging Biol 10:192–200.
6. Itoh T, Wakahara S, Nakano T, Suzuki K, Kobayashi K, Inoue O (2005) Effects of anesthesia upon 18F-FDG uptake in rhesus monkey brains. Ann Nucl Med 19:373–7.
7. Kyme AZ, Zhou VW, Meikle SR, Fulton RR (2008) Real-time 3D motion tracking for small animal brain PET. Phys Med Biol 53:2651–66.
8. Vaska P, Woody CL, Schlyer DJ, Shokouhi S, Stoll SP, Pratte J-F, et al. (2004) RatCAP: miniaturized head-mounted PET for conscious rodent brain imaging. IEEE Trans Nucl Sci 51:2718–2722.
9. Tsukada H, Kakiuchi T, Shizuno H, Nishiyama S (1998) Interactions of cholinergic and glutamatergic neuronal systems in the functional activation of cerebral blood flow response: a PET study in unanesthetized monkeys. Brain Res 796:82–90.
10. Ansaldi D, Smith, S., Urban, K., Vigil, M., Rathbun, B., Ninov, V., Troy, T., Whalen, J., Rice, B., Francis, K., Lassota, P.. Dual Bioluminescence and Fluorescence Fast Imager for Biological Applications Requiring Continuous Monitoring in Real Time. Caliper Life Sciencesx. Available at www.caliperls.com/assets/016/7463.pdf
11. Suckow C, Kuntner C, Chow P, Silverman R, Chatziioannou A, Stout D (2009) Multimodality rodent imaging chambers for use under barrier conditions with gas anesthesia. Mol Imaging Biol 11:100–6.
12. Bigelow WG, Lindsay WK, Greenwood WF (1950) Hypothermia; its possible role in cardiac surgery: an investigation of factors governing survival in dogs at low body temperatures. Ann Surg 132:849–66.
13. Bunag RD (1983) Facts and fallacies about measuring blood pressure in rats. Clin Exp Hypertens A 5:1659-81.
14. David, John M1; Chatziioannou, Arion F2; Taschereau, Richard2; Wang, Hongkai2, Stout, David B2 The Hidden Cost of Housing Practices: Using Noninvasive Imaging to Quantify the Metabolic Demands of Chronic Cold Stress of Laboratory Mice Comparative Medicine, 1 October 2013, vol. 63, no. 5, pp. 386–391(6).
15. Kampinga HH (2006) Cell biological effects of hyperthermia alone or combined with radiation or drugs: a short introduction to newcomers in the field. Int J Hyperthermia 22:191–6.
16. Arora A, Hakim I, Baxter J, Rathnasingham R, Srinivasan R, Fletcher DA, et al. (2007) Needle-free delivery of macromolecules across the skin by nanoliter-volume pulsed microjets. Proc Natl Acad Sci U S A 104:4255–60.
17. Carson RE, Channing MA, Blasberg RG, Dunn BB, Cohen RM, Rice KC, et al. (1993) Comparison of bolus and infusion methods for receptor quantitation: application to [18F] cyclofoxy and positron emission tomography. J Cereb Blood Flow Metab 13:24–42.
18. Jilge B, Kunz E (2004) *The Laborartory Mouse*: Elsevier Academic Press.
19. Wu HM, Sui G, Lee CC, Prins ML, Ladno W, Lin HD, et al. (2007) In vivo quantitation of glucose metabolism in mice using small-animal PET and a microfluidic device. J Nucl Med 48:837–45.

20. Convert L, Morin-Brassard G, Cadorette J, Archambault M, Bentourkia M, Lecomte R (2007) A new tool for molecular imaging: the microvolumetric beta blood counter. J Nucl Med 48:1197–206.
21. Colwell CS, Kaufman CM, Menaker M, Ralph MR (1993) Light-induced phase shifts and Fos expression in the hamster circadian system: the effects of anesthetics. J Biol Rhythms 8:179–88.
22. Collaco AM, Rahman S, Dougherty EJ, Williams BB, Geusz ME (2005) Circadian regulation of a viral gene promoter in live transgenic mice expressing firefly luciferase. Mol Imaging Biol 7:342–50.
23. Stout DB, Huang SC, Melega WP, Raleigh MJ, Phelps ME, Barrio JR (1998) Effects of large neutral amino acid concentrations on 6-[F-18]Fluoro-L-DOPA kinetics. J Cereb Blood Flow Metab 18:43–51.
24. Dahlbom MY, D.-C.; Cherry, S.R.; Chatziioannou, A.; Hoffman, E.J., (1991) Methods for improving image quality in whole body PET scanning. Conference Record of the 1991 IEEE 3:1587–1591.
25. Chow PL, Stout DB, Komisopoulou E, Chatziioannou AF (2006) A method of image registration for small animal, multi-modality imaging. Phys Med Biol 51:379–90.
26. Davies B, Morris T (1993) Physiological parameters in laboratory animals and humans. Pharm Res 10:1093–5.
27. Yang Y, Rendig S, Siegel S, Newport DF, Cherry SR (2005) Cardiac PET imaging in mice with simultaneous cardiac and respiratory gating. Phys Med Biol 50:2979–89.
28. Kreissl MC, Wu HM, Stout DB, Ladno W, Schindler TH, Zhang X, et al. (2006) Noninvasive measurement of cardiovascular function in mice with high-temporal-resolution small-animal PET. J Nucl Med 47:974–80.
29. Whalen M, Shapiro JI (1991) Controlled ventilation during NMR spectroscopic studies: hemodynamic and biochemical consequences. Magn Reson Imaging 9:229–34.
30. Kerbel RS (2003) Human tumor xenografts as predictive preclinical models for anticancer drug activity in humans: better than commonly perceived-but they can be improved. Cancer Biol Ther 2:S134–9.
31. Wang II, Huang II (2000) Adenovirus technology for gene manipulation and functional studies. Drug Discov Today 5:10–16.
32. Suckow CE, Stout DB (2008) MicroCT liver contrast agent enhancement over time, dose, and mouse strain. Mol Imaging Biol 10:114–20.
33. Willekens I, Lahoutte T, Buls N, Vanhove C, Deklerck R, Bossuyt A, et al. (2009) Time-course of contrast enhancement in spleen and liver with Exia 160, Fenestra LC, and VC. Mol Imaging Biol 11:128–35.
34. MacLaurin SA, Bouchard, M., Dwyer, P., Levenson, R., Mansfield, J., Krucker, T. (2006) Reduction of skin and food autofluorescence in different mouse strains through diet changes. Mol Imaging Biol 5:252.
35. Huang SC, Phelps ME, Hoffman EJ, Sideris K, Selin CJ, Kuhl DE (1980) Noninvasive determination of local cerebral metabolic rate of glucose in man. Am J Physiol 238:E69–82.
36. Kreissl M, Stout D, Wu H-M, Ladno W, Caglayan E, Zhang X, et al. (2006) Influence of insulin and fasting on myocardial, muscle and brain [18F]-FDG uptake and kinetics in mice. J Nucl Med 47:71P.
37. Lee KH, Ko BH, Paik JY, Jung KH, Choe YS, Choi Y, et al. (2005) Effects of anesthetic agents and fasting duration on 18F-FDG biodistribution and insulin levels in tumor-bearing mice. J Nucl Med 46:1531–6.
38. Huang SC, Truong D, Wu HM, Chatziioannou AF, Shao W, Wu AM, et al. (2005) An internet-based "kinetic imaging system" (KIS) for MicroPET. Mol Imaging Biol 7:330–41.

Chapter 19
Applications of Small-Animal Imaging in Neurology and Psychiatry

Cindy Casteels, Habib Zaidi, and Koen Van Laere

1 Introduction

Next to genetical testing and behavioural observations, neuroimaging studies are increasingly performed on primates and rodents to model a variety of human diseases and traits. Animal models of brain disease are available for all major neurodegenerative diseases, epilepsy, stroke, but also psychiatric diseases such as anorexia nervosa, obesity, depression and anxiety [1].

Most commonly, animal models of brain disease are used to elucidate the mechanisms underlying the human condition and to translationally evaluate pharmacological, behavioural or other treatments for the disease. There are at least two criteria that an experimental model must satisfy: (i) reliability and (ii) predictive validity. Even though also other types of validity such as construct, etiological, convergent, discriminant and face validity are relevant to animal models (for an overview see [2]), predictive validity and reliability are the only necessary and sufficient criteria that will justify the model's use for a particular application. Briefly, (i) reliability refers to the consistency and stability with which the disease variables are observed; (ii) predictive validity incorporates specificity of responses to treatments that are effective in the human disease. Undoubtedly, the more types of validity a model satisfies; the greater its value, utility and relevance to the human disorder or condition.

Developing models that fully mimic human neurological or psychiatric disorders is in many cases troublesome. Preclinical studies often need a choice between models that reproduce cardinal pathological features of the disorders by

C. Casteels (✉) • K. Van Laere
Division of Nuclear Medicine, Leuven University Hospital, Leuven, Belgium
e-mail: Cindy.Casteels@med.kuleuven.be; koen.vanlaere@uz.kuleuven.ac.be

H. Zaidi
Department of Radiology & Medical Informatics, Geneva University Hospital, Geneva, Switzerland
e-mail: habib.zaidi@hcuge.ch

H. Zaidi (ed.), *Molecular Imaging of Small Animals: Instrumentation and Applications*,
DOI 10.1007/978-1-4939-0894-3_19,

mechanisms that may not necessarily occur in humans versus models that are based on known pathophysiological mechanisms but may not reproduce all the features seen in patients.

Neurological and psychiatric models can be subdivided in three groups on the basis of the underlying mechanism: (i) genetically engineered; (ii) pharmacology based; or (iii) produced through advanced biotechnology such as viral vector technology. They may encompass several species, both primates and rodents. The use of mice in functional neuroimaging research is limited by the small size of the brain compared to the resolution limitations of current preclinical imaging systems.

The most commonly applied neuroimaging techniques for studying in vivo disease models are positron emission tomography (PET), single-photon emission computed tomography (SPECT) and magnetic resonance imaging (MRI), each of which has its own advantages and disadvantages (see Chaps. 4, 5, and 7). In this chapter, we will focus on how functional imaging technologies (PET and SPECT) have advanced our understanding of human neurological and psychiatric diseases. In particular, we will focus on the role of these techniques in evaluating models of Parkinson's disease, Huntington's disease, Alzheimer, epilepsy, stroke, addiction, depression, mania and eating disorders.

In general, the development of dedicated small-animal PET/SPECT systems offers the ability to study in vivo molecular changes during (i) normal development, (ii) biological processes and responses, and (iii) disease initiation and progression. As such, they may provide surrogate markers and allow assessment of therapeutic interventions by using serial scans over an extended period in the same animal. Selective radioligands for many neurotransmitter receptors [3] and other cellular proteins [4], which act as enzyme substrates [5] or allow the interference of neuronal function [6], are available.

PET imaging offers certain advantages over SPECT including: the acquisition of relatively fast dynamic data (order of seconds) and the potential to quantify these observations [7]. The spatial resolution when compared to structural imaging techniques such as MRI, is relatively limited, with the highest resolution scanners today giving at best 1–2 mm full width at half maximum (FWHM). The sensitivity of dedicated SPECT is typically an order of magnitude lower than PET. The spatial resolution of state-of-the-art preclinical SPECT scanners can be as low as 0.35 mm, although a trade-off between sensitivity and resolution is always needed [8, 9]. However, the detection of pico- and femtomolar concentrations of radioligand is feasible with both PET and SPECT [10].

When designing or performing in vivo small-animal studies of the brain, the following methodological issues must additionally be considered:

- *Motion prevention*:
  - Immobilizing the animal in the PET/SPECT scanner is the first issue that has to be taken into consideration. Although systems and procedures have been developed to use awake monkeys in PET studies [11] and dedicated instrumentation developed to scan rats in their living environment [12], anaesthesia is still the standard for ensuring immobility during in vivo imaging of small-animals. A fundamental requirement of imaging is not to disturb the

biological system under investigation. However, in many instances, anaesthesia can have several effects on the studied brain parameter. These effects are not predictable since changes are often of different magnitude and direction amongst target receptor, enzyme or transporter systems. The choice of anaesthetics is therefore of great importance to investigate, as it needs to minimally interfere with the tracer dynamics and the research question to obtain biologically valid outcomes (see Chap. 18). For example, the anaesthetic isoflurane was found to alter the expression of the plasma membrane dopamine transporter (DAT) in the brain [13], excluding its use for DAT imaging. Matsumara et al. investigated the effect of six different anaesthetics agents on the uptake of [^{18}F]-FDG in the rat brain [14] and demonstrated significant effects of the different anaesthetics agents on [^{18}F]-FDG metabolism when administered during the uptake period. Only when anaesthesia was started after the initial uptake phase, i.e. 40 min after [^{18}F]-FDG injection, did the small-animal PET images reflect glucose metabolism of the conscious state, as measured with ex vivo autoradiography [14]. However, delaying the induction of anaesthesia with respect to the administration of the PET ligand is not always possible. It limits imaging to a static state, delays imaging protocol and negates the opportunity for dynamic imaging protocols that are required for fully quantitative and compartmental modelling.

- *Absolute quantification*:
  - Fully quantitative and compartmental modelling is a prerequisite for the accurate determination of various biological parameters, such as receptor density (B_{max}) and affinity (K_D) or derived combined parameters such as binding potential. Kinetic modelling generally requires arterial blood sampling to calculate the blood activity concentration over time (input function) [15]. Techniques that have been established to measure blood activity concentrations in humans need to be carefully considered for animal experiments because the vascular access is more problematic, the blood volume smaller and the heart rate much higher than in humans [16]. Arterial blood sampling in rodents is technically demanding; requires extensive animal preparation, complex catheter manipulation and physiological monitoring. Besides, it hampers serial small-animal PET/SPECT studies over weeks or months. Other techniques deriving the input function from a reference tissue devoid of receptors [17], from images of the heart [18] or from the use of an (arterial) probe [19], have also been developed and could reduce the need for blood sampling. They are, however, highly dependent on the radiotracer used and the molecular target. The last two options, for example, are only feasible when the radiotracer does not undergo significant metabolism [20], or when a standard curve describing the metabolism is usable.
- *Tracer principle*:
  - Assessment of the mass effect of injection is an additional issue, especially in the case of receptor imaging [21]. In human imaging studies, only a small chemical amount of radiotracer is injected, in the range of pico- to microgram.

This dose has several advantages, including conforming to true tracer kinetics and giving lower or negligible toxicity. However, in order to obtain sufficient count rates in the brain of small-animals, relatively high doses need to be injected. Indeed, in small-animal imaging, the increase in dose with increasing resolution and the decrease in dose with decreasing body weight cancel one another. Consequently, the concentration of radioligand in the animal will be higher in the ratio of human to rodent body mass, potentially saturating vulnerable systems. In the case of binding sites of low density such as receptors, the increased mass injected can lead to physiological effects and non-linear kinetics. One must therefore reduce the injected dose of small-animals as low as possible and necessary.

- *Quantitative analysis*:
  - By its very nature, SPECT and particularly PET are quantitative imaging modalities provided appropriate corrections for physical degrading factors are incorporated in the imaging protocol (see Chap. 17). The automated quantitative assessment of metabolic PET data is attractive and will certainly revolutionize the practice of molecular imaging since it can lower variability across facilities and may enhance the consistency of image interpretation independent of reader experience. For example, the development of tracer-specific small-animal PET probabilistic atlases [22] correlated with anatomical (e.g. MRI) templates enabled automated volume-of-interest (VOI) or voxel-based analysis of small-animal PET data with minimal end-user interaction [23]. One such software tool was developed by Kesner et al. [24] to enable the assessment of the biodistribution of PET tracers using small-animal PET data. This is achieved through non-rigid coregistration of a digital mouse anatomical model with the animal PET image followed by automated calculation of tracer concentrations in 22 predefined VOIs representing the whole body and major organs. The development of advanced anatomical models including both stylized and more realistic voxel-based mouse [25–27] and rat [28, 29] models obtained from serial cryo-sections or dedicated high resolution small-animal CT and MRI scanners will certainly help to support ongoing research in this area [30, 31]. For neuroscience applications, a high-resolution rat brain was also recently developed [32].

2 Applications in Neurology

2.1 Parkinson's Disease

Parkinson's disease (PD) is a progressive neurodegenerative disorder, characterized by massive degeneration of dopaminergic neurons in the substantia nigra (SN) pars compacta [33]. This nigral neuronal loss leads to a striatal dopamine deficiency, which is considered to underlie the most overt symptoms of the disease.

PD affects approximately more than 2 % of the general population over the age of 65. The mean onset of the disease is around 60 years, although up to 10 % of those affected are 45 years of age or younger, referred to as young-onset PD. Clinical signs of PD are evident when about 80 % of striatal dopamine and 50 % of nigral neurons are lost [34].

Traditional models of PD fall into two major categories: (i) pharmacological, for example reserpine or amphetamine administration to deplete dopamine, a largely reversible treatment; and (ii) lesioning using neurotoxins which is permanent, for example intraparenchymal injection of 6-hydroxydopamine (6-OHDA) or systemic administration of 1-methyl-4-phenyl-1,2,3,6-tetrahydropyridine (MPTP), as reviewed by Hantraye et al. [35]. Newer approaches in the development of PD models have been attempted as well based on the identification of monogenic familial forms of the disease (at least 11 different linkages with 6 gene mutations have been identified) [36], resulting in transgenic and non-transgenic experimental models [37]. Each of the abovementioned models have its own strengths and weaknesses in representing the human condition, and have all been extensively characterized behaviourally and neurochemically (for an overview see [38]).

Imaging experimental PD models has largely been in the domain of PET imaging with the availability of radioligands to monitor both pre- and postsynaptic striatal dopaminergic function in order to follow the disease process and to examine compensatory mechanisms. The presynaptic nigrostriatal terminal function can be assessed with radioligands suitable for imaging at least three different functions, (i) aromatic amino acid decarboxylase activity (AADC), (ii) vesicular monoamine transporter type 2 (VMAT2) and (iii) the plasma membrane dopamine transporter (DAT). Imaging of postsynaptic dopaminergic function has focused on the dopamine D_2-like receptor system.

Changes in dopamine metabolism have been widely identified in PD patients and MPTP-treated nonhuman primates using either 6-[^{18}F]-fluoro-L-DOPA ([^{18}F]FDOPA) [39–42] or 6-[^{18}F]-fluoro-L-methyl-tyrosine ([^{18}F]FMT) [43, 44], tracers of catabolism and trapping of dopamine, or its analogs. Somewhat surprisingly, [^{18}F]FDOPA showed no significant brain uptake in the rat [45], although it can be used successfully in vivo in mice [46]. Mouse models of PD, either genetically modified or MPTP-treated, have not been extensively studied with in vivo imaging techniques so far, primarily because of the small size of the brain. However, due to the relatively large size of the striatum, a number of studies have shown that it is feasible. Sharma and colleagues have shown that striatal [^{18}F]FDOPA uptake is reduced in the striatum of homozygous weaver mutant mice (a genetic model of PD) compared to both heterozygous and wild-type control animals [46]. Additionally, homozygous weaver mutant mice show an age-related decline in striatal [^{18}F]FDOPA uptake [47].

Most imaging studies performed in rat PD models measure the loss of presynaptic dopamine terminals primarily using tracers for the DAT using cocaine analogs. After unilateral lesions of the nigrostriatal projection through injection in the medial forebrain bundle (MFB), decreased [^{11}C]-CFT and [^{11}C]RTI-121 binding have been noticed [48], as a result of decreased density of the transporter, without concomitant

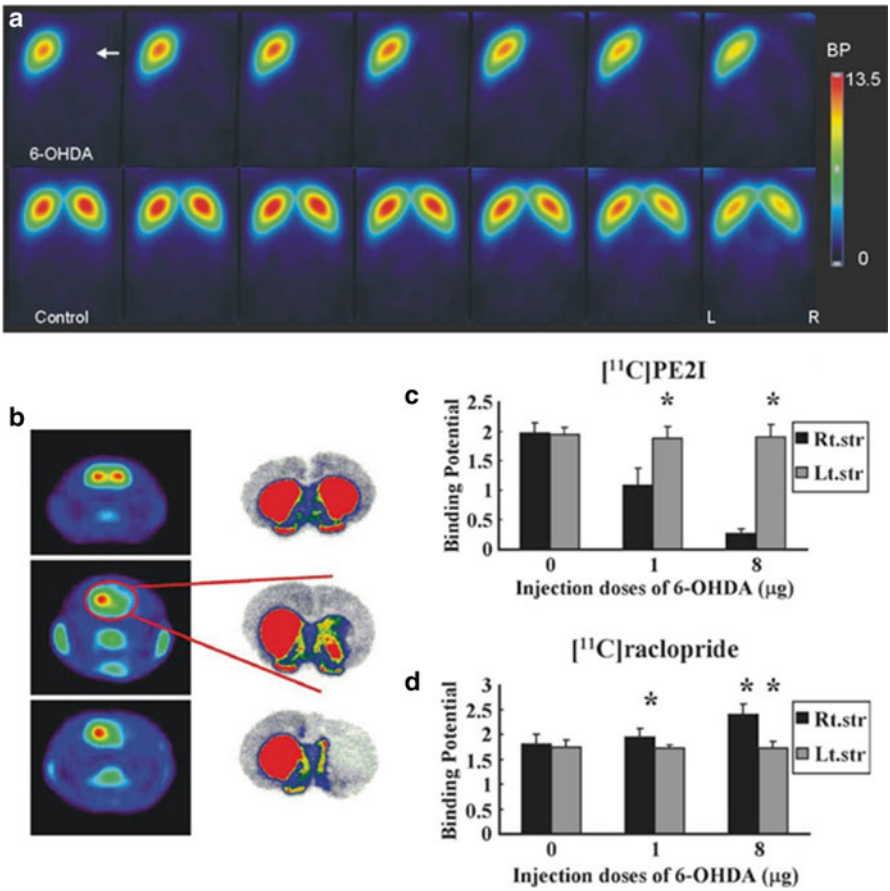

Fig. 19.1 Overview of both pre- and postsynaptic striatal function in the 6-OHDA model of Parkinson's disease. (**a**) Series of axial sections (ventral to dorsal, slice interval 1.0 mm) showing decreased DAT availability in the dorsal striatum of 6-OHDA-treated rats in comparison to controls, as measured using [^{18}F]-FECT. *Color bars* indicate binding indices for the dopamine transporter. (**b**) Also in the same model, reductions in VMAT2 density using [^{11}C]DTBZ with microPET (*left*) and autoradiography (*right*) have been identified. *Top image*: A normal control animal for comparison; *middle image*: an animal with a mild right unilateral lesion; *bottom image*: an animal with a severe right unilateral lesion. (**b**–**d**) PET measures of the integrity of the striatal dopamine function correlates to the amount of 6-OHDA injected. [^{11}C]PE2I binding to DAT (**c**) and [^{11}C]-raclopride binding to D_2 receptors (**d**) decreased and increased, respectively, with injected dose of 6-OHDA. Reprinted from [48, 54, 56] with permission from Springer and Elsevier

changes in affinity [49]. $VMAT_2$ density changes have also been identified (Fig. 19.1b) [48], as have increased [^{11}C]-raclopride binding to the D_2 receptors [50, 51], consistent with human PET studies in early PD patients [52]. Whether the D_2 receptor upregulation is a result of changes in receptor density or affinity is still unresolved, as both characteristics have been found to be altered [51, 53]. Besides, longitudinal microPET analysis of striatal D_2 binding in the same animals

demonstrated that the increase in D_2 receptor density after unilateral 6-OHDA lesions occurs bilaterally [53]. Nikolaus and co-workers found that the D_2 receptor density starts to increase in both striata within 2 days post-lesion, while a trend toward a significant increase in the contralateral striatum was noticed at day 14. The authors attributed the change in the contralateral striatum to be indicative of compensatory changes upon unilateral dopamine depletion [53]. Decreased presynaptic dopamine terminal binding have also been observed after unilateral lesions of the nigrostriatal tract through injection of 6-OHDA in the SN with [^{18}F]-FECT (Fig. 19.1a) [54], and through lentiviral vector-based mediated overexpression of alpha-synuclein in the striatum using [^{123}I]FPCIT [55].

These PET measures of the integrity of the striatal dopamine system have been shown to correlate to the amount of 6-OHDA injected. One study showed that 6-OHDA lesioning causes reciprocal, dose-dependent changes in [^{11}C]PE2I binding to DAT compared to [^{11}C]-raclopride binding to D_2 receptors, decreasing and increasing the binding respectively (Fig. 19.1c, d) [56]. Another study also intended to measure the relationship between the 6-OHDA dose and the integrity of the striatal dopamine system using [^{11}C]DTBZ, confirmed previous correlation [48].

As functional imaging of the striatal dopaminergic system can objectively follow loss of dopamine terminal function in PD, it also provides a potential means of monitoring the efficacy of putative therapeutic strategies. Possible restorative approaches evaluated in PD models include: striatal implants of human and porcine fetal mesencephalic cells, retinal cells that release levodopa/dopamine, embryonic stem cells and neurotrophic factors.

In unilateral 6-OHDA-lesioned rats, striatal transplantation of foetal dopamine neurons restores both the regional cerebral blood volume (rCBV) response to amphetamine as measured with pharmacological MRI, as well as the [^{11}C]CFT binding in the lesioned striatum [57]. Behavioural recovery does not occur until [^{11}C]CFT binding is restored in the same model to 75–85 % of the intact side [58]. The logistic, practical and ethical issues associated with foetal cells, however, contributed to a shift away from this particular line of investigation to the evaluation of alternative source of cells.

Alternative cells such as retinal pigmented epithelial (RPE) cells have so far only been studied in larger animals. RPE cells produce levodopa (L-DOPA), the biochemical precursor of dopamine, as an intermediate in neuromelanin production. Implanted human RPE cells, unilaterally into the striata of bilateral MPTP-treated monkeys, results in improved motor function and increased [^{18}F]-FDOPA uptake with a concomitant decrease in [^{11}C]-raclopride binding 2 months after implant [59].

The potential of embryonic stem (ES) cells as other viable source of cells for transplantation in PD has been evaluated in the unilateral 6-OHDA rat model. Bjorklund et al. [60] have shown that when transplanted into the rat striatum, mouse ES cells differentiate into dopamine neurons and decrease behavioural asymmetries. In addition, [^{11}C]CFT binding was increased in the grafted striatum and correlated with the number of TH+ neurons in the graft [60]. Also in the same model, infusion of GDNF, a neurotrophic factor, into the SN and lateral ventricles prevents the 6-OHDA-induced reduction in DAT, as measured by [^{11}C]-RTI-121 [61, 62].

Despite both histological and PET evidence in animals, neither of the abovementioned graft techniques demonstrated clinical efficacy in controlled trials so far [63, 64]. In those trials "off" period dyskinesias were often problematic. There are suggestions, however, that less severely affected PD patients could benefit more from those intrastriatal implantations.

Apart from the dopaminergic system, another active field of research in recent years has become the study of the contribution of inflammation to the progression of neurodegenerative disorders, as it may provide alternative therapeutic opportunities. Microglia cells are the macrophages of the brain and respond to noxious stimuli by changing morphology and expression of cell-surface markers and releasing pro-inflammatory cytokines [65]. Activated microglia cells may play a major role in the extension of neuronal loss after a lesion or insult. Migration of activated microglia and macrophages towards the lesion site correlates with the secondary damage after an acute neurotoxic event [66]. Moreover, a similar mechanism might amplify and perpetuate neuronal damage in chronic neurodegenerative disorders, such as PD.

Cicchetti and coworkers have used a ^{11}C-labeled tracer that binds to the peripheral benzodiazepine receptor ([^{11}C]-PK11195) to study activated microglia in PD models. Unilateral striatal infusion of 6-OHDA has been shown to increase [^{11}C]-PK11195 binding in the lesioned striatum, at 3 weeks post lesion compared to baseline [67]. In the same model, chronic treatment with a selective inhibitor of the inducible form of cyclooxygenase (COX-2) constrained this inflammatory response at 12 days postlesion and limited, to a certain extent, the progressive dopamine neuronal death in the SN, as measured using [^{11}C]-CFT and immunohistochemistry [68].

Cerebral metabolic mapping with autoradiography has also been used in previous animal research to determine the regional alterations in brain activity related to the pathogenesis of PD [69, 70]. The technique has additionally been used to map regions responsive to levodopa in the 6-OHDA lesioned rat [71]. Nowadays, [^{14}C]-2-deoxyglucose autoradiography is often replaced by [^{18}F]-FDG PET imaging. [^{18}F]-FDG is considered to be a marker of cerebral glucose consumption based on neuronal entrapment and accumulation of [^{18}F]-FDG-6-PO_4, indicating neuronal viability [6]. In PD patients, specific cortical-subcortical metabolic alterations have been described using [^{18}F]-FDG based on direct regional analysis [72] or network analysis approaches [73]. So far, only one study in small-animals has been performed. It was recently demonstrated that the unilateral intranigral lesion produced with 6-OHDA causes a severe metabolic impairment in the ipsilateral sensorymotor cortex of 6-OHDA lesioned rats, while metabolism was relatively increased in the contralateral midbrain, comprising the SN [54]. The change in the contralateral midbrain was attributed to be indicative of compensatory changes to unilateral dopamine depletion, in line with the previous mentioned contralateral D_2 receptor upregulation [53]. It was concluded that the model shows metabolically strong functional correspondence to the cortico-subcortical impairments seen in PD patients [54].

2.2 Huntington's Disease

Huntington's disease (HD), or Huntington's chorea, is an autosomal dominant progressive neurodegenerative disorder affecting approximately 1 in 10,000 individuals and is characterized by involuntary movements such as chorea, emotional disturbances and cognitive impairment [74]. Typically, onset of symptoms occur in middle-age. HD is caused by a cytosine-adenine-guanine (CAG) repeat expansion within exon 1 of the HD gene (IT15) on chromosome 4 [75]. The number of CAG repeats accounts for about 60 % of the variation in age of onset, with the remainder represented by modifying genes and environment [76].

The earliest animal models of HD are based on the selective vulnerability of striatal neurons to excitotoxic amino acids [77]. Intrastriatal injection of quinolinic acid (QA) [78] or systemic administration of 3-nitropropionic acid (3-NP) [79] results in 'pathogenic models' of the disease. Since the recent discovery of the gene mutation for the disease, new transgenic models are also being developed. Transgenic animal models of HD were first created in mice [80] and subsequently in *Drosophila* [81]; later on, a transgenic rat model of HD was reported [82].

Small-animal imaging data on HD are largely PET-based using similar markers described for Parkinson's disease with more experimental data utilizing fluorodeoxyglucose to map regions of reduced metabolism, indicative of cell loss [6]. Imaging of HD models has been used extensively to evaluate both the validity of the models and the effects of various interventions.

In the QA-lesioned rat striatum, [^{18}F]-FDG uptake is substantially decreased at 1 week post lesioning, and decreases further at 5 and 7 weeks postlesion [83]. In contrast, lesion-induced effects on dopamine D_2 receptor binding were more progressive, with an initial upregulation of [^{18}F]-FESP binding apparent 1 week postlesion followed by a decline 5 and 7 weeks thereafter [83]. Additional experiments revealed that the marked upregulation of dopamine D_2 receptors consequent to QA injections could be detected as early as 3 days after the initial insult [83]. Using [^{11}C]KFI8446, Ishiwata et al. have shown that adenosine A_{2A} receptor binding is decreased to a similar extent as [^{11}C]-raclopride binding to D_2 receptors in the lesioned striatum, but to a greater extent than [^{11}C]SCH23390 binding to D_1 receptors [84]. Also in the same model, the QA injury did not affect [^{11}C]flumazenil binding to benzodiazepine receptors at day 5 postlesion [85]. In addition, Moresco et al. have shown that the loss of adenosine A_{2A} and dopamine D_2 receptors are paralleled by an increase of microglia activation, as measured using [^{11}C]PK11195 [86]. At the very first time point investigated, from QA administration (24 h), only a slight non-significant increase in [^{11}C]PK11195 binding was observed. At 8, 30 and 60 days, however, [^{11}C]PK11195 binding values were on average three times higher than the controls.

Compared to intrastriatal QA, repeated systemic administration of 3-NP results in more widespread striatal lesions. A longitudinal [^{18}F]-FDG study aimed to explore the acute and chronic effects of systemic 3-NP administration, showed a significant interanimal variation in response to the toxin [87]. Rats that developed

large striatal lesions had decreased glucose utilization in the striatum and cortex 1 day after starting 3-NP injections. Rats that did not develop lesions showed reversible enhancement in cortical glucose utilization and no changes in striatal glucose metabolism. Progressive degeneration was observed by a decrease in glucose metabolism in the striatum [87].

Transgenic rodents expressing a mutant form of the huntingtin gene are used in the study of disease progression and the effects of treatments. A recent longitudinal study, following up R6/2 mice with [^{18}F]-FDG, demonstrated an exponential decrease in glucose metabolism, starting at the age of 8 weeks and continuing through the 6 weeks follow-up time in the striatum, cortex and cerebellum [88]. Treatment with the transglutaminase inhibitor cystamine in these animals has been shown to have a neuroprotective effect in a dose-dependent manner, attenuating the decrease in striatal, cortical and cerebellar [^{18}F]-FDG [88].

2.3 Alzheimer's Disease

Alzheimer's disease (AD) is the most common cause of progressive cognitive decline in aged humans, comprising 50–70 % of all cases [89]. AD begins with great difficulty in new learning and memory, which leads to forgetfulness of recent events. AD worsens over time, usually over many years, leading to problems in word finding and reasoning, difficulty completing daily activities of living and ultimately death. The most severe neuropathological changes occur in the hippocampus, followed by the association cortices and some subcortical structures, such as the amygdala [90]. The neuropathological changes are characterized by massive neuronal cell and synapse loss [91], as well as beta-amyloid plaques and neurofibrillary lesions [90]. The major protein component of plaques is the polypeptide *Abeta* that is derived from amyloid precursor protein (APP). The neurofibrillary lesions contain hyperphosphorylated aggregates of the microtubule-associated protein *tau* and are found in cell bodies and apical dendrites as neurofibrillary tangles (NFT).

Less than 1 % of the total number of AD cases are caused by autosomal dominant mutations in three genes, among which APP [92]. Mutations in the gene encoding *tau* have also been linked to neurodegeneration and dementia [93]. The fact that these genes encode for proteins that are deposited in plagues and NFTs further confirms their causal role in the disease and led to the generation of transgenic animal models [94]. Most widely used animal models comprise both mouse and invertebrate; rat models of AD are rare. As far as neuro-anatomy, memory and motor functions are concerned, the transgenic mouse models are superior to the invertebrate ones in resembling the human condition [95]. Many different strains exist, but most of these overexpress human APP.

Not all PET studies of transgenic mice have been very successful so far because of the small size of the mouse brain and the inherent limitations in resolution of the first generation of small-animal PET scanners [96]. Considering that [^{18}F]-FDG is becoming one of the most widely used diagnostic adjuncts for AD [97], the

expectation that this technique would also be widely used in transgenic mice has for this reason not been met. Whereas autoradiographic studies show decreased cerebral glucose metabolism in the posterior cingulate cortex, in vivo imaging does not allow the identification of this change [98].

Visualizing Abeta deposition in vivo is another novel diagnostic tool, which might contribute to a definite diagnosis of AD and to monitor the success of treatments. The earliest probe was a dye called BSB (*trans*,*trans*)-1-bromo-2,5-bis-(3-hydroxycarbonyl-4-hydroxy)styrylbenzene, which was used to label Abeta-plaques in Tg2576 mice [99]. In recent years, the novel PET tracer ^{11}C-labeled Pittsburgh Compound-B (PIB) has gained significant attention [100]. PIB was shown to enter the brain quickly and label plaques within minutes [101]. It was used as a PET tracer in APP transgenic mice but initially failed to reflect the amount of Abeta [102]. In APP23 mice, an age-dependent increase in radioligand binding was found to be consistent with progressive Abeta accumulation [103]. Importantly, Abeta reductions upon vaccination with an anti-Abeta-antibody were reflected by reduced binding of [^{11}C]-PIB. The use of transgenic mice in preclinical studies is however limited as species-differences in Abeta accumulation have been reported [103].

In order to diminish the spatial resolution limitations of PET, high-field strength MRI can be combined with preclinical PET imaging for more accurate anatomical localization. In a study combining a transgenic mouse model of AD and the use of the toxin *N*-(2-chloroethyl)-*N*-ethyl-bromo-benzylamine (dsp4), which specifically targets the noradrenergic neurons of the locus coeruleus, Heneka et al. demonstrated an interaction effect between beta-amyloid deposition and noradrenergic neurotransmission [104]. Only transgenic mice who were also treated with dsp4 showed decreased cortex/cerebellum ratios in [^{18}F]-FDG uptake, [^{11}C]flumazenil binding and [^{11}C]*N*-methyl-4-piperidyl-acetate trapping, indicative of reduced cerebral glucose metabolism, decreased neuronal integrity and attenuated acetylcholinesterase activity, respectively.

2.4 Epilepsy

Epilepsy is a common chronic neurological disorder that is characterized by recurrent, unprovoked seizures [105] and affects approximately 3 % of the population during their life-time [106]. Seizures arise from excessive abnormal hypersynchronized firing of a population of cortical neurons [107]. About 60–70 % of patients experience focal or partial seizures, and about 30–40 % generalized seizures [108]. Epileptic seizures are controlled with medication in approximately 70 % of the cases. When seizures are medically intractable, resection of the epileptogenic cortex may be considered.

Many epilepsy syndromes, particularly temporal lobe epilepsy (TLE), are associated with structural and functional abnormalities of the brain. The relationship of these abnormalities to the development (i.e. epileptogenesis), progression and prognosis of epilepsy are still incompletely understood.

Animal models in epilepsy neuroimaging research have long been important for the investigation of the neurobiology, consequences and treatment of seizures and epilepsy. The use of animal models particularly enables the investigation of the neurobiological changes during epileptogenesis, which is difficult to study in humans, given that in most patients, the chronic rather than the early epileptogenic stage is represented. Besides, prospective studies, in which patients at risk are followed up until the onset of the first seizure, are time-consuming, costly and practically difficult to undertake.

The animal models used in epilepsy research can be divided into models of seizures and models of epilepsy itself [109]. In the case of the former, the seizures are induced by the application of an acute brain insult, usually electrical and chemical, while in the latter the seizures occur spontaneously as in human epilepsy. In these chronic models, epileptogenesis is generally induced by a precipitating insult (genetic or acquired) that initiates a cascade of processes that transform a normal to a hyperexcitable epileptic brain, resulting in the occurrence of recurrent spontaneous seizures after a latent or silent period.

In 2000, Kornblum et al. were the first to publish in vivo [^{18}F]-FDG findings during acute seizures using small-animal PET [110]. [^{18}F]-FDG is one of the most commonly used radiotracers for PET imaging in clinical epilepsy practice and research, and is used in patients with refractory epilepsy to presurgically localize the functional deficit zone [111]. In the model of kainic-acid induced seizures, during status epilepticus (SE) a dramatic enhancement in glucose metabolism in several brain regions was demonstrated, most notably in hippocampus and entorhinal cortex [110]. Rats displaying moderate to severe seizures demonstrated 1.6- and 2.3-fold increases in [^{18}F]-FDG uptake in the hippocampus, respectively. This correlation between [^{18}F]-FDG uptake and seizure activity was also confirmed in C57BI/6 mice [112]. Using pilocarpine induced SE in these animals, [^{18}F]-FDG uptake in the hippocampus (+33.2 %) was directly correlated with seizure activity during the uptake period.

Wang et al. studied a mouse model for GLUT-1 haploinsufficiency using [^{18}F]-FDG small-animal PET [113]. GLUT-1 is the predominant glucose transporter expressed in the blood–brain barrier and is responsible for glucose entry into the brain [114]. GLUT-1 haploinsufficient mice were found to display among others spontaneous epileptiform discharges on electroencephalography, paralleled by a diffuse hypometabolism in the brain as compared to the wild-type strain [113].

Recently, longitudinal small-animal PET imaging was used to study brain glucose metabolism during epileptogenesis in two chronic epilepsy models of TLE [115]. In the amygdala kindling model, rats were found to have decreased glucose uptake in the ipsilateral hippocampus at the end of the kindling period that persisted at the 2 weeks post-kindling scan. In the post kainic acid induced SE model, a global hypometabolism was presented as early as 24 h after the kainic acid treatment. This hypometabolism remained persistently decreased for the following 6 weeks and was not affected by the onset of spontaneous seizures.

More recently, the relationship between brain glucose metabolism and epileptogenesis was further investigated in the rat lithium-pilocarpine model of epilepsy

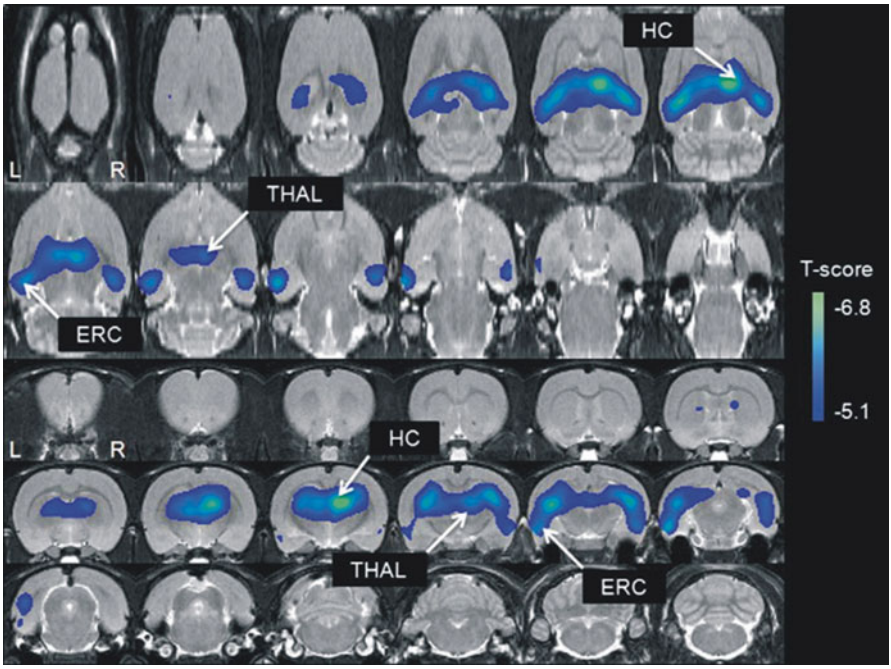

Fig. 19.2 Comparison of brain glucose metabolism between SE and control animals on day 3. Differences for the brain regions have been color-coded and are superimposed on a MRI template. Axial (*top 2 rows*) and coronal (*bottom 3 rows*) brain sections showing significantly decreased [^{18}F]-FDG uptake on day 3 in SE rats compared to controls, most pronounced in hippocampus (*HC*), entorhinal cortex (*ERC*) and thalamus (*THAL*) bilaterally (*white arrows*). Significance at the voxel level is shown with a T statistic color scale. Reprinted from [116], with permission from Elsevier

using a voxel-based analysis approach [116]. Early in the silent phase of epileptogenesis (day 3), rats displayed a severely hypometabolism in the entire cerebrum, although no electro-encephalographic or behavioural seizure activity was present at that time. This hypometabolism was most pronounced in the hippocampus, entorhinal cortex and thalamus bilaterally (Fig. 19.2); regions all characterized by the highest [^{18}F]-FDG uptake during SE. During the chronic epileptic phase, a normalization of the glucose metabolism was seen.

Apart from [^{18}F]-FDG, as marker of neuronal activity, specific neurochemical changes can be measured by the use of specific receptor ligands. Several of these receptor systems represent existing or possible therapeutic targets.

The receptor that has most commonly been imaged using PET in human epilepsy studies has been the central benzodiazepine (cBZ) receptor using radiolabeled flumazenil (FMZ). Changes in expression and function of the $GABA_A$/cBZ receptor complex are well described in human focal epilepsy [111]. Liefaard et al. used a population pharmacokinetic model to study the changes in GABAa/cBZ complex in the kindling model of TLE [117]. After injection of an excess amount of [^{11}C]FMZ

to fully saturate the receptors, the concentration-time curves of [^{11}C]FMZ in blood and brain were measured, from which K_D and B_{max} were estimated. After kindling, K_D was unaffected, but B_{max} in epileptic rats decreased to 64 % of controls. Also in fully kindled rats, the brain volume of distribution was found to be increased with 180 %, indicating, in these animals, reductions in transport of [^{11}C]FMZ outside the brain [117].

Another receptor radiotracer with potential for small-animal epilepsy models is (*N*-[2-(3-cyano-phenyl)-3-(4-(2-[^{18}F]fluorethoxy)phenyl)-1-methylpropyl]-2-(5-methyl-2-pyridyloxy)-2-methyl proponamide) ([^{18}F]MK-9470), which labels brain type 1 cannabinoid (CB_1) receptors [3]. Cerebral CB_1 receptors belong to the endocannabinoid system (ECS), together with a family of naturally occurring lipids, the endocannabinoids, and with transport and degradation proteins [118]. The endocannabinoid system would provide an 'on-demand' protection against acute excitotoxicity in neurons of the central nervous system and would contribute to a signaling system that protects neurons against the consequences of abnormal discharge activity [119]. In rodent models of epilepsy, administration of cannabinoids is protective against seizures [120, 121] and affects seizures' frequency and duration. Endocannabinoids and CB_1 receptor levels are increased in these epileptic animals [122]. Using small-animal PET, the involvement of the ECS was recently demonstrated, more precisely the CB_1 receptor, in the mechanism-of-action of the antiepileptic drug valproate (VPA) [123]. A significant increase (+32 %) was found in global cerebral [^{18}F]MK-9470 binding after 2-week chronic VPA administration compared to sham-treated animals. As VPA does not exhibit high affinity for the CB_1 receptor, such upregulation is likely caused by an indirect effect on the ECS, since, as mentioned before, activation of the CB_1 receptor has been shown to decrease excitability and excitotoxicity on demand [119].

At present, none of the abovementioned neurobiological changes have been shown to be a biological marker, predictive for seizures outcome.

2.5 Cerebral Ischaemia

Stroke is the second most common cause of death and major cause of disability worldwide [124]. Stroke results from a transient or permanent reduction in cerebral blood flow (CBF), usually secondary to thromboembolic occlusion of one or more cerebral arteries. The compromised blood supply leads to functional impairment, followed by structural disintegration of neurons in the absence of reperfusion. The initial phase of dysfunction is potentially reversible, prior to subsequent cell death. While some brain tissue may be irreversibly damaged, other hypoperfused areas may be at risk but are potentially salvageable. These latter areas are called the penumbra [125]. If people reach their life expectancy, one in four men will have had a disabling stroke by age 80, and one in five women by age 85 [126]. The burden of stroke on patients, their families, and society in general is enormous.

The use of animal models in neuroimaging stroke research has focused on a number of areas which include: (i) defining and understanding the concept of the penumbra; (ii) development of new imaging techniques for the diagnosis and prognosis of stroke; and (iii) the investigation both of the underlying processes that lead to cell death, and of possible therapies for the treatment of stroke.

Over the last decade, comprehensive reviews have described the numerous possible animal models of cerebral ischaemia and their relevance to the human disease [127]. Experimental models may be broadly classified by the reduction in cerebral blood flow (CBF), as either global or focal models, which may in turn be permanent or reversible in nature. Models of focal ischemia most often involve unilateral, transient, or permanent occlusion of the middle cerebral artery (MCA-O), leading to ischemic damage in the neocortex and/or caudate-putamen [128]. Models of global ischemia are usually transient, since persistent global cerebral ischemia readily leads to death. Transient global ischemia can be induced with hypoxic ventilation and/or multi-vessel occlusions [129].

The penumbra is the most important target for acute stroke therapy. Since the penumbra can be considered as a temporary phase of potential viability through which ischemic tissue progresses into infarction, the therapeutic time-window is limited, possibly to a few hours; therefore early detection is essential. In humans, multitracer PET measuring blood flow and metabolism is still the current gold-standard technique for penumbral identification [130]. Diffusion/perfusion-weighted MRI and perfusion CT are more commonly used because of their simplicity and suitability for repeat studies; however, they may not differentiate infarct, penumbra and oligemia (i.e. deficiency in blood volume) reliably after stroke [130]. Following occlusion of the MCA in male spontaneously hypertensive and male normotensive Wistar Kyoto rats, CBF was decreased 1 h after the occlusion to <30 % of the control hemisphere in both groups, cerebral metabolic rate of oxygen consumption ($CMRO_2$) was diminished to a similar extent and oxygen extraction fraction (OEF) was increased, indicating misery perfusion [131]. During permanent occlusion, the underlying physiological disturbances were greater in spontaneously hypertensive rats as compared to the normotensive ones, revealing that hypertension is a risk factor for the onset of stroke as well as for poorer outcome after stroke [131]. In the same models, a collapse of the compensatory OEF mechanism was found 24 h after occlusion [132].

In rats undergoing distal MCA occlusion surgery, sequential [^{18}F]-FDG PET studies demonstrated decreased glucose metabolism in the stroke area delineated by MRI [133]. The [^{18}F]-FDG uptake in the stroke area was about 0.5 % of the injected dose per gram (ID/g) at days 1, 15 and 22. At day 8, the stroke area appeared to be smaller and the uptake was higher, likely attributable to inflammation.

Other PET studies have started to validate new ways of identifying infarction and penumbra in experimental models. [^{18}F]-FMISO PET was evaluated in rats undergoing permanent and temporary MCA occlusion [134]. Nitroimidazole compounds such as FMISO are trapped in hypoxic cells [135], but not in necrotic tissue [136], thereby providing a simple direct image of the penumbra. In the hyperacute phase (until 30 min) after permanent MCA occlusion, there was increased [^{18}F]-FMISO

binding in the entire ipsilateral MCA territory, which normalized 48 h later, in line with a nearly complete MCA territory infarct. In contrast, there was no demonstrable tracer retention in temporary MCA occlusion models, which histopathologically showed ischemic changes only, supporting the validity of [^{18}F]-FMISO as a marker of the penumbra after stroke.

Recently, Reshef et al. reported on ^{18}F-labeled-5-fluoropentyl-2-methyl-malonic acid ([^{18}F]-ML-10) as potential radioligand for imaging apoptosis among others in cerebral stroke [137]. Although necrosis predominates as the mode of cell death during the hyperacute stage of stroke, apoptosis plays an important role in ensuing staged of active disease [138]. Following permanent MCA occlusion in mice, increased [^{18}F]-ML-10 uptake was observed selectively in the ischemic MCA territory, and correlated with the histological evidence of cell death. The degree, however, to which a defective blood–brain-barrier (BBB) contribute to the specific uptake of [^{18}F]-ML-10 has not been determined.

No treatment currently exists to restore the lost neurological function after stroke. Increased vascularisation in the stroke border zone within a few days after stroke is associated with neurological recovery [139], and may be valuable not only as prognostic factor but also as measurement of success to help guide proangiogenic therapies. Using [^{64}Cu]-DOTA-VGEF$_{121}$ in rats undergoing distal MCA occlusion surgery, Cai et al. found that angiogenesis appeared very rapidly after stroke (i.e. 2 days post occlusion) [133]. [^{64}Cu]-DOTA-VGEF$_{121}$ uptake peaked in the stroke border zone ~10 days after surgery, confirmed by histology and autoradiography, after which it decreases. No correlation of [^{64}Cu]-DOTA-VGEF$_{121}$ uptake with long term stroke outcome has been performed yet to evaluate the potential prognostic value.

In a SPECT study, ^{99m}TC-HYNIC-annexin V, another radioligand for imaging apoptosis, was used to monitor the response of neuroprotective therapy with monoclonal antibody raised against FasL in a rodent model of transient MCA occlusion [140]. FasL is the cognate ligand for the Fas death receptor, a member of the tumour necrosis receptor subfamily [141]. FasL rapidly increased its expression within the neurons of the penumbra following ischemic injury, thereby inducing pro-apoptotic mechanisms [142]. Blankenberg et al. demonstrated that radiolabeled annexin V detects the early phases of neuronal ischemic injury and its response to anti-FasL therapy. Anti-FasL treatment significantly reduced annexin uptake by 92 % with a 60 % decrease in the number of apoptotic neurons on day 1. On day 6, treated rat had an 80 % reduction in tracer uptake with a 75 % decrease in infarct size as compared to controls. Annexin V uptake was in both controls and treated animals linearly correlated with infarct size and the number of apoptotic nuclei.

The same radioligand was also used in sequential SPECT studies to demonstrate the neuroprotective potential of minocycline, an antibiotic with antiapoptotic properties [143], in CB6/F1 mice undergoing unilateral distal MCA occlusion [144]. Seven-day minocycline treatment was found to significantly reduce annexin V uptake between 1 and 30 days after injury, in line with the infarct size. Annexin V uptake was in control and treated-animal maximal on days 1 and 7, followed by a decline at 30 days.

3 Applications in Psychiatry

The application of small-animal PET/SPECT in the field of biological psychiatry is hampered by the limited presence of suitable animal models. Despite a significant number of human PET/SPECT studies, there is a paucity of functional imaging studies in animals. It is indeed more difficult to reproduce human psychiatric diseases using animals in view of the large symptomatic heterogeneity of psychiatric illness, even inside the same clinical definition (endophenotypes). For example, it is particularly difficult to model specific human emotions and to evaluate this in rodents. Moreover, the aberrant behaviours symptomatic of human mental illness are mostly uniquely human, particularly those that are mediated by brain pathways without homology in rodents, e.g. the expanded prefrontal cortex of the human brain.

Despite these difficulties inherent in modelling human psychiatric phenotypes, there has been some recent success, mainly in mice, identifying genetic mutations that give rise to some of the characteristic features of anxiety, depression, schizophrenia, autism, obsessive-compulsive disorder and bipolar disorder [145]. Also here, the application of mice models in small-animal PET/SPECT research has been limited by the small size of the mouse brain. We give an overview of the various neurochemical systems that may provide possible molecular targets for small-animal PET/SPECT research.

Among the various neurotransmitter systems, the dopaminergic system is of particular interest in drug abuse and addiction. Research into brain mechanisms of additive behaviour have traditionally focused on the nucleus accumbens and dopamine inputs to this region from the ventral tegmental area [146]. The potentially significant involvements of the oribitofrontal cortex, anterior cingulate cortex, and other limbic cortical areas have more recently been recognized and investigated [147–149]. Although the precise aetiology of drug addiction is poorly understood, it is widely known to be linked to certain personality traits (e.g. risk-takers, sensation- or novelty-seekers) [150, 151] and individuals diagnosed with particular brain disorders such as attention-deficit hyperactivity disorder (ADHD) [152].

In a recent small-animal PET study, Dalley et al. investigated dopamine $D_{2/3}$ receptor availability in the dorsal and ventral striatum of high impulsive rats compared with non-impulsive rats to evaluate the causal relationship between impulsivity and drug abuse vulnerability [153]. Rats were scanned using the radioligand [^{18}F]fallypride prior to drug exposure. The authors found that [^{18}F]fallypride binding was significantly reduced in the nucleus accumbens but not the dorsal striatum of high impulsive rats compared with non-impulsive subjects. Extracellular dopamine levels were also measured in the nucleus accumbens using in vivo microdialysis [153]; there was no difference between both groups suggesting that dopamine $D_{2/3}$ receptors were likely fewer in number in the nucleus accumbens of high impulsive rats. The authors hypothesized from their PET findings that low dopamine $D_{2/3}$ receptors associated with certain personality traits may be a susceptible neurobiological marker that confers vulnerability to drug experimentation and encourage excessive drug use.

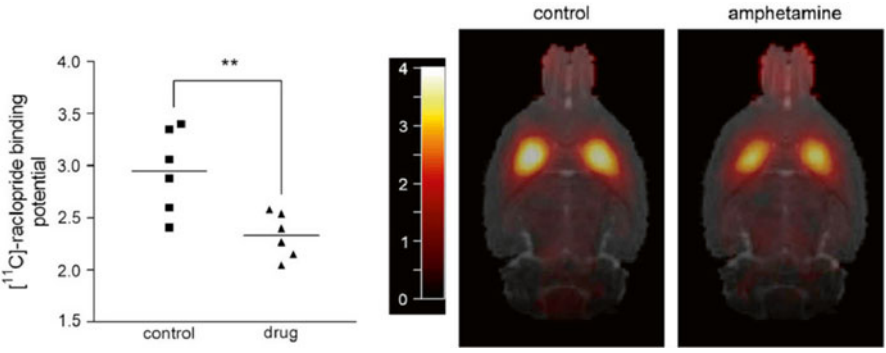

Fig. 19.3 Reduced binding potential of the dopamine $D_{2/3}$ receptor antagonist [^{11}C]-raclopride in the dorsal striatum of rats exposed to intravenous D-amphetamine self-administration compared with control rats receiving yoked infusions of saline (*left hand* graph). Shown also are co-registered [^{11}C]-raclopride binding potential maps and MRI images for a saline control rat and an amphetamine-exposed rat. **$p < 0.01$ (Student's unpaired *t*-test). Reprinted from [158], with permission from Elsevier

In addition, the origin of inter-individual variability in impulsive behaviour is still unknown, but potentially involves both genetic and environmental influences [154, 155]. The importance of environment on dopamine D_2 receptor availability was demonstrated in the monkey striatum [156]. Dopamine D_2 receptor availability measured by [^{18}F]fluoroclebopride was found to be lower in the subordinate monkeys than dominant monkeys. Crucially, this difference was present only when the monkeys were housed together—not before—suggesting this effect to be related to social context rather than to traits variables. The authors also demonstrated a link between low dopamine D_2 receptor availability in the striatum and cocaine self-administration. This finding was substantiated in a recent longitudinal PET study in the monkey brain, demonstrating that baseline dopamine D_2 receptor availability inversely predicts cocaine self-administration and that cocaine itself further reduce the dopamine D_2 receptor availability in this region [157].

This latter finding was also observed in rats, self-administering the psychostimulant D-amphetamine [158]. Drug-exposed and saline control rats were scanned 24 h after the discontinuation of self-administration using PET and [^{11}C]-raclopride. Consistent with the abovementioned study in monkey, chronic administration of amphetamine significantly decreased [^{11}C]-raclopride binding potential in the dorsal striatum (Fig. 19.3).

Besides drug abuse and addiction, molecular neuroimaging studies are also consistent with the notion that dopaminergic dysregulation is a key pathological feature of schizophrenia. Schizophrenia affects 1 % of the population [159] and usually begins in late adolescence or early adulthood. It is characterized by positive psychotic symptoms, such as delusions and hallucinations and disorganized speech, and negative psychotic symptoms, such as emotional blunting and loss of drive. PET and SPECT human imaging studies have shown that schizophrenia is associated with increased presynaptic striatal dopamine synthesis and storage [160, 161],

and increased striatal release of dopamine following amphetamine administration [162, 163]. Treatment consequently involves the use of antipsychotic drug, all of which act as antagonists at central dopamine D_2 receptors [164].

The application of small-animal PET/SPECT in schizophrenia research is mainly focused on the development and evaluation of these antipsychotic drugs for the treatment of this disorder. Despite extensive clinical experience with antipsychotics, there has long been no broad consensus on the doses of these substances that should be administered. Formerly, most antipsychotics were administered empirically according to clinical dose-finding studies, in which arbitrarily selected doses were tested to find the "most efficient" dose range in a patient population, with no regard for the molecular effects of the tested drug. Brain PET imaging studies in healthy rats have indicated that occupancy of at least 65 % of dopamine D_2 receptors is needed for clinical response to antipsychotics, and that occupancy rates exceeding 72 and 78 % are associated with a high risk for motor adverse effects, providing a rationale for the use of relatively low doses of typical antipsychotics [165].

PET studies in patients with schizophrenia that assessed the level of dopamine D_1 receptors in the prefrontal cortex using [^{11}C]SCH23390 and [^{11}C]NCC112 [166–168], have generated contradictory findings. Small-animal PET in healthy rats provided evidence to elucidate this inconsistency [169]. Sprague–Dawley rats subjected to acute dopamine depletion did not show alterations in [^{11}C]NCC112 in the striatum and prefrontal cortex, while paradoxically striatal [^{11}C]SCH23390 binding was decreased. On the other hand, subchronic dopamine depletion was associated with increased [^{11}C]NCC112 binding and decreased [^{11}C]SCH23390 binding in these regions, suggesting that the binding of these tracers in the prefrontal cortex of patients with schizophrenia might reflect changes in dopamine D_1 receptors secondary to sustained deficit in the prefrontal dopamine function.

Apart from the dopaminergic system, the central serotonergic system has received great interest in depression research [170]. Modifications of serotonergic activity contribute to many of the symptoms, for example, mood, appetite, sleep, sexual and cognitive dysfunction. Depression has the highest prevalence of all psychiatric disorders and occurs twice as frequently in women as in men. It can begin at any age, but has its average age of onset in the mid-20s [171].

The involvement of the serotonergic system in depression is also based partly on the observation that selective serotonin reuptake inhibitors (SSRIs) exert antidepressant effects and that most antidepressant drugs either directly or indirectly enhance serotonin (5-HT) transmission [172]. The most promising evidence for a deficit in central serotonin neurotransmission that is compensated by antidepressant pharmacotherapy involves postsynaptic serotonin-1A receptors (5-HT_{1A}). In human PET studies, changes in expression and function of the 5-HT_{1A} receptor are well described, particularly in the mesiotemporal cortex and raphe nucleus (for review see [173]). Currently, most of the radiopharmaceuticals developed to image 5-HT_{1A} receptors have also been validated in rodents, but not yet applied in depression research. 5-HT_{1A} receptor subtypes have been extensively visualized with small-animal PET using [^{11}C]WAY-100635 [174]. A new promising tool for the in vivo imaging of this receptor subtype in rodents is recently presented by [^{18}F]

MPPF [175]. Aznavour and colleagues demonstrated using [^{18}F]MPPF in rats that values of binding potential for hippocampus (1.2), entorhinal cortex (1.1), medial prefrontal cortex (1.0) and raphe nuclei (0.6) were comparable to those previously measured with PET in cats, non-human primates or humans [175]. Test-retest variability was also in the order of 10 % in the larger brain regions and less than 20 % in small nuclei.

Individuals affected by depression may also suffer from mania in bipolar disorder, which affects approximately 1 % of the world's population [176]. Hougland et al. performed in vivo [^{18}F]-FDG imaging in a rat model of mania [177]. Following ICV ouabain administration, brain [^{18}F]-FDG uptake was reduced compared to those animals receiving equal volumes of artificial cerebrospinal fluid. Pretreatment with lithium, a standard treatment for mania, normalized this [^{18}F]-FDG uptake. Imaging of ill bipolar patients has revealed consistent findings [178, 179].

The dopaminergic and serotonergic neurotransmitter systems have also been central in functional imaging research of patients with eating disorders. Patients with anorexia nervosa (AN) and bulimia nervosa (BN) display anxiety, depression, and suicide or have symptoms related to altered reward and excessive motor activity [180]. In human imaging studies of AN, involvement of the parietal, frontal and cingulate cortices in the pathophysiology have been well demonstrated using radioligands for the serotonergic pathways [181], as well as [^{18}F]-FDG [182].

In an animal model of AN, Barabarich-Marsteller et al. investigated using [^{18}F]-FDG whether the psychobiological changes that occur following 'voluntary' starvation in individuals are comparable to the changes that result from involuntary food restriction (i.e., an experimental procedure leading to activity-based anorexia or ABA) [183]. Briefly, rats were restricted to 40 % of their baseline daily food intake until a 30 % weight loss occurred. Combining the food restriction with access to a running wheel induced hyperactivity and a spontaneous restriction of food intake, as seen in humans [184]. Only the food-restricted rats displayed an increase in [^{18}F]-FDG uptake in the cerebellum, while a decrease was observed in the hippocampus and striatum; the latter is in line with previous reports in the clinical condition [182].

More recently, these cerebral metabolic changes in the same ABA model were monitored using a voxel-based analysis approach [185]. In line with Barabarich-Marsteller et al., a higher regional metabolism in the cerebellum and hypometabolism was found in the ventral striatum. In addition, relative [^{18}F]-FDG uptake was increased in the mediodorsal thalamus and ventral pontine nuclei, while body weight loss was positively correlated with cerebral metabolism in the cingulate cortex and the adjacent somato-sensory cortex. It was concluded that the activity-based rat model of AN share indeed several characteristics with the human disease, encompassing complex interplays between different circuitries involving motor activity, food-related behaviour and somato-sensory regions, thus adding proof to the validity of this model.

Despite the abovementioned body of evidence indicating a prominent role of dopamine and serotonin neurotransmission in various psychiatric disorders, there is a limited base of PET/SPECT studies investigating the role of other neurochemical

systems in patients or models for psychiatry. Human studies have suggested that GABAergic abnormalities are associated with stress, anxiety, and depression [186–188]. Glutamate neurotransmission, on the other hand, may be involved in obsessive compulsive behaviour and schizophrenia [189, 190]. Although radioligands to image both systems have been validated in small-animals [191, 192], none of them have yet been utilized in psychiatric animal research.

4 Conclusion

Preclinical in vivo imaging techniques such as PET and SPECT have played a role in validating animal models of neurological and psychiatric diseases at a basic science level, and therefore contributed to improve our understanding of human diseases. In particular, the key advantages of these research tools is that subjects can be followed longitudinally, over time, thus allowing investigation of the disease process, the development of compensatory changes, and the long-term evaluation of the safety and efficacy of drug-based, surgical, cellular or gene-therapy based interventions.

The preclinical evaluation of potential therapies using small-animal imaging has mainly been applied in the field of neurology. The use of small-animal PET/SPECT imaging in psychiatry is hampered by the lack of suitable animal models, as preclinical neuroimaging research is only as good as the animal model being employed.

Acknowledgments CC is a Postdoctoral Researcher for the Research Council of the Katholieke Universiteit Leuven, Belgium; KVL is Senior Clinical Researcher for the Fund for Scientific Research Flanders (FWO), Belgium. This work was funded in part by the European Community FP7-Network-of-Excellence INMiND (grant agreement no. 278850). HZ knowledge support provided by the Swiss National Science Foundation under grant SNSF 31003A-125246.

References

1. Lythgoe MF, Sibson NR, Harris NG (2003) Neuroimaging of animal models of brain disease. Br Med Bull 65:235-257.
2. Hitzemann R (2000) Animal models of psychiatric disorders and their relevance to alcoholism. Alcohol Res Health 24:149-158.
3. Burns HD, Van Laere K, Sanabria-Bohorquez S et al (2007) [18F]MK-9470, a positron emission tomography (PET) tracer for in vivo human PET brain imaging of the cannabinoid-1 receptor. Proc Natl Acad Sci U S A 104:9800-9805.
4. Chitneni SK, Garreau L, Cleynhens B et al (2008) Improved synthesis and metabolic stability analysis of the dopamine transporter ligand [(18)F]FECT. Nucl Med Biol 35:75-82.
5. Birchfield NB and Casida JE (1996) Protoporphyrinogen oxidase: high affinity tetrahydrophthalimide radioligand for the inhibitor/herbicide-binding site in mouse liver mitochondria. Chem Res Toxicol 9:1135-1139.
6. Wienhard K (2002) Measurement of glucose consumption using [(18)F]fluorodeoxyglucose. Methods 27:218-225.

7. Myers R and Hume S (2002) Small animal PET. Eur Neuropsychopharmacol 12:545-555.
8. Vastenhouw B and Beekman F (2007) Submillimeter total-body murine imaging with U-SPECT-I. J Nucl Med 48:487-493.
9. van der Have F, Vastenhouw B, Ramakers RM et al (2009) U-SPECT-II: An Ultra-High-Resolution Device for Molecular Small-Animal Imaging. J Nucl Med 50:599-605.
10. Massoud TF and Gambhir SS (2003) Molecular imaging in living subjects: seeing fundamental biological processes in a new light. Genes Dev 17:545-580.
11. Tsukada H (1999) Delivery of radioligands for positron emission tomography (PET) in the central nervous system. Adv Drug Deliv Rev 37:175-188.
12. Vaska P, Woody CL, Schlyer DJ et al (2004) RatCAP: miniaturized head-mounted PET for conscious rodent brain imaging. IEEE Trans Nucl Sci 51:2718-2722.
13. Votaw J, Byas-Smith M, Hua J et al (2003) Interaction of isoflurane with the dopamine transporter. Anesthesiology 98:404-411.
14. Matsumura A, Mizokawa S, Tanaka M et al (2003) Assessment of microPET performance in analyzing the rat brain under different types of anesthesia: comparison between quantitative data obtained with microPET and ex vivo autoradiography. Neuroimage 20:2040-2050.
15. Ingvar M, Eriksson L, Rogers GA, Stone-Elander S, Widen L (1991) Rapid feasibility studies of tracers for positron emission tomography: high-resolution PET in small animals with kinetic analysis. J Cereb Blood Flow Metab 11:926-931.
16. Laforest R, Sharp TL, Engelbach JA et al (2005) Measurement of input functions in rodents: challenges and solutions. Nucl Med Biol 32:679-685.
17. Gunn RN, Lammertsma AA, Hume SP, Cunningham VJ (1997) Parametric imaging of ligand-receptor binding in PET using a simplified reference region model. Neuroimage 6:279-287.
18. Wu HM, Huang SC, Allada V et al (1996) Derivation of input function from FDG-PET studies in small hearts. J Nucl Med 37:1717-1722.
19. Pain F, Laniece P, Mastrippolito R et al (2004) Arterial input function measurement without blood sampling using a beta-microprobe in rats. J Nucl Med 45:1577-1582.
20. Sossi V and Ruth TJ (2005) Micropet imaging: in vivo biochemistry in small animals. J Neural Transm 112:319-330.
21. Jagoda EM, Vaquero JJ, Seidel J, Green MV, Eckelman WC (2004) Experiment assessment of mass effects in the rat: implications for small animal PET imaging. Nucl Med Biol 31:771-779.
22. Casteels C, Vermaelen P, Nuyts J et al (2006) Construction and Evaluation of Multitracer Small-Animal PET Probabilistic Atlases for Voxel-Based Functional Mapping of the Rat Brain. J Nucl Med 47:1858-1866.
23. Rubins DJ, Melega WP, Lacan G et al (2003) Development and evaluation of an automated atlas-based image analysis method for microPET studies of the rat brain. Neuroimage 20:2100-2118.
24. Kesner AL, Dahlbom M, Huang SC et al (2006) Semiautomated analysis of small-animal PET data. J Nucl Med 47:1181-1186.
25. Segars WP, Tsui BM, Frey EC, Johnson GA, Berr SS (2004) Development of a 4-D digital mouse phantom for molecular imaging research. Mol Imaging Biol 6:149-159.
26. Dogdas B, Stout D, Chatziioannou AF, Leahy RM (2007) Digimouse: a 3D whole body mouse atlas from CT and cryosection data. Phys Med Biol 52:577-587.
27. Taschereau R, Chow PL, Chatziioannou AF (2006) Monte carlo simulations of dose from microCT imaging procedures in a realistic mouse phantom. Med Phys 33:216-224.
28. Stabin MG, Peterson TE, Holburn GE, Emmons MA (2006) Voxel-based mouse and rat models for internal dose calculations. J Nucl Med 47:655-659.
29. Wu L, Zhang G, Luo Q, Liu Q (2008) An image-based rat model for Monte Carlo organ dose calculations. Med Phys 35:3759-3764.
30. Zaidi H and Xu XG (2007) Computational anthropomorphic models of the human anatomy: the path to realistic Monte Carlo modeling in radiological sciences. Annu Rev Biomed Eng 9:471-500.

31. Zaidi H and Tsui BMW (2009) Review of anthropomorphic computational anatomical and physiological models. Proceedings of the IEEE 97:1938-53.
32. Beekman F, Vastenhouw B, vander Wilt G et al (2009) 3D rat phantom for ultra-high resolution molecular imaging. Proceedings of the IEEE 97:1997-2005.
33. Samii A, Nutt JG, Ransom BR (2004) Parkinson's disease. Lancet 363:1783-1793.
34. Fearnley JM and Lees AJ (1991) Ageing and Parkinson's disease: substantia nigra regional selectivity. Brain 114 (Pt 5):2283-2301.
35. Hantraye P (1998) Modeling dopamine system dysfunction in experimental animals. Nucl Med Biol 25:721-728.
36. Schapira AH (2006) Etiology of Parkinson's disease. Neurology 66:S10-S23.
37. Recchia A, Debetto P, Negro A et al (2004) Alpha-synuclein and Parkinson's disease. FASEB J 18:617-626.
38. Jenner P (2008) Functional models of Parkinson's disease: a valuable tool in the development of novel therapies. Ann Neurol 64 Suppl 2:S16-S29.
39. Doudet DJ, Chan GL, Holden JE et al (1998) 6-[18F]Fluoro-L-DOPA PET studies of the turnover of dopamine in MPTP-induced parkinsonism in monkeys. Synapse 29:225-232.
40. Yee RE, Irwin I, Milonas C et al (2001) Novel observations with FDOPA-PET imaging after early nigrostriatal damage. Mov Disord 16:838-848.
41. Melega WP, Raleigh MJ, Stout DB et al (1996) Longitudinal behavioral and 6-[18F]fluoro-L-DOPA-PET assessment in MPTP-hemiparkinsonian monkeys. Exp Neurol 141:318-329.
42. Doudet DJ, Wyatt RJ, Cannon-Spoor E et al (1993) 6-[18F]fluoro-L-dopa and cerebral blood flow in unilaterally MPTP-treated monkeys. J Neural Transplant Plast 4:27-38.
43. Eberling JL, Bankiewicz KS, Jordan S, VanBrocklin HF, Jagust WJ (1997) PET studies of functional compensation in a primate model of Parkinson's disease. Neuroreport 8: 2727-2733.
44. Eberling JL, Pivirotto P, Bringas J, Bankiewicz KS (2000) Tremor is associated with PET measures of nigrostriatal dopamine function in MPTP-lesioned monkeys. Exp Neurol 165:342-346.
45. Hume SP, Lammertsma AA, Myers R et al (1996) The potential of high-resolution positron emission tomography to monitor striatal dopaminergic function in rat models of disease. J Neurosci Methods 67:103-112.
46. Sharma SK and Ebadi M (2005) Distribution kinetics of 18F-DOPA in weaver mutant mice. Brain Res Mol Brain Res 139:23-30.
47. Sharma SK, El Refaey H, Ebadi M (2006) Complex-1 activity and 18F-DOPA uptake in genetically engineered mouse model of Parkinson's disease and the neuroprotective role of coenzyme Q10. Brain Res Bull 70:22-32.
48. Strome EM, Cepeda IL, Sossi V, Doudet DJ (2006) Evaluation of the integrity of the dopamine system in a rodent model of Parkinson's disease: small animal positron emission tomography compared to behavioral assessment and autoradiography. Mol Imaging Biol 8:292-299.
49. Sossi V, Holden JE, Topping GJ et al (2007) In vivo measurement of density and affinity of the monoamine vesicular transporter in a unilateral 6-hydroxydopamine rat model of PD. J Cereb Blood Flow Metab 27:1407-1415.
50. Nguyen TV, Brownell AL, Iris Chen YC et al (2000) Detection of the effects of dopamine receptor supersensitivity using pharmacological MRI and correlations with PET. Synapse 36:57-65.
51. Hume SP, Myers R, Bloomfield PM et al (1992) Quantitation of carbon-11-labeled raclopride in rat striatum using positron emission tomography. Synapse 12:47-54.
52. Kaasinen V, Ruottinen HM, Nagren K et al (2000) Upregulation of putaminal dopamine D2 receptors in early Parkinson's disease: a comparative PET study with [11C] raclopride and [11C]N-methylspiperone. J Nucl Med 41:65-70.
53. Nikolaus S, Larisch R, Beu M et al (2003) Bilateral increase in striatal dopamine D2 receptor density in the 6-hydroxydopamine-lesioned rat: a serial in vivo investigation with small animal PET. Eur J Nucl Med Mol Imaging 30:390-395.

54. Casteels C, Lauwers E, Bormans G, Baekelandt V, Van Laere K (2007) Metabolic-dopaminergic mapping of the 6-hydroxydopamine rat model for Parkinson's disease. Eur J Nucl Med Mol Imaging
55. Lauwers E, Beque D, Van Laere K et al (2007) Non-invasive imaging of neuropathology in a rat model of alpha-synuclein overexpression. Neurobiol Aging 28:248-257.
56. Inaji M, Okauchi T, Ando K et al (2005) Correlation between quantitative imaging and behavior in unilaterally 6-OHDA-lesioned rats. Brain Res 1064:136-145.
57. Chen YI, Brownell AL, Galpern W et al (1999) Detection of dopaminergic cell loss and neural transplantation using pharmacological MRI, PET and behavioral assessment. Neuroreport 10:2881-2886.
58. Brownell AL, Livni E, Galpern W, Isacson O (1998) In vivo PET imaging in rat of dopamine terminals reveals functional neural transplants. Ann Neurol 43:387-390.
59. Doudet DJ, Cornfeldt ML, Honey CR, Schweikert AW, Allen RC (2004) PET imaging of implanted human retinal pigment epithelial cells in the MPTP-induced primate model of Parkinson's disease. Exp Neurol 189:361-368.
60. Bjorklund LM, Sanchez-Pernaute R, Chung S et al (2002) Embryonic stem cells develop into functional dopaminergic neurons after transplantation in a Parkinson rat model. Proc Natl Acad Sci U S A 99:2344-2349.
61. Opacka-Juffry J, Ashworth S, Hume SP et al (1995) GDNF protects against 6-OHDA nigrostriatal lesion: in vivo study with microdialysis and PET. Neuroreport 7:348-352.
62. Sullivan AM, Opacka-Juffry J, Blunt SB (1998) Long-term protection of the rat nigrostriatal dopaminergic system by glial cell line-derived neurotrophic factor against 6-hydroxydopamine in vivo. Eur J Neurosci 10:57-63.
63. Olanow CW, Goetz CG, Kordower JH et al (2003) A double-blind controlled trial of bilateral fetal nigral transplantation in Parkinson's disease. Ann Neurol 54:403-414.
64. Freed CR, Greene PE, Breeze RE et al (2001) Transplantation of embryonic dopamine neurons for severe Parkinson's disease. N Engl J Med 344:710-719.
65. Minghetti L and Levi G (1998) Microglia as effector cells in brain damage and repair: focus on prostanoids and nitric oxide. Prog Neurobiol 54:99-125.
66. Ullrich O, Diestel A, Eyupoglu IY, Nitsch R (2001) Regulation of microglial expression of integrins by poly(ADP-ribose) polymerase-1. Nat Cell Biol 3:1035-1042.
67. Cicchetti F, Brownell AL, Williams K et al (2002) Neuroinflammation of the nigrostriatal pathway during progressive 6-OHDA dopamine degeneration in rats monitored by immunohistochemistry and PET imaging. Eur J Neurosci 15:991-998.
68. Sanchez-Pernaute R, Ferree A, Cooper O et al (2004) Selective COX-2 inhibition prevents progressive dopamine neuron degeneration in a rat model of Parkinson's disease. J Neuroinflammation 1:6-
69. Palombo E, Porrino LJ, Bankiewicz KS et al (1988) Administration of MPTP acutely increases glucose utilization in the substantia nigra of primates. Brain Res 453:227-234.
70. Porrino LJ, Burns RS, Crane AM et al (1987) Changes in local cerebral glucose utilization associated with Parkinson's syndrome induced by 1-methyl-4-phenyl-1,2,3, 6-tetrahydropyridine (MPTP) in the primate. Life Sci 40:1657-1664.
71. Wooten GF and Collins RC (1983) Effects of dopaminergic stimulation on functional brain metabolism in rats with unilateral substantia nigra lesions. Brain Res 263:267-275.
72. Kuhl DE, Metter EJ, Riege WH (1984) Patterns of local cerebral glucose utilization determined in Parkinson's disease by the [18F]fluorodeoxyglucose method. Ann Neurol 15:419-424.
73. Lozza C, Baron JC, Eidelberg D et al (2004) Executive processes in Parkinson's disease: FDG-PET and network analysis. Hum Brain Mapp 22:236-245.
74. Walker FO (2007) Huntington's disease. Lancet 369:218-228.
75. The Huntington's Disease Collaborative Research Group (1993) A novel gene containing a trinucleotide repeat that is expanded and unstable on Huntington's disease chromosomes. The Huntington's Disease Collaborative Research Group. Cell 72:971-983.

76. Wexler NS, Lorimer J, Porter J et al (2004) Venezuelan kindreds reveal that genetic and environmental factors modulate Huntington's disease age of onset. Proc Natl Acad Sci U S A 101:3498-3503.
77. Coyle JT and Schwarcz R (1976) Lesion of striatal neurones with kainic acid provides a model for Huntington's chorea. Nature 263:244-246.
78. Beal MF, Kowall NW, Ellison DW et al (1986) Replication of the neurochemical characteristics of Huntington's disease by quinolinic acid. Nature 321:168-171.
79. Borlongan CV, Koutouzis TK, Sanberg PR (1997) 3-Nitropropionic acid animal model and Huntington's disease. Neurosci Biobehav Rev 21:289-293.
80. Mangiarini L, Sathasivam K, Seller M et al (1996) Exon 1 of the HD gene with an expanded CAG repeat is sufficient to cause a progressive neurological phenotype in transgenic mice. Cell 87:493-506.
81. Marsh JL, Pallos J, Thompson LM (2003) Fly models of Huntington's disease. Hum Mol Genet 12 Spec No 2:R187-R193.
82. von Horsten S, Schmitt I, Nguyen HP et al (2003) Transgenic rat model of Huntington's disease. Hum Mol Genet 12:617-624.
83. Araujo DM, Cherry SR, Tatsukawa KJ, Toyokuni T, Kornblum HI (2000) Deficits in striatal dopamine D(2) receptors and energy metabolism detected by in vivo microPET imaging in a rat model of Huntington's disease. Exp Neurol 166:287-297.
84. Ishiwata K, Ogi N, Hayakawa N et al (2002) Adenosine A2A receptor imaging with [11C] KF18446 PET in the rat brain after quinolinic acid lesion: comparison with the dopamine receptor imaging. Ann Nucl Med 16:467-475.
85. Ishiwata K, Ogi N, Hayakawa N et al (2002) Positron emission tomography and ex vivo and in vitro autoradiography studies on dopamine D2-like receptor degeneration in the quinolinic acid-lesioned rat striatum: comparison of [11C]raclopride, [11C]nemonapride and [11C] N-methylspiperone. Nucl Med Biol 29:307-316.
86. Moresco RM, Lavazza T, Belloli S et al (2008) Quinolinic acid induced neurodegeneration in the striatum: a combined in vivo and in vitro analysis of receptor changes and microglia activation. Eur J Nucl Med Mol Imaging 35:704-715.
87. Brownell AL, Chen YI, Yu M et al (2004) 3-Nitropropionic acid-induced neurotoxicit--ssessed by ultra high resolution positron emission tomography with comparison to magnetic resonance spectroscopy. J Neurochem 89:1206-1214.
88. Wang X, Sarkar A, Cicchetti F et al (2005) Cerebral PET imaging and histological evidence of transglutaminase inhibitor cystamine induced neuroprotection in transgenic R6/2 mouse model of Huntington's disease. J Neurol Sci 231:57-66.
89. Fratiglioni L, De Ronchi D, Guero-Torres H (1999) Worldwide prevalence and incidence of dementia. Drugs Aging 15:365-375.
90. Jellinger KA (2008) Neuropathological aspects of Alzheimer disease, Parkinson disease and frontotemporal dementia. Neurodegener Dis 5:118-121.
91. Selkoe DJ (2002) Alzheimer's disease is a synaptic failure. Science 298:789-791.
92. Williamson J, Goldman J, Marder KS (2009) Genetic aspects of Alzheimer disease. Neurologist 15:80-86.
93. Spillantini MG, Murrell JR, Goedert M et al (1998) Mutation in the tau gene in familial multiple system tauopathy with presenile dementia. Proc Natl Acad Sci U S A 95:7737-7741.
94. Gotz J, Deters N, Doldissen A et al (2007) A decade of tau transgenic animal models and beyond. Brain Pathol 17:91-103.
95. Gotz J and Ittner LM (2008) Animal models of Alzheimer's disease and frontotemporal dementia. Nat Rev Neurosci 9:532-544.
96. Levin CS and Zaidi H (2007) Current trends in preclinical PET system design. PET Clinics 2:125-160.
97. Herholz K, Carter SF, Jones M (2007) Positron emission tomography imaging in dementia. Br J Radiol 80 Spec No 2:S160-S167.

98. Valla J, Chen K, Berndt JD et al (2002) Effects of image resolution on autoradiographic measurements of posterior cingulate activity in PDAPP mice: implications for functional brain imaging studies of transgenic mouse models of Alzheimer's Disease. Neuroimage 16:1-6.
99. Skovronsky DM, Zhang B, Kung MP et al (2000) In vivo detection of amyloid plaques in a mouse model of Alzheimer's disease. Proc Natl Acad Sci U S A 97:7609-7614.
100. Klunk WE, Engler H, Nordberg A et al (2004) Imaging brain amyloid in Alzheimer's disease with Pittsburgh Compound-B. Ann Neurol 55:306-319.
101. Bacskai BJ, Hickey GA, Skoch J et al (2003) Four-dimensional multiphoton imaging of brain entry, amyloid binding, and clearance of an amyloid-beta ligand in transgenic mice. Proc Natl Acad Sci U S A 100:12462-12467.
102. Klunk WE, Lopresti BJ, Ikonomovic MD et al (2005) Binding of the positron emission tomography tracer Pittsburgh compound-B reflects the amount of amyloid-beta in Alzheimer's disease brain but not in transgenic mouse brain. J Neurosci 25:10598-10606.
103. Maeda J, Ji B, Irie T et al (2007) Longitudinal, quantitative assessment of amyloid, neuroinflammation, and anti-amyloid treatment in a living mouse model of Alzheimer's disease enabled by positron emission tomography. J Neurosci 27:10957-10968.
104. Heneka MT, Ramanathan M, Jacobs AH et al (2006) Locus ceruleus degeneration promotes Alzheimer pathogenesis in amyloid precursor protein 23 transgenic mice. J Neurosci 26:1343-1354.
105. Fisher RS, Van Emde BW, Blume W et al (2005) Epileptic seizures and epilepsy: definitions proposed by the International League Against Epilepsy (ILAE) and the International Bureau for Epilepsy (IBE). Epilepsia 46:470-472.
106. Hauser WA and Kurland LT (1975) The epidemiology of epilepsy in Rochester, Minnesota, 1935 through 1967. Epilepsia 16:1-66.
107. Gram L (1990) Epileptic seizures and syndromes. Lancet 336:161-163.
108. The Commission on Classification and Terminology of the International League Against Epilepsy (1981) Proposal for revised clinical and electroencephalographic classification of epileptic seizures. Epilepsia 22:489-501.
109. Purpura DP, Penry JK, Woodbury DM, Tower DB, Walter RD (1972) Experimental Models of Epilepsy - A Manual for the Laboratory Worker. New York, Raven
110. Kornblum HI, Araujo DM, Annala AJ et al (2000) In vivo imaging of neuronal activation and plasticity in the rat brain by high resolution positron emission tomography (microPET). Nat Biotechnol 18:655-660.
111. Goffin K, Dedeurwaerdere S, Van Laere K, Van Paesschen W (2008) Neuronuclear assessment of patients with epilepsy. Semin Nucl Med 38:227-239.
112. Mirrione MM, Schiffer WK, Siddiq M, Dewey SL, Tsirka SE (2006) PET imaging of glucose metabolism in a mouse model of temporal lobe epilepsy. Synapse 59:119-121.
113. Wang D, Pascual JM, Yang H et al (2006) A mouse model for Glut-1 haploinsufficiency. Hum Mol Genet 15:1169-1179.
114. Dick AP, Harik SI, Klip A, Walker DM (1984) Identification and characterization of the glucose transporter of the blood-brain barrier by cytochalasin B binding and immunological reactivity. Proc Natl Acad Sci U S A 81:7233-7237.
115. Jupp B, Williams J, Binns D, Hicks R, O'Brien T (2007) Imaging small animal models of epileptogenesis. Neurology Asia 12 (supplement 1):51-54.
116. Goffin K, Van Paesschen W, Dupont P, Van Laere K (2009) Longitudinal microPET imaging of brain glucose metabolism in rat lithium-pilocarpine model of epilepsy. Exp Neurol
117. Liefaard LC, Ploeger BA, Molthoff CF et al (2009) Changes in GABAA receptor properties in amygdala kindled animals: in vivo studies using [11C]flumazenil and positron emission tomography. Epilepsia 50:88-98.
118. Di Marzo V, Melck D, Bisogno T, De Petrocellis L (1998) Endocannabinoids: endogenous cannabinoid receptor ligands with neuromodulatory action. Trends Neurosci 21:521-528.

119. Marsicano G, Goodenough S, Monory K et al (2003) CB1 cannabinoid receptors and on-demand defense against excitotoxicity. Science 302:84-88.
120. Wallace MJ, Wiley JL, Martin BR, Delorenzo RJ (2001) Assessment of the role of CB1 receptors in cannabinoid anticonvulsant effects. Eur J Pharmacol 428:51-57.
121. Wallace MJ, Martin BR, Delorenzo RJ (2002) Evidence for a physiological role of endocannabinoids in the modulation of seizure threshold and severity. Eur J Pharmacol 452:295-301.
122. Wallace MJ, Blair RE, Falenski KW, Martin BR, Delorenzo RJ (2003) The endogenous cannabinoid system regulates seizure frequency and duration in a model of temporal lobe epilepsy. J Pharmacol Exp Ther 307:129-137.
123. Goffin K, Bormans G, Casteels C et al (2008) An in vivo [(18)F]MK-9470 microPET study of type 1 cannabinoid receptor binding in Wistar rats after chronic administration of valproate and levetiracetam. Neuropharmacology
124. Murray CJ and Lopez AD (1997) Mortality by cause for eight regions of the world: Global Burden of Disease Study. Lancet 349:1269-1276.
125. Paciaroni M, Caso V, Agnelli G (2009) The Concept of Ischemic Penumbra in Acute Stroke and Therapeutic Opportunities. Eur Neurol 61:321-330.
126. Seshadri S and Wolf PA (2007) Lifetime risk of stroke and dementia: current concepts, and estimates from the Framingham Study. Lancet Neurol 6:1106-1114.
127. Wiebers DO, Adams HP, Jr., Whisnant JP (1990) Animal models of stroke: are they relevant to human disease? Stroke 21:1-3.
128. Carmichael ST (2005) Rodent models of focal stroke: size, mechanism, and purpose. NeuroRx 2:396-409.
129. McBean DE and Kelly PA (1998) Rodent models of global cerebral ischemia: a comparison of two-vessel occlusion and four-vessel occlusion. Gen Pharmacol 30:431-434.
130. Heiss WD (2000) Ischemic penumbra: evidence from functional imaging in man. J Cereb Blood Flow Metab 20:1276-1293.
131. Temma T, Kuge Y, Sano K et al (2008) PET O-15 cerebral blood flow and metabolism after acute stroke in spontaneously hypertensive rats. Brain Res 1212:18-24.
132. Temma T (2008) In-vivo positron emission tomography (PET) measurement of cerebral oxygen metabolism in small animals. Yakugaku Zasshi 128:1267-1273.
133. Cai W, Guzman R, Hsu AR et al (2009) Positron emission tomography imaging of poststroke angiogenesis. Stroke 40:270-277.
134. Takasawa M, Beech JS, Fryer TD et al (2007) Imaging of brain hypoxia in permanent and temporary middle cerebral artery occlusion in the rat using 18F-fluoromisonidazole and positron emission tomography: a pilot study. J Cereb Blood Flow Metab 27:679-689.
135. Nunn A, Linder K, Strauss HW (1995) Nitroimidazoles and imaging hypoxia. Eur J Nucl Med 22:265-280.
136. Miller GG, Ngan-Lee J, Chapman JD (1982) Intracellular localization of radioactively labeled misonidazole in EMT-6-tumor cells in vitro. Int J Radiat Oncol Biol Phys 8: 741-744.
137. Reshef A, Shirvan A, Waterhouse RN et al (2008) Molecular imaging of neurovascular cell death in experimental cerebral stroke by PET. J Nucl Med 49:1520-1528.
138. Mattson MP, Duan W, Pedersen WA, Culmsee C (2001) Neurodegenerative disorders and ischemic brain diseases. Apoptosis 6:69-81.
139. Krupinski J, Kaluza J, Kumar P, Kumar S, Wang JM (1994) Role of angiogenesis in patients with cerebral ischemic stroke. Stroke 25:1794-1798.
140. Blankenberg FG, Kalinyak J, Liu L et al (2006) 99mTc-HYNIC-annexin V SPECT imaging of acute stroke and its response to neuroprotective therapy with anti-Fas ligand antibody. Eur J Nucl Med Mol Imaging 33:566-574.
141. French LE and Tschopp J (2003) Protein-based therapeutic approaches targeting death receptors. Cell Death Differ 10:117-123.

142. Martin-Villalba A, Hahne M, Kleber S et al (2001) Therapeutic neutralization of CD95-ligand and TNF attenuates brain damage in stroke. Cell Death Differ 8:679-686.
143. Wang X, Zhu S, Drozda M et al (2003) Minocycline inhibits caspase-independent and -dependent mitochondrial cell death pathways in models of Huntington's disease. Proc Natl Acad Sci U S A 100:10483-10487.
144. Tang XN, Wang Q, Koike MA et al (2007) Monitoring the protective effects of minocycline treatment with radiolabeled annexin V in an experimental model of focal cerebral ischemia. J Nucl Med 48:1822-1828.
145. Flint J and Shifman S (2008) Animal models of psychiatric disease. Curr Opin Genet Dev 18:235-240.
146. Roberts DC, Corcoran ME, Fibiger HC (1977) On the role of ascending catecholaminergic systems in intravenous self-administration of cocaine. Pharmacol Biochem Behav 6:615-620.
147. Everitt BJ, Hutcheson DM, Ersche KD et al (2007) The orbital prefrontal cortex and drug addiction in laboratory animals and humans. Ann N Y Acad Sci 1121:576-597.
148. Hester R and Garavan H (2004) Executive dysfunction in cocaine addiction: evidence for discordant frontal, cingulate, and cerebellar activity. J Neurosci 24:11017-11022.
149. Volkow ND, Fowler JS, Wang GJ, Goldstein RZ (2002) Role of dopamine, the frontal cortex and memory circuits in drug addiction: insight from imaging studies. Neurobiol Learn Mem 78:610-624.
150. Adams JB, Heath AJ, Young SE et al (2003) Relationships between personality and preferred substance and motivations for use among adolescent substance abusers. Am J Drug Alcohol Abuse 29:691-712.
151. Dawe S and Loxton NJ (2004) The role of impulsivity in the development of substance use and eating disorders. Neurosci Biobehav Rev 28:343-351.
152. Levin FR and Kleber HD (1995) Attention-deficit hyperactivity disorder and substance abuse: relationships and implications for treatment. Harv Rev Psychiatry 2:246-258.
153. Dalley JW, Fryer TD, Brichard L et al (2007) Nucleus accumbens D2/3 receptors predict trait impulsivity and cocaine reinforcement. Science 315:1267-1270.
154. Crabbe JC and Cunningham CL (2007) Trait or state? Science 317:1033-1035.
155. Uhl G (2007) Premature poking: impulsivity, cocaine and dopamine. Nat Med 13:413-414.
156. Morgan D, Grant KA, Gage HD et al (2002) Social dominance in monkeys: dopamine D2 receptors and cocaine self-administration. Nat Neurosci 5:169-174.
157. Nader MA, Morgan D, Gage HD et al (2006) PET imaging of dopamine D2 receptors during chronic cocaine self-administration in monkeys. Nat Neurosci 9:1050-1056.
158. Dalley JW, Fryer TD, Aigbirhio FI et al (2009) Modelling human drug abuse and addiction with dedicated small animal positron emission tomography. Neuropharmacology 56 Suppl 1:9-17.
159. Lopez AD and Murray CC (1998) The global burden of disease, 1990-2020. Nat Med 4: 1241-1243.
160. Hietala J, Syvalahti E, Vilkman H et al (1999) Depressive symptoms and presynaptic dopamine function in neuroleptic-naive schizophrenia. Schizophr Res 35:41-50.
161. McGowan S, Lawrence AD, Sales T, Quested D, Grasby P (2004) Presynaptic dopaminergic dysfunction in schizophrenia: a positron emission tomographic [18F]fluorodopa study. Arch Gen Psychiatry 61:134-142.
162. Laruelle M, Bi-Dargham A, Gil R, Kegeles L, Innis R (1999) Increased dopamine transmission in schizophrenia: relationship to illness phases. Biol Psychiatry 46:56-72.
163. Breier A, Su TP, Saunders R et al (1997) Schizophrenia is associated with elevated amphetamine-induced synaptic dopamine concentrations: evidence from a novel positron emission tomography method. Proc Natl Acad Sci U S A 94:2569-2574.
164. Seeman P, Chau-Wong M, Tedesco J, Wong K (1975) Brain receptors for antipsychotic drugs and dopamine: direct binding assays. Proc Natl Acad Sci U S A 72:4376-4380.
165. Mukherjee J, Christian BT, Narayanan TK, Shi B, Mantil J (2001) Evaluation of dopamine D-2 receptor occupancy by clozapine, risperidone, and haloperidol in vivo in the rodent and nonhuman primate brain using 18F-fallypride. Neuropsychopharmacology 25:476-488.

166. Okubo Y, Suhara T, Suzuki K et al (1997) Decreased prefrontal dopamine D1 receptors in schizophrenia revealed by PET. Nature 385:634-636.
167. Karlsson P, Farde L, Halldin C, Sedvall G (2002) PET study of D(1) dopamine receptor binding in neuroleptic-naive patients with schizophrenia. Am J Psychiatry 159:761-767.
168. Bi-Dargham A, Mawlawi O, Lombardo I et al (2002) Prefrontal dopamine D1 receptors and working memory in schizophrenia. J Neurosci 22:3708-3719.
169. Guo N, Hwang DR, Lo ES et al (2003) Dopamine depletion and in vivo binding of PET D1 receptor radioligands: implications for imaging studies in schizophrenia. Neuropsychopharmacology 28:1703-1711.
170. Arango V, Underwood MD, Mann JJ (2002) Serotonin brain circuits involved in major depression and suicide. Prog Brain Res 136:443-453.
171. Doris A, Ebmeier K, Shajahan P (1999) Depressive illness. Lancet 354:1369-1375.
172. Neumeister A, Nugent AC, Waldeck T et al (2004) Neural and behavioral responses to tryptophan depletion in unmedicated patients with remitted major depressive disorder and controls. Arch Gen Psychiatry 61:765-773.
173. Drevets WC, Thase ME, Moses-Kolko EL et al (2007) Serotonin-1A receptor imaging in recurrent depression: replication and literature review. Nucl Med Biol 34:865-877.
174. Mathis CA, Simpson NR, Mahmood K, Kinahan PE, Mintun MA (1994) [11C]WAY 100635: a radioligand for imaging 5-HT1A receptors with positron emission tomography. Life Sci 55:L403-L407.
175. Aznavour N, Benkelfat C, Gravel P et al (2009) MicroPET imaging of 5-HT 1A receptors in rat brain: a test-retest [18F]MPPF study. Eur J Nucl Med Mol Imaging 36:53-62.
176. Goodwin R and Jamison KR (1990) Manic-depressive illness. Oxford University Press, New York
177. Hougland MT, Gao Y, Herman L et al (2008) Positron emission tomography with fluorodeoxyglucose-F18 in an animal model of mania. Psychiatry Res 164:166-171.
178. Baxter LR, Jr., Phelps ME, Mazziotta JC et al (1985) Cerebral metabolic rates for glucose in mood disorders. Studies with positron emission tomography and fluorodeoxyglucose F 18. Arch Gen Psychiatry 42:441-447.
179. Al-Mousawi AH, Evans N, Ebmeier KP et al (1996) Limbic dysfunction in schizophrenia and mania. A study using 18F-labelled fluorodeoxyglucose and positron emission tomography. Br J Psychiatry 169:509-516.
180. Sigel E (2008) Eating disorders. Adolesc Med State Art Rev 19:547-72, xi.
181. Bailer UF, Frank GK, Henry SE et al (2005) Altered brain serotonin 5-HT1A receptor binding after recovery from anorexia nervosa measured by positron emission tomography and [carbonyl11C]WAY-100635. Arch Gen Psychiatry 62:1032-1041.
182. Delvenne V, Lotstra F, Goldman S et al (1995) Brain hypometabolism of glucose in anorexia nervosa: a PET scan study. Biol Psychiatry 37:161-169.
183. Barbarich-Marsteller NC, Marsteller DA, Alexoff DL, Fowler JS, Dewey SL (2005) MicroPET imaging in an animal model of anorexia nervosa. Synapse 57:85-90.
184. Casper RC, Sullivan EL, Tecott L (2008) Relevance of animal models to human eating disorders and obesity. Psychopharmacology (Berl) 199:313-329.
185. Van Kuyck K, Casteels C, Vermaelen P et al (2007) Motor- and food-related metabolic cerebral changes in the activity-based rat model for anorexia nervosa: A voxel-based microPET study. Neuroimage 35:214-221.
186. Tokunaga M, Ida I, Higuchi T, Mikuni M (1997) Alterations of benzodiazepine receptor binding potential in anxiety and somatoform disorders measured by 123I-iomazenil SPECT. Radiat Med 15:163-169.
187. Kaschka W, Feistel H, Ebert D (1995) Reduced benzodiazepine receptor binding in panic disorders measured by iomazenil SPECT. J Psychiatr Res 29:427-434.
188. Geuze E, van Berckel BN, Lammertsma AA et al (2008) Reduced GABAA benzodiazepine receptor binding in veterans with post-traumatic stress disorder. Mol Psychiatry 13:74-83, 3.
189. McGuire P, Howes OD, Stone J, Fusar-Poli P (2008) Functional neuroimaging in schizophrenia: diagnosis and drug discovery. Trends Pharmacol Sci 29:91-98.

190. Rosenberg DR, Mirza Y, Russell A et al (2004) Reduced anterior cingulate glutamatergic concentrations in childhood OCD and major depression versus healthy controls. J Am Acad Child Adolesc Psychiatry 43:1146-1153.
191. Dedeurwaerdere S, Gregoire MC, Vivash L et al (2009) In-vivo imaging characteristics of two fluorinated flumazenil radiotracers in the rat. Eur J Nucl Med Mol Imaging
192. Shetty HU, Zoghbi SS, Simeon FG et al (2008) Radiodefluorination of 3-fluoro-5-(2-(2-[18F](fluoromethyl)-thiazol-4-yl)ethynyl)benzonitrile ([18F]SP203), a radioligand for imaging brain metabotropic glutamate subtype-5 receptors with positron emission tomography, occurs by glutathionylation in rat brain. J Pharmacol Exp Ther 327:727-735.

Chapter 20
Applications of Molecular Small-Animal Imaging in Cardiology

Ravi Marfatia, Sina Tavakoli, and Mehran M. Sadeghi

1 Introduction

Cardiovascular disease (CVD) is a leading cause of death in both industrialized and developing countries, claiming more than 800,000 lives in the US and millions more in the rest of the world in recent years. Despite recent reduction in age-specific CVD mortality rate, increasing longevity, urbanization and industrialization has led to a rapid increase in the prevalence of CVD in both developed and developing nations. With surging health care costs the focus is shifting from treatment to prevention of disease as well as developing cost effective diagnostic and prognostic strategies. Conventional imaging modalities such as coronary angiography, echocardiography, myocardial perfusion imaging, computed tomography (CT) and magnetic resonance imaging (MRI), have been historically used to define structure and function as well as to monitor response to therapy, relying on the contrast provided by heterogeneity of anatomy, physiology and metabolism. As such, they provide valuable anatomical and physiological information about vasculature (e.g., extent of the disease, location, presence of calcification) and the myocardium (e.g., ejection fraction, wall thickening, dilatation, viability and cardiac output). However, traditional imaging modalities have limited use in detecting molecular and cellular events that determine the course of disease and its response to therapeutic interventions. Emerging molecular imaging modalities utilizing probes targeted at relevant molecular and cellular events can advance research on pathophysiology, allow early detection of disease, assist in the design of novel therapies, facilitate monitoring disease activity and response to therapy, and provide prognostic information.

We have seen considerable progress in the development of cardiovascular molecular imaging over the past decade, and in specific cases cardiovascular molecular

R. Marfatia • S. Tavakoli • M.M. Sadeghi (✉)
Cardiovascular Molecular Imaging Laboratory, Yale University School of Medicine, New Haven, CT 06520-8017, USA
e-mail: marfatia@uchc.edu; tavakoli@uthscsa.edu; mehran.sadeghi@yale.edu

H. Zaidi (ed.), *Molecular Imaging of Small Animals: Instrumentation and Applications*,
DOI 10.1007/978-1-4939-0894-3_20,

imaging is on the verge of reaching clinical practice. Preclinical imaging studies in small animals have played, and continue to play, a key role in this progress. In this review, we will first focus on applications of molecular small animal imaging in common pathological processes, such as inflammation, apoptosis and thrombosis that affect the cardiovascular and other systems. This will be followed by a more detailed review of the state of the art molecular small animal imaging in specific vascular and cardiac pathologies.

2 Imaging in Common Pathophysiological Processes

2.1 Inflammation

The role of inflammation in the pathogenesis of cardiovascular diseases has been increasingly recognized in recent years. Atherosclerosis represents a chronic inflammatory process triggered, amongst others, by modified lipoproteins [1]. Similarly, inflammation plays a central role in the development and progression of heart failure. Despite context-specific differences, various inflammatory processes share many common features, including endothelial activation which is an early step in the recruitment of inflammatory cells. The normal endothelium maintains a dynamic barrier between blood, containing circulatory cells and macromolecules, and subendothelial structures. Activation of endothelial cells (ECs) by pro-inflammatory cytokines and other macromolecules [such as modified low-density lipoprotein (LDL)] triggers the expression of endothelial adhesion molecules [such as E-selectin, intercellular adhesion molecule-1 (ICAM-1) and vascular cell adhesion molecule-1 (VCAM-1)] and loss of anti-adhesive properties. The complex and hierarchic interactions of adhesion molecules expressed by ECs and their counterparts on circulatory leukocytes mediate rolling, adherence and subsequent transmigration of inflammatory cells across the endothelium into the subendothelial compartment. Chemokines, e.g., monocyte chemoattractant protein-1 (MCP-1), provide a chemoattractant gradient to direct inflammatory cells to the sites of inflammation. Various cellular and molecular players of innate and adaptive immunity play predominant roles in specific inflammatory conditions.

Upregulation of endothelial adhesion molecules appears as a promising target for imaging early stages of inflammation. VCAM-1 is absent on resting ECs, and is upregulated in response to pro-inflammatory stimuli. Expression of VCAM-1 is an early event in the course of atherogenesis [2]. Thus, VCAM-1 may be a potentially useful target for detection of early atherosclerotic plaque. Because of its expression on the endothelium, VCAM-1 can be easily targeted and imaged using molecular imaging modalities which are dependent on targeting agents with limited access to sub-endothelial structures (e.g., MRI and ultrasound imaging). The low level of VCAM-1 expression on activated ECs is a potential limiting factor for its detection by conventional radiotracer-based imaging modalities [3]. However, alternative

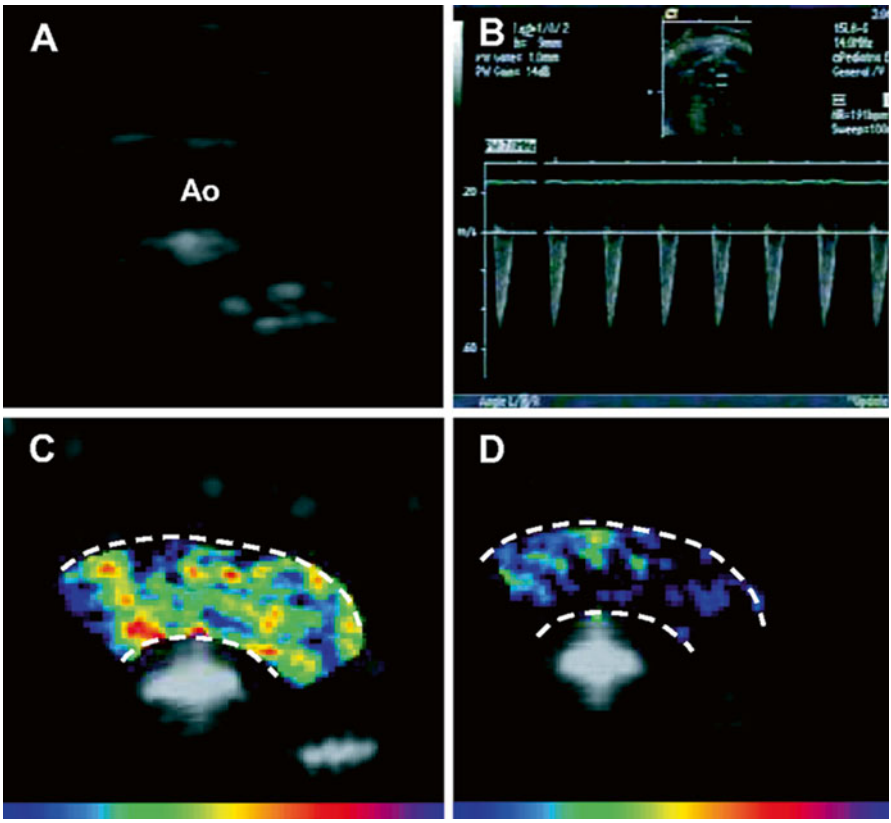

Fig. 20.1 Contrast-enhanced ultrasound imaging of endothelial activation in the aorta of high cholesterol-fed apoE$^{-/-}$ mice using VCAM-1-targeted microbubbles. Images (**a**) and (**b**) show the aortic arch (*Ao*) detected by two-dimensional and pulsed wave Doppler imaging. There is considerably higher enhancement of the arch 10 min after intravenous injection of VCAM-1-targeted (**c**), as compared to non-targeted, control (**d**) microbubbles. Reprinted with permission from Kauffman et al. [7]

approaches have been developed to enhance VCAM-1-dependent signal and improve target-to-background ratios. One such approach uses a peptide with homology to the α-chain of very late antigen-4 (VLA-4, a natural binding partner for VCAM-1 on activated leukocytes) which may be involved in VCAM-1 mediated ligand internalization [4]. When incorporated into magneto-fluorescent nanoparticles, this peptide allowed for in vivo detection of activated endothelium overlaying atherosclerotic lesions of high cholesterol-fed apoprotein E (apoE)$^{-/-}$ mice by MRI and optical imaging [5]. Alternatively, conjugation of P-selectin and VCAM-1 antibodies to microparticles of iron oxide [6] or VCAM-1 antibody to microbubbles (Fig. 20.1) [7, 8] has been used to detect endothelial activation by MRI and ultrasound imaging in atherosclerosis and arteriogenesis.

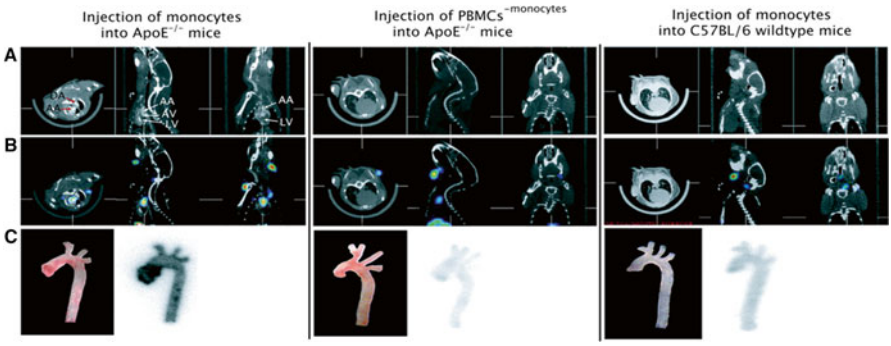

Fig. 20.2 Imaging of monocyte recruitment to atherosclerotic plaques. CT (**a**) and fused Micro-SPECT/CT (**b**) images obtained 5 days after introduction of ^{111}In-oxine-labeled murine monocytes (*left* panel) or monocyte-depleted peripheral blood mononuclear cells (*middle* panel) to high cholesterol-fed apoE$^{-/-}$ mice. Labeled-monocytes introduced to C57BL/6 wild-type mice (*right* panel) served as a control. Substantial ^{111}In-oxine-labeled monocytes recruitment was observed in the ascending aorta of apoE$^{-/-}$ mice but not elsewhere, which was verified by autoradiography of harvested aortas (**c**) (*LV* left ventricle, *AV* aortic valve region, *AA* ascending aorta, *DA* descending aorta). Reprinted with permission from Kircher et al. [10]

Molecular imaging technologies provide highly valuable experimental tools for tracking leukocyte trafficking and activation in the sites of inflammation in small animal models of cardiovascular disease. Direct labeling of murine monocytes with ^{111}In-oxine allowed investigators to track and study trafficking of different monocyte subsets into the myocardium after myocardial infarction and further define their function [9]. The inhibitory effect of statin therapy on monocyte trafficking into atherosclerotic lesions in the apoE$^{-/-}$ mouse has been demonstrated by micro-SPECT-CT imaging using ^{111}In-oxine labeled monocytes (Fig. 20.2) [10]. Other examples of promising approaches to imaging leukocyte biology in animal models of cardiovascular disease include using radiolabeled chemokines (e.g., ^{99m}Tc-labeled MCP-1) to target chemokine receptors on activated monocytes [11], targeting enhanced cellular metabolism (e.g., by ^{18}F-FDG imaging) [12], detecting the phagocytic activity of macrophages [13, 14] and imaging proteases produced by activated leukocytes [15, 16]. These will be discussed in more detail in the following sections. Such imaging approaches have provided information on cellular and molecular biology of inflammation complementary to those obtained by classical in vitro studies, opening new avenues of research to elucidate the role of inflammation in cardiovascular diseases.

2.2 Apoptosis and Cell Death

Apoptosis, a highly regulated, energy-dependant, complex program of cell death is an integral component of normal development and homeostasis. In the cardiovascular system, apoptosis plays an important role in the pathogenesis of many pathologic

processes, including atherosclerotic plaque rupture, MI and ischemia-reperfusion injury, heart failure and transplant rejection. The cardiomyocyte is a highly differentiated cell with limited regenerative capacity. Therefore, cardiomyocyte loss by apoptosis (or otherwise) has a significant impact on deteriorating cardiac function, and inhibition of apoptosis in rodent models of ischemia-reperfusion has shown to be cardioprotective [17]. Imaging apoptosis can help elucidate this process in vivo and pave the way for the development of novel apoptosis-preventing therapeutic and therapy-monitoring strategies.

Apoptosis is one of the several morphologically and biochemically distinct, but overlapping, pathways to cell death, and unlike necrosis, does not produce an inflammatory response [18]. The biologic induction of apoptosis occurs via the so-called "extrinsic" or "intrinsic" pathways and presents several targets for molecular imaging. The extrinsic pathway is initiated by external stimuli such as cytokines or toxins and involves the binding of transmembrane death receptors to their ligands. The resulting complexes activate a cascade of downstream proteases known as caspases which commit the cell to apoptosis. In the intrinsic pathway, the intracellular release of caspase-activating proteins by mitochondria in response to cellular stresses such as hypoxia, viral infections, radiation, etc. causes apoptosis through formation of the apoptosome complex and activating the caspase cascade. A non-specific, aspect of apoptosis used commonly as target for imaging is the externalization of phosphatidyl serine (PS) (reviewed in [19]). PS is a negatively charged aminophospholipid that is actively maintained internally in normal cells and is translocated to the outer surface of the cell membrane early on in the course of apoptosis, functioning as a marker for macrophages to phagocytose the apoptotic cell [20]. The surface expression of PS and its high expression level facilitate its targeting for imaging apoptosis. However, PS externalization and exposure to its ligands are not exclusive to apoptosis and are observed in other forms of cell death, certain forms of leukocyte activation [21–23] and activated platelets [24]. Another important factor to consider in targeting PS for detection of apoptosis is that PS externalization can be a reversible process and not all cells with surface expression of PS undergo apoptosis [25]. Annexin A5 (also called annexin V), a protein with a high binding affinity for PS, has been studied extensively for imaging apoptosis. Annexin A5 has been conjugated with various radioisotopes (^{99m}Tc, ^{18}F and ^{124}I) [26–28], fluorescent agents [29, 30] or incorporated into magnetic nanoparticles [31] and used for imaging apoptosis in small animals and in humans. Other PS binding tracers have been developed (reviewed in [32]) and are in various stages of evaluation.

Sequential activation of several caspases in both extrinsic and intrinsic pathways of apoptosis makes them appealing targets for imaging apoptosis. Furthermore, unlike PS externalization, the caspase activation cascade is reasonably specific for apoptosis. Strategies for optical imaging and PET imaging using radiolabeled caspase binding molecules [33] and caspase-sensitive reporter probes [34] have been developed. However, caspases-targeted imaging of apoptosis in the cardiovascular system is in early stages of development and awaits further experimental validation.

Annexin V imaging of apoptosis in the cardiovascular system has rapidly moved from preclinical studies to humans [27, 35]. However, many issues regarding the specificity of different tracers for apoptosis and the biological significance of cell death in cardiovascular pathologies remain unresolved. Imaging apoptosis in small animal models of atherosclerosis, ischemia-reperfusion, heart failure, and transplant rejection can help address many of the unresolved issues which have impeded the use of apoptosis imaging in the clinic. Some of these applications will be discussed in the following sections.

2.3 Angiogenesis

Angiogenesis and atherogenesis, formation of new blood vessels from pre-existing vessels, are integral parts of development, wound healing and response to ischemia. In recent years, much attention has been paid to therapeutic angiogenesis to treat myocardial and peripheral ischemia. However, angiogenesis is also involved in the development of atherosclerosis and may participate in plaque vulnerability. Therefore, modulation of angiogenesis in the cardiovascular system requires a complex balancing act between these two opposite effects.

Angiogenesis can occur through different mechanisms. One mechanism, sprouting, is induced by hypoxia, inflammation and other cellular and molecular cues that stimulate production of pro-angiogenic factors. Hypoxia initiates angiogenesis through transcriptional regulation of gene expression. The binding of hypoxia-induced factors (HIFs), which are inactivated by proteosomal degradation under normoxia and are stabilized under hypoxia, to the promoter of hypoxia-inducible genes leads to upregulation of pro-angiogenic factors [e.g., vascular endothelial growth factor (VEGF)] [36]. Local secretion of cytokines, growth factors and proteases from inflammatory cells also contributes to this pro-angiogenic milieu. This leads to increased endothelial permeability, dissolution of the basement membrane and reorganization of extracellular matrix, migration of the so-called tip cells and proliferation of ECs, and the subsequent reconstruction of vascular conduits. These primitive vascular structures are stabilized with the recruitment of pericytes and vascular smooth muscle cells (VSMCs).

Numerous pro- and anti-angiogenic molecules contribute to this complex process [36], some of which have been utilized as imaging targets [8, 37–39]. Nitric oxide (NO) induces vasodilatation and is in part responsible for local VEGF production. Matrix metalloproteinases (MMPs) contribute to angiogenesis by remodeling matrix and release of growth factors, such as VEGF, basic fibroblast growth factor (bFGF) and insulin-like growth factor (IGF)-1 that are normally retained by extracellular proteins. Additionally, MMP action on matrix proteins exposes novel adhesion epitopes for vascular cells. Angiostatin, an inhibitor of EC proliferation, is generated through proteolytic cleavage of plasminogen by MMP-7 and -9. Growth factors, e.g., VEGF, FGF and platelet-derived growth factor, participate in angiogenesis through induction of endothelial proliferation and recruitment of

VSMCs and pericytes. Integrins are involved in cell-matrix interactions and play a key role in EC migration, proliferation and survival. The αvβ3 integrin is probably the most extensively studied target for imaging angiogenesis in the cardiovascular system [37, 40].

VEGF imaging is an alternative promising approach for in vivo detection of angiogenesis [39]. The VEGF family of growth factors consists of 6 members, namely VEGF-A, -B, -C, -D, PIGF and Orf VEGFs (also called VEGF-E) [41]. VEGF-A, the prototypic angiogenic growth factor, is a homodimeric protein with several isoforms which are generated through alternative splicing. VEGF-121, and -165 are soluble secreted proteins while VEGF-189 and -206 are mostly bound to the cell surface or extracellular matrix [42]. VEGFs bind to three high affinity VEGF receptors (VEGFRs), with each member of the VEGF family exhibiting a distinct binding pattern. VEGFR-1 and -2 are expressed by arterial, capillary and venous endothelium, while VEGFR-3 expression is confined to the lymphatic endothelium. Many of the VEGF effects on EC, including endothelial proliferation, survival and hyperpermeability, are attributable to VEGFR-2 signaling and VEGFR-1 appears to serve as a regulator of VEGFR-2 signaling in ECs. In addition to aforementioned VEGFR, VEGF binds to neuropilins which also serve as co-receptors and potentiate VEGFR-2 signaling. Labeled VEGF-121 which lacks the heparin binding domain of VEGF-165, and therefore thought to be specific for classical VEGFRs, has been extensively used for imaging angiogenesis in various animal models of angiogenesis [43]. However, recent data indicate that VEGF-121 can also bind to neuropilins, potentially complicating the interpretation of those studies [44].

Investigation with therapeutic angiogenesis utilizing growth factor, gene, and cell therapy in animal models of ischemia has led to promising results. However, these original successes have not been reproduced in large clinical trials. The development and validation of reliable imaging modalities for in vivo detection of angiogenesis will help understand the underlying causes of these failures and help develop and evaluate novel therapeutic approaches for vaso-occlusive diseases.

2.4 Matrix Remodeling

The extracellular space of multi-cellular organisms is composed of a network of macromolecules which constitute the extracellular matrix (ECM). ECM is organized in the vicinity of cells that produce it, and actively regulates their function. Variations in ECM components, including glycosaminoglycans usually linked to proteoglycans, and fibrous proteins (e.g., collagen, elastin, fibronectin and elastin) are in part responsible for differences in physical properties of various tissues, and may be targeted for imaging. Integrins bind to ECM proteins, mainly through a specific tripeptide sequence (Arginine-Glycine-Aspartate, RGD), and anchor cells to the surrounding matrix. In addition to their role in cell survival, proliferation and migration, integrins serve as mechanoreceptors, transducing mechanical stimuli into intracellular signaling events. Several RGD-based tracers have been developed

and studied for detection of integrin expression and activation in vivo [37, 45, 46]. In response to altered biology and hemodynamics the ECM undergoes major structural and functional changes, a process termed as 'matrix remodeling'. ECM remodeling may occur through protein synthesis, contraction and proteolytic degradation and is an integral part of development, tissue repair and fibrosis. Alteration of ECM homeostasis, i.e., matrix remodeling, is a main pathological feature of myocardial and vascular remodeling. Cardiac fibroblasts synthesize ECM proteins and modulate responses to chemical, mechanical and electrical stimuli. They can also differentiate into myofibroblasts, cells characterized by the presence of smooth muscle markers (e.g. smooth muscle α-actin) which contribute to matrix remodeling through enhanced production of ECM molecules and generation of tension [47]. Various growth factors, inflammatory molecules and mechanical stimuli regulate cardiac myofibroblast formation and function, stimulating increased collagen secretion (predominantly types I and III) and resulting in myocardial fibrosis [48].

MMPs are a family of proteases involved in matrix remodeling. They constitute a group of nearly 25 zinc-dependant proteases responsible for the degradation and removal of specific components of ECM. Inflammatory cells are major sources of MMPs, which are produced as inactive pro-enzymes and are activated by proteolytic cleavage which exposes a catalytic site. Tissue inhibitors of metalloproteinases (TIMPs) regulate MMP activity, which is modulated by the expression level, activation state and presence of inhibitors. In addition to their role in matrix remodeling, MMPs also contribute to cardiovascular biology by digesting other proteins, including troponin, myosin light chain and poly(ADP-ribose) polymerase [49]. Most notably for this discussion, MMPs play an important role in many common cardiovascular diseases. MMP-2 [50] and MMP-9 [51], both gelatinases, have been shown to play a key role in the development of cardiac rupture in gene deletion mice. TIMP-3 deficient mice are shown to have dysfunctional matrix homeostasis causing severe cardiac dysfunction [52]. In rat models of chronic volume overload MMP upregulation occurs prior to left ventricular (LV) remodeling and MMP inhibition reduces LV dysfunction [53]. MMP-2 and -9 plasma levels are elevated post-MI [54] and elevated MMP-13 levels, which is normally low, are noted in end stage heart failure [55]. MMPs are also critical in vascular remodeling and their involvement there is discussed separately. As such, MMPs constitute a formidable target for molecular imaging of matrix remodeling in many cardiovascular diseases.

Various strategies have been employed to detect in vivo MMP activity. Near infrared fluorescent probes which are activated through proteolytic cleavage by MMPs have been used for optical imaging of MMP activity post-MI in mice [56, 57]. As the MMP signal is dependent on enzymatic activity, this approach considerably amplifies the signal and may allow for detection of activities that are otherwise difficult to detect. While this is a very powerful approach for imaging in small animals which may be more or less easily extended to specific MMPs, the restricted penetration depth of optical imaging limits its utility in larger animals and humans. An alternative approach uses radio-labeled tracers (such as ^{111}In-labeled RP782 and ^{99m}Tc-labeled RP805 [58, 59]) which directly bind to a specific site (in the case of RP782 and RP805, the activated catalytic site) on MMP molecules (Fig. 20.3).

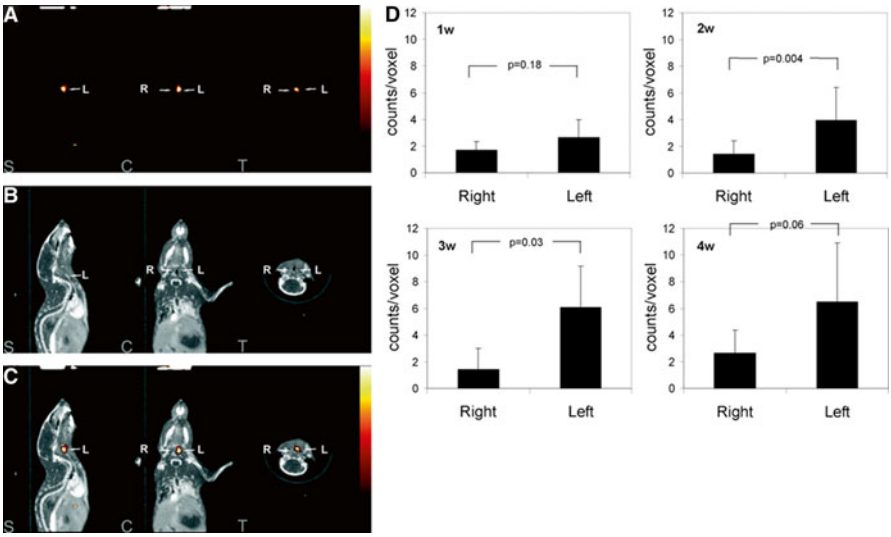

Fig. 20.3 Imaging MMP activation in vascular remodeling using RP782, an ^{111}In-labeled MMP-targeting tracer. In vivo microSPECT (**a**), CT angiography (**b**), and fused microSPECT/CT (**c**) images at 3 weeks after left carotid injury in apoE$^{-/-}$ mice demonstrate enhanced MMP activation in the injured left (*L*) as compared to control right (*R*) carotid arteries (*S* sagittal, *C* coronal, and *T* transverse slices, *w* weeks). Image-derived quantitative analyses of carotid RP782 uptake at different time points after injury are shown in (**d**). Reprinted with permission from Zhang et al. [59]

Many of the existing MMP-targeted tracers have broad target specificity. The challenge is to develop novel tracers with specificity for individual members of the MMP family which may be more appropriate for imaging specific conditions. Nevertheless, existing tracers have been proved useful in studying many cardiovascular pathologies and their use will be discussed in the following sections.

2.5 Vascular Remodeling

Adult arteries undergo changes in morphology, cell content and matrix composition in response to injury. This process is broadly labeled as vascular remodeling. In atherosclerosis, remodeling is triggered by modified lipids and other pro-inflammatory molecules in conjunction with hemodynamic factors which potentiate the effect of injury. The effect of arterial injury may be even more dramatic in specific pathologies. Mechanical injury to the vessel wall at the time of percutaneous coronary angioplasty (PTCA) leads to transient dilatation of the artery which is followed by elastic recoil and development of neointimal hyperplasia, both playing an important role in post-PTCA restenosis. Immune injury is the main mediator of graft arteriosclerosis (GA) after cardiac transplantation. GA is associated with concentric narrowing of coronary arteries and small vessel pruning that ultimately leads

to myocardial ischemia and loss of the transplant. Aneurysm is another example of vascular remodeling which is a major cause of morbidity and mortality. In the case of abdominal aortic aneurysm, expansion of the artery is associated with changes in mechanical strain which may ultimately lead to aneurysm rupture and death.

VSMC proliferation and migration as well as extracellular matrix remodeling are two major components of vascular remodeling which have been targeted for imaging. In every vascular pathology the balance between these factors and concomitant inflammation determines the outcome in terms of the vessel morphology and biology. Resting VSMCs in the media are in a differentiated or contractile state. In response to injury, they undergo phenotypic modulation and transform into highly proliferative and synthetic cells, which participate in vascular remodeling through migration into the neointima and extracellular matrix synthesis [60]. This phenotypic modulation of VSMCs is associated with dramatic changes in their molecular structure, including a reduction in VSMC-specific marker gene expression, a reduction in myofilaments and an increase in synthetic cellular organelles, which seems to contribute to repair processes. Many of these changes provide potential targets for imaging VSMC proliferation in remodeling arteries. Z2D3 is an antibody to a poorly characterized antigen expressed in atherosclerosis, which is found to be upregulated in proliferating VSMCs. Molecular imaging of vascular remodeling using radio-labeled Z2D3 more than a decade ago was one of the first examples of successful molecular imaging of vessel wall biology [61]. Integrin αvβ3 is upregulated in vascular remodeling and undergoes conformational changes which can be targeted, providing additional specificity to imaging. RP748, a ^{111}In-labeled peptidomimetic molecule that preferentially binds to activated (high affinity conformation) αvβ3 (and potentially other αv) integrins localizes to injured carotid arteries of apoE$^{-/-}$ mice and may be detected by autoradiography [45]. RP748 uptake in this model was found to parallel cell proliferation, providing a potential tool to detect VSMC proliferation induced by mechanical injury to the arterial wall.

2.6 Thrombosis

The primary function of the coagulation system is to maintain the integrity of the circulatory system and to prevent blood loss in case of injury. Under pathological conditions activation of this system can lead to thrombosis and partial or total occlusion of the blood vessel. Deep venous thrombosis, pulmonary embolism, and acute coronary syndromes are examples of the most common cardiovascular diseases where thrombosis plays a causal role, and molecular imaging can provide important diagnostic information. Platelet activation is central to blood clot formation. Thrombin is a pro-inflammatory molecule that, amongst other functions, cleaves fibrinogen into fibrin and activates platelets. Activation of a cascade of coagulation proteases in conjunction with their co-factors through intrinsic or extrinsic (mainly due to tissue factor) pathways of coagulation converge on prothrombin to generate thrombin. Platelet activation may also occur independent of thrombin through exposure to subendothelial collagen [62].

Thrombus formation over a disrupted atherosclerotic plaque leads unstable angina and MI. Rupture of the plaque's fibrous cap or erosion of the endothelial layer exposes blood to the thrombogenic subendothelial components. The interplay between blood, plaque components, and local homodynamic factors determines the final consequence of these events which may be self-limited mural thrombus, a common autopsy finding in clinically silent patients, or fatal MI. Plaque inflammation is one of the determinants of its thrombogenicity [63]. Expression of tissue factor by plaque macrophages has been implicated in potentiation of thrombosis formation when blood is exposed to the subendothelial compartment. Endothelial shedding and apoptosis (mediated in part by myeloperoxidase) can also expose the platelets to subendothelial component.

Different aspects of thrombosis formation, including platelet activation [64], fibrinogen cross linking [65], and fibrin deposition [66] have been targets of molecular imaging in animal models or early clinical studies. Integrin αIIbβ3 plays an important role in platelet activation and recruitment. Activation of αIIbβ3 integrin is associated with conformational changes that increase it affinity for fibrinogen and von Willebrand factor. Apcitide is a ^{99m}Tc-labeled peptide that binds to integrin αIIbβ3 and has been extensively studied for imaging acute deep venous thrombosis [67, 68]. By characterizing components of thrombosis molecular imaging can help elucidate the pathogenesis of acute coronary syndromes and help track the response to therapeutic interventions.

Recent advances in molecular imaging which have contributed to unraveling the molecular and cellular basis of cardiovascular diseases, their progression and development of complications will be discussed here (Table 20.1). Although we have organized our discussion into sections focused on specific pathologies, we acknowledge that this separation is somewhat arbitrary and artificial, as many of the issues discussed under specific topics are also applicable to other vascular and cardiac pathologies.

3 Molecular Imaging of Cardiovascular Pathology

3.1 Atherosclerosis

3.1.1 Endothelial Cell Activation

As previously discussed, EC activation is an early event in the course of atherogenesis. ECs form a barrier between blood and the rest of the vessel wall that is impermeable to most macromolecules in normal conditions. However, EC activation triggered by factors such as pro-inflammatory cytokines, changes in shear stress and hypercholesterolemia disrupts this barrier and results in non-specific diffusion of macromolecules into the subendothelial space. The non-specific hyper-permeability of activated ECs has served as the basis for imaging atherosclerosis with non-specific contrast agents (e.g., gadolinium-diethylenetriamine pentaacetic acid or

Table 20.1 Selected examples of small-animal cardiovascular imaging

Disease process	Molecular process	Target	Agent	Animal species	Imaging modality
Atherosclerosis	Inflammation	Endothelial cell activation	VCAM-1 internalizing nanoparticle-28 [101]	Mice	MRI/optical imaging
	Inflammation	Endothelial cell activation	VCAM-1-targeted microbubbles [59]	Mice	Ultrasound
	Inflammation	Monocyte trafficking	^{111}Indium-oxine-labeled monocytes [3]	Mice	MicroSPECT
	Inflammation	Macrophage burden	Iodinated nanoparticulate contrast agent (N1177) [6]	Rabbits	CT
	Inflammation	Macrophage burden	HDL-nanoparticles [75, 76]	Mice	MRI
	Inflammation	Macrophage burden	Ferumoxtran-10 [77]	Rabbits	MRI
	Matrix remodeling	Protease activity (MMPs)	P947 [96, 97]	Mice/rabbits	MRI
	Matrix remodeling	Protease activity (MMPs)	Activatable near-infrared fluorescence probe [98]	Mice	Optical imaging
	Matrix remodeling	Protease activity (Cathepsin K)	Cathepsin-K sensitive protease-activatable agent [99]	Mice	Optical imaging
	Lipid biology	LDL oxidation	Gadolinium labeled micelles containing MDA2, E06, IK17 [90]	Mice	MRI
	Apoptosis	Phosphatidylserine redistribution	^{99m}Tc-annexin-V [106]	Mice	MicroSPECT
	Angiogenesis	$\alpha_v\beta_3$ Integrin	Paramagnetic nanoparticles [34]	Rabbits	MRI
Aneurysm	Thrombus renewal	Platelet activity	^{99m}Tc-annexin-V [107]	Rats	SPECT
Vascular remodeling	Matrix remodeling	Protease (MMP) activity	^{111}In-RP782 (58)	Mice	Dual MicroSPECT/CT
	Remodeling	VSMC proliferation	^{111}In-labeled conventional Z2D3 [120]	Rabbits	Scintigraphy

Myocardial infarction/ischemia	Apoptosis	Phosphatidylserine redistribution	^{99m}Tc-annexin-V and ^{111}In-antimyosin-antibodies [131]	Rats	Scintigraphy
	Apoptosis	Phosphatidylserine redistribution	Magnetic and near infrared fluorescence nanoparticle (AnxCLIO-Cy5.5) [132]	Mice	MRI/optical imaging
	Apoptosis	C2A domain of synaptotagmin	^{99m}Tc-C2A-GST [135]	Rats	SPECT
	Inflammation	Myeloperoxidase activity	Gadolinium-based myeloperoxidase activatable sensor (MPO-Gd) [137]	Mice	MRI
	Inflammation	Cathepsin activity/phagocyte recruitment	Protease-activatable fluorescence sensor (Prosense-680)/magneto-fluorescent iron oxide nanoparticle (CLIO-VT750) [9]	Mice	Fluorescent molecular tomography
	Matrix remodeling	MMP activity	Near-infrared fluorescent probe [53]	Mice	Optical imaging
	Remodeling	VEGF receptor expression	^{64}Cu-DOTA-VEGF$_{121}$ [139]	Rats	PET
	Remodeling	FXIII activity	^{111}In-labeled affinity peptide [144, 145]	Mice	SPECT
	Fibrosis	Collagen	^{99m}Tc-B-collagelin [141]	Rats	SPECT
	Fibrosis	Myofibroblasts	^{99m}Tc-Cy5.5-RGD imaging peptide [142]	Mice	MicroSPECT
	Angiogenesis	$\alpha_v\beta_3$ Integrin	^{99m}Tc-labeled RGD peptide (NC100692) [138]	Mice	MicroSPECT
	Angiogenesis	$\alpha_v\beta_3$ Integrin	^{18}F-Galacto-RGD [42]	Rats	PET

(continued)

Table 20.1 (continued)

Disease process	Molecular process	Target	Agent	Animal species	Imaging modality
Transplant rejection	Inflammation	Protease activity/ phagocyte recruitment	Protease-activatable fluorescence sensor (Prosense-680)/ magneto-fluorescent iron oxide nanoparticle (CLIO-VT750) [11]	Mice	Fluorescent molecular tomography/MRI
	Inflammation	Macrophages	Microparticles of iron oxide [158]	Rats	MRI
	Inflammation	Macrophages	Dextran-coated ultra-small particles of iron oxide [159]	Rats	MRI
Gene and cell therapy	Cell tracking	Transplanted cells	Iron-labeled bone marrow derived stem cells [166]	Rats	MRI
	Cell tracking	Transplanted cells	Reporter genes [167]	Mice	Optical imaging/PET

Gd-DTPA) [69]. However, this leakiness and accumulation of macromolecules may also interfere with molecular imaging of more specific markers.

A number of strategies have been employed to detect endothelial activation as an early step in the development of atherosclerosis in vivo. Endothelial activation is associated with upregulation of a number of adhesion molecules on ECs (e.g., VCAM-1) which through interactions with their counterparts mediate the recruitment of circulatory leukocytes and their transmigration to subendothelial compartments. Direct radiolabeling of VCAM-1 binding peptides [70] or conjugation of VCAM-1 binding peptides or antibodies to nanoparticles [5] or microbubbles [7] has been successfully used to image atherogenesis in small animals. Multi-targeting of P-selectin and VCAM-1 (using microparticles of iron oxide conjugated to specific antibodies) as well as ICAM-1 and selectins (using sialyl Lewis x and anti-ICAM-1 antibodies conjugated microbubbles) have been introduced as an approach to increase the sensitivity and specificity for early plaque imaging [6]. The direct contact between ECs and blood facilitates the delivery of tracers for molecular imaging. This is especially through for larger particles needed for MRI and ultrasound-based imaging, which by carrying multiple binding sites can overcome the technical challenges related to low expression level of adhesion molecules. Targeting endothelial activation to detect atherosclerosis can be helpful as a research tool to investigate atherogenic factors and potentially to track the effect of novel preventive therapies. However, at the present time potential clinical applications of imaging endothelial activation in atherosclerosis remain undefined.

3.1.2 Inflammatory Cell Trafficking and Activation

Inflammatory cells, including macrophages, T-cells, dendritic cells and mast cells, can be detected even in the earliest atherosclerotic lesions [1]. Technical challenges have restricted studies of leukocyte trafficking into the plaque using standard molecular and cell biology techniques. However, recent advances in molecular imaging have opened unique opportunities to study leukocyte biology in atherosclerosis. In a series of proof of principle experiments, murine monocytes directly labeled with ^{111}In-oxine were successfully used to detect monocyte trafficking to atherosclerotic lesions in apoE$^{-/-}$ mice by microSPECT imaging (Fig. 20.2) [10]. Several monocyte/macrophage and lymphocyte subpopulations with distinct biological activities have been identified, and their role in the development of atherosclerosis and other vascular pathologies is under intensive investigation. However, using classical research tools it is often difficult to establish whether these cells are recruited to the plaque as such, or if they are differentiated in situ. Tracking trafficking of specific leukocyte subpopulations by molecular imaging, using similar approaches may help address this critical issue in vascular pathology.

In addition to direct labeling of cells, several alternative approaches for imaging inflammatory cell biology have been developed and tested in small animal models of atherosclerosis. Targeting phenotypic changes associated with differentiation of monocytes to macrophages and their activation is one example of a promising

approach to imaging macrophage biology in vivo. Monocyte differentiation is associated with up-regulation of several scavenger receptors (e.g. scavenger receptor A, scavenger receptor BI, CD36 and CD68). Uptake of highly oxidized and otherwise modified lipoproteins by differentiated macrophages also leads to morphological changes and formation of foam cells, a histological hallmark of fatty streaks. Several macrophage membrane proteins, such as scavenger receptors [71–73] and lectin-like oxidized LDL receptor 1 [74], have been successfully targeted by radiotracers and other targeting agents. Enhanced metabolic activity of macrophage-rich atherosclerotic plaques may also be detected by ^{18}F-FDG PET imaging [75, 76]. Another aspect of macrophage biology is the phagocytic activity which can be non-invasively detected by MRI using a high density lipoprotein-based nanoparticles contrast agent or derivative agents [77, 78]. Using ultrasmall superparamagnetic nanoparticles of iron oxide, such as ferumoxtran-10, that accumulate in macrophages is another approach to detection of macrophage burden of atherosclerotic plaques [79]. N1177, an iodinated nanoparticle contrast agent that is phagocytized and accumulates in macrophages, has been successfully used to image atherosclerotic plaques in rabbits utilizing a clinical CT scanner (Fig. 20.4) [13]. Chemokines, e.g., MCP-1, play a key role in inflammatory cell recruitment [80], and imaging chemokine receptors is an alternative approach to imaging tissue macrophages in atherosclerosis. CCR-2 the receptor for MCP-1 is upregulated on monocytes in the course of inflammation and has been targeted with ^{125}I- or ^{99m}Tc-labeled MCP-1 to detect monocyte recruitment in various cardiovascular pathologies [11, 81].

3.1.3 Lipid Accumulation

Lipid retention and modification are integral to the pathogenesis of various stages of atherogenesis, and lipid-targeted imaging may provide important information about this process. LDL was the first agent to be labeled with ^{125}I to study lipid trafficking in damaged arterial wall of rabbits [82]. Subsequent studies have used various radiolabeled LDL preparations to study lipid accumulation and image atherosclerosis [83, 84]. Despite some promising initial data, imaging atherosclerosis with radiolabeled LDL has proved to be ineffective due to tracers' slow blood clearance [84] and the investigators have moved on to labeling other lipids to study plaque biology [85].

Alternative approaches to imaging lipid biology in atherosclerosis focus on oxidized LDL, LDL derivatives, and LDL-targeting antibodies [86–88]. LDL undergoes chemical modifications that enhance its pro-atherogenic and pro-inflammatory properties. One such modification generates oxidized LDL which has higher binding to macrophage scavenger receptors and faster blood clearance than native LDL [87]. Oxidized LDL triggers MMP production by macrophages [89]. MDA2, an antibody to an epitope on oxidized LDL (and other similarly modified proteins) localizes to atherosclerotic lesions in hypercholesterolemic rabbits and apoE$^{-/-}$ and LDL receptor (LDLR)$^{-/-}$ mice and its uptake can track the effect of dietary

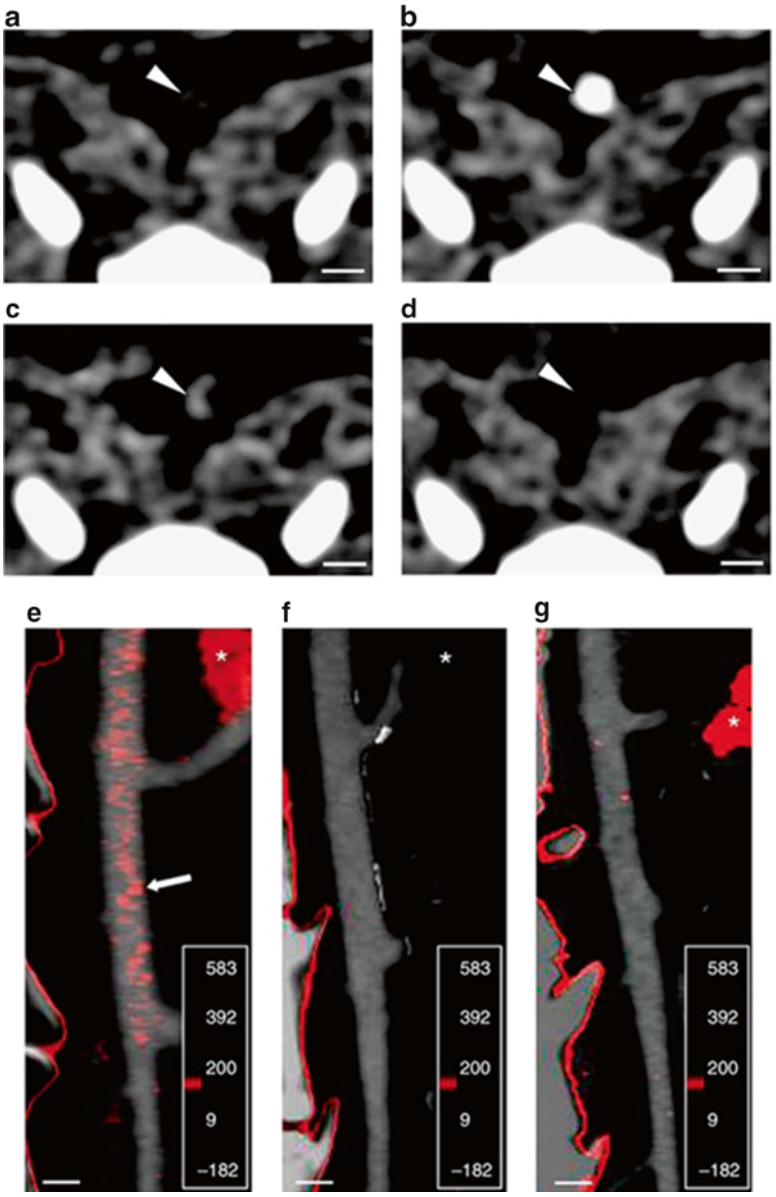

Fig. 20.4 CT imaging of macrophage activity in atherosclerosis using N1177, an iodinated nanoparticle contrast agent. Axial CT images of balloon-injured hypercholesterolemic rabbit aorta obtained before (**a**), during (**b**), and 2 h after the injection of N1177 (**c**) or a conventional contrast agent (**d**) demonstrating aortic enhancement with N1177 but not with the conventional contrast agent. Color-coded images show aortic enhancement with N1177 (**e**), but not with the conventional contrast (**f**) in hypercholesterolemic nor with N1177 in a control (**g**) rabbit. Reprinted with permission from Hyafil et al. [13]

interventions on plaque progression [88, 90]. Furthermore, a reduction in MDA2 uptake has been linked to increased VSMC and collagen expression in the plaque, features of plaque stability [91]. More recently, a number of LDL oxidation-specific antibodies, MDA2, E06 and IK17 have been incorporated into targeted micelles containing gadolinium for imaging of atherosclerosis by MRI [92]. MRI in atherosclerotic apoE$^{-/-}$ mice demonstrated aortic enhancement with targeted micelles which could be blocked with excess free antibody. This uptake was linked to the presence of macrophages in the plaque. While oxidized LDL has been the main target of these imaging studies, it is important to note that the similar epitopes are present on other modified lipids which are expressed by other cells, including apoptotic macrophages [93].

3.1.4 Plaque Vulnerability

Atherosclerotic plaque rupture or erosion exposes the blood to subendothelial structures and promotes local intra-arterial thrombosis which can manifest as an acute coronary syndrome. Therefore, there is a great need for non-invasive imaging approaches to characterize plaque biology in vivo. Plaques that are vulnerable to rupture are characterized by the presence of a thin fibrous cap, large necrotic core, marked infiltration of inflammatory cells and loss of collagen and VSMCs [94]. Many of these features have been studied in small animal models of atherosclerosis through novel molecular imaging approaches, some of which were discussed in previous paragraphs. The imbalance between matrix synthesis and degradation as a result of increased expression of diverse groups of proteases by inflammatory cells seems to contribute to destabilization of plaque's physical integrity. Apoptotic loss of VSMCs leads to reduced matrix synthesis and further destabilizes the plaques. The presence of neovessels in the plaque, which are fragile, may contribute to plaque destabilization through inflammatory cell recruitment and intra-plaque hemorrhage which results in necrotic core enlargement.

Protease activation is a highly promising target for imaging plaque vulnerability. MMPs and cathepsins are examples of proteolytic enzymes that are induced and activated by inflammatory cells and are believed to play a causal role in plaque rupture. Radiolabeled MMP-targeted tracers have been used to image atherosclerosis and changes in its biology following therapeutic interventions in a variety of small animal models, including spontaneous atherosclerosis or accelerated atherosclerosis following carotid artery ligation in apoE$^{-/-}$ or LDLR$^{-/-}$ mice [95, 96] or atherosclerosis induced by abdominal aorta de-endothelialization in hypercholesterolemic rabbits [97]. While some of these studies have shown a strong correlation between tracer uptake and plaque macrophage content and MMP-2 and -9 expression [95, 97], it is still unclear how the uptake of broad spectrum MMP tracers relates to activation of specific MMPs and presence of tissue inhibitors. In addition to scintigraphic-based imaging, conjugation of gadolinium to a tetrapeptide inhibitor of MMPs has been successfully used for MRI of atherosclerosis in mice and rabbits [98, 99]. The proteolytic activity of MMP-2 and -9 can also be targeted using

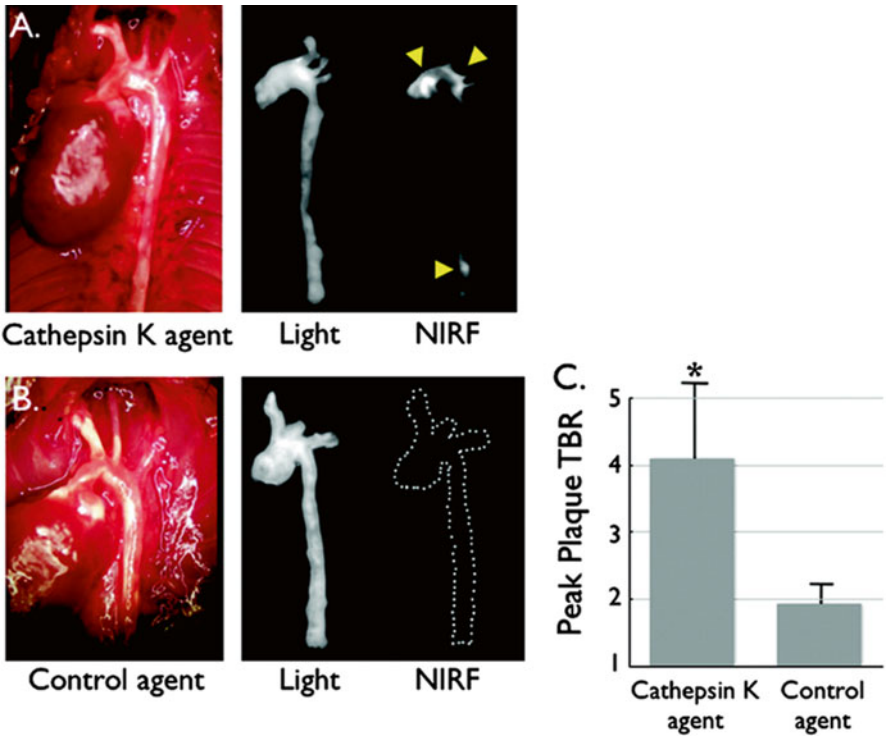

Fig. 20.5 Near-infrared fluorescence imaging of cathepsin K activity using a cathepsin K-sensitive protease-activatable agent. Fluorescence reflectance imaging demonstrates a strong focal signal in the aortic root, aortic arch, and abdominal aorta (*arrowheads*) of apoE$^{-/-}$ mice (**a**) which corresponds to visible atherosclerotic plaques. Injection of a control agent (**b**) demonstrates minimal near-infrared fluorescent signal. Plaque target-to-background ratio is significantly higher in the cathepsin K group (**c**). Reprinted with permission from Jaffer et al. [101]

"activatable" near-infrared fluorescence substrate of gelatinases that allows optical imaging of atherosclerosis in apoE$^{-/-}$ mice [100]. A similar methodology has been used to develop near-infrared fluorescence probes to image the activity of specific cathepsins, such as cathepsins B and K, in atherosclerosis (Fig. 20.5) [101, 102]. Although not directly tested for imaging plaque vulnerability, myeloperoxidase, an enzyme produced by neutrophils and macrophages, contributes to the pathogenesis of atherosclerosis and may be imaged by bioluminescence imaging in vivo [103].

The presence of apoptotic cells has been linked to plaque vulnerability [104, 105]. Dead macrophages and other cells in the plaque contribute to enlargement of the necrotic core. Therefore, imaging apoptosis appears a promising approach to gain information on plaque vulnerability. ^{99m}Tc-labeled annexin V has been extensively studied for imaging atherosclerotic lesions from small animals to humans [35, 106, 107] and its uptake in the plaque has been correlated with the presence of macrophages and indices of apoptosis. As discussed previously, a confounding factor in the interpretation of annexin V studies is the limited specificity of its target,

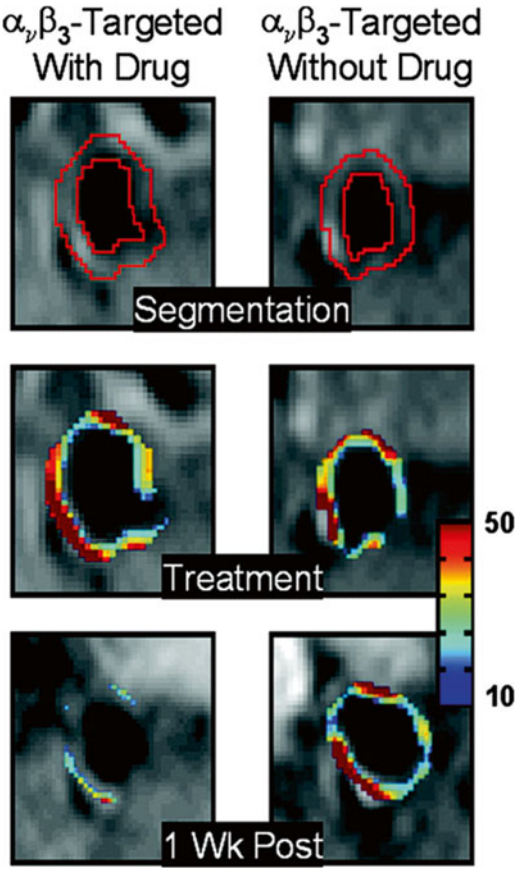

Fig. 20.6 MRI αvβ3 integrin-targeted paramagnetic nanoparticles containing the antiangiogenic agent, fumagillin, in hyperlipidemic rabbits. Images of the abdominal aorta were obtained prior to (*top* panel), 4 h (*middle* panel) and 1 week (*lower* panel) after injection of αvβ3-targeted nanoparticles with (*left* panel) or without (*right* panel) fumagillin. The effectiveness of targeted drug delivery is confirmed by decreased enhancement in the drug-treated group at 1 week. Reprinted with permission from Winter et al. [112]

externally exposed PS, for apoptosis, and has formed the basis for using annexin V imaging in studies of platelet activation and thrombus formation in aneurysm [108] and experimental endocarditis [109]. It is also important to note that recent studies have demonstrated that the role of apoptosis in atherogenesis depends on its stage, with apoptosis being protective in early stages and contributing to plaque enlargement in more developed lesions [110].

Increased neovascularization, whether ectopic neovascularization or hyperplasia of vasa vasorum, in the plaque is another pathological feature of plaques that are prone to rupture [111]. The direct exposure of neovascular endothelium to blood facilitates its access to intravascular imaging probes. This can potentially increase targeting specificity by limiting access of probes to structure beyond the vasculature. An early example of imaging plaque angiogenesis used αvβ3 integrin-targeted paramagnetic nanoparticles to detect early atherosclerotic lesions in rabbit by MRI [38]. This approach has provided an opportunity to deliver therapeutic agents carried by targeted nanoparticles to plaque neovessels, whether alone or in combination with systemic therapies (Fig. 20.6) [112, 113]. While technically challenging,

it may also be possible to use targeted microbubbles (e.g., to αvβ3 integrin) to detect plaque angiogenesis by ultrasound imaging. Radiotracer-based imaging is an alternative approach to imaging plaque angiogenesis [114]. Given the broad distribution of many of the targets used for imaging angiogenesis (e.g., αvβ3 integrin, VEGF receptors), it is unlikely that in this case the signal originates solely from the neovessels.

Geometrical remodeling plays a role in symptomatic presentation of atherosclerosis [115]. Early on in the course of atherogenesis the artery undergoes expansive remodeling to maintain lumen size and blood flow. At some point in the development, this expansive remodeling cannot compensate for the increased plaque burden, resulting in luminal stenosis and reduction in flow. Under certain conditions, the artery undergoes constriction, rather than expansion, increasing the likelihood of luminal stenosis and symptoms of chronic ischemia. In advanced atherosclerosis, expansive remodeling has been linked to plaque vulnerability [116]. As such, molecular imaging the remodeling process in small animals may provide important information on plaque biology and its propensity to complications [45, 59].

Imaging metabolic activity in atherosclerosis is the most clinically advanced molecular imaging approach for assessing plaque biology. Increased ^{18}F-FDG uptake in the carotid arteries of a subset of patients has been linked to the risk of plaque rupture and stroke [75, 76]. Investigation in animal models of atherosclerosis has related ^{18}F-FDG uptake to plaque inflammation and macrophage burden [117]. More recent work has demonstrated that ^{18}F-FDG uptake in the plaque is reduced in the course of statin therapy [118], raising the possibility that ^{18}F-FDG imaging may be used as a surrogate for tracking the effect of therapeutic intervention on plaque inflammation. However, there remain many unanswered questions about the nature and specificity of ^{18}F-FDG uptake in atherosclerosis and molecular imaging in small animals will undoubtedly play an important role in addressing these issues.

Given the biological complexity of atherogenesis, it is likely that imaging a single molecular or cellular process will not be sufficient to provide a full picture of its complex biology. The overlap between biology in different pathological states (e.g., presence of macrophages and neovascularization between “stable” and vulnerable plaque [119]) adds extra difficulty to interpretation of imaging studies of atherosclerosis. There is considerable value in assessing plaque morphology and burden with classical imaging (for example to assess fibrous cap thickness, lipid content, artery size, and presence of calcification). Recognizing these issues, many investigators have focused their efforts on multimodality imaging of atherosclerosis to combine anatomical and functional imaging. The small animal models of atherosclerosis provide a valuable tool to study many aspects of atherosclerosis biology. However, atherosclerosis in these animal models lacks some salient features of human disease, and therefore caution is warranted in extrapolating findings in small animals to human pathology. This is especially true for imaging plaque vulnerability, as despite the presence of extensive atherosclerosis burden, none of the existing animal models exhibit spontaneous plaque rupture and/or acute coronary events.

3.2 Other Vascular Pathologies

While atherosclerosis is the most common vascular disease, other vascular diseases are fairly prevalent and play important roles in vascular morbidity and mortality in humans. In many cases (e.g., in post-angioplasty restenosis, graft arteriosclerosis and aneurysm) atherosclerosis is involved in the development and complications of these pathologies. Similar to its role in atherosclerosis, small animal imaging can contribute to our understanding of pathophysiology, diagnosis and treatment of these vascular pathologies. Restenosis is the main long-term complication of PTCA, and occurs in ~40 % of cases. Although the use of stents (bare metal or drug eluting) stents has dramatically reduced the incidence of restenosis, restenosis remains the prototypic example of arterial response to injury. Animal models of mechanical injury provide a unique tool to study the pathogenesis of restenosis and other vascular pathologies that are associated with geometrical remodeling and neointimal hyperplasia. As discussed in previous sections, VSMC proliferation and matrix remodeling, key pathogenic processes in restenosis have been targets of molecular imaging in various small animal models [45, 59, 120]. Expression and activation of αv integrins parallels cell proliferation in a model of wire injury to carotid artery in apoE$^{-/-}$ mice, providing the molecular basis for integrin-targeted imaging of cell proliferation in vascular remodeling [45].

GA, the main cause of late transplant failure in cardiac transplantation, is characterized by diffuse concentric narrowing of coronary lumen secondary to neointimal hyperplasia. Immunity plays a central role in the development of GA which shares many cellular and molecular features of restenosis. GA is often diagnosed in advanced stages when the effect of therapeutic interventions may be limited. Molecular imaging targeted at relevant pathological features in small animals may lead to the development of an imaging approach for early GA, and help improve our understanding of pathogenesis. However, there is some debate about the relevance of various animal models of transplantation to human GA. The most widely used model of GA is based on aortic allotransplantation across a minor antigen or in the presence of immunosuppression, which leads to medial VSMC loss and their replacement with cells of donor origin. In an alternative approach, segments of human artery can be transplanted to immunodeficient mice. Adoptive transfer of human mononuclear cells in this models leads to an arteriopathy which mimics many features of human GA [121]. It has been shown that similar to neointimal hyperplasia in restenosis, cell proliferation in this chimeric human/mouse model of GA may be detected by targeting avb3 integrin activation in vivo [121]. Recent development of imaging approaches to study leukocyte trafficking and inflammation in atherosclerosis [10] raises the possibility that the same methodologies can be applied to imaging GA.

Aortic aneurysm is another example of a fairly prevalent vascular disease with considerable morbidity and mortality [122]. Aortic aneurysm rupture or dissection can be lethal, justifying surgical intervention in the subset of aneurysms that are at high risk for complication. While aneurysm size is the best known predictor of its

propensity to rupture, it is likely that molecular and cellular features which are associated with aneurysm expansion, rupture or dissection can be targeted by molecular imaging and help identify high risk small aneurysms [123]. Aneurysm thrombosis may lead to highly morbid embolic events, and it may be helpful to detect thrombus formation in aneurysm by molecular imaging. As previously discussed, ^{99m}Tc-Annexin V has been used to detect arterial thrombosis in a rat model of abdominal aortic aneurysm [108].

3.3 Myocardial Pathology

Despite species-specific differences in myocardial biology, small animal models have served as the starting point for many observations on myocardial pathology, imaging and therapy that were later on validated in larger animals and in humans. Molecular imaging of the myocardium which started with studies of myocardial metabolism has markedly extended and now includes studies of myocardial structure, neurohormonal dysfunction, inflammation and immunity, and therapeutic interventions, which will be reviewed in the following sections.

3.3.1 Ischemia and Infarction

Myocardial ischemia triggers changes in substrate utilization from fatty acids to glucose. This change has served as the basis for imaging ischemic memory with either ^{18}F-FDG [124] or radiolabeled fatty acid and their analogues such as ^{123}I-iodophenylpentadecanoic acid and β-methyl-*p*-iodophenyl-pentadecanoic acid (BMIPP) [125]. Like other fatty acids, BMIPP uptake is facilitated by CD36 or fatty acid translocase (FAT) [126] and BMIPP retention is dependent on its irreversible and ATP-dependent metabolism which is reduced in the setting of myocardial ischemia [127]. Although imaging in small animal models of myocardial ischemia can still provide important information on cardiac metabolism, much of the investigation in this field has moved to imaging in large animals and humans.

Following prolonged ischemia or as a result of reperfusion injury the myocardium undergoes apoptotic and necrotic cell death. Disruption of membrane integrity in necrotic and apoptotic cells exposes intracellular myosin which is normally not accessible to imaging tracers. As such, anti-myosin imaging with labeled antibodies has been extensively studied to image MI in various animal models and in humans [128–130]. This approach to imaging myocardial damage has evolved to include targeting other biologically relevant processes using tracers with better pharmacokinetic profiles. Myocardial apoptosis has been imaged using different imaging modalities. Labeled Annexin V has been used to image cell death following ischemia-reperfusion by scintigraphic imaging in rats [131], and an annexin-labeled magnetofluorescent nanoparticle, AnxCLIO-Cy5.5 has provided high resolution images in murine models of cardiomyocyte apoptosis [132]. Other investigators

have used fluorescent-labeled annexin V to image the kinetics of apoptosis following reperfusion injury in real time in beating mouse heart [133]. More recently, the C2A domain of synaptotagmin I, a transmembrane trafficking protein, which specifically binds with high affinity to PS and phosphatidylinositides has been labeled and used for imaging cell death by MRI in tumors [134] and by scintigraphic imaging in rat models of ischemia-reperfusion [135].

3.3.2 Healing, Remodeling and Heart Failure

Following acute injury the myocardium is inundated with an inflammatory infiltrate which initiates the healing process. Activation of the transcription factor nuclear factor (NF)-κB is an early event in this inflammatory response to ischemia-reperfusion. The kinetics of NF-κB activation following MI has been studied by in vivo molecular imaging using a transgenic mouse expressing luciferase under the control of NF-κB [136]. NF-κB activation is an upstream regulatory event for many endothelial adhesion molecules (e.g., VCAM-1) which are upregulated following ischemia-reperfusion, and may be detected by molecular imaging in vivo. The cellular composition of the inflammatory infiltrate is dynamic, and includes elements of both innate and adaptive immunity. As such, molecular imaging of various leukocyte subpopulations and their products can play an important role in studies of post-MI healing [9, 15, 137]. Myeloperoxidase an inflammatory enzyme produced by activated neutrophils and monocyte-macrophages following MI has been imaged in mouse using an activatable MRI tracer [137]. Other studies have focused on imaging cathepsins and MMPs which in conjunction with other inflammatory components play an important role in myocardial healing, angiogenesis, and remodeling.

MMPs play a significant role in post-MI remodeling by directly altering ECM components or indirectly by affecting other molecular and cellular processes. Inhibition of MMPs, through pharmacological interventions or gene deletion, favorably alters post-MI ventricular remodeling and shows therapeutic potential for prevention of heart failure. Various imaging strategies have been devised to assess in vivo MMP activity to further delineate its role in post-MI remodeling as well as to evaluate therapeutic interventions. MMP-2 and -9 activity has been longitudinally tracked in a murine model of MI by optical imaging using a enzyme-activated near-infrared fluorescence probe [57]. A family of ^{111}In- or ^{99m}Tc-labeled broad-spectrum MMP tracers (RP782, RP805), which target multiple activated MMPs, have been used for non-invasive imaging of MI and remodeling in rodents (Fig. 20.7) [58]. In addition to their uptake in the infarct area, these probes are also taken up in the remote, presumable healthy areas, reflecting the diffuse nature of MMP activation following MI. These studies have provided novel insight into the temporal and spatial pattern of MMP activation which precedes pathological ventricular remodeling, stressing out the contribution of small animal molecular imaging to studies of cardiovascular diseases. Similar approaches will help further elucidate the roles of individual members of the MMP family in the pathogenesis of cardiomyopathy and

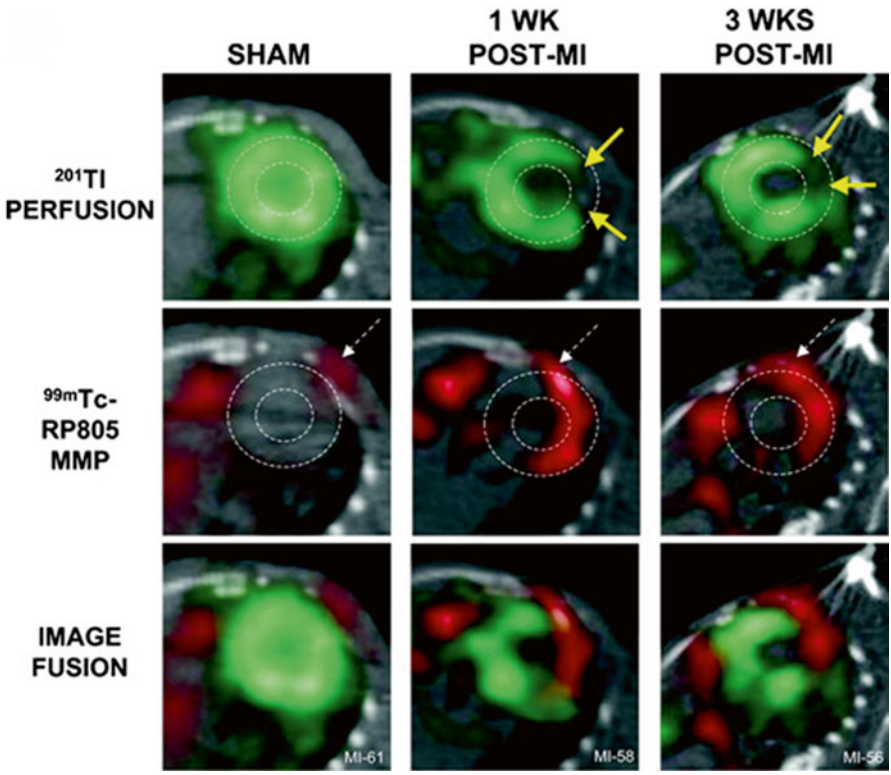

Fig. 20.7 MicroSPECT/CT imaging of MMP activation in post-myocardial infarction remodeling. Dual tracer imaging in mice at 1 and 3 weeks after myocardial infarction or sham operation demonstrated enhanced ^{99m}Tc-labeled MMP tracer (RP805) uptake in the areas of decreased perfusion detected by ^{201}Tl. Reprinted with permission from Su et al. [58]

ventricular remodeling and may serve as a clinical tool to predict and assess the effect of therapeutic intervention for ventricular remodeling.

Angiogenesis and arteriogenesis are integral to the healing process after MI. While a primary function may be to increase blood supply to reduce ischemia, they play an equally important role in regulating pathological remodeling and preventing the development of heart failure. The feasibility of molecular imaging of angiogenesis was initially demonstrated in a rat model of MI [37]. Ex vivo analysis demonstrated significant uptake of RP748, an ^{111}In-labeled quinolone targeting activated αvβ3 integrin in the regions of decreased perfusion detected by reduced ^{201}Thallium retention. In subsequent studies, the pro-angiogenic effect of MMP-9 gene deletion on ischemia-induced angiogenesis was demonstrated by SPECT imaging in the wild type and MMP-9$^{-/-}$ mice using NC100692, a ^{99m}Tc-labeled RGD peptide [138]. The time course of neovascularization and integrin expression following MI in rats was studies by PET imaging using ^{18}F-Galacto-RGD [46]. While there was no significant uptake of the tracer at 1 day after MI, tracer uptake was clearly detectable as early as 3 days and peaked at 1–3 weeks after reperfusion.

VEGF receptors are upregulated during ischemia and as described earlier, have been targeted effectively to image angiogenesis. In addition to their role in neovascularization, growth factors and their receptors are also involved in post-MI remodeling. A PET tracer, ^{64}Cu-6DOTA-VEGF$_{121}$ has been successfully utilized to monitor kinetics of VEGF receptor expression in the rat myocardium after MI [139]. Similar to αvβ3 integrin, VEGF receptors are expressed by ECs and other cells, including inflammatory cells which play an important role in ventricular remodeling, and caution is warranted in attributing tracer uptake solely to neovascularization in the infarct region.

The healing process after myocardial injury often leads to myocardial fibrosis, the detection of which may be useful for studies of cardiomyopathy. Myocardial fibrosis whether regional, as in post-infarct scar, or diffuse, as in the case of non-ischemic cardiomyopathy, is readily detectable by MRI [140]. While a growing number of targeted probes accumulate in the scar [141, 142], none has been shown to detect the diffuse fibrosis in cardiomyopathy. The non-specific uptake of probes by the scar tissue mandates careful attention to appropriate controls in investigational studies of novel tracers.

The blood coagulation factor, transglutaminase factor XIII (FXIII), which is activated by thrombin [143] plays a cardioprotective role in post-MI remodeling by its involvement in ECM metabolism and its regulatory effect on the inflammatory response to stabilize the infarct. SPECT imaging of in vivo FXIII activity has been performed using a FXIIIa-sensitive probe (^{111}In-NQEQVSPLTLLK) [144]. Cross-linking of this probe with ECM components led to focal probe retention, reflecting the presence of FXIII activity. Using this probe in a murine model of MI investigators were able to directly monitor FXIII activity in vivo [145], demonstrating that treatment with thrombin inhibitor dalteparin decreases FXIII activity and increases incidence of ventricular rupture. Thus, imaging FXIII activity post-MI would allow monitoring healing and possibly predicting prognosis.

3.3.3 Neurohormonal System and Cardiac Innervation

Activation of the renin-angiotensin system contributes to pathological remodeling and progressive cardiac dysfunction. Many of the effects of the renin-angiotensin system activation are mediated by angiotensin II, which in addition to enhancing VSMC tone and salt and water retention, promotes cardiomyocyte hypertrophy, fibroblast hyperplasia [146] and extracellular matrix deposition [147]. A number of clinical trials have demonstrated improved survival, decreased progression of heart failure and reversal of LV remodeling following treatment with angiotensin converting enzyme (ACE) inhibitors [148, 149], angiotensin II type I receptor (AT1R) blocking agents [150] and aldosterone inhibitors [151]. To date, several radiolabeled ACE inhibitors and AT1R antagonists have been labeled and evaluated in preliminary experiments for defining the kinetics of angiotensin receptor expression after myocardial infarction and detection of ventricular remodeling [152, 153]. Ongoing imaging studies in small animal models will establish the utility of this approach for predicting pathological ventricular remodeling and response to therapy.

Abnormalities in myocardial innervation are common findings in myocardial ischemia, heart failure and arrhythmia. ^{123}I-metaiodobenzylguanidine (MIBG), a false neurotransmitter and an analog of norepinephrine and ^{11}C-hydroxyephedrine (HED) have been extensively studied for assessment of global and regional cardiac sympathetic innervation by planar, SPECT and PET imaging [154], and are under clinical evaluation in heart failure and arrhythmia. Similarly, other tracers under evaluation in small animal models for imaging various aspects of cardiac innervation provide novel opportunities for assessing prognosis and the effect of therapeutic interventions in heat failure [155].

3.3.4 Acute Transplant Rejection

Cardiac transplantation, often used for treatment of end stage heart failure, is complicated by acute rejection in a large group of patients. The surveillance of heart transplant recipients involves obtaining multiple endomyocardial biopsies at regular intervals, which is an invasive procedure and prone to sampling error. Molecular imaging may provide a noninvasive method of graft surveillance with earlier detection of rejection, a higher predictive value and fewer complications. Initial clinical trials to evaluate molecular imaging strategies for non-invasive detection of acute rejection in heart transplants using an ^{111}In-labeled anti-myosin antibody to detect cardiomyocyte death [156] and ^{99m}Tc-annexin V to target cardiomyocyte apoptosis [157] have not led to widespread clinical use. Recent animal studies have focused on imaging immune response in the course of acute rejection and have targeted phagocytic activity and protease expression of macrophages for imaging transplant rejection [16, 158, 159].

3.3.5 Tracking Gene and Cell Therapies

Gene and cell therapy are novel and promising therapeutic approaches to a variety of diseases, including heart failure [160]. Following the initial enthusiasm with gene therapy, this approach has faced a number of obstacles, including safety concerns, which have limited its use in clinical trials. In animal studies, regenerative therapy using a variety of cells has shown to improve cardiac function and reduce infarct size. However, the mechanisms of these beneficial effects are yet to be elucidated, and may include paracrine effects, differentiation into or fusion with cardiac myocytes, enhanced neovascularization and recruitment of beneficial cells to the infarct area. The optimal cell types and delivery methods have not been defined and translation to clinical application has been difficult with studies showing inconclusive and at times conflicting results. Molecular imaging can help assess the distribution and survival of transplanted cells and understand their mechanism of action.

One strategy to track the fate of transplanted cells involves their labeling with radioisotopes prior to delivery and high sensitivity SPECT or PET imaging. Several approaches for cell labeling, including ^{111}In-oxine [161, 162], ^{111}In-tropolone [163],

^{99m}Tc-exametazime [164], and ^{18}F-FDG [165] have been tested in animal studies. These and other studies have established the usefulness of radiolabeling cells for in vivo imaging by scintigraphy, demonstrating an overall low uptake and retention of transplanted cell in the infarct area in rodents. Imaging ^{111}In-oxine labeled hematopoietic progenitor cells introduced directly into the ventricular cavity of rats with normal or infarcted myocardium supported the presence of a possible homing mechanism directing cells to the infarct area [161]. Limitations of this approach include the short half lives of radiotracers, restricting the tracking of transplanted cells to a few days, possible radiotoxicity and low spatial resolution. An alternative labeling approach involves loading cells with paramagnetic iron-oxide particles which generate signals on T2-weighted MRI images. Using this approach, iron-labeled bone marrow stromal cells have been tracked in a rat model of MI for a period of 16 weeks [166]. Limitations of MRI include the inability to differentiate viable from non viable cells or with macrophages which retain iron particles.

An alternative method for tracking transplanted cells involves indirect labeling with reporter genes. Reporter genes are incorporated into cells using viral or non-viral vectors and encode proteins that interact with an imaging probe to produce signals detectable by MRI, SPECT, PET and optical imaging. Longitudinal tracking of cells is possible as transcription and translation only occur in viable cells and their progeny. Bioluminescence- and fluorescence-based optical imaging has proven especially useful in tracking stem cells in small animals. In a recent study, murine embryonic stem cells transfected with a triple-fusion reporter gene consisting of firefly luciferase, red fluorescence protein, and truncated herpes virus thymidine kinase were introduced in a rat model MI and their survival, migration and proliferation was successfully tracked using optical and PET imaging (Fig. 20.8) [167]. Despite the high detection sensitivity of optical imaging, its use with the current technology is limited by the depth of penetration and restricted to imaging in small animals.

4 Summary

Recent advances in imaging technologies and tracer development have opened the way for the progress in molecular imaging of the cardiovascular system in small animals, as discussed in detail here. While this review of the state of the art is by no means exhaustive and due to space limitations a number of highly informative original studies are omitted, it is clear that after a decade of experimentation and development, we are now entering a new era in cardiovascular molecular imaging. We see some of the approaches validated in small animals tested in patients and are on the verge of entering routine clinical practice. Pilot studies have established many molecular and cellular aspects of cardiovascular pathobiology as potential targets for molecular imaging. Additional developmental work is necessary to establish better or representative animal models, e.g., for atherosclerotic plaque rupture and

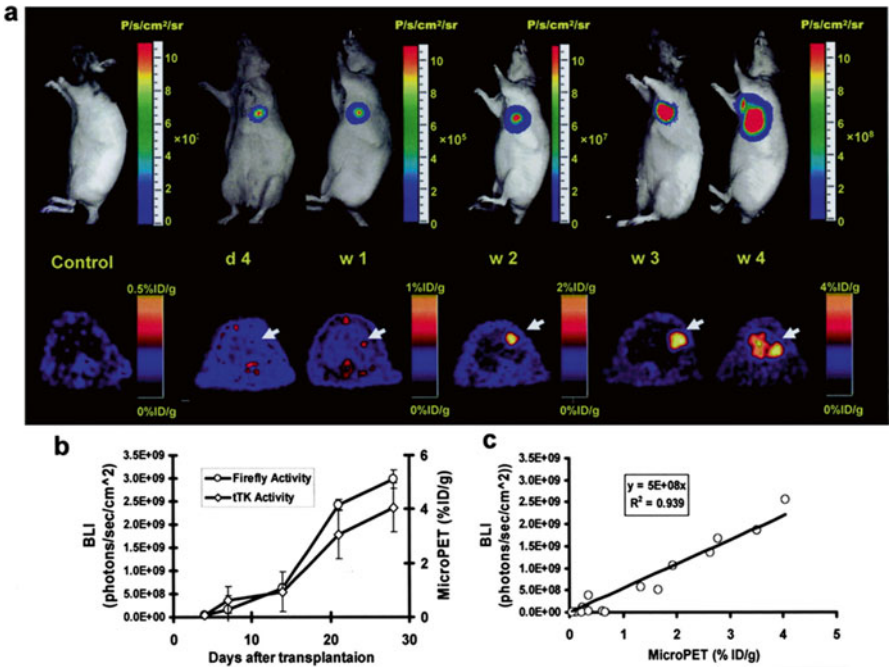

Fig. 20.8 Tracking of transplanted embryonic stem cells by serial bioluminescence and PET imaging. Murine cells transduced with a triple-fusion reporter gene construct containing firefly luciferase, truncated thymidine kinase, and monomeric red fluorescence protein were injected into adult athymic rat hearts and animals were imaged over a 4 week period. Bioluminescence (*top*) and PET (*bottom*) signals progressively increased from day 4 to week 4 (**a**, **b**) and displayed a strong correlation (**c**). (*BLI* bioluminescence). Reprinted with permission from Cao et al. [58]

erosion, aortic aneurysm, chronic rejection and non-ischemic cardiomyopathy. Standard protocols are yet to be established for molecular imaging in small animals, including image reconstruction and analysis. Novel tracers are needed for neglected areas of investigation, including cardiovascular complications of diabetes and other systemic diseases. Although from an economical and regulatory stand point it may be necessary to focus on a few highly promising tracers with broad clinical application, the complexity of cardiovascular biology cannot be accurately reflected by a few tracers selected for clinical development. Therefore, it is important to pursue the validation of existing tracers and work on identifying novel targets and probes for imaging cardiovascular processes. In conjunction with advances in multimodality imaging, which has helped overcome some of the limitations of individual imaging technologies, this is expected to lead to remarkable expansion of cardiovascular molecular imaging in small animals as a tool for understanding pathobiology and drug development.

Acknowledgments This work was supported by National Institutes of Health R01 HL85093, and a Department of Veterans Affairs Merit Award to MMS.

References

1. Hansson GK, Robertson AK, Soderberg-Naucler C (2006) Inflammation and atherosclerosis. Annu Rev Pathol 1:297-329.
2. Cybulsky MI, Gimbrone MA, Jr. (1991) Endothelial expression of a mononuclear leukocyte adhesion molecule during atherogenesis. Science 251:788-91.
3. Sadeghi MM, Schechner JS, Krassilnikova S, Gharaei AA, Zhang J, Kirkiles-Smith N, et al. (2004) Vascular cell adhesion molecule-1-targeted detection of endothelial activation in human microvasculature. Transplant Proc 36:1585-91.
4. Kelly KA, Allport JR, Tsourkas A, Shinde-Patil VR, Josephson L, Weissleder R (2005) Detection of vascular adhesion molecule-1 expression using a novel multimodal nanoparticle. Circ Res 96:327-36.
5. Nahrendorf M, Jaffer FA, Kelly KA, Sosnovik DE, Aikawa E, Libby P, et al. (2006) Noninvasive vascular cell adhesion molecule-1 imaging identifies inflammatory activation of cells in atherosclerosis. Circulation 114:1504-11.
6. McAteer MA, Schneider JE, Ali ZA, Warrick N, Bursill CA, von zur Muhlen C, et al. (2008) Magnetic resonance imaging of endothelial adhesion molecules in mouse atherosclerosis using dual-targeted microparticles of iron oxide. Arterioscler Thromb Vasc Biol 28:77-83.
7. Kaufmann BA, Sanders JM, Davis C, Xie A, Aldred P, Sarembock IJ, et al. (2007) Molecular imaging of inflammation in atherosclerosis with targeted ultrasound detection of vascular cell adhesion molecule-1. Circulation 116:276-84.
8. Behm CZ, Kaufmann BA, Carr C, Lankford M, Sanders JM, Rose CE, et al. (2008) Molecular imaging of endothelial vascular cell adhesion molecule-1 expression and inflammatory cell recruitment during vasculogenesis and ischemia-mediated arteriogenesis. Circulation 117: 2902-11.
9. Nahrendorf M, Swirski FK, Aikawa E, Stangenberg L, Wurdinger T, Figueiredo JL, et al. (2007) The healing myocardium sequentially mobilizes two monocyte subsets with divergent and complementary functions. J Exp Med 204:3037-47.
10. Kircher MF, Grimm J, Swirski FK, Libby P, Gerszten RE, Allport JR, et al. (2008) Noninvasive in vivo imaging of monocyte trafficking to atherosclerotic lesions. Circulation 117:388-95.
11. Hartung D, Petrov A, Haider N, Fujimoto S, Blankenberg F, Fujimoto A, et al. (2007) Radiolabeled Monocyte Chemotactic Protein 1 for the detection of inflammation in experimental atherosclerosis. J Nucl Med 48:1816-21.
12. Ogawa M, Ishino S, Mukai T, Asano D, Teramoto N, Watabe H, et al. (2004) (18)F-FDG accumulation in atherosclerotic plaques: immunohistochemical and PET imaging study. J Nucl Med 45:1245-50.
13. Hyafil F, Cornily JC, Feig JE, Gordon R, Vucic E, Amirbekian V, et al. (2007) Noninvasive detection of macrophages using a nanoparticulate contrast agent for computed tomography. Nat Med 13:636-41.
14. Nahrendorf M, Zhang H, Hembrador S, Panizzi P, Sosnovik DE, Aikawa E, et al. (2008) Nanoparticle PET-CT imaging of macrophages in inflammatory atherosclerosis. Circulation 117:379-87.
15. Nahrendorf M, Sosnovik DE, Waterman P, Swirski FK, Pande AN, Aikawa E, et al. (2007) Dual channel optical tomographic imaging of leukocyte recruitment and protease activity in the healing myocardial infarct. Circ Res 100:1218-25.
16. Christen T, Nahrendorf M, Wildgruber M, Swirski FK, Aikawa E, Waterman P, et al. (2009) Molecular imaging of innate immune cell function in transplant rejection. Circulation 119:1925-32.
17. Yaoita H, Ogawa K, Maehara K, Maruyama Y (1998) Attenuation of ischemia/reperfusion injury in rats by a caspase inhibitor. Circulation 97:276-81.
18. Edinger AL, Thompson CB (2004) Death by design: apoptosis, necrosis and autophagy. Curr Opin Cell Biol 16:663-9.

19. Jaffer FA, Sosnovik DE, Nahrendorf M, Weissleder R (2006) Molecular imaging of myocardial infarction. J Mol Cell Cardiol 41:921-33.
20. Zhou Z (2007) New phosphatidylserine receptors: clearance of apoptotic cells and more. Dev Cell 13:759-60.
21. Fischer K, Voelkl S, Berger J, Andreesen R, Pomorski T, Mackensen A (2006) Antigen recognition induces phosphatidylserine exposure on the cell surface of human CD8+ T cells. Blood 108:4094-101.
22. Martin S, Pombo I, Poncet P, David B, Arock M, Blank U (2000) Immunologic stimulation of mast cells leads to the reversible exposure of phosphatidylserine in the absence of apoptosis. Int Arch Allergy Immunol 123:249-58.
23. Dillon SR, Mancini M, Rosen A, Schlissel MS (2000) Annexin V binds to viable B cells and colocalizes with a marker of lipid rafts upon B cell receptor activation. J Immunol 164: 1322-32.
24. Thiagarajan P, Tait JF (1990) Binding of annexin V/placental anticoagulant protein I to platelets. Evidence for phosphatidylserine exposure in the procoagulant response of activated platelets. J Biol Chem 265:17420-3.
25. Balasubramanian K, Mirnikjoo B, Schroit AJ (2007) Regulated externalization of phosphatidylserine at the cell surface: implications for apoptosis. J Biol Chem 282:18357-64.
26. Keen HG, Dekker BA, Disley L, Hastings D, Lyons S, Reader AJ, et al. (2005) Imaging apoptosis in vivo using 124I-annexin V and PET. Nucl Med Biol 32:395-402.
27. Kietselaer BL, Reutelingsperger CP, Boersma HH, Heidendal GA, Liem IH, Crijns HJ, et al. (2007) Noninvasive detection of programmed cell loss with 99mTc-labeled annexin A5 in heart failure. J Nucl Med 48:562-7.
28. Murakami Y, Takamatsu H, Taki J, Tatsumi M, Noda A, Ichise R, et al. (2004) 18F-labelled annexin V: a PET tracer for apoptosis imaging. Eur J Nucl Med Mol Imaging 31:469-74.
29. Petrovsky A, Schellenberger E, Josephson L, Weissleder R, Bogdanov A, Jr. (2003) Near-infrared fluorescent imaging of tumor apoptosis. Cancer Res 63:1936-42.
30. Medarova Z, Bonner-Weir S, Lipes M, Moore A (2005) Imaging beta-cell death with a near-infrared probe. Diabetes 54:1780-8.
31. Schellenberger EA, Bogdanov A, Jr., Hogemann D, Tait J, Weissleder R, Josephson L (2002) Annexin V-CLIO: a nanoparticle for detecting apoptosis by MRI. Mol Imaging 1:102-7.
32. Tait JF (2008) Imaging of apoptosis. J Nucl Med 49:1573-6.
33. Smith G, Glaser M, Perumal M, Nguyen QD, Shan B, Arstad E, et al. (2008) Design, synthesis, and biological characterization of a caspase 3/7 selective isatin labeled with 2-[18F]fluoroethylazide. J Med Chem 51:8057-67.
34. Laxman B, Hall DE, Bhojani MS, Hamstra DA, Chenevert TL, Ross BD, et al. (2002) Noninvasive real-time imaging of apoptosis. Proc Natl Acad Sci U S A 99:16551-5.
35. Kietselaer BL, Reutelingsperger CP, Heidendal GA, Daemen MJ, Mess WH, Hofstra L, et al. (2004) Noninvasive detection of plaque instability with use of radiolabeled annexin A5 in patients with carotid-artery atherosclerosis. N Engl J Med 350:1472-3.
36. Semenza GL (2003) Angiogenesis in ischemic and neoplastic disorders. Annu Rev Med 54:17-28.
37. Meoli DF, Sadeghi MM, Krassilnikova S, Bourke BN, Giordano FJ, Dione DP, et al. (2004) Noninvasive imaging of myocardial angiogenesis following experimental myocardial infarction. J Clin Invest 113:1684-91.
38. Winter PM, Morawski AM, Caruthers SD, Fuhrhop RW, Zhang H, Williams TA, et al. (2003) Molecular imaging of angiogenesis in early-stage atherosclerosis with alpha(v)beta3-integrin-targeted nanoparticles. Circulation 108:2270-4.
39. Lu E, Wagner WR, Schellenberger U, Abraham JA, Klibanov AL, Woulfe SR, et al. (2003) Targeted in vivo labeling of receptors for vascular endothelial growth factor: approach to identification of ischemic tissue. Circulation 108:97-103.
40. Hua J, Dobrucki LW, Sadeghi MM, Zhang J, Bourke BN, Cavaliere P, et al. (2005) Noninvasive imaging of angiogenesis with a 99mTc-labeled peptide targeted at alphavbeta3 integrin after murine hindlimb ischemia. Circulation 111:3255-60.

41. Veikkola T, Karkkainen M, Claesson-Welsh L, Alitalo K (2000) Regulation of angiogenesis via vascular endothelial growth factor receptors. Cancer Res 60:203-12.
42. Ferrara N, Houck KA, Jakeman LB, Winer J, Leung DW (1991) The vascular endothelial growth factor family of polypeptides. J Cell Biochem 47:211-8.
43. Ferrara N, Gerber HP, LeCouter J (2003) The biology of VEGF and its receptors. Nat Med 9: 669-76.
44. Pan Q, Chathery Y, Wu Y, Rathore N, Tong RK, Peale F, et al. (2007) Neuropilin-1 binds to VEGF121 and regulates endothelial cell migration and sprouting. J Biol Chem 282: 24049-56.
45. Sadeghi MM, Krassilnikova S, Zhang J, Gharaei AA, Fassaei HR, Esmailzadeh L, et al. (2004) Detection of injury-induced vascular remodeling by targeting activated alphavbeta3 integrin in vivo. Circulation 110:84-90.
46. Higuchi T, Bengel FM, Seidl S, Watzlowik P, Kessler H, Hegenloh R, et al. (2008) Assessment of alphavbeta3 integrin expression after myocardial infarction by positron emission tomography. Cardiovasc Res 78:395-403.
47. Powell DW, Mifflin RC, Valentich JD, Crowe SE, Saada JI, West AB (1999) Myofibroblasts. I. Paracrine cells important in health and disease. Am J Physiol 277:C1-9.
48. Diez J, Lopez B, Gonzalez A, Querejeta R (2001) Clinical aspects of hypertensive myocardial fibrosis. Curr Opin Cardiol 16:328-35.
49. Nagase H, Visse R, Murphy G (2006) Structure and function of matrix metalloproteinases and TIMPs. Cardiovasc Res 69:562-73.
50. Hayashidani S, Tsutsui H, Ikeuchi M, Shiomi T, Matsusaka H, Kubota T, et al. (2003) Targeted deletion of MMP-2 attenuates early LV rupture and late remodeling after experimental myocardial infarction. Am J Physiol Heart Circ Physiol 285:H1229-35.
51. Romanic AM, Harrison SM, Bao W, Burns-Kurtis CL, Pickering S, Gu J, et al. (2002) Myocardial protection from ischemia/reperfusion injury by targeted deletion of matrix metalloproteinase-9. Cardiovasc Res 54:549-58.
52. Fedak PW, Smookler DS, Kassiri Z, Ohno N, Leco KJ, Verma S, et al. (2004) TIMP-3 deficiency leads to dilated cardiomyopathy. Circulation 110:2401-9.
53. Chancey AL, Brower GL, Peterson JT, Janicki JS (2002) Effects of matrix metalloproteinase inhibition on ventricular remodeling due to volume overload. Circulation 105:1983-8.
54. Kai H, Ikeda H, Yasukawa H, Kai M, Seki Y, Kuwahara F, et al. (1998) Peripheral blood levels of matrix metalloproteases-2 and -9 are elevated in patients with acute coronary syndromes. J Am Coll Cardiol 32:368-72.
55. Spinale FG (2002) Matrix metalloproteinases: regulation and dysregulation in the failing heart. Circ Res 90:520-30.
56. Bremer C, Tung CH, Weissleder R (2001) In vivo molecular target assessment of matrix metalloproteinase inhibition. Nat Med 7:743-8.
57. Chen J, Tung CH, Allport JR, Chen S, Weissleder R, Huang PL (2005) Near-infrared fluorescent imaging of matrix metalloproteinase activity after myocardial infarction. Circulation 111:1800-5.
58. Su H, Spinale FG, Dobrucki LW, Song J, Hua J, Sweterlitsch S, et al. (2005) Noninvasive targeted imaging of matrix metalloproteinase activation in a murine model of postinfarction remodeling. Circulation 112:3157-67.
59. Zhang J, Nie L, Razavian M, Ahmed M, Dobrucki LW, Asadi A, et al. (2008) Molecular imaging of activated matrix metalloproteinases in vascular remodeling. Circulation 118: 1953-60.
60. Doran AC, Meller N, McNamara CA (2008) Role of smooth muscle cells in the initiation and early progression of atherosclerosis. Arterioscler Thromb Vasc Biol 28:812-9.
61. Johnson LL, Schofield LM, Verdesca SA, Sharaf BL, Jones RM, Virmani R, et al. (2000) In vivo uptake of radiolabeled antibody to proliferating smooth muscle cells in a swine model of coronary stent restenosis. J Nucl Med 41:1535-40.
62. Furie B, Furie BC (2008) Mechanisms of thrombus formation. N Engl J Med 359:938-49.

63. Libby P (2008) The molecular mechanisms of the thrombotic complications of atherosclerosis. J Intern Med 263:517-27.
64. Bates SM, Lister-James J, Julian JA, Taillefer R, Moyer BR, Ginsberg JS (2003) Imaging characteristics of a novel technetium Tc 99m-labeled platelet glycoprotein IIb/IIIa receptor antagonist in patients With acute deep vein thrombosis or a history of deep vein thrombosis. Arch Intern Med 163:452-6.
65. Jaffer FA, Tung CH, Wykrzykowska JJ, Ho NH, Houng AK, Reed GL, et al. (2004) Molecular imaging of factor XIIIa activity in thrombosis using a novel, near-infrared fluorescent contrast agent that covalently links to thrombi. Circulation 110:170-6.
66. Botnar RM, Perez AS, Witte S, Wiethoff AJ, Laredo J, Hamilton J, et al. (2004) In vivo molecular imaging of acute and subacute thrombosis using a fibrin-binding magnetic resonance imaging contrast agent. Circulation 109:2023-9.
67. Taillefer R, Edell S, Innes G, Lister-James J (2000) Acute thromboscintigraphy with (99m) Tc-apcitide: results of the phase 3 multicenter clinical trial comparing 99mTc-apcitide scintigraphy with contrast venography for imaging acute DVT. Multicenter Trial Investigators. J Nucl Med 41:1214-23.
68. Dunzinger A, Hafner F, Schaffler G, Piswanger-Soelkner JC, Brodmann M, Lipp RW (2008) 99mTc-apcitide scintigraphy in patients with clinically suspected deep venous thrombosis and pulmonary embolism. Eur J Nucl Med Mol Imaging 35:2082-7.
69. Cai J, Hatsukami TS, Ferguson MS, Kerwin WS, Saam T, Chu B, et al. (2005) In vivo quantitative measurement of intact fibrous cap and lipid-rich necrotic core size in atherosclerotic carotid plaque: comparison of high-resolution, contrast-enhanced magnetic resonance imaging and histology. Circulation 112:3437-44.
70. Broisat A, Riou LM, Ardisson V, Boturyn D, Dumy P, Fagret D, et al. (2007) Molecular imaging of vascular cell adhesion molecule-1 expression in experimental atherosclerotic plaques with radiolabelled B2702-p. Eur J Nucl Med Mol Imaging 34:830-40.
71. Mulder WJ, Strijkers GJ, Briley-Saboe KC, Frias JC, Aguinaldo JG, Vucic E, et al. (2007) Molecular imaging of macrophages in atherosclerotic plaques using bimodal PEG-micelles. Magn Reson Med 58:1164-70.
72. Lipinski MJ, Amirbekian V, Frias JC, Aguinaldo JG, Mani V, Briley-Saebo KC, et al. (2006) MRI to detect atherosclerosis with gadolinium-containing immunomicelles targeting the macrophage scavenger receptor. Magn Reson Med 56:601-10.
73. Amirbekian V, Lipinski MJ, Briley-Saebo KC, Amirbekian S, Aguinaldo JG, Weinreb DB, et al. (2007) Detecting and assessing macrophages in vivo to evaluate atherosclerosis noninvasively using molecular MRI. Proc Natl Acad Sci U S A 104:961-6.
74. Ishino S, Mukai T, Kuge Y, Kume N, Ogawa M, Takai N, et al. (2008) Targeting of lectinlike oxidized low-density lipoprotein receptor 1 (LOX-1) with 99mTc-labeled anti-LOX-1 antibody: potential agent for imaging of vulnerable plaque. J Nucl Med 49:1677-85.
75. Tawakol A, Migrino RQ, Bashian GG, Bedri S, Vermylen D, Cury RC, et al. (2006) In vivo 18F-fluorodeoxyglucose positron emission tomography imaging provides a noninvasive measure of carotid plaque inflammation in patients. J Am Coll Cardiol 48:1818-24.
76. Rudd JH, Warburton EA, Fryer TD, Jones HA, Clark JC, Antoun N, et al. (2002) Imaging atherosclerotic plaque inflammation with [18F]-fluorodeoxyglucose positron emission tomography. Circulation 105:2708-11.
77. Frias JC, Ma Y, Williams KJ, Fayad ZA, Fisher EA (2006) Properties of a versatile nanoparticle platform contrast agent to image and characterize atherosclerotic plaques by magnetic resonance imaging. Nano Lett 6:2220-4.
78. Chen W, Vucic E, Leupold E, Mulder WJ, Cormode DP, Briley-Saebo KC, et al. (2008) Incorporation of an apoE-derived lipopeptide in high-density lipoprotein MRI contrast agents for enhanced imaging of macrophages in atherosclerosis. Contrast Media Mol Imaging 3:233-42.
79. Hyafil F, Laissy JP, Mazighi M, Tchetche D, Louedec L, Adle-Biassette H, et al. (2006) Ferumoxtran-10-enhanced MRI of the hypercholesterolemic rabbit aorta: relationship between signal loss and macrophage infiltration. Arterioscler Thromb Vasc Biol 26:176-81.

80. Libby P (2002) Inflammation in atherosclerosis. Nature 420:868-74.
81. Blankenberg FG, Wen P, Dai M, Zhu D, Panchal SN, Tait JF, et al. (2001) Detection of early atherosclerosis with radiolabeled monocyte chemoattractant protein-1 in prediabeteic Zucker rats. Pediatr Radiol 31:827-35.
82. Roberts AB, Lees AM, Lees RS, Strauss HW, Fallon JT, Taveras J, et al. (1983) Selective accumulation of low density lipoproteins in damaged arterial wall. J Lipid Res 24:1160-7.
83. Rosen JM, Butler SP, Meinken GE, Wang TS, Ramakrishnan R, Srivastava SC, et al. (1990) Indium-111-labeled LDL: a potential agent for imaging atherosclerotic disease and lipoprotein biodistribution. J Nucl Med 31:343-50.
84. Lees AM, Lees RS, Schoen FJ, Isaacsohn JL, Fischman AJ, McKusick KA, et al. (1988) Imaging human atherosclerosis with 99mTc-labeled low density lipoproteins. Arteriosclerosis 8:461-70.
85. Nielsen LB, Stender S, Kjeldsen K, Nordestgaard BG (1996) Specific accumulation of lipoprotein(a) in balloon-injured rabbit aorta in vivo. Circ Res 78:615-26.
86. Hardoff R, Braegelmann F, Zanzonico P, Herrold EM, Lees RS, Lees AM, et al. (1993) External imaging of atherosclerosis in rabbits using an 123I-labeled synthetic peptide fragment. J Clin Pharmacol 33:1039-47.
87. Iuliano L, Signore A, Vallabajosula S, Colavita AR, Camastra C, Ronga G, et al. (1996) Preparation and biodistribution of 99m technetium labelled oxidized LDL in man. Atherosclerosis 126:131-41.
88. Tsimikas S, Palinski W, Halpern SE, Yeung DW, Curtiss LK, Witztum JL (1999) Radiolabeled MDA2, an oxidation-specific, monoclonal antibody, identifies native atherosclerotic lesions in vivo. J Nucl Cardiol 6:41-53.
89. Rajavashisth TB, Xu XP, Jovinge S, Meisel S, Xu XO, Chai NN, et al. (1999) Membrane type 1 matrix metalloproteinase expression in human atherosclerotic plaques: evidence for activation by proinflammatory mediators. Circulation 99:3103-9.
90. Tsimikas S, Shortal BP, Witztum JL, Palinski W (2000) In vivo uptake of radiolabeled MDA2, an oxidation-specific monoclonal antibody, provides an accurate measure of atherosclerotic lesions rich in oxidized LDL and is highly sensitive to their regression. Arterioscler Thromb Vasc Biol 20:689-97.
91. Torzewski M, Shaw PX, Han KR, Shortal B, Lackner KJ, Witztum JL, et al. (2004) Reduced in vivo aortic uptake of radiolabeled oxidation-specific antibodies reflects changes in plaque composition consistent with plaque stabilization. Arterioscler Thromb Vasc Biol 24: 2307-12.
92. Briley-Saebo KC, Shaw PX, Mulder WJ, Choi SH, Vucic E, Aguinaldo JG, et al. (2008) Targeted molecular probes for imaging atherosclerotic lesions with magnetic resonance using antibodies that recognize oxidation-specific epitopes. Circulation 117:3206-15.
93. Chang MK, Binder CJ, Miller YI, Subbanagounder G, Silverman GJ, Berliner JA, et al. (2004) Apoptotic cells with oxidation-specific epitopes are immunogenic and proinflammatory. J Exp Med 200:1359-70.
94. Aikawa M, Libby P (2004) The vulnerable atherosclerotic plaque: pathogenesis and therapeutic approach. Cardiovasc Pathol 13:125-38.
95. Ohshima S, Petrov A, Fujimoto S, Zhou J, Azure M, Edwards DS, et al. (2009) Molecular imaging of matrix metalloproteinase expression in atherosclerotic plaques of mice deficient in apolipoprotein e or low-density-lipoprotein receptor. J Nucl Med 50:612-7.
96. Schafers M, Riemann B, Kopka K, Breyholz HJ, Wagner S, Schafers KP, et al. (2004) Scintigraphic imaging of matrix metalloproteinase activity in the arterial wall in vivo. Circulation 109:2554-9.
97. Fujimoto S, Hartung D, Ohshima S, Edwards DS, Zhou J, Yalamanchili P, et al. (2008) Molecular imaging of matrix metalloproteinase in atherosclerotic lesions: resolution with dietary modification and statin therapy. J Am Coll Cardiol 52:1847-57.
98. Amirbekian V, Aguinaldo JG, Amirbekian S, Hyafil F, Vucic E, Sirol M, et al. (2009) Atherosclerosis and matrix metalloproteinases: experimental molecular MR imaging in vivo. Radiology 251:429-38.

99. Lancelot E, Amirbekian V, Brigger I, Raynaud JS, Ballet S, David C, et al. (2008) Evaluation of matrix metalloproteinases in atherosclerosis using a novel noninvasive imaging approach. Arterioscler Thromb Vasc Biol 28:425-32.
100. Deguchi JO, Aikawa M, Tung CH, Aikawa E, Kim DE, Ntziachristos V, et al. (2006) Inflammation in atherosclerosis: visualizing matrix metalloproteinase action in macrophages in vivo. Circulation 114:55-62.
101. Jaffer FA, Kim DE, Quinti L, Tung CH, Aikawa E, Pande AN, et al. (2007) Optical visualization of cathepsin K activity in atherosclerosis with a novel, protease-activatable fluorescence sensor. Circulation 115:2292-8.
102. Chen J, Tung CH, Mahmood U, Ntziachristos V, Gyurko R, Fishman MC, et al. (2002) In vivo imaging of proteolytic activity in atherosclerosis. Circulation 105:2766-71.
103. Gross S, Gammon ST, Moss BL, Rauch D, Harding J, Heinecke JW, et al. (2009) Bioluminescence imaging of myeloperoxidase activity in vivo. Nat Med 15:455-61.
104. Bjorkerud S, Bjorkerud B (1996) Apoptosis is abundant in human atherosclerotic lesions, especially in inflammatory cells (macrophages and T cells), and may contribute to the accumulation of gruel and plaque instability. Am J Pathol 149:367-80.
105. Kolodgie FD, Narula J, Burke AP, Haider N, Farb A, Hui-Liang Y, et al. (2000) Localization of apoptotic macrophages at the site of plaque rupture in sudden coronary death. Am J Pathol 157:1259-68.
106. Kolodgie FD, Petrov A, Virmani R, Narula N, Verjans JW, Weber DK, et al. (2003) Targeting of apoptotic macrophages and experimental atheroma with radiolabeled annexin V: a technique with potential for noninvasive imaging of vulnerable plaque. Circulation 108:3134-9.
107. Isobe S, Tsimikas S, Zhou J, Fujimoto S, Sarai M, Branks MJ, et al. (2006) Noninvasive imaging of atherosclerotic lesions in apolipoprotein E-deficient and low-density-lipoprotein receptor-deficient mice with annexin A5. J Nucl Med 47:1497-505.
108. Sarda-Mantel L, Coutard M, Rouzet F, Raguin O, Vrigneaud JM, Hervatin F, et al. (2006) 99mTc-annexin-V functional imaging of luminal thrombus activity in abdominal aortic aneurysms. Arterioscler Thromb Vasc Biol 26:2153-9.
109. Rouzet F, Dominguez Hernandez M, Hervatin F, Sarda-Mantel L, Lefort A, Duval X, et al. (2008) Technetium 99m-labeled annexin V scintigraphy of platelet activation in vegetations of experimental endocarditis. Circulation 117:781-9.
110. Gautier EL, Huby T, Witztum JL, Ouzilleau B, Miller ER, Saint-Charles F, et al. (2009) Macrophage apoptosis exerts divergent effects on atherogenesis as a function of lesion stage. Circulation 119:1795-804.
111. Doyle B, Caplice N (2007) Plaque neovascularization and antiangiogenic therapy for atherosclerosis. J Am Coll Cardiol 49:2073-80.
112. Winter PM, Neubauer AM, Caruthers SD, Harris TD, Robertson JD, Williams TA, et al. (2006) Endothelial alpha(v)beta3 integrin-targeted fumagillin nanoparticles inhibit angiogenesis in atherosclerosis. Arterioscler Thromb Vasc Biol 26:2103-9.
113. Winter PM, Caruthers SD, Zhang H, Williams TA, Wickline SA, Lanza GM (2008) Antiangiogenic synergism of integrin-targeted fumagillin nanoparticles and atorvastatin in atherosclerosis. JACC Cardiovasc Imaging 1:624-34.
114. Matter CM, Schuler PK, Alessi P, Meier P, Ricci R, Zhang D, et al. (2004) Molecular imaging of atherosclerotic plaques using a human antibody against the extra-domain B of fibronectin. Circ Res 95:1225-33.
115. Abrams J (2005) Clinical practice. Chronic stable angina. N Engl J Med 352:2524-33.
116. Raffel OC, Merchant FM, Tearney GJ, Chia S, Gauthier DD, Pomerantsev E, et al. (2008) In vivo association between positive coronary artery remodelling and coronary plaque characteristics assessed by intravascular optical coherence tomography. Eur Heart J 29:1721-8.
117. Zhang Z, Machac J, Helft G, Worthley SG, Tang C, Zaman AG, et al. (2006) Non-invasive imaging of atherosclerotic plaque macrophage in a rabbit model with F-18 FDG PET: a histopathological correlation. BMC Nucl Med 6:3.
118. Tahara N, Kai H, Ishibashi M, Nakaura H, Kaida H, Baba K, et al. (2006) Simvastatin attenuates plaque inflammation: evaluation by fluorodeoxyglucose positron emission tomography. J Am Coll Cardiol 48:1825-31.

119. Fleiner M, Kummer M, Mirlacher M, Sauter G, Cathomas G, Krapf R, et al. (2004) Arterial neovascularization and inflammation in vulnerable patients: early and late signs of symptomatic atherosclerosis. Circulation 110:2843-50.
120. Narula J, Petrov A, Bianchi C, Ditlow CC, Lister BC, Dilley J, et al. (1995) Noninvasive localization of experimental atherosclerotic lesions with mouse/human chimeric Z2D3 F(ab')2 specific for the proliferating smooth muscle cells of human atheroma. Imaging with conventional and negative charge-modified antibody fragments. Circulation 92:474-84.
121. Zhang J, Krassilnikova S, Gharaei AA, Fassaei HR, Esmailzadeh L, Asadi A, et al. (2005) Alphavbeta3-targeted detection of arteriopathy in transplanted human coronary arteries: an autoradiographic study. Faseb J 19:1857-9.
122. Isselbacher EM (2005) Thoracic and abdominal aortic aneurysms. Circulation 111:816-28.
123. Longo GM, Xiong W, Greiner TC, Zhao Y, Fiotti N, Baxter BT (2002) Matrix metalloproteinases 2 and 9 work in concert to produce aortic aneurysms. J Clin Invest 110:625-32.
124. Dilsizian V (2008) 18F-FDG uptake as a surrogate marker for antecedent ischemia. J Nucl Med 49:1909-11.
125. Dilsizian V, Bateman TM, Bergmann SR, Des Prez R, Magram MY, Goodbody AE, et al. (2005) Metabolic imaging with beta-methyl-p-[(123)I]-iodophenyl-pentadecanoic acid identifies ischemic memory after demand ischemia. Circulation 112:2169-74.
126. Abumrad NA, el-Maghrabi MR, Amri EZ, Lopez E, Grimaldi PA (1993) Cloning of a rat adipocyte membrane protein implicated in binding or transport of long-chain fatty acids that is induced during preadipocyte differentiation. Homology with human CD36. J Biol Chem 268:17665-8.
127. Hosokawa R, Nohara R, Fujibayashi Y, Okuda K, Ogino M, Hata T, et al. (1997) Myocardial kinetics of iodine-123-BMIPP in canine myocardium after regional ischemia and reperfusion: implications for clinical SPECT. J Nucl Med 38:1857-63.
128. Khaw BA, Fallon FT, Strauss HW, Haber E (1980) Myocardial infarct imaging of antibodies to canine cardiac myosin with indium-111-diethylenetriamine pentaacetic acid. Science 209:295-7.
129. Khaw BA, Gold HK, Yasuda T, Leinbach RC, Kanke M, Fallon JT, et al. (1986) Scintigraphic quantification of myocardial necrosis in patients after intravenous injection of myosin-specific antibody. Circulation 74:501-8.
130. Weissleder R, Lee AS, Khaw BA, Shen T, Brady TJ (1992) Antimyosin-labeled monocrystalline iron oxide allows detection of myocardial infarct: MR antibody imaging. Radiology 182:381-5.
131. Sarda-Mantel L, Hervatin F, Michel JB, Louedec L, Martet G, Rouzet F, et al. (2008) Myocardial uptake of 99mTc-annexin-V and 111In-antimyosin-antibodies after ischemia-reperfusion in rats. Eur J Nucl Med Mol Imaging 35:158-65.
132. Sosnovik DE, Schellenberger EA, Nahrendorf M, Novikov MS, Matsui T, Dai G, et al. (2005) Magnetic resonance imaging of cardiomyocyte apoptosis with a novel magneto-optical nanoparticle. Magn Reson Med 54:718-24.
133. Dumont EA, Reutelingsperger CP, Smits JF, Daemen MJ, Doevendans PA, Wellens HJ, et al. (2001) Real-time imaging of apoptotic cell-membrane changes at the single-cell level in the beating murine heart. Nat Med 7:1352-5.
134. Zhao M, Beauregard DA, Loizou L, Davletov B, Brindle KM (2001) Non-invasive detection of apoptosis using magnetic resonance imaging and a targeted contrast agent. Nat Med 7:1241-4.
135. Liu Z, Zhao M, Zhu X, Furenlid LR, Chen YC, Barrett HH (2007) In vivo dynamic imaging of myocardial cell death using 99mTc-labeled C2A domain of synaptotagmin I in a rat model of ischemia and reperfusion. Nucl Med Biol 34:907-15.
136. Tillmanns J, Carlsen H, Blomhoff R, Valen G, Calvillo L, Ertl G, et al. (2006) Caught in the act: in vivo molecular imaging of the transcription factor NF-kappaB after myocardial infarction. Biochem Biophys Res Commun 342:773-4.
137. Nahrendorf M, Sosnovik D, Chen JW, Panizzi P, Figueiredo JL, Aikawa E, et al. (2008) Activatable magnetic resonance imaging agent reports myeloperoxidase activity in healing

infarcts and noninvasively detects the antiinflammatory effects of atorvastatin on ischemia-reperfusion injury. Circulation 117:1153-60.
138. Lindsey ML, Escobar GP, Dobrucki LW, Goshorn DK, Bouges S, Mingoia JT, et al. (2006) Matrix metalloproteinase-9 gene deletion facilitates angiogenesis after myocardial infarction. Am J Physiol Heart Circ Physiol 290:H232-9.
139. Rodriguez-Porcel M, Cai W, Gheysens O, Willmann JK, Chen K, Wang H, et al. (2008) Imaging of VEGF receptor in a rat myocardial infarction model using PET. J Nucl Med 49:667-73.
140. Rodriguez E, Soler R (2008) New MR insights of cardiomyopathy. Eur J Radiol 67: 392-400.
141. Muzard J, Sarda-Mantel L, Loyau S, Meulemans A, Louedec L, Bantsimba-Malanda C, et al. (2009) Non-invasive molecular imaging of fibrosis using a collagen-targeted peptidomimetic of the platelet collagen receptor glycoprotein VI. PLoS One 4:e5585.
142. van den Borne SW, Isobe S, Verjans JW, Petrov A, Lovhaug D, Li P, et al. (2008) Molecular imaging of interstitial alterations in remodeling myocardium after myocardial infarction. J Am Coll Cardiol 52:2017-28.
143. Muszbek L, Yee VC, Hevessy Z (1999) Blood coagulation factor XIII: structure and function. Thromb Res 94:271-305.
144. Nahrendorf M, Hu K, Frantz S, Jaffer FA, Tung CH, Hiller KH, et al. (2006) Factor XIII deficiency causes cardiac rupture, impairs wound healing, and aggravates cardiac remodeling in mice with myocardial infarction. Circulation 113:1196-202.
145. Nahrendorf M, Aikawa E, Figueiredo JL, Stangenberg L, van den Borne SW, Blankesteijn WM, et al. (2008) Transglutaminase activity in acute infarcts predicts healing outcome and left ventricular remodelling: implications for FXIII therapy and antithrombin use in myocardial infarction. Eur Heart J 29:445-54.
146. Sadoshima J, Izumo S (1993) Molecular characterization of angiotensin II-induced hypertrophy of cardiac myocytes and hyperplasia of cardiac fibroblasts. Critical role of the AT1 receptor subtype. Circ Res 73:413-23.
147. Lijnen PJ, Petrov VV (2003) Role of intracardiac renin-angiotensin-aldosterone system in extracellular matrix remodeling. Methods Find Exp Clin Pharmacol 25:541-64.
148. (1991) Effect of enalapril on survival in patients with reduced left ventricular ejection fractions and congestive heart failure. The SOLVD Investigators. N Engl J Med 325:293-302.
149. St John Sutton M, Pfeffer MA, Plappert T, Rouleau JL, Moye LA, Dagenais GR, et al. (1994) Quantitative two-dimensional echocardiographic measurements are major predictors of adverse cardiovascular events after acute myocardial infarction. The protective effects of captopril. Circulation 89:68-75.
150. Cohn JN, Tognoni G (2001) A randomized trial of the angiotensin-receptor blocker valsartan in chronic heart failure. N Engl J Med 345:1667-75.
151. Pitt B (2009) Aldosterone blockade in patients with heart failure and a reduced left ventricular ejection fraction. Eur Heart J 30:387-8.
152. Shirani J, Narula J, Eckelman WC, Narula N, Dilsizian V (2007) Early imaging in heart failure: exploring novel molecular targets. J Nucl Cardiol 14:100-10.
153. Verjans JW, Lovhaug D, Narula N, Petrov AD, Indrevoll B, Bjurgert E, et al. (2008) Noninvasive imaging of angiotensin receptors after myocardial infarction. JACC Cardiovasc Imaging 1:354-62.
154. Henneman MM, Bengel FM, van der Wall EE, Knuuti J, Bax JJ (2008) Cardiac neuronal imaging: application in the evaluation of cardiac disease. J Nucl Cardiol 15:442-55.
155. Tipre DN, Fox JJ, Holt DP, Green G, Yu J, Pomper M, et al. (2008) In vivo PET imaging of cardiac presynaptic sympathoneuronal mechanisms in the rat. J Nucl Med 49:1189-95.
156. Frist W, Yasuda T, Segall G, Khaw BA, Strauss HW, Gold H, et al. (1987) Noninvasive detection of human cardiac transplant rejection with indium-111 antimyosin (Fab) imaging. Circulation 76:V81-5.
157. Narula J, Acio ER, Narula N, Samuels LE, Fyfe B, Wood D, et al. (2001) Annexin-V imaging for noninvasive detection of cardiac allograft rejection. Nat Med 7:1347-52.

158. Wu YL, Ye Q, Foley LM, Hitchens TK, Sato K, Williams JB, et al. (2006) In situ labeling of immune cells with iron oxide particles: an approach to detect organ rejection by cellular MRI. Proc Natl Acad Sci U S A 103:1852-7.
159. Kanno S, Wu YJ, Lee PC, Dodd SJ, Williams M, Griffith BP, et al. (2001) Macrophage accumulation associated with rat cardiac allograft rejection detected by magnetic resonance imaging with ultrasmall superparamagnetic iron oxide particles. Circulation 104:934-8.
160. Fuster V, Sanz J (2007) Gene therapy and stem cell therapy for cardiovascular diseases today: a model for translational research. Nat Clin Pract Cardiovasc Med 4 Suppl 1:S1-8.
161. Aicher A, Brenner W, Zuhayra M, Badorff C, Massoudi S, Assmus B, et al. (2003) Assessment of the tissue distribution of transplanted human endothelial progenitor cells by radioactive labeling. Circulation 107:2134-9.
162. Brenner W, Aicher A, Eckey T, Massoudi S, Zuhayra M, Koehl U, et al. (2004) 111In-labeled CD34+ hematopoietic progenitor cells in a rat myocardial infarction model. J Nucl Med 45:512-8.
163. Jin Y, Kong H, Stodilka RZ, Wells RG, Zabel P, Merrifield PA, et al. (2005) Determining the minimum number of detectable cardiac-transplanted 111In-tropolone-labelled bone-marrow-derived mesenchymal stem cells by SPECT. Phys Med Biol 50:4445-55.
164. Barbash IM, Chouraqui P, Baron J, Feinberg MS, Etzion S, Tessone A, et al. (2003) Systemic delivery of bone marrow-derived mesenchymal stem cells to the infarcted myocardium: feasibility, cell migration, and body distribution. Circulation 108:863-8.
165. Hofmann M, Wollert KC, Meyer GP, Menke A, Arseniev L, Hertenstein B, et al. (2005) Monitoring of bone marrow cell homing into the infarcted human myocardium. Circulation 111:2198-202.
166. Stuckey DJ, Carr CA, Martin-Rendon E, Tyler DJ, Willmott C, Cassidy PJ, et al. (2006) Iron particles for noninvasive monitoring of bone marrow stromal cell engraftment into, and isolation of viable engrafted donor cells from, the heart. Stem Cells 24:1968-75.
167. Cao F, Lin S, Xie X, Ray P, Patel M, Zhang X, et al. (2006) In vivo visualization of embryonic stem cell survival, proliferation, and migration after cardiac delivery. Circulation 113: 1005-14.

Chapter 21
Applications of Molecular Small-Animal Imaging in Oncology

Marybeth A. Pysz and Jürgen K. Willmann

1 Introduction

1.1 Characteristics of Cancer: Defining Molecular Targets

Extensive research has characterized, and will continue to explore, the complexity of tumorigenesis (i.e., the process by which a normal cell transforms). In addition to acquisition of genetic mutations (Table 21.1), recent advances in molecular genetics have also implicated transcriptional regulatory mechanisms (e.g., epigenetic alterations [1]) and post-transcriptional modifications (e.g., microRNAs (miRNAs) [2]) as major contributors to the cancer phenotype. While these individual events may transform a single cell, a tumor is composed of cancerous cells, stromal cells, fibroblasts, cancer stem cells, and inflammatory cells, among others, which create a stable microenvironment for the tumor as a whole to survive and thrive [3, 4]. Together, the altered tumor cell proteome and extracellular communication set the stage for a signaling network re-programmed for uncontrolled proliferation and replication, self-sufficiency, resistance to apoptosis/cell death, stimulation of angiogenesis, and invasion and metastasis [5]. These physiological properties and genetic alterations associated with cancer can be utilized as molecular targets to (a) create molecular probes for detecting cancer with various molecular imaging modalities; (b) design new chemotherapeutic therapies; and (c) (combine *a* and *b*) create delivery systems to target chemotherapeutic drugs to the tumor in order to decrease cytotoxic effects on normal cells/tissue.

M.A. Pysz • J.K. Willmann (✉)
Departments of Radiology and MIPS, Stanford University, Stanford, CA, USA
e-mail: willmann@stanford.edu

H. Zaidi (ed.), *Molecular Imaging of Small Animals: Instrumentation and Applications*,
DOI 10.1007/978-1-4939-0894-3_21,

Table 21.1 Frequent genetic mutations and/or altered gene/protein expression patterns in several types of cancer

Cancer type	Subtypes (most common)	Common genetic mutations and/or differential expression changes
Breast	1. Ductal	*BRCA1, BRAC2, ERα, PTEN, LKB1, p53, Casp8, TGFβ1, FGFR2, M4P3K1, PGR, FOX P3, ATF2, HER2* [188, 189]. *CCND1, cMYC* [190]
Lung	1. Non-small cell lung carcinoma (NSCLC)	*K-Ras-2, H-Ras-1*[191], *ERBB2, EGFR, RARβ, RB, p53, p16, cMYC, EIF4e, CCND1, COX2, VEGF* [190]
	2. Small cell lung carcinoma (SCLC)	
	3. Bronchial carcinoid	
Colorectal	1. Colon cancer	*APC, CTNNB, p16, SMAD4, CCKBR, TGFβRII, COX2, DCC, BCL2 p53, K-Ras, hMSH2, PI3KCA, cMYC, BAX, CCND1*[21, 190]
	2. GIST (Gastrointestinal Stromal Tumor)	
	3. Rectal cancer	
Skin	1. Melanoma	*NRas, BRAF, c-Kit, MITF, PTEN* [192]
	2. Basal cell carcinoma	
	3. Squamous cell carcinoma	
Liver	1. Hepatocellular carcinoma	*CTNNB1, p53, APC, HNF1a* [193], *K-Ras, PDGF, TGFβ,DDR1, IGF2R, M6F, PTEN, CCND1, IEGF, MMP9/14, cMYC, EGFR* [194]
Pancreas	1. Ductal adenocarcinoma	*K-Ras2, pl6/INK4A, p53, DPC4/SMAD4, BRCA2, TGFβRII* [195]
Brain	1. Glioblastoma	*p53, VEGF, p16, PTEN, COX2, CCNE, CCNA,p27, HER2/HER4, INK4a, cMYC, EGFR* [196]
	2. Medullablastoma	
Hematological	1. Leukaemia (AML/ALL)	*RB* (and *p130), p16^{INK4A}, p15 ^{INK4B}, p53, MDM-2, ATM, CBP/p300, NF1,AML1, WT-1,* IκBα *DCC, MSH2, PTEN, SMAD4/TGFβ, BAX, FAS/APO-1, hMLH1*[190, 197]
	2. Non-Hodgkin's lymphoma	
	3. Hodgkin's lymphoma	
	4. Multiple myeloma	
Prostate	1. Androgen dependent	*cMYC, c-Met, CCND1, CKN1B, FGF8, FLT1, VEGF, TGFβ, PTEN, BLC2,pl6, p53, RAF, RB, AR* [190]
	2. Androgen independent	
Ovarian		*K-Ras, BRAF, AKT, p53, RB, PTEN, BRCA1/2, HOX* [198]

1.2 Clinical Cancer Detection by Molecular Imaging

Clinical imaging of cancer can be divided into three purposes: (1) detection and diagnosis; (2) staging; and (3) treatment monitoring. *First*, cancer detection and diagnosis is most commonly investigated using anatomical imaging techniques—mainly computed tomography (CT), but also, magnetic resonance imaging (MRI) [6, 7] and ultrasound (US) [6, 8]. These techniques explore abnormal lesions based on anatomical-morphological changes, and most often detect tumors when the diameter is greater than 1 cm [8]; this is mostly due to the fact that patients often do not exhibit symptoms until they have a sizable tumor and imaging is performed at rather late stages of the tumor. Once an abnormal lesion is detected, then an imaging-guided biopsy can be taken and analyzed by histology/pathology in order to determine if the lesion is malignant or benign. If it is malignant, the *second* step of cancer imaging is staging, which serves to determine the extent to which the cancer has spread (i.e., detection of local or distant metastases), and to recommend proper treatment options (i.e., surgery and/or chemotherapy/radiotherapy) [6]. Post-surgical imaging is also necessary to determine the presence/absence of residual disease [6]. Imaging of micrometastases and/or residual cancer cells requires highly sensitive imaging techniques. For this reason, scintigraphic imaging modalities (i.e., single photon emission computed tomography (SPECT) and positron emission tomography (PET)) are often used in combination with anatomical-morphological imaging for cancer staging in the clinical environment [9, 10]. More specifically, ^{18}F-fluorodeoxy glucose (^{18}F-FDG) is the most commonly used PET radiotracer (~95 % of all clinical PET [8, 10]) that accumulates in tumors due to their higher cellular metabolic rate compared with normal tissue [10, 11]. The success rate of cancer imaging with ^{18}F-FDG PET exceeds 85 % in part because of the high sensitivity (subnanomolar to submillimolar range [11, 12]) and low background signal from normal tissue (except brain, kidneys, and bladder). Moreover, the high sensitivity of ^{18}F-FDG PET/CT enables detection of early stage tumors and/or pre-cancerous lesions, as well as, early characterization of therapeutic response [11]. However, some cancers may not be imaged using ^{18}F-FDG PET/CT because some cancers do not uptake the probe (e.g., thyroid and neuroendocrine [11]), or, background signal in normal tissue is too high due to sites of inflammation or high metabolic activity of normal cells (e.g., brain) [10]. One example of another molecular imaging modality used for staging is MRI detection of lymph node metastases. Contrast enhanced MRI using magnetic nanoparticles targeted to macrophages in lymph nodes was able to detect mm-sized micrometastases of prostate cancer in lymph nodes [13], and this method has been approved for detection of lymph node metastases common to other forms of cancer (e.g., genitourinary cancers, breast cancer, and head and neck cancer) [8]. Sensitive and quantitative detection of cancer is also required for the *third* step in imaging: treatment monitoring. ^{18}F-FDG-PET/CT is the most common molecular imaging modality used for monitoring changes in tumor size (i.e., volume measurement) as a read-out for response to chemotherapy. However, several studies have established non-specific uptake (i.e., due to

tumor hypoxia and multi-drug resistance (discussed further below)), and the push is toward monitoring molecular events specific to the type of therapy administered [8]. For these reasons, it is imperative to develop other molecular probes and/or improve upon the sensitivities of other molecular imaging modalities. Most pre-clinical evaluations of new molecular probes and/or contrast agents involve extensive biodistribution, pharmacokinetics, sensitivity, and toxicity measurements in small animal models of cancer, which are discussed in the next paragraph.

1.3 Small-Animal Models in Oncology

Several rodent models exist for studying neoplastic phenotypes in vivo, and these include: (1) a sub-cutaneous tumor graft; (2) injection of tumor cells or surgical transplantation of solid tumor orthotopically to organ/site of interest, (3) genetic modification of animals to promote tumorigenesis, and (4) treatment of the animal with a known carcinogen to induce cancer [14]. The *first* model—a sub-cutaneous tumor graft—involves the injection of established tumor cell lines (often human (i.e., xenograft), see Table 21.2 for list of commonly used cancer cell lines) under the skin, forming a bleb. This model type is extremely useful for proof-of-principle molecular imaging studies, since several different genotypic cell lines are available; therefore, the researcher can easily find or manipulate cell lines for proper positive and/or negative controls. For example, RKO colon cancer cells are wild-type for expression of adenomatous polyposis coli (*APC*), while most colon cancer cells express a mutated, functionally inactive form of *APC*. If a researcher wanted to design a probe to target only colon cancer cells expressing mutant *APC*, then they could use RKO colon cancer cells as a negative control. Scientists may also opt to use primary cancer cells extracted from human patient neoplasms; however, these are often less characterized for genetic alterations. Another advantage to this model is that a three-dimensional tumor forms quickly (often within 1–4 weeks), and has some phenotypical characteristics (such as hyperproliferation, angiogenesis, and necrosis) commonly observed in tumors. One disadvantage of this model is inherent in the use of cell lines, which will only contain one type of cancer cell, thereby making the tumor relatively homogeneous. Another disadvantage of sub-cutaneous tumor grafts is that the microenvironment does not accurately reflect that which may be experienced in the organ. For example, a sub-cutaneous tumor graft of pancreatic cancer cells would be surrounded by skin and muscle, and most angiogenic vessels would be recruited from the muscle side. This environment is quite different than the pancreas, which is rich in blood vessels and varied structure (ducts, acinar cells, fibrous).

The *second* type of model—orthotopic tumor model—is used to compensate for the issues associated with microenvironment and is established by injecting tumor cells in or transplanting solid tumor to a specific organ/site. There are several advantages to orthotopic tumor models: (1) Like sub-cutaneous tumors, orthotopic tumors grow relatively quickly (though may be slower because less cells are typically

Table 21.2 Methodologies for induction of cancer in rodents: genetic engineering, application of chemical carcinogens, or injection of human cancer cell lines

Cancer type	Examples of transgenic mouse/rat models[a]	Examples of chemically-induced models	Common human cell lines[b]
Breast	*BRCA1/2*$^{-/-}$, *ATM*$^{-/-}$, *Tp53*$^{-/-}$, *FoxP*$^{+/-}$, *Atf2*$^{+/-v}$ [188, 199]	Mouse mammary tumor virus (MMTV) [188]	MCF7, SK-BR-3, MCF-10A, MCF-10F, MCF-12A, MCF-I2F
Lung	Protein C-promoter driven *craf-BxB,* adenoviral Cre-^{V600E}*BRaf* [200] or LSL-K-*ras*^{G12D} and/or *LSL-p53R276H* [19, 201]	Methylene chloride, chloroprene, vanadium pentoxide [202]	A549, HT-1080, NCI-H2126, NCI-HI688, NCI-H1755, WI-26 VA4, DMS 79, DMS 53, Hs 573.T, A-427, SK-MES-I, SK-LU-I, Hs 57.T
Colon	*APC*$^{Min/+}$ [203], *APC*^{4638N} [204], *Muc2*$^{-/-}$ [205], *KRas*^{V12G} [20]	Azoxymethane [206, 207], high fat diet, docosahexaenoic acid, high caloric intake [208]	Colo 320DM, DLD-I, HCT-116, HCT-15, RCA, Colo205, Colo201, LoVo, SW48, SW403, SWI116, SW837, SW948, SWI417, HCT-8, T84, LSI23, CaCo-2, RKO, GEO, LS174T/LS180, SW620, SW480, HT-29
Skin	Tg.AC [209], RasH2 [210] SENCAR, Tyr-*H-ras*; *Ink4a/Arf*(del2/3), Tyr-*H-ras p53*$^{-/-}$ [211]	12-O-tetra-decanoyl phorbol-13-acetate (TPA), UV irradiation. 7,12-dimethvl benz[a]anthracene (DMBA) [212]	A-375, Hs 834.T, Hs 839.T, Hs 852.T, A2058, HT-144
Liver	Albumin promoter driven expression of Hepatitis B or C viral transgene [213], Mdr2-KO mice [214], 4 LAP-tTA/TRE-MET [215]	Ethanol, 2-acetyl-aminofluorene, 4-dimethylaminoazobenzene, herbicides, estradiol [216], infection with *Opisthorchis viverrini* or *Helicobacter hepaticus* [213]	HEP G2, HEP 3B, SNU-398, SNU-449, SNU-182, SNU-475, SNU-387, SNU-423, SK-HEP-I, C3A
Pancreas	Pdx 1-Cre, Kras^{G12D} [22], Pdx l-Cre, Trp53R172H/Kras^{G12D} [28]	Caerulein [217]	PANC-1 MiaPaCa-2, SU86.86, Capan-l, Capan-2. HPAC, HPAF-II, BxPC-3
Brain	GFAP-Cre, RCAS-Cre, Math 1-Cre, Nestin-Cre, Olig2-Cre, or Tlx-Cre driven: *Ptch*$^{+/-}$, *SmoM2, Brca2*$^{-/-}$-*p53*$^{-/-}$, *Nf1*$^{+/-}$-*p53*$^{+/-}$, *Kras-Pten–/–* (see [218] for review)	Lead compounds, acetonitrile, acrylamide, 2-methylaziridine, 1,2-propane sulfone, alkylnitrosureas [219]	U87MG, M059K, M059J, DBTRG-05MG, Hs, 683, A-172, LN-229, LN-18

(continued)

Table 21.2 (continued)

Cancer type	Examples of transgenic mouse/rat models[a]	Examples of chemically-induced models	Common human cell lines[b]
Hematological	*Mx1/Cre-^{V600E}BRaf* or *^{G12D}Kras* [200], *RB$^{-/-}$ p16INK4A$^{-/-}$/p19ARF$^{-/-}$, p53$^{-/-}$/BCR-ABL-expressing* bone marrow cells [197], *BCR-ABL^{p210}, PML-RARa, Mll* fusion knock-in mice [211, 220]	Benzene [221], formaldehyde [222], 1,3-butadiene [223]	HL-60, U937, Ml, CCRF-CEM, CCRF-SB, RPMI 6666, Mo-B, KG-1, CCRF-HSB-2, MOLT-3, NALM-1, ARH-77, RS4;11, GA-10, A3, AML-193, TALL-104, NC-37, HS-Sultan, BC-1
Prostate	ARKO(1-5), SCARKO, SPARKI (AR Knock-in and Knockout models, see [224]), TRAMP [225], PB- or C3-promoter driven expression of oncogenes (e.g., *KRas, cMYC*), *p27$^{Kipl-/-}$, PTEN$^{+/-}$, p53$^{-/-}$, pRB$^{-/-}$* [226]	*N*-methyl-*N*-nitrosourea, *N*-nitrosobis (2-oxopropyl. Amine), 3,2′-dimethyl-4-amino-biphenyl, and 2-amino-l-methyl-6-phenylimidazo[4,5-*b*] xpyridine [227]	PC-3, LNCaP, DU-145, CA-HPV-10
Ovarian	*TP53$^{-/-}$, RB1$^{-/-}$* [228], MSIIRI-driven SV40 Tag [198, 229], Cre-recombinase *APC$^{-/-}$/PTEN$^{-/-}$* [230]	7,12-Dimethylbenz(a)anthracene [231]	SKOV-3, SW626, Caov-3, Caov-4, ES-2, OVCAR-3

[a]Many transgenic mice are commercially available through Jackson Laboratories (http://www.jax.org)
[b]Available through American Tissue Culture Collection (ATCC) (http://www.atcc.org)

injected to accommodate for the smaller size and increased density in organs); (2) These models are also particularly useful for development of molecular imaging because implantation in the site of interest aids in confirmation that there is differential imaging signal between the cancerous and normal tissue; and (3) Orthotopic models can be useful for studying metastatic disease [15]. There are several types of metastatic orthotopic models, depending on the site of injection. For example, metastasis of hepatocellular cell carcinoma (HCC) has been studied by surgically transplanting human patient HCC specimens onto the mouse liver [16], or by injecting a suspension of human HepB HCC cell line into the surgically-exposed liver of SCID mice [17]. Another method used for studying metastasis is to inject tumor cells intravenously in the small animal, and observe where they "home" (i.e., adhere) to [18]. A major disadvantage of orthotopic models is the fact that they still do not recapitulate site specificity associated with cancer initiation (e.g., pancreatic ductal adenocarcinoma arises in pancreatic ducts, and invasive disease spreads to regions of acinar cells, but pancreatic tumor cells injected orthotopically in the pancreas would likely be mixed with acinar cells).

The *third* type of rodent model commonly used in cancer research is genetically engineered, or transgenic mice. There are two strategies to genetically modify a rodent: (1) "knock-in" strategy involves introducing a new gene into the rodent genome; or, (2) "knock-out" strategy whereby a rodent gene is substituted with an inactive rodent gene or human gene. The "knock-out" strategy is employed frequently to understand the effects of various genetic alterations associated with cancer (Table 21.1). These alterations include the overexpression of oncogenes (e.g., *CCND1*, which encodes cyclin D1, a mitogenic protein), expression of mutated oncogenes (e.g., oncogenic $KRas^{V12G}$), deletion or down-regulation of tumor suppressor gene expression (e.g., *p53*), and finally, expression of a mutated, non-functional tumor suppressor gene (e.g., APC^{I1638N}). Notably, several of these genetic abnormalities, including expression of oncogenic $KRas^{V12G}$ and deletion or suppression of *p53*, are common between cancer types; however, caution must be exercised as each of these mutations contribute differently to each type of cancer. For example, *KRas* mutations occur early during lung tumorigenesis and have been implicated with tumor initiation [19], whereas *KRas* mutations occur later in colon cancer tumorigenesis, and are associated with tumor progression [20, 21]. The "knock-out" transgenic mouse/rodent is bred by combining two transgenic mice: one with a "knock-in" expression of an enzyme named Cre recombinase, and one with a "knock-in" of a plasmid expressing the target gene with two LoxP sites (i.e., recognition sites inserted one before and one after the target gene sequence) followed by the 'replacement' gene. When offspring inherit both the Cre recombinase expression and target gene expression system, the Cre recombinase binds the two LoxP sites preventing expression of the target gene, and the 'replacement' gene is then transcribed. This method is called Cre-Lox site-specific recombination, and can also be used to direct expression of a gene (e.g., a mutation or truncated gene) to a specific organ using a tissue-specific promoter in front of the 'replacement' gene (see review [14]). For example, mutation(s) in *KRas* ($KRas^{V12D}$ or $KRas^{G12D}$) is/are frequently observed in several cancers, including breast, colon, pancreas, and lung. If all the tissues express the mutation, then several tumors can form in

the animal, which may not be desirable because the animal can have inflammatory reactions affecting tumor growth, and/or the health of the animal may be compromised before the tumor at the site of interest is optimal for the planned experiment. For this reason, it is optimal to direct expression to a specific organ/tissue using a tissue-specific promoter. Several mouse models (Table 21.2) have been developed to study the effects of oncogenic *Kras* in tumor formation within specific tissues. The tissue-specific promoters include: (1) pVillin (colorectal) [20]; Pdx1 (pancreas) [22]; (2) thyroglubulin (thyroid) [23], and (3) LA1 (lung) [24]. Several other tissue-specific promoters are described in a review by Ristevski et al. [25]. Caution must be exercised to ensure that the tissue-specific promoter is fully characterized [25]. For example, Tuveson et al. [26] used a Mist1 promoter to drive pancreatic tumorigenesis in pancreatic acinar cells, but also observed hepatocellular carcinoma. Taken together, Cre-LoxP recombination-generated transgenic mice are an exquisite tool for studying the effects of specific genetic alterations. Another advantage of this system is that they closely resemble the patterns of tumorigenesis in humans. For example, the Pdx1-Cre LoxP-Stop-LoxP(*LSL*)-$KRas^{V12G}$ mouse model develops Pancreatic Intraepithelial Neoplasias (PanINs) with similar progression patterns and kinetics to that histologically observed in humans [22, 27]: (1) ductal epithelial cells lengthen forming a columnar shape (as opposed to cuboidal), and begin to produce copious amounts of cytoplasmic mucin (stage PanIN-1A starting at age 2 weeks in mice); (2) formation of papillary or micropapillary ductal lesions (i.e., growth of abnormal ductal epithelium inwards towards ducts; stage PanIN-1B); and, (3) atypical nuclei and loss of cell polarity occur in moderate (stage PanIN-2) or significant (PanIN-3) frequencies. In addition, the authors demonstrated that the stromal/acinar compartment associated with the tumor had abnormalities including an influx of inflammatory cells and fibroblasts, as well as collagen deposition [22]. This example clearly demonstrates the ability of the transgenic mouse model to appropriately mimic human cancer. In addition, the effects of multiple oncogenes can be examined by multiple breeding. Hingorani et al. [22, 28] extended the Pdx1-Cre *LSL-*$KRas^{V12G}$ model studies by crossing them with a $p53^{R172H}$ mutant mouse to study the effects of both mutant *KRas* and *p53* (mouse model: Pdx1-Cre *LSL-*$KRas^{V12G}$/$p53^{R172H}$), and found that the double mutation promoted increased invasion and liver metastases. The median survival time for these mice was 5 months; however, in some cases (especially important for when investigating the effects of genes not previously reported), the genetic alterations may result in embryonic lethalities. In this situation, it is desirable to conditionally express the oncogene such that expression can be under temporal control [25, 29]. This is accomplished by the use of inducible-gene expression systems, where the promoter of the 'replacement' gene depends on the presence/absence of a chemical. Several inducible systems are available: (1) metallothionien promoter (relies on presence of heavy metals); (2) interferon-inducible promoter (e.g., *6-16, Mx1,* or *OAS*; relies on presence of interferons); (3) hormone-inducible (e.g., insect hormone 20-OH ecdysone, or synthetic estrogen; relies on expression of receptor to bind to hormone and presence of hormone); and (4) antibiotic-inducible (e.g., tetracycline (Tet); requires expression of Tet receptor to take up Tet, and presence/absence of Tet) (see Ristevski et al. [25] for review). Inducible-systems can provide better control over gene expression; however,

they involve adding a chemical (and sometimes, expression of receptor/activator) in circulation. The disadvantages of adding a circulating chemical are that the dose must be properly evaluated to induce uniform gene expression throughout the target, and the chemical may be toxic to the animal or cause other systemic effects that can affect the experiment (e.g., administration of heavy metals to induce the metallothionein promoter may be toxic) [25]. Taken together, transgenic models have many applications, especially for molecular imaging, as they can be used to develop methodologies for early detection, better sensitivity, and better resolution (since pre-neoplastic and small focal lesions can develop in these models). The major disadvantages of using a transgenic mouse model are the time and cost of intricate preparation steps, including cloning, breeding, genotyping, histological assessment, and characterization of kinetics, among others. Indeed, a transgenic mouse may take years to develop; however, as discussed, this unique methodology for studying spontaneous tumor initiation and progression can offer invaluable information about human cancer, and may be worth the effort when evaluating novel molecular imaging strategies.

The *fourth* model used to study tumorigenesis in animals is cancer induction via chemicals (e.g., toxins such as pesticides, alcohol, and viruses) or physical means (e.g., dietary changes, UV radiation exposure, or prevention of exercise) (see Table 21.2). These models can represent more realistic situations in which humans acquire cancer. For example, excessive alcohol consumption in humans can result in "alcoholic fatty liver," which is associated with increased liver weight, accumulation of triglycerides, and altered lipid metabolism [30, 31]. These conditions result in altered gene expression and a chemically altered environment (e.g., alcohol increases the production of free radicals that can lead to cellular damage [32]) in the tissue, which can promote inflammation (i.e., development of hepatitis) and an increased risk for carcinogenesis. These animal models are mostly used to study cancer prevention (i.e., to analyze what lifestyle behaviors and/or chemicals can increase the risk for cancer), but can also be used to study agents that directly cause cancer (e.g., certain types of human papilloma virus (HPV) are known to cause cervical cancer). There are several advantages to using this model. First, many human cancers have been associated with lifestyle behaviors (e.g., smoking, excessive alcohol consumption, lack of exercise) and/or chemical exposure (e.g., toxins in environment such as lead paint or asbestos materials); therefore, these models can analyze the biological effects of these cancers. Second, these models are invaluable for risk assessment. Patients at high risk often undergo more frequent cancer screening, and it is imperative to have the ability to discriminate between the cancerous tissue, a benign but abnormal lesion on tissue, an inflamed tissue, and/or normal tissue. There is a broad literature base describing the give-and-take relationship between inflammation and cancer—both chronic inflammation has been shown to cause tumorigenesis [33], and cancer has been shown to induce an inflammatory response [34]. Often, inflammation and cancer are associated with similar characteristics: genomic instability, altered gene expression, altered physical structure, angiogenesis, and generation of reactive oxygen species, among others [34, 35]. Therefore, the difference between inflammation and cancer can be difficult, and these animal models can provide a method for establishing discrimination criteria.

For example, since angiogenesis is commonly observed in both inflammation and cancer, it may not be feasible to use a general imaging technique to observe angiogenic microvessels for discriminating between inflammation and cancer. Instead, it may be optimal to compare molecular markers associated with angiogenic vessels in inflamed tissue or tumor. Some disadvantages to using chemically- or physically-induced animal models of tumorigenesis include the fact that they may take time to develop and optimize (e.g., dose, administration technique, kinetics), can be extremely toxic to the animals, and may result in a non-uniform distribution of reaction (though some may argue this is an advantage as this would be expected in human cases, it can be difficult for imaging and ex vivo tissue sampling if it is not equally distributed).

All of these small animal models are used to develop new molecular imaging strategies and contrast agents for (1) developing screening criteria (e.g., comparison of inflammatory to cancerous diseases), (2) detecting pre-cancerous and cancerous lesions; (3) staging tumorigenesis and characterizing metastases; and, (4) developing and monitoring therapeutic treatment and remission status. The following sections will discuss the various molecular imaging techniques as they are used in small animal models of cancer.

2 Identifying Molecular Targets for Molecular Imaging Contrast Agents in Oncology

2.1 Targeting the Cancer Physiome

The cancer phenotype involves several behaviors that set cancer cells apart from non-transformed, normal cells, including uncontrolled proliferation/replication, ability to evade cell death/apoptosis, enhanced cell survival (i.e., insensitivity to growth inhibitory signals), self-sufficiency through angiogenesis, and unconfined growth through invasion and metastases [5]. Certainly cellular reprogramming through genetic mutations (Table 21.1), epigenetic events, and post-transcriptional/post-translational modifications contribute to the observed neoplastic phenotype. However, a tumor, composed of many cancer cells as a whole, behaves differently than individual cancer cells. While most tumors start from a single cancer cell that expands itself (i.e., initiation process of carcinogenesis is “clonal”), cells that comprise the tumor can also change during progression due to changing microenvironment. As Fig. 21.1 shows, a single initiating cell expands itself in a disorganized pattern, but in a three-dimensional form, a tumor can comprise different factors, growth stimuli, chemical and/or cellular signals that can vary depending on the location of the cell. All of these factors can affect the phenotype; therefore, even though one transformed cell is “clonally expanded”, the tumor becomes *heterogeneous* in composition of angiogenic vessels, hypoxic cells, invading and metastasizing cells, inflammatory cells (e.g., leukocytes), among others (e.g., fibroblasts) [34].

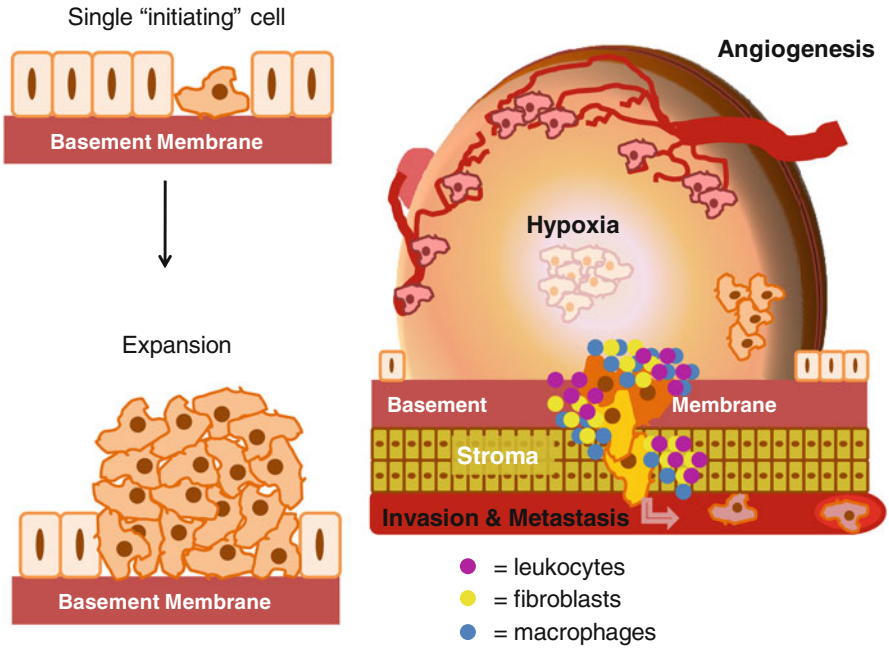

Fig. 21.1 One model of carcinogenesis involves a single "initiating" cell which has been transformed (i.e., acquired genetic alteration(s)), which expands to form a three-dimensional tumor. This tumor can be thought of as a sphere with a gradient of cellular signals, such that the cells within the tumor experience different cell-cell interactions depending on the location. For example, cells near angiogenic vessels (in *pink*) are in close proximity to nutrients and other stimuli, whereas, cells in the center may be located away from growth stimuli and are "starving" for nutrients, oxygen, etc. In addition, an inflammatory response is initiated and involves infiltration of leukocytes (*purple*), fibroblasts (*yellow*), and macrophages (*blue*). Thus, each cell within the tumor may be interacting/communicating with different cells in the changing tumor microenvironment [40, 41]

Recent studies have also demonstrated that hematological malignancies [36] and solid tumors [37] contain a small subset of cells are cancer stem cells, or cells that express both epithelial- and stem-cell antigens. Indeed, stem cells and cancer cells are similar in their abilities to self-renew (Wnt and Sonic hedgehog signaling pathways are in common), and, to evade apoptosis (e.g., through increased expression of anti-apoptotic gene *bcl2*) (see Reya et al. [38] for review). Normal stem cells can also be transformed to become initiating cancer stem cells, resulting in malignancy; this has been demonstrated in acute myeloid leukemia [39].

The impact of the evolving (i.e., continually changing over time [40, 41]) heterogeneous tumor on molecular imaging is tremendous, since the molecular targets may be changing over time. Early detection is the key to increasing the probability of survival; however, this requires that the molecular target for detection must be present in pre-neoplastic cells and/or initiating transformed cells. Molecular imaging modalities are also often used to monitor therapeutic efficacy, which may affect some tumor subpopulations, but not others, once again potentially affecting the

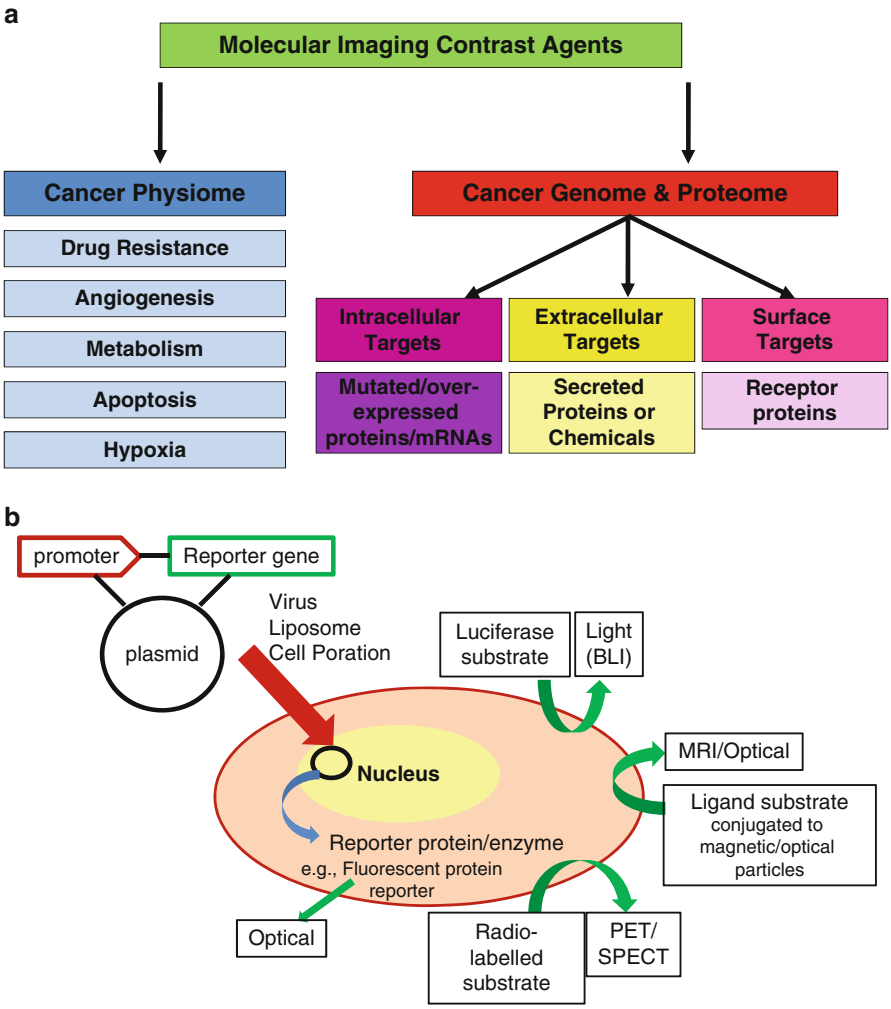

Fig. 21.2 Molecular imaging of cancer detection, monitoring, and/or evaluation of therapeutic treatment involves "labelling" the tumor with either (**a**) a contrast agent directed at a tumor characteristic (cancer physiome) or a cancer cell-specific characteristic (cancer genome/proteome), or (**b**) a reporter protein/enzyme produced by the cancer cell after it has been introduced with the DNA encoding the reporter. For more details please refer to the text

molecular target of interest. Contrast agents that are used to target the cancer phenotype prey upon the ability of the tumor to rapidly proliferate, metabolize growth factors, resist chemotherapeutic treatment, form angiogenic vessels, and to contain hypoxic areas (Fig. 21.2a). Many of these phenotype characteristics have been characterized such that the genes/proteins involved can be targeted. For example, it is well-established that angiogenesis, or the recruitment of blood vessels to

grow within the tumor, is facilitated by endothelial cells expressing high levels of vascular endothelial growth factor receptor type 2 (VEGFR2) and integrin $\alpha_V\beta_3$ [42]. Several contrast agents have been developed to target either VEGFR2 and/or integrin $\alpha_V\beta_3$ using PET, SPECT, MRI, and ultrasound imaging modalities (this is discussed in more detail in the subsequent parts of this chapter).

2.2 Targeting the Cancer Genome and/or Proteome

Many cancers have similar genetic alterations (Table 21.1) such that it may seem obvious that such a common alteration or protein product (e.g., such as mutated K-Ras; though there may be different mutations between cancers) would be a feasible target for a molecular imaging probe and/or cancer therapy. However, most molecular imaging contrast agents are developed to target the phenotype since it is easier to visualize larger molecular events (e.g., proliferative activity or angiogenesis) or extracellular/cell surface protein expression. Post-imaging biopsies of resected tumors or aspirated fluids are commonly used to verify these mutations, but it would be highly advantageous to have real-time (i.e., instantaneous) and non-invasive (i.e., not a surgical procedure) images that verify this genetic information. This scenario would be especially ideal for screening patients at high risk for developing cancer, and utilizing imaging agents to discriminate for example between inflammatory and cancerous disease(s) (discussed above). That is, some macromolecular events (e.g., angiogenesis) may be common to inflammation and cancer, but other micromolecular events (e.g., altered gene/protein expression) may be different. Recent studies utilizing an mRNA-targeted quenched fluorescent molecular probe (i.e., fluorescent signal is released when mRNA oligo probe binds to its target RNA; see Sect. 3.6 below) to detect mutated K-Ras and survivin transcript expression in vitro in pancreatic cancer cells [43] show promise in strategies for non-invasive imaging of intracellular genetic targets. However, contrast agents that are internalized by cells to demonstrate intracellular enzyme activity or gene/transcript expression face considerable challenges in an in vivo setting: (1) they are extremely susceptible to being degraded prior to reaching the target, which means that (2) they can result in unspecific fluorescent signal due to premature quenching, and (3) they must be able to be internalized by the cells without additional chemical means (e.g., transfection vehicles such as liposomes, or viral packaging), among others [44]. For DNA- or RNA-based molecular probes, nucleic acid target sequences can be linked to peptides, or small molecules, such as phosphorothioates (inhibit endonucleases), that may offer some protection from degradation [44]. Fluorescent detection is also limiting for detection of low copy number, and has limited translation to human applications. Recently, bioluminescent detection of mutant p53 using a RNA-based reporter gene strategy has been successfully used in vivo in a murine tumor xenograft model [45]. In this study, a target mRNA sequence connected to the reporter mRNA sequence encoding luciferase, which can be visualized by

adding the D-luciferin substrate to produce bioluminescence (both the reporter gene imaging approach and bioluminescence will be explained in more detail later in this chapter). Another strategy employed for visualizing mRNA expression is peptide-nucleic acid (PNA) chimeras, which involve a 12 nucleotide sequence (similar to idea of antisense RNA or short-interfering RNA (siRNA)) flanked with two basic peptide sequences (e.g., *N*-Gly-D-Ala-Gly-Gly-Aba- [46]) on either side, providing stability and resistance to endo-/exo-nucleases and proteases [47]. These PNAs have been successfully employed with SPECT imaging (^{99m}Tc labeling) or PET imaging (^{64}Cu labeling) to detect *MYC, CCND1* (cyclin D1), and oncogenic *K-Ras* mRNA expression in breast and pancreatic cancer murine models [46, 48–50]. Similar chimeras have been used in conjugation to nanoparticles for ^{64}Cu PET imaging of *K-Ras*^{G12D} mRNA expression in pancreatic cancer [51], and are currently under development for oncogenic *K-Ras* mRNA detection with Gd^{3+}-particles and MRI [52].

In addition to cancer-specific gene expression imaging, protein expression can be visualized similarly with peptides, proteins (e.g., ligands to bind to receptors), or antibodies. Because they cannot cross the cell membrane, peptides/proteins are mostly limited to extracellular or cell surface proteins. For example, image detection of cell surface or extracellular proteins can be performed using antibody/protein-protein interactions, peptide (short protein sequence)-protein interactions. Several studies exemplify this concept by imaging the role of vascular endothelial growth factor (VEGF) receptor type 2 (VEGFR2) signaling in angiogenesis either by (1) anti-VEGFR2 antibody targeted VEGFR2 on endothelial cells (e.g., targeted microbubbles bound to antibody [53]); (2) peptides targeting VEGFR2 on endothelial cells (e.g., targeted microbubbles conjugated to peptide [54]); or, (3) anti-VEGF antibody targeting VEGF bound to VEGFR and/or VEGF secreted by tumor and tumor-associated stroma cells (e.g., radioisotype-labelling and PET imaging: ^{89}Zr-VEGF antibody [42, 55]). To image intracellular protein expression, one strategy that has been employed is conjugation of a peptide to poly-arginine (since poly-arginine can penetrate cells), and studies have been limited to optical imaging (see Sect. 3.6 for further description of this type of contrast agent).

2.3 Use of Reporter Systems in Molecular Imaging

Another method for visualization of tumor-specific gene/protein expression is to deliver a reporter construct to the target (i.e., cancer) cells. The reporter construct is a plasmid with a promoter-enhancing element driving the expression of a reporter gene/product (Fig. 21.2b). The plasmids are then introduced into the cells using viral delivery systems (e.g., adenovirus, lentivirus, retrovirus), liposomal/micelle particles, or mechanical poration (e.g., sonoporation with ultrasound) [56]. Alternatively, animals can be genetically engineered to express the reporter gene

(e.g., transgenic mice expressing estrogen-response-element (ERE)-promoter driven luciferase [57]). Reporter genes/products can then be imaged with optical imaging (e.g., fluorescent proteins or luciferase enzymes), MRI (e.g., ferritin), or PET/SPECT (e.g., HSV1-tk) [58]. The reporter genes/products and molecular probes to detect them will be discussed in the following section for each imaging modality. Promoters used to drive reporter gene expression can be "always on" (e.g., *CMV, RSV, LTR*) as for their use in imaging cell trafficking, or they can be "inducible" by specific intracellular or extracellular proteins/molecules. For example, cancer cells stably-expressing a reporter gene driven by an "inducible" promoter can be used in a tumor xenograft model, and then this promoter can be activated later by the researcher. Korpal et al. [59] used this idea to investigate the role of transforming growth factor β (TGFβ) in breast cancer skeletal metastases. SP28 breast cancer cells, which were previously known to metastasize to the lung and bone, were transfected with several types of expression systems: (1) an inducible expression system to control SMAD4 expression (SMAD4 stimulated TGFβ signaling), consisting of (a) a CMV-driven tetracycline activator (tTA) gene, and (b) a tetracycline-responsive element (TRE)-driven SMAD4 gene; (2) a CMV-driven Renilla luciferase gene (Rluc); and (3) a SMAD-binding element-driven Firefly luciferase gene (Fluc) (see Sect. 3.6 for a detailed description of these luciferases). In this system, SMAD4 expression was controlled by the ability of the tetracycline activator to bind to the TRE element. When the animals were administered doxycycline (Dox; a tetracycline analog; administered 0.5 mg/ml via drinking water), Dox would bind to the tTA protein and prevent it from binding to the TRE promoter (i.e., SMAD4 expression would be turned off; also called a Tet-off system). In the absence of Dox, the tTA protein could bind to TRE (i.e., SMAD4 expression would occur). Using bioluminescence imaging, Korpal et al. [59] could determine the percentage of total tumor cells (i.e., signal obtained from CMV (constitutively on)-driven Rluc) had TGFβ signaling (i.e., signal from SMAD-dependent expression of Fluc) (please see below (Sect. 3.6) for description on use of Fluc, Rluc, and bioluminescence imaging). This study was able to demonstrate that bone metastasis burden can be reduced if TGFβ signaling is interrupted early, but has no effect if bone lesions are already well-established [59]. In addition to using reporter cells in rodents, transgenic mouse models of reporter systems have been developed. Recently, Woolfenden et al. [60] developed a Cre-LoxP-driven luciferase mouse model (please see Sect. 2.3 for a detailed description of the Cre-LoxP recombination method), and when this strain was crossed with a $KRas^{tm4tyj/J}$ mouse (transgenic mouse model of non-small cell lung cancer expressing oncogenic $KRas^{G12D}$), bioluminescent imaging was able to measure lung tumor growth over time.

In addition to use of reporter systems for imaging, these constructs have been engineered as gene therapy, as in the case of the suicide gene herpes simplex virus-1-driven thymidine kinase (HSV1-TK). The idea of suicide gene therapy relies on an enzyme (e.g., thymidine kinase) to convert a non-toxic pro-drug (e.g., ganciclovir) to a toxic drug; therefore, if this reporter gene can be delivered to specific target cells (e.g., cancer cells), then surrounding non-targeted (e.g., normal tissue) will not

be affected [61]. Targeting cancer cells can be achieved by choosing to drive HSV1-TK expression by a tumor-specific promoter (i.e., an "inducible" promoter that has high activity in cancer cells compared with normal cells). Several studies have demonstrated cancer-specific HSV1-TK gene therapy using cancer-specific promoters: COX-2 [62], eIF4E [61], and heat shock protein [63], among others. Reporter gene therapies will be discussed in Sect. 4. HSV1-TK expression can also be used as a reporter, and its expression can be detected with molecular imaging using a substrate for the enzyme. Since TK phosphorylates thymidine or pyrimidine, analogs of these substrates can be radiolabelled for detection by PET or SPECT imaging.

3 Molecular Imaging Modalities Used in Small-Animal Imaging of Oncology

Molecular imaging technologies (Fig. 21.4) are progressing towards the goal of "real-time cancer biopsies" for instantaneous diagnosis and therapy monitoring. Development of these technologies highly relies on in vivo small animal cancer imaging to understand the feasibility of probe design and scale up to clinical use in humans. Strategies for imaging cancer in small animals often depend on the experimental goal, which may be: (1) detection of primary tumor versus metastases; (2) detection of larger, late-stage carcinoma versus early stage or pre-neoplastic lesion; (3) quantitative measurement of therapeutic treatment/delivery; or, (4) cell- or molecule-tracking for visualization of biodistribution; among others. These factors dictate the resolution, speed, quantification, signal-to-noise, and contrast agent of choice for the researcher. For example, FDG-PET imaging is a widely used imaging modality for cancer detection and therapeutic monitoring, but ^{18}F-FDG is also taken up in the brain and heart, and excreted through the bladder; thus, if the tumor of interest is located in/near these organs, it may be difficult to discern between nearby signal versus actual signal from the tumor. Commonly used contrast agents in each modality will be reviewed in these subsections. There are many overlapping themes associated with contrast agent design, and all strive to serve the best signal-to-noise ratio in an optimal time frame (i.e., allowing enough time for uptake and clearance of non-targeted or unused contrast agent). Contrast agents can be directly-labelled small chemicals (e.g., 2-deoxyglucose (2-DG)), biomolecules (e.g., antibodies, nucleic acids, or peptides), vesicles (e.g., liposomes), microparticles (e.g., microbubbles (MBs)), or nanoparticles (NPs; e.g., quantum dots (QDs) or superparamagnetic iron oxide (SPIO) NPs) (Fig. 21.3). Multiple labels on molecules and/or particles can be used for multi-modality imaging. For example, Cai et al. [64] labelled QDs (detectable with fluorescent imaging) with an RGD-peptide (targets $\alpha_V\beta_3$ integrin in tumor angiogenic vessels) and also ^{64}Cu for detection with PET imaging. Dual-labelling is common for verification of target and signal measurement, as well as assessing biodistribution of the imaging probe

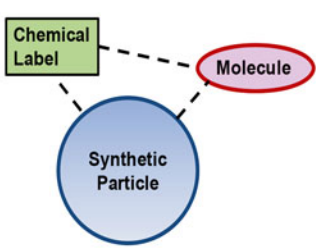

Molecule to be targeted/taken up by cells:

1. Small Molecule/Chemical (e.g., fluorodeoxygluose)
2. Nucleotide Sequence (RNA/DNA) (e.g., molecular beacon, reporter gene plasmid)
3. Protein
   a) Peptide
   b) Antibody/Antibody Fragment

Chemical Labels:

1. Radionuclides
   a) PET: ^{18}F, ^{64}Cu, ^{11}C, ^{68}Ga, ^{89}Zr, ^{86}Y, ^{90}Y, ^{124}I, ^{177}Lu
   b) SPECT: ^{125}I,^{131}I, ^{111}In, ^{99m}Tc
2. Metals
   a) MRI: Fe_2O_3, FePt, Gd^{3+}
3. Enzymes
   a) Optical: Luciferase

Synthetic Particles

Particle Type	Size	Materials	Imaging Modality
Quantum Dots (QDs)	2-12 nm	CdSe/ZnS core semiconductor nanoparticle	Optical, PET
		Paramagnetic coating	MRI
		Conjugated to Fe_2O_3 , FePt,or Gd^{3+}	MRI
Nanoparticles (NPs)	2-100 nm	Monocrystalline iron oxide (MION)	MRI
		Superparamagnetic iron oxide (SPIO)	MRI
		Magnetism-engineered iron oxide (MEIO)	MRI
		Manganese Oxide (MnO)	MRI
		Gold Nanoshells	Optical
		Single-walled Carbon Nanotubes (SWNT)	PET, Optical
		Perfluorocarbons	SPECT, MRI, US
		Polymer Micelles	All
Microbubbles (MBs)	1-10 μm	Lipid bilayer shell	US
Liposomes	100-200 nm	Lipid bilayer shell	MRI, US

Fig. 21.3 Design of molecular imaging probes involves a molecule. chemical label, and/or synthetic particle. Synthetic particles with various sizes and materials are used with various small animal imaging modalities (compiled from several reviews: [65, 71, 171, 179, 187])

to other organs/tissues. In a similar fashion, multiple molecular moieties may also be used for both targeting and therapeutic applications. For example, Blanco and colleagues [65] have constructed a multifunctional probe, which contains an SPIO NP (for detection with MRI) fused to Doxyrubicin (anti-cancer drug) and packaged in a micelle (liposome) with an RGD-peptide on the shell. Using this probe, they were able to observe the localization of their probe in the tumor with MRI imaging, and used bioluminescence (optical) imaging to measure decreases in tumor volume following treatment (i.e., tumor cells stably expressing luciferase were used in a murine tumor xenograft model). The combinations are infinite in number, though the same rules of probe design apply to multi-functional probes, as they do for more simplified probes.

Imaging modalities are also utilized to understand cancer biology, and the interaction of normal cells with cancer cells. To understand metastases of cancer

cells, for example, labelled cancer cells may be injected into the circulation and their location can be tracked via an imaging modality to detect the labelled cell(s). Recent studies have also shown with optical imaging that immune cells [66] and mesenchymal stem cells [67, 68] can home to tumors and be used for therapeutic treatment. A green fluorescent protein (GFP)-expressing transgenic mouse model has also been developed to understand the interaction of host tissue with tumor. Using dual-color fluorescent whole-body imaging, the interaction between the mouse host tissue and implanted red fluorescent protein (RFP)-expressing tumor cells could be observed [69].

3.1 Positron Emission Tomography (PET)

Positron emission tomography (PET) is a highly sensitive and quantitative imaging technique with unlimited penetration depth (see Chap. 5); however, it involves administration of radioactivity and is expensive (based on instrumentation and cost of radiotracer synthesis). As discussed in previous chapters, PET detects coincidence of two γ rays (~511 keV each; two rays separated by 180°) emitted when a radionuclide emits a positron, which in turn annihilates a neighboring electron. A detector ring records the coincidence and converts it to light; the electrons are then mapped to specific locations in the living subject. Several radionuclides are used in PET (see Chap. 9 and [70]), and the most common used for cancer imaging include ^{18}F (half-life ($t_{1/2}$) = 1.83 h) and ^{64}Cu ($t_{1/2}$ = 12.7 h) [70–73]. While ^{18}F is commonly produced in large quantities in cyclotrons, its shorter half-life makes exploratory research in small animals more difficult in terms of synthesizing new tracers. Labelling a molecule with ^{18}F can be performed in several ways: (1) a fluorine-containing molecule can be modified to replace F with the ^{18}F; (2) a "bridging" molecule with a fluorine can be attached to the targeting molecule (e.g., peptide/protein, antibody; example study: comparison of thiol groups 4-^{18}F-fluorobenzaldehyde-O-(2-[2-[2-(pyrrol-2,5-dione-1-yl)ethoxy]-ethoxy]-ethyl)xime (^{18}F-FBOM), 4-^{18}F-fluorobenzaldehyde-O-[6-(2,5-dioxo-2,5-dihydro-pyrrol-1-yl)-hexyl]o xime (^{18}F-FBAM), and succinimidyl-4-^{18}F-fluorobenzoate (^{18}F-SFB) as bridging groups between ^{18}F and cysteine-containing tripeptide glutathione, a cysteine-containing dimeric neurotensin derivative, and human native low-density lipoprotein [74]); and, (3) an H, OH, or another atom can be replaced with ^{18}F (though this method is time-intensive, and can change the binding properties) (see [71]). Advantages of using ^{18}F include its wide availability (it is produced in cyclotrons where available for clinical use) and its short half-life (i.e., fast decay rate) allows repetitive imaging of the same animal. Recent studies have demonstrated that the chemical reactions involved can be performed in under 2 h (e.g., ^{18}F-FBEM labelling of RGD peptide [75]); however, in this case, the amount of radioactivity injected and corrected decay rate must be accounted for to obtain optimal sensitivity of PET scanning. On the other hand, ^{64}Cu can be easily coupled to biomolecules using a variety of chelators (e.g., DOTA, TETA) [76], and because

of its longer half-life (12.7 h), there is less concern of time due to radiolabelling reactions. A large disadvantage of ^{64}Cu is that it is not as widely available (often must be purchased from a commercial vendor and, thus, is expensive to use) and is not as feasible for longitudinal studies as ^{18}F (due to the relatively long half-time).

Table 21.3 lists several examples of PET tracers developed for imaging a variety of cancer targets, including those associated with the cancer physiome (i.e., cell metabolism, angiogenesis, and hypoxia) and those associated with the cancer genome/proteome (i.e., tumor receptors); in addition, several PET tracers are available to detect expression of HSV1-TK reporter. ^{18}F-Fluorodeoxyglucose (^{18}F-FDG) is by far the most commonly used PET tracer, and is readily available in most cyclotrons since it is approved for clinical use [76]. ^{18}F-FDG is taken up by rapidly proliferating cells, which have increased expression of glucose transporters (GLUT) and glycolytic enzymes; therefore, it is an indicator of increased cell metabolism. Notably, the increased GLUT expression has been found to be driven by hypoxia conditions (i.e., expression of hypoxia inducible factor (HIF)-1α), and studies in mice have demonstrated direct correlation between separate PET scans using ^{18}F-FDG and ^{18}F-FMISO (class of nitroimidazole compounds which get highly reduced/reactive in hypoxic (≤1,000 ppm oxygen) environments, and covalently binds to intracellular macromolecules preventing ^{18}F-FMISO from exiting the cell [77]) (see [78] for review). A tracer used for imaging tumor proliferation is 3-deoxy-3-^{18}F-fluorodeoxythymidine (^{18}F-FLT), which is transported through the cell membrane and trapped by thymidine kinase 1 (TK1), an enzyme under tight regulation of the cell cycle. Alternatively, ^{18}F-1-(29-deoxy-29-fluoro-b-D-arabinofuranosyl) thymine (^{18}F-FMAU) is trapped by thymidine kinase 2 (TK2). Both versions of radiolabelled thymidine/thymine can be incorporated into DNA; therefore, these tracers are indicators of DNA synthesis [77]. So, how do they differ? TK1 is a cytosolic protein expressed at high levels during G_1, S, and G_2/M phases of the cell cycle, whereas TK2 is localized in the mitochondria, and its expression is independent of the cell cycle. As a result, ^{18}F-FLT and ^{18}F-FMAU have different pharmacodynamics (e.g. ^{18}F-FLT uptake is high in bone, heart, intestines, and brain, while significant uptake of ^{18}F-FMAU was observed in the liver and kidneys) [77]. ^{18}F-fluorethylcholine (^{18}F-FEC) is another PET tracer that images tumor proliferation by integration into membrane phospholipids; therefore, rapidly dividing cells would produce daughter cells with ^{18}F-FEC-containing membranes. While these four PET tracers are aimed at imaging rapidly proliferating cancer cells, they behave quite differently when compared to each other. As introduced briefly in this section, optimizing signal-to-background ratio is a key component to molecular imaging probe design. von Forstner et al. [79] compared the performance of ^{18}F-FDG, ^{18}F-FLT, and ^{18}F-FEC in detection of pancreatic cancer using different human cell lines implanted orthotopically in mice. It has been shown that in addition to tumor uptake, tissue uptake of ^{18}F-FDG was seen in the heart, liver, and bladder, and, ^{18}F-FLT was observed in gallbladder, liver, kidneys, and bladder. Notably, ^{18}F-FLT was strongly taken up by all the tumors, whereas ^{18}F-FDG was taken up by only half of the tumors. In contrast, ^{18}F-FEC was not taken up by the tumors, and was observed in the liver,

Table 21.3 PET tracers developed and utilized in in vivo small-animal molecular imaging of cancer

Molecular event/ type	Molecular target	PET tracer	Example studies in animal models of cancer
Cell metabolism (compared in [79])	GLUT	^{18}F-fluorodeoxyglucose (^{18}F-FDG; FDG)	Pancreatic [79]
	TK1	^{18}F-fluorothymidine (^{18}F-FLT)	Pancreatic [79]
		^{18}F-fluorethylcholine (^{18}F-FEC)	Pancreatic [79]
Angiogenesis (reviews: [42, 55])	VEGFR-1/2	^{89}Zr-VEGF (antibody)	Ovarian [42, 55]
		^{64}Cu-DOTA-VEGF (peptide)	Glioma [232], Breast [233]
		^{64}Cu-DOTA-VEGF (peptide) (QD)	Glioma [234]
		^{18}F-SNB-anti VEFGR-2 (Ab) (MB)	Angiosarcoma [119]
	$\alpha_v\beta_3$ integrin	^{64}Cu-RGD (SWNT)	Glioma [84]
		^{64}Cu-RGD (QD)	Glioma [64]
		^{64}Cu-RGD (SPIO)	Glioma [42, 55]
		^{64}Cu-knottin peptides	Glioma [235]
Hypoxia (reviews: [236, 237])	Carbonic anhydrase (IX)	^{124}I-anti-cG250 (CAIX Ab)	Renal [236, 237]
		^{18}F-FMISO	Colon [238]
	Hypoxia response element (9HRE) dual reporter with HSV1-tk	^{124}I-FIAU	Colon [238]
		^{18}F-FAZA	Breast [239]
Tumor cell receptors	HER-2	^{90}Y, ^{86}Y, ^{68}Ga-anti-HER-2 (Ab)	Ovarian [240]
		^{64}Cu-trastuzumab	Ovarian [241]
	ER	^{94m}Tc-cyclofenil	Breast [242]
		^{18}F-estradiol(FES)	Breast [243]
		^{18}F-tamoxifen	Breast [244]
	Folate Receptor	^{18}F-folic acid	Nasopharyngeal epidermal [245]
		^{66}Ga, ^{68}Ga-deferoxamine -folate	Nasopharyngeal epidermal [246]
Prostate specific antigen (PSA and PSMA)		^{64}Cu-anti PSMA Ab	Prostate [247]
Apoptosis	Annexin V	^{124}I-Annexin	Liver [248]
Reporter imaging	HSV1-TK	^{18}F-FHBG	Glioma [82]
		^{18}F-FHPG	Glioma [82]
		^{18}F-FMAU	Glioma [82]
		^{18}F-FEAU	Glioma [82]

kidneys, and duodenum. This study demonstrates clear differences in distribution and levels of tumor uptake. Most importantly, the study highlights the importance of comparing ^{18}F-FDG and ^{18}F-FLT for differentiating between a tumor with a normal tissue background versus an inflamed tissue background [79, 80]. Another

study comparing ^{18}F-FDG and ^{18}F-FMISO in sarcoma-bearing mice and mice with inflammatory lesions (induced by injection of turpentine oil) demonstrated that ^{18}F-FDG was taken up in both tumor and inflammatory lesions, whereas ^{18}F-FMISO uptake was specific to the sarcoma [81]. Similar issues must be taken into account when designing tracers for imaging angiogenesis, since angiogenesis has been found to occur during inflammatory processes [35].

In addition to imaging the cancer phenotype (e.g., angiogenesis, proliferation, and hypoxia, among others), cancer gene/protein expression has been imaged with various PET tracers. Several PET tracers have been developed to target receptor proteins that are often overexpressed in cancer cells; this long list is not limited to, but includes, estrogen receptor (ER), folate receptor, epidermal growth factor receptor (EGFR), and human epidermal growth factor receptor type 2 (HER-2; mouse homolog of this receptor is ErbB-2), among others (see Table 21.3). Since radionuclides can be internalized, PET tracers have also been developed for detection of intracellular genes/proteins. For example, Tian et al. [49] constructed a multi-targeting probe for detection of breast cancer. A ^{64}Cu-labelled probe for targeting insulin-like growth factor receptor (IGF1R) expression and cyclin D1 (an important protein involved in mitogenesis) mRNA levels was developed. Notably, this study demonstrated that multiple targeting can improve sensitivity, and it allows for visualization of the localized tumor uptake: PET imaging revealed that the center of the MCF-7 tumor xenografts showed the highest levels of cyclin D1 mRNA expression, suggesting that PEt allows spatial in vivo genetic profiling in cancer.

PET tracers have also been developed for detection of reporter proteins. The most common reporter proteins are HSV1-TK (discussed in Sect. 2.3) and a mutated form, HSV1-sr293TK. The wild-type form of TK phosphorylates thymidine and pyrimidine, while the mutated form, sr293TK, phosphorylates acycloguanosine. Radiolabelled substrates for these enzymes include thymidine analogs [^{18}F-FEAU (1-(2′-deoxy-2′-fluoro-beta-D-arabinofuranosyl)-5-ethyluridine) and ^{18}F-FFEAU(1-(2′-deoxy-2′-fluoro-beta-D-arabinofuranosyl)-5-(2-fluoroethyl)uridine)], pyrimidine analogs [^{18}F-FIAU (1-(2′-deoxy-2′-fluoro-beta-D-arabinofuranosyl)-5-iodouridine), ^{18}F-FMAU (1-(2′-deoxy-2′-fluoro-b-D-arabinofuranosyl)-5-methyluridine), ^{18}F-FIAC (1-(2′-deoxy-2′-fluoro-beta-D-arabinofuranosyl)-5-iodocytosine)], and guanosine analogs [^{18}F-FHBG (9-[4-fluoro-3-(hydoxymethyl)butyl]guanine), ^{18}F-FHPG FHBG compound name was confirmed to be (9-[4-fluoro-3-(hydoxymethyl)butyl]guanine) (9-[(1-^{18}F-fluoro-3-hydroxy-2-propoxy)methyl]guanine)]. Direct comparisons of these PET tracers for HSV1-TK reporter detection show differences in biodistribution and emphasize the importance of tumor-to-background ratio for different applications [82]. For example, ^{18}F-FEAU and ^{18}F-FFEAU produce a more sensitive signal (i.e., higher signal-to-noise ratio) than ^{18}F-FHBG or ^{18}F-FHPG, but they cannot cross the blood–brain barrier; therefore, they would not be optimal for detection of HSV1-TK-expressing gliomas [82].

As discussed, a highly important consideration when developing molecular imaging probes is how to achieve the highest tumor-to-background ratio. Radiochemistry can be optimized to achieve different biodistribution patterns to enhance tumor-to-background ratios in cancer imaging. In addition to different

choices of chemical "cross-bridges" between the radioisotope and biomolecule (discussed above), options for moiety additions or changes in stereochemistry to the targeting molecule can affect biodistribution and tumor-to-background ratio. For example, Urakami et al. [83] compared the effects of D and L stereochemistry on the PET tracer O-^{18}F-fluoromethyl-D-tyrosine (^{18}F-FMT; used for indication of high levels of protein synthesis/amino acid metabolism), and found that radiolabelled D-tyrosine produced a ~1.5-fold higher tumor-to-background ratio than L-tyrosine. Other attempts to improve tumor-to-background ratios include the use of radiolabelled nanoparticles (NPs), including QDs, single-walled carbon nanotubes (SWNTs) [84], and SPIOS (reviews: [42, 55]) to provide stability for the tracer. Liu et al. [84] compared the ability to image a subcutaneous tumor with PET and two tracers: (1) a radiolabelled peptide targeting $\alpha_V\beta_3$ integrin (PEG-RGD-DOTA-^{64}Cu) and (2) a radiolabelled SWNT targeted to $\alpha_V\beta_3$ integrin (i.e., SWNTs was labelled with two entities: PEG-RGD to target $\alpha_V\beta_3$ integrin, and PEG-DOTA-^{64}Cu radiolabel). Notably, the presence of SWNT-associated PEG-RGD/PEG-DOTA-^{64}Cu provided five times more tumor uptake compared with PEG-RGD-DOTA-^{64}Cu, which was rapidly cleared from the mouse; thus, the SWNT stabilized the probe for enhanced tumor-to-background ratios.

PET-based molecular imaging of cancer is often combined with anatomical imaging methods such as CT (Chap. 13) and MRI (Chap. 15) to provide co-registration of structural and molecular information [70, 85]. Moreover, dual-modality approaches to molecular imaging with multi-labelled nanoparticles can provide highly sensitive measurements and verification of targets. In addition to multimodality imaging, PET can be multifunctional in terms of using tracers for radiodetection and radiotherapy. For example, the ^{90}Y radioisotope emits γ rays for PET imaging, but also β particles for radiotherapy. Further studies are needed to fully characterize the whole-body effects of γ/β particles (see review [86] for additional details on radionuclide therapy).

3.2 Single Photon Emission Tomography (SPECT)

SPECT imaging, like PET imaging, detects γ rays generated as a result of photon emission. However, a disadvantage is that it has less spatial resolution (~1 mm^3 in small animals; 12–15 mm^3 in humans) than PET (PET spatial resolution: ~1–2 mm^3 in small animals; 4–8 mm^3 in humans) (Fig. 21.4 and [71]). Continuing technological advances in SPECT scanners (e.g., pinhole cameras) and software (e.g., to account for photon scattering and attenuation) have potential for improved resolution, sensitivity, and quantification [87]. SPECT devices are also less expensive than PET scanners. SPECT imaging devices are constructed with rotating γ cameras that detect parallel γ rays (see Chap. 4), and then convert them to an electrical signal proportional to the γ ray energy [71]. Because separate energies can be measured, several radioisotopes with different γ-ray energies can be measured in one scan. Radioisotopes are typically used with SPECT imaging: ^{99m}Tc (emits 1 γ ray:

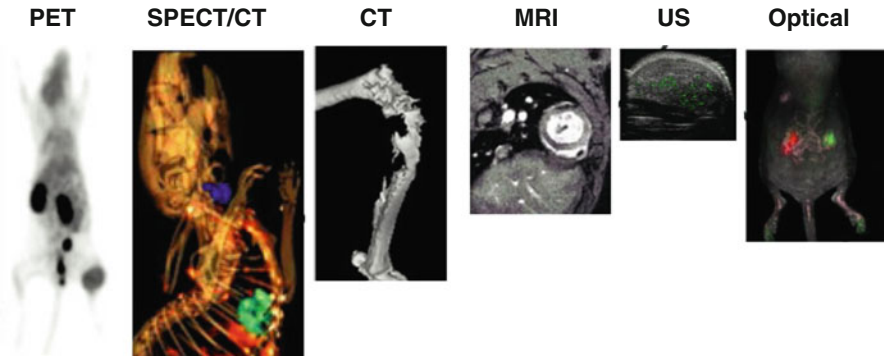

Imaging Modality	Cost	Spatial Resolution	Penetration Depth	Acquisition Time	Clinically Translatable?	Other Pros/Cons
PET	$$$	1-2 mm	No limit	Min	Yes	Radiation
SPECT	$$	1-2 mm	No limit	Min	Yes	Radiation
CT	$$	50 μm	No limit	Min	Yes	1. Radiation 2. Limited targeted contrast 3. Poor soft-tissue contrast
MRI	$$$	10-100 μm	No limit	Min/Hrs	Yes	1. Anatomical/ structural image 2. Targeted contrast agents
US	$-$$	50 μm	mm	Min/real time imaging possible	Yes	1. Operator dependency 2. Current contrast agents only for vasculature 3. Cannot image whole body, bone, or lungs
Optical (FRI/BLI)	$-$$	1-several mm	≤ 1 cm	Sec/Min	Limited applications	1. High-throughput 2. High sensitivity

Fig. 21.4 Example images generated using common small animal imaging modalities [71]. Comparison of modalities used for in vivo cancer research in small animals highlights advantages (*red*) and disadvantages (*blue*). Adapted from reviews [71, 179]

140 keV; t1/2 = 6 h), ^{111}In (emits 2 γ rays: 171 keV and 245 keV; t1/2 =2.8 d), and ^{123}I (emits 2 γ rays: 27 keV and 159 keV; t1/2 = 8 d). Several isotopes (except iodine) are conjugated to biomolecules via a chelator/bridging molecule [71], and the chemistry is often easier than radioisotopes used for PET tracers [73]. Table 21.4 lists several SPECT tracers used for cancer detection in small animals. Note that there are many molecular targets similar to those used for PET tracers (Table 21.3), and they only differ by the chelating moiety and radioisotope. Similarly, like ^{90}Y (discussed above in 3.1), ^{131}I (emission of β particles) or ^{111}In (emission of Auger particles) can be used for both SPECT imaging (detection of γ rays) and radiotherapy [70, 86]. Considerations for SPECT tracer design are similar as that for PET: the goal is always for high tumor-to-background signal. As with PET, coregistration of SPECT molecular imaging data with anatomical images acquired with CT or MRI will also allow verification of targets and provide sensitive measurements.

Table 21.4 SPECT tracers developed and utilized in in vivo small-animal molecular imaging of cancer

Molecular event/type	Molecular target	SPECT tracer	Example studies in animal models of cancer
Angiogenesis (review: [42, 55])	VEGFR-1/2	^{125}I-VEGF$_{165}$, (^{125}I or ^{99}Tc)-VEGF$_{121}$, ^{111}In-hnTf-VEGF	Glioblastoma, breast (review: [42, 55])
	$\alpha_v\beta_3$ integrin	^{111}In-perfluorocarbon NP-RGD	Lung [249]
Tumor cell receptors	HER-2	^{111}In-, ^{131}I-, or ^{99m}Tc-labeled anti-HER-2 antibodies/ fragments	Breast (review: [240])
	ER	^{131}I-tamoxifen	Breast [244]
		tridentate ^{99m}Tc(I)-estradiol-pyridin-2-yl hydrazine	Breast, endometrial [250]
	Folate receptor	^{111}In-DTPA-folate	Ovarian [251]
		^{99m}Tc-folate	Nasopharyngeal epidermal [252]
Apoptosis	Annexin V	^{99m}Tc-Annexin	Fibrosarcoma [253]
Reporter genes	HSV1-TK	^{123}I-FIAU	Glioma [254]

3.3 Computed Tomography (CT)

CT imaging is not a molecular imaging technique per se; however, advances in nanoparticles are probing into the development of targeted contrast agents. CT scanners are constructed with a rotating X-ray source and a detector (separated by 180º), which measures the absorption by tissue (see Chap. 6). As a result, a high-resolution anatomical X-ray image is obtained. CT is routinely used to detect cancer in the clinic, and in small animal imaging studies, it is mostly used for co-registration of anatomical images with molecular images obtained by other imaging modalities (e.g., PET, SPECT; discussed above and in Chaps. 12 and 13) [71]. While CT has high resolution delineation between air, bone, fat, and soft tissue, it often cannot offer high contrast differences between soft tissues; therefore, contrast agents are used to highlight particular organs, tissues, and/or blood vessels. They include solutions of iodine, barium, or barium sulphate. Recent advances in nanotechnology have focused on developing iodinated nanoparticles for use with CT; however, studies are elementary and highly dependent on the location of interest. Moreover, the high amounts of contrast agent (e.g., iodine) required for CT image enhancement may be compromised by the stability and toxicity of NPs, especially for clinical translation. Aviv et al. [88] synthesized and characterized iodinated copolymeric nanoparticles (i.e., copolymerization of 2-methacryloyloxyethyl (2,3,5-triiodobenzoate) and 2-hydroxyethyl methacrylate) for CT detection of liver lesions in mice and rats. Few reports describe targeted contrast agents for CT. Wyss et al. [89] attached an E-selectin (i.e., protein that is often overexpressed in cancer and is involved in cellular adhesion)-binding peptide to an iodinated liposome, and visualized enhanced signalling (compared to non-targeted liposome-iodine) of human colon cancer

xenografts in mice with CT scanning. Attention has drifted from traditional contrast agents, and recent studies are focusing on different materials, including gold nanoparticles (i.e., gold induces a strong X-ray attenuation). Jackson et al. [90] observed ~88–115 % greater contrast enhancement with gold NPs compared with iodine in in vitro characterization studies using phantoms. Indeed, gold NPs were able to "highlight" tumor microvessels in CT-scans of human fibrosarcoma xenografts [91]. Similarly, Rabin et al. [92] developed polymer-coated bismuth sulphide nanocrystals that had 5-fold greater x-ray absorption than iodine and a >2 h circulation time. These agents are typically used for imaging angiogenic vessels and lymph node imaging [92].

3.4 Magnetic Resonance Imaging (MRI)

MRI is based on the principles of nuclear magnetic resonance (NMR): Application of a magnetic field to some nuclei (e.g., ^{1}H, ^{19}F) causes them to change alignment to either a parallel or anti-parallel alignment. In MRI, emission of radiofrequency waves excites nuclei to a higher energy state, and this energy is proportional to the applied magnetic field. Most MRI studies take advantage of the high concentrations of water in biological tissues (^{1}H concentration is about 80 M), and image intensities are generated by measuring local/regional changes in water content/density. Upon release of this energy emission, the nuclei return (i.e., "relaxes") to its original energy state in a characteristic time, T_1 (rate constant for *longitudinal* relaxation), and also interact with other nuclei (e.g., through spin-spin interactions) with a characteristic time, T_2 (also known as *transverse* relaxation). The changes in magnetic field resulting from changing nuclei excitation/relaxation and nuclei density are measured and converted to signal intensities representing an anatomical image of soft tissue (see Chap. 7 and reviews [71, 93] for more detailed background on MRI instrumentation and concepts). Like CT, MRI is often used in conjunction with PET or SPECT to co-register anatomical and molecular information (see Chaps. 14 and 15). MRI Spectroscopy (MRS) is another related imaging technique, which uses MRI to measure protons/nuclei of metabolites (e.g., choline, lactate, lipids, and polyamines; see [94] for methodology and properties of these metabolites), which as mentioned above, can be altered in tumors. Notably, this technique allows for measurement of multiple metabolites with a single scan. For example, concentration profile mapping of metabolites in a mouse model of cerebral metastases of breast cancer cells revealed signature differences in metabolite concentrations over time: *N*-acetylacetate decreases were measured early, while choline, creatine, lactate, and lipids increased as the tumors evolved [95].

MRI contrast agents serve to reduce T_1 and/or T_2: T_1-shortening contrast agents (e.g., paramagnetic ions such as Gd^{3+}) influence protons/nuclei in close proximity to themselves, and result in a brightened image contrast; whereas T_2-shortening contrast agents (e.g., superparamagnetic and ferromagnetic compounds) cause a local disturbance in the magnetic field, and result in a darkened contrast image (see [93]

Table 21.5 Targeted contrast agents developed and utilized for in vivo small-animal molecular MRI of cancer

Molecular event/type	Molecular target	MRI contrast agent/substrate	Example studies in animal models of cancer
Angiogenesis	$\alpha_v\beta_3$ integrin	RGD peptide-Gd containing paramagnetic and fluorescent liposomes	Colon [255]
		RGD peptide-SPIOs	Squamous cell carcinoma [98]
Tumor cell receptors	HER-2	Avidin-Gd^{3+}-anti-HER-2 antibody	Breast [104]
		Herceptin-IO NPs	Breast [256]
	EGFR	Anti-EGFR antibody-IO NPs	Pancreatic [257]
	uPA/uPAR	uPA/uPAR-specific peptide—IO NPs	Breast (uPA, [258]), pancreatic (uPAR, [259])
	Folate Receptor	PEG-G3-(Gd-DTPA)11-(folate)5	Fibrosarcoma [260]
Reporter imaging [105]	β-gal	EgadMe	Prostate [261]
	Trasferrin receptor	Transferrin-MION	Breast [262]
	Ferritin	iron	Glioma [106]
	Lysine-rich protein	–	Glioma [263]

for review). Dynamic contrast enhanced (DCE)-MRI utilizes non-targeted contrast agents (e.g., Gd-diethylenetrinitrilopentaacetic acid (DPTA)) to image blood vessels and has been used for highlighting angiogenic vessels associated with tumor [96] and tumor stroma [97]. DCE-MRI techniques for imaging angiogenesis include assessment of contrast agent perfusion, blood vessel permeability, and/or tissue blood volume (see [98] for a review of methodologies), and have been used for measuring tumor response to chemotherapy (e.g., Gd-DOTA perfusion imaging confirmed VEGFR inhibition of melanoma growth [99]). While these heavy metal ion-based non-targeted contrast agents provide some contrast, advances in nanotechnology have enabled coupling of and/or embedding of heavy metals (e.g., Gd^{3+}, Fe^{2+}) to/in synthetic nanoparticles and/or liposomes. NPs and/or liposomes allow for loading of thousands of heavy metal ions resulting in much higher contrast [93] and allowing for quantitative biomarker detection on the nanomolar level [100]. For example, Gd^{3+} by itself has a T_1 constant of 4.5, but a perfluorocarbon nanoparticle with ~74,000 Gd^{3+} ions has a T_1 constant of 34 [101]. Several nanoparticles with different relaxation properties have been developed for use with MRI (Fig. 21.3, [101]), and have been used for perfusion [102] or, conjugated to targeting molecules for cancer detection (Table 21.6; [103]). Although direct conjugation of heavy metals to molecules has been performed (e.g., Gd^{3+}-anti-HER-2 antibody to detect breast cancer [104]), most recent targeted contrast agents involve nanoparticles: iron oxide (IO NPs, SPIOs, etc., Fig. 21.3) or Gd^{3+}-loaded liposomes, perfluorocarbons, or dendrimers (Table 21.5). To target the cancer physiome, several contrast

agents targeting $\alpha_V\beta_3$ integrin have been developed using RGD peptide, $\alpha_V\beta_3$ integrin peptide antagonist, or anti- $\alpha_V\beta_3$ integrin antibody (see [98] for review). Other targeted contrast agents have been constructed to target cancer cell receptors, including HER-2, epidermal growth factor receptor (EGFR), urokinase-plasminogen activator (uPA)/receptor (uPAR), and folate receptor (Table 21.5), among others [101, 103]. Reporter gene imaging of cancer with MRI mostly utilizes iron uptake by cells using an iron receptor as a reporter (Table 21.5, [105]). For example, a tumor xenograft mouse model using C6 glioma cells expressing a tetracycline-inducible eGFP-ferritin reporter was utilized to verify the feasibility of using MRI to detect reporter genes, as it was consistent with fluorescent imaging quantitation [106]. Notably, a ferritin-expressing transgenic mouse has been developed for tracking organ (and potentially, cancer) gene expression with MRI [107]. MRI-applicable reporter genes and/or NPs have been used also for cell tracking. As described above, cell tracking studies are performed to understand cancer metastases as well as delivery immune- and/or cell-based therapies (e.g., mesenchymal stem cells). For example, Partlow et al. [108] used ^{19}F (another proton/nuclei) MRI imaging to track perfluorocarbon NP-labelled stem cells following intravenous injection in a mouse. Similarly, perfluoropolyether-labelled dendritic cells tracked to lymph nodes for investigation of use as immunotherapy [109]. Magnetic nanoparticles have also been used for "theranostics" (i.e., multifunctional use as diagnostic and therapeutic) [103]. In addition to multifunctional polymer micelles carrying heavy ions and chemotherapeutic drugs (as described above from [65]), magnetic nanoparticles are used for "thermal therapy." When a strong magnetic field is applied, IO NPs absorb energy and convert it to heat. If these IO NPs are localized within a tumor, then it results in a localized temperature increase to 42–45 °C, which sensitizes tumor cells to die (a process known as tumor hyperthermia). Wang et al. [110] demonstrated that magnetic fluid hyperthermia (i.e., magnetic field applied to Fe_2O_3 and As_2O_3/Fe_2O_3 magnetic microspheres to induce heat) induced necrosis in liver tumor-bearing mice.

3.5 Ultrasound (US)

Ultrasound is a non-invasive, real-time, inexpensive, portable, and non-radiological imaging technique. US images are generated by sending a high frequency sound wave (>1 MHz) to tissue and recording the echoes that scatter back from the tissue. Several US techniques are used for imaging in 2D cross-sectional views: (1) Brightness modulation (B-mode), in which returning sound waves from tissue of varying densities were registered by their intensities (i.e., echo intensities are converted to different shades of gray: hypoechoic (decreased echoes) regions containing liquid (e.g., blood) appears as black, and hyperechoic (increased echoes) regions containing solids appear as white); (2) Color Doppler records shifts in emitted frequency and responding echoes to measure liquid flow velocity and flow direction. This method is used frequently in cardiovascular imaging (see Chap. 20), but can be

used for imaging blood flow in microvessels (e.g., tumor angiogenic vessels); and (3) Contrast-enhanced molecular ultrasound (CEMUS) involves ultrasound detection of contrast agents. US contrast agents (e.g., microbubbles (Fig. 21.3)) are usually filled with gas and are confined to vasculature (i.e., travel through blood vessels and do not leak out; however, they are small enough to travel through capillaries enabling visualization of small blood vessels) [111]. Microbubbles (MBs: 1–4 μm phospholipid-shelled perfluorobutane-filled bubbles) are the most widely used contrast agent with US. When US waves are emitted onto MBs, the gas expands/contracts resulting in particle oscillation and echo scattering. In addition to oscillating, the US wave can also cause MBs to compress such that differences in pressure result in asymmetric echoes/frequencies, also known as harmonics. Harmonics are expressed relative to the emitted US sound wave—either larger (overtones) or smaller (undertones). Higher amplitude harmonic imaging is often used to obtain high contrast with improved signal-to-noise ratio from contrast agents compared with surrounding tissue. Another method for separating signals from tissue and contrast agents is pulse-inversion, which involves emitting 2 US waves and recording the difference between the echoes received back from these waves. Since tissue is not moving, oscillating, or compressing, the returned echoes cancel each other resulting in no signal. But, since MBs oscillate and compress resulting in multiple, asymmetrical echoes, the two waves result in a positive signal intensity. Several US machines with high frequency transducers are produced for dedicated high-resolution small-animal molecular imaging (e.g., 40 MHz transducers and US machines made by VisualSonics, Inc.), and clinical US machines have also been used on small animals (though the resolution is significantly lower using approximately 15 MHz transducer frequency). Three-dimensional US imaging systems (e.g., Vevo2100, VisualSonics, Inc.) provide the additional information by adding a motor to move the transducer and acquire 2D frames over mm ranges; thus, the frames are then stacked together to form a 3D image. Additional background material about US imaging is available in the following references: [71, 112–115].

One advantage of molecular imaging includes the ability to quantify molecular events in vivo, and several techniques are available for US imaging with contrast agents; however, all methods represent different ways to quantify vascularity. First, perfusion of contrast agent into an organ/tumor can be calculated to assess blood flow pattern and "highlight" abnormal regions (e.g., highlight tumor blood vessels to distinguish between vascularized regions and necrotic regions of a tumor). The intensities observed by the influx of contrast agent is plotted over time, and comparison of these curves can distinguish between experimental conditions. For example, Ding et al. [116] performed US imaging with non-targeted microbubbles on fibrosarcoma xenografts to measure the effects of mitogen activated protein kinase kinase (MAPK/MKK) signalling on tumor angiogenesis. This study demonstrated that inhibition of MKK signalling resulted in decreased tumor perfusion as measured with US (while it did not affect perfusion in kidneys), which then correlated with decreased amounts of microvessels as assessed by ex vivo quantitative methods. Several reports have analyzed perfusion parameters and correlated with Doppler sonography. Krix et al. [117] used perfusion calculations and Doppler

Table 21.6 Targeted contrast agents developed and utilized in in vivo small-animal molecular US imaging of cancer

Molecular event/ type	Molecular target	US contrast agents	Example studies in animal models of cancer
Angiogenesis	$\alpha_V\beta_3$ integrin	Echistatin-coated MBs	Glioma [264, 265]
		Anti-β_3 Ab-MB	Ovarian [123], squamous cell carcinoma [266]
		β_3-Targeted perfluorocarbon NP	Breast [123]
	VEGFR-2	Anti-VEGFR-2 Ab-MB	Ovarian [121], angiosarcoma [53], glioma [53], squamous cell [267], breast [122], pancreatic [268], melanoma [121]
		KDR-peptide-MB	Colon [54]
	Endoglin	Anti-endoglin Ab-MB	Pancreatic [268]
	Tumor endothelium (target not known)	Tripeptide arginine-arginine-leucine (R-R-L)-liposome	Squamous cell carcinoma [269]

sonography to identify reductions in tumor vascularity following anti-angiogenic therapy treatment. A second method for quantifying vascularity is to use contrast agents molecularly targeted to tumor angiogenic vessels. Since most US contrast agents are confined to the vasculature, these contrast agents are targeted to endothelial cells lining the tumor microvessels. Studies have shown that tumor angiogenic vessels express different levels of genes/proteins, such as vascular endothelial growth factor receptor 2 (VEGFR2) or $\alpha_V\beta_3$ integrins, compared to blood vessels in normal tissue [118]. Willmann et al. [53, 119, 120] and others [121] have published several studies on the use of VEGFR2- and/or $\alpha_V\beta_3$ integrin-targeted MBs for quantification of expression levels of these markers in tumor microvessels (Table 21.6). Pysz et al. [54] reports the use of clinically-translatable MBs (i.e., constructed by direct binding of a peptides to lipid-shelled MBs; as opposed to using an antibody conjugated to the MB via streptavidin-biotin chemistry, which is toxic in humans) targeting human kinase domain receptor (KDR, the human analog of VEGFR2) for measuring response to anti-angiogenic therapy in murine colon tumor xenografts (i.e., after the study characterized the cross-reactivity to murine VEGFR2). Quantification can be performed using a pulse-replenishment method: (1) measuring the signal intensity of bound and unbound MBs after MBs have been given sufficient time to attach; (2) application of a high-frequency pulse to destroy the bubbles; and (3) measuring the signal intensity of the replenished unbound MBs [53]. Using this method in a breast cancer mouse model, Lee et al. [122] has also found that VEGFR2-targeted ultrasound signal intensities correlate with VEGFR2 expression levels (assessed by ex vivo methods); therefore, US has capabilities of in vivo gene/protein expression quantification. Tumor detection with β_3 integrin-targeted nanoparticles has also been evaluated with US by quantifying differences

in entropy levels [123]; however, the use of NPs (e.g., perfluorocarbon-filled lipid-shelled nanobubbles, polylactic acid/air-filled polymer-shelled nanobubbles, solid nanoparticles, etc. Review: [112]) with US is just emerging. Given that NPs have longer retention times and their smaller size will enable them to leak out of tumor angiogenic vessels to bind to cancer cells, intensity measurements will rely on enhancement from accumulation of NPs in a particular area. Acoustic properties with nanoparticles filled with various gases/liquids and constructed with various shells (e.g., polymer-shelled nano/microcapsules [124], gold nanoparticles [125], SPIOs [126]) are currently under investigation, and the use of targeted nanoparticles have been demonstrated in vitro (e.g., HER-2 targeted polylactic acid nanoparticles with breast cancer cells [127]). However, much work is still needed for in vivo optimization of circulation time prior to measurement, amount of NP contrast agent, and intensity quantification methods for future considerations of NPs with US-mediated tumor detection [128].

In addition to its direct role in cancer detection as a molecular imaging modality, US has been used indirectly with other molecular imaging modalities for cancer detection and gene therapy through sonoporation. When US waves are emitted onto MBs, oscillation and MB expansion can create shear forces that result in cavitation (i.e., create pores/holes in cell membranes for enhanced permeability) of endothelial cells. Alternatively, cavitation can also occur by applying higher frequencies for rapid expansion/compression of the MB, which generates high pressures and temperatures and creates membrane pores. Several studies have shown that US waves can also create pores in the absence of MBs ([129]; also, see Newman et al. [130] for review on sonoporation). For example, US-mediated sonoporation was used to label sarcoma cells with SPIO NPs for cell tracking with MRI [131]. With advanced US machines having 3D capabilities, this sonoporation technique also has potential for use with enhancing nanoparticle delivery in vivo for molecular imaging with other modalities (e.g., MRI and optical). US-mediated sonoporation is also utilized for gene transfection [132], and has been characterized using transfection of reporter genes (e.g., luciferase (see Sect. 3.6)). Moreover, combinations of certain microbubbles (e.g., positively charged MBs) and DNA have been shown to protect DNA from endonuclease degradation, which may contribute to higher transfection in vivo [133–135]. Several studies have used US-mediated sonoporation for gene therapy, including delivery of suicide gene (HSV1-TK) therapy (e.g., [136]), siRNA (e.g., siRNA targeting Akt3 and mutant B-Raf [137]), and interferon beta (e.g., [138]), among others. Tumor-specific gene therapy has also been reported to avoid expression in the liver (i.e., due to MB accumulation). Nie et al. [139] used a VEGFR2-promoter to drive expression of thymidine kinase in a hepatocellular carcinoma murine model; since VEGFR2 expression is increased in tumor microvessel cells and US can be applied in a specific anatomical region to provide regional sonoporation, this study demonstrates that tumor-specific gene therapy is highly feasible using US-mediated sonoporation. Similarly, US-mediated sonoporation has been used for targeted delivery of chemotherapeutic drugs, such as doxorubicin [140, 141], paclitaxel [142], and protein-type drugs [143] (e.g., antibodies) (see Gao et al. [144] for review). These studies utilized microbubbles

encapsulating the chemotherapeutic drugs; however, US-enhanced therapeutic effects have also been demonstrated with circulating chemotherapeutic drugs [145]. Other applications for US imaging in oncology include guidance of invasive procedures (e.g., surgery, needle injections/aspirations for therapy or biopsies), as well as direct thermal ablation of cancer cells (i.e., high intensity focused ultrasound applied at surfaces) [146].

3.6 Optical Imaging

Optical imaging can be divided into subgroups: fluorescent imaging, bioluminescent imaging, photoacoustic imaging, and spectral imaging. Chapters 8 and 16 review the optical instrumentation used in small-animal optical imaging. Advances are continually working towards increased spatial resolution, decreased acquisition time, accurate quantitation, deeper tissue penetration, and increased tumor-to-background ratio for potential translation to clinical oncology [147]. For example, Sokolov et al. [148] has demonstrated an approach to development of a real-time, portable, and inexpensive optical confocal endomicroscopy system to successfully image cervical cell morphology in vivo, and produced real-time images closely resembling ex vivo histology. Furthermore, molecularly-targeted fluorescent contrast agents (e.g., gold nanoparticles targeting epidermal growth factor receptor (EGFR) [149]) can provide a real-time, in vivo "biopsy" with gene/protein expression information in addition to the morphology. Fiber-optic microscopy has been clinically used to explore early-stage colorectal and lung neoplasms [147, 150, 515], and these smaller imaging devices are currently being developed for small-animal imaging in conjunction with various contrast agents. Contrast agents used with optical imaging systems, include fluorescently (green, far red, and photoswitchable)-labelled molecules, cells, or particles; light-scattering particles (e.g., gold, metal, or polymer nanoparticles, quantum-dots (semiconductor nanocrystals)); and, bioluminescent proteins/enzymes (e.g., luciferase). Optically-detected labels (or particles) can involve (1) direct conjugation to the compound/particle that will bind its molecular target; or (2) a reporter system where the cell(s) express the optically-detected protein/enzyme. The first example is most commonly used; however, reporter systems are becoming increasingly popular with new advances in in vivo transfection/delivery methods.

Fluorescent labels include green or red fluorescent protein, Cy5.5, Alexa series of dyes, and indocyanine green, among others [152]. Fluorophores are safe, inexpensive, chemically stable, and nonradiological [8], and improvements in brightness, solubility, and photostability are continuing to advance [153]. They can be directly attached to a molecular probe as in the Veiseh et al. [154] study, which used Cy5.5-labelled chlorotoxin to optically visualize glioma cells in the brain. Just as ^{18}F-labelling for use with PET imaging, fluorescently-labelled 2-DG has been successfully used to image cancer cells in vivo; however, a smaller, non-NIRF fluorescent dye is required to ensure that uptake is through glucose transporters rather than

additional mechanisms used for uptake of larger, NIRF dyes (e.g., natural tumor uptake of the dye) [44]. Self-quenching fluorescent dyes can also be packaged in liposome-like vesicles that are targeted to and bind to specific cell surface receptors (e.g., LDL receptor) for internalization into cancer cells; once the vesicle releases the dyes into the cells, the dyes become active and emit light [44]. Fluorescent dyes can also be attached to molecular probe associated with a quencher such that it is activated only when the probe has "associated" with its target. In this case, the dye and quencher are in close proximity (within 100 Å) to each other, and when this distance is lengthened, the dye transfers energy to the quencher, and releases light. The dye-quencher separation distance can be lengthened by the molecular "linker" connecting the dye and quencher, and is either broken (e.g., linker is made of a peptide sequence susceptible to protease cleavage) or changed in conformation (e.g., the linker is made of an RNA hairpin that is processed in cells similar to shRNAs, linearized, and then bound to its target mRNA) (see Stefflova et al. [44] for review). This dye-quencher system, also known as a molecular beacon, has been implemented by Weissleder and colleagues ([155–159]) for imaging a variety of cathepsin- and MMP-type proteases, which are often overexpressed in many cancers. NIRF-labelled protease-activatable probes have been used for multi-modality cancer imaging, such as NIRF-imaging microcatheter/endoscope for colonic adenocarcinoma lesions [160, 161] and peripheral lung cancers [162], as well as fluorescent molecular tomographic (FMT) and MRI of gliomas [163]. These cathepsin- and MMP-activatable probes, as well as other as well as directly-labelled targeted probes (e.g., $\alpha_V\beta_3$ integrin, EGFR, and 2DG), are commercially (e.g., VisEn Medical, LiCor Biosciences) available for small animal imaging studies. In addition to use for cancer detection, the highly-quantitative abilities of fluorescent probe imaging also enable accurate measurement of therapeutic monitoring. Fluorescently-conjugated therapeutic antibodies (e.g., Avastin anti-human VEGF antibody) can be used to verify target, and discriminate on-target and off-target effects, as well as measure longitudinal effects of decreasing target expression over time [164]. Moreover, these probes can be used to specifically target therapy to cancer cells to minimize normal tissue damage; for example, MMP-7-protease cleavable molecular beacon releases a photosensitizer in the localized tumor region (i.e., because of high extracellular MMP-7 activity near cancer cells), and this photosensitizer can be activated by photodynamic therapy to produce cell-killing single oxygen species [44, 165] (Table 21.7).

Bioluminescence imaging of luciferase (from bacteria, insects, or sea pansy) expression is another type of optical imaging, which detects light released from enzymatic ATP-dependent conversion of D-luciferin (administered to animal) to oxyluciferin. The wavelength depends on the luciferase type. Firefly (*Photinus pyralis*) luciferase-catalyzed reaction emits light at ~580 nm. Click-beetle (*Pyrophorus plagiophthalamus*) luciferase has been engineered to produce green-orange (544 nm) or red (611 nm) light following reaction. *Renilla* (sea pansy) and *Gaussia* (marine capecod) luciferase react with coelenterazine substrate in an ATP-independent manner to produce blue light (480 nm) [152]. Since tissue does not emit significant levels of bioluminescence, background signal is very low, and can

Table 21.7 Contrast agents developed and utilized in in vivo small-animal optical molecular imaging of cancer

Molecular event/type	Molecular target	Optical contrast agents	Example studies in animal models of cancer
Angiogenesis	VEGFR-1/2	Cy5.5-VEGF	Breast [270]
		^{64}Cu-DOTA-VEGF (peptide) (QD)	Glioma [234]
	$\alpha_v\beta_3$ integrin	RGD-QD705	Glioma [271]
		Rhodamine/ PE-RGD-liposomes	Colon [255]
		Cy5.5-knottin peptides	Glioma [235]
Tumor cell receptors	HER-2	Cy5.5-anti-HER-2 Ab	Breast [272]
	ER	Luciferase reporter (BLI)	Breast [57], brain [267]
	Folate receptor	Pyropheophorbide-peptide-folate	Fibrosarcoma [273]
Proteases	Cathepsin (H, K, D, Z) [44, 274]	Cyanine-peptide	Breast [275]
	MMP-(2, 7, 9)	Cy5.5-peptide	Fibrosarcoma, lung [276, 277]
Prostate specific membrane antigen (PSMA)		QD-anti PSMA Ab	Prostate [187]
Apoptosis	Caspase activity	Fluorescently labelled [278]	Pancreatic [279]
	Annexin V	Fluorescently labelled	Colon [280]
Reporter gene	Luciferase	Enzyme substrates D-luciferin, coelenterazine	Breast [59]
	GFP/RFP	Fluorescent protein	Mesenchymal stem cells trafficking to gliomas [68]

detect as few as 100–10,000 cells, depending on the tissue-depth of injection [166]. Moreover, stable expression of the luciferase enzyme can enable longitudinal studies over significant periods of time, as substrate is delivered only prior to imaging. Because it is a highly sensitive and quantitative method, bioluminescent imaging is used commonly in two applications: (1) measuring volumetric changes in implanted luciferase-expressing tumor cells (e.g., following therapy treatment [65]); and (2) reporter imaging of cell trafficking and/or protein expression (e.g., Korpal et al. [59]) used BLI to track metastases of luciferase-expressing breast cancer cells to bone (detailed description of methods in Sect. 2.3). Recent reports also describe conjugation of luciferase to synthetic particles for targeted imaging (e.g., QDs [167]) with enhanced sensitivity. Since QDs require an external light source to be excited and emit fluorescence, attachment of luciferase can provide this light source: addition of luciferase substrate to react with the enzyme will produce light. Thus, a light source localized around the QD can be generated even in deep-tissues for in vivo imaging.

As with other imaging modalities, contrast agents used to detect cancer cells with optical imaging devices have evolved to include peptide- or antibody-conjugated nanoparticles, including quantum dots, metal nanoparticles, and carbon nanotubes [168]. Quantum dots are semiconductor crystals (2-12 nm diameter) that naturally emit fluorescence, and depending on their size and composition, they can emit multiple colors (i.e., different wavelengths with the same emission wavelength); therefore, they can be used for multi-targeting applications. In addition, they are brighter (e.g., 10–50 times larger molar extinction coefficient than fluorophores), more photostable, and chemically stable than fluorophores [169]. Most notably, their light emitting and size properties are highly flexible and tunable for specific interests. They can also be used with multiple imaging modalities to gain more information. Quantum dots have been coupled with Fe_2O_3, FePt, or Gd^{3+} for imaging with 3-D optical imaging systems (e.g., fluorescence molecular tomography (FMT) from VisEn Medical, Inc.) and MRI to respectively obtain molecular target and anatomical information (see Nie et al. [169] for review). Quantum dots can be conjugated with various moieties for molecular targeting, including streptavidin (e.g., for conjugation of a biotinylated moiety such as an antibody or DNA plasmid), luciferase, or direct conjugation of moiety to a PEG-coated QD. They may also be coated with polycationic peptides, which promote cellular uptake of quantum dots for intracellular targeting (similar to molecular beacon construction strategies discussed above) [170]. In contrast to QDs, metal NPs have both absorptive and scattering properties, and can be visualized with NIRF, darkfield microscopy, and photoacoustic imaging (see Hirsch et al. [171] for review).

Photoacoustic imaging involves optical stimulation of nanoparticles, which absorb light, and then convert the light energy to heat. The generated heat results in a thermoelastic expansion of the tissue and increase in pressure, which generates an ultrasonic wave [172]. Li et al. [173] reported the use of HER-2- and EGFR-targeted gold nanorods activated at 785 nm and 1,000 nm respectively for in vivo detection of squamous cell carcinoma in a murine tumor xenograft model. In vivo photoacoustic imaging of cancer in small animals has also been performed with gold nanoshells [171] and SWNTs [174]. Carbon and metal NPs also demonstrate surface-enhanced Raman scattering of photons, and can be used with Raman spectroscopy, which measures scattered photons. Zavaleta and colleagues [175, 176] have described the use of RGD-targeted SWNTs and non-targeted gold NPs to image subcutaneous tumor xenografts with a Raman microscope. Both Raman spectroscopy and photoacoustic imaging techniques have increased spatial resolution and soft tissue depth compared with traditional optical imaging, and have potential for implementation in surface scanning instruments, especially endoscopy [172], or for applications requiring low light penetration (e.g., skin or breast). For more detailed description of Raman spectroscopy and photoacoustic imaging techniques, please see the following reviews: [171, 177, 178].

4 Molecular Imaging for Development, Monitoring, and Delivery of Cancer Therapy

4.1 The Road from Bench to Bedside for Development of Cancer Therapeutics

Pre-clinical research in small animals plays a critical role in evaluating medical practices and drug development. The steps of bench-to-bedside translational research (Fig. 21.5) can be very time-consuming and expensive; therefore, accurate, quantitative, and robust methodologies like molecular imaging are invaluable for molecular probe and drug development [71, 147, 179].

The first step in this process is to identify potential targets of interest. As discussed above and is shown in Table 21.1, several genetic alterations common to various cancers have been well characterized. At first glance, it perhaps seems very straightforward to utilize the wealth of available genetic/proteomic/phenotypic information to identify potential targets for imaging and treatment of cancer.

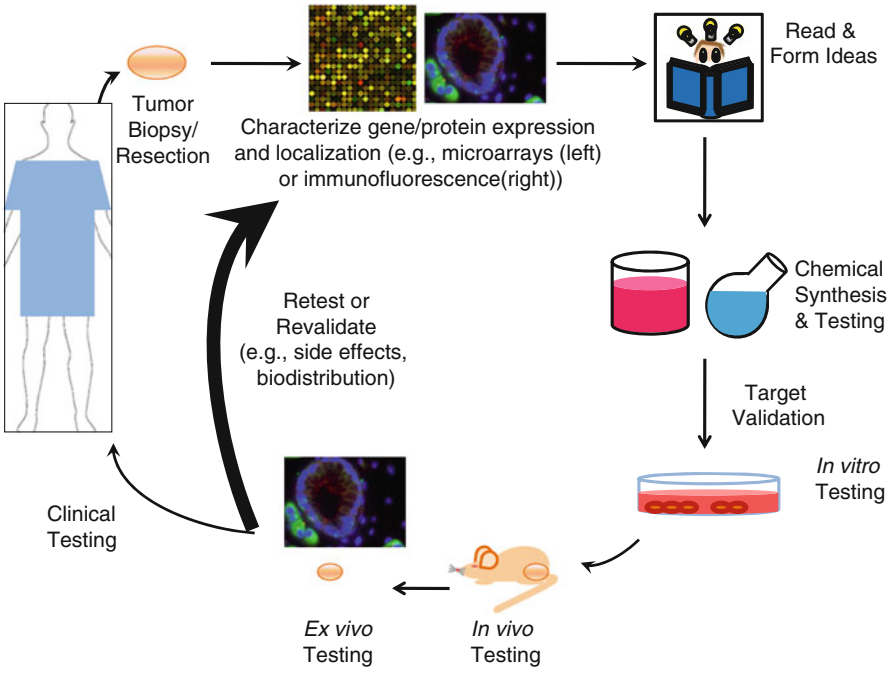

Fig. 21.5 Bench-to-bedside translational research involves intense pre-clinical investigation and validation in vitro, in vivo, and ex vivo before coming full circle to the patient. This process is performed for both molecular imaging probe design and cancer therapeutics

However, several factors can complicate the process, especially when considering what happens in the clinic. Cancer is a progressing disease, with changing gene/protein expression and tumor characteristics over (1) time and (2) localization. For example, hypoxic regions can develop during tumor growth, and studies have shown that these regions are dynamically "moving." Hypoxia induces expression levels and activity of HIF-1α, which facilitates expression of proteins that can act on free radicals; thus, a cycle of hypoxia-reoxygenation occurs. Radio- and chemical-based therapeutics most often require oxygen or oxygen radicals to produce cytotoxic effects; therefore, in absence of oxygen, these hypoxic regions are often multidrug resistant [180]. Other factors that contribute to therapeutic resistance include:

1. Enhanced survival of endothelial and tumor cells (via continuing tumormicroenvironment (i.e., tumor cells interacting with normal cells, tumor stroma, infiltrating immune cells, etc.) interactions (i.e., cell-cell communications via secreted cytokines, growth factors, enzymes, and other proteins/chemicals), and
2. Hypoxia-induced genomic instability promoting resistance to DNA damage (e.g., by radiotherapy) or to apoptosis (e.g., by chemical inducers such as TRAIL ligand) (see Teicher et al. [180] for a review on drug resistance).

Hypoxia also induces angiogenesis, whereby the host's blood vessels are recruited to form new vessels through the tumor (Fig. 21.1); thus, the tumor forms its own vascular supply of nutrients. Because of varying regions of hypoxia and cell-cell communications, these angiogenic vessels are often disorganized (in direction/location) and leaky [180]. Molecular imaging and cancer therapy is highly dependent on angiogenic vessels for delivery of molecular imaging probes (e.g., targeted microbubbles or nanoparticles) and chemotherapeutic drugs. Taken together, amounts of hypoxia affect levels of angiogenesis, which in turn affect the accessibility to the tumor. All of these factors change over time, which emphasizes the need to have different strategies for different stages of cancer. This rationale has led to construction of multi-targeted probes. Willmann et al. [120] demonstrated the used of dual-targeting microbubbles for detection of $\alpha_V\beta_3$ integrin and VEGFR2 expression with ultrasound. The idea behind this study was that early, new formed angiogenic vessels may have different gene expression than previous established, older angiogenic vessels; therefore, an imaging probe targeting two key proteins involved in angiogenesis may demonstrate the "activity" of angiogenesis.

In addition to considerations of tumor progression, the location and manner in which the tumor acts with the microenvironment can also affect imaging and therapeutic strategies. For example, the tumor-stroma component is an important contribution to the invasive behavior of pancreatic cancer [181]; therefore, targeting the tumor-stroma component may be a better strategy. Molecular imaging has the ability to provide this information by demonstrating in vivo mapping of localized gene/protein expression. Other factors affecting target optimization include primary tumor compared to metastatic disease and tumor subtypes (e.g., androgen-dependent prostate cancer versus androgen-independent prostate cancer). Thus, molecular imaging

provides a platform for detection and staging of cancer (as discussed throughout the chapter), but also for optimizing targets for "personalized" (i.e., tumor-characteristic dependent) and specific (i.e., tumor targeted) cancer therapy [182].

The *second* step in the bench-to-bedside process is target evaluation and validation. Once targets have been identified, drugs and/or targeting molecules for imaging probes are synthesized and rigorously tested in vitro and in vivo. Thousands of chemical compounds may be tested, with often only one compound ultimately qualifying for clinical testing. Several rounds of in vitro and in vivo testing may occur to ensure (1) specificity of targeting; (2) identification of off-target effects (both non-specific targets in tumor cells and effects on normal cells); (3) uptake and metabolic efficiency; (4) evaluation of toxicity to both tumor and/or normal cells; (5) efficiency of in vivo delivery and pharmacokinetics; (6) measurement of overall effects (e.g., level of tumor eradification); and (7) dose optimization, among others [71]. Molecular imaging can be used for all of these steps both in vitro (e.g., use of bioluminescence imaging to quantitate the differential effects of thousands of drug compounds on cells) and in vivo (several similar examples for molecular imaging probes described throughout chapter) [71]. In this section we will focus solely on evaluating cancer therapy with cancer imaging, though the process (Fig. 21.5) for evaluating targets of molecular imaging probes is similar. There are two main uses for molecular imaging in pre-clinical evaluation of cancer therapeutics: (1) measurement of tumor response (e.g., tumor cell death, tumor volume, endpoint effect, etc.) using established molecular imaging probes (discussed throughout the chapter), and (2) measurement of biodistribution and/or tumor localization of the drug.

4.2 Evaluating Cancer Therapeutic Efficacy

The ultimate goal of cancer therapeutics is to completely eradicate all the tumor cells for complete remission of the patient. This process can take time, and may involve treatment with multiple therapeutic drugs for synergistic effects. Molecular imaging can play several roles in evaluating the effect of therapy on the target. First, the tumor size/volume can be measured. Anatomical modalities like CT, MRI, and even 3D ultrasound can provide a physical measurement of the tumor. Secondly, measurements of molecular activities/events can be used to assess changes in tumor response. Several FDA-approved cancer chemotherapy drugs target proteins (e.g., EGFR, HER-2, ER) or cellular processes (e.g., microtubule breakdown) associated with proliferation (Table 21.8). Changes in metabolic activity or proliferation rates can then be measured using ^{18}F-FDG-PET or ^{18}F-FLT-PET respectively. As discussed above, increased FDG uptake is observed in hypoxic regions, and therefore, may not accurately reflect decreased proliferation [71]. Anti-angiogenic therapy (e.g., Avastin (Genentech, Inc.)) is FDA-approved for the treatment of some cancers (e.g., colorectal). To monitor the efficacy of this chemotherapeutic treatment, molecular imaging of angiogenesis can be used. Clinical imaging of angiogenesis includes CT [72],

Table 21.8 FDA-approved chemotherapeutic drugs have been labeled for imaging cancer in small animals

Therapy	Target	Label type	Imaging modality	Example studies in animal models of cancer
Bevacizumab/Avastin	VEGFR	^{89}Zr	PET	Ovarian [281, 282]
		^{111}In	SPECT	Ovarian [282]
Trastuzamab (review: [240, 283])	HER-2	^{111}In	SPECT	Ovarian, breast [240, 283]
		^{90}Y, ^{86}Y, ^{68}Ga	PET	Ovarian [240, 283]
		MnO NP	MRI	Breast [240, 283]
		Cy5.5	Optical	Breast [240, 283]
Tamoxifen [244]	ER	^{131}I	SPECT	Breast [244]
		^{18}F	PET	Breast [244]
Gefitnib	EGFR tyrosine kinase	^{11}C	PET	Breast [284]
Cetuximab	EGFR	^{64}Cu	PET	Head and neck squamous carcinoma [240]
		Cy5.5	Optical	Head and neck squamous carcinoma [285]
Erlotinib/Tarceva	EGFR	^{11}C	PET	Lung [286]
Paclitaxel	Microtubule breakdown	^{18}F	PET	Breast [287]

MRI, and US [71] perfusion studies, as well as ^{18}F-RGD-PET imaging [71]. Other methods for evaluating secondary effects (e.g., imaging of apoptosis with radiolabelled annexin V (see Sects. 3.1 and 3.2) or levels of hypoxia (e.g., ^{18}F-FAZA-PET) of anti-proliferative or anti-angiogenic drugs) have been described (see review: [71]).

Another method used to measure the efficacy of the chemotherapeutic drug is to directly radiolabel it and use it as both an imaging probe and therapy. Table 21.8 lists several common chemotherapeutic drugs that have been chemically labelled with radioisotopes, NPs, or fluorescent dyes for cancer detection in small animals. PET imaging of radiolabelled chemotherapeutics have also been used in patients (see reviews: [71, 182]). This method is useful for determining if the drug can penetrate the tumor, as well as characterizing distribution to other organs. Subsequent longitudinal imaging scans will reflect drug activity. For example, radiolabelled anti-VEGF antibody will bind VEGF, and therefore, be a measurement of angiogenesis with the tumor. Assuming that the therapeutic effect is to inhibit angiogenesis resulting in lack of nutrients and increases in cell death, there will be a decrease in the number of vascular endothelial cells expressing VEGF receptors, and it is expected that a second scan would reflect decreased signal associated with the tumor. Kurdziel et al. [182] also reports direct-labelling of chemotherapies are useful for evaluating multidrug resistance. This strategy involves using molecular imaging of tumor uptake/penetration of the drug such that if the drug is not/weakly taken up by the tumor, alternative or additional/synergistic therapies may be suggested to improve outcome and avoid unwanted side-effects.

4.3 Molecular Imaging for Targeted Therapy and/or Site-Specific Resection

As mentioned, the specific localization of the drug to the tumor can be directly visualized by chemically labelling the drug. Several examples of tumor-targeted drug delivery mechanisms were discussed in Sect. 3 with each imaging modality. These include (1) suicide gene therapy driven by a tumor specific promoter; (2) US-mediated sonoporation during chemotherapeutic administration; (3) drugs encapsulated in targeted-synthetic particles; and (4) use of γ- and β/α-emitting radioisotopes to label targeting molecules for dual PET and/or SPECT imaging and radiotherapy.

Imaging modalities providing anatomical information, such as MRI, CT, or optical (e.g., endoscopy) modalities, can also be used to assist in surgical tumor removal, or provide direct therapy (e.g., MRI radiowaves delivering "thermotherapy" to induce tumor hyperthermia). For example, MRI-guided HIFU ablation is commonly performed for removal of prostate [183, 184], and has been evaluated for treatment of other cancers (e.g., liver [185], breast [186]).

5 Conclusions and Future Directions

Preclinical molecular imaging in small animals plays an invaluable role in translational cancer research. Developments in instrumentation technologies (e.g., increased resolution, or combining modalities with single instruments such as PET/CT, PET/MRI, or endoscopy/US), material chemistries (e.g., new synthetic materials such as nanoparticles), and identification of new molecular targets and/or therapies have greatly advanced our current understanding of cancer from the molecular level (e.g., tumor gene/protein expression) to the macromolecular level (e.g., interaction of tumor with microenvironment). However, the actual translation of many of the aforementioned molecular imaging probes and/or therapies to clinical practice remains a significant challenge. Regulatory requirements are strictly imposed by the Food and Drug Administration (FDA) for approval of molecular imaging probes and/or cancer therapies; though these can be reduced for exploratory trials with micro-doses of imaging probes (e.g., PET tracers which are injected in trace amounts) [71]. For example, it may take exhaustive resources and an average of 14.2 years to move a cancer therapy drug from target identification to FDA-approval and clinical use (cycle highlighted in Fig. 21.5) [71]. Future directions in cancer research hope to improve on the cost/time factors for research scientists, but most importantly, on clinical oncology through (1) early detection, (2) in vivo molecular characterization of cancer, and (3) tumor-targeted and tumor-specific therapies for ultimately enhanced survival and/or complete remission—all of which can be accomplished with molecular imaging.

Acknowledgments This work was supported by funding from the Radiological Society of North America (RSNA; grant RSD0809), and the National Institutes of Health/National Cancer Institute (NIH/NCI; grants CA139279-01A1, CA114747, and CA118681).

References

1. Delcuve G. P., Rastegar M., and Davie J. R., Epigenetic control. *J Cell Physiol* **219:**243-50 (2009)
2. Osaki M., Takeshita F., and Ochiya T., MicroRNAs as biomarkers and therapeutic drugs in human cancer. *Biomarkers* **13:**658-70 (2008)
3. Ischenko I., Seeliger H., Schaffer M.*, et al.*, Cancer stem cells: How can we target them? *Curr Med Chem* **15:**3171-84 (2008)
4. Polyak K., Haviv I., and Campbell I. G., Co-evolution of tumor cells and their microenvironment. *Trends Genet* **25:**30-8 (2009)
5. Hanahan D. and Weinberg R. A., The hallmarks of cancer. *Cell* **100:**57-70 (2000)
6. Benaron D. A., The future of cancer imaging. *Cancer Metastasis Rev* **21:**45-78 (2002)
7. Pomper M. G., Translational molecular imaging for cancer. *Cancer Imaging* **5 Spec No A:**S16-26 (2005)
8. Weissleder R., Molecular imaging in cancer. *Science* **312:**1168-71 (2006)
9. Wong F. C. and Kim E. E., A review of molecular imaging studies reaching the clinical stage. *Eur J Radiol* **70:**205-11 (2009)
10. Gambhir S. S., Molecular imaging of cancer with positron emission tomography. *Nat Rev Cancer* **2:**683-93 (2002)
11. Ben-Haim S. and Ell P., ^{18}F-FDG PET and PET/CT in the evaluation of cancer treatment response. *J Nucl Med* **50:**88-99 (2009)
12. Massoud T. F. and Gambhir S. S., Molecular imaging in living subjects: Seeing fundamental biological processes in a new light. *Genes Dev* **17:**545-80 (2003)
13. Harisinghani M. G., Barentsz J., Hahn P. F.*, et al.*, Noninvasive detection of clinically occult lymph-node metastases in prostate cancer. *N Engl J Med* **348:**2491-9 (2003)
14. Mather S., Molecular imaging with bioconjugates in mouse models of cancer. *Bioconjug Chem* **20:**631-43 (2009)
15. Kerbel R. S., Human tumor xenografts as predictive preclinical models for anticancer drug activity in humans: Better than commonly perceived-but they can be improved. *Cancer Biol Ther* **2:**S134-9 (2003)
16. Tang Z. Y., Sun F. X., Tian J.*, et al.*, Metastatic human hepatocellular carcinoma models in nude mice and cell line with metastatic potential. *World J Gastroenterol* **7:**597-601 (2001)
17. Finn R. S., Bentley G., Britten C. D.*, et al.*, Targeting vascular endothelial growth factor with the monoclonal antibody bevacizumab inhibits human hepatocellular carcinoma cells growing in an orthotopic mouse model. *Liver Int* **29:**284-90 (2009)
18. Bani M. R., Garofalo A., Scanziani E.*, et al.*, Effect of interleukin-1-beta on metastasis formation in different tumor systems. *J Natl Cancer Inst* **83:**119-23 (1991)
19. Shaw A. T., Kirsch D. G., and Jacks T., Future of early detection of lung cancer: The role of mouse models. *Clin Cancer Res* **11:**4999 s-5003s (2005)
20. Janssen K. P., El-Marjou F., Pinto D.*, et al.*, Targeted expression of oncogenic K-Ras in intestinal epithelium causes spontaneous tumorigenesis in mice. *Gastroenterology* **123:**492-504 (2002)
21. Vogelstein B., Fearon E. R., Hamilton S. R.*, et al.*, Genetic alterations during colorectal-tumor development. *N Engl J Med* **319:**525-32 (1988)
22. Hingorani S. R., Petricoin E. F., Maitra A.*, et al.*, Preinvasive and invasive ductal pancreatic cancer and its early detection in the mouse. *Cancer Cell* **4:**437-50 (2003)

23. Chiappetta G., Fabien N., Picone A., *et al.*, Transgenic mice carrying the human Kras oncogene under the control of a thyroglobulin promoter: Kras expression in thyroids analyzed by in situ hybridization. *Oncol Res* **8:**85-93 (1996)
24. Yang Y., Wislez M., Fujimoto N., *et al.*, A selective small molecule inhibitor of c-Met, PHA-665752, reverses lung premalignancy induced by mutant K-ras. *Mol Cancer Ther* **7:**952-60 (2008)
25. Ristevski S., Making better transgenic models: Conditional, temporal, and spatial approaches. *Mol Biotechnol* **29:**153-63 (2005)
26. Tuveson D. A., Zhu L., Gopinathan A., *et al.*, Mist1-KrasG12D knock-in mice develop mixed differentiation metastatic exocrine pancreatic carcinoma and hepatocellular carcinoma. *Cancer Res* **66**:242-7 (2006)
27. Feldmann G., Beaty R., Hruban R. H., *et al.*, Molecular genetics of pancreatic intraepithelial neoplasia. *J Hepatobiliary Pancreat Surg* **14:**224-32 (2007)
28. Hingorani S. R., Wang L., Multani A. S., *et al.*, Trp53R172H and KrasG12D cooperate to promote chromosomal instability and widely metastatic pancreatic ductal adenocarcinoma in mice. *Cancer Cell* **7:**469-83 (2005)
29. Sun Y, Chen X, and Xiao D. Tetracycline-inducible expression systems: new strategies and practices in the transgenic mouse modeling. *Acta Biochim Biophys Sin (Shanghai)* **39**:235-46 (2007)
30. Baillie M., Alcohol and the liver. *Gut* **12:**222-9 (1971)
31. Forgione A., Miele L., Cefalo C., *et al.*, Alcoholic and nonalcoholic forms of fatty liver disease. *Minerva Gastroenterol Dietol* 53:83-100 (2007)
32. Mufti S. I., Eskelson C. D., Odeleye O. E., *et al.*, Alcohol-associated generation of oxygen free radicals and tumor promotion. *Alcohol Alcohol* **28:**621-8 (1993)
33. Balkwill F. and Mantovani A., Inflammation and cancer: Back to Virchow? *Lancet* **357:**539-45 (2001)
34. Colotta F., Allavena P., Sica A., *et al.*, Cancer-related inflammation, the seventh hallmark of cancer: Links to genetic instability. *Carcinogenesis* **30:**1073-81 (2009)
35. Porta C., Larghi P., Rimoldi M., *et al.*, Cellular and molecular pathways linking inflammation and cancer. *Immunobiology* **214:**761-77 (2009)
36. Bonnet D. and Dick J. E., Human acute myeloid leukemia is organized as a hierarchy that originates from a primitive hematopoietic cell. *Nat Med* **3:**730-7 (1997)
37. Ailles L. E. and Weissman I. L., Cancer stem cells in solid tumors. *Curr Opin Biotechnol* **18:**460-6 (2007)
38. Reya T., Morrison S. J., Clarke M. F., *et al.*, Stem cells, cancer, and cancer stem cells. *Nature* **414:**105-11 (2001)
39. Miyamoto T., Weissman I. L., and Akashi K., AML1/ETO-expressing nonleukemic stem cells in acute myelogenous leukemia with 8;21 chromosomal translocation. *Proc Natl Acad Sci U S A* **97:**7521-6 (2000)
40. Merlo L. M., Pepper J. W., Reid B. J., *et al.*, Cancer as an evolutionary and ecological process. *Nat Rev Cancer* **6:**924-35 (2006)
41. Polyak K. and Weinberg R. A., Transitions between epithelial and mesenchymal states: Acquisition of malignant and stem cell traits. *Nat Rev Cancer* **9:**265-73 (2009)
42. Cai W. and Chen X., Multimodality molecular imaging of tumor angiogenesis. *J Nucl Med* 49 Suppl **2:**113S-28S (2008)
43. Yang L., Cao Z., Lin Y., *et al.*, Molecular beacon imaging of tumor marker gene expression in pancreatic cancer cells. *Cancer Biol Ther* **4:**561-70 (2005)
44. Stefflova K., Chen J., and Zheng G., Using molecular beacons for cancer imaging and treatment. *Front Biosci* **12:**4709-21 (2007)
45. So M. K., Gowrishankar G., Hasegawa S., *et al.*, Imaging target mRNA and siRNA-mediated gene silencing in vivo with ribozyme-based reporters. *Chembiochem* **9:**2682-91 (2008)
46. Rao P. S., Tian X., Qin W., *et al.*, 99mTc-peptide-peptide nucleic acid probes for imaging oncogene mRNAs in tumours. *Nucl Med Commun* **24:**857-63 (2003)

47. Good L. and Nielsen P. E., Progress in developing pna as a gene-targeted drug. *Antisense Nucleic Acid Drug Dev* **7:**431-7 (1997)
48. Tian X., Aruva M. R., Qin W.*, et al.*, Noninvasive molecular imaging of MYC mRNA expression in human breast cancer xenografts with a [99mTc]peptide-peptide nucleic acid-peptide chimera. *Bioconjug Chem* **16:**70-9 (2005)
49. Tian X., Aruva M. R., Zhang K.*, et al.*, PET imaging of CCND1 mRNA in human MCF7 estrogen receptor positive breast cancer xenografts with oncogene-specific [64Cu]chelator-peptide nucleic acid-IGF1 analog radiohybridization probes. *J Nucl Med* **48:**1699-707 (2007)
50. Tian X., Chakrabarti A., Amirkhanov N. V.*, et al.*, External imaging of CCND1, MYC, and KRAS oncogene mRNAs with tumor-targeted radionuclide-PNA-peptide chimeras. *Ann N Y Acad Sci* **1059:**106-44 (2005)
51. Chakrabarti A., Zhang K., Aruva M. R.*, et al.*, Radiohybridization PET imaging of Kras G12D mRNA expression in human pancreas cancer xenografts with [(64)Cu]DO3A-peptide nucleic acid-peptide nanoparticles. *Cancer Biol Ther* **6:**948-56 (2007)
52. Amirkhanov N. V., Dimitrov I., Opitz A. W.*, et al.*, Design of (Gd-DO3A) n-polydiamidopropanoyl-peptide nucleic acid-D(cys-ser-lys-cys) magnetic resonance contrast agents. *Biopolymers* **89:**1061-76 (2008)
53. Willmann J. K., Paulmurugan R., Chen K.*, et al.*, US imaging of tumor angiogenesis with microbubbles targeted to vascular endothelial growth factor receptor type 2 in mice. *Radiology* **246:**508-18 (2008)
54. Pysz M. A., Foygel K., Rosenberg J., *et al.*, Antiangiogenic cancer therapy: monitoring with molecular US and a clinically translatable contrast agent (BR55). *Radiology* **256**:519-27 (2010)
55. Cai W., Gambhir S. S., and Chen X., Chapter 7. Molecular imaging of tumor vasculature. *Methods Enzymol* **445:**141-76 (2008)
56. Serganova I., Mayer-Kukuck P., Huang R.*, et al.*, Molecular imaging: Reporter gene imaging. *Handb Exp Pharmacol* **185(Part 2):**167-223 (2008)
57. Rando G., Ramachandran B., Rebecchi M.*, et al.*, Differential effect of pure isoflavones and soymilk on estrogen receptor activity in mice. *Toxicol Appl Pharmacol* **237:**288-97 (2009)
58. Kang J. H. and Chung J. K., Molecular-genetic imaging based on reporter gene expression. *J Nucl Med* **49 Suppl 2:**164S-79S (2008)
59. Korpal M., Yan J., Lu X.*, et al.*, Imaging transforming growth factor-beta signaling dynamics and therapeutic response in breast cancer bone metastasis. *Nat Med* **15:**960-6 (2009)
60. Woolfenden S., Zhu H., and Charest A., A CRE/LoxP conditional luciferase reporter transgenic mouse for bioluminescence monitoring of tumorigenesis. *Genesis* **47:**659-66 (2009)
61. Mathis J. M., Williams B. J., Sibley D. A.*, et al.*, Cancer-specific targeting of an adenovirus-delivered herpes simplex virus thymidine kinase suicide gene using translational control. *J Gene Med* **8:**1105-20 (2006)
62. Wang Z. X., Bian H. B., Yang J. S.*, et al.*, Adenovirus-mediated suicide gene therapy under the control of Cox-2 promoter for colorectal cancer. *Cancer Biol Ther* **8:**1480-8 (2009)
63. Isomoto H., Ohtsuru A., Braiden V.*, et al.*, Heat-directed suicide gene therapy mediated by heat shock protein promoter for gastric cancer. *Oncol Rep* **15:**629-35 (2006)
64. Cai W., Chen K., Li Z. B.*, et al.*, Dual-function probe for PET and near-infrared fluorescence imaging of tumor vasculature. *J Nucl Med* **48:**1862-70 (2007)
65. Blanco E., Kessinger C. W., Sumer B. D.*, et al.*, Multifunctional micellar nanomedicine for cancer therapy. *Exp Biol Med (Maywood)* **234:**123-31 (2009)
66. Edinger M., Cao Y. A., Verneris M. R.*, et al.*, Revealing lymphoma growth and the efficacy of immune cell therapies using in vivo bioluminescence imaging. *Blood* **101:**640-8 (2003)
67. Wang H., Cao F., De A.*, et al.*, Trafficking mesenchymal stem cell engraftment and differentiation in tumor-bearing mice by bioluminescence imaging. *Stem Cells* **27:**1548-1558 (2009)
68. Sasportas L. S., Kasmieh R., Wakimoto H.*, et al.*, Assessment of therapeutic efficacy and fate of engineered human mesenchymal stem cells for cancer therapy. *Proc Natl Acad Sci U S A* **106:**4822-7 (2009)

69. Yang M., Reynoso J., Jiang P., *et al.*, Transgenic nude mouse with ubiquitous green fluorescent protein expression as a host for human tumors. *Cancer Res* **64:**8651-6 (2004)
70. Maurer A. H., Combined imaging modalities: PET/CT and SPECT/CT. *Health Phys* **95:**571-6 (2008)
71. Willmann J. K., Van Bruggen N., Dinkelborg L. M., *et al.*, Molecular imaging in drug development. *Nat Rev Drug Discov* **7:**591-607 (2008)
72. Fass L., Imaging and cancer: A review. *Mol Oncol* **2:**115-52 (2008)
73. Mariani G., Bruselli L., and Duatti A., Is PEt always an advantage versus planar and SPECT imaging? *Eur J Nucl Med Mol Imaging* **35:**1560-5 (2008)
74. Wuest F., Kohler L., Berndt M., *et al.*, Systematic comparison of two novel, thiol-reactive prosthetic groups for ^{18}F labeling of peptides and proteins with the acylation agent succinimidyl-4-[^{18}F]fluorobenzoate ([^{18}F]SFB). *Amino Acids* **36:**283-95 (2009)
75. Cai W., Zhang X., Wu Y., *et al.*, A thiol-reactive ^{18}F-labeling agent, n-[2-(4-^{18}F-fluorobenzamido)ethyl]maleimide, and synthesis of RGD peptide-based tracer for PET imaging of alpha v beta 3 integrin expression. *J Nucl Med* **47:**1172-80 (2006)
76. Shokeen M. and Anderson C. J., Molecular imaging of cancer with copper-64 radiopharmaceuticals and positron emission tomography (PET). *Acc Chem Res* **42:**832-41 (2009)
77. Dunphy M. P. and Lewis J. S., Radiopharmaceuticals in preclinical and clinical development for monitoring of therapy with PET. *J Nucl Med* **50 Suppl 1:**106S-21S (2009)
78. Dierckx R. A. and Van De Wiele C., FDG uptake, a surrogate of tumour hypoxia? *Eur J Nucl Med Mol Imaging* **35:**1544-9 (2008)
79. von Forstner C., Egberts J. H., Ammerpohl O., *et al.*, Gene expression patterns and tumor uptake of ^{18}F-FDG, ^{18}F-FLT, and ^{18}F-FEC in PET/MRI of an orthotopic mouse xenotransplantation model of pancreatic cancer. *J Nucl Med* **49:**1362-70 (2008)
80. Pakzad F., Groves A. M., and Ell P. J., The role of positron emission tomography in the management of pancreatic cancer. *Semin Nucl Med* **36:**248-56 (2006)
81. Liu R. S., Chou T. K., Chang C. H., *et al.*, Biodistribution, pharmacokinetics and PET imaging of [(18)F]FMISO, [(18)F]FDG and [(18)F]FAC in a sarcoma- and inflammation-bearing mouse model. *Nucl Med Biol* **36:**305-12 (2009)
82. Miyagawa T., Gogiberidze G., Serganova I., *et al.*, Imaging of HSV-tk reporter gene expression: Comparison between [^{18}F]FEAU, [^{18}F]FFEAU, and other imaging probes. *J Nucl Med* **49:**637-48 (2008)
83. Urakami T., Sakai K., Asai T., *et al.*, Evaluation of o-[(18)F]fluoromethyl-D-tyrosine as a radiotracer for tumor imaging with positron emission tomography. *Nucl Med Biol* **36:**295-303 (2009)
84. Liu Z., Cai W., He L., *et al.*, In vivo biodistribution and highly efficient tumour targeting of carbon nanotubes in mice. *Nat Nanotechnol* **2:**47-52 (2007)
85. Bolus N. E., George R., Washington J., *et al.*, PET/MRI: The blended-modality choice of the future? *J Nucl Med Technol* **37:**63-71; quiz 72-3 (2009)
86. Williams L. E., Denardo G. L., and Meredith R. F., Targeted radionuclide therapy. *Med Phys* **35:**3062-8 (2008)
87. Rahmim A. and Zaidi H., PET versus SPECT: Strengths, limitations and challenges. *Nucl Med Commun* **29:**193-207 (2008)
88. Aviv H., Bartling S., Kieslling F., *et al.*, Radiopaque iodinated copolymeric nanoparticles for X-ray imaging applications. *Biomaterials* **30:**5610-6 (2009)
89. Wyss C., Schaefer S. C., Juillerat-Jeanneret L., *et al.*, Molecular imaging by micro-CT: Specific E-selectin imaging. *Eur Radiol* **19:**2487-94 (2009)
90. Jackson P. A., Rahman W. N., Wong C. J., *et al.*, Potential dependent superiority of gold nanoparticles in comparison to iodinated contrast agents. *Eur J Radiol* **75**:104-9
91. Cai Q. Y., Kim S. H., Choi K. S., *et al.*, Colloidal gold nanoparticles as a blood-pool contrast agent for X-ray computed tomography in mice. *Invest Radiol* **42:**797-806 (2007)
92. Rabin O., Manuel Perez J., Grimm J., *et al.*, An X-ray computed tomography imaging agent based on long-circulating bismuth sulphide nanoparticles. *Nat Mater* **5:**118-22 (2006)

93. Tran T. D., Caruthers S. D., Hughes M., *et al.*, Clinical applications of perfluorocarbon nanoparticles for molecular imaging and targeted therapeutics. *Int J Nanomedicine* **2:**515-26 (2007)
94. Serkova N. J., Hasebroock K. M., and Kraft S. L., Magnetic resonance spectroscopy of living tissues. *Methods Mol Biol* **520:**315-27 (2009)
95. Simoes R. V., Martinez-Aranda A., Martin B., *et al.*, Preliminary characterization of an experimental breast cancer cells brain metastasis mouse model by mri/mrs. *MAGMA* **21:** 237-49 (2008)
96. Palmowski M., Schifferdecker I., Zwick S., *et al.*, Tumor perfusion assessed by dynamic contrast-enhanced mri correlates to the grading of renal cell carcinoma: Initial results. *Eur J Radiol* **74**:e176-80
97. Farace P., Merigo F., Fiorini S., *et al.*, DCE-MRI using small-molecular and albumin-binding contrast agents in experimental carcinomas with different stromal content. *Eur J Radiol* **78**:52-9 (2011)
98. Kiessling F., Morgenstern B., and Zhang C., Contrast agents and applications to assess tumor angiogenesis in vivo by magnetic resonance imaging. *Curr Med Chem* **14:**77-91 (2007)
99. Rudin M., Mcsheehy P. M., Allegrini P. R., *et al.*, PTK787/ZK222584, a tyrosine kinase inhibitor of vascular endothelial growth factor receptor, reduces uptake of the contrast agent gddota by murine orthotopic B16/BL6 melanoma tumours and inhibits their growth in vivo. *NMR Biomed* **18:**308-21 (2005)
100. Morawski A. M., Winter P. M., Crowder K. C., *et al.*, Targeted nanoparticles for quantitative imaging of sparse molecular epitopes with mri. *Magn Reson Med* **51:**480-6 (2004)
101. Artemov D., Bhujwalla Z. M., and Bulte J. W., Magnetic resonance imaging of cell surface receptors using targeted contrast agents. *Curr Pharm Biotechnol* **5:**485-94 (2004)
102. Reichardt W., Hu-Lowe D., Torres D., *et al.*, Imaging of VEGF receptor kinase inhibitor-induced antiangiogenic effects in drug-resistant human adenocarcinoma model. *Neoplasia* **7:**847-53 (2005)
103. Mccarthy J. R. and Weissleder R., Multifunctional magnetic nanoparticles for targeted imaging and therapy. *Adv Drug Deliv Rev* **60:**1241-51 (2008)
104. Artemov D., Mori N., Ravi R., *et al.*, Magnetic resonance molecular imaging of the HER-2/NEU receptor. *Cancer Res* **63:**2723-7 (2003)
105. Gilad A. A., Ziv K., Mcmahon M. T., *et al.*, MRI reporter genes. *J Nucl Med* **49:**1905-8 (2008)
106. Cohen B., Dafni H., Meir G., *et al.*, Ferritin as an endogenous MRI reporter for noninvasive imaging of gene expression in C6 glioma tumors. *Neoplasia* **7:**109-17 (2005)
107. Cohen B., Ziv K., Plaks V., *et al.*, MRI detection of transcriptional regulation of gene expression in transgenic mice. *Nat Med* **13:**498-503 (2007)
108. Partlow K. C., Chen J., Brant J. A., *et al.*, 19F magnetic resonance imaging for stem/progenitor cell tracking with multiple unique perfluorocarbon nanobeacons. *FASEB J* **21:**1647-54 (2007)
109. Ahrens E. T., Flores R., Xu H., *et al.*, In vivo imaging platform for tracking immunotherapeutic cells. *Nat Biotechnol* **23:**983-7 (2005)
110. Wang Z. Y., Song J., and Zhang D. S., Nanosized As2O3/Fe2O3 complexes combined with magnetic fluid hyperthermia selectively target liver cancer cells. *World J Gastroenterol* **15:**2995-3002 (2009)
111. Kiessling F., Huppert J., and Palmowski M., Functional and molecular ultrasound imaging: Concepts and contrast agents. *Curr Med Chem* **16:**627-42 (2009)
112. Deshpande N. S. and Willmann J. K., "Micro- and nano-particle based contrast-enhanced ultrasound imaging". in: *Nanoplatform based molecular imaging*, Edited by Chen X., Wiley Publications (2011)
113. Balaban R. S. and Hampshire V. A., Challenges in small animal noninvasive imaging. *ILAR J* **42:**248-62 (2001)
114. Qin S., Caskey C. F., and Ferrara K. W., Ultrasound contrast microbubbles in imaging and therapy: Physical principles and engineering. *Phys Med Biol* **54:**R27-57 (2009)

115. Ferrara K., Pollard R., and Borden M., Ultrasound microbubble contrast agents: Fundamentals and application to gene and drug delivery. *Annu Rev Biomed Eng* **9:**415-47 (2007)
116. Ding Y., Boguslawski E. A., Berghuis B. D., *et al.*, Mitogen-activated protein kinase kinase signaling promotes growth and vascularization of fibrosarcoma. *Mol Cancer Ther* **7:**648-58 (2008)
117. Krix M., Kiessling F., Vosseler S., *et al.*, Sensitive noninvasive monitoring of tumor perfusion during antiangiogenic therapy by intermittent bolus-contrast power doppler sonography. *Cancer Res* **63:**8264-70 (2003)
118. Folkman J., Angiogenesis. *Annu Rev Med* **57:**1-18 (2006)
119. Willmann J. K., Cheng Z., Davis C., *et al.*, Targeted microbubbles for imaging tumor angiogenesis: Assessment of whole-body biodistribution with dynamic micro-PET in mice. *Radiology* **249:**212-9 (2008)
120. Willmann J. K., Lutz A. M., Paulmurugan R., *et al.*, Dual-targeted contrast agent for us assessment of tumor angiogenesis in vivo. *Radiology* **248:**936-44 (2008)
121. Rychak J. J., Graba J., Cheung A. M., *et al.*, Microultrasound molecular imaging of vascular endothelial growth factor receptor 2 in a mouse model of tumor angiogenesis. *Mol Imaging* **6:**289-96 (2007)
122. Lee D. J., Lyshchik A., Huamani J., *et al.*, Relationship between retention of a vascular endothelial growth factor receptor 2 (VEGFR2)-targeted ultrasonographic contrast agent and the level of VEGFR2 expression in an in vivo breast cancer model. *J Ultrasound Med* **27:**855-66 (2008)
123. Hughes M. S., Marsh J. N., Zhang H., *et al.*, Characterization of digital waveforms using thermodynamic analogs: Detection of contrast-targeted tissue in vivo. *IEEE Trans Ultrason Ferroelectr Freq Control* **53:**1609-16 (2006)
124. Pisani E., Tsapis N., Paris J., *et al.*, Polymeric nano/microcapsules of liquid perfluorocarbons for ultrasonic imaging: Physical characterization. *Langmuir* **22:**4397-402 (2006)
125. Yadav R. R., Mishra G., Yadawa P. K., *et al.*, Ultrasonic properties of nanoparticles-liquid suspensions. *Ultrasonics* **48:**591-3 (2008)
126. Nolte I., Vince G. H., Maurer M., *et al.*, Iron particles enhance visualization of experimental gliomas with high-resolution sonography. *AJNR Am J Neuroradiol* **26:**1469-74 (2005)
127. Liu J., Li J., Rosol T. J., *et al.*, Biodegradable nanoparticles for targeted ultrasound imaging of breast cancer cells in vitro. *Phys Med Biol* **52:**4739-47 (2007)
128. Liu J., Levine A. L., Mattoon J. S., *et al.*, Nanoparticles as image enhancing agents for ultrasonography. *Phys Med Biol* **51:**2179-89 (2006)
129. Manome Y., Nakamura M., Ohno T., *et al.*, Ultrasound facilitates transduction of naked plasmid DNA into colon carcinoma cells in vitro and in vivo. *Hum Gene Ther* **11:**1521-8 (2000)
130. Newman C. M. and Bettinger T., Gene therapy progress and prospects: Ultrasound for gene transfer. *Gene Ther* **14:**465-75 (2007)
131. Mo R., Lin S., Wang G., *et al.*, Preliminary in vitro study of ultrasound sonoporation cell labeling with superparamagnetic iron oxide particles for MRI cell tracking. *Conf Proc IEEE Eng Med Biol Soc* **2008:**367-70 (2008)
132. Feril L. B., Jr., Ultrasound-mediated gene transfection. *Methods Mol Biol* **542:**179-94 (2009)
133. Wang D. S., Panje C., Pysz M. A., *et al.*, Cationic versus neutral microbubbles for ultrasound-mediated gene delivery in cancer. *Radiology* **264**:721-32 (2012)
134. Lentacker I., De Geest B. G., Vandenbroucke R. E., *et al.*, Ultrasound-responsive polymer-coated microbubbles that bind and protect DNA. *Langmuir* **22:**7273-8 (2006)
135. Christiansen J. P., French B. A., Klibanov A. L., *et al.*, Targeted tissue transfection with ultrasound destruction of plasmid-bearing cationic microbubbles. *Ultrasound Med Biol* **29:**1759-67 (2003)
136. Aoi A., Watanabe Y., Mori S., *et al.*, Herpes simplex virus thymidine kinase-mediated suicide gene therapy using nano/microbubbles and ultrasound. *Ultrasound Med Biol* **34:**425-34 (2008)
137. Tran M. A., Gowda R., Sharma A., *et al.*, Targeting V600EB-Raf and Akt3 using nanoliposomal-small interfering rna inhibits cutaneous melanocytic lesion development. *Cancer Res* **68:**7638-49 (2008)

138. Hayashi S., Mizuno M., Yoshida J., *et al.*, Effect of sonoporation on cationic liposome-mediated IFNbeta gene therapy for metastatic hepatic tumors of murine colon cancer. *Cancer Gene Ther* **16:**638-43 (2009)
139. Nie F., Xu H. X., Lu M. D., *et al.*, Anti-angiogenic gene therapy for hepatocellular carcinoma mediated by microbubble-enhanced ultrasound exposure: An in vivo experimental study. *J Drug Target* **16:**389-95 (2008)
140. Lentacker I., Geers B., Demeester J., *et al.*, Design and evaluation of doxorubicin-containing microbubbles for ultrasound-triggered doxorubicin delivery: Cytotoxicity and mechanisms involved. *Mol Ther* **18:**101-8 (2009)
141. Rapoport N., Gao Z., and Kennedy A., Multifunctional nanoparticles for combining ultrasonic tumor imaging and targeted chemotherapy. *J Natl Cancer Inst* **99:**1095-106 (2007)
142. Xing W., Gang W. Z., Yong Z., *et al.*, Treatment of xenografted ovarian carcinoma using paclitaxel-loaded ultrasound microbubbles. *Acad Radiol* **15:**1574-9 (2008)
143. Zhao Y. Z., Lu C. T., Fu H. X., *et al.*, Phospholipid-based ultrasonic microbubbles for loading protein and ultrasound-triggered release. *Drug Dev Ind Pharm* **35:**1121-7 (2009)
144. Gao Z., Kennedy A. M., Christensen D. A., *et al.*, Drug-loaded nano/microbubbles for combining ultrasonography and targeted chemotherapy. *Ultrasonics* **48:**260-70 (2008)
145. Larkin J. O., Casey G. D., Tangney M., *et al.*, Effective tumor treatment using optimized ultrasound-mediated delivery of bleomycin. *Ultrasound Med Biol* **34:**406-13 (2008)
146. Sibille A., Prat F., Chapelon J. Y., *et al.*, Characterization of extracorporeal ablation of normal and tumor-bearing liver tissue by high intensity focused ultrasound. *Ultrasound Med Biol* **19:**803-13 (1993)
147. Weissleder R. and Pittet M. J., Imaging in the era of molecular oncology. *Nature* **452:**580-9 (2008)
148. Sokolov K., Aaron J., Hsu B., *et al.*, Optical systems for in vivo molecular imaging of cancer. *Technol Cancer Res Treat* **2:**491-504 (2003)
149. Sokolov K., Follen M., Aaron J., *et al.*, Real-time vital optical imaging of precancer using anti-epidermal growth factor receptor antibodies conjugated to gold nanoparticles. *Cancer Res* **63:**1999-2004 (2003)
150. Dekker E. and Fockens P., New imaging techniques at colonoscopy: Tissue spectroscopy and narrow band imaging. *Gastrointest Endosc Clin N Am* **15:**703-14 (2005)
151. Herth F. J., Eberhardt R., and Ernst A., The future of bronchoscopy in diagnosing, staging and treatment of lung cancer. *Respiration* **73:**399-409 (2006)
152. Luker G. D. and Luker K. E., Optical imaging: Current applications and future directions. *J Nucl Med* **49:**1-4 (2008)
153. Ballou B., Ernst L. A., and Waggoner A. S., Fluorescence imaging of tumors in vivo. *Curr Med Chem* **12:**795-805 (2005)
154. Veiseh M., Gabikian P., Bahrami S. B., *et al.*, Tumor paint: A chlorotoxin:Cy5.5 bioconjugate for intraoperative visualization of cancer foci. *Cancer Res* **67:**6882-8 (2007)
155. Chen J., Tung C. H., Allport J. R., *et al.*, Near-infrared fluorescent imaging of matrix metalloproteinase activity after myocardial infarction. *Circulation* **111:**1800-5 (2005)
156. Jiang T., Olson E. S., Nguyen Q. T., *et al.*, Tumor imaging by means of proteolytic activation of cell-penetrating peptides. *Proc Natl Acad Sci U S A* **101:**17867-72 (2004)
157. Mahmood U., Tung C. H., Bogdanov A., Jr., *et al.*, Near-infrared optical imaging of protease activity for tumor detection. *Radiology* **213:**866-70 (1999)
158. Tung C. H., Bredow S., Mahmood U., *et al.*, Preparation of a cathepsin D sensitive near-infrared fluorescence probe for imaging. *Bioconjug Chem* **10:**892-6 (1999)
159. Weissleder R., Tung C. H., Mahmood U., *et al.*, In vivo imaging of tumors with protease-activated near-infrared fluorescent probes. *Nat Biotechnol* **17:**375-8 (1999)
160. Alencar H., Funovics M. A., Figueiredo J., *et al.*, Colonic adenocarcinomas: Near-infrared microcatheter imaging of smart probes for early detection--study in mice. *Radiology* **244:**232-8 (2007)

161. Gounaris E., Tung C. H., Restaino C., *et al.*, Live imaging of cysteine-cathepsin activity reveals dynamics of focal inflammation, angiogenesis, and polyp growth. *PLoS One* **3:**e2916 (2008)
162. Figueiredo J. L., Alencar H., Weissleder R., *et al.*, Near infrared thoracoscopy of tumoral protease activity for improved detection of peripheral lung cancer. *Int J Cancer* **118:**2672-7 (2006)
163. McCann C. M., Waterman P., Figueiredo J. L., *et al.*, Combined magnetic resonance and fluorescence imaging of the living mouse brain reveals glioma response to chemotherapy. *Neuroimage* **45:**360-9 (2009)
164. Chang S. K., Rizvi I., Solban N., *et al.*, In vivo optical molecular imaging of vascular endothelial growth factor for monitoring cancer treatment. *Clin Cancer Res* **14:**4146-53 (2008)
165. Zheng G., Chen J., Stefflova K., *et al.*, Photodynamic molecular beacon as an activatable photosensitizer based on protease-controlled singlet oxygen quenching and activation. *Proc Natl Acad Sci U S A* **104:**8989-94 (2007)
166. Edinger M., Cao Y. A., Hornig Y. S., *et al.*, Advancing animal models of neoplasia through in vivo bioluminescence imaging. *Eur J Cancer* **38:**2128-36 (2002)
167. So M. K., Xu C., Loening A. M., *et al.*, Self-illuminating quantum dot conjugates for in vivo imaging. *Nat Biotechnol* **24:**339-43 (2006)
168. Smith B. R. and Gambhir S. S., "Chapter 17: Nanoparticle-based molecular imaging in living subjects." in: *Molecular imaging in oncology*, Edited by: Pomper M. G. and Gelovani J. G., Taylor & Francis, Inc., (2008), *pp*. 261-282.
169. Nie S., Xing Y., Kim G. J., *et al.*, Nanotechnology applications in cancer. *Annu Rev Biomed Eng* **9:**257-88 (2007)
170. Smith A. M., Duan H., Mohs A. M., *et al.*, Bioconjugated quantum dots for in vivo molecular and cellular imaging. *Adv Drug Deliv Rev* **60:**1226-40 (2008)
171. Hirsch L. R., Gobin A. M., Lowery A. R., *et al.*, Metal nanoshells. *Ann Biomed Eng* **34:**15-22 (2006)
172. Wang L. V., Prospects of photoacoustic tomography. *Med Phys* **35:**5758-67 (2008)
173. Li P. C., Wang C. R., Shieh D. B., *et al.*, In vivo photoacoustic molecular imaging with simultaneous multiple selective targeting using antibody-conjugated gold nanorods. *Opt Express* **16:**18605-15 (2008)
174. De La Zerda A., Zavaleta C., Keren S., *et al.*, Carbon nanotubes as photoacoustic molecular imaging agents in living mice. *Nat Nanotechnol* **3:**557-62 (2008)
175. Keren S., Zavaleta C., Cheng Z., *et al.*, Noninvasive molecular imaging of small living subjects using raman spectroscopy. *Proc Natl Acad Sci U S A* **105:**5844-9 (2008)
176. Zavaleta C., De La Zerda A., Liu Z., *et al.*, Noninvasive raman spectroscopy in living mice for evaluation of tumor targeting with carbon nanotubes. *Nano Lett* **8:**2800-5 (2008)
177. Haisch C., Quantitative analysis in medicine using photoacoustic tomography. *Anal Bioanal Chem* **393:**473-9 (2009)
178. Nijssen A., Koljenovic S., Bakker Schut T. C., *et al.*, Towards oncological application of raman spectroscopy. *J Biophotonics* **2:**29-36 (2009)
179. Weissleder R., Scaling down imaging: Molecular mapping of cancer in mice. *Nat Rev Cancer* **2:**11-8 (2002)
180. Teicher B. A., Acute and chronic in vivo therapeutic resistance. *Biochem Pharmacol* **77:** 1665-73 (2009)
181. Vonlaufen A., Phillips P. A., Xu Z., *et al.*, Pancreatic stellate cells and pancreatic cancer cells: An unholy alliance. *Cancer Res* **68:**7707-10 (2008)
182. Kurdziel K. A., Kalen J. D., Hirsch J. I., *et al.*, Imaging multidrug resistance with 4-[^{18}F]fluoropaclitaxel. *Nucl Med Biol* **34:**823-31 (2007)
183. Barqawi A. B. and Crawford E. D., Emerging role of HIFU as a noninvasive ablative method to treat localized prostate cancer. *Oncology (Williston Park)* **22:**123-9; discussion 129, 133, 137 passim (2008)

184. Grenier N., Quesson B., De Senneville B. D., *et al.*, Molecular MR imaging and MR-guided ultrasound therapies in cancer. *JBR-BTR* **92:**8-12 (2009)
185. Maruyama H., Yoshikawa M., and Yokosuka O., Current role of ultrasound for the management of hepatocellular carcinoma. *World J Gastroenterol* **14:**1710-9 (2008)
186. Lu P., Zhu X. Q., Xu Z. L., *et al.*, Increased infiltration of activated tumor-infiltrating lymphocytes after high intensity focused ultrasound ablation of human breast cancer. *Surgery* **145:**286-93 (2009)
187. Gao X., Cui Y., Levenson R. M., *et al.*, In vivo cancer targeting and imaging with semiconductor quantum dots. *Nat Biotechnol* **22**:969-76 (2004)
188. Szpirer C., and Szpirer J., Mammary cancer susceptibility: Human genes and rodent models. *Mamm Genome* **18:**817-31 (2007)
189. Winter S. F., and Hunter K. W., Mouse modifier genes in mammary tumorigenesis and metastasis. *J Mammary Gland Biol Neoplasia* **13:**337-42 (2008)
190. Garnis C., Buys T. P., and Lam W. L., Genetic alteration and gene expression modulation during cancer progression. *Mol Cancer* **3:**9 (2004)
191. Jackson M. A., Lea I., Rashid A., *et al.* Genetic alterations in cancer knowledge system: Analysis of gene mutations in mouse and human liver and lung tumors. *Toxicol Sci* **90:**400-18 (2006)
192. Singh M., Lin J., Hocker T. L., *et al.* Genetics of melanoma tumorigenesis. *Br J Dermatol* **158:**15-21 (2008)
193. Rebouissou S., Bioulac-Sage P., and Zucman-Rossi J., Molecular pathogenesis of focal nodular hyperplasia and hepatocellular adenoma. *J Hepatol* **48:**163-70 (2008)
194. Lemmer E. R., Friedman S. L., and Llovet J. M., Molecular diagnosis of chronic liver disease and hepatocellular carcinoma: The potential of gene expression profiling. *Semin Liver Dis* **26:**373-84 (2006)
195. Ottenhof N. A., Milne A. N., Morsink F. H., *et al.*, Pancreatic intraepithelial neoplasia and pancreatic tumorigenesis: Of mice and men. *Arch Pathol Lab Med* **133:**375-81 (2009)
196. Shiraishi T. and Tabuchi K., Genetic alterations of human brain tumors as molecular prognostic factors. *Neuropathology* **23:**95-108 (2003)
197. Krug U., Ganser A., and Koeffler H. P., Tumor suppressor genes in normal and malignant hematopoiesis. *Oncogene* **21**:3475-95 (2002)
198. Shan W. and Liu J., Epithelial ovarian cancer: Focus on genetics and animal models. *Cell Cycle* **8:**731-5 (2009)
199. Borowsky A., Special considerations in mouse models of breast cancer. *Breast Dis* **28:**29-38 (2007)
200. Pritchard C., Carragher L., Aldridge V., *et al.*, Mouse models for braf-induced cancers. *Biochem Soc Trans* **35:**1329-33 (2007)
201. Dutt A. and Wong K. K., Mouse models of lung cancer. *Clin Cancer Res* **12:**4396 s-4402s (2006)
202. Wakamatsu N., Devereux T. R., Hong H. H., *et al.*, Overview of the molecular carcinogenesis of mouse lung tumor models of human lung cancer. *Toxicol Pathol* **35**:75-80 (2007).
203. Moser A. R., Pitot H. C., and Dove W. F., A dominant mutation that predisposes to multiple intestinal neoplasia in the mouse. *Science* **247:**322-4 (1990)
204. Fodde R., Edelmann W., Yang K., *et al.*, A targeted chain-termination mutation in the mouse APC gene results in multiple intestinal tumors. *Proc Natl Acad Sci U S A* **91:**8969-73 (1994)
205. Velcich A., Yang W., Heyer J., *et al.*, Colorectal cancer in mice genetically deficient in the mucin MUC2. *Science* **295:**1726-9 (2002)
206. Hirose Y., Hata K., Kuno T., *et al.*, Enhancement of development of azoxymethane-induced colonic premalignant lesions in C57BL/KSJ-DB/DB mice. *Carcinogenesis* **25:**821-5 (2004)
207. Reddy B. S., Studies with the azoxymethane-rat preclinical model for assessing colon tumor development and chemoprevention. *Environ Mol Mutagen* **44:**26-35 (2004)
208. Taketo M. M. and Edelmann W., Mouse models of colon cancer. *Gastroenterology* **136:**780-98 (2009)

209. Leder A., Kuo A., Cardiff R. D., *et al.*, V-Ha-Ras transgene abrogates the initiation step in mouse skin tumorigenesis: Effects of phorbol esters and retinoic acid. *Proc Natl Acad Sci U S A* **87:**9178-82 (1990)
210. Saitoh A., Kimura M., Takahashi R., *et al.*, Most tumors in transgenic mice with human C-Ha-Ras gene contained somatically activated transgenes. *Oncogene* **5:**1195-200 (1990)
211. Borowsky A. D., Munn R. J., Galvez J. J., *et al.*, Mouse models of human cancers (part 3). *Comp Med* **54:**258-70 (2004)
212. Lynch D., Svoboda J., Putta S., *et al.*, Mouse skin models for carcinogenic hazard identification: Utilities and challenges. *Toxicol Pathol* **35:**853-64 (2007)
213. Rogers A. B., and Fox J. G., Inflammation and cancer. I. Rodent models of infectious gastrointestinal and liver cancer. *Am J Physiol Gastrointest Liver Physiol* **286:**G361-6 (2004)
214. Katzenellenbogen M., Mizrahi L., Pappo O., *et al.*, Molecular mechanisms of liver carcinogenesis in the MDR2-knockout mice. *Mol Cancer Res* **5:**1159-70 (2007)
215. Tward A. D., Jones K. D., Yant S., *et al.* Distinct pathways of genomic progression to benign and malignant tumors of the liver. *Proc Natl Acad Sci U S A* **104:**14771-6 (2007)
216. Kohle C., Schwarz M., and Bock K. W., Promotion of hepatocarcinogenesis in humans and animal models. *Arch Toxicol* **82:**623-31 (2008)
217. Carriere C., Young A. L., Gunn J. R., *et al.*, Acute pancreatitis markedly accelerates pancreatic cancer progression in mice expressing oncogenic KRas. *Biochem Biophys Res Commun* **382:**561-5 (2009)
218. Huse J. T. and Holland E. C., Genetically engineered mouse models of brain cancer and the promise of preclinical testing. *Brain Pathol* **19:**132-43 (2009)
219. Rice J. M. and Wilbourn J. D., Tumors of the nervous system in carcinogenic hazard identification. *Toxicol Pathol* **28:**202-14 (2000)
220. Bernardi R., Grisendi S., and Pandolfi P. P., Modelling haematopoietic malignancies in the mouse and therapeutical implications. *Oncogene* **21:**3445-58 (2002)
221. Huff J. E., Haseman J. K., Demarini D. M., *et al.*, Multiple-site carcinogenicity of benzene in Fischer 344 rats and B6C3FL mice. *Environ Health Perspect* **82:**125-63 (1989)
222. Bosetti C., McLaughlin J. K., Tarone R. E., *et al.*, Formaldehyde and cancer risk: A quantitative review of cohort studies through 2006. *Ann Oncol* **19:**29-43 (2008)
223. Melnick R. L. and Huff J., 1,3-butadiene: Toxicity and carcinogenicity in laboratory animals and in humans. *Rev Environ Contam Toxicol* **124:**111-44 (1992)
224. Kerkhofs S., Denayer S., Haelens A., *et al.*, Androgen receptor knockout and knock-in mouse models. *J Mol Endocrinol* **42:**11-7 (2009)
225. Gingrich J. R., Barrios R. J., Morton R. A., *et al.*, Metastatic prostate cancer in a transgenic mouse. *Cancer Res* **56:**4096-102 (1996)
226. Kasper S., Survey of genetically engineered mouse models for prostate cancer: Analyzing the molecular basis of prostate cancer development, progression, and metastasis. *J Cell Biochem* **94:**279-97 (2005)
227. Shirai T., Takahashi S., Cui L., *et al.*, Experimental prostate carcinogenesis - rodent models. *Mutat Res* **462:**219-26 (2000)
228. Flesken-Nikitin A., Choi K. C., Eng J. P., *et al.*, Induction of carcinogenesis by concurrent inactivation of p53 and Rb1 in the mouse ovarian surface epithelium. *Cancer Res* **63:**3459-63 (2003)
229. Connolly D. C., Bao R., Nikitin A. Y., *et al.*, Female mice chimeric for expression of the simian virus 40 TAG under control of the MISIIR promoter develop epithelial ovarian cancer. *Cancer Res* **63:**1389-97 (2003)
230. Wu R., Hendrix-Lucas N., Kuick R., *et al.*, Mouse model of human ovarian endometrioid adenocarcinoma based on somatic defects in the Wnt/beta-catenin and PI3K/PTEN signaling pathways. *Cancer Cell* **11:**321-33 (2007)
231. Wang Y., Zhang Z., Lu Y., *et al.*, Enhanced susceptibility to chemical induction of ovarian tumors in mice with a germ line p53 mutation. *Mol Cancer Res* **6:**99-109 (2008)
232. Chen K., Cai W., Li Z. B., *et al.*, Quantitative PET imaging of VEGF receptor expression. *Mol Imaging Biol* **11:**15-22 (2009)

233. Wang H., Cai W., Chen K., *et al.*, A new PET tracer specific for vascular endothelial growth factor receptor 2. *Eur J Nucl Med Mol Imaging* **34:**2001-10 (2007)
234. Chen K., Li Z. B., Wang H., *et al.*, Dual-modality optical and positron emission tomography imaging of vascular endothelial growth factor receptor on tumor vasculature using quantum dots. *Eur J Nucl Med Mol Imaging* **35:**2235-44 (2008)
235. Kimura R. H., Cheng Z., Gambhir S. S., *et al.*, Engineered knottin peptides: A new class of agents for imaging integrin expression in living subjects. *Cancer Res* **69:**2435-42 (2009)
236. Reischl G., Dorow D. S., Cullinane C., *et al.*, Imaging of tumor hypoxia with [124I]IAZA in comparison with [^{18}F]FMISO and [^{18}F]FAZ--irst small animal PET results. *J Pharm Pharm Sci* **10:**203-11 (2007)
237. Ljungkvist A. S., Bussink J., Kaanders J. H., *et al.*, Dynamics of tumor hypoxia measured with bioreductive hypoxic cell markers. *Radiat Res* **167:**127-45 (2007)
238. He F., Deng X., Wen B., *et al.*, Noninvasive molecular imaging of hypoxia in human xenografts: Comparing hypoxia-induced gene expression with endogenous and exogenous hypoxia markers. *Cancer Res* **68:**8597-606 (2008)
239. Piert M., Machulla H. J., Picchio M., *et al.*, Hypoxia-specific tumor imaging with ^{18}F-Fluoroazomycin arabinoside. *J Nucl Med* **46:**106-13 (2005)
240. Niu G., Cai W., and Chen X., Molecular imaging of human epidermal growth factor receptor 2 (HER-2) expression. *Front Biosci* **13:**790-805 (2008)
241. Niu G., Li Z., Cao Q., *et al.*, Monitoring therapeutic response of human ovarian cancer to 17-DMAG by noninvasive pet imaging with (64)Cu-DOTA-trastuzumab. *Eur J Nucl Med Mol Imaging* **36:**1510-9 (2009)
242. Bigott H. M., Parent E., Luyt L. G., *et al.*, Design and synthesis of functionalized cyclopentadienyl tricarbonylmetal complexes for technetium-94 m PET imaging of estrogen receptors. *Bioconjug Chem* **16:**255-64 (2005)
243. Aliaga A., Rousseau J. A., Ouellette R., *et al.*, Breast cancer models to study the expression of estrogen receptors with small animal PET imaging. *Nucl Med Biol* **31:**761-70 (2004)
244. Yang D. J., Li C., Kuang L. R., *et al.*, Imaging, biodistribution and therapy potential of halogenated tamoxifen analogues. *Life Sci* **55:**53-67 (1994)
245. Bettio A., Honer M., Muller C., *et al.*, Synthesis and preclinical evaluation of a folic acid derivative labeled with ^{18}F for PET imaging of folate receptor-positive tumors. *J Nucl Med* **47:**1153-60 (2006)
246. Mathias C. J., Lewis M. R., Reichert D. E., *et al.*, Preparation of 66Ga- and 68Ga-labeled Ga(iii)-deferoxamine-folate as potential folate-receptor-targeted pet radiopharmaceuticals. *Nucl Med Biol* **30:**725-31 (2003)
247. Elsasser-Beile U., Reischl G., Wiehr S., *et al.*, PET imaging of prostate cancer xenografts with a highly specific antibody against the prostate-specific membrane antigen. *J Nucl Med* **50:**606-11 (2009)
248. Keen H. G., Dekker B. A., Disley L., *et al.*, Imaging apoptosis *in vivo* using 124I-Annexin V and PET. *Nucl Med Biol* **32:**395-402 (2005)
249. Hu G., Lijowski M., Zhang H., *et al.*, Imaging of VX-2 rabbit tumors with alpha(nu)beta3-integrin-targeted 111In nanoparticles. *Int J Cancer* **120:**1951-7 (2007)
250. Nayak T. K., Hathaway H. J., Ramesh C., *et al.*, Preclinical development of a neutral, estrogen receptor-targeted, tridentate 99mTc(i)-estradiol-pyridin-2-yl hydrazine derivative for imaging of breast and endometrial cancers. *J Nucl Med* **49:**978-86 (2008)
251. Muller C., Schibli R., Krenning E. P., *et al.*, Pemetrexed improves tumor selectivity of 111In-DTPA-folate in mice with folate receptor-positive ovarian cancer. *J Nucl Med* **49:**623-9 (2008)
252. Muller C., Hohn A., Schubiger P. A., *et al.*, Preclinical evaluation of novel organometallic 99mTc-folate and 99mTc-pteroate radiotracers for folate receptor-positive tumour targeting. *Eur J Nucl Med Mol Imaging* **33:**1007-16 (2006)
253. Mukherjee A., Kothari K., Toth G., *et al.*, 99mTc-labeled Annexin V fragments: A potential SPECT radiopharmaceutical for imaging cell death. *Nucl Med Biol* **33:**635-43 (2006)

254. Choi S. R., Zhuang Z. P., Chacko A. M., *et al.*, SPECT imaging of herpes simplex virus type1 thymidine kinase gene expression by [(123)I]FIAU(1). *Acad Radiol* **12:**798-805 (2005)
255. Mulder W. J., Strijkers G. J., Habets J. W., *et al.*, MR molecular imaging and fluorescence microscopy for identification of activated tumor endothelium using a bimodal lipidic nanoparticle. *FASEB J* **19:**2008-10 (2005)
256. Chen T. J., Cheng T. H., Chen C. Y., *et al.*, Targeted herceptin-dextran iron oxide nanoparticles for noninvasive imaging of HER2/Neu receptors using MRI. *J Biol Inorg Chem* **14:**253-60 (2009)
257. Yang L., Mao H., Wang Y. A., *et al.*, Single chain epidermal growth factor receptor antibody conjugated nanoparticles for *in vivo* tumor targeting and imaging. *Small* **5:**235-43 (2009)
258. Yang L., Peng X. H., Wang Y. A., *et al.*, Receptor-targeted nanoparticles for *in vivo* imaging of breast cancer. *Clin Cancer Res* **15:**4722-32 (2009)
259. Yang L., Mao H., Cao Z., *et al.*, Molecular imaging of pancreatic cancer in an animal model using targeted multifunctional nanoparticles. *Gastroenterology* **136:**1514-25 e2 (2009)
260. Chen W. T., Thirumalai D., Shih T. T., *et al.*, Dynamic contrast-enhanced folate-receptor-targeted MR imaging using a Gd-loaded PEG-dendrimer-folate conjugate in a mouse xenograft tumor model. *Mol Imaging Biol* **12:**145-54 (2009)
261. Liu L., Kodibagkar V. D., Yu J. X., *et al.*, 19F-NMR detection of LacZ gene expression via the enzymic hydrolysis of 2-fluoro-4-nitrophenyl beta-D-galactopyranoside *in vivo* in PC3 prostate tumor xenografts in the mouse. *FASEB J* **21:**2014-9 (2007)
262. Shan L., Wang S., Sridhar R., *et al.*, Dual probe with fluorescent and magnetic properties for imaging solid tumor xenografts. *Mol Imaging* **6:**85-95 (2007)
263. Gilad A. A., McMahon M. T., Walczak P., *et al.*, Artificial reporter gene providing mri contrast based on proton exchange. *Nat Biotechnol* **25:**217-9 (2007)
264. Kumar C. C., Nie H., Rogers C. P., *et al.*, Biochemical characterization of the binding of echistatin to integrin alphaVbeta3 receptor. *J Pharmacol Exp Ther* **283:**843-53 (1997)
265. Ellegala D. B., Leong-Poi H., Carpenter J. E., *et al.*, Imaging tumor angiogenesis with contrast ultrasound and microbubbles targeted to alpha(v)beta3. *Circulation* **108:**336-41 (2003)
266. Palmowski M., Huppert J., Ladewig G., *et al.*, Molecular profiling of angiogenesis with targeted ultrasound imaging: Early assessment of antiangiogenic therapy effects. *Mol Cancer Ther* **7:**101-9 (2008)
267. Stell A., Belcredito S., Ciana P., *et al.*, Molecular imaging provides novel insights on estrogen receptor activity in mouse brain. *Mol Imaging* **7**:283-92 (2008)
268. Korpanty G., Carbon J. G., Grayburn P. A., *et al.*, Monitoring response to anticancer therapy by targeting microbubbles to tumor vasculature. *Clin Cancer Res* **13:**323-30 (2007)
269. Weller G. E., Wong M. K., Modzelewski R. A., *et al.*, Ultrasonic imaging of tumor angiogenesis using contrast microbubbles targeted via the tumor-binding peptide arginine-arginine-leucine. *Cancer Res* **65:**533-9 (2005)
270. Backer M. V. Gaynutdinov T. I., Patel V., *et al.*, Vascular endothelial growth factor selectively targets boronated dendrimers to tumor vasculature. *Mol Cancer Ther* **4:**1423-9 (2005)
271. Cai W., Shin D. W., Chen K., *et al.*, Peptide-labeled near-infrared quantum dots for imaging tumor vasculature in living subjects. *Nano Lett* **6:**669-76 (2006)
272. Hilger I., Leistner Y., Berndt A., *et al.*, Near-infrared fluorescence imaging of HER-2 protein over-expression in tumour cells. *Eur Radiol* **14:**1124-9 (2004)
273. Stefflova K., Li H., Chen J., *et al.*, Peptide-based pharmacomodulation of a cancer-targeted optical imaging and photodynamic therapy agent. *Bioconjug Chem* **18:**379-88 (2007)
274. Funovics M., Weissleder R., and Tung C. H., Protease sensors for bioimaging. *Anal Bioanal Chem* **377:**956-63 (2003)
275. Bremer C., Tung C. H., Bogdanov A., Jr., *et al.*, Imaging of differential protease expression in breast cancers for detection of aggressive tumor phenotypes. *Radiology* **222**:814-8 (2002)

276. Allport J. R. and Weissleder R., Murine lewis lung carcinoma-derived endothelium expresses markers of endothelial activation and requires tumor-specific extracellular matrix *in vitro*. *Neoplasia* **5:**205-17 (2003)
277. Bremer C., Tung C. H., and Weissleder R., *In vivo* molecular target assessment of matrix metalloproteinase inhibition. *Nat Med* **7:**743-8 (2001)
278. Edgington L. E., Berger A. B., Blum G., *et al.*, Noninvasive optical imaging of apoptosis by caspase-targeted activity-based probes. *Nat Med.* **15:**967-73 (2009)
279. Kizaka-Kondoh S., Itasaka S., Zeng L., *et al.*, Selective killing of hypoxia-inducible factor-1-active cells improves survival in a mouse model of invasive and metastatic pancreatic cancer. *Clin Cancer Res* **15:**3433-41 (2009)
280. Manning H. C., Merchant N. B., Foutch A. C., *et al.*, Molecular imaging of therapeutic response to epidermal growth factor receptor blockade in colorectal cancer. *Clin Cancer Res* **14:**7413-22 (2008)
281. Nagengast W. B., De Vries E. G., Hospers G. A., *et al.*, *In vivo* VEGF imaging with radiolabeled bevacizumab in a human ovarian tumor xenograft. *J Nucl Med* **48:**1313-9 (2007)
282. Dijkers E. C., Kosterink J. G., Rademaker A. P., *et al.*, Development and characterization of clinical-grade 89Zr-trastuzumab for HER2/Neu immunopet imaging. *J Nucl Med* **50:**974-81 (2009)
283. Mankoff D. A., Link J. M., Linden H. M., *et al.*, Tumor receptor imaging. *J Nucl Med* 49 Suppl **2:**149S-63S (2008)
284. Kawamura K., Yamasaki T., Yui J., *et al.*, *In vivo* evaluation of P-glycoprotein and breast cancer resistance protein modulation in the brain using [(11)C]gefitinib. *Nucl Med Biol* **36:**239-46 (2009)
285. Kulbersh B. D., Duncan R. D., Magnuson J. S., *et al.*, Sensitivity and specificity of fluorescent immunoguided neoplasm detection in head and neck cancer xenografts. *Arch Otolaryngol Head Neck Surg* **133:**511-5 (2007)
286. Memon A. A., Jakobsen S., Dagnaes-Hansen F., *et al.*, Positron emission tomography (PET) imaging with [11C]-labeled erlotinib: A micro-PET study on mice with lung tumor xenografts. *Cancer Res* **69:**873-8 (2009)
287. Gangloff A., Hsueh W. A., Kesner A. L., *et al.*, Estimation of paclitaxel biodistribution and uptake in human-derived xenografts *in vivo* with (18)F-Fluoropaclitaxel. *J Nucl Med* **46:**1866-71 (2005)

Chapter 22
Applications of Molecular Small-Animal Imaging in Inflammation and Infection

Alberto Signore, Eri F.J. de Vries, Filippo Galli, and Gaurav Malviya

1 Introduction

In the past decades, the field of molecular imaging of inflammation/infection has enormously expanded because of the huge clinical need for diagnostic, prognostic and therapeutic purposes.

Imaging inflammation and infection is an exquisite example of imaging histopathological changes with very little morphological alterations of tissues and organs. This makes it difficult to be detected using conventional radiological techniques, such as ultrasound (US), computed tomography (CT) and even magnetic resonance imaging (MRI). The best chance for infection imaging and to evaluate its extent and severity is the use of radiolabeled probes (radiopharmaceuticals) that specifically bind to relevant target molecules highly expressed in the site of inflammation/infection [1].

A very important application of molecular imaging of infection, beside diagnosis, is to help clinicians for therapy decision making and early therapy follow-up. We aim at providing a wide range of radiopharmaceutical to guide clinicians to

A. Signore (✉)
Nuclear Medicine Unit, II Faculty of Medicine and Surgery, 'Sapienza' University of Rome, St. Andrea Hospital, Rome, Italy

Department of Nuclear Medicine and Molecular Imaging, University of Groningen, University Medical Centre Groningen, Groningen, The Netherlands
e-mail: alberto.signore@uniroma1.it

E.F.J. de Vries • G. Malviya
Department of Nuclear Medicine and Molecular Imaging, University of Groningen, University Medical Centre Groningen, Groningen, The Netherlands
e-mail: e.f.j.de.vries@umcg.nl; g.malviya@umcg.nl

F. Galli
Nuclear Medicine Unit, II Faculty of Medicine and Surgery, 'Sapienza' University of Rome, St. Andrea Hospital, Rome, Italy
e-mail: filippo.galli@hotmail.com

H. Zaidi (ed.), *Molecular Imaging of Small Animals: Instrumentation and Applications*,
DOI 10.1007/978-1-4939-0894-3_22,

select the most appropriate therapy, based on what target is more expressed than others, and to early assess the efficacy of therapy with obvious economical other than clinical relevance.

In this view, specificity of radiolabeled probes is the key. We must be able to distinguish between a sterile inflammation and a microbial infection, being the two events not always associated. Indeed a sterile inflammation can be found in organ-specific autoimmune diseases, degenerative diseases, atherosclerosis, chronic graft rejection and others. By contrast acute or chronic infections are characterized by the presence of micro-organisms in the infected tissue and a predominant polymorphonuclear cell type of infiltration with variable levels of edema.

The terms "inflammation", "infection", "acute" and "chronic" have, therefore, different meanings for histo-pathologists, clinicians and nuclear medicine physicians. For imaging purposes we define an inflammation, a reactive inflammatory sterile process (often chronic and with predominant tissue infiltration of mononuclear cells); an infection, the presence of foreign micro-organisms (often acute and with predominant tissue infiltration of polymorphonuclear cells); acute, a process that develops within days or weeks (with endothelial cell activation, polymorphonuclear cell infiltration and large tissue exudate); chronic, a process that develops in months or years, often after an acute event (with little endothelial cell activation, mononuclear cell infiltration and little transudate).

To achieve the goal of molecular imaging of different events occurring in inflammation or infection we require a combination of highly advanced and sophisticated imaging devices with tailored radiopharmaceuticals.

2 Imaging Tools

To image inflammation and infection in small animals, high resolution and sensitive imaging tools are mandatory, because foci can be small and inflammatory processes can be mild. Several imaging modalities are available for small animals, which can roughly be divided in morphological and functional, depending on the main information they provide. Characteristics of imaging modalities for small animal imaging are summarized in Table 22.1. In the following paragraphs, we will briefly discuss the most important ones in relation to infection and inflammation imaging in small animals.

2.1 CT

CT is a morphological imaging technique that consists of a rotating x-ray tube and a detector system [3]. Dedicated small animal CT cameras, that provide high-resolution (<50 μm) 3D information of body structure, due to differential attenuation of X-rays by various tissues, are available. Although CT is ideally suited for

Table 22.1 Characteristics of imaging modalities for small animal imaging

	PET	SPECT	Bio-luminescence	Fluorescence	MRI	CT
Probe concentration	pM	nM-pM	pM-fM	nM-pM	mM-μM	Not applicable
Functional information	Very high	High	High	High	Intermediate	Very low
Anatomical information	Low	Low	Low	Low	Very high	Very high
Tissue dept	Not limited	Not limited	0.1–1 cm	0.1–5 cm	Not limited	Not limited
Spatial resolution (mm)[a]	1–4	0.5–5	3–10	2–10	0.025–0.1	0.03–0.4
Acquisition time (s)(per frame)[a]	1–300	60–2,000	10–300	10–2,000	60–3,000	1–300
Signal quantification	High	Intermediate	Low—intermediate	Low—intermediate	Intermediate	Very low

[a]Adapted from Lecchi et al. [2] with modifications

imaging of structures like bone, the contrast between different soft tissues is poor. To improve visualization of soft tissues, blood pool contrast agents can be used. However, CT contrast agents that specifically target the site of inflammation are not available. Since inflammation and infection do not often induce morphological changes of affected tissues that can be observed by CT, this technique usually is not useful for investigating infection and inflammation, but it could provide complementary anatomical information when used in combination with functional imaging modalities.

2.2 MRI

MRI is a high-resolution imaging technique that is predominantly used to investigate soft tissue morphology [4]. MRI measures the electromagnetic flux that is generated when nuclei that have been excited by a radiofrequency pulse in a magnetic field return to their low energy spin state. MRI images can be acquired base on the longitudinal (realignment) relaxation time T1 or on the transverse (spin phase) relaxation time T2. The signal of T1 and T2-weighted MRI is dependent on the environment of the relaxating nucleus. MRI usually measures the spin relaxation of protons present in water. However, other atoms like ^{13}C, ^{23}Na and ^{31}P can also be used for MRI, but these atoms generate a much weaker signal and are far less abundant in vivo than ^{1}H. MRI cameras consist of a magnet that generates a homogeneous static magnetic field, a radiofrequency transmitter and receiver and three orthogonal magnetic gradient coils. For small animal imaging, dedicated MRI systems have been developed with increased sensitivity and resolution (as low as a few cubic micrometers) by using higher strength magnetic fields (up to 20 T), smaller bore and dedicated radiofrequency coils. To increase the specificity of MRI different contrast agents have been exploited. Two classes of contrast agents can be discriminated: paramagnetic and super-paramagnetic. Paramagnetic contrast agents, usually gadolinium complexes, enhance the signal in T1-weighted MRI, whereas super-paramagnetic contrast agents like iron oxide particles reduce the T2 signal.

MRI can discriminate different tissues on basis of their water content. Consequently, morphological MRI could be exploited to visualize the higher water concentration in edema that is formed as a result of inflammation or infection [5]. With the exception of edema, infection and inflammation do usually not induce substantial morphological changes that can be monitored by anatomical MRI.

In addition to morphological information, MRI can also provide functional information when targeted contrast agents are used [6]. For targeted imaging of infection and inflammation, ultra-small super-paramagnetic iron oxide (USPIO) particles could be of particular interest. When injected in the blood stream, USPIO particles are rapidly taken up by macrophages via phagocytosis. Subsequently, migration of the labeled macrophages to the site of infection can be monitored by MRI [7]. The difference in accumulation of macrophages in infectious and sterile inflammation would allow discrimination between the different types of inflammation. In

addition, immune cells (leukocytes, NK cells) can be labeled in vitro with iron oxide particles for cell tracking with MRI. Iron oxide particles can also be used to label bioactive molecules. For example, USPIO have been conjugated to an antibody directed against CD4 [8]. This labeled antibody could successfully detect CNS infiltrating helper T cells in various models of inflammation. Likewise, antibodies have also been conjugated with the chelator DTPA for labeling with gadolinium [6]. Although targeted imaging with MRI contrast agents is feasible, the technique is not sensitive, as it requires concentrations of the contrast agents at the target site to be in the micro- to millimolar range. For instance, 100–1,000 gadolinium atoms have to be bound to a single antibody molecule in order to get a suitable signal. Such a high gadolinium load can easily result in loss of affinity of the antibody. USPIOs generate a stronger signal than gadolinium and could therefore be more sensitive.

2.3 Optical Imaging

Optical molecular imaging is a low-cost, fast and sensitive non-invasive imaging technique that monitors the propagation of light through tissue [9, 10]. The most widely used optical imaging techniques are fluorescence and bioluminescence imaging. In fluorescence imaging, an external light source excites a fluorescent imaging probe inside an animal to a higher energy state. The fluorescent reporter probe subsequently returns to its ground energy state by emission of light with a longer wavelength. The emitted light is detected outside the animal by a light sensitive camera. When multiple fluorophores are used that emit light at different wavelengths, various processes can in principle be studied simultaneously using the appropriate light emission filters. The instrumentation for fluorescence imaging typically consists of a charge-coupled device (CCD) camera, mounted on a light-tight chamber with an animal support device, an external light source and excitation and emission filters. The sensitivity of fluorescence imaging is limited by tissue optics and background light. To reduce baseline noise, the CCD camera can be cooled to −105 °C. The major limitations to the sensitivity of fluorescence imaging are autofluorescence and poor penetration of light through tissues, due to absorption and scattering. Classical fluorescent probes like GFP and DsRed emit light in the visible spectrum from 400 to 650 nm. At wavelengths <600 nm, light is highly attenuated by haemoglobin and other proteins and consequently only superficial inflammatory foci (<1 cm deep) can be imaged with probes that emit light in this range of the spectrum. To overcome this problem, new probes like dyes that absorb and emit light in the near-infrared (NIR) region (700–1,000 nm) and quantum dots (semiconductor nanocrystals) have been developed for fluorescence imaging [11]. Most tissues show less autofluorescence and absorption in the NIR region than in the visible region and therefore visualization of deeper tissues can be achieved with NIR fluorophores. Still, fluorescence imaging is mainly suitable for application in small animals. The nonlinear attenuation of light by tissue makes quantification of optical imaging data a complicated task. Two-dimensional optical images

preferentially show superficial activity and cannot resolve depth. Tomographic optical imaging devices have now been developed to overcome these limitations [12]. Improved quantification and volumetric localization can be achieved using transmission images that can be generated with light source-detector pairs at multiple angles [13].

In bioluminescence imaging [14], cells within the animal have been engineered to produce a light-producing enzyme (luciferase). Firefly luciferase is most frequently used for bioluminescence imaging. In the presence of oxygen en adenosine triphosphate, firefly luciferase oxidizes its substrate luciferin and produces yellow-green light with an emission peak of approximately 560 nm. Luciferases of other species, such as click beetle, and luciferases that react with different substrates, such as sea pansy (Renilla) and marine copepod (Gaussia), have also been used. Besides these luciferases, the lux operons of bacteria like *P. luminescence* could also be used for bioluminescence imaging. Since the bacterial operon encodes all proteins that are required for bioluminescence, administration of an external substrate is not required. Unfortunately, attempts to transfect the bacterial operon into mammalian cells have remained unsuccessful. For bioluminescence imaging the same equipment can be used as for fluorescence imaging, although the external light source is not needed. Bioluminescence of firefly luciferase generates an emission spectrum, of which about 30 % is above 600 nm. Although a major portion of the light signal is absorbed and scattered by tissue, the low background associated with bioluminescence makes this technique more sensitive than fluorescence imaging.

In the context of infection and inflammation imaging, two types of optical imaging approaches can be discriminated: reporter gene imaging and imaging of a targeted ligand. For cell tracking, for example, the reporter gene approach is often used. Immune cells or pathogens (e.g. lymphocytes, bacteria, viruses) can be genetically engineered to express a fluorescent or luminescent reporter gene (e.g. GFP, luciferase, lux operon). After in vivo administration of the engineered cells, their migration can be repetitively monitored, as well as the effect of therapeutic intervention. Bioluminescence imaging is especially attractive for this purpose, since the low background associated with this technique allows detection of only a small concentration of cells [15]. The targeting ligand approach is frequently used in fluorescence imaging, but is not suitable for bioluminescence. In this method, a fluorophore is linked to a ligand with affinity for a specific process in infection or inflammation, such as a biomolecule that is overexpressed by a pathogen or an immune cell. Various fluorescently labeled ligands have been labeled, including antibodies [16], enzyme substrates [17], antimicrobial peptides [18] and antibiotic drugs [19].

2.4 Nuclear Imaging

Positron emission tomography (PET) and single photon emission computed tomography (SPECT) are nuclear imaging techniques that provide functional information about biochemical and physiological processes. Both PET and SPECT imaging are

based on the detection of radioactive radiation from a targeted tracer by a dedicated camera [20, 21]. After intravenous injection, the radioactive tracer migrates to the target organ, where it is trapped by interaction with e.g. receptors, transporters, enzymes or antigens. The accumulation of radioactivity in the target organ is a measure of the biological parameter that was investigated. PET and SPECT differ in the radionuclide that are employed to label the tracer and in the detection technology of the camera.

PET tracers are usually labeled with short-lived isotopes, like ^{11}C, ^{13}N, ^{15}O, ^{18}F, ^{64}Cu, ^{68}Ga, ^{89}Zr and ^{124}I with a half-life that varies from 2 min to 4 days. These isotopes decay all by emission of a positron, which travels a short distance in tissue, depending on its energy. When the positron has lost most of its energy, it interacts with an electron and undergoes a process called annihilation. In this process, the positron and electron are converted into two 511 keV photons that are emitted in opposite directions. Outside the body the electrons are detected by the PET camera. The PET camera contains ring of detectors that are located around the bore where the subject is placed. The PET camera only registers photons with the proper energy that are detected in coincidence (i.e. within 10 ns) by opposite detectors. The mostly used detectors are made from lutetium oxyorthosilicate (LSO) or its equivalent (LYSO) and gadolinium orthosilicate (GSO), because of the high gamma-ray stopping power of these materials. PET is high sensitive (picomolar concentration) because it does not require the use of a collimator. In contrast to e.g. optical imaging, PET is independent of tissue depth, because absorption of radiation by the body can be compensated for by attenuation correction using a transmission scan that is made with an external radioactive source or a CT scan (for hybrid systems). The spatial resolution of PET depends on the energy of the positron, the detector size and the bore size of the camera. Most clinical PET cameras currently have a spatial resolution of about 5 mm. Dedicated small animal PET scanners are now available with a spatial resolution of about 1 mm, which is mainly due to a reduction in bore and detector crystal size. For most animal scanners, however, the spatial resolution rapidly declines when moving away from the centre of the field-of-view. A major advantage of PET over other imaging techniques is that it allows absolute quantification of the biochemical parameter of interest by pharmacokinetic modeling. For quantification, not only the data from a dynamic PET scan, but also information on the plasma radioactivity and plasma metabolites over time are required. The plasma input function and plasma metabolites can be determined by repetitive arterial blood sampling during the PET scan. Arterial blood sampling for quantification is a major challenge in very small animals like mice [22]. In rats, the procedure is generally feasible, but longitudinal protocols are usually not possible, because of the arterial canulation and the relatively large volume of blood that is withdrawn. For some tracers, the tracer input curve that is required for quantification can be derived from the PET image itself by regions-of-interest analysis of the blood pool of the heart or a reference tissue.

For SPECT imaging, radionuclides that emit single photons are applied, such as ^{99m}Tc, ^{111}In and ^{123}I. In SPECT cameras a collimator is placed in front of the detector system. A collimator is a perforated plate—usually lead or tungsten—that rejects all

photons that do not travel in a specific direction. Because the collimator blocks most photons, the sensitivity of SPECT is about 2 orders of magnitude lower than that of PET. In most systems, the collimator and detector rotate around the subject in order to obtain data in three dimensions. Collimators with parallel holes perpendicular to the detector are usually applied in clinical SPECT cameras. For SPECT cameras with parallel-hole collimators the resolution is mainly determined by the geometry of the collimator and detector size. The resolution that is obtained with parallel-hole collimators (7–15 mm) is insufficient for small animal imaging. Therefore, pinhole collimators are used for small animal SPECT. Pinhole collimators can magnify an object according to the same principle as for a *camera obscura*. The magnification factor that can be obtained by the pinhole system equals the ratio of the distance between the detector and the pinhole and the distance between the subject and the pinhole. Pinhole systems with a resolution under 0.5 mm in mice and under 1 mm in rats are now commercially available. In pinhole systems, there is a trade-off between resolution, sensitivity and field-of-view. To improve the imaging performance, dedicated stationary systems with multiple pinholes have been developed [23]. These systems use a large number of small detectors in combination with multiple pinhole geometries, which significantly improves the sensitivity of these systems. However, the field-of-view that can simultaneously be covered by the multiple pinhole SPECT systems is very small (about 1 cm^3). Consequently, the acquisition of a "whole body scan" can be quite time-consuming. Quantification of SPECT data is a major technological challenge, due to limitations of the instrumentation and imaging process [24]. Attenuation and scatter are dependent on the photon energy—and thus the isotope—and the subject size. In rodents, attenuation of photons by soft tissue can be up to 50 % for ^{125}I and 25 % for ^{99m}Tc, whereas scatter may contribute 10–25 % to the total counts. Attenuation correction can easily be performed using an external radiation source or by acquiring a CT scan, followed by post-processing of the SPECT images. Methods for scatter correction, however, are still under development. Because of the low sensitivity of SPECT, the count rate of the system may severely affect the temporal resolution for dynamic imaging. In contrast to PET, multiple energy windows can be used in SPECT. This allows simultaneous imaging of different tracers with different isotopes, provided that proper correction for crosstalk of the different isotopes in other energy windows.

At present, various radiolabeled targeted probes are available for PET and SPECT imaging of infection and inflammation. These include antibodies, receptor ligands and enzyme substrates. An overview of the available radiotracers will be presented in the next section.

2.5 Hybrid Imaging

Each of the imaging modalities mentioned above has advantages and disadvantages. In a multi-modular approach, information from complementary imaging modalities is combined, so weaknesses of one modality can be compensated for by another

modality [2]. Usually, morphological imaging modality (i.e. CT, MRI) is used in combination with a molecular imaging modality (i.e. PET, SPECT, optical) to integrate anatomical and functional information. In this manner the exact location of a lesion can be pinpointed. For imaging of infection and inflammation, however, anatomical image fusion is not always important as it is in oncology and neurology. On the other hand, combination of two functional imaging modalities (e.g. optical and PET) could also be useful in, for example, translational research. There are basically two methods to integrate information from different modalities: software fusion and integrated hardware. For software integration, the images from different modalities should be transformed to align the objects, after which images can be fused. This methods, however, is prone to errors, because functional images can have too little anatomical information for correct realignment and internal organs (especially in the abdomen) can have shifted, when the subject was moved from one modality to the other. For small animal imaging, the realignment could be facilitated by the use of external fiducial markers or animal restraining systems. Integrated hardware systems do not suffer from these disadvantages. For clinical applications, integrated hardware systems like PET/CT and SPECT/CT are now routinely used, especially for tumor imaging. For small animal imaging, combined PET/CT and SPECT/CT systems and even triple PET/SPECT/CT systems have become available in the last years as well (Table 22.1). For brain and soft tissue imaging hybrid PET/MRI systems would be extremely useful. Combining PET or SPECT with MRI, however, is a technological challenge, because the photomultipliers that are currently used for PET and SPECT detector read-out do not function in the magnetic field of the MRI. Consequently, hybrid PET/MRI systems are still in the experimental phase of development. Attempts are made to place the photomultipliers outside the magnetic field of the MRI, or to use avalanche photodiodes instead of photomultipliers [25]. Prototype PET/MRI systems have already been built and the first results are promising. More detailed information about hybrid imaging systems can be found elsewhere in this book.

3 Radiopharmaceuticals

Conventionally used radiopharmaceuticals for imaging infections are ^{99m}Tc-albumin nanocolloids and radiolabeled leukocytes exploiting respectively the enhanced vascular permeability and the influx of leukocytes in inflamed tissues. During the past two decades various analogues of receptor-binding ligands for receptors expressed on leukocyte subsets have been tested for imaging infection and inflammation in small animals and also in humans. Apart from the defensive proteins in plasma, a large variety of chemical mediators (e.g. interleukins, chemotactic factors, vascular mediators) appears in the affected region that regulate the activity of the immune cells in the region. The immune cells involved (granulocytes, monocytes and lymphocytes) have specific receptors on their cell surface for these chemical mediators. In general, these chemical mediators have a high affinity

($Kd = 10^{-8}$–10^{-10} M) for the receptors on the leukocyte plasma membrane. Their high affinity makes these mediators suitable vehicles for the scintigraphic visualization of the homing of leukocytes in infectious and inflammatory foci [25]. Main radiopharmaceuticals for imaging inflammation/infection are summarized in Table 22.2.

3.1 Monoclonal Antibodies and Their Fab' Fragments

An antibody monomer has a Y-shaped structure with a molecular weight of approximately 150,000 Da, and the structure is composed of two identical light and heavy chains, which could be murine, chimeric, humanised and fully human. Monoclonal antibodies (mAbs) specifically bind to their target that could be adhesion molecules, activation markers, antigens or receptors. Several monoclonal antibodies and their Fab' fragments including anti-TNF-α, anti-CD25, anti-CD20, anti-DR, anti-CD3, anti-CD4, anti-MIF, anti-granulocyte and anti-E-selectin antibody, radiolabeled mainly with ^{99m}Tc, ^{111}In or ^{125}I, are used for the imaging of inflammation/infection lesions. Scintigraphic studies with these radiolabeled mAbs offer an exciting possibility for the detection of their specific targets in different inflammatory disease animal models; moreover, a positive scintigraphic image shows the presence of their target molecules in the inflammatory lesion. This technique allows whole body imaging and detects inflammation in an early stage of disease that might be difficult to assess clinically or by means of radiography. These monoclonal antibodies target pro-inflammatory cytokines (e.g. TNF-α, IL-1 and IL-6) and membrane bound receptors (e.g. CD3 and CD4). The use of antibodies against surface granulocyte or lymphocyte antigens may improve the ability to detect inflammatory processes compared to the use of radiolabeled autologous leukocytes, because of their higher specificity. The commercially available ^{99m}Tc-labeled mAbs are the BW250/183 (Antigranulocyte®), an IgG1 recognizing the nonspecific cross-reacting antigen 95 (NCA-95) expressed on human granulocytes, pro-myelocytes and myelocytes, the Fab' fragment IMMU-MN3 (Leukoscan®), and the SSEA-1, an anti-CD15 IgM (LeuTech®) with high affinity binding. Moreover, radiolabeled mAbs are always injected in a tracer (non-pharmacological) dose for scintigraphic imaging purpose which rarely induce any clinical or side-effects in the subject.

3.2 Peptides, Cytokines, Chemokines, Interferons and Growth Factors

Studies of peptides/receptor systems are providing a novel means by which, one can characterize cellular structures and tissues. Peptides are small, low molecular weight proteins (usually less than 10,000 kDa, and less than 100 amino acids). Different radioisotopes are currently used for peptide labeling. Among these, iodine isotopes (^{123}I and ^{131}I), ^{111}In and ^{99m}Tc are most frequently used. ^{99m}Tc is the most popular

Table 22.2 Radiopharmaceuticals for imaging inflammation/infection

Radiopharmaceutical	Target	Isotopes for labeling	Application in molecular imaging	Reference
Monoclonal antibodies and Fab' fragments				
Infliximab (Remicade®) [chimeric IgG1 mAb]	TNF-α	^{99m}Tc	Crohn's disease, rheumatoid arthritis imaging	[26–28]
Adalimumab (Humira®) [fully human IgG1 mAb]	TNF-α	^{99m}Tc	Rheumatoid arthritis imaging	[29]
1D09C3 [humanised IgG4 mAb]	HLA-DR	^{99m}Tc	Lymphoma imaging (experimental stage)	[30]
Basiliximab (Simulect®) [chimeric IgG1 mAb]	CD25	^{211}At	T-cell leukemia imaging	[31]
Daclizumab (Zenapax®) [humanised IgG1 mAb]	CD25	^{18}F, ^{99m}Tc, ^{111}In, ^{125}I, ^{212}Bi, ^{67}Ga	T-cell leukemia imaging	[32]
OKT-3 (Muromonab®) [murine IgG2a mAb]	CD3	^{99m}Tc	Rheumatoid arthritis and renal transplant rejection imaging in animal model and humans	[33]
Visilizumab (Nuvion®) [humanized IgG2 mAb]	CD3	^{99m}Tc	T-lymphocyte imaging in animal model	[34]
MAX.16H5 [murine IgG1 mAb]	CD4	^{99m}Tc	Rheumatoid arthritis imaging in animal model and humans	[35]
Anti-MIF mAb	MIF	^{125}I	Inflammation imaging in animal model	[36]
Anti E-Selectin [murine IgG1 mAb]	E-Selectin	^{111}In	Rheumatoid arthritis imaging in animal model and humans	[37]
Rituximab (Mabthera®) [chimeric IgG1 mAb]	CD20	^{99m}Tc	Sentinel lymph node (SLN) and rheumatoid arthritis imaging in animal model and humans	[38, 39]
Anti-granulocyte mAb (Leukoscan, sulesomab) [IgG1 mAb]	Human granulocytes	^{99m}Tc, ^{111}In	Imaging of fever of unknown origin and other acute inflammatory disorders, in human and animal models	[40, 41]

(continued)

Table 22.2 (continued)

Radiopharmaceutical	Target	Isotopes for labeling	Application in molecular imaging	Reference
Peptides, cytokines, chemokines, interferons and growth factors				
IL-1 α/β	IL1RI[a]=B, Mo, N, IL1RII=En, Fi, He, Ke, T	^{123}I, ^{125}I	Inflammatory process imaging in animal model	[42]
IL-1ra (receptor antagonist)	IL-1R	^{123}I, ^{125}I	Rheumatoid arthritis, Inflammatory process imaging in animal model and human	[43]
IL-2	T, B, NK	^{123}I, ^{125}I, ^{99m}Tc, ^{35}S	Graves' ophthalmopathy, type 1 diabetes, celiac disease, Crohn's disease, thyroid autoimmune disease, kidney graft rejection, cutaneous melanoma, atherosclerosis, kidney allograft imaging in animal model and humans	[44–48]
IL-8	N, Ba, T	^{99m}Tc, ^{123}I, ^{125}I, ^{131}I	Detection of infectious foci (abscesses), sterile inflammation and osteomyelitis in animal model and in humans	[49, 50]
IL-6, IL-10 G-CSF	T, B, Mϕ, He, HP, N, phagocytes	^{125}I	Infectious foci imaging in animal model	[51]
IL-12	T, NK	^{125}I	T-lymphocytes and lymphocytic infiltrates imaging in animal models	[52]
MCP-1	Mo, Mϕ, Gr	^{99m}Tc	Subacute inflammation imaging in animal model	[53, 54]
IFN-g	Many different cells	^{123}I	Lung inflammatory diseases imaging	[55]
Epidermal growth factor (EGF)	EGFR	^{123}I, ^{111}In, ^{125}I	Metastatic lymph nodes in humans, imaging of breast cancer, study of skin wounds	[56]
Tumour growth factor beta (TGF-β)	TGF-RI-V, many different cells	^{125}I	Imaging study of angiogenesis	[57]
Leukotriene (LTB_4)	BLT1, BLT2	^{99m}Tc	Inflammation/infection imaging in animal model	[58]
LTB_4 receptor antagonist (RP517; DPC 11870-11; MB88, fMLFK)	LTB_4 receptors	^{99m}Tc, ^{111}In	Infection imaging in animal model	[59, 60]

IIa-IIIb receptor antagonist (DMP444)	IIa-IIIb	^{99m}Tc	Imaging of infective experimental endocarditis	[61]
Neutrophil elastase inhibitor (EPI-HNE-2/4)	Neutrophil elastase	^{99m}Tc	Inflammation/infection imaging in animal model	[62]
Antimicrobial peptides (UBI 29-41, P483H, HNP1-3, hLF)	Bacteria and fungi infection	^{99m}Tc	Infection imaging in animal model and in humans	[25, 63, 64]
Bacteriophage	Bacteria	^{99m}Tc	Infection imaging in animal model	[65]
Antibiotics				
Ciprofloxacin (Infecton™)	Prokaryotic topoisomerase IV and DNA gyrase	^{99m}Tc	Microbial infection imaging in animal model and in humans	[66]
Sparfloxacin	Gram-positive and gram-negative bacteria	^{99m}Tc	Bacterial infection imaging in animal model	[67]
Ceftizoxime	Bacterial wall	^{99m}Tc	Bacterial infection imaging in animal model	[68]
Isoniazid	Mycobacteria	^{99m}Tc	*Mycobacterium tuberculosis* infection in animal model	[69]
Ethambutol	Mycobacteria	^{99m}Tc	Mycobacterial infection imaging in animal model	[70]
Fluconazole	Fungal infections	^{99m}Tc	Fungal infection imaging in animal model	[71]
Other radiopharmaceuticals				
Human polyclonal immunoglobulin (HIG)	Non-specific	^{99m}Tc, ^{111}In	Inflammation/infection imaging in animal model and humans	[72, 73]
Fluorodeoxyglucose (FDG)	Activated lymphocytes, monocytes and granulocytes	^{18}F	Imaging in animal model and humans for inflammatory disorders such as lymphoma, vasculitis, sarcoidosis, rheumatoid arthritis, Alzheimer's and Parkinson's disease etc., and in infections such as osteomyelitis, spondylodiscitis, prosthetic joint infection etc.	[74]
^{67}Ga-citrate	Transferrin receptors (CD71)	^{67}Ga	Imaging in animal tumor model and imaging of fever of unknown origin in HIV patients	[75]

(continued)

Table 22.2 (continued)

Radiopharmaceutical	Target	Isotopes for labeling	Application in molecular imaging	Reference
Autologous human leukocytes	Active migration in inflammatory lesion	^{111}In, ^{99m}Tc-HMPAO	Acute inflammation imaging in animal model and humans	[76]
Albumin nanocolloids	Non-specific extravasation	^{99m}Tc	Rheumatoid arthritis, and other inflammatory lesion imaging	[77]
JOO1X	CD11b, CD14 (macrophages, monocytes)	^{99m}Tc	Arthritis, chronic berilliosis, and other inflammatory lesions imaging in animal model	[78]
Octreotide (Octreoscan®)	Somatostatin receptor	^{111}In, ^{123}I, ^{99m}Tc	Imaging of granulomatous and chronic inflammation in animal model and human	[79]
Liposomes	Cells of reticuloendothelial system	^{111}In, ^{99m}Tc	Small animal models of osteomyelitis, experimental colitis and focal infection	[80, 81]
Avidin-biotin	Non-specific extravasation	^{111}In	Osteomyelitis and endocarditis imaging	–

Abbreviations: *B* B lymphocytes, *Ba* basophils, *EGFR* epidermal growth factor receptor, *Ep* epithelial cells, *En* endothelial cells, *Fi* fibroblast, *Gr* granulocyte, *He* haematopoietic cells, *HP* haematopoietic precursor, *Ke* keratinocyte, *Lym* lymphocytes, *Mo* monocytes, *Mϕ* macrophage, *T* T lymphocytes, *N* neutrophil, *NC* neoplastic cells, *NK* natural killer cells, *SMS* smooth cell muscle

[a]IL1RI, IL1RII, TNF-R1, TNF-R2: receptor types I and II

isotope for nuclear medicine studies, due to its favorable physical and dosimetric features, wide availability and relatively low cost. Although, radiolabeling with transitional metals, like ^{99m}Tc, can be rather cumbersome and quite complex; especially for small peptides, direct labeling can be unstable and non-specific, and for these reasons peptide labeling with ^{99m}Tc is usually performed using a bifunctional chelating agent. Compared with larger molecules, like proteins and mAbs, peptides are rapidly taken up and retained in target tissues, in accordance with the usually rapid plasma clearance due to the renal excretion. Major peptide features include (i) rapid pharmacokinetics, (ii) possibility of modification in the excretion route, (iii) biologically active, (iv) usually not immunogenic, and (v) high receptor binding affinity. For both monoclonal antibodies and small peptides, the choice of radioisotope and radiolabeling method can play a major role in the overall in vivo distribution and in the target to non-target ratios achieved.

A cationic human antimicrobial peptide fragment, ubiquicidin 29-41 (MW 1.69 kDa) with the aminoacid sequence Thr-Gly-Arg-Ala-Lys-Arg-Arg-Met-Gln-Tyr-Asn-Arg-Arg, and 6 positively charged residues (5 Arg + 1 Lys) was labeled with ^{99m}Tc. In animal studies ^{99m}Tc-UBI showed rapid visualization of infections with gram-positive and gram-negative bacteria but little accumulation was found in sterile inflammation processes. A very recent study described the quantitative uptake of ^{99m}Tc-UBI 29-41 in rabbits with *S. aureus* infections during treatment with ciprofloxacin. The results showed that the uptake of the radiotracer was significantly decreased after treatment and was proportional to the number of bacteria suggesting that the tracer might be used for monitoring the efficacy and duration of treatment [82].

Cytokines are proteins and glycoproteins members of a family of overlapping and interdependent molecules with important roles in the homeostatic control of the immune system and other organs, in physiology and pathology. Most cytokines are between 15 and 25 kDa and they are often similar in size, charge and glycosylation. The major sources of cytokines are T cells and macrophages but their production varies depending on the individual cytokine; IL-2 is produced mainly by activated T cells whereas IL-1 can be produced by macrophages, endothelial cells, large granular lymphocytes, T and B cells, fibroblasts, epithelial cells, astrocytes, keratinocytes and osteoblasts. Cytokines act via the interaction with specific cell surface receptors expressed on a known cell population; cytokine receptors, usually of high affinity, are generally expressed at low levels on resting cells but their expression can be upregulated during activation. Many cytokines have good characteristics as radiopharmaceuticals and they are characterised by (i) small molecular weight as compared to other radiopharmaceuticals, (ii) rapid half life and plasma clearance, (iii) high-affinity binding to specific receptors, (iv) ready availability by DNA recombinant technique, and (v) human recombinant origin and lack of immunogenicity.

Several groups, pioneered by Signore et al. [44, 83], have radiolabeled IL2 with ^{123}I or ^{99m}Tc to target T lymphocytes and monocytes in chronic, mononuclear cell-mediated inflammatory processes such as autoimmune diseases, kidney graft rejection and melanoma characterized by over-expression of CD25 (IL2 receptors). Clinical studies have demonstrated the efficacy of using scintigraphy to detect

radiolabeled IL2 specifically targeted to activated lymphocytes, which correlates with the severity of tissue lymphocytic infiltration and can be used to monitor the efficacy of therapies. In animal models, ^{125}I labeled IL12p40, a peptide derived from IL12, a Th1-specific cytokine, has shown specific binding to tissue-infiltrating lymphocytes. Radiolabeled IL1 and IL1 receptor antagonist (IL1ra) have also been extensively studied in animal models of acute inflammation, where they have shown specific binding to granulocytes, and in humans in rheumatoid arthritis.

Other cytokines have also been used for the detection of specific receptors in several pathologies. ^{125}I-labeled tumor growth factor beta (TGF-β) has been used for the study of angiogenesis and radiolabeled epidermal growth factor (EGF) has been used for the study of metastatic lymph nodes, for imaging breast cancer and for the study of skin wounds. Most radiolabeled cytokines have been used for the study of inflammatory diseases, e.g. ^{99m}Tc-labeled monocyte chemotactic peptide-1 (MCP-1) for specific imaging of macrophages in animal models of subacute inflammatory diseases, IL6 for targeting of acute inflammation and ^{123}I-interferon-gamma for investigation of lung disease.

Chemokine receptor ligands have also been labeled for in vivo imaging of inflammatory sites. Studies have extensively investigated IL8 in the preclinical setting. IL8 is a member of the CXC family of chemokines that binds with high affinity to the type I and II CXC receptors abundantly expressed on neutrophils and monocytes. Radiolabeled IL8 reveals high and specific accumulation at the focus of acute infection within a few hours after injection both in animals and in humans.

3.3 Antibiotics

Imaging agents that target cell receptors expressed on the cells infiltrating inflamed tissue, which are recruited during the inflammatory response, and accumulate in the focus due to a common feature of infection and inflammation, cannot be used to differentiate between infection and inflammation. Agents that specifically target the infectious organisms (e.g. bacteria, fungi or viruses) have the potential to distinguish microbial from non-microbial inflammation. During the last decade a few agents have been presented, that aim to specifically visualize infectious foci by targeting the infectious organisms. In search for an infection diagnosis agent, antibiotic radiolabeling was first introduced by Solanki et al. in early 1990s. Ideally, the radiolabeled antibiotic should be metabolised and specifically incorporated by the micro organisms present in the infection, so that accumulation of radioactivity is directly proportional to the number of micro organisms present in the infection. Several antibiotics have been radiolabeled so far, such as ciprofloxacin, sparfloxacin, enrofloxacin, levofloxacin, norfloxacin and ofloxacin, and most of them of these are members of quinolones class. Although radiolabeled antibiotics opened a new and promising door in the search of an infection specific imaging agent, published results are controversial and, still more studies are required to understand the efficacy of this radiopharmaceutical in differentiating infection foci from sterile inflammation [45].

3.4 Other Radiopharmaceuticals

3.4.1 Human Polyclonal Immunoglobulin (HIG)

Human polyclonal immunoglobulin is a non-antigen specific IgG antibody that can be labeled with ^{99m}Tc or ^{111}In and has been proposed for the detection of acute and subacute inflammation/infections; since HIGs are of human origin, they do not produce allergic reactions. Furthermore, they are commercially available as kits. The use of ^{111}In involves a few disadvantages: it causes a relatively high radiation burden, its gamma radiation is sub-optimal for in vivo imaging, it is not always easily available and expensive. ^{99m}Tc is a more attractive alternative due to its short half-life, availability and lower cost. The mechanisms of HIG uptake in inflamed tissues are not yet fully known. Among various hypotheses, the increase of vascular permeability seems to be the main mechanism of their accumulation [72, 73]. Nevertheless, further binding mechanisms such as to the Fc receptor expressed by infiltrating cells, to the extracellular matrix proteins and to bacteria have been described. HIGs have proven to be very useful in lung inflammation imaging, for the detection of joint and bone inflammations and infections, and the study of fever of unknown origin.

3.4.2 Fluorodeoxyglucose (FDG)

The FDG (2′-deoxy-2′-fluro-D-glucose) accumulation in activated lymphocytes, monocytes and granulocytes is based on the fact that these cells use glucose as an energy source only after activation during the metabolic burst. Transport of FDG across the cellular membrane is mediated by glucose transporter protein. ^{18}F is a positron emitter with a physical half-life of 1 h and 50 min. Intracellular FDG is subsequently phosphorylated to ^{18}F-FDG-6 phosphate by hexokinase enzyme and phosphorylated molecule remains trapped inside the cell in contrast to phosphorylated glucose that enters the glycolysis cycle. However, ^{18}F-FDG is an unspecific tracer for imaging inflammation/infection and can show uptake in any kind of cell with high glycolytic activity and may provide a false-positive result. Several recent studies with ^{18}F-FDG PET (^{18}F- fluorodeoxyglucose positron emission tomography) demonstrated very promising results for imaging in different inflammation/infection, although it is quite expensive [74].

3.4.3 ^{67}Ga-Citrate

^{67}Ga-citrate was discovered in 1971, for imaging infection and inflammation. ^{67}Ga-citrate binds in ionic form to circulating transferrin as an analogue of iron. It uses transferrin receptors (CD71) to access the cell and then becomes highly stable within the cells. During acute inflammation condition, ^{67}Ga-citrate extravasates at

the site of inflammation due to the locally enhanced vascular permeability, where it binds with high affinity to lactoferrin excreted by leukocyte or to siderophores, produced by micro organisms grown in a low-iron environment [75]. Approximately, 25 % of the total injected dose is excreted through urinary system and rest is retained in the bone, bone marrow, liver and soft tissues. However, the radiopharmaceutical has long physical half-life (78 h) and high energy gamma radiation, which are unfavorable characteristics for scintigraphic imaging and cause high radiation absorbed dose. The use of this radiopharmaceutical is mainly involved the study of chronic osteomyelitis, lung infection and fever of unknown origin (FUO).

3.4.4 Autologous Human Leukocytes

Radiolabeled leukocytes are considered as a 'gold standard' for the imaging inflammation techniques in nuclear medicine. These autologous leukocytes are characterized by high specificity, because they only accumulate as a consequence of active migration into inflamed joints. After intravenous injection, the radionuclide shows a rapid clearance of activity from normal lungs and blood-pool, because of the high uptake in neutrophilic infiltrates [76]. Radiolabeled leukocytes first adhere to vascular endothelium and then migrate towards the inflammatory focus through endothelium and basal membrane. Thus, these radiopharmaceuticals are specific indicator for leukocytic infiltration, but not for bacterial contamination. There is no kidney, bladder or bowel excretion showed by ^{111}In-leukocytes, so the whole abdomen is an excellent field for localization of infectious or inflammatory disease. In contrast, ^{99m}Tc-HMPAO is released from the leukocytes within few minutes after administration and excreted by kidneys up to 7 % of the injected dose per hour. However, ^{111}In-oxine has a long half-life of 67 h and radiation energy of 173 and 247 keV that gives an extra radiation burden, whereas ^{99m}Tc has short half-life of 6 h and ideal γ-radiation energy of 140 keV. Leukocytes must be separated from other blood cells before labeling, otherwise ^{111}In/^{99m}Tc being lipophilic, label every cell type indiscriminately.

3.4.5 Albumin Nanocolloids

As the name indicates these are albumin derived small particles of 30–80 nm diameters. Non-specific extravasation due to increased vascular permeability cause the leakage of ^{99m}Tc-nanocolloids into inflamed tissue followed by accumulation through the phagocytosis by macrophages in the reticulo-endothelial system [77]. These are characterized by rapid blood clearance and satisfactory target to background ratio early after the administration which allows completion of study usually within 1 h. This technique is easy to perform and inexpensive.

3.4.6 JOO1X

J001X is a non-pyrogenic acylated polygalactoside, purified from the from the membrane proteoglycans of a non-pathogenic strain of *Klebsiella pneumoniae*. It selectively binds to CD11b, complement receptor 3 expressed on monocytes, NK cells and macrophages, as well as to CD14, the lipopolysaccharide receptor expressed on macrophages and monocytes. It preferably binds to macrophages, mainly in their activated state. In principle, ^{99m}Tc-J001X could image inflammatory foci because these are also characterised by the recruitment of macrophages. Radiolabeled J001X has been used in several experimental animal studies including alveolitis and inflammatory lymph nodes in chronic berylliosis in baboons, inflammatory lesions in pigs and rabbit arthritis model [78].

3.4.7 Octreotide

The somatostatin analogue ^{111}In-labeled octreotide (Octreoscan®) was officially introduced in 1994, and its use to visualize various somatostatin receptor-positive tumours and tissues is widely accepted. Somatostatin receptors are expressed on normal and activated lymphocytes and macrophages. A study was performed with ^{111}In-octreotide in patients with sarcoidosis, aspergillosis, tuberculosis and Wegener's granulomatosis [79]. Whole body images were acquired after administration of ^{111}In-octreotide. In this study, granuloma localizations were clearly visualized in all patients studied. Binding of ^{111}In-octreotide at sites of granulomatous inflammation was also verified by in vitro autoradiography. In contrast to the potential of octreotide in the detection of chronic inflammation, studies in animal models of *Staphylococcus aureus* induced foci in rats revealed that ^{111}In-octreotide is not suitable for the detection of experimental abscesses, as lower accumulation than control ^{111}In-HIG was noted with no retention with time.

3.4.8 Liposomes

Liposomes are microscopic lipid vescicles that are usually used as carriers for drugs to increase their solubility and to achieve selective deposition or to reduce toxicity. These are rapidly taken by the reticuloendothelial (RES) cells. Liposomes are radiolabeled with ^{99m}Tc and have been used for the detection of infection and inflammation [80, 81]. Sterically stabilized liposomes have been formulated; they show decreased uptake by the RES, a longer half-life and enhanced localization in tumors and site of infection. Several studies with ^{111}In or ^{99m}Tc labeled liposome in different small animal models demonstrated its ability for the scintigraphic detection of infection and inflammation, such as focal infection in rats and experimental colitis in rabbits.

3.4.9 Avidin-Biotin

Avidins are family of proteins present in the eggs of amphibians, reptiles, and avians; streptavidin, produced by *Streptomyces avinii*, is also part of the same family. Both avidin and streptavidin (MW 64-60 kDa) have four sites for the binding of biotin with very high affinity ($K_d = 10^{15}$). Biotin, also known as vitamin H, is a compound of low molecular weight that can be radiolabeled with variety of different radiometals. The avidin-biotin system has been used for the in vivo labeling of monoclonal antibodies for the radioimmunodiagnosis of tumors. Radiolabeled biotin readily accumulates in the inflamed tissue where it binds irreversibly to streptavidin, whereas non-bound biotin is rapidly cleared through the kidneys with minimal accumulation in normal tissues [84, 85]. However, they are of heterologous origin and can cause immune responses, but there is no evidence to date that avidin or streptavidin are toxic.

The use of avidin-biotin system has been studied in animal model of acute infection where it accumulated in the infected focus more than ^{111}In-HIG. The major advantages of this approach are increased concentration of the radiotracer at the target tissue, a good target to background ratio and early acquisition of images.

4 Animal Models

In the development process of any new radiopharmaceutical, the in vivo testing is an important and unavoidable step, since it represents the link between in vitro specificity tests and clinical evaluation. Performing an evaluation at an early stage of the candidate tracer in an animal model would give useful information regarding its biodistribution, toxicity, route and extent of excretion, interaction with the host and micro-organisms and of course its in vivo specificity. Moreover the animal data are placed as a prerequisite by the guidelines for the clinical evaluation of a new radiopharmaceutical together with the reliability of the model. It is important to underline that the more the model can mimic a human pathology the more it is possible to use the obtained data as a starting point for the subsequent human studies, even if their predictive value could be low due to different factors, e.g. receptors variability, kinetic and biodistribution of the tracer in different species, etc. So, on the way that leads a radiopharmaceutical to be developed the choice of the best model is a crucial point in order to obtain reliable results that justify, or not, the passage at the clinical stage. This choice is not always an easy task, since the models of infection and inflammation are many and present different advantages and drawbacks, like in the case of the thigh muscle model, which is one of the most common for imaging infection and a convenient screening tool, but that present a very artificial condition which is nearly impossible to verify in humans. On the basis of these findings, the nature and course of the pathology should be kept in mind by the investigator in order to choose and design the appropriate model, and it is worthy to mention that there is not a perfect model and depending on the aim of the study variations can be introduced in the chosen one. Here we report a few examples of some models for infection and inflammation which can be used for imaging studies.

4.1 Thigh Muscle Model

The thigh muscle model is widely used to assess the in vivo specificity of radiopharmaceuticals to bacteria and provide a simple and versatile screening tool. It was born as a model for pharmacokinetic experiments in 1940 [86], but it is suitable for imaging infection like many other models that were born for different purposes. It is based on the induction of an abscess in the thigh or calf muscle of the animal. The infection can be performed under anaesthesia through the injection of a 1:1 solution of autologous blood and saline with the micro-organism of interest in the growing phase. The evaluation of the infection can be performed 24 h after the infection by palpation, since local swelling should be evident, or alternatively by aspiration of a fluid sample from the muscle, that can be put in culture into agar plates. As a supplementary test, the grown colonies can be fixed on a slide, stained and then observed at the microscope for the identification of the strain. The sterile control can be performed with the injection of saline, while the sterile inflammation can be performed with the injection of heat killed bacteria or alternatively zymosan, which cause infiltration of granulocytes, and turpentine oil, which cause increased hyperaemia. The animal can be infected with many of the common used micro-organisms such as *Staphylococcus aureus, Streptococcus pneumoniae, Haemophilus influenzae, Escherichia coli, Klebsiella pneumoniae, Pseudomonas aeruginosa* and *Candida albicans*. This model of infection is one of the most common, easy and fast to reproduce in different species such as mice, rats and rabbits with many advantages. It is not needed neither a surgical procedure nor specialized housing or care of the animals. The model is reproducible with low variability and if performed in mice the costs would be highly reduced. Anyway the cons of the model consist in the too rapid infection, generated by the injection of a consistent amount of CFU, which is not such a 'natural' condition, with the exception of pyomyositis which is a very rare infection [87].

4.2 Endocarditis Model

Infective endocarditis is a diagnostic and therapeutic challenge characterized by a particular interaction between the pathogen and the host tissue which may lead, through the formation of a septic thrombus to injury of both underlying valvular and cardiac tissue and a septic state caused by the spread of the micro-organism due to the thrombus degradation. One of the developed model is based on the induction of an aortic valve thrombotic vegetation by the insertion of a polyethylene catheter into the left ventricle through the right carotid artery under anesthesia (intramuscular injection with ketamine hydrochloride 15 mg/kg). In detail keeping the animal in a dorsal position, an incision should be done along the right side of the trachea, exposing the carotid artery to permit a ligature with a silk suture. In order to mark the portion of artery where the catheter will be introduced via a guide-wire, upstream of the ligature should be placed a clamp on which the catheter can be fixed after

removing the guide. After removing the clamp, the catheter can be introduced further until there is some resistance, which it means that the tip is some millimetres far from the semilunar cusps of the aortic valves [88]; alternatively to check the position of the catheter, a manometer can be connected to it [89]. The end of the catheter remaining outside the vessel can be folded and the incision closed with silk, keeping the catheter in situ until the end of the experiment. This procedure is necessary to obtain valvular lesions with the formation of aseptic vegetations typical of nonbacterial thrombotic endocarditis, triggered by the deposition of platelets and fibrin on the damaged areas. After 24 h from the surgery the micro-organism of interest can be inoculated through the i.v. injection of bacteria that will interact with the platelets forming septic vegetations. There are other variants of this model in which the bacteria are inoculated directly through the catheter which can be also removed after the surgery, but this situation is much less comparable to the clinical one in human. The infection can be monitored counting the colony forming units (CFU) of bacteria per gram of vegetations, but usually the animals will suffer of the classic symptoms of endocarditis corresponding to the human ones such as fever, anemia, positive blood cultures, peripheral emboli and secondary septic localizations. The model can be used either in rabbits or rats; the former present larger vegetations and is more expensive, whereas the latter are easier to handle and cheaper. The developed endocarditis is very close to the infective one in human, with the limit imposed by the differences between the species. The pathophysiology of the damage caused by the catheter differs from the events that predispose humans to endocarditis, with the exception of the one associated with prosthetic valve infections. Finally, the bacteremia produced in the animals is much higher and characterized by a single strain, whereas the one that leads to endocarditis in humans is more often heterogeneous and with possible different septic vegetations.

4.3 Tissue Cage Fluid Model

In pharmacokinetic studies, the tissue cage model is one of the best to reproduce the characteristics of human device-associated implants. In this model a perforated cylinder of teflon is implanted subcutaneously and then a bacteria inoculum is injected directly inside the cage. The surgery is quite simple, under anesthesia, it is only needed to make an incision in the skin and dissect the subcutaneous epifascial space in which the cage can finally be implanted and the lesion closed with metal clips. The interstitial fluid will start to accumulate inside the cage the week following the surgery and can be aspirated for sterility controls. Also granulocytes will colonize the cage, but they showed a limited phagocytic activities and a lower oxidative metabolism, maybe due to the continue exposure to the inert surface of the cage. Histologically, a richly vascularized granulation tissue is present, containing lymphocytes, fibroblasts and collagen fibers. At this point the bacteria can be injected and they will colonized the space inside the cage. Even if this model was born for different purposes it is a promising tool for radiopharmaceutical screening since it

presents a lot of advantages. As mentioned above, the main one is that it closely resembles a human infection; it is cheap and easy to develop. Different species can be used such as mice, rats, rabbits and guinea pigs and they do not need any specialized housing or care. Anyway it has his own pitfalls, since most devices fulfill mechanical functions and they are not subcutaneous but in the blood stream, near bones or in brain tissue.

4.4 Inflammatory Bowel Disease Models

Inflammatory bowel disease (IBD) is a group of inflammatory conditions that may affect the whole gastrointestinal tract and the most representatives types of the disease are Crohn's disease (CD) and ulcerative colitis (UC).

4.4.1 Ulcerative Colitis

Acute colitis can be easily induced by an intracolonic administration of 50 % ethanol containing trinitrobenzene sulfonic acid (TNBS). The mice should be anesthetized so that a cannula or a catheter can be inserted rectally to deliver the solution into the lumen. The cannula can be removed after some seconds and the animal will develop an acute colitis in 24–48 h post administration [90, 91]. The controls can be obtained with the administration of saline or 50 % ethanol. Histologically, multiple areas of mucosal necrosis (ulceration) can be observed at the site of instillation and the part of the colon between the instillation site and rectum. The submucosa becomes edematous and massive transmural granulocytic infiltration is present [92]. Alternatively, chronic colitis can be induced in mice adding a 5 % solution (wt/vol) of dextran sulfate sodium (DSS) to the drinking water for 5 days, then the solution can be replaced with normal water for 11 days. In a first moment the animals will develop an acute colitis with the classic symptoms represented by body weight and lose fecal consistency. In a second moment the acute colitis will turn into a chronic one and the symptoms will be attenuated. The ex vivo assessment of the inflammatory markers can confirm an ongoing local and systemic inflammatory response. The DSS damages the colonic epithelium and ulceration, mucosal damage, production of cytokines and other inflammatory mediators, and leukocyte infiltration will occur, resembling the human disease [93]. Even if the symptoms are similar, the mechanisms is very different and in the DSS model still not well known [94], so the investigator should keep it in mind when analyzing the data from the studies. The reproducibility of these models is good, but in the same group of animals a high degree of variation can be observed, depending on the variability of the animal response to the inflammatory stimuli [95]. Regarding the former model, the developed colitis is a very bad condition for the animals with high risk of peritonitis, which can be avoided with fasting. Anyway these models provide a valid tool to study many important aspects of the disease, even if they do not represent the complexity of the human condition.

4.4.2 Crohn's Disease

The SAMP1/Yit mouse is a model of intestinal inflammation which resembles the characteristic of CD developing a spontaneous and chronic ileitis without any chemical, immunologic, or genetic manipulations and described by Kosiewicz et al. [96]. Like in Crohn's disease, the T cells in the mouse lesions produce IFN-γ and the disease can be transferred through these cells to normal recipient mice. In 20 weeks of age the mice will develop spontaneous ileitis with a penetrance of the 100 % and a progression of severity over time and characterized by discontinuous inflammation containing granulomata is present mainly in the small intestine. Other typical symptoms of CD such as alterations in intestinal mucosal architecture, thickening of the bowel wall, and phenotypic alterations of the intestinal epithelial cell population in inflamed areas are present. Finally, in recipient mice the disease can largely be prevented by administering anti-TNF-α delimitating a significant parallel with human Crohn's disease, which makes the model much more reliable than the others.

4.5 Atherosclerosis Models

A common hypercholesterolemic model of atherosclerosis is easily obtained in rabbits feeding them with a cholesterol enriched diet for 8 weeks. The cholesterol levels can be monitored through blood analysis whereas lesions of the aortic valve with infiltration of extracellular lipid deposits and myofibroblast cells can be observed with light microscopy and immunostaining. A wide used model is the apolipoprotein E-deficient mouse ($ApoE^{-/-}$), that develops spontaneously fatty streaks (accumulation of macrophages) throughout the vasculature by 3 months of age and coronary artery occlusion within the first year of life. The rate of atherosclerosis can be enhanced by feeding them with a high-fat diet. It represents an early optimal model of rapidly advancing atherosclerosis with a limitation that consists in the difficult follow-up of the progression or regression of atherosclerosis in vivo, which it makes necessary to sacrifice the animals at different time points. Regarding this topic, the development of MRI techniques represents a promising tool that can provide a non-invasive monitoring of atherosclerotic lesions degree [97]. The $LDLr^{-/-}ApoB^{100/100}$ mice is another model predisponed to develop on a chow diet, a calcific aortic valve stenosis, a pathology that shares common features and risk factors with atherosclerosis and reveals parallels such as lipid deposition, inflammation, cellular reaction and matrix remodelling [98]. If the animals are kept on a high cholesterol diet, they develop a severe hyperlipidemia and steatohepatitis, which reduce their viability. The model develops moderate hypercholesterolemia with a level of cholesterol in serum of 271 mg/dL and a consequent reduction of the systolic aortic valve orifice diameter by 50 %. These two genetically engineered mouse models have a lot in common with the syndrome in human, obesity included and have been studied extensively, so that they can be considered a first choice when planning an animal study on atherosclerosis.

4.6 Animal Models with Induced Inflammation

For the study of inflammatory processes a delayed- type hypersensitivity reaction (DTHR), which are involved in several common autoimmune disorders in humans, can be induced in mice sensitizing the abdominal skin with a hapten provoking contact hypersensitivity reactions (CHSRs). It is needed the application of 5 % 2,4,6-trinitrochlorobenzene (TNCB), dissolved in a mixture of acetone and olive oil. After 1 week, an acute TNCB-specific CHSR can be elicited by challenging the mice on both sides of one ear with 1 % TNCB, dissolved again in a mixture of acetone and olive oil. The application of TNCB should be repeated every 48 h, up to 13 times, to induce chronic skin inflammation. The assessment of the degree of inflammation can be performed after the elicitation of CHSR at an ear, through measurement of ear thickness before the first TNCB challenge and 12 h after every subsequent ear challenge [99]. Histologically, the presence of typical changes found in acute inflammatory responses, such as a dense dermal infiltration of polymorphonuclear leukocytes and lymphocytes, as well as the formation of subepidermal abscesses can be confirmed by examination of ear tissue, hematoxylin- and eosinstained, 12 h after the first TNCB challenge. Chronic TNCB-specific inflammation should present symptoms acanthosis and hyperkeratosis. In general inflammatory processes possess a high degree of vascularization that can cause an unspecific uptake of radiopharmaceuticals in scintigraphic tests, so it is needed to find expedients to avoid this situation, e.g. assessing the specificity of the tracer with competition tests.

4.7 Rheumatoid Arthritis (RA) Model

The collagen-induced arthritis model is the best known induced model. It is reproducible in susceptible strains such as DBA/1, B10.Q and B10.RIII by immunization with type II collagen (CII) in complete Freund's adjuvant. Since the immunity of B and T cells against the autologous CII is required, the injected one should be obviously from a different source like bovine or porcine and should be as much purified as possible in order to avoid false positives or less arthritogenic events. As mentioned above the model is very well known, reproducible and resembles in many aspects the human disease. Alternatively a hybrid animal/human system has been developed implanting human cartilage biopsies subcutaneously in severe combined immunodeficiency (SCID) mice. Afterwards human fibroblasts can be isolated from rheumatoid synovium and injected in the bloodstream with the consequent invasion of the implanted cartilage that is not dependent on B and T cells stimulation. Whereas the former gives an overview of the main events that occur in the human disease, the latter remarks the role of the fibroblasts in long-lasting RA, which is damaging even in the absence of inflammatory stimuli. It is important to underline this concept, since the model is much more suitable for studies that target the cellular components of arthritis.

5 Small-Animal Imaging in Inflammation and Infection

5.1 Single Photon Emission Computed Tomography (SPECT)

Number of studies has been performed in different inflammation and/or infection animal models by SPECT using different radiopharmaceuticals. These studies are mainly concerned with the evaluation of new radiopharmaceuticals in small animal models for their specificity and sensitivity. Some examples are discussed below.

5.1.1 SPECT for Inflammation Imaging

Mice Model of TNBS Induced Colitis

A study was undertaken to evaluate a scintigraphic technique, to assess lymphocyte trafficking in a trinitrobenzene sulfonic acid (TNBS) induced Balb/c mouse model of colitis [100]. Colitis was induced by rectal administration of 0.5–2 mg TNBS dissolved in 40 % ethanol, using a vinyl catheter that is positioned 3 cm from the anus. Control mice undergo identical procedures, but are instilled with saline (NaCl 0.9 %). Murine splenocytes were radiolabeled in vitro with ^{111}In-oxine and injected into either TNBS colitis or control mice. Specific radioactive uptake, representing transferred cells, was determined by serial dedicated animal planar scintigraphy and pinhole SPECT of the abdomen 4, 24 and 48 h post injection of ^{111}In-oxine lymphocytes (Fig. 22.1).

The highest visible uptake was detected in colitis mice injected with sensitized lymphocytes. Planar pinhole scintigraphy performed on cleaned colon resection specimen showed clear uptake in colitis mice injected with sensitized lymphocytes, and no or minimal uptake in control groups. There was a significant higher mean visual uptake ($p<0.01$) on transverse SPECT slices in TNBS colitis recipient mice injected with sensitized lymphocytes as compared with control groups. There was a significant higher uptake ratio ($p<0.01$) of sensitized (TNBS) lymphocytes in TNBS colitis recipient mice as compared with control groups. Histological scoring confirmed the presence of colitis in the TNBS treated groups.

This study concluded that the homing of TNBS-sensitized lymphocytes can be assessed in vivo by an animal pinhole SPECT modality.

Rodent Model of Occlusion/Reperfusion Injury

In a recent study, ^{99m}Tc-HYNIC-annexin V small animal SPECT radionuclide imaging was used to follow the response of neuroprotective therapy with monoclonal antibody raised against FasL in a rodent model of transient left middle cerebral artery (MCA) intraluminal thread occlusion [101].

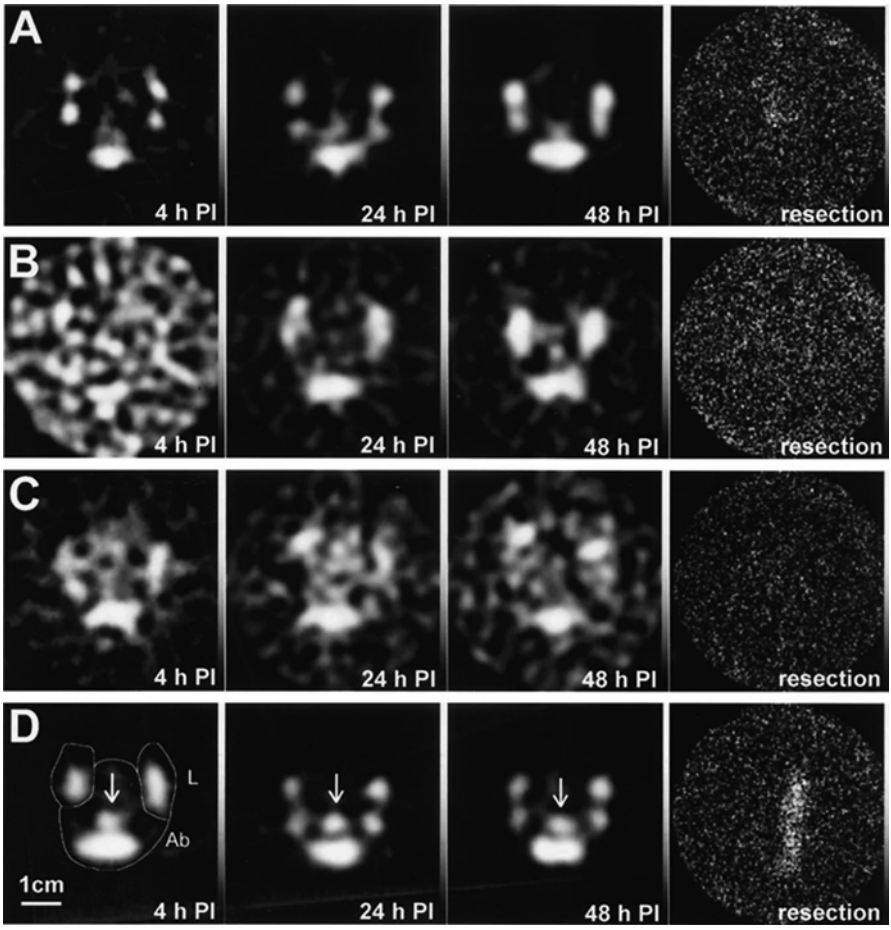

Fig. 22.1 Transverse pinhole SPECT slices of the pelvic region of group (**a**) (NaCl donor/NaCl recipient), (**b**) (TNBS donor/NaCl recipient), (**c**) (NaCl donor/TNBS recipient) and (**d**) (TNBS donor/TNBS recipient) 4, 24 and 48 h p.i. The mouse body contour is outlined and, abdomen (*Ab*) and limbs (*L*) are also identified, on the 4 h image (**d**). On the *right* panel, planar pinhole scintigraphy of corresponding colon resection specimen has been shown. Specific colon uptake is observed and verified by a positive resection specimen, in group (**d**). (Reproduced from Bennink et al. [100])

For animal model, in Sprague-Dawley rats a cervical midline incision was then made and the left carotid artery and branches isolated. The common carotid, external carotid, and pterygopalatine arteries were identified and ligated. An uncoated 30-mm-long segment of 3-0 nylon monofilament suture was inserted into the internal carotid artery and advanced under direct visualization so that it was placed approximately 19–20 mm from the bifurcation in order to occlude the ostium of the MCA. The occluding suture was kept in place for 120 min. Animals were then allowed to recover and underwent imaging at either 24 h or 6 days after the

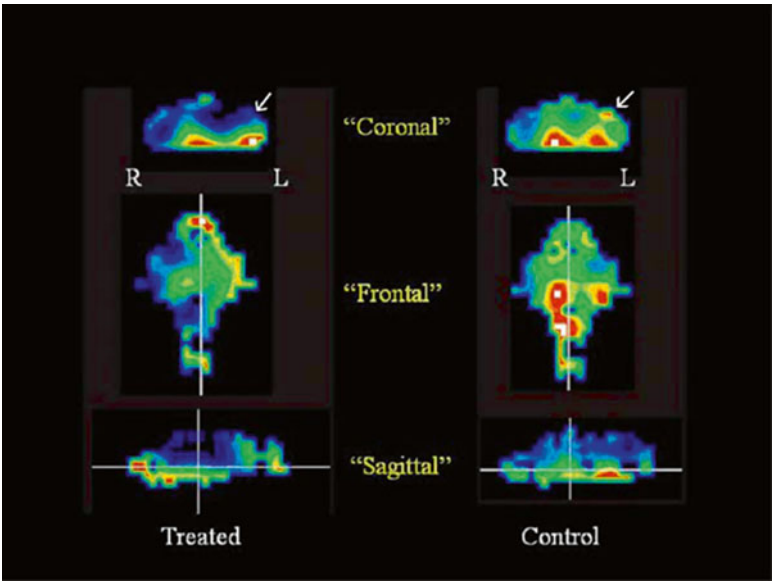

Fig. 22.2 Small animal SPECT images obtained 6 days after left MCA occlusion/reperfusion injury, show multiple sites of abnormally increased uptake scattered throughout the brains of both antibody-treated and control animals. False color image representation of annexin V activity; *white/red* pixels = highest values of tracer uptake, *blue/black* pixels = lowest tracer uptake. (Reproduced from Blankenberg et al. [101])

initiation of MCA, then euthanized at 1 or 7 days. Human recombinant annexin V was radiolabeled with ^{99m}Tc, with 92–97 % radiochemical purity and 100–200 μCi/μg specific activity. Animals received 185–370 MBq of ^{99m}Tc-HYNIC-annexin V, 1 h prior to the start of imaging via penile injection. SPECT images were recorded with a 1-mm aperture pinhole collimator into a 64 × 64 imaging matrix for the projection data (and 643 for the reconstructed data), 30 s per step, 3° per step, for a 360° rotation.

On day 6, antibody-treated rats (n = 5) demonstrated a strikingly lower intralesional uptake of annexin V compared with controls (n = 8) as shown in Fig. 22.2. Region of interest (ROI) analysis of the image data confirmed that the total intralesional activity within each cerebral hemisphere was significantly lower in treated animals than in controls. At 24 h, antibody-treated animals (n = 3) demonstrated significantly decreased intralesional uptake of annexin V in both the left and the right cerebral hemisphere, by 92 % and 75 %, respectively, compared with controls (n = 3). The uptake of annexin V in the midbrain and posterior fossa was also significantly decreased in the 24-h treatment group as compared with controls.

The study demonstrated that ^{99m}Tc-labeled annexin V small animal SPECT radionuclide imaging can detect the early phases of neuronal ischemic injury, and also monitor the effects of anti-FasL antibody therapy in a rodent model of focal ischemic cerebral injury.

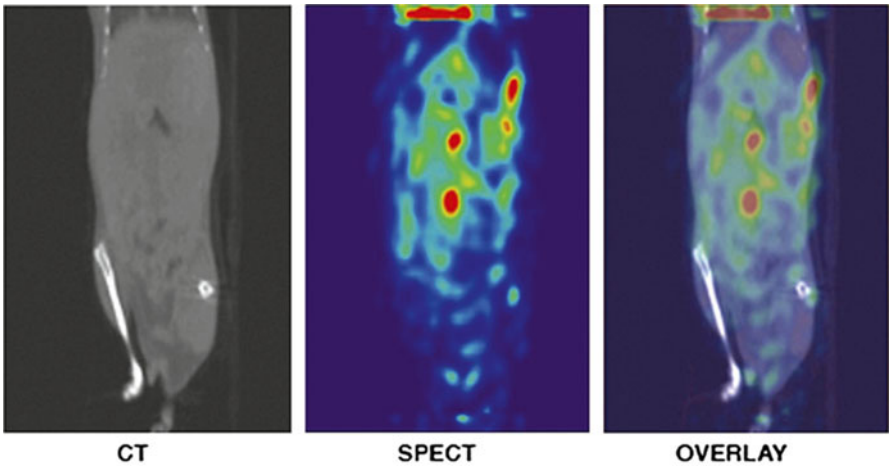

Fig. 22.3 An example of the overlay strategy with a CT, SPECT, and overlay SPECT-CT image of a 5 % DSS mouse. (Reproduced from Kanwar et al. [102])

Mice Model of DSS Induced Inflammatory Bowel Disease (IBD)

A recent study was performed for the in vivo imaging of mucosal CD4 positive cells in Balb/c mice model of human inflammatory bowel disease [102]. This model was developed by the oral administration of dextran sulfate sodium (DSS). For the imaging study, mice were divided into 3 groups: a control group receiving no DSS, a mild colitis group given 3 % DSS, and a moderate colitis group given 5 % DSS in drinking water. Rat monoclonal antibody against murine CD4 (clone YTS 177) was labeled with ^{111}In, with the specific activity of 82.6 + 16.9 MBq/mg. 34.26 + 0.26 MBq of ^{111}In-labeled CD4 antibody was injected in the tail vein of mice, 48 h prior to imaging. Imaging was performed with a small animal combined modality single photon emission computed tomography imaging gamma camera (X-SPECT; Gamma Medica, Northridge, CA) using a 2 mm pinhole collimator (360° of rotation, 64 projection, 15 s/projection, and an 82 × 82 imaging matrix).

In Fig. 22.3, sagittal images of a mouse injected with 5 % DSS and regions of specific antibody uptake are graded by color with red indicating maximum uptake. The amount of labeled antibody (in microcuries/mg) found in the colons of each group was compared; colonic activity was greater with increasing doses of DSS ($p < 0.05$). The results of the AMIDE software analysis of reconstructed SPECT-CT images for the colon uptake ratio (CUR) showed, statistically significant differences between all groups. The degree and extent of colitis correlated with SPECT-CT imaging, regression analyses were performed to relate the CUR to the colon length, total lymphocytes, histopathologic scores, and total CD4+ T cells. Except in the case of colon length ($p < 0.05$), all of these analyses showed significant differences. ^{111}In-labeled anti-CD4 antibody localized to areas of colonic inflammation and

correlated with the degree of pathology, as assessed by total cell counts, CD4+ T cell counts, and histopathology.

This study in murine model of DSS-induced colitis, demonstrated that SPECT-CT imaging can be used for the localization and quantitative assessment of inflammation.

5.1.2 SPECT for Infection Imaging

Mice Model of Infection (*Staphylococcus aureus* and *Klebsiella pneumonia*)

Another study was performed with a radiolabeled human neutrophil peptide-1 (HNP-1), an antibacterial peptide derived from human neutrophils, in a mice model of infection (*Staphylococcus aureu*s or *Klebsiella pneumonia*) to evaluate its potential for the imaging of bacterial infection [103]. Authors used two kind of mice models in this study.

Thigh muscle model: A bolus of approximately 1×10^6 colony-forming units (CFUs) *S. aureus* or *K. pneumoniae* was injected into the right thigh muscle. Five minutes later, either ^{99m}Tc-HNP-1 (0.8 MBq) or ^{99m}Tc-IgG (0.8 MBq) was injected intravenously as a control.

Peritoneum model: A peritoneal *K. pneumoniae* infection model was used to quantify the binding of tracers to both bacteria and leukocytes from the site of infection. Briefly, approximately 1×10^6 CFUs of *K. pneumoniae* was injected into the peritoneal cavity of mice, and 5 min later, ^{99m}Tc-HNP-1 (0.8 MBq) or ^{99m}Tc-IgG (0.8 MBq) was injected i.v. as a control.

At different intervals, comprehensive information about clearance and accumulation of ^{99m}Tc-HNP-1 at sites of infection (*S. aureus* or *K. pneumonia)* and in various organs was obtained by scintigraphy; for comparison purpose ^{99m}Tc-IgG was used. Whole-body images were acquired every 60 s during the first hour after tracer injection. Four hours after tracer injection, a 5 min image was acquired. Visualization of foci with *S. aureus* or *K. pneumonia* was already achieved 5 min after injection of ^{99m}Tc-HNP-1, as indicated by a ratio of 1.3 or higher between the targeted thigh muscle (containing bacteria) and the nontargeted (contralateral) thigh muscle (T/NT). Similar T/NT for ^{99m}Tc-IgG were obtained 4 h after injection of the tracer, indicating that imaging of foci of bacteria with ^{99m}Tc-HNP-1 is much faster than with ^{99m}Tc-lgG. Binding of ^{99m}Tc-HNP-1 to bacteria was approximately 1,000 times higher than binding to leukocytes. Although the number of bacteria in the peritoneum was 1,000-fold lower than the number of leukocytes, a significant correlation between binding of ^{99m}Tc-HNP-1 to bacteria on the one hand and accumulation of tracer on the other was still found, in contrast to ^{99m}Tc-lgG. This study demonstrated that the scintigraphy with ^{99m}Tc-HNP-1 allows rapid visualization of bacterial infections.

5.2 *Positrons Emission Tomography (PET)*

5.2.1 FDG PET for Imaging of Bone Infections

In response to an inflammatory stimulus, the glucose metabolism of immune cells like macrophages, granulocytes and leukocytes is increased. Consequently, elevated uptake of the radiolabeled glucose analogue [^{18}F]FDG is observed at the site of inflammation. [^{18}F]FDG PET is a useful tool for imaging of bone infections, but may give false positive results, due to normal bone healing. Normal bone healing is associated with an acute inflammatory phase, which could be hard to distinguish from a bone infection by [^{18}F]FDG PET. Several [^{18}F]FDG PET imaging studies in rodents have been conducted to tackle this problem [104–106]. An experimental rabbit model for osteomyelitis was created by surgical removal of a segment from the leg bone, infection of the bone with *Staphylococcus aureus* and refilling the bone either with the removed bone segment or with orthopedic bone cement. Control animals, representing normal bone healing, underwent the same surgical procedure, but saline was injected in the bone instead of the bacterial solution. FDG PET showed an increase in tracer uptake both in the healing bone and in the infected bone at 3 weeks after surgery, with the uptake ratio between affected and contralateral bone being 2.4 ± 0.3 and 3.9 ± 1.7, respectively [107]. At 6 weeks, however, FDG uptake in the healing bone was almost normalized (uptake ratio 1.3 ± 0.5), whereas tracer uptake remained elevated in the infected bone (uptake ratio 4.2 ± 1.0). Comparable results were obtained in similar FDG PET study in this animal model, in which the animals were investigated at day 1, 8, 15, 22 and 29 after surgery [104]. FDG uptake was increased in both the healing bone and the infected bone from day 1 after infection, whereas X-ray was unable to detect osteolytic lesions until day 15. From day 15 onward, the infected bone could be discriminated from the normal healing bone by FDG PET, due to a reduction in tracer uptake in de healing bone. In addition, increased FDG uptake in the regional lymph nodes was observed in 67–89 % of the infected animals at day 8–29 after surgery. In contrast, enhanced lymph node FDG uptake was found in only one uninfected animal at a single time point (day 8). These results show that FDG PET can be an attractive tool to discriminate between osteomyelitis and normal bone healing. Two to three week after surgery, osteomyelitis could be diagnosed by visual analysis of FDG PET images with sensitivity, specificity, accuracy, positive and negative predictive value of at least 93 %.

FDG PET proved also useful to monitor the efficacy of impregnation of orthopedic materials with antimicrobial agents for treatment or prevention of bone infections. Thus, a biodegradable osteoconductive bone defect filler, containing the antimicrobial agent ciproflaxacin, was tested in the osteomyelitis rabbit model [105]. Two weeks after bone infection with *S. aureus*, debris was surgically removed from the infected bone lesion and the lesion was filled with the ciprofloxacin-releasing orthopedic composite, or with control composite without antibiotic agent. At 6 weeks, sham-treated animals exhibited highly elevated FDG uptake in the bone

lesion (SUV 1.7 ± 0.9). In contrast, animals treated with ciprofloxacin-releasing osteoconductive bone defect filler had markedly reduced FDG uptake (SUV 0.6 ± 0.2), approaching the normal bone uptake in negative control animals. The reduction in FDG uptake in treated animals correlated with successful eradication of the infection and restoration of bone formation.

In a similar manner, FDG PET was used to test the efficacy of a bioabsorbable ciprofloxacin-containing bone screw [108]. The ciprofloxacin-impregnated bone screw or a stainless steel control screw were contaminated with *S. aureus* and implanted in the proximal tibia of a rabbit. In control animals noncontaminated screws were implanted. At 6 weeks after surgery, animals that were implanted with a contaminated stainless steel screw showed significantly augmented FDG uptake at the site of implantation, as compared to noncontaminated controls (SUV 0.76 ± 0.34 and 0.52 ± 0.07, respectively). Contamination of the ciproflaxacin-impregnated bioabsorbable screw with *S. aureus*, on the other hand, did not evoke any increase in FDG uptake (SUV 0.44 ± 0.10 vs. 0.59 ± 0.10 for noncontaminated screws). X-ray images showed marked signs of bone infection due to the infected stainless steel screws, but not for the impregnated screws.

These examples show that FDG PET can not only be used in small animal models of bone infection for investigation of the diagnostic value of the imaging method, but also for evaluation of new orthopedic materials.

5.2.2 PET Imaging of Antibiotic Drugs

Fluoroquinolones belong to a class of antibiotic drugs that inhibit bacterial DNA gyrase and topoisomerase-IV. Several representatives of this class of antibiotics, including ciprofloxacin [109], fleroxacin [110], lomefloxacin [111] and trovafloxacin [112] have been labeled with ^{18}F for PET imaging. Only for [^{18}F]fleroxacin and [^{18}F]trovafloxacin, the evaluation of the tracer in an animal model of infection was published [113, 114]. Both labeled compounds were investigated in Sprague-Dawley rats and New Zealand White rabbits that were injected with E. coli in a thigh muscle. [^{18}F]fleroxacin was administered at a dose of 10 mg/kg in both species and tissue distribution was determined by ex vivo biodistribution (rats) or PET imaging (rabbits) [115]. These studies showed that sufficiently high drug concentrations could be obtained in all extra-cranial tissues to achieve antimicrobial activity. The drug concentration in the brain was low, suggesting that CNS toxicity is unlikely. In both species, uptake of the radiolabeled drug in the infected muscle was not significantly different from uptake in the control muscle, although it should be emphasized that a pharmacological concentration of the labeled drug was used and not a tracer dose. Similar results were obtained in a comparable study with [^{18}F] trovafloxacin [113]. Taken together, these animal studies and also studies in humans suggest that PET imaging of radiolabeled fluoroquinolones is a useful tool for determining pharmacokinetic parameters of the drug noninvasively. Since no tracer-dose studies with radiolabeled fluoroquinolones in animal models of infection have been published, it remains to be investigated whether these radiolabeled antibiotics are suited for imaging of infections.

5.2.3 PET Imaging of Herpes Virus Infection

Herpes viruses are the most common cause for encephalitis. The viral thymidine kinase is an attractive target for imaging of herpes virus infections, since this enzyme is only expressed in replicating viruses. Several tracers are currently available for imaging of herpes simpex virus thymidine kinase (HSVtk) activity [115]. These tracers are specifically phosphorylated by the viral thymidine kinase and subsequently. Bennett and coworkers have shown that imaging of replication-competent herpes simplex virus type 1 viruses is feasible using PET and the tracer 2′-fluoro-5-[^{124}I]iodo-1-β-D-arabinofuranosyluracil ([^{124}I]FIAU) [116]. They injected virus particles into subcutaneous tumors in the flanks of rats and could clearly visualize the HSV-infected tumors with [^{124}I]FIAU PET, whereas control tumors could not be discerned. Tracer uptake correlated with the HSV-1 dose and with the interval between virus infection and PET imaging (and as a result with viral replication). These results indicate that [^{124}I]FIAU PET might be useful for detection of herpes virus infection and for monitoring of oncolytic viral treatment of cancer [117].

An important characteristic of herpes viruses is that they establish latency in the central nervous system after primary infection. Both primary infection and reactivation of herpes viruses may sporadically result in herpes encephalitis. The acyclic guanosine derivatives 9-[(3-[^{18}F]fluoro-1-hydroxy-2-propoxy)methyl]guanine ([^{18}F]FHPG) and 9-[4-[^{18}F]fluoro-3-(hydroxymethyl)butyl]guanine ([^{18}F]FHBG) are radiolabeled analogs of the antiviral agents ganciclovir and penciclovir, respectively. [^{18}F]FHPG and [^{18}F]FHBG have been investigated in an animal model of herpes simplex encephalitis as potential PET tracers for detection of replicating HSV in the brain [118, 119]. Thus, rats were infected by inoculation of HSV-1 via the nose, which induced severe herpes simplex encephalitis within one week. Ex vivo autoradiography and consecutive metabolite analysis demonstrated that [^{18}F]FHPG selectively accumulated in infected brain regions, where it was phosphorylated by the virus [117]. In the same animal model, comparable selective accumulation of [^{18}F]FHBG was observed in ex vivo biodistribution and PET imaging studies (Fig. 22.4), although uptake was very low, even in infected brain regions [118]. [^{18}F]FHPG and [^{18}F]FHBG are both hydrophilic tracers that hardly penetrate the intact blood-brain barrier, but might enter the brain when the blood-brain barrier is disrupted during infection and inflammation. However, [^{18}F]FHBG PET imaging studies could not demonstrate any enhanced tracer uptake in the HSV-infected brain by visual analysis, which is probably due to a combination of low brain uptake and technical limitation of the imaging method, such as partial volume and spill-over effects.

As an alternative approach, the immune response to the HSV infection of the brain was exploited as a target for imaging [119]. In response to the viral invasion of the brain, the macrophages of the brain, microglia cells, are activated, which is accompanied by an increased expression of the peripheral benzodiazepine receptor (PBR, also called translocator protein) on the mitochondria of the microglia cells. The expression of the PBR is low in the healthy brain, but is highly upregulated in neuroinflammation. Several tracers have been developed for PET imaging of the PBR, of which [^{11}C]PK11195 (*(R)-N*-methyl-*N*-(1-methylpropyl)-1-(2-chlorophenyl)isoquinoline-3-carboxamide) has been used most frequently [120].

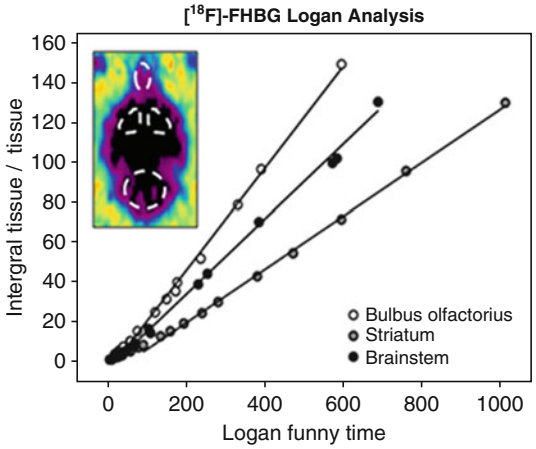

Brain area	Distribution volume		
Bulbus olfactorius	0.267	±	0.015
Frontal cortex	0.226	±	0.039
Striatum	0.149	±	0.005
Midbrain	0.166	±	0.023
Brainstem	0.248	±	0.055
Cerebellum	0.190	±	0.012

Fig. 22.4 Graphical Patlak analysis of [18F]FHBG uptake in the brain of a rat suffering from an HSV encephalitis. The corresponding PET image is depicted in the *insert* of the graph. The distribution volumes for different brain areas, as obtained by [18F]FHBG PET, corresponded well with the migration of the virus

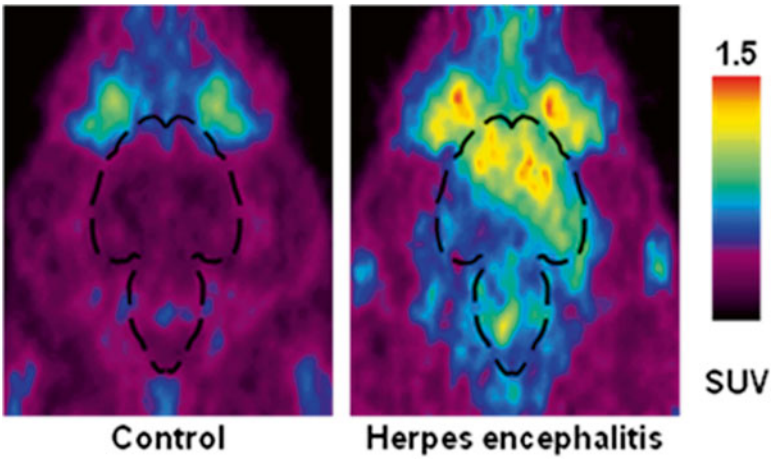

Fig. 22.5 [11C]PK11195 PET images of the brains of a control rat and a rat that was intranasally infected with HSV-1 7 days before. The brain is outlined by the *black dotted line*. Increased tracer uptake is observed in the bulbus olfactorius, frontal cortex, brain stem and cerebellum, which corresponds to the migration pattern of the virus

PET imaging with [11C]PK11195 and other tracers for the PBR was applied to study the activation of microglia cells in the herpes simplex encephalitis rat model [119]. PET imaging and ex vivo biodistribution studies showed that uptake of [11C]-PK11195 was increased in the bulbus olfactorius, frontal cortex, parietal/temporal/occipital cortex, cerebellum and brainstem in HSV-infected rats (Fig. 22.5). This

increase in tracer uptake correlated well with the distribution of activated microglia, as determined by immunohistochemistry.

Taken together, these studies indicate that specific tracers for imaging of herpes virus infections are available, but these tracers appear unable to penetrate into the brain sufficiently to allow imaging of brain infections. PET imaging of the PBR on activated microglia is a suitable alternative to monitor brain infections.

5.3 Other Imaging Modalities

Imaging of infection and/or inflammation can be performed with other modalities such as MRI, optical imaging and US.

5.3.1 MRI

Concerning atherosclerosis, Fayad et al. [97] were the first to describe a non-invasive high-resolution MRI of atherosclerotic lesions in the ApoE$^{-/-}$ mice. The animal model was identical to the one described above; an apolipoprotein E deficient mouse that, even feeded on chow diet, develops spontaneous atherosclerosis. After acquiring the images they sacrificed the mice and prepared the tissues for histological analysis. The MRI and histopathological sections images from the same mouse were correlated and in a second step analyzed separately by two different investigators. The authors found that it was possible to visualize the arteries of wild-type and atherosclerotic mice identifying lesions (of which they had not prior knowledge) and obtaining a high grade of agreement with the histopathological findings. So they concluded that MRI could have provided a tool to study atherosclerosis and improve its understanding, diagnosis and treatment. Although they found their results were promising, they also found out that there was some limitations including vessel motion during cardiac cycle and respiratory acts, that could cause a series of artifacts with a negative influence in the images analysis (Fig. 22.6). This study was followed by many others, aiming to find a procedure for the follow up of the atherosclerotic events without sacrificing the mice at different time points or simply to improve the sensitivity and accuracy of the technique.

Alsaid et al. [121] conducted a study trying to assess the feasibility and performance of high-resolution MRI in combination with two different gating strategies. They tested double-sensor cardiac and respiratory gating, using both ECG and respiratory sensor signals and single-sensor cardiorespiratory gating using demodulated ECG; in order to avoid artifacts as much as possible and to see which one of the two procedure was the best. They used the ApoE$^{-/-}$ mouse model and performed the experiments on a 2-T horizontal MRI equipped with a 180 mT/m gradient set, acquiring image using a two-dimensional (2D) gradient echo (GE) sequence. They

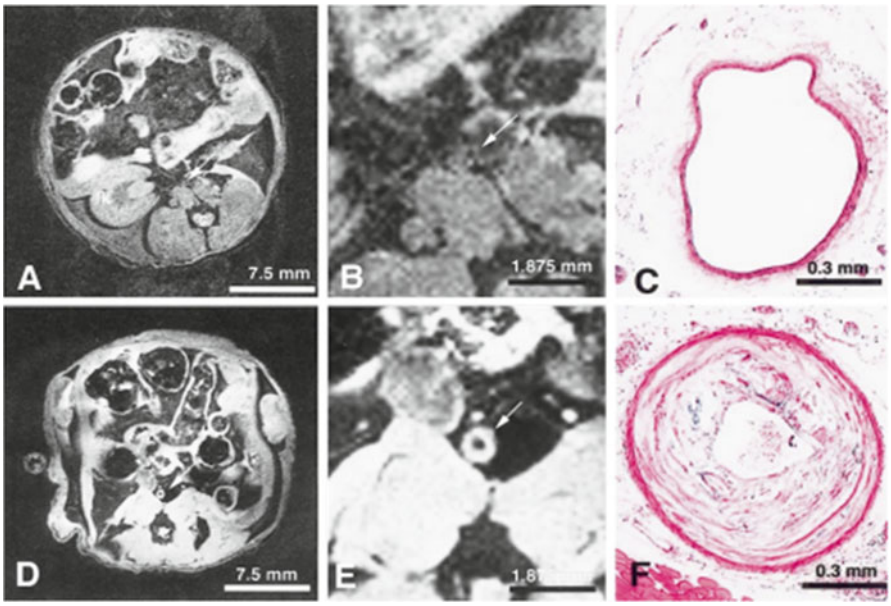

Fig. 22.6 MRI imaging and histology of normal mouse aorta (**a**, **b**, **c**) and of a mouse aorta affected by severe atherosclerosis (**d**, **e**, **f**). (Reproduced from Fayad et al. [97])

were able to obtain high-resolution MRI images of atherosclerotic plaque at the aortic root and the carotid origin and concluded that even if the single-sensor cardiorespiratory gating using demodulated ECG presented some advantages respect to the other, both gating systems were good to visualize lesions in the thoracic area and could prevent the obtaining of artifacts.

5.3.2 US

Clavel et al. [122] tried to determine if ultrasonography analysis could accurately detect arthritis lesions in a the collagen-induced mouse model described earlier, even if the small size of a mouse is a limit to the use of US, which could potentially be a useful non-invasive technique to follow up the disease in the same animal, which is a recurring task in many different diseases.

After acquiring images in both Doppler and B mode the mice were sacrificed and the legs were collected for histological studies, so that they could compare the obtained results with ultrasonographic and clinical evaluations. They showed that it is possible to follow up the development of arthritis in mice with US and also to define parameters that permitted to distinguish five grades of arthritis, even if it was not possible to visualize cartilage destruction, which is a feature of RA. Eventually they concluded that US presents several advantages such as low costs, innocuity and

precision, supplemented by Doppler analysis that are able to give information on joint vascularization and angiogenesis which participates in the disease.

5.3.3 Optical Imaging

Infection

The use of a molecular probe with a fluorescent reporter group can permit to image bacteria through optical imaging, even if it is not so much developed like MRI, SPECT and PET/CT.

Leevy et al. [123] used a fluorescent molecular probe containing synthetic zinc(II) dipicolylamine (Zn-DPA) coordination complexes as affinity groups that could selectively bind to the outer anionic surface of the bacterial membrane. The probe contained a near-infrared (NIR) fluorophore attached to the affinity group with an emission wavelengths in the region of 650 – 900 nm that could propagate through more than 2 cm of tissue. Then they used the probe for targeted, fluorescence imaging of bacterial infection in a thigh muscle mouse model. The mice were infected with *S. aureus* and *E. coli* and they found that it could be possible to discriminate between infected and non-infected thigh. Moreover they showed that using a probe with a different affinity group as a control, they couldn't detect any fluorescent from the infected tissue. Anyway, more studies are needed to check the reliability of this technique, since the range of the NIR light has limited penetration that permits the imaging of infection only in sites such as throat, skin and urinary tract.

Inflammation

Since RA mainly affects the joints of hand and feet, Simon et al. [124], proposed that optical imaging with labeled leukocytes could be an innovative and alternative imaging modality, avoiding the problem of imaging deeper tissues. To prove their hypothesis they induced arthritis in rats and injected autologous leukocytes labeled with DiD, a liphophilic carbocyan marker with an absorption window between 650 and 900 nm. The images were acquired from rats treated and untreated with cortisone, which is known to reduce the effects of the inflammatory response and they noticed that while in the former group there was an accumulation of labeled leukocytes in the joints, in the latter the signal was markedly reduced. The concluded that their approach could have provided a higher sensitivity compared to the previous ones, which were based on the labeling of dedicated antigens, but that their study could only be a starting point for the improvement of the technique since their dye was not clinically approved. Moreover the study had several limitations, including the impossibility to know which subpopulation of cells was migrating to the joints and if the fluorescence detected in the joints was truly due to the initially labeled cells (Fig. 22.7).

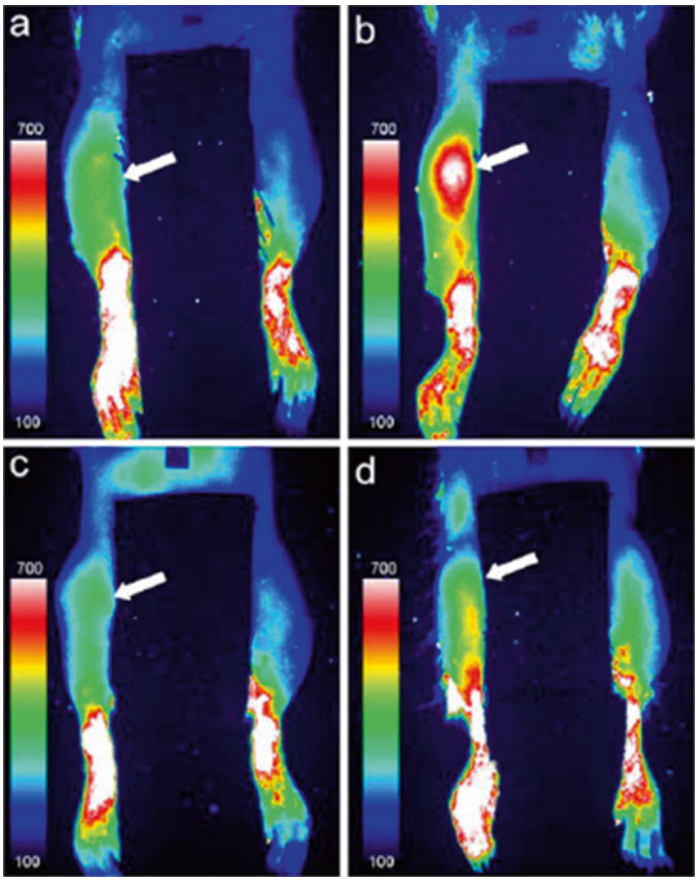

Fig. 22.7 Optical imaging of arthritis in rats injected with autologous leukocytes labeled with DiD, a liphophilic carbocyan marker with an absorption window between 650 and 900 nm. (**a**, **b**) induced arthritis in right knee; (**c**, **d**) cortisone treated arthritis; (**a**, **c**) before and (**b**, **d**) 4 h after injection of DiD-labeled leukocytes. (Reproduced from Simon et al. [124])

6 Extrapolation of Animal Results to Human Studies

Although extrapolation of animal data to humans is always difficult and requires particular attention, in the field of inflammation/infection, this is even more difficult. However, pre-clinical screening in animals of different molecules or different analogues of a given molecule is always necessary. It is necessary because, although some considerations on the quality and properties of a labeled probe can be done a priori on a theoretical basis or can be obtained by in vitro studies, most necessary information can only be obtained by studying in vivo the biodistribution of the labeled probe.

Theoretical considerations can be made for the choice of the isotope to attach to the molecule and for the labeling method to choose, accordingly. Factors influencing the choice of isotope are the biological half life of the molecule and of the isotope (that should be as similar as possible), the type of imaging modality to be used (PET, SPECT), the biochemical structure of the molecule (molecular weight, structure, presence of S-S bonds, others), the need of having a spacer (or a linker) between the isotope and the molecule, the sensitivity of the molecule to oxidizing/reducing chemicals, etc. These considerations may help to orientate to the correct choice and save time to following steps of research.

In vitro information that can be obtained are related to the type of quality controls that are performed and include labeling efficiency and stability of the labeled probe in different conditions (in saline, plasma, room temperature or 37 °C, challenge with different isotope chelators, etc.), biochemical quality controls on the structure of the compound (SDS-PAGE, ITLC, HPLC, Maldi-TOF, etc.), test of immunoreactive fraction, binding assay to cells (including displacement with unlabeled probe and Scatchard plot analysis), biological assay to cells, autoradiography to tissues or cells. These tests will define the structure, stability and binding affinity/activity of the probe to its target and will also provide initial information on the possible use of the probe.

Animal studies, finally, provide information on the biodistribution, metabolism, kinetic and pharmacological interactions. When performing these experiments it must be considered that animals of different sex, age, strain and conditions, may give different responses. The most influencing conditions are the food and water intake of animals, the body temperature during the experiments, heart and breading rate of animals, the kind and duration of anesthesia, the host response to induced infection. All these factors are extremely variable and different from small animals to humans.

Some other anatomical considerations can be done when extrapolating animal results to humans, such as the deepness of an organ and its proximity with other organs that have high uptake of labeled probe for metabolic reasons. For instance, a pancreatic lesion in a mouse or rat, will hardly be seen using a radiopharmaceutical that is metabolized by the kidneys, but this may not be the case in humans; and vice versa, an infection in a highly vascularised tissue (i.e. endocarditis) can be better seen in a mouse than in man using a short half-life probe because of the faster heart rate and liver metabolism in mice than humans.

Last but not least, we must take into consideration that infections induced in animals are much more severe and extended than those we normally observe in humans and that the host response to infection is much different in rodents than in humans. In rodents, the inoculation of bacteria induces high vascular damage, edema and macrophage infiltration. In humans, latent infections appear with little vascular phenomena, poor edema and mainly granulocytic infiltration. The cytokine/chemokine response to the inflammatory/infective agent is also different, in different species, as well as the immunoglobulin production.

In conclusion, although very important, animal data should be taken with caution when extrapolated to humans, particularly in the study of inflammatory/infective diseases that are very different for physiological and pathological reasons.

7 Conclusions

Small animals are frequently used in clinical research field as models of inflammation/infection. In particular, mice are the first choice in radiopharmaceutical research because they are economical, may provide suitable model for different human disorders and also their production is rapid. The mouse genome sequence has been already determined and the knockout mice are also available as models of different human abnormalities. Human tumor xenografted animal models have been used in the field of inflammation imaging from several years. Therefore, these small animal models are playing a key role in the radiopharmaceutical research.

A number of radiopharmaceuticals for imaging inflammation have been proposed that differ in their specificity and mechanism of uptake in inflamed foci as compared to the traditional inflammation imaging agents such as human autologous leukocytes. Radiolabeled cytokines and mAbs represents a reliable tool for the diagnosis of chronic inflammatory processes, moreover, the introduction of radiolabeled antibiotics and antimicrobial peptides now made the field of inflammation/infection imaging highly specific and precise. Sophisticated techniques like PET, SPECT and other hybrid modalities improve the quality of scintigraphic images and often allowed to screen quickly and efficiently different radiolabeled molecules in a given model, thus providing a useful tool for pre-clinical screening of radiolabeled probes and for predicting biodistribution and clinical use in humans.

Acknowledgements Authors wish to thank Lori Camillo Sforza for help in editing the chapter and ISORBE for providing useful information, PhD thesis and other scientific literature on the topic.

References

1. Signore A, Chianelli M, D'Alessandria C, Annovazzi A (2006) Receptor targeting agents for imaging infection/inflammation: where are we now? Q J Nucl Med Mol Imaging 50: 236-242
2. Lecchi M, Ottobrini L, Martelli C, Del Sole A, Lucignani G (2007) Instrumentation and probes for molecular and cellular imaging. Q J Nucl Med Mol Imaging 51(2):111-126
3. Ohlerth S, Scharf G (2007) Computed tomography in small animals - Basic principles and state of the art applications. Vet J 173:254-271
4. Pirko I, Fricke ST, Johnson AJ, Rodriguez M, Macura SI (2005) Magnetic resonance imaging, microscopy, and spectroscopy of the central nervous system in experimental animals. NeurRx 2:250-264
5. Tournebize R, Doan BT, Dillies MA, Maurin S, Beloeil JC, Sansonetti PJ (2006) Magnetic resonance imaging of Klebsiella pneumoniae-induced pneumonia in mice. Cell Microbiol 8:33-43
6. Artemov (2003) Molecular magnetic resonance imaging with targeted contrast agents. J Cell Biochem 90:518-524
7. Corot C, Petry KG, Trivedi R, Saleh A, Jonkmanns C, Le Bas JF, Blezer E, Rausch M, Brochet B, Foster-Gareau P, Balériaux D, Gaillard S, Dousset V (2004) Macrophage imaging

in central nervous system and in carotid atherosclerotic plaque using ultrasmall superparamagnetic iron oxide in magnetic resonance imaging. Invest Radiol 39:619-625
8. Pirko I, Ciric B, Johnson AJ, Gamez J, Rodriguez M, Macura S (2003) Magnetic resonance imaging of immune cells in inflammation of central nervous system. 44: 463-468
9. Choy G, Choyke P, Libutti S (2003) Current advances in molecular imaging: non-invasive in vivo bioluminescent and fluorescent optical imaging in cancer research. Mol Imaging 2:303-312
10. Luker GD, Luker KE (2008) Optical imaging: current applications and future directions. J Nucl Med 49:1-4
11. Rao J, Dragulescu-Andrasi A, Yao H (2007) Fluorescence imaging in vivo: recent advances. Curr Opinion Biotechnol 18:17-25
12. Zacharakis G, Kambara H, Shih H, Ripoll J, Grimm J, Saeki Y, Weisleder R, Ntziachristos V (2005) Volumetric tomography of fluorescent proteins through small animals in vivo. Proc Natl Acad Sci 102:18252-18257
13. Ntziachristos V, Ripoll J, Wang LV, Weisleder R (2005) Looking and listening to light: the evolution of whole body photonic imaging. Nat Biotechnol 23:313-320
14. Doyle TC, Burns SM, Contag CH (2004) In vivo bioluminescence imaging for integrated studies of infection. Cell Microbiol 6:303-317
15. Engelsman AF, van der Mei HC, Francis KP, Busscher HJ, Ploeg RJ, van Dam GM (2009) Real time noninvasive Monitoring of contaminating bacteria in a soft tissue implant infection model. Inc Biomed Mater Res Part B: Appl Biomater 88B:123-129
16. Zhao X, Hilliard LR, Mechery SJ, Wang Y, Bagwe RP, Jin S, Tan W (2004) A rapid bioassay for single bacterial cell quantitation using bioconjugated nanoparticles. Proc Natl Acad Sci 101:15027-15032
17. Hennig A, Florea M, Roth D, Enderle T, Nau WM (2007) Design of peptide substrates for nanosecond time-resolved fluorescence assays of proteases: 2,3-diazabicyclo[2.2.2]oct-2-ene as a noninvasive fluorophore. Anal Biochem 360:255-265
18. Sood R, Domanov Y, Kinnunen PK (2007) Fluorescent temporin B derivative and its binding to liposomes. J Fluoresc 17:223-234
19. Gee KR, Kang HC, Meier TI, Zhao G, Blaszcak LC (2001) Fluorescent Bocillins: synthesis and application in the detection of penicillin-binding proteins. Electrophoresis 22:960-965
20. Chatziioannou AF (2005) Instrumentation for molecular imaging in preclinical research. Micro-PET and micro-SPECT. Proc Am Thorac Soc 2:533-536
21. Rahmin A, Zaidi H (2008) PET versus SPECT: strengths, limitations and challenges. Nucl Med Commun 29:193-207
22. Shoghi KI, Welch MJ (2007) Hybrid image and blood sampling input function for quantification of small animal dynamic PET data. Nucl Med Biol 34:989-994
23. Beekman F, van der Have F (2007) The pinhole: gateway to ultra-high-resolution three-dimensional radionuclide imaging. Eur J Nucl Med Mol Imaging 34:151-161
24. Franc BL, Acton PD, Mari C, Hasegawa BH (2008) Small-animal SPECT and SPECT/CT: important tools for preclinical investigation. J Nucl Med 49:1651-1563
25. Chianelli M, Mather SJ, Martin-Comin J, Signore A (1997) Radiopharmaceuticals for the study of inflammatory processes: a review. Nucl Med Commun 18(5):437-455
26. Conti F, Priori R, Chimenti MS, Coari G, Annovazzi A, Valesini G, et al (2005) Successful treatment with intraarticular infliximab for resistant knee monarthritis in a patient with spondylarthropathy a role for scintigraphy with ^{99m}Tc-infliximab. Arthritis Rheum 52 (4):1224-1226
27. Tsopelas C, Penglis S, Ruskiewicz A, Bartholomeusz DL (2006) Scintigraphic imaging of experimental colitis with technetium-99m-infliximab in the rat. Hell J Nucl Med 9(2):85-89
28. D'Alessandria C, Malviya G, Viscido A, Aratari A, Maccioni F, Amato A, et al (2007) Use of a 99m-Technetium labeled anti-TNFα monoclonal antibody in Crohn's Disease: in vitro and in vivo studies. Q J Nucl Med Mol Imaging 51:1-9
29. Malviya G, D'Alessandria C, Lanzolla T, Lenza A, Conti F, Valesini G, Scopinaro F, Dierckx RA, Signore A (2008) 99m-Technetium labeled anti-TNFα antibodies for the therapy

decision making and follow-up of patients with rheumatoid arthritis. Q J Nucl Med Mol Imaging 52Suppl 1(2):13
30. Malviya G, Lagàna B, Signore A, Dierckx RA (2008) Radiolabeled peptides and monoclonal antibodies for therapy decision making in inflammatory diseases. Curr Pharm Design 14(24):2401-2414
31. Zhang M, Yao Z, Zhang Z, Garmestani K, Talanov VS, Plascjak PS, et al (2006) The Anti-CD25 Monoclonal Antibody 7G7/B6, Armed with the α-Emitter ^{211}At, Provides Effective Radioimmunotherapy for a Murine Model of Leukemia. Cancer Res 66(16): 8227-8232
32. Choi CW, Lang L, Lee JT, Webber KO, Yoo TM, Chang HK, et al (1995) Biodistribution of 18F- and 125I-labeled anti-Tac disulfide-stabilized Fv fragments in nude mice with interleukin 2 alpha receptor-positive tumor xenografts. Cancer Res 55(22):5323-5329
33. Martins FPP, Gutfilen B, DE Souza SAL, DE Azevedo MNL, Cardoso LR, Fraga R, et al (2008) Monitoring rheumatoid arthritis synovitis with 99mTc-anti-CD3. Br J Radiol 81: 25-29
34. Malviya G, D'Alessandria C, Trotta C, Massari R, Soluri A, Scopinaro F, Dierckx RA, Signore A (2008) Radiolabeled-Visilizumab, a humanized anti-CD3 monoclonal antibody, for in vivo targeting of human CD3+ lymphocytes. Eur J Nucl Med Mol Imaging 35Suppl 2:S142
35. Kinne RW, Becker W, Schwab J, Horneff G, Schwarz A, Kalden JR, et al (1993) Comparison of 99Tcm-labeled specific murine anti-CD4 monoclonal antibodies and nonspecific human immunoglobulin for imaging inflamed joints in rheumatoid arthritis. Nucl Med Commun 14(8):667-675
36. Zhang C, Hou G, Han J, Song J, Liang T (2007) Radioiodine Labeled Anti-MIF McAb: A Potential Agent for Inflammation Imaging. Mediators Inflamm 2007:50180
37. Jamar F, Chapman PT, Manicourt D-H, Glass DM, Haskard DO, Peters AM (1997) A comparison between ^{111}In-anti-E-selectin mAb and ^{99}Tc^{m}-labeled human non-specific immunoglobulin in radionuclide imaging of rheumatoid arthritis. Brit J Radiol 70:473-81
38. Stopar TG, Mlinaric-Rascan I, Fettich J, Hojker S, Mather SJ (2006) 99mTc-rituximab radiolabeled by photo-activation: a new non-Hodgkin's lymphoma imaging agent. Eur J Nucl Med 33:53--59
39. Malviya G, Laganà B, Milanetti F, Del Mastro C, Familiari D, Dierckx RA, Scopinaro F, D'Amelio R, Signore A (2008) Use of 99m-technetium labeled Rituximab for imaging of patients with chronic inflammatory diseases. Eur J Nucl Med Mol Imaging 35Suppl 2:S142
40. Kjaer A, Lebech AM, Eigtved A, Hojgaard L (2004) Fever of unknown origin: prospective comprison of diagnostic value of ^{18}F-FDG PET and ^{111}In-granulocyte scintigraphy. Eur J Nucl Med Mol Imaging 31:622-626
41. Vicente AG, Almoguera M, Alonso JC, Heffernan AJ, Gomez A, Contreras PI, Martin-Comin J (2004) Diagnosis of orthopedic infection in clinical practice using Tc-99m sulesomab (antigranulocyte monoclonal antibody fragment Fab'2). Clin Nucl Med 29:781-785
42. van der Laken CJ, Boerman OC, Oyen WJ, van de Ven MT, van der Meer JW, Corstens FH (1998) Imaging of infection in rabbits with radioiodinated interleukin-1 (alpha and beta), its receptor antagonist and a chemotactic peptide: a comparative study. Eur J Nucl Med 25: 347-352
43. Van der Laken CJ, Boerman OC, Oyen WJG, Van der Ven MTP, Claessens RAMJ, Van der Meer JWM, Corstens FHM (1996) Different behaviour of radioiodinated human recombinant interleukin-1 and its receptor antagonist in an animal model of infection. Eur J Nucl Med 23:1531-1535
44. Chianelli M, Parisella MG, Visalli N, Mather SJ, D'Alessandria C, Pozzilli P, Signore A (2008) IMDIAB study group. Pancreatic scintigraphy with 99mTc-interleukin-2 at diagnosis of type 1 diabetes and after 1 year of nicotinamide therapy. Diabetes Metab Res Rev 24(2): 115-122
45. Signore A, D'Alessandria C, Lazzeri E, Dierckx R (2008) Can we produce an image of bacteria with radiopharmaceuticals? Eur J Nucl Med Mol Imaging 35(6):1051-1055

46. Signore A, Chianelli M, Toscano A, Monetini L, Ronga G, Nimmon CC, et al (1992) A radiopharmaceutical for imaging areas of lymphocytic infiltration: 123I-interleukin-2. Labeling procedure and animal studies. Nucl Med Commun 13(10):713-722
47. Chianelli M, Signore A, Fritzberg AR, Mather SJ (1997) The development of technetium-99m-labeled interleukin-2: a new radiopharmaceutical for the in vivo detection of mononuclear cell infiltrates in immune-mediated diseases. Nucl Med Biol 24(6):579-86
48. Chianelli M, Mather SJ, Grossman A, Sobnak R, Fritzberg A, Britton KE, Signore A (2008) (99m)Tc-interleukin-2 scintigraphy in normal subjects and in patients with autoimmune thyroid diseases: a feasibility study. Eur J Nucl Med Mol Imaging 35(12):2286-2293
49. Hay RV, Skinner RS, Newman OC, Kunkel SL, Lyle LR, Shapiro B, et al (1997) Scintigraphy of acute inflammatory lesions in rats with radiolabeled recombinant human interleukin-8. Nucl Med Commun 18:367-378
50. Gratz S, Rennen HJ, Boerman OC, Oyen WJ, Corstens FH (2001) Rapid imaging of experimental colitis with (99m)Tc-interleukin-8 in rabbits. J Nucl Med 42:917-923
51. Van der Laken CJ, Boerman OC, Oyen WJG, Van de Ven MPT, Laverman P, Van der Meer JWM, Corstens FHM (1997) Targeting inflammation with radiolabeled interleukin-1 and other cytokines in various mouse models. Nucl Med Commun 18:478
52. Annovazzi A, D'Alessandria, Bonanno E, Mather SJ, Cornelissen B, Van de Wiele C, et al (2006) Synthesis of 99mTc-HYNIC-interleukin-12, a new specific rediopharmaceutical for imaging T lymphocytes. Eur J Nucl Med Mol Imaging 33(4):474-482
53. Hartung D, Petrov A, Haider N, Fujimoto S, Blankenberg F, Fujimoto A, et al (2007) Radiolabeled Monocyte Chemotactic Protein 1 for the detection of inflammation in experimental atherosclerosis. J Nucl Med 48(11):1816-1821
54. Blankenberg FG, Tait JF, Blankenberg TA, Post AM, Strauss HW (2001) Imaging macrophages and the apoptosis of granulocytes in a rodent model of subacute and chronic abscesses with radiolabeled monocyte chemotactic peptide-1 and annexin V. Eur J Nucl Med 28(9): 1384-1393
55. Virgolini I, Kurtaran A, Leimer M, Smith-Jones P, Agis H, Angelberger P, et al (1997) Inhalation scintigraphy with Iodine-123-labeled interferon g-1b: pulmonary deposition and dose escalation study in healthy volunteers. J Nucl Med 38:1475-1481
56. Shatten C, Pateisky N, Vavra N, Ehrenbock P, Angelberger P, Sivolapenko G, Epenetos A (1991) Lymphoscintigraphy with 123I-labeled epidermal growth factor. Lancet 337:395-396
57. Dickson KM, Bergeron JJ, Philip A, O'Connor-McCourt M, Warshawsky H (2001) Localization of specific binding sites for ^{125}I-TGF-beta1 to fenestrated endothelium in bone and anastomosing capillary networks in enamel organ suggests a role for TGF-beta1 in angiogenesis. Calcif Tissue Int 68:304-315
58. Brouwers AH, Laverman P, Boerman OC, Oyen WJG, Barrett JA, Harris TD, et al (2000) A 99mTc-labeled leukotriene B4 receptor antagonist for scintigraphic detection of infection in rabbits. Nucl Med Commun 21:1043-50
59. van Eerd JE, Oyen WJ, Harris TD, Rennen HJ, Edwards DS, Liu S, et al (2003) A bivalent leukotriene B4 antagonist for scintigraphic imaging of infectious foci. J Nucl Med 44: 1087-1091
60. van Eerd JE, Laverman P, Oyen WJ, Harris TD, Edwards DS, Ellars CE, et al (2004) Imaging of experimental colitis with a radiolabeled leukotriene B4 antagonist. J Nucl Med 45:89-93
61. Oyen WJ, Boerman OC, Brouwers FM, Barrett JA, Verheugt FW, Ruiter DJ, Corstens FH, van der Meer JW (2000) Scintigraphic detection of acute experimental endocarditis with the technetium-99m labeled glycoprotein IIb/IIIa receptor antagonist DMP444. Eur J Nucl Med 27:392-399
62. Rusckowski M, Qu T, Pullman J, Marcel R, Ley AC, Ladner RC, Hnatowich DJ (2000) Inflammation and infection imaging with a 99mTc-neutrophil elastase inhibitor in monkeys. J Nucl Med 41:363-374
63. Welling MM, Paulusma-Annema A, Balter HS, Pauwels EK, Nibbering PH (2000) Technetium-99m labeled antimicrobial peptides discriminate between bacterial infections and sterile inflammations. Eur J Nucl Med 27:292-301

64. Welling MM, Hiemstra PS, van den Barselaar MT, Paulusma-Annema A, Nibbering PH, Pauwels EK, Calame W (1998) Antibacterial activity of human neutrophil defensins in experimental infections in mice is accompanied by increased leukocyte accumulation. J Clin Invest 102(8):1583-1590
65. Rusckowski M, Gupta S, Liu G, Dou S, Hnatowich DJ (2004) Investigations of a (99m) Tc-labeled bacteriophage as a potential infectionspecific imaging agent. J Nucl Med 45:1201-1208
66. Sarda L, Saleh-Mghir A, Peker C, Meulemans A, Cremieux AC, Le Guludec D (2002) Evaluation of 99mTc-ciprofloxacin scintigraphy in a rabbit model of Staphylococcus aureus prosthetic joint infection. J Nucl Med 43:239-245
67. Singh AK, Verma J, Bhatnagar A, Ali A (2003) Tc-99m Labeled Sparfloxacin: A Special Infection Imaging Agent. World J Nucl Med 2:103-109
68. Martin-Comin J, Soroa V, Rabiller G, Galli R, Cuesta L, Roca M (2004) Diagnosis of bone infection with 99mTc-ceftizoxime. Rev Esp Med Nucl 23: 357.
69. Singh AK, Verma J, Bhatnagar A, Sen S, Bose M (2003) Tc-99 isoniazid: a specific agent for diagnosis of tuberculosis. World J Nucl Med 2:292-305
70. Causse JE, Pasqualini R, Cypriani B, Weil R, Van der Valk R, Bally P, et al (1990) Descomps. Labeling of Ethambutol with 99mTc; using a new reduction procedure. Pharmacokinetic study in the mouse and rat. Int J Rad Appl Instrum(A) 41:493-506
71. Lupetti A, Welling MM, Mazz U, Nibbering PH, Pauwels EKJ (2002) Technetium-99m labeled fluconazole and antimicrobial peptides for imaging of Candida albicans and Aspergillus fumigatus infections. Eur J Nucl Med 29:674-679
72. Nijhof MW, Oyen WJG, van Kampen A, Claessens RA, van der Meer JW, Corstens FHM (1997) Evaluation of infections of the locomotor system with indium-111-labeled human IgG scintigraphy. J Nucl Med 38:1300-1305
73. Oyen WJG, Claessens RAMJ, van der Meer JWM, Rubin RH, Strauss HW, Corstens FHM (1992) Indium-111-labeled human nonspecific immunoglobulin G: a new radiopharmaceutical for imaging infectious and inflammatory foci. Clin Infect Dis 14:1110-1118
74. Beckers C, Jeukens X, Ribbens C, Andre B, Marcellis S, Leclercq P et al (2006) ^{18}F-FDG PET imaging of rheumatoid knee synovitis correlates with dynamic magnetic resonance and sonographic assessment as well as with the serum level of metalloproteinase-3. Eur J Nucl Med 33(3):275-280
75. Sohn M, Jones B, Whiting JJ et al (1993) Distribution of gallium-67 in normal and hypotransferrinemic tumour-bearing mice. J Nucl Med 34:2135-2143
76. McAfee JG, Thakur ML (1976) Survey of radioactive agents for the in vitro labeling of phagocytic leucocytes. I Soluble agents. II Particles. J Nucl Med 17:480-492
77. Liberatore M, Clemente M, Turilli AP, Zorzin L, Marini M, Di Rocco E et al (1992) Scintigraphic evaluation of disease activity in rheumatoid arthritis a comparison of technetium-99m human non-specific immunoglobulins, leucocytes and albumin nanocolloids. Eur J Nucl Med 19:853-857
78. Diot P, Le Pape A, Nolibe D, Normier G, Binz H, Revillard JP, Lasfargues G, Lavandier M, Lemarie E (1992) Scientigraphy with J001X, a Klebsiella membrane glycolipid, for the early diagnosis of chronic berilliosis: Results from an experimental model. Br J Int Med 49:359-364
79. Vanhagen PM, Krenning EP, Reubi JC, et al (1994) Somatostatin analogue scintigraphy in granulomatous diseases. Eur J NuclMed 21:497-502
80. Boerman OC, Storm G, Oyen WJG, et al (1995) Sterically stabilized liposomes labeled with ^{111}In to image focal infection in rats. J Nucl Med 36:1639-1644
81. Dams ETM, Oyen WJG, Boerman OC, et al (1998) Tc-99m-labeled liposomes to image experimental colitis in rabbits: Comparison with Tc-99m-HMPAO-granulocytes and Tc-99m-HYNIC-IgG. J Nucl Med 39:2172-2178
82. Akhtar MS, Khan ME, Khan B, Irfanullah J, Afzal MS, Khan MA, et al (2008) An imaging analysis of 99mTc-UBI (29-41) uptake in S. aureus infected thighs of rabbits on ciprofloxacin treatment. Eur J Nucl Med Mol Imaging 35:1056-1064

83. Signore A (2007) Radiolabelled interleukin-2 for in vivo imaging of activated T-lymphocytes. PhD thesis. University of Groningen, The Netherlands. ISBN-13: 978-90-9021462-7
84. Rusckowski M, Paganelli G, Hnatowich DJ, Magnani P, Virzi F, Fogarasi M, DiLeo C, Sudati F, Fazio F (1996) Imaging osteomyelitis with streptavidin and indium-111-labeled biotin. J Nucl Med 37:1655-1662
85. Samuel A, Paganelli G, Chiesa R, Sudati F, Calvitto M, Melissano G, Grossi A, Fazio F (1996) Detection of prosthetic vascular graft infection using avidin/indium-111-biotin scintigraphy. J Nucl Med 37:55-61
86. Eagle H, Fleischman R, Musselman AD (1950) The bactericidal action of penicillin in vivo: the participation of the host, and the slow recovery of the surviving organisms. Ann Intern Med 33**:**544-571
87. Adams EM, Gudmundsson S, Yocum DE, Haselby RC, Craig WA, Sundstrom WR (1985) Streptococcal myositis. Arch Intern Med 145(6):1020-1023
88. Perlman BB, Freedman LR (1971) Experimental endocarditis. II. Staphylococcal infection of the aortic valve following placement of a polyethylene catheter in the left side of the heart. Yale J Biol Med 44(2):206-213
89. Rouzet F, Dominguez Hernandez M, Hervatin F, Sarda-Mantel L, Lefort A, Duval X, Louedec L, Fantin B, Le Guludec D, Michel JB (2008) Technetium 99m-labeled annexin V scintigraphy of platelet activation in vegetations of experimental endocarditis. Circulation 117(6):781-789
90. Teng X, Xu LF, Yhou P, Sun M (2009) Effects of trefoil peptide 3 on expression of TNF-alpha, TLR4, and NF-kappaB in trinitrobenzene sulphonic acid induced colitis mice. Inflammation 32(2):120-129
91. Bai A, Lu N, Guo Y, Chen J, Liu Z (2009) Modulation of inflammatory response via alpha2-adrenoceptor blockade in acute murine colitis. Clin Exp Immunol 156(2):353-362
92. Oyen et al (1997) Scintigraphic evaluation of experimental colitis in rabbits. J Nucl Med 38(10):1596-1600
93. Bennink RJ, Hamann J, de Bruin K, ten Kate FJ, van Deventer SJ, te Velde AA (2005) Dedicated pinhole SPECT of intestinal neutrophil recruitment in a mouse model of dextran sulfate sodium-induced colitis. J Nucl Med 46(3):526-531
94. van Montfrans C, Bennink RJ, de Bruin K, de Jonge W, Verberne HJ, Ten Kate FJ, van Deventer SJ, Te Velde AA (2004) In vivo evaluation of 111In-labeled T-lymphocyte homing in experimental colitis. J Nucl Med 45(10):1759-1765
95. Melgar S, Gillberg PG, Hockings PD, Olsson LE (2007) High-throughput magnetic resonance imaging in murine colonic inflammation. Biochem Biophys Res Commun. 355(4): 1102-1107
96. Kosiewicz MM, Nast CC, Krishnan A, Rivera-Nieves J, Moskaluk CA, Matsumoto S, Kozaiwa K, Cominelli F (2001) Th1-type responses mediate spontaneous ileitis in a novel murine model of Crohn's disease. J Clin Invest 107(6):695-702
97. Fayad ZA, Fallon JT, Shinnar M, Wehrli S, Dansky HM, Poon M, Badimon JJ, Charlton SA, Fisher EA, Breslow JL, Fuster V (1998) Noninvasive in vivo High-Resolution Magnetic Resonance Imaging of atherosclerotic lesions in genetically engineered Mice. Circulation 98: 1541-1547
98. Weinreb DB, Aguinaldo JG, Feig JE, Fisher EA, Fayad ZA (2007) Non-invasive MRI of mouse models of atherosclerosis. NMR Biomed 20(3):256-264
99. Pichler BJ, Kneilling M, Haubner R, Braumüller H, Schwaiger M, Röcken M, Weber WA (2005) Imaging of delayed-type hypersensitivity reaction by PET and 18F-galacto-RGD. J Nucl Med 46(1):184-189
100. Bennink RJ, van Montfrans C, de Jonge WJ, de Bruin K., van Deventer SJ, te Velde AA (2004) Imaging of intestinal lymphocyte homing by means of pinhole SPECT in a TNBS colitis mouse model. Nucl Med Biol 31:93-101
101. Blankenberg FG, Kalinyak J, Liu L, Koike M, Cheng D, Goris ML, Green A, Vanderheyden JL, Tong DC, Yenari MA (2006) ^{99m}Tc-HYNIC-annexin V SPECT imaging of acute stroke

and its response to neuroprotective therapy with anti-Fas ligand antibody. Eur J Nucl Med Mol Imaging 33:566-574
102. Kanwar B, Gao DW, Hwang AB, Grenert JP, Williams SP, Franc B, McCune JM (2008) In vivo imaging of mucosal CD4+ T cells using single photon emission computed tomography in a murine model of colitis. J Immunol Methods 329:21-30
103. Welling MM, Nibbering PH, Paulusma-Annema A, Hiemstra PS, Pauwels EKJ, Calame W (1999) Imaging of Bacterial Infections with 99mTc Labeled Human Neutrophil Peptide-1. J Nucl Med 40:2073-2080
104. Jones-Jackson L, Walker R, Purnell G, McLaren SG, Skinner RA, Thomas JR et al (2005) Early detection of bone infection and differentiation from post-surgical inflammation using 2-deoxy-2-[18F]-fluoro-D-glucose positron emission tomography (FDG-PET) in an animal model. J Orthop Res 23(6):1484-1489
105. Koort JK, Makinen TJ, Suokas E, Veiranto M, Jalava J, Knuuti J et al (2005) Efficacy of ciprofloxacin-releasing bioabsorbable osteoconductive bone defect filler for treatment of experimental osteomyelitis due to Staphylococcus aureus. Antimicrob Agents Chemother 49(4):1502-1508
106. Makinen TJ, Lankinen P, Poyhonen T, Jalava J, Aro HT, Roivainen A (2005) Comparison of 18F-FDG and 68Ga PET imaging in the assessment of experimental osteomyelitis due to Staphylococcus aureus. Eur J Nucl Med Mol Imaging 32(11):1259-1268
107. Koort JK, Makinen TJ, Knuuti J, Jalava J, Aro HT (2004) Comparative 18F-FDG PET of experimental Staphylococcus aureus osteomyelitis and normal bone healing. J Nucl Med 45(8):1406-1411
108. Makinen TJ, Veiranto M, Knuuti J, Jalava J, Tormala P, Aro HT (2005) Efficacy of bioabsorbable antibiotic containing bone screw in the prevention of biomaterial-related infection due to Staphylococcus aureus. Bone 36(2):292-299
109. Langer O, Mitterhauser M, Brunner M, Zeitlinger M, Wadsak W, Mayer BX et al (2003) Synthesis of fluorine-18-labeled ciprofloxacin for PET studies in humans. Nucl Med Biol 30(3):285-291
110. Livni E, Babich J, Alpert NM, Liu YY, Thom E, Cleeland R et al (1993) Synthesis and biodistribution of 18F-labeled fleroxacin. Nucl Med Biol 20(1):81-87
111. Tewson TJ, Yang D, Wong G, Macy D, DeJesus OJ, Nickles RJ et al (1996) The synthesis of fluorine-18 lomefloxacin and its preliminary use in human studies. Nucl Med Biol 23(6): 767-772
112. Babich JW, Rubin RH, Graham WA, Wilkinson RA, Vincent J, Fischman AJ (1996) 18F-labeling and biodistribution of the novel fluoro-quinolone antimicrobial agent, trovafloxacin (CP 99,219). Nucl Med Biol 23(8):995-998
113. Fischman AJ, Babich JW, Alpert NM, Vincent J, Wilkinson RA, Callahan RJ et al (1997) Pharmacokinetics of 18F-labeled trovafloxacin in normal and Escherichia coli-infected rats and rabbits studied with positron emission tomography. Clin Microbiol Infect 3(1):63-72
114. Fischman AJ, Livni E, Babich J, Alpert NM, Liu YY, Thom E et al (1992) Pharmacokinetics of 18F-labeled fleroxacin in rabbits with Escherichia coli infections, studied with positron emission tomography. Antimicrob Agents Chemother 36(10):2286-2292
115. Buursma AR, Rutgers V, Hospers GA, Mulder NH, Vaalburg W, de Vries EF (2006) 18F-FEAU as a radiotracer for herpes simplex virus thymidine kinase gene expression: in-vitro comparison with other PET tracers. Nucl Med Commun 27(1):25-30
116. Bennett JJ, Tjuvajev J, Johnson P, Doubrovin M, Akhurst T, Malholtra S et al (2001) Positron emission tomography imaging for herpes virus infection: Implications for oncolytic viral treatments of cancer. Nat Med 7(7):859-863
117. Buursma AR, De Vries EFJ, Garssen J, Kegler D, van Waarde A, Schirm J et al (2005) [^{18}F] FHPG positron emission tomography for detection of herpes simplex virus (HSV) in experimental HSV encephalitis. J Virol 79(12):7721-7727
118. Doorduin J, De Vries EFJ, Dierckx RA, Klein HC (2007) PET imaging of herpes simplex encephalitis in rats. J Labelled Cmp Radiopharm 50 Suppl 1:S60

119. Doorduin J, Klein HC, Dierckx RA, James M, Kassiou M, de Vries EF (2009) [(11) C]-DPA-713 and [(18)F]-DPA-714 as New PET Tracers for TSPO: A Comparison with [(11) C]-(R)-PK11195 in a Rat Model of Herpes Encephalitis. Mol Imaging Biol doi: 10.1007/s11307-009-0211-6
120. Doorduin J, de Vries EF, Dierckx RA, Klein HC (2008) PET imaging of the peripheral benzodiazepine receptor: monitoring disease progression and therapy response in neurodegenerative disorders. Curr Pharm Des 14(31):3297-3315
121. Alsaid H, Sabbah M, Bendahmane Z, Fokapu O, Felblinger J, Desbleds-Mansard C, Corot C, Briguet A, Crémillieux Y, Canet-Soulas E (2007) High-resolution contrast-enhanced MRI of atherosclerosis with digital cardiac and respiratory gating in mice. Magn Reson Med 58(6): 1157-1163
122. Clavel G, Marchiol-Fournigault C, Renault G, Boissier MC, Fradelizi D, Bessis N (2008) Ultrasound and Doppler micro-imaging in a model of rheumatoid arthritis in mice. Ann Rheum Dis 67(12):1765-1772
123. Leevy WM, Gammon ST, Jiang H, Johnson JR, Maxwell DJ, Jackson EN, Marquez M, Piwnica-Worms D, Smith BD (2006) Optical imaging of bacterial infection in living mice using a fluorescent near-infrared molecular probe. J Am Chem Soc 128(51):16476-16477
124. Simon GH, Daldrup-Link HE, Kau J, Metz S, Schlegel J, Piontek G, Saborowski O, Demos S, Duyster J, Pichler BJ (2006) Optical imaging of experimental arthritis using allogeneic leukocytes labeled with a near-infrared fluorescent probe. Eur J Nucl Med Mol Imaging 33(9):998-1006

Chapter 23
Applications of Small-Animal Molecular Imaging of Gene Expression

June-Key Chung, Hyewon Youn, Joo Hyun Kang, and Keon Wook Kang

1 Introduction

Recent advances in molecular imaging allow us to visualize both cellular and subcellular processes within living subjects at the molecular level as well as at the anatomical level [1]. Molecular imaging is molecular-genetic imaging for visualizing cellular processes by combination of molecular biology and biomedical imaging. This marvelous technique provides research attention not only in molecular cell biology but also in related fields. Remarkable improvement of molecular imaging was achieved in visualization, characterization, and quantification of biological

J.-K. Chung (✉)
Department of Nuclear Medicine, Cancer Research Institute, Tumor Micro-environment Global Core Research Center, College of Medicine, Seoul National University, Seoul, South Korea
e-mail: jkchung@snu.ac.kr

H. Youn
Department of Nuclear Medicine, Cancer Research Institute, Tumor Micro-environment Global Core Research Center, College of Medicine, Seoul National University, Seoul, South Korea

Cancer Imaging Center, Seoul National University Hospital, Seoul, South Korea
e-mail: hwyoun@snu.ac.kr

J.H. Kang
Molecular Imaging Research Center, Korea Institute of Radiological and Medical Science, Seoul, South Korea
e-mail: kang2325@kirams.re.kr

K.W. Kang
Department of Nuclear Medicine, Cancer Research Institute, College of Medicine, Seoul National University, Seoul, South Korea

Institute of Radiation Medicine, Medical Research Center, Seoul National University, Seoul, South Korea
e-mail: kangkw@snu.ac.kr

H. Zaidi (ed.), *Molecular Imaging of Small Animals: Instrumentation and Applications*,
DOI 10.1007/978-1-4939-0894-3_23,

processes by integration of many different fields such as genetics, pharmacology, chemistry, physics, engineering and medicine.

Especially, the development of controlled gene delivery and gene expression vector systems promotes generation of various types of reporter genes for visualization, for example, chlorampenicol acetyltransferase (CAT) [2], β-galactosidase (lacZ) [3], luciferases [4], and fluorescent proteins [5]. Conventionally, a recombinant plasmid, which contains a target gene and a reporter gene, has been used to monitor target gene expression by assaying reporter gene expression. However, this method cannot be used directly in living animals because the invariable light intensity from reporter proteins was not enough to be visualized in animals for non-invasive imaging. Different strategies are required for monitoring gene expression in vivo imaging. Accumulation of specific imaging signal for amplifying its intensity makes it possible to visualize localization, quantification, and repetitive determination of gene expression in vivo non-invasive imaging [6, 7]. More effective strategies have been tried to overcome the obstacles for monitoring gene expression in vivo by recruiting methods from radio-pharmaceutics and physics. Radio-labeled small compounds and paramagnetic probes were developed for imaging specific proteins and magnetic signals, accelerating non-invasive molecular imaging technology [8, 9]. In recent publications, these strategies have been reviewed by researchers for introducing the concept of molecular imaging [10–12].

The development of molecular imaging technologies has been facilitated by associated development of imaging instruments as well as imaging materials such as enhancement agents, probes, ligands and reporter constructs. Small animal models have a great advantage in disease studies that are difficult or impossible to be performed in human. Repetitive observation is a virtue of non-invasive small animal imaging, which provides information about a spatial and temporal dimension in disease development and progression. Multiple imaging modalities, including micro-CT (computed tomography), micro-SPECT (single photon emission computed tomography), micro-PET (positron emission tomography), micro-MRI (magnetic resonance), micro-US (ultrasound), and various optical techniques using fluorescence and bioluminescence, are available for small animal imaging. Recently, the resolution of some imaging modality is approaching cellular level [13], and the advances in imaging technology have resulted in developing combined imaging modalities, such as PET/CT, SPECT/CT, and PET/MRI [14, 15]. Using the newly developed instrumental merging techniques, more precise localization information of both anatomical and molecular activity can be acquired in a single imaging session [16]. Advantages of multimodal approaches to molecular imaging provide better images for visualizing cellular, functional, and morphological changes.

Molecular and genetic changes usually precede biochemical, physiological, and anatomical changes. Anatomic morphology changes can be visualized by conventional imaging modalities such as CT, MRI, US and radiography. Biochemical and physiological changes can be monitored by PET, SPECT and MRI. Molecular genetic imaging offers several different options in visualizing molecular genetic changes, which is occurring at the beginning of most diseases. The strategies for monitoring gene expression in small animal molecular imaging are broadly defined as direct and indirect imaging (Table 23.1). Direct imaging strategies usually consist

Table 23.1 Applicable molecular imaging methods for visualizing gene expression in small animals

Direct imaging			
Target	Probes	Imaging modality	References
Biomarker (ex. glucose transporter)	[F-18] FDG	Nuclear	[18–20]
Receptor	Antibody	Nuclear, MRI	[22, 23]
	Minibody	Nuclear	[24]
	Affibody	Nuclear	[25]
	Peptide ligand	Nuclear, MRI	[26–28]
	Peptide ligand	Nuclear, optical	[29]
mRNA, protein	Synthetic small molecular tracer		
	Antisense oligonucleotide	Nuclear	[30–33]
	Aptamer	Nuclear, optical	[34]
Receptor, transporter, biomarker	Paramagnetic iron oxide SPIO, MION	MRI	[43, 44]
Indirect imaging (reporter gene imaging)			
Reporter	Probes/contrasting agents	Imaging modality	References
Fluorescent protein	GFPs, RFPs	Optical	[46, 47]
Enzyme type reporter			
Luciferase		Optical	[48–51]
HSV1-TK	[F-18] FEAU, FHBG, [I-124] FIAU, etc.	Nuclear	[52, 53, 55–58]
Tyrosinase	Paramagnetic iron oxide	MRI	[84, 85]
Receptor type			
D2R	[F-18] FESP	Nuclear	[59–62]
SSTr	[I-123,124,131,Tc-99m] octreotide	Nuclear	[63, 69–75]
hNET	[I-123,124,131] MIBG, [C-11]ephedrine	Nuclear	[76–79]
Transferrin	Paramagnetic iron oxide	MRI	[82]
Ferritin	Paramagnetic iron oxide	MRI	[86, 87]
LRP	H^+	MRI	[88]
Transporter type			
NIS	[I-123,124,131]. [Tc-99m]O_4	Nuclear	[64–68]

of a specific target and a target-specific probe, and the interaction between a target and a probe is directly related with the intensity of imaging signal. Synthetic radiolabeled antisense oligonucleotide can be used as a probe for direct imaging to visualize endogenous gene expression at the transcription level.

For indirect imaging, reporter gene based techniques, which have been identified and widely used to study cell biology, are most frequently performed for monitoring gene expression in vivo. Reporter genes are genetic markers that easily encode detectable proteins, or involve in metabolism of labeled probe. These markers are great tools to determine activities of specific promoters and the factors when they are located at the downstream of a specific promoter/enhancer sequence. Many genes contain more than one promoter, and promoter activities may be specific for a disease process. By placing an imaging reporter gene under the control of such promoter, promoter activity can be dynamically visualized and gene expression can

be monitored. The reporter proteins are accumulated in the cells with promoter-reporter construct, and the measurements of specific imaging signals from accumulated reporter proteins provide indirect information that reflects the level of reporter gene expression. A variety of molecular imaging techniques, including optical, nuclear, magnetic resonance modalities, can be used for reporter imaging. Since reporter based imaging system represents a part of molecular signature in cellular process, it may be useful in gene therapy as well as imaging tool.

2 Direct Imaging for Small Animal Molecular Imaging

The strategies of direct imaging for small animal molecular imaging have been established using nuclear medicine, optical and MRI modalities with a specific target and a target-specific probe for gene expression. The localization and the concentration of a probe are directly related to its interaction with a target. In biomarker imaging, the metabolic trapping of specific probe molecule reflects the molecular events of a disease. Specific ligands for receptors, antibodies or antibody fragments (i.e. minibody or affibody, etc.) for specific antigen, and synthetic small molecular tracers are other examples of direct imaging probes. Recently, synthetic small molecular tracers, such as antisense oligonucleotide or aptamer probes for targeting specific mRNA or protein, have been developed to visualize gene expression (Fig. 23.1).

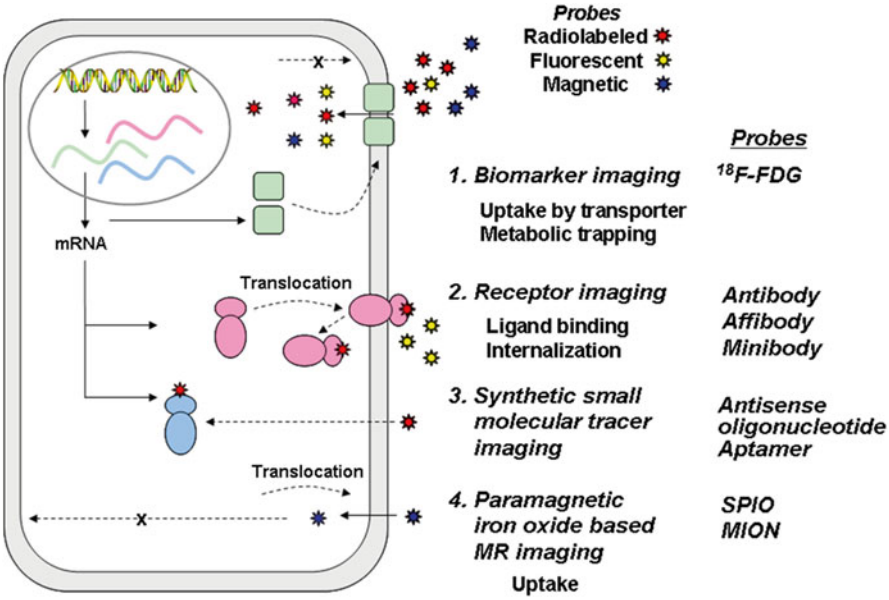

Fig. 23.1 Schematic illustration of direct imaging with target-specific probe. *Stars* are radioisotope labeled, fluorescent, or magnetic probes

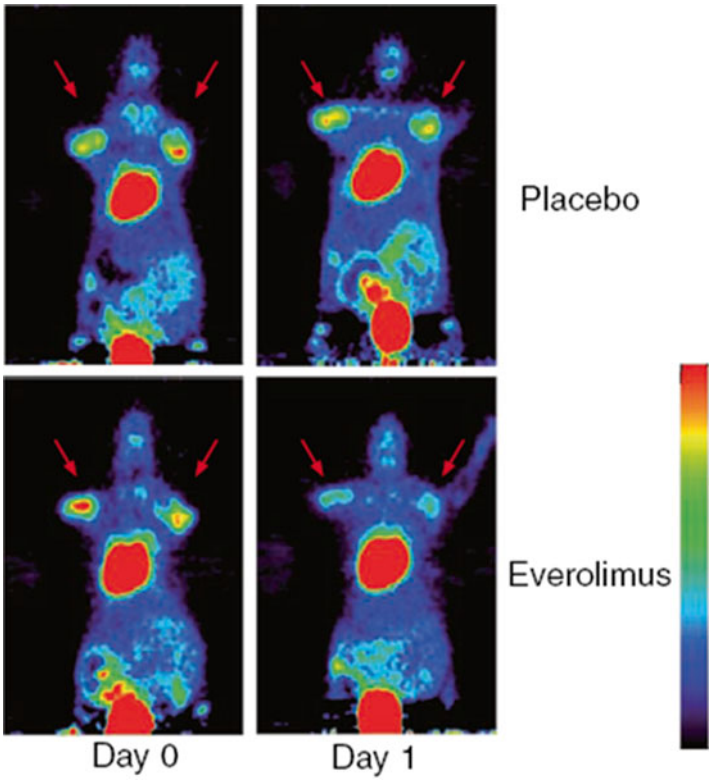

Fig. 23.2 An application of FDG-PET as a biomarker imaging for visualizing tumor to evaluate the efficacy of the mTOR inhibitor everolimus. Reprinted with permission from [18]

2.1 Biomarker Imaging

For visualizing downstream effects of changes in specific molecular events, biomarker imaging can be useful. One good example of biomarker imaging is based on the fact that malignant tumors frequently show elevated level of glucose utilization and glycolysis [17]. This imaging strategy utilizes a radiolabeled glucose analogue (2′-fluoro-2′-deoxyglucose-[F-18]FDG) and positron emission tomography (PET), which reflects increased glucose transport and hexokinase activity. [F-18]FDG PET has been widely used in clinic to access tumor diagnosis and monitor therapeutic effect.

However, biomarker imaging may reflect more than a single protein or signaling pathway. For [F-18]FDG PET, glucose metabolism is regulated by many different kinds of extracellular signals such as PI3 Kinase/Akt pathway, mTOR, c-kit, and Hif-1α activation [11]. Nonetheless, [F-18]FDG PET whole body imaging is most widely used in clinic for tumor diagnosis and monitoring the efficacy of anti-cancer therapy taking advantages of the pre-developed radiolabeled probe. Especially, the application of biomarker imaging for monitoring the response of treatment is commonly used for evaluating the efficacy of newly developed drugs [18–20] (Fig. 23.2).

2.2 Receptor Imaging

Since the enhanced intensity of probe signal is directly related to its interaction with a specific target, imaging specific receptors has been evolved to improve probe sensitivity and specificity. For this reason, radiolabeled antibodies for a specific receptor have been used over last 20 years to visualize the localization of the receptor. However, the use of conventional radiolabeled antibody has a major problem of higher background signal from non-specific binding, slow penetration and prolonged clearance by a larger size. More recently, genetically engineered small fragments of antibody, such as minibodies or affibodies, have been introduced as imaging probes for reducing size disturbance and increasing affinity [21]. In addition, small sized radiolabeled peptide ligands have been also used for specific receptor imaging. Moreover, recent advances have increased the detection sensitivity, which provides more options for selecting probes including fluorescent or paramagnetic nanoparticle based probes.

Tyrosine kinase HER2 is overexpressed in most breast cancers, and a radiolabeled monoclonal HER2 antibody for targeting HER2 is a good example of target specific receptor imaging [22]. A gadolinium-chelated HER2 specific antibody was also successfully used for magnetic resonance based molecular imaging of HER2 receptor [23]. A series of small fragmented antibodies was derived from a parental HER2 monoclonal antibody. A variant of anti-$p185^{HER2}$ minibodies showed high affinity to $p185^{HER2}$ and rapid clearance. However, their results demonstrated that the tumor targeting properties in vivo mouse studies were less effective than in vitro [24]. Instead of antibody libraries, affibody molecules are selected from phage display. A new type of molecule named $(Z_{her2:4})_2$ showed high affinity to HER2 and the tumor was easily visualized with a gamma camera in a xenografted mouse [25].

Radiolabeled glycosylated RGD peptides are also developed for targeting alpha(v) beta3 integrin, which is highly expressed on tumor vasculature and plays an important role in tumor metastasis, and angiogenesis [26, 27]. Recent researches focus on the wider use of a different imaging modality or multimodality using RGD. Kiessling et al. reported that the RGD-labeled ultra-small super paramagnetic iron oxide (USPIO) for MRI successfully accumulated in the tumor vasculature of xenograft mouse model [28]. Multimodal imaging approach using RGD peptide was also tried, and tumor selective localization was observed by bioluminescence, fluorescence, gamma scintigraphy, and SPECT imaging [29].

2.3 Synthetic Small Molecular Tracer Imaging

The development of synthetic small molecular tracer that specifically hybridizes to target mRNAs or proteins provided another strategy for direct imaging, including radiolabeled antisense (or aptamer) oligonucleotide probes (RASONs). Some efficacy of RASONs was demonstrated for endogenous gene expression, using a gamma camera and PET imaging [30]. Recently, the successful uses of ^{99m}Tc-RASON

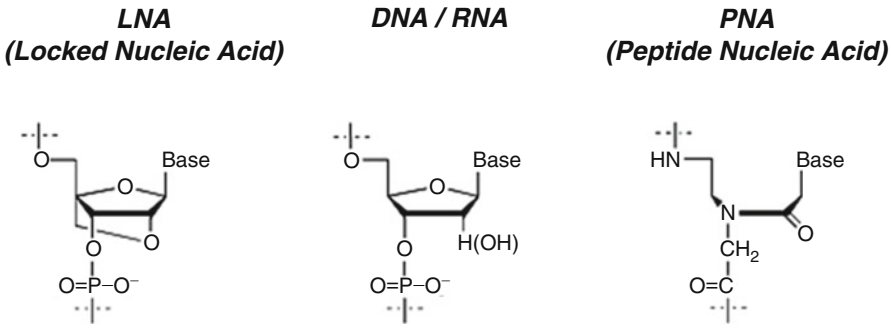

Fig. 23.3 Structures of some oligonucleotide analogues; locked nucleic acid and peptide nucleic acid

targeting human telomerase reverse transcriptase (hTERT) [31], proliferating cell nucleus antigen (PCNA) [32], and multidrug resistance gene-1 (MDR-1) mRNA [33] were reported in xenografted mouse models. Newly developed oligonucleotide based molecule, named aptamer, which can bind to almost any targets including proteins, peptides, antibodies, and small molecules such as DNAs and RNAs, provides a wide range of possible probes for specific targeting. An efficient targeting example using MUC-1 specific aptamer has been demonstrated in most tumors [34]. However, RASON imaging still has several serious limitations, such as high background activity, limited tracer delivery, and poor stability.

A further development of direct radiotracer imaging strategies is required for a specific probe for each molecular target. In recent studies, the application of cell penetrating peptide (CPP) with oligonucleotide probe is suggested to improve the delivery efficiency of tracing probe across the cell membrane, and the use of modified oligonucleotide is also recommended for longer stability of the tracing probe. Positively charged CPPs, such as TAT (transactivator of transcription) protein transduction domain and Arginine/Lysine rich peptide domain, have been used as conjugating peptides for intracellular delivery of a variety of small molecules including oligonucleotides [35, 36]. Many types of oligonucleotide analogues including locked nucleic acid (LNA) or peptide nucleic acid (PNA), have been reported [36, 37], and the structural modification prevents enzymatic degradation of oligonucleotides from nucleases (Fig. 23.3).

2.4 Paramagnetic Iron Oxide Based MRI

Recently, the application of super paramagnetic nanoparticle based probe has increase for high resolution of in vivo MRI. This strategy uses MRI based on T2 effect by superparamagnetic ion oxide (SPIO) nanoparticle for visualization [38]. The clinically approved SPIO containing Fe^{2+} and Fe^{3+} ion oxide core, is coated

with carboxydextran. A larger amount of ion oxide can be loaded into the nanoparticle, and micrometer sized particles harboring iron oxide (MPIOs) are available for this purpose [39]. Especially, paramagnetic iron oxide has been successfully used with a better spatial resolution in monocyte-macrophage based liver imaging and stem cell trafficking [40, 41]. For imaging the gene expression, the conjugation with a targeting peptide or oligonucleotide with paramagnetic ion oxide, have been widely used [42, 43]. Though the possible toxicity of iron oxide nanoparticle has always challenged, recent findings have shown that SPIO can be safely used in mesenchymal stem cells trafficking without changing the viability, proliferation, and differentiation capability [44].

3 Reporter Gene Imaging for Small Animal Molecular Imaging

Although the originally devised reporter genes have been widely utilized to study in vitro cell biology, recent technical developments allow direct in vivo visualization to analyse gene expression and regulation. Reporter genes, located at the downstream of a specific promoter, are genetic markers that encode easily detectable proteins, and these markers become extraordinary tools to determine the activities of specific promoters. Imaging reporter genes uses genetic markers that involve in metabolism of labeled probes [6], which are great tools for determining activities of specific promoters and the factors when they are located at the downstream of a specific promoter/enhancer sequence. By placing an imaging reporter gene under the control of such a promoter, dynamic visualization of promoter activity can be achieved [45].

3.1 Optical Reporter Imaging

Major advantages of optical imaging modalities, such as fluorescence and bioluminescence imaging, are suggested that they are simpler, cheaper, more convenient, and more user friendly than other imaging modalities. Another advantage, especially for bioluminescence imaging, is highly sensitivity for detecting low levels of gene expression. Various optical reporter genes construct which have been already used in vitro, are available for testing the same biological hypotheses in living animal models. Combining the fluorescence and bioluminescence reporter genes into a single gene product could provide a better resolution for the analysis of gene expression by taking advantages of fluorescence in vitro as well as bioluminescence in vivo (Fig. 23.4).

Though one of the critical components of the optical imaging modalities is the sensitivity of detecting devices, the recent advances have greatly increased their sensitivity. The charged coupled device (CCD) camera is the detection device

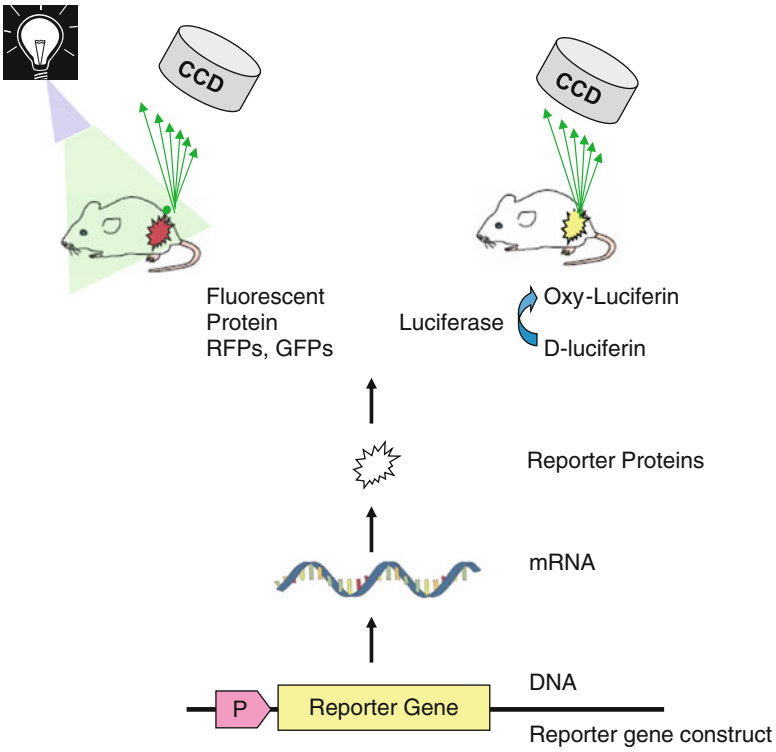

Fig. 23.4 Strategy of promoter-reporter gene construct for monitoring gene expression using optical imaging. P is a promoter/enhancer sequence

which captures photons by photocathode, which converts photon to electron for amplification. For final detection using phosphorscreen, another conversion of amplified electron to photon is required. For reducing thermal noise, this device can be cooled down to −120 °C. The sensitive range of this system is across the entire visible and near infrared wavelengths. However, the blue, green, yellow range of the light spectrum can be easily absorbed by mammalian tissue, the red or longer wavelength of light is preferable for in vivo optical imaging.

3.1.1 Fluorescent Protein Based Reporter System

Recently, a fluorescent protein based reporter system has become very popular for monitoring gene expression, localization, movement and protein–protein interaction in vitro [5]. Imaging fluorescent proteins is measured by the light emission from the excitation of external source of light. Various factors are involved in the brightness of fluorescent proteins, including folding, maturation, extinction coefficient, quantum yield, and the photo-stability of proteins. For this reason, many types of genetically engineered variants from natural fluorescent proteins are also developed for better imaging.

Green fluorescent protein (GFP) has been widely used in molecular cell biology, and most GFP variants have come from spectral shifted variants [5, 46]. Synthetic variants including an enhanced GFP (eGFP) have been developed for improving stability and brightness of fluorescence. A number of red fluorescent proteins (RFPs) have also been developed by genetic modification to overcome its limitations, such as tetrameric toxicity and incomplete maturation. Since many wild types fluorescent proteins have tetrameric structure which causes aggregation and toxicity, a variety of genetically engineered mutant RFPs shows with longer emission wavelength. Bright, less toxic and more suitable RFPs for mammalian cell studies have been generated by Tsien's group. Monomers or tandem dimers of tetrameric fluorescent proteins with very bright fluorescence and higher photo-stability have been developed, and named such as mPlum, mCherry and tdTomato [46, 47].

However, fluorescent reporter imaging for in vivo small animal imaging has major limitations such as the requirement of an external light source and the exponentially decreasing intensity of light with increasing depth of the target localization. Moreover, the sensitivity and specificity of fluorescence imaging are frequently disturbed by endogenous tissue autofluorescence resulting in substantial background emissions. For this reason, the proper use of selective filters or the application of spectral analysis is required in order to reduce the interference of autofluorescence to the acquired images.

3.1.2 Bioluminescent Protein Based Reporter System

Among the various kinds of reporter genes, luciferases are the only ones that produce light, and do not require an external excitation source. As mammalian tissue does not emit a significant amount of light, luciferase imaging offers lower background signal compared to fluorescence imaging. The family of luciferase enzymes presents in certain bacterial, marine crustaceans, fish and insects. The Firefly luciferase (FLuc) and Renilla luciferase (RLuc) are most commonly used luciferase genes, and their corresponding substrates are luciferin and coeleterazine.

Native luciferase of American firefly, *Photinus pyralis*, produces light with broad emission that peaks at 560 nm and above 600 nm fraction, making it suitable for in vivo imaging. Since the first report of Luc gene, this reporter gene has been modified for improving expression in mammalian cells by codon optimization. The peroxisomal targeting sequence was also deleted for higher expression in cytosol, and the some amino acids were substituted for shifting emission wave length towards the red region above 600 nm [48]. More recently, a synthetically-derived luciferase Fluc2 is developed with humanized codon optimization that is designed for high expression and reduced anomalous transcription. The native substrate, D-luciferin [D-(-)-2-(6′-hydroxy-2′-benzothiazolyl) thiazone-4-carboxylic acid], is converted into oxyluciferin in an Mg-ATP dependent process. These luciferases generate a visible light through the oxidation of an enzyme-specific substrate in the presence of oxygen, and ATP is also required as an additional co-factor for luciferase imaging. For in vivo administration, it was reported that luciferin found to be non toxic

and well distributed in the whole body of mouse after exogenous application (usually intraperitoneal injection, also can use intravenous route), even crossed the blood–brain or placental barrier. In a mouse model, luciferase reaction peaked at 20 min after the injection.

Another type of commonly used luciferase from Renilla, emits blue light with 480 nm peak, limiting its use in vivo. Firefly and RLuc are distinguishable because they use different substrates and emit different light spectra. For these reasons, RLuc has been used for the normalization of FLuc expression. Fast induction of luminescence and short half-life of luciferin and luciferase in bioluminescence system provide a suitable method for monitoring transcriptional activation using these two luciferases [49, 50].

In vivo bioluminescence imaging was originally developed using bacterial infection model [51], and a set of genes from soil bacterium *Photohabus luminescens* was first introduced into Salmonella bacteria. Bacterial luciferase Lux operon consists of five polycistronic genes under same promoter, named Lux A, B, C, D, E. Lux A and B encode heterodimeric bacterial luciferase and additional genes encode substrate synthesizing enzymes such as fatty acid reductase enzyme complex. The lux operon has also been reorganized and optimized for expression. Labeled bacteria can be detected in the mouse model and represented the location of an infection. Reduced form of flavin mononucleotide (FMNH2) can be used as a substrate for bacterial luciferase, and emission peak is 490 nm [48, 51].

For whole-body imaging of small animals, bioluminescence reporter genes have been more widely used than fluorescence imaging due to the higher sensitivity and the lower background luminescence or autoluminescence. However, the basic problem of optical imaging system is the attenuation of light photons. About 90 % of bioluminescence signal flux is lost per centimeter of tissue, thus, photon intensities detected by CCD cameras may not proportionately or sufficiently reflect endogenous reporter gene expression in the inner organs of even small animals [48].

3.2 Nuclear Medicine Reporter Imaging

Many radionuclides emitting positrons and gamma rays have been used for a diagnosis and therapeutic purpose. PET scanners produce the image of positron emitters such as F-18, C-11, and I-124. To generate planar images and tomography of gamma ray emitters, a conventional gamma camera and SPECT have been routinely used. I-131, I-123, In-111 and Tc-99m are the source of gamma emitters in these cases. For small animal studies, several small animal imaging instruments for nuclear imaging have been developed to meet the level of spatial resolution for the basic research requirement. Recently commercialized micro-PET scanners have resolution of ca. 2 mm^3, and newly developed micro-SPECT systems have pinhole collimators for high resolution [7]. Various positron and gamma ray emitting probes and reporter genes for nuclear imaging have been developed, but choices have to be made by particular situations considering unique advantages and disadvantages of each strategy (Fig. 23.3).

3.2.1 The Herpes Simplex Virus-1 Thymidine Kinase (HSV-tk) System

The HSV1-tk has been most widely used as a reporter gene for radionuclide based molecular imaging, and a therapeutic suicidal gene for targeted gene therapy. The expressed viral thymidine kinase (TK) phosphorylates thymidine to thymidine-monophosphate, which is then phosphorylate di- and/or tri-phosphorylated by many cellular kinases. These phosphorylated compounds can serve as inhibitors of DNA replication, blocking DNA polymerization, which leads to cell death. Unlike mammalian TK, HSV1-tk can phosphorylates modified thymidine analogues, for example, F-18 labeled 2′-fluoro-2′-deoxy-1-β-D-arabinofuranosyl-5-iodouracil (FIAU). Phosphorylated FIAU cannot traverse the cellular membrane and it is retained in the cell. PET can detect HSV1-tk gene expression by visualizing positron emission from a reporter probe, F-18 labeled phosphorylated FIAU in this case. The magnitude of radioactive reporter probe accumulation reflects HSV1-tk enzyme activity, which represents HSV1-tk gene expression.

Two types of substrates for HSV1-tk have been reported [6, 52], which are pyrimidine nucleoside derivatives and acycloguanosine derivatives. Pyrimidine nucleoside derivatives are similar to natural thymidine in their structure, and they can be more sensitive probes than acycloguanosine derivatives for HSV1-tk imaging. Pyrimidine nucleoside derivatives include FIAU, 2′-fluoro-2′-deoxy-5-methyl-1-β-D-arabinofuranosyl-uracil (FMAU) and 2′-fluoro-2′-deoxy-5-ethyl-1-β- D-arabino furanosyl uracil (FEAU). A tracer dose of these drugs with radioisotopes can be successfully utilized as a probe for monitoring HSV1-tk expression by taking advantage of high sensitivities of PET and SPECT [53–56]. Since HSV1-tk is less substrate specific, it can phosphorylate acycloguanosine derivatives. Acycloguanosine derivatives have been used, and newly developed anti-herpetic drugs, such as F-18 labeled acyclovir (ACV), ganciclovir (GCV), penciclovir (PCV), and 9-(4-fluoro-3-hydroxymethylbutyl)-guanine (FHBG) have been found to accumulate better than older drugs in HSV1-tk transfected cells [55] (Fig. 23.5).

A mutant HSV1-tk (HSV1-sr39tk) containing six amino acid substitutions, has been developed. Tumor uptake of F-18 PCV was elevated in C6 rat glioma cells stably transfected with mutant HSV1-sr39tk (C6-stb-sr39tk1+). The tumor uptake was 3.7 times higher than that of C6 cells with wild type HSV1-tk [57]. From the stable mammalian cell transfectants, sensitive clones were screened and selected, representing 43-fold more sensitive to ganciclovir and 20-fold more sensitive to acyclovir. This mutant HSV1-TK enzyme seems to use fluorinated acycloguanosines more effectively compared to pyrimidine nucleoside derivatives as substrates. HSV1-sr39tk/F-18 FHBG offers more effective PET reporter gene/probe combination with higher sensitivity and higher selectivity. F-18 FHBG showed favorable pharmacokinetic profiles, not crossing the blood–brain barrier (BBB) and rapid renal clearance [58].

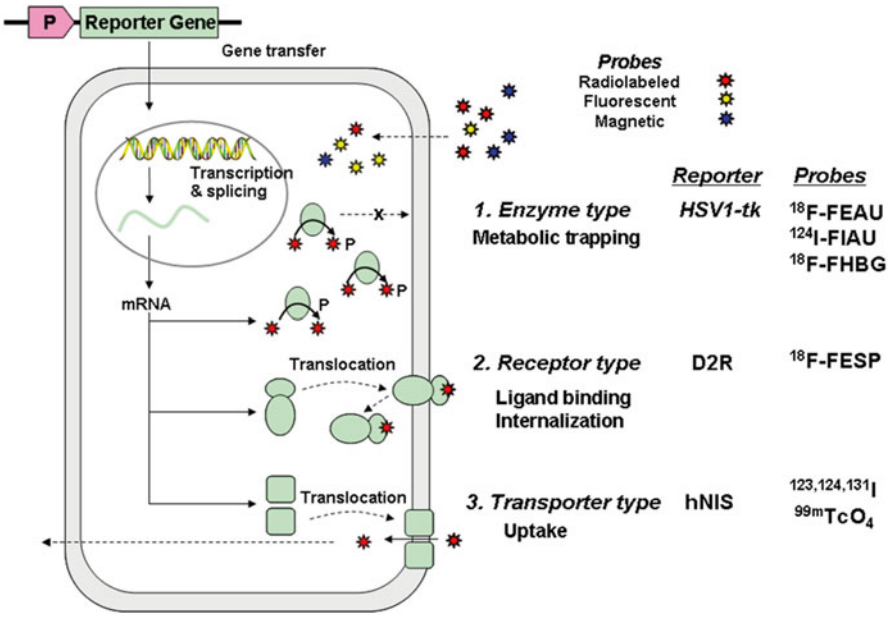

Fig. 23.5 Schematic illustration of three type reporter gene expression used nuclear imaging modalities. *Stars* are radioisotope labeled substrates (enzyme) or ligands (receptor) or radioisotope itself (transporter type)

3.2.2 The Dopamine 2 Receptor (D2R) System

Since most thymidine kinase substrates do not cross the BBB very rapidly, the development of a new kind of reporter gene/probe has been requested. Dopamine D2 receptor (D2R) system has been introduced for this reason, which uses D2R as an imaging reporter gene and F-18-fluoroethyl spiperone (FESP) as a radiolabeled probe [59]. D2R, found in striatum and pituitary, is a seven transmembrane domain protein with 415 amino acids [60]. Besides the crossing availability of FESP through BBB, quantitative PET signals from accumulated radioactive F-18 FESP in D2R expressing cells were reported to reflect D2R expression [61]. However, this system has potential problems, resulting from an ectopic expression of D2R. High level of receptor expression cannot be achieved on cellular membrane because of the competition with other receptors, and D2R can be occupied by endogenous natural ligands. Moreover, when a ligand activates D2R, cellular levels of cAMP may be affected, which could stimulate many unexpected signaling cascades. To prevent this, mutant strains of D2R have been developed, which will not activate such signal pathways [62].

3.2.3 The Sodium/Iodide Symporter (NIS) System

Since conventional PET reporter gene imaging requires the complicated substrates and expensive PET equipment, the development of simpler and less expensive system is requested [63]. The sodium iodide symporter (NIS) gene system which utilize iodide uptake driven by the sodium ion concentration gradient across the membrane has been shown to be the simplest and most applicable reporter system [64, 65]. In thyroid cells, sodium ion gradient is generated and maintained by the sodium–potassium pump (Na+-K+ATPase). An iodide enters with two sodiums through a specific transporter, NIS. In addition to iodide, several other anions are transported by NIS, i.e., $ClO_4^- > ReO_4^- > I^- \geq SCN^- > ClO_3^- > NO_3^-$ in order of transport rates. Pertechnetate (TcO_4^-) and perrhenate (ReO_4^-) are also transported by NIS, and radioactive forms (Tc-99m or Re-188) of such anions are important in terms of nuclear medicine imaging and radionuclide therapy. The NIS gene was first identified in the rat by Dai and Carrasco in 1996 and the human equivalent (hNIS) was isolated with 84 % homology with rat NIS [66]. The hNIS gene consists of 15 exons interrupted by 14 introns, and encodes a 3.9 kb mRNA transcript for 643 amino acids. NIS is an intrinsic membrane protein with 13 putative transmembrane domains, an extracellular N-terminal domain, and an intracellular carboxy domain. The level of NIS on the surface of cell membrane is proportional to total NIS protein level in cultured cells, and radioiodide uptake is also proportional to total NIS protein amount [67].

NIS has many advantages as an imaging reporter gene because various probes are available, such as radioiodines and Tc-99m, and their metabolism are well understood. Unlike D2R or HSV1-tk system using radiolabeled ligand, NIS has no problem with associated labeling stability because NIS directly uses radioiodine or Tc-99m. In addition, NIS seems less perturb cells because iodide is not metabolized in most tissues and no adverse effects have been observed except for sodium influx. Availability of less immunoactive human origin gene is another important merit of NIS. Since NIS genes are expressed on cell surfaces, reporter probes can reach to the cells easily. Importantly, reporter gene imaging with NIS may be more convenient, because most nuclear medicine departments have easily access to a gamma camera, SPECT, radioiodines, and Tc-99m. Nevertheless, NIS also has several limitations. NIS occurs naturally at high concentrations in the thyroid, stomach, and urinary tract causing difficulties of interpretating image. NIS system is also hampered by the rapid efflux of radionuclides from cells, but co-transfection with the thyroid peroxidase gene may improve radioiodine retention in target cells [68].

3.2.4 The Somatostatin Receptor (SSTr) System

The somatostatin receptors (SSTr) are G-protein-linked receptors with seven transmembrane domains. Among the six SSTr genes, the expression of SSTr2 is basically restricted to the pituitary [69]. Somatostatin binds to all hSSTr subtypes with high affinity, and octreotide, a somatostatin analog peptide, binds to hSSTr2 with highest affinity and lower affinity to hSSTr1, hSSTr3, hSSTr4, and hSSTr5 [70]. Several types of radiolabeled octereotides have been developed, i.e., I-123 labeled

Tyr3-octereotide [71], Tc-94m Tyr3-octreotate [72], and In-111 DTPA-D-Phe-octereotide [73, 74]. Human ovarian tumor xenografts expressing human SSTr2 with adenoviral vector, have been monitored by In-111 DTPA-D-Phe-octereotide-binding in vivo and in vitro [75].

However, natural expression of hSSTr2 and potential disturbance by an intracellular ligand binding to hSSTr2 in a number of normal tissues are major flaws of this system. A model epitope-tagged receptor was constructed by fusing hemagglutinin (HA) sequence of the influenza virus, which is novel and is not found in normal tissues within the extracellular N-terminus of hSSTr2 gene [76]. Therefore, the HA epitope can be used as a specific marker for determining gene transfer.

3.2.5 The Human Norepinephrine Transporter (hNET) System

The human norepinephrine transporter (hNET) is a transmembrane protein that is involved in the transport of norepinephrine analogs into cells at adrenergic nerve terminals. It has been used clinically for imaging myocardial sympathetic innervation and neural crest tumors using I-123, I-131 MIBG and C-11 ephedrine [77]. Major advantage of hNET as a reporter is its small gene size (<2 kb), which allow its easy incorporation into the expression cassette of the delivery vehicle [78]. In addition, this system is less immunogenic to human and safety of radiolabeled probes is confirmed. Moreover, the slow clearance of tracer from gene-transfected tumors allows a "late imaging" paradigm after injecting I-124 MIBG. It was reported that tumors expressing hNET showed a tenfold higher accumulation of I-131 MIBG than control tumors in a nude mouse xenograft model.

However, low sensitivity and narrow dynamic range are the disadvantages of this system. In addition, only one reporter probe molecule can be retained per receptor molecule, which hinders signal amplification. The feasibility of hNET as a reporter gene was evaluated using C-11 ephedrine, and only one of three hNET transduced tumors is managed to be visualized. At least 10^4 transduced T cells were required for the visualization of T cells injected into tumors by SPECT or PET [79].

3.2.6 The Estrogen Receptor Ligand (ERL) System

A new reporter gene imaging system that uses F-18 labeled estradiol (FES) and a human estrogen receptor ligand (hERL) binding domain was designed by Furukawa et al. [80]. This system takes advantage of the fact that FES has an easy access to a wide range of tissues, including a brain. The endogenous level of hERL is relatively lower in tissues other than the uterus, ovaries, and mammary glands that provide a major advantage of this system. Lacking N-terminal activation and DNA binding domains, hERL loses its binding ability to target DNA, and can no longer work as a transcription factor, which is used as an imaging reporter. Estrogen receptor concentrations and FES tumor uptakes are well-correlated in human breast cancer [81], and cells, expressing estrogen receptors at a level of 3 pmol/mg protein, can be visualized in vivo.

3.3 Magnetic Resonance Reporter Imaging

Recently developed micro-MRI units with higher tesla have made it possible to image small animals at higher resolution (~50 μm) [12]. Though MRI has not developed for reporter imaging, many trials have made on the development of new MRI reporters for imaging molecular events of interaction including the binding of specific MRI contrasting agents with specific surface receptors, proton exchange mediated by enzymatic cleavage of functional group and the binding of metalloprotein or MRI contrasting agents [82, 83].

3.3.1 The Transferrin Receptor System

The transferrin proteins are easy to bind with iron, and the iron-loaded transferrin proteins rapidly binds to transferrin receptors. The transferrin receptor-transferrin-Fe complex is internalized by receptor mediated endocytosis. The iron is then released from the endosome by the acidic environment, and the released iron decreases T2 MRI signals. As a reporter gene, the transferrin gene was cloned and transfected into the target cells, showing elevated level of transferring receptor gene expression. Successful MRI was demonstrated using superparamagnetic iron oxide for imaging the expression of transferrin receptor [82].

3.3.2 The Tyrosinase/Ferritin System

As another type of MRI reporter gene, the use of iron binding metalloprotein such as tyrosinase and ferritin has been suggested [84–86]. Tyrosinase is involved in melanin biosynthesis, and melanin has a higher affinity to iron. The human tyrosinase enzyme coded gene was successfully introduced and imaged in mouse fibroblast by iron induced T1 hyperintensities in vitro [84]. As an iron reservoir, ferritin also has roles in MRI reporter imaging [85]. Successful delivery of transferrin transgene using adenovirus was reported, and clear visualization was demonstrated in a rat glioma xenograft model [86].

3.3.3 The LRP System

Recent advances in cloning techniques allow the development of new reporter constructs. Nonmetallic, biodegradable MRI reporter gene encoding lysine rich protein (LRP) is the prototype of a potential family of genetic engineered reporter, expressing artificial proteins with frequency-selective contrast [87, 88]. The endogenous contrast is based on the transfer from amide protons or LRP to water protons, and this proton exchange reduces MRI signal intensity. Different changes of MRI signal intensity between control and LRP-expressing xenografts in mice demonstrated that LRP is a potential reporter for MRI [88].

4 Multimodality Imaging for Small Animal Molecular Imaging

Because each imaging technology has unique advantages and disadvantages, it is useful to develop multimodal reporter gene system and detectors compatible with several imaging modalities. PET/bioluminescent imaging appears to be the most amenable technology because PET can provide 3D images and allow quantitative analyses of reporter expression, and optical bioluminescent imaging can easily and rapidly produce bi-dimensional images with high sensitivity [89]. The development of instruments for combined modality, such as microPET/microCT and micro-SPECT/microCT, has been increased [90], and instruments that permit concurrent, coregistered optical imaging as well as nuclear medicine imaging are under development. These multimodal instruments should provide convenient and sensitive means of bioluminescent noninvasive reporter gene imaging with the advantage of different modalities.

For generating multimodal reporter gene system, several strategies are being used to link the expressions of multiple reporter genes (Fig. 23.6). Most genomic DNA is involved in the regulation of gene expression, which can be exercised at the transcriptional level or at the post-translational level. Many genes contain more than one promoter, and the activity of a particular promoter may be specific to a diseases process. These types of promoter are of particular interest. First because they are a part of the molecular signature of the pathological process concerned, and second, they are potentially useful as specific promoters for gene therapy.

Dual promoter or co-administration approach may be used according to the purpose of research, but the level of expression is relatively low and not controllable. The most widely used strategy is bi-cistronic approach using an internal ribosomal entry site (IRES) sequence between the two genes. Both genes are then transcribed

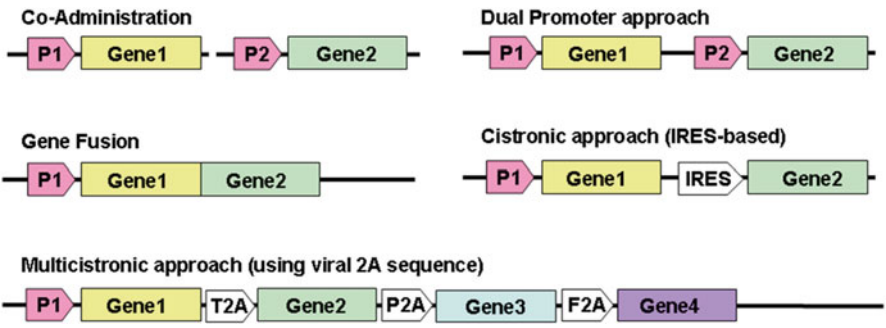

Fig. 23.6 Strategies of promoter-reporter gene constructs for monitoring gene expression. P1, P2 are promoter/enhancer sequences; Gene1, Gene2 can be reporter gene; internal ribosomal entry site (IRES); ribosomal skipping 2A sequence from foot-and-mouth disease virus (F2A), equine Rhinitis A virus, porcine teschovirus-1 (P2A) and Thosea asigna virus (T2A)

into a single mRNA, and later translated into two different proteins. However, biscistronic approach including IRES system, has demonstrated that a biased expression of the two transgenes with the second gene is under expressed [91, 92]. As an alternative option for multiple reporter gene expressions is the use of ribosomal skipping via 2A peptides [93, 94]. Several viruses use 2A peptides to mediate protein cleavage, including foot-and-mouth disease virus (F2A), equine Rhinitis A virus, porcine teschovirus-1 (P2A) and Thosea asigna virus (T2A). The 2A peptide consensus motif (DVEXNPGP) is extremely rare and is associated with cleavage-like activity through a ribosomal skip mechanism; the 2A peptide impairs normal peptide bond formation without affecting the translation of other gene. 2A peptides have been shown to initiate the production of up to four proteins both in vitro and in vivo [94].

Another strategy involves the use of a fusion gene vector, whereby two genes are connected, and their coding sequences are in the same reading frame to generate a single protein. Fusion between the two reporter genes, such as fLuc and GFP or its color shift variants allow a dual mode of optical imaging. This has been conventionally used to monitor the biological process in vitro. Since the fusion of engineered eGFP with other reporter gene, such as fLuc or NIS gene, has provided successful employment without changing their functional properties. Chimeric fusion genes or bi-cistronic vectors have been used for the noninvasive imaging of reporter gene expression, monitored by bioluminescence and fluorescence, microPET and fluorescence, microPET and bioluminescence, and by microPET, fluorescence and bioluminescence [95–98].

5 Application of Small-Animal Molecular Imaging

5.1 Monitoring Gene Therapy with Targeted Gene Expression

Linking molecular imaging to gene therapy could allow real-time assessments of therapeutic efficacy, and also linking an imaging reporter gene with a therapeutic gene could become a general approach to the monitoring of the in vivo expression of the therapeutic gene. For example, HSV1-TK was designed to kill target cells in the presence of pharmacologic concentrations of these prodrugs (suicide gene therapy). The location and magnitude of HSV1-tk gene expression can be monitored repeatedly by PET, using either F-18 FEAU, FHBG or I-124 FIAU [52, 56, 57]. NIS expression has been used in both imaging thyroid cancer and concentrating I-131 in cancer cells. NIS has also been investigated as an exogenous therapeutic gene that kills target cells in the presence of pharmacologic concentrations of I-131 or Re-188 (radionuclide gene therapy). Exogenous NIS gene expression can be determined with radioiodines or Tc-99m pertechnetate [65, 67, 68].

5.2 Monitoring Endogeneous Gene Expression

Several investigators have designed specific reporter gene constructs named, "The Cis-Promoter/Enhancer Reporter Gene System" under the control of upstream promoter/enhancer elements, possessing binding sites for specific transcription factors. Once a promoter/enhancer element has been activated due to the expression or activation of an endogenous gene product, imaging reporter gene expression occurs, thus enabling visualization. Using cis-promoter/enhancer imaging reporter genes, some intracellular biological events, such as, the activation of specific signal transduction pathways and nuclear receptors can be visualized.

The visualization of endogenous p53, an important anti-oncogenic gene, is a good example of endogenous gene expression [98, 99]. In this study, we used the p53RE-hNIS reporter system, in which the hNIS reporter gene is expressed under the control of an artificial enhancer p53 responsive element (p53RE). Adriamycin was used to induce the enhanced expression of endogenous p53, and adriamycin treated cells were found to accumulate more I-125 than non-treated cells. Xenografted tumors of these cells also showed increased radionuclide accumulation after adriamycin treatment (Fig. 23.7).

5.3 Visualizing Intracellular Biologic Phenomenon

For TGF-beta receptor imaging, HSV1-tk/GFP fusion retroviral reporter vector controlled by a promoter with a Smad binding site was constructed. When TGF-beta binds to its receptor, a specific intracellular signal transduction pathway is activated and the production of several Smad proteins occurs. In vivo images were acquired using a mouse xenograft model with cancer cells having reporter construct. I-124 FIAU images visualized target tumors after injecting TGF-beta, indicating the presence of Smads and the successful TGF-beta signal transduction in tumors.

Our group also generated images of the activities of estrogen and retinoic acid nuclear receptors, using a cis-enhancer reporter imaging system with an internal ribosome entry site (IRES) [100, 101]. NIS and luciferase genes were linked with IRES to express simultaneously two reporter genes under the control of a cis-acting retinoic acid responsive element (RARE). I-125 uptake and bioluminescent intensity were observed to increase after retinoic acid treatment by scintigraphic and optical bioluminescent images (Fig. 23.8).

5.4 Monitoring Tumor Mass and Metastases

The expression of a noninvasive reporter imaging gene in small animals offers excellent opportunities to understand cancer progression, metastasis, and therapy. Individual animals can be visually monitored for tumor burden at primary sites, and

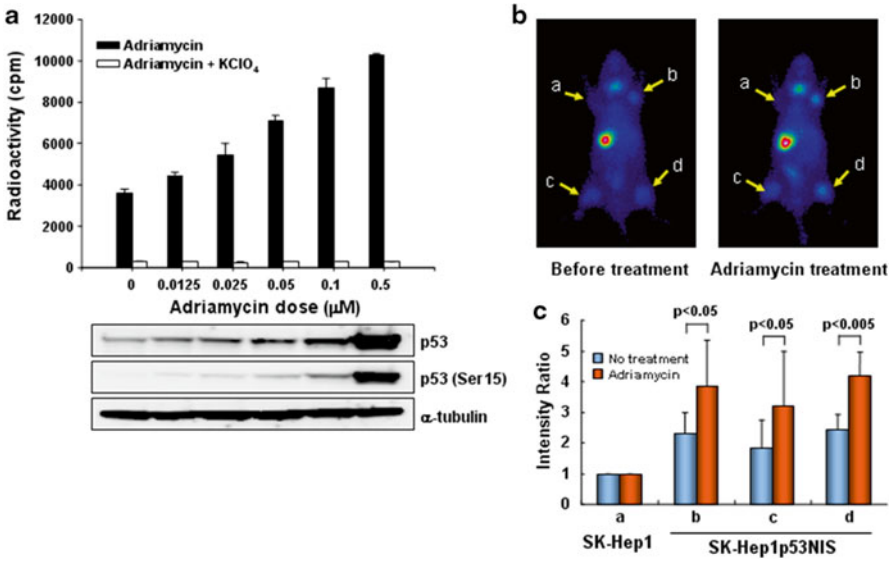

Fig. 23.7 Relation between p53 gene expression and the accumulation of radioiodines in SK-Hep1 cells expressing p53RE-hNIS (SK-Hep1p53NIS) after adriamycin treatment. (**a**) Dose dependent induction of p53RE-hNIS by adriamycin treatment. After 24 h, 125-I uptake of cells was increased with the adriamycin dose. Western blot analysis for total p53 and activated p53 (p53-Ser15) protein levels and their dependence on adriamycin dose in SK-Hep1p53NIS cells. Expressions of total p53 and activated p53 protein were increased in a dose-dependent manner by adriamycin treatment in SK-Hep1p53NIS cells. (**b**) Scintigraphic image of endogenous p53 activation. Tumors were established in vivo by s.c. injection into four different nude mice sites: 1×10^7 of SK-Hep1 (*a*, negative control); SK-Hep1p53NIS (*b*, 5×10^6; *c*, 1×10^7; *d*, 2×10^7). After 7 days, planar scintigraphic images of [^{99m}Tc]-pertechnetate uptake before and after treatment of adriamycin (2 mg/kg) in the same mouse were obtained. Scintigraphies showed increased uptake of [^{99m}Tc]-pertechnetate in test tumors (SK-Hep1p53NIS) after adriamycin treatment compared with the control tumor (SK-Hep1). (**c**) Intensity ratio of SK-Hep1p53NIS to SK-Hep1 in mice ($n=5$) before and after adriamycin treatment. When adriamycin was given to these mice, significantly higher [^{99m}Tc]-pertechnetate uptake was observed in SKHep1p53NIS than in SK-Hep1 xenografts ($p<0.05$) or in nontreated SK-Hep1p53NIS xenografts (*, $p<0.05$, modified from [99])

the differences in tumor progression rates can be distinguished by reporter imaging. The possibility of metastases can be investigated, and individual responses to alternative therapies can be repeatedly monitored. Moreover, therapies can be altered and the consequences of these alterations observed.

Using animal models, the effects of anticancer therapeutic regimens can be easily monitored using a gamma camera system and radioiodine or Tc-99m with NIS gene expression. We found an excellent correlation ($R^2=0.99$) between the accumulated radioiodine activity in cells and numbers of viable cancer cells [102]. It is likely that radioactivity reflects viable cancer cell numbers more accurately than tumor weight, because tumor tissues contain immune cells, necrotic, and fibrous tissues as well as cancer cells. In addition, our group developed a lentiviral vector system carrying sodium iodide symporter (hNIS) gene under UbC promoter to establish stable and long-term gene expression in vitro and in vivo and subsequently demonstrated a marked therapeutic effect by radioiodine gene therapy using I-131 in a tumor xenograft model [103].

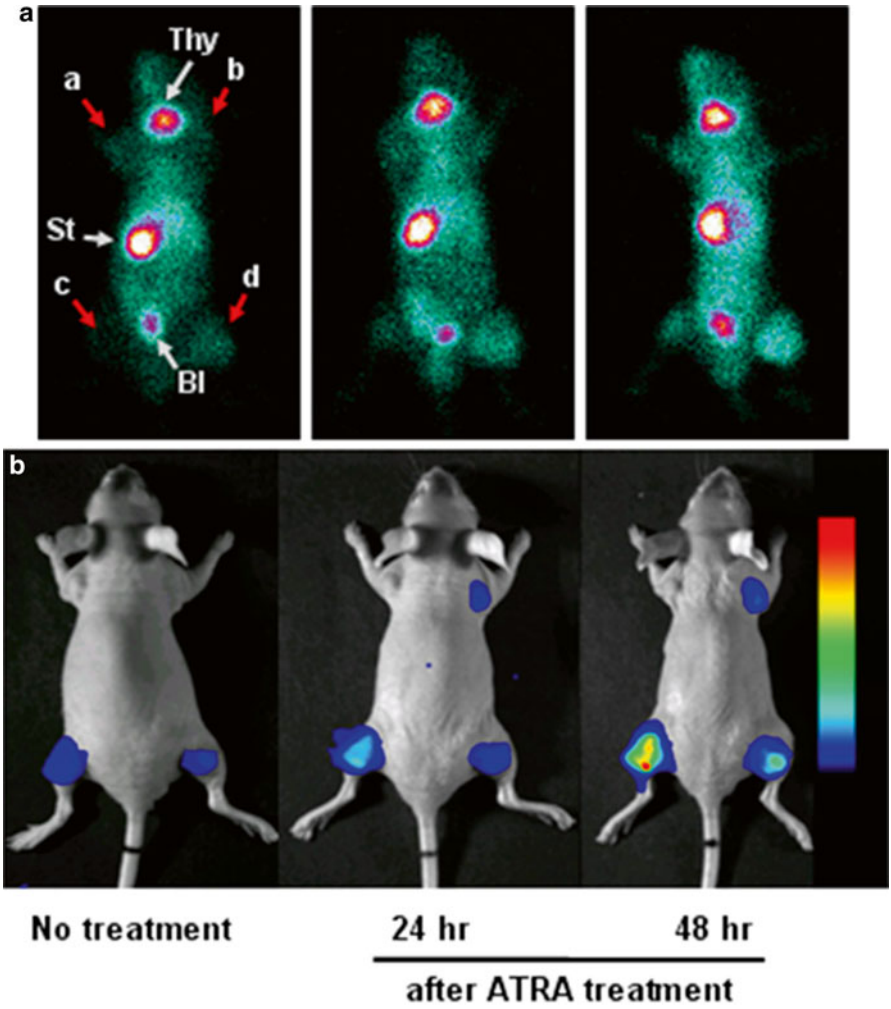

Fig. 23.8 Noninvasive and repetitive Tc-99m accumulation imaging by NIS (**a**) and bioluminescence imaging by luciferase (**b**) to the response of RA in nude mice bearing SK-HEP1 and SK-RARE/NL tumors. Xenograft tumors derived from SK-HEP1 (*a*, 1×10^7 wild-type) and SK-RARE/NL cells (*b*, 1×10^6; *c*, 1×10^7; *d*, 1×10^8) were grown in male nude mice. Serial planar gamma camera images of nude mice before all trans retinoic acid (ATRA) oral administration and 24 or 48 h after treatment were taken (*Thy* thyroid, *St* stomach, *Bl* bladder). Xenograft tumors derived from SK-HEP1 (*a*, 8×10^6 SK-HEP1 cells) and SK-RARE/NL cells (*b*, 1×10^6 cells; *c*, 4×10^6 cells; *d*, 8×10^6) were grown in three male nude mice by subcutaneous injection. Three days after injection, mice were imaged at 20 min after i.p. injection of luciferin (no treatment). After mice were treated with ATRA orally, mice were again imaged for time-dependent luciferase expression at 24 and 48 h. After 24 and 48 h after systemic ATRA administration, elevated Tc-99m uptake and bioluminescent images were observed than those of no treated tumors (modified from [100])

5.5 Evaluation Cell Therapy

Small animal molecular imaging can also be applied to monitoring in vivo distributions of immune and stem cells. The imaging of targeted T-cell trafficking using optical luciferase bioluminescence imaging has been demonstrated in several models of autoimmunity, including collagen-induced arthritis [104] and experimental autoimmune encephalomyelitis [105]. In addition, the transplantation of cells, such as, stem cells or progenitor cells, into damaged tissues has tremendous potential for the treatment of a number of disorders. Once stem cells have been administered systemically or locally, they may be able to migrate and repopulate pathologic sites. Three important aspects of cellular implants, i.e., cell tracking, cell viability, and cell numbers can be monitored by molecular imaging [106]. For example, the locations, numbers, and survival duration of embryonic cardiomyoblasts in rat have been noninvasively monitored using HSV1-tk and luciferase gene as an imaging reporter [107]. Neural stem cell migration was also demonstrated with the NIS and luciferase genes [108]. The successful differentiation and functional maturation of neuronal stem cells were also visualized using NIS-Luc gene controlled by neuron specific enolase (NSE) promoter, which induces neural differentiation [109]. Recently, the translation into a large animal model was successfully performed for evaluating the possibility of clinical application. Though in vivo imaging of transplanting mesenchima stem cell in porcine heart provides sign of inflammation [110], this kind of pilot study could provide precious information toward future clinical trials.

5.6 Identifying Drug Target and Preclinical Testing

Small animal gene expression imaging techniques provide a new means of identifying drug targets and of preclinical testing. The ability to noninvasively image endogenous gene expression and various intracellular biologic phenomena, such as signal transduction, nuclear receptor activation, and protein–protein interactions, has important implications for drug discovery. Current imaging strategies, based on a suitable reporter or imaging probes, can provide new information on the level, timing, and duration of action of many biologically active gene products. The selection of optimal probes or promoters for reporter gene expression control should be carefully considered when monitoring the effects of drugs on cells. Reporter gene expression imaging has emerged as a useful means of monitoring tumor growth and regression in preclinical models at subcutaneous, orthotopic, or intraperitoneal sites [111, 112]. For example, we reported that genotoxic stress, such as that induced by doxoribicin, enhanced transgene expression via NF-kB activation, and strong viral promoter (cytomegalovirus promoter) has consensus binding sites for NF-kB in its enhancer region [113].

6 Conclusion

The remarkable efforts that are made on molecular imaging technologies demonstrate its potential importance and range of applications. Continued improvements in the instrumentation, the identification of novel targets and genes, and the availability of improved imaging probes, should be made, and multimodal imaging probe should provide easier transition between laboratory studies including small animal study and clinical application. The generation of disease-specific animal models, and the developments of target-specific probes and genetically encoded reporters are another important component. For this reason, the multidisciplinary team approach becomes increasingly important, and effective communication and cooperation within such teams are essential requirements of success.

In conclusion, molecular imaging embraces proteomic, metabolic, cellular biologic processes, and genetic imaging. Several imaging probes and reporter genes have been developed, and successful transitions from bench to bedside have already occurred [114, 115]. Unique roles of small animal molecular imaging allow us to increase our knowledge on the critical biological pathways involved in disease progression by characterizing biological processes or tumor properties, and provide bridges to clinical application, i.e., in diagnosis, staging, determination of therapeutic targets, monitoring therapy, and in the evaluation of prognoses.

Acknowledgments This work was supported by the Korea Science and Engineering Foundation (KOSEF) grant funded by the Korea government, the Ministry of Education, Science and Technology (MEST) (No. 20090065586). This research was also supported by Basic Science Research Program through the National Research Foundation of Korea (NRF) funded by the Ministry of Education, Science and Technology (R13-2002-025-03001-02008).

References

1. Blasberg RG, Gelovani-Tjuvajev J (2002) In vivo molecular-genetic Imaging. J Cell Biochem Suppl 39:172–183
2. Overbeek PA, Chepelinsky AB, Khillan JS, Piatigorsky J, Westphal H (1985) Lens-specific expression and developmental regulation of the bacterial chloramphenicol acetyltransferase gene driven by the murine alpha A-crystallin promoter in transgenic mice. Proc Natl Acad Sci USA 82:7815–7819
3. Forss-Petter S, Danielson PE, Catsicas S, Battenberg E, Price J, Nerenberg M, Sutcliffe JG (1990) Transgenic mice expressing beta-galactosidase in mature neurons under neuron-specific enolase promoter control. Neuron 5:187–197
4. Yu YA, Timiryasova T, Zhang Q, Beltz R, Szalay AA (2003) Optical imaging: bacteria, viruses, and mammalian cells encoding light-emitting proteins reveal the locations of primary tumors and metastases in animals. Anal Bioanal Chem 377:964–972
5. Shaner NC, Steinbach PA, Tsien RY (2005) A guide to choosing fluorescent proteins. Nat Methods 2:905–909
6. Tjuvajev JG, Stockhammer G, Desai R, Uehara H, Watanabe K, Gansbacher B, Blasberg RG (1995) Imaging the expression of transfected genes in vivo. Cancer Res 55:6126–6132

7. Gambhir SS, Barrio JR, Phelps ME, Iyer M, Namavari M, Satyamurthy N, Wu L, Green LA, Bauer E, MacLaren DC, Nguyen K, Berk AJ, Cherry SR, Herschman HR (1999) Imaging adenoviral-directed reporter gene expression in living animals with positron emission tomography. Proc Natl Acad Sci USA 96:2333–2338
8. Brown RS, Leung JY, Fisher SJ, Frey KA, Ethier SP, Wahl RL (1996) Intratumoral distribution of tritiated-FDG in breast carcinoma: correlation between Glut-1 expression and FDG uptake. J Nucl Med 37:1042–1047
9. Ichikawa T, Hogemann D, Saeki Y, Tyminski E, Terada K, Weissleder R, Chiocca EA, Basilion JP (2002) MRI of transgene expression: correlation to therapeutic gene expression. Neoplasia 4:523–530
10. Min JJ, Gambhir SS (2004) Gene therapy progress and prospects: noninvasive imaging of gene therapy in living subjects. Gene Ther 11:115–125
11. Serganova I, Mayer-Kukuck P, Huang R, Blasberg R (2008) Molecular Imaging: Reporter Gene Imaging. Handb Exp Pharmacol 185 Pt 2:167–223
12. Kang JH, Chung JK (2008) Molecular-genetic imaging based on reporter gene expression. J Nucl Med 49 Suppl2:164S–79S
13. Hoffman JM, Gambhir SS (2007) Molecular Imaging: the vision and opportunity for radiology in the future. Radiology 244:39–47
14. Townsend DW, Carney JP, Yap JT, Hall NC (2004) PET/CT today and tomorrow. J Nucl Med 45 Suppl1:4S–14S
15. Pichler BJ, Judenhofer MS, Catana C, Walton JH, Kneilling M, Nutt RE, Siegel SB, Claussen CD, Cherry SR (2006) Performance test of an LSO-APD detector in a 7-T MRI scanner for simultaneous PET/MRI. J Nucl Med 47:639–647
16. Meera I, Makoto S, Mai J, et al. (2005) Application of molecular imaging in cancer therapy. Curren Cancer Ther 5:607–618
17. Warburg O (1956) On the origin of cancer cells. Science 123:309–314
18. Cejka D, Kuntner C, Preusser M, Fritzer-Szekeres M, Fueger BJ, Strommer S, et al. (2009) FDG uptake is a surrogate marker for defining the optimal biological dose of the mTOR inhibitor everolimus in vivo. Br J Cancer 100:1739–1745
19. Ma WW, Jacene H, Song D, Vilardell F, Messersmith WA, Laheru D, et al. (2009) [18F]fluorodeoxyglucose positron emission tomography correlates with Akt pathway activity but is not predictive of clinical outcome during mTOR inhibitor therapy. J Clin Oncol 27:2697–2704
20. McLarty K, Fasih A, Scollard DA, Done SJ, Vines DC, Green DE, et al. (2009) 18F-FDG small-animal PET/CT differentiates trastuzumab-responsive from unresponsive human breast cancer xenografts in athymic mice. J Nucl Med 50:1848–1856
21. Wu AM, Senter PD (2005) Arming antibodies: prospects and challenges for immunoconjugates. Nat Biotechnol 23:1137–1146
22. Blend MJ, Stastny JJ, Swanson SM, Brechbiel MW (2003) Labeling anti-HER2/neu monoclonal antibodies with In-111 and Y-90 using a bifunctional DTPA chelating agent. Cancer Biother Radiopharm 18:355–363
23. Artemov D, Mori N, Ravi R, Bhujwalla ZM (2003) Magnetic resonance molecular imaging of the HER-2/neu receptor. Cancer Res 63:2723–2727
24. Olafsen T, Kenanova VE, Sundaresan G, Anderson AL, Crow D, Yazaki PJ, et al. (2005) Optimizing radiolabeled engineered anti-p185HER2 antibody fragments for in vivo imaging. Cancer Res 65:5907–5916
25. Steffen AC, Orlova A, Wikman M, Nilsson FY, Ståhl S, Adams GP, et al. (2006) Affibody-mediated tumour targeting of HER-2 expressing xenografts in mice. Eur J Nucl Med Mol Imaging 33:631–638
26. Haubner R, Wester HJ, Weber WA, Mang C, Ziegler SI, Goodman SL, et al. (2001) Noninvasive imaging of alpha(v)beta3 integrin expression using F-18 labeled RGD-containing glycopeptide and positron emission tomography. Cancer Res 61:1781–1785
27. Wadas TJ, Deng H, Sprague JE, Zheleznyak A, Weilbaecher KN, Anderson CJ. (2009) Targeting the alphavbeta3 integrin for small-animal PET/CT of osteolytic bone metastases. J Nucl Med 50:1873–1880

28. Kiessling F, Huppert J, Zhang C, Jayapaul J, Zwick S, Woenne EC, et al. (2009) RGD-labeled USPIO inhibits adhesion and endocytotic activity of alpha v beta3-integrin-expressing glioma cells and only accumulates in the vascular tumor compartment. Radiology 253: 462–469
29. Edwards WB, Akers WJ, Ye Y, Cheney PP, Bloch S, Xu B, Laforest R, Achilefu S. (2009) Multimodal imaging of integrin receptor-positive tumors by bioluminescence, fluorescence, gamma scintigraphy, and single-photon emission computed tomography using a cyclic RGD peptide labeled with a near-infrared fluorescent dye and a radionuclide. Mol Imaging 8:101–10
30. Dewanjee MK, Ghafouripour AK, Kapadvanjwala M, Dewanjee S, Serafini AN, Lopez DM, et al. (1994) Noninvasive imaging of c-myc oncogene messenger RNA with indium-111-antisense probes in a mammary tumor-bearing mouse model. J Nucl Med 35:1054–1063
31. Liu M, Wang RF, Zhang CL, Yan P, Yu MM, Di LJ, et al. (2007). Noninvasive imaging of human telomerase reverse transcriptase (hTERT) messenger RNA with 99mTc-radiolabeled antisense probes in malignant tumors. J Nucl Med 48:2028–2036
32. Zhang YR, Zhang YX, Cao W, Lan XL. (2005) Uptake kinetics of 99mTc-MAG3-antisense oligonucleotide to PCNA and effect on gene expression in vascular smooth muscle cells. J Nucl Med 46:1052–1058
33. Fan C, Hnatowich DJ. (2008) Preparation and quality control of 99mTc labeled MDR1 oligonucleotide DNAs. Sheng Wu Yi Xue Gong Cheng Xue Za Zhi 25:712–715
34. Pieve CD, Perkins AC, Missailidis S. (2009) Anti-MUC1 aptamers: radiolabelling with (99m)Tc and biodistribution in MCF-7 tumour-bearing mice. Nucl Med Biol 36:703–710
35. Abes R, Arzumanov AA, Moulton HM, Abes S, Ivanova GD, Iversen PL, et al. (2007). Cell-penetrating-peptide-based delivery of oligonucleotides: an overview. Biochem Soc Trans 35:775–779
36. Lebleu B, Moulton HM, Abes R, Ivanova GD, Abes S, Stein DA, et al. (2008). Cell penetrating peptide conjugates of steric block oligonucleotides. Adv Drug Deliv Rev 60:517–29
37. Karkare S, Bhatnagar D (2006) Promising nucleic acid analogs and mimics: characteristic features and applications of PNA, LNA, and morpholino. Appl Microbiol Biotechno 71:575–586
38. Bulte JW, Arbab AS, Douglas T, Frank JA (2004) Preparation of magnetically labeled cells for cell tracking by magnetic resonance imaging. Methods Enzymol 386:275–299
39. Hinds KA, Hill JM, Shapiro EM, Laukkanen MO, Silva AC, Combs CA, Varney TR, Balaban RS, Koretsky AP, Dunbar CE (2003) Highly efficient endosomal labeling of progenitor and stem cells with large magnetic particles allows magnetic resonance imaging of single cells. Blood 102:867–872
40. Kostura L, Kraitchman DL, Mackay AM, Pittenger MF, Bulte JW (2004) Feridex labeling of mesenchymal stem cells inhibits chondrogenesis but not adipogenesis or osteogenesis. NMR Biomed 17:513–517
41. Rief M, Wagner M, Franiel T, Bresan V, Taupitz M, Klessen C, et al. (2009) Detection of focal liver lesions in unenhanced and ferucarbotran-enhanced magnetic resonance imaging: a comparison of T2-weighted breath-hold and respiratory-triggered sequences. Magn Reson Imaging 27:1223–9
42. Zhang CY, Lu J, Tsourkas A. (2008) Iron chelator-based amplification strategy for improved targeting of transferrin receptor with SPIO. Cancer Biol Ther 7:889–95
43. Wen M, Li B, Ouyang Y, Luo Y, Li S (2009) Preparation and quality test of superparamagnetic iron oxide labeled antisense oligodeoxynucleotide probe: a preliminary study. Ann Biomed Eng 37:1240–50
44. Liu ZY, Wang Y, Liang CH, Li XH, Wang GY, Liu HJ, Li Y. (2009) In vitro labeling of mesenchymal stem cells with superparamagnetic iron oxide by means of microbubble-enhanced US exposure: initial experience. Radiology 253:153–9
45. Blasberg RG, Tjuvajev JG (2003) Molecular-genetic imaging: current and future perspectives. J Clin Invest 111:1620–1629

46. March JC, Rao G, Bentley WE (2003) Biotechnological applications of green fluorescent protein. Appl Microbiol Biotechnol 62:303–315
47. Shaner NC, Lin MZ, McKeown MR, Steinbach PA, Hazelwood KL, Davidson MW, Tsien RY (2008) Improving the photostability of bright monomeric orange and red fluorescent proteins. Nat Methods 5:545–551
48. Contag, CH and Bachmann MH (2002) Advances in in vivo bioluminescence imaging of gene expression. Annu Rev Biomed Eng 4:235–260
49. Bhaumik S, Gambhir S (2002) Optical imaging of renilla luciferase reporter gene expression in living mice. Proc Natl Acad Sci USA 99:377–382
50. Contag PR, Olomu IN, Stevenson DK, Contag CH (1998) Bioluminescent indicators in living mammals. Nature Med 2:245–247
51. Contag CH, Contag PR, Mullins JI, Spilman SD, Stevenson DK, Benaron DA. (1995) Photonic detection of bacterial pathogens in living hosts. Mol Microbiol 18:593–603
52. Abbruzzese JL, Schmidt S, Raber MN, Levy JK, Castellanos AM, Legha SS, Krakoff IH (1989) Phase I trial of 1-(2′-deoxy-2′-fluoro-1-beta-D-arabino furanosyl)-5-methyluracil (FMAU) terminated by severe neurologic toxicity. Invest New Drugs 7:195–201
53. Chitneni SK, Deroose CM, Fonge H, Gijsbers R, Dyubankova N, Balzarini J, Debyser Z, Mortelmans L, Verbruggen AM, Bormans GM. (2007) Synthesis and biological evaluation of an I-123 labeled bicyclic nucleoside analogue (BCNA) as potential SPECT tracer for VZV-tk reporter gene imaging. Bioorg Med Chem Lett 17:3458–3462
54. Kim JS, Lee JS, Im KC, Kim SJ, Lee DS, Moon DH (2007) Performance measurement of the microPET Focus 120. J Nucl Med 48:1527–1535
55. Kang JH, Chung JK (2008) Molecular-genetic imaging based on reporter gene expression. J Nucl Med Suppl 2:164S–79S
56. Cui L, Yoon S, Schinazi RF, Sommadossi JP (1995) Cellular and molecular events leading to mitochondrial toxicity of 1-(2-deoxy-2-fluoro-1-beta-D-arabinofuranosyl)-5-iodouracil in human liver cells. J Clin Invest 95:555–563
57. Black ME, Newcomb TG, Wilson HMP, Lobe LA (1996) Creation of drug-specific herpes simplex virus type 1 thymidine kinase mutant for gene therapy. Proc Nat Acad Sci USA 93:3525–3529
58. Gambhir SS, Bauer E, Black ME, Liang Q, Kokoris MS, Barrio JR, et al. (2000) A mutant herpes simplex virus type 1 thymidine kinase reporter gene shows improved sensitivity for imaging reporter gene expression with positron emission tomography. Proc Natl Acad Sci USA 97:2785–2790
59. MacLaren DC, Gambhir SS, Satyamurthy N, Barrio JR, Sharfstein S, Toyokuni T, et al. (1999) Repetitive, noninvasive imaging of the dopamine D2 receptor as a reporter gene in living animals. Gene Ther 5:785–791
60. Missale C, Nash SR, Robinson SW, Jaber M, Caron MG (1998) Dopamine receptors: from structure to function. Physiol Rev 78:189–225
61. Bahn MM, Huang SC, Hawkins RA, Satyamurthy N, Hoffman JM, Barrio JR, et al. (1989) Models for in vivo kinetic interactions of dopamine D2 neuroreceptors and 3-(2'-[F-18] Fluoroethyl)spiperone examined by positron emission tomography. J Cerebral Blood Flow Metab 9:840–849
62. Liang Q, Gotts J, Satyamurthy N, Barrio J, Phelps ME, Gambhir SS, et al. (2002) Noninvasive, repetitive, quantitative measurement of gene expression from a bicistronic message by positron emission tomography, following gene transfer with adenovirus. Mol Ther 6:73–82
63. Rogers BE, Zinn KR and Buchsbaum DJ (2000) Gene transfer strategies for improving radiolabeled peptide imaging and therapy. Q J Nucl Med 44:208–223
64. Dai G, Levy O, Carrasco N (1996) Cloning and characterization of the thyroid iodide transporter. Nature 379:458–460
65. Chung JK (2002) Sodium/iodide symporter; its role in nuclear medicine. J Nucl Med 43:1188–1200

66. Smanik PA, Lui Q, Furminger TL, Ryu K, Xing S, Mazzaferri EL, et al. (1996) Cloning of the human sodium lodide symporter. Biochem Biophys Res Commun 226:339–345
67. Vadysirisack DD, Shen DH, Jhiang SM (2006) Correlation of Na^+/I^- symporter expression and activity: implications of Na^+/I^- symporter as an imaging reporter gene. J Nucl Med 47:182–190
68. Huang M., Batra RK, Kogai T, Lin YQ, Hershman JM, Lichtenstein A, et al. (2001) Ectopic expression of the thyroidperoxidase gene augments radioiodide uptake and retention mediated by the sodium iodide symporter in non-small cell lung cancer. Cancer Gene Ther 8:612–618
69. Rogers BE, McLean SF, Kirkman RL, Della Manna D, Bright SJ, Olsen CC, et al. (1999) In vivo localization of [^{111}In]-DTPA-D-Phe1-octreotide to human ovarian tumor xenografts induced to express the somatostatin receptor subtype 2 using an adenoviral vector. Clin Cancer Res 5:383–393
70. Woltering, E. A., O'Dorisio, M. S., and O'Dorisio, T. M. (1995) The role of radiolabeled somatostatin analogs in the management of cancer patients. *In:* V. T. DeVita, Jr., S. Hellman, and S. A. Rosenberg (eds.), Principles and Practice of Oncology, Ed. 4, Vol. 9, pp. 1–16. Philadelphia: Lippincott-Raven
71. Krenning EP, Bakker WH, Breeman WA, Koper JW, Kooij PP, Ausema L, et al. (1989) Localisation of endocrine-related tumours with radioiodinated analogue of somatostatin. Lancet 863:242–244
72. Roger BE, Parry JJ, Andrews R, Cordopitis P, Nock BA, Maina T. MicroPET imaging of gene transfer with a somatostatin receptor-based reporter gene and Tc-94m Demotate 1. J Nucl Med 46:1889–1897
73. Bakker WH, Albert R, Bruns C, Breeman WA, Hofland LJ, Marbach P, et al. (1991) [^{111}In-DTPA-D-Phe1]-octreotide, a potential radiopharmaceutical for imaging of somatostatin receptor-positive tumors: synthesis, radiolabeling and in vitro validation. Life Sci 49:1583–1591
74. Van Den Bossche B, Van de Wiele C. (2004) Receptor imaging in oncology by means of nuclear medicine: current status. J Clin Oncol 22:3593–3607
75. Roger BE, Chaudhuri TR, Reynolds PN, Della Manna D, Zinn KR.(2003) Non-invasive gamma camera imaging of gene transfer using an adenoviral vector encoding an epitope-tagged receptor as a reporter. Gene Ther 10:105–114
76. Buursma AR, Beerens AMJ, de Vries EFJ, van Waarde A, Rots MG, Hospers GA, Vaalburg W, Haisma HJ. (2005) The human norepinephrine transporter in combination with C-11-m-hydroxyephedrine as a reporter gene/probe for PET of gene therapy. J Nucl Med 46:2068–2075
77. Moroz MA, Serganova I, Zanzonico P, Ageyeva L, Beresten T, Dyomina E, Burnazi E, Finn RD, Doubrovin M, Blasberg RG. (2007) Imaging hNET reporter gene expression with I-124 MIBG. J Nucl Med 48:827–836
78. Doubrovin MM, Doubrovin ES, Zanzonico P, Sadelain M, Larson SM, O'Reilly RJ. (2007) In vivo imaging and quantitation of adoptively transferred human antigen-specific T cells transduced to express a human norepinephrine transporter gene. Cancer Res 67:11959–11969
79. Haberkorn U, Altmann A, Mier W, Eisenhut M. (2004) Impact of functional genomics and proteomics on radionuclide imaging. Seminars Nucl Med 34:4–22
80. Furukawa T, Lohith TG, Takamatsu S, Mori T, Tanaka T, Fujibayashi Y. (2006) Potential of the FES-hERL PET reporter gene system – basic evaluation for gene therapy monitoring. Nucl Med Biol 33:145–151
81. Mintun MA, Welch MJ, Siegel BA, Mathias CJ, Brodack JW, McGuire AH, Katzenellenbogen JA. (1988) Breast cancer: PET imaging of estrogen receptors. Radiology 169:45–48
82. Koretsky A, Lin Y-J, Schorle H, Jaenisch R. (1996) Genetic control of MRI contrast by expression of the transferrin receptor. In: Proceedings of the International Society of Magnetic Resonance Medicine 4:69

83. Louie AY, Huber MM, Ahrens ET, Rothbächer U, Moats R, Jacobs RE, et al. (2000) In vivo visualization of gene expression using magnetic resonance imaging. Nat Biotechnol 18: 321–325
84. Weissleder R, Simonova M, Bogdanova A, Bredow S, Enochs WS, Bogdanov A Jr. (1997) MR imaging and scintigraphy of gene expression through melanin induction. Radiology 204:425–429
85. Alfke H, Stoppler H, Nocken F, et al. (2003) In vitro MR imaging of regulated gene expression. Radiology 228:488–492
86. Cohen B, Dafni H, Meir G, Harmelin A, Neeman M. (2005) Ferritin as an endogenous MRI reporter for noninvasive imaging of gene expression in C6 glioma tumors. Neoplasia 7:109–117
87. Genove G, DeMarco U, Xu H, Goins WF, Ahrens ET. (2005) A new transgene reporter for in vivo magnetic resonance imaging. Nat Med 11:450–454
88. Gilad AA, McMahon MT, Walczak P, Winnard PT Jr, Raman V, van Laarhoven HW, et al. (2007) Artificial reporter gene providing MRI contrast based on proton exchange. Nat Biotechnol 25:217–219
89. Ottobrini L, Ciana P, Biserni A, Lucignani G, Maggi A (2006) Molecular imaging: a new way to study cellular processes in vivo. Mol Cell Endo 246:69–75
90. Goertzen AL, Meadors AK, Silverman RW, Cherry SR (2002) Simultaneous molecular and anatomical imaging of the mouse in vivo. Phys Med Biol 47:4315–4328
91. Yu X, Zhan X, D'Costa J, Tanavde VM, Ye Z, Peng T, et al. Lentiviral vectors with two independent internal promoters transfer high-level expression of multiple transgenes to human hematopoietic stem-progenitor cells. Mol Ther 2003;7:827–838
92. Osti D, Marras E, Ceriani I, Grassini G, Rubino T, Vigano D, et al. Comparative analysis of molecular strategies attenuating positional effects in lentiviral vectors carrying multiple genes. J Virol Methods 2006;136:93–101
93. Szymczak AL, Vignali DA. Development of 2A peptide-based strategies in the design of multicistronic vectors. Expert Opin Biol Ther 2005;5:627–638
94. Szymczak AL, Workman CJ, Wang Y, Vignali KM, Dilioglou S, Vanin EF, et al. Correction of multigene deficiency *in vivo* using a single 'self-cleaving' 2A peptide-based retroviral vector. Nat Biotechnol 2004;22:589–594
95. Dubey P, Su H, Adonai N, Du S, Rosato A, Braun J, Gambhir SS, Witte ON. (2003) Quantitative imaging of the T cell antitumor response by positron-emission tomography. Proc Natl Acad Sci USA 100:1232–1237
96. De A, Lewis XA, Gambhir SS (2003) Noninvasive imaging of lentiviral-mediated reporter gene expression in living mice. Mol Ther 7:681–691
97. Ray P, De A, Min JJ et al. (2004) Imaging tri-fusion multimodality reporter gene expression in living subjects. Cancer Res 64:1323–1330
98. Doubrovin M, Ponomarev V, Beresten T, Balatoni J, Bornmann W, Finn R, et al. (2001) Imaging transcriptional regulation of p53-dependent genes with positron emission tomography in vivo. Proc Natl Acad Sci USA 98:9300–9305
99. Kim KI, Chung JK, Kang JH, Lee YJ, Shin JH, Oh HJ, et al. (2005) Visualization of endogenous p53-mediated transcription in vivo using sodium iodide symporter. Clin Cancer Res 11:123–128
100. So MK, Kang JH, Chung JK, Chung JK, Lee YJ, Shin JH, et al. (2004) In vivo imaging of retinoic acid receptor activity using a sodium/iodide symporter and luciferase dual imaging reporter gene. Mol Imaging 3:163–171
101. Kang JH, Chung JK, Lee YJ, Kim KI, Jeong JM, Lee DS, et al. (2006) Evaluation of transcriptional activity of the oestrogen receptor with sodium iodide symporter as an imaging reporter gene. Nucl Med Commun 27:773–777
102. Shin JH, Chung JK, Kang JH, Lee YJ, Kim KI, So Y, et al. (2004) Noninvasive imaging for monitoring of viable cancer cells using dual-imaging reporter gene. J Nucl Med 45: 2109–2115

103. Kim HJ, Jeon YH, Kang JH, Lee YJ, Kim KI, Chung HK, et al. (2007) In vivo long-term Imaging and radioiodine therapy by sodium iodide symporter gene expression using a lentiviral system containing ubiquitin C promoter. Cancer Biol Ther 6:1130–1135
104. Nakajima A, Seroogy CM, Sandora MR, Tarner IH, Costa GL, Taylor-Edwards C, et al. (2001) Antigen-specific T cell-mediated gene therapy in collagen-induced arthritis. J Clin Invest 107:1293–1301
105. Costa GL, Sandora MR, Nakajima A, Nguyen EV, Taylor-Edwards C, Slavin AJ, et al. (2001) Adoptive immunotherapy of experimental autoimmune encephalomyelitis via T cell delivery of the IL-12 p40 subunit. J Immunol 167:2379–2387
106. Acton PD, Zhou R (2005) Imaging reporter genes for cell tracking with PET and SPECT. Q J Nucl Mol Imaging 49:349–360
107. Wu JC, Chen IY, Sundaresan G, Chen IY, Sundaresan G, Min JJ, et al. (2003) Molecular imaging of cardiac cell transplantation in living animals using optical bioluminescence and positron emission tomography. Circulation 108:1302–1305
108. Sheikh AY, Lin SA., Cao F, Cao Y, van der Bogt KE, Chu P, et al. (2007) Molecular imaging of bone marrow mononuclear cell homing and engraftment in ischemic myocardium. Stem Cells 25:2677–2684
109. Hwang DW, Kang JH, Jeong JM, Chung JK, Lee MC, Kim S, et al. (2008) Noninvasive in vivo monitoring of neuronal differentiation using reporter driven by a neuronal promoter. Eur J Nucl Med Mol Imaging 35:135–145
110. Lyngbæk S, Ripa RS, Haack-Sørensen M, Cortsen A, Kragh L, Andersen CB, et al (2008) Serial noninvasive in vivo positron emission tomographic tracking of percutaneously intramyocardially injected autologous porcine mesenchymal stem cells modified for transgene reporter gene expression. Circ Cardiovasc Imaging 1:94–103
111. Minn AJ, Kang Y, Serganova I, Gupta GP, Giri DD, Doubrovin M, et al. (2005) Distinct organ-specific metastatic potential of individual breast cancer cells and primary tumors. J Clin Invest 115:44–55
112. Lyons SK, Lim E, Clermont AO, Dusich J, Zhu L, Campbell KD, et al. (2006) Noninvasive bioluminescence imaging of normal and spontaneously transformed prostate tissue in mice. Cancer Res 66:4701–4707
113. Kim KI, Kang JH, Chung JK, Lee YJ, Jeong JM, Lee DS, et al. (2007) Doxorubicin enhances the expression of transgene under control of the CMV promoter in anaplastic thyroid carcinoma cells. J Nucl Med 48:1553–1561
114. Ambrosini V, Quarta C, Nanni C, Pettinato C, Franchi R, Grassetto G, et al (2009) Small animal PET in oncology: the road from bench to bedside. Cancer Biother Radiopharm 24:277–285
115. O'Connor JP, Carano RA, Clamp AR, Ross J, Ho CC, Jackson A, et al (2009) Quantifying antivascular effects of monoclonal antibodies to vascular endothelial growth factor: insights from imaging. Clin Cancer Res 15:6674–6682

Chapter 24
Applications of Small-Animal Molecular Imaging in Drug Development

Gang Niu and Xiaoyuan Chen

1 Introduction

The gauntlet for a new drug to succeed is a daunting one. The reduction in the time and cost required for modern drug discovery and development serves as a crucial need. An important element to accelerate drug discovery and development process is the rapid identification of promising drug candidates as opposed to the non-starters before unnecessary vast sums are invested. The aim of molecular imaging is to precisely visualize, characterize, and measure biological processes at the molecular and cellular levels in humans and other living systems [1]. By introducing molecular imaging probes into traditional diagnostic imaging techniques, researchers can determine the expression of indicative molecular markers at different stages of diseases. The introduction of new imaging probes, methods, and advanced imaging instrumentation is significantly speeding up the processes of drug discovery and development. The convergence of innovations has created more sensitive, specific and higher resolution measurements within living organism, especially small animals. This is expected to improve a wide range of discovery activities such as target biology, compound screening, pharmacokinetics (PK), and pharmacodynamics (PD) evaluation in animal disease models and, eventually, clinical trials. In this chapter, we will summarize and evaluate the applications of various advanced small animal imaging techniques in drug development process.

G. Niu
National Institute Biomedical Imaging and Bioengineering (NIBIB), NIH, Bethesda, MD, USA
e-mail: niug@mail.nih.gov

X. Chen (✉)
National Institute of Biomedical Imaging and Bioengineering (NIBIB), National Institutes of Health (NIH), Bethesda, MD, USA
e-mail: chenx5@mail.nih.gov

H. Zaidi (ed.), *Molecular Imaging of Small Animals: Instrumentation and Applications*,
DOI 10.1007/978-1-4939-0894-3_24,

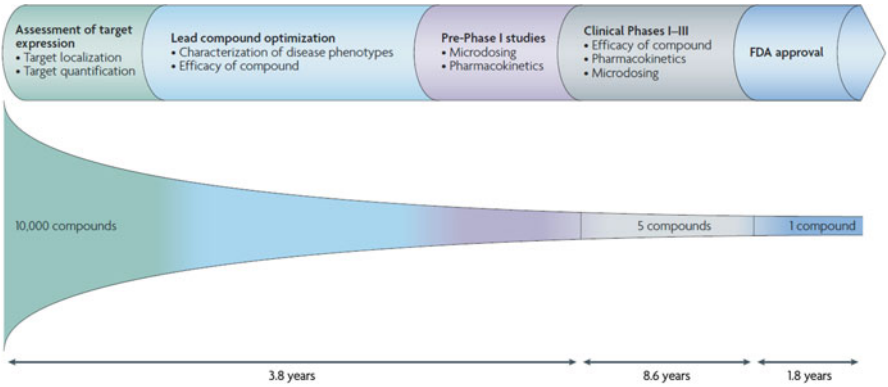

Fig. 24.1 The drug development process. Reproduced with permission from [23]

2 Overview of Drug Development

As shown in Fig. 24.1, on average, for ~10,000 compounds evaluated in preclinical studies, about five compounds enter clinical trials and about one compound finally receives regulatory approval by the FDA [2]. The mean time from synthesis of a new compound to marketing approval in the United States is 14.2 years, which can be broken down into pre-clinical development, Phase I testing, Phase II testing, Phase III testing, and FDA approval [3]. The cost of advancing a drug to the point of applying for FDA approval has been estimated to be $802 million based on a survey of ten pharmaceutical firms in 2001 and was estimated to be $1.9 billion in 2013 [4]. Therefore, both the time and cost need to be minimized for the modern drug discovery and development processes.

Early drug development involves several phases from target identification to preclinical development [5]. Currently, target identification is the most important step in the arduous process of drug development, especially in the post-genomic era which the number of potential protein targets is in the hundreds of thousands, up from the mere hundreds of potential targets under study before the sequence became available. The identification of small molecule modulators of protein function and the process of transforming these into high-content lead series are key activities in modern drug discovery. The next step is target validation, which usually occurs through a number of proteomics methods including two-dimensional gel separation of protein mixtures followed by mass spectrometry (2D-MS), transcriptional profiling of mRNAs and functional screening [6]. More often, the process of finding a new drug against a chosen target for a particular disease usually involves high-throughput screening (HTS), wherein large libraries of chemicals are tested for their ability to interact with the target [7]. After HTS, one or more pharmacophores can be developed if these compounds share common chemical features. Certain features of the lead compound such as affinity, specificity and pharmacokinetic properties of the molecule can be improved through using structure-activity relationships (SAR) [8, 9]. Structure can be determined by nuclear magnetic resonance (NMR) spectroscopy or through high-throughput X-ray crystallography [10].

The hit-to-lead phase is usually the follow up of HTS, including hit confirmation, hit explosion, lead generation, and lead optimization [11]. Hit confirmation will retest compounds with the same assays performed in HTS as well as alternative assays to confirm the activity against the selected target and generate a dose response curve to calculate half maximal inhibitory concentration (IC_{50}) and half maximal effective concentration (EC_{50}) values. Once the compounds of acceptable affinity and selectivity are identified, their physical properties, i.e., solubility, pKa, logP (the logarithm of the partition coefficient) and passage through a monolayer of Caco-2 cells, are then determined. Each of those parameters is critical and can be a reason for the failure of a given drug candidate. Drug metabolism is then studied in the hepatocytes in which later toxicology studies will be performed. Following hit confirmation, several compound clusters will be chosen according to their characteristics in the previously defined tests. Drug–drug interactions are assayed and then the absorption, distribution, metabolism and excretion (ADME—pharmacokinetics) of the candidate drug are determined in rodents and in other species. Further characterization involves radiolabeling the drug candidate and performing whole-body autoradiography and toxicokinetics, the correlation of changes in plasma and tissue concentrations with toxicity. At this point the drug candidate is ready to enter clinical trials. Phase I clinical trials consist of determining a safe dose of the drug candidate in healthy volunteers, and in phase II the drug candidate is administered to patient volunteers to evaluate efficacy and search for side effects. Effectiveness is further monitored in phase III, as is the presence of long-term side effects. As described in the following section, small animal molecular imaging can be used at various stages in the drug development process, which may help reduce attrition rates and allow the selection of the most promising drug candidates early on in development.

3 Small Animal Molecular Imaging

Experimental small animals include rodents, birds, snakes and other animals with a head or body diameter <5 cm. Among them, the mouse remains the premier animal model for biomedical research because they are accessible, easy to maintain, have a short reproductive cycle, and are easily genetically manipulated. The human and mouse genomes are highly homologous, thus knowledge of the complete gene sequence of another mammal will enable the construction of relevant animal models of human disease at an unprecedented rate and with high specificity [12]. Moreover, transgenic animals have been made to contain a corresponding mutation for many human genetic diseases for which a specific gene has been identified and characterized. Transgenic animals are used to study the effects of genetic mutations on development, immunity, host response and other metabolic diseases [13, 14]. Orthotopic xenograft models provide a more physiologic microenvironment for tumors [15]. So far, the rodent models provide the best first guess at drug candidate pharmacokinetics and effects.

Small animals are prerequisite in several steps of drug development including target identification/validation and following pharmacodynamics and pharmacokinetics study and toxicity study. Conventionally, invasive tissue or body fluid is sampled for laboratory-based analysis of pharmacokinetic information and therapeutic endpoints. Plasma and tumor samples can be assessed by a range of assays, including northern and western blotting, enzyme-linked immunosorbent assay (ELISA), immunohistochemistry, real-time polymerase chain reaction (RT-PCR), and gene expression microarrays. However, the selection bias and the low sensitivity of traditional immunohistochemical techniques for identifying partial, rather than complete reductions in protein expression limit the feasibility of such studies [16]. Therefore, there has been growing interest in the use of non-invasive functional and molecular imaging techniques in the process of drug discovery. This is especially important given the recent shift in oncology drug discovery from conventional cytotoxic agents to novel agents acting on specific molecular targets [5]. The recognition that the latter class of drugs may be more likely to be cytostatic than cytotoxic means that the traditional methods of evaluating antitumor activity by reduction in tumor size [17, 18] may no longer be appropriate or adequate [19]. For example, imaging endpoints included in clinical trials, such as the RECIST (Response Evaluation Criteria in Solid Tumors) criteria, rely on anatomic changes to assess the efficacy of antitumor drugs, with progression defined as a 20 % increase in tumor long axis diameter [20]. But physiologic changes detected with molecular imaging techniques antedate anatomic changes and should be more sensitive in assessing efficacy [21].

Molecular imaging usually exploits specific molecular probes as well as intrinsic tissue characteristics as the source of image contrast, and provides the potential for understanding of integrative biology, earlier detection and characterization of disease, and evaluation of treatment [22]. Imaging technologies can yield tremendous amounts of high quality experimental data per protocol by increasing the number of times that quantitative data can be collected, and guiding tissue sampling for subsequent biochemical or histological analyses, resulting in a rapid and powerful combination of analyses. By imaging the whole animal at multiple time points, researchers can better understand disease pathology, pharmacokinetics and other contextual aspects of the biomolecular processes taking place in the living animal. The images can provide both the structural and functional information under physiologic conditions, mimicking the situation observed in the clinic. In addition, non-invasive and repetitive study of the same living subject at different time points decreases statistical variance and reduces the number of animals required and cost [23]. Pharmacokinetic knowledge obtained from imaging enables continuous monitoring of the disposition of the drug candidate, not just snapshots of the plasma concentration of the unmetabolized component, which may have little relevance to the concentration of the drug candidate at the intended site of action. Use of molecular imaging techniques in early phases of drug development can: (1) identify specific molecular targets; (2) provide information on the optimal biological dose and PK/PD relationships; and (3) provide in vivo PD evaluation of compounds [24]. Such information will help answer several key questions in drug discovery and

development, especially targeted therapy. For example, as anti-cancer strategies become more directed towards a defined molecular target, real-time information relevant to whether the molecular target is expressed, the selectivity and binding of the compound for that target, and the effects of such an interaction is required.

Consequently, molecular imaging of small animals has begun to play important role in identifying new targets, validating in vivo targets, accelerating drug development, and halting compound development early if it proves not to have the desired mechanism and appropriate PK and PD characteristics. In the following section, we will address several important aspects of the role of small animal molecular imaging in the drug discovery and development process after brief discussion of several routinely used molecular imaging modalities.

The advance of various small animal modalities is discussed in other chapters in this book. In general, most of the diagnostic techniques that are routinely used in clinics have a counterpart in the experimental research setting, which include computed tomography (CT), positron emission tomography (PET), single-photon emission computed tomography (SPECT), magnetic resonance imaging (MRI) and ultrasound. Moreover, several imaging modalities have developed to use more appropriately in small animals such at optical imaging (bioluminescence imaging and fluorescence imaging), photoacoustic imaging, and intravital microscopy [22]. For preclinical evaluation, the imaging technique must have adequate spatial resolution for small animals (mainly in the range of 10–100 μm to mm) and sensitivity to detect biochemical events (mainly in the range of millimolar to nanomolar), as well as small clinically relevant changes over time. Each imaging modality has certain advantages as well as limitations, and the choice for an imaging modality, or combination of techniques, is determined by the specific biological questions being asked. In general, the different imaging techniques are more complementary than competitive [23]. Therefore, many hybrid systems that combine two or more modalities are commercially available to take the synergistic advantage, while others are under active development [25–27]. Computer software and algorithms have also been developed to allow co-registration of different imaging modalities [28]. Continued development and wider availability of scanners dedicated to small animal imaging studies will enable the smooth transfer of knowledge and molecular measurements between species, thereby facilitating clinical translation.

4 Applicatons of SAMI in Drug Development

4.1 Target Identification/Validation

The target identification/validation stage during drug development aims to elucidate of pathophysiology of the underlying mechanism under study. For example, epidermal growth factor receptors (EGFR or HER-2) overexpression during tumorigenesis, VEGF/VEGFRs overexpression during angiogenesis, hypoxia-inducible factor-1

(HIF-1a) expression during hypoxia, or overexpression of the prostate specific membrane antigen (PMSA) in prostate cancer. Molecular imaging allows detection of specific targets in vivo, including assessment of the presence of the targets, as well as the quantification of their spatial and temporal distribution. A target may be a single key protein or a particular pathway related to certain pathologic process [29]. For example, epidermal growth factor receptor 2 (HER-2) is a cell membrane surface-bound receptor tyrosine kinase [30]. Overexpression of HER-2 increases cell proliferation, anchorage-independent cell growth, cell migration, and invasiveness [31–33]. HER-2 overexpression has been detected in up to 30 % of breast and ovarian cancers [34] and overexpression of HER-2 has been correlated with invasive and poor prognostic features [35]. Due to its crucial role in carcinogenesis and tumor progression, HER-2 has been intensively investigated as a target for cancer therapy with specific antibodies including trastuzumab (Herceptin, Genentech, Inc., San Francisco, CA) [12] and pertuzumab (Omnitarg, rhu mAb-2C4, Genentech) [36], and small molecular tyrosine kinase inhibitors (TKIs) such as Lapatibib [37]. With ^{111}In labeled murine monoclonal antibody SV2-61r that recognizes the extracellular domain of HER-2, HER-2 positive tumors in nude mice were localized well with a gamma camera [38]. Tumor expression of HER-2 in animal models also successfully visualized by both SPECT imaging using ^{125}I ($t_{1/2}$=59.4 d) and ^{111}In ($t_{1/2}$=67.2 h) labeled affibodies [39, 40] and PET imaging using ^{68}Ga ($t_{1/2}$=68 min) labeled antibody fragments [41, 42].

Another example is endothelial growth factor and receptor (VEGF/VEGFR), which has been identified as anti-angiogenesis target for cancer therapy. Development of VEGF- or VEGFR-targeted molecular imaging probes could serve as a new paradigm for the assessment of anti-angiogenic therapeutics and for better understanding the role and expression profile of VEGF/VEGFR in many angiogenesis-related diseases. Due to the soluble and more dynamic nature of VEGF, imaging VEGF expression is very difficult. The more rationale design is to use radiolabeled VEGF isoforms for SPECT or PET imaging of VEGFR expression. With SPECT imaging, recombinant human $VEGF_{121}$ was labeled with ^{111}In for identification of ischemic tissue in a rabbit model, where unilateral hind-limb ischemia was created by femoral artery excision [43]. $VEGF_{121}$ has also been labeled with ^{99m}Tc through an "Adapter/Docking" strategy and the tracer was tested in a murine mammary carcinoma with tumor uptake of about 3 %ID/g [44, 45]. Cai et al. have labeled $VEGF_{121}$ with ^{64}Cu for PET imaging of tumor angiogenesis and VEGFR expression [46]. MicroPET imaging revealed rapid, specific, and prominent uptake of ^{64}Cu-DOTA-$VEGF_{121}$ (~15 %ID/g) in highly vascularized small U87MG tumor with high VEGFR-2 expression but significantly lower and sporadic uptake (~3 %ID/g) in large U87MG tumor with low VEGFR-2 expression (Fig. 24.2). This study also demonstrated the dynamic nature of VEGFR expression during tumor progression in that even for the same tumor model, VEGFR expression level can be dramatically different at different stages. Successful demonstration of the ability of ^{64}Cu-DOTA-$VEGF_{121}$ to visualize VEGFR expression in vivo should allow for clinical translation of this tracer to image tumor angiogenesis and to guide VEGFR-targeted cancer therapy. All VEGF-A isoforms bind to both VEGFR-1 and VEGFR-2 [47]. In the imaging studies reported to date, specificity to either VEGFR-1 or VEGFR-2 has rarely been

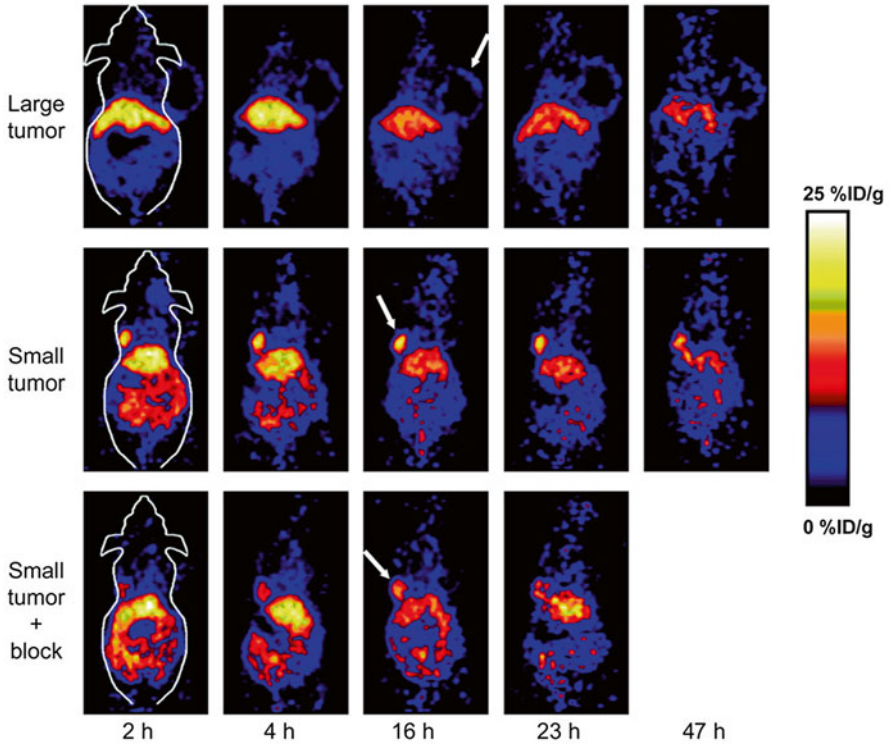

Fig. 24.2 Serial microPET scans of large and small U87MG tumor-bearing mice injected intravenously with 5–10 MBq of ^{64}Cu-DOTA-VEGF$_{121}$. Mice injected with ^{64}Cu-DOTA-VEGF$_{121}$ 30 min after injection of 100 μg VEGF$_{121}$ are denoted as "Small tumor + block". Reproduced with permission from [46]

achieved as most of the tracers are based on VEGF isoforms. Recently, a VEGFR-2-specific PET tracer has been developed using the D63AE64AE67A mutant of VEGF$_{121}$ (VEGF$_{DEE}$) generated by recombinant DNA technology. The renal uptake of ^{64}Cu-DOTA-VEGF$_{DEE}$ was significantly lower than that of ^{64}Cu-DOTA-VEGF$_{121}$ as rodent kidneys expressed high levels of VEGFR-1 based on immunofluorescence staining [48]. With radioisotopes labeled anti-VEGF antibody, SPECT or PET imaging of VEGF has also been performed [49]. Whole-animal PET imaging studies revealed a high tumor-to-background contrast [50].

Integrins, a family of cell adhesion molecules related to angiogenesis, are also intensively investigated mainly with RGD based imaging probes. First in vivo application of radioiodinated RGD peptides revealed the receptor-specific tumor uptake but also predominantly hepatobiliary elimination, resulting in high activity concentration in the liver and small intestine [51]. Consequently, several strategies to improve the pharmacokinetics of radiohalogenated peptides have been studied including conjugation with sugar moieties, hydrophilic amino acids and polyethylene glycol (PEG)

[52–54]. Besides radiohalogenated RGD peptides, a variety of radiometalated tracers have been developed as well, including peptides labeled with ^{111}In, ^{99m}Tc, ^{64}Cu, ^{90}Y, ^{188}Re and ^{68}Ga [55–58]. Most of them are based on the cyclic pentapeptide and are conjugated via the γ-amino function of a lysine with different chelator systems, like DTPA, the tetrapeptide sequence H-Asp-Lys-Cys-Lys-OH, 1,4,7,10-tetraazacyclododecane-N-N″-N″-N‴-tetraacetic acid (DOTA) and 1,4,7-triazacyclononane-1,4,7-triacetic acid (NOTA). While all these compounds have shown high receptor affinity and selectivity and specific tumour accumulation, the pharmacokinetics of most of them still have to be improved [59]. Therefore, multimeric RGD peptides have been developed in order to provide more effective antagonists with better targeting capability and higher cellular uptake through the integrin-dependent endocytosis pathway [60]. The underlying rationale is that the interaction between integrin $\alpha_v\beta_3$ and RGD-containing ECM-proteins involves multivalent binding sites with clustering of integrins. Our group has developed a series of multimeric RGD peptides labelled with ^{18}F or ^{64}Cu for PET imaging, using PEGylation and polyvalency to improve the tumor-targeting efficacy and pharmacokinetics [56, 61–64]. ^{18}F-FB-E[c(RGDyK)]$_2$ (abbreviated as ^{18}F-FRGD2) showed predominantly renal excretion and almost twice as much tumor uptake in the same animal model compared with the monomeric tracer ^{18}F-FB-c(RGDyK) [61, 62]. Tumor uptakes quantified by microPET scans in six tumor xenograft models correlated well with integrin $\alpha_v\beta_3$ expression level measured by SDS-PAGE autoradiography. The tetrameric RGD peptide-based tracer, ^{64}Cu-DOTA-E[E[c(RGDfK)]$_2$]$_2$, showed significantly higher receptor binding affinity than the corresponding monomeric and dimeric RGD analogues and demonstrated rapid blood clearance, high metabolic stability, predominant renal excretion and significant receptor-mediated tumor uptake with good contrast in xenograft-bearing mice (Fig. 24.3) [65].

Currently, there is already a large library of imaging probes that are directed against a large number of known targets and molecular imaging allows confirmation of many targets for drug development. However, for relatively new targets, this direct approach requires synthesizing a new customized imaging probe, and the sensitivity and specificity of detection and interaction with the target need to be characterized individually. This can often be laborious, costly and time-consuming [23]. For currently available imaging probes, much research is needed in the future to improve the in vivo stability, target affinity/specificity, and pharmacokinetics. Another key problem is that quantitative imaging is highly desirable instead of qualitative imaging. Although it is generally assumed that non-invasive imaging results correlate with the target expression level, such assumption has not been extensively validated. In most reports, two tumor models are studied where one acts as a positive control and the other as a negative control. Such correlation is critical for evaluation of target expression level and future treatment monitoring applications, as it would be ideal to be able to monitor the changes in the target expression level quantitatively, rather than qualitatively, in each individual patient [66].

Alternative indirect strategies also can be adopted in the case that direct imaging is impossible or difficult. A common method to fit this goal is fusion protein, which usually achieved by fusing a detectable reporter gene with the target. Then the target

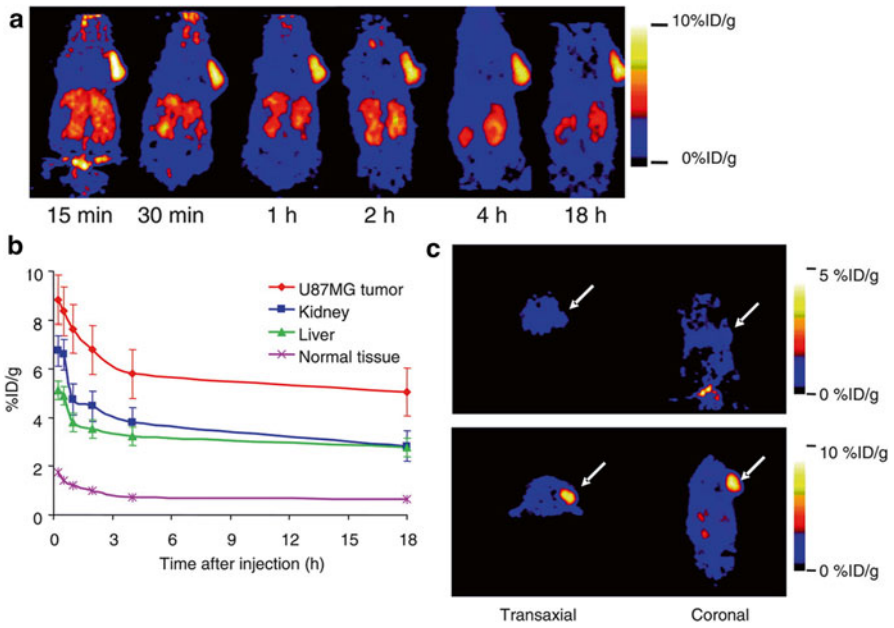

Fig. 24.3 (**a**) Decay-corrected whole-body coronal microPET images of nude mouse bearing human U87MG tumor at 15 and 30 min and at 1, 2, 4, and 18 h after injection of 9.1 MBq of ^{64}Cu-DOTA-E{E[c(RGDfK)]$_2$}$_2$. (**b**) Time–activity curves derived from multiple time-point microPET study. (**c**) Comparison of tumor uptakes in mice injected with ^{64}Cu-DOTA-E{E[c(RGDfK)]$_2$}$_2$ at a dose of 9.3 MBq with (*top*) or without (*bottom*) 10 mg/kg c(RGDyK). Reproduced with permission from [65]

expression or changes during therapy process could be evaluated through measuring the reporter gene expression. For instance, Mayer-Kuckuk et al. [67] has fused dihydrofolate reductase (DHFR) with a PET reporter gene, herpes simplex virus 1 thymidine kinase (HSV1 TK), to encode a fusion protein DHFR-HSV1 TK. In a xenograft model, the fusion-protein increase after treated with antifolate could be visualized with PET using ^{124}I-FIAU, 2′-fluoro-2′-deoxy-1-beta-D-arabinofuranosyl-5-[^{124}I] iodouracil (substrate of HSV1 TK), as imaging probe. That is an example that drug-induced modulation of gene expression can be imaged indirectly by reporter gene. This strategy can be used to test the effectiveness of different therapies that act through DHFR.

4.2 Measurement of Pharmacodynamic Endpoints

Pharmacodynamics studies the biochemical and physiological effects of drugs on the targets within the body and the mechanisms of drug action. Therapeutic efficacy is one of the key questions needed to be answered for each drug or drug candidate [68]. Molecular imaging is able to provide information to evaluate pharmacological

effects. For instance, solid tumors are often characterized by having high glucose utilization, tumour cell proliferation, hypoxia with sustained angiogenesis and evasion of apoptosis [69]. The influence of compounds targeting these characteristics of cancer biology can be selectively visualized by molecular imaging techniques [23]. Examples include FDG PET to image glucose transport and metabolism and FLT PET to evaluate proliferation. In addition, some imaging strategies can focus on one particular pathway or single molecular target to access specific drugs.

4.2.1 Imaging of Metabolism and Proliferation with FDG and FLT PET

Accelerated glucose metabolism is one of the phenotypic or functional changes observed in cancer tissue [70]. Tumor cells are known to be highly glycolytic because of increased expression of glycolytic enzymes, especially hexokinase. FDG is a model PET radiopharmaceutical and has been lauded as the "molecule of the century" in nuclear medicine [71]. As a glucose analogue, FDG enters the cell similar to the way glucose does, through specific glucose transporters on the cell membrane and is converted to FDG 6-phosphate, which is trapped in the cell in proportion to the metabolism of glucose [72]. As the magnitude of FDG uptake in certain tumors relates quite directly to the number of viable cells, FDG-PET imaging provides high specificity and sensitivity in several kinds of cancer with many applications in the clinical management of patients with malignant diseases. However, various tissues and processes in the body, including inflammatory cells and macrophages have greater glucose metabolic rates and thus accumulate higher amounts of FDG than normal tissues, which explains the rate of false-positives seen in the imaging data of FDG PET [71].

FDG PET has been extensively applied to monitor therapeutic responses of radiation therapy and chemotherapy both preclinically and clinically [73, 74]. Using small animal PET, FDG uptake in gastrointestinal stromal tumor (GIST) xenografts was significantly decreased 24 h after the treatment with imatinib, which correlated with a response to treatment [75]. In one study to evaluate the use of FDG PET in monitoring chemotherapy effects in a human non-small cell lung cancer (NSCLC) xenograft model, tumor-FDG uptakes and volumes were measured after administrating a single dose of mitomycin (MMC) and vinblastine (VLB). A significant reduction in tumor volume after chemotherapy occurred and was associated with significantly lower FDG uptake values than the control group, as early as on day 1 [76]. As shown in Fig. 24.4, with subcutaneous U87MG human glioblastoma xenografts treated with CE-355621, an antibody against c-Met, FDG small animal PET visualized significant inhibition of FDG accumulation only 3 days after drug treatment, which was earlier than the inhibition of tumor volume growth seen at 7 days after drug treatment [77]. With a B16F10 murine melanoma model, Dandekar et al. [78] evaluated the reproducibility of FDG small-animal PET studies. FDG small-animal PET mouse xenograft studies were reproducible with moderately low variability, indicating that serial small-animal PET studies may be performed with reasonable accuracy to measure tumor response to therapy.

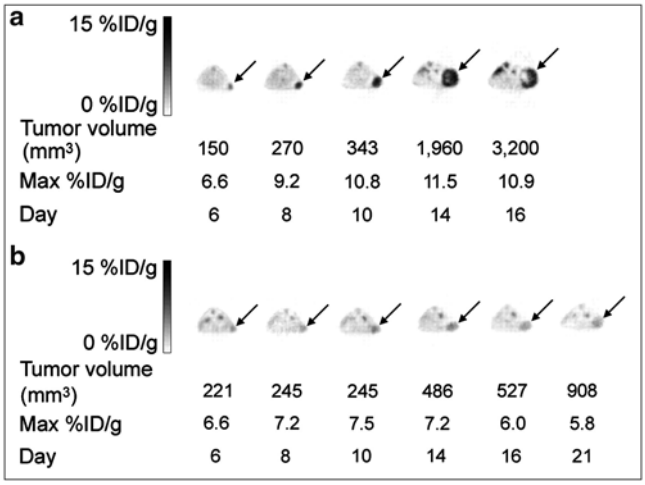

Fig. 24.4 Representative axial ^{18}F-FDG microPET images from nude mice with U87MG xenografts (*arrows*). CE-355621 or control vehicle was administered on day 7. (**a**) ^{18}F-FDG accumulation increased over time in a representative control mouse xenograft. (**b**) ^{18}F-FDG accumulation on days 8–21 in a representative drug-treated mouse xenograft was similar to that of baseline day 6. Reproduced with permission from [77]

Increased mitotic rate, cell proliferation, and lack of differentiation were regarded as the main factors responsible for accelerated growth of malignant tissue. Molecular imaging probes have been designed to specifically measure proliferation, among which [^{18}F] fluoro-L-thymidine (FLT) is the most extensively investigated tracer to image cell proliferation. FLT is transported into cells similar to the thymidine pathway and phosphorylated to FLT-5′-monophosphate by the enzyme thymidine kinase 1 (TK-1). FLT phosphates are impermeable to the cell membrane, resistant to degradation, and metabolically trapped inside the cells. The level of TK-1 in a cell increases several fold as it goes from a resting state to the proliferative phase and is destroyed at the end of S-phase [79]. Therefore, radiolabeled thymidine analogues provide a measure of DNA synthesis and tumor cell proliferation. Several other radiolabeled nucleotide analogues have also been developed to measure DNA synthesis including [^{18}F]fluorouridine and 2′-[^{18}F] fluoro-5-methyl-1-β-D-arabinofuranosyluracil (FMAU) [80].

Although increased glucose metabolism is a feature of tumors, it is also associated with a variety of other processes, whereas cellular proliferation is specific to tumors. In addition, certain anticancer drugs were designed to stop the cell division but may not necessarily lead to cell death. Consequently, the tumor cellular proliferation may drop without any significant changes in the tumor energy metabolism. For instance, FLT PET has been used to measure early cytostasis and cytotoxicity induced by cisplatin treatment of radiation-induced fibrosarcoma 1 (RIF-1) tumor-bearing mice. The decrease in [^{18}F]FLT uptake at 24 h was associated with a decrease in cell proliferation assessed immunohistochemically, despite the lack of a change

in tumor size [81]. It also has been demonstrated that FLT microPET mouse tumor xenograft studies are reproducible with moderately low variability [82]. Drawbacks of FLT PET include low tumor uptake, different uptake and metabolic pathway from thymidine and unconfirmed specificity to malignant diseases, which are against its role in reflecting tumor proliferation [83].

4.2.2 Imaging Blood Flow and its Relevance to Antivascular Agents

Angiogenesis refers to the process by which new blood vessels are formed. It has been recognized as a key element in the pathophysiology of tumor growth and metastasis [84]. Antiangiogenic and antivascular agents are intensively investigated for tumor therapy. Traditionally, tumor angiogenesis and anti-angiogenic therapy have been evaluated by methods such as measurement of circulating angiogenic markers and histological estimate of microvascular density (MVD). In contrast, imaging can provide a noninvasive means of detecting angiogenesis within and about the perimeter of the whole tumor and give functional information.

As mentioned above, ultrasound (particularly microbubble contrast enhanced ultrasound) is a valuable imaging modality to determine the tumor microvascular blood volume and blood velocity [62]. In particular, dynamic contrast-enhanced ultrasonography (DCE-US) allows repeated examinations and provides both morphologic and functional analyses. US modes, based on the second harmonic signal generated by the nonlinear properties of contrast agents, have provided access to tumor blood flow with the quantification of the contrast-uptake kinetics within tumors after a bolus injection of contrast agent [85]. Several quantitative parameters considered as indicators of tumor flow such as the peak intensity (PI) or time-to-PI can be extracted from the time-intensity curves of contrast uptake [86]. Using DCE-US, the antitumor efficacy of AVE8062, a tumor vasculature disruptive agent, has been assessed in melanoma-bearing nude mice [87].

PET studies with ^{15}O-oxygen and related tracers can offer *direct* physiological measurement of circulatory parameters of regional blood flow and vascular volume [88]. Dynamic contrast-enhanced MRI (DCE-MRI) has also been well established to investigate angiogenesis within tumors, and in particular the response to antiangiogenic therapy. The leakage of MRI contrast agent through tumor vessels results in a fast "wash-in" of contrast coupled with the rapid "wash-out," and allows a functional analysis of the tumor microcirculation [89]. DCE-MRI can be performed with low-molecular-weight contrast media (LMCM) such as Gd-diethylenetriamine pentaacetic acid (Gd-DTPA) or macromolecular contrast media (MMCM) such as Gd conjugated human serum albumin (Gd-HSA) [90].

K^{trans}, k_{ep}, fpV, and v_e are standardized output parameters derived from a two-compartment general kinetic model, which is the most widely accepted model and can be readily derived from first principles [91]. K^{trans} represents the rate of contrast agent transfer from blood to interstitium, and k_{ep} is the reverse rate constant, representing backflow. The term fpV is the fraction of plasma volume, related to whole tissue volume, and v_e is the fractional extravascular, extracellular leakage volume. These parameters can be depicted numerically or as color-encoded images.

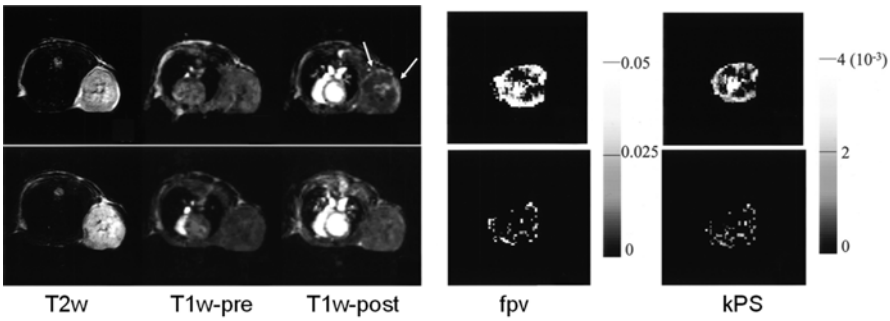

Fig. 24.5 T2w, T1w-pre, and T1w-postcontrast images for animal before (*upper panel*) and 24 h after (*lower panel*) treatment with SU6668. T2w, axial T2w RARE image; T1w-pre and T1w-post, axial T1w GRE images acquired before and 50 min after injection of Gd-DTPA-albumin. kPS, transendothelial permeability. Reproduced with permission from [97]

It has been shown that DCE-MRI parameters correlate with vascular permeability, and hence angiogenesis, within tumor tissue [92]. DCE-MRI can be used to demonstrate the antiangiogenic effects of drugs early after their administration, and can predict traditional treatment response parameters such as changes in tumor size. The ability to accurately monitor angiogenesis response to therapy means that drug efficacy can be established at a very early stage of treatment so that non-responding patients may be detected and management plans altered on a timely basis [93].

DCE-MRI can detect responses to PTK/ZK (a VEGF receptor tyrosine kinase inhibitor) therapy as early as 2 days after therapy with significant reductions in area under gadolinium-contrast-medium curve (AUGC) [94] or permeability parameters [95], which also predict subsequent response. LMCM DCE-MRI has also shown significant reductions in permeability values in patients treated with the antivascular agents AG-013736 (an inhibitor of the VEGF, PDGF, c-Kit receptor tyrosine kinases) and SU5416 (a selective inhibitor of VEGFR-2 tyrosine kinase) activity [96]. Although consensus is still lacking on the exact kinetic model to be used in analyzing DCE-MRI data, the differences among the various methods are often marginal. Therefore, DCE-MRI is rapidly emerging as the imaging technique of choice for monitoring clinical response in trials of new antiangiogenic and antivascular therapies.

Unlike LMCM, the increased size of MMCMs makes them less diffusible, and K^{trans} values may reflect permeability within tumors more accurately [89]. MMCMs can also give more accurate estimates of tumor blood volume since they are excellent blood pool agents. For example, SU6668 is an oral, small molecule inhibitor of angiogenic receptor tyrosine kinases such as vascular endothelial growth factor receptor 2 (Flk-1/KDR), platelet-derived growth factor (PDGF) receptor, and fibroblast growth factor (FGF) receptor. DCE-MRI clearly detected the early effect (after 24 h of treatment) of SU6668 on tumor vasculature as a 51 and 26 % decrease in the average vessel permeability measured in the tumor rim and core, respectively. A substantial decrease was also observed in average fractional plasma volume in the rim (59 %) and core (35 %) of the tumor (Fig. 24.5) [97, 98].

4.2.3 Imaging of Hypoxia

Hypoxia has been shown to be present in many disease states and the degree of hypoxia is highly relevant in functional recovery in ischemic events such as stroke and myocardial ischemia. In solid tumors, hypoxia develops through the inadequate supply of oxygen by the vascular supply to the growing tumor mass. Tumor hypoxia is an important determinant of treatment response, relapse-free survival, and overall prognosis [99]. The traditional "gold standard" for measuring oxygen tension in tissue has been with the pO_2 electrode [100], but this method is invasive and restricted to easily accessible tumors. To avoid the problems of invasiveness and lack of representativity, PET protocols have been developed which permit in vivo mapping of tumor hypoxia with anatomical resolution [101, 102].

The principal strategy for PET tracer imaging of tissue hypoxia to date has been the use of compounds that are preferentially absorbed and trapped within cells in the reduced state [103]. The most frequently studied radiotracers are ^{18}F labeled nitroimidazole derivatives including ^{18}F-fluoromisonidazole (FMISO), ^{18}F-fluoroazomycin arabinoside (FAZA), and ^{18}F-fluoroerythronitroimidazole (FETNIM) (Fig. 24.6). ^{18}F-FMISO enters cells by passive diffusion, where it is reduced by nitroreductase enzymes to become trapped in cells with reduced tissue oxygen partial pressure. When oxygen is abundant in normally oxygenated cells, the parent compound is quickly regenerated by reoxidation and metabolites do not accumulate. However, in hypoxic cells, the low oxygen partial pressure prevents reoxidation of ^{18}F-FMISO metabolites. Because FMISO only accumulates in hypoxic cells with functional nitroreductase enzymes, there will be no accumulation in dead necrotic cells [104]. Multiple studies correlating direct oxygen measurements with ^{18}F-FMISO uptake have been performed and the degree of ^{18}F-FMISO uptake correlated with direct pO_2 histographic measurement in both renal cell carcinoma and head and neck cancers [105, 106]. ^{18}F-FMISO has been used to image hypoxia in human tumors in vivo and to monitor the effects of conventional therapy [107, 108]. ^{18}F-FMISO has also been used in the non-oncologic setting including cerebral hypoxia and myocardial hypoxia [12, 109].

Although ^{18}F-FMISO remains the most extensively investigated radiotracer of hypoxia, it is still far from an ideal hypoxia tracer. The main problem is the limited rate and extent of uptake into hypoxic tissue, such that it takes between 2 and 4 h to achieve an adequate target/background ratio for imaging [103]. Therefore, other compounds including second-generation nitromidazoles have also been synthesized for imaging of hypoxia. Both ^{18}F-FAZA and ^{18}F-FETNIM demonstrated comparable intratumoral uptake with ^{18}F-FMISO and faster clearance from the blood, viscera and muscle tissues, via the renal system in animal models [110, 111]. However, a lower tumor/blood ratio with ^{18}F-FAZA compared with ^{18}F-FMISO has also been reported [112]. Another nitroimidazole-based compound iodoazomycin galactopyranoside (IAZGP) labeled with ^{124}I ($t_{1/2} = 4.2$ day) has yielded considerably higher tumor-to-background contrast at later time point, i.e., 1–2 days after administration [113].

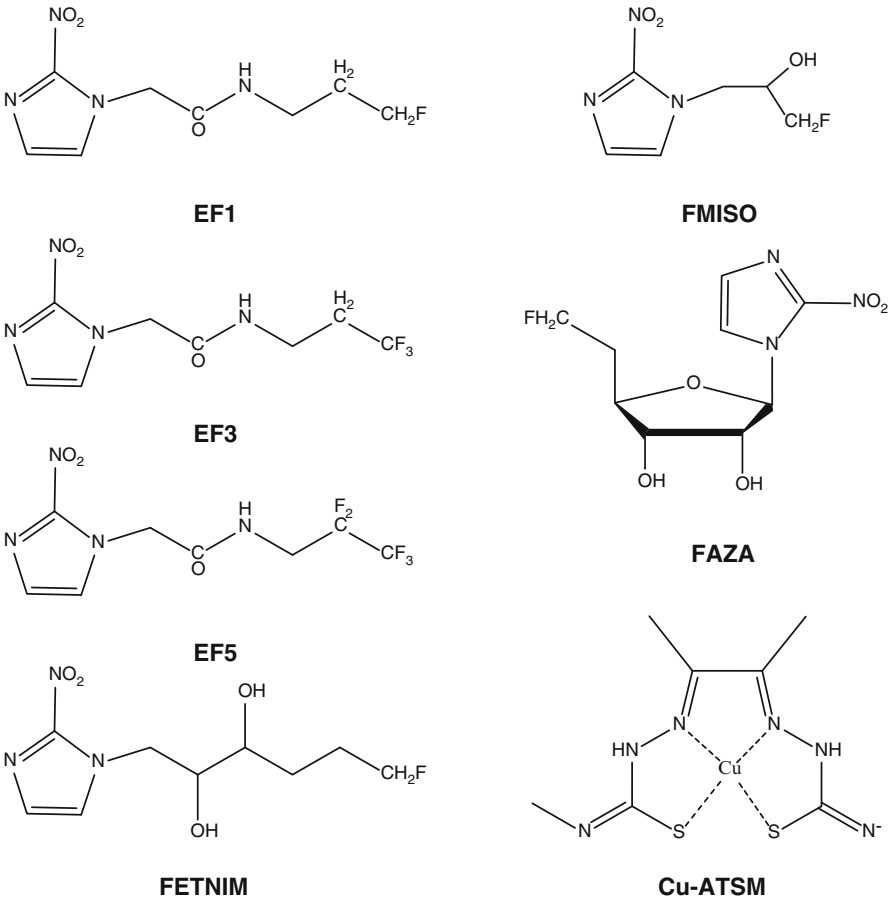

Fig. 24.6 Schematic structures of hypoxia sensitive probes

The 2-nitroimidazole EF5 (2-(2-nitro-1H-imidazol-1-yl)-N-(2,2,3,3,3-pentafluoropropyl)acetamide) is another example of a hypoxia marker and has a uniform biodistribution and stable structure in vivo [114]. Highly specific monoclonal antibodies (mAbs) against EF5 and its adducts have been made, allowing a number of clinically relevant biopsy techniques [115]. A 3-monofluoro analog of EF5, EF1, has been labeled with ^{18}F [116] to image hypoxia in the hypoxic Morris 7777 (Q7) hepatoma and the oxic 9LF glioma tumor models [117]. The results demonstrated that PET imaging with ^{18}F-EF1 was able to differentiate hypoxic versus aerobic tumors in rodents. ^{18}F-EF5 has also been synthesized [118] and PET imaging with ^{18}F-EF5 was carried out in a rat tumor model [113]. Tumors were easily visible by 60 min postinjection (p.i.) when the final tumor to muscle ratios (based on gamma counts) were greater than 2. Another fluorinated etanidazole compound, EF3, has been successfully radiolabeled using ^{18}F for PET-based hypoxia evaluation [119]. Ex vivo pharmacokinetics and biodistribution studies demonstrated that ^{18}F-EF3

could be a good alternative for ^{18}F-FMISO for the detection of tumor hypoxia [120]. However, a recent comparative study performed by Dubois et al. indicated that the maximal ^{18}F-EF3 tumor uptake, compared to the maximum ^{18}F-FMISO uptake, was significantly lower at 2 h p.i., although reached similar levels at 4 h p.i. [121]. Reduced polarity of EF5 and its analogues will result in a longer drug half-life, which may cause binding to aerobic cells and slower excretion of the un-metabolized marker from normal tissues.

An alternative compound evaluated for tissue hypoxia imaging is Cu-diacetyl-bis(N4-methylthiosemicarbazone) (Cu-ATSM) [36]. The mechanism of hypoxia selectivity of Cu-ATSM and related complexes is thought to involve an initial intracellular proton-coupled reduction to produce a copper(I) species, followed by reoxidation and efflux from cells with high oxygen tension or by ligand dissociation and trapping of the copper in cells with low oxygen tension [122]. ^{60}Cu-ATSM has been shown to be predictive of radiotherapy treatment outcome in small-scale clinical studies [123, 124]. Recently, a Cu-ATSM–glucose (ATSE/A-G) has been synthesized in order to improve the biodistribution properties such as high levels of liver and kidney uptake [125]. In vivo PET showed that ^{64}Cu-ATSE/A-G retained hypoxia selectivity and had improved characteristics when compared with ^{64}Cu-ATSM, with a shift from primarily hepatointestinal for ^{64}Cu-ATSM to partially renal with ^{64}Cu-ATSE/A-G [125].

4.2.4 Imaging of Apoptosis

Apoptosis, or programmed cell death, has been recognized as an active regulatory mechanism, complementary, but functionally opposite, to proliferation with important roles in shaping and maintaining tissue size and prevention of disease [126]. Diseases such as transplant rejection, myocardial or cerebral infarctions, and (neuro) degenerative diseases are characterized by relative excess of cell death [127]. In tumors, however, the amount of programmed cell death is too low compared to cell proliferation or apoptosis is completely inactivated [128]. Most of the chemotherapy agents cause tumor cell death primarily by induction of apoptosis and resistance to anticancer treatment is widely believed to involve mutations that lead to deregulated cellular proliferation and suppression of mechanisms that control apoptosis [129]. Thus, imaging of apoptotic response could provide a much faster way to predict effectiveness of cancer chemotherapy than currently used morphologic measurements [130]. In cardiovascular medicine, imaging of apoptosis could be highly useful in managing myocardial infarction, unstable atherosclerotic plaques, and cardiac allograft rejection [131].

Phosphatidylserine exposure is a near-universal event in apoptosis, it occurs within a few hours of the apoptotic stimulus, and it presents a very abundant target (millions of binding sites per cell) that is readily accessible on the extracellular face of the plasma membrane [132]. Due to high affinity for apoptotic cells, no immunogenicity and lack of in vivo toxicity, annexin V is the dominant probe to detect and image apoptosis [130]. Annexin V has been labeled with ^{99m}Tc after conjugated with

hydrazinonicotinamide (HYNIC), a bi-functional nicotinic acid analogue, to detect apoptosis in vivo [133]. In anti-Fas antibody induced massive hepatic apoptosis model, there was a 134 and a 304 % increase in the liver uptake of ^{99m}Tc-HYNIC-annexin V above controls at 1 and 2 h, respectively. In a rat model of heterotopic cardiac allografts, in which transplant rejection is mediated by apoptosis, all of the cardiac allografts were visualized readily on imaging with ^{99m}Tc-HYNIC-annexin V by 5 days after transplantation. The third was a xenograft tumor model in which apoptosis was induced by a chemotherapeutic agent, cyclophosphamide. Twenty hours after drug administration, treated tumors showed readily visualizable increases in ^{99m}Tc-HYNIC-annexin V activity of 78 % above control values in untreated animals [133]. The experiments along with other studies performed by this group [134, 135] demonstrated the feasibility of ^{99m}Tc-annexin V for the noninvasive in vivo imaging of PS expression associated with apoptosis. Apoptosis induced by another chemotherapeutic drug, paclitaxel, also resulted in increased uptake of ^{99m}Tc-annexin V, which was readily visualized by scintigraphy [136]. Besides annexin V, the C2A domain of synpaptotagmin I [137] and a small-molecule peptide based on phage display [138] also showed binding affinity for phosphatidylserine and can be potential apoptosis imaging agents. Imaging agents derived from Annexin V also have been further refined by introducing a short N-terminal peptide via recombinant DNA methods for site-specific labeling of different radionuclides, fluorophores for multiple modality imaging of apoptosis [139–141].

Besides phosphatidylserine exposure, caspase activation and mitochondrial membrane potential collapse are also featured apoptotic characteristics [139]. Caspases play central role in the execution of cell death and both the intrinsic (mitochondrial) and extrinsic (death receptor) pathways of apoptosis eventually activate several effector caspases [142]. Caspase-3 is one of the key effector caspases which recognizes and cleave DEVD (aspartic acid-glutamic acid-valine-aspartic acid) peptide sequence presenting in many cellular proteins [poly(ADPribose) polymerase], lamins, etc. [143]. DEVD containing molecules targeting caspase-3 have been developed to image apoptosis [144–146]. Most of these studies utilized fluorescence imaging and bioluminescence imaging, which is suitable for cellular and small animal investigation. However, the clinical translation is limited. Isatin (1-H-indole-2,3-dione) was identified as an inhibitor of caspase 3 by high throughput screening and further structural optimization led to the discovery of the highly potent derivative, isatin sulfonamide, with caspases 3 and 7 inhibiting efficacy in the 2–6 nM range [147]. Realizing the potential of radiolabeled isatins for imaging of apoptosis, several groups developed the ^{18}F-labeled agents as a putative tracer for PET imaging of activated caspase 3 levels [148–150]. With a ^{18}F labeled isatin sulfonamide analogue, ^{18}F-WC-II-89, microPET imaging studies revealed a high uptake of the radiotracer in the liver of a cycloheximide-treated rat relative to the untreated control (Fig. 24.7) [151]. Another strategy to image apoptosis aims to mitochondrial membrane potential collapse, which is also one of the central events in apoptosis [142]. Radiolabeled probes based on phosphonium cations show the predicted decrease in cellular uptake in vitro as mitochondrial potential is decreased, and in vivo these probes show highest uptake in the heart and kidneys [152, 153].

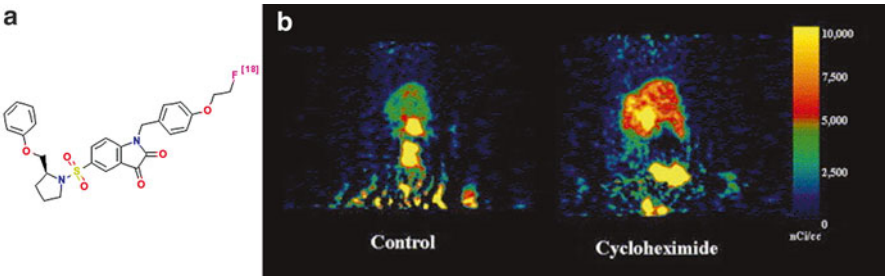

Fig. 24.7 (**a**) Structure of the isatin sulfonamide analogue, ^{18}F-WC-II-89; (**b**) whole-body microPET images of ^{18}F-WC-II-89 distribution in a control rat (*left*) and cycloheximide-treated rat (*right*). Reproduced with permission from [153]

4.2.5 Imaging Particular Downstream Targets

FDG/FLT PET and DCE MRI have generic values for a wide range of anti-tumor and antivascular drugs. Molecular imaging strategies have also been developed to apply to only a narrow group of compounds. A good example here is the response of client proteins of heat shock protein 90 (HSP90) to HSP90 inhibitors. HSP90 is a key member of molecular chaperones that promote the proper folding of nascent polypeptides and ensure that protein–protein interactions occur in a productive manner under basal conditions [154]. The downstream effects of HSP90 inhibition affect a wide range of signaling processes that make possible the malignant properties of cancer cells. Therefore, HSP90 inhibitors exhibit a broad spectrum of anticancer activities. In addition, analysis of treatment-induced changes in relevant HSP90 client proteins could be used as PD end points for evaluation of therapeutic response of HSP90 inhibitors.

Human epidermal growth factor receptor 2 (HER-2) has been established as clients of HSP90 and HER-2 is dependent upon HSP90 for its stability throughout the whole life span of the receptor, including the maturation process in the endoplasmic reticulum (ER), and during the residency of the receptor at the plasma membrane. HER-2 is depleted within 2 h of HSP90 inactivation [155]. A positron emitter Galium-68 ($t_{1/2}=68$ min) labeled F(ab′)$_2$ fragment of trastuzumab (herceptin, humanized antibody against HER-2) has been used to assess the degradation of HER-2 by HSP90 inhibitor, 17-allylaminogeldanamycin (17-AAG). Based on the microPET quantification, HER-2 expression was reduced by almost 80 % in the animals 24 h after 17-AAG treatment [41]. In a follow-up study, tumor response to 17-AAG treatment was assessed by ^{68}Ga-DOTA-F(ab′)$_2$-trastuzumab and ^{18}F-FDG PET. Within 24 h after treatment, a significant decrease in HER-2 was measured by HER-2 PET, whereas ^{18}F-FDG PET uptake was virtually unchanged. This indicates that HER-2 PET with ^{68}Ga-DOTA-F(ab′)$_2$-herceptin could provide accurate information for the tumor's early response to 17-AAG treatment [42].

Epidermal growth factor receptor (EGFR), another member of HER family, has also been established as a client of HSP90 [156, 157]. Quantitative PET imaging of EGFR expression in tumor-bearing mice using copper-64 ($t_{1/2}$ = 12.7 h) labeled cetuximab (Erbitux; C255; ImClone and Bristol-Myers Squibb) showed that the tumor uptake of ^{64}Cu-DOTA-cetuximab measured by PET had a good linear correlation (r^2 = 0.80) with the EGFR expression level as quantified by Western blotting [158]. Quantitative microPET showed that ^{64}Cu-DOTA-cetuximab has prominent tumor activity accumulation in untreated tumors but significantly lower uptake in 17-AAG-treated tumors at 24 h post-injection. Both immunofluorescence staining and Western blot confirmed the significantly lower EGFR expression level in the tumor tissue upon 17-AAG treatment. The results indicate that this approach may be valuable in monitoring therapeutic responses to HSP90 inhibitor 17-AAG in EGFR-positive cancer patients [159].

Another example is the serine/threonine kinase Akt. Akt functions as a signaling hub where many upstream signaling pathways converge [160]. Because Akt and its upstream regulators are dysregulated in some forms of cancer, they are promising targets for pharmaceutical intervention [161, 162]. Zhang et al. [90] have constructed a bioluminescent Akt reporter that contains an Akt consensus substrate peptide and a domain that binds phosphorylated amino acid residues (FHA2) flanked by the N-terminal (N-Luc) and C-terminal (C-Luc) domains of the firefly luciferase reporter molecule. With this reporter construction, Akt activity in cultured cells and tumor xenografts can be monitored quantitatively *and* dynamically in response to activation or inhibition of receptor tyrosine kinase, inhibition of phosphoinositide 3-kinase, or direct inhibition of Akt. The in vivo results indicated that this technology could facilitate the determination of PD of drugs in animal models. Moreover, this platform may be expanded to other key kinases in cancer.

Imaging probes targeting a particular therapeutic response has also been investigated. For example, with the goal to determine whether recombinant peptides can be used to differentiate responding from nonresponding cancers immediately after initiation of treatment, Han et al. [163] designed a series of seminal experiments. After six rounds of in vivo biopanning with a T7 phage-based random peptide library, an HVGGSSV peptide was isolated to be the predominant sequence from both Lewis lung carcinoma and GL261 tumors treated with combined radiation and a VEGF receptor tyrosine kinase inhibitor. The peptide was labeled with Cy7 and near infrared (NIR) imaging revealed that HVGGSSV peptide could differentiate between responding and nonresponding tumors (Fig. 24.8) [163]. Moreover, a direct correlation between the amount of increased peptide binding and the responsiveness of the cancer also has been established. Thus, rapid, noninvasive assessment of the pharmacodynamic response was achieved with this peptide, which promises to accelerate drug development and minimize the duration of treatment with ineffective regimens in patients.

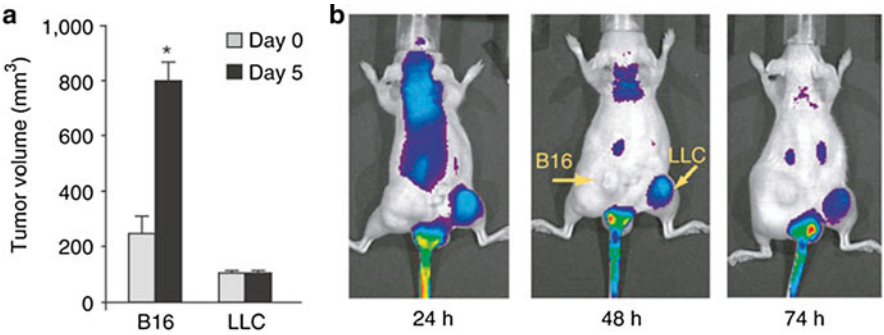

Fig. 24.8 Lewis lung carcinoma tumors were implanted into the right hind limb and B16F0 tumors were implanted into the left hind limb of the same mouse. Both the Lewis lung carcinoma and B16F0 tumors were treated with SU11248 and 3 Gy for 5 consecutive days. (**a**) Tumor volumes were measured at day 0 and day 5. Four hours after the first treatment, Cy7-labeled HVGGSSV peptide was infused and NIR imaging was used to study peptide binding to treated tumors. (**b**) Shown are NIR images of mice obtained at indicated times after the first treatment. Reproduced with permission from [163]

4.3 Imaging Therapeutic Gene Expression with Relevance to Gene Therapy

Gene therapy is an evolving technique that seeks to use nucleic acids (DNA or RNA) to treat or prevent diseases. There are several approaches to gene therapy, including forced expression of a therapeutic gene on the background of a mutant gene (gene addition), replacing a mutated gene that causes disease with a healthy copy of the gene (gene replacement), inactivating or "knocking out" a mutated gene that is functioning improperly, and introducing a novel gene into the body to help prevent or fight diseases [164]. To deliver a therapeutic gene to the patient's target cells, an appropriate carrier molecule or gene delivery vehicle, often called a vector, may be used. Efforts are being directed towards cell-type specific targeting for which both payload delivery and gene expression which can be visualized currently by biodistribution and transduction imaging, respectively. In addition, the treatment outcome can also be monitored by non-invasive imaging methods. Transduction imaging visualizes the transgene-mediated protein production, whereas biodistribution imaging visualizes the actual systemic distribution of gene delivery vectors [165]. It is important to evaluate both particle kinetics and transgene expression in vivo to generate an accurate picture of gene delivery and expression [166]. Molecular imaging of gene expression is usually achieved with the use of particular genes, called "imaging reporter genes." Reporter genes can be used to study promoter/enhancer elements (both constitutive and inducible) involved in gene expression and endogenous gene expression through the use of transgenes containing endogenous promoters fused to the reporter [167]. In some cases, the therapeutic genes themselves are reporter genes and can be imaged

directly, such as HSV-1 thymidine kinase (HSV1-tk) [168] and sodium idodie symporter (NIS) [169]. The expression of most other therapeutic genes which have no ligands or substrates for functional image analysis can be studied if they are linked to the expression of a reporter gene [170]. Usually, the therapeutic gene with expressing vectors will be replaced by or fused with a reporter gene. The spatial and temporal expression of reporter genes could be visualized and quantitated by multiple non-invasive imaging modalities. The rapid progress in molecular imaging, especially in the field of imaging gene expression, will greatly aid some of the gene therapy requirements and likely contribute to the success of this promising therapeutic modality [171].

For example, heat-shock protein promoters, particularly HSP70 promoters, have been commonly used for gene therapy strategies because they are both heat-inducible and efficient [172]. A series of studies has been performed for tumor treatment by introducing into tumor cells a suicide gene such as that coding for thymidine kinase (TK) or cytosine deaminase (CD) under the control of an HSP promoter [173, 174]. Green fluorescence protein (GFP) has been utilized extensively as reporter gene to evaluate the spatial and temporal control of gene expression driven by HSP70 promoters [175–178]. On a microscope heating stage using GFP as a reporter, HSP70 expression kinetics were visualized continuously in cultured bovine aortic endothelial cells (BAECs). BAECs were transfected with a DNA vector expressing an HSP70-GFP fusion protein under the control of HSP70 promoter. The kinetic profile for HSP70-GFP fusion protein is consistent with the endogenous HSP70 [179].

The expression of the reporter gene coding for TK can be probed with pyrimidine nucleoside derivatives, such as 2′-deoxy-2′-fluoro-β-D-arabinofuranosyl-5-iodouracil (FIAU), and acycloguanosine derivative, such as 9-[4-fluoro-3-(hydroxymethyl) butyl]guanine (FHBG). With PET imaging, spontaneous in vivo activation of the HSV1-tk suicide gene driven by the *Grp78* promoter, a member of HSP70 family, in growing tumors and its activation by photodynamic therapy (PDT) in a controlled manner has been observed [174]. NIS is responsible for the physiologic uptake of iodide. NIS is also able to concentrate pertechnetate (TcO_4^-), bromide (Br^-), and perrhenate (ReO_4^-). With corresponding radionuclides, NIS gene expression could be visualized by SPECT or PET imaging [180]. Che and co-workers have constructed a retroviral vector, pQHSP70/hNIS-IRES-eGFP (pQHNIG70), containing the hNIS-IRES-eGFP dual-reporter genes under the control of an inducible human HSP70 promoter. A stable ratio of radiotracer uptake to eGFP fluorescence and to HSP70 protein was demonstrated over a wide range of expression levels, induced by different levels of heating. The local application of heat thus can effectively induce hNIS and eGFP gene expression in vivo, and this expression can be efficiently visualized by fluorescence, scintigraphic, and micro-PET imaging [181].

Native ferritin receptors can concentrate the body's natural iron to quantities detectable by MRI, thus making it an elegant MRI reporter gene. This method was used to image viral transduction in rat brain in a non-invasive manner without any external ligands. Genove et al. [182] used adenoviruses to deliver a ferritin transgene into specific host tissues and imaged cells that took up endogenous iron and

became superparamagnetic. In this context, the overexpressed ferritin receptors have been imaged using a heavy chain of murine ferritin, an iron storage molecule with ferrioxidase activity, for the detection of gene expression by MRI in vivo [183].

4.4 Evaluation of Pharmacokinetics

Information from small animal imaging studies can be extremely helpful at the ligand synthesis/optimization stage, particularly in elucidating pharmacokinetics of the drug candidate. Pharmacokinetic imaging requires the drug candidate to be tagged in some way, usually radiolabeled, but increasingly with fluorescent labels and, for larger molecules, with magnetic labels. In almost all cases, except for radiolabeling an identical site in the drug candidate with carbon-11 for PET, one must be mindful that an analogue, rather than the drug candidate, is being studied. Central nervous system (CNS) drugs can be tagged and tracked in vivo in a single animal to determine blood–brain barrier (BBB) permeability. Quantitative kinetic evaluation of drug candidates can be performed with PET, allowing calculation of relevant rate constants that describe tissue extraction, receptor-specific binding, nonspecific binding and/or enzyme turnover. Pharmacokinetic knowledge obtained from imaging enables continuous monitoring of the disposition of the drug candidate, not just snapshots of the plasma concentration of the unmetabolised component, which may have little relevance to the concentration of the drug candidate at the intended site of action. That is true of CNS drugs, where brain and plasma kinetics invariably diverge and for oncologic agents, where heterogeneous tumor perfusion presents the lesion with an uneven or inadequate dose, not reflected in peripheral samples. Pharmacodynamic information, i.e., the effects of the drug candidate on the tissues, is also readily available through small animal imaging. Changes in blood flow critical to anti-angiogenic therapies can be assessed by PET, MRI or US. Drug–drug interactions can be studied by radiotracers designed to probe the activity of multidrug resistance (MDR) pumps under the influence of MDR modulators, for example. All of that information can be used in an iterative fashion for structural refinement of lead compounds. The objective of the following lead generation phase is to synthesize lead compounds, new analogues with improved potency, reduced off-target activities, and physiochemical/metabolic properties suggestive of reasonable in vivo pharmacokinetics. While lead optimization is accomplished through empirical modification of the hit structure and/or by employing structure-based design if structural information about the target is available. A key component of the lead optimization process involves optimization of the lead compound with respect to suitable “drug-like” properties in experimental animals, measuring absorption, distribution, metabolism and excretion (ADME) in pharmacokinetic (PK) studies. This is critically important because a frequent point of failure in drug discovery programs is suboptimal PK properties when the new agent is first tested in the intact animal [184].

Studies of the kinetics of drug absorption, distribution, metabolism and excretion (ADME) form an important part of any drug development process. Poor pharmacokinetics is a major cause of drug "failure." Conventionally, PK studies are performed by measuring drug concentrations in the plasma by high performance liquid chromatography (HPLC) and an appropriate detection method such as ultraviolet, mass spectrometry or radioactivity counting if the drug labeled with a radioisotope such as tritium. Due to its extremely high sensitivity (as low as 10^{-12} mol/L), quantitative PET imaging can provide information on the kinetics, dosimetry and distribution of drugs in diseased and normal tissues within the field of view of the scanner, in addition to information on hepatobiliary and renal clearance. Small animal PET scanners allow scans to be carried out in small rodents and canine or primate models to screen candidate compounds and refine the imaging paradigm before implementation in humans. Many drugs can be labeled with carbon-11 or with fluorine-18 with minimal or no effect on the chemical/physicochemical properties of the compound, allowing the monitoring of the drug biodistribution non-invasively [185, 186].

Based on PET imaging, general pharmacokinetic parameters can be quantified and calculated, including peak radioactivity (C_{max}), time to reach peak radioactivity (t_{max}), area under the radioactivity–time curve (AUC), uptake [standardized uptake value (SUV)], and proportions of the drug in various tissues relative to those in the blood. Other important kinetic parameters relating to the uptake, distribution, and washout also can be derived from mathematical modeling of tissue data, such as clearance from plasma to tissue (K_1), clearance from tissue to plasma (K_2), selective binding (K_3), permeability–product surface area (PS product), net unidirectional influx constant from plasma to tissue (K_I), mean residence time, binding potential, and tissue volume of distribution (partitioning between blood and tissue) [187]. In most PET pharmacokinetic studies, only trace amounts of drugs are administered. It may also be necessary to carry out studies with a formulation containing the appropriate pharmacological dose combined with the radiotracer to acquire more precise pharmacokinetic information at pharmacological doses.

For instance, fleroxacin is a promising fluoroquinolone used to treat urinary tract infections, skin and soft tissue infections, gastrointestinal infections, and acute bacterial exacerbations of chronic bronchitis [188]. In order to evaluate the pharmacokinetics of fleroxacin, [^{18}F]fleroxacin was synthesized and shown to be identical physically, chemically, and in its antimicrobial activity to the commercially produced product. The pharmacokinetics of [^{18}F]fleroxacin was measured in healthy and infected animals by positron emission tomography (PET) and tissue radioactivity measurements [189, 190]. The similar strategy was also applicable to humans [191]. Another example, 1,3-Bis-(2-chloroethyl)-1-nitrosourea (BCNU), a lipophilic alkylating agent, is one of the most effective agent for the treatment of intracerebral gliomas. Pharmacokientics study by PET imaging demonstrated that intra-arterial administration of ^{11}C-BCNU achieved concentrations of the drug in the tumor that averaged 50 times higher than the level found with a comparable intravenous dose [192]. $VEGF_{121}$/rGel is a VEGFR-2 specific fusion toxin composed of $VEGF_{121}$ linked with a G_4S tether to recombinant plant toxin gelonin [193]. Our group used $VEGF_{121}$/rGel to treat orthotopic glioblastoma in a mouse model. Before

initiation of treatment, microPET imaging with ^{64}Cu-labeled $VEGF_{121}$/rGel was performed to evaluate the tumor targeting efficacy and the pharmacokinetics. It was found that ^{64}Cu-DOTA-$VEGF_{121}$/rGel exhibited high tumor accumulation/retention and high tumor-to-background contrast up to 48 h after injection. Based on the in vivo pharmacokinetics of ^{64}Cu-DOTA-$VEGF_{121}$/rGel, $VEGF_{121}$/rGel was administered every other day for the treatment of orthotopic U87MG glioblastomas [128].

Another promising application uses radioimmunoimaging (RII) to localize the biodistribution of radioimmunoconjugates (RIC) and calculate the dosimetry for effective radioimmunotherapy (RIT). Biodistribution of ^{90}Y for dosimetry calculations is typically obtained by imaging using the surrogate radiometal ^{111}In because ^{90}Y does not emit photons. ^{111}In has a half-life almost identical to that of ^{90}Y, emits two γ-rays of 171 and 245 keV, and can be readily incorporated into the same metal chelating agents as ^{90}Y. For these reasons, ^{111}In has been considered an excellent analogue for ^{90}Y. For example, the FDA-approved RIC ibritumomab tiuxetan (Zevalin™, BiogenIDEC) is labeled with ^{90}Y to treat non-Hodgkin's lymphoma (NHL), and it requires the use of ^{111}In-ibritumomab tiuxetan to produce images of the tumor and normal organs for dosimetry and biodistribution studies [194]. However, it has been reported that ^{111}In-trastuzumab did not parallel the uptake of ^{86}Y-trastuzumab in the bone, and thus may not accurately predict the level of ^{90}Y accumulation in the bone for clinical RIT applications [147, 195]. Thus, quantitative information offered by PET through ^{86}Y radiolabels could enable more accurate absorbed dose estimation for ^{90}Y RIT [147]. It has also been reported that ^{99m}Tc-MAb conjugates showed a similar pharmacokinetic behavior as ^{186}Re-MAb conjugates, and can thus be used to predict the localization of ^{186}Re-labeled MAbs and make dosimetric predictions in individual patients [196].

4.5 Imaging of Therapeutic Cells Trafficking

The development of stem cells for therapeutic purposes, including cell therapy and regenerative medicine, is emerging as a major field of pharmaceutical research. For example, bone marrow cells have been used to regenerate infarcted myocardium [197, 198] and mesenchymal stem cell (MSC) based cancer therapy is very promising [199]. Non-invasive monitoring the disposition, migration and destination of therapeutic cells will facilitate the development of cell based therapy. The cells can be labeled directly by introducing a marker into or onto the cells before transplant/implant that is stably incorporated or attached to the cells. For example, Aicher et al. [200] labeled endothelial and hematopoietic progenitor cells with ^{111}In-oxine and the increase in ischemia-induced heart uptake compared with sham-operated controls was readily visible using a pinhole collimator though only 5 % of the injected dose of radioactivity was found in the heart. ^{64}Cu-pyruvaldehyde-bis-(*N^4-methylthiosemicarbazone*) (^{64}Cu–PTSM) also has been used radiolabel cells ex vivo for in vivo positron-emission tomography (PET) imaging studies of cell trafficking in mice. The images indicated that tail-vein-injected labeled C6 cells traffic to the lungs and

liver. In addition, transient splenic accumulation of radioactivity was clearly detectable in a mouse scanned at 3.33 h postinfusion of ^{64}Cu–PTSM-labeled lymphocytes [201]. ^{18}F-HFB [202] and ^{18}F-FDG [203] also have been investigated as a marker to label mesenchymal stem cells for in vivo PET imaging. Direct labeling of cells with radionuclides can only determine short-term circulation and homing properties of infused stem cells because the imaging signal decreases with radio-decay, or becomes more diffused with cell division and cell dispersion [77, 201]. Instead of radionuclides labeling, iron oxide particles or perfluorocarbon nanobeacons also can be utilized to label cells for MRI imaging [204, 205]. Amado and coworkers injected iron-oxide labeled MSCs intramyocardially 3 days after a myocardial infarct (MI) was induced by balloon occlusion of the left anterior descending (LAD). The iron oxide labeled cells created hypoenhanced regions and 42 % of the signal still remained at 8 weeks [206]. Compared with radionuclide imaging, the main advantage of MRI is its capacity for high anatomic resolution. However, MRI currently lacks the sensitivity of radionuclide based labeling (SPECT/PET), which limits its ability to detect small numbers of cells (>10^5 cells are needed to be detectable) [204]. Moreover, the detected signal does not necessarily indicate whether the cells are viable for dead cells still generate signals for days before macrophage clearance of cellular debris [207].

An alternative strategy to image cell trafficking relies on the expression of imaging reporter genes transduced into the cells before transplantation, which are then visualized by corresponding imaging modalities including optical imaging, SPECT/PET or MRI, upon injection of appropriate probes or substrates. Bioluminescence imaging (BLI) with firefly luciferase (fLuc) or renilla luciferase (rLuc) has been used to monitor the oncogenic transformation of MSCs and track the MSCs distribution in various disease models include tumor models, acute kidney injury, tissue engineering constructs, genetic disease and angiogenesis [199, 208, 209]. MSCs had been successfully transfected with the herpes simplex virus type 1 thymidine kinase (*HSV1-TK*) reporter gene [30]. The engraftment and proliferation of *HSV1-TK*$^+$MSCs in tumor stroma were detected by PET imaging with ^{18}F-labeled 9-(4-fluoro-3-hydroxymehtybutyl)-guanine (^{18}F-FHBG). Human sodium iodide symporter (*hNIS*) was also used as a reporter gene to image stem cell trafficking. Hwang et al. infected with MSCs lentiviral vector carrying NIS (MSC-NIS) and gamma camera scintigraphy with ^{99m}Tc-pertechnetate showed higher uptake by MSC-NIS on a polymer scaffolds than by MSC-NIS not seeded on a scaffold [210].

Comparing with direct labeling method, reporter gene based cell imaging facilitates longitudinal measurements of viable cells. In addition, with tissue specific promoter, such as collagen α1 type I promoter (Col2.3) specifically for osteogenic differentiation, the destination and differentiation of transplanted stem cells can also be evaluated. However, there are also issues related to reporter gene imaging including the low transfect efficiency, gene silence along with time, and possible effect of transfection on the proliferation and differentiation potential of the labeled stem cells. Recently, Li et al. performed a comparison study between reporter gene and iron particle labeling for tracking human embryonic stem cells (hESC) in living subjects. After transfected with lentivirus containing a fLuc and GFP fusion reporter gene, hES cells were colabeled with superparamagnetic iron oxide particles before

transplantation into murine hind limbs. Longitudinal magnetic resonance imaging (MRI) showed persistent MRI signals that lasted up to 4 weeks. While, bioluminescence signals from hESCs increased dramatically during the same period. These data indicate that reporter gene is a better marker for monitoring cell viability, whereas iron particle labeling is a better marker for high-resolution detection of cell location by MRI [211]. Another comparison study also showed that fLuc BLI reporter gene imaging is a more accurate gauge of transplanted cell survival as compared to MRI of Feridex-labeled cells [212].

5 Conclusions and Perspectives

Small-animal molecular imaging is becoming more widely used as a non-invasive tool for drug discovery and drug screening. Compared with conventional methods for the evaluation of PK/PD, molecular imaging has several major advantages. The use of molecular imaging endpoints for in vivo studies, rather than time-consuming conventional dissection and histology, substantially decreases the workload. Furthermore, because imaging is noninvasive and allows for longitudinal studies in a single animal, it also provides much more precise data of statistical relevance. Significant advances have been made in developing novel probes for multimodality molecular imaging of tumor angiogenesis. Small molecules, peptides, peptidomimetics, proteins, and antibodies have been labeled with radioisotopes, superparamagnetic nanoparticles, fluorescent dyes, quantum dots, and microbubbles for PET, SPECT, magnetic resonance imaging, near-IR fluorescence, and ultrasound imaging of small animal tumor models. Thus, an important advantage of molecular imaging techniques is that they can bridge the gap between preclinical and clinical research to develop candidate drugs that have the optimal target specificity, pharmacodynamics, and efficacy.

In addition, the exploratory investigational new drug (eIND) mechanism from FDA will allow faster first-in-human studies. Compared to time-consuming conventional methods, microdosing studies with novel imaging probes can provide an opportunity for early assessment of the safety profile and pharmacokinetics in healthy volunteers. Such rapid initial clinical studies will definitely accelerate the translation from animal test to clinical application, and so as to drug discovery process. Furthermore, the molecular imaging field has grown at a furious pace over the last decade, and the value of molecular imaging in drug development and screening is more widely accepted by pharmaceutical companies. Due to the high sensitivity and versatility, PET is the dominant imaging strategy in drug discovery and development at the present. Labeling with carbon, oxygen, fluorine will minimize the change to the chemical structure or even keep the structure identical. Thus the biodistribution of imaging probes can model the drug distribution perfectly. Even if the drug target is different from the imaging target, one can still use the imaging result as a useful surrogate to test the efficacy of the drug at a given dose. For these reasons, molecular imaging is widely expected to be regularly applied in many steps of the drug development process in the near future.

Though molecular imaging of small animals is being adopted as an attractive tool in drug development, there are several challenges in this relative new field. Firstly, the imaging based quantification and explanation still need to be refined to reflect target expression or activity more accurately. For example, the imaging probes accumulation on certain regions reflected by images relates mainly to targets expression and probe-target interaction. However, other factors such as blood flow, extravasculation of the probes, and interstitial pressure also count. Thus, a more accurate decipher of the images acquired by multiple molecular imaging modalities is critical to completely replace the conventional sampling methods for PK parameters and PD endpoints evaluation. To achieve this goal, probes with optimal specificity and affinity to target molecules must be developed. In addition, further improvements in sensitivity and spatial/temporal resolution of the imaging techniques are still needed. In addition, advanced quantification algorithms and models may also be required. Another hurdle of direct translation of small animal imaging results from rodent to humans is species-specific differences such as the difference between cytochrome-P450 enzymes [213]. Sometimes the knockout mice are phenotypically heterogeneous, which may cause difficulty in extrapolation to human disease. The introduction of "humanized mouse" models may alleviate this situation. The "humanized mouse" is a mouse in which normal or abnormal human tissue that retains human biofunction can be transplanted and the biofunctions can be observed by medical researchers from a clinical standpoint. It is still a mouse but it maintains the identical biofunctions of human tissues such as immunological function [214]. The NOD/Shi-*scid IL2rγ* ^{null} (NOG) mouse [215], an excellent immunodeficient mouse used as the basis for the humanized mouse, are now being used for studies in human hematopoiesis, innate and adaptive immunity, autoimmunity, infectious diseases, cancer biology, and regenerative medicine [216]. Humanized mice may serve as a "preclinical" bridge for translating data from animal models to human cells and tissues before their application in the clinic.

The next, but not the last, challenge is the continued discovery and development of imaging probes. Despite the superficial similarity between developing imaging agents and drugs, the two processes are much different. An imaging agent must clear from regions other than the region of interest (ROI) during the time course of an imaging study in vivo to get a good target/non-target ratio, while the biodistribution of a drug is of little consequence, as long as its binding to non-target sites is nontoxic while maintaining activity at the target [217]. For imaging probes development, active collaborations among researchers in different disciplines must take place. These efforts include investigations by cellular/molecular biologists to identify and validate molecular imaging targets, by chemists/radiochemists to synthesize and characterize the imaging probes, and by medical physicists/mathematicians to develop high sensitivity/high resolution imaging devices/hybrid instruments and to develop better algorithms to further improve signal-to-noise ratio of a given imaging device. Close partnerships among academic researchers, clinicians, pharmaceutical industries, and the regulatory agencies are essential to promote further development of imaging probes, to apply molecular/functional imaging approaches to predict and evaluate drugs' effects during and after treatment, to move molecular imaging guided intervention strategy quickly into the clinic, and to accelerate drug development.

Acknowledgments This project was supported by National Institute of Biomedical Imaging and Bioengineering (NIBIB) (R21 EB001785), National Cancer Institute (NCI) (R21 CA102123, P50 CA114747, U54 CA119367, and R24 CA93862), Department of Defense (DOD) (W81XWH-04-1-0697, W81XWH-06-1-0665, W81XWH-06-1-0042, and DAMD17-03-1-0143), and a DOD Prostate Postdoctoral Fellowship from Department of Defense (to G. Niu).

References

1. Mankoff DA (2007) A definition of molecular imaging. J Nucl Med 48:18N, 21N.
2. Zambrowicz BP, Sands AT (2003) Knockouts model the 100 best-selling drug--ill they model the next 100? Nat Rev Drug Discov 2:38-51.
3. Dimasi JA (2001) New drug development in the United States from 1963 to 1999. Clin Pharmacol Ther 69:286-96.
4. DiMasi JA, Hansen RW, Grabowski HG (2003) The price of innovation: new estimates of drug development costs. J Health Econ 22:151-85.
5. Seddon BM, Workman P (2003) The role of functional and molecular imaging in cancer drug discovery and development. Br J Radiol 76 Spec No 2:S128-38.
6. Butcher SP (2003) Target discovery and validation in the post-genomic era. Neurochem Res 28:367-71.
7. MacBeath G, Schreiber SL (2000) Printing proteins as microarrays for high-throughput function determination. Science 289:1760-3.
8. Andricopulo AD, Montanari CA (2005) Structure-activity relationships for the design of small-molecule inhibitors. Mini Rev Med Chem 5:585-93.
9. Ertl P, Schuffenhauer A (2008) Cheminformatics analysis of natural products: lessons from nature inspiring the design of new drugs. Prog Drug Res 66:217, 219-35.
10. Montelione GT (2001) Structural genomics: an approach to the protein folding problem. Proc Natl Acad Sci U S A 98:13488-9.
11. Smith A (2002) Screening for drug discovery: The leading question. Nature 418:453-459.
12. Gregory SG, Sekhon M, Schein J, Zhao S, Osoegawa K, Scott CE, et al. (2002) A physical map of the mouse genome. Nature 418:743-50.
13. Polites HG (1996) Transgenic model applications to drug discovery. Int J Exp Pathol 77:257-62.
14. Zhang W, Feng JQ, Harris SE, Contag PR, Stevenson DK, Contag CH (2001) Rapid in vivo functional analysis of transgenes in mice using whole body imaging of luciferase expression. Transgenic Res 10:423-34.
15. Perez-Soler R, Kemp B, Wu QP, Mao L, Gomez J, Zeleniuch-Jacquotte A, et al. (2000) Response and determinants of sensitivity to paclitaxel in human non-small cell lung cancer tumors heterotransplanted in nude mice. Clin Cancer Res 6:4932-8.
16. Massoud TF, Gambhir SS (2007) Integrating noninvasive molecular imaging into molecular medicine: an evolving paradigm. Trends Mol Med 13:183-91.
17. Miller AB, Hoogstraten B, Staquet M, Winkler A (1981) Reporting results of cancer treatment. Cancer 47:207-14.
18. Therasse P, Arbuck SG, Eisenhauer EA, Wanders J, Kaplan RS, Rubinstein L, et al. (2000) New guidelines to evaluate the response to treatment in solid tumors. European Organization for Research and Treatment of Cancer, National Cancer Institute of the United States, National Cancer Institute of Canada. J Natl Cancer Inst 92:205-16.
19. Gelmon KA, Eisenhauer EA, Harris AL, Ratain MJ, Workman P (1999) Anticancer agents targeting signaling molecules and cancer cell environment: challenges for drug development? J Natl Cancer Inst 91:1281-7.
20. Padhani AR, Ollivier L (2001) The RECIST (Response Evaluation Criteria in Solid Tumors) criteria: implications for diagnostic radiologists. Br J Radiol 74:983-6.

21. Hoekstra CJ, Hoekstra OS, Stroobants SG, Vansteenkiste J, Nuyts J, Smit EF, et al. (2002) Methods to monitor response to chemotherapy in non-small cell lung cancer with 18F-FDG PET. J Nucl Med 43:1304-9.
22. Massoud TF, Gambhir SS (2003) Molecular imaging in living subjects: seeing fundamental biological processes in a new light. Genes Dev. 17:545-80.
23. Willmann JK, van Bruggen N, Dinkelborg LM, Gambhir SS (2008) Molecular imaging in drug development. Nat Rev Drug Discov 7:591-607.
24. Price P, Jones T (2002) Molecular imaging: what picture does it paint for future oncology? Drug Discov Today 7:741-3.
25. Beyer T, Townsend DW, Brun T, Kinahan PE, Charron M, Roddy R, et al. (2000) A combined PET/CT scanner for clinical oncology. J Nucl Med 41:1369-79.
26. Even-Sapir E, Lerman H, Lievshitz G, Khafif A, Fliss DM, Schwartz A, et al. (2003) Lymphoscintigraphy for sentinel node mapping using a hybrid SPECT/CT system. J Nucl Med 44:1413-20.
27. Catana C, Wu Y, Judenhofer MS, Qi J, Pichler BJ, Cherry SR (2006) Simultaneous acquisition of multislice PET and MR images: initial results with a MR-compatible PET scanner. J Nucl Med 47:1968-76.
28. Loening AM, Gambhir SS (2003) AMIDE: a free software tool for multimodality medical image analysis. Mol Imaging 2:131-7.
29. Druker BJ, Tamura S, Buchdunger E, Ohno S, Segal GM, Fanning S, et al. (1996) Effects of a selective inhibitor of the Abl tyrosine kinase on the growth of Bcr-Abl positive cells. Nat Med 2:561-6.
30. Schechter AL, Hung MC, Vaidyanathan L, Weinberg RA, Yang-Feng TL, Francke U, et al. (1985) The neu gene: an erbB-homologous gene distinct from and unlinked to the gene encoding the EGF receptor. Science 229:976-978.
31. Tan M, Yao J, Yu D (1997) Overexpression of the c-erbB-2 gene enhanced intrinsic metastasis potential in human breast cancer cells without increasing their transformation abilities. Cancer Res. 57:1199-205.
32. Bacus SS, Ruby SG, Weinberg DS, Chin D, Ortiz R, Bacus JW (1990) HER-2/neu oncogene expression and proliferation in breast cancers. Am J Pathol. 137:103-11.
33. Wiercioch R, Balcerczak E, Byszewska E, Mirowski M (2003) Uptake of radiolabelled herceptin by experimental mammary adenocarcinoma. Nucl Med Rev Cent East Eur 6:99-103.
34. Traish AM, Wotiz HH (1987) Prostatic epidermal growth factor receptors and their regulation by androgens. Endocrinology 121:1461-7.
35. Solit DB, Zheng FF, Drobnjak M, Munster PN, Higgins B, Verbel D, et al. (2002) 17-Allylamino-17-demethoxygeldanamycin induces the degradation of androgen receptor and HER-2/neu and inhibits the growth of prostate cancer xenografts. Clin Cancer Res 8:986-93.
36. Agus DB, Akita RW, Fox WD, Lewis GD, Higgins B, Pisacane PI, et al. (2002) Targeting ligand-activated ErbB2 signaling inhibits breast and prostate tumor growth. Cancer Cell 2:127-37.
37. Konecny GE, Pegram MD, Venkatesan N, Finn R, Yang G, Rahmeh M, et al. (2006) Activity of the dual kinase inhibitor lapatinib (GW572016) against HER-2-overexpressing and trastuzumab-treated breast cancer cells. Cancer Res. 66:1630-9.
38. Saga T, Endo K, Akiyama T, Sakahara H, Koizumi M, Watanabe Y, et al. (1991) Scintigraphic detection of overexpressed c-erbB-2 protooncogene products by a class-switched murine anti-c-erbB-2 protein monoclonal antibody. Cancer Res 51:990-4.
39. Orlova A, Magnusson M, Eriksson TL, Nilsson M, Larsson B, Hoiden-Guthenberg I, et al. (2006) Tumor imaging using a picomolar affinity HER2 binding affibody molecule. Cancer Res 66:4339-48.
40. Tolmachev V, Nilsson FY, Widstrom C, Andersson K, Rosik D, Gedda L, et al. (2006) 111In-benzyl-DTPA-ZHER2:342, an affibody-based conjugate for in vivo imaging of HER2 expression in malignant tumors. J Nucl Med 47:846-53.

41. Smith-Jones PM, Solit DB, Akhurst T, Afroze F, Rosen N, Larson SM (2004) Imaging the pharmacodynamics of HER2 degradation in response to Hsp90 inhibitors. Nat Biotechnol 22:701-6.
42. Smith-Jones PM, Solit D, Afroze F, Rosen N, Larson SM (2006) Early tumor response to Hsp90 therapy using HER2 PET: comparison with ^{18}F-FDG PET. J Nucl Med 47:793-6.
43. Sollars V, Lu X, Xiao L, Wang X, Garfinkel MD, Ruden DM (2003) Evidence for an epigenetic mechanism by which Hsp90 acts as a capacitor for morphological evolution. Nat Genet 33:70-4.
44. Blankenberg FG, Mandl S, Cao YA, O'Connell-Rodwell C, Contag C, Mari C, et al. (2004) Tumor imaging using a standardized radiolabeled adapter protein docked to vascular endothelial growth factor. J Nucl Med 45:1373-80.
45. Backer MV, Levashova Z, Patel V, Jehning BT, Claffey K, Blankenberg FG, et al. (2007) Molecular imaging of VEGF receptors in angiogenic vasculature with single-chain VEGF-based probes. Nat Med
46. Cai W, Chen K, Mohamedali KA, Cao Q, Gambhir SS, Rosenblum MG, et al. (2006) PET of vascular endothelial growth factor receptor expression. J Nucl Med 47:2048-56.
47. Dayton PA, Pearson D, Clark J, Simon S, Schumann PA, Zutshi R, et al. (2004) Ultrasonic analysis of peptide- and antibody-targeted microbubble contrast agents for molecular imaging of alphavbeta3-expressing cells. Mol Imaging 3:125-34.
48. Wang H, Cai W, Chen K, Li ZB, Kashefi A, He L, et al. (2007) A new PET tracer specific for vascular endothelial growth factor receptor 2. Eur J Nucl Med Mol Imaging
49. Nagengast WB, de Vries EG, Hospers GA, Mulder NH, de Jong JR, Hollema H, et al. (2007) In vivo VEGF imaging with radiolabeled bevacizumab in a human ovarian tumor xenograft. J Nucl Med 48:1313-9.
50. Collingridge DR, Carroll VA, Glaser M, Aboagye EO, Osman S, Hutchinson OC, et al. (2002) The development of [^{124}I]iodinated-VG76e: a novel tracer for imaging vascular endothelial growth factor *in vivo* using positron emission tomography. Cancer Res 62:5912-9.
51. Haubner R, Wester HJ, Reuning U, Senekowitsch-Schmidtke R, Diefenbach B, Kessler H, et al. (1999) Radiolabeled alpha(v)beta3 integrin antagonists: a new class of tracers for tumor targeting. J Nucl Med 40:1061-71.
52. Haubner R, Wester HJ, Weber WA, Mang C, Ziegler SI, Goodman SL, et al. (2001) Noninvasive imaging of $\alpha_v\beta_3$ integrin expression using ^{18}F-labeled RGD-containing glycopeptide and positron emission tomography. Cancer Res 61:1781-5.
53. Haubner R (2006) $\alpha_v\beta_3$-integrin imaging: a new approach to characterise angiogenesis? Eur J Nucl Med Mol Imaging 33 Suppl 1:54-63.
54. Chen X, Park R, Shahinian AH, Bading JR, Conti PS (2004) Pharmacokinetics and tumor retention of ^{125}I-labeled RGD peptide are improved by PEGylation. Nucl Med Biol 31:11-9.
55. Noiri E, Goligorsky MS, Wang GJ, Wang J, Cabahug CJ, Sharma S, et al. (1996) Biodistribution and clearance of ^{99m}Tc-labeled Arg-Gly-Asp (RGD) peptide in rats with ischemic acute renal failure. J Am Soc Nephrol 7:2682-8.
56. Chen X, Hou Y, Tohme M, Park R, Khankaldyyan V, Gonzales-Gomez I, et al. (2004) Pegylated Arg-Gly-Asp peptide: ^{64}Cu labeling and PET imaging of brain tumor alphavbeta3-integrin expression. J Nucl Med 45:1776-83.
57. Dijkgraaf I, Liu S, Kruijtzer JA, Soede AC, Oyen WJ, Liskamp RM, et al. (2007) Effects of linker variation on the in vitro and in vivo characteristics of an ^{111}In-labeled RGD peptide. Nucl Med Biol 34:29-35.
58. Li ZB, Chen K, Chen X (2008) (68)Ga-labeled multimeric RGD peptides for microPET imaging of integrin $\alpha_v\beta_3$ expression. Eur J Nucl Med Mol Imaging 35:1100-8.
59. van Hagen PM, Breeman WA, Bernard HF, Schaar M, Mooij CM, Srinivasan A, et al. (2000) Evaluation of a radiolabelled cyclic DTPA-RGD analogue for tumour imaging and radionuclide therapy. Int J Cancer 90:186-98.
60. Boturyn D, Coll JL, Garanger E, Favrot MC, Dumy P (2004) Template assembled cyclopeptides as multimeric system for integrin targeting and endocytosis. J Am Chem Soc 126: 5730-9.

61. Chen X, Tohme M, Park R, Hou Y, Bading JR, Conti PS (2004) Micro-PET imaging of $\alpha_v\beta_3$-integrin expression with 18F-labeled dimeric RGD peptide. Mol Imaging 3:96-104.
62. Hughes MS, Marsh JN, Zhang H, Woodson AK, Allen JS, Lacy EK, et al. (2006) Characterization of digital waveforms using thermodynamic analogs: detection of contrast-targeted tissue *in vivo*. IEEE Trans Ultrason Ferroelectr Freq Control 53:1609-16.
63. Chen X, Park R, Tohme M, Shahinian AH, Bading JR, Conti PS (2004) MicroPET and autoradiographic imaging of breast cancer alpha v-integrin expression using ^{18}F- and ^{64}Cu-labeled RGD peptide. Bioconjug Chem 15:41-9.
64. Chen X, Liu S, Hou Y, Tohme M, Park R, Bading JR, et al. (2004) MicroPET imaging of breast cancer alphav-integrin expression with ^{64}Cu-labeled dimeric RGD peptides. Mol Imaging Biol 6:350-9.
65. Wu Y, Zhang X, Xiong Z, Cheng Z, Fisher DR, Liu S, et al. (2005) microPET imaging of glioma integrin $\alpha_v\beta_3$ expression using ^{64}Cu-labeled tetrameric RGD peptide. J Nucl Med 46:1707-18.
66. Cai W, Niu G, Chen X (2008) Imaging of integrins as biomarkers for tumor angiogenesis. Curr Pharm Des 14:2943-73.
67. Mayer-Kuckuk P, Banerjee D, Malhotra S, Doubrovin M, Iwamoto M, Akhurst T, et al. (2002) Cells exposed to antifolates show increased cellular levels of proteins fused to dihydrofolate reductase: a method to modulate gene expression. Proc Natl Acad Sci U S A 99:3400-5.
68. Workman P (2003) How much gets there and what does it do?: The need for better pharmacokinetic and pharmacodynamic endpoints in contemporary drug discovery and development. Curr Pharm Des 9:891-902.
69. Hanahan D, Weinberg RA (2000) The hallmarks of cancer. Cell 100:57-70.
70. Warburg O (1956) On the origin of cancer cells. Science 123:309-14.
71. Vallabhajosula S (2007) (18)F-labeled positron emission tomographic radiopharmaceuticals in oncology: an overview of radiochemistry and mechanisms of tumor localization. Semin Nucl Med 37:400-19.
72. Sols A, Crane RK (1954) Substrate specificity of brain hexokinase. J Biol Chem 210: 581-95.
73. Ichiya Y, Kuwabara Y, Otsuka M, Tahara T, Yoshikai T, Fukumura T, et al. (1991) Assessment of response to cancer therapy using fluorine-18-fluorodeoxyglucose and positron emission tomography. J Nucl Med 32:1655-60.
74. Berlangieri SU, Brizel DM, Scher RL, Schifter T, Hawk TC, Hamblen S, et al. (1994) Pilot study of positron emission tomography in patients with advanced head and neck cancer receiving radiotherapy and chemotherapy. Head Neck 16:340-6.
75. Prenen H, Deroose C, Vermaelen P, Sciot R, Debiec-Rychter M, Stroobants S, et al. (2006) Establishment of a mouse gastrointestinal stromal tumour model and evaluation of response to imatinib by small animal positron emission tomography. Anticancer Res 26:1247-52.
76. Tian M, Zhang H, Higuchi T, Oriuchi N, Inoue T, Endo K (2004) Effect of mitomycin C and vinblastine on FDG uptake of human nonsmall-cell lung cancer xenografts in nude mice. Cancer Biother Radiopharm 19:601-5.
77. Tseng JR, Kang KW, Dandekar M, Yaghoubi S, Lee JH, Christensen JG, et al. (2008) Preclinical efficacy of the c-Met inhibitor CE-355621 in a U87 MG mouse xenograft model evaluated by 18F-FDG small-animal PET. J Nucl Med 49:129-34.
78. Dandekar M, Tseng JR, Gambhir SS (2007) Reproducibility of 18F-FDG microPET studies in mouse tumor xenografts. J Nucl Med 48:602-7.
79. Sherley JL, Kelly TJ (1988) Regulation of human thymidine kinase during the cell cycle. J Biol Chem 263:8350-8.
80. Shields AF (2003) PET imaging with 18F-FLT and thymidine analogs: promise and pitfalls. J Nucl Med 44:1432-4.
81. Leyton J, Latigo JR, Perumal M, Dhaliwal H, He Q, Aboagye EO (2005) Early detection of tumor response to chemotherapy by 3'-deoxy-3'-[18F]fluorothymidine positron emission

tomography: the effect of cisplatin on a fibrosarcoma tumor model in vivo. Cancer Res 65:4202-10.
82. Tseng JR, Dandekar M, Subbarayan M, Cheng Z, Park JM, Louie S, et al. (2005) Reproducibility of 3'-deoxy-3'-^{18}F-fluorothymidine microPET studies in tumor xenografts in mice. J Nucl Med 46:1851-7.
83. Dimitrakopoulou-Strauss A, Strauss LG (2008) The role of ^{18}F-FLT in cancer imaging: does it really reflect proliferation? Eur J Nucl Med Mol Imaging 35:523-6.
84. Folkman J (2002) Role of angiogenesis in tumor growth and metastasis. Semin Oncol 29: 15-8.
85. Lassau N, Lamuraglia M, Chami L, Leclere J, Bonvalot S, Terrier P, et al. (2006) Gastrointestinal stromal tumors treated with imatinib: monitoring response with contrast-enhanced sonography. AJR Am J Roentgenol 187:1267-73.
86. Li PC, Yang MJ (2003) Transfer function analysis of ultrasonic time-intensity measurements. Ultrasound Med Biol 29:1493-500.
87. Lavisse S, Lejeune P, Rouffiac V, Elie N, Bribes E, Demers B, et al. (2008) Early quantitative evaluation of a tumor vasculature disruptive agent AVE8062 using dynamic contrast-enhanced ultrasonography. Invest Radiol 43:100-11.
88. Miller KD, Soule SE, Calley C, Emerson RE, Hutchins GD, Kopecky K, et al. (2005) Randomized phase II trial of the anti-angiogenic potential of doxorubicin and docetaxel; primary chemotherapy as Biomarker Discovery Laboratory. Breast Cancer Res Treat 89:187-97.
89. Padhani AR (2003) MRI for assessing antivascular cancer treatments. Br J Radiol 76 Spec No 1:S60-80.
90. Zhang C, Jugold M, Woenne EC, Lammers T, Morgenstern B, Mueller MM, et al. (2007) Specific targeting of tumor angiogenesis by RGD-conjugated ultrasmall superparamagnetic iron oxide particles using a clinical 1.5-T magnetic resonance scanner. Cancer Res 67:1555-62.
91. Tofts PS, Brix G, Buckley DL, Evelhoch JL, Henderson E, Knopp MV, et al. (1999) Estimating kinetic parameters from dynamic contrast-enhanced T_1-weighted MRI of a diffusable tracer: standardized quantities and symbols. J Magn Reson Imaging 10:223-32.
92. Padhani AR, Husband JE (2001) Dynamic contrast-enhanced MRI studies in oncology with an emphasis on quantification, validation and human studies. Clin Radiol 56:607-20.
93. Barrett T, Brechbiel M, Bernardo M, Choyke PL (2007) MRI of tumor angiogenesis. J Magn Reson Imaging 26:235-49.
94. Liu G, Rugo HS, Wilding G, McShane TM, Evelhoch JL, Ng C, et al. (2005) Dynamic contrast-enhanced magnetic resonance imaging as a pharmacodynamic measure of response after acute dosing of AG-013736, an oral angiogenesis inhibitor, in patients with advanced solid tumors: results from a phase I study. J Clin Oncol 23:5464-73.
95. Thomas AL, Morgan B, Horsfield MA, Higginson A, Kay A, Lee L, et al. (2005) Phase I study of the safety, tolerability, pharmacokinetics, and pharmacodynamics of PTK787/ZK 222584 administered twice daily in patients with advanced cancer. J Clin Oncol 23:4162-71.
96. Medved M, Karczmar G, Yang C, Dignam J, Gajewski TF, Kindler H, et al. (2004) Semiquantitative analysis of dynamic contrast enhanced MRI in cancer patients: Variability and changes in tumor tissue over time. J Magn Reson Imaging 20:122-8.
97. Marzola P, Degrassi A, Calderan L, Farace P, Crescimanno C, Nicolato E, et al. (2004) In vivo assessment of antiangiogenic activity of SU6668 in an experimental colon carcinoma model. Clin Cancer Res 10:739-50.
98. Faccioli N, Marzola P, Boschi F, Sbarbati A, D'Onofrio M, Pozzi Mucelli R (2007) Pathological animal models in the experimental evaluation of tumour microvasculature with magnetic resonance imaging. Radiol Med (Torino) 112:319-28.
99. Tatum JL, Kelloff GJ, Gillies RJ, Arbeit JM, Brown JM, Chao KS, et al. (2006) Hypoxia: importance in tumor biology, noninvasive measurement by imaging, and value of its measurement in the management of cancer therapy. Int J Radiat Biol 82:699-757.

100. Stone HB, Brown JM, Phillips TL, Sutherland RM (1993) Oxygen in human tumors: correlations between methods of measurement and response to therapy. Summary of a workshop held November 19-20, 1992, at the National Cancer Institute, Bethesda, Maryland. Radiat Res 136:422-34.
101. Foo SS, Abbott DF, Lawrentschuk N, Scott AM (2004) Functional imaging of intratumoral hypoxia. Mol Imaging Biol 6:291-305.
102. Vikram DS, Zweier JL, Kuppusamy P (2007) Methods for noninvasive imaging of tissue hypoxia. Antioxid Redox Signal 9:1745-56.
103. Laking GR, Price PM (2003) Positron emission tomographic imaging of angiogenesis and vascular function. Br J Radiol 76 Spec No 1:S50-9.
104. Lee ST, Scott AM (2007) Hypoxia positron emission tomography imaging with 18f-fluoromisonidazole. Semin Nucl Med 37:451-61.
105. Lawrentschuk N, Poon AM, Foo SS, Putra LG, Murone C, Davis ID, et al. (2005) Assessing regional hypoxia in human renal tumours using ^{18}F-fluoromisonidazole positron emission tomography. BJU Int 96:540-6.
106. Zimny M, Gagel B, Dimartino E, Hamacher K, Coenen HH, Westhofen M, et al. (2006) FDG-a marker of tumour hypoxia? A comparison with [^{18}F]fluoromisonidazole and pO (2)-polarography in metastatic head and neck cancer. Eur J Nucl Med Mol Imaging 33:1426-31.
107. Koh WJ, Rasey JS, Evans ML, Grierson JR, Lewellen TK, Graham MM, et al. (1992) Imaging of hypoxia in human tumors with [F-18]fluoromisonidazole. Int J Radiat Oncol Biol Phys 22:199-212.
108. Rasey JS, Koh WJ, Evans ML, Peterson LM, Lewellen TK, Graham MM, et al. (1996) Quantifying regional hypoxia in human tumors with positron emission tomography of [18F] fluoromisonidazole: a pretherapy study of 37 patients. Int J Radiat Oncol Biol Phys 36:417-28.
109. Markus R, Reutens DC, Kazui S, Read S, Wright P, Pearce DC, et al. (2004) Hypoxic tissue in ischaemic stroke: persistence and clinical consequences of spontaneous survival. Brain 127:1427-36.
110. Sorger D, Patt M, Kumar P, Wiebe LI, Barthel H, Seese A, et al. (2003) [F-18] Fluoroazomycinarabinofuranoside (^{18}FAZA) and [F-18]Fluoromisonidazole ((FMISO)-F-18): A comparative study of their selective uptake in hypoxic cells and PET imaging in experimental rat tumors. Nuclear Medicine and Biology 30:317-326.
111. Gronroos T, Bentzen L, Marjamaki P, Murata R, Horsman MR, Keiding S, et al. (2004) Comparison of the biodistribution of two hypoxia markers [F-18]FETNIM and [F-18]FMISO in an experimental mammary carcinoma. European Journal of Nuclear Medicine and Molecular Imaging 31:513-520.
112. Piert M, Machulla HJ, Picchio M, Reischl G, Ziegler S, Kumar P, et al. (2005) Hypoxia-specific tumor imaging with F-18-fluoroazomycin arabinoside. Journal of Nuclear Medicine 46:106-113.
113. Ziemer LS, Evans SM, Kachur A, Shuman AL, Cardi CA, Jenkins WT, et al. (2003) Noninvasive imaging of tumor hypoxia in rats using the 2-nitroimidazole F-18-EF5. European Journal of Nuclear Medicine and Molecular Imaging 30:259-266.
114. Koch CJ (2002) Measurement of absolute oxygen levels in cells and tissues using oxygen sensors and 2-nitroimidazole EF5. Methods Enzymol 352:3-31.
115. Evans SM, Jenkins WT, Joiner B, Lord EM, Koch CJ (1996) 2-Nitroimidazole (EF5) binding predicts radiation resistance in individual 9L s.c. tumors. Cancer Res 56:405-11.
116. Kachur AV, Dolbier WR, Jr., Evans SM, Shiue CY, Shiue GG, Skov KA, et al. (1999) Synthesis of new hypoxia markers EF1 and [18F]-EF1. Appl Radiat Isot 51:643-50.
117. Evans SM, Kachur AV, Shiue CY, Hustinx R, Jenkins WT, Shive GG, et al. (2000) Noninvasive detection of tumor hypoxia using the 2-nitroimidazole [18F]EF1. J Nucl Med 41:327-36.
118. Dolbier WR, Jr., Li AR, Koch CJ, Shiue CY, Kachur AV (2001) [18F]-EF5, a marker for PET detection of hypoxia: synthesis of precursor and a new fluorination procedure. Appl Radiat Isot 54:73-80.

119. Josse O, Labar D, Georges B, Gregoire V, Marchand-Brynaert J (2001) Synthesis of [^{18}F]-labeled EF3 [2-(2-nitroimidazol-1-yl)-N-(3,3,3-trifluoropropyl)-acetamide], a marker for PET detection of hypoxia. Bioorg Med Chem 9:665-75.
120. Mahy P, De Bast M, Leveque PH, Gillart J, Labar D, Marchand J, et al. (2004) Preclinical validation of the hypoxia tracer 2-(2-nitroimidazol-1-yl)- N-(3,3,3-[^{18}F]trifluoropropyl)acetamide, [^{18}F]EF3. Eur J Nucl Med Mol Imaging 31:1263-72.
121. Dubois L, Landuyt W, Cloetens L, Bol A, Bormans G, Haustermans K, et al. (2008) [^{18}F]EF3 is not superior to [^{18}F]FMISO for PET-based hypoxia evaluation as measured in a rat rhabdomyosarcoma tumour model. Eur J Nucl Med Mol Imaging
122. Vavere AL, Lewis JS (2007) Cu-ATSM: a radiopharmaceutical for the PET imaging of hypoxia. Dalton Trans:4893-902.
123. Dehdashti F, Grigsby PW, Mintun MA, Lewis JS, Siegel BA, Welch MJ (2003) Assessing tumor hypoxia in cervical cancer by positron emission tomography with ^{60}Cu-ATSM: relationship to therapeutic response-a preliminary report. Int J Radiat Oncol Biol Phys 55:1233-8.
124. Dehdashti F, Mintun MA, Lewis JS, Bradley J, Govindan R, Laforest R, et al. (2003) In vivo assessment of tumor hypoxia in lung cancer with ^{60}Cu-ATSM. Eur J Nucl Med Mol Imaging 30:844-50.
125. Bayly SR, King RC, Honess DJ, Barnard PJ, Betts HM, Holland JP, et al. (2008) In Vitro and In Vivo Evaluations of a Hydrophilic 64Cu-Bis(Thiosemicarbazonato)-Glucose Conjugate for Hypoxia Imaging. J Nucl Med
126. Henson PM, Hume DA (2006) Apoptotic cell removal in development and tissue homeostasis. Trends Immunol 27:244-50.
127. Schoenberger J, Bauer J, Moosbauer J, Eilles C, Grimm D (2008) Innovative strategies in in vivo apoptosis imaging. Curr Med Chem 15:187-94.
128. Hsu AR, Cai W, Veeravagu A, Mohamedali KA, Chen K, Kim S, et al. (2007) Multimodality molecular imaging of glioblastoma growth inhibition with vasculature-targeting fusion toxin VEGF121/rGel. J Nucl Med 48:445-54.
129. Evan GI, Vousden KH (2001) Proliferation, cell cycle and apoptosis in cancer. Nature 411:342-8.
130. Lahorte CM, Vanderheyden JL, Steinmetz N, Van de Wiele C, Dierckx RA, Slegers G (2004) Apoptosis-detecting radioligands: current state of the art and future perspectives. Eur J Nucl Med Mol Imaging 31:887-919.
131. Wolters SL, Corsten MF, Reutelingsperger CP, Narula J, Hofstra L (2007) Cardiovascular molecular imaging of apoptosis. Eur J Nucl Med Mol Imaging 34 Suppl 1:S86-98.
132. Boersma HH, Kietselaer BL, Stolk LM, Bennaghmouch A, Hofstra L, Narula J, et al. (2005) Past, present, and future of annexin A5: from protein discovery to clinical applications. J Nucl Med 46:2035-50.
133. Blankenberg FG, Katsikis PD, Tait JF, Davis RE, Naumovski L, Ohtsuki K, et al. (1998) In vivo detection and imaging of phosphatidylserine expression during programmed cell death. Proc Natl Acad Sci U S A 95:6349-54.
134. Blankenberg FG, Naumovski L, Tait JF, Post AM, Strauss HW (2001) Imaging cyclophosphamide-induced intramedullary apoptosis in rats using ^{99m}Tc-radiolabeled annexin V. J Nucl Med 42:309-16.
135. Blankenberg FG, Robbins RC, Stoot JH, Vriens PW, Berry GJ, Tait JF, et al. (2000) Radionuclide imaging of acute lung transplant rejection with annexin V. Chest 117:834-40.
136. Yang DJ, Azhdarinia A, Wu P, Yu DF, Tansey W, Kalimi SK, et al. (2001) In vivo and in vitro measurement of apoptosis in breast cancer cells using ^{99m}Tc-EC-annexin V. Cancer Biother Radiopharm 16:73-83.
137. Zhu X, Li Z, Zhao M (2007) Imaging acute cardiac cell death: temporal and spatial distribution of ^{99m}Tc-labeled C2A in the area at risk after myocardial ischemia and reperfusion. J Nucl Med 48:1031-6.
138. Shao R, Xiong C, Wen X, Gelovani JG, Li C (2007) Targeting phosphatidylserine on apoptotic cells with phages and peptides selected from a bacteriophage display library. Mol Imaging 6:417-26.

139. Tait JF (2008) Imaging of apoptosis. J Nucl Med 49:1573-6.
140. Tait JF, Smith C, Levashova Z, Patel B, Blankenberg FG, Vanderheyden JL (2006) Improved detection of cell death in vivo with annexin V radiolabeled by site-specific methods. J Nucl Med 47:1546-53.
141. Yagle KJ, Eary JF, Tait JF, Grierson JR, Link JM, Lewellen B, et al. (2005) Evaluation of ^{18}F-annexin V as a PET imaging agent in an animal model of apoptosis. J Nucl Med 46:658-66.
142. Riedl SJ, Shi Y (2004) Molecular mechanisms of caspase regulation during apoptosis. Nat Rev Mol Cell Biol 5:897-907.
143. Grutter MG (2000) Caspases: key players in programmed cell death. Curr Opin Struct Biol 10:649-55.
144. Angres B, Steuer H, Weber P, Wagner M, Schneckenburger H (2008) A membrane-bound FRET-based caspase sensor for detection of apoptosis using fluorescence lifetime and total internal reflection microscopy. Cytometry A
145. Ray P, De A, Patel M, Gambhir SS (2008) Monitoring caspase-3 activation with a multimodality imaging sensor in living subjects. Clin Cancer Res 14:5801-9.
146. Coppola JM, Ross BD, Rehemtulla A (2008) Noninvasive imaging of apoptosis and its application in cancer therapeutics. Clin Cancer Res 14:2492-501.
147. Lovqvist A, Humm JL, Sheikh A, Finn RD, Koziorowski J, Ruan S, et al. (2001) PET imaging of ^{86}Y-labeled anti-Lewis Y monoclonal antibodies in a nude mouse model: comparison between (86)Y and (111)In radiolabels. J Nucl Med 42:1281-7.
148. Sunkuk K, Shi K, Houston JP, Wei W, Qingping W, Chun L, et al. (2005) Imaging dose-dependent pharmacokinetics of an RGD-fluorescent dye conjugate targeted to $\alpha_v\beta_3$ receptor expressed in Kaposi's sarcoma. Mol Imaging 4:75-87.
149. Kopka K, Faust A, Keul P, Wagner S, Breyholz HJ, Holtke C, et al. (2006) 5-pyrrolidinylsulfonyl isatins as a potential tool for the molecular imaging of caspases in apoptosis. J Med Chem 49:6704-15.
150. Smith G, Glaser M, Perumal M, Nguyen QD, Shan B, Arstad E, et al. (2008) Design, synthesis, and biological characterization of a caspase 3/7 selective isatin labeled with 2-[^{18}F]fluoroethylazide. J Med Chem 51:8057-67.
151. Zhou D, Chu W, Rothfuss J, Zeng C, Xu J, Jones L, et al. (2006) Synthesis, radiolabeling, and in vivo evaluation of an 18F-labeled isatin analog for imaging caspase-3 activation in apoptosis. Bioorg Med Chem Lett 16:5041-6.
152. Min JJ, Biswal S, Deroose C, Gambhir SS (2004) Tetraphenylphosphonium as a novel molecular probe for imaging tumors. J Nucl Med 45:636-43.
153. Madar I, Ravert H, Nelkin B, Abro M, Pomper M, Dannals R, et al. (2007) Characterization of membrane potential-dependent uptake of the novel PET tracer ^{18}F-fluorobenzyl triphenylphosphonium cation. Eur J Nucl Med Mol Imaging 34:2057-65.
154. Nollen EA, Morimoto RI (2002) Chaperoning signaling pathways: molecular chaperones as stress-sensing 'heat shock' proteins. J Cell Sci 115:2809-16.
155. Citri A, Alroy I, Lavi S, Rubin C, Xu W, Grammatikakis N, et al. (2002) Drug-induced ubiquitylation and degradation of ErbB receptor tyrosine kinases: implications for cancer therapy. Embo J 21:2407-17.
156. Murakami Y, Mizuno S, Uehara Y (1994) Accelerated degradation of 160 kDa epidermal growth factor (EGF) receptor precursor by the tyrosine kinase inhibitor herbimycin A in the endoplasmic reticulum of A431 human epidermoid carcinoma cells. The Biochemical journal 301 (Pt 1):63-68.
157. Sakagami M, Morrison P, Welch WJ (1999) Benzoquinoid ansamycins (herbimycin A and geldanamycin) interfere with the maturation of growth factor receptor tyrosine kinases. Cell Stress Chaperones 4:19-28.
158. Cai W, Chen K, He L, Cao Q, Koong A, Chen X (2007) Quantitative PET of EGFR expression in xenograft-bearing mice using ^{64}Cu-labeled cetuximab, a chimeric anti-EGFR monoclonal antibody. Eur J Nucl Med Mol Imaging 34:850-858.
159. Niu G, Cai W, Chen K, Chen X (2008) Non-Invasive PET Imaging of EGFR Degradation Induced by a Heat Shock Protein 90 Inhibitor. Mol Imaging Biol 10:99-106.

160. Lemmon MA, Schlessinger J (1994) Regulation of signal transduction and signal diversity by receptor oligomerization. Trends Biochem Sci 19:459-63.
161. Hennessy BT, Smith DL, Ram PT, Lu Y, Mills GB (2005) Exploiting the PI3K/AKT pathway for cancer drug discovery. Nat Rev Drug Discov 4:988-1004.
162. Kondapaka SB, Singh SS, Dasmahapatra GP, Sausville EA, Roy KK (2003) Perifosine, a novel alkylphospholipid, inhibits protein kinase B activation. Mol Cancer Ther 2:1093-103.
163. Han Z, Fu A, Wang H, Diaz R, Geng L, Onishko H, et al. (2008) Noninvasive assessment of cancer response to therapy. Nat Med 14:343-9.
164. Miller AD (1990) Progress toward human gene therapy. Blood 76:271-8.
165. Kootstra NA, Verma IM (2003) Gene therapy with viral vectors. Annu Rev Pharmacol Toxicol 43:413-39.
166. Kristian Raty J, Liimatainen T, Unelma Kaikkonen M, Grohn O, Airenne KJ, Yla-Herttuala S (2007) Non-invasive Imaging in Gene Therapy. Mol Ther 15:1579-86.
167. Massoud TF, Singh A, Gambhir SS (2008) Noninvasive molecular neuroimaging using reporter genes: part I, principles revisited. AJNR Am J Neuroradiol 29:229-34.
168. Liang Q, Nguyen K, Satyamurthy N, Barrio JR, Phelps ME, Gambhir SS, et al. (2002) Monitoring adenoviral DNA delivery, using a mutant herpes simplex virus type 1 thymidine kinase gene as a PET reporter gene. Gene Ther 9:1659-66.
169. Niu G, Krager KJ, Graham MM, Hichwa RD, Domann FE (2005) Noninvasive radiological imaging of pulmonary gene transfer and expression using the human sodium iodide symporter. Eur J Nucl Med Mol Imaging 32:534-40.
170. Niu G, Anderson RD, Madsen MT, Graham MM, Oberley LW, Domann FE (2006) Dual-expressing adenoviral vectors encoding the sodium iodide symporter for use in noninvasive radiological imaging of therapeutic gene transfer. Nucl Med Biol 33:391-8.
171. Wunderbaldinger P, Bogdanov A, Weissleder R (2000) New approaches for imaging in gene therapy. Eur J Radiol 34:156-65.
172. Rome C, Couillaud F, Moonen CT (2005) Spatial and temporal control of expression of therapeutic genes using heat shock protein promoters. Methods 35:188-98.
173. Blackburn RV, Galoforo SS, Corry PM, Lee YJ (1998) Adenoviral-mediated transfer of a heat-inducible double suicide gene into prostate carcinoma cells. Cancer Res 58:1358-62.
174. Dong D, Dubeau L, Bading J, Nguyen K, Luna M, Yu H, et al. (2004) Spontaneous and controllable activation of suicide gene expression driven by the stress-inducible grp78 promoter resulting in eradication of sizable human tumors. Hum Gene Ther 15:553-61.
175. Huang Q, Hu JK, Lohr F, Zhang L, Braun R, Lanzen J, et al. (2000) Heat-induced gene expression as a novel targeted cancer gene therapy strategy. Cancer Res 60:3435-9.
176. Vekris A, Maurange C, Moonen C, Mazurier F, De Verneuil H, Canioni P, et al. (2000) Control of transgene expression using local hyperthermia in combination with a heat-sensitive promoter. J Gene Med 2:89-96.
177. Borrelli MJ, Schoenherr DM, Wong A, Bernock LJ, Corry PM (2001) Heat-activated transgene expression from adenovirus vectors infected into human prostate cancer cells. Cancer Res 61:1113-21.
178. Guilhon E, Quesson B, Moraud-Gaudry F, de Verneuil H, Canioni P, Salomir R, et al. (2003) Image-guided control of transgene expression based on local hyperthermia. Mol Imaging 2:11-7.
179. Wang S, Xie W, Rylander MN, Tucker PW, Aggarwal S, Diller KR (2008) HSP70 kinetics study by continuous observation of HSP-GFP fusion protein expression on a perfusion heating stage. Biotechnol Bioeng 99:146-54.
180. Niu G, Gaut AW, Ponto LL, Hichwa RD, Madsen MT, Graham MM, et al. (2004) Multimodality noninvasive imaging of gene transfer using the human sodium iodide symporter. J Nucl Med 45:445-9.
181. Che J, Doubrovin M, Serganova I, Ageyeva L, Beresten T, Finn R, et al. (2007) HSP70-inducible hNIS-IRES-eGFP reporter imaging: response to heat shock. Mol Imaging 6:404-16.
182. Genove G, DeMarco U, Xu H, Goins WF, Ahrens ET (2005) A new transgene reporter for in vivo magnetic resonance imaging. Nat Med 11:450-4.

183. Cohen B, Dafni H, Meir G, Harmelin A, Neeman M (2005) Ferritin as an endogenous MRI reporter for noninvasive imaging of gene expression in C6 glioma tumors. Neoplasia 7:109-17.
184. Workman P (2001) New drug targets for genomic cancer therapy: successes, limitations, opportunities and future challenges. Curr Cancer Drug Targets 1:33-47.
185. Halldin C, Gulyas B, Farde L (2001) PET studies with carbon-11 radioligands in neuropsychopharmacological drug development. Curr Pharm Des 7:1907-29.
186. Fischman AJ, Alpert NM, Rubin RH (2002) Pharmacokinetic imaging: a noninvasive method for determining drug distribution and action. Clin Pharmacokinet 41:581-602.
187. Aboagye EO, Price PM, Jones T (2001) In vivo pharmacokinetics and pharmacodynamics in drug development using positron-emission tomography. Drug Discov Today 6:293-302.
188. Machka K, Braveny I (1987) Comparative in vitro activity of RO 23-6240 (fleroxacin), a new 4-quinolone derivative. Eur J Clin Microbiol 6:482-5.
189. Fischman AJ, Livni E, Babich J, Alpert NM, Liu YY, Thom E, et al. (1992) Pharmacokinetics of ^{18}F-labeled fleroxacin in rabbits with Escherichia coli infections, studied with positron emission tomography. Antimicrob Agents Chemother 36:2286-92.
190. Rubin RH, Livni E, Babich J, Alpert NM, Liu YY, Tham E, et al. (1993) Pharmacokinetics of fleroxacin as studied by positron emission tomography and [^{18}F]fleroxacin. Am J Med 94:31S-37S.
191. Fischman AJ, Livni E, Babich JW, Alpert NM, Bonab A, Chodosh S, et al. (1996) Pharmacokinetics of [^{18}F]fleroxacin in patients with acute exacerbations of chronic bronchitis and complicated urinary tract infection studied by positron emission tomography. Antimicrob Agents Chemother 40:659-64.
192. Tyler JL, Yamamoto YL, Diksic M, Theron J, Villemure JG, Worthington C, et al. (1986) Pharmacokinetics of superselective intra-arterial and intravenous [^{11}C]BCNU evaluated by PET. J Nucl Med 27:775-80.
193. Veenendaal LM, Jin H, Ran S, Cheung L, Navone N, Marks JW, et al. (2002) In vitro and in vivo studies of a VEGF121/rGelonin chimeric fusion toxin targeting the neovasculature of solid tumors. Proc Natl Acad Sci U S A 99:7866-71.
194. Wiseman GA, Kornmehl E, Leigh B, Erwin WD, Podoloff DA, Spies S, et al. (2003) Radiation dosimetry results and safety correlations from ^{90}Y-ibritumomab tiuxetan radioimmunotherapy for relapsed or refractory non-Hodgkin's lymphoma: combined data from 4 clinical trials. J Nucl Med 44:465-74.
195. Garmestani K, Milenic DE, Plascjak PS, Brechbiel MW (2002) A new and convenient method for purification of ^{86}Y using a Sr(II) selective resin and comparison of biodistribution of ^{86}Y and ^{111}In labeled Herceptin. Nucl Med Biol 29:599-606.
196. van Gog FB, Visser GW, Klok R, van der Schors R, Snow GB, van Dongen GA (1996) Monoclonal antibodies labeled with rhenium-186 using the MAG3 chelate: relationship between the number of chelated groups and biodistribution characteristics. The Journal of nuclear medicine 37:352-362.
197. Orlic D, Kajstura J, Chimenti S, Jakoniuk I, Anderson SM, Li B, et al. (2001) Bone marrow cells regenerate infarcted myocardium. Nature 410:701-5.
198. Strauer BE, Brehm M, Zeus T, Kostering M, Hernandez A, Sorg RV, et al. (2002) Repair of infarcted myocardium by autologous intracoronary mononuclear bone marrow cell transplantation in humans. Circulation 106:1913-8.
199. Wang H, Chen X (2008) Imaging mesenchymal stem cell migration and the implications for stem cell-based cancer therapies. Future Oncol 4:623-8.
200. Aicher A, Brenner W, Zuhayra M, Badorff C, Massoudi S, Assmus B, et al. (2003) Assessment of the tissue distribution of transplanted human endothelial progenitor cells by radioactive labeling. Circulation 107:2134-9.
201. Adonai N, Nguyen KN, Walsh J, Iyer M, Toyokuni T, Phelps ME, et al. (2002) Ex vivo cell labeling with ^{64}Cu-pyruvaldehyde-bis(N4-methylthiosemicarbazone) for imaging cell trafficking in mice with positron-emission tomography. Proc Natl Acad Sci U S A 99:3030-5.

202. Ma B, Hankenson KD, Dennis JE, Caplan AI, Goldstein SA, Kilbourn MR (2005) A simple method for stem cell labeling with fluorine 18. Nucl Med Biol 32:701-5.
203. Drevs J, Hofmann I, Hugenschmidt H, Wittig C, Madjar H, Muller M, et al. (2000) Effects of PTK787/ZK 222584, a specific inhibitor of vascular endothelial growth factor receptor tyrosine kinases, on primary tumor, metastasis, vessel density, and blood flow in a murine renal cell carcinoma model. Cancer Res 60:4819-24.
204. Bulte JW, Kraitchman DL (2004) Iron oxide MR contrast agents for molecular and cellular imaging. NMR Biomed 17:484-99.
205. Partlow KC, Chen J, Brant JA, Neubauer AM, Meyerrose TE, Creer MH, et al. (2007) ^{19}F magnetic resonance imaging for stem/progenitor cell tracking with multiple unique perfluorocarbon nanobeacons. Faseb J 21:1647-54.
206. Amado LC, Saliaris AP, Schuleri KH, St John M, Xie JS, Cattaneo S, et al. (2005) Cardiac repair with intramyocardial injection of allogeneic mesenchymal stem cells after myocardial infarction. Proc Natl Acad Sci U S A 102:11474-9.
207. Pearl J, Wu JC (2008) Seeing is believing: tracking cells to determine the effects of cell transplantation. Semin Thorac Cardiovasc Surg 20:102-9.
208. Degano IR, Vilalta M, Bago JR, Matthies AM, Hubbell JA, Dimitriou H, et al. (2008) Bioluminescence imaging of calvarial bone repair using bone marrow and adipose tissue-derived mesenchymal stem cells. Biomaterials 29:427-37.
209. Vilalta M, Degano IR, Bago J, Gould D, Santos M, Garcia-Arranz M, et al. (2008) Biodistribution, long-term survival, and safety of human adipose tissue-derived mesenchymal stem cells transplanted in nude mice by high sensitivity non-invasive bioluminescence imaging. Stem Cells Dev 17:993-1003.
210. Hwang do W, Jang SJ, Kim YH, Kim HJ, Shim IK, Jeong JM, et al. (2008) Real-time in vivo monitoring of viable stem cells implanted on biocompatible scaffolds. Eur J Nucl Med Mol Imaging 35:1887-98.
211. Li Z, Suzuki Y, Huang M, Cao F, Xie X, Connolly AJ, et al. (2008) Comparison of reporter gene and iron particle labeling for tracking fate of human embryonic stem cells and differentiated endothelial cells in living subjects. Stem Cells 26:864-73.
212. Chen IY, Greve JM, Gheysens O, Willmann JK, Rodriguez-Porcel M, Chu P, et al. (2008) Comparison of Optical Bioluminescence Reporter Gene and Superparamagnetic Iron Oxide MR Contrast Agent as Cell Markers for Noninvasive Imaging of Cardiac Cell Transplantation. Mol Imaging Biol
213. Schellens JH, Malingre MM, Kruijtzer CM, Bardelmeijer HA, van Tellingen O, Schinkel AH, et al. (2000) Modulation of oral bioavailability of anticancer drugs: from mouse to man. Eur J Pharm Sci 12:103-10.
214. Nomura T, Tamaoki N, Takakura A, Suemizu H (2008) Basic concept of development and practical application of animal models for human diseases. Curr Top Microbiol Immunol 324:1-24.
215. Cao T, Leroux-Roels G (2000) Antigen-specific T cell responses in human peripheral blood leucocyte (hu-PBL)-mouse chimera conditioned with radiation and an antibody directed against the mouse IL-2 receptor beta-chain. Clin Exp Immunol 122:117-23.
216. Pearson T, Greiner DL, Shultz LD (2008) Humanized SCID mouse models for biomedical research. Curr Top Microbiol Immunol 324:25-51.
217. Pomper MG, Lee JS (2005) Small animal imaging in drug development. Curr Pharm Des 11:3247-72.

Chapter 25
Multimodality Molecular Imaging: A Futuristic Outlook

Habib Zaidi and Abass Alavi

1 Multimodality Imaging: Clinical Perspective

Over the past few decades, there have been significant advances in medical imaging, which have modernized the assessment of a large number of disorders and provided high accuracy. The advent of X-ray CT in 1973 unlocked a new-fangled era in structural imaging, which has improved over the years to further increase the number of clinical applications using this very powerful modality [1]. This technology had a profound impact on clinical practice and proved to be valuable in almost every disorder, predominantly in situations where surgical intervention is required for optimal patient management. Subsequent to the introduction of CT, MRI became the major spotlight owing to its high soft tissue contrast, which enabled the investigation of soft tissue abnormalities, mostly in the central nervous and musculoskeletal systems [2, 3]. For virtually all neurological diseases, MRI has become and still is the preferred modality for detection and accurate characterization of the underlying disorder. Similarly, MRI provided superior value for the characterization of many musculoskeletal abnormalities owing to its high spatial and contrast resolutions that enable improved lesion detectability in this organ system.

Notwithstanding the pivotal role played by these two very powerful structural imaging modalities since their introduction, clinical practice has demonstrated that CT and MRI only depict alterations related to later manifestations of the disease and as such, these techniques are less sensitive for early disorders. It is nowadays evident that changes in cellular metabolism at the molecular level are the early signs

H. Zaidi (✉)
Department of Radiology & Medical Informatics, Geneva University Hospital, Geneva, Switzerland
e-mail: habib.zaidi@hcuge.ch

A. Alavi
Division of Research, Department of Radiology, University of Pennsylvania, Philadelphia, PA, USA
e-mail: abass.alavi@uphs.upenn.edu

H. Zaidi (ed.), *Molecular Imaging of Small Animals: Instrumentation and Applications*,
DOI 10.1007/978-1-4939-0894-3_25,

of disease activity. Therefore, early detection of these alterations may substantiate subtle abnormalities not detectable by structural imaging modalities. It is worth emphasizing that changes at the molecular level may or may not be seen as structural abnormalities and in the former case, this may be delayed for weeks or months after the initiation of the disease process. Similarly, changes occurring following treatment are not perceptible on these images for some time after accomplishment of therapeutic interventions. Given that some therapeutic strategies may not be successful and should be terminated and substituted with alternative treatments, such delays may negatively affect the optimal management of numerous severe diseases such as cancer, cardiac diseases, and central nervous and orthopedic disorders. Consequently, it was realized that improvement upon the limitations of structural imaging modalities was necessary.

Molecular imaging technologies based on the tracer principle [4], such as SPECT and PET, have surmounted many of the shortcomings of structural imaging techniques. For instance, PET, which utilizes positron-emitting tracers, proved to be a very powerful imaging modality providing the exquisite spatial and contrast resolutions needed for early stage disease detection, thus allowing swift implementation of therapeutic interventions. PET also emerged as the molecular imaging modality of choice owing to its capability of providing accurate quantification of disease activity as well as high precision and reproducibility.

The introduction of ^{18}F-Fluorodeoxyglucose (FDG) by investigators at the University of Pennsylvania initiated a new period in medical imaging which has expanded into many areas of study over the past three decades [5]. While the intent of these scientists when introducing this compound was to investigate neuropsychiatric disorders, soon after its introduction it became apparent that FDG is an outstanding marker for evaluating disease activity in cancer. Today FDG-PET is routinely used for managing many kinds of malignancies not only at diagnosis, but also during staging, assessing response to treatment, and detection of recurrence. However, FDG is a nonspecific tracer for detecting cancer since it is also taken up by the inflammatory cells in various settings. This has led the utility of this compound in evaluating infection, inflammation, atherosclerosis, thrombosis and muscle disease [6].

The term hybrid imaging implies acquiring scans with a single imaging instrument that provides two data sets that can be reviewed alone or fused together. During the last two decades, SPECT or PET scanners have been assembled with CT as a hybrid unit enabling a large number of clinical studies to be performed worldwide with the utilization of both modalities. This approach permits the correlation of images produced by both instruments either fused together or side by side for precise localization of molecular abnormalities at various anatomical sites as visualized on CT images. Similarly, PET and MRI images can be fused electronically to pinpoint the position of abnormalities detected on PET on MRI. Different configurations of hybrid PET/MRI systems are since few years commercially available and it is expected that such assemblies will be valuable in many disorders [7–9]. Therefore, it is appropriate to review the use of combined PET, CT and MRI in various clinical and research settings in order to understand their potential role in current and future clinical practice.

Based on what has been learned over the past decade, the impact of hybrid imaging in managing patients in a multitude of disorders has been enormous. This also is applicable to improving the ability of clinical scientists to conduct research in a variety of disorders. A large number of scientific reports have shown that hybrid imaging with either SPECT or PET combined with CT provided valuable information not achievable with either technique alone. In addition, with hybrid imaging, the number of equivocal results is reduced compared to the use of one imaging technique without the other. For decades, physicians have used side-by-side visual interpretation of images generated by different modalities, necessarily obtained at different times. Now, along with the introduction of combined hybrid imaging instruments, major efforts have focused on developing software-based solutions for image registration that allow image fusion of different organs for research as well as clinical purposes. This is of particular value in organs such as the brain where anatomic landmarks allow successful co-registration of structural and functional imaging with submillimetric accuracy. However, the role of such approaches may become less in the future, as hybrid imaging with dedicated instruments becomes widely available. This is particularly true for combined PET/MRI for examining brain, pelvis, head and neck, and musculoskeletal systems.

It must be pointed out that perfect co-registration of functional and structural imaging techniques may not be feasible because of physiologic activities that continue to occur between acquisitions of two sets of images. For example, CT images are obtained within a short period of time for most of the body, whereas PET images require a longer period of time for completion. Therefore, respiratory motion and bowel contractions may prevent perfect registration between the two sets of images. Fortunately, with improvements in software capabilities, the effects of such biologic factors have been minimized recently.

It should also be emphasized that combination of structural and functional images allows more accurate quantification than that achievable with functional imaging alone. The use of structural imaging along with functional techniques made it possible to correct for partial volume effects. Also, increasingly global assessment of disease activity is becoming of great interest to the medical community for cancer and other disorders. By generating partial volume corrected quantitative data and measuring volumes by functional/structural techniques, one can assess global disease burden which allows accurate characterization of disease activity and following the natural course and the effect of treatments at different time points soon after they are initiated.

2 The Promise of Preclinical Multimodality Imaging

Beside the enormous potential of PET as a clinical tool, the technique is also being exploited in biomedical research involving the use of small laboratory animals to visualize and track a number of molecular processes associated with diseases such as cancer, cardiovascular disease and neurological disorders in living small animal

models of human disease. Multimodality small-animal molecular imaging has become increasingly important as transgenic and knockout mice are produced to model human diseases. With the ever increasing number and importance of human disease models, particularly in rodents (mice and rats), the ability of high resolution and high sensitivity multimodality molecular imaging technology to contribute unique information is becoming more common and indispensable. Multimodality imaging offers the capability of combining various modalities and recording either sequentially or simultaneously complementary information gathered from SPECT, PET, CT, MRI, optical, fluorescence, and bioluminescence imaging. Such information proved to be useful in many basic research experiments involving laboratory animals [10].

Recent advances in radiochemistry/radiopharmacy and tracer production technology combined with innovations in molecular/cell biology made it possible to design specific molecular imaging probes enabling to selectively target molecular pathways and to visualize in vivo events in small-animals to investigate disease processes non-invasively [11]. Murine models are now playing a pivotal role in devising contemporary concepts of mammalian biology and human disease, thus enabling large scale studies aiming at evaluating novel diagnostic and therapeutic strategies to be conducted [12, 13]. In addition, manipulation of the genome using transgenic and knock-out techniques is now feasible, making it possible to adapt animal models replicating accurately biological and biochemical processes in humans. The development of tumors in rodents representative of the main types of human cancers is also possible using currently available mouse models. Similarly, the potential role of molecular imaging using small-animals in neuroscience [14] and cardiovascular [15] research is well acknowledged. With the unrestricted possibilities they offer, transgenic and knockout mice are playing a pivotal role in biomedical research, and at the present time, transgenic rodents can be developed to address many basic research questions related to the genetic, molecular, and cellular basis of biology and a variety of diseases [16]. In addition to facilitating the investigation of disease in its natural state, in vivo preclinical imaging assays are employed to guide the discovery and design of new therapeutic strategies of human disease.

During the last two decades much worthwhile research and development efforts were devoted to the development of small-animal imaging instrumentation resulting in the design of highly sophisticated systems with submillimetric spatial resolution and very high sensitivity. Recent advances seem to suggest that with the physical performance of current small-animal imaging units, we are approaching the intrinsic physical performance achievable. This has stimulated the investigation and conceptual design of novel ground-breaking strategies and approaches allowing improved performance at similar or even reduced cost, compared to existing technologies. The use of small-animal molecular imaging instrumentation is expected to continue to grow as more molecular targeted imaging agents are being developed. Today, there are more than 70,880 PUBMED entries when searching for the mesh terms shown in Fig. 25.1. The arguments supporting the need of multimodality imaging in the context of clinical imaging are equally valid for small-animal imaging where the prospective advantages of combining molecular and structural imaging has been well documented [10].

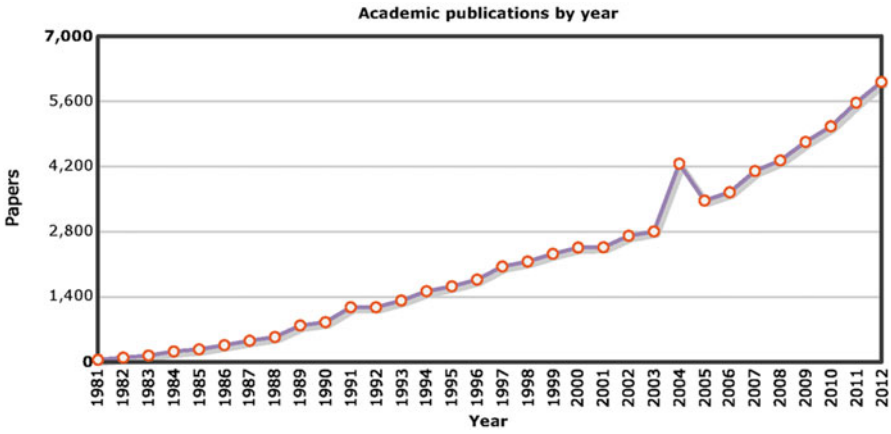

Fig. 25.1 The increasing number of annual peer-reviewed publications reporting on the use of small-animal molecular imaging in preclinical research demonstrates the growing interest in this technology. This graph is based on a PubMed query with using the following mesh terms: "ANIMAL" OR "MOUSE" OR "RAT" AND "POSITRON EMISSION TOMOGRAPHY" OR "SINGLE PHOTON EMISSION COMPUTED TOMOGRAPHY" OR "PET" OR "SPECT". A time line was created with MEDSUM: an online MEDLINE summary tool by Galsworthy, MJ. Hosted by the Institute of Biomedical Informatics (IBMI), Faculty of Medicine, University of Ljubljana, Slovenia (www.medsum.info)

3 Challenges of Multimodality Preclinical Imaging

There are several challenges that face the use of preclinical multimodality imaging in biomedical research beyond those faced in clinical setting and that may represent inherent limitations in these technologies. First, preclinical imaging is commonly performed in experimental laboratories rather than in clinical facilities, thus putting additional requirements in terms of accessibility, user-friendless and running cost. Second, the dedicated small-animal scanner must have excellent performance characteristics including high spatial resolution and high sensitivity required for improved detectability of small lesions and the possibility to acquire data within 1 h during which the rodent can be safely anesthetized. In addition, the high sensitivity enables to decrease the amount of the radiotracer that needs to be injected to the animal, thus reducing the radiation dose which at higher levels can change the model characteristics or cause lethality [17].

Small-animal imaging brings about problematic challenges to design and construct scanners with micron level tolerances and resolution/sensitivity issues are not straightforwardly determined. Much worthwhile research was carried out to address the important challenges that must be overcome in implementing and operating novel and innovative PET design concepts and technologies on the horizon that are under development in academic and corporate settings. Many of these systems are yet to be

implemented to overcome the current challenges for advancing multimodality small-animal imaging technology [18]. An important asset of small-animal compared to clinical instrumentation is the small size of the scanner, which enables new detection modules, promising design concepts and innovative reconstruction strategies to be implemented and evaluated at a reasonable cost (see Chaps. 4–8).

When combining different imaging modalities, there are always trade-offs to be made that can cause undesired complications. For instance, a sequential dual-modality PET/CT scanner requires longer time to acquire both images compared to acquiring data on two scanners in parallel. The additional cost and complexity may generate inconveniences with system operation and funding. The size of the hybrid system may be much bigger than expected. Accurate knowledge of the precise location of the subject within each modality becomes vital for image coregistration, which can be influenced by many physical and instrumentation related factors. Depending on the modalities and energies involved, there may also be significant crosstalk between them, further degrading image quality and quantitative accuracy. For small-animal imaging, the combination of multiple imaging modalities into one gantry seems to be driven by market forces that are not always supported by scientifically sounds arguments and justifications. Nevertheless, it is up to the user to decide what is useful and what should be in the market to satisfy their requirements.

There are many other challenges that need to be addressed on a daily basis in small-animal facilities (see Chap. 18). This includes animal handling to make available a large cohort of various rodent models of human disease, optimal use of anesthesia and heating, providing easy animal access, monitoring of physiological parameters such as heart rate, temperature, respiration or blood pressure, hydration during the course of the study, enabling sub-millimeter reproducible positioning, dealing with the lack of standardized image format standard across modalities (e.g. similar to DICOM used in clinical imaging), and biosafety issues related to the use of immune compromised animals, biohazardous and infectious agents [10]. Most likely the main challenge to multimodality preclinical systems is that adding more options increases the gantry size, further limiting access to the animals. This is a relevant issue, particularly when monitoring the rodent welfare and interventions or when blood sampling is required. Since animal physiology support has become more widely adopted and supported, newer systems were carefully designed to include physiological and video monitoring [19].

4 Summary and Future Directions

In this volume of hot topics on multimodality small-animal molecular imaging, we present some of the most innovative and novel approaches that have been introduced to biomedical research by using state-of-the-art molecular imaging technology ranging from single-modality scanners to systems combining two or three different imaging modalities. Current trends and new horizons in preclinical

multimodality imaging in vivo and their role in biomedical research are described in detail. Future prospects, research trends and challenges are identified and directions for future research are discussed.

Molecular imaging techniques based on the tracer principle using either single-photon or positron-emitting compounds by using SPECT or PET contain limited anatomic information about the location of the body part being examined, which is further enhanced by combining the results with the corresponding structural imaging information available from CT or MRI. Although other approaches are being explored including ultrasound and endoscopic imaging studies, it was decided not to include these latter techniques in this volume. There is still scope for groundbreaking designs of hybrid units combining functional (SPECT, PET) and other imaging modalities (CT, MRI, US, optical) and given the imagination and creativity of currently active research groups, the future of preclinical multimodality imaging is definitely bright.

This is an exciting time for translational molecular imaging. During the last two decades, the number of published papers reporting on the development or use of multimodality small-animal imaging technology has been growing steadily, which motivated the compilation of this volume as a snapshot of this dynamically changing field. The development of small-animal imaging instrumentation has been very rapid and exciting, and there is every reason to believe the field will move forward more rapidly in the near future with the advent of novel technologies and methodologies and the unlimited imagination of active researchers. Despite the remarkable achievements summarized in this volume and other peer-reviewed journals, there is still scope for further research. There is no shortage of challenges and opportunities for small-animal imaging instrumentation and quantitative imaging techniques at the present time. We hope that in this limited space we were able to give the reader a flavor of recent developments in the field and their potential applications in preclinical setting. We found the compilation of this volume to be a rewarding and educational experience and hope that the reader is left with the same experience.

In summary, multimodality small-animal molecular imaging is an area of considerable research interest and many research groups are very active in this field, leading the molecular imaging community to predict a promising progress during the next few years.

Acknowledgment This work was supported by the Swiss National Science Foundation under grant SNSF 31003A-125246.

References

1. G. N. Hounsfield (1979) Nobel lecture: Computed medical imaging. Available at http://www.nobelprize.org/nobel_prizes/medicine/laureates/1979/hounsfield-lecture.pdf
2. P. Mansfield (2003) Nobel lecture: Snap-Shot MRI. Available at http://www.nobelprize.org/nobel_prizes/medicine/laureates/2003/mansfield-lecture.html

3. P. C. Lauterbur (2003) Nobel lecture: All Science is Interdisciplinary—from Magnetic Moments to Molecules to Men. Available at http://www.nobelprize.org/nobel_prizes/medicine/laureates/2003/lauterbur-lecture.html
4. G. C. de Hevesy (1944) Nobel lecture: Some applications of isotopic indicators. Available at http://www.nobelprize.org/nobel_prizes/chemistry/laureates/1943/hevesy-lecture.pdf
5. A. Alavi, M. Reivich (2002) Guest editorial: the conception of FDG-PET imaging. Semin Nucl Med 32:2-5
6. B. Hesse, A. Alavi (2011) Editorial [Hybrid Imaging]. Curr Med Imaging Rev 7: 167-168
7. H. Zaidi, N. Ojha, M. Morich, et al. (2011) Design and performance evaluation of a whole-body Ingenuity TF PET-MRI system. Phys Med Biol 56: 3091-3106
8. G. Delso, S. Furst, B. Jakoby, et al. (2011) Performance measurements of the Siemens mMR integrated whole-body PET/MR scanner. J Nucl Med 52: 1914-1922
9. P. Veit, C. Kuehle, T. Beyer, et al. (2005) Whole-body PET/CT tumour staging with integrated PET/CT- colonography: technical feasibility and first experiences in patients with colorectal cancer. Gut 55: 68-73
10. D. B. Stout, H. Zaidi (2008) Preclinical multimodality imaging in vivo. PET Clin 3: 251-273
11. H. Zaidi, B. Hasegawa: Overview of nuclear medical imaging: physics and instrumentation. In Quantitative analysis in nuclear medicine imaging. H. Zaidi, Ed. Springer, New York, 2006. pp 1-34
12. S. S. Gambhir (2002) Molecular imaging of cancer with positron emission tomography. Nat Rev Cancer 2: 683-693
13. R. Weissleder (2006) Molecular imaging in cancer Science 312: 1168-71
14. A. H. Jacobs, H. Li, A. Winkeler, et al. (2003) PET-based molecular imaging in neuroscience. Eur J Nucl Med Mol Imaging 30: 1051-1065
15. I. Y. Chen, J. C. Wu (2011) Cardiovascular molecular imaging: focus on clinical translation. Circulation 123: 425-443
16. D. Tuveson, D. Hanahan (2011) Translational medicine: Cancer lessons from mice to humans Nature 471: 316-317
17. T. Xie, H. Zaidi (2013) Monte Carlo-based evaluation of S-values in mouse models for positron-emitting radionuclides. Phys Med Biol 58: 169-182
18. C. S. Levin (2012) Promising new photon detection concepts for high-resolution clinical and preclinical PET. J Nucl Med 53: 167-170
19. K. Herrmann, M. Dahlbom, D. Nathanson, et al. (2013) Evaluation of the Genisys4, a bench-top preclinical PET scanner. J Nucl Med 54: 1162-1167